University of Liège - School of Engineering
Department of Aerospace and Mechanical Engineering
Non-Linear Computational Mechanics - MN2L Research Group

Numerical Modeling of Friction in Lubricated Cold Rolling

Dominik Boemer
M. Sc. Eng., Mechanical Engineer
FNRS Research Fellow

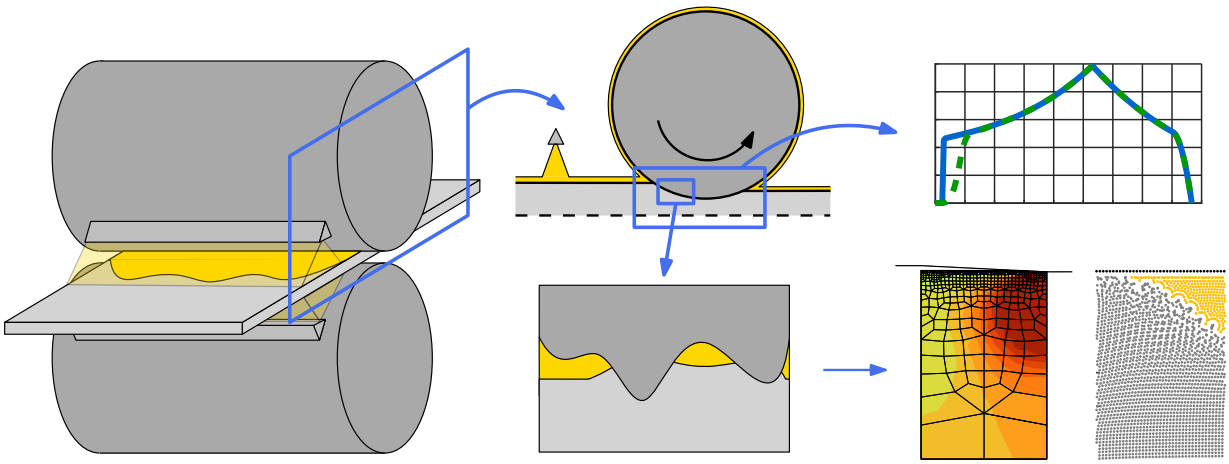

Thesis submitted in partial fulfillment of the requirements
for the Ph.D. Degree in Engineering Sciences and Technology
("Docteur en Sciences de l'Ingénieur et Technologie")

February 2020

First printing, February 2020

Members of the Examination Committee

Prof. Ludovic Noels (President of the Committee)
University of Liège/CM3 (Liège, Belgium)
Email: l.noels@uliege.be

Prof. Jean-Philippe Ponthot (Adviser)
University of Liège/MN2L (Liège, Belgium)
Email: jp.ponthot@uliege.be

Dr. Romain Boman (Adviser)
University of Liège/MN2L (Liège, Belgium)
Email: r.boman@uliege.be

Prof. Diego Celentano
Pontificia Universidad Católica de Chile (Santiago de Chile, Chile)
Email: dcelentano@ing.puc.cl

Prof. Laurent Duchêne
University of Liège/ArGEnCo (Liège, Belgium)
Email: l.duchene@uliege.be

Ir. Maxime Laugier
Lubrication-Tribology R&D Coordinator ArcelorMittal (Maizières-lès-Metz, France)
Email: maxime.laugier@arcelormittal.com

Prof. Pierre Montmitonnet
Mines ParisTech/CEMEF (Paris, France)
Email: pierre.montmitonnet@mines-paristech.fr

Funding

The research described in the present thesis was financially supported by the Fonds de la Recherche Scientifique de Belgique (F.R.S.-FNRS) through an F.R.S.-FNRS Research Fellowship, which is here acknowledged.

Computational resources have been provided by the Consortium des Équipements de Calcul Intensif (CÉCI), funded by the Fonds de la Recherche Scientifique de Belgique (F.R.S.-FNRS) under Grant No. 2.5020.11 and by the Walloon Region.

University of Liège - School of Engineering
Department of Aerospace and Mechanical Engineering

Numerical modeling of friction in lubricated cold rolling

by Dominik BOEMER

Abstract

Thinner and harder steel strips, which are in great demand in the production of lighter car bodies, challenge cold rolling mills like never before. The objective of this thesis is therefore to *accurately model friction in lubricated cold rolling* to ultimately minimize friction while preventing skidding between the rolls and the strip by flexible lubrication, i.e. by adjusting the lubrication conditions in real-time depending on the current rolling conditions.

Accordingly, the *most comprehensive experimental data of lubricated cold rolling* are analyzed to identify the underlying physical mechanisms that have to be included in the rolling model. Furthermore, these data are post-processed to test this model.

By means of the previous data, the *most powerful model of lubricated cold rolling* available so far is completely rederived, documented, and improved while its computer implementation is entirely refactored. This model, which is called METALUB, is a 2D cold rolling model in the mixed lubrication regime with a thermo-elastoviscoplastic description of the strip, a thermo-piezoviscous description of the lubricant, non-circular roll flattening and lubricant starvation. In particular, strain rate hardening and thermal softening are added to the model in addition to improvements regarding its robustness.

METALUB is then tested based on the previous experimental data to evaluate its predictive capabilities and shortcomings. After the first systematic calibration of its numerical parameters, this model allowed to *improve predictions of earlier research by more physically consistent hypotheses*. Nevertheless, the model is still *limited* by unavailable material parameters, the simplicity of its thermal model as well as manual adjustments of the lubricant film thickness and the boundary coefficient of friction, if starvation or micro-plasto-hydrodynamic/static (MPH) lubrication (permeation of the lubricant from microscopic surface pockets into the solid/solid contact zone between asperities) occur, respectively.

Thus, the *first coupling procedure between METALUB and the finite element (FE) solver METAFOR* is developed to replace analytical asperity flattening equations by FE simulations of *lubricated asperity flattening* and to ultimately include MPH lubrication in the model.

Finally, *lubricated asperity flattening is for the first time simulated by the Lagrangian meshless particle method "smoothed particle hydrodynamics"* (SPH) to eliminate mesh-related weaknesses of FE asperity flattening models.

Keywords: friction, lubrication, cold rolling, METALUB, finite element method, smoothed particle hydrodynamics

Acknowledgments

Although this thesis only bears my name, I would like to gratefully acknowledge a number of people who contributed to its completion and who made the journey more enjoyable during the past years.

First and foremost, I would like to express my deepest gratitude to my advisers, *Jean-Philippe Ponthot* and *Romain Boman*.

Prof. Ponthot, thank you for your proposal to write my PhD thesis in your research group, for your immediate availability when questions arose (even during weekends or late at night), for your careful proofreading of my documents and for the freedom to orient my research (especially, when I tried to turn DEM simulations into a real industrial tool). I also want to thank you for organizing holiday dinners and the Feast of Saint Nicolas, which strengthened the team spirit of our research group.

Romain, it is clear that this thesis would also not exist without your help. On the one hand, your strong interest and experience in software development rendered it possible to fully capitalize on earlier research. On the other hand, our weekly meetings gave me an opportunity to confront my ideas with yours to improve them by regular feedback. I also want to thank you for your openness, which allows thoughtful disagreement, and your words of encouragement.

I would like to thank the further members of the examination committee, *Diego Celentano*, *Laurent Duchêne*, *Maxime Laugier*, *Pierre Montmitonnet* and *Ludovic Noels* for the time that they spent reading, reviewing and evaluating this thesis, especially, in consideration of its size. Maxime, thank you for sharing your passion about lubricated cold rolling by inviting me to the ArcelorMittal research center, for the experimental data and for accepting to be a member of the committee despite difficult circumstances.

Among other things, I enjoyed coming to work because of my colleagues in the department of Aerospace and Mechanical Engineering, in particular, those of the MN2L research group and those in my office, *Luc Papeleux*, *Yves Carretta*, *Gaëtan Wautelet*, *Cristian Canales Cárdenas*, *Lina Homsy*, *Goeffrey Deliége*, *Marco Lucio Cerquaglia*, *Yannick Crutzen*, *Pierre Joris*, *Cédric Laruelle*, *Billy-Joe Bobach* and many more. In particular, *Luc*, thank you for taking the time to answer my numerous questions, for sharing your thoughtful opinion about the economy, the environment, society and politics, as well as, for staying at the office with me long after regular working hours. *Yves*, thank you for helping me to build on your research in lubricated cold rolling, especially, by answering my long questions even after you finished working at the university. *Marco*, thank you for introducing me to PFEM when everything started for me in Barcelona during PARTICLES 2015, and for taking the time to confront our opinions about SPH.

Furthermore, I would like to thank *Nicolas Legrand* at ArcelorMittal as well as *Axel Kohlmeyer* and *Steve Plimpton* for answering my questions about cold rolling and LAMMPS, respectively.

Since sharing struggles makes you stronger, I want to gratefully acknowledge some fellow PhD students, who finished their undergraduate studies with me: *Artium Belet*, *Fabian Belleflamme*, *Kevin Bulthuis*, *Joffrey Coheur*, *Adrien Crovato*, *Christophe Dubussy* and *Kim Liégeois*.

Finally, I would like to thank my friends, my parents *Renate* and *Bruno*, my brother *David* and my grandparents for their support during this thesis.

Contents

Nomenclature

In this nomenclature, most of the acronyms and symbols are defined in *alphabetical order* in the following *topic-specific sections*: acronyms, units, mathematics, indexing, continuum mechanics, kinematics, strains, stresses, material parameters, plasticity, thermodynamics, finite element method, smoothed particle hydrodynamics, rolling, tribology, other symbols.

Symbols might exist with a different meaning in different sections but *duplication was minimized as much as possible*. Furthermore, the following rules apply:

- Units: standard text characters, like m, kg, s, ...
- Scalars: italic characters, like x, ρ, i, ...
- Vectors (first-order tensors): bold lower case or bold greek characters, like $\mathbf{x}$, $\boldsymbol{\phi}$, $\mathbf{v}$, ...
- Tensors (second-order tensors): bold upper case or bold greek characters, like $\mathbf{F}$, $\boldsymbol{\sigma}$, $\mathbf{W}$, ...

The scalar components of a tensor in a Cartesian coordinate system are denoted by the same symbol, which is not written in bold. For instance, the components of the Cauchy stress tensor $\boldsymbol{\sigma}$ are σ_{ij}, or in their expanded version

$$\begin{bmatrix} \sigma_{xx} & \sigma_{xy} & \sigma_{xz} \\ \sigma_{yx} & \sigma_{yy} & \sigma_{yz} \\ \sigma_{zx} & \sigma_{zy} & \sigma_{zz} \end{bmatrix}$$

The main diagonal terms or eigenvalues of a tensor are written by dropping the second index. In the previous example,

$$\sigma_x, \sigma_y, \sigma_z$$

Acronyms

Acronym	Meaning
AHSS	Advanced high-strength steel
ALE	Arbitrary Lagrangian Eulerian
CFD	Computational fluid dynamics
CIEFS	Couplage itératif et étagé fluid structure (iterative and staggered fluid structure coupling) solver by Stephany [305]
CPU	Central processing unit (processor)
ESPH	Eulerian smoothed particle hydrodynamics
FE	Finite element
FEM	Finite element method
FSI	Fluid-structure interaction
L1, L2, L3	Lubricant 1, 2 or 3 of the experimental campaign at Maizières-lès-Metz
LAMMPS	Large-scale Atomic/Molecular Massively Parallel Simulator
METAFOR	Metal forming; non-linear finite element solver for large deformations
METALUB	Metal lubrication; cold rolling model in the mixed lubrication regime
MN2L	Numerical non-linear mechanics (Mécanique numérique non-linéaire)
MPH	Micro-plasto-hydrodynamic/static
MPHDL	Micro-plasto-hydrodynamic lubrication
MPHSL	Micro-plasto-hydrostatic lubrication
MPM	Material point method
O/W	Oil-in-water (emulsion)
PFEM	Particle finite element method
RMS	Root-mean-square
S1, S2, S3	Rolled product (strip) 1, 2 or 3 of the experimental campaign at Maizières-lès-Metz
SPH	Smoothed particle hydrodynamics
TLSPH	Total Lagrangian smoothed particle hydrodynamics
ULSPH	Updated Lagrangian smoothed particle hydrodynamics
USER-SMD	USER Smooth Mach Dynamics SPH package in LAMMPS
TRIP	Transformation induced plasticity
WLF	Williams-Landel-Ferry viscosity law
W&S	Wilson and Sheu (asperity flattening equation)
WCSPH	Weakly compressible smoothed particle hydrodynamics

Units

Symbol	Meaning
bar	Bar (1 bar = 10^5 Pa)
°	Degree (angle)
°C	Degree Celsius
h	Hour
Hz	Hertz
kg	Kilogram
kgf	Kilogram-force
l	Liter
m	Meter
min	Minute
N	Newton
P	Poiseuille
Pa	Pascal
rad	Radian
s	Second
t	Tonne (metric ton)
W	Watt

Mathematics

Symbol	Meaning
$\lvert(\cdot)\rvert$	Absolute value function
$\times$	Cross product
$\mathrm{cov}(X, Y)$	Covariance of the random variables X and Y
$\delta(\cdot)$	Dirac delta function
δ_{ij}	Kronecker delta
$\dot{(\cdot)}$	Total time derivative
$\ddot{(\cdot)}$	Second total time derivative
$\frac{\partial(\cdot)}{\partial(\cdot\cdot)}$	Partial derivative
$\frac{\mathrm{d}(\cdot)}{\mathrm{d}(\cdot\cdot)}$	Total derivative
$\det(\cdot)$	Determinant
$\mathrm{dev}(\cdot)$	Deviator
$\cdot$	Dot product, e.g. $\mathbf{a} \cdot \mathbf{b} = a_i b_i$, $(\mathbf{A} \cdot \mathbf{b})_i = A_{ij} b_j$

$:$	Double dot product ($\mathbf{A} : \mathbf{B} = A_{ij}B_{ji}$)
$\emptyset$	Empty set
$\mathbf{E}(\cdot)$	Expected value
$f(\cdot)$	Scalar function
$\mathbf{f}(\cdot)$	Vector-valued function
$\mathbf{I}$	Identity matrix
$\int (\cdot)\ \mathrm{d}(\cdot\cdot)$	Integral
$(\cdot)^{-1}$	Inverse of a matrix
$\log_{10}(\cdot)$	Logarithm with base 10
$\ln(\cdot)$	Natural logarithm
$\max(\cdot)$	Maximum
$\min(\cdot)$	Minimum
$\nabla(\cdot)$	Gradient
$\nabla \cdot (\cdot)$	Divergence
$\mathcal{O}(\cdot)$	Bachmann–Landau notation
$\otimes$	Dyadic product
$\Pr[(\cdot)]$	Probability
$\mathbb{R}^3$	Real coordinate space of 3 dimensions
$\mathrm{sign}(\cdot)$	Sign function
$\mathrm{tr}(\cdot)$	Trace
$(\cdot)^T$	Transpose of a matrix
$(\cdot)^{-T}$	Transpose of an inverse of a matrix

Indexing

Symbol	Meaning	Units
$i, j, k, \ldots$	Indices of tensor components (with Einstein notation)	-
$a, b, c, \ldots$	Indices of interacting particles in SPH (without Einstein notation)	-

Continuum mechanics

Symbol	Meaning	Units
$\delta\mathcal{M}$	Virtual work done by inertia forces	J
$\delta\mathbf{u}(\mathbf{x})$	Virtual displacement	m
$\delta\mathcal{W}_{\text{ext}}$	Virtual work done by external forces	J

$\delta\mathcal{W}_{\text{int}}$	Virtual work done by internal forces	J
$\mathbf{e}_i$	Unit vectors of a coordinate system	-
$\mathbf{E}_A$	Unit vectors of a coordinate system in the reference configuration	-
$\mathbb{H}$	Hooke tensor	Pa
$\mathbb{M}$	Material tensor	Pa
$\mathbf{n}$	Unit normal to a surface	-
$\mathbf{n}_0$	Unit normal to a surface in the reference configuration	-
$\boldsymbol{\phi}(\cdot)$	Mapping function	m
$\mathbb{S}$	Set of surface points of a continuum	-
$\mathbb{S}_\sigma$	Set of surface points of a continuum, to which forces are applied	-
$\mathbb{S}_u$	Set of surface points of a continuum with imposed displacements	-
$\mathbb{V}$	Continuum space in the current configuration or its volume	m^3
$\mathbb{V}_0$	Continuum space in the reference configuration or its volume	m^3

Kinematics

Symbol	**Meaning**	**Units**
x_i	Components of the position vector	m
$\mathbf{x}$	Position vector	m
X_A	Components of the position vector in the reference configuration	m
$\mathbf{X}$	Position vector in the reference configuration	m
u_i	Components of the displacement vector	m
$\mathbf{u}$	Displacement vector	m
v_i	Components of the velocity vector	m/s
$\overline{v}_i$	Non-dimensional components of the velocity vector	-
$\mathbf{v}$	Velocity vector	m/s
a_i	Components of the acceleration vector	m/s^2
$\mathbf{a}$	Acceleration vector	m/s^2

Strains

Symbol	Meaning	Units
$\mathbf{D}$	Strain rate tensor	s^{-1}
$\mathbf{D}^d$	Deviatoric strain rate tensor	s^{-1}
$\mathbf{D}^e$	Elastic strain rate tensor	s^{-1}
$\mathbf{D}^p$	Plastic strain rate tensor	s^{-1}
$\overline{D}^p$	Effective plastic strain rate	s^{-1}
$\boldsymbol{\epsilon}$	Strain tensor	-
$\boldsymbol{\epsilon}^e$	Elastic strain tensor	-
$\overline{\epsilon}$	Effective strain	-
$\overline{\epsilon}^p$	Effective plastic strain	-
$\mathbf{E}^N$	Natural or logarithmic strain tensor	-
$\mathbf{F}$	Deformation gradient tensor	-
J	Jacobian determinant or jacobian	-
$\mathbf{L}$	Velocity gradient tensor	s^{-1}
$\mathbf{R}$	Rotation tensor	-
$\mathbf{U}$	Right stretch tensor	-
$\mathbf{W}$	Spin tensor	s^{-1}

Stresses

Symbol	Meaning	Units
$\mathbf{b}$	Applied force per unit mass vector	$m.s^{-2}$
J_2	Second invariant of the deviatoric stress tensor	Pa^2
p	Mechanical pressure or simply pressure ($p > 0$, in compression)	Pa
p_{th}	Thermodynamic pressure	Pa
$\overline{p}_{\text{th}}$	Non-dimensional thermodynamic pressure	-
$\mathbf{P}$	First Piola-Kirchhoff stress tensor	Pa
σ_{hyd}	Hydrostatic stress	Pa
σ_{VM}	Equivalent/effective Von Mises stress	Pa
$\boldsymbol{\sigma}$	Cauchy stress tensor, true stress	Pa
$\mathbf{s}$	Deviatoric Cauchy stress tensor	Pa
$\mathbf{t}$	Surface traction or stress vector	Pa
$\mathbf{t}_0$	Stress vector in the reference configuration	Pa

Material parameters

Symbol	Meaning	Units
α_s	Thermal diffusivity	m^2/s
A	Material constant in the Ludwik or Smatch hardening law	Pa
A_1	Material constant in the extended WLF model	°C
A_2	Material constant in the extended WLF model	Pa^{-1}
β_l	Percentage of the friction energy that is transformed into thermal energy of the lubricant	-
β_s	Taylor-Quinney coefficient of the strip	-
b_1	Material constant in the extended WLF model	Pa^{-1}
b_2	Material constant in the extended WLF model	-
B	Material constant in the Ludwik or Smatch hardening law	Pa
B_1	Material constant in the extended WLF model	-
B_2	Material constant in the extended WLF model	Pa^{-1}
c	Speed of sound	m/s
c_l	Specific heat capacity of the lubricant	J/(kg.°C)
c_s	Specific heat capacity of the strip	J/(kg.°C)
C	Material constant in the Krupkowski or Smatch hardening law	-
C_1	Material constant in the extended WLF model	-
C_2	Material constant in the extended WLF model	°C
D	Material constant in the Smatch hardening law	-
$\overline{D}_0^p$	Reference value of the effective plastic strain rate in the viscoplastic hardening law	s^{-1}
$\overline{\epsilon}_0^p$	Initial effective plastic strain of the strip	-
η	Dynamic viscosity	Pa.s
η^*	Average dynamic viscosity	Pa.s
η_0	Dynamic viscosity in the reference state	Pa.s
η_g	Material constant in the extended WLF model, dynamic viscosity at glass transition	Pa.s
η_s	Viscoplasticity coefficient in the viscoplastic hardening law	-
$\overline{\eta}$	Non-dimensional dynamic viscosity	-
E	Material constant in the Smatch hardening law	Pa
E_r	Young's modulus of the roll	Pa
E_s	Young's modulus of the strip	Pa
F	Intermediate variables in the extended WLF model	-
γ_l	Barus pressure-viscosity coefficient	Pa^{-1}

G	Shear modulus	Pa
G_s	Shear modulus of the strip	Pa
h_i	Isotropic hardening coefficient	Pa
$h_{i,s}$	Isotropic hardening coefficient of the strip	Pa
H	Hardness	Pa
K	Bulk modulus	Pa
K_l	Bulk modulus of the lubricant	Pa
K_s	Bulk modulus of the strip	Pa
m	Material constant in the thermoplastic hardening law	-
ν	Poisson's ratio	-
ν_r	Poisson's ratio of the roll	-
ν_s	Poisson's ratio of the strip	-
n	Exponent in the Krupkowski or Ludwik hardening law	-
p_r	Material constant in the Roelands equation	Pa
ρ	Density	kg/m^3
ρ^*	Average density	kg/m^3
ρ_0	Density in the reference state	kg/m^3
ρ_l	Density of the lubricant	kg/m^3
ρ_s	Density of the strip	kg/m^3
$\overline{\rho}$	Non-dimensional density	-
σ_Y^*	Conventional yield stress, i.e. without the viscoplastic component	Pa
σ_Y	Yield stress (extended, i.e. including the viscoplastic component)	Pa
σ_Y^0	Initial yield stress	Pa
S_0	Temperature index of the viscosity in the Roelands equation	-
τ_Y	Shear yield stress	Pa
$\tau_{Y,a}$	Shear strength of the solid interface (asperities)	Pa
T_0	Reference temperature in the Roelands equation or the thermoplastic hardening law	°C
T_g	Glass transition temperature	°C
T_m	Melting temperature in the thermoplastic hardening law	°C
ζ	Second viscosity parameter	Pa.s
ζ^*	Average second viscosity parameter	Pa.s
$\overline{\zeta}$	Non-dimensional second viscosity parameter	-
z_{p_l}	Pressure index of the viscosity in the Roelands equation	-

Plasticity

Symbol	Meaning	Units
$f_Y(\cdot)$	Yield function	Pa^2
Γ	Integral of the flow intensity over a time step	-
$g(\cdot)$	Plastic flow potential	Pa^2
λ	Flow intensity	s^{-1}
N_{ij}	Components of the unit normal to the plastic flow potential	-
$\mathbf{N}$	Unit normal to the plastic flow potential	-
$\mathbf{p}$	Internal material parameters	-
Υ	Plastic multiplier	$Pa^{-1}.s^{-1}$

Thermodynamics

Symbol	Meaning	Units
e	Internal energy per unit mass	J/kg
Pe	Péclet number	-
$\mathbf{q}$	Heat flux	W/m^2
s	Heat source per unit time and per unit mass	W/kg

Finite element method

Symbol	Meaning	Units
α_F, α_M	Numerical parameters of the generalized α-method	-
β, β_0	Numerical parameters of the Newmark algorithm	-
$\mathbf{B}$	Strain-displacement matrix	m^{-1}
γ, γ_0	Numerical parameters of the Newmark algorithm	-
g_n	Normal gap	m
g_t	Tangential gap	m
i	Mechanical iteration index	-
I, J	Indices of nodes	-
$\mathbf{J}$	Jacobian matrix of motion	-
k_n	Normal penalty coefficient	Pa/m
k_t	Tangential penalty coefficient	Pa/m
$\mathbf{E}_{n,n+1}$	Incremental natural strain matrix from time step n to time step $n+1$	-

$\mathbf{F}_{\text{ext}}$	External force vector	N
$\mathbf{F}_{\text{inert}}$	Inertial force vector	N
$\mathbf{F}_{\text{int}}$	Internal force vector	N
$\mathbf{F}_{n,n+1}$	Incremental deformation gradient matrix from time step n to time step $n+1$	-
$\mathbf{M}$	Mass matrix	kg
n	Time step index	-
N^I	Shape function of node I	-
$\mathbf{R}_{n,n+1}$	Incremental rotation matrix from time step n to time step $n+1$	-
$\mathbf{S}$	Tangent jacobian matrix	N/m
$\text{tol}_{\Delta\mathbf{F}}$	Tolerance of the mechanical iterations	-
$\mathbf{x}^I$	Position vector of node I	m
$\boldsymbol{\zeta}$	Position vector in the parent space of the shape functions	m

Smoothed particle hydrodynamics

Symbol	Meaning	Units
$\langle\cdot\rangle^k$	Kernel approximation	-
$\langle\cdot\rangle^{kp}$	Kernel and particle approximation	-
α	Parameter of the artificial Monaghan-type bulk viscosity	-
α_d	Kernel normalization factor in dimension d	-
$\mathbf{b}_a$	Applied force per unit mass to the particle a	m.s^{-2}
β_c	Contact scale factor	-
β_t	Time step factor	-
c_a	Speed of sound at the particle a	m/s
$\mathbf{D}_a$	Strain rate tensor at the particle a	s^{-1}
Δt^c_{cr}	Critical time step due to the contact formulation	s
$\Delta t^{\text{SPH}}_{\text{cr}}$	Critical time step in SPH due to the CFL condition	s
$\overline{\epsilon}^p_a$	Effective plastic strain at the particle a	-
E^*	Effective contact stiffness	Pa
$\mathcal{E}_{ab}$	Error vector due to zero-energy modes	m
$\mathbf{f}_a$	Total force applied to the particle a	N
$\mathbf{f}_{ab}$	Total force applied to the particle a by the particle b	N
$\mathbf{f}^c_{ab}$	Contact force applied to the particle a by the particle b	N
$\mathbf{f}^{\text{HG}}_{ab}$	Force to suppress zero-energy modes, which is applied to the particle a by the particle b	N

$\mathbf{f}_{ab}^{\mathrm{HG},e}$	Penalty force to suppress zero-energy modes in elastic deformations, which is applied to the particle a by the particle b	N
$\mathbf{f}_{ab}^{\mathrm{HG},v}$	Artificial viscous force to suppress zero-energy modes in plastic deformations, which is applied to the particle a by the particle b	N
$\mathbf{f}_{a}^{\mathrm{int}}$	Internal force applied to the particle a	N
$\mathbf{f}_{ab}^{\mathrm{int}}$	Internal force applied to the particle a by the particle b	N
$\mathbf{F}_a$	Deformation gradient tensor at the particle a	-
$\dot{\mathbf{F}}_a$	Rate-of-deformation gradient tensor at the particle a	s^{-1}
h	Smoothing length	m
J_a	Jacobian determinant or jacobian at the particle a	-
K_a	Effective bulk modulus at the particle a	Pa
$\mathbf{K}_a$	Shape matrix of the particle a in the current configuration	-
$\mathbf{K}_{0,a}$	Shape matrix of the particle a in the reference configuration	-
l_0	Particle spacing, i.e. the distance between neighboring nodes of a square lattice along its principal directions	m
$\mathbf{L}_a$	Velocity gradient tensor at the particle a	s^{-1}
m_a	Particle mass of the particle a	kg
n_p	Total number of particles	-
n_t	Total number of time steps	-
Π_{ab}	Artificial Monaghan-type bulk viscosity term applied to the particle a by the particle b	$\mathrm{m}^5.\mathrm{kg}^{-1}.\mathrm{s}^{-2}$
p_a	Pressure at the particle a	Pa
$\mathbf{P}_a$	First Piola-Kirchhoff stress tensor at the particle a	Pa
R_a	Contact radius of the particle a	m
$\mathbf{R}_a$	Rotation tensor at the particle a	-
ρ_a	Density at the particle a in the current configuration	$\mathrm{kg/m}^3$
ρ_a^0	Density at the particle a in the reference configuration	$\mathrm{kg/m}^3$
s	Skin distance	m
$\mathbf{s}_a$	Deviatoric Cauchy stress tensor at the particle a	Pa
$\mathcal{S}_a$	Support domain of the kernel function of the particle a in the current configuration	-
$\mathcal{S}_a^0$	Support domain of the kernel function of the particle a in the reference configuration	-
$\sigma_{Y,a}$	Yield stress at the particle a	Pa
$\boldsymbol{\sigma}_a$	Cauchy stress tensor at the particle a	Pa
$\mathbf{u}_a$	Displacement of the particle a	m
$\mathbf{U}_a$	Right stretch tensor at the particle a	-

$\mathbf{v}_a$	Velocity vector of the particle a	m/s
V_a	Particle volume of the particle a in the current configuration	m^2 or m^3
V_a^0	Particle volume of the particle a in the reference configuration	m^2 or m^3
$W(\cdot)$	Kernel function	m^{-2} or m^{-3}
$\mathbf{x}_a$	Position vector of the particle a in the current configuration	m
$\mathbf{x}_{ab}$	Position vector from the particle a to the particle b in the current configuration, i.e. $\mathbf{x}_b - \mathbf{x}_a$	m
$\mathbf{X}_a$	Position vector of the particle a in the reference configuration	m
$\mathbf{X}_{ab}$	Position vector from the particle a to the particle b in the reference configuration, i.e. $\mathbf{X}_b - \mathbf{X}_a$	m
ξ	Parameter of the anti-hourglass or zero-energy mode suppression algorithm	-
ζ	Kernel dependent scaling factor	-

Rolling

Symbol	Meaning	Units
α	Angle between the roll and the strip at the entry of the roll bite	°
e_x	Elongation of the strip	-
$\mathbf{e}_x, \mathbf{e}_y, \mathbf{e}_z$	Unit vectors of the coordinate system in cold rolling with $\mathbf{e}_z$ being vertical (Fig. 4.2)	-
$\mathbf{e}_\xi, \mathbf{e}_\eta, \mathbf{e}_\zeta$	Unit vectors of the coordinate system in cold rolling with $\mathbf{e}_\zeta$ being orthogonal to the contact interface between the roll and the strip (Fig. 4.2)	-
F_r	Rolling force	N
$\overline{F}_r$	Rolling force per width of the strip	N/m
JIF$(\cdot)$	Jortner influence function	-
l	Distance between two material points of the strip along the rolling direction	m
l_{in}	Distance between two material points of the strip along the rolling direction before passing between the rolls	m
l_{out}	Distance between two material points of the strip along the rolling direction after passing between the rolls	m
l_{rb}	Length of the roll bite	m
$l_{x,l}$	Out-of-plane length of the lubricant portion	m
$l_{x,s}$	Out-of-plane length of the strip portion	m

L_{in}	Back tension load	kgf
L_{out}	Front tension load	kgf
L_r	Rolling load	t
$\overline{L}_r$	Rolling load per width of the strip	t/m
$\text{MIF}_{r,p}$, $\text{MIF}_{r,\tau}$, $\text{MIF}_{\theta,p}$, $\text{MIF}_{\theta,\tau}$	Meindl influence functions to compute the radial (r) and tangential (θ) deformations of the roll due to pressure (p) and shear stress (τ)	-
M_r	Rolling torque (norm)	Nm
$M_{r,b}$	Rolling torque of the bottom roll	Nm
$M_{r,t}$	Rolling torque of the top roll	Nm
$\overline{M}_r$	Rolling torque per width (of the strip)	N
$\mathbf{M}_r$	Rolling torque vector	Nm
$\overline{\mathbf{M}}_r$	Rolling torque vector per width (of the strip)	N
ω_r	Angular rotation speed of the roll	rad/s
r	Thickness reduction ratio	-
R	Deformed roll radius	m
R_0	Undeformed roll radius	m
σ_{in}	Back tension (at the entry of the roll bite)	Pa
σ_{out}	Front tension (at the exit of the roll bite)	Pa
s_f	Forward slip, i.e. the relative exit speed of the strip with respect to the rolling speed	-
θ	Angular coordinate of the roll	rad
t_{in}	Thickness of the strip at the entry of the roll bite, i.e. its initial thickness	m
t_{out}	Thickness of the strip at the exit of the roll bite, i.e. its final thickness	m
t_s	Local thickness of the strip	m
T_{in}	Temperature of the strip at the entry of the roll bite	°C
T_{out}	Temperature of the strip at the exit of the roll bite	°C
T_s	Local temperature of the strip	°C
$T_{s,\text{in}}$	Temperature of the strip at the entry of the bite	°C
$\overline{T}$	Average temperature in the roll bite	°C
u_θ	Tangential displacement of the roll profile due to flattening	m
u_r	Radial displacement of the roll profile due to flattening	m
v_{in}	Speed of the strip at the entry of the roll bite (inlet)	m/s
v_{out}	Speed of the strip at the exit of the roll bite (outlet)	m/s
v_r	Rolling speed, i.e. the linear velocity of the roll at its periphery along the rolling direction	m/s

$v_{r,b}$	Rolling speed of the bottom roll	m/s
$v_{r,t}$	Rolling speed of the top roll	m/s
v_s	Strip speed, i.e. the linear velocity of the strip along the rolling direction	m/s
w	Width of the strip	m
x	Coordinate along the rolling direction	m
x_{im}	Position of the transition to the mixed inlet zone	m
x_{in}	Position of the entry of the roll bite, where the first contact occurs between the rolls and the strip	m
x_{iw}	Position of the transition to the work zone	m
x_{omhs}	Position of the transition to the (mixed) high-speed outlet zone	m
x_{omls}	Position of the transition to the (mixed) low-speed outlet zone	m
x_{out}	Position of the end of the roll bite, where the contact between the roll and the strip ends	m
x_r	Position of the roll profile along the rolling direction	m
x_{wmhs}	Position of the transition to the (mixed) high-speed work zone	m
x_{wmls}	Position of the transition to the (mixed) low-speed work zone	m
y	Coordinate along the transverse direction, i.e. perpendicular to the rolling direction (in the horizontal plane)	m
z	Coordinate along the vertical axis pointing upwards	m
z_0	Vertical z-coordinate of the center of the roll with respect to the neutral plane of the strip	m
$z_r(x)$	Macroscopic profile of the roll along the rolling direction	m
$z_r(y)$	Microscopic roughness profile of the roll along the transverse direction	m
$z_s(y)$	Microscopic roughness profile of the strip along the transverse direction	m

Tribology

Symbol	Meaning	Units
A	Fractional/relative area of contact, also known as contact ratio	-
A_a	Apparent area of contact	m^2
A_r	Real area of contact	m^2

d_a	Limiting depth of the local deformation field due to indentation	m
ϵ	Non-dimensional small number or film thickness below which the continuum hypothesis is not valid anymore	-/m
E_p	Non-dimensional plastic strain rate	-
f_1, f_2	Intermediate variable in the asperity flattening equation by Wilson and Sheu	-
$f_Z(\cdot)$	Height distribution function, i.e. the probability density function of Z	-
$f_Z^*(\cdot)$	Height distribution function, i.e. the probability density function of Z after asperity flattening	-
F_n	Normal force (norm) to a surface	N
F_t	Tangential force (norm) to a surface	N
$\mathbf{F}_a$	Contribution of the contact force supported by solid/solid (asperity) contact	N
$\mathbf{F}_i$	Interface contact force	N
$\mathbf{F}_l$	Contribution of the contact force supported by the lubricant	N
γ	Peklenik surface pattern parameter	-
γ_r	Peklenik surface pattern parameter of the roll surface	-
γ_s	Peklenik surface pattern parameter of the strip surface	-
h	Signed distance from the non-updated mean line of the strip roughness to the non-updated mean line of the roll roughness, also known as the nominal lubricant film thickness	m
h_l	Local lubricant film thickness, i.e. the distance between the surface asperities of two surfaces	m
$h_{l,\mathrm{iw}}$	Lubricant film thickness at the transition from the inlet to the work zone, i.e. where the strip starts to deform plastically	m
h_L	Lubricant film thickness provided by the lubrication system	m
H_0	Thickness of the substrate in the FE/SPH micro-model of asperity flattening	m
h_t	Distance between the updated mean line of the strip roughness and the updated mean line of the roll roughness, also known as the mean lubricant film thickness	m
$h_{t,c}$	Critical value of the mean lubricant film thickness h_t corresponding to the percolation threshold	m
$h_{t,\mathrm{in}}$	Lubricant film thickness at the entry of the roll bite	m
h_u	Signed distance from the non-updated mean line of the strip roughness to its updated mean line	m
h_v	Mean film thickness in the valleys	m

H	Non-dimensional nominal lubricant film thickness	-
H_a	Non-dimensional effective hardness	-
H_t	Non-dimensional mean lubricant film thickness	-
$\lambda_{0.5x}$	Length at which the autocorrelation function of the roughness height profile along $\mathbf{e}_x$ reduces to 50% of its initial value	m
$\lambda_{0.5y}$	Length at which the autocorrelation function of the roughness height profile along $\mathbf{e}_y$ reduces to 50% of its initial value	m
$\overline{l}$	Half spacing between asperities along the transverse direction, i.e. the direction orthogonal to the rolling direction in the horizontal plane	m
L	Length of an asperity profile	m
L_{xy}	Characteristic length scale in the xy-plane	m
L_z	Characteristic length scale in the z direction	m
μ	Local coefficient of friction	-
μ_C	Coulomb coefficient of friction in the solid/solid contact zone	-
μ_T	Tresca coefficient of friction also known as the friction factor, i.e. the shear strength of the solid interface with respect to the shear yield stress of the underlying bulk material, in the solid/solid contact zone	-
$\overline{\mu}$	Equivalent coefficient of friction in the roll bite	-
N	Number of discrete measuring points of an asperity profile	-
N_a	Normal component of the solid/solid (asperity) contact force with respect to the contact interface	N
N_i	Normal component of the interface contact force with respect to the contact interface	N
N_l	Normal lubricant contact force with respect to the contact interface	N
ϕ_f	First shear stress factor	-
ϕ_{fs}	Second shear stress factor	-
ϕ_{fp}	Third shear stress factor	-
ϕ_s	Shear flow factor of the contacting surfaces	-
ϕ_x	Pressure flow factor along $\mathbf{e}_x$	-
ϕ_y	Pressure flow factor along $\mathbf{e}_y$	-
Φ_s	Shear flow factor of a single surface	-
p_a	Asperity contact pressure, i.e. contact pressure in the solid/-solid contact region	Pa

p_i	Interface pressure	Pa
p_l	Lubricant pressure	Pa
$p_{l,d}$	Hydrodynamic contribution of the lubricant pressure	Pa
$p_{l,s}$	Hydrostatic contribution of the lubricant pressure	Pa
q'_x, q'_y	Volume flow rates per unit width in the directions $\mathbf{e}_x$ and $\mathbf{e}_y$	m^2/s
$\overline{q}'_x, \overline{q}'_y$	Average volume flow rates per unit width in the directions $\mathbf{e}_x$ and $\mathbf{e}_y$	m^2/s
Q	Volumetric flow rate per width	m^2/s
R_a	Arithmetical average roughness	m
$R_{a,r}$	Arithmetical average roughness of the roll(s)	m
$R_{a,r,b}$	Arithmetical average roughness of the bottom roll	m
$R_{a,r,t}$	Arithmetical average roughness of the top roll	m
R_ϵ	Reduced Reynolds number	-
Re	Reynolds number	-
$R_{\max}$	Maximum peak to valley height	m
R_p	Maximum peak height with respect to the mean line	m
R_{pc}	Peak count, i.e. number of peaks per unit length	peaks/m
$R_{pc,r,b}$	Peak count, i.e. number of peaks per unit length, of the bottom roll	peaks/m
$R_{pc,r,t}$	Peak count, i.e. number of peaks per unit length, of the top roll	peaks/m
R_q	(Composite) root-mean-square roughness	m
R_q (C)	(Composite) root-mean-square roughness computed with the assumption that the roughness profile follows a Christensen height distribution	m
R_q (T)	(Composite) root-mean-square roughness computed with the assumption that the roughness profile is triangular	m
$R_{q,r}$	Root-mean-square roughness of the roll	m
$R_{q,r}$ (C)	Root-mean-square roughness of the roll computed with the assumption that the roughness profile follows a Christensen height distribution	m
$R_{q,r}$ (T)	Root-mean-square roughness of the roll computed with the assumption that the roughness profile is triangular	m
$R_{q,s}$	Root-mean-square roughness of the strip	m
$R_{q,s}$ (C)	Root-mean-square roughness of the strip computed with the assumption that the roughness profile follows a Christensen height distribution	m
$R_{q,s}$ (T)	Root-mean-square roughness of the strip computed with the assumption that the roughness profile is triangular	m

R_{sk}	Skewness of a roughness profile	-
R_t	Total height of a roughness profile	m
R_z	Average peak to valley height of a roughness profile	m
τ_a	Shear stress between surface asperities, i.e. shear stress in the solid contact region	Pa
τ_i	Interface shear stress	Pa
τ_l	Lubricant shear stress	Pa
T_a	Tangential component of the solid/solid (asperity) contact force with respect to the contact interface	N
T_i	Tangential component of the interface contact force with respect to the contact interface	N
T_l	Tangential lubricant contact force with respect to the contact interface	N
T_l	Lubricant temperature	°C
T_l^*	User-specified lubricant temperature	°C
U_{xy}	Characteristic velocity in the xy-plane	m/s
v_a	Downward indentation speed	m/s
v_b	Upward speed of the free surface	m/s
W_s	Velocity along z of the strip	m/s
W_r	Velocity along z of the roll	m/s
$\overline{x}$	Non-dimensional x coordinate	-
y_i	Horizontal coordinate of an asperity profile at a discrete measurement point i	m
$\overline{y}$	Non-dimensional y coordinate	-
z	Asperity profile height/coordinate	m
z_a, z_b	Specific heights of a surface	m
z_i	Asperity profile height at a discrete measurement point i	m
z_m	Vertical coordinate of the mean line	m
$z_{\max}$	Maximum roughness height with respect to the mean line	m
$z_{\min}$	Minimum roughness height with respect to the mean line	m
$\overline{z}$	Non-dimensional z coordinate	-
Z	Random variable representing the height (roughness) of a surface	m
Z_r	Random variable representing the height (roughness) of the roll surface	m
Z_s	Random variable representing the height (roughness) of the strip surface	m

Other symbols

Symbol	Meaning	Units
$\Delta\overline{F}_r$	Relative numerical error of the prediction of the rolling force per width with respect to the most accurate prediction	-
Δs_f	Relative numerical error of the prediction of the forward slip with respect to the most accurate prediction	-
$\Delta\theta_1, \Delta\theta_2, \Delta\theta_3$	Angular discretization steps of the roll in Jortner's and Meindl's methods	°
Δt	Time step	s
Δt_0	Initial time step	s
$\Delta t_{\max}$	Maximum time step	s
Δx	Spatial integration step	m
Δx_1	Big spatial integration step outside the roll bite	m
Δx_2	Small spatial integration step inside the roll bite	m
$\Delta x_{\text{extr},1}$	Big data extraction step outside the roll bite	m
$\Delta x_{\text{extr},2}$	Small data extraction step inside the roll bite	m
$\Delta x_{\max}$	Maximum spatial integration step	m
$\Delta x_{\min}$	Minimum spatial integration step	m
π	Pi constant, 3.14159265	-
t	Time	s
$\bar{t}$	Non-dimensional time	-
tol_{abs}	Integration error tolerance for small values	Depends
tol_{crit}	Tolerance of the zone transition criterion	-
$\text{tol}_{\overline{F}_r}$	Tolerance of the rolling force per width	-
tol_{int}	Tolerance of the integration error	-
tol_Q	Tolerance of the adjustment loop of the lubricant flow rate	-
tol_R	Tolerance of the adjustment loop of the roll profile	-
$\text{tol}_{\sigma_{\text{out}}}$	Tolerance of the adjustment loop of the strip speed at the entry of the roll bite	-
tol_{s_f}	Tolerance of the forward slip	-
$\text{tol}_{t_{\text{out}}}$	Tolerance of the adjustment loop of the vertical roll position	-
$w^{(0)}$	Weighting coefficient of the roll profile relaxation if it does not change from one iteration to the next of the roll profile adjustment loop	-
$w^{(i)}$	Weighting coefficient of the roll profile relaxation at iteration i	-

x_{12}	Coordinate along the rolling direction, where the fine discretization of the roll or the roll bite starts	m
x_{23}	Coordinate along the rolling direction, where the fine discretization of the roll ends	m

Chapter 1

Introduction

This introduction starts by defining the *context* of this thesis, which leads to its *objectives* in the following section. Based on these objectives, the *outline* of this document is then described before highlighting our *original contributions*.

1.1 Context

Harder, thinner and more diverse steel strips are in great demand to optimally satisfy the requirements in the production of car bodies or packaging, like tin cans. Increased hardness of strip materials usually leads to a reduced product thickness for a given functionality, which implies less material usage and thus, smaller weight as well as, possibly, lower costs and less waste. Especially, *weight reduction* has become more and more important in recent years due to the emission targets of carbon dioxide, the main greenhouse gas, for new cars by the EU legislation [100]. Therefore, Advanced High-Strength Steels (AHSS) with yield stresses over 750 MPa were introduced in automotive sheet products [182, 370]. In consequence, new challenges arose in the production of steel strips, and specifically, in cold rolling.

After the production of steel by a blast furnace and a converter, the liquid metal is shaped in a continuous caster to several-centimeter-thick slabs, which are hot rolled at about 1000°C since the high temperature decreases the resistance of the material. To simplify its processing, the strip is commonly separated into coils after hot rolling, which can later be welded together again. When the strip reaches several millimeters in thickness, it is further reduced by *cold rolling* at about 100°C to satisfy very strict geometrical tolerances without significant surface oxidation. Cold rolling occurs in tandem mills that consist of successive mill stands. In each stand, the strip is pulled by friction between work rolls, which gradually reduce its thickness.

The process is strongly dependent on *friction*: if friction forces are too low, skidding occurs between the rolls and the strip, which could favor stand vibrations that lead to undesired variations of the strip gauge and, potentially, strip breakage. If friction forces are, however, greater than

required to prevent skidding, they unnecessarily increase the rolling force, the energy consumption and wear of the work rolls.

Especially, the increase of the *rolling force*, which is the force that pushes the rolls against the strip, is detrimental in the current context. In fact, most of the existing European tandem mills were constructed at least 30 years ago, when rather soft steel grades were produced [182]. Today, harder and thinner rolled products, however, reach their technological capacity limits, i.e. the maximum rolling forces. Accordingly, friction should be controlled as well as possible to maximize the production output instead of wasting this capacity due to unnecessary friction.

Even before becoming crucial due to harder and thinner strips, the key to better friction control in cold rolling was *flexible lubrication* [183]. Oil-in-water emulsions are generally sprayed onto the strip and the rolls to cool them down and to prevent excessive friction and surface wear (seizure/scuffing) by reaching the mixed lubrication regime. In this regime, the interface pressure between the rolls and the strip is partially supported by the solid-to-solid contact between their microscopic surface asperities and partially by the lubricant that was entrained into the roll bite. Conventional lubrication systems operate, however, passively unlike flexible lubrication, which continuously adjust the lubrication conditions as a function of the current rolling conditions. Thus, flexible lubrication could minimize friction while preventing skidding at three characteristic time scales, i.e. (1) during the whole rolling campaign by adapting itself to the decreasing roughness of the rolls due to wear, which reduces friction until they have to be replaced, (2) for each coil, whose characteristics (format, material, surface condition, ...) could be different from the preceding coil since the product diversity increases, and (3) between coils when the rolling speed is reduced to roll the weld between them, which increases the rolling force since less lubricant is entrained into the bite.

Research about the concept of flexible lubrication as such was started between 1998 and 2000 by M. Laugier, who was supported by G. Hauret, at Irsid (Institut de recherche de la sidérurgie; in English, Research institute of the steel industry; now ArcelorMittal Maizières Research SA), which is currently a part of the *ArcelorMittal* group [178, 181, 182, 183]. This research was essentially focused on the development of a predictive tool, which determines the required lubrication conditions to minimize friction while preventing skidding, and an effective control technology, which imposes these conditions in the rolling mill. In 2010, after laboratory tests, such a technology was implemented on an industrial production line by ArcelorMittal via a static mixer that allows to adjust the oil concentration in the emulsion within seconds. The development of the predictive tool to determine the oil concentration, however, turned out to be less straightforward.

The lubrication conditions (oil concentration, viscosity, ...) that minimize friction while preventing skidding can be identified experimentally or by mathematical modeling, also referred to as numerical modeling, if these models are solved on a computer. *Experimental and numerical approaches* are commonly combined to take advantage of their respective strengths. In general, experimental rolling tests provide the data to build, to calibrate and to validate rolling models, which should be able to extrapolate these data to different rolling conditions than those in the experiments. By this predictive ability of the model, new rolling conditions can be numerically

investigated in a cheaper and faster way than experimental testing, before experimentally checking specific results, which possibly allow to further refine the model.

Considerable efforts went into the *development of rolling models* that can be classified into three generations regarding friction and lubrication. In first generation models, friction is solely described by Coulomb or Tresca friction with a constant (assumed) coefficient of friction, so that lubrication is not directly taken into account. In second generation models, lubrication is included in the prediction via the Reynolds equation and asperity flattening equations by assuming that more of a single-phase lubricant is available at the entry of the roll bite than it can absorb. Finally, third generation models should be able to determine friction directly based on the lubrication conditions, i.e. including lubrication by oil-in-water emulsions and more sophisticated lubrication mechanisms in the roll bite, which will be explained hereafter.

To develop such models, the following *research projects* were conducted during the past two and a half decades[1] in collaboration with ArcelorMittal Maizières Research SA (previously, Irsid):

- *Marsault (1998)* [215] developed the second-generation rolling model LAM2DTRIBO, which clearly is the foundation of the following research efforts, within the context of the research project "Contact: Metal-Tool-Lubricant" from 1995 to 2000 under the direction of P. Montmitonnet (CEMEF).
- *Cassarini (2007)* [63] developed a model of the lubricant film formation in emulsion-lubricated cold rolling. The objective of this model is to predict the lubricant film thickness at the entry of the roll bite based on the lubrication conditions in order to include it in the previous rolling model.
- *Stephany (2008)* [305] extended Marsault's model by developing the software METALUB based on Boman's (1999) [36] significantly faster implementation of LAM2DTRIBO. This model rendered it possible to impose the lubricant film thickness at the entry of the roll bite so that numerous experimental rolling scenarios were reproduced. Various simulation parameters, however, still had to be adjusted since, for instance, a coupling between this model and the film formation model by Cassarini never converged.
- *Guillaument (2010)* [128] simulated the impact of emulsion droplets on the strip and the phase separation between oil and water that leads to the lubricant film formation before the entry of the bite by computational fluid dynamics (CFD). This so-called film formation by plate-out was less thoroughly studied in Cassarini's thesis, which focused more on the dynamic concentration mechanism at the entry of the bite.
- *Carretta (2014)* [54] developed the first finite element (FE) model of micro-plasto-hydrodynamic/static (MPH) lubrication. More precisely, in 1998, a decrease of friction with increasing strip reduction was experimentally observed at Irsid [180]. This observation was ultimately explained by MPH lubrication, i.e. the permeation of the lubricant from microscopic surface pockets into the solid/solid contact zone between asperities. Since this

[1]The thesis by *Counhaye (2000)* [86] could also be cited, but it focuses more on strip geometry in cold rolling than on friction modeling.

physical mechanism was not included in the previous rolling models, Carretta attempted to couple a new and more robust version of METALUB with his MPH lubrication model.

Despite significant advances in friction modeling during these projects and many more (see Chap. 2 for details), friction in lubricated cold rolling can still not be accurately predicted, i.e. *no full third generation rolling model exists so far*. On the one hand, the previous models require a few parameter adjustments to reproduce the experimental data because some parameters were not measured and because some physical mechanisms are not included in these models. On the other hand, coupling the models to include the missing mechanisms is not straightforward. For instance, METALUB does not yet model the lubricant film formation, if less lubricant is available at the entry of the roll bite than it can absorb. This condition is called starvation. Hence, the film thickness at the entry of the bite has to be manually adjusted to reproduce the experimental rolling force, if starvation occurs. Prior attempts to couple METALUB with Cassarini's film formation model, which computes this thickness, were, however, unsuccessful.

1.2 Objectives

This thesis is the continuation of the preceding research efforts with the long-term objective of ***accurately modeling friction in lubricated cold rolling to minimize friction while preventing skidding by flexible lubrication***.

More specifically, within the framework of this document, this objective is divided into several intermediate goals to *build a strong foundation on prior research before extending it*. First, as indicated in the previous section, the research in lubricated cold rolling is relatively extensive due to the ongoing demand of steel strip and the complexity of this process. Hence, *the state of the art is reviewed to identify the most effective ways to improve the existing models*.

Secondly, models are usually built and validated by experimental observations. Experimental rolling data of previous research are, however, less comprehensive than data that have been measured more recently on the pilot mill of ArcelorMittal. Hence, physical mechanisms that were observed by these recent data might not be included in older models, which are based on more limited data. Moreover, this limitation has required hypotheses and parameter adjustments in older models to reproduce the experimental results, so that the real predictive capabilities and the shortcomings of the model cannot be identified clearly. To eliminate these drawbacks, it is necessary to *determine the physical mechanisms that should be included in the rolling model based on the most comprehensive available data and to evaluate this model by these data*.

Over the past years, METALUB has become the most powerful numerical model of lubricated cold rolling (to the best of our knowledge). Nevertheless, different versions of the model existed in the past and modifications were not always recorded with ample explanations so that no centralized and detailed documentation exists, thus hindering future research. Moreover, the previous experimental data show that earlier versions of METALUB lack some physical mechanisms to accurately model lubricated cold rolling. Hence, the third objective is *to thoroughly rederive, to document and to extend the METALUB model*.

Fourthly, as mentioned earlier, rolling models were tested by less complete data than the data that are currently available. Therefore, hypotheses and parameter adjustments were required in the past to reproduce the experimental results although totally different material parameters or physical mechanisms could be at the origin of these results. In addition to the experimental data, the modeling capabilities of METALUB are extended. For these reasons, the fourth intermediate goal consists in *precisely evaluating the current predictive capabilities and limitations of the model by the most comprehensive available experimental data to determine how to further improve this model*.

One significant drawback of METALUB is its analytical model of lubricated asperity flattening, which is not able, among other things, to predict MPH lubrication. Hence, the fifth intermediate goal is to pursue Carretta's work by attempting to *couple METALUB with a more versatile FE model of lubricated asperity flattening to replace the analytical model*.

Finally, the model of MPH lubrication by Carretta is limited by the mesh-based nature of the finite element (FE) method. To overcome this restriction, the sixth intermediate goal consists in *exploring the truly meshless method "smoothed particle hydrodynamics" (SPH) to model lubricated asperity flattening*.

Thus, the previous objectives can be summarized as follows:

1. *Review the literature* to identify the most effective ways to improve friction modeling in lubricated cold rolling.
2. Determine which physical mechanisms should be included in a rolling model based on the *most comprehensive available experimental data*.
3. Completely rederive, document and extend the *METALUB* model to include the previous mechanisms.
4. *Evaluate* the predictive capabilities and shortcomings of *METALUB* based on the preceding data to determine how to further improve this model.
5. *Couple METALUB with a FE model of lubricated asperity flattening* to remove shortcomings of analytical asperity flattening equations.
6. *Explore SPH modeling of lubricated asperity flattening* to eliminate drawbacks of the FE MPH lubrication model.

1.3 Outline

The *structure* of this thesis is based on the previous objectives and a brief summary is given hereafter. ***Due to the size of this document, each chapter is thoroughly summarized in its conclusion so that chapters do not have to be read in their entirety to understand key findings. Moreover, numerous developments were transferred to the appendix for greater ease of reading.***

In Chap. 2, the *context of friction modeling in lubricated cold rolling is set and the corresponding literature is reviewed* to lay the foundations for the following chapters. Initially, *cold rolling* is described by situating this process within the steelmaking process and by explaining fundamental concepts, like the forward slip, as well as the lubrication in cold rolling. Then, the *physics of friction* is introduced by focusing on the characterization of solid surfaces, asperity flattening, dry friction and friction in lubricated cold rolling. Ultimately, the research about *friction modeling in lubricated cold rolling* is categorized into three generations of rolling models to identify the current state of the art.

In Chap. 3, the *most comprehensive experimental rolling data* to the best of our knowledge are presented. First, it is explained how these data were measured by ArcelorMittal. Then, they are analyzed to determine the physical mechanisms that have to be included in a cold rolling model to accurately predict the rolling force and the forward slip, amongst others. The data, which were post-processed to simplify their usage in METALUB, can be found in appendix E.

In Chap. 4, the cold rolling model *METALUB is meticulously rederived and extended*. Due to more than 20 years of development of this model, its *historical context* is reviewed before defining its components: (1) the *rolling process description*, in which fundamental parameters and hypotheses are introduced, (2) the *load sharing equation* between asperities and the lubricant in the mixed lubrication regime, (3) the *geometric contact description of a rough surface* to write the solid/solid contact area as a function of the distance between surfaces, (4) the *mechanics of the strip* that relates the internal stresses of the strip to its geometrical modification and the stresses at the interface between the strip and the rolls, (5) *roll flattening* due to these stresses, which are determined by (6) *solid contact* and (7) *lubricant flow modeling*, as well as (8) the *thermal model*. Finally, all these components are combined in one model and its solution method is explained. The underlying *system of equations* can be found in appendix N.

In Chap. 5, the *predictive capabilities and the limitations of METALUB are evaluated* by the experimental data of Chap. 3. At the beginning, a *literature review about the validation of METALUB* demonstrates why this model has to be further validated. Then, the *numerical parameters of the model are for the first time systematically calibrated* (details in appendix O) before also calibrating some *physical parameters*. Eventually, several *validation cases* of Chap. 3 are numerically reproduced.

In Chap. 6, a *coupling procedure between METALUB and the FE solver METAFOR* is developed to simulate lubricated asperity flattening by the FE method instead of analytical flattening equation. First, the *coupling procedure by Carretta*, which is based on his FE model of MPH lubrication, is described. Due to several shortcomings of this method, a *new coupling procedure* is then developed and *tested* by a rolling scenario of Chap. 3.

In Chap. 7, *lubricated asperity flattening is simulated for the first time by the meshless method "smoothed particle hydrodynamics"* (SPH) to eliminate mesh-related drawbacks of FE asperity flattening models. Initially, *SPH* is introduced based on an extensive literature review, the complete derivation of the method and simulations of fluid-structure-interaction (FSI) tests via the USER-SMD SPH package in the molecular dynamics simulator LAMMPS (Large-scale Atom-

ic/Molecular Massively Parallel Simulator). Then, this method is applied to gradually *simulate lubricated asperity flattening* after modeling separately the compression of an elastoplastic solid, dry asperity flattening and the compression of a lubricant.

In addition to the appendices mentioned earlier, numerous further appendices complete explanations of the previous chapters, in which they are referenced. In short, the *height distribution function of a triangular asperity profile* is derived in appendix A. The *composite root-mean-square roughness* of two surfaces is computed in appendix B. More *sophisticated dry friction models* than Coulomb's law with a constant coefficient are reviewed in appendix C. The prediction of the *lubricant film thickness by Wilson and Walowit* [368] is proven in appendix D. The *conversion factor from the arithmetical to the root-mean-square roughness* is calculated in appendix F. The *graphical user interface* (GUI) of the METALUB software is illustrated in appendix G. Some *fundamentals of mechanics*, i.e. continuum mechanics, the conservation equations, solid mechanics and fluid mechanics, are summarized in appendix H. An *incoherence in the formula of roll deformation by Jortner et al.* [163] is corrected in appendix I. The corresponding *influence functions* in this formula are listed in appendix J. Their extension, i.e. the *Meindl influence functions*, are specified in appendix K. The form of the *Roelands viscosity equation* in METALUB is derived in appendix L. The computation of viscous shear stresses between lubricated surfaces based on *shear stress factors* to take the roughness into account is explained in appendix M. *Additional validation cases of METALUB* are presented in appendix P. Some details about the *coupling procedure between METALUB and METAFOR by Carretta* are described in appendix Q. And finally, the *radial return algorithm* for the explicit integration of the elastoplastic constitutive equations in the SPH solver is explained in appendix R.

1.4 Original contributions

In this section, the ***original contributions***, which differentiate this thesis from earlier research, are listed and referenced to easily find them in this document.

Chapter 3: Experimental data

- The ***experimental data***, which were provided by ArcelorMittal, ***are the most comprehensive data of lubricated cold rolling*** to the best of our knowledge, since they include, among other things, (1) roughness measurements of the roll and strip surfaces, (2) hardening laws of the strip materials by plane-strain compression tests, (3) thermo-piezoviscous material laws of the lubricants for high pressures and (4) a large design space so that the isolated influences of numerous operating parameters were tested. These data are summarized in Sec. 3.1 and in appendix E, where they were carefully post-processed and documented to simplify their usage in future research.
- ***The influences of numerous physical parameters on the rolling load and forward slip in lubricated cold rolling are for the first time explained via the underlying physical mechanisms in one single document with the corresponding experimental rolling data***

(to the best of our knowledge), i.e. in Sec. 3.2. They were, however, described separately in different references, e.g. Roberts [276], Zhang et al. [379] and Marsault [215], sometimes with the respective experimental data.

Chapter 4: METALUB - A Mixed Lubrication Cold Rolling Model

- The ***METALUB model, which seems to be the most powerful model of lubricated cold rolling, is completely rederived in this document*** with unified notations and equations, i.e. all equations are deduced from initial definitions and assumption, either directly in this document (Chap. 4 and appendix E) or via references to the original research, in which they were derived. In earlier research about the METALUB model, equations sometimes appeared without any derivation or meaningful reference, different notations were used in the research and the computer code, and the equations of different types of roll bites (dry, lubricated, coupling) were not unified, so that the extension of the model was nearly impossible.
- The ***METALUB model is corrected and extended***:
  - The *distance between the rolls and the strip* was inconsistently computed in the past, so that they could overlap. This inconsistency is corrected in Sec. 4.5.1.
  - ***Thermo-viscoplasticity of the strip*** is included in METALUB in Secs. 4.5.2.3 and 4.5.2.4 since the previous rolling data and earlier research indicated noticeable thermal softening and strain rate hardening of the strip.
  - The elastic *roll flattening model by Meindl* [220] is added to METALUB in Sec. 4.6.4 and appendix K. This model includes all flattening modes of the roll, i.e. radial and tangential deformations due to pressure and shear stress, while previous models only considered at most radial deformations due to pressure.
  - The regression equation by Sutcliffe [313] of the *asperity flattening equation by Korzekwa et al.* [169] (Sec. 4.7.1.3) is introduced in METALUB. Contrary to Wilson and Sheu [367], who modeled asperity flattening by the upper bound method, Korzekwa et al. used the FE method, which is expected to return more realistic results.
  - The possibility to include different roughness values for the rolls and the strip is added in the computation of the *shear flow factor* by Eqs. (4.163) and (4.174), which were derived by Patir and Cheng [254]. Moreover, some regression equations of this factor are corrected in Eq. (4.182).
  - The possibility to take the roughness into account in the computation of the lubricant shear stresses is included in METALUB via *shear stress factors* by Patir and Cheng [254] for small relative contact areas in Sec. 4.8.3 and appendix M.
  - Simplified *thermal models* of the strip and the lubricant are added to METALUB in Sec. 4.9. In the past, the thermal solver THERMROLL [42] was coupled with Stephany's version of METALUB, which was, however, abandoned due to its programming style.

  - To prevent the lubricant pressure from becoming greater than the interface pressure, which is physically inconsistent, a transition to the *high-speed outlet zone* is added to the integration zones of the roll bite in Secs. 4.10.1 and 4.10.2.6.
  - The ***robustness of the model*** *and the speed of its resolution are* ***improved*** in Sec. 4.10 by eliminating unnecessary convergence criteria, by nondimensionalizing the remaining criteria and by choosing better initial conditions in iterative solvers. The improvement of the robustness is absolutely necessary before attempting to couple METALUB with other independent solvers.
  - A *method to alleviate the high-speed hypothesis*, i.e. the imposed identity of the lubricant pressure to the interface pressure and the negligence of the Poiseuille term in the Reynolds equation, based on Stephany's CIEFS solver [305] is added to METALUB in Sec. 4.10.5.

- The ***METALUB source code and its graphical user interface (appendix G) were entirely refactored*** *to increase its robustness, to improve the programming style and to extend the model*, i.e. almost all of the current 20,878 lines in the 169 core C++ files (`/lub/src`) were changed. In total, the project contains about 1,100 files and 200 regression tests.

Chapter 5: METALUB - Numerical Results

- The *numerical parameters in METALUB are for the first time systematically calibrated* to eliminate convergence issues and to reduce the computation time with a controlled accuracy of the results in Sec. 5.2 and appendix O.
- ***METALUB predictions are significantly improved*** (mainly, by strain rate hardening, thermal softening via a thermal model and the negligence of the lubricant shear stress in the roll bite) and ***limitations*** (essentially, the temperature prediction of the lubricant, film formation and MPH lubrication) are illustrated by test cases on a semi-industrial pilot mill (Secs. 5.3 and 5.4).

Chapter 6: Coupling of METALUB with METAFOR - FE Asperity Flattening

- The ***first coupling procedure between a rolling model, i.e. METALUB, and a FE model of lubricated asperity flattening*** *including the bulk elongation along the rolling direction* is described in Chap. 6.

Chapter 7: SPH Simulation of Lubricated Asperity Flattening in LAMMPS

- *Numerous validation tests of fluid, solid and fluid-structure-interaction problems are for the first time reproduced by the USER-SMD SPH implementation* in the molecular dynamics solver LAMMPS (to the best of our knowledge, Sec. 7.1.5).
- ***Dry and lubricated asperity flattening are for the first time simulated by SPH*** in Secs. 7.2.3 and 7.2.5. Since SPH is a meshless method, it allows to simulate fluids and solids with

large deformations without mesh distortions, unlike the FE method.

Chapter 2

Contextualization and Literature Review

In this chapter, the *context of friction modeling in lubricated cold rolling is set and the corresponding literature is reviewed*, thereby laying the foundations for the following chapters. First, the *cold rolling* process is described. Then, the physics of *friction* is explained. And finally, these elements are combined to sum up the current development status of *friction modeling in lubricated cold rolling*.

2.1 Cold rolling

In this section, cold rolling is positioned within the *steelmaking process* to review the operations that affect the strip during cold rolling and its final properties. Then, the *cold rolling process* as such is explained. Finally, the *lubrication in cold rolling* is highlighted separately because of its current potential to further optimize the process.

2.1.1 Steelmaking process

Steel is an essential component of our everyday life with a use per capita of about 350 kg/year in the European Union and a worldwide production of around 1,690 million tons in 2017 according to the World Steel Association [371]. It is produced by eliminating the excess carbon of pig iron, from *blast furnaces*, in *oxygen-blown converters* or by recycling scrap metal via *electric furnaces* [276, p. 407]. Major steps of the steelmaking process are schematically illustrated in Fig. 2.1. The liquid steel is then solidified as billets, blooms or slabs by continuous casting, or very rarely by ingot casting. While *billets* and *blooms* are semi-finished steel products with a square cross section up to 155 mm $\times$ 155 mm or higher, respectively, *slabs* have a rectangular cross section [10]. This leads to the distinction of long and flat products in the steel industry depending on whether the thickness has about the same size as the width, e.g. bars and beams, or not, e.g. plates and strips, respectively [235].

In this work, we focus on *flat products* and more specifically on strip rolling. To transform several-

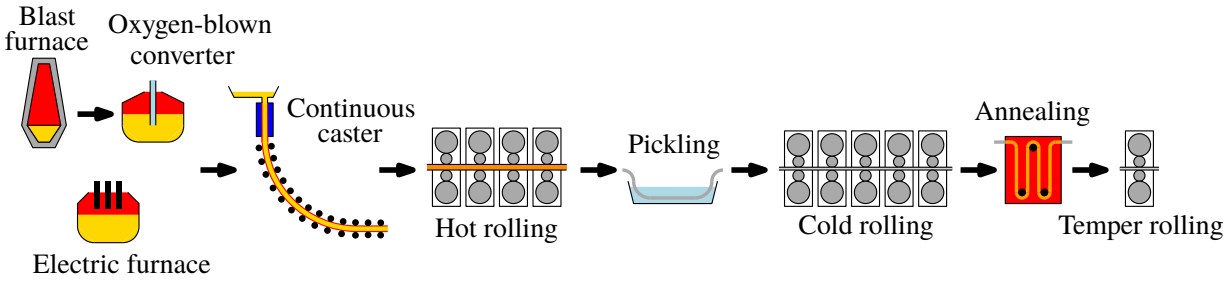

Figure 2.1: Schematic diagram of some major steps in the steelmaking process.

centimeter-thick slabs into millimeter-thick *strips* at reasonable rolling loads, they are *hot rolled* at about 1000°C (around 73% of its melting temperature) since the high temperature reduces the material resistance. *Rolling* can be defined as "a forming operation by plastic deformation, aimed at decreasing the section of a long metal part, through two or more axisymmetric tools (rolls) rotating around their axes; the entrainment of the product is primarily effected by the rotation of the rolls" [235]. To transport the strip easily from one operation to the next, strips are rolled up to *coils*. About 12.5% of the total annual steel production consists of hot rolled strip below 3 mm [371].

After hot rolling, the cooled strip is covered with an oxide layer, which is removed by the *pickling line*. More precisely, the oxide layer is broken open by scalebreakers and the strip is pickled in tanks filled with acid. The strip is finally rinsed, dried and possibly oiled to prevent further oxidation before being cold rolled [276, p. 407].

In contrast to hot rolling, *cold rolling* occurs at relatively low temperatures, i.e. at about 100°C, for the three following reasons [235]: first, it is possible to satisfy stricter *geometrical tolerances* by cold rolling than by hot rolling due to less significant thermal expansion of the workpiece and the rolls, and due to very limited oxide film thicknesses. Secondly, less oxidation also results in a better *surface quality* by cold rolling than by hot rolling. And finally, lower temperatures prevent recrystallization. Dislocations can therefore be multiplied to reach *mechanical properties* by work-hardening which could otherwise be insufficient. Further details about the cold rolling process are explained in the following section.

Cold rolling is followed by the *annealing* of the strip in a batch-type annealing furnace or a continuous annealing line at about 650 to 750°C, prior to which it generally has to be degreased. Increasing the temperature of the strip at high temperature leads to a more homogeneous microstructure with reduced internal stresses and thus, improved mechanical properties by partial recrystallization [235].

After the annealing process, the strip is again cold rolled but with a very small thickness reduction, i.e. 0.2 to 2%, on a single mill stand. This process is called *temper or skin-pass rolling* [171]. It has essentially four objectives: to eliminate the yield point elongation[1], to imprint a specific

[1]The yield point elongation is a plateau following yielding in the stress–strain curve. The corresponding flow behavior leads to Lüders bands, which can be at the origin of breakage in subsequent forming processes [171].

surface texture, to improve strip flatness and to create the required hardness or temper of the strip. Instead of temper rolling, light-gauge steel strips are further reduced by *secondary cold mills*.

Finally, *surface treatments* can be applied, either before or after temper rolling depending on the treatment. For instance, strips are painted or hot dip galvanized to prevent corrosion of tin cans in the food packaging industry.

2.1.2 Cold rolling process

In the cold rolling process, the thickness of a metal strip is reduced close to the ambient temperature, as mentioned previously. The initial thickness classically ranges from 1.5 to 5 mm, while the final thickness can be 0.5 to 0.8 mm as required in the automotive industry or 0.15 to 0.3 mm in the food packaging industry. The strip width ranges from about 700 mm up to 1800 mm [235].

In the following sections, the *structure of cold rolling mills* is described before explaining some *fundamental concepts of cold rolling*.

2.1.2.1 Structure of cold rolling mills

A *cold rolling mill or train* can either be discontinuous or continuous. In a *discontinuous* mill, a coil is rolled separately of other coils and therefore mounting and demounting the coil, as well as stopping the mill is required. *Continuous* trains, in which successive coils are welded together, are therefore preferred to discontinuous trains. In modern cold rolling facilities, the strip is directly transferred from the pickling line to the cold rolling mill without any intermediate separation into coils (Fig. 2.2).

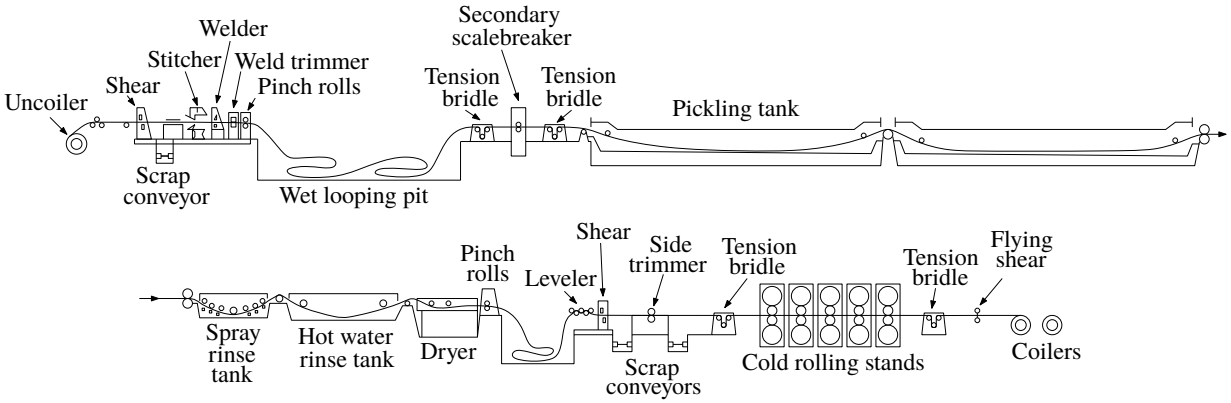

Figure 2.2: Schematic diagram of a continuous cold rolling train with a 5-stand cold rolling mill and the preceding pickling line. Adapted from Figs. 2-39 and 8-11 in [276].

A cold rolling mill is composed of a tandem mill in between an uncoiler and a coiler with intermediate tension bridles. The *uncoiler* unrolls the hot rolled strip while the *coiler* rolls up the cold rolled strip. *Tension bridles* allow to apply tension to the strip before it enters into the tandem mill and when it comes out of it.

A *tandem mill* consists of four to six successive *mill stands* in the steel industry depending on the total required reduction of thickness (Eq. 2.1) and the maximum reduction of each stand, which is limited by its rolling capacity, i.e. the maximum rolling load. The reduction by a single stand is around 30%. Hence, reducing the strip thickness from 3 to 0.5 mm requires about 5 stands.

Different designs of individual mill stands have been developed over time, as illustrated in Fig. 2.3 [276, p. 23]. Initially, the *two-high configuration* with a top and a bottom work roll was introduced. Due to bending of these rolls because of significant rolling forces, top and bottom backup rolls were added in the same vertical plane. The resulting *four-high configuration* is the most popular configuration for cold rolling of steel strip today. The diameter of the work rolls is typically 600 mm, while that of the backup rolls is 1400 mm. Other designs, like a *6-high configuration* with additional intermediate rolls to improve flatness, or the *cluster Sendzimir mill* with 20 rolls for hard stainless steel, can also be mentioned. In this work, we focus, however, on the most wide-spread four-high configuration. Since the work and back up rolls have to be harder than the material that has to be rolled, they are made of cast or forged chrome steel [14, p. 236] with yield stresses in compression up to 3000 MPa [86].

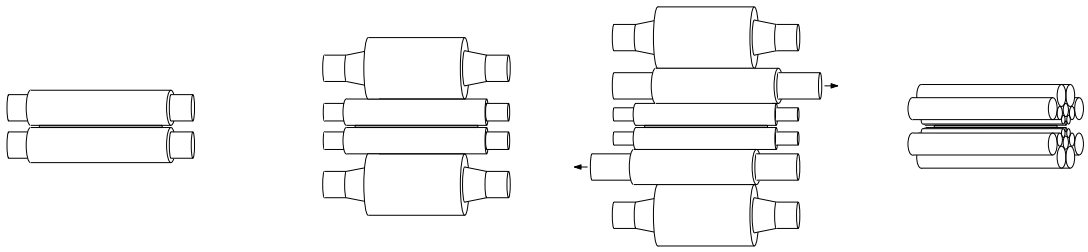

(a) 2-high. **(b)** 4-high. **(c)** 6-high. **(d)** Sedzimir.

Figure 2.3: Schematic representation of roll configurations in single mill stands.

To reduce the thickness of the strip when it moves in-between the work rolls, the position of the rolls and thus, the force that they exert on the workpiece are applied by *mill screws* and *hydraulic systems* to speed up the roll positioning. The *rolling torque*, that is required to rotate the rolls, is generated by electric motors [276].

Finally, since cold rolling is strongly dependent on friction and thermal expansion, a *cooling and lubrication system* is required in each mill stand. It consists of several tanks, pumps and nozzles to apply either water, an oil-in-water emulsion, or the pure oil, as well as other additives, which will be discussed in Sec. 2.1.3.

2.1.2.2 Fundamental concepts in cold rolling

In this section, *fundamental concepts in cold rolling* are described. These include rolling as such, the importance of friction, back and front tensions, mill stand and roll deformations, roll wear, chatter and the current objectives in cold rolling.

Concept of rolling

Rolling consists in the reduction of the strip thickness from an initial thickness t_{in} to a final thickness t_{out} when the strip moves in-between the work rolls. Fig. 2.4 illustrates this reduction in the top zone of the mill stand due to symmetry, which is classically assumed to exist between the top and bottom parts [215]. The resulting *reduction* or *reduction ratio* r is defined as follows:

$$r = \frac{t_{\text{in}} - t_{\text{out}}}{t_{\text{in}}} \tag{2.1}$$

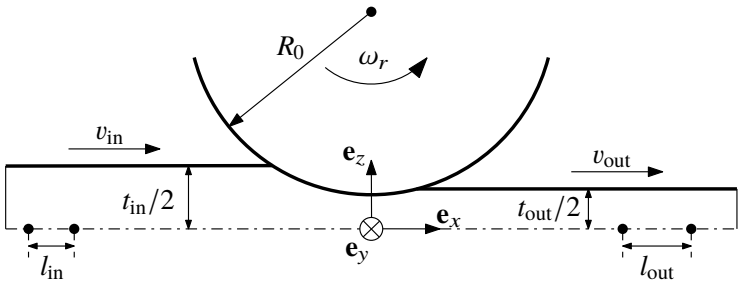

Figure 2.4: Schematic diagram of rolling.

Due to the incompressible nature of plastic deformations [48, 49], the speed of the strip at the entry of the bite v_{in} can be related to the speed at the exit v_{out} by the conservation of mass and the plane-strain state in cold rolling, which prevents the strip from spreading in the transverse direction $\mathbf{e}_y$ (see next section):

$$v_{\text{in}} t_{\text{in}} = v_{\text{out}} t_{\text{out}} \quad \text{or} \quad l_{\text{in}} t_{\text{in}} = l_{\text{out}} t_{\text{out}} \tag{2.2}$$

where l_{in} and l_{out} are the horizontal distances between two material points of the strip along the rolling direction before passing between the rolls and afterwards, respectively (Fig. 2.4). Instead of quantifying the reduction by the reduction ratio r, it can also be measured by the engineering strain in the rolling direction, which is usually called the *elongation* e_x:

$$e_x = \frac{l_{\text{out}} - l_{\text{in}}}{l_{\text{in}}} \tag{2.3}$$

The contact zone between the work rolls and the strip is called the *roll bite*. The length of the roll bite can be approximated by the following formula due to the relatively small thickness of the strip with respect to the radius of the non-deformed roll R_0 and the small elastic increase of thickness after the closest point between the rolls (Eq. D.3 in appendix D). The roll bite is therefore about 1 to 3 centimeters long in cold rolling:

$$l_{\text{rb}} \approx \sqrt{R_0 (t_{\text{in}} - t_{\text{out}})} \tag{2.4}$$

Due to the volume conservation in Eq. (2.2) and the thickness reduction, the velocity of the strip increases along the roll bite, i.e. $v_{\text{out}} > v_{\text{in}}$. Moreover, since the work roll speed is usually not

greater than the strip speed along the entire roll bite, the strip is slower than the roll at the entry of the bite and faster at its exit, i.e. $v_{\text{in}} < v_r < v_{\text{out}}$, where $v_r = R_0\omega_r$ is the peripheral speed of the roll, or simply, the *rolling speed*. The final speed of the strip is about 1200 m/min for thin/hard strips and 1800 to 2100 m/min for packaging steel after the last mill stand [167, 235]. The position inside the roll bite, where the speed of the strip v_s becomes equal to that of the roll v_r is called the *neutral point*. In general, only one neutral point exists in the roll bite, but multiple neutral points or neutral zones can exist, too [171].

When the entry speed of the strip v_{in} decreases due to changing friction conditions in the bite at a constant rolling speed (and constant back and front tensions), the neutral point becomes closer and closer to the exit of the roll bite and the exit speed v_{out} decreases as well due to volume conservation. A significant parameter in cold rolling that characterizes this mechanism is the *forward slip* s_f. It is defined as the relative speed of the strip at the exit of the roll bite with respect to the rolling speed [276, p. 596]:

$$s_f = \frac{v_{\text{out}} - v_r}{v_r} \tag{2.5}$$

In general, the forward slip amounts to a few percent, while its critical level is $s_f \in]0\%,\ 0.5\%]$ to ensure the stability of the process [179]. As will be explained in the following section, the forward slip decreases when friction is reduced. Hence, the forward slip is a criterion that quantifies by how much friction can be reduced before skidding occurs.

Importance of friction

In cold rolling, the strip is moved through the roll bite by the rolls via friction. Hence, the friction force between the strip and the rolls is a fundamental component of rolling. At the entry of the bite, the interface shear stress τ_i *pushes the material towards the neutral point* since the velocity of the rolls is greater than that of the strip before the neutral point (Fig. 2.5). After the neutral point, the friction force tries to prevent the strip from leaving the roll bite since it still pushes the strip towards the neutral point in the bite due to the greater speed of the strip with respect to that of the rolls.

In the transverse direction $\mathbf{e}_y$, friction forces prevent the strip from spreading in this direction. In addition to the small thickness of the strip in cold rolling, this is the reason why the process is generally assumed to occur in the *plane-strain state*, i.e. without deformations along $\mathbf{e}_y$ [276, p. 246].

At the entry of the roll bite, the strip is in a tension state because of the applied back tension σ_{in}, which is introduced in the following section. Due to the friction forces, which compress more and more the strip along the axial direction, as explained before, the axial stress σ_x (positive in tension) decreases towards the neutral point. The same is true from the exit of the bite towards the neutral point for similar reasons. Hence, σ_x varies along the roll bite as illustrated in Fig. 2.5 (blue curve).

In addition to these friction forces, the rolls apply a pressure p_i (positive in compression) onto the strip, which leads to its reduction. This pressure is related to the axial stress σ_x by the resistance

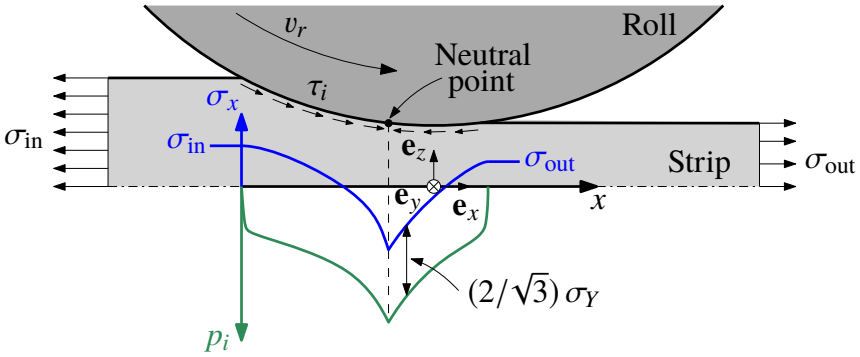

Figure 2.5: Influence of the interface shear stress τ_i, which is applied by the roll to the strip through friction, on the axial stress σ_x (positive in tension). This traction is related to the interface pressure p_i (positive in compression) in the plastic deformation zone by the yield criterion. The evolution of p_i along the roll bite exhibits the characteristic friction hill while the blue curve represents the axial stress profile $\sigma_x(x)$. The stresses σ_{in} and σ_{out} are the back and front tensions.

of the material. In the plane-strain state, for a rigid perfectly plastic material, the Von Mises yield criterion is written as follows with the yield stress σ_Y (see Eqs. 3.11 and 3.12 for details):

$$p_i + \sigma_x = \frac{2}{\sqrt{3}}\sigma_Y \tag{2.6}$$

In consequence, the interface pressure p_i increases towards the neutral point and then decreases afterwards. This evolution, which is shown in Fig. 2.5 (green curve), is called the *friction hill* [276, p. 248]. The maximum pressure is reached at the neutral point, where the axial compression is highest, too.

The resultant vertical force of the interface pressure over the entire roll bite is called the *rolling force* F_r, or *rolling load* L_r, when it is written in units of mass, e.g. metric tons. In general, these values are written per unit width of the strip. Hence, $\overline{F}_r$ and $\overline{L}_r$ are the rolling force and rolling load per width, which are commonly equal to about 16 kN/mm or 1600 t/m, respectively.

One of the most important consequences of the previous explanation is the *increase of the rolling force with friction* (Sec. 3.2.1.1 for more details). The rolling force is, however, restricted by the technological limit, also known as the capacity of the mill stand, e.g. $\overline{L}_r = 3000$ t, which is why minimizing friction (while avoiding skidding) is of major importance in cold rolling. Moreover, the neutral point moves towards the exit of the bite, when friction is reduced, which implies that the *forward slip decreases with decreasing friction*, too.

Furthermore, friction in the roll bite also impacts the *energy consumption* of rolling either directly by the dissipation of frictional energy at the interface between the rolls and the strip, or indirectly by increasing the rolling load. In fact, if the rolling load rises, frictional energy losses increase in the backup roll bearings, at contacts between work rolls and back-up rolls, in the pinions, reductions gears, ... [276]. For instance, the ratio of power dissipated by friction to the total power consumption in the last mill stand of a 5-stand tandem mill was estimated at around 40%,

with a possible total power reduction of 35% when the coefficient of friction in the bite is reduced from 0.03 to 0.01 (in a specific rolling scenario) [86, 87].

While friction should be minimized, it should also not be so small that *skidding*, where the work roll speed is higher than the strip speed along the entire roll bite, occurs. Besides degrading the surface quality of the product, skidding results in the reduction of thickness and tension control, which could ultimately lead to strip rupture, as explained in the following section.

Back and front tensions

Referring to the previous section, the strip is in a tension state at the entry of the bite. In fact, tension forces are applied to the strip not only before but also after the roll bite by tension bridles or the neighboring mill stands to ensure the *stability* of the process. Otherwise, the strip could deform uncontrollably between the stands by buckling. The tension stresses are called *back and front tensions*, σ_{in} and σ_{out}, which are respectively applied before and after the roll bite with respect to the rolling direction (Fig. 2.5).

In addition to ensuring the stability of the process, back and front tensions *reduce the rolling force* by increasing the axial stress σ_x in the bite, which in turn reduces the interface pressure (Fig. 2.5). They should, however, not be too significant in order to decrease the risk of strip rupture between the stands, which is one of the most frequent incidents in cold rolling [86].

Mill stand and roll deformations

Due to the significant rolling forces, the deformation of the mill stand and the rolls can have an influence on the strip thickness and flatness [86]. Concerning the deformations of the roll, one distinguishes roll deflection and roll flattening. Both effects are illustrated in Fig. 2.6.

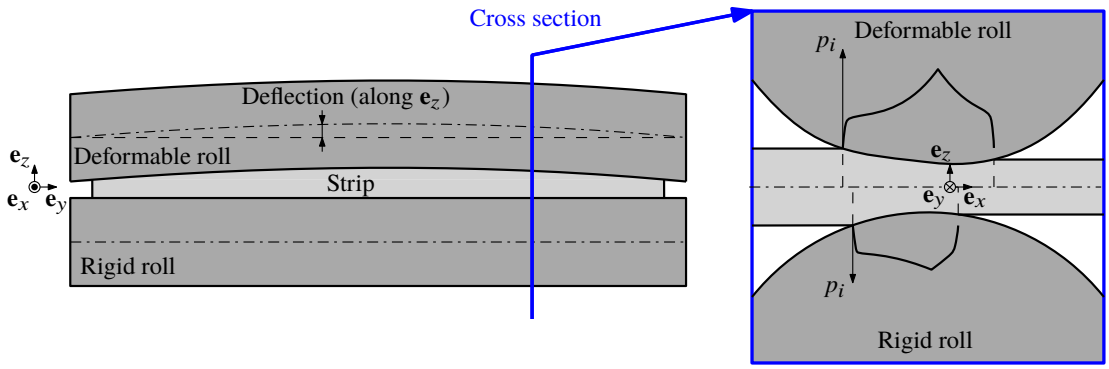

Figure 2.6: Roll deflection and roll flattening with the resulting interface pressure profile p_i along the roll bite. Comparison between the configurations with a deformable roll and a rigid roll.

Roll deflection is the displacement of the roll centerline due to bending and shear strains, which is usually modeled by beam theory [234]. Various techniques exist to compensate for roll deflection to obtain strips with more homogeneous thickness along the transverse direction $\mathbf{e}_y$ [276, p. 153].

For instance, rolls are cambered or crowned, which means that they are given a slight barrel-shape with a greater diameter at its center than at its extremities. Moreover, backup rolls are introduced as explained previously.

Roll flattening consists in the variation of the roll radius with respect to the centerline due to the interface pressure and shear stress between the rolls and the strip, and possibly, the backup rolls, too, depending on the rolling configuration [236].

Roll wear

Since the rolls move the strip through the roll bite via friction, their roughness has an important influence on the process. This roughness of about 0.2 to 0.4 μm (R_a, Sec. 2.2.1.1) [235] is initially provided to the rolls by *grinding*, i.e. their surface is ground by an abrasive wheel while they are rotated around their axis as in a lathe [276, p. 129]. For this reason, the roughness of the roll changes mainly along the direction of its axis, which implies that the grooves of the strip roughness are usually oriented along the rolling direction $\mathbf{e}_x$ as illustrated in Fig. 2.7 [312, 314].

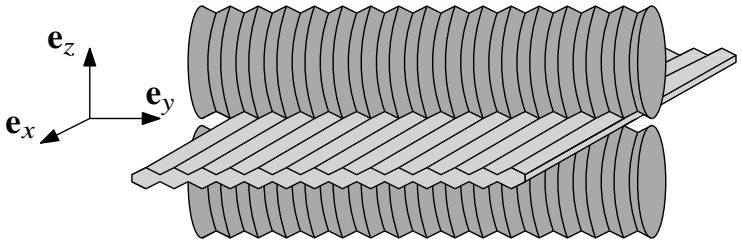

Figure 2.7: Schematic representation of the roughness lay direction, which has been significantly magnified. The roughness of the roll due to grinding is transferred to the softer strip during rolling.

Due to abrasion between the roll and strip, the surface roughness of the roll is gradually worn away until friction forces are not sufficient anymore to move the strip through the bite in a controlled way, i.e. skidding may occur, or the surface profile becomes unacceptable [276, p. 167]. To reuse the rolls, they have therefore to be ground again, usually after rolling several hundred kilometers of strip [86].

Chatter

Chatter consists in self-excited vibrations of the mill stand [376]. The most serious type of vibration is 3$^{\text{rd}}$ octave chatter at around 150 Hz, which leads to variations of the strip gauge by vertical vibrations of the rolls, and ultimately, strip breakage. Practically, chatter is *eliminated by reducing the rolling speed* as soon as it is detected, which decreases the production efficiency. Hence, technological solutions were developed to prevent chatter [233, 235, 330], for instance, by damping devices or by keeping the difference between friction coefficients of neighboring stands within certain ranges [110].

Current objectives in cold rolling

The general objective in cold rolling is to *roll thinner strips of harder materials at smaller costs*. For instance, in the *packaging industry*, the thickness of beverage cans was reduced by 50% during the past 30 years, effectively decreasing its weight from 36g in 1983 to below 18g in 2012 [377].

Rolling thinner Advanced High-Strength Steel (AHSS) strips with yield stresses of about 1000 MPa is currently of prime importance in the cold rolling industry so that *car manufacturers* can satisfy the emission targets of carbon dioxide by the EU legislation [100]. In fact, 97.3 million vehicles were produced worldwide in 2017 [251], each requiring about 900 kg of steel. Due to the increased resistance of AHSS, thinner AHSS strips compared to conventional steel are sufficient to satisfy specifications of car manufacturers without compromising occupant safety requirements. Hence, the vehicle weight can be reduced by 25 to 39%, thus saving 3 to 4.5 tons of greenhouse gases over its lifetime, which is equivalent to more than the total amount of CO_2 emitted during the production of all steel in the vehicle [370].

The increased hardness of these steel strips and their small thickness challenge the current capacity limits of European mills since these requirements strongly increase the rolling force. In fact, European rolling mills were not designed in the past to roll such hard steel grades today [182]. Since friction increases the rolling force but enables skidding and chatter, when it is too low, *controlling friction in the roll bite* is of crucial importance today. Besides *improving hard and thin AHSS strip rolling*, efficiently adjusting friction could also have the following benefits [183]:

- *Prevention of strip out-of-gage due to rolling force shoot-up during transients*: for instance, the rolling speed is reduced to roll the weld between two coils. A lower rolling speed implies less efficient lubrication, which leads to an increase of the rolling force because of more friction. If the capacity limit of the mill was reached, the strip thickness would exceed the requested thickness.
- *Prevention of chatter and related rolling incidents*: as mentioned previously, chatter is related to the friction conditions in the bite, although their dependence is not yet completely understood [235].
- *Increase of rolling speed*: since chatter appears preferentially when the rolling speed increases, the previous benefit allows to increase the rolling speed and thus, the production rate.
- *Reduction of energy consumption*, if friction is decreased.
- *Increase of roll campaign length*: wear reduces the roughness of the rolls and thus friction until they have to be replaced to prevent skidding. If friction could be decreased at the beginning of the campaign to reduce wear and if friction could be increased at its end to delay skidding, the rolls could be used longer. This could be achieved by gradually reducing the lubricant film thickness in the roll bite as the roughness of the rolls decreases, so that friction and wear are kept as small as possible during the entire campaign.

- *Improved strip cleanliness*: reduced friction goes along with milder contact conditions between the rolls and the strip. Hence, less iron fines are produced by wear.

The key to better friction control in cold rolling and to reach the previous objectives is *lubrication* and specifically, *flexible lubrication*, which continuously adapts the lubrication conditions to the specific rolling conditions as suggested by Laugier et al. [182, 183]. For this reason, lubrication in cold rolling is explained in the following section.

2.1.3 Lubrication in cold rolling

Strips have been extensively cold rolled with lubricants since the early 1930's, mainly to reduce friction and wear [276, p. 243]. This reduction is possible since the lubricant, which is entrained into the bite because of its viscosity, partially supports the contact pressure between the strip and the roll while transferring only a very limited shear stress between both. The lubrication regime, in which the rolling load is partially supported by the asperity tops and partially by the lubricant is called the *mixed lubrication regime* (Fig. 2.8, Sec. 2.2.4.2).

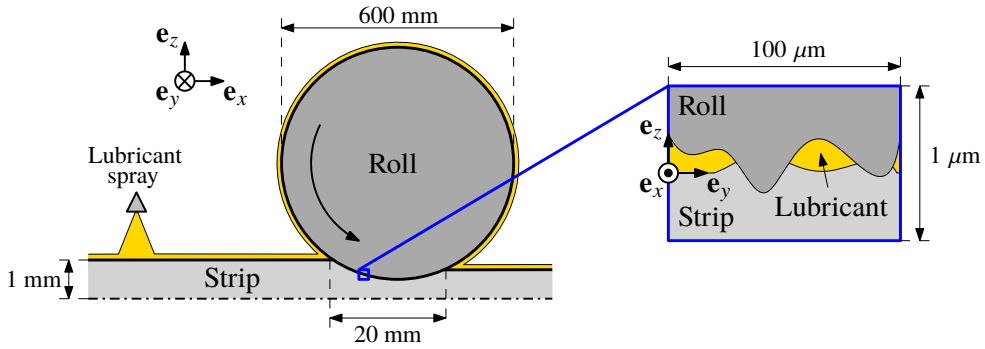

Figure 2.8: Mixed lubrication regime in cold rolling, in which the rolling load is partially supported by the asperity tops of the roll and the strip, and the lubricant.

The roll bite is either lubricated by *neat oils* or *oil-in-water (O/W) emulsions*. These emulsions consist of small oil droplets (about 10 μm) in water, stabilized by an emulsifier, which is a substance with a lipophilic and hydrophilic part [63, 128]. Other additives, like extreme-pressure additives (to prevent seizure), oiliness agents (to increase the viscosity), anti-oxydants (to extend the operating life of the oil) and rust inhibitors are commonly blended in emulsions [235, 276, p. 255]. The water in the emulsion cools the roll bite due to its important heat capacity, which prevents the viscosity of the lubricant to decrease due to heating and which reduces the impact of thermal expansion, while it also carries the oil into the roll bite.

Because of the relatively small concentration of oil, which can be provided to the bite via O/W emulsions, e.g. 2%, hydrodynamic lubrication with free surface roughening (Sec. 2.2.2.4) and the resulting possible risk of skidding and chatter due to reduced friction, which could occur with neat oils, can be prevented by starvation. *Starvation* consists in less oil being available at the entry of the roll bite than it can absorb [63, 271], so that less oil is entering into the roll bite by

viscous entrainment than it can absorb. This effect is crucial, when friction has to be controlled by the lubrication. In fact, if less oil is available at the entry of the roll bite than it can absorb and if this oil quantity further decreases, the oil film in the bite decreases and friction increases due to the reduced support by this film. If, however, more oil is available than it can absorb, friction is not significantly impacted. In this case, the roll bite is said to operate in *full-flooded lubrication*.

Different *lubrication systems* are used in cold rolling: direct application lubrication, recirculating lubrication and hybrid or flexible lubrication (Fig. 2.9).

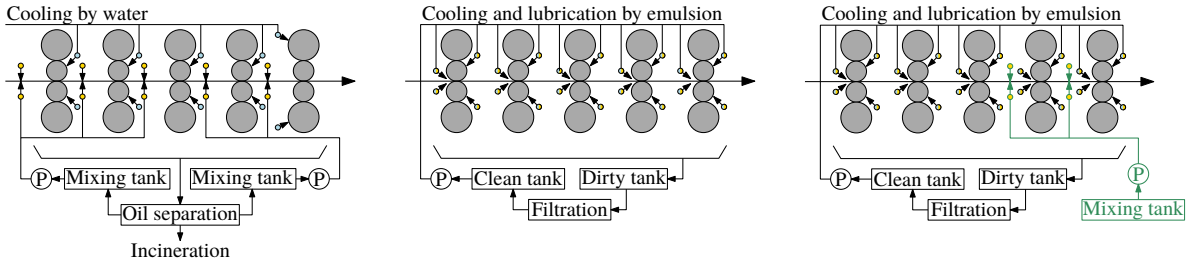

(a) Direct application system. **(b)** Recirculating system. **(c)** Hybrid/flexible system.

Figure 2.9: Different lubrication systems in cold rolling [167].

Direct application lubrication systems (Fig. 2.9a) apply an unstable O/W emulsion with a high oil concentration (5 - 15%) at a certain distance, i.e. about 1 m, from the roll bite to the strip [167]. The mill and the strip are cooled by a water cooling system, which is indepentent of the lubrication system [276, p. 387]. The emulsion in direct application systems is unstable to facilitate the oil film formation on the strip by adding no emulsifier or only a small quantity. This film formation process is explained by the plate-out theory (Sec. 2.2.4.1). Direct application lubrication systems are used for resistant thin gauge high-speed rolling because of the efficient lubricant film formation. In fact, the rolling mill with the highest rolling speed of around 2800 m/min is lubricated by a direct application system [280]. The disadvantage of these systems is that the emulsion cannot simply be reused since the oil separates from the water because of its unstable nature. Hence, the oil consumption and the resulting waste volume is significant.

Recirculating lubrication systems (Fig. 2.9b) use stable O/W emulsions with a low concentration of oil (1 - 3%) as a lubricant and coolant [167, 276, p. 389]. Stable emulsions have the benefit of being reusable since the oil droplets are maintained even after recirculated use. While recirculating systems generate less waste emulsion than direct application systems, their ability to supply the oil to the roll bite is, however, inferior to that of direct application systems, especially in high-speed rolling. Oil film formation by recirculating systems is described by the dynamic concentration theory, which is briefly explained in Sec. 2.2.4.1. A conventional recirculating system typically reduces the coefficient of friction $\overline{\mu}$ of dry rolling from about 0.12 to $\overline{\mu} \in [0.025, 0.065]$ [179, 276].

Hybrid lubrication systems (Fig. 2.9c) were first introduced in the 1980's by Muramoto et al. [242] according to Kimura et al. [167] by combining direct application and recirculating lubrication systems, although earlier undocumented implementations of these systems can be expected. Hybrid lubrication systems are a technological solution of the *flexible lubrication concept* by

Laugier et al. [183] according to which friction is controlled via the lubrication at the three process time scales, i.e. the rolling campaign, for each coil and in transient states between coils, to reach the objectives of the previous section. Therefore, special direct application systems are added to conventional recirculating systems (Fig. 2.10), especially in the last stands, where rolling conditions are more severe than in the preceding stands [86, p. 8]. These direct application systems are special in the sense that the oil quantity, which they provide to the strip, can be adjusted either by changing the flow rate of the emulsion or the concentration of oil in the emulsion. They are expected to reduce the coefficient of friction to $\overline{\mu} \in [0.020, 0.035]$ [182] in order to roll AHSS strips with the desired final thickness. Lubrication conditions such that $\overline{\mu} \in [0.010, 0.015]$ were already reached for different materials [167]. By eliminating chatter through controlled friction via the lubrication, such a system allowed, for instance, to consistently reach a rolling speed of 2100 m/min for T4CA grade strip rolling in a five-stand tandem mill [110, 167].

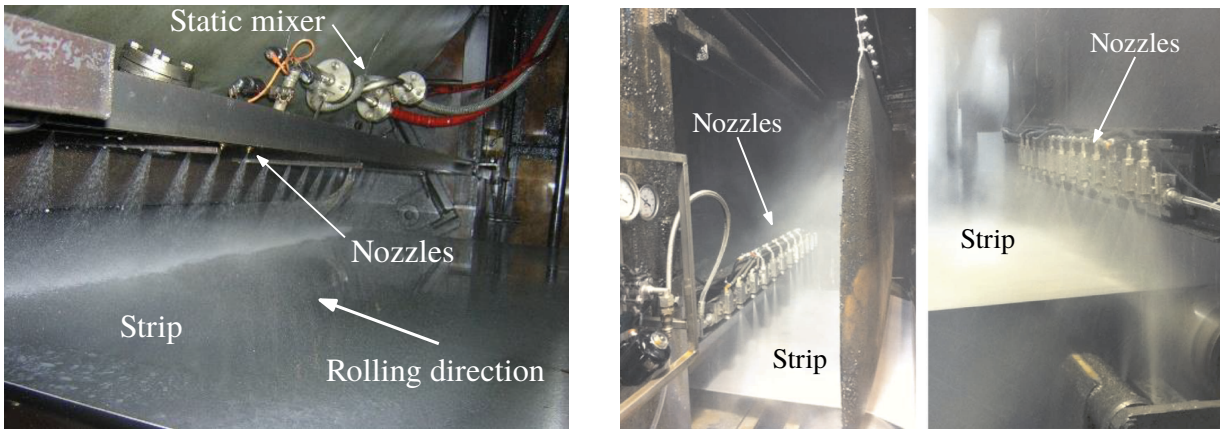

(a) Flexible lubrication industrial pilot (FLIP) tested at stand 4 of the tandem mill in the Sagunto facility of ArcelorMittal from mid 2010 until mid 2011 [183].

(b) Flexible lubrication system installed in september 2011 at the first and third stand of the 4-stand tandem mill at Tilleur by ArcelorMittal [54].

Figure 2.10: Illustration of implemented flexible lubrication systems.

The introduction of flexible lubrication systems inevitably leads to the question *which values lubrication parameters* (oil concentration in the emulsion, spray conditions of the emulsion, oil viscosity, ...) should take to *minimize friction while preventing skidding and chatter for given rolling conditions* (strip format, strip material, surface characteristics of the strip and the rolls, mill stand technology, ...). This question can be answered by *experimental testing* and by *numerical models*, which are a necessity due to the important number of parameters in cold rolling. For this reason, the physics of friction is introduced, and friction modeling in lubricated cold rolling is reviewed in the following sections.

2.2 Physics of friction

As explained previously, friction is an essential component of the rolling process. More precisely, friction is "the resisting force tangential to the common boundary between two bodies when, under

the action of an external force, one body moves or tends to move relative to the surface of the other" [250]. Over time, numerous theories and models have been developed to understand and to predict this force. In this section, they are introduced to ultimately model friction in lubricated cold rolling.

First, some concepts about the *characterization of solid surfaces* are defined. When these surfaces interact their geometry changes. Hence, *asperity flattening* is described in the second section. This mechanism influences *friction*, which is reviewed without a lubricant in the third section and, finally with a *lubricant* in the context of cold rolling in the last section.

2.2.1 Characterization of solid surfaces

Although solid surfaces in metal forming usually appear to be homogeneous and smooth at the macro-scale, they are heterogeneous and rough at the micro-scale [281]. On the one hand, Fig. 2.11 illustrates the *material heterogeneity* that usually exists at the tool-workpiece interface. It consists of a work hardened surface layer due to previous processing steps, as well as a relatively hard and brittle oxide film with an adsorbed film due to chemical and physical interactions with air, its humidity and lubricants.

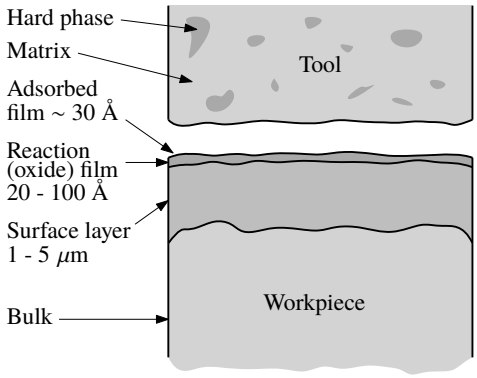

Figure 2.11: Tool-workpiece interface at the micro-scale according to Schey [281, p. 28].

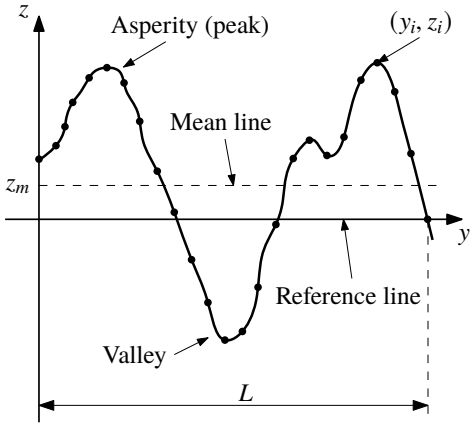

Figure 2.12: Surface roughness profile $z(y)$ with measurement points (y_i, z_i).

On the other hand, the tool and workpiece have a *geometrical surface* with peaks, which are called *asperities*, and valleys. Numerous methods to characterize them are described in the literature, see e.g. [31, 221].

2.2.1.1 Amplitude parameters

Amplitude parameters are introduced to characterize the height of rough surfaces with respect to a reference plane. If a surface roughness profile, like the one in Fig. 2.12, is measured with a

profilometer, the following amplitude parameters can be defined:

- *Arithmetical average roughness* R_a:

$$R_a = \frac{1}{L}\int_0^L |z - z_m|\,\mathrm{d}y \quad \text{or, for discrete measuring points,} \quad R_a = \frac{1}{N}\sum_{i=1}^{N} |z_i - z_m| \tag{2.7}$$

  where L is the sampling length of the profile, N the number of discrete equidistant measuring points along y and z_m the vertical coordinate of the mean line, which is assumed to be zero hereafter:

$$z_m = \frac{1}{L}\int_0^L z\,\mathrm{d}y \quad \text{or, for discrete measuring points,} \quad z_m = \frac{1}{N}\sum_{i=1}^{N} z_i \tag{2.8}$$

- *Root-mean-square roughness* R_q:

$$R_q = \sqrt{\frac{1}{L}\int_0^L z^2\,\mathrm{d}y} \quad \text{or, for discrete measuring points,} \quad R_q = \sqrt{\frac{1}{N}\sum_{i=1}^{N} z_i^2} \tag{2.9}$$

2.2.1.2 Surface height distribution function

Besides the amplitude parameters, the surface roughness can be described by probability density functions. In fact, if the height of a surface is a random variable Z, the probability density function of Z, which is also known as the *height distribution function* $f_Z(z)$, can be integrated to determine the probability of the surface having a height between z_a and z_b [31, p. 30]:

$$\Pr\left[z_a \leq Z \leq z_b\right] = \int_{z_a}^{z_b} f_Z(z)\,\mathrm{d}z \tag{2.10}$$

The height distribution function of an asperity profile with *triangular asperities* (Fig. 2.13) is given by the following equation (Fig. 2.14), as shown in appendix A:

$$f_Z(z) = \begin{cases} \dfrac{1}{2\sqrt{3}R_q} & \text{, if } z \in [-\sqrt{3}R_q; \sqrt{3}R_q] \\ 0 & \text{, otherwise.} \end{cases} \tag{2.11}$$

Moreover, the *Christensen height distribution* function was introduced to approximate the Gaussian height distribution with a finite support (Figs. 2.13 and 2.14), i.e. $z \in [-3R_q; 3R_q]$ [77]:

$$f_Z(z) = \begin{cases} \dfrac{35}{96R_q}\left[1 - \left(\dfrac{z}{3R_q}\right)^2\right]^3 & \text{, if } z \in [-3R_q; 3R_q] \\ 0 & \text{, otherwise.} \end{cases} \tag{2.12}$$

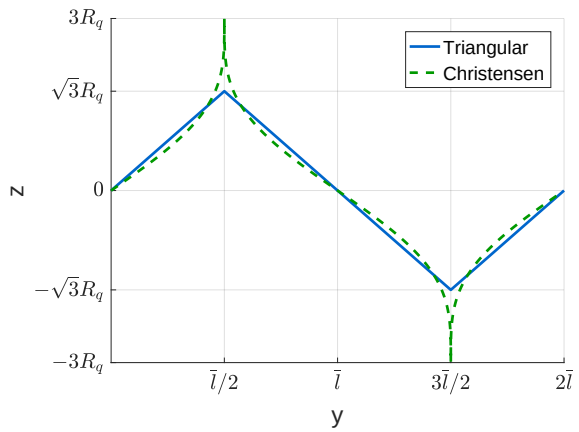

Figure 2.13: Triangular asperity profile and profile with a Christensen height distribution. The variable $\bar{l}$ denotes the half spacing between asperities, which will be introduced in Eq. (4.89).

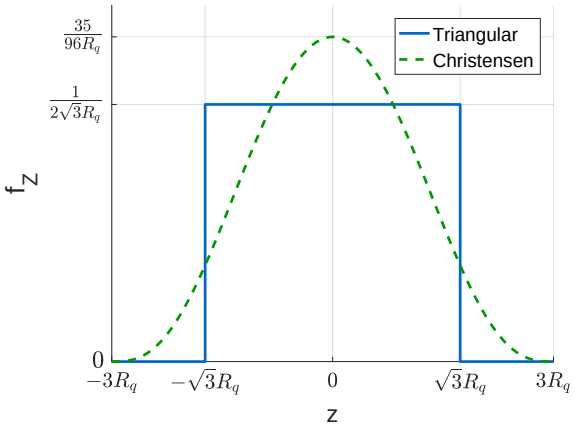

Figure 2.14: Surface height distribution function of a triangular asperity profile and the Christensen height distribution function.

The coordinate of the mean line z_m as well as the amplitude parameters R_a and R_q can also be computed on the basis of the surface height distribution function [31, p. 26]:

$$z_m = \int_{-\infty}^{+\infty} z f_Z(z)\,\mathrm{d}z; \qquad R_a = \int_{-\infty}^{+\infty} |z - z_m|\, f_Z(z)\,\mathrm{d}z; \qquad R_q = \sqrt{\int_{-\infty}^{+\infty} z^2 f_Z(z)\,\mathrm{d}z} \tag{2.13}$$

2.2.1.3 Composite roughness

The *composite roughness* of two rough surfaces, like those of the roll Z_r and the strip Z_s, can be defined as the sum of the random variables, which represent their height, i.e. $Z = Z_r + Z_s$. If $R_{q,r}$ and $R_{q,s}$ are the root-mean-square roughness of the roll and the strip, and if Z_r and Z_s are *uncorrelated*, their composite root-mean-square (RMS) roughness is given by the following equation (appendix B) [31, p. 44]:

$$R_q = \sqrt{R_{q,r}^2 + R_{q,s}^2} \tag{2.14}$$

2.2.2 Asperity flattening

Due to their roughness, solid surfaces first enter into contact at the highest points and the contact patches then usually grow depending on different asperity flattening mechanisms as shown in Fig. 2.15. Hence, the *real area of contact* A_r, which is the area of the projected contact patches on a reference plane, is not necessarily equal to the *apparent area of contact* A_a. The reference plane is parallel to the mean plane of the asperity surfaces, which is the extension of the mean line concept from an asperity profile to a surface (Sec. 2.2.1). The contact level is characterized by the *relative area of contact* A, which is also called the contact ratio or the fractional area of contact:

$$A = A_r / A_a \tag{2.15}$$

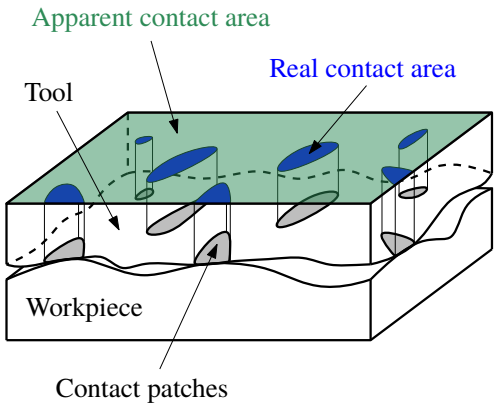

Figure 2.15: Contact patches between rough contacting surfaces with their projection onto the horizontal plane to define the real contact area with respect to the apparent contact area.

Asperity flattening is essentially due to three mechanisms, which are not mutually exclusive: normal loading, deformation of the underlying bulk material and sliding. One should also notice that the real area of contact might decrease under certain conditions due to a lubricant or surface roughening. These mechanisms and the corresponding models are briefly explained and reviewed since friction depends on asperity flattening. Detailed reviews can be found in the theses by Westeneng [358] and Carretta [54].

2.2.2.1 Flattening due to normal loading

When a force F_n pushes rough surfaces together in the normal direction to the interface, the relative contact area A increases until the real contact area A_r is sufficient to support the load. Electrical resistance measurements by Bowden and Tabor [45] showed essentially a linear relationship between the real contact area and the load. Hence, it was initially assumed that asperities deform *plastically* such that $A_r = F_n/H$ where $H \approx 3\sigma_Y$ is the penetration hardness and σ_Y the yield stress of the softer material [324].

Although the linear relationship between A_r and F_n could first not be explained by the *elastic* contact theory of Hertz [138], it was later shown to be possible when the number of contact spots increases with the load by Archard [11]. Thus, this proportionality is not necessarily due to the plasticity but also the *statistics of surface roughness* with possible elastic contact.

In one of the most popular *asperity flattening models due to normal loading*, i.e. the model by Greenwood and Williamson [125], the *interaction of flattened asperities* was not included. Later on, it was, however, shown by Pullen and Williamson [264] that the relative contact area A increases only linearly with the normal load F_n at small loads and that it becomes less than proportional to F_n at higher load, when the asperties of a specimen in a rigid holder are flattened (Figs. 2.16 and 2.17). This *persistence effect of asperities*, which allows them to support greater contact pressure than their hardness, was explained by their interaction via plastic incompressibility [48, 49] that *rises the surface valleys almost uniformly*, when the asperities are flattened.

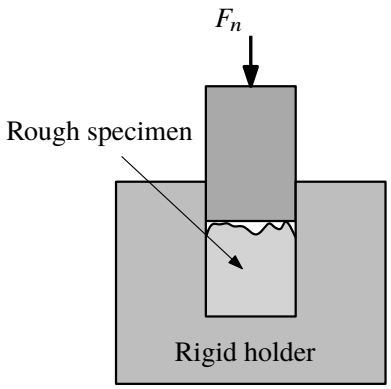

Figure 2.16: Flattened surface of a specimen in a rigid holder, which prevents bulk deformation [264].

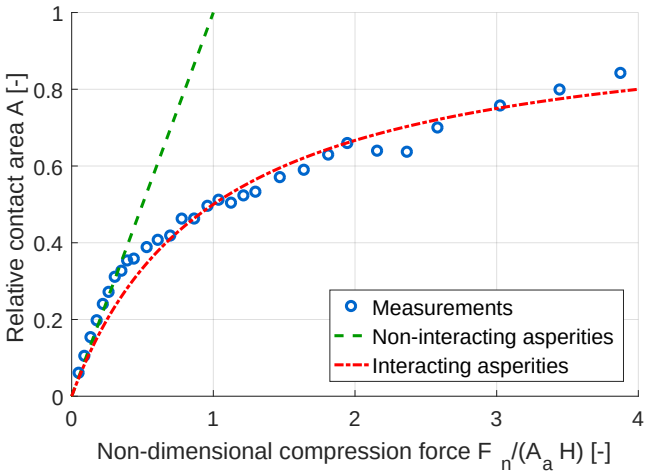

Figure 2.17: Measured relation between the non-dimensional compression force $F_n/(A_a H)$ and the relative contact area A, as well as predictions by models with non-interacting or interacting asperities according to [264].

The *finite element method* finally allowed to simulate asperity flattening due to normal loading of arbitrarily shaped surfaces with complex material models: rigid-viscoplastic plane-strain indentation of a smooth strip surface by a roll with triangular asperities in a rolling model [164, 165], elastic flattening in 3D [151] and elastoplastic flattening in 3D [255].

2.2.2.2 Flattening due to underlying bulk deformations

If the underlying bulk material below asperities is deformed, for instance, by applying tension to normally loaded rough specimens as illustrated in Fig. 2.18, asperity flattening increases with this deformation [124]. Experimental measurements by Fogg [106] in Fig. 2.18 illustrate the increase of the relative contact area with the tension σ.

Asperity flattening with normal load and underlying bulk deformation seems first to have been modeled successfully by Wilson and Sheu [367] via the *upper bound method* with roughness grooves parallel to the direction of bulk deformation. Sutcliffe [311] shortly afterwards modeled this flattening mechanism by the *slip-line field theory* with roughness grooves perpendicular to the direction of bulk deformation.

Flattening by the combined effect of normal loading and underlying bulk deformations was later predicted by numerous *finite element models*. First, Makinouchi et al. [212] flattened three triangular asperities with an elastoplastic material law by a flat frictionless die in the plane-strain state. Later on, Korzekwa et al. [169] generalized the existing theories, in particular those of Wilson and Sheu [367] and Sutcliffe [311], by simulating viscoplastic asperity flattening as a function of the straining direction with respect to the orientation of the roughness grooves, without strain hardening. More complex asperity profiles were then simulated by flattening

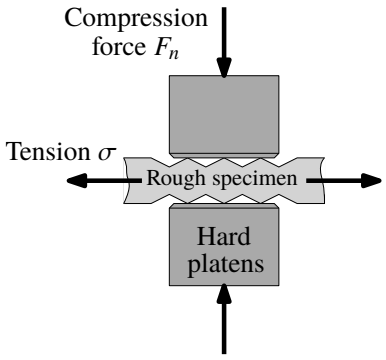

Figure 2.18: Compression of rough specimen by a force F_n with applied tension σ [106].

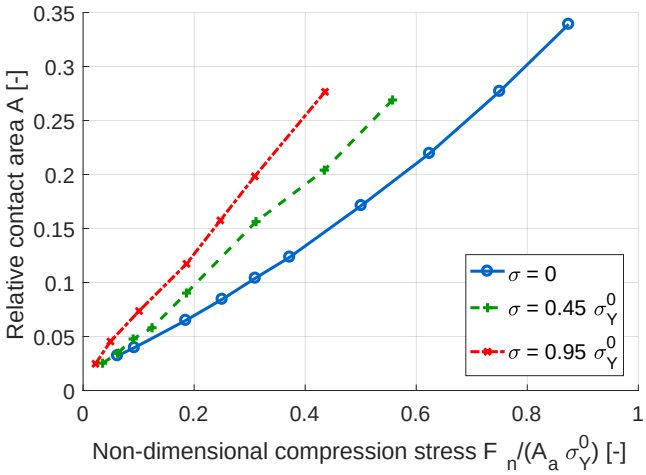

Figure 2.19: Experimental measurement of the relative contact area as a function of the normal compression force F_n for different tensions σ based on Fig. 42.11 in [106]. The variables A_a and σ_Y^0 denote the apparent contact area and the initial yield stress of the specimen.

profiles with up to three-wavelengths of triangular asperities [209, 210]. Recently, Nielsen et al. [248] validated elastoplastic FE asperity flattening simulations with bulk deformation and strain hardening experimentally.

Asperity flattening in the context of cold rolling was simulated by Carretta et al. [54, 56, 57, 61] using the non-linear finite element solver Metafor (Sec. 6.2.2.1). In particular, he simulated the flattening of an asperity profile, which was extruded along the rolling direction to 3D, by a rigid plane and by bulk deformations via tension along this direction (Fig. 2.20).

Since finite element models are usually costly, especially if the complexity of the geometry increases, Westeneng [358] developed an *asperity flattening model based on bars* with non-linear work hardening to reduce the computational cost of the discretization.

2.2.2.3 Flattening due to shear stresses

Flattening due to shear stresses was introduced by McFarlane and Tabor [219] to explain the increase of friction during sliding of clean metals. This mechanism is called *junction growth* [325]. More precisely, if a 2D asperity deforms plastically when it is in contact with a rigid surface, it has to satisfy the Von Mises yield criterion [219] (Fig. 2.22):

$$p_a^2 + 3\tau_a^2 = \sigma_Y^2 \tag{2.16}$$

where p_a, τ_a and σ_Y are the contact pressure and the shear stress on top of the asperity, as well as the yield stress, respectively. If the shear stress τ_a increases due to a rising tangential force F_t, the pressure p_a has to decrease to satisfy the previous equation. Hence, the real contact area increases by plastic flow, if the normal force $F_n = A_r p_a$ remains constant.

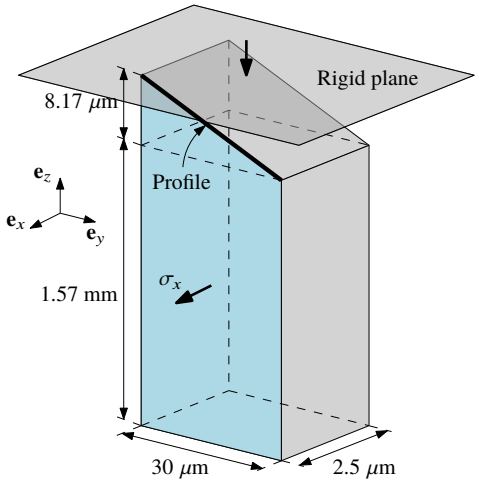

Figure 2.20: Flattening of an asperity profile (extruded to 3D along the rolling direction $\mathbf{e}_x$) by a downwards moving plane and the bulk deformation due to the applied tension σ_x [54].

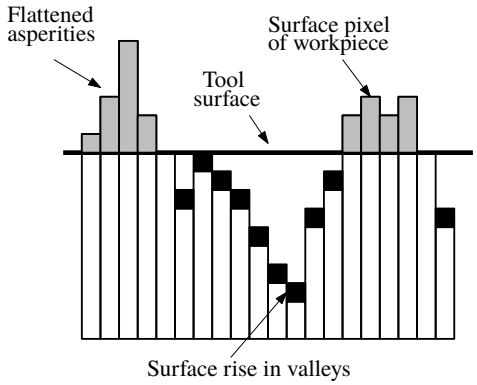

Figure 2.21: Asperity flattening model based on bars that discretize the workpiece surface [358]. When asperities are flattened the surface in the valleys has to rise due to volume conservation [264].

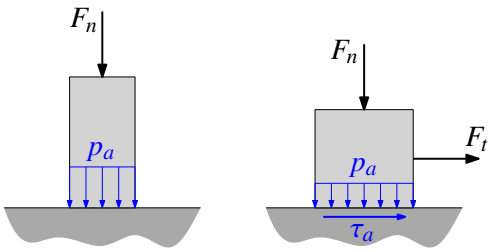

Figure 2.22: Increase of the real contact area due to shear stress, when an asperity is pushed against another surface.

2.2.2.4 Influence of a lubricant on asperity flattening

In the context of asperity flattening, a *lubricant* has essentially two influences: on the one hand, it separates the contacting solid surfaces and on the other hand, it enables free surface roughening.

The *resistance to asperity flattening due to the lubricant* was included in flattening models by reducing directly the interface pressure p_i by the lubricant pressure p_l to compute the pressure on top of the asperities $p_a = p_i - p_l$ [144, 147, 245], by considering the lubricant pressure in the analytical equilibrium equation at the interface [367] or via hydrostatic elements in finite element models [12]. Recently, Shvarts and Yastrebov [290] modeled asperity flattening in the presence of a Poiseuille flow from a pressure p_{in} to a pressure p_{out} through a wavy channel, that separates an elastic solid from an rigid flat tool, which is pushed against it, with the help of the FE method.

Besides preventing asperity flattening, the lubricant can also permeate into the interface between contacting surfaces at sufficiently high pressure and thus reduce the relative contact area. Such micro-plasto-hydrodynamic or hydrostatic effects and the corresponding models are described in Sec. 2.2.4.3.

Surface roughening is due to the crystalline structure of metals whose free surfaces tend to roughen, when the bulk is deformed plastically. The same is true when surfaces are in contact with a lubricant film since this film acts as a cushion, that allows the emergence of grains at the surface of the workpiece unlike the contact with a hard die [204, 279, 281].

2.2.3 Dry friction

Before considering friction with a lubricant, friction and the most influential models in the literature are briefly explained when no lubricant is intentionally applied. This condition is called *dry friction* [281, p. 30]. A recent overview of friction modeling in metal forming processes was compiled by Nielsen and Bay [247].

Friction was first mentioned in the scientific literature by Amontons [8] and Coulomb [85], who suggested that the friction force F_t is proportional to the normal force F_n (*Amontons' first law*, also known as *Coulomb's law*):

$$F_t = \mu F_n \tag{2.17}$$

where μ is the coefficient of friction. Coulomb explained the existence of this force by the interlocking of surface asperities. It was, however, shown that friction still existed, when the contacting surfaces were very smooth. This led to the publication of the *adhesion theory of friction* by Holm [148], Ernst and Merchant [99] and Bowden and Tabor [46, 47] according to which strong atomic forces between interfaces exist where *surface films* (Sec. 2.2.1) are broken through and direct metal-to-metal junctions are created [281, p. 34].

The combination of this theory with *asperity flattening* (Sec. 2.2.2) then allowed to explain why the friction force is independent of the apparent area of contact (*Amontons' second law*), why friction increases during sliding of clean metals (junction growth, Sec. 2.2.2.3) and why the

friction stress becomes at most equal to the shear yield stress of the bulk material, when the normal force increases. This last friction mode is called *sticking friction* [252, 283].

Hence, dry friction can be explained by adhesion and the mechanical interaction of asperities, e.g. plowing of the softer surface by the harder surface in the presence of contaminant films that are penetrated at least by some asperities [46]. More elaborate dry friction models than Coulomb's law with a constant coefficient of friction are reviewed in appendix C.

2.2.4 Friction in lubricated cold rolling

As mentioned in Sec. 2.1.3, lubricants are mainly introduced in cold rolling to minimize friction. In this section, it is briefly explained *how* the lubricant influences friction. First, the *mechanisms of oil film formation* are described. Then, the rolls-strip-lubricant interaction in the roll bite is characterized by introducing different *lubrication regimes and mechanisms*. And finally, *micro-plasto-hydrodynamic/static lubrication* is highlighted separately due to the recent interest in modeling this phenomenon and its potential benefit for the cold rolling industry.

2.2.4.1 Mechanisms of oil film formation

As mentioned previously in Sec. 2.1.3, oil is provided to the roll bite in its pure form or in oil-in-water emulsions via direct application systems, recirculating systems or combinations of these systems. A significantly smaller quantity of oil can be returned to the entry of the roll bite from its exit by the roll surface depending on the wash-off by cooling water jets and wiping by the backup rolls.

The oil film formation by direct application and recirculating systems are generally explained by the *plate-out* and *dynamic concentration theories*, respectively, which are thoroughly analyzed in the thesis by Cassarini [63].

Plate-out theory

The *plate-out theory*, which was proposed by Roberts [275, p. 103] according to Kimura et al. [167], consists in the oil film formation on the strip due to its lipophilic surface when oil droplets in O/W emulsions are projected onto the strip (Fig. 2.23).

Experimental investigations showed that the applied oil film increases when the oil concentration in the emulsion increases, when the oil droplet size increases, when air atomizing nozzles are used and when the elapsed time after spraying and before entering the roll bite increases, which explains the distance between the nozzles and the bite (Fig. 2.23) [109, 167]. From a *numerical* stand point, a 3D CFD model of emulsion droplets impacting a moving strip was developed by Guillaument et al. [128, 129] to determine the oil film thickness. This model suggests that plate-out depends more significantly on the ballistics of the droplets than on the elapsed time after spraying. The computation time amounts, however, to several days on hundreds of CPUs to simulate a small fraction of a second (e.g. 360 hours on 512 CPUs to simulate 50 ms, [128, p. 109]).

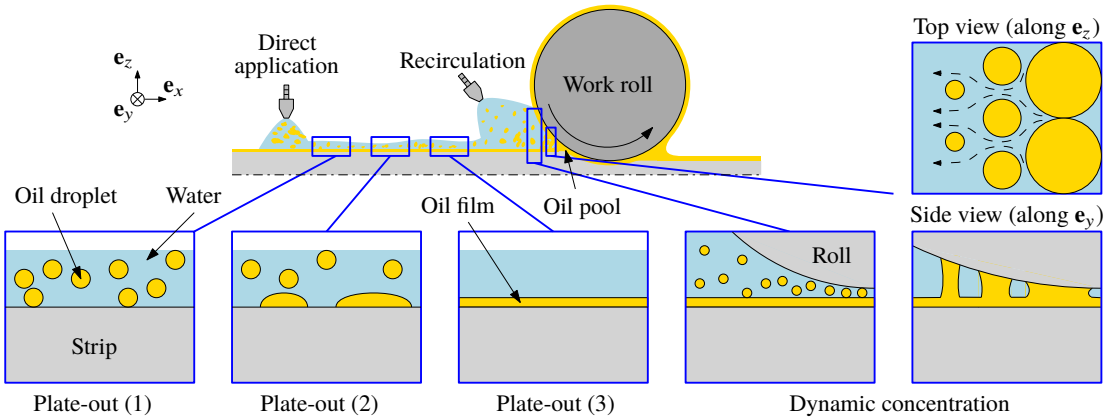

Figure 2.23: Mechanisms of oil film formation. Far from the roll bite, the direct application systems creates an oil film by the plate-out mechanism, i.e. when more and more droplets come into contact with the lipophilic strip. In the convergent near the bite, the oil film is created by dynamic concentration: when droplets are small compared to the film thickness, the model by Szeri [321] describes the film formation, while the theory by Wilson et al. [365] applies when the droplet size becomes similar to the distance between the roll and the strip. Due to the greater viscosity of oil, water is pushed out of the entry zone of the roll bite.

Dynamic concentration theory

The *dynamic concentration theory* was introduced by Wilson et al. [365, 366] to explain how significantly thicker lubricant films can be created by O/W emulsions with low oil concentrations than by pure water. This explanation is based on the idea that oil droplets are in general greater than the film thickness inside the bite. Thus, when the space between the roll and the strip decreases at the entry of the bite, the oil droplets, which are carried to the bite by the water, are flattened and they take a column-like form in contact with the lipophilic surfaces of the roll and the strip as shown in Fig. 2.23 (dynamic concentration, right). Due to the greater viscosity of the oil, the water is pushed more easily out of the bite, where the concentration of oil increases. Hence, this theory explains the formation of an oil pool at entry of the bite, if more oil is provided to the roll bite than it can absorb; otherwise, starvation occurs [63] (Sec. 2.1.3). Furthermore, it explains why the oil almost exclusively enters into the bite, if the rolling speed is not high enough to entrain water, too [380].

Cassarini [63] combined the plate-out theory with the dynamic concentration theory by Wilson et al. [365] and the theory by Szeri [321], which considers the oil droplets to be significantly smaller than the film thickness. This last hypothesis is, in fact, reasonable at the entry of the bite as shown in Fig. 2.23 (dynamic concentration, left). More recently, Lo et al. [202] developed an analytical model, which was later included in a rolling model [203], for oil-in-water emulsions based on CFD simulations of dynamic concentration.

2.2.4.2 Lubrication regimes and mechanisms

Depending on the mean lubricant film thickness h_t in the roll bite with respect to the roughness of the roll and the strip, i.e. classically, the composite root-mean-square (RMS) roughness R_q (Eq. 2.14), different lubrication regimes can be defined [14, 281, 361]. Since different lubrication mechanisms are dominant in these regimes, the evolution of the coefficient of friction with the film thickness changes from one regime to another. This behavior is generally illustrated by the *Stribeck curve* (Fig. 2.24), which represents the coefficient of friction as a function of the parameter $\eta v/p_i$ where η, v and p_i are the dynamic viscosity, the sliding speed and the normal interface pressure, respectively.

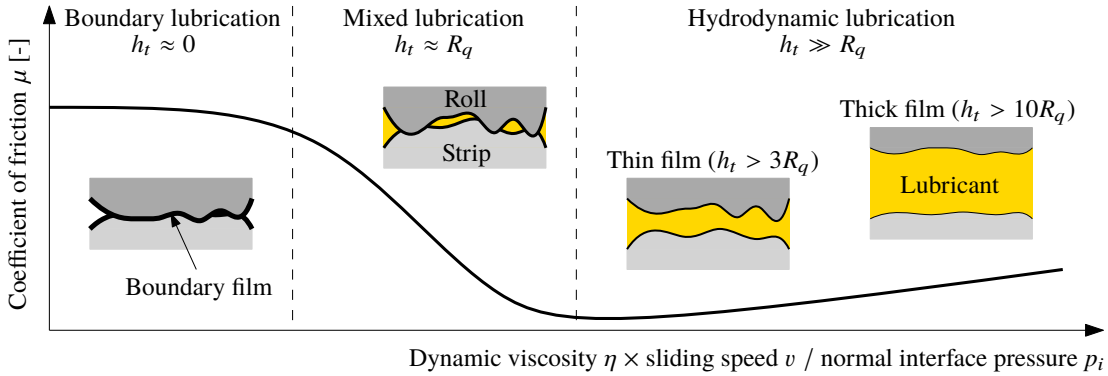

Figure 2.24: Stribeck curve with different lubrication regimes, in which the coefficient of friction changes due to different dominant lubrication mechanisms.

The different lubrication regimes and the respective dominant lubrication mechanisms are explained in the following sections.

Hydrodynamic lubrication regime

In the *hydrodynamic lubrication regime* no contact exists between the solid interfaces, e.g. the roll and the strip, since the lubricant film thickness is significantly greater than the amplitude of the roughness. Hence, the load is entirely supported by the lubricant film. In the literature, one distinguishes thick film lubrication ($h_t > 10R_q$) from thin film lubrication ($3R_q < h_t < 10R_q$), in which the asperities have a noticeable influence on the lubricant flow [361].

Hydrodynamic lubrication is generally modeled by the *Reynolds equation* [273] (Sec. 4.8.1), either with or without *flow factors*, which are included to take into account the influence of the roughness on the lubricant flow [200, 253, 254, 363, 364]. The Reynolds equation quantifies the mechanism of hydrodynamic lubrication, i.e. the increase in lubricant pressure when a viscous fluid is entrained into a convergent space between two surfaces, as in rolling. The increase of the coefficient of friction with the sliding speed in the hydrodynamic regime in Fig. 2.24 is due to increasing viscous friction forces.

A *prediction of the film thickness* $h_{l,\mathrm{iw}}$ at the transition from the inlet zone to the work zone of the roll bite, where the strip starts to deform plastically (Sec. 4.10.1), was derived by Wilson

and Walowit [368]. It is based on the Reynolds equation in thick film lubrication and on the assumption of full-flooded lubrication by an isoviscous or piezoviscous lubricant according to the Barus equation (Eq. 4.192), respectively (appendix D):

$$h_{l,\mathrm{iw}} = \frac{3\eta_0(v_{\mathrm{in}} + v_r)R_0}{\sigma_Y^0\, l_{\mathrm{rb}}} \qquad \text{or} \qquad h_{l,\mathrm{iw}} = \frac{3\eta_0(v_{\mathrm{in}} + v_r)\gamma_l R_0}{\left[1 - \exp\left(-\gamma_l\, \sigma_Y^0\right)\right] l_{\mathrm{rb}}} \tag{2.18}$$

where η_0 is the dynamic viscosity of the lubricant at the reference pressure, v_{in} the speed of the strip at the entry of the bite, v_r the rolling speed, R_0 the roll radius, σ_Y^0 the initial yield stress of the strip, l_{rb} the length of the roll bite (Eq. 2.4) and γ_l the pressure-viscosity coefficient (Eq. 4.192). Since these equations are based on the assumption of full-flooded lubrication, they provide a threshold value of the lubricant film thickness provided by the lubrication system, above which starvation does not occur and above which flexible lubrication can therefore not operate. This clearly illustrates that flexible lubrication depends on numerous parameters, even in a relatively simple model.

Hydrodynamic lubrication is usually not desired in cold rolling of steel for two reasons. On the one hand, only *low friction* forces are created by hydrodynamic lubrication. Hence, the strip could easily skid in the roll bite and the occurence of chatter is facilitated [235]. On the other hand, surface roughening can occur due to the relatively thick lubricant film as explained in Sec. 2.2.2.4. Roughening strongly affects the *surface appearance* of the strip, i.e. that the brightness decreases when the roughness increases [14].

When the hydrodynamic lubrication mechanism is influenced by elastic deformations of the surface or the increase of the lubricant viscosity due to pressure, the lubrication mode is known as *elasto-hydrodynamic lubrication* [381]. In cold rolling, elastic deformations are, however, small with respect to plastic deformations, which is why, this lubrication mode is rather called *plasto-hydrodynamic lubrication* in this context [232], or *macro-plasto-hydrodynamic lubrication* at the bulk level [14] to contrast with *micro-plasto-hydrodynamic lubrication* at the asperity level (Sec. 2.2.4.3).

Boundary lubrication regime

In the *boundary lubrication regime* [134], the surfaces of the roll and the strip are in contact without the lubricant acting as a pressure cushion. Hence, the load is essentially carried by the contacting surface asperities, which are only separated by a very thin boundary film (Fig. 2.24). This means that friction forces are relatively significant. The boundary film generally consists of some molecular layers of physically adsorbed or chemically reacted organic compounds, like those in the lubricant [14, 281].

Boundary friction is usually *modeled* like dry friction due to adhesion and plowing (Sec. 2.2.3). The complexity of adhesion in the presence of the boundary film is then hidden in the friction factor $\mu_T = \tau_{Y,a}/\tau_Y$, which quantifies the shear strength of the interface at the top of the asperities with respect to the yield shear stress of the bulk material, if asperity flattening is simulated, e.g. [144]. Otherwise, this complexity is hidden in the Coulomb coefficient μ_C, see e.g. [215].

Mixed lubrication regime

In the *mixed lubrication regime*, forces between surfaces are transmitted partially by the contact between their asperities and partially by the lubricant (Fig. 2.24). This regime is thus a trade-off between the hydrodynamic and the boundary regimes, which provides enough friction to pull the strip in between the rolls while limiting undesired consequences of significant friction forces, like excessive rolling loads and roll wear. Hence, metal strips are cold rolled in the mixed lubrication regime.

Besides macro-plasto-hydrodynamic lubrication and boundary lubrication, *hydrostatic lubrication* is an additional mechanism in the mixed lubrication regime, which occurs when some lubricant gets trapped and compressed in pockets (or valleys) of contacting rough surfaces [14, 172]. When this lubricant of the pockets permeates into the real contact area due to compression, this lubrication mechanism is called *micro-plasto-hydrostatic lubrication*. If the reason of permeation is, however, hydrodynamics, i.e. the combined action of velocity and viscosity in a convergent space, this mechanism is called *micro-plasto-hydrodynamic lubrication*. These two mechanisms are explained more thoroughly in the following section.

2.2.4.3 Micro-plasto-hydrodynamic/static lubrication

Micro-plasto-hydrodynamic/static (MPH) lubrication is described in this section because of its possible capacity to increase production rates in cold rolling [180], if its occurrence and impact can be predicted systematically. Experimental observations and models of MPH lubrication are reviewed thoroughly by Azushima [13], by Bay et al. [23] and more recently, by Carretta [54].

In this section, the focus will be on the most significant *experimental observations*, the importance of *MPH lubrication in cold rolling* and the most popular *models of MPH lubrication*.

Experimental observations of MPH lubrication

In plane-strain compression-friction tests, Mizuno and Okamoto [222] observed that friction increased with the drawing speed and the viscosity of the lubricant, which is a known phenomenon in the hydrodynamic lubrication regime (Sec. 2.2.4.2), while surface pockets, that trapped the lubricant, became smaller. They named this phenomenon *micro-plasto-hydrodynamic lubrication* since it consists in the creation of a hydrodynamic lubrication regime at the micro-level of the asperities, which are plastically deformed by hydrodynamic shear stresses, thus allowing the lubricant to flow out of the surface pockets to contact regions, where boundary lubrication would otherwise prevail (Fig. 2.25).

The permeation of the lubricant into the contact zone was later confirmed by Azushima et al. [16] via a *sheet drawing* apparatus with a transparent quartz die, a microscope and a camera (Fig. 2.26). When a strip with pyramidal macro-indentations, which are filled with a lubricant, is pulled through the dies, the permeation of the lubricant into the contact zone around the indentation can be directly observed depending on the lubrication conditions. Similar experiments were

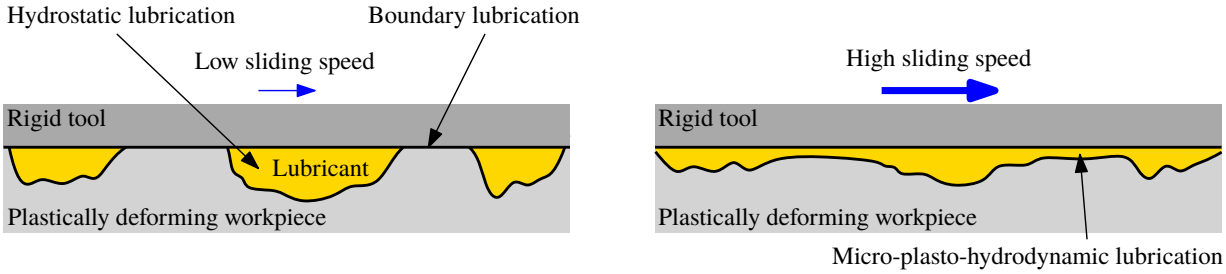

Figure 2.25: Schematic representation of changing lubrication conditions when the sliding speed increases. At low sliding speed, hydrostatic and boundary lubrication co-exist in the mixed lubrication regime. At higher sliding speeds, the lubricant, that was trapped in surface pockets, flows out of them and this creates a hydrodynamic film at the level of the asperities, which are plastically deformed by hydrodynamic shear stresses. Hence, micro-plasto-hydrodynamic lubrication occurs at higher sliding speeds [222].

carried out later on by Bech et al. [24, 25], who studied the influence of additional parameters on lubricant permeation (Fig. 2.27).

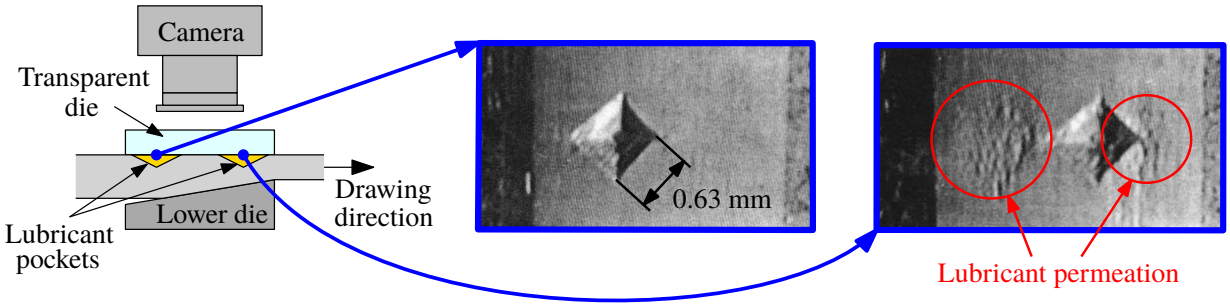

Figure 2.26: Schematic representation of the plane strip drawing set-up of Bech et al. [24] on the left. A similar set-up was used by Azushima et al. [16] to take the photographs on the right, which allow to observe the escape mechanisms of the lubricant from the pyramidal pockets of the strip [13].

As shown in Fig. 2.27, the lubricant can either permeate into the solid contact zone in front of or behind the pocket. Hence, *two different micro-plasto lubrication mechanisms* are defined [16, 24]. On the one hand, backward permeation can be explained by the lubricant pressure p_l becoming greater than the solid/solid contact pressure p_a at the end of the pocket due to hydrodynamic lubrication, i.e. the effect of viscosity and speed in the convergent space at the back of the pocket (Fig. 2.28). Therefore, backward permeation is caused by *micro-plasto-hydrodynamic lubrication (MPHDL)*. On the other hand, forward permeation occurs when the hydrostatic lubricant pressure in the pocket becomes greater than the solid/solid contact pressure at the front of the pocket (Fig. 2.28). Thus, this mechanism is called *micro-plasto-hydrostatic lubrication (MPHSL)*. While increasing the lubricant viscosity and the drawing speed favors MPHDL, increasing the back tension or the coefficient of friction (with respect to the bottom die in Fig. 2.26) favors MPHSL. The influence of numerous additional parameters, like the reduction, the pocket volume, the slope and the radius of curvature at the edges of the pockets, was studied by [24, 287, 295].

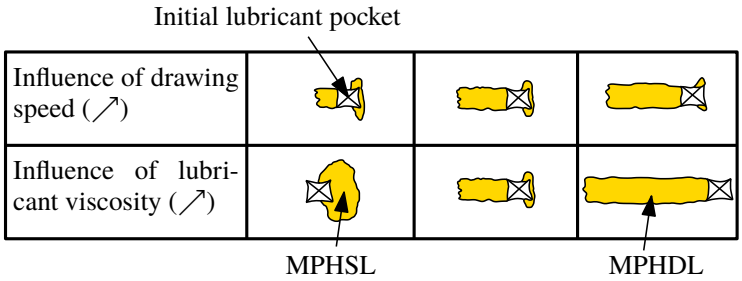

Figure 2.27: Influence of the drawing speed and the lubricant viscosity (increasing from left to right) on the permeation region by plane strip drawing experiments (drawing direction from left to right) of Bech et al. [24] with pyramidal indentations, that have a different orientation than those of Azushima et al. [16].

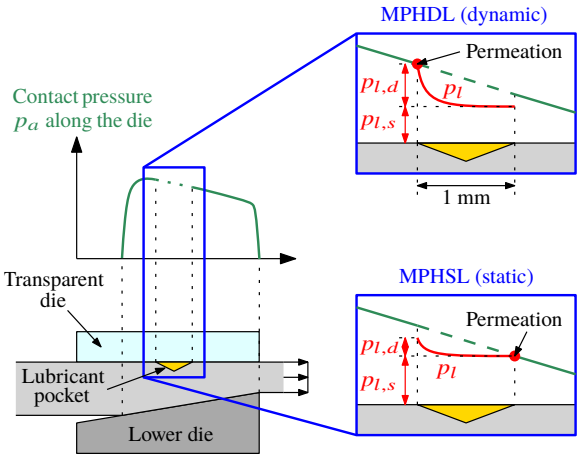

Figure 2.28: Explanation of MPH lubrication. In MPHDL, the hydrodynamic contribution $p_{l,d}$ of the lubricant pressure p_l becomes so important that the lubricant pressure becomes greater than the solid/solid contact pressure p_a. Hence, the lubricant flows out of the pocket at its back. In MPHSL, the hydrostatic contribution $p_{l,s}$ of the lubricant pressure p_l becomes greater than the contact pressure p_a at the front of the pocket, where the lubricant then permeates into the contact zone [16, 24].

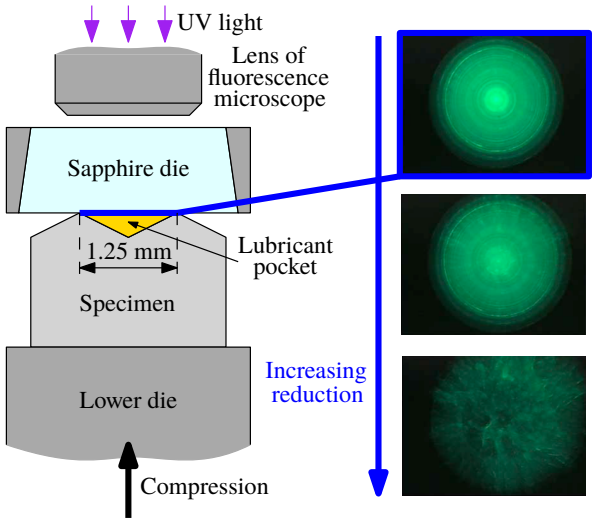

Figure 2.29: Permeation of the lubricant into the real contact zone in upsetting tests. A lubricant pocket in a metallic specimen is pushed by a bottom die against a transparent saphire die. The UV light causes the fluorescent dye in the lubricant to emit visible light, which can be observed by a microscope. When the thickness reduction of the specimen increases, the lubricant permeates into the real contact area as can be seen on the right, where the outline of the conical pocket becomes blurred [17].

Besides plane strip drawing, micro-plasto-hydrostatic lubrication was also investigated in the *upsetting of metals*, which consists in compressing billets between two dies with a lubricant pocket. Permeation of the lubricant into the real contact area due to the increase of hydrostatic pressure occured for significant reductions in this process [195]. In particular, Azushima et al. [17] observed directly the permeation by estimating the oil film thickness via light intensity measurements of a fluorescent dye in the lubricant (Fig. 2.29).

Up to this point, micro-plasto-hydrodynamic/static lubrication was essentially described for macro-indentations at the millimeter scale, which are filled with a lubricant, in plane strip drawing and upsetting experiments. Azushima and Kudo [15], however, also filmed the *contact interface of a rough lubricated surface* in contact with the smooth transparent quartz die of their strip drawing apparatus, which was explained previously. Fig. 2.30 shows how the bright solid contact zones initially grow before the lubricant permeates into the contact zones. This permeation is accompanied by a reduction of the measured coefficient of friction, since the normal load is increasingly carried by the lubricant.

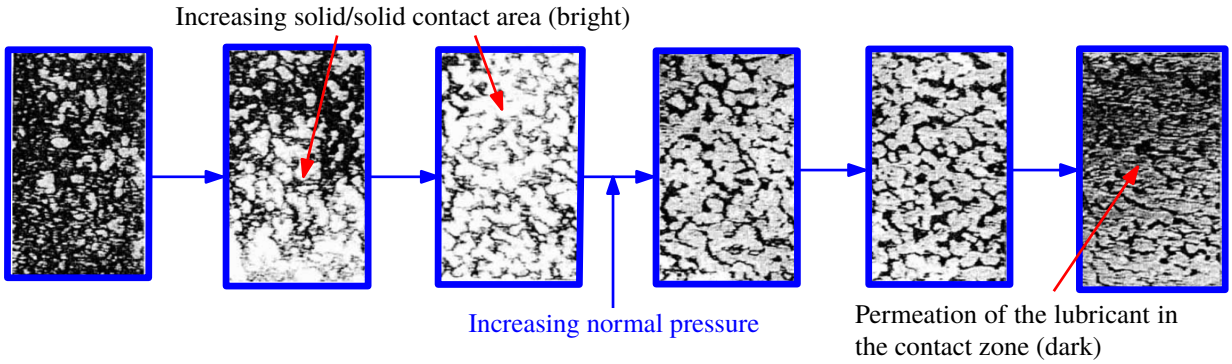

Figure 2.30: Photographs of a rough and lubricated workpiece surface that is pushed against a smooth transparent die by increasing normal pressure. Initially, the solid/solid contact zones (bright) grow and the lubricant gets trapped in between those zones (dark). At relatively significant pressure levels, some bright zones become dark, which suggests that the lubricant permeates into the contact zones with simulteanous free surface roughening [15].

Finally, the *occurrence of micro-plasto-hydrodynamic lubrication with respect to macro-plasto-hydrodynamic lubrication*, is studied by Ahmed and Sutcliffe [6] via strip drawing and rolling tests. They conclude that micro-plasto-hydrodynamic lubrication seems only to apply when macro-hydrodynamic lubrication is not too significant, so that the lubricant pockets are isolated instead of being connected by a hydrodynamic inlet film.

Importance of MPH lubrication in cold rolling

A *decrease of friction with increasing strip reduction was first observed in the context of cold rolling* at ArcelorMittal during the year 1998. For instance, Fig. 2.31 shows the decreasing back-calculated coefficient of friction with the reduction in the context of pilot mill trials. Similar

observations were made on an industrial tandem tin plate mill, especially on the last stands, where the sliding speeds and pressure gradients are most significant [180].

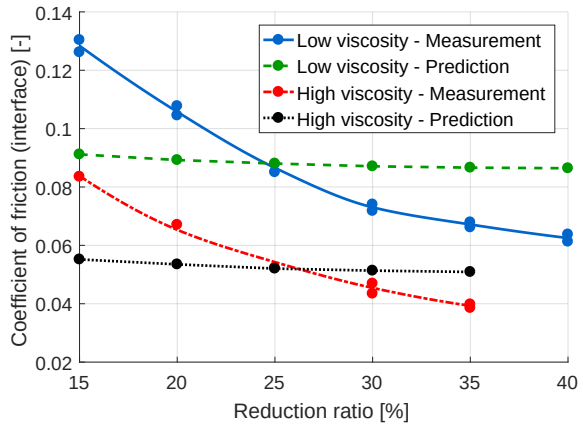

Figure 2.31: Decreasing back-calculated coefficients of friction (via rolling force and forward slip in rolling model with constant coefficient of friction) and almost constant predicted coefficients of friction in a rolling scenario with a low-viscosity oil (8 mPa.s) and a scenario with a high-viscosity oil (155 mPa.s): TRIP steel (yield stress of about 800 MPa), initial thickness 3.27 to 3.30 mm, strip width 75 mm, front tension 2000 kg, back tension 1200 kg, work roll diameter 480 mm, work roll roughness 0.6-0.7 μm, rolling speed 50 m/min, emulsion concentration 2.2% [180].

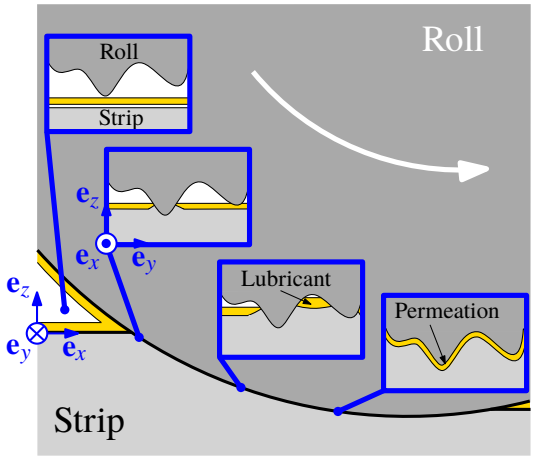

Figure 2.32: Schematic illustration of MPH lubrication in cold rolling. Initially, the lubricant separates the surfaces of the roll and the strip. Then, surface asperities break the lubricant film and the asperities of the harder roll indent the surface of the strip. Finally, at sufficiently high pressure levels, sliding speeds, viscosity, ..., the lubricant permeates into the solid/solid contact zones, where it reduces friction by reducing the load supported by the solid asperities [54, 180].

Initial doubts about these observations were later resolved by assuming *MPH lubrication* to exist in cold rolling. In fact, it is expected that the lubricant permeates the solid/solid contact regions at sufficiently high pressure levels, sliding speeds, viscosity, ..., where it then reduces friction, as illustrated in Fig. 2.32.

Even the most sophisticated numerical models of cold rolling are, however, *incapable of predicting* this reduction of friction as shown in Fig. 2.31, where the estimated coefficient of friction is essentially constant when the reduction increases. In fact, cold rolling models were only able to reproduce experimental results when the boundary coefficient of friction, i.e. the Coulomb coefficient in the solid/solid contact zone, is reduced manually to fit these results (Fig. 2.33), which is conceptually equivalent to reducing friction by MPH lubrication [305]. Since accurate friction control is, however, necessary in cold rolling (Sec. 2.1.2.2), this explains why including MPH lubrication models in cold rolling models is required. The most important models of MPH lubrication are reviewed in the following section.

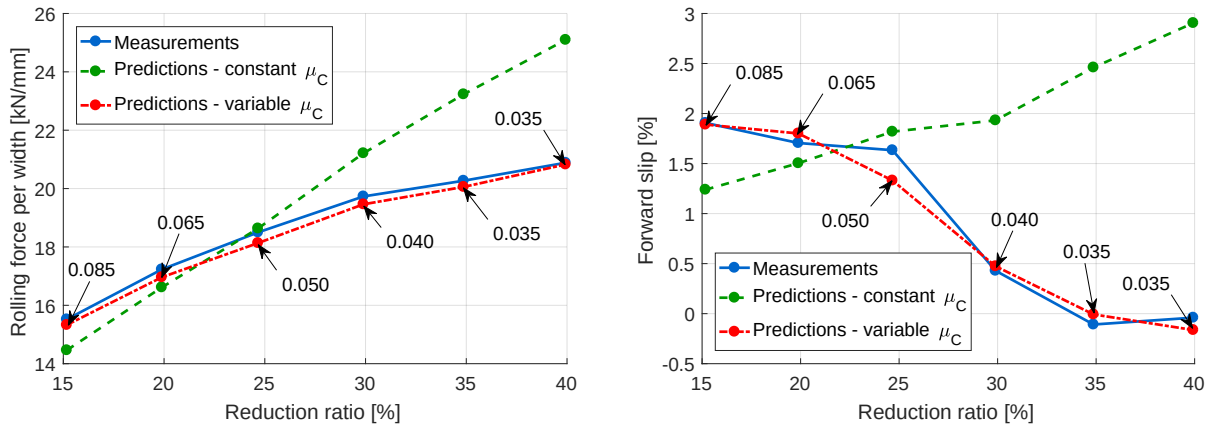

(a) Rolling force per width.

(b) Forward slip.

Figure 2.33: Illustration of the necessity of MPH lubrication models in cold rolling models. The experimental measurements were taken in essentially the same rolling conditions as those for the low-viscosity lubricant in Fig. 2.31; these figures are probably based on the same experimental data [305, p. 224] (wrong units in this reference: MN/m or kN/mm instead of MN). The predictions by Stephany's version of the METALUB model (Sec. 4.1) with a constant coefficient of friction μ_C in the solid/solid contact region deviate from the measurements for increasing reduction ratios. Reducing this coefficient as the reduction increases allows to reproduce the experimental evolution of the rolling force and the forward slip.

Modeling of MPH lubrication

MPH lubrication was first qualitatively modeled by Azushima et al. [16] in the context of indentations filled with a lubricant in plane strip drawing (Fig. 2.28), before this lubrication mechanism was quantitatively modeled by Bech et al. [25, 24]. In fact, they calculated the contact pressure without the lubricant by the slab method, while the hydrostatic and hydrodynamic pressure components of the lubricant were respectively computed by the volume reduction of the pocket and by the Reynolds equation.

The *first analytical model* of micro-plasto-hydrodynamic lubrication *including the opening of the lubricant pocket by plastic deformation* was developed by Lo and Wilson [201], who combined the Reynolds equation, the mass conservation equation and the asperity flattening equation by Wilson and Sheu [367]. This model was extended and integrated in a simplified rolling model by Sutcliffe et al. [316]. More precisely, the roll is assumed to draw oil out of surface pockets in the strip by the combined action of the lubricant viscosity and the sliding speed, after the pressure in the pockets and in the solid contact region become identical, as shown in Fig. 2.34. This model was later extended to include the lubricant flow due to MPHDL from one pocket to the following pocket [186]. Numerous hypotheses were introduced in these models, like the lubricant outflow mode in front of the pocket, a smooth rigid roll, a rigid perfectly plastic strip and an unchanging slope of the pocket edges.

Modeling MPH lubrication via the *finite element method* started by simulations of the upsetting

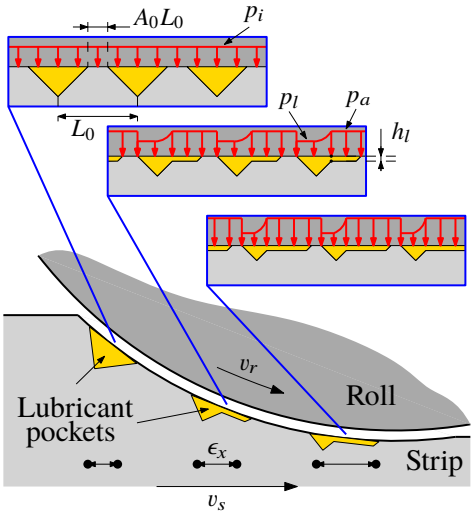

Figure 2.34: Illustration of the MPHDL model by Lo and Wilson [201] in the rolling model by Sutcliffe et al. [316]. Based on the material characteristics, the geometry (the pocket angle, the initial pocket spacing L_0 and the initial relative contact area A_0, when the lubricant pressure p_l and the pressure on top of the asperities p_a are identical and equal to the interface pressure p_i), the sliding speed $v_r - v_s$, and the strip elongation ϵ_x, the model allows to compute the MPHDL film thickness h_l and the progressive flattening of the pocket.

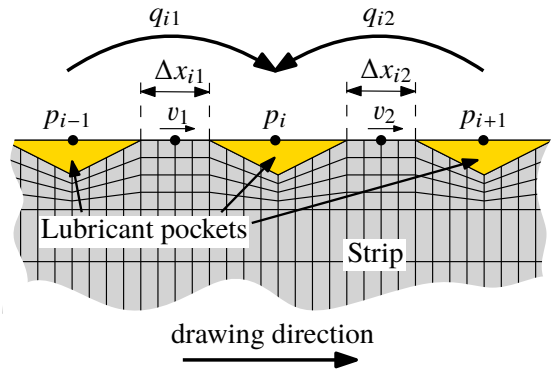

Figure 2.35: Schematic representation of the finite element discretization of the strip with lubricant pockets in the model by Dubar et al. [95]. The flow rates q_{i1} and q_{i2} are due to the pressure gradients $(p_i - p_{i-1})/\Delta x_{i1}$ and $(p_{i+1} - p_i)/\Delta x_{i2}$ between neighboring pockets and viscous entrainment by the sliding speeds v_1 and v_2 of the strip with respect to the tool surface.

process (Fig. 2.29) with a lubricant pocket [12]. In this model, the metallic specimen is assumed to be rigid-perfectly plastic, while the lubricant pressure is computed by hydrostatic elements. More recently, the plane strip drawing tests with lubricant pockets by Sørensen et al. [295] (Fig. 2.28) were simulated in a two-step procedure by Shimizu et al. [288]. First, the strip is simulated without the lubricant pocket and the velocities of the nodes around the pocket are recorded. In a second computation, these velocities are then applied to the nodes around the pocket, which is simulated exclusively to calculate the increasing hydrostatic pressure in it. Strictly speaking these models do, however, not describe MPH lubrication yet, since the permeation of the lubricant into the real contact area is not included.

Permeation was first introduced in FE simulations of the upsetting process by assuming that the lubricant volume, which leaves the surface pocket, is proportional to the pressure in the pocket by Stephany et al. [306]. This idea was further developed by Dubar et al. [95], who simulated lubricant pockets in plane strip drawing (Fig. 2.28) by the finite element method and by taking fluid flow from one pocket to another into account. Their model is based on a two-step procedure for each time step. First, a FE computation with hydrostatic elements for the lubricant pockets determines the state of the strip, when it is drawn through the dies. Based on these results, i.e. the pressure differential $p_i - p_{i-1}$, the plateau length Δx_{ij} and the relative tool/workpiece velocity v_j, where $j = 1$ or 2 for the previous or subsequent pocket, respectively, the lubricant flow rates q_{ij} from one pocket to another are computed by the Reynolds equation (Fig. 2.35):

$$q_{i1} = -\frac{h^3}{12\eta}\frac{p_i - p_{i-1}}{\Delta x_{i1}} - v_1 h \quad \text{and} \quad q_{i2} = \frac{h^3}{12\eta}\frac{p_{i+1} - p_i}{\Delta x_{i2}} + v_2 h \tag{2.19}$$

where h and η are the user-specified film thickness and dynamic viscosity of the lubricant.

Up to this point, *full MPH lubrication*, i.e. with the reduction of the real contact area due to permeation of the lubricant into the solid/solid contact zone, has not been modeled by the finite element method, but only via the analytical model by Lo and Wilson [201]. Such a reduction for MPH-*static* lubrication was simulated via hydrostatic elements by Azushima et al. [17] in the context of the rigid-plastic upsetting process with a linearly compressible fluid and more recently by Shvarts and Yastrebov [291] for a non-linearly compressible fluid in surface pockets of an elastoplastic material.

The simultaneous occurrence of MPHSL and MPHDL was first simulated by Carretta [54, 55], who developed a 2D plane-strain *FE model with the solver* Metafor [258] *to predict MPHDL and MPHSL*, i.e. the permeation behind and in front of the lubricant pocket, in the context of the strip drawing experiments by Bech et al. [24] (Fig. 2.28). This model is based on a two-step procedure with a full and a reduced model around the lubricant pocket, similar to the one by Shimizu et al. [288]. While the *full model* computes the displacements of a rectangular boundary around the lubricant pocket (Fig. 2.36a), a *reduced model* simulates this zone by imposing the recorded displacements to its boundary (Fig. 2.36b). This is necessary to reduce the computation time while refining the mesh as much as required around the pocket. In these simulations, the strip has an elastoplastic material law, while the lubricant is assumed to be Newtonian and compressible with a pressure-dependent bulk modulus. This model is exceptionally original due

to the particular choice of the boundary conditions and the Arbitrary Lagrangian Eulerian (ALE) formulation in the domain of the lubricant to prevent mesh-distortions [35, 94]. While contact is generally enforced by the penalty method with Coulomb friction, the top edge of the lubricant can move freely along the horizontal direction for reasons of numerical stability. In order to predict, however, MPHDL and MPHSL in the reduced model, very thin lubricant pipes were added behind and in front of the pocket, as well as an adherence condition of the lubricant to the top die. More precisely, due to the discretization by a mesh, the lubricant can only flow inside the deforming mesh and therefore these small pipes had to be added, while the adherence is necessary to create the hydrodynamic pressure build-up in MPHDL. Although, Carretta's model is a 2D model at the limit of the continuum mechanics hypothesis with a simple isoviscous lubricant, it allows to reproduce the experimental results of Bech et al. [24]. The most important drawbacks of the model are the hypothesis of artificial lubricant pipes and the significant computation time of about 10 days.

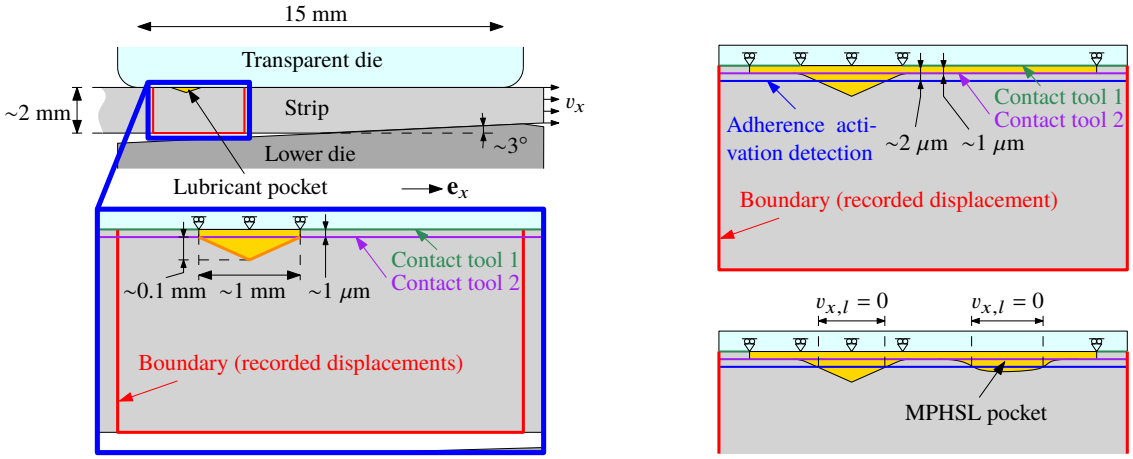

(a) Full model in which the whole strip is simulated by drawing it through the dies at a constant speed v_x. The displacement of a rectangular boundary around the pocket is recorded to apply it in the reduced model. The top edge of the strip is in contact with the contact tool 1, except for the edges in the pocket (orange), which are in contact with the contact tool 2. The offset between these tools 1 and 2 is required to prevent the pocket from closing completely, which would lead to mesh distortions.

(b) Initial geometry of the reduced model (top) and the computed geometry with a MPHSL pocket (bottom). The displacement of the full model is applied to the boundary of the reduced model. Very thin lubricant pipes are added to the model so that the lubricant can flow out of the initial pocket. Moreover, the adherence of the lubricant to the top die is activated by setting its velocity $v_{x,l}$ at the top dies to zero, when the thickness of the outflow becomes greater than a certain limit value.

Figure 2.36: MPHDL and MPHSL model by Carretta et al. [54, 55] in the context of plane strip drawing experiments with a lubricant pocket by Bech et al. [24].

2.3 Friction modeling in lubricated cold rolling

In order to minimize friction in cold rolling while preventing skidding and chatter, the adequate lubrication conditions should be applied. In the past, their determination was mainly performed by trial-and-error experimental testing, which is rather expensive due to the numerous testing

scenarios as well as the cost of the experimental set-up and the operators. For this reason, *numerical modeling was suggested as a complementary approach.*

In this section, the *most significant rolling models* are mentioned and briefly described to situate the METALUB model of Chap. 4 within the vast literature about cold rolling models. Excellent reviews about these models were compiled by Roberts [276], Sutcliffe [314] and Montmitonnet et al. [234, 236].

This section is divided into three subsections corresponding to the *three generations of rolling models regarding friction and lubrication*: in first generation models, friction is described by the Coulomb or Tresca friction law for the entire contact interface in the bite, so that lubrication is not really taken into account. In second generation models, lubrication and asperity flattening are taken into account to predict friction via the Reynolds equation and asperity flattening equations by assuming that more of a single-phase lubricant is available at the entry of the roll bite than it could absorb. Third generation models have at least the capabilities of second generation models and, in addition, friction can be directly determined on the basis of the lubrication and operating conditions. Hence, they include models of the lubricant film formation (starvation) and micro-plasto-hydrodynamic/static lubrication.

Although numerical models have become relatively predictive, one should notice that *experimental testing is still a requirement to advance in cold rolling research*. For instance, various sensors have been developed recently to measure the temperature and friction conditions in the roll bite [188], in particular, the lubricant film thickness by ultrasound [60, 150].

2.3.1 First generation models - Rolling models without lubrication

Rolling modeling can be traced back to von Karman [348], who derived a differential equation of the interface pressure between the roll and the strip along the roll bite by writing the equilibrium equations for a vertical element of the workpiece in plane-strain conditions. For this reason, this method is called the *slab method* (Sec. 4.5.3). In the von Karman equation, friction is modeled by Coulomb's law, i.e. that the interface shear stress τ_i between the roll and the strip is proportional to the interface pressure p_i so that $\tau_i = \mu_C p_i$, where μ_C is the Coulomb coefficient of friction. The von Karman equation was later solved by various methods. In particular, Nadai [243] introduced different friction laws, like the constant interface shear stress along the roll bite, in this model.

By eliminating previous assumptions, e.g. mathematical approximations and a constant yield stress, Orowan [252] noticed significant discrepancies between experimental measurements and predicted interface pressure variations of past models along the roll bites. These incongruencies were removed by assuming slipping friction according to Coulomb's law when the predicted interface shear stress τ_i is smaller than the bulk shear yield stress τ_Y, and *sticking friction* according to Tresca's law $\tau_i = \mu_T \tau_Y$ with $\mu_T = 1$, i.e. $\tau_i = \tau_Y$, otherwise.

Bland and Ford [32] developed a cold rolling model, which can be regarded as an approximation of the model by Orowan [252], to compute rolling forces and other rolling results quicker than this previous model [107]. Up to this point, roll flattening was computed by Hitchcock's theory

[142], which was extended by Bland and Ford [33] to take elastic deformations due to back and front tensions into account. Non-circular roll flattening was introduced by Jortner et al. [163] who adapted Orowans's theory [252] for this purpose (Sec. 4.6 explores roll flattening models). Based on Jortner's work, Cosse and Economopoulos [84] developed an elastoplastic cold rolling model with a minimum number of assumptions. Later, Alexander [7] emphasized the ease with which the previous equations of the slab method can be integrated by digital computers.

Most of the previous models are *1D models*, in which field variables, like the deformations or the interface pressure, are functions of the position along the rolling direction solely. Due to their excellent ratios of predictive quality to computational cost and methodological complexity, they are the most widespread and most used models in the rolling industry. Currently, one of the best 1D rolling models is probably the skin pass model by Krimpelstätter [171] since it includes elastoviscoplastic strip deformations with internal elastic zones in the bite and non-vanishing shear strains, as well as normal and tangential roll flattening due to normal and tangential stresses. *2D and 3D models* were, however, also developed by various methods like finite difference or finite element methods [234]. In particular, the FE model LAM3 by Hacquin et al. [130, 131], which is based on the integration along streamlines for stationary processes by a Eulerian-Lagrangian Heterogeneous Time Step (ELHTS) formulation, can be mentioned due to its advanced features, namely thermo-elastoviscoplastic strip deformations with thermo-elastic roll deformations. In these multidimensional models, friction is, however, usually described by Coulomb-Tresca friction, i.e. without taking lubrication directly into account, since these models are already sufficiently complex and costly themselves. Some exceptions are the FE rolling models by Boman and Ponthot [37], who used the ALE formulation and a FE discretization of the Reynolds equation, and more recently, Wu et al. [374], who solved the Reynolds equation by finite differences. In this document, we will focus on 1D rolling models due to their relatively small computation time and intricacy, which allows the addition of more physical complexity, i.e. lubrication, without compromising large industrial parameter studies.

2.3.2 Second generation models - Lubricated rolling models

In *second generation rolling models*, friction is generally not modeled exclusively by constant coefficients of friction or constant shear stresses anymore, although these laws are usually still applied in the boundary lubrication region of models with mixed lubrication.

The first model with *hydrodynamic lubrication* was developed by Nadai [243], which was mentioned previously and which includes this lubrication mode by assuming the interface shear stress to be proportional to the slip speed between the roll and the strip. After various other cold rolling models with hydrodynamic lubrication, like the one by Cheng [76], and the derivation of the inlet film thickness by Wilson and Walowit [368] (Sec. 2.18), the first *mixed lubrication* model for cold rolling was developed by Tsao and Sargent [333]. In their model, the lubricant film thickness is computed by the Reynolds equation without the Poiseuille term. The fractional contact area, which determines the relative importance of solid and viscous friction, is then determined by Greenwood and Williamson's asperity flattening model [125].

In contrast to Tsao and Sargent [333], Sutcliffe [315] and Sheu and Wilson [285] developped cold rolling models in the mixed regime based on their respective *asperity flattening models* [311, 367], which include flattening due to plastic bulk elongation that is an inherent component of rolling (Sec. 2.2.2.2). Furthermore, the Reynolds equation with the Poiseuille term is solved in these models, in particular, by taking into account lubricant flow modifications due to roughness via the average Reynolds equation by Patir and Cheng [253, 254] in [285]. The model by Keife and Sjögren [165] should also be mentioned since it is similar to the previous models and since the asperity flattening is computed via the finite element method, similarly to the idea in Chap. 6, but without plastic bulk elongation in their model.

The previous models are considered to be *high-speed models*, because the hydrodynamic pressure is assumed to build up in the inlet zone of the bite [231, 232]: hence, (1) the lubricant pressure p_l is supposed to be equal to the interface pressure p_i in the work zone, where the strip is plastically deformed, (2) the Reynolds equation is solved without the Poiseuille term, which has become negligible with respect to the Couette term, and (3) the asperity flattening equation is not useful anymore in the work zone because $p_l = p_i$ implies that $p_a = p_l$ (by the load sharing equation, which will be introduced in Eq. 4.4). Since the hydrodynamic pressure could, however, also increase later on in the work zone, such that the previous hypotheses are invalidated, *low-speed models* were introduced by Wilson and Chang [72, 363]. *Low- and high-speed models were later combined* in mixed rolling models by Lin, Marsault and Wilson [194, 215]. In these models, the explicit integration along the roll bite switches from the equations of the low-speed system to those of the high-speed system, when the Poiseuille term becomes negligible with respect to the Couette term [194] or when the lubricant pressure becomes equal to the interface pressure [215].

More specifically, Marsault [215] developed the LAM2DTRIBO model in the context of the research contract program about "Contact: Metal-tool-lubricant" (Contrat de Programme de Recherche, CPR, "Contact: Métal-outil-lubrifiant"), which was a collaboration between Irsid (Usinor group, now ArcelorMittal group), Pechiney CRV, CNRS, amongst others, and which was directed by Pierre Montmitonnet at Mines ParisTech/CEMEF. This model is the basis of the METALUB model, which will be described more thoroughly in Chap. 4. The research based on this model during the past 20 years at the University of Liège is reviewed in Sec. 4.1 and not in this section to prevent redundancy.

Instead of switching from one system of equations to another in the combined low- and high-speed models, Qiu et al. [265] suggested a seemingly more robust solution method [231], in which the Reynolds equation is solved by the finite difference method rather than the explicit integration of this equation along the bite in the rolling direction.

Discrepancies between experimental results by Tabary et al. [323] and numerical results led Le and Sutcliffe to develop rolling models with a two-wavelength roughness along the rolling direction [184] or a semi-empirical friction model [185]. In this second model, boundary friction in a rolling model with mixed lubrication was estimated by measuring coefficients of friction via a strip drawing rig, instead of classically using these coefficients as fitting parameters to reproduce measured rolling results [215]. Finally, in the last article by Sutcliffe (and Le) about cold rolling models [187], a multi-scale friction model is developed since discrepancies between experimental

and numerical results could not be fully eliminated by the two-wavelength roughness model, and due to the dependence of the semi-empirical model on experimental strip drawing tests. In this model, a transverse roughness is introduced on top of a primary-scale longitudinal roughness, as suggested by surface topographies of ground rolls.

2.3.3 Third generation models - Lubricated rolling models with film formation and MPH lubrication

Despite the already existing complexity of second generation models, they are still missing additional components to predict rolling results, like the rolling force and the forward slip, directly on the basis of industrial lubrication conditions, like the oil concentration in the emulsion. These components in *third generation models* are essentially methods to predict the *oil film formation* at the entry of the bite, including the dynamic concentration and plate-out mechanisms with possible starvation (Sec. 2.2.4.1), and *micro-plasto-hydrodynamic/static lubrication* in the roll bite (Sec. 2.2.4.3), although *thermal effects* should also be estimated (Sec. 4.9.1).

For these reasons, after the second generation model by Marsault [215], the successive theses about oil film formation by dynamic concentration [63], starvation and further development of Marsault's model [305], oil film formation by plate-out [128], and micro-plasto-hydrodynamic/static lubrication [54] were realized in a *joined effort of the research groups* at ArcelorMittal (Maxime Laugier, Nicolas Legrand), Mines ParisTech/CEMEF (Pierre Montmitonnet), Bordaux I (Jean-Paul Caltagirone) and ULiège (Jean-Philippe Ponthot, Romain Boman) to develop third generation models. While a simplified starvation model was successfully introduced in Metalub by Stephany [305], the coupling between this model and the film formation model by Cassarini [63] did not converge yet [237]. Similarly, it is still unclear how the plate-out model by Guillaument [128] can be coupled with the Metalub model in addition to the significant computational cost of this CFD model. Finally, after reproducing numerically the strip drawing experiments with a lubricant pocket by Bech et al. [24], Carretta [54] was in the process of developing a coupling procedure between Metalub and the FE solver Metafor to introduce MPH lubrication in the rolling model. Thorough testing of this procedure was, however, still required (Chap. 6).

Besides these research efforts, Kosasih et al. [170] included *emulsion lubrication* in a rolling model via the dynamic concentration mechanism. This model was coupled to a finite difference resolution of the *thermal equations* for the roll and the strip to compute the lubricant temperature [329]. Finally, Lo et al. [203] recently developed a rolling model with emulsion lubrication based on CFD computations to determine to which extent the continuous and disperse phases contribute to the total lubricant pressure [202].

2.4 Conclusion

In this chapter, the *context of friction modeling in lubricated cold rolling was set and the corresponding literature was reviewed* to lay the foundations for the following chapters.

Cold rolling is a manufacturing method in the steelmaking process, where it reduces the thickness of strips from several millimeters to several tenths of a millimeter at about 100°C, classically in five-stand four-high tandem mills. The cold rolling process is strongly dependent on friction, which increases the rolling load, that pushes the work rolls against the strip in the roll bite, and the forward slip, i.e. the relative exit speed of the strip with respect to the rolling speed. To optimize the production, friction has to be controlled tightly because the rolling force of a mill stand is limited and because undesired mill vibrations as well as skidding of the strip between the rolls also depend on friction. This has become even more important in recent years, since thinner and harder Advanced High-Strength Steel strips have to be produced for the automotive industry, which tries to minimize the weight of cars due to emission targets of carbon dioxide. Therefore, flexible lubrication systems are crucial. With the help of these systems, friction can be controlled by adjusting the oil quantity at the entry of the roll bite, for instance, via the oil concentration in the oil-in-water emulsion, which is sprayed onto the strip. To determine the optimal values of lubrication parameters, like this concentration, for given rolling conditions, experimental testing and especially numerical models are required because of the important number of parameters in cold rolling.

Therefore, the *physics of friction* is introduced in the second part of this chapter. Metallic surfaces are generally rough at the micro-scale and their roughness can be characterized by amplitude parameters and surface height distribution functions. In consequence, contacting surfaces initially enter only into contact at their peaks, which are called asperities. These asperities are essentially flattened by three mechanisms, which thus increase the relative contact area, i.e. the ratio of the real contact area to the apparent contact area: normal loading, underlying bulk deformations (with normal loading), and shearing (with normal loading). Asperity flattening is directly linked to dry friction, which can be explained by adhesion in the real contact area and the mechanical interaction of asperities in the presence of contaminant films. Various dry friction models have been developed over time: Amontons' first law, also known as Coulomb's law, sticking friction, ... Furthermore, the lubricant influences friction in cold rolling in different ways. Before entering into the roll bite, an oil film is formed by the plate-out mechanism, which consists in oil drops getting stuck to the lipophilic surface of the strip, and by dynamic concentration, according to which water is pushed out of the oil concentration zone near the entry of the roll bite due to its lower viscosity. Depending on the oil film thickness with respect to the roughness amplitude, different lubrication regimes exist: (1) the hydrodynamic regime with low friction where the lubricant film is so thick that it totally separates the solid surfaces, (2) the mixed regime with medium friction due to a shared load between asperity contacts and the lubricant, and (3) the boundary regime with high friction due to asperity contact. The mixed lubrication regime, which usually occurs in cold rolling, is characterized by different lubrication mechanisms: (1) macro-plasto-hydrodynamic lubrication, i.e. a lubricant film is created by its viscosity, the speed differential and the convergent geometry between plastically deforming surfaces, (2) boundary lubrication at the contact of asperities, (3) hydrostatic lubrication where the lubricant is compressed in surface pockets and (4) micro-plasto-hydrodynamic/static (MPH) lubrication. This latter mechanism consists in the lubricant permeating from pressurized surface pockets into the solid contact zone at sufficiently high sliding speed and hydrostatic pressure with simultaneous plastic deformations

at the scale of the asperities. The discovery of decreasing friction in lubricated cold rolling, when the reduction increases, can be explained by this mechanism, so that it should be included in rolling models. In addition to rolling tests on a pilot mill, MPH lubrication was experimentally studied by strip drawing and upsetting tests, usually, with macroscopic lubricant pockets, which were reproduced numerically, requiring, however, significant computation times.

Finally, *friction modeling in lubricated cold rolling* was reviewed. These models can be assigned to three categories regarding friction and lubrication: first, second and third generation models. In first generation models, friction is modeled by the Coulomb or Tresca laws for the entire contact interface in the roll bite. In second generation models, mixed lubrication is introduced by combining the Reynolds equation with asperity flattening equations, which take the underlying bulk deformation into account. The METALUB model in Chap. 4 is such a second generation model, in which numerous features were introduced in order to develop a third generation model. These third generation models should allow to predict rolling results, like the rolling force, directly based on industrial lubrication conditions, so that these conditions can be adjusted optimally by flexible lubrication systems. Hence, third generation models should include models of oil film formation at the entry of the roll bite, micro-plasto-hydrodynamic/static lubrication in the bite and the thermal state of the lubricant, the rolls and the strip. Currently, friction models in cold rolling include some of these components but others are missing. The difficulty lies in combing all of them into one single model, which is able to provide industrial results after reasonable computation times.

Chapter 3

Experimental Data

In the previous chapter, the theory about friction and lubrication in cold rolling was introduced. For instance, phenomena like hydrodynamic lubrication and lubricant starvation were explained. These phenomena are *illustrated* in this chapter by the most comprehensive experimental data of cold rolling to the best of our knowledge.

As will be explained in Sec. 5.1, cold rolling data in the literature, e.g. in Stephany's thesis [305], are usually less complete than the data in this chapter. Our objective is, however, to predict rolling results, like the rolling load and the forward slip, as accurately as possible. This accuracy commonly suffers from required hypotheses and parameter adjustments due to the limited data. In order to remedy this shortcoming and thus, in order to *quantify the predictive capabilities of our model* as well as possible, very complete experimental data are presented in this chapter and later used in Chaps. 5 and 6 for this reason.

Besides the description of the experimental setup, the *resulting data are thoroughly analyzed* to determine what influences operating parameters, like the rolling speed or the lubricant viscosity, have on the rolling force and forward slip. Explanations of these influences by physical mechanisms are then suggested *to determine which mechanisms should be included in the rolling model of the following chapter* to predict, amongst others, the rolling force and forward slip accurately.

The current chapter is thus structured in two parts. In the first part, it is explained *how the experimental data were measured*, and in the second part, these *data are analyzed*. In order to keep the data for the future without having to post-process them again and to accelerate future cold rolling research, these data were added in appendix E.

3.1 Experimental setup

In this section, the *experimental measurements* and the data post-processing are described. Particular attention was obviously paid to extracting the parameters that are required in the cold rolling model of the following chapter.

The experimental data were measured in March 2014 within the framework of the *roll gap sensors* project, which was partially funded by the RFCS (Research Fund for Coal and Steel) program of the European Commission [188], on a *semi-industrial pilot mill* based at ArcelorMittal's research campus in Maizières-lès-Metz, France.

The different components of the experimental campaign are successively described hereafter: the *mill*, the *strip*, the *lubrication/cooling system* and the *resulting measurements*.

3.1.1 Mill

As explained by Hunter [150], the semi-industrial pilot mill (single stand) was used in a two-high configuration with work rolls having a diameter of 391 mm. While the rolling load is applied by a hydraulic screw, the back and front tensions are exerted by tension bridles between the coiler and uncoiler as shown in Fig. 3.1. Additional data are provided in Tab. 3.1 for reasons of completeness.

Parameters	Values	Units
Mill barrel width	300	mm
Mill load capacity	1.96	MN
Maximum rolling speed	1500	m/min
Roll gap	0.05 - 4	mm
Strip width	50 - 200	mm
Power of mill drive	300	kW
Power of coiler/uncoiler (each)	110	kW
Power of tension bridels (each)	70	kW
Max. force by tension bridels at 100 m/min	4216	kgf
Max. force by tension bridels at 1500 m/min	222	kgf
Angle between strip and horizontal at roll bite entry	0.7	°

Table 3.1: Additional data of the semi-industrial pilot mill at ArcelorMittal's research campus in Maizières-lès-Metz, France [150].

The roughness of the work rolls was quantified by taking a cast of the roll surfaces (Fig. 3.2 and then measuring the roughness parameters by the Mahr Perthometer S2 profilometer [150] as shown in Tab. 3.2. It can be seen that the roughness of the top and bottom rolls is almost the same and that it decreases during the testing campaign due to wear, except for one measurement and this for unknown reasons (change of rolls, measurement error, ...).

3.1.2 Strip

During the test campaign, essentially 14 different coils of 3 different types were rolled [150]:

- DD14 Ti grade steel [51] after hot rolling, 100 mm width, 2.8 mm thickness, abbreviation: S1

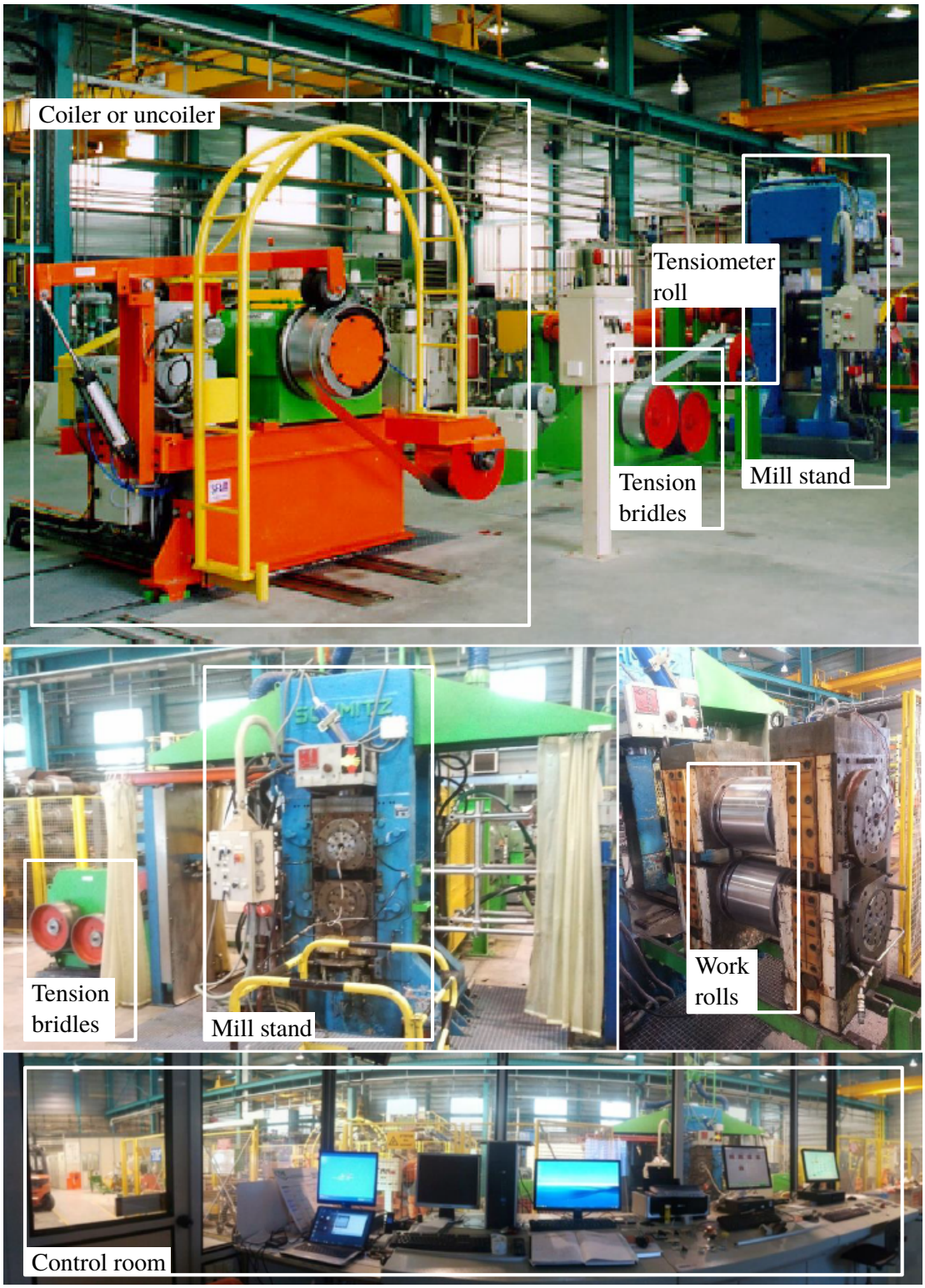

Figure 3.1: Semi-industrial pilot mill and control room at ArcelorMittal's research campus in Maizières-lès-Metz, France [150].

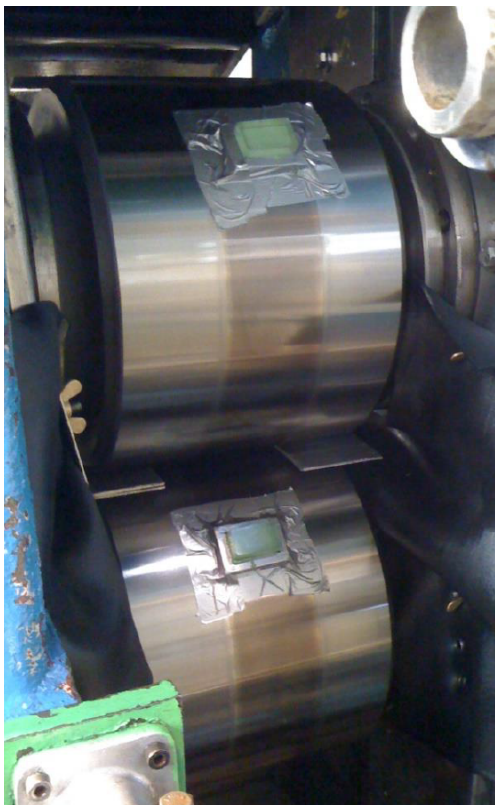

Figure 3.2: Roughness castings of the work rolls [150].

- DC06 grade [52] aluminium-killed steel after cold rolling, 75 mm width, 0.75 mm thickness, abbreviation: S2
- DC06 grade [52] aluminium-killed steel after cold rolling, 100 mm width, 0.634 mm thickness, abbreviation: S3

One of the most important material characteristics of the strip in cold rolling is its yield stress σ_Y and furthermore, the evolution of the yield stress as a function of the effective plastic strain $\overline{\epsilon}^p$, i.e. its hardening law. Thermo-viscoplastic effects were unfortunately not measured. The isotropic hardening law was determined by *plane-strain compression tests*, which are similar to the rolling process [26, 355][276, p. 458], at low deformation speeds ($\overline{D}^p \approx 0.02\ \mathrm{s}^{-1}$). The measured hardening laws for the three different rolled products are shown in Fig. 3.3. The values of the yield stresses are probably more important than those in the norms [51, 52] because they were measured during the rolling process and not after the final heat treatment. The *effective strain* $\overline{\epsilon}$, which will be assumed to be equal to the effective plastic strain $\overline{\epsilon}^p$ due to small elastic deformations with respect to plastic deformations, was computed by the following formula (Eq. 4.32) based on the initial thickness of the strip t_{in} and its thickness t_s at a given stage of deformation:

$$\overline{\epsilon} = \frac{2}{\sqrt{3}} \ln\left(\frac{t_{\mathrm{in}}}{t_s}\right) \tag{3.1}$$

Time	R_a	R_z	$R_{\max}$	R_t	R_{pc}	R_{sk}
-	μm	μm	μm	μm	peaks/cm	-
After coil 2	0.618	4.389	5.114	5.434	89	-0.42
After coil 5	0.617	4.621	5.841	5.841	92	-0.34
After coil 11	0.563	4.204	4.882	5.194	75	-0.53
After coil 12	0.563	4.194	4.811	5.186	83	-0.53
After coil 14	0.543	4.022	4.849	5.136	67	-0.48

(a) Top roll.

Time	R_a	R_z	$R_{\max}$	R_t	R_{pc}	R_{sk}
-	μm	μm	μm	μm	peaks/cm	-
After coil 2	0.614	4.413	5.160	5.422	103	-0.28
After coil 5	0.651	4.567	5.494	5.917	103	-0.18
After coil 11	0.577	4.065	4.823	4.991	73	-0.33
After coil 12	0.569	4.309	5.395	5.801	72	-0.25
After coil 14	0.535	3.697	4.481	4.849	71	-0.26

(b) Bottom roll.

Table 3.2: Roughness of the rolls.

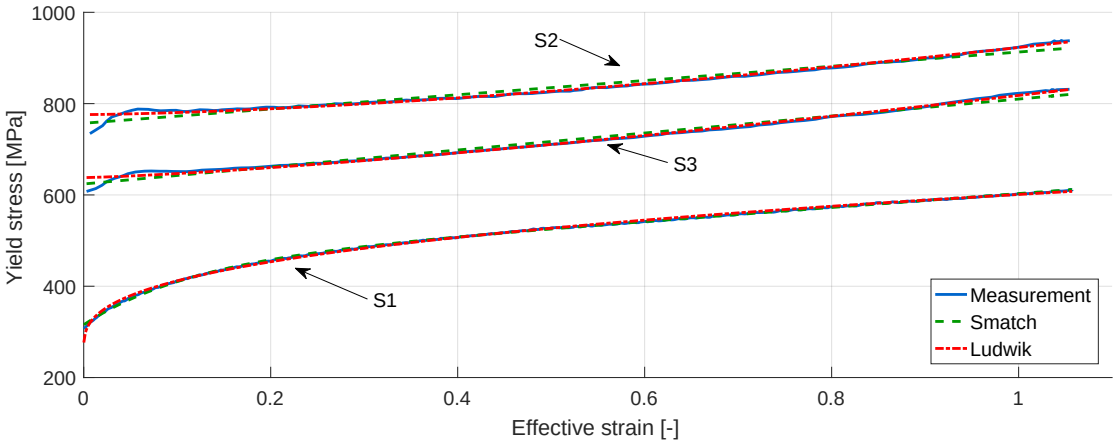

Figure 3.3: Measured and fitted hardening laws.

In order to easily evaluate these hardening laws for a given effective plastic strain and to compute their local derivatives in the METALUB model, the coefficients of the *Smatch hardening law* [3, 4] were provided in the documentation of the experimental campaign:

$$\sigma_Y = (A + B\overline{\epsilon}^p)\left(1 - Ce^{-D\overline{\epsilon}^p}\right) + E \tag{3.2}$$

where the values of the material constants are mentioned in Tab. 3.3. The Smatch law resembles a combination of the Swift and Voce laws [319, 347]. The coefficient E was set equal to 0 before fitting the data because it is commonly used as an adjustment parameter [54, 305]. Since the Smatch law seems to be overly complex (e.g. $C = 0$ in two cases), the material constants of the *Ludwik hardening law* were also determined [208]. This law is similar to the Johnson-Cook law, which is limited to its first components, i.e. without the thermo-viscoplastic factors, due to the available data [161]:

$$\sigma_Y = A + B\,(\overline{\epsilon}^p)^n \tag{3.3}$$

It can be seen in Fig. 3.3 that the fitting is very good for important plastic strains, while some discrepancies exist at low strains. The material of the rolled product S2 is the most resistant one, then S3 and finally S1.

Parameters	S1	S2	S3	Units
A	451	757	624	MPa
B	152	156	186	MPa
C	0.3	0	0	-
D	9.13	0	0	-
E	0	0	0	MPa

(a) Smatch hardening law.

Parameters	S1	S2	S3	Units
A	263	776	638	MPa
B	338	147	180	MPa
n	0.356	1.52	1.31	-

(b) Ludwik hardening law.

Table 3.3: Material parameters of the strips.

The *roughness of the strip* was measured by the same profilometer as the rolls (Sec. 3.1.1). The results are shown in Tab. 3.4. It can be seen that the material of the S1 coils is much rougher than the S2 and S3 coils because the S1 coils come from the hot rolling mill, while the others have already been cold rolled. Although 5 different samples were taken per measurement, some differences still exist between coils 4 and 14, possibly due to the wear of the rolls, by which they were rolled prior to the test campaign.

3.1.3 Lubrication and cooling systems

Three different *lubrication and cooling systems* can be activated simultaneously:

- *flexible lubrication circuit* (of direct application type) by 4 nozzles, with transverse flow, which are supplied from two 100 l tanks, with temperature control and agitation, by 2 centrifugal pumps (max. 1 m^3/h at 10 bar) and 2 volumetric pumps (max. 1 m^3/h at 10 bar);

Strip	R_a	R_z	$R_{\max}$	R_t	R_{pc}	R_{sk}
	μm	μm	μm	μm	peaks/cm	-
Coil 2 (S1)	1.505	9.653	12.09	12.50	75	-0.09
Coil 4 (S2)	0.101	1.136	1.360	1.481	0	-2.38
Coil 12 (S3)	0.189	1.400	2.596	2.683	3.5	-1.05
Coil 14 (S2)	0.079	0.915	1.219	1.271	0	-2.41

Table 3.4: Roughness of the strips.

- *recirculating circuit* of emulsion by 4 nozzles, which are supplied from two 2000 l tanks, with temperature control and agitation, by 2 pumps delivering at most 18 m^3/h at 10 bar;
- *water cooling circuit* via 2 nozzles supplied by a centrifugal pump (max. 50 m^3/h at 10 bar).

In the thesis by Hunter [150], the location of the nozzles is schematized as in Fig. 3.4 for the flexible lubrication and recirculating circuits. The lubricant and water are applied to the top and bottom sides of the strip as well as the top and bottom rolls. Only the top side is shown in the figure.

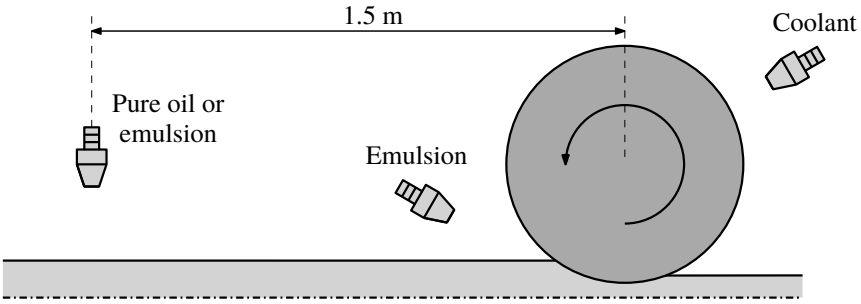

Figure 3.4: Lubrication and cooling circuit arrangements with the nozzles of the flexible lubrication circuit on the left and those of the recirculating circuit just in front of the roll bite.

Three different *oils* were used during the test campaign either in their pure form or in emulsions. They will be called L1, L2 and L3. As stated in Sec. 2.2.4.2, one of the most important physical property of a lubricant in the context of lubrication is its viscosity. The dynamic viscosity of the previous pure oils was determined by Bouscharain and Vergne [44] by a coaxial cylinder rheometer at atmospheric pressure and by a falling ball viscometer at higher pressure for different temperatures. Based on these measurements, the coefficients of the extended WLF law (see Sec. 4.8.2.3) were determined in order to evaluate the *dynamic viscosity as a function of the lubricant pressure* p_l *and temperature* T_l:

$$\log_{10}\eta(p_l,T_l)=\log_{10}\eta_g-\frac{C_1\left[T_l-T_g(p_l)\right]F(p_l)}{C_2+\left[T_l-T_g(p_l)\right]F(p_l)}\quad\text{with}\quad\begin{cases}T_g(p_l)=T_g(0)+A_1\ln\left(1+A_2p_l\right)\\F(p_l)=(1+b_1p_l)^{b_2}\end{cases}\tag{3.4}$$

where the different material parameters are given in Tab. 3.5. Fig. 3.5 illustrates the evolution of the dynamic viscosity of the different lubricants as a function of pressure for different temperatures. The measured data were added in order to show the good agreement between them and the predictions by the material law. This figure also shows that the viscosity for high pressures at low temperatures was not measured. This is due to the solidification of the lubricant. More precisely, the L1, L2 and L3 lubricants *solidify* at 40°C, when the pressure becomes greater than 200, 300 and 200 MPa, and at 75°C, when the pressure becomes greater then 600, 700 and 500 MPa, respectively. Fig. 3.5 also shows that L1 is much more viscous than L2 and L3. The concentration of the oil in the recirculated emulsion was kept between 1.95% to 2.25% and the oil particle size was measured: 6.9 μm for L1, and 3.4 μm or later 4.8 μm for L2.

Parameters	L1	L2	L3	Units
A_1	102.77	47.67	49.64	°C
A_2	0.000226	0.000704	0.000365	MPa^{-1}
b_1	0.00573	0.00611	0.00578	MPa^{-1}
b_2	−0.547	−0.517	−0.565	-
C_1	15.95	16.08	16.11	-
C_2	26.98	25.80	26.00	°C
η_g	10^6	10^6	10^6	MPa.s
$T_g(0)$	−73.16	−90.60	−85.96	°C

Table 3.5: Material parameters of the lubricants.

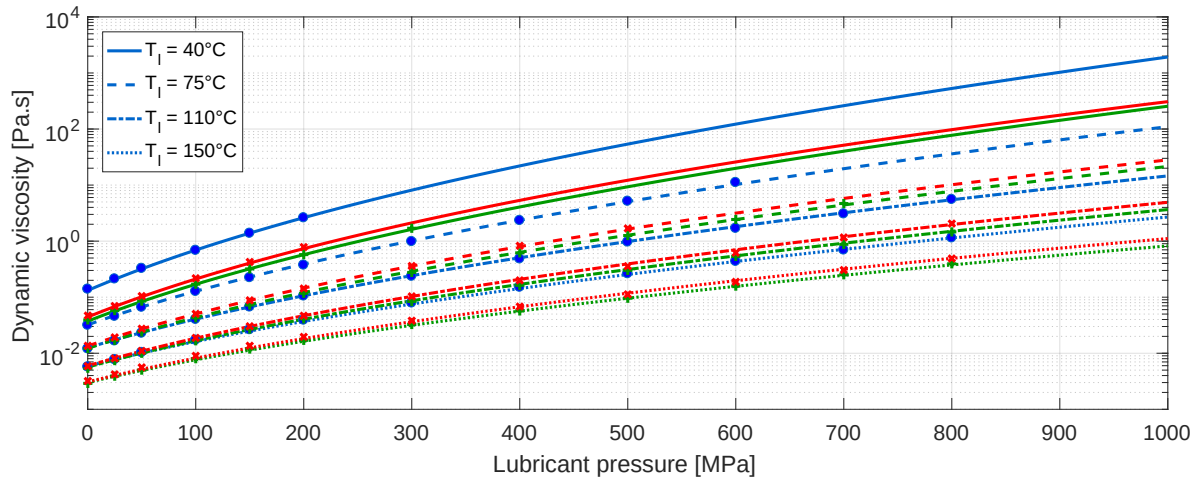

Figure 3.5: Dynamic viscosity η of the different lubricants L1 (blue), L2 (green) and L3 (red) as a function of pressure p_l for different temperatures T_l.

The *lubricant density* ρ_l, which is required in the falling ball viscometer experiments [18] and which probably has an influence on the micro-plasto-hydrostatic effect via the compressibility

(Sec. 2.2.4.3), was computed by the Tait equation [19]:

$$\frac{V}{V_0} = 1 - \frac{1}{1+K_0'} \ln\left[1 + \frac{p_l}{K_0}(1+K_0')\right] \tag{3.5}$$

where

- V is the current volume of the lubricant, which has a mass m, i.e. $V = m/\rho_l$;
- V_0 is the volume at atmospheric pressure of the lubricant, which has a mass m:

$$V_0 = \frac{m}{\rho_l^0}\left[1 + \alpha_v\left(T_l - T_l^0\right)\right] \tag{3.6}$$

- T_l is the lubricant temperature (in °C);
- ρ_l^0 is the lubricant density at atmospheric pressure and at the reference temperature T_l^0. For all three lubricants, $\rho_l^0 = 0.91$ g/cm^3 at $T_l^0 = 20$°C;
- $\alpha_v = 0.0008\ °C^{-1}$ is the coefficient of thermal expansion;
- $K_0' = 11$ is the pressure rate of change of the bulk modulus K at atmospheric pressure;
- p_l is the lubricant pressure (in MPa);
- K_0 is the bulk modulus at atmospheric pressure:

$$K_0 = K_{00}\exp\left[\beta_K\left(T_l + 273.15\right)\right] \quad \text{with} \quad \begin{cases}\beta_K = -0.0065\ °C^{-1}\\ K_{00} = 9000\ \text{MPa}\end{cases} \tag{3.7}$$

Besides the values of the lubricant density at atmospheric pressure, all other material parameters were selected from Bair [19]. On the basis of the previous equations, the lubricant density is finally computed as follows:

$$\rho_l(p_l, T_l) = \frac{\rho_l^0}{\left[1 + \alpha_v(T_l - T_l^0)\right]\left\{1 - \frac{1}{1+K_0'}\ln\left[1 + \frac{p_l}{K_0}(1+K_0')\right]\right\}} \tag{3.8}$$

3.1.4 Measurements during rolling

On the basis of the previous elements, e.g. the rolled product or the lubricant, different experimental scenarios were defined to study their influence on the rolling process, i.e. mainly on the rolling force and the forward slip, while keeping all other operating parameters constant. The different influences can be assigned to three categories: the rolled product, the lubrication conditions and the mill operating conditions via the rolling speed and the reduction ratio (or

elongation). The resulting *experimental scenarios* are summarized in Tab. 3.6. Some values were rounded in this table for reasons of synthesis. The exact values can be found in appendix E.

The number of a test in Tab. 3.6 corresponds to the *number of the coil*, except for Test 15, in which the rest of coil 8 is rolled. It is possible that a coil is used in multiple test scenarios. Hence, the suffixes A and B are added to the test number, like Tests 4A and 4B.

Test number	Rolled product	Flexible lubrication	Recirculated	Rolling speed [m/min]	Elongation [%]
1	S1	-	L2 2%	25 - 400	30
2	S1	L3 20%	L2 2%	25 - 400	30
3	S1	L3 0-20%	L2 0-2%	300	30
4A	S2	-	L2 2%	25 - 500	30
4B	S2	L3 20%	L2 2%	25 - 500	30
5A	S2	L3 0-20%	L2 2%	400	30
5B	S2	L3 100%	-	25 - 500	30
6	S1	L3 100%	-	25 - 400	30
7	S1	L3 100%	-	100	5 - 40
8	S2	L3 100%	-	100	5 - 40
9	S3	L3 100%	-	700 - 1200	30
10A	S2	L1 100%	-	25 - 500	30
10B	S2	L1 100%	-	25 - 500	30
11	S1	L1 100%	-	25 - 400	30
12A	S3	L1 100%	-	25 - 1200	30
12B	S3	-	L1 2%	25	30
13	S1	-	L1 2%	25 - 400	30
14A	S2	L1 100%	-	100	5 - 50
14B	S2	L1 100%	-	500	10 - 40
15	S2	L3 100%	-	50	11 - 50

Table 3.6: Summary of the tested scenarios.

For each test, the following *data were recorded* by the mill control system, which was developed by the company *iba AG*:

- Time in [s]
- Front tension load L_{out} in [t]
- Back tension load L_{in} in [t]
- Elongation e_x in [%]
- Forward slip s_f in [%]
- Rolling load L_r in [t]

- Peripheral rolling speed of the top roll $v_{r,t}$ in [m/min]
- Peripheral rolling speed of the bottom roll $v_{r,b}$ in [m/min]
- Torque of the top roll $M_{r,t}$ in [N.m]
- Torque of the bottom roll $M_{r,b}$ in [N.m]
- Entry temperature of the strip T_{in} in [°C]
- Exit temperature of the strip T_{out} in [°C]

These data are *post-processed* according to the rules explained in appendix E to values that can be compared more easily and that are required in the cold rolling model, which is explained in Chap. 4. For instance, the rolling load L_r in tons cannot be directly used to compare strips of different widths. Moreover, forces are usually numerically written in Newtons in the mathematical model. Hence, the rolling load L_r in tons is converted to the rolling force per width $\overline{F}_r$ in kN/mm for brevity. In addition to the post-processing rules, the resulting data can be found in appendix E.

3.2 Analysis of the experimental data

In this section, the *influences of various parameters*, i.e. the rolling speed, the lubricant quantity, the lubricant type, the lubricant temperature, the strip elongation/reduction and the rolled product, on the rolling force and the forward slip are presented based on the previous experimental data. These influences are *illustrated* in Figs. 3.6 to 3.14 and the *underlying physical mechanisms are explained*, as far as possible. In fact, this analysis *does not claim to be exhaustive* because of the large number of mechanisms in lubricated cold rolling and their complex interaction (see e.g. [215]). Since some measurements were taken in a state more or less unsteady (appendix E), a color code was introduced in the figures to highlight this property: red (unsteady), orange (almost steady) and green (steady). The different measurements were connected by line segments to enhance their readability. If measurements of the rolling force or the forward slip were taken multiple times in almost the same conditions, their average was computed to increase the statistical significance of the results. The line segments pass through this average instead of the different measurements themselves, again in order to improve the readability.

3.2.1 Influence of the rolling speed

Fig. 3.6 shows that the rolling force can either increase or decrease with the *rolling speed*, while the forward slip decreases, provided that enough lubricant is available at the entry of the bite (see Sec. 3.2.2 concerning the influence of the lubricant quantity) and provided that all other parameters, like the elongation or the back and front tensions, are unchanged. These conditions seem to be satisfied in the test cases in Fig. 3.6 since a pure oil is applied (full-flooded lubrication) and since the other parameters were kept almost constant during the experiments. The resulting observations can be explained by the hydrodynamic effect and viscoplasticity.

3.2.1.1 Hydrodynamic effect

The decrease of the rolling force and the forward slip can be explained by *hydrodynamic lubrication*, which is also known as the *speed effect*[1] in this context [276]. In fact, if the rolling speed v_r increases, the lubricant film thickness h_t rises by viscous entrainment of the lubricant into the roll bite as suggested by Wilson and Walowit [368] (Eq. 2.18). In consequence, the relative contact area A decreases so that less solid friction occurs, which results in lower average friction. The notion of average friction can be characterized quantitatively by the equivalent coefficient of friction $\overline{\mu}$ in the bite (Eq. 4.311). Decreasing friction finally implies that the rolling force F_r and the forward slip s_f are reduced, as will be explained hereafter. The previous reasoning can be summarized[2] as follows:

$$v_r \nearrow \quad \rightarrow \quad h_t \nearrow \quad \rightarrow \quad A \searrow \quad \rightarrow \quad \overline{\mu} \searrow \quad \rightarrow \quad F_r \searrow, s_f \searrow \tag{3.9}$$

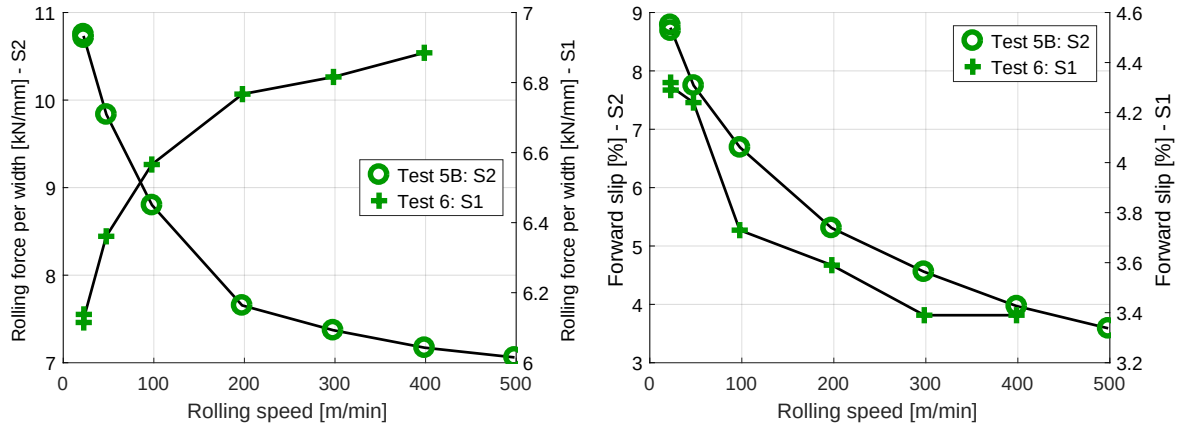

(a) Rolling force per width.

(b) Forward slip.

Figure 3.6: Influence of the rolling speed with flexible lubrication by pure L3 and constant elongation (30%) for different rolled products (S1 and S2).

The *decrease of the rolling force due to decreasing friction* can be explained as follows. If friction decreases, the interface shear stress applied by the roll to the strip decreases in absolute value. Since the roll has a greater speed than the strip at the entry of the bite, this implies that the strip is less compressed along the rolling direction. Less compression along this direction implies that less compression along the vertical direction is required to reach the yield stress, which enables plastic deformation. Hence, the rolling force decreases, when friction decreases.

In more mathematical terms, the stress σ_x (positive in tension) in the rolling direction inside the strip becomes less negative, when friction decreases. This can be illustrated by the equilibrium

[1] This term is, however, ambiguous since viscoplasticity is also a speed effect.

[2] The equations with arrows are simplifications to facilitate the explanations. In lubricated cold rolling, these variables are usually interdependent.

equation in the rolling direction of the strip by the slab method (Eq. 4.65):

$$\frac{\partial \sigma_x}{\partial x} = -\frac{1}{t_s}\left[(\sigma_x + p_i)\frac{\partial t_s}{\partial x} + 2\tau_i\right] \approx -\frac{2\tau_i}{t_s} \tag{3.10}$$

where t_s is the thickness of the strip, p_i the applied interface pressure and τ_i the applied interface shear stress to the strip, at a given position of the bite. The approximation holds for thin strips and rolls with relatively important diameters like those in cold rolling. Since τ_i is positive, i.e. oriented in the rolling direction, at the entry of the bite (Fig. 4.7), its smaller value due to smaller friction results in a less negative axial stress σ_x according to Eq. (3.10). Because the axial stress σ_x is less negative, when friction decreases, the vertical stress σ_z has to be less negative to reach the yield stress. In fact, by the Von Mises yield criterion for a rigid plastic material in the plane-strain state (Eq. H.125), the plastic deformation starts when the following equation is satisfied

$$\sigma_x - \sigma_z = \frac{2}{\sqrt{3}}\sigma_Y \tag{3.11}$$

where σ_Y is the yield stress and where the absolute value function was removed in consideration of the stress values. The vertical stress σ_z (positive in tension) is related to the interface pressure between the roll and the strip, which is positive in compression, by the equilibrium equation in the vertical direction of the slab method (Eq. 4.67):

$$\sigma_z = -p_i + \frac{1}{2}\tau_i\frac{\partial t_s}{\partial x} \approx -p_i \tag{3.12}$$

where the previous approximation holds again for the same reasons as previously. If the interface pressure thus decreases, when friction decreases, the rolling force decreases (Eq. 4.296), too. In short,

$$\overline{\mu}\searrow \;\rightarrow\; |\tau_i|\searrow \;\rightarrow\; \sigma_x\nearrow \;\rightarrow\; \sigma_z\nearrow \;\rightarrow\; p_i\searrow \;\rightarrow\; F_r\searrow \tag{3.13}$$

The *decrease of the forward slip due to decreasing friction* can be explained in a simplified way by considering that skidding starts, when friction becomes insufficient. This implies that the final speed of the strip is lower than that of the rolls, which means, by definition, that the forward slip becomes negative. Thus, the forward slip decreases, when friction decreases [206, 276]. Quantitatively, this statement can be expressed by the following formula [107, 199]:

$$s_f = \frac{R}{t_{\text{out}}}\left(\frac{\alpha}{2} - \frac{\alpha^2}{4\mu}\right)^2 \tag{3.14}$$

where R is the deformed roll radius, t_{out} the final strip thickness, α the angle at the entry of the roll bite (Fig. D.1) and μ the (constant) coefficient of friction. One should notice that the forward slip could decrease, while friction increases due to other influences in the previous equation. For instance, when the reduction ratio decreases, the final strip thickness increases, if the initial thickness is constant, so that the forward slip would decrease according to the previous equation.

Simultaneously, friction could increase since less lubricant permeates into the solid/solid contact region by MPH lubrication (Sec. 2.2.4.3) due to the smaller reduction.

Furthermore, the forward slip decreases much more for the S2 strip than the S1 strip, i.e. from about 9% to 3.5% instead of 4.4% to 3.4% (Fig. 3.6b), respectively. Among other things, this could possibly be explained by the difference in *roughness* of the different strips since the S2 strip is much smoother than the S1 strip, so that an equal increment of the lubricant film thickness with the rolling speed would reduce the solid/solid contact, and thus, friction more significantly for the smoother strip. The different *initial thicknesses* of the S1 and S2 strips also influence these values via the contact angle of the roll bite or the final thickness in Eq. (3.14), since the reduction ratio is constant for both strips.

3.2.1.2 Viscoplasticity

The increase of the rolling force in Fig. 3.6a, which seems to be in contradiction with the previous reasoning, seems mainly to be due to *viscoplasticity*. In fact, if the rolling speed increases, the deformation rate, or more specifically, the effective plastic strain rate $\overline{D}^p$ (Eq. H.58) increases. If the metal is viscoplastic, this leads to an increase of its resistance, which is quantified by its (extended)[3] yield stress σ_Y. As explained in the previous section, the vertical stress σ_z and, thus, the interface pressure p_i directly depend on the yield stress. If it increases, the interface pressure increases and therefore, the rolling force, too. In short,

$$v_r \nearrow \quad \rightarrow \quad \overline{D}^p \nearrow \quad \rightarrow \quad \sigma_Y \nearrow \quad \rightarrow \quad \sigma_z \searrow \quad \rightarrow \quad p_i \nearrow \quad \rightarrow \quad F_r \nearrow \tag{3.15}$$

The increase of the rolling force in Test 6 could (theoretically) also be explained by *starvation*, which will be clarified in the following section. A simultaneous drop of the forward slip due the starvation seems, however, unlikely because of the increased friction, when not enough oil is provided to the roll bite. For this reason, the coexistence of viscoplasticity with a simultaneous decrease of friction due to the hydrodynamic effect seems to be a more consistent explanation of the increasing rolling force and decreasing forward slip with the rolling speed in Fig. 3.6: while viscoplasticity has a significant impact on the rolling force, the forward slip mainly depends on the friction state. This explanation is also provided by Zhang and Lenard [379] in a similar scenario. An extreme case of this scenario is dry rolling as illustrated by Fig. 6.6 in Roberts [276], which shows that the rolling force increases with the rolling speed while the forward slip remains constant according to experiments.

[3]The *extended* yield stress σ_Y is the combination of the conventional yield stress σ_Y^*, for which the effective plastic strain rate $\overline{D}^p$ is theoretically 0, and the viscoplastic component in the material equation of the effective stress σ_{VM} (here the Von Mises stress), e.g. $\sigma_{\mathrm{VM}} = \sigma_Y^* + A\overline{D}^p$, where A is a material constant [158]. In the literature, this combination is sometimes directly called yield stress, e.g. [130, 349], or not, e.g. [158, 258, 259]. To simplify the explanations, the extended yield stress σ_Y is usually called *yield stress* in this document.

3.2.2 Influence of the lubricant quantity

Figs. 3.7 and 3.8 show that the *rolling force and the forward slip generally increase, when the available quantity of lubricant decreases, if it is below a certain threshold*. This observation is less obvious in Fig. 3.8a than in Fig. 3.7a due to the measurement in the unsteady state at 200 m/min (red triangle)[4], and the small differences of the rolling force for different lubrication condition, which could be caused, amongst others, by slightly different operating conditions.

The increase of the rolling force and the forward slip with the decreasing lubricant quantity can be explained as follows. If the lubricant film thickness provided by the lubrication system h_L decreases, and if it becomes smaller than the maximum lubricant film thickness passing through the roll bite in full-flooded lubrication (Wilson and Walowit, Eq. 2.18), the lubricant film thickness h_t in the bite decreases. Otherwise, it remains equal to this maximum film thickness since the roll bite cannot absorb more lubricant. If the film thickness in the roll bite decreases, more significant contact between solid surfaces increases friction. And finally, as explained in Sec. 3.2.1.1, friction increases the rolling load and forward slip. In short,

$$h_L \searrow \rightarrow h_t \searrow \rightarrow A \nearrow \rightarrow \overline{\mu} \nearrow \rightarrow F_r \nearrow, s_f \nearrow \tag{3.16}$$

The previous condition, in which less lubricant enters into the roll bite than it can absorb, is called *starvation*.

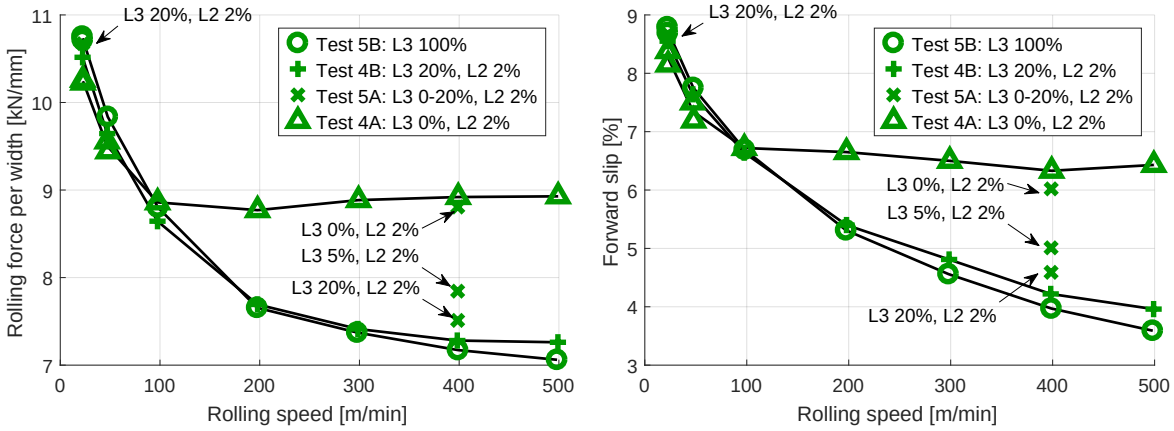

(a) Rolling force per width. **(b)** Forward slip.

Figure 3.7: Influence of the lubricant quantity with the rolled product *S2* and constant elongation (30%). The L3 lubricant is introduced by the flexible lubrication circuit, while the L2 lubricant is applied by the recirculating circuit.

Starvation can occur for different reasons. First, it can occur when the *rolling speed is increasing*. In this case, the roll bite can absorb more lubricant, which is not necessarily available. In fact, if

[4]In fact, the rolling force was still increasing at 200 m/min since the final thickness was not reached yet, when the measurement was taken. Hence, it can be expected that the rolling force at 200 m/min in the steady state is more important than the one shown in Fig. 3.8a.

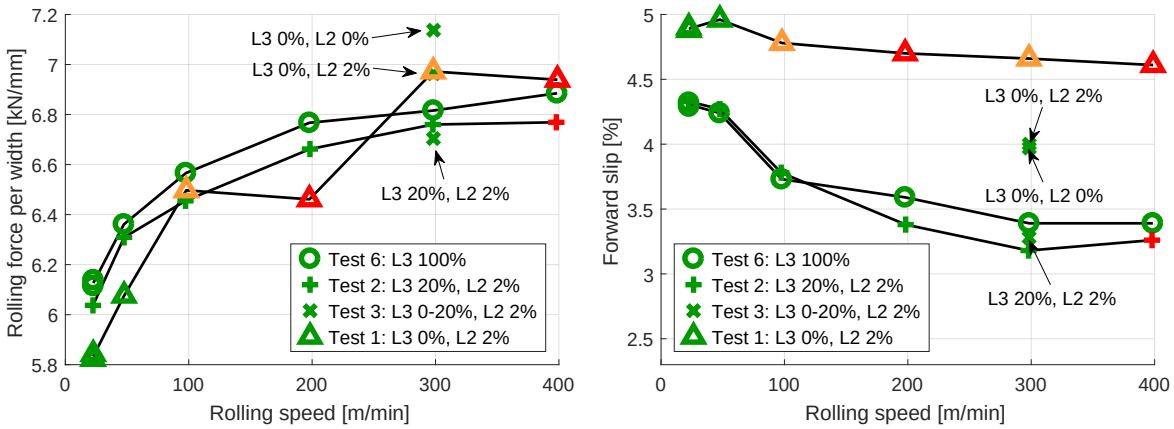

(a) Rolling force per width.

(b) Forward slip.

Figure 3.8: Influence of the lubricant quantity with the rolled product *S1* and constant elongation (30%). The L3 lubricant is introduced by the flexible lubrication circuit, while the L2 lubricant is applied by the recirculating circuit. The color code indicates the state, in which the measurements were taken, as explained at the beginning of Sec. 3.2 (green: steady state; orange: almost steady; red: unsteady).

an emulsion is applied, the lubricant film thickness in the roll bite first increases with the rolling speed like in full-flooded lubrication. If the rolling speed is further increased, this thickness either becomes constant or it decreases [63]. The decrease could be explained by less and less lubricant being available per unit length of the strip when the lubricant spray rate is constant. In addition, the lubricant film formation could be less efficient per unit length of the strip at higher rolling speeds [63], e.g. due to the reduction of the time available for the oil to connect to the lipophilic surfaces of the strip (Sec. 2.2.4.1). The occurrence of starvation with the rolling speed is shown in Fig. 3.7 by the Test 4A. At low rolling speed, the oil film thickness increases with this speed by viscous entrainment, and the rolling forces and forward slips are almost identical for all lubrication conditions. At rolling speeds greater than 100 m/min, the thickness of the film seems, however, to become constant in Test 4A because the rolling force and the forward slip become almost constant with the rolling speed, too. In consequence, the rolling force and forward slip are greater than in the other test cases, in which more lubricant is provided to the roll bite. Secondly, starvation can occur when the *concentration of the lubricant in the emulsion is reduced* [271]. This is shown specifically in Test 5A in Fig. 3.7 and in Test 3 in Fig. 3.8. *Conversely, it is important to mention that this mechanism is the underlying principle of flexible lubrication, which consists in adjusting the lubrication conditions to minimize friction and thus, the rolling force, while preventing skidding.* In fact, Fig. 3.7a clearly shows that the rolling force obtained with a conventional recirculating system (emulsion with a low oil concentration and a low viscosity oil) can be significantly reduced, if the lubricant quantity is increased by flexible lubrication in the *domain of starvation*. Outside of this domain, e.g. at low rolling speeds, the flexible lubrication system has essentially no influence in the considered test cases. Furthermore, higher oil concentrations than 20% also have no significant influence in these cases.

Concerning Tests 5A and 3 in Figs. 3.7 and 3.8, it is interesting to notice that the respective results

in Tests 4A and 4B, and Tests 1 and 2 are almost identical at 300 m/min (except for the forward slip in Fig. 3.8b). The cross in Fig. 3.8 at 300 m/min, which has no immediate counterpart in Tests 1 or 2, corresponds seemingly to rolling without the recirculating and flexible lubrication systems. It is unclear why the corresponding forward slip in Fig. 3.8b is not more significant.

3.2.3 Influence of the lubricant type and spray temperature

Figs. 3.9 and 3.10 illustrate the influence of the *lubricant type* and its spray temperature. These tests were carried out with two pure oils, L1 and L3, which is the less viscous one. It can be observed that the rolling force and the forward slip decrease with increasing viscosity. This observation can be explained by the hydrodynamic effect, which was described in Sec. 3.2.1.1. More precisely, if the viscosity η increases, the mean film thickness of lubricant h_t in the bite increases due to viscous entrainment. This mechanism is included in the equation by Wilson and Walowit [368] (Eq. 2.18). If the mean film thickness increases, the load supported by the solid/solid interface decreases. Hence, friction decreases, as well as the rolling force and the forward slip.

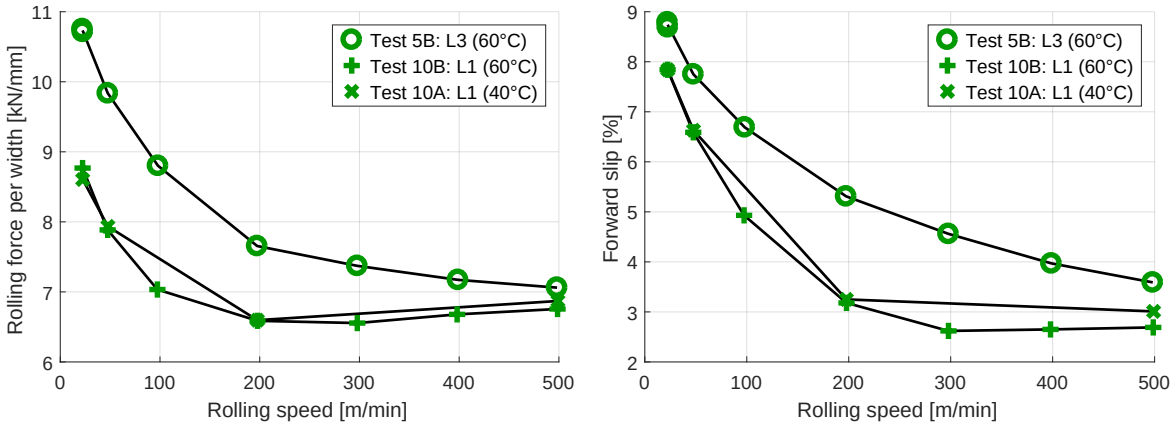

(a) Rolling force per width.

(b) Forward slip.

Figure 3.9: Influence of the lubricant type (flexible lubrication by pure and less viscous L3 or pure and more viscous L1) and its temperature (40°C or 60°C) with the rolled product *S2* and constant elongation (30%).

In addition to the comparison of results for two different lubricants, results were also obtained for a single lubricant at different *spray temperatures* in Fig. 3.9. These results are almost identical. In general, the lubricant spray temperature therefore seems to have no influence on the rolling force or the forward slip, at least in the analyzed rolling conditions, probably because of heat exchanges with the strip and the rolls. The lubricant temperature at the immediate entry of the bite $T_{l,\text{in}}$, i.e. not its spray temperature, has however a significant influence on the rolling load since it influences its viscosity. In fact, the rolling force and the forward slip decrease, when the lubricant temperature $T_{l,\text{in}}$ decreases due to the resulting increase of its viscosity. The influence

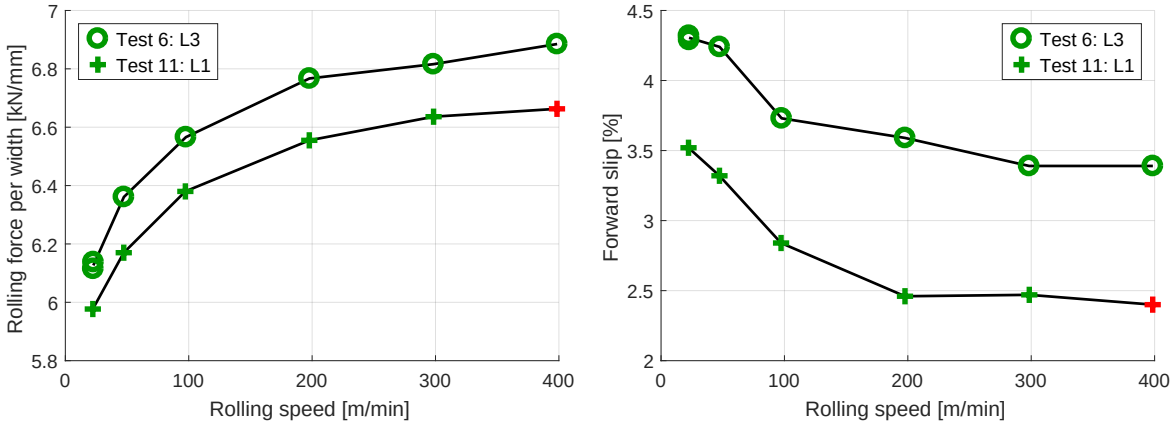

(a) Rolling force per width.

(b) Forward slip.

Figure 3.10: Influence of the lubricant type (flexible lubrication by pure and less viscous L3 or pure and more viscous L1) with the rolled product *S1* and constant elongation (30%). The color code indicates the state, in which the measurements were taken, as explained at the beginning of Sec. 3.2 (green: steady state; orange: almost steady; red: unsteady).

of the lubricant type and its temperature can be summarized as follows:

$$T_{l,\text{in}} \searrow \rightarrow \eta \nearrow \rightarrow h_t \nearrow \rightarrow A \searrow \rightarrow \overline{\mu} \searrow \rightarrow F_r \searrow, s_f \searrow \tag{3.17}$$

One can also notice that the rolling force and the forward slip increase slightly at higher rolling speeds in Fig. 3.9 for the more viscous L1 lubricant in Tests 10A and 10B. This might be due to increasing starvation at higher rolling speeds, when the lubricant inlet flow rate is constant, as explained in Sec. 3.2.2. This hypothesis seems, however, unlikely since it supposes that not enough pure oil was sprayed onto the strip during the experimental campaign.

An alternative explanation might be *viscous friction*, which becomes more significant at high rolling speeds if the oil remains Newtonian. In fact, the lubricant shear stress τ_l between the rolls and the strip increases with the rolling speed v_r, because the speed differential $|v_r - v_s|$ between their surfaces rises. In consequence, the resulting increase of friction raises the rolling force and the forward slip:

$$v_r \nearrow \rightarrow |v_r - v_s| \nearrow \rightarrow \tau_l \nearrow \rightarrow \overline{\mu} \nearrow \rightarrow F_r \nearrow, s_f \nearrow \tag{3.18}$$

Finally, the increase of the rolling force and the forward slip with the rolling speed could also be explained by the *heating of the roll* since more energy is dissipated by friction and plastic deformation per unit of time, when the rolling speed increases. In consequence, the heat of the roll could reduce the lubricant film thickness by decreasing the viscosity of the lubricant:

$$v_r \nearrow \rightarrow T_{l,\text{in}} \nearrow \rightarrow \eta \searrow \rightarrow h_t \searrow \rightarrow A \nearrow \rightarrow \overline{\mu} \nearrow \rightarrow F_r \nearrow, s_f \nearrow \tag{3.19}$$

The *influence of the lubricant type* is also illustrated *for recirculated emulsions* in Fig. 3.11 instead of directly applied pure oils, as shown previously. The recirculated emulsion contains either about 2% L1 or 2% L2, which is less viscous than L1. As expected, the forward slip is greater for the emulsion with the less viscous lubricant. The tendency is, however, inverted for the rolling force, which could be explained by the measurements in the transient state in Test 1.

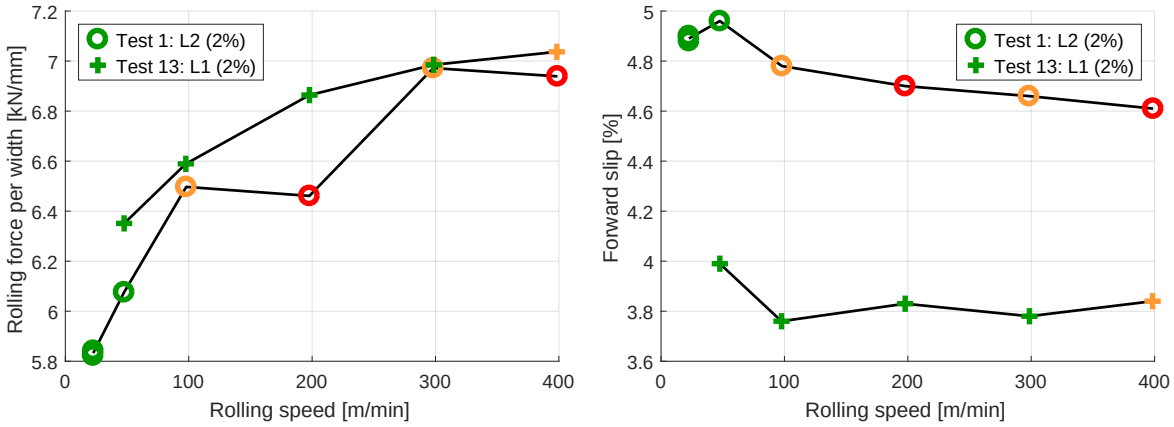

(a) Rolling force per width.

(b) Forward slip.

Figure 3.11: Influence of the lubricant type (recirculated emulsion with either 2% less viscous L2 or 2% more viscous L1) with the rolled product S1 and constant elongation (30%). The color code indicates the state, in which the measurements were taken, as explained at the beginning of Sec. 3.2 (green: steady state; orange: almost steady; red: unsteady).

3.2.4 Influence of the elongation/reduction

Figs. 3.12 and 3.13 show the influence of the *elongation*, which is equivalent to the influence of the reduction, on the rolling force and forward slip. The elongation in this context is defined (Eq. 2.3) as the engineering strain $e_x = (l_{\text{out}} - l_{\text{in}})/l_{\text{in}}$, where l_{in} is the distance between two points of the strip in the rolling direction before the bite and where l_{out} is this distance after the bite.

The *rolling force* increases with the elongation in all of the previous cases. This can be explained as follows. On the one hand, the *length of the roll bite* l_{rb} increases, when the elongation increases, due to the geometrical configuration (Eq. 2.4). And since the interface pressure is generally at least equal to the yield stress in the plane-strain state, the resulting force of the vertical stresses, increases, too:

$$\epsilon_x \nearrow \quad \rightarrow \quad l_{\text{rb}} \nearrow \quad \rightarrow \quad F_r \nearrow \tag{3.20}$$

This phenomenon is further amplified by roll flattening (Sec. 2.1.2.2), which increases the length of the roll bite, due to important stresses between the rolls and the strip.

On the other hand, the strain and, in consequence, the effective plastic strain $\overline{\epsilon}^p$ increase with the elongation. Hence, *work hardening* increases the yield stress σ_Y of the material, which raises the

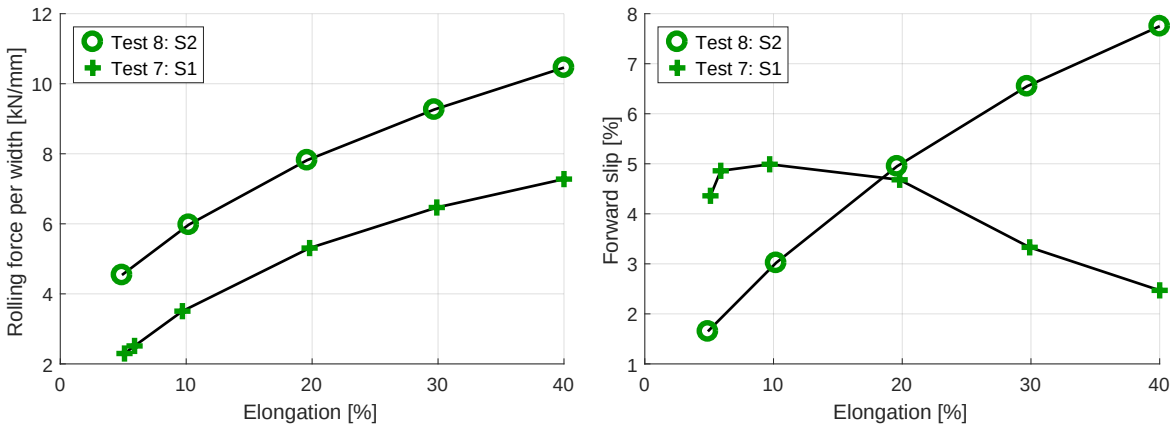

(a) Rolling force per width. **(b)** Forward slip.

Figure 3.12: Influence of the elongation at the rolling speed $v_r = 100$ m/min with flexible lubrication by pure L3 for different rolled products (S2 and S1).

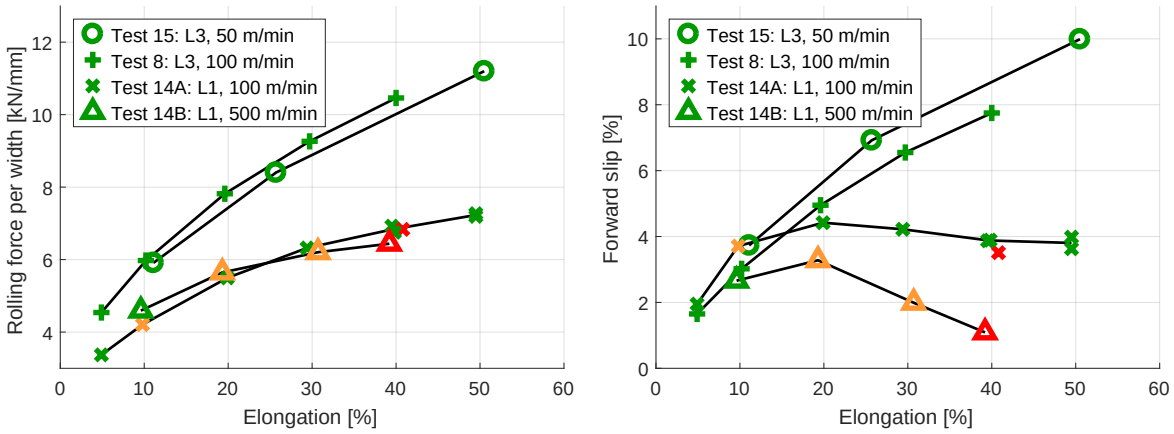

(a) Rolling force per width. **(b)** Forward slip.

Figure 3.13: Influence of the elongation with the rolled product S2 at different rolling speeds with flexible lubrication by pure and less viscous L3 or pure and more viscous L1. The color code indicates the state, in which the measurements were taken, as explained at the beginning of Sec. 3.2 (green: steady state; orange: almost steady; red: unsteady).

rolling force, as explained in Sec. 3.2.1.2:

$$e_x \nearrow \quad \rightarrow \quad \overline{\epsilon}^p \nearrow \quad \rightarrow \quad \sigma_Y \nearrow \quad \rightarrow \quad F_r \nearrow \tag{3.21}$$

The rolling force is greater for the S2 strip than for the S1 strip, if their elongation is identical, as shown in Fig. 3.12a. This observation could be explained by the greater yield stress of the S2 strip, although further mechanisms influence its value, as detailed hereafter.

Concerning the *forward slip*, Fig. 3.12b shows that the behavior can be totally different depending on the rolled product. Previously, it was already suggested by Eq. (3.14), that the forward slip is the result of *different interacting mechanisms*.

First, the increase of the forward slip is at least partially due to *the increased length of the contact arc between the roll and the strip*, when the elongation increases. The converse case can be considered to clarify this explanation. In fact, if the elongation is reduced and if the forward slip is positive (no skidding), the neutral point gradually approaches the exit of the roll bite until the strip and the roll are (hypothetically) only touching at one point (in 2D), where their speeds are identical, so that the forward slip is 0. Conversely, the forward slip increases, when the elongation increases according to this mechanism:

$$e_x \nearrow \quad \rightarrow \quad l_{\mathrm{rb}} \nearrow \quad \rightarrow \quad s_f \nearrow \tag{3.22}$$

Secondly, the *contact angle* α between the roll and the strip (Fig. D.1) increases, when the elongation increases. Hence, the lubricant film thickness decreases (Sec. D), so that the rolling force and the forward slip increase since friction increases:

$$e_x \nearrow \quad \rightarrow \quad \alpha \nearrow \quad \rightarrow \quad h_t \searrow \quad \rightarrow \quad A \nearrow \quad \rightarrow \quad \overline{\mu} \nearrow \quad \rightarrow \quad F_r \nearrow, s_f \nearrow \tag{3.23}$$

Thirdly, the increase of the forward slip with the elongation can also partially be explained by *asperity flattening*. In fact, if the elongation increases, the resistance of the material to indentation decreases. Hence, the relative contact area increases, as explained in Sec. 2.2.2.2. Since the load is less supported by the lubricant, friction increases and the forward slip, too. Besides increasing the forward slip, this mechanism also increases the rolling load due to the resulting increase in friction, when the reduction increases. In short,

$$e_x \nearrow \quad \rightarrow \quad A \nearrow \quad \rightarrow \quad \overline{\mu} \nearrow \quad \rightarrow \quad F_r \nearrow, s_f \nearrow \tag{3.24}$$

In the case of the S1 strip, the forward slip mainly decreases with the reduction except for the first few measurements. This can potentially be explained as follows. When the elongation increases, the lubricant in the valleys is more and more compressed until it flows to the asperity tops where it progressively separates the solid/solid contact. Both strips in Fig. 3.12b differ, amongst others, by their roughness and their yield stress. In addition to a greater quantity of trapped lubricant with the S1 strip, its smaller yield stress might facilitate the permeation. In consequence, friction is reduced and the forward slip drops with increasing reduction. This description corresponds

to *micro-plasto-hydrodynamic/static (MPH) lubrication*, which was explained in Sec. 2.2.4.3. It also impacts the rolling force since friction is reduced. The rolling force does, however, not decrease with the elongation in the analyzed test cases due to other mechanisms, which increase its value more significantly, as explained previously. A decreasing rolling force with an increasing reduction is, however, possible. In a nutshell,

$$e_x \nearrow \rightarrow p_l \nearrow \rightarrow A \searrow \rightarrow \overline{\mu} \searrow \rightarrow F_r \searrow, s_f \searrow \tag{3.25}$$

The *effects of the rolling speed and the lubricant type* on the rolling load at constant reduction were analyzed in Secs. 3.2.1 and 3.2.3. These effects explain the smaller rolling forces (Fig. 3.13a), if the viscosity increases and the smaller forward slips (Fig. 3.13b), if the rolling speed or the viscosity increase. Concerning the differences between rolling forces for different rolling speeds in Fig. 3.13a, one would expect the force corresponding to greater rolling speeds to be smaller than those corresponding to smaller speeds due to decreased friction by an increased lubricant film thickness. The opposite is, however, experimentally observed with the L3 lubricant, and with the L1 lubricant at smaller rolling speeds. Overall, the respective differences are, however, relatively small. Thus, it is difficult to determine the precise underlying physical reason.

Interestingly, the forward slip decreases at higher reductions in the scenarios with the more viscous L1 oil in Fig. 3.13b, in contrast to the evolution with the L3 lubricant, while it increases in all scenarios at low reductions. Thus, MPH lubrication seems to be more pronounced when the rolling speed and the viscosity increase, possibly because of rolling conditions in favor of micro-plasto-hydro*dynamic* lubrication due to greater sliding speeds and viscosity (Sec. 2.2.4.3).

3.2.5 Higher rolling speeds

In Tests 9 and 12A, *higher rolling speeds*, i.e. 700 to 1200 m/min, were tested with the S3 coils and they are compared to the equivalent tests with the S2 coils in Fig. 3.14.

Fig. 3.14a shows that the rolling force per width with the rolled product S3 is much smaller than that required for the product S2. This can be explained by the smaller material resistance of the product S3 ($\sigma_Y^0 \approx 650$ MPa) with respect to the product S2 ($\sigma_Y^0 \approx 750$ MPa). The ratio of their respective rolling forces per width is, however, more significant than the simple ratio of their yield stresses probably due to more significant roll flattening with the more resistant material, which increases the length of the roll bite, and thus the rolling force per width (Eq. 3.20).

The rolling load and forward slip in Test 12A first decreases and then increases with the rolling speed, presumably for the reasons that were previously mentioned in Sec. 3.2.3: the lubricant film thickness increases with the rolling speed so that friction is reduced until viscous friction becomes significant.

Concerning Test 9, it is surprising to see that the rolling force per width and the forward slip are on average smaller than in Test 12A, although the L1 lubricant is more viscous than L3. Maybe these observations could be explained by the interaction of the hydrodynamic and viscous friction

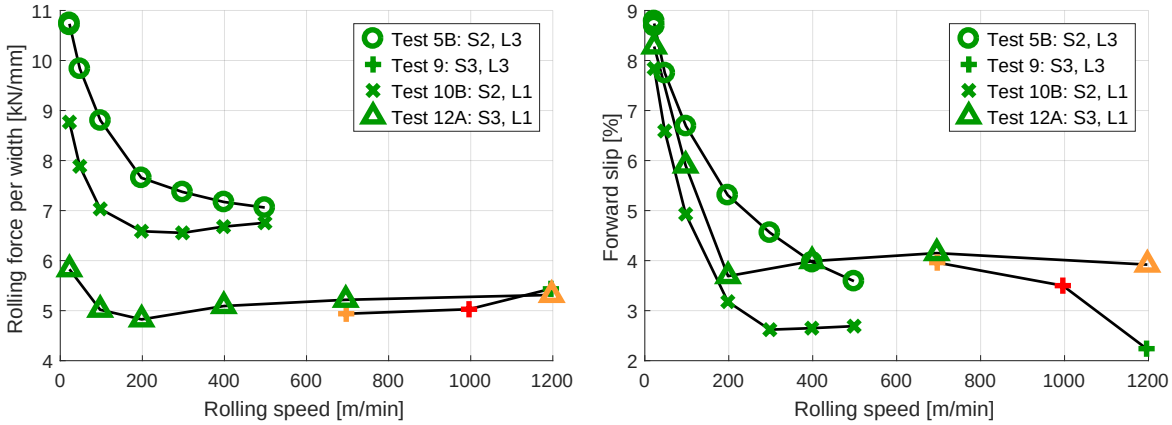

(a) Rolling force per width.

(b) Forward slip.

Figure 3.14: Influence of the rolling speed with flexible lubrication by pure and less viscous L3 or pure and more viscous L1, and constant elongation (30%) for different rolled products (more resistant S2 and less resistant S3). The color code indicates the state, in which the measurements were taken, as explained at the beginning of Sec. 3.2 (green: steady state; orange: almost steady; red: unsteady).

effects, which are not totally symmetric: if the viscosity rises, it might increase total friction more by viscous friction than it decreases total friction by increasing the lubricant film thickness.

3.3 Conclusion

In this chapter, the most comprehensive experimental data of lubricated cold rolling (to the best of our knowledge) were presented by describing the experimental setup and by analyzing the resulting data for two reasons: first, *to determine* which *physical mechanisms* have to be introduced in a cold rolling model to predict the rolling force and forward slip (amongst others) as well as possible, and secondly, to use the experimental *data* later on *to calibrate and validate this model* (Chap. 5).

In the first part of this chapter, the *experimental setup* is described. It consists of a semi-industrial, single stand, two-high pilot *mill*, which was used to roll three different *strip products* (format, steel grade, surface characteristics) with different *lubrication configurations*, different *rolling speeds* and different *elongations* (reductions). The input and output data of numerous experimental scenarios were measured. Concerning the input data, the roughness of the rolls and the strips was determined by a profilometer, while the yield curve of the strips was quantified by plane-strain compression tests. Unfortunately, the thermo-viscoplastic behavior of the strips was not measured. Three different lubricants were introduced in the bite either by the flexible lubrication system or by the recirculating circuit, in their pure form or by oil-in-water emulsions. The thermo-piezoviscous properties of the lubricants were determined by a coaxial cylinder rheometer and by a falling ball viscometer. Based on this input data, numerous test scenarios were defined. For each of these scenarios, the rolling force and the forward slip as well as other results were

measured.

In the second part of this chapter, the *influence* of the rolling speed, the rolled product, the lubricant quantity, the lubricant type, the lubricant temperature, and the elongation on the rolling force and the forward slip was *analyzed* based on the experimental results. Different *interacting physical mechanisms* were suggested to explain these influences, as far as possible, mainly:

- *Hydrodynamic effect*: if the rolling speed increases, the rolling force and the forward slip might decrease, if enough lubricant is provided, since a growing layer of lubricant, which is entrained in the roll bite, reduces friction. The same is true, if the viscosity of the lubricant increases.
- *Starvation*: when less and less lubricant is provided to the bite than it can absorb, the rolling force and the forward slip increase due to the decreasing thickness of the lubricant film.
- *Viscous friction*: at high rolling speeds, the rolling force and the forward slip can increase due to viscous shear stresses, if the speed increases.
- *Viscoplasticity*: if the strip is strain-rate-dependent, the rolling force can increase with the rolling speed due to the increase of the yield stress.
- *Work hardening*: work hardening increases the yield stress, when the elongation increases. In consequence, the rolling force increases with the elongation.
- *Modification of the roll bite geometry*: when the elongation of the strip increases, the length of the contact arc between the roll and the strip increases. Hence, the resultant force of the vertical stresses in the bite, i.e. the rolling force, and the forward slip increase. These consequences are amplified by the increase of friction since the hydrodynamic effect decreases due to the greater contact angle at the entry of the bite (when the elongation increases).
- *Asperity flattening*: the elongation of the strip reduces the resistance of asperities to their flattening, which increases the real contact area between the roll and the strip. Since less load is thus supported by the lubricant, friction increases, as well as the rolling force and the forward slip.
- *Micro-plasto-hydrodynamic/static lubrication*: when the elongation increases, the lubricant pressure might increase so strongly that the lubricant rises to the top of the asperities where it permeates into the solid/solid contact area. The resulting reduction of friction reduces the rolling force and the forward slip. This effect seems to become more important, if the rolling speed and the viscosity of the lubricant increase, which can be explained by micro-plasto-hydro*dynamic* lubrication.

Chapter 4

METALUB - A Mixed Lubrication Cold Rolling Model

In this chapter, the *mixed lubrication cold rolling model* METALUB, which will be used to reproduce the experimental data of the previous chapter in the following chapter, is explained. It is based on the LAM2DTRIBO model by Marsault (1998) [215], which was reimplemented and extended during the past 20 years at the LTAS-MN2L research group (University of Liège).

In the first section of this chapter, the *historical context* of the METALUB model with some implementation details is summarized, while the different model components are described in the remaining sections: *rolling process description, mixed lubrication, geometric contact description of rough surfaces, mechanics of the strip, roll flattening, asperity flattening, lubricant flow, thermal model, full model and its solution method*.

Due to the complexity and extensiveness of the numerous model components with changing implementations and sometimes incomplete explanations in the past, particular attention was paid to create a *solid foundation for future developments by being as comprehensive as possible* in this document. To provide, however, this information efficiently to the reader, significant parts of these explanations were moved to the appendix.

4.1 Historical context

In 1998, *Nicolas Marsault* finished his PhD thesis at École des Mines de Paris (CEMEF) during which he developed LAM2DTRIBO, a FORTRAN77 software of 2D cold rolling in the mixed lubrication regime, under the supervision of Pierre Montmitonnet [215]. LAM2DTRIBO is a second generation cold rolling model (Sec. 2.3.2), which includes elastoplastic strip deformations, elastic roll deformations by the finite element method, lubricant flow and asperity flattening. Nevertheless, its numerical robustness is limited (no results in some test scenarios), the computation time is relatively long (several minutes for one computation) and lubricant starvation is not modeled.

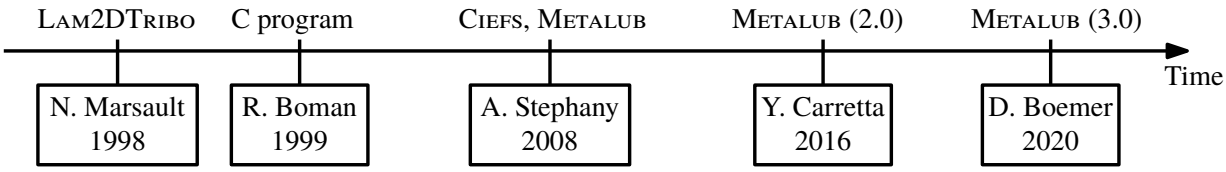

Figure 4.1: Development history of the cold rolling model Metalub with the respective program names (or specifications) and the dates, when researches either finished their PhD or stopped working full time on Metalub.

In 1999, *Romain Boman* reimplemented Marsault's model in the C programming language at the University of Liège [36]. During a collaboration with Pascal Gratacos at Irsid (now ArcelorMittal), they discovered that Boman's code is 10 to 100 times faster than Marsault's Lam2DTribo model.

In 2008, *Antoine Stephany* finished his PhD thesis, which was partially financed by ArcelorMittal, in which he developed two solvers on the basis of Boman's code [304, 305, 306, 307]. First, he developed Ciefs (Couplage Itératif et Étagé Fluid Structure, iterative and staggered fluid structure coupling), which is a combination of Marsault's model and the model with finite difference resolution of the Reynolds equation by Qiu et al. (1999) [265] to prevent the application of the high-speed simplification ($p_i = p_l$, Sec. 2.3.2). This model was, however, abandoned by Stephany due to its limited numerical robustness. Secondly, Stephany developed a C++ implementation of Boman's Lam2DTribo model in C, which he called Metalub, with the computation of elastic non-circular roll deformations by Jortner's method [163] (Sec. 4.6.3), a starvation model (Sec. 4.10.4) and extensive experimental validation (Sec. 5.1). His model was, however, abandoned by Carretta due to an overly complex programming style.

In 2014, *Yves Carretta* finished his thesis and he continued to work on lubricated cold rolling until 2016 at the University of Liège [54, 55, 56, 57, 58, 59, 60, 61, 62, 149, 180]. Carretta developed a new version of Metalub (2.0) in C++ by combining the best elements of Boman's and Stephany's codes. In particular, he used code management practices and software features of the finite element (FE) solver Metafor [35, 258], which is another software project in the LTAS-MN2L research group, to transform Metalub into a truly industrial tool with a long term development strategy: strongly object-oriented programming style in C++ for computational performance, version control via Svn, Python wrapper via Swig to construct data sets, automated regression tests, and a graphical user interface (GUI) in PyQt. Besides comparing Metalub results to those of the FE rolling code Lam3 (Sec. 2.3.1) without lubrication, reproducing rolling results with flexible lubrication (Sec. 2.1.3) by Metalub in the context of Nicolas Bockiau's internship [34] and comparing lubricant film thicknesses of Metalub to ultrasound measurements, Carretta coupled Stephany's version of Metalub with ThermRoll [42] to model heat transfers (Sec. 4.9.1) and Metalub (2.0) with Metafor to model asperity flattening as well as micro-plasto-hydrodynamic/static lubrication by the finite element method (Chap. 6).

In 2015, *Dominik Boemer*, the author of this document, started his PhD thesis by reviewing the past expertise in modeling of lubricated cold rolling and by extending it. In the following sections, the components of the current Metalub model are described in its most recent version (3.0). The

graphical user interface (GUI) of the underlying computer code is illustrated in appendix G.

4.2 Rolling process description

A metal strip of width w and thickness t_{in} enters the roll bite with a velocity v_{in}. The two rolls have a nominal, i.e. non-deformed, radius R_0 and an angular rotation speed ω_r. The strip exits the roll bite still with a width w (Sec. 2.1.2.2), a thickness t_{out} and a velocity v_{out}, which is equal to $v_{\text{in}} t_{\text{in}} / t_{\text{out}}$ by the conservation of mass, disregarding negligible elastic volume changes. The adjacent uncoiler, recoiler, mill stand or tension bridles apply the back and front tensions σ_{in} and σ_{out}, which are assumed to be constant through the cross-section. Due to the symmetry, this scenario can be modeled by considering only one half of the system as represented in Fig. 4.2. The coordinate system was oriented in such a way that $\mathbf{e}_x$ is the rolling direction and $\mathbf{e}_z$ the vertical axis. The direction $\mathbf{e}_y$ is deduced from the previous directions, since the coordinate system is supposed to be dextrorsum, i.e. right-handed. In the past [54, 215, 305], $\mathbf{e}_y$ was assumed to be the vertical axis, which is less popular and less optimal than choosing $\mathbf{e}_z$ as the vertical axis, in consideration of future extensions of the model.

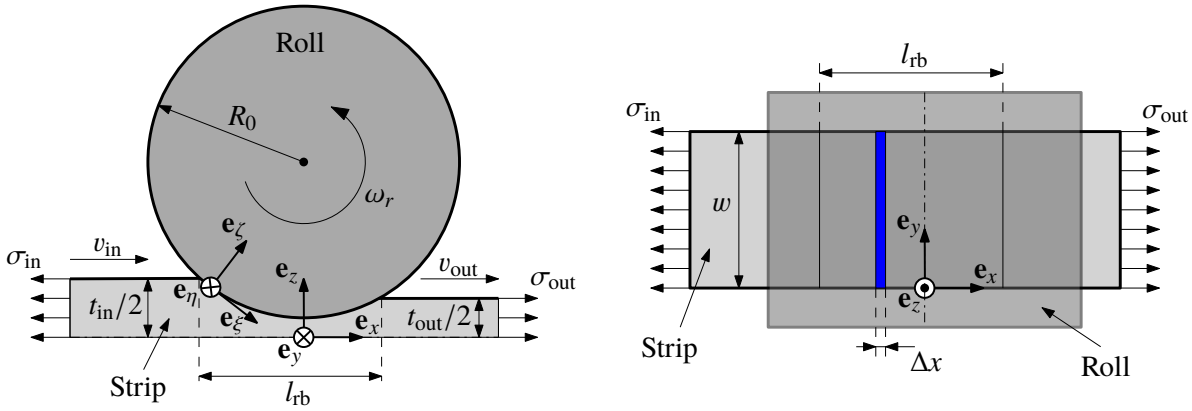

(a) Side view (plane symmetry with respect to $z = 0$).

(b) Top view. The blue area is the representative area of the contact state at a position x in the roll bite ($\Delta x \ll$).

Figure 4.2: Rolling process with coordinate systems, as well as geometric, kinematic and dynamic variables.

In strip rolling, the thickness of the strip is in general much smaller than the width of the strip and the length of the roll bite. For instance, in Test 5B-4, which was introduced in Chap. 3, the initial thickness $t_{\text{in}} = 0.75$ mm is significantly smaller than the width $w = 75$ mm and the length of the roll bite $l_{\text{rb}} \approx 10$ mm [150, p. 218]. Moreover, the process is assumed to be geometrically identical in different $\mathbf{e}_x\mathbf{e}_z$-planes along $\mathbf{e}_y$, since roll deflection by bending is reduced as much as possible [276, p. 153]. Because of the previous reasons, state variables, like strains and stresses, are expected to depend mainly on the Eulerian x-coordinate in the roll bite [235, p. 62], which is a reasonable hypothesis provided that the ratio of the roll bite length l_{rb} and the strip thickness t_s is greater than 3 according to Montmitonnet [234].

4.3 Load sharing equation in mixed lubrication

METALUB was created to model cold rolling in the mixed lubrication regime. In this regime, forces from the roll are transmitted to the strip partially by the contact between solid asperities and partially by the lubricant as explained in Sec. 2.2.4.2. If $\mathbf{F}_i$ is the total force resulting from the asperity contact force $\mathbf{F}_a$ and the lubricant force $\mathbf{F}_l$ at a position x of the roll bite for a small representative area around x (Fig. 4.2b), then

$$\mathbf{F}_i = \mathbf{F}_a + \mathbf{F}_l \tag{4.1}$$

In a 2D case, like cold rolling by assumption (Fig. 4.2a), the previous equation can be related to the local pressure and shear stresses by defining normal and tangential force components with respect to the contact plane:

$$\mathbf{F}_i = N_i\mathbf{e}_\xi + T_i\mathbf{e}_\zeta \qquad \mathbf{F}_a = N_a\mathbf{e}_\xi + T_a\mathbf{e}_\zeta \qquad \mathbf{F}_l = N_l\mathbf{e}_\xi + T_l\mathbf{e}_\zeta \tag{4.2}$$

Since rough surfaces are generally not entirely in contact with each other due to this roughness, one can distinguish the real contact area A_r from the apparent contact area A_a (Sec. 2.2.2). If the interface pressure p_i is defined with respect to the apparent contact area A_a, the asperity contact pressure p_a with respect to the real contact area A_r and the lubricant pressure with respect to the remaining area $A_a - A_r$, these pressures can be combined in the following equation:

$$N_i = N_a + N_l \qquad \Rightarrow \qquad A_a p_i = A_r p_a + (A_a - A_r)p_l \tag{4.3}$$

A more convenient way of writing the previous equation without the extensive quantities of the area can be obtained by the *relative contact area* $A = A_r/A_a$ (Eq. 2.15). Hence, the following *load sharing equation* can be written based on Eqs. (4.3) and (2.15):

$$p_i = Ap_a + (1 - A)p_l \tag{4.4}$$

Similarly, the local shear stress is the combination of the asperity shear stress τ_a and the shear stress created by the viscosity of the lubricant τ_l:

$$\tau_i = A\tau_a + (1 - A)\tau_l \tag{4.5}$$

In the following sections, it will be explained how the different components in the previous equations can be computed along the roll bite thanks to a roughness description (for A), strip and roll mechanics (for p_i and τ_i), asperity contact (for p_a and τ_a) and lubricant flow (for p_l and τ_l).

4.4 Geometric contact description of rough surfaces

In this section, some *geometric contact parameters*, i.e. the distance between non-updated mean lines h, the mean film thickness h_t and the relative contact area A, will be defined and written as functions of each other based on some hypotheses as shown in Fig. 4.3.

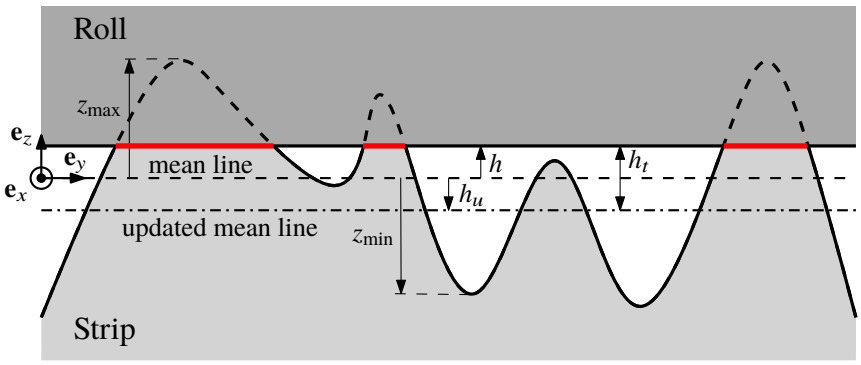

Figure 4.3: Geometric contact parameters, essentially, the distance between non-updated mean lines h and the distance between updated mean lines h_t.

Thus, when the surface of the strip is flattened by the roll, the *roll is supposed to be and to remain locally flat*. The influence of these assumptions is reduced by taking into account the RMS roughness of the roll $R_{q,r}$ in the RMS composite roughness R_q (Sec. 2.2.1.3), and by considering the fact that the hardness of the roll is significantly greater than that of the strip [276, p. 109]. Concerning the strip, the *shape of its asperities is assumed to be preserved* during their flattening but the material which trespasses the mean line of the roll surface is eliminated from the system (see dotted lines in Fig. 4.3). This is equivalent to assuming that the profile increases uniformly its height in the valleys of the asperities, which is reasonable according to the findings by Pullen and Williamson (Sec. 2.2.2.1) [264]. In fact, the shape preservation can be explained by the material rise in the valleys of the roughness due to the asperity flattening and the incompressibility of a plastically deforming metal [48, 49].

4.4.1 Distance between non-updated mean lines

The *distance h between non-updated mean lines* in Fig. 4.3 is the signed distance between the non-updated mean line of the strip and the non-updated mean line of the roll. These mean lines are computed according to Eq. (2.8). The distance between them is measured from the strip to the roll (positive sign). It decreases, when the surface asperities of the strip are flattened during the rolling process. In consequence, h can become negative.

4.4.2 Relative contact area

The relative contact area A (Sec. 2.2.2) between the strip and the roll can be related to the surface height distribution function (Sec. 2.2.1.2) of the strip, if the profile is assumed to be preserved during asperity flattening:

$$A(h) = \begin{cases} \int_h^{z_{max}} f_Z(z)\,\mathrm{d}z & \text{, if } h \leq z_{max} \\ 0 & \text{, otherwise.} \end{cases} \tag{4.6}$$

4.4.3 Mean film thickness

The *mean film thickness* h_t is defined as the distance between the updated mean lines of the strip roughness and the roll (Fig. 4.3). It can be computed as follows:

$$h_t(h) = \begin{cases} \displaystyle\int_{z_{\min}}^{h} (h-z) f_Z(z)\, \mathrm{d}z & \text{, if } h \leq z_{\max} \\ h & \text{, otherwise.} \end{cases} \tag{4.7}$$

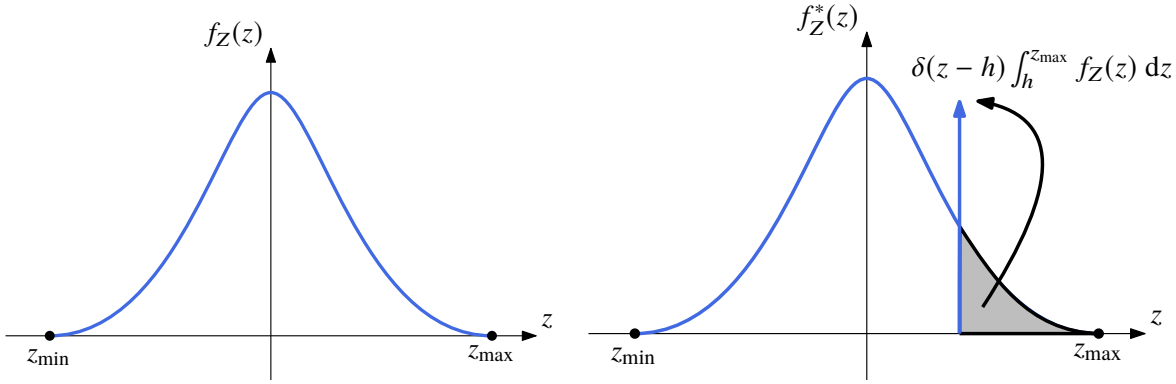

(a) Before flattening. **(b)** After flattening.

Figure 4.4: Modification of the surface height distribution function during asperity flattening.

In fact, the surface height distribution $f_Z(z)$ of the strip (and the roll via R_q) before flattening can be represented by the function in Fig. 4.4a. When the asperities are crushed due to the contact between the strip and the roll, a new surface height distribution $f_Z^*(z)$ is obtained as shown in Fig. 4.4b. This illustration is based on the idealized material elimination hypothesis. Hence, the material, which trespasses the surface of the roll, is simply deleted as explained earlier, and a delta Dirac function at $z = h$ replaces the contribution of these heights. In consequence, the non-trivial part of Eq. (4.7) can be proven by assuming that $h \leq z_{\max}$:

$$\begin{aligned} h_t &= h - h_u && (4.8)\\ &= h - \int_{z_{\min}}^{z_{\max}} z f_Z^*(z)\, \mathrm{d}z && (4.9)\\ &= h - \left[\int_{z_{\min}}^{h} z f_Z(z)\, \mathrm{d}z + h \int_{h}^{z_{\max}} f_Z(z)\, \mathrm{d}z \right] && (4.10)\\ &= \int_{z_{\min}}^{h} (h-z) f_Z(z)\, \mathrm{d}z && (4.11) \end{aligned}$$

where h_u is defined in Fig. 4.3 as the signed distance from the mean line of the strip to its updated mean line. In the previous reasoning, we used the following relation, which simply states that all heights z are in between $z_{\min}$ and $z_{\max}$:

$$\int_{z_{\min}}^{z_{\max}} f_Z(z)\, \mathrm{d}z = 1 = \int_{z_{\min}}^{h} f_Z(z)\, \mathrm{d}z + \int_{h}^{z_{\max}} f_Z(z)\, \mathrm{d}z \tag{4.12}$$

4.4.4 Application

Based on Eqs. (4.6) and (4.7), it is possible to compute analytically the relative contact area A and the mean film thickness h_t of the triangular asperity (Eq. 2.11) and Christensen (Eq. 2.12) height distributions as a function of the distance h between non-updated mean lines, i.e. $A(h)$ and $h_t(h)$. Other relations, like the inverse relation $h(h_t)$ and the derivatives $\partial A(h)/\partial h$ and $\partial h_t(h)/\partial h$ will also be required in the METALUB model. Hence, they are derived, too.

4.4.4.1 Triangular asperity height distribution

- Relative contact area:

$$A(h) = \begin{cases} \frac{1}{2} - \frac{h}{2\sqrt{3}R_q} & \text{, if } h < \sqrt{3}R_q \\ 0 & \text{, otherwise.} \end{cases} \tag{4.13}$$

$$\frac{\partial A}{\partial h}(h) = \begin{cases} -\frac{1}{2\sqrt{3}R_q} & \text{, if } h < \sqrt{3}R_q \\ 0 & \text{, otherwise.} \end{cases} \tag{4.14}$$

- Mean film thickness:

$$h_t(h) = \begin{cases} \frac{\sqrt{3}R_q}{4}\left(1 + \frac{h}{\sqrt{3}R_q}\right)^2 & \text{, if } h < \sqrt{3}R_q \\ h & \text{, otherwise.} \end{cases} \tag{4.15}$$

- Distance between non-updated mean lines:

$$h(h_t) = \begin{cases} \sqrt{3}R_q\left(\sqrt{\frac{4h_t}{\sqrt{3}R_q}} - 1\right) & \text{, if } h_t < \sqrt{3}R_q \\ h_t & \text{, otherwise.} \end{cases} \tag{4.16}$$

$$\frac{\partial h}{\partial h_t}(h_t) = \begin{cases} \sqrt{\frac{\sqrt{3}R_q}{h_t}} & \text{, if } h_t < \sqrt{3}R_q \\ 1 & \text{, otherwise.} \end{cases} \tag{4.17}$$

The previous equations were obtained by inverting Eq. (4.15) and taking the derivative of the resulting equation (Eq. 4.16) with respect to h_t.

4.4.4.2 Christensen height distribution

To simplify the notations, the variables $H = h/(3R_q)$ and $H_t = h_t/(3R_q)$ are introduced.

- Relative contact area:

$$A(h) = \begin{cases} \frac{1}{32}\left(16 - 35H + 35H^3 - 21H^5 + 5H^7\right) & \text{, if } H < 1 \\ 0 & \text{, otherwise.} \end{cases} \tag{4.18}$$

$$\frac{\partial A}{\partial h}(h) = \begin{cases} -\frac{35}{96R_q}\left(1-H^2\right)^3 & \text{, if } H < 1 \\ 0 & \text{, otherwise.} \end{cases} \tag{4.19}$$

- Mean film thickness:

$$h_t(h) = \begin{cases} \frac{3R_q}{256}\left(35 + 128H + 140H^2 - 70H^4 + 28H^6 - 5H^8\right) & \text{, if } H < 1 \\ h & \text{, otherwise.} \end{cases} \tag{4.20}$$

- Distance between non-updated mean lines:

$$h(h_t) = \begin{cases} 3R_q\left[-1 + 2H_t^{0.2235} + 0.5142H_t^{0.2222}(H_t - 1)\right] & \text{, if } H_t < 1 \\ h_t & \text{, otherwise.} \end{cases} \tag{4.21}$$

$$\frac{\partial h}{\partial h_t}(h_t) = \begin{cases} 0.4470H_t^{-0.7765} + 0.1143H_t^{-0.7778}(1 - H_t) \\ \quad +0.5142H_t^{0.2222} & \text{, if } H_t < 1 \\ 1 & \text{, otherwise.} \end{cases} \tag{4.22}$$

Deriving the inverse relation of Eq. (4.20) to obtain the function $h(h_t)$ in Eq. (4.21) is not as straightforward as inverting Eq. (4.15) due to the polynomial dependence. Instead of numerically solving the polynomial for a particular solution, which can be computationally time-consuming, a fitted relation, which satisfies the following conditions, was determined and its coefficients were chosen by the least squares method:

- $H = -1$ at $H_t = 0$
- $\partial H/\partial H_t \to +\infty$ as $H_t \to 0$
- $H = 1$ at $H_t = 1$

Eq. (4.22) was then computed by taking the derivative of Eq. (4.21) with respect to h_t. As shown in Fig. 4.5, the fitted relations seem to be sufficiently accurate approximations of the exact relations.

4.5 Mechanics of the strip

In this section, the *mechanics of the strip* are described. First, the strains of the strip are derived as functions of kinematic variables, i.e. the variations of the strip thickness and the strip speed along the roll bite. These strains can then be used to compute the stresses in the strip by the constitutive equations of the strip material. And finally, these stresses have to satisfy the equilibrium equations, which are derived by the slab method.

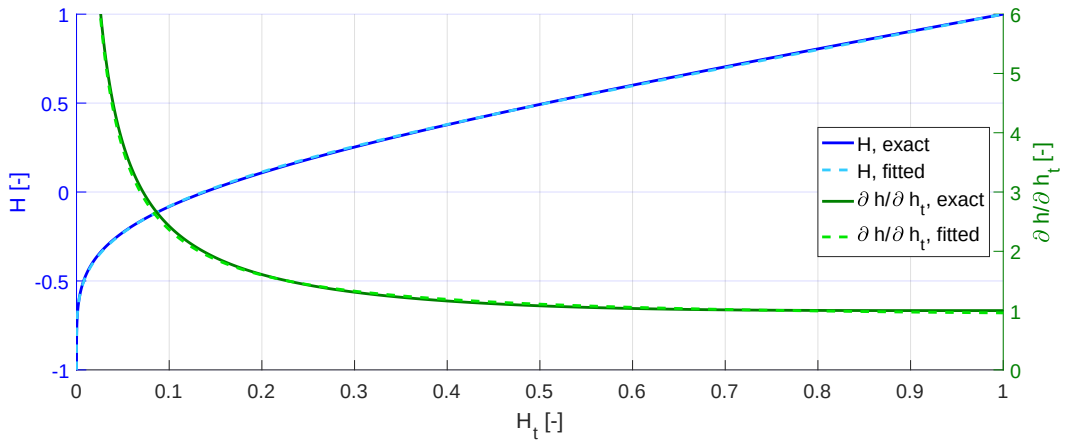

Figure 4.5: Comparison of the exact and fitted relations of the distance between non-updated mean lines and its derivative as a function of the mean film thickness. The corresponding functions are overlapping, if no visual differences can be seen although different colors were used.

4.5.1 Strain computation

The *strains* of the strip are essentially created by the space restriction between the rolls. Based on the previous definition of the distance between updated mean lines h_t, i.e. the mean film thickness, the thickness of the strip t_s can be related to the profile of the roll z_r, which does not necessarily remain circular, as shown in Fig. 4.6. Thus, at a specific position x in the roll bite:

$$h_t = z_r - \frac{t_s}{2} \tag{4.23}$$

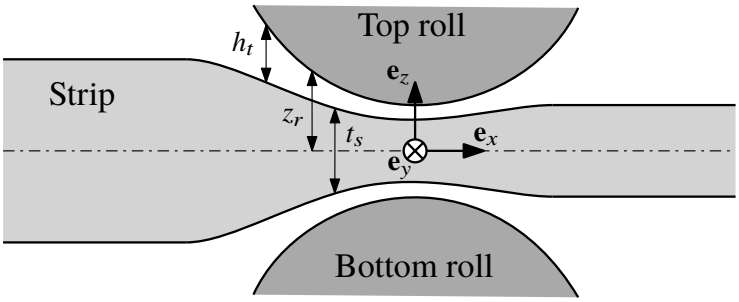

Figure 4.6: Profile of the roll $z_r(x)$, which is defined based on the distance between the updated mean lines of the rolls and the strip $h_t(x)$ and the thickness of the strip $t_s(x)$. The distances in the figure are computed along the vertical direction $\mathbf{e}_z$.

One should notice that the previous equation was rather $h = z_r - t_s/2$ *in the past* [54, 215, 305]. This formulation could result in a configuration with slightly *overlapping* roll and strip since h can become negative by definition. Since this overlapping is non physical, the previous equation was replaced by Eq. (4.23), which required the derivation of the inverse relation $h = h(h_t)$ in

Sec. 4.4.4. This correction changed the rolling forces and forward slips of the regression tests in METALUB on average by about 0.5% and 3% (relative change), respectively.

The local deformations of the strip are quantified by its strain tensor $\boldsymbol{\epsilon}$, which can be simplified in the scenario of strip rolling. Due to the assumed symmetry along $\mathbf{e}_y$, the shear terms ϵ_{xy}, ϵ_{yx}, ϵ_{yz} and ϵ_{zy} can be neglected. Moreover, the shear terms ϵ_{xz} and ϵ_{zx} are assumed to be zero due to the small thickness. A potential future solution to alleviating the previous hypothesis is introduced by Krimpelstätter [171, p. 178-185]. Furthermore, a classical hypothesis in strip rolling is the constant strip width inside the roll bite due to its small thickness and friction [276, p. 246]. In other words, the strain $\epsilon_y = 0$ vanishes by this *plane-strain hypothesis*. Supposing that the remaining deformations are homogeneous over the strip thickness due to the small thickness, the strain state can be entirely described by $\epsilon_x(x)$ and $\epsilon_z(x)$.

The evolution of these variables can be deduced from the evolution of the strip speed $v_s(x)$, which is also assumed to be uniform along $\mathbf{e}_z$ due to the small thickness, and its thickness $t_s(x)$. In fact, different strain measures can be defined in continuum mechanics (Sec. H.1.5.1). In this context, the *natural (or logarithmic) strain tensor* is chosen because the hardening laws in the previous chapter were determined based on this strain measure (Sec. 3.1.2). More precisely, the natural strain matrix is given by the following equation due to the previous simplifications:

$$\mathbf{E}^N = \begin{pmatrix} \epsilon_x & 0 & 0 \\ 0 & 0 & 0 \\ 0 & 0 & \epsilon_z \end{pmatrix} \tag{4.24}$$

with

$$\epsilon_x = \ln\left(\frac{l}{l_{\text{in}}}\right) \tag{4.25}$$

$$\epsilon_z = \ln\left(\frac{t_s}{t_{\text{in}}}\right) \tag{4.26}$$

where l_{in} is the distance between two very close material particles along the rolling direction $\mathbf{e}_x$ before the deformation of the strip, while l is this distance between the same particles but during the deformation of the strip, i.e. $l = l(x)$. Similarly, t_{in} is the initial thickness of the strip, while t_s is its thickness along the roll bite.

The *evolution of the strains*, i.e. $\partial\epsilon_x/\partial x$ and $\partial\epsilon_z/\partial x$, along the roll bite can be derived from the previous strain measures. First, for the longitudinal strain ϵ_x, the strain tensor $\mathbf{E}^N$ has to be related to the velocity gradient $\mathbf{L}$ (Eq. H.14) in order to write $\partial\epsilon_x/\partial x$ as a function of v_s. Since the strain matrix $\mathbf{E}^N$ is diagonal according to the previous hypotheses, the stretch matrix $\mathbf{U}$ (Eq. H.13) can be deduced:

$$\mathbf{U} = \exp \mathbf{E}^N = \begin{pmatrix} e^{\epsilon_x} & 0 & 0 \\ 0 & 0 & 0 \\ 0 & 0 & e^{\epsilon_z} \end{pmatrix} \tag{4.27}$$

The deformation gradient $\mathbf{F} = \mathbf{RU}$ is then equal to the stretch tensor (Eq. H.12), because, no rotation of the strip material occurs in the model, i.e. $\mathbf{R} = \mathbf{I}$, by assumption. Hence, the velocity gradient can be computed via the deformation gradient (Eq. H.15):

$$\mathbf{L} = \dot{\mathbf{F}}\mathbf{F}^{-1} = \begin{pmatrix} \dot{\epsilon}_x e^{\epsilon_x} & 0 & 0 \\ 0 & 0 & 0 \\ 0 & 0 & \dot{\epsilon}_z e^{\epsilon_z} \end{pmatrix} \begin{pmatrix} 1/e^{\epsilon_x} & 0 & 0 \\ 0 & 0 & 0 \\ 0 & 0 & 1/e^{\epsilon_z} \end{pmatrix} = \begin{pmatrix} \dot{\epsilon}_x & 0 & 0 \\ 0 & 0 & 0 \\ 0 & 0 & \dot{\epsilon}_z \end{pmatrix} \tag{4.28}$$

Thus, by the definition of the velocity gradient (Eq. H.14),

$$\dot{\epsilon}_x = \frac{\partial v_s}{\partial x} \tag{4.29}$$

The spatial evolution of the axial strain in the steady state ($\partial \epsilon_x / \partial t = 0$) is consequently given by the following equation (derivative of a Eulerian function, Eq. H.8 with flow along $\mathbf{e}_x$ solely):

$$\frac{\partial \epsilon_x}{\partial x} = \frac{1}{v_s} \frac{\partial v_s}{\partial x} \tag{4.30}$$

Secondly, the evolution of the vertical strain ϵ_z can be obtained by differentiating Eq. (4.26) with respect to x:

$$\frac{\partial \epsilon_z}{\partial x} = \frac{1}{t_s} \frac{\partial t_s}{\partial x} \tag{4.31}$$

Finally, the *relation between the effective strain $\bar{\epsilon}$ and t_s in the experimental plane-strain compression test* (Eq. 3.1) can be derived by the assumption that elastic strains are small with respect to plastic strains in cold rolling, i.e. $\bar{\epsilon} = \bar{\epsilon}^p$, by the definition of the effective plastic strain rate (Eq. H.58) and by the incompressibility of plastic deformations [48, 49], i.e. $\epsilon_x + \epsilon_z = 0$ (Eq. H.21 and $\epsilon_y = 0$):

$$\bar{\epsilon} = \sqrt{\frac{2}{3}\left(\epsilon_x^2 + \epsilon_z^2\right)} = \frac{2}{\sqrt{3}} |\epsilon_z| = \frac{2}{\sqrt{3}} \ln\left(\frac{t_{\text{in}}}{t_s}\right) \tag{4.32}$$

4.5.2 Constitutive equations of the strip

The material deformation mode changes along the roll bite. It is commonly assumed that the deformation of the strip is elastic at the entry and exit of the roll bite, while it is elastoplastic in between [332]. The existence of elastic zones inside the plastic zone seems, however, possible because of strong roll flattening [105, p. 121] as shown in a model by Grimble et al. [126] and later included in a temper rolling model by Krimpelstätter [171]. The possibility of detecting internal elastic zones was also introduced in the CIEFS model by Stephany (Sec. 4.1) via the radial return algorithm [305, 307]. Based on these previous references, it is, however, unclear to what extent the inclusion of these zones quantitatively impacts the prediction of the rolling force and

the forward slip. For this reason and the apparent incompatibility[1] of our solution model with a radial return method, the inclusion of elastic zones in the central plastic zone is not taken into account in the present work.

Furthermore, the stress state is supposed to neither change along the transverse direction $\mathbf{e}_y$ nor along the vertical direction $\mathbf{e}_z$ due to the assumed symmetry along $\mathbf{e}_y$ and the small thickness of the strip. Hence, the stress state only depends on the position x in the roll bite along the rolling direction.

Moreover, the internal shear stresses are neglected, either because they vanish by the supposed symmetry along $\mathbf{e}_y$, i.e. $\sigma_{xy} = \sigma_{yx} = \sigma_{yz} = \sigma_{zy} = 0$, or because they are assumed to be zero due to the small thickness, which keeps the cross sections flat and perpendicular to the rolling direction, i.e. $\sigma_{xz} = \sigma_{zx} = 0$. Thus, all elements of the Cauchy stress tensor are zero except for its diagonal terms, which only depend on x.

In the following sections, the classical *elastic* and *elastoplastic* components of the model are described. Moreover, a *thermo-viscoplastic* extension was added based on the Johnson-Cook material law [161] to numerically reproduce the experimental findings of Chap. 3, which seemingly require a constitutive model with a rate-dependent component at least.

4.5.2.1 Elastic model

The elastic deformation of the material is linear and isotropic by hypothesis. The constitutive equation is therefore *Hooke's law* for isotropic materials. As explained before, the strain and stress tensors are assumed to be diagonal due to symmetry and the small thickness of the strip with respect to the other dimensions. The diagonal terms of the elastic deformation tensor $\boldsymbol{\epsilon}^e$ are thus provided by the following equation:

$$\epsilon_i^e = \frac{1}{E_s}\left[\sigma_i - \nu_s(\sigma_j + \sigma_k)\right] \tag{4.33}$$

where E_s and ν_s are the Young's modulus and the Poisson's ratio of the strip.

Due to the plane-strain condition in the $\mathbf{e}_x\mathbf{e}_z$-plane, the previous equation can be simplified for $i = y$. Hence, the elastic material equation for the strip can be written as follows:

$$\epsilon_x^e = \frac{1}{E_s}\left[\sigma_x - \nu_s(\sigma_y + \sigma_z)\right] \tag{4.34a}$$

$$\sigma_y = \nu_s(\sigma_x + \sigma_z) \tag{4.34b}$$

[1]This apparent incompatibility stems from the combination of the different model equations in appendix N to obtain an explicitly integratable system of equations. Such a system could certainly be derived for the elastic predictor. It is, however, unclear how to later correct the evolution of lubrication properties, like the lubricant pressure, based on the correction of the stresses. Further research is required to solve this problem, if necessary. In Stephany's thesis [305], this problem did not arise since the strip deformation model was coupled to the lubrication model by successive relaxations, if our understanding of his method is correct. Stephany's CIEFS method was, however, not developed further due to its limited robustness and inability to include more complex rolling features, like starvation.

$$\epsilon_z^e = \frac{1}{E_s}\left[\sigma_z - \nu_s(\sigma_x + \sigma_y)\right] \tag{4.34c}$$

4.5.2.2 Elastoplastic model

In between the entry and exit elastic zones, the strip is assumed to be deformed elastoplastically. This material behavior is described by the *Prandtl-Reuss equations*, which are derived in Sec. H.3.3 for the 3D case (Eqs. H.112 and H.122):

$$\dot{p} = -K_s \operatorname{tr}\mathbf{D} \tag{4.35}$$

$$\dot{s}_{ij} = 2G_s\left(D_{ij} - \frac{D_{kk}}{3}\delta_{ij} - \beta_1 s_{ij} s_{kl} D_{kl}\right) \tag{4.36}$$

where

$$K_s = \frac{E_s}{3-6\nu_s} \qquad \beta_1 = \frac{1}{\frac{2}{3}\sigma_Y^2\left(1+\frac{h_{i,s}}{3G_s}\right)} \qquad h_{i,s} = \frac{\mathrm{d}\sigma_Y}{\mathrm{d}\overline{\epsilon}^p} \qquad G_s = \frac{E_s}{2(1+\nu_s)} \tag{4.37}$$

are respectively, the bulk modulus, an intermediate variable, the isotropic hardening coefficient, and the shear modulus of the strip. The variable $\mathbf{D}$ denotes the strain rate tensor, which is defined in Eq. (H.17).

The equations for $\dot{p}$, $\dot{s}_{ij}$ and $\mathbf{D}$ can be simplified by the previous hypotheses, which consist in assuming diagonal strain and stress matrices. Moreover, the strain rate along $\mathbf{e}_y$ is zero due to the plane-strain hypothesis. Hence, the elastoplastic constitutive equations are the following ones:

$$\dot{p} = -K_s(D_x + D_z) \tag{4.38}$$

$$\dot{s}_x = \frac{2G_s}{3}\left[\left(2 - 3\beta_1 s_x^2\right)D_x - \left(1 + 3\beta_1 s_x s_z\right)D_z\right] \tag{4.39}$$

$$\dot{s}_z = \frac{2G_s}{3}\left[-\left(1 + 3\beta_1 s_x s_z\right)D_x + \left(2 - 3\beta_1 s_z^2\right)D_z\right] \tag{4.40}$$

The equation for $\dot{s}_y$ was not added because it can easily be deduced from the other components by the zero-trace property of the deviatoric stress tensor (Eq. H.27).

Furthermore, the components of the strain rate tensor in Eqs. (4.38), (4.39) and (4.40) are computed as follows by the definition of the velocity gradient and the strain rate tensors (Eqs. H.14 and H.17), since $v_x = v_s$ due to the small thickness:

$$D_x = \frac{\partial v_s}{\partial x} \tag{4.41}$$

$$D_z = \frac{\partial v_z}{\partial z} \tag{4.42}$$

By a similar reasoning than the one to derive Eq. (4.30),

$$\frac{\partial v_z}{\partial z} = v_s \frac{\partial \epsilon_z}{\partial x} \tag{4.43}$$

Substituting the result of Eq. (4.31) in the previous equation, then yields an expression of D_z, which is a function of the strip thickness:

$$D_z = \frac{v_s}{t_s}\frac{\partial t_s}{\partial x} \tag{4.44}$$

One should notice that p, s_x and s_z are Eulerian variables in the METALUB model. Because of the steady state analysis, their total time derivatives become spatial derivatives (Eq. H.8, with $\partial(\cdot)/\partial t = 0$):

$$\dot{p} = v_s\frac{\partial p}{\partial x} \qquad \dot{s}_x = v_s\frac{\partial s_x}{\partial x} \qquad \dot{s}_y = v_s\frac{\partial s_y}{\partial x} \tag{4.45}$$

The previous elastoplastic equations depend on the evolution of the yield stress σ_Y as function of the effective plastic strain $\overline{\epsilon}^p$, i.e. the hardening law. The evolution of the effective plastic strain along the roll bite can be obtained by expanding its definition in Eq. (H.57) and by simplifying the resulting expression due to the steady state hypothesis:

$$\overline{D}^p = v_s\frac{\partial\overline{\epsilon}^p}{\partial x} \tag{4.46}$$

The effective plastic strain rate can be computed by its definition in Eq. (H.58), by the additive decomposition of strain rates in Eq. (H.52), and by the plane-strain state assumption[2]:

$$\overline{D}^p = \sqrt{\frac{2}{3}\left[(D_x - D_x^e)^2 + (D_z - D_z^e)^2\right]} \tag{4.47}$$

The elastic strain rates D_x^e and D_z^e can finally be related to the elastic strains by the definition of the elastic strain rates (similar to Eq. H.17 but restricted to elastic deformations) and by a similar reasoning as for Eq. (4.30):

$$D_x^e = \frac{\partial v_x^e}{\partial x} = v_s\frac{\partial\epsilon_x^e}{\partial x} \tag{4.48}$$

$$D_z^e = \frac{\partial v_z^e}{\partial x} = v_s\frac{\partial\epsilon_z^e}{\partial x} \tag{4.49}$$

By combining the equations of this section, it is ultimately possible to compute the stresses of the strip by the evolution of the kinematic variables provided that the experimental yield curve of the material (Chap. 3) is fitted by a hardening law. The following laws have been implemented in METALUB.

[2]In this equation, $D_y^p = D_y - D_y^e$ was assumed to be negligible. It could, however, be included in the model in the future, since $D_y = 0$ and since D_y^e can be derived by Hooke's law and Eq. (4.48), in which x is replaced by y.

Perfect plasticity

In this case, the material of the strip is perfectly plastic, i.e.

$$\sigma_Y(\overline{\epsilon}^p) = \sigma_Y^0 \tag{4.50}$$

where σ_Y^0 is the initial yield stress. By Eq. (4.37), the isotropic hardening coefficient is thus equal to zero:

$$h_{i,s}(\overline{\epsilon}^p) = 0 \tag{4.51}$$

Krupkowski power law

The Krupkowski power law [215], which is also known as the Swift law [319], is defined as follows:

$$\sigma_Y(\overline{\epsilon}^p) = \sigma_Y^0 \left(1 + C\overline{\epsilon}^p\right)^n \tag{4.52}$$

where σ_Y^0, C and n are the initial yield stress and two isotropic hardening material parameters, respectively. The isotropic hardening coefficient can be computed as follows

$$h_{i,s}(\overline{\epsilon}^p) = nC\sigma_Y^0 \left(1 + C\overline{\epsilon}^p\right)^{n-1} \tag{4.53}$$

Ludwik law

The Ludwik law [208] is identical to the first component of the Johnson-Cook hardening law [161]:

$$\sigma_Y(\overline{\epsilon}^p) = A + B\left(\overline{\epsilon}^p\right)^n \tag{4.54}$$

where A, B and n are material constants. The parameter A can be identified as the initial yield stress. The corresponding isotropic hardening coefficient is the following one:

$$h_{i,s}(\overline{\epsilon}^p) = nB\left(\overline{\epsilon}^p\right)^{n-1} \tag{4.55}$$

Smatch law

The Smatch law is defined by the following equation on the basis of [3, 4], which was used by [54, 305]:

$$\sigma_Y(\overline{\epsilon}^p) = \left(A + B\overline{\epsilon}^p\right)\left(1 - Ce^{-D\overline{\epsilon}^p}\right) + E \tag{4.56}$$

where A, B, C, D and E are material constants. Based on the previous definition, the isotropic hardening coefficient is equal to

$$h_{i,s}(\overline{\epsilon}^p) = Ce^{-D\overline{\epsilon}^p}\left[AD + B\left(D\overline{\epsilon}^p - 1\right)\right] + B \tag{4.57}$$

Experimental yield curve

It was also added the possibility to compute directly the yield stress and the isotropic hardening coefficient based on the data points of a measured experimental yield curve $\sigma_Y = \sigma_Y(\overline{\epsilon}^p)$ by linear interpolation and finite differentiation. It might be necessary to smooth the experimental curve to ensure the convergence of the model in this case.

4.5.2.3 Viscoplastic model

The analysis of experimental results in the previous chapter suggested that *viscoplasticity* plays an important role in certain cold rolling scenarios (Sec. 3.2.1.2). More precisely, the rolling load increased with the rolling speed while the forward slip decreased, see e.g. Test 6. A decreasing forward slip implies decreasing friction. Decreasing friction would then imply a decreasing rolling load. This load, however, increased, which looked like a contradiction. The current explanation of this observation is viscoplasticity. In fact, the greater the rolling speed, the more resistant becomes the strip material and the more increases the rolling load, although friction decreases by increased viscous entrainment of the lubricant.

Viscoplasticity has never been considered in the context of the METALUB model before, except for [305, p. 237]. Besides the previous experimental observations, other sources, however, also emphasize its importance in cold rolling [171]. According to Roberts [276, p. 480], the strain rate effect is an intrinsic component of rolling, where strain rates of 10 to 1000 s^{-1} are usual, and it should therefore not be neglected in cold rolling models. Roberts suggests the following expression of the constrained yield stress σ_c [276, pp. 296, 454]:

$$\sigma_c = 1.155 \left(\sigma_Y^* + a \log_{10} 1000\dot{\epsilon}\right) \tag{4.58}$$

where $1.155 \approx 2/\sqrt{3}$ is the conversion factor to the plane-strain state (i.e. constrained, Eq. H.125), σ_Y^* is the conventional yield stress (without strain rate dependence), a is a material constant with a value of about 6250 psi = 43 MPa per decade change of strain rate and $\dot{\epsilon}$ is the strain rate in s^{-1}.

Besides this law in Roberts [276], numerous material models have been developed in the literature to take into account strain rate hardening [158]. In particular, the purely empirical Johnson-Cook law seems to be one of the most popular models for metals subjected to large strains, high-strain rates and high-temperatures due its simplicity, the reduced number of experiments to determine the material constants and the resulting availability of material parameters in the literature [161]:

$$\sigma_Y(\overline{\epsilon}^p, \overline{D}^p, T) = \left[A + B\,(\overline{\epsilon}^p)^n\right] \left(1 + \eta_s \ln \frac{\overline{D}^p}{\overline{D}_0^p}\right) \left[1 - \left(\frac{T - T_0}{T_m - T_0}\right)^m\right] \tag{4.59}$$

where

- $\overline{\epsilon}^p$ is the effective plastic strain;
- $\overline{D}^p$ is the effective plastic strain rate;
- T is the temperature;
- A, B, η_s, n, m are material constants;
- T_0 is the reference temperature;
- T_m is the melting temperature.

This law combines the influences of plastic strain, strain rate and thermal softening. The strain rate component is assumed to be equal to 1, when the plastic strain rate $\overline{D}^p$ is smaller than the reference strain rate $\overline{D}_0^p$. This reference strain rate is commonly equal to 1 s^{-1} in the literature, but different values were also chosen [158]. It is important to notice that its choice impacts the values of the material constant η_s. The Johnson-Cook law has two drawbacks in the context of cold rolling. First, it could not adequatly model the material behavior since it seems to become insufficient for strain rates exceeding 1000 s^{-1} [158, 349]. For instance, the Hensel-Spittel dependence, which is a power law with respect to the effective plastic strain rate, was used in the temper rolling model by Krimpelstätter [171, p. 51]. Secondly, the material laws, which were used in the past, in particular the Smatch law, included a more complex strain influence than the power law in the Johnson-Cook model, which could be insufficient.

Despite the first drawback, the viscous component of the Johnson-Cook law was implemented in METALUB because *choosing an exceedingly complex model instead makes no sense at the current stage of development*. In fact, the strain rate dependent material constants were not measured in the context of the data in Chap. 3. When better data will be available, better material laws can be easily added to the model in the future. The current goal is to test the qualitative influence of viscoplasticity on the results.

The second drawback can be solved on the basis of the current hardening laws in METALUB. More precisely, the hardening laws that are implemented in METALUB are similar to the first term in the Johnson-Cook law in the sense that the yield stress is computed as a function of the plastic strain rate. Hence, a natural extension of these laws is their *multiplication by the viscous component of the Johnson-Cook law*. The resulting viscoplastic hardening law and the hardening coefficient are the following ones:

$$\sigma_Y(\overline{\epsilon}^p, \overline{D}^p) = \sigma_Y(\overline{\epsilon}^p)\left(1 + \eta_s \ln \frac{\overline{D}^p}{\overline{D}_0^p}\right) \tag{4.60}$$

$$h_{i,s}(\overline{\epsilon}^p, \overline{D}^p) = h_{i,s}(\overline{\epsilon}^p)\left(1 + \eta_s \ln \frac{\overline{D}^p}{\overline{D}_0^p}\right) \tag{4.61}$$

where $\sigma_Y(\overline{\epsilon}^p)$ is one of the hardening laws in Eqs. (4.50), (4.52), (4.54) or (4.56). The standard values of the material constants η_s and $\overline{D}_0^p$ in METALUB are 0.01 and 1 s^{-1}, which seem to be realistic average values for steel according to [158, 161].

While an evolution equation was previously derived for the effective plastic strain $\overline{\epsilon}^p$ (see Eq. 4.47), no such equation seems to be easily derivable for the effective plastic strain rate. This is the reason why, the yield stress and the isotropic hardening coefficient at the following spatial step in the roll bite are evaluated *explicitly* on the basis of the effective plastic strain rate at the previous step (see Sec. 4.10.1).

4.5.2.4 Thermo-viscoplastic model

The previous model can be extended to take into account *thermal softening* effects provided that a prediction of the strip temperature T_s is available along the roll bite. The corresponding thermal model to compute $T_s(x)$ is explained in Sec. 4.9. By neglecting thermal expansion and thermoelastic effects, we can introduce thermal softening in the model by computing the yield stress and the respective hardening coefficient as follows, again based on the Johnson-Cook law (Eq. 4.59):

$$\sigma_Y\left(\overline{\epsilon}^p, \overline{D}^p, T_s\right) = \sigma_Y\left(\overline{\epsilon}^p, \overline{D}^p\right)\left[1 - \left(\frac{T_s - T_0}{T_m - T_0}\right)^m\right] \tag{4.62}$$

$$h_{i,s}\left(\overline{\epsilon}^p, \overline{D}^p, T_s\right) = h_{i,s}\left(\overline{\epsilon}^p, \overline{D}^p\right)\left[1 - \left(\frac{T_s - T_0}{T_m - T_0}\right)^m\right] \tag{4.63}$$

where

- $\sigma_Y\left(\overline{\epsilon}^p, \overline{D}^p\right)$ is the yield stress without its thermal component. In METALUB, it can either be the yield stress $\sigma_Y\left(\overline{\epsilon}^p\right)$ (Eqs. 4.50, 4.52, 4.54 or 4.56) or this yield stress multiplied by the viscous component of the Johnson-Cook law (Eq. 4.60), if viscoplasticity is activated.
- $h_{i,s}\left(\overline{\epsilon}^p, \overline{D}^p\right)$ is the hardening coefficient without its thermal component. Like the yield stress, it can either be $h_{i,s}\left(\overline{\epsilon}^p\right)$ (Eqs. 4.51, 4.53, 4.55 or 4.57) or $h_{i,s}\left(\overline{\epsilon}^p, \overline{D}^p\right)$ (Eq. 4.61), if viscoplasticity is activated.
- T_0 is the reference temperature. By default, it is equal to 25°C.
- T_m is the melting temperature. By default, it is assumed to be equal to the average value for steel in [161], i.e. 1500°C.
- m is a material constant. By default, its value is set equal to 1 according to the average value for steel in [161].

4.5.3 Equilibrium equations

By the strain computation and the constitutive equations of the previous sections, it is possible to determine the stresses of the strip and vice versa. The equilibrium equation between these stresses and the applied surface tractions are computed in this section by the *slab method* (Sec. 2.3.1).

If the interface pressure p_i and the interface shear stress τ_i (Sec. 4.3) are applied to a part of the strip as shown in Fig. 4.7 and if dynamic effects and volume forces are neglected, the equilibrium equations along $\mathbf{e}_x$ and $\mathbf{e}_z$ can be formulated as follows. Along $\mathbf{e}_x$,

$$-\sigma_x\, t_s + 2\,\tau_i\, l\, \cos\theta + 2\, p_i\, l\, \sin\theta + (\sigma_x + \Delta\sigma_x)(t_s + \Delta t_s) = 0 \tag{4.64}$$

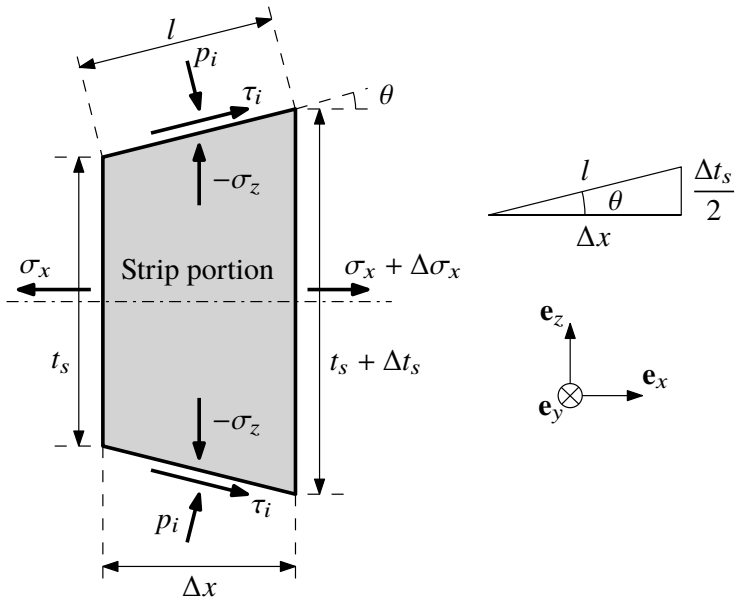

Figure 4.7: Strip portion with stresses (σ_x and σ_z) and surface tractions (p_i and τ_i) to compute the equilibrium of forces by the slab method.

By noticing that $\cos\theta = \Delta x/l$, $\sin\theta = \Delta t_s/(2l)$, $\Delta\sigma_x\,\Delta t_s \approx 0$ and by $\Delta x \to 0$, the previous equation becomes

$$\frac{\partial(\sigma_x\, t_s)}{\partial x} = -p_i \frac{\partial t_s}{\partial x} - 2\tau_i \tag{4.65}$$

Along the $\mathbf{e}_z$-axis, the equilibrium equation is the following one:

$$-\,p_i\, l\, \cos\theta + \tau_i\, l\, \sin\theta - \sigma_z\, \Delta x = 0 \tag{4.66}$$

By the previous explanations, this equation can be simplified as:

$$\sigma_z = -p_i + \frac{1}{2}\tau_i \frac{\partial t_s}{\partial x} \tag{4.67}$$

In the METALUB model, the influence of the shear stress in the previous equation is neglected to simplify the resulting system of equations in appendix N. Thus,

$$\sigma_z = -p_i \tag{4.68}$$

The previous hypothesis seems reasonable since $(1/2)\tau_i \partial t_s/\partial x$ is equal[3] to about 1 MPa, if the interface pressure $p_i = 800$ MPa, the coefficient of friction $\mu = 0.1$, the roll bite length $l_{\text{rb}} = 10$ mm, the initial strip thickness $t_{\text{in}} = 0.75$ mm and the reduction $r = 30$ % as in Test 5B-4 in Chap. 3.

[3]

$$\left|\frac{1}{2}\tau_i \frac{\partial t_s}{\partial x}\right| \approx \left|\frac{1}{2}\mu p_i \frac{(1-r)t_{\text{in}} - t_{\text{in}}}{l_{\text{rb}}}\right| = 0.9 \text{ MPa} \tag{4.69}$$

4.6 Roll flattening

Due to the important stresses that are applied to the rolls and the mill stand, their elastic deformations can affect the final strip thickness and its flatness (Sec. 2.1.2.2). In the following sections, methods to compute *roll flattening* of linearly elastic, isotropic and homogeneous rolls due to the contact pressure and shear stress in the $\mathbf{e}_x\mathbf{e}_z$-plane are presented, i.e. roll deflections due to bending are not taken into account. In fact, it is assumed that this latter deformation mode was minimized by choosing crowned rolls with a sufficient diameter and optional back-up rolls as explained in Sec. 2.1.2.2. Elastic deformations of the mill stand are also not included in the model since the position of the roll axis will be explicitly imposed to obtain a specific final thickness of the strip (Sec. 4.10.3.3).

Based on these hypotheses, the roll profile in the METALUB model is defined by the position of its axis, which passes through the point $(0, 0, z_0)$ along $\mathbf{e}_y$ and its profile $z_r(x)$ as shown in Fig. 4.8 for a circular roll model.

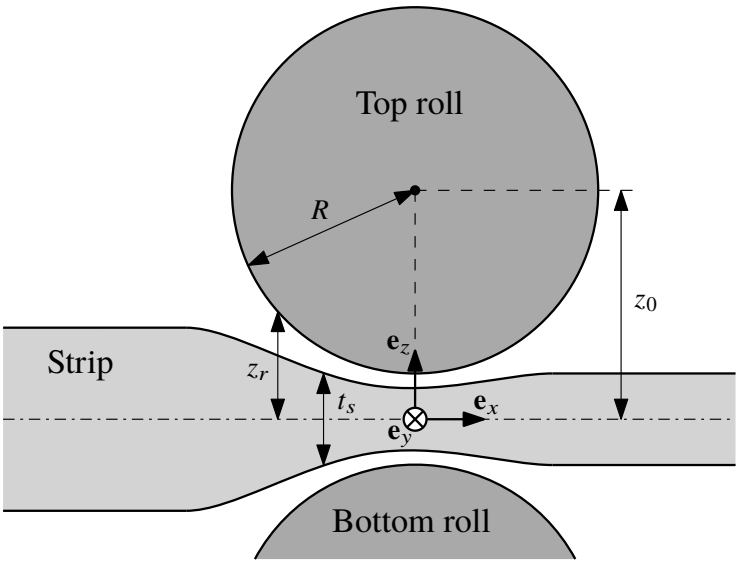

Figure 4.8: Profile of the roll z_r, vertical position of its axis z_0, the strip thickness t_s and the roll radius R of a circular roll model, which is not necessarily equal to the radius R_0 of the undeformed roll.

In the following sections, different models to compute the roll flattening as a function of the stresses in the roll bite are described in the order of increasing ability to compute the real roll profile: *Hitchcock, Bland and Ford, Jortner et al. and Meindl*. All these models are implemented in METALUB and the most accurate method, i.e. Meindl's method, was implemented in the framework of this thesis. Besides deformed rolls, the model obviously also includes *rigid circular rolls and prescribed non-circular roll profiles*, which are respectively defined by a radius R_0 or a data file of profile coordinates that are interpolated.

4.6.1 Hitchcock's roll flattening model

The model by *Hitchcock* [142] is based on Hertz contact theory [261, p. 638]. Hence, the real pressure distribution is replaced by an elliptical distribution in the symmetry plane $\mathbf{e}_x\mathbf{e}_z$ for an infinitely long cylinder in contact with a plane. Moreover, the shear component of the stresses, which are applied to the roll, are not taken into account. The deformed roll is supposed to remain cylindrical but with an increased radius R for the contact arc due to the local flattening:

$$R = R_0 \left(1 + \frac{16(1-\nu_r^2)}{\pi E_r} \frac{F_r}{w(t_{\text{in}} - t_{\text{out}})}\right) \tag{4.70}$$

where R_0 is the radius of the undeformed roll, ν_r its Poisson's ratio, E_r its Young's modulus, F_r the rolling force, w the width of the strip (i.e. F_r/w is the force per unit width), t_{in} the initial strip thickness and and t_{out} its final thickness. The derivation of this formula can be found in Roberts [276, pp. 482-490].

Once the roll flattening is computed, it is necessary to extract the roll profile z_r at given positions x along the roll bite to include its influence on the other elements of the rolling scenario in the model, i.e. it is necessary to determine $z_r(x)$, which is defined in Fig. 4.8 for a circular roll. Besides the roll profile, its derivative $\partial z_r(x)/\partial x$ is also required in the cold rolling model:

$$z_r(x) = z_0 - \sqrt{R^2 - x^2} \tag{4.71}$$

$$\frac{\partial z_r}{\partial x}(x) = \frac{x}{\sqrt{R^2 - x^2}} \tag{4.72}$$

4.6.2 Bland and Ford's roll flattening model

Hitchcock's model was further improved by taking into account elastic entry and exit zones of the strip in the roll bite as well as back and front tensions by *Bland and Ford* [33]:

$$R = R_0 \left(1 + \frac{16(1-\nu_r^2)}{\pi E_r} \frac{F_r}{w\left(\sqrt{t_{\text{in}} - t_{\text{out}} + \delta_1 + \delta_2} + \sqrt{\delta_2}\right)^2}\right) \tag{4.73}$$

with

$$\delta_1 = \frac{\nu_s(1+\nu_s)}{E_s}\left(t_{\text{out}}\sigma_{\text{out}} - t_{\text{in}}\sigma_{\text{in}}\right) \tag{4.74}$$

$$\delta_2 = \frac{(1-\nu_s)^2}{E_s} t_{\text{out}}\left(\sigma_Y^0 - \sigma_{\text{out}}\right) \tag{4.75}$$

where σ_{in}, σ_{out} and σ_Y^0 are the back tension, the front tension and the initial yield stress of the strip. The roll profile $z_r(x)$ and its derivative $\partial z_r(x)/\partial x$ can again be computed by Eqs. (4.71) and (4.72).

4.6.3 Jortner's roll flattening model

Since the pressure distribution is usually different from the elliptical one, which is predicted by Hertz theory and since the contact arc is *not circular* anymore when important rolling forces are applied, a more sophisticated model is required to predict the flattening of the roll.

Such a model was developed by *Jortner et al.* [163]. It is based on a roll, which has a radius R_0 in its undeformed configuration, in the plane-strain state with diametrically applied pressure loads p as illustrated in Fig. 4.9. This configuration is obtained in practice when the back-up roll (or axis) supplies the balancing load. Although the back-up pressure distribution is not strictly identical to the pressure distribution in the roll bite, Saint-Venant's principle suggests that this difference does not have a significant influence on the results. In other words, Jortner's model provides an almost exact determination of the elastic flattening of the roll locally subjected to a given pressure distribution.

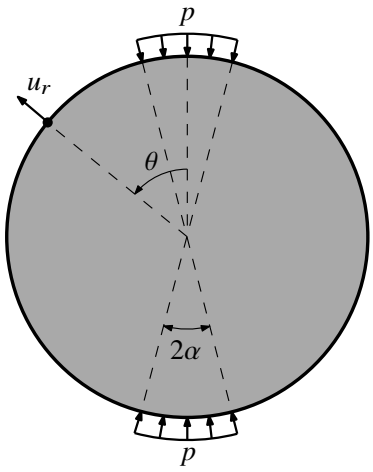

Figure 4.9: Loading and geometry in Jortner's roll flattening model.

According to Jortner et al. [163], the *radial elastic displacement* u_r of the roll profile due to the pressure load p is given by the following equation for $\alpha \to 0$ (Fig. 4.9):

$$u_r(R_0, \theta, \alpha, p, E_r, \nu_r) = \frac{pR_0}{\pi E_r} \mathrm{JIF}(\theta, \alpha, \nu_r) \tag{4.76}$$

where p is the radial pressure applied to the arc, which has an angle 2α, θ is the angle at which the radial displacement u_r is calculated, E_r is the Young's modulus of the roll and ν_r is its Poisson's ratio. The term $\mathrm{JIF}(\theta, \alpha, \nu_r)$ is the *Jortner influence function*, which is defined as follows:

$$\mathrm{JIF}(\theta, \alpha, \nu_r) = \begin{cases} \mathrm{jif}(\theta, \alpha, \nu_r) & , \text{if } |\theta| > \alpha \\ \mathrm{jif}(\theta, \alpha, \nu_r) - \pi(1 - \nu_r - 2\nu_r^2) & , \text{if } |\theta| < \alpha \end{cases} \tag{4.77}$$

with

$$\mathrm{jif}(\theta,\alpha,\nu_r) = \left(1-\nu_r-2\nu_r^2\right)\cos(\beta)\left(\tan^{-1}\frac{1+\cos(\beta)}{\sin(\beta)}+\tan^{-1}\frac{1-\cos(\beta)}{\sin(\beta)}\right)+\left(1-\nu_r^2\right)\sin(\beta)\ln\frac{1-\cos(\beta)}{1+\cos(\beta)}\Bigg|_{\beta=\theta-\alpha}^{\beta=\theta+\alpha} \tag{4.78}$$

The previous notation is defined as follows:

$$f(\beta)|_{\beta=a}^{\beta=b} = f(b)-f(a) \tag{4.79}$$

The coefficient π in Eq. (4.77) was added in this work since it was not included in Jortner et al. [163]. In fact, Eq. (8) in the article by Jorter et al. is wrong: π should be replaced by E in this equation (nomenclature of the article). A *proof* of this necessary correction can be found in appendix I.

Moreover, the function $\mathrm{jif}(\theta,\alpha,\nu_r)$ is not defined, when $\theta=\alpha$ in Eq. (4.78). In fact, it is discontinuous at $\theta=\alpha$ since its value for $\theta\to\alpha^+$ is different from its value for $\theta\to\alpha^-$. Hence, the function $\mathrm{jif}(\theta,\alpha,\nu_r)$ was extended in appendix J in order to lead to no numerical problem.

By the principle of *superposition* in linear elasticity, the *total displacement along the radial direction* $u_{r,i}$ at a location θ_i of the roll, which is stressed by multiple pressure zones p_j, as shown in Fig. 4.10, can be computed as follows:

$$u_{r,i} = \frac{R_0}{\pi E_r}\sum_{j=1}^{n}\mathrm{JIF}(\theta_j-\theta_i,\alpha_j,\nu_r)p_j \tag{4.80}$$

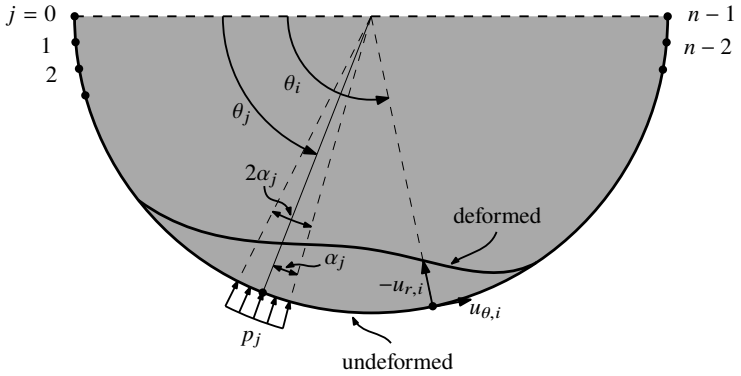

Figure 4.10: Computation of the roll flattening due to pressure by the superposition principle.

In METALUB, the *roll profile is discretized* by specifying three different angular steps, $\Delta\theta_1$, $\Delta\theta_2$ and $\Delta\theta_3$ as well as two coordinates x_{12} and x_{23}. Fig. 4.11 shows that the roll is discretized by sectors having an angle $\Delta\theta_1$ until x_{12}, then $\Delta\theta_2$ until slightly after x_{23} and finally $\Delta\theta_3$. The first

and the last (small) sectors were reduced to start precisely at x_{12} with the fine discretization and to use the step $\Delta\theta_2$ between x_{12} and x_{23}. The value of x_{12} can be different from x_{12} in Eq. (4.218), which determines when the refined integration zone starts, although they are usually set to the same value since a finer roll discretization is also required where a smaller integration step is required (Sec. 4.10.1), i.e. in the roll bite.

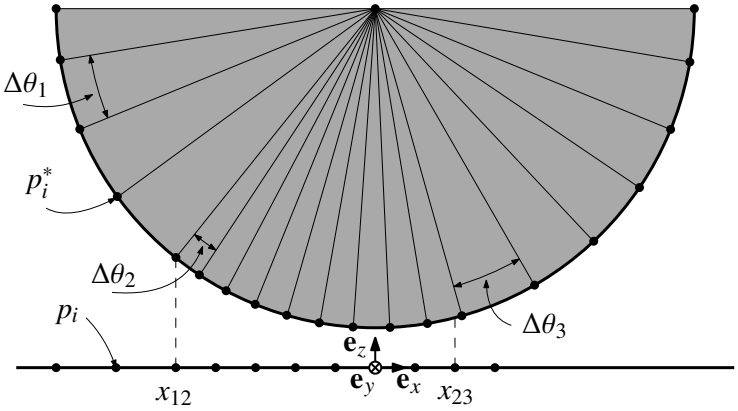

Figure 4.11: Discretization of the roll in METALUB.

As shown in Fig. 4.11, the roll bite is discretized by the spatial integration step (Sec. 4.10.1) at a number of x-positions, where the interface pressure p_i will be computed. This pressure is then linearly interpolated along x to evaluate it at the discretization points of the roll, which will be noted[4] p_i^*. The angular step α_j in Eq. (4.80) is computed as follows:

$$\alpha_0 = \frac{\theta_1 - \theta_0}{2}; \qquad \alpha_j = \frac{\theta_{j+1} - \theta_{j-1}}{4} \text{ for } j \in \{1, \ldots, n-2\}; \qquad \alpha_{n-1} = \frac{\theta_{n-1} - \theta_{n-2}}{2} \tag{4.81}$$

In the case of a non-circular roll profile, as in this Jortner model or the Meindl model in the next section, the final roll profile can be computed by transforming the polar coordinates to Cartesian coordinates (Figs. 4.8 and 4.10):

$$x_r = -(R_0 + u_r)\cos\theta + u_\theta \sin\theta \tag{4.82}$$

$$z_r = -(R_0 + u_r)\sin\theta - u_\theta \cos\theta \tag{4.83}$$

where the tangential (or circumferential) displacement u_θ is assumed to be zero in Jortner's method. The profile height z_r at an arbitrary x-position is then computed by linear interpolation of the profile at the discretization points of the roll. The slope of this interpolation line is used as an approximation of $\partial z_r(x)/\partial x$.

Finally, in addition to *not taking into account the tangential flattening* of the roll due to the interface pressure, Jortner's method does also *not include radial and tangential deformations*

[4]The notation of the interface pressure p_i, where i stands for interface, might lead to confusion due to the previous introduction of p_j, which is the pressure that is applied in a certain sector to the roll, where j is an index corresponding to the sector. These pressures are related by the following equation $p_j = p_i^*(\theta_j)$.

due to shear stresses. This hypothesis is usually reasonable when the interface shear stress is relatively small with respect to the interface pressure, i.e. in cold rolling except for skin pass or temper rolling [171]. Therefore, Golten's shear influence functions were added to Jortner's influence functions [116] by Grimble et al. [126]. Hence, the radial deformation due to the interface pressure and the interface shear stress can be computed.

4.6.4 Meindl's roll flattening model

In order to finally *add all possible flattening modes*, i.e. radial and tangential deformations due to the interface pressure and the interface shear stress, to the METALUB model, *Meindl*'s semi-analytical roll flattening method [220] was implemented on the basis of Krimpelstätter's thesis [171]. Meindl derived the linear elastic deformation of the homogeneous, isotropic roll in a similar way to how Jortner derived the radial deformation due to the interface pressure. Besides the loading and geometry of Jortner's roll flattening model in Sec. 4.9, a similar *scenario but with shear stresses* was required. This scenario is shown in Fig. 4.12. Although shear stresses were added on the left, right and top of the work roll to obtain an equilibrated configuration that can be solved analytically, and although these stresses differ from those in the real rolling scenario, their influence on the local solution in the roll bite is again limited by the Saint-Venant principle and the small roll bite length with respect to the diameter of the roll.

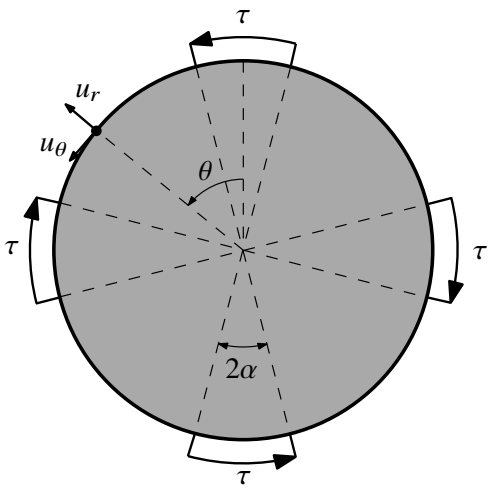

Figure 4.12: Shear stress loading and geometry of Meindl's roll flattening model.

The resulting *displacements of the roll profile* due to the loading cases in both scenarios is the following for $\alpha \to 0$:

$$u_r(R_0, \theta, \alpha, p, \tau, E_r, \nu_r) = \frac{pR_0}{\pi E_r}\mathrm{MIF}_{r,p}(\theta, \alpha, \nu_r) + \frac{\tau R_0}{\pi E_r}\mathrm{MIF}_{r,\tau}(\theta, \alpha, \nu_r) \tag{4.84}$$

$$u_\theta(R_0, \theta, \alpha, p, \tau, E_r, \nu_r) = \frac{pR_0}{\pi E_r}\mathrm{MIF}_{\theta,p}(\theta, \alpha, \nu_r) + \frac{\tau R_0}{\pi E_r}\mathrm{MIF}_{\theta,\tau}(\theta, \alpha, \nu_r) \tag{4.85}$$

where $\text{MIF}_{r,p}$, $\text{MIF}_{r,\tau}$, $\text{MIF}_{\theta,p}$ and $\text{MIF}_{\theta,\tau}$ are the *Meindl influence functions* for the radial (r) and tangential (θ) deformations due to pressure (p) and shear stress (τ). They are defined in appendix K for different deformation states [171]: the generalized plane-strain state (ϵ_y = constant along the axis and $\sigma_y = 0$ at the lateral free surfaces of the roll), the plane-strain state ($\epsilon_y = 0$) and the plane-stress state ($\sigma_y = 0$). Although, cold rolling is commonly modeled in plane strain, the plane-stress formulation was added for completeness. Surprisingly, this plane-stress formulation was used by Dbouk et al. [89, 90] to model roll flattening in cold rolling instead of the plane-strain formulation. The generalized plane-strain state is the best model of the real roll flattening according to Meindl [220] since it considers the fact that the roll can very slightly elongate along the axial direction, i.e. the bearings do not strictly limit its axial expansion as in the plane-strain state.

Fig. 4.13 illustrates the evolution of the different influence functions in the plane-strain state. The Jortner influence function (JIF) was also represented to show that it is equal to the corresponding Meindl influence function ($\text{MIF}_{r,p}$). By algebraic operations it is certainly possible to mathematically prove that Jortner's function in Eq. (J.1) is equal to Meindl's function in Eq. (K.6), and so on for the remaining equations. Fig. 4.13 can also be physically interpreted. For instance, the interface pressure flattens the roll ($\text{MIF}_{r,p}$ in Fig. 4.13), while the (positive) shear stress pushes the profile to the right ($\text{MIF}_{\theta,\tau}$ in Fig. 4.13).

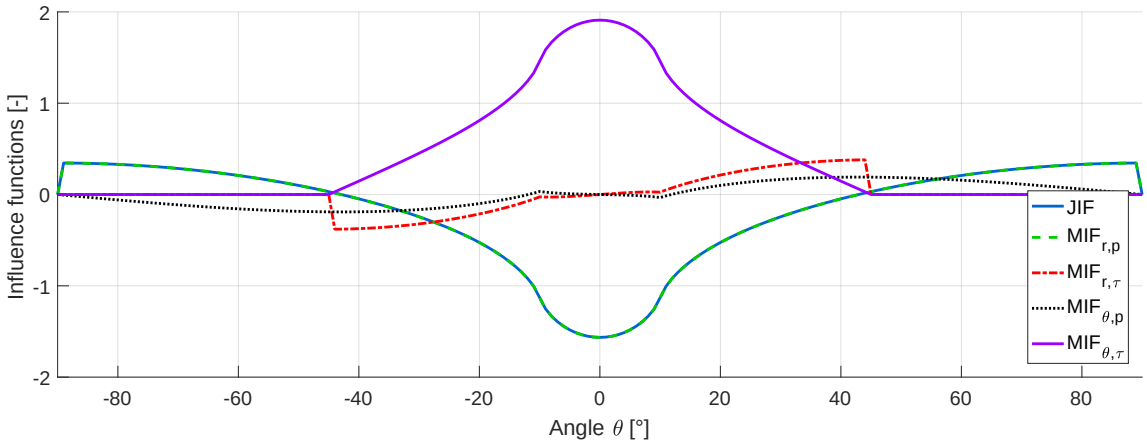

Figure 4.13: Jortner (JIF) and Meindl (MIF) influence functions in plane-strain state with $\alpha = 10°$ and $\nu_r = 0.3$. The Jortner influence function JIF and the Meindl influence function $\text{MIF}_{r,p}$ are overlapping.

In the same way as in Jortner's method, the resulting *total displacement of the roll profile* can be computed by the superposition principle of linear elasticity theory. Hence, according to Figs 4.10 and 4.14,

$$u_r(\theta_i) = \frac{R_0}{\pi E_r}\left(\sum_{j=1}^{n} \text{MIF}_{r,p}(\theta_j - \theta_i, \alpha_j, \nu_r)p_j + \text{MIF}_{r,\tau}(\theta_j - \theta_i, \alpha_j, \nu_r)\tau_j\right) \tag{4.86}$$

$$u_\theta(\theta_i) = \frac{R_0}{\pi E_r}\left(\sum_{j=1}^{n} \mathrm{MIF}_{\theta,p}(\theta_j - \theta_i, \alpha_j, \nu_r)p_j + \mathrm{MIF}_{\theta,\tau}(\theta_j - \theta_i, \alpha_j, \nu_r)\tau_j\right) \tag{4.87}$$

$$\tag{4.88}$$

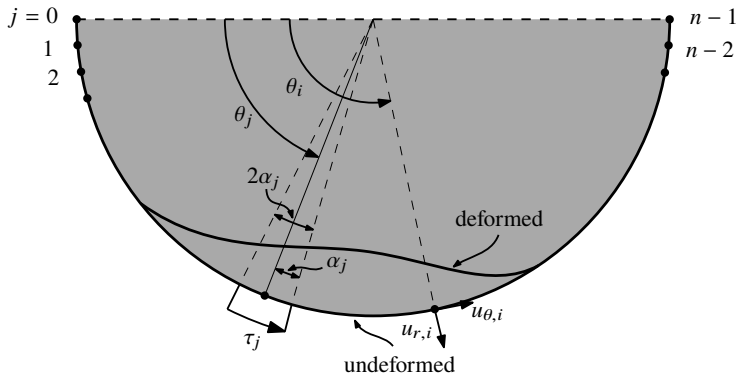

Figure 4.14: Computation of the roll flattening due to shear stress by the superposition principle.

The meaning and the computation of the previous values, α_j, p_j, ... is identical to those in the explanation of Jortner's method (Sec. 4.6.3). The shear stress τ_j is evaluated at the discretization points of the roll by linear interpolation of the interface shear stress evolution $\tau_i(x)$ in the same way as p_j is computed by $p_i(x)$. The deformed roll profile $z_r(x)$ and its derivative $\partial z_r(x)/\partial x$ can finally be computed by Eqs. (4.82) and (4.83) and the explanations in Sec. 4.6.3.

4.7 Solid contact modeling

In dry and lubricated cold rolling, the strip moves through the roll bite due to the friction (essentially boundary friction) between the rolls and the strip, and the difference of back and front tension in some cases. Boundary friction obviously only applies where the rolls and the strip are actually in contact. In order to determine the real contact area and the resulting friction, *solid contact modeling* by asperity flattening equations and boundary friction models is explained in the following sections.

4.7.1 Asperity flattening

The asperity flattening equations implemented in METALUB relate the *normal load and the plastic bulk deformation of the strip* to the real contact area. In other words, they allow to compute the relative contact area A as a function of the interface pressure p_i, or its components, i.e. the pressure on top of the asperities p_a and the lubricant pressure p_l, and the elongation of the strip e_x. Flattening due to shear stresses and free surface roughening, which were described in Sec. 2.2.2, are thus not included in the model.

In the following sections, three different asperity flattening equations are introduced: *Wilson and Sheu* [367], *Sutcliffe and Marsault* [215, 311] and *Korzekwa et al.* [169, 313]. Moreover, the *generalized asperity flattening equation* is derived to compute the evolution of the contact level along the roll bite by the flattening equation.

4.7.1.1 Asperity flattening equation by Wilson and Sheu

Wilson and Sheu's asperity flattening equation [367] is based on the indentation scenario in Fig. 4.15, which is assumed to be equivalent to the asperity flattening problem. Rigid indenters are pressed against the rigid, perfectly plastic workpiece with a pressure p_a, while the lubricant pressure p_l is applied in between them. The problem is symmetric along $\mathbf{e}_y$ and in the plane-strain state, i.e. no expansion occurs in the direction $\mathbf{e}_y$ as in cold rolling (Sec. 2.1.2.2). A uniform elongation rate D_x of the workpiece is assumed to exist along $\mathbf{e}_x$, where $\mathbf{e}_x$ is the rolling direction. Since the material is supposed to be rigid perfectly plastic, $D_x = D_x^p$. The indenters are considered to be much longer in the $\mathbf{e}_x$-direction than in the $\mathbf{e}_y$-direction similar to the roll and strip roughness, which usually have parallel grooves to the rolling direction due to roll grinding (Sec. 2.1.2.2).

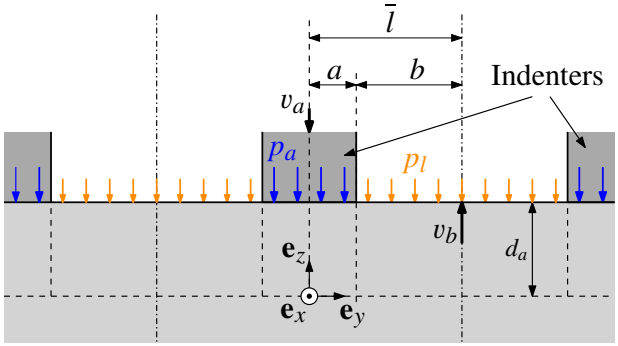

Figure 4.15: Indentation of a rigid, perfectly plastic workpiece by rigid indenters, which is represented in a normal plane to the rolling direction $\mathbf{e}_x$.

Two different trial velocity fields of the workpiece were assumed: a sticking (Figs. 4.16a and 4.16b) and a sliding field (Figs. 4.16c and 4.16d). These fields are not the real velocity fields but approximations. The variable d_a in Fig. 4.15 limits the depth of the local deformation field. Moreover, the following non-dimensional variables were defined to derive the asperity flattening equation:

- *the non-dimensional plastic strain rate*:

$$E_p = \frac{D_x^p \bar{l}}{v_a + v_b} \tag{4.89}$$

where $\bar{l}$, v_a and v_b are the half spacing between asperities, the average downward indentation speed and the average upward speed of the free surface as shown in Fig. 4.15.

- *the non-dimensional effective hardness*:

$$H_a = \frac{p_a - p_l}{\tau_Y} \tag{4.90}$$

where $\tau_Y = \sigma_Y/\sqrt{3}$ is the shear yield stress (Eq. H.56) of the workpiece.

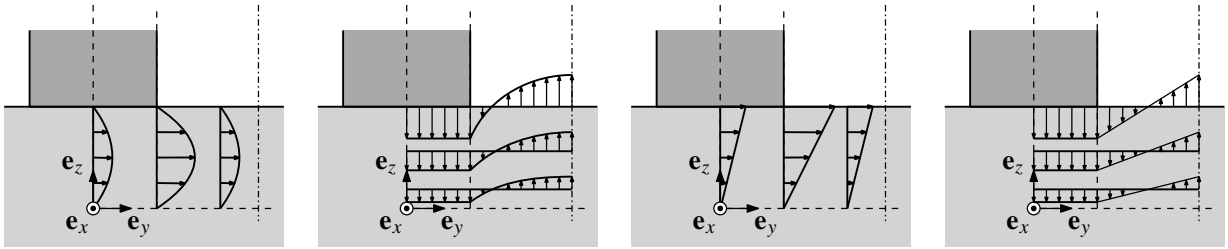

(a) Sticking, $\mathbf{e}_y$. **(b)** Sticking, $\mathbf{e}_z$. **(c)** Sliding, $\mathbf{e}_y$. **(d)** Sliding, $\mathbf{e}_z$.

Figure 4.16: Assumed velocity fields of the workpiece along $\mathbf{e}_y$ and $\mathbf{e}_z$.

The internal power dissipation due to the plastic deformation and the power due to external forces can be estimed based on the previous velocity fields. By the conservation of energy, the applied external power must balance the internal plastic power dissipation, if no other dissipation sources exist. The resulting energy balance combines the applied pressure via H_a, the elongation of the strip via E_p and the relative contact area A in one equation. This equation, however, still depends on d_a, which is the limiting depth of the local deformation field due to indentation. This remaining arbitrariness is eliminated by choosing the value of d_a which minimizes the internal power since the real velocity field is the one that minimizes that power [135, p. 114][260]. The previous method thus leads to an *upper bound solution*, which overpredicts the internal power dissipation, since the underlying velocity fields are still idealized and not the actual one.

The results of this analysis are relatively similar for the sticking and sliding velocity fields from Fig. 4.16 as shown in Fig. 4.17. In general, the relative contact area A increases, if the non-dimensional effective hardness H_a, e.g. the indenter pressure, increases or if the non-dimensional plastic strain rate E_p increases. Nevertheless this behavior cannot be observed in all scenarios in Fig. 4.17. In fact, the increase of H_a at small values of A in Fig. 4.17 is believed to be an artifact of the velocity fields which were introduced [367]. In other words, these fields are only an approximation of the real velocity fields and they might be wrong estimations for small values of A.

Finally, a *fitting relation* was developed by Wilson and Sheu [367] to compute H_a, A or E_p relatively quickly without having to minimize the power dissipation. The detailed method, which explains how this relation was derived, is not described in the reference. It is, however, mentioned that the upper bound results are used for building the approximation, if A and E_p are relatively large, i.e. when the constructed velocity fields are relatively accurate. At small values of A and E_p, the relation was adjusted to reproduce the value

$$H_a = 2 + \pi \approx 5.142 \tag{4.91}$$

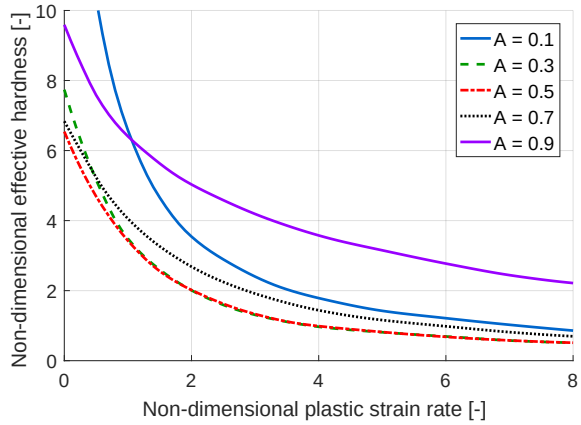

(a) Sticking case.

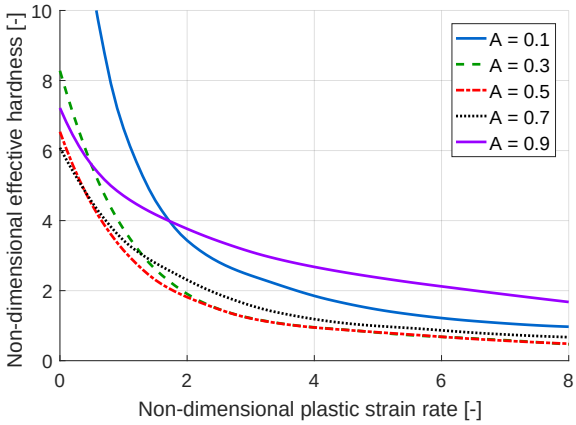

(b) Sliding case.

Figure 4.17: Upper bound results of the non-dimensional effective hardness H_a for a non-dimensional plastic strain rate E_p and a given relative contact area A by Wilson and Sheu [367].

which is computed by the slip-line field analysis of indentation [139, p. 254]. In conclusion, the following equation, which is illustrated in Fig. 4.18a, was derived:

$$E_p = \frac{1}{0.515 + 0.345A - 0.860A^2}\left(\frac{2}{H_a} - \frac{1}{2.571 - A - A\ln(1-A)}\right) \tag{4.92}$$

or

$$\frac{2}{H_a} = f_1 E_p + f_2 \quad \text{with} \quad \begin{cases} f_1 &= 0.515 + 0.345A - 0.860A^2 \\ f_2 &= 1/[2.571 - A - A\ln(1-A)] \end{cases} \tag{4.93}$$

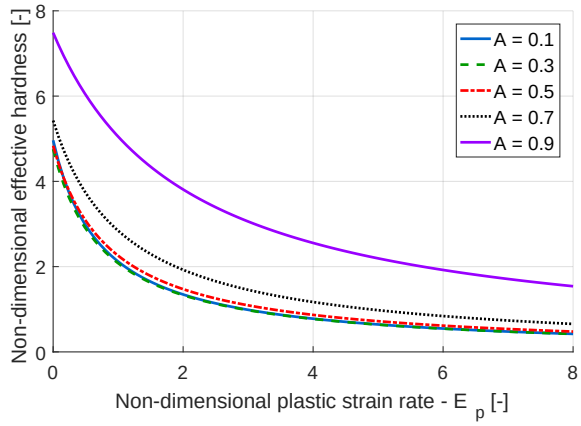

(a) Wilson and Sheu's equation by Eq. (4.92).

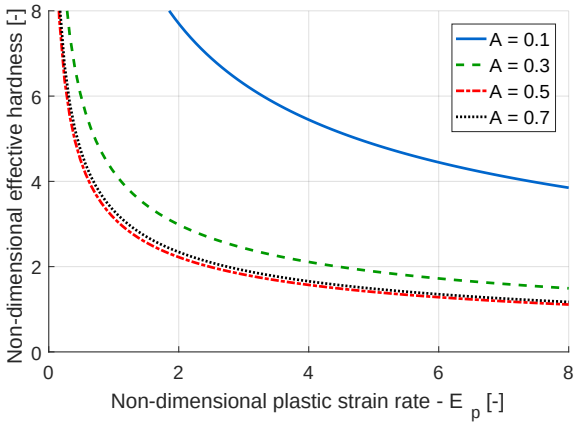

(b) Sutcliffe and Marsault's equation by Eq. (4.96).

Figure 4.18: Representation of some asperity flattening equations.

Although this equation was developed for a rigid perfectly plastic material, it is also assumed to approximate asperity flattening when the strip deforms elastically at the macro-scale in METALUB.

In this case, $E_p = 0$ and the relation between the pressures and the relative contact area is deduced from Eq. (4.92):

$$H_a = 2\left[2.571 - A - A\ln\left(1 - A\right)\right] \tag{4.94}$$

The derivative of the non-dimensional effective hardness H_a in the previous equation with respect to the relative contact area A, which is also required in the METALUB model, is given by the following equation:

$$\frac{\partial H_a}{\partial A} = -2 - 2\ln\left(1 - A\right) + \frac{2A}{1 - A} \tag{4.95}$$

4.7.1.2 Asperity flattening equation by Sutcliffe and Marsault

According to *Marsault* [215], the following asperity flattening equation can be determined based on *Sutcliffe*'s asperity flattening equation [311]:

$$E_p = \frac{4}{H_a^2 A^2 (3.81 - 4.38A)} \tag{4.96}$$

How exactly this relation was deduced from Sutcliffe's equation is not explained by Marsault [215] but it is mentioned that the same method as for transverse asperities by Sutcliffe [311] was applied for longitudinal asperities, whose grooves are aligned with the bulk deformation.

One notices in Eq. (4.96) that $E_p \to +\infty$, when $A \to 0$, or rather, $A \to 0$, when $E_p \to +\infty$, which seems *not realistic*. More generally, Fig. 4.18 shows that there are important differences between Wilson and Sheu's asperity flattening equation and Sutcliffe and Marsaults's equation, when A is relatively small while the similarity increases for larger fractional contact areas. In consequence, Eq. (4.94), i.e. Wilson and Sheu's equation, is used in zones with elastic bulk deformations in METALUB, when Sutliffe and Marsault's equation is selected. This latter equation, however, also *degenerates for very large fractional contact areas* since $3.81 - 4.38A$ in Eq. (4.96) becomes negative. In conclusion, although Sutcliffe and Marsaults's equation is implemented in METALUB, it is almost never included in a rolling computation because of its clear drawbacks with respect to Wilson and Sheu's equation.

4.7.1.3 Asperity flattening equation by Korzekwa, Dawson and Wilson

Korzekwa et al. [169] generalized Wilson and Sheu's asperity flattening equation [367] by *viscoplastic finite element simulations of asperity flattening with arbitrary straining directions* of the underlying bulk material. Fig. 4.19 shows the results of their flattening model by the finite element method (FEM) as well as those of Wilson and Sheu. It is clearly visible that significant discrepancies exist between these results. On the one hand, the differences between the upper bound method and the flattening equation by Wilson and Sheu for $A \leq 0.3$ can be explained by the construction of the flattening equation, i.e. the upper bound solution was only thought to be adequate at higher relative contact areas (Sec. 4.7.1.1). On the other hand, the results of the upper bound method overpredict the hardness of the FE method [169] at low contact ratios because

of the method's upper bound nature, while the results are very close at higher fractional contact area.

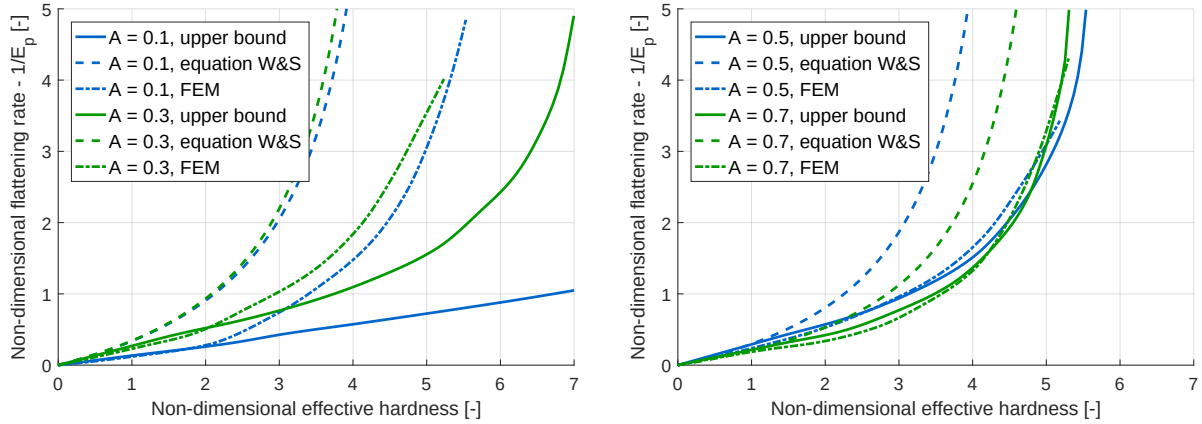

(a) $A \leq 0.3$. **(b)** $A \geq 0.5$.

Figure 4.19: Comparison of the upper bound solution and the asperity flattening equation by Wilson and Sheu [367] with the FE solution by Korzekwa et al. [169].

In order to use Korzekwa et al.'s model in a rolling model, Sutcliffe [313] *fitted* their results relatively well by the following relation, which was implemented in METALUB, as shown in Fig. 4.20:

$$E_p = \frac{1}{A\,(1-A)\left(c_1 + c_2 A + c_3 A^2\right)} \tag{4.97}$$

with

$$c_1 = 5.1206\,\Delta - 4.5258\,\Delta^2 + 3.5599\,\Delta^3 \tag{4.98}$$

$$c_2 = -9.5761\,\Delta + 11.3854\,\Delta^2 - 8.6069\,\Delta^3 \qquad \text{where} \qquad \Delta = \frac{H_a}{2} \tag{4.99}$$

$$c_3 = 8.3193\,\Delta - 11.7954\,\Delta^2 + 7.6475\,\Delta^3 \tag{4.100}$$

Finally, it is important to notice that the system of equations in METALUB (appendix N) has to evaluate H_a as a function of A in the mixed inlet zone. Since inverting Eq. (4.97) is non-trivial, Eqs. (4.94) and (4.95) (Wilson and Sheu's equation) are used in this short inlet zone.

4.7.1.4 Generalized asperity flattening equation

The *generalized asperity flattening equation* is derived to compute the evolution of the relative contact area along the roll bite as a function of the interface pressures and the strip elongation. In fact, it seems not possible to reformulate Eq. (4.92), (4.96) or (4.97) analytically in order to compute A as a function of H_a and E_p.

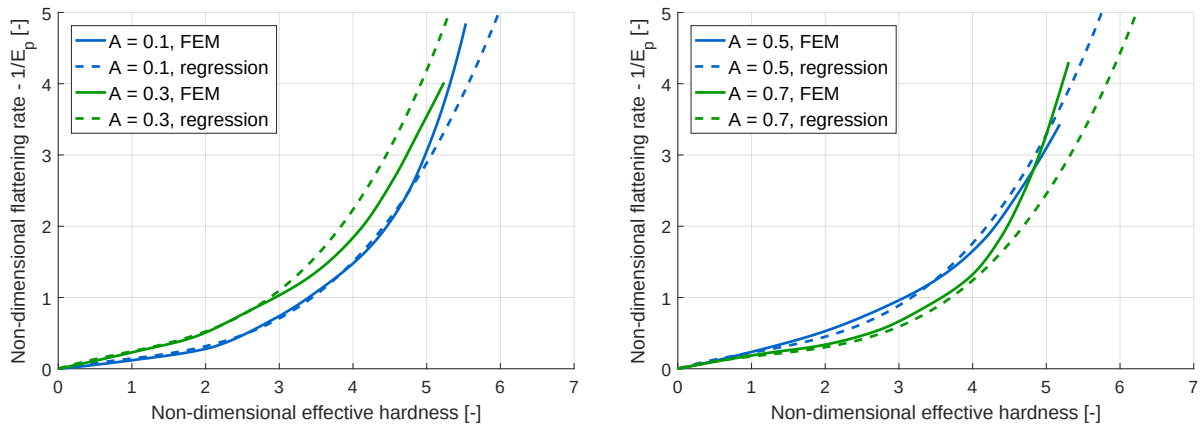

(a) $A \leq 0.3$. **(b)** $A \geq 0.5$.

Figure 4.20: Comparison of the FE solution by Korzekwa et al. [169] and the regression relation (Eq. 4.97) by Sutcliffe [313].

As explained in Sec. 4.4, it was assumed that the roll is flat and therefore, that it has no surface roughness. To account, however, for the roughness of the real roll, the composite root-mean-square roughness R_q combines the roughness characteristics of the roll and the strip. This value is used to determine the surface height distribution function $f_Z(z)$ of the idealized strip by Eqs. (2.11) or (2.12).

Previously, $f_Z(z)$ was introduced without any dependence on time. During cold rolling, the strip moves, however, through the roll bite. Thus, the asperity tops are flattened at a speed v_a, while the valleys are pushed upwards at a speed v_b due to the incompressibility of a plastically deforming metal. In consequence, the surface height distribution function depends on time, i.e. $f_Z(z,t)$. This time-dependence is illustrated in Fig. 4.21.

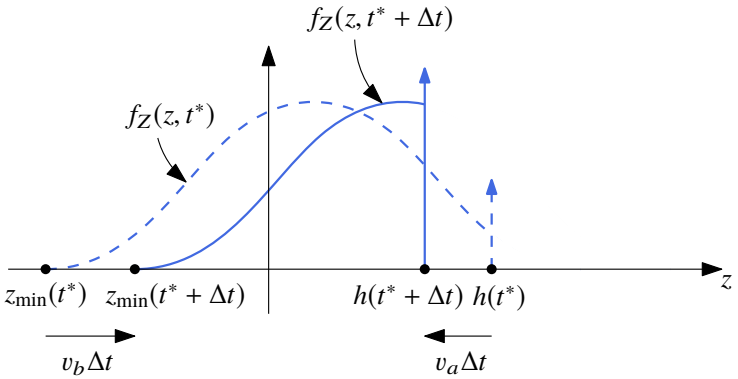

Figure 4.21: Time-dependence of the surface height distribution function from time t^* to time $t^* + \Delta t$.

It might seem surprising that the height distribution is simply translated by $v_b \Delta t$ during a time step Δt, i.e. that the increase in height for all heights in the valley is the same. This behavior was, however, measured experimentally by Pullen and Williamson [264] (Sec. 2.2.2.1) for a sample

which was prevented from flowing sideways, like commonly assumed in cold rolling. Based on the previous explanations,

$$z_{\min}(t^* + \Delta t) = z_{\min}(t^*) + v_b \Delta t \tag{4.101}$$

$$h(t^* + \Delta t) = h(t^*) - v_a \Delta t \tag{4.102}$$

$$f_Z(z, t^* + \Delta t) = f_Z(z + v_b \Delta t, t^*) \tag{4.103}$$

The generalized asperity flattening equation can be obtained by computing the derivative of the relative contact area with respect to time:

$$\left.\frac{\mathrm{d}A}{\mathrm{d}t}\right|_{t=t^*} = \lim_{\Delta t \to 0} \frac{A(t^* + \Delta t) - A(t^*)}{\Delta t} \tag{4.104}$$

The relative contact areas at t^* and $t^* + \Delta t$ can be substituted in the previous equation by the following relation, which can be derived by the relation between the relative contact area and the surface height distribution function (Eq. 4.6):

$$A(t^*) = \int_{h(t^*)}^{z_{\max}(t^*)} f_Z(z, t^*)\, \mathrm{d}z = 1 - \int_{z_{\min}(t^*)}^{h(t^*)^-} f_Z(z, t^*)\, \mathrm{d}z \tag{4.105}$$

The minus sign in $h(t^*)^-$ was introduced to mention that the delta Dirac at $h(t^*)$ is not included in the integral. Otherwise, it would be equal to 1 since all heights are in the interval $[z_{\min}(t^*), h(t^*)]$. Hence,

$$\left.\frac{\mathrm{d}A}{\mathrm{d}t}\right|_{t=t^*} = \lim_{\Delta t \to 0} \frac{1}{\Delta t} \left(\int_{z_{\min}(t^*)}^{h(t^*)^-} f_Z(z, t^*)\, \mathrm{d}z - \int_{z_{\min}(t^* + \Delta t)}^{h(t^* + \Delta t)^-} f_Z(z, t^* + \Delta t)\, \mathrm{d}z \right) \tag{4.106}$$

By Eqs. (4.101), (4.102) and (4.103), the previous equation becomes

$$\left.\frac{\mathrm{d}A}{\mathrm{d}t}\right|_{t=t^*} = \lim_{\Delta t \to 0} \frac{1}{\Delta t} \left(\int_{z_{\min}(t^*)}^{h(t^*)^-} f_Z(z, t^*)\, \mathrm{d}z - \int_{z_{\min} + v_b \Delta t}^{h(t^*)^- - v_a \Delta t} f_Z(z + v_b \Delta t, t^*)\, \mathrm{d}z \right) \tag{4.107}$$

Introducing the change of variables

$$z' = z - v_b \Delta t \tag{4.108}$$

$$\mathrm{d}z' = \mathrm{d}z \tag{4.109}$$

one obtains

$$\left.\frac{\mathrm{d}A}{\mathrm{d}t}\right|_{t=t^*} = \lim_{\Delta t \to 0} \frac{1}{\Delta t} \left(\int_{z_{\min}(t^*)}^{h(t^*)^-} f_Z(z, t^*)\, \mathrm{d}z - \int_{z_{\min}(t^*)}^{h(t^*)^- - (v_a + v_b)\Delta t} f_Z(z, t^*)\, \mathrm{d}z \right) \tag{4.110}$$

If $F_Z(z,t)$ is an antiderivative of $f_Z(z,t)$,

$$\left.\frac{\mathrm{d}A}{\mathrm{d}t}\right|_{t=t^*} = \lim_{\Delta t\to 0} -\left(\frac{F_Z\left[h(t^*)^- - (v_a+v_b)\Delta t, t^*\right] - F_Z\left[h(t^*)^-, t^*\right]}{\Delta t}\right) \tag{4.111}$$

Defining $\Delta z = -(v_a+v_b)\Delta t$,

$$\left.\frac{\mathrm{d}A}{\mathrm{d}t}\right|_{t=t^*} = \lim_{\Delta z\to 0} -\left(\frac{F_Z\left[h(t)^- + \Delta z, t^*\right] - F_Z\left[h(t)^-, t^*\right]}{\Delta z}\right)\left[-(v_a+v_b)\right] \tag{4.112}$$

By recognizing the definition of the derivative, one obtains

$$\left.\frac{\mathrm{d}A}{\mathrm{d}t}\right|_{t=t^*} = (v_a+v_b) f_Z(h(t^*)^-, t^*) \tag{4.113}$$

The derivative of the relative contact area can also be written with respect to space by the material derivative expansion (Eq. H.8), in which the partial time derivative vanishes, since the stationary process of cold rolling is studied:

$$\frac{\mathrm{d}A}{\mathrm{d}t} = \underbrace{\frac{\partial A}{\partial t}}_{=0} + \frac{\partial A}{\partial x}\frac{\partial x}{\partial t} \quad \Rightarrow \quad \left.\frac{\partial A}{\partial x}\right|_{x=x(t^*)} = \frac{(v_a+v_b) f_Z(h(t^*)^-, t^*)}{v_s} \tag{4.114}$$

where v_s is the speed of the strip. By Eq. (4.89),

$$\left.\frac{\partial A}{\partial x}\right|_{x=x(t^*)} = \frac{D_x^p \bar{l}}{v_s E_p} f_Z(h(t^*)^-, t^*) \tag{4.115}$$

Finally, this contact evolution along the roll bite can also be written for the signed distance between non-updated mean lines h. In fact[5], by Eq. (4.105),

$$\left.\frac{\partial A}{\partial h}\right|_{x=x(t^*)} = \left.\frac{\partial}{\partial h}\left(1 - \int_{z_{\min}(t)}^{h^-} f_Z(z,t^*)\,\mathrm{d}z\right)\right|_{x=x(t^*)} = -f_Z(h(t^*)^-, t^*) \tag{4.120}$$

[5]The mathematical operation can be proven as follows by Taylor series:

$$\frac{\partial}{\partial b}\left(\int_a^b f(x)\,\mathrm{d}x\right) = \lim_{\Delta b\to 0}\frac{1}{\Delta b}\left(\int_a^{b+\Delta b} f(x)\,\mathrm{d}x - \int_a^b f(x)\,\mathrm{d}x\right) \tag{4.116}$$

$$= \lim_{\Delta b\to 0}\frac{1}{\Delta b}\int_b^{b+\Delta b} f(x)\,\mathrm{d}x \tag{4.117}$$

$$= \lim_{\Delta b\to 0}\frac{1}{\Delta b}\left[f(b)\Delta b + \mathcal{O}(\Delta b^2)\right] \tag{4.118}$$

$$= f(b) \tag{4.119}$$

Hence,

$$\left.\frac{\partial A}{\partial x}\right|_{x=x(t^*)} = \left.\frac{\partial A}{\partial h}\right|_{x=x(t^*)} \left.\frac{\partial h}{\partial x}\right|_{x=x(t^*)} = -\left.\frac{\partial h}{\partial x}\right|_{x=x(t^*)} f_Z(h(t^*)^-, t^*) \tag{4.121}$$

Therefore, Eq. (4.115) becomes

$$\frac{\partial h}{\partial x} = -\frac{D_x^p \bar{l}}{v_s E_p} \tag{4.122}$$

which is the generalized asperity flattening equation.

4.7.2 Boundary friction models

In this section, the *boundary friction models* in METALUB are mentioned and the friction regularization for thin gauge rolling computations is explained.

4.7.2.1 Friction models

Numerous dry friction models were summarized in Sec. 2.2.3. These models can also be applied on top of the asperities in the boundary friction regime [362]. The following models are thus implemented in METALUB to compute the *shear stress on top of the asperities* τ_a in the solid contact region:

- *Coulomb friction law* [85]:

$$\tau_a = \text{sign}\,(v_r - v_s)\mu_C p_a \tag{4.123}$$

  where μ_C is the Coulomb coefficient of friction. If the shear stress τ_a exceeds the shear yield stress τ_Y of the workpiece or the boundary film, the material will rather shear inside the body of this workpiece. This behaviour is called sticking friction [281] and it can be described by the following law as explained in Sec. 2.2.3.

- *Tresca friction law* [252, 373]:

$$\tau_a = \text{sign}\,(v_r - v_s)\mu_T \tau_Y \tag{4.124}$$

  where μ_T is the Tresca coefficient of friction. The previous laws can finally be combined to take both friction mechanisms into account.

- *Coulomb-Tresca friction law*, also known as *Coulomb limited by Tresca friction law*:

$$\tau_a = \text{sign}\,(v_r - v_s)\,\min\,(\mu_C p_a, \mu_T \tau_Y) \tag{4.125}$$

  If $\mu_T = 1$, this law is called the *Coulomb-Orowan friction law* [252].

4.7.2.2 Friction regularization

Applying the previous models directly might be problematic when roll flattening is significant as in *thin gauge rolling*. In this case, the neutral point is rather a neutral zone, where no slip exists between the roll and the strip due to the identity of the rolling speed to the strip speed [105]. Since the previous laws quantify the tangential force, when slip occurs, they overpredict the tangential forces in these zones, which deteriorates the convergence capabilities of the model. For these reasons, *friction regularization* was included in LAM2DTRIBO by Sutcliffe and Montmitonnet [317] based on the regularization by Gratacos et al. [118] of a FEM rolling model, and in Stephany's METALUB version [305, p. 175] based on an arc tangent function. In the current METALUB version, Carretta [54] introduced a linear friction regularization as suggested by Counhaye [86, pp. 71 and 109]:

$$\tau_{a,\mathrm{reg}} = \alpha\tau_a \quad \text{with} \quad \alpha = \begin{cases} s/s_{\max} & \text{, if } s < s_{\max} \\ 1 & \text{, otherwise.} \end{cases} \quad \text{and} \quad s = \frac{|v_s - v_r|}{v_r} \tag{4.126}$$

According to the previous equation, the shear stress $\tau_{a,\mathrm{reg}}$ becomes smaller when the speed of the strip approaches that of the roll. The threshold is defined by the numerical parameter $s_{\max}$, which should be sufficiently small to not impact the tangential force, where slip actually occurs, while being sufficiently large to allow convergence, as explained in a recent study of friction regularization by Shigaki et al. [286]. Typically, $s_{\max}$ takes a value between 0.001 and 0.01.

4.8 Lubricant flow

As explained in Sec. 2.1.3, oil-in-water emulsions are commonly used in cold rolling to reduce friction and to cool the roll bite. Due to the complexity of lubrication by emulsions, the METALUB model is first derived by assuming lubrication by pure oil without starvation. Starvation is then introduced later in Sec. 4.10.4.

Fluid film lubrication between two moving solid interfaces as in cold rolling can generally be described by the *Reynolds equation*. In this section, the particular form of this equation, which is solved in METALUB, is derived. Since the pressure generation between the solid interfaces is strongly dependent on the viscosity of the lubricant, multiple constitutive equations are then introduced in a section about *lubricant rheology*. Finally, besides separating the strip from the roll by the lubricant pressure, shear forces are transmitted from the roll to the strip via the lubricant. Models to compute these *shear stresses* are included at the end of this section.

4.8.1 Reynolds equation

In this section, a *thin film approximation* of the lubricant flow is derived first. The *Reynolds equation* [273] is then deduced from this approximation by a *control volume approach* to facilitate the introduction of the *average Reynolds equation*, which takes into account the influence of

roughness on the lubricant flow. Moreover, an alternative derivation of the Reynolds equation by the *continuity equation* can be found in Sec. H.4.3. These derivations are based on Hamrock et al. [132] and Szeri [322]. Finally, the average Reynolds equation is simplified to be included in the METALUB model.

4.8.1.1 Thin film approximation

A thin-film approximation can be derived from the Navier-Stokes equation (Eq. H.129) by taking into account the particular geometry of the lubricant film (Fig. 4.22). In fact, the characteristic length scale L_z in the $\mathbf{e}_z$ direction is assumed to be significantly smaller than the length scale L_{xy} in the $\mathbf{e}_x\mathbf{e}_y$-plane, i.e. $\epsilon = L_z/L_{xy}$ is $\mathcal{O}(10^{-3})$. For instance, thin film lubrication in cold rolling occurs for a mean film thickness h_t below 10 R_q according to Wilson [361]. In Sec. 3, 10 R_q is equal to about 10 μm, while the roll bite length and the width of the strip are equal to about 10 mm and 1 m, respectively.

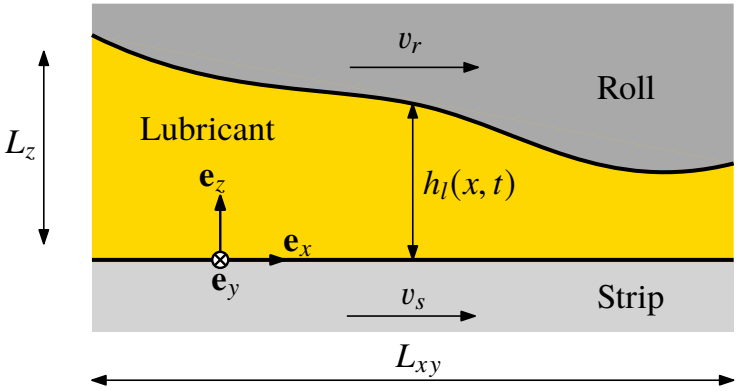

Figure 4.22: Thin fluid film between two moving boundaries with their characteristic length scales.

In order to obtain the thin film approximation, the quantities in the Navier-Stokes equation (Eq. H.131) are normalized, i.e. such that the normalized values are $\mathcal{O}(1)$:

$$(\overline{x}, \overline{y}, \overline{z}) = \frac{1}{L_{xy}} \left(x, y, \frac{1}{\epsilon} z \right) \tag{4.127}$$

Similarly, the characteristic velocity of the fluid in the $\mathbf{e}_x\mathbf{e}_y$-plane is U_{xy}. It can be expected that the velocity along z is much smaller than U_{xy} because the flow is supposed to be almost parallel to the $\mathbf{e}_x\mathbf{e}_y$-plane due to the small thickness. Hence,

$$(\overline{v}_x, \overline{v}_y, \overline{v}_z) = \frac{1}{U_{xy}} \left(v_x, v_y, \frac{1}{\epsilon} v_z \right) \tag{4.128}$$

By introducing the average density ρ^*, the average dynamic viscosity η^* and the average second viscosity parameter ζ^* (Sec. H.4.1), which are assumed to be independent of the geometry, the

following quantities can be normalized:

$$\bar{t} = \frac{U_{xy} t}{L_{xy}}; \quad \overline{\rho} = \frac{\rho}{\rho^*}; \quad \overline{\eta} = \frac{\eta}{\eta^*}; \quad \overline{\zeta} = \frac{\zeta}{\zeta^*} \tag{4.129}$$

After replacing the unnormalized parameters and variables in the Navier-Stokes equation along $\mathbf{e}_x$ (Eq. H.132a) by their normalized counterparts, neglecting the volume forces (except the inertia forces) and multiplying the equation by $\epsilon^2 L_{xy}^2/(\eta^* U_{xy})$, the following equation with the thermodynamic pressure p_{th} (Sec. H.4.1) is obtained:

$$\begin{aligned}\epsilon^2 \frac{\rho^* L_{xy} U_{xy}}{\eta^*} \overline{\rho} \left(\frac{\partial \overline{v}_x}{\partial \bar{t}} + \overline{v}_x \frac{\partial \overline{v}_x}{\partial \overline{x}} + \overline{v}_y \frac{\partial \overline{v}_x}{\partial \overline{y}} + \overline{v}_z \frac{\partial \overline{v}_x}{\partial \overline{z}} \right) &= -\epsilon^2 \frac{L_{xy}}{\eta^* U_{xy}} \frac{\partial p_{\text{th}}}{\partial \overline{x}} + \frac{\partial}{\partial \overline{z}} \left(\overline{\eta} \frac{\partial \overline{v}_x}{\partial \overline{z}} \right) \\ &+ \epsilon^2 \left\{ \left(\frac{\zeta^*}{\eta^*} \right) \frac{\partial}{\partial \overline{x}} \left[\overline{\zeta} \left(\frac{\partial \overline{v}_x}{\partial \overline{x}} + \frac{\partial \overline{v}_y}{\partial \overline{y}} + \frac{\partial \overline{v}_z}{\partial \overline{z}} \right) \right] + \frac{\partial}{\partial \overline{x}} \left(2\overline{\eta} \frac{\partial \overline{v}_x}{\partial \overline{x}} \right) \right. \\ &\left. + \frac{\partial}{\partial \overline{y}} \left[\overline{\eta} \left(\frac{\partial \overline{v}_x}{\partial \overline{y}} + \frac{\partial \overline{v}_x}{\partial \overline{x}} \right) \right] + \frac{\partial}{\partial \overline{z}} \left(\frac{\partial \overline{v}_z}{\partial \overline{x}} \right) \right\}\end{aligned} \tag{4.130}$$

If $\epsilon \to 0$, the last term in the previous equation disappears definitely. This is not necessarily true for the other terms because quantities, like a significant length L_{xy}, can compensate for the small ϵ. Hence,

$$\epsilon^2 \frac{\rho^* L_{xy} U_{xy}}{\eta^*} \overline{\rho} \left(\frac{\partial \overline{v}_x}{\partial \bar{t}} + \overline{v}_x \frac{\partial \overline{v}_x}{\partial \overline{x}} + \overline{v}_y \frac{\partial \overline{v}_x}{\partial \overline{y}} + \overline{v}_z \frac{\partial \overline{v}_x}{\partial \overline{z}} \right) = -\epsilon^2 \frac{L_{xy}}{\eta^* U_{xy}} \frac{\partial p_{\text{th}}}{\partial \overline{x}} + \frac{\partial}{\partial \overline{z}} \left(\overline{\eta} \frac{\partial \overline{v}_x}{\partial \overline{z}} \right) \tag{4.131}$$

In contrast to the positions, velocities, density and viscosity, no characteristic value is known for the pressure. Multiple ways of nondimensionalizing the pressure are, however, possible, e.g.

$$\overline{p}_{\text{th}} = \frac{p_{\text{th}}}{\rho^* U_{xy}} \quad \text{or} \quad \overline{p}_{\text{th}} = \frac{p_{\text{th}} L_{xy}}{\eta^* U_{xy}} \quad \text{or} \quad \overline{p}_{\text{th}} = \epsilon^2 \frac{p_{\text{th}} L_{xy}}{\eta^* U_{xy}} \tag{4.132}$$

Considering that the creation of an oil film, which separates the roll from the strip, has to be modeled by the simplified Navier-Stokes equation, the pressure term should not be eliminated. Hence, the last way of normalizing the pressure is chosen in the previous equation. Thus, Eq. (4.131) becomes

$$\mathrm{R}_\epsilon \overline{\rho} \left(\frac{\partial \overline{v}_x}{\partial \bar{t}} + \overline{v}_x \frac{\partial \overline{v}_x}{\partial \overline{x}} + \overline{v}_y \frac{\partial \overline{v}_x}{\partial \overline{y}} + \overline{v}_z \frac{\partial \overline{v}_x}{\partial \overline{z}} \right) = -\frac{\partial \overline{p}_{\text{th}}}{\partial \overline{x}} + \frac{\partial}{\partial \overline{z}} \left(\overline{\eta} \frac{\partial \overline{v}_x}{\partial \overline{z}} \right) \tag{4.133}$$

where R_ϵ is a reduced Reynolds number based on the Reynolds number Re:

$$\mathrm{R}_\epsilon = \epsilon \mathrm{Re} \qquad \mathrm{Re} = \frac{\rho^* L_z U_{xy}}{\eta^*} \tag{4.134}$$

Similarly, the Navier-Stokes equations along the $\mathbf{e}_y$ and $\mathbf{e}_z$-axis can be normalized and simplified for $\epsilon \to 0$. Thus, the thin film approximation of the Navier-Stokes equations can be written as follows:

$$\mathrm{R}_\epsilon \overline{\rho}\left(\frac{\partial \overline{v}_x}{\partial \overline{t}} + \overline{v}_x\frac{\partial \overline{v}_x}{\partial \overline{x}} + \overline{v}_y\frac{\partial \overline{v}_x}{\partial \overline{y}} + \overline{v}_z\frac{\partial \overline{v}_x}{\partial \overline{z}}\right) = -\frac{\partial \overline{p}_{\mathrm{th}}}{\partial \overline{x}} + \frac{\partial}{\partial \overline{z}}\left(\overline{\eta}\frac{\partial \overline{v}_x}{\partial \overline{z}}\right) \tag{4.135a}$$

$$\mathrm{R}_\epsilon \overline{\rho}\left(\frac{\partial \overline{v}_y}{\partial \overline{t}} + \overline{v}_x\frac{\partial \overline{v}_y}{\partial \overline{x}} + \overline{v}_y\frac{\partial \overline{v}_y}{\partial \overline{y}} + \overline{v}_z\frac{\partial \overline{v}_y}{\partial \overline{z}}\right) = -\frac{\partial \overline{p}_{\mathrm{th}}}{\partial \overline{y}} + \frac{\partial}{\partial \overline{z}}\left(\overline{\eta}\frac{\partial \overline{v}_y}{\partial \overline{z}}\right) \tag{4.135b}$$

$$0 = -\frac{\partial \overline{p}_{\mathrm{th}}}{\partial \overline{z}} \tag{4.135c}$$

Up to this point, the following hypotheses were made: the continuum description is valid, the Navier-Stokes equations hold and the fluid film along z is thin. Moreover, if the lubricant flow is supposed to be laminar with dominant viscous forces relative to inertia forces, as in lubricated cold rolling, $\mathrm{R}_\epsilon \to 0$. In fact, $\rho^* \approx 900$ kg/m^3, $L_z \approx 10$ μm, $L_{xy} \approx 10$ mm, $U_{xy} \approx 200$ m/min and $\eta^* \approx 0.1$ Pa.s implies that $R_\epsilon \approx 3 \cdot 10^{-4}$. Thus, Eqs. (4.135) can be further simplified:

$$\frac{\partial p_l}{\partial x} = \frac{\partial}{\partial z}\left(\eta\frac{\partial v_x}{\partial z}\right) \tag{4.136a}$$

$$\frac{\partial p_l}{\partial y} = \frac{\partial}{\partial z}\left(\eta\frac{\partial v_y}{\partial z}\right) \tag{4.136b}$$

One might notice that the previous equations are not normalized anymore, since the left and right hand sides have been multiplied by the appropriate factors, which were simplified before. Moreover, the thermodynamic pressure p_{th} was replaced by the (mechanical) lubricant pressure p_l according to the Stokes assumption (Eq. H.127).

These equations can be integrated twice with respect to z since the thin film hypothesis implies that $\partial p_l/\partial x$, $\partial p_l/\partial y$ and the dynamic viscosity η are no functions of z:

$$v_x = \frac{1}{2\eta}\frac{\partial p_l}{\partial x}z^2 + Az + B \tag{4.137a}$$

$$v_y = \frac{1}{2\eta}\frac{\partial p_l}{\partial y}z^2 + Cz + D \tag{4.137b}$$

The constants A, B, C and D can be determined by imposing the following no-slip boundary conditions, where W_r and W_s are the vertical speeds of the roll and strip surfaces (appendix H.4.3):

$$v_x = v_s \qquad v_y = 0 \qquad v_z = W_s \qquad \text{at } z = 0 \tag{4.138a}$$

$$v_x = v_r \qquad v_y = 0 \qquad v_z = W_r \qquad \text{at } z = h_l \tag{4.138b}$$

The velocities along $\mathbf{e}_y$ at the surfaces of the roll and the strip are assumed to be zero due to the plane-strain hypothesis in cold rolling. Therefore,

$$v_x = \frac{1}{2\eta}\frac{\partial p_l}{\partial x}(z^2 - h_l z) + \left(1 - \frac{z}{h_l}\right)v_s + \frac{z}{h_l}v_r \tag{4.139a}$$

$$v_y = \frac{1}{2\eta}\frac{\partial p_l}{\partial y}(z^2 - h_l z) \tag{4.139b}$$

4.8.1.2 Reynolds equation from control volume approach

The Reynolds equation can be derived by applying the principle of mass conservation to the *control volume* in Fig. 4.23. The volume flow rates per unit width in the directions $\mathbf{e}_x$ and $\mathbf{e}_y$ in this figure are defined as:

$$q'_x = \int_0^{h_l} v_x \, \mathrm{d}z \tag{4.140}$$

$$q'_y = \int_0^{h_l} v_y \, \mathrm{d}z \tag{4.141}$$

Based on Eq. (4.139), these integrals can be computed:

$$q'_x = -\frac{h_l^3}{12\eta}\frac{\partial p_l}{\partial x} + \frac{v_s + v_r}{2}h_l \tag{4.142}$$

$$q'_y = -\frac{h_l^3}{12\eta}\frac{\partial p_l}{\partial y} \tag{4.143}$$

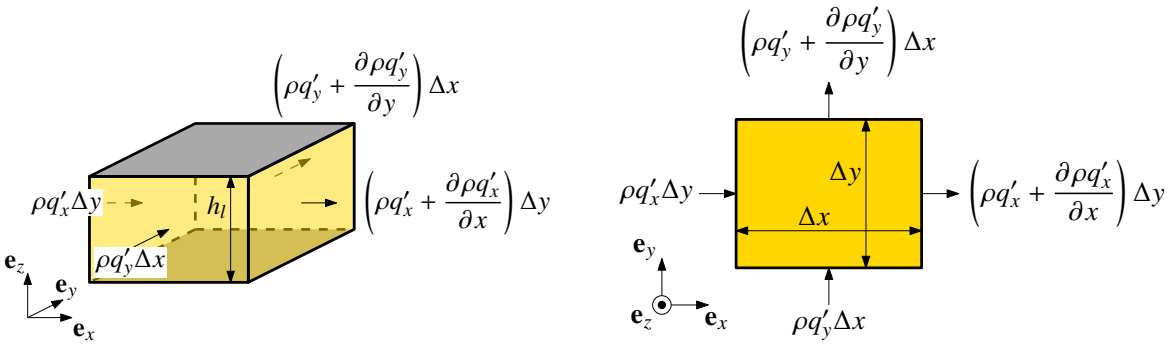

(a) 3D view. **(b)** Top view.

Figure 4.23: Control volume with inflow and outflow values.

Moreover, the variation of mass inside the control volume can only change due to inflows and outflows by the conservation of mass:

$$\rho q'_x \Delta y - \left(\rho q'_x + \frac{\partial(\rho q'_x)}{\partial x}\Delta x\right)\Delta y + \rho q'_y \Delta x - \left(\rho q'_y + \frac{\partial(\rho q'_y)}{\partial y}\Delta y\right)\Delta x = \frac{\partial(\rho h_l)}{\partial t}\Delta x \Delta y \tag{4.144}$$

After simplifying this expression,

$$-\frac{\partial(\rho q'_x)}{\partial x}-\frac{\partial(\rho q'_y)}{\partial y}=\frac{\partial(\rho h_l)}{\partial t} \tag{4.145}$$

Substituting Eqs. (4.142) and (4.143) in the previous equation, one obtains the general *Reynolds equation* in cold rolling:

$$\frac{\partial}{\partial x}\left(\frac{\rho h_l^3}{12\eta}\frac{\partial p_l}{\partial x}\right)+\frac{\partial}{\partial y}\left(\frac{\rho h_l^3}{12\eta}\frac{\partial p_l}{\partial y}\right)=\frac{\partial}{\partial x}\left(\rho h_l\frac{v_s+v_r}{2}\right)+\frac{\partial(\rho h_l)}{\partial t} \tag{4.146}$$

The first two terms in the previous equation are called Poiseuille terms due to their similarity to the terms describing a Poiseuille flow, while the third term is called the Couette term for similar reasons.

4.8.1.3 Average Reynolds equation

Previously, is was assumed that the surfaces of the roll and the strip are smooth and that they are never in contact. This is, however, not true for real rough surfaces (Fig. 4.24). Therefore, an *average Reynolds equation* was derived to model the lubricant flow between rough surfaces with asperity contacts.

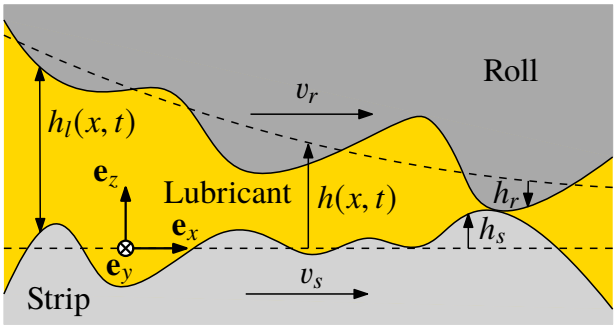

Figure 4.24: Thin film lubrication between rough surfaces. The dashed lines are the non-updated mean lines of the surface profiles. The roughness deviations from the mean lines h_s and h_r are actually both positive in the directions, which are represented.

Below, two approaches will be introduced: one for *small fractional contact areas* and one for *large fractional areas*, where the nominal film thickness h, i.e. the signed distance from the non-updated mean line of the strip to the non-updated mean line of the roll, becomes zero or negative. Then, the *transition between both models* is analyzed.

Average Reynolds equation for small relative contact areas

This first approach was developed by Patir and Cheng [253, 254]. A simplified explanation and implementation of the following method can be found in Vyas [350]. Instead of assuming that the

volume flow rates per unit width, q'_x and q'_y, do not change respectively along $\mathbf{e}_y$ and $\mathbf{e}_x$ as in the previous section, it is more realistic to assume that they do because of the local surface roughness. In order to deduce macroscopic characteristics of these microscopic variations, average volume flow rates per unit width are defined by

$$\overline{q}'_x = \frac{1}{\Delta y}\int_y^{y+\Delta y} q'_x \, \mathrm{d}x = \frac{1}{\Delta y}\int_y^{y+\Delta y}\left(-\frac{h_l^3}{12\eta}\frac{\partial p_l}{\partial x} + \frac{v_s+v_r}{2}h_l\right)\mathrm{d}y \tag{4.147}$$

$$\overline{q}'_y = \frac{1}{\Delta x}\int_x^{x+\Delta x} q'_y \, \mathrm{d}x = \frac{1}{\Delta x}\int_x^{x+\Delta x}\left(-\frac{h_l^3}{12\eta}\frac{\partial p_l}{\partial y}\right)\mathrm{d}x \tag{4.148}$$

The values of the previous integrals depend on the surface roughness. If these values can be computed either analytically or numerically for a flow configuration with asperities, flow factors ϕ_x, ϕ_y and ϕ_s can be deduced such that the following equations are satisfied:

$$\overline{q}'_x = -\phi_x\frac{h^3}{12\eta}\frac{\partial \overline{p}_l}{\partial x} + \frac{v_s+v_r}{2}\overline{h}_l + \frac{v_s-v_r}{2}R_q\phi_s \tag{4.149}$$

$$\overline{q}'_y = -\phi_y\frac{h^3}{12\eta}\frac{\partial \overline{p}_l}{\partial y} \tag{4.150}$$

where the variables $\overline{p}_l$ and $\overline{h}_l$ denote respectively the average lubricant pressure and the average gap as defined by Patir and Cheng [253]:

$$\overline{h}_l = \int_{-\infty}^{h}(h-z)f_Z(z)\,\mathrm{d}z \tag{4.151}$$

where $z = h_s + h_r$ is the combined roughness with composite root-mean-square roughness R_q and the probability density function $f_Z(z)$. The average gap $\overline{h}_l$ in the previous equation is actually the distance between updated mean lines, i.e. the mean film thickness h_t, which was defined in Eq. (4.7).

The conservation equation of the previous section, i.e. Eq. (4.145), is still valid in this context. To obtain the average Reynolds equation, the volume flow rates per width can be replaced by the respective average flow rates and the local film thickness by the average gap, $\overline{h}_l = h_t$. If the compressibility of the lubricant is neglected ($\partial\rho/\partial x = \partial\rho/\partial y = \partial\rho/\partial t = 0$), Eq. (4.145) becomes:

$$-\frac{\partial \overline{q}'_x}{\partial x} - \frac{\partial \overline{q}'_y}{\partial y} = \frac{\partial h_t}{\partial t} \tag{4.152}$$

Substituting the average volume flow rates of Eqs. (4.149) and (4.150) in the previous equation, the average Reynolds equation is written as follows, where $\overline{p}_l$ was replaced by p_l to simplify the notations although it should be understood to be the average lubricant pressure:

$$\frac{\partial}{\partial x}\left(\phi_x\frac{h^3}{12\eta}\frac{\partial p_l}{\partial x}\right) + \frac{\partial}{\partial y}\left(\phi_y\frac{h^3}{12\eta}\frac{\partial p_l}{\partial y}\right) = \frac{\partial}{\partial x}\left(\frac{v_s+v_r}{2}h_t\right) + \frac{\partial}{\partial x}\left(\frac{v_s-v_r}{2}R_q\phi_s\right) + \frac{\partial h_t}{\partial t} \tag{4.153}$$

One notices that, if $\phi_x, \phi_y \to 1$ and $\phi_s \to 0$, when $h/R_q \to +\infty$, one recovers the Reynolds equation without surface roughness. The flow factors are provided for triangular asperity and Gaussian height distributions hereafter.

Triangular asperity height distribution The pressure flow factor ϕ_x can be computed analytically for *triangular asperities, whose grooves are aligned with the rolling direction*, as explained by Wilson and Chang [363]. More explicitly, by Eqs. (4.147) and (4.149),

$$\phi_x = \frac{\dfrac{1}{\Delta y}\displaystyle\int_y^{y+\Delta y} \left(\frac{h_l^3}{12\eta}\frac{\partial p_l}{\partial x}\right) \mathrm{d}y}{\dfrac{h^3}{12\eta}\dfrac{\partial \overline{p}_l}{\partial x}} \tag{4.154}$$

This integral can be simplified since η is assumed to be independent of y, and since $\partial p_l/\partial x$ is assumed to be equal to the derivative of the average pressure in the lubricant, i.e. $\partial \overline{p}_l/\partial x$. Hence,

$$\phi_x = \frac{\dfrac{1}{\Delta y}\displaystyle\int_y^{y+\Delta y} h_l^3 \, \mathrm{d}y}{h^3} \tag{4.155}$$

If the strip is not in contact with the roll, the interface can be represented as shown in Fig. 4.25. In this case, the integral in Eq. (4.155) can be computed with

$$h_l = h - \sqrt{3}R_q + \frac{2\sqrt{3}R_q}{\Delta y} y \tag{4.156}$$

according to this figure. Thus, if no contact exists between the strip and the roll, the pressure flow factor is given by the following equation:

$$\phi_x = \frac{\dfrac{1}{\Delta y}\displaystyle\int_0^{\Delta y} \left(h - \sqrt{3}R_q + \frac{2\sqrt{3}R_q}{\Delta y} y\right)^3 \mathrm{d}y}{h^3} = 1 + \frac{3R_q^2}{h^2} \tag{4.157}$$

The shear flow factor of the triangular asperity height distribution is equal to zero [215] due to the longitudinal lay of the triangular asperities. In fact,

$$\frac{1}{\Delta y}\int_y^{y+\Delta y} \left(\frac{v_s + v_r}{2} h_l\right) \mathrm{d}y = \frac{v_s + v_r}{2}\frac{1}{\Delta y}\int_y^{y+\Delta y} h_l \, \mathrm{d}y = \frac{v_s + v_r}{2}\overline{h}_l \tag{4.158}$$

Combining the previous equation with Eqs. (4.147) and (4.149) yields:

$$\phi_s = 0 \tag{4.159}$$

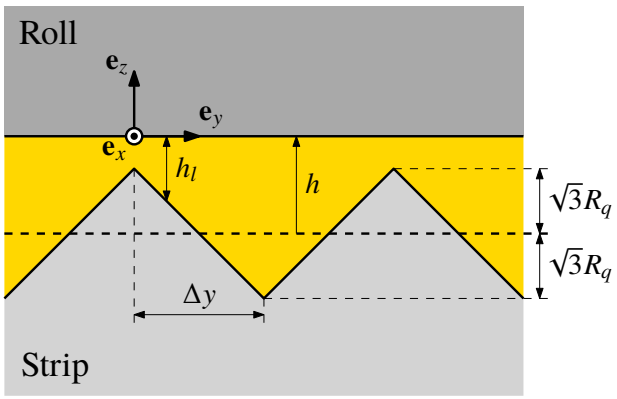

Figure 4.25: Contact interface between the roll and the strip with a longitudinal triangular asperity height distribution and no contact between them.

Gaussian surface height distribution The *pressure flow factors* ϕ_x and ϕ_y were obtained by Patir and Cheng [253] through flow simulations (CFD) by considering the pure rolling case [132, p. 224, Tab. 7.1], i.e. $v_s = v_r$. This is obviously an approximation of cold rolling, where a peripheral material point of the roll has a greater horizontal velocity than the corresponding point of the strip before the neutral point and a smaller velocity after the neutral point. It is, however, true that both velocities are not significantly different. Moreover, it was assumed that $\partial p_l / \partial y = 0$ at the minimum and maximum y-coordinates. This hypothesis is realistic due to the symmetry of strip and the roll along the y-axis. Finally, the rough surfaces in the numerical simulations have a *Gaussian surface height distribution*. Based on the previous hypotheses, the pressure flow factors take the following values:

$$\phi_x = \begin{cases} 1 - C_x e^{-\frac{r_x h}{R_q}} \text{ with } \begin{cases} C_x = 0.89679 - 0.26591 \ln \gamma \\ r_x = 0.43006 - 0.10828\gamma + 0.23821\gamma^2 \end{cases} & \text{, if } \gamma \leq 1 \\ 1 + C_x \left(\dfrac{h}{R_q} \right)^{-1.5} \text{ with } C_x = -0.10667 + 0.10750\gamma & \text{, otherwise.} \end{cases} \tag{4.160}$$

and

$$\phi_y(\gamma) = \phi_x(1/\gamma) \tag{4.161}$$

where γ is the *Peklenik surface pattern parameter*, which is defined by the ratio

$$\gamma = \frac{\lambda_{0.5x}}{\lambda_{0.5y}} \tag{4.162}$$

The values $\lambda_{0.5x}$ and $\lambda_{0.5y}$ are the lengths at which the autocorrelation function of z, which is the composite roughness height of the roll and the strip, reduces to 50% of its initial value, respectively along x and along y according to Peklenik [256]. This number characterizes the directional orientation of the roughness. Figure 4.26 gives a visual explanation by showing the typical contact areas for longitudinally ($\gamma > 1$), isotropic ($\gamma = 1$) and transversely ($\gamma < 1$) oriented

surface roughness. Due to these roughness orientations, the parameter R_q represents the area and not the profile based composite root-mean-square roughness, although R_q is usually the profile based composite root-mean-square roughness due to limited measurement data. The expressions of C_x and r_x in Eq. (4.160) were determined via least squares curve fitting by Marsault [215] of the values in Patir and Cheng [253].

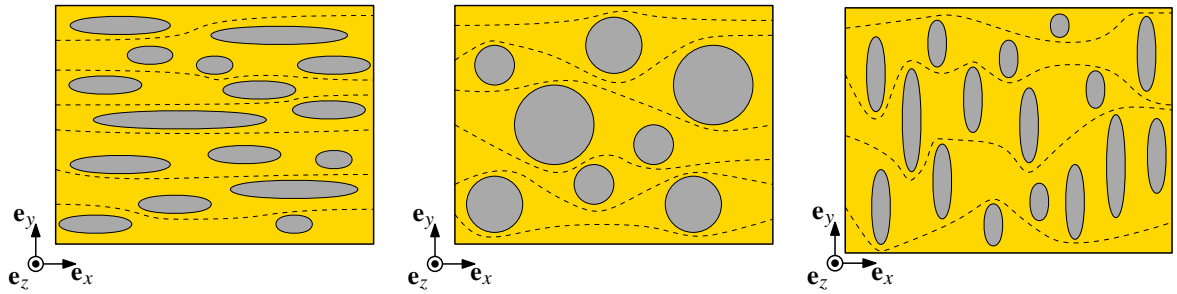

(a) $\gamma > 1$. **(b)** $\gamma = 1$. **(c)** $\gamma < 1$.

Figure 4.26: Typical contact areas for longitudinally ($\gamma > 1$), isotropic ($\gamma = 1$) and transversely ($\gamma < 1$) oriented surfaces with schematic dashed streamlines.

The *shear flow factor* ϕ_s was computed numerically by Patir and Cheng [254] with similar assumptions than ϕ_x in Patir and Cheng [253], except for the pure shearing hypothesis, i.e. $v_s = -v_r$ instead of $v_s = v_r$. Moreover, the resulting value of ϕ_s depends on the root-mean-square roughness of each surface separately instead of the composite RMS roughness R_q. In fact, more fluid is transported in the valleys of a rough moving surface than a smooth moving surface. In past versions of METALUB, the roll was assumed to be smooth, while the strip was assumed to be rough in the computation of the flow factors [54, 215, 305]: the roughness of the strip was assumed to be equal to the composite roughness of the roll and the strip. This inconsistency was corrected by introducing the roughness values of the roll $R_{q,r}$ and the strip $R_{q,s}$ in the model and by using the following definition of the shear flow factor according to Patir and Cheng [254]:

$$\phi_s = \frac{R_{q,s}^2}{R_q^2}\Phi_s\left(\frac{h}{R_q}, \gamma_s\right) - \left(1 - \frac{R_{q,s}^2}{R_q^2}\right)\Phi_s\left(\frac{h}{R_q}, \gamma_r\right) \tag{4.163}$$

with

$$\Phi_s = A_s e^{-0.25\frac{h}{R_q}} \quad \text{with} \quad A_s = 1.0766 - 0.37758\ln\gamma \tag{4.164}$$

if $h/R_q > 5$. The expression of A_s was again determined via curve fitting by Marsault [215] based on the values in Patir and Cheng [254]. The Peklenik surface pattern parameters of the roll, the strip and the composite roughness are usually assumed to be identical, i.e. $\gamma_r = \gamma_s = \gamma$, due to roughness transfer and limited measurement data.

If the nominal film thickness h, i.e. the signed distance from the non-updated mean line of the strip to the non-updated mean line of the roll, becomes negative or, in other words, if the fractional contact area A becomes relatively large, the previous results are not valid anymore since they

were developed for small fractional contact areas (or no contact at all for the triangular asperity ridges).

Average Reynolds equation for large relative contact areas

The previous model was extended by Wilson and Marsault [364] to account for large fractional contact areas. In fact, the variable h in Eq. (4.153) is replaced by h_t, which cannot become zero or negative unlike h, but which is equal to h as long as no contact exists between contacting surfaces:

$$\frac{\partial}{\partial x}\left(\phi_x \frac{h_t^3}{12\eta}\frac{\partial p_l}{\partial x}\right) = \frac{\partial}{\partial x}\left(\frac{v_s + v_r}{2} h_t\right) + \frac{\partial}{\partial x}\left(\frac{v_s - v_r}{2} R_q \phi_s\right) + \frac{\partial h_t}{\partial t} \tag{4.165}$$

In this equation, the derivative of the average lubricant pressure along $\mathbf{e}_y$ was removed since the lubricant flow in this direction is assumed to be small, i.e. $v_y \approx 0$ in Eq. (4.139b). This hypothesis is consistent with the longitudinal orientation of the roughness in cold rolling (Sec. 2.1.2.2), which partially prevents the lubricant from flowing in the transverse direction $\mathbf{e}_y$ in the mixed lubrication regime. Moreover, the area based composite root-mean-square roughness S_q instead of the profile based R_q is used in [364]. Due to limited measurement data, R_q is commonly used in METALUB, as mentioned earlier.

Triangular asperity height distribution If the strip and the roll are in contact as shown in Fig. 4.27, the flow factor is computed by the following formula, which is similar to Eq. (4.154) except for the substitution of h by h_t in the denominator:

$$\phi_x = \frac{\dfrac{1}{\Delta y}\displaystyle\int_y^{y+\Delta y}\left(\frac{h_l^3}{12\eta}\frac{\partial p_l}{\partial x}\right)\,\mathrm{d}y}{\dfrac{h_t^3}{12\eta}\dfrac{\partial p_l}{\partial x}} \tag{4.166}$$

This equation can again be simplified as explained in Sec. 4.8.1.3 to obtain:

$$\phi_x = \frac{\dfrac{1}{\Delta y}\displaystyle\int_y^{y+\Delta y} h_l^3\,\mathrm{d}y}{h_t^3} \tag{4.167}$$

It can be evaluated as follows:

$$\phi_x = \frac{1}{h_t^3 \Delta y}\int_{\Delta y\left(\frac{1}{2}-\frac{h}{2\sqrt{3}R_q}\right)}^{\Delta y}\left(h - \sqrt{3}R_q + \frac{2\sqrt{3}R_q}{\Delta y}y\right)^3\,\mathrm{d}y = \frac{2\sqrt{3}R_q}{h_t} \tag{4.168}$$

The shear flow factor of the triangular asperity height distribution is equal to zero for the same reasons as in Eq. (4.159):

$$\phi_s = 0 \tag{4.169}$$

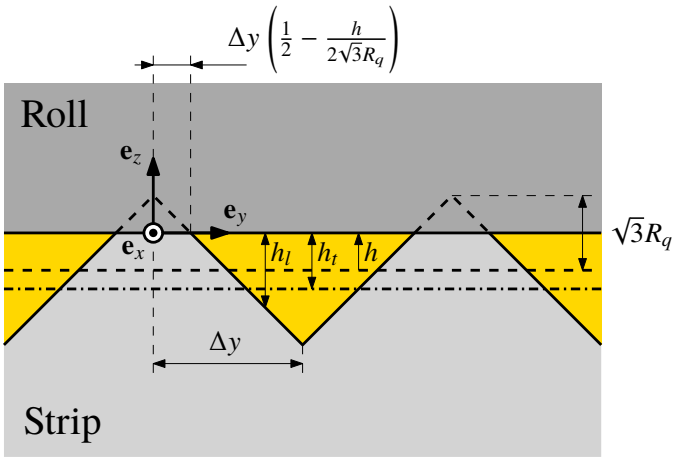

Figure 4.27: Contact interface between the roll and the strip with a triangular asperity height distribution and no contact between them.

Gaussian surface height distribution The corresponding flow factors for a surface with a quasi-Gaussian Christensen surface height distribution (Eq. 2.12) were determined by Wilson and Marsault [364] based on Patir and Cheng [253, 254], Tripp [331] and Lo [200]. In Tripp [331], the flow factors are computed by an analytical perturbation approach, which can be considered to be the analytical counterpart of the numerical approach by Patir and Cheng [253, 254]. The analytical solution breaks, however, down due to the contact growth between the surfaces. Hence, the authors suggest that an approach, which takes *percolation*, where the lubricant is trapped in surface pockets, into account, is more appropriate than their model for important relative contact areas. In Lo [200], the flow factor method, a *porous medium model* and percolation theory are combined. The previous results are later extended by Wilson and Marsault [364] to obtain the *pressure flow factors for large fractional contact areas* of surfaces with a Christensen surface height distribution. Thus, if $h_t/R_q < 3$,

$$\phi_x h_t^3 = a_2 R_q (h_t - h_{t,c})^2 + a_3 (h_t - h_{t,c})^3 \tag{4.170}$$

where $h_{t,c}$ is the critical value of h_t corresponding to the percolation threshold, i.e. the mean film thickness below which the lubricant is captured in isolated, non-connected valleys. For the longitudinal triangular asperity height distribution, the grooves are always assumed to be parallel to the rolling direction. Hence, the lubricant gets never trapped and the percolation limit is zero. For the quasi-Gaussian Christensen height distribution, the percolation limit is, however, not always zero. Its value and the values of a_2 and a_3 in the previous equation are given by the following equations. Fig. 4.28 shows that the *percolation threshold* decreases when γ increases, i.e. when the asperities do not block the pressure driven flow:

$$h_{t,c} = 3R_q \left(1 - \frac{1}{(0.47476/\gamma + 1)^{0.25007}}\right) \tag{4.171}$$

$$a_2 = 0.051375 \ln^3(9\gamma) - 0.0071901 \ln^4(9\gamma) \tag{4.172}$$

$$a_3 = 1.0019 - 0.17927 \ln\gamma + 0.047583 \ln^2\gamma - 0.016417 \ln^3\gamma \tag{4.173}$$

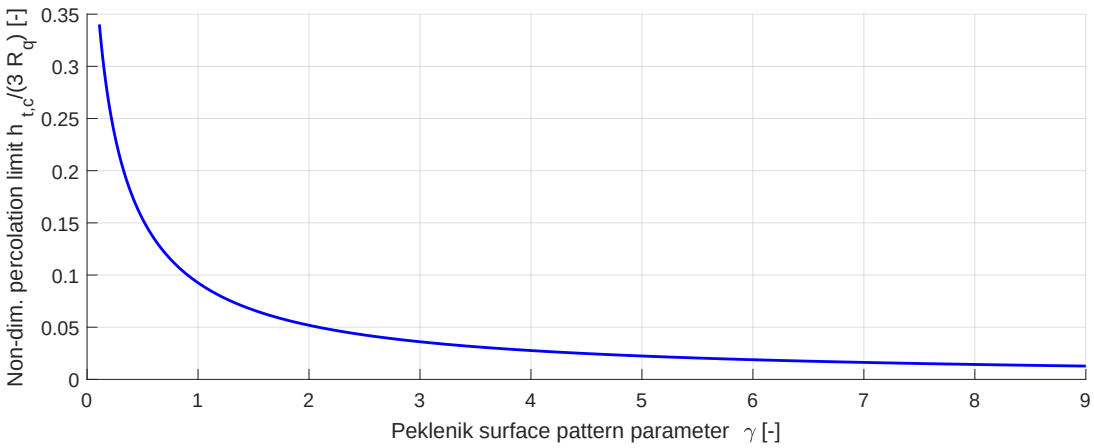

Figure 4.28: Evolution of the percolation threshold in Eq. (4.171) as a function of the surface pattern orientation, which is described by the Peklenik parameter.

Concerning the *shear flow factor for large fractional contact areas*, the mathematical form is assumed to be the same as for small fractional contact areas (Eq. 4.163) to take the increased lubricant transport in the valleys of a rougher surface with respect to a smoother one into account:

$$\phi_s = \frac{R_{q,s}^2}{R_q^2}\Phi_s\left(\frac{h_t}{R_q}, \gamma_s\right) - \left(1 - \frac{R_{q,s}^2}{R_q^2}\right)\Phi_s\left(\frac{h_t}{R_q}, \gamma_r\right) \tag{4.174}$$

where the Peklenik surface pattern parameters of the roll, the strip and the composite roughness are assumed to be identical, again, i.e. $\gamma_r = \gamma_s = \gamma$, due to roughness transfer and limited measurement data. Like for small fractional contact areas, the assumption of past METALUB versions [54, 215, 305], i.e. $\phi_s = \Phi_s$, is not made anymore. The following expression of Φ_s was derived for $h_t/R_q < 5$ by Wilson and Marsault [364]:

$$\Phi_s = b_0 + b_1\left(\frac{h_t}{R_q}\right) + b_2\left(\frac{h_t}{R_q}\right)^2 + b_3\left(\frac{h_t}{R_q}\right)^3 + b_4\left(\frac{h_t}{R_q}\right)^4 + b_5\left(\frac{h_t}{R_q}\right)^5 \tag{4.175}$$

with

$$b_0 = 0.12667\gamma^{-0.6508} \tag{4.176}$$

$$b_1 = \exp\left(-0.38768 - 0.44160\ln\gamma - 0.12679\ln^2\gamma + 0.042414\ln^3\gamma\right) \tag{4.177}$$

$$b_2 = -\exp\left(-1.1748 - 0.39916\ln\gamma - 0.11041\ln^2\gamma + 0.031775\ln^3\gamma\right) \tag{4.178}$$

$$b_3 = \exp\left(-2.8843 - 0.36712\ln\gamma - 0.10676\ln^2\gamma + 0.028039\ln^3\gamma\right) \tag{4.179}$$

$$b_4 = -0.004706 + 0.0014493\ln\gamma + 0.00033124\ln^2\gamma - 0.00017147\ln^3\gamma \tag{4.180}$$

$$b_5 = 0.00014734 - 4.255\cdot 10^{-5}\ln\gamma - 1.057\cdot 10^{-5}\ln^2\gamma + 5.0292\cdot 10^{-6}\ln^3\gamma \tag{4.181}$$

Flow factor transition from small to large relative contact areas

Previously, pressure and shear flow factors were computed to take the influence of the surface roughness on the lubricant flow into account. These factors were derived for longitudinal triangular asperity and Gaussian/Christensen height distributions either for small or large relative contact areas. In this section, the *transition from small to large relative contact areas* is analyzed.

Figure 4.29 shows the *pressure flow factor* evolution as a function of the mean film thickness h_t for the triangular asperity and the Christensen height distributions. The curve of the triangular asperity height distribution was obtained by Eqs. (4.168) and (4.157), with the smooth transition from the first to the second formula, when h_t becomes greater than $\sqrt{3}R_q$. A similar transition also exists for the flow factors obtained with the Christensen height distribution from Eq. (4.170) to Eq. (4.160), when h_t becomes greater than $3R_q$ (see black dashed vertical line in Fig. 4.29). This transition is relatively smooth as shown in the magnification in the top right corner. Moreover, the magnification in the center of Fig. 4.29 shows that some flow factor might become smaller than 0 due to fitting inaccuracies, especially for $\gamma = 1/9$, which is not realistic. This inconsistency was partially corrected by setting ϕ_x equal to 0, when it becomes negative.

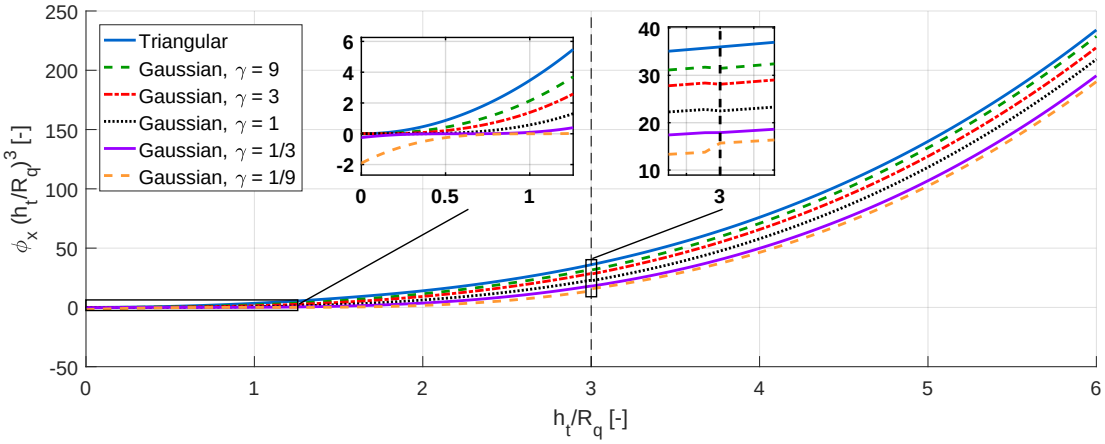

Figure 4.29: Pressure flow factors ϕ_x for longitudinal triangular asperity and Christensen/Gaussian height distributions, and for small and large relative contact areas as a function of the mean film thickness h_t.

Figure 4.30 shows the *shear flow factor* evolution as a function of the mean film thickness for the Christensen/Gaussian height distribution. The transition from Eq. (4.175) to Eq. (4.163) occurs at $h_t/R_q = 5$, when the mean film thickness increases. The results in Fig. 4.30 can be criticized for three reasons. First, there seems to been an error in Eq. (4.175). In fact, ϕ_s for $\gamma = 1/9$ is smaller than ϕ_s for $\gamma = 1/3$ just before $h_t/R_q = 5$ in Fig. 4.30. This erroneous evolution is not represented in Fig. 4 in Wilson and Marsault [364], which should be identical to Fig. 4.30. Secondly, the shear flow factor ϕ_s should be equal to h_t/R_q, when h_t is smaller than the percolation limit given in Eq. (4.171), according to Wilson and Marsault [364]. A comparison of Fig. 4 in this reference [364] and Fig. 4.30 shows again that this is not true in the current version of METALUB. Finally, the transition at $h_t/R_q = 5$ is discontinuous. After some investigations, it was found that this is

partially due to the fitting function of A_s in Eq. (4.163) based on the values of Patir and Cheng [254].

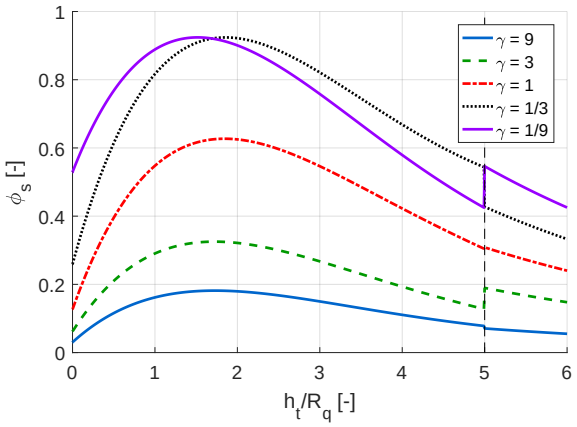

Figure 4.30: Old shear flow factors for the Gaussian/Christensen height distribution according to Eqs. (4.163) and (4.175).

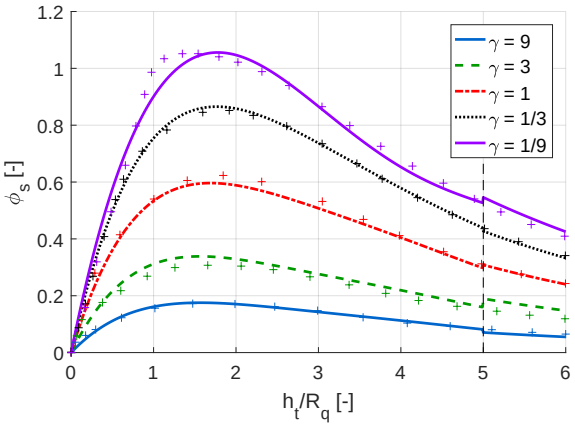

Figure 4.31: New shear flow factors for the Gaussian/Christensen height distribution according to Eqs. (4.163) and (4.182). The crosses represent the data used to derive the fitting relation from Fig. 4 in Wilson and Marsault [364].

To remove or at least reduce the previous inconsistency of Eq. (4.175), a *new fitting relation* of the function Φ_s in the shear flow factor ϕ_s was derived for $h_t \leq 5R_q$ based on Fig. 4 in Wilson and Marsault [364]:

$$\Phi_s = b_1 \left(\frac{h_t}{R_q}\right) + b_2 \left(\frac{h_t}{R_q}\right)^2 + b_3 \left(\frac{h_t}{R_q}\right)^3 + b_4 \left(\frac{h_t}{R_q}\right)^4 + b_5 \left(\frac{h_t}{R_q}\right)^5 \tag{4.182}$$

with

$$b_1 = 9.7038 \cdot 10^{-1} - 3.4234 \cdot 10^{-1} \ln\gamma - 1.9633 \cdot 10^{-2} \ln^2\gamma + 1.7168 \cdot 10^{-2} \ln^3\gamma \tag{4.183}$$

$$b_2 = -5.7008 \cdot 10^{-1} + 1.5732 \cdot 10^{-1} \ln\gamma + 3.2603 \cdot 10^{-2} \ln^2\gamma - 1.1655 \cdot 10^{-2} \ln^3\gamma \tag{4.184}$$

$$b_3 = 1.5264 \cdot 10^{-1} - 2.9864 \cdot 10^{-2} \ln\gamma - 1.6539 \cdot 10^{-2} \ln^2\gamma + 4.3583 \cdot 10^{-3} \ln^3\gamma \tag{4.185}$$

$$b_4 = -2.0511 \cdot 10^{-2} + 2.6452 \cdot 10^{-3} \ln\gamma + 3.2798 \cdot 10^{-3} \ln^2\gamma - 8.0194 \cdot 10^{-4} \ln^3\gamma \tag{4.186}$$

$$b_5 = 1.0997 \cdot 10^{-3} - 8.8689 \cdot 10^{-5} \ln\gamma - 2.2337 \cdot 10^{-4} \ln^2\gamma + 5.4110 \cdot 10^{-5} \ln^3\gamma \tag{4.187}$$

To illustrate the improvement, Fig. 4.30 shows the old shear flow factor evolution based on Eqs. (4.163) and (4.175), while Fig. 4.31 shows that evolution for the new shear flow factors based on Eqs. (4.163) and (4.182), as well as the data points taken from Fig. 4 in Wilson and Marsault [364]. The improvement is clearly visible, although the shear flow factors only have a very small influence on the results of the full rolling model since v_s is almost equal to v_r along the roll bite.

Finally, the *derivative of the shear flow factor* ϕ_s with respect to h_t, which is required in the METALUB system of equations, can be computed as follows:

$$\frac{\partial \phi_s}{\partial h_t} = \frac{R_{q,s}^2}{R_q^2} \frac{\partial \Phi_s}{\partial h_t} \left(\frac{h_t}{R_q}, \gamma_s \right) - \left(1 - \frac{R_{q,s}^2}{R_q^2} \right) \frac{\partial \Phi_s}{\partial h_t} \left(\frac{h_t}{R_q}, \gamma_r \right) \tag{4.188}$$

with

$$\frac{\partial \Phi_s}{\partial h_t} = \frac{1}{R_q} \left[b_1 + b_2 \left(\frac{h_t}{R_q} \right) + b_3 \left(\frac{h_t}{R_q} \right)^2 + b_4 \left(\frac{h_t}{R_q} \right)^3 + b_5 \left(\frac{h_t}{R_q} \right)^4 \right] \tag{4.189}$$

where the Peklenik surface pattern parameters are again assumed to be equal, i.e. $\gamma = \gamma_r = \gamma_s$ due to roughness transfer and the limited experimental data.

4.8.1.4 Simplified average Reynolds equation

The average Reynolds equations in Eqs. (4.153) and (4.165) for small and large relative contact areas, respectively, can be simplified by some hypotheses in the METALUB model.

Simplified average Reynolds equation for small relative contact areas

Equation (4.153) can be simplified by removing the term along $\mathbf{e}_y$ since the lubricant flow along this direction is assumed to be negligible, i.e. $v_y \approx 0$ in Eq. (4.139b). As mentioned previously, this assumption is consistent with the longitudinal orientation of the roughness in cold rolling (Sec. 2.1.2.2), which partially prevents the lubricant from flowing in the transverse direction $\mathbf{e}_y$ in the mixed lubrication regime. Moreover, in the stationary state, $\partial h_t / \partial t = 0$. If the resulting equation is integrated along $\mathbf{e}_x$, one obtains:

$$\frac{\partial p_l}{\partial x} = \frac{12\eta}{\phi_x h^3} \left(\frac{v_s + v_r}{2} h_t + \frac{v_s - v_r}{2} R_q \phi_s - Q \right) \tag{4.190}$$

The value of the unknown constant Q, which represents the volumetric flow rate of the lubricant per width, is determined by imposing the condition $p_l = 0$ at the outlet of the roll bite.

Simplified average Reynolds equation for large relative contact areas

Equation (4.165) for large relative contact areas can also be simplified by considering the steady state ($\partial h_t / \partial t = 0$) and by integrating the equation along $\mathbf{e}_x$. The difference between Eq. (4.190) and Eq. (4.191) is the variable h or h_t in the factor on the right-hand side. Since $h_t = h$, when no contact exists between the surfaces, the following equation can be used in both cases, i.e. for small and large relative contact areas:

$$\frac{\partial p_l}{\partial x} = \frac{12\eta}{\phi_x h_t^3} \left(\frac{v_s + v_r}{2} h_t + \frac{v_s - v_r}{2} R_q \phi_s - Q \right) \tag{4.191}$$

4.8.2 Lubricant rheology

Since the lubricant is assumed to be incompressible and since inertial effects are neglected in the simplified Reynolds equation (Eq. 4.191), the only property of the lubricant that has an influence on the pressure generation in the model is its *viscosity*. Since this viscosity essentially depends on the pressure and temperature, constitutive laws of increasing complexity and accuracy have been developed over time. These laws are briefly described in this section.

4.8.2.1 Barus equation

The viscosity increases in general with pressure since the lubricant molecules are more packed-up. This pressure dependence was first modeled by the *Barus equation* [21]:

$$\eta(p_l) = \eta_0 e^{\gamma_l p_l} \tag{4.192}$$

where η_0 is the viscosity at the reference pressure and where γ_l is the pressure-viscosity coefficient.

4.8.2.2 Roelands equation

According to *Roelands* [278], the dynamic viscosity η (in MPa.s) depends on the lubricant pressure p_l (in MPa) and its temperature T_l (in °C) as follows:

$$\eta = \eta_0 \exp\left\{\left[\ln\left(10^6\,\eta_0\right) + 9.67\right]\left[\left(1 + \frac{p_l}{p_r}\right)^{z_{p_l}}\left(\frac{T_0 + 135}{T_l + 135}\right)^{S_0} - 1\right]\right\} \tag{4.193}$$

where

- the factor 10^6 was introduced since the previous laws were initially written for a dynamic viscosity in Pa.s. In the METALUB model, the units MPa.s are, however, used since the unit system in this model was chosen to be N, mm, s.
- η_0 is the reference viscosity (in MPa.s),
- $p_r = 196.2$ MPa is a constant,
- z_{p_l} is the pressure index of the viscosity. In METALUB its value is chosen such that the slope of the Roelands equation, i.e. $\partial\eta/\partial p_l$, is equal to the slope of the Barus equation at $p_l = 0$, with $T_l = T_0$, as suggested by Marsault [215, p. 54]:

$$z_{p_l} = \frac{p_r \gamma_l}{\ln\left(10^6\,\eta_0\right) + 9.67} \tag{4.194}$$

- T_0 is the reference temperature corresponding to η_0,
- S_0 is the temperature index of the viscosity.

The previous form of the Roelands equation is derived in appendix L to understand why its form in Eqs. (A2.11), (A2.56), (A2.104), (A2.155), (A2.192) and (A2.219) in Marsault's thesis [215] is incorrect.

4.8.2.3 Extended Williams-Landel-Ferry (WLF) model

One of the most accurate models to describe the dependence of viscosity on pressure and temperature is the *extended WLF model*, which is based on the model by Williams, Landel and Ferry [360] and which was first extended by Yasutomi et al. [375] to add the pressure dependence and then by Bair et al. [20] to refine this dependence:

$$\log_{10}\eta(p_l,T_l)=\log_{10}\eta_g-\frac{C_1\left[T_l-T_g(p_l)\right]F(p_l)}{C_2+\left[T_l-T_g(p_l)\right]F(p_l)}\quad\text{with}\quad\begin{cases}T_g(p_l) & =T_g(0)+A_1\ln\left(1+A_2p_l\right)\\ \eta_g & =10^{12}\text{ Pa.s}\end{cases} \tag{4.195}$$

and with

$$F(p_l)=1-B_1\ln\left(1+B_2p_l\right)\quad\text{(standard version, [375])} \tag{4.196}$$

$$F(p_l)=\left(1+b_1p_l\right)^{b_2}\quad\text{(enhanced version, [20])} \tag{4.197}$$

where T_g is the glass transition temperature and where A_1, A_2, b_1, b_2, B_1, B_2, C_1 and C_2 are material parameters. These values can be found in the technical reports by Bouscharain and Vergne [43, 44] for specific lubricants, in particular those described in Sec. 3.1.3.

4.8.3 Lubricant shear stress

Besides transferring pressure to the strip, the lubricant also applies shear forces due to the velocity difference between the strip and the roll, and the viscosity. The shear stress σ_{zx} acting on the solid interfaces at $z=0$ (strip) and $z=h_l$ (roll) can be computed by the constitutive equation of a *Newtonian fluid* (Eq. H.126):

$$\sigma_{zx}=\eta\left(\frac{\partial v_z}{\partial x}+\frac{\partial v_x}{\partial z}\right) \tag{4.198}$$

By the order of magnitude evaluation in Sec. 4.8.1.1, it was shown that $\partial v_z/\partial x$ is much smaller than $\partial v_x/\partial z$ for thin films. Moreover, $\partial v_x/\partial z$ can be computed based on Eq. (4.139a):

$$\frac{\partial v_x}{\partial z}=\left(\frac{2z-h_l}{2\eta}\right)\frac{\partial p_l}{\partial x}-\frac{v_s-v_r}{h_l} \tag{4.199}$$

Hence,

$$\sigma_{zx}|_{z=0}=-\frac{h_l}{2}\frac{\partial p_l}{\partial x}-\frac{\eta(v_s-v_r)}{h_l} \tag{4.200}$$

$$\sigma_{zx}|_{z=h_l}=\frac{h_l}{2}\frac{\partial p_l}{\partial x}-\frac{\eta(v_s-v_r)}{h_l} \tag{4.201}$$

The shear stress τ_l, which is applied to the strip by the lubricant, can then be computed by Eq. (4.200) and by neglecting the *pressure gradient term, which is assumed to be negligible* due

to the multiplication by the local film thickness h_l while the speed differential term is divided by the film thickness. Furthermore, this film thickness h_l can be replaced by the *mean film thickness in the valleys* h_v to take into account the surface roughness in the lubricant shear stress computation according to Marsault [215]. In contrast to h_v, the mean film thickness h_t represents the mean film thickness over all, i.e. in the regions of solid contact and in the valleys, according to its definition in Eq. (4.10). Fig. 4.32 illustrates the definition of the different values for the triangular asperity height distribution. Hence,

$$(A_a - A_r)h_v + A_r\ 0 = A_a h_t \tag{4.202}$$

where A_a and A_r are the apparent and real contact areas. Dividing the previous equation by A_a yields

$$(1 - A)h_v = h_t \quad \Rightarrow \quad h_v = \frac{h_t}{1 - A} \tag{4.203}$$

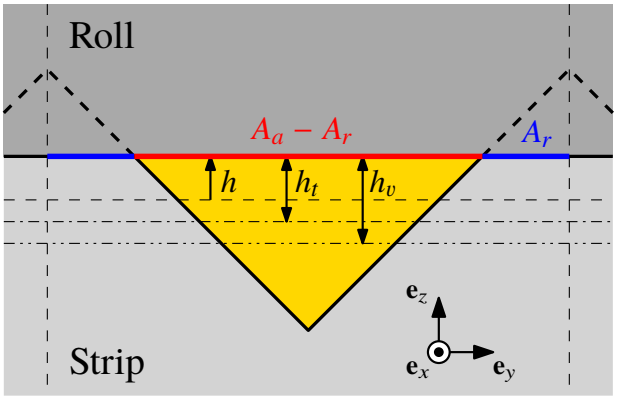

Figure 4.32: Illustration of the signed distance between non-updated mean lines, i.e. the nominal film thickness h, the mean film thickness h_t and the mean film thickness in the valleys h_v for a triangular roughness profile. In addition, A_r represents the real contact area, while A_a is the apparent contact area.

Thus, the *lubricant shear stress* is calculated as follows in the METALUB model:

$$\tau_l = \frac{\eta(v_r - v_s)}{h_v} \quad \text{with} \quad h_v = \frac{h_t}{1 - A} \tag{4.204}$$

An alternative formulation of the lubricant shear stress, which is based on *shear stress factors* as suggested by Patir and Cheng [254], was also added to METALUB. Shear stress factors are an equivalent concept to flow factors in the average Reynolds equation but in the computation of lubricant shear stresses to consider the influence of roughness. Since shear stress factors were only derived in the literature for small fractional contact areas, i.e. $h > 0$, the *lubricant shear stress with stress factors* takes the following form, in which the pressure gradient terms were not neglected for completeness:

$$\tau_l = \begin{cases} \dfrac{\eta(v_r - v_s)}{h}(\phi_f - \phi_{fs}) - \phi_{fp}\dfrac{h}{2}\dfrac{\partial p_l}{\partial x} & \text{, if } h > 0 \\ \dfrac{\eta(v_r - v_s)}{h_v} - \dfrac{h_v}{2}\dfrac{\partial p_l}{\partial x} & \text{, otherwise.} \end{cases} \tag{4.205}$$

where ϕ_f, ϕ_{fs} and ϕ_{fp} are the shear stress factors. The full derivation of the previous equations is explained in appendix M.

4.9 Thermal model

Considering the significant dependence of the lubricant viscosity on its temperature as shown in Fig. 3.5, it seems necessary to include at least a simplified thermal model in METALUB. In the following sections, the *context* of thermal modeling in METALUB, an *adiabatic thermal model of the strip* and *thermal models of the lubricant* are explained.

4.9.1 Context of thermal modeling in METALUB

In the past, Carretta coupled Stephany's version of METALUB [305] with the thermal solver THERMROLL [42] to take the thermal aspect of rolling lubrication into account [54, 58]. In simple words, METALUB was used to compute the *heat generation by plastic deformation and friction*. Based on this heat generation and the heat sinks mainly due to cooling of the rolls, *temperature profiles* along the roll and the strip were predicted by THERMROLL, which is based on the finite volume method. These temperature profiles were then used in a new METALUB computation to adapt the *lubricant viscosity* and ultimately, to quantify the heat generation again. This iterative process continued until the temperature did not change anymore from one iteration to the next.

Unfortunately, the quantitative results of this coupling procedure are *questionable* since the evolution of the exit temperature of the strip as a function of the mean film thickness (starvation) is not monotonous in Fig. 5.6 on page 137 of Carretta's thesis [54]. Besides these questionable results, the *limited documentation* of THERMROLL never allowed us to completely check its correctness. Moreover, the coupling procedure with THERMROLL was never implemented in Carretta's final version of METALUB, which is extended in this thesis. In fact, the coupling procedure was implemented in Stephany's version of METALUB, which was abandoned due to overly complex programming choices.

Because of the previous reasons, it would be required to verify the underlying equations of THERMROLL and its implementation. To keep THERMROLL in the METALUB project for the future with regression tests, the additional investment of re-implementing it directly into METALUB would make sense. Due to the significant time investment of the previous solution, a more time efficient but simplified way of including the thermal effect on the lubricant in METALUB computations was developed, i.e. an *adiabatic thermal model*.

4.9.2 Adiabatic thermal model of the strip

This model is obviously much simpler than THERMROLL due to the limited development time, but more consistent with the reality than the existing thermal model in METALUB, which assumes that the lubricant temperature in the roll bite is constant and provided by the user.

In the new model, the temperature evolution of the strip $T_s(x)$ along the roll bite is computed by specifying the entry temperature of the strip $T_{s,\text{in}}$ and by integrating an equation for $\partial T_s/dx$ along the roll bite. This latter equation can be derived by assuming that the thermal model is partially adiabatic in the sense that *almost all the energy by plastic deformation and half the energy by friction increases the local temperature of the strip homogeneously*. Hence, neither explicit heat conduction inside the strip nor heat exchanges with the rolls or the environment are considered, except for half the friction energy. If fact, the heat due to friction is commonly assumed to be distributed evenly between the roll and the strip [337]. These are obviously strong hypotheses, which seem, however, better than including no temperature increase at all. These hypotheses can be partially mitigated by the following arguments. First, the strip is relatively thin in cold rolling. Hence, the temperature difference between the surface and the core should be relatively small, although it is not negligible as shown by Tseng [336]. Secondly, conduction along the rolling direction is also small with respect to the convective term due to the high Péclet number Pe. For instance, in the rolling scenario of Tseng [336], $\text{Pe} = v_r t_s/\alpha_s \approx 1357$, with the rolling speed $v_r = 688$ m/min, the strip thickness $t_s = 0.15$ cm and the thermal diffusivity[6] $\alpha_s = 1.267 \cdot 10^{-5}$ m^2/s.

On the basis of the initial temperature of the strip, its evolution along the roll bite, i.e. $\partial T_s/\partial x$ can be computed by the *conservation of energy* (Eq. H.35):

$$\rho_s \frac{\mathrm{d}e}{\mathrm{d}t} = \mathbf{D} : \boldsymbol{\sigma} - \nabla \cdot \mathbf{q} + \rho_s s \tag{4.206}$$

where ρ_s is the density of the strip, e the internal energy per unit mass, t the time, $\mathbf{D} = \mathbf{D}^e + \mathbf{D}^p$ the strain rate tensor, $\boldsymbol{\sigma}$ the Cauchy stress tensor, $\mathbf{q}$ the heat flux per unit area and s the heat source per unit mass.

This equation can be simplified by assuming that it applies only to the *adiabatic strip* and by *neglecting the internal energy created by elastic deformations*. Moreover, plastic deformation work is not entirely transformed into heat as first observed by Farren, Taylor and Quinney [101, 327]. The fraction of work that is actually transformed into heat is called the *Taylor-Quinney coefficient* β_s, which is generally assumed to be equal to 0.9 for metals according to Rittel et al. [274]. Thus,

$$\rho_s \frac{\mathrm{d}e}{\mathrm{d}t} = \beta_s \mathbf{D}^p : \boldsymbol{\sigma} + \rho_s s \tag{4.207}$$

Moreover, *friction* is a heat source. Since friction is applied by the top and the bottom rolls, and since only half of this energy (on one side) is assumed to increase the temperature of the strip, half the energy rate per width per length (of the control volume), i.e. $\tau_i(v_r - v_s)/2$, has to be divided by half of the strip thickness t_s. The interface shear stress τ_i instead of the shear stress on the asperity tops τ_a was included in the previous equation to take into account the friction energy by viscous dissipation, too. Moreover, it is important to notice that the difference between v_r and

[6]The thermal diffusivity is defined as the thermal conductivity k_s divided by the density ρ_s and the specific heat capacity c_s (here of the strip), i.e. $\alpha_s = k_s/(\rho_s c_s)$. It measures the heat transfer rate by conduction from a hot to a cold end of a material block.

v_s is computed in the following order to obtain an increase of the internal energy due to friction (positive value):

$$\rho_s \frac{\mathrm{d}e}{\mathrm{d}t} = \beta_s \mathbf{D}^p : \boldsymbol{\sigma} + \frac{\tau_i (v_r - v_s)}{t_s} \tag{4.208}$$

Because only the *steady state* rolling process is modeled, the following equation is satisfied:

$$\frac{\mathrm{d}e}{\mathrm{d}t} = \underbrace{\frac{\partial e}{\partial t}}_{=0} + v_s \frac{\partial e}{\partial x} \tag{4.209}$$

In addition, for small temperature changes,

$$e = c_s (T_s - T_{\mathrm{ref}}) \tag{4.210}$$

where c_s is the supposedly constant *specific heat capacity* of the strip, commonly 500 J/(kg.°C) for steel. By combining the previous equations, by applying the plane-strain hypothesis in cold rolling and by taking into account the previous simplifications of the stress tensor (Sec. 4.5.2), one finally obtains the *simplified evolution equation of the strip temperature along the roll bite*:

$$\frac{\partial T_s}{\partial x} = \frac{1}{\rho_s c_s v_s} \left[\beta_s \left(D_x^p \sigma_x + D_z^p \sigma_z \right) + \frac{\tau_i (v_r - v_s)}{t_s} \right] \tag{4.211}$$

The resulting temperature of the strip can be used in the thermo-viscoplastic hardening law in Sec. 4.5.2.4 to include *thermal softening* in the model. Moreover, the temperature of the strip can be used to predict the lubricant temperature as explained in the following section. The obvious drawback of this model is that it does not include the full *energy exchange with the roll*.

4.9.3 Thermal models of the lubricant

Different *thermal models* were defined in the Metalub model to test which method could best predict the temperature of the *lubricant* $T_l(x)$ in the roll bite, although heat exchanges with the roll are not included.

4.9.3.1 Isothermal lubricant

The classical hypothesis in Metalub is that the lubricant *temperature is constant* and equal to a user-specified value T_l^*:

$$T_l(x) = T_l^* \tag{4.212}$$

This model does, however, not take into account the temperature increase of the lubricant along the roll bite. Therefore, the following model was added to Metalub.

4.9.3.2 Strip temperature

Since the temperature of the roll is not computed in the adiabatic model of the strip and since the thermal capacity of the lubricant is smaller than that of the strip, if its quantity is relatively low, the temperature of the lubricant could be assumed to be equal to the *temperature of the strip*:

$$T_l(x) = T_s(x) \tag{4.213}$$

The previous method could be problematic at the entry of the bite, if the temperature of the roll is significantly higher than that of the strip since the lubricant temperature would be underpredicted during the film formation.

4.9.3.3 Conditional strip temperature

To prevent the previous problem but to include the temperature increase of the lubricant in the model, the following *conditional temperature law* can be defined:

$$T_l(x) = \begin{cases} T_l^* & \text{, if } T_s(x) < T_l^* \\ T_s(x) & \text{, otherwise.} \end{cases} \tag{4.214}$$

This hypothesis is, however, questionable since the adiabatic model of the strip distributes the energy homogeneously along the thickness of the strip. In reality, it can be expected that the lubricant temperature increases much more significantly due to its small quantity and its proximity to highly dissipative solid friction zones. This mechanism is modeled in the following section.

4.9.3.4 Heating by friction

In this model, it is assumed that a *percentage β_l of the friction energy is transformed into thermal energy of the lubricant*. Hence, the thermal equation of the lubricant can be derived in the same way as the thermal equation of the strip in Sec. 4.9.2:

$$\frac{\partial T_l}{\partial x} = \frac{\beta_l}{\rho_l c_l v_s} \frac{\tau_i (v_r - v_s)}{h_t} \tag{4.215}$$

where ρ_l and c_l are the density and the specific heat capacity of the lubricant, respectively. This equation is integrated along the roll bite, like the other equations of the model, by starting with the user-specified temperature T_l^* at the entry of the bite.

4.10 Full model and its solution method

In the previous sections, the different components of a mixed lubrication cold rolling model were described. In this section, these *components are combined* and a *solution method* is suggested to solve the resulting system of equations.

First, the *spatial integration in the roll bite* is explained in general. Secondly, the specific *equations that are integrated and their boundary conditions* are combined to define the full system of equations. Based on this system of equations and its integration, the model returns some solutions, which do, however, not satisfy all boundary conditions yet. For this reason, the *general* METALUB *algorithm* is explained in the third section. Finally, methods to include *starvation*, to *alleviate the high-speed hypothesis* and to *post-process* the results of the integration are explained.

4.10.1 Spatial integration of the roll bite

Because of the analysis of the steady state rolling process, the small thickness of the strip and the symmetry along the transverse direction $\mathbf{e}_y$, the *independent variable* of the underlying system of equations is the *position* x along the roll bite. In this model, the state at each position x will be characterized by the following *dependent variables*:

- v_s: strip speed;
- t_s: strip thickness;
- h, h_t: nominal and mean film thickness
- A: relative contact area;
- p_a, p_l, p_i: asperity contact, lubricant and interface pressures;
- τ_a, τ_l, τ_i: asperity contact, lubricant and interface shear stresses;
- σ_x, σ_y and σ_z: principal Cauchy stresses of the strip (negligible shear stresses, Sec. 4.5.2);
- s_x, s_z: deviatoric stresses along $\mathbf{e}_x$ and $\mathbf{e}_z$ of the strip;
- p: mechanical pressure of the strip;
- $\overline{\epsilon}^p$: effective plastic strain of the strip.

The evolution of the dependent variables can be described by the equations of the previous sections, which were written on purpose in their *Eulerian form* since x is chosen as the independent variable.

Different integration methods of these equations were tested in the past. Stephany [305] combined the most promising methods, i.e. the final algorithm by Marsault [215], which will be explained hereafter, and the one by Qiu et al. [265], in his CIEFS (Couplage Itératif et Étagé Fluide-Solide) solver (Sec. 4.10.5). Although this method allowed him to alleviate the high-speed hypothesis (Sec. 4.10.2.4), which is not possible by Marsault's algorithm, this improvement did only insignificantly change the results, if these could actually be obtained. In fact, Stephany's method was not very robust and the introduction of additional physical phenomena in the cold rolling model, like starvation, were very complex. Hence, his algorithm was not further developed.

To date, the most robust way of solving the equations of the previous sections seems to be their *explicit integration with the division of the roll bite into zones* depending on the contact status between the roll and the strip, and the deformation mode of the strip as suggested by Marsault [215] (Fig. 4.33):

- Zone 1: *Hydrodynamic inlet zone*: hydrodynamic lub., elastic strip;
- Zone 2: *Mixed inlet zone*: mixed lub., elastic strip;
- Zone 3: *Low-speed (mixed) work zone*: mixed lub., elastoplastic strip;
- Zone 3': *High-speed (mixed) work zone*: mixed lub., elastoplastic strip, high-speed hyp.;
- Zone 4: *Low-speed (mixed) outlet zone*: mixed lub., elastic strip;
- Zone 4': *High-speed (mixed) outlet zone*: mixed lub., elastic strip, high-speed hyp.

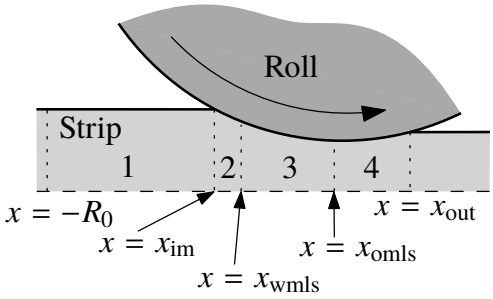

Figure 4.33: General division of the roll bite in 4 zones.

At the entry of the roll bite, there is first no solid-to-solid contact between the roll and the strip, which is deformed elastically due to the back tension and the hydrodynamic interaction with the lubricant. This first zone is therefore called the hydrodynamic inlet zone. When the roll and the strip enter into contact at $x = x_{\text{im}}$ (inlet mixed), the mixed inlet zone, in which deformations of the strip are still elastic, begins. In the work zone, these deformations then become elastoplastic at $x = x_{\text{wmls}}$ (work mixed low-speed). And finally, in the outlet zone, which starts at $x = x_{\text{omls}}$ (outlet mixed low-speed), the deformations of the strip are again exclusively elastic. The outlet zone finally ends at $x = x_{\text{out}}$.

In the work and outlet zones, an additional distinction between subzones is introduced when the lubricant flow rate in Eq. (4.191) cannot be adjusted such that the lubricant pressure becomes equal to zero at the end of the roll bite. This issue will be explained more thoroughly in Sec. 4.10.2.4. Hence, an additional high-speed work zone (zone 3') and a high-speed outlet zone (zone 4') are introduced. These high-speed zones either start in the low-speed work zone (zone 3) at $x = x_{\text{wmhs}}$ (work mixed high-speed) or in the low-speed outlet zone (zone 4) at $x = x_{\text{omhs}}$ (outlet mixed high-speed). The resulting arrangement of zones is illustrated in Fig. 4.34.

As explained before, the evolution of the state variables in each of the six zones is mainly described by the equations in the previous sections (Secs. 4.3-4.9). For each zone, a *system of first-order*

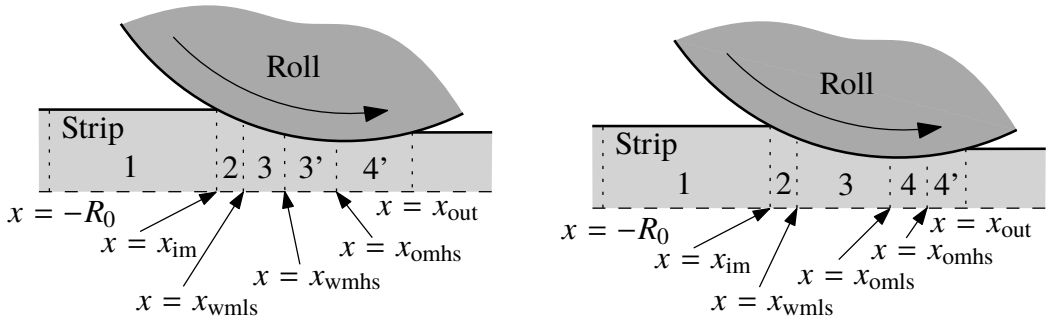

(a) Transition in the work zone. **(b)** Transition in the outlet zone.

Figure 4.34: Zones with high-speed transition.

differential equations, which will be specified in Sec. 4.10.2, can therefore can be written in vector form:

$$\frac{\partial \mathbf{y}}{\partial x} = \mathbf{f}(x, \mathbf{y}) \tag{4.216}$$

where $\mathbf{y} = [y_1, y_2, \ldots]$ is the vector of variables that are integrated and where $\mathbf{f}$ is the vector of the corresponding right-hand side expressions of the differential equations. The integration of these equations starts at $x = -R_0$ for reasons of simplicity (see e.g. Fig. 4.33). In any case, the contribution of the lubricant pressure by the Reynolds equation is very small far from the roll bite, i.e. far from x_{im}. The integration then proceeds from zone to zone until reaching the end of the roll bite. Various numerical *integration methods and spatial discretization strategies* exist to solve the previous ordinary differential equations [114, 262]. Several methods have been implemented in MATALUB for different reasons, which will be explained hereafter, although many more were tested in the past by Marsault [215].

4.10.1.1 Forward Euler method

The *forward Euler method* [114] was introduced in MATALUB to simplify the *debugging* of some rolling test cases, since it is a one-step method, i.e. it requires only a single evaluation of $\mathbf{f}(x, \mathbf{y})$ at position x to predict the value of $\mathbf{y}$ at the next position $x + \Delta x$, where Δx is the spatial step. If the functions $\mathbf{y}(x)$ are sufficiently smooth, their first-order Taylor expansion can be written at $x + \Delta x$. Hence,

$$\mathbf{y}_{n+1} = \mathbf{y}_n + \Delta x \, \mathbf{f}(x_n, \mathbf{y}_n) \tag{4.217}$$

where $\mathbf{y}_n = \mathbf{y}(x_n)$.

Using the same spatial step Δx from the beginning of the integration at $x = -R_0$ until its end at $x = x_{\text{out}}$ would, however, unnecessarily increase the computation time since significant variations of the key variables only occur in the roll bite. Therefore, two different step sizes Δx_1 and Δx_2 ($< \Delta x_1$) are commonly used in MATALUB such that

$$\Delta x = \begin{cases} \Delta x_1 & \text{, if } x < x_{12} \\ \Delta x_2 & \text{, otherwise.} \end{cases} \tag{4.218}$$

Practical guidelines, about which values Δx_1, Δx_2 and x_{12} should take are provided in Sec. 5.2.

4.10.1.2 Runge-Kutta 4 method

While the forward Euler method is a first-order method, i.e. the global truncation error[7] is $\mathcal{O}(\Delta x)$ and the local truncation error $\mathcal{O}(\Delta x^2)$, the *Runge-Kutta 4 method* is a fourth-order method [114], i.e. $\mathcal{O}(\Delta x^4)$ and $\mathcal{O}(\Delta x^5)$, respectively. For a given step size, the Runge-Kutta 4 method thus leads to a much more accurate result than the forward Euler method, although four evaluations of $\mathbf{f}(x, \mathbf{y})$ instead of one are required [114, p. 35]:

$$\mathbf{y}_{n+1} = \mathbf{y}_n + \frac{\mathbf{k}_1}{6} + \frac{\mathbf{k}_2}{3} + \frac{\mathbf{k}_3}{3} + \frac{\mathbf{k}_4}{6} \tag{4.219}$$

with

$$\mathbf{k}_1 = \Delta x\, \mathbf{f}(x_n, \mathbf{y}_n) \tag{4.220}$$

$$\mathbf{k}_2 = \Delta x\, \mathbf{f}\left(x_n + \frac{\Delta x}{2}, \mathbf{y}_n + \frac{\mathbf{k}_1}{2}\right) \tag{4.221}$$

$$\mathbf{k}_3 = \Delta x\, \mathbf{f}\left(x_n + \frac{\Delta x}{2}, \mathbf{y}_n + \frac{\mathbf{k}_2}{2}\right) \tag{4.222}$$

$$\mathbf{k}_4 = \Delta x\, \mathbf{f}(x_n + \Delta x, \mathbf{y}_n + \mathbf{k}_3) \tag{4.223}$$

The Runge-Kutta 4 method is usually used in METALUB computations with the same *step adaptation method* as the Euler method, i.e. Eq. (4.218). Other step adaptation methods were, however, implemented to satisfy certain conditions more accurately. While these methods were mostly used in the past, they are rarely used now due to their important number of numerical parameters that have to be adjusted (Sec. 5.2).

4.10.1.3 Runge-Kutta 4 method with partially adaptive step size

The *Runge-Kutta 4 method with partially adaptive step size* is very similar to the previous method. It distinguishes itself from this method by the step adaptation near the transition from one zone to the next. For instance, as will be explained in Sec. 4.10.2, the transition from the mixed inlet zone to the low-speed work zone occurs when the Von Mises stress σ_{VM} reaches the yield stress σ_Y. In the Runge-Kutta 4 method with constant step size (before and after x_{12} in the previous section), the transition to the next zone thus simply occurs when

$$\sigma_{\text{VM}} > \sigma_Y \tag{4.224}$$

[7] The *global truncation error* is the difference at the last iteration between the computed value by the method and the exact solution of the differential equation, starting with the same initial conditions. The *local truncation error* is the difference at the current iteration between the computed value by the method and the exact solution of the differential equation, which passes through the computed value of the previous iteration. Hence, the local truncation error quantifies the error of one iteration, while the global error quantifies the cummulative error over the entire integration domain.

In the Runge-Kutta 4 method with partially adaptive step size, this step is, however, divided by 2 until the following condition is satisfied:

$$\sigma_{\mathrm{VM}} > \sigma_Y \quad \text{and} \quad \frac{\sigma_{\mathrm{VM}} - \sigma_Y}{\sigma_Y} < \mathrm{tol}_{\mathrm{crit}} \tag{4.225}$$

where $\mathrm{tol}_{\mathrm{crit}}$ is the tolerance of the transition criterion. In this way, the transition criterion can be enforced in a more controlled manner.

Instead of using Eq. (4.218) to again increase the step size after the transition, or at the beginning of the integration, the selection of either Δx_1 or Δx_2 is no more based on the user-specified value of x_{12} but rather on the transition to the mixed inlet zone. More precisely, the spatial step is equal to Δx_1 in the hydrodynamic inlet zone and it is equal to Δx_2 in the remaining zones, apart from near the transitions from one zone to the next.

This method has two drawbacks: on the one hand, the transition criteria between zones, like the one in Eq. (4.225), requires the introduction of an *additional numerical parameter*, i.e. $\mathrm{tol}_{\mathrm{crit}}$, which unnecessarily complicates the numerical calibration. On the other hand, reducing the integration step from Δx_1 to Δx_2 at the transition from the hydrodynamic inlet zone to the mixed inlet zone is too late in scenarios, in which the lubricant pressure becomes significant before transitioning to the mixed inlet zone. Hence, its evolution might not be accurately captured by the greater integration step Δx_1 of the hydrodynamic inlet zone than Δx_2 in the remaining zones. This step adaptation method has, however, the benefit of *automatically reducing the integration step in the roll bite*, while x_{12} has to be chosen manually if the approach in Eq. (4.218) is selected.

4.10.1.4 Runge-Kutta 4 method with fully adaptive step size

Finally, in addition to an increased control of the transition criterion and the automatic step reduction at the transition to the mixed inlet zone, the *Runge-Kutta 4 method with fully adaptive step size* also changes this size depending on a prediction of the *integration error* by step doubling [114, p. 81]. This approach was introduced by Marsault [215], certainly, in order to achieve a given accuracy in the solution with a minimum computational effort. The underlying principle of this method is to evaluate $\mathbf{y}_{n+1}$ in two different ways. First, $\mathbf{y}_{n+1}$ is evaluated by starting from $\mathbf{y}_n$ and reaching $\mathbf{y}_{n+1}$ in one step Δx. This estimation of $\mathbf{y}_{n+1}$ is denoted by $\mathbf{y}^{(1)}$. Then, $\mathbf{y}_{n+1}$ is evaluated in two steps, which have both a size $\Delta x/2$; this value is denoted by $\mathbf{y}^{(2)}$. If the following condition is satisfied, i.e. if the integration error is too important, the integration is restarted from $\mathbf{y}_n$ but with the half step $\Delta x/2$:

$$\mathrm{tol}_{\mathrm{int}} < \Delta_{\mathrm{int}} = \max_i \begin{cases} \left| \dfrac{y_i^{(1)} - y_i^{(2)}}{y_i^{(1)} + y_i^{(2)}} \right| & \text{, if } |y_i^{(1)}| > \mathrm{tol}_{\mathrm{abs}} \text{ and } |y_i^{(2)}| > \mathrm{tol}_{\mathrm{abs}} \\ \left| y_i^{(1)} - y_i^{(2)} \right| & \text{, otherwise.} \end{cases} \tag{4.226}$$

where $\mathrm{tol}_{\mathrm{int}}$ and $\mathrm{tol}_{\mathrm{abs}}$ are the integration error tolerances. The separation of the previous criterion into relative and absolute error cases is necessary, for instance, if $y_i^{(1)} = 10^{-10}$ and $y_i^{(2)} = 10^{-12}$. In this case, both values are very small but the relative error is close to 1.

The initial step Δx is the user-specified value Δx_1. Depending on the integration error Δ_{int}, the user-specified minimum integration step $\Delta x_{\min}$ and the maximum integration step $\Delta x_{\max}$, which is either the user-specified Δx_1 in the hydrodynamic inlet zone or the user-specified Δx_2 in the remaining zones, the subsequent integration steps are computed in the following way:

$$\Delta x = \begin{cases} \Delta x_{\max} & \text{, if } \Delta x > \Delta x_{\max} \\ 2\Delta x & \text{, if } \Delta x < \Delta x_{\min} \\ \Delta x & \text{, otherwise.} \end{cases} \quad \text{where} \quad \Delta x = \begin{cases} \dfrac{\text{tol}_{\text{int}} \Delta x}{2\Delta_{\text{int}}} & \text{, if } \Delta_{\text{int}} > \Delta x_{\min} \\ 2\Delta x & \text{, otherwise.} \end{cases} \tag{4.227}$$

In simple words, these conditions ensure that the integration step is increased, when the integration error is small compared to the integration tolerance, and that the integration step is greater than $\Delta x_{\min}$ and smaller than $\Delta x_{\max}$.

Due to its *important number of numerical parameters*, i.e. Δx_1, Δx_2, tol_{int}, tol_{abs}, tol_{crit}, which are almost impossible to calibrate simultaneously, the fully adaptive Runge-Kutta 4 integrator was replaced by the partially adaptive Runge-Kutta 4 integrator. Since a relatively small integration step is required in the roll bite as shown in Sec. 5.2, the criterion tolerance tol_{crit} in the partially adaptive Runge-Kutta 4 was not required anymore, too. Finally, the transition from Δx_1 to Δx_2 at the transition from the hydrodynamic inlet zone to the mixed inlet zone might be too late to capture an increase of the lubricant pressure in the hydrodynamic inlet zone, as mentioned earlier. For these reasons, the *current best choice* because of its accuracy and efficient numerical parameter calibration is the simple *Runge-Kutta 4 method in which the spatial steps are chosen according to Eq.* (4.218).

4.10.2 Equations and boundary conditions

As explained in the previous section, the roll bite is divided into zones, which each have their own system of equations depending on the contact status between the roll and the strip, and the deformation mode of the strip. These equations were mainly derived in the previous sections (Secs. 4.3-4.9). On the basis of these equations, a *system of equations*, which can be integrated by the previous methods, was written for each zone. This is easier said than done because of the strong coupling between the numerous equations. This complexity, which will be explained in more detail hereafter, is illustrated in appendix N.

In the past, *Marsault* [215] derived what seemed to be the most complete system of equations at his time. *Stephany* [305] later improved this system by correcting an equation of Marsault's system, by reformulating this system to simplify his computer code, and by introducing also the elastic deformation in the work zone, which was previously neglected.

In this thesis, strong emphasis was put on *deriving the system of equation as clearly and meticulously as possible* while introducing mainly two significant changes with respect to the systems by Marsault [215] and its corrections by Stephany [305]. In the past, it was difficult to know which equations were actually implemented in METALUB since these equations were either only

summarized, i.e. not the full system of equations was provided, or derived partially, i.e. it was unclear how some equations were obtained. This was changed in this thesis to accelerate future developments by specifying all *underlying equations* in appendix N, with references to their definitions or derivations in Secs. 4.3-4.9 or appendix H. Moreover, a significant difficulty in solving these equations is to structure them so that they can be integrated without having to solve an algebraic system of equations for each position x. In other words, it has to be possible to directly evaluate the derivatives in Eq. (4.216) at position x based on the values $\mathbf{y}$ at this position, although numerous equations of derivatives are written as functions of other derivatives. Instead of having to solve a linear system of equations at each position, the equations were structured in such a way that they can be evaluated directly. In other words, they were solved by hand. Since solving them is not easy because of the numerous variables and equations, the *full derivation* based on the underlying equations and the *final form* are provided in appendix N.

Two *changes of the system of equation* are introduced in this thesis. First, the following equation of Marsault [215], Stephany [305] and also Carretta [54], although not directly mentioned in this last thesis, i.e.

$$h = z_r - \frac{t_s}{2} \tag{4.228}$$

was replaced by the more consistent equation (Eq. 4.23)

$$h_t = z_r - \frac{t_s}{2} \tag{4.229}$$

In fact, in the first version, the nominal film thickness can by definition become negative, which means that the roll and strip can overlap. In other words, the strip can become thicker than the rolls geometrically allow it to become. This is not possible with h_t, which cannot become negative by definition. In the past, this correction was probably not introduced because it only has a small influence on the results, and because it requires to invert the relation $h_t = h_t(h)$, which can be cumbersome for the Christensen height distribution (Sec. 4.4.4.2).

Secondly, besides coherence, the previous correction was also introduced to use the *same system of equations in a classical* Metalub *computation and a coupled one with the finite element (FE) solver* Metafor, obviously except for the equation that is replaced by the FE computation. More details are provided in Chap. 6, in which the analytical asperity flattening equation by Wilson and Sheu, Sutcliffe and Marsault or Korzekwa et al. are replaced by FE asperity flattening simulations. In consequence, the constraint of changing only the equations that are directly impacted by the asperity flattening equation, and the strong interdependence of all equations required to entirely *re-derive the system of equations from the underlying equations*, although similarities with the final system by Marsault and Stephany obviously remain. In addition to these major changes, it was also paid attention to being consistent between the derived equations from one zone to the next, since multiple formulations are usually possible.

Before explaining the significant details of each integration zone, like the end-of-zone criteria, it is, however, necessary to mention that some variables in the system have to take a certain value

before the integration process starts. On the one hand, the following *boundary conditions* are imposed at $x = -R_0$:

$$p_l = 0 \tag{4.230}$$
$$t_s = t_{\text{in}} \tag{4.231}$$
$$\sigma_x = \sigma_{\text{in}} \tag{4.232}$$
$$v_s = v_{\text{in}} \tag{4.233}$$

On the other hand, it is necessary to specify the *lubricant flow rate* Q, the *vertical position of the roll axis* z_0 and the *profile of the roll* z_r in order to close the system of equations. While t_{in} and σ_{in} are user-specified variables, v_{in}, Q, z_0 and z_r are adjusted to satisfy different conditions, e.g. the lubricant flow rate is adjusted so that the lubricant pressure $p_l = 0$ at the end of the roll bite. These conditions and the way in which they are applied are explained in Sec. 4.10.3.

In the following subsections, the *details of the different zones* are briefly explained, i.e. the system of equations and the end-of-zone criteria.

4.10.2.1 Hydrodynamic inlet zone (zone 1)

The *hydrodynamic inlet zone* starts at $x = -R_0$. Although the lubricant film thickness is not small in this region and probably not laminar due to recirculations near the roll-strip convergent, the Reynolds equation, which was derived for a small film thickness with laminar flow, is integrated in this zone by assumption. This hypothesis seems, however, reasonable since the pressure build-up only becomes important when the mean film thickness becomes small (Eq. 4.191). Hence, the contribution far from the roll bite is relatively insignificant.

The *underlying equations* of the hydrodynamic inlet zone are summarized in Sec. N.1.1.1. Although the asperity contact pressure p_a is by definition zero in the hydrodynamic inlet zone, its value is rather set equal to $p_l + 5.142\tau_Y$ in order to have a continuous transition to p_a in the mixed inlet zone, which is commonly computed by Wilson and Sheu's flattening equation (Eq. 4.91) in the classical METALUB model. In any case, the value of p_a in this zone has no influence on the results since the relative contact area A is zero. The *derivation of the structured system of equations*, which is actually implemented in METALUB, and this *system* can be found in Secs. N.1.1.2 and N.1.1.3.

The hydrodynamic inlet zone ends at $x = x_{\text{im}}$ where the *asperities of the roll and the strip enter into contact*. On the basis of the composite root-mean-square roughness and the choice of the surface height distribution, this occurs in the following cases[8]:

- Triangular asperity height distribution:

$$h_t < \sqrt{3}R_q \quad \text{and} \quad \frac{\sqrt{3}R_q - h_t}{R_q} < \text{tol}_{\text{crit}} \tag{4.234}$$

[8] In the following end-of-zone criteria strict inequalities are used since those are implemented. Non-strict inequalities are, however, also valid.

- Christensen height distribution:

$$h_t < 3R_q \quad \text{and} \quad \frac{3R_q - h_t}{R_q} < \text{tol}_{\text{crit}} \tag{4.235}$$

where the second condition is only required, if an integration method with adaptive step size is used, as explained in Sec. 4.10.1.3.

4.10.2.2 Mixed inlet zone (zone 2)

In the *mixed inlet zone*, the core of the strip deforms elastically and the asperities of the roll and the strip are in contact. The underlying equations are summarized in Sec. N.1.2.1. Mainly, the *asperity flattening equation* and a *boundary friction model* had to be added to the equations of the hydrodynamic inlet zone to compute the asperity contact pressure p_a and the shear stress τ_a. The derivation of the structured system of equations in METALUB and this system can be found in Secs. N.1.2.2 and N.1.2.3.

The mixed inlet zone ends at $x = x_{\text{wmls}}$ when the *strip starts to deform plastically*, i.e.

$$\sigma_{\text{VM}} > \sigma_Y \quad \text{and} \quad \frac{\sigma_{\text{VM}} - \sigma_Y}{\sigma_Y} < \text{tol}_{\text{crit}} \tag{4.236}$$

4.10.2.3 Low-speed work zone (zone 3)

In the *low-speed work zone*, the core of the strip deforms plastically. Hence, the *plastic material description* had to be added to the underlying system of equations (Sec. N.1.3.1). The derivation of the structured system of equations in METALUB and this system can be found in Secs. N.1.3.2 and N.1.3.3.

The low-speed work zone either ends at $x = x_{\text{omls}}$, when the *deformations become elastic again* (unloading), or at $x = x_{\text{wmhs}}$, when the *lubricant pressure is about to become greater than the interface pressure at the end of the lubricant flow rate adjustment* (Sec. 4.10.3.1). The position x_{omls}, at which the first condition is satisfied, is always assumed to be the x-coordinate at which the top roll profile has its minimum z-coordinate, i.e. where the top and bottom rolls are the closest to each other [215]. In this case, the integration algorithm transitions to the low-speed outlet zone. The second condition depends at least partially on the choice of the lubricant flow rate Q, which will be explained in Sec. 4.10.3.1. In short, if it is impossible to find a lubricant flow rate such that the lubricant pressure becomes zero at the end of the bite, the maximum flow rate, for which the lubricant pressure can become greater than the interface pressure before the end of the bite, is chosen. In this case, the integration algorithm transitions to the high-speed work zone, if the following condition is satisfied:

$$p_l > p_i \quad \text{and} \quad \frac{p_l - p_i}{\sigma_Y} < \text{tol}_{\text{crit}} \tag{4.237}$$

where the second condition is only required in an integration method with adaptive step size.

4.10.2.4 High-speed work zone (zone 3')

According to the previous section, the *high-speed work zone* was introduced to proceed with the integration of the roll bite when the lubricant pressure is about to become greater than the interface pressure. This is necessary since a greater lubricant pressure p_l than interface pressure p_i implies by the load sharing law (Eq. 4.4) that the lubricant pressure p_l becomes greater than the pressure on top of the asperities p_a. According to Montmitonnet [231], this is a physical impossibility. Furthermore, the current asperity flattening models in METALUB were derived for a positive non-dimensional hardness $H_a = (p_a - p_l)/\tau_Y$ (Eq. 4.90). Hence, they are unable to treat the case $p_l > p_a$. It is, however, questionable whether eliminating this case from the model is a good idea in the long term. In fact, lubricant permeation in the solid/solid contact region (micro-plasto-hydrodynamic/static lubrication, Sec. 2.2.4.3) seems only possible when the lubricant pressure becomes at least locally slightly greater than the pressure on top of the contacting asperities.

The transition to the high-speed work zone typically occurs when the rolling speed is relatively important, which explains why this zone is called the *high-speed* work zone, or near to the percolation threshold. Under these circumstances, the simplified and rearranged Reynolds equation (based on Eq. 4.191), i.e.

$$\frac{\phi_x h_t^3}{12\eta}\frac{\partial p_l}{\partial x} = \frac{v_s + v_r}{2}h_t + \frac{v_s - v_r}{2}R_q\phi_s - Q \tag{4.238}$$

can be re-written as a *volume conservation equation*, i.e.

$$Q = \frac{v_s + v_r}{2}h_t + \frac{v_s - v_r}{2}R_q\phi_s \tag{4.239}$$

since the *Poiseuille term becomes negligible with respect to the Couette term* [215]. In fact, when the mean film thickness is close to the percolation threshold, the lubricant becomes trapped in the surface pockets and it is carried along in them. For instance, the equation of the pressure flow factor for the Christensen asperity height distribution (Eq. 4.170) clearly illustrates that the Poiseuille term becomes negligible when h_t approaches the percolation threshold $h_{t,c}$ since $\phi_x \to 0$.

In both cases, i.e. when the lubricant pressure becomes close to the interface pressure due to the important rolling speed or the percolation threshold, the Reynolds equation is replaced by the previous volume conservation equation in the underlying system of equations of the low-speed work zone to describe the high-speed work zone in Sec. N.1.4.1. An additional hypothesis was, however, introduced by Marsault [215] in order to ensure the integrability of the equations.

If the full Reynolds equation (Eq. 4.191) is replaced by the volume conservation equation (Eq. 4.239), the lubricant pressure has to be determined by another equation. This seems possible by inverting the order, in which the equations are evaluated. Instead of computing the lubricant pressure by the Reynolds equation and the mean film thickness by the asperity flattening equation, the lubricant pressure is computed by the asperity flattening equation and the mean

film thickness by the Reynolds equation without the Poiseuille term. Practically, this procedure is, however, not possible without solving implicitly a system of equations. More precisely, the system of equations in Sec. N.1.5.1 has to be structured in a way such that it allows explicit integration, as in the other zones, i.e. it should be possible to evaluate the derivatives of variables at a position x by the values of these variables at this position and not by values at the previous step. This is, however, not possible due to the computation of $\tau_a = \tau_a(v_s, v_r, p_a, \tau_Y)$, which cannot be inverted to compute $p_a = p_a(v_s, v_r, \tau_a, \tau_Y)$ because of possible Tresca friction. The full explanation can be found in Sec. N.1.5.2. Marsault [215] mentioned that the computation with this modified system of equations did not converge for an important number of rolling scenarios. It remains, however, unclear how the equations were structured in [215] to solve them explicitly because they are not provided in the thesis.

Since solving the previous system explicitly is not possible, an additional hypothesis was introduced by Marsault [215], which consists in imposing

$$p_l = p_i \tag{4.240}$$

in the high-speed zones. The underlying equations, the derivation of the structured system and this system can be found in Sec. N.1.4. Several reasons are mentioned by Marsault [215] to justify this approach: (1) Sheu and Wilson [285] made the same hypothesis in their model, (2) Azushima and Kudo [15] showed experimentally the rising of the lubricant on the asperity tops at the percolation limit, which implies that the lubricant pressure becomes equal to the interface pressure, and (3) Liu et al. [195] demonstrated by finite element computations that the lubricant pressure approaches the asperity contact pressure at the percolation limit. As mentioned at the beginning of this section, a slightly greater lubricant pressure than the pressure on the asperity tops seems, however, to be required locally in order to allow the permeation of the lubricant in the solid/solid contact zone during micro-plasto-hydrodynamic/static lubrication, which is currently not included in the model.

The previous hypothesis has the drawback that the *lubricant pressure will be equal to the interface pressure until the end of the roll bite*. A decrease of the lubricant pressure prior to the decrease of the interface pressure as shown in the theses by Marsault[9] [215, Fig. 5.7] and Stephany [305, Fig. 3.9] is therefore not possible, when the lubricant pressure becomes equal to the interface pressure in the roll bite. In both references, the method, which allowed to compute the prior decrease of the lubricant pressure, were, however, abandoned due to their numerical instability. An additional method to solve this problem is explained in Sec. 4.10.5. Unfortunately, to date, none of these methods solved this problem satisfactorily. Nevertheless, its influence on the key results, i.e. the rolling force and the forward slip, seems to be negligible [215, 305].

In a similar way to the low-speed work zone, the high-speed work zone transitions to the high-speed outlet zone at $x = x_{\mathrm{omhs}}$, when the *strip deformations become elastic again*, i.e. at the position, where the top roll profile has its minimum z-coordinate.

[9] It is unclear how Marsault generated Fig. 5.7 in his thesis since it seems not possible to write the system of equations, which has to be solved to obtain this figure, in an explicitly integrable way as explained in Sec. N.1.5.2.

4.10.2.5 Low-speed outlet zone (zone 4)

The strip deforms again elastically in the *low-speed outlet zone*. Therefore, the underlying equations in Sec. N.1.6.1 are almost identical to those in the mixed inlet zone (Sec. N.1.2.1). Instead of using again the asperity flattening equation by Wilson and Sheu in this elastic zone, which is a hypothesis since the equation was derived for a perfectly plastic material, the *asperity profile is assumed to remain unchanged*. This assumption seems reasonable since elastic deformations of metals are in general very small. Based on the equations in Sec. N.1.6.1, the structured system of equations in Sec. N.1.6.3 was derived in Sec. N.1.6.2.

The outlet zone finally ends at $x = x_{\text{out}}$, *when the interface pressure becomes zero*, i.e.

$$p_i < 0 \tag{4.241}$$

if an integrator without step adaptation is used or

$$\frac{p_i}{\sigma_Y} < \text{tol}_{\text{crit}} \quad \text{and} \quad p_i > 0 \tag{4.242}$$

if an integrator with step adaption is used.

Moreover, a *high-speed transition* at $x = x_{\text{omhs}}$ was added since the lubricant pressure became greater than the interface pressure in the low-speed outlet zone of some rolling scenarios. This transition simply consist in using the equations of the high-speed outlet zone, when the condition in Eq. (4.237) is satisfied.

4.10.2.6 High-speed outlet zone (zone 4')

The equations in the *high-speed outlet zone* (Sec. N.1.7) are identical to those in the low-speed outlet zone (Sec. N.1.6) except for the Reynolds equation, which is replaced by $p_l = p_i$, as explained before (Sec. 4.10.2.4).

The end-of-zone criterion of the high-speed outlet zone is the same as in the low-speed outlet zone, i.e. the interface pressure vanishes (Eq. 4.241 or Eq. 4.242).

4.10.3 General METALUB algorithm

The METALUB algorithm is historically based on a *shooting method* [308] in Marsault [215], which allows to solve this boundary value problem by transforming it into an initial value problem. On the one hand, some initial conditions at $x = -R_0$ are directly enforced, i.e. that

$$p_l = 0 \tag{4.243}$$

$$t_s = t_{\text{in}} \tag{4.244}$$

$$\sigma_s = \sigma_{\text{in}} \tag{4.245}$$

since the reference pressure is zero, and since the initial thickness of the strip t_{in} and the back tension σ_{in} are input parameters of the model. On the other hand, *some variables are adjusted in order to satisfy further conditions*:

1. the *lubricant flow rate* Q has to be adjusted so that the lubricant pressure is zero at the end of the roll bite (Sec. 4.191):

$$p_l = 0 \quad \text{at} \quad x = x_{\text{out}} \tag{4.246}$$

2. the *initial speed of the strip* v_{in} is adjusted so that the tension in the strip at the end of the roll bite is equal to the imposed front tension:

$$\sigma_x = \sigma_{\text{out}} \quad \text{at} \quad x = x_{\text{out}} \tag{4.247}$$

3. the *vertical position of the roll axis* z_0 is adjusted so that the thickness of the strip at the end of the roll bite is equal to the imposed final thickness of the strip:

$$t_s = t_{\text{out}} \quad \text{at} \quad x = x_{\text{out}} \tag{4.248}$$

4. the *profile of the roll* $z_r(x)$ is adjusted so that it corresponds to the resulting deformation by the interface pressure profile $p_i(x)$ and the interface shear stress profile $\tau_i(x)$.

Practically, these conditions are imposed by *4 nested loops*, whose order is the same as in previous versions of the model [54, 215, 305], as shown in Fig. 4.35. This flowchart only shows the *general* Metalub *algorithm*. The details of the adjustment loops will be explained in the following subsection. The algorithm starts with an initial guess of $z_r(x)$, z_0, v_{in} and Q. Then, the lubricant flow rate Q is adjusted until the lubricant pressure becomes equal to zero at the end of the roll bite, provided that the bite is not dry. When this condition is satisfied, the entry speed v_{in} of the strip is adjusted to satisfy $\sigma_x = \sigma_{\text{out}}$ at $x = x_{\text{out}}$. A third loop, which contains the two previous ones, then computes the vertical position of the roll to attain the specified exit thickness of the strip. Finally, the outermost loop gradually adapts the profile of the roll, if a non-rigid roll model was selected. This order of the adjustments was initially chosen by Marsault [215] and it was continued to be used by Stephany [305] and Carretta [54].

The precise way of adjusting the lubricant flow rate Q, the entry speed v_{in}, the vertical position of the roll axis z_0 and the profile of the roll z_r is explained in the following subsections.

4.10.3.1 Adjustment of the lubricant flow rate

The volumetric lubricant flow rate (per unit width) Q has to be adjusted such that the lubricant pressure is zero at the end of the roll bite, i.e. $p_l = 0$ at $x = x_{\text{out}}$ (Sec. 4.8.1.4). As suggested by the simplified Reynolds equation (Eq. 4.191) and the formulations in Secs. N.1.2.3, N.1.3.3 and N.1.6.3, the lubricant pressure becomes either negative, if Q is relatively important, or it becomes greater than the interface pressure before the end of the roll bite, if Q is too small. This behavior is illustrated in Fig. 4.36.

The classical method to adjust the flow rate in Metalub is the *bisection method* [53]. This method is based on an initial interval $[Q^{(0)}_{\text{min}}, Q^{(0)}_{\text{max}}]$ such that $p_l > p_i$ for $Q^{(0)}_{\text{min}}$ and $p_l < 0$ for

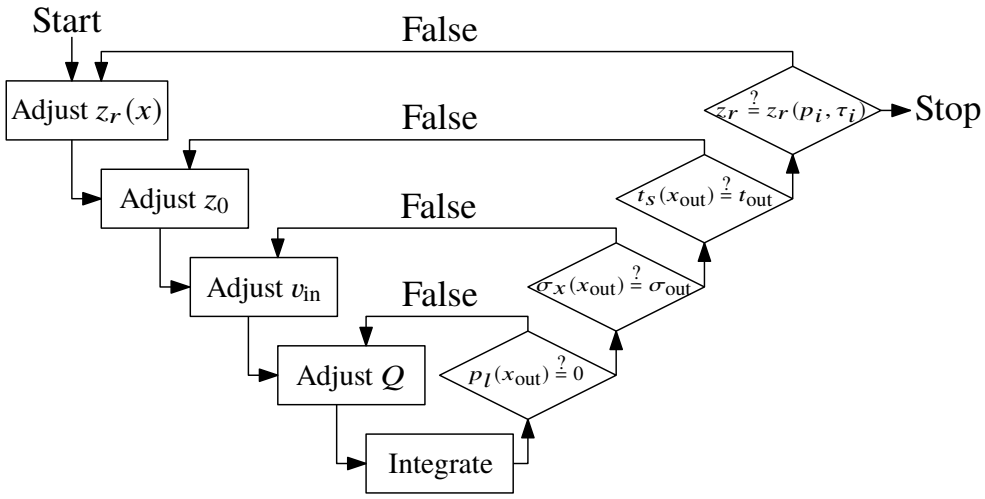

Figure 4.35: Flowchart of the general resolution method in METALUB, which is based on 4 nested loops. These loops adjust the roll profile $z_r(x)$, the vertical position of the roll axis z_0, the entry speed of the strip v_{in} and the volumetric flow rate of the lubricant per width Q.

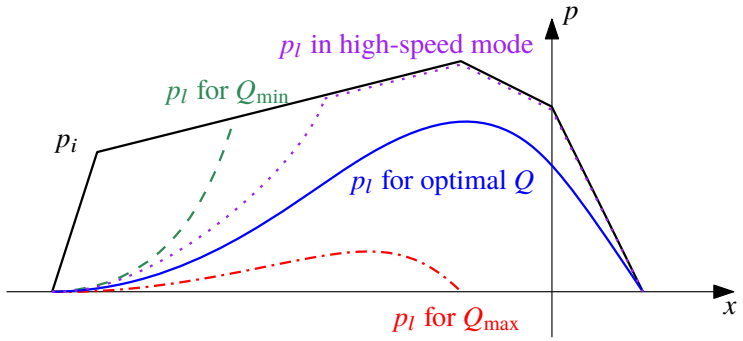

Figure 4.36: Schematic representation of lubricant pressure evolution $p_l(x)$ along the roll bite depending on the choice of the lubricant flow rate Q. The interface pressure evolution $p_i(x)$ is also represented.

$Q^{(0)}_{max}$ at some point of the roll bite. This interval is then iteratively divided based on the following condition depending on the new flow rate:

$$Q^{(i)} = \frac{Q^{(i)}_{min} + Q^{(i)}_{max}}{2} \tag{4.249}$$

Hence,

$$[Q^{(i+1)}_{min}, Q^{(i+1)}_{max}] = \begin{cases} [Q^{(i)}_{min}, Q^{(i)}] & \text{, if } p_l < 0 \\ [Q^{(i)}, Q^{(i)}_{max}] & \text{, if } p_l > p_i \end{cases} \tag{4.250}$$

The *initial interval* of the lubricant flow rate was chosen to be the following one:

$$[Q^{(0)}_{min}, Q^{(0)}_{max}] = [0, v_r R_p] \tag{4.251}$$

where R_p is the maximum peak height with respect to the mean line, i.e. $\sqrt{3}R_q$ for the triangular asperity height distribution and $3R_q$ for the Christensen height distribution. The maximum flow rate can be deduced from the Reynolds equation (Eq. 4.8.1.4). In fact,

$$Q = \frac{v_s + v_r}{2} h_t + \frac{v_s - v_r}{2} R_q \phi_s - \frac{\phi_x h_t^3}{12\eta} \frac{\partial p_l}{\partial x} \tag{4.252}$$

At the first contact between the roll and the strip, $\partial p_l / \partial x > 0$, $v_s < v_r$, and $h_t = R_p$. In any case, $\phi_x \geq 0$ and $\phi_s \geq 0$. Therefore, the maximum flow rate is smaller than $v_r R_p$. In the past, Stephany set the minimum flow rate equal to $v_r R_p / 1000$ after some numerical tests [305, p. 170]. It appeared, however, that some rolling cases with important starvation could only converge, if the minimum flow rate is lower than Stephany's limit. Otherwise, the lubricant pressure becomes smaller than 0 before the end of the roll bite for the minimum and maximum flow rates. Hence, the more reasonable limit $Q_{\min}^{(0)} = 0$ was chosen.

The *computation speed* of the Metalub model [54, 215, 305] was greatly improved by a simple idea. More precisely, instead of computing the initial flow rate $Q^{(0)}$ by Eq. (4.249) at the beginning of each adjustment loop of the lubricant flow rate, it is rather set equal to the final flow rate of the previous adjustment loop of this rate, which is usually closer to the solution than the prediction by Eq. (4.249). In the very first adjustment loop of the lubricant flow rate in a Metalub run, a previous estimation of Q is not available and thus, Eq. (4.249) is used in this case. Hence, the total computation time of almost 200 software regression tests was reduced by a factor 2. This speed-up is, however, also due to similar improvements in the adjustment loop of the strip speed (Sec. 4.10.3.2).

Previously, it was explained how to update the flow rate but not *when to stop its adjustment*. In earlier versions of Metalub, it was stopped when the lubricant pressure p_l became close to 0 at the end of the roll bite (boundary condition to derive Eq. 4.190 and thus, Eq. 4.191), i.e. at the position where the interface pressure p_i converges to 0. This condition is easily satisfied in a mixed lubrication regime, which tends towards the boundary regime. However, when the rolling speed increases, the lubricant pressure becomes more and more sensitive to its flow rate up to the point where the previous condition cannot be satisfied anymore since the difference between the interval limits of the bisection method $Q_{\min}^{(i)}$ and $Q_{\max}^{(i)}$ becomes close to the machine epsilon. Even the introduction of a quadruple precision instead of the usual double precision in Marsault's Lam2DTribo software as well as different integration strategies could not solve this problem [215]. In addition, Marsault cites Letalleur [190] (private communication) who observed a similar sensitivity in a simpler scenario than cold rolling. Hence, he concludes that this sensitivity with respect to Q is an intrinsic property of the Reynolds equation in the low-speed zones since the lubricant pressure is computed by the Poiseuille term, which becomes negligible when the rolling speed increases or close to the percolation threshold (Sec. 4.10.2.4). For this reason, the adjustment loop of the lubricant flow rate in Lam2DTribo is stopped either when p_l becomes close to 0 at the end of the roll bite, as explained previously, or when the following condition is satisfied:

$$\frac{Q_{\max}^{(i)} - Q_{\min}^{(i)}}{Q_{\max}^{(i)} + Q_{\min}^{(i)}} < \text{tol}_Q \tag{4.253}$$

with $\text{tol}_Q = 10^{-14}$. In this latter case, Marsault integrates the roll bite one final time with $Q_{\min}^{(i)}$ and he switches to the high-speed equations, when the lubricant pressure becomes equal to the interface pressure. In fact, the choice of $Q_{\min}^{(i)}$ instead of $Q_{\max}^{(i)}$ allows the lubricant pressure to become equal to the interface pressure, so that their equality in the high-speed zones renders it possible that the lubricant pressure becomes close to 0 at the end of the roll bite.

In the current version of METALUB, this method was slightly modified for two reasons: first, the lubricant pressure can either become slightly negative or slightly greater than the interface pressure at the end of the roll bite in previous implementations, which is non-physical. Secondly, two different tolerance, one for the lubricant pressure at the end of the roll bite and tol_Q are required. Our objective, is, however, to reduce the number of tolerances in METALUB to simplify their systematic adjustment (Sec. 5.2). Therefore, the possibility to transition to the high-speed equations, when the lubricant pressure becomes equal to the interface pressure in the low-speed outlet zone, was added (Sec. 4.10.1). Furthermore, the condition regarding the lubricant pressure becoming sufficiently small at the end of the roll bite was removed. More specifically, the lubricant flow rate is adjusted until Eq. (4.253), in which tol_Q is calibrated as explained in Sec. 5.2, is satisfied. All preceding integrations of the roll bite are stopped, either if the lubricant becomes negative or greater than the interface pressure before the end of the roll bite, since this information is sufficient to update the flow rate. The final integration is then executed with $Q_{\min}^{(i)}$, as explained previously. Overall, these modifications have a very small impact on the results, but the algorithm is simplified.

To integrate the full Reynolds equation along the roll bite instead of neglecting the Poiseuille term in the high-speed zones, Stephany [305] developed his CIEFS solver. Nevertheless, he later abandoned this solver because it was not robust enough and very difficult to extend to cold rolling with lubricant starvation. In any case, CIEFS only insignificantly improved the results in the cases, in which it converged. *A similar method to solve the Reynolds equation without removing the Poiseuille term* was introduced by Carretta and the author of this thesis (Sec. 4.10.5). The previous method with high-speed zones remains, however, the most robust and most accurate resolution method so far.

Previously, the bisection method was introduced to adjust the lubricant flow rate. This method is very robust because a solution will ultimately be obtained, if the respective hypotheses are satisfied, which is the case. Its convergence rate, is however, relatively slow. This is due to the fact that it does not use the value but only the sign of the successive evaluations, i.e. of the lubricant pressure at the end of the roll bite. To improve the convergence rate, it would be necessary to extend the underlying equations at least numerically such that a specific lubricant pressure $p_l(x_{\text{out}}, Q_i)$ at the end of the roll bite is computed in any rolling scenario. In fact, if such a value was known and if the initial prediction was not too far from the solution, the flow rate could be adjusted by *Newton-Raphson iterations* based on a numerical finite difference estimation

of the derivative [53], as follows:

$$Q^{(i+1)} = Q^{(i)} - \frac{p_l(x_{\text{out}}, Q^{(i)})}{p_l'(x_{\text{out}}, Q^{(i)})} \quad \text{with} \quad p_l'(x_{\text{out}}, Q^{(i)}) = \frac{p_l(x_{\text{out}}, Q^{(i)} + \Delta Q) - p_l(x_{\text{out}}, Q^{(i)})}{\Delta Q} \tag{4.254}$$

Due to the complexity of the underlying system of equations in METALUB and despite numerous trials, it was, however, not possible to extend these equations in order to compute a lubricant pressure at the end of the roll bite, which is at least numerically consistent. This strategy would require the introduction of numerous additional tolerances, although an important number of them is already required (Sec. 5.2).

4.10.3.2 Adjustment of the strip speed at the entry of the bite

The *bisection method* is also the classical method in METALUB to *adjust the entry speed of the strip* in order to reach the specified front tension. The initial interval of the entry speed is for obvious reasons the following one, since the strip can initially not move faster than the roll at its periphery:

$$\left[v_{\text{in,min}}^{(0)}, v_{\text{in,max}}^{(0)}\right] = [0, v_r] \tag{4.255}$$

Different adjustment methods were tested over the years. First, the *initial guess* can be computed by the midpoint value:

$$v_{\text{in}}^{(i)} = \frac{v_{\text{in,min}}^{(i)} + v_{\text{in,max}}^{(i)}}{2} \tag{4.256}$$

In his thesis, Stephany introduces, however, a *more realistic initial guess* than the midpoint [305, p. 169]:

$$v_{\text{in}}^{(0)} = \min\left(1, 1.1\frac{t_{\text{out}}}{t_{\text{in}}}\right) v_r \tag{4.257}$$

This value was chosen since it corresponds to a forward slip $s_f = (v_{\text{out}} - v_r)/v_r$ of 10%, which is a realistic value in cold rolling. In fact, the definition of the forward slip can be combined with the conservation of mass equation, i.e. $v_{\text{in}} t_{\text{in}} = v_{\text{out}} t_{\text{out}}$, in which elastic deformations were neglected:

$$v_{\text{out}} = (1 + s_f)\frac{t_{\text{out}}}{t_{\text{in}}} v_r \tag{4.258}$$

Equation (4.257) is then obtained by setting s_f equal to 10% and by limiting the entry speed to its physical limit, i.e. the peripheral speed of the roll.

In this thesis, an *even better initial guess* of the entry speed in the subsequent iterations of the vertical roll position loop was implemented in METALUB. This guess is simply the final entry speed of the previous vertical roll position iteration. As mentioned earlier (Sec. 4.10.3.1), this idea, which was also applied to improve the initial guess of the lubricant flow rate, significantly reduced

the computation time of METALUB. In conclusion, Eq. (4.257) is currently used in METALUB for the very first adjustment of the entry strip speed, while the final value of the previous roll position adjustment is used as the initial guess in the subsequent adjustment.

Besides these initial guesses $v_{\text{in}}^{(0)}$ of v_{in} (for each vertical position update of the roll), it is also necessary to adapt its *values during the iterations of the bisection method*, i.e. $v_{\text{in}}^{(i)}$. The classical *midpoint method* in Eq. (4.256) is generally used. A *more efficient method* was, however, introduced in METALUB by Carretta on the basis of Stephany's work for the second guess of v_{in}, i.e. $v_{\text{in}}^{(2)}$. Neither of them seems to have published this method. In fact, by reducing the interval of the bisection method as efficiently as possible, the total number of integrations can be significantly reduced. This can be achieved by the following second guess:

$$v_{\text{in}}^{(2)} = \begin{cases} v & \text{, if } v \in \left[v_{\text{in,min}}^{(1)}, v_{\text{in,max}}^{(1)}\right] \\ \frac{v_{\text{in,min}}^{(1)} + v_{\text{in,max}}^{(1)}}{2} & \text{, otherwise.} \end{cases} \tag{4.259}$$

with

$$v = \left[1 - 0.1 \operatorname{sign}\left(\frac{\sigma_x(x_{\text{out}}) - \sigma_{\text{out}}}{\sigma_Y^0}\right) \max\left(1, \left|\frac{\sigma_x(x_{\text{out}}) - \sigma_{\text{out}}}{\sigma_Y^0}\right|\right)\right] v_{\text{in}}^{(1)} \tag{4.260}$$

In simple words, the previous formula slightly reduces (increases) the entry speed of the strip if the computed front tension $\sigma_x(x_{\text{out}})$ is greater (resp. smaller) than the user-specified front tension σ_{out}. In the following integration, the computed front tension will thus be reduced (resp. increased) since it generally decreases with a decreasing entry speed of the strip.

In contrast to the lubricant flow rate adjustment, the value of the condition that is enforced, i.e. $\sigma_x(x_{\text{out}}) - \sigma_{\text{out}}$, is precisely known at each adjustment of the entry speed of the strip. Hence, a computation speed-up by a *Newton-Raphson prediction* [53] of the next entry speed is possible. This method was implemented in METALUB with a forward finite difference prediction of the derivative:

$$v_{\text{in}}^{(i+1)} = v_{\text{in}}^{(i)} - \frac{\sigma_x(x_{\text{out}}, v_{\text{in}}^{(i)}) - \sigma_{\text{out}}}{\sigma_x'(x_{\text{out}}, v_{\text{in}}^{(i)})} \quad \text{with} \quad \sigma_x'(x_{\text{out}}, v_{\text{in}}^{(i)}) = \frac{p_l(\sigma_x(x_{\text{out}}, v_{\text{in}}^{(i)} + \Delta v_{\text{in}}) - \sigma_x(x_{\text{out}}, v_{\text{in}}^{(i)})}{\Delta v_{\text{in}}} \tag{4.261}$$

Although this method is fully functional in METALUB and although Stephany [305] introduced even another method, i.e. the false position method (regula falsi), the *bisection method is generally preferred* because of its robustness, its good convergence rate due to the considered guesses of $v_{\text{in}}^{(0)}$ and $v_{\text{in}}^{(1)}$, which usually only require 3 iterations, and due to the non-introduction of additional parameters, unlike the step Δv_{in} in the finite difference of the Newton-Raphson method. Especially, this last condition is important since the systematic calibration of the METALUB model is relatively complex (Sec. 5.2).

Finally, the adjustment of v_{in} *converges*, if the following condition is satisfied. A strategy to

determine the tolerance $\text{tol}_{\sigma_{\text{out}}}$ is explained in Sec. 5.2:

$$\frac{|\sigma_x(x_{\text{out}}) - \sigma_{\text{out}}|}{\sigma_Y^0} < \text{tol}_{\sigma_{\text{out}}} \tag{4.262}$$

4.10.3.3 Adjustment of the vertical roll position

Once the lubricant flow rate and the entry speed of the strip have been calculated, the *vertical position of the roll is adjusted* in order to obtain a final strip thickness, which corresponds to the specified thickness t_{out}. Initially, the vertical position of the roll axis z_0 is *predicted* by the following equation (Fig. 4.8):

$$z_0 = \frac{t_{\text{out}}}{2} + R_0^* \tag{4.263}$$

where R_0^* is either the radius of the underformed roll R_0 or the vertical distance between the lowest point the top roll and its axis, if the roll profile has been discretized (Secs. 4.6.3 or 4.6.4). Although the previous equation is a good approximation of z_0, this value will usually change in the following iterations due to the elastic spring back of the strip and roll flattening.

Hence, after the successive convergences of the entry speed adjustment, the vertical position of the roll axis is *updated* as follows by approaching the optimal value by half of the required variation (under-relaxation) in order to introduce no numerical instability [305, p. 179]:

$$z_0(x) = z_0(x) - \frac{t_s(x_{\text{out}}) - t_{\text{out}}}{4} \tag{4.264}$$

The adjustment of the vertical roll position finally *converges* when the following condition is met:

$$\frac{|t_s(x_{\text{out}}) - t_{\text{out}}|}{t_{\text{out}}} < \text{tol}_{t_{\text{out}}} \tag{4.265}$$

where $\text{tol}_{t_{\text{out}}}$ is an additional tolerance. As mentioned earlier, a systematic way of determining the numerous tolerances in METALUB is explained in Sec. 5.2.

4.10.3.4 Adjustment of the roll profile

After the convergence of the previous three nested adjustment loops of Q, v_{in} and z_0 with an initially circular roll, interface pressure and shear stress profiles $p_i(x)$ and $\tau_i(x)$ are known along the roll bite. These profiles can then be used to compute the *resulting profile of the roll* $z_r(x)$ due to elastic deformations, which are caused by $p_i(x)$ and $\tau_i(x)$, via Hitchcock's, Bland and Ford's, Jortner's and Meindl's methods (Secs. 4.6.1-4.6.4).

Using the resulting profile $z_r(x)$ of these methods directly in a new integration of the roll bite generally leads to *convergence issues*, especially for hard and thin strips. On the one hand, for circular roll flattening models, the rolling load increases the roll radius, which in turn might increase again the rolling load since the length of the bite increases and so on [238, 286]. On the other hand, for non-circular roll flattening models, the roll profile might become locally concave

near the neutral point due to the significant interface pressure increase around this point. In the subsequent iteration with this new roll profile and its "numerical punching" [236] or "trough" [286], artificial thickening of the strip and its possible elastic unloading render convergence difficult or impossible. This phenomenon was observed by Krimpelstatter [171, p. 298] with Meindl's method and by Stephany [305] with Jortner's method. It usually implies that more than one plastic zone exist in an intermediate configuration of the roll profile adjustment loop. METALUB is, however, based on the hypothesis that a single continuous plastic zone is located in the roll bite. Since this inconsistency is most likely at the origin of the convergence issues, different solution strategies were introduced in the past.

First, Fleck and Johnson [104] prevented explicitly an increase of the strip thickness in the bite by allowing the roll profile at most to become horizontal. According to Montmitonnet et al. [236], Matsumoto [217] introduced a less stringent condition with a very small elastic thickening of the strip, while a plastic thickness is decreasing or at most held constant.

Furthermore, *relaxations* were introduced to gradually update the profile of the roll by Montmitonnet et al. [238], and later Marsault [215], Stephany [305] and Carretta [54]. Thus, the recalculated radius $R_*^{(i)} = R(p_i^{(i)})$ in Hitchcock's and Ford and Bland's models or the roll profile $[x_{r,*}^{(i)}, z_{r,*}^{(i)}] = [x_r, z_r](p_i^{(i)}, \tau_i^{(i)})$ in Jortner's or Meindl's models for each discretization point of the roll is combined with the previous radius $R^{(i-1)}$ or profile $[x_r^{(i-1)}, z_r^{(i-1)}]$, i.e.

$$R^{(i)} = w^{(i)} R_*^{(i)} + \left(1 - w^{(i)}\right) R^{(i-1)} \quad \text{or} \quad \begin{cases} x_r^{(i)} & = w^{(i)} x_{r,*}^{(i)} + \left(1 - w^{(i)}\right) x_r^{(i-1)} \\ z_r^{(i)} & = w^{(i)} z_{r,*}^{(i)} + \left(1 - w^{(i)}\right) z_r^{(i-1)} \end{cases} \tag{4.266}$$

where $w^{(i)}$ is the relaxation coefficient at iteration i of the roll adjustment loop. A typical value of $w^{(i)}$ is 0.5. In practice, it usually has to be reduced to about 0.1 or smaller values for rolling scenarios with relatively important rolling loads.

In the past, various ways were introduced to improve the convergence rate by *adapting the relaxation coefficient*. These methods will be briefly described here. In general, they require, however, the calibration of additional numerical parameters, which is why they were not used in this thesis to reduce the complexity of the numerical parameter calibration (Sec. 5.2).

For instance, Stephany [305, p. 178] mentioned that the weighting coefficient should, initially, be relatively close to 1 to converge quickly to the solution and then it should become smaller and smaller to introduce no oscillations around the final solution. This approach was implemented by the following equation:

$$w^{(i)} = \max\left(w_{\min}, w^{(0)} C^i\right) \tag{4.267}$$

where C is a constant such that $0 \leq C \leq 1$. The values $w_{\min} = 0.1$, $w^{(0)} = 0.5$ and $C = 0.95$ seem to be good choices according to a convergence study by Stephany [305].

Carretta [54] introduced the length of the roll bite in the updating method of the relaxation coefficient. This method was developed by Matsumoto and Shiraishi [217, 218] and applied by

Dbouk et al. [90]. It is based on the following idea: as long as the length of the roll bite increases from one roll profile adjustment to the next, the relaxation coefficient is kept constant. If the length decreases, however, this is a sign that the final deformation has almost been reached. In consequence, the coefficient should be reduced to limit oscillations around the solution. This reasoning can be explained as follows. If one imagines that the roll becomes less and less stiff from one roll profile adjustment to the next, starting with a rigid roll, the length of the roll bite increases from one iteration to the next. When the roll finally reaches its imposed level of stiffness, the length of the roll bite should become constant. The process of reducing the stiffness of the roll is almost equivalent to performing the previous relaxations in Eq. (4.266) starting from a circular roll profile. By including only a part of the deformed radius, this is as if only a part of the elastic deformation was considered, i.e. as if the roll becomes less and less stiff in each iteration. This idea was implemented as follows:

- $l_{\mathrm{rb}}^{(i)} \geq l_{\mathrm{rb}}^{(i-1)}$ for less than 20 successive iterations:

$$w^{(i)} = w^{(i-1)} \tag{4.268}$$

- $l_{\mathrm{rb}}^{(i)} \geq l_{\mathrm{rb}}^{(i-1)}$ for 20 successive iterations to increase the convergence speed:

$$w^{(i)} = \min\left(1.5w^{(i-1)}, 1\right) \tag{4.269}$$

- $l_{\mathrm{rb}}^{(i)} < l_{\mathrm{rb}}^{(i-1)}$ to decrease oscillations around the solution:

$$w^{(i)} = \max\left(w_{\min}, \frac{w^{(i-1)}}{2}\right) \tag{4.270}$$

In this procedure, the minimum relaxation coefficient $w_{\min}$ and the initial relaxation coefficient $w^{(0)}$ respectively take the values 0.01 and 0.5 in Matsumoto [217] or 0.05 and 0.5 in Dbouk et al. [90].

Finally, a *convergence criterion* has to be defined in order to end the adjustment of the roll profile and thus, to end the execution of a Metalub computation. This criterion should quantify the fact, that the final roll profile corresponds to the applied interface pressure and shear stress. While a maximum number of roll adjustment iterations was used by Marsault [215], the following roll flattening criterion was introduced by Stephany [305]:

$$\frac{\max_x |z_{r_*}^{(i)} - z_r^{(i-1)}|}{\min_x z_r^{(i)}} < \mathrm{tol}_{z_r} \tag{4.271}$$

Carretta replaced Stephany's criterion by two criteria of more macroscopic final variables, i.e. the rolling force F_r and the length of the roll bite l_{rb}, which had to be satisfied simultaneously:

$$\frac{|F_r^{(i)} - F_r^{(i-1)}|}{F_r^{(i)}} < \mathrm{tol}_{F_r} \qquad \text{and} \qquad \frac{|l_{\mathrm{rb}}^{(i)} - l_{\mathrm{rb}}^{(i-1)}|}{l_{\mathrm{rb}}^{(i)}} < \mathrm{tol}_{l_{\mathrm{rb}}} \tag{4.272}$$

These criteria by Carretta were, however, replaced because they require two tolerance values instead of a single one, which unnecessarily complicates the calibration of the procedure. Moreover, synthetic variables like the rolling force can be unchanged from one iteration to the next although the roll profile changes significantly.

The criterion that is currently implemented in METALUB is similar to the one by Stephany. Instead of dividing the profile difference by the minimum profile height as in Eq. (4.271), it is rather divided by the radius of the undeformed roll to have an easier interpretation and a constant reference value. Moreover, Stephany's criterion only accounts for the profile variation along the vertical direction, it would, however, be more reasonable to account for the variations along the radial and tangential directions in the context of non-circular roll flattening. Hence, the new criteria for the methods by Hitchcock and Bland and Ford, and the methods by Jortner and Meindl, respectively, are the following:

$$\frac{|R_*^{(i)} - R^{(i-1)}|}{R_0} < \mathrm{tol}_R \quad \text{or} \quad \frac{\max \sqrt{\left(x_{r,*}^{(i)} - x_r^{(i-1)}\right)^2 + \left(z_{r,*}^{(i)} - z_r^{(i-1)}\right)^2}}{R_0} < \mathrm{tol}_R \tag{4.273}$$

where tol_R is the tolerance of the roll profile adjustment loop, which will be determined in Sec. 5.2. The maximum value in the previous equation is computed with respect to all discretization points of the roll profile in Jortner's and Meindl's methods. It is also important to notice that new values, like $R_*^{(i)}$, are compared with previous values, like $R^{(i-1)}$, to guarantee a certain independence of the relaxation method. This is important to eliminate the occurrence of artificial convergence, i.e. if the relaxation coefficient becomes smaller and smaller from one roll flattening adjustment to the next, for instance, by Matsumoto's method, the difference between $R^{(i)}$ and $R^{(i-1)}$ also becomes smaller and smaller. Hence, the method could converge because the relaxation coefficient becomes very small instead of the good correspondence between the roll profile and the stresses, which it is subjected to.

4.10.4 Lubricant starvation

Previously, it was assumed that as much lubricant as possible enters into the roll bite. In reality, the amount of lubricant can, however, be less significant. This is called *lubricant starvation*, as explained in Sec. 2.1.3. Depending on the amount of lubricant, the contact between the roll and the strip can therefore be mainly dry at the inlet of the roll bite and then become more and more lubricated. In fact, due to asperity crushing, the lubricant in the surface valleys comes increasingly into contact with the other interface along the roll bite as shown in Fig. 4.37.

Lubricant starvation was introduced in METALUB by Stephany [305]. It is simulated by specifying the lubricant film thickness at the entry of the bite $h_{t,\mathrm{in}}$. As long as the average distance between the surface asperities h_t is smaller than $h_{t,\mathrm{in}}$, rolling is assumed to be *dry*, i.e. without lubricant (Fig. 4.37). Once the inlet film thickness becomes, however, larger than the mean distance between surface asperities, i.e. $h_t < h_{t,\mathrm{in}}$, the *equations of a fully lubricated roll bite are integrated*.

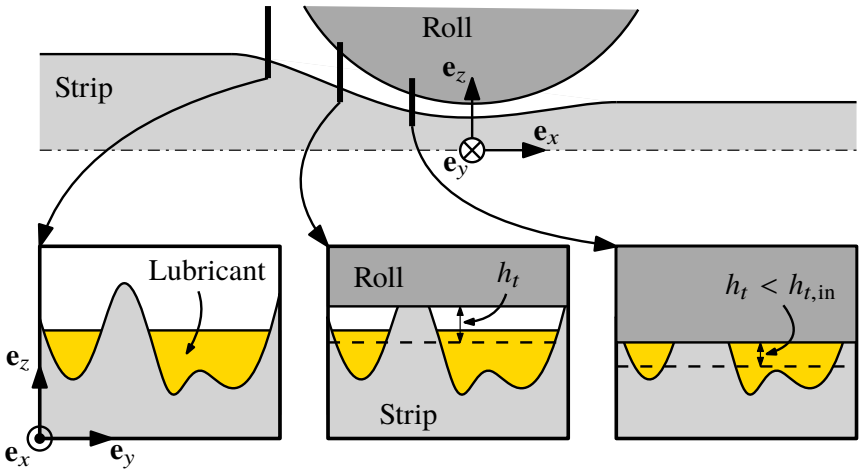

Figure 4.37: Schematic illustration of starvation with a smooth roll and a longitudinally rough strip to simplify the representation. The lubricant comes in contact with the lubricant, when the mean film thickness h_t becomes smaller than the lubricant film thickness at the entry of the bite $h_{t,\text{in}}$.

In practice, the previous condition can be evaluated, when the end-of-zone criteria are checked at each integration step Δx of the bite. If it is proven true, i.e. if $h_t < h_{t,\text{in}}$, the *system of equations of the dry roll bite is replaced by the system, which was explained previously for the lubricated roll bite* (Secs. 4.10.2 and N.1). The system, which corresponds to the roll bite without lubricant, is similar to the one with lubricant except for the lubricant pressure p_l and shear stress τ_l being equal to zero. Since the derivation of this system is relatively straightforward and based on that of the lubricated roll bite, it is presented in the same section, i.e. Sec. N.1. Moreover, although no lubricant is in the dry roll bite, the same zone structure and naming convention as that of the lubricated roll bite is maintained in order to simplify the presentation and the implementation. High-speed zones do, however, obviously not exist without the lubricant. The resulting equations are different from and more complete than those provided by Stephany [305, p. 184-185].

In the previous paragraphs, it is mentioned that only the system of equations has to change in order to model starvation. This implies that the *different adjustment loops of the lubricant flow rate, the entry speed of the strip, . . . do not have to be modified*. This is mainly true aside from *one exception*. In fact, it might happen that the specified inlet film thickness $h_{t,\text{in}}$ is so small, that the distance between updated mean lines h_t will never become smaller than $h_{t,\text{in}}$. In this case, the lubricant pressure will neither become negative nor greater than the interface pressure, simply because it is zero. If this is true for the limiting flow rates $Q^{(0)}_{\text{min}}$ and $Q^{(0)}_{\text{max}}$ of the initial interval in the adjustment loop of the lubricant flow rate, this loop can be ended since the result is independent of Q, which is equal to $h_{t,\text{in}} v_{\text{in}}$.

Finally, it is important to notice that the equations of a *dry roll bite* with rough rolls and strip, which were introduced to model starvation, can also be used *independently of starvation* in MATLAB. In this scenario, the equations are directly integrated in the adjustment loop of the strip entry speed, without the adjustment loop of the lubricant flow rate.

4.10.5 Method to alleviate the high-speed hypothesis

The *high-speed hypothesis*, i.e. $p_l = p_i$ and neglecting the Poiseuille term in the Reynolds equation, was introduced to render the full integration of the roll bite possible (Secs. 4.10.2.4 and 4.10.3.1). In the past, it was tried to solve the underlying equations of the roll bite without this hypothesis in order to understand its effects on the results. This is the reason why Stephany developed the CIEFS solver [305, p. 135-155], which was later, however, abandoned due to its limited numerical robustness and insignificant improvement of the solution. Although Stephany's findings showed only small improvements, Carretta tried to include this algorithm partially in METALUB for the coupling procedure with the FE solver METAFOR (Sec. 6.1.3). Although the *CIEFS-like procedure* in METALUB is generally not used because it has some major drawbacks, it will be documented hereafter with the hope that it might help in future research.

This method is introduced as a post-processing method in METALUB. In fact, the evolution of the key variables, like the mean film thickness $h_t(x)$, the speed of the strip $v_s(x)$, ..., and the adjusted parameters, i.e. the lubricant flow rate Q, the entry speed of the strip v_{in}, the vertical position of the roll axis z_0 and the roll profile $z_r(x)$, are first determined by a classical METALUB computation, as shown in Fig. 4.38. These results are then used to *solve the Reynolds equation by the finite difference method* to obtain a new lubricant pressure evolution p_l^*. Since this pressure evolution has an influence on all the other variables of the system, these variables are gradually updated by *fixed-point iterations with relaxations* [53, p. 56].

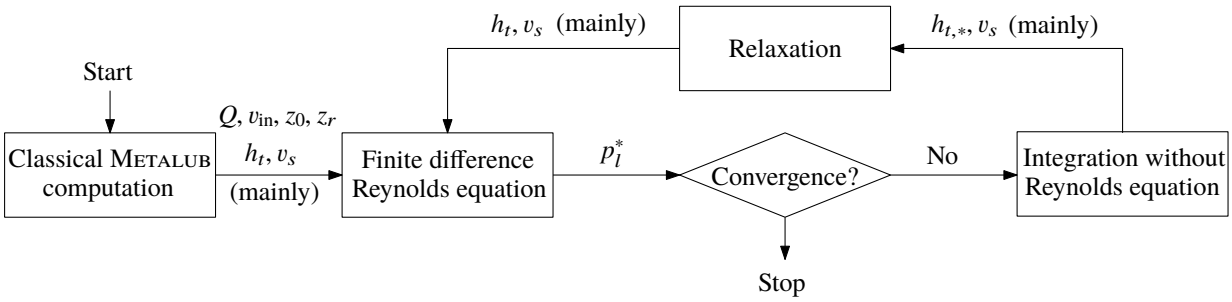

Figure 4.38: Flowchart of the METALUB computation with fixed-point iterations in order to solve the rolling problem with a finite difference resolution of the Reynolds equation.

In more detail, if the evolution of the mean film thickness is stationary, which is true in the case of METALUB since the stationary rolling process is modeled, the *Reynolds equation* in Eq. (4.165) can be written as follows:

$$\underbrace{\frac{\partial}{\partial x}\left(\phi_x \frac{h_t^3}{12\eta}\frac{\partial p_l}{\partial x}\right)}_{(*)} = \underbrace{\frac{\partial}{\partial x}\left(\frac{v_s+v_r}{2}h_t\right)}_{(**)} + \underbrace{\frac{\partial}{\partial x}\left(\frac{v_s-v_r}{2}R_q\phi_s\right)}_{(***)} \tag{4.274}$$

The *finite difference method* then allows to determine a new lubricant pressure evolution $p_l^*(x)$ based on the previous equation and:

- the old lubricant pressure $p_l(x)$ to compute the dynamic viscosity $\eta(x)$,

- the old mean film thickness $h_t(x)$, in particular to evaluate $\phi_x(h_t)$ and $\phi_s(h_t)$,
- the old strip speed $v_s(x)$ and
- some boundary conditions, which will be defined hereafter.

The *peripheral speed of the roll* v_r is assumed to be constant at each position of the roll bite in METALUB due to the small thickness of the strip and the small radial elastic deformations of the roll.

The Reynolds equation is, however, *not necessarily solved by finite differences along the whole roll bite* in METALUB. In fact, if the mean film thickness h_t becomes smaller than the *percolation threshold* $h_{t,c}$ (Sec. 4.8.1.3), the first term in the previous equation (Eq. 4.274) vanishes and it cannot be solved by finite differences. Based on the results of the classical METALUB computation, the discretization points of the position along the roll bite x_i with $i = 0, 1, \ldots, n_2 - 1$ can be partitioned such that x_i with $i = 0, 1, \ldots, n_1 - 1$ are those before $h_t(x_i) < h_{t,c}$ and x_i with $i = n_1, n_1 + 1, \ldots, n_2 - 1$ those after $h_t(x_i) > h_{t,c}$. Hence, x_{n_1} is precisely the first discrete position at which $h_t < h_{t,c}$ (Fig. 4.39). If the mean film thickness becomes smaller than the percolation threshold, the new variable n is equal to n_1, and to n_2 otherwise.

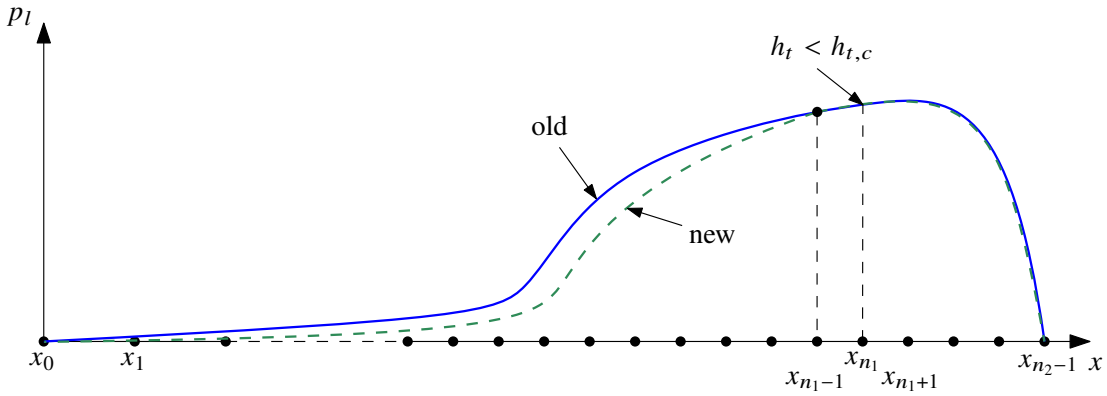

Figure 4.39: Partition of discretization points depending on the percolation threshold. The evolution of the lubricant pressure is also represented in order to illustrate that it is only recomputed in the first part of the roll bite, if the mean film thickness becomes smaller than the percolation threshold.

To solve the previous Reynolds equation by finite differences for p_l at x_i ($i = 0, 1, \ldots, n - 1$), the derivatives have to be *approximated by a centered-difference formula* [53, p. 685], i.e. for an arbitrary function $f(x)$:

$$\frac{\partial f}{\partial x}(x_i) \approx \frac{f(x_{i+1}) - f(x_{i-1})}{x_{i+1} - x_{i-1}} \tag{4.275}$$

where $x_{i-1} < x_i < x_{i+1}$ are three consecutive locations at which the value of the function f is known. The steps between two consecutive locations are not necessarily the same for each neighboring pair. To simplify the notations, the following variables are introduced:

$$f_0 = \phi_x \frac{h_t^3}{12\eta} \tag{4.276}$$

$$g_0 = f_0 \frac{\partial p_l}{\partial x} \tag{4.277}$$

$$f_1 = \frac{v_s + v_r}{2} h_t \tag{4.278}$$

$$f_2 = \frac{v_s - v_r}{2} R_q \phi_s \tag{4.279}$$

Based on these notations, the first term in Eq. (4.274) can be discretized as follows:

$$(*) = \frac{g_0(x_{i+1/2}) - g_0(x_{i-1/2})}{x_{i+1/2} - x_{i-1/2}} \tag{4.280}$$

where $x_{i+1/2}$ and $x_{i-1/2}$ can be approximated by

$$x_{i+1/2} = \frac{x_{i+1} + x_i}{2} \qquad x_{i-1/2} = \frac{x_i + x_{i-1}}{2} \tag{4.281}$$

and where $g_0(x_{i+1/2})$ and $g_0(x_{i-1/2})$ can be approximated by

$$g_0(x_{i+1/2}) = \frac{f_0(x_{i+1}) + f_0(x_i)}{2} \frac{p_l(x_{i+1}) - p_l(x_i)}{x_{i+1} - x_i} \tag{4.282}$$

$$g_0(x_{i-1/2}) = \frac{f_0(x_i) + f_0(x_{i-1})}{2} \frac{p_l(x_i) - p_l(x_{i-1})}{x_i - x_{i-1}} \tag{4.283}$$

Introducing Eqs. (4.281), (4.282) and (4.283) in Eq. (4.280) and grouping the terms according to the different values of p_l, one gets

$$\begin{aligned}(*) = {} & p_l(x_{i+1}) \underbrace{\frac{f_0(x_{i+1}) + f_0(x_i)}{2a(x_{i+1} - x_i)}}_{A_i} \\ & + p_l(x_i) \left(-\frac{f_0(x_{i+1}) + f_0(x_i)}{2a(x_{i+1} - x_i)} - \frac{f_0(x_i) + f_0(x_{i-1})}{2a(x_i - x_{i-1})} \right) \\ & + p_l(x_{i-1}) \underbrace{\frac{f_0(x_i) + f_0(x_{i-1})}{2a(x_i - x_{i-1})}}_{B_i}\end{aligned} \tag{4.284}$$

where

$$a = \frac{x_{i+1} + x_i}{2} - \frac{x_i + x_{i-1}}{2} \tag{4.285}$$

Applying also Eq. (4.275) to the second and third terms of Eq. (4.280), we obtain

$$(**) = \frac{f_1(x_{i+1}) - f_1(x_{i-1})}{x_{i+1} - x_{i-1}} = C_i \qquad (***) = \frac{f_2(x_{i+1}) - f_2(x_{i-1})}{x_{i+1} - x_{i-1}} = D_i \tag{4.286}$$

Combining Eqs. (4.284) and (4.286) in Eq. (4.274) yields a system of equations for $i = 1, \ldots n-1$ that can be solved for $p_l^*(x_i)$, i.e. the new values of $p_l(x_i)$, provided that adequate boundary conditions are applied:

$$p_l^*(x_{i+1})A_i - p_l^*(x_i)(A_i + B_i) + p_l^*(x_{i-1})B_i = C_i + D_i \tag{4.287}$$

Two different sets of *boundary conditions* are implemented in METALUB depending on the percolation threshold. First, the lubricant pressure is assumed to be zero at the beginning of the roll bite, i.e. at $x = -R_0$, in either case. Secondly, if the mean film thickness h_t is greater than the percolation threshold $h_{t,c}$ along the entire roll bite, the Reynolds equation can be solved by finite differences from the beginning of the roll bite to its end, where the lubricant pressure is also assumed to be zero:

$$\begin{cases} p_l^*(x_0) = 0 \\ p_l^*(x_{n_2-1}) = 0 \end{cases} \tag{4.288}$$

Otherwise, the Reynolds equation is only solved until the mean film thickness becomes smaller than the percolation threshold, i.e. for x_i with $i = 0, 1, \ldots, n_1 - 1$. In this case,

$$\begin{cases} p_l^*(x_0) = 0 \\ p_l^*(x_{n_1-1}) = p_l(x_{n_1-1}) \end{cases} \tag{4.289}$$

It is also important to notice that the remaining lubricant pressure values of the roll bite, i.e. those for $i = n_1, n_1 + 1, \ldots, n_2 - 1$ are equal to the old values, since the Reynolds equation is not solved in this part of the roll bite.

Based on these boundary conditions, the remaining lubricant pressure values can be computed by *solving the following tridiagonal matrix system*:

$$\begin{bmatrix} -(A_1+B_1) & A_1 & & & & & & \\ B_2 & \ddots & \ddots & & & & & \\ & \ddots & & & & & & \\ & & B_i & -(A_i+B_i) & A_i & & & \\ & & & & \ddots & & & \\ & & & & \ddots & \ddots & A_{n-2} & \\ & & & & & B_{n-2} & -(A_{n-2}+B_{n-2}) \end{bmatrix} \begin{bmatrix} p_l^*(x_1) \\ \vdots \\ p_l^*(x_{i-1}) \\ p_l^*(x_i) \\ p_l^*(x_{i+1}) \\ \vdots \\ p_l^*(x_{n-2}) \end{bmatrix} = \begin{bmatrix} C_1 + D_1 \\ \vdots \\ C_{i-1} + D_{i-1} \\ C_i + D_i \\ C_{i+1} + D_{i+1} \\ \vdots \\ C_{n-2} + D_{n-2} + E \end{bmatrix} \tag{4.290}$$

where

$$E = \begin{cases} 0 & \text{, if } h_t > h_{t,c} \text{ in the whole roll bite,} \\ -p_l(x_{n-1})A_{n-2} & \text{, otherwise.} \end{cases} \tag{4.291}$$

After solving this system, the lubricant pressure evolution is locally *truncated* by 0 or $p_i(x)$, if it becomes negative or greater than the interface pressure, respectively, so that it can be used

in further integrations of the roll bite, as will be explained hereafter. The elimination of the high-speed hypothesis by this procedure is, however, questionable after the previous operation.

The new lubricant pressure distribution $p_l^*(x)$ obviously has an influence on the other variables in the roll bite, if it is significantly different from the old distribution $p_l(x)$. To check whether this is true or not, the following *convergence criterion* computes a non-dimensional maximum variation from the old to the new values:

$$\max_i \frac{\left|p_l(x_i) - p_l^*(x_i)\right|}{\sigma_Y^0} < \text{tol}_{p_l} \tag{4.292}$$

If this criterion is not satisfied, the new lubricant pressure is most likely inconsistent with the values of the other variables in the roll bite. Therefore, the key values in the roll bite are *iteratively updated by fixed-point iterations with relaxations* as shown in Fig. 4.38. In simple words, the full roll bite is integrated again, however, with the new lubricant pressure evolution $p_l^*(x)$. Based on these integration results, the Reynolds equation is solved again by finite differences. This process continues until the lubricant pressure does not change significantly anymore from one finite difference resolution to the next.

More precisely, on the basis of the adjusted parameters, i.e. the lubricant flow rate Q, the entry speed of the strip v_{in}, the vertical position of the roll z_0 and the profile of the roll $z_r(x)$, of the classical METALUB computation and the lubricant pressure p_l^* by the finite difference method, it is possible to integrate again the roll bite. In contrast to the classical METALUB computation, the lubricant pressure gradient (precisely in Eqs. N.59, N.165, N.283 and N.536) is, however, not computed by the explicit integration of the Reynolds equation (Eq. 4.191) but by the integration of the linearly interpolated finite difference:

$$\frac{\partial p_l}{\partial x}(x_i) = \begin{cases} \dfrac{p_l^*(x_{i+1}) - p_l^*(x_i)}{x_{i+1} - x_i} & \text{, if } i = 0 \\ \dfrac{p_l^*(x_i) - p_l^*(x_{i-1})}{x_i - x_{i-1}} & \text{, if } i = n_2 - 1 \\ \dfrac{p_l^*(x_{i+1}) - p_l^*(x_{i-1})}{x_{i+1} - x_{i-1}} & \text{, otherwise.} \end{cases} \tag{4.293}$$

where $p_l^*(x_i)$ quantifies the spatial lubricant pressure evolution, which was computed by the finite difference method. Moreover, no transition to the high-speed equations is neither allowed (small integration errors) nor required since the lubricant pressure was previously truncated to values between 0 and p_i.

This previous method is called a *fixed-point method* because a lubricant pressure distribution is injected into the METALUB system of equations to compute a new pressure distribution by the finite difference method, and so on.

When the roll bite is integrated again with the lubricant pressure of the finite difference resolution, a significantly different mean film thickness, $h_{t,*}^{(i)}$, with respect to the one that was computed

initially by the classical METALUB computation, $h_t^{(0)}$, or by the previous integration of the roll bite, $h_t^{(i-1)}$, could be obtained. To prevent resulting oscillations of the solution, the mean film thickness is updated by *relaxations* before solving the Reynolds equation again by finite differences:

$$h_t^{(i)} = w^{(i)} h_{t,*}^{(i)} + (1 - w^{(i)}) h_t^{(i-1)} \tag{4.294}$$

where $w^{(i)}$ is the relaxation coefficient. This coefficient can either be constant or not. If it is constant, it has to be relatively small in order to induce no visible oscillations of the solution. Carretta introduced a method, which is similar to the Matsumoto method for roll flattening (Sec. 4.10.3.4), in order to improve the convergence speed. Instead of comparing the length of the roll bite from one iteration to the next, the method is this time based on the evolution of the maximum lubricant pressure. As long as it increases, the evolution is assumed to be stable and the relaxation coefficient is kept constant.

Finally, the method, which was presented in this section, has several *drawbacks*. First, this method introduces *additional numerical parameters*, i.e. tol_{p_l}, $w^{(0)}$, $w_{\min}$ and the 10 first iterations (like the 20 iterations in Matsumoto and Shiraishi's method in Sec. 4.10.3.4), although the method already depends on a significant number of them (Sec. 5.2). Secondly, the most important drawback is the following one: the *method does not update the adjustment parameters* v_{in}, z_0 and $z_r(x)$. In fact, the adjusted values of the initial classical METALUB computation are used but not updated, although the lubricant pressure evolution changes. Since the entry speed of the strip v_{in} is, for instance, adjusted in the classical METALUB computation to reach the imposed front tension, this *constraint is not necessarily satisfied anymore after the fixed-point iterations*. The solution is therefore inconsistent with the imposed process parameters. For these reasons, this method is generally not used.

In the future, the previous problem could possibly be solved by *redesigning METALUB with an additional loop* as shown in Fig. 4.40. This additional loop contains the fixed-point iterations, which were explained in this section. Such a solution obviously resembles the one that was introduced by Stephany [305, p. 138-147], but it seems more robust and simpler, though still complex. Moreover, while it was tried in this document to be as clear as possible by introducing all systems of equations that are actually implemented in METALUB and by minimizing as much as possible the introduction of numerical parameters, it is difficult to understand how Stephany's method works precisely based on his thesis alone. In addition, he introduced *numerous convergence criteria*. Although calibrating the tolerances in our convergence criteria is certainly also one of the major challenges, our method seems, however, simpler than Stephany's method for the previous reasons.

4.10.6 Post-processing

Once the resolution method of this chapter has been applied to solve the equations of the roll bite, the following values are known along the roll bite at each integration point x:

$$v_s, t_s, A, h, h_t, p_a, p_l, p_i, \tau_a, \tau_l, \tau_i, \sigma_x, \sigma_y, \sigma_z, s_x, s_z, p, \overline{\epsilon}^p \tag{4.295}$$

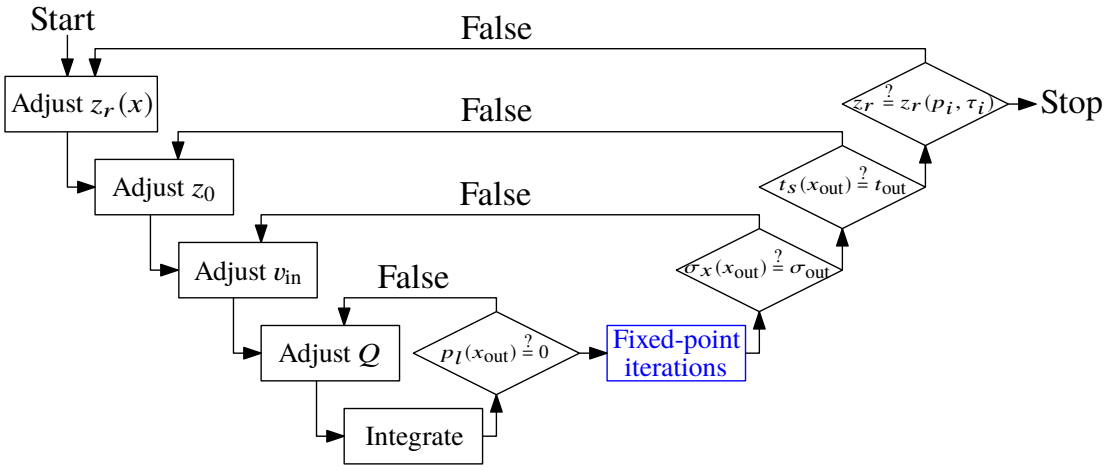

Figure 4.40: Modified flowchart of METALUB (Fig. 4.35) in order to alleviate the high-speed hypothesis by introducing fixed point iterations with the resolution of the Reynolds equation by finite differences.

Since the number of integration points can be relatively significant due to the small integration steps, the *available data are sampled at a reduced frequency*, i.e. when the distance to the last extraction point becomes greater than $\Delta x_{\text{extr},1}$ before the coordinate x_{12} (with the integrators in Secs. 4.10.1.1 and 4.10.1.2) or in the hydrodynamic inlet zone (with the integrators in Secs. 4.10.1.3 and 4.10.1.4) and $\Delta x_{\text{extr},2}$ after x_{12} (resp.) or in the remaining zones (resp.). Using two different steps is required since the *sampling frequency should be greater in the roll bite than far from it* due to the significant variations of the previous variables in the roll bite. The values of $\Delta x_{\text{extr},1}$ and $\Delta x_{\text{extr},2}$ are determined in Sec. O.5.

Based on the extracted values, different key values in cold rolling, i.e. the *rolling force*, the *rolling torque*, the *forward slip* and the *equivalent coefficient of friction*, can be computed. The way to determine these values is explained hereafter.

4.10.6.1 Rolling force

The *rolling force* F_r is the vertical force applied by the roll on the strip. In METALUB, the rolling force per width is computed as follows, by assuming that the interface pressure is oriented vertically:

$$\overline{F}_r = \int_{x_{\text{in}}}^{x_{\text{out}}} p_i \, \mathrm{d}x = \frac{F_r}{w} \tag{4.296}$$

where w is the width of the strip.

4.10.6.2 Torque

To compute the *torque* that has to be applied to the roll in order to reduce the thickness of the strip, the geometry was parameterized as shown in Fig. 4.41. The deformed roll is rotating around O' negatively around $\mathbf{y}$. The usual system of coordinates is defined by the point O and the basis

$(\mathbf{e}_x, \mathbf{e}_y, \mathbf{e}_z)$. A second system of coordinates can be defined by the point P, whose coordinates in the first system are (x_P, y_P, z_P), the local tangent unit vector to the roll $\mathbf{t}$, the local outward-pointing normal $\mathbf{n}$, and the vector $\mathbf{e}_y$. In the current configuration, the values of the angles α and β are negative since they are oriented counterclockwise.

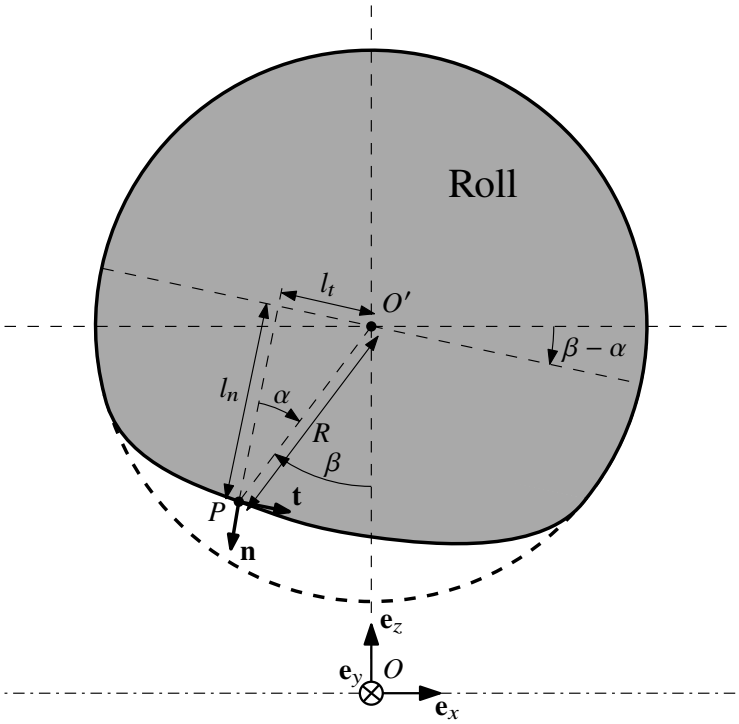

Figure 4.41: Geometrical parameters to compute the torque, which has to be applied to the deformed roll.

Based on the previous definitions, the rolling torque per width (applied by on roll to the strip) is given by

$$\overline{\mathbf{M}}_r = \int_{x_{\text{in}}}^{x_{\text{out}}} \mathbf{O'P} \times \mathbf{dF} \tag{4.297}$$

where

$$\mathbf{O'P} = l_n \mathbf{n} + l_t \mathbf{t} \tag{4.298}$$

$$\mathbf{dF} = p_i \, dl \, \mathbf{n} + \tau_i \, dl \, \mathbf{t} \tag{4.299}$$

Since the *torque applied by the roll to the strip* is computed, a positive interface pressure p_i is pointing along $\mathbf{n}$ and a positive shear stress τ_i along $\mathbf{t}$ according to the directions given in Fig. 4.7.

The signed distance quantities can be written as a function of the deformed radius R and the angles α and β. Hence,

$$l_n = R \cos \alpha \tag{4.300}$$

$$l_t = R \sin \alpha \tag{4.301}$$

Notice that l_t is negative since α is negative. Furthermore, the infinitesimal length element dl can be written as a function of dx:

$$dx = dl\cos(\beta-\alpha) \quad \Rightarrow \quad dl = \frac{dx}{\cos(\beta-\alpha)} \tag{4.302}$$

Combining the previous relations finally results in the following expressions of the rolling torque per width $\overline{\mathbf{M}}_r$ and its norm:

$$\overline{\mathbf{M}}_r = (-\mathbf{e}_y)\int_{x_{\text{in}}}^{x_{\text{out}}} R\left(\frac{\tau_i\cos\alpha - p_i\sin\alpha}{\cos(\beta-\alpha)}\right)\mathrm{d}x \quad \Rightarrow \quad \overline{M}_r = \int_{x_{\text{in}}}^{x_{\text{out}}} R\left(\frac{\tau_i\cos\alpha - p_i\sin\alpha}{\cos(\beta-\alpha)}\right)\mathrm{d}x \tag{4.303}$$

If the roll remains circular, $\alpha = 0$, i.e.

$$\overline{\mathbf{M}}_r = (-\mathbf{e}_y)R\int_{x_{\text{in}}}^{x_{\text{out}}}\left(\frac{\tau_i}{\cos\beta}\right)\mathrm{d}x \quad \Rightarrow \quad \overline{M}_r = R\int_{x_{\text{in}}}^{x_{\text{out}}}\left(\frac{\tau_i}{\cos\beta}\right)\mathrm{d}x \tag{4.304}$$

Finally, to compute the torque, the deformed radius R and the angles α and β have to be determined.

Rigid circular roll

In the case of a rigid circular roll, the deformed radius R is equal to the undeformed radius R_0, i.e. $R = R_0$. Instead of calculating explicitly the angle β, its cosine can directly be determined as follows:

$$\cos\beta = \frac{y_{O'} - y_P}{R} \tag{4.305}$$

Deformed roll

In the case of a deformed roll, the local radius and the angles are given by the following equations:

$$R = \sqrt{x_P + (y_{O'} - y_P)^2} \tag{4.306}$$

$$\beta = \arcsin\left(\frac{x_P}{R}\right) \tag{4.307}$$

$$\alpha = \beta - \arctan\left(\frac{\partial z_r}{\partial x}\right) \tag{4.308}$$

where the last relation follows from the fact that $\partial z_r/\partial x = \tan(\beta-\alpha)$, which is the third component of the tangent vector $\mathbf{t}$ provided that its first component is one, i.e. $\mathbf{t} = (1, 0, \partial z_r/\partial x)$.

4.10.6.3 Forward slip

The *forward slip* is computed as follows:

$$s_f = \frac{v_s(x_{\text{out}}) - v_r}{v_r} \tag{4.309}$$

4.10.6.4 Equivalent coefficient of friction

If μ is the *local coefficient of friction* at a position x, i.e.

$$\mu = \left| \frac{\tau_i}{p_i} \right|, \tag{4.310}$$

the *equivalent coefficient of friction* is defined as follows:

$$\overline{\mu} = \frac{1}{x_{\text{out}} - x_{\text{in}}} \int_{x_{\text{in}}}^{x_{\text{out}}} \mu \, \mathrm{d}x \tag{4.311}$$

It is important that the value of the local coefficient of friction is meaningful in this definition, i.e. p_i and τ_i are sufficiently large. For this reason, the bounds of the integral in Eq. (4.311) are determined such that only values, for which p_i is larger than 1/100 of the maximum interface pressure, are considered.

4.11 Conclusion

In this chapter, the mixed lubrication cold rolling model METALUB was *derived and extended*. This model was initially developed by Marsault (1998) [215] and refined by Boman (1999) [36], Stephany (2008) [305] and Carretta (2014) [54]. Due to various versions of the model over the past years, particular attention was paid to *meticulously rederive the entire model with unified notations (appendix N) by combining the best features of past developments while further enhancing it*. These features and enhancements are summarized hereafter.

METALUB is a 2D cold rolling model with applied back and front tensions, and mixed lubrication. Hence, the interface pressure in the roll bite is computed by a *load sharing equation* between the lubricant and solid asperity contact.

The load sharing depends on the *geometric contact description of the rough rolls and strip*. They are characterized by a composite mean-square-roughness, the half-spacing between asperities, the surface pattern orientation and a surface height distribution, which is either that of triangular asperities or the quasi-Gaussian Christensen distribution. These distributions relate the relative contact area to the distance between mean lines and the mean film thickness of the lubricant.

The *mechanics of the strip* is described by elastoplastic constitutive equations, which were extended to take into account viscoplasticity and thermal softening, via numerous hardening laws: perfect plasticity, Krupkowski power law, Ludwik law, Smatch law, experimental yield curve and their combinations with the thermo-viscoplastic components of the Johnson-Cook law. The equilibrium equations of the strip were derived by the slab method. Furthermore, the strain computation of previous models was corrected so that the roll and the strip cannot overlap anymore.

Besides including rigid circular and non-circular roll profiles, the model takes into account *roll flattening* via the methods by Hitchcock [142], Bland and Ford [33], Jortner et al. [163] or

Meindl [220]. This last method, which is the most accurate of them all since it includes radial and circumferential profile modifications due to pressure and shear, was added in this thesis.

Solid contact in the bite is computed by asperity flattening equations and boundary friction models. More precisely, asperity flattening by normal loading and plastic bulk deformation is calculated via the equations by Wilson and Sheu [367], Sutcliffe and Marsault [215, 311] or Korzekwa et al. [169, 313], which is probably the most accurate one. This latter model was added in this thesis. Friction in the solid contact region is then computed by the Coulomb, Tresca or the Coulomb-Tresca law with linear regularization when roll flattening is significant.

The *lubricant flow* is modeled by the average Reynolds equation with flow factors for triangular asperity and Christensen height distributions. The shear flow factors were corrected in this thesis. The lubricant rheology can be modeled via the laws by Barus [21], Roelands [278] or the extended WLF law [20, 375]. The lubricant shear stress is either computed on the basis of the film thickness in the valleys or a newly added shear stress factor approach, which was, however, not extended to large fractional contact areas.

Since Stephany's version of METALUB was replaced by Carretta's version, the coupling with the *thermal model* THERMROLL was abandoned. To include, however, the influence of temperature in METALUB, an adiabatic model for the strip with some thermal laws for the lubricant was implemented in this thesis.

All the previous components were finally combined by describing the *full model and its solution method*. The roll bite is divided into zones, depending on the contact status and the deformation modes of the strip. The equations in each zone are integrated explicitly from zone to zone along the roll bite via different integration and discretization strategies. The general METALUB algorithm is based on four nested loops to adjust some parameters, with the integration of the roll bite in the innermost loop. Towards the outermost loop, the lubricant flow rate is first adjusted to have a zero lubricant pressure at the end of the bite. This might require a high-speed transition, after which the interface pressure is assumed to be equal to the lubricant pressure, when the rolling speed is significant or when the state in the bite is close to the percolation threshold. Secondly, the entry speed of the strip is adjusted to reach the imposed front tension. Thirdly, the position of the roll bite is shifted vertically until the final strip thickness is equal to the imposed final thickness and ultimately, the profile of the roll is adapted depending on the stresses that it is subjected to. In this thesis, the number of numerical parameters and the computation time of the model was significantly reduced by smarter initial guesses. The previous method can also be used to model rolling with lubricant starvation by assuming that the bite is dry before the distance between asperities becomes smaller than the lubricant film thickness at the inlet. And eventually, a method to partially alleviate the high-speed hypothesis is explained before post-processing methods are introduced to compute the rolling force, torque, forward slip and the equivalent coefficient of friction.

Besides the rederivation of the entire underlying system of equations, one of the major highlights of this thesis is the *implementation* of the model in C++ with a Python wrapper, regression tests and version control. Carretta's METALUB (2.0) version was completely refactored to use exactly

the same notations in this document as in the software and to implement the model as robustly as possible, which is required due to the complexity of the interacting physics in lubricated cold rolling. Furthermore, Carretta's graphical user interface (GUI) of METALUB was also completely refactored and extended to simplify the interaction with the model (appendix G).

Chapter 5

METALUB - Numerical Results

In the past, different versions of the METALUB model or its predecessor LAM2DTRIBO were used in numerous studies, most notably the PhD theses by Marsault (1998) [215], Stephany (2008) [305] and Carretta (2014) [54], to predict, amongst others, the rolling load and the forward slip in cold rolling. Their results are briefly summarized in the next section to illustrate *why it is necessary to further quantify the predictive ability* of the METALUB model.

Before being able to quantify this ability, the model has first to return a solution. This is not obvious as illustrated by Stephany abandoning his CIEFS model, which was used to solve the same problem as the METALUB model [305]. In fact, although METALUB is more robust than CIEFS, it has still convergence issues due to various reasons. One of these reasons is the choice of the numerical parameters in the model. These parameters were never systematically calibrated in the past, probably due to the complex nested loop structure of the model, which renders any other calibration strategy than an heuristic one quite difficult. This is the reason why a strategy to *calibrate the numerical parameters*, e.g. the spatial integration steps, the tolerances, ..., is provided in the second section of this chapter. Besides convergence, the objective of this strategy is to choose numerical parameters, which minimize the computation time while achieving a guaranteed accuracy on the results. This strategy is illustrated on the basis of an experimental test scenario that was described in Chap. 3, i.e. Test 5B-4 in Sec. E.7.

Then, the *influence of physical parameters*, like the yield stress and the boundary coefficient of friction, is studied in the context of Test 5B to calibrate the most influential and most uncertain parameters in order to numerically reproduce the experimental results as accurately as possible. This procedure should allow quantifing to which degree METALUB computations can predict friction in lubricated cold rolling.

Finally, in a last section, several *validation cases* are presented in order to show which adjustments are systematically required to accurately estimate the rolling load and forward slip, and what the limitations of the model are. The different validation cases correspond to experimental scenarios, which were presented in Chap. 3.

5.1 Literature review about the validation of METALUB

Marsault (1998) [215] carried out a comprehensive sensitivity analysis to identify the most important parameters in the determination of the lubrication conditions, which are the thickness reduction ratio, the rolling speed, the composite RMS roughness, the initial viscosity of the lubricant and its pressure dependence. Its thermal dependence seems only to be important at the entry of the roll bite, where the lubricant film is created.

Based on these results, two industrial rolling cases were studied. In the model of the first case, the rolls are assumed to be rigid, although the initial yield stress of the stainless strip amounts to 500 MPa with subsequent hardening. At a reduction of 33%, it therefore seems not necessarily possible to precisely predict the rolling load and forward slip, even though the roll diameter is small. The experimental values were, however, predicted more or less accurately by adjusting the Tresca coefficient of friction, which was used as a fitting parameter. In the second industrial case, roll flattening was considered but the final results were not compared to the measured rolling load and forward slip. Moreover, the half spacing between asperities was determined in both cases by assuming that the triangular asperities form a 7° angle with the mean plane, i.e. seemingly without any experimental confirmation.

Besides these industrial cases, the computed mean film thickness was satisfactorily compared to the measured thickness by oil drop experiments of Sutcliffe (1990) [312]. Furthermore, it was shown that the Tresca coefficient of friction had to be reduced with the rolling speed in order to fit experimental effective coefficients of friction by Tabary et al. (1996) [323].

In conclusion to Marsault's thesis (1998) [215], the previous results gave very limited quantitative information about the predictive capabilities of the model in industrial scenarios due to few industrial comparisons, estimated roughness data and fitting adjustments by the boundary coefficients of friction, although experimental assessments were promising.

Stephany (2008) [305] calibrated and validated his version of the METALUB model by analyzing numerous cold rolling scenarios. On the one hand, he showed that the model can reproduce dry rolling results, which were computed by another rolling model. On the other hand, his predictions were *limited by the available experimental data*. For instance, the lubricant viscosity was not known but estimated in the predictions of the strong slip scenarios by Shiraishi et al. (1995) [289]. In addition, the half-distance between asperity tops $\bar{l}$ and the Peklenik surface pattern parameter γ were also estimated instead of being measured. Furthermore, the hardening law and the boundary coefficient of friction μ_C in the boundary region were adjusted in the models of the tandem mill at Tilleur (Belgium).

Besides the limitation due to experimental data, the predictive capabilities of the METALUB model also seem to be *limited by the physical phenomena that are not included* in Stephany's model. While the prediction of the rolling force is satisfactory for the tandem mill at Tilleur, the forward slip is largely overpredicted. This conclusion was also drawn, when the influence of the reduction ratio was studied by Stephany. In this particular case, the overprediction of the forward slip seems to be due to micro-plasto-hydrodynamic/static lubrication, which was not included in the

model. Moreover, the hardening law is manually adjusted in two of his applications by reducing the yield stress: influence of rolling speed on the tandem mill at Sollac (Sainte-Agathe, Florange) and influence of starvation in double reduction rolling on the pilot mill. The underlying physical mechanism, which is most likely thermal softening, is, however, not directly modeled via the computation of the temperature increase in the roll bite.

In summary, Stephany (2008) [305] studied extensively the predictive capabilities of his METALUB model, which are limited by the incomplete experimental data (viscosity, roughness parameters, ...) and the physical mechanisms that are not included in his model (thermal softening, micro-plasto-hydrodynamics, ...).

Carretta (2014) [54] modeled the flexible lubrication conditions of the mill at Tilleur by adjusting the yield stress and the Coulomb coefficient of friction in the boundary region for a rolled product. Based on these values, the rolling force and forward slip were then relatively accurately predicted by adjusting the lubricant film thickness at the entry of the bite when the rolling speed or the lubricant concentration in the emulsion changed. Because this thickness was adjusted for each operating point separately, it is difficult to judge the real predictive ability of the model.

The previous versions of the METALUB model can clearly reproduce industrial results. Nevertheless, this prediction is usually only valid close to operation conditions for which the boundary coefficient of friction, the yield stress and the lubricant film thickness at the entry were adjusted due to limited experimental data. In addition to these limitations, surface roughness parameters, like the half spacing between asperities, were generally chosen without any underlying measurements.

The experimental data in Chap. 3, which seem to be the *most complete available data to our knowledge*, are therefore the opportunity to assess the predictive ability of the model more thoroughly. For instance, thermo-piezoviscosity of the lubricant and surface roughness parameters were measured, as well as temperature changes after the roll bite. Such data are absolutely required to test possible improvements of the model, like viscoplasticity, the lubricant temperature dependence or the FE asperity crushing model, which is described in Chap. 6.

5.2 Numerical parameter calibration

The values of the *numerical parameters* should be chosen to *minimize the computation time with the constraint of having an acceptably small influence on the key results* of the computation, which are the rolling force per width $\overline{F}_r$ and the forward slip s_f. Maximum absolute variations of $\overline{F}_r$ and s_f by about 0.05 kN/mm and 0.05% seem acceptable (e.g. Fig. 3.6 with product S1). These variations correspond to about 1% of relative change in both cases[1].

[1]This value can further be justified by considering the reproducibility differences of the experimental results. For instance, Fig. 3.7 shows different measurements at v_r = 400 m/min for operating conditions, which should be identical. If the measurements in Test 4B are compared to the corresponding measurements in Test 5A, the relative change is (7511-7281)/7511 = 3% for the rolling force and (4.59-4.22)/4.59 = 8% for the forward slip. Hence, the required maximum variation of 1% seems reasonable.

In the following section, a METALUB model of Test 5B-4, i.e. Test 5B at 197.5 m/min in Sec. E.7, which was introduced in Chap. 3, is defined in order to choose the numerical tolerances in a way to satisfy the previous constraint.

5.2.1 Definition of the baseline model

The *base case* in Tab. 5.1 defines the METALUB model, which corresponds to the rolling scenario at about 200 m/min in Test 5B of Chap. 3 (Sec. E.7). This scenario was chosen because it is one of the least complex scenarios, i.e. no starvation is observed, a pure oil is used as lubricant and the variations of the rolling load and forward slip are relatively smooth. Hence, it is one of the *most likely reproducible* scenarios by METALUB. Moreover, the following choices were made in Tab. 5.1:

- The roll bite is modeled with the full-flooded lubrication hypothesis, i.e. without starvation.
- The heating of the strip due to friction and plastic deformation is activated for later parametric studies although the temperature variation of the strip has no impact in the current model since neither thermoplasticity nor the thermal dependence of the lubricant viscosity on the strip temperature are activated.
- The values of the Young's modulus and the Poisson's ratio of the strip are assumed to be equal to classical values of steel since no other values could be found in the experimental data. The same is true for the material parameters of the roll.
- Viscoplasticity and thermoplasticity are for now not included in the model.
- A standard density of 7850 kg/m^3 and mean specific heat capacity of 500 J/(kg.°C) are chosen since the real values are very close to these values [300, p. 284 (DC06)][2] and since increasing the accuracy of these parameters would not significantly improve the results for two reasons. First, the thermoplasticity material constants are not known. Secondly, our thermal model is very simple because it neglects heat exchanges with the roll.
- The lubricant temperature is assumed to be constant along the roll bite and equal to its application temperature, which also corresponds to the average of the entry and exit temperatures of the strip.
- The Peklenik surface pattern parameter γ was not measured in the tests of Chap. 3. Hence, it is assumed to be equal to 9, as in all previous METALUB computations, since the asperity lay is mainly longitudinal in cold rolling (Sec. 2.1.2.2).
- The Coulomb-Tresca friction law is chosen to model solid friction. The value of the Coulomb coefficient μ_C in the boundary region was adjusted slightly to obtain a good prediction of the rolling force (before adjusting any other parameters) since no measurement of this value is known in the context of the experimental campaign. The Tresca coefficient

[2]The units of the mean specific heat capacity in this reference should be J/(kg.°C) instead of kJ/(kg.°C).

μ_T was set equal to 1 since the friction stress can at most be equal to the plane-strain yield shear stress $\tau_Y = \sigma_Y/\sqrt{3}$ [252].

- The shear stress factors are not activated as in any other models of the past. Their influence will be studied later on.
- Meindl's roll flattening model (Sec. 4.6.4) is selected since it is the most accurate method that is implemented in METALUB.
- The relaxation method for roll deformations (Sec. 4.10.3.4) with a constant relaxation coefficient $w^{(0)}$ is selected since it is the simplest method. Only if the reduction of the computation time is necessary after studying this basic method, more complex methods should be considered.
- The Runge-Kutta 4 integration method without partially or fully adaptive step size (aside from the step reduction at x_{12}, Sec. 4.10.1.2) is selected for reasons that were explained in Sec. 4.10.1.

5.2.2 Reduction of the problem into sub-problems

In this section, the interdependence of numerical parameters in METALUB is first explained before the *full problem is reduced into sub-problems to systematically calibrate these parameters*.

Due to the *nested loop structure* of the resolution method in METALUB (Sec. 4.10.3), the value of an outer loop criterion depends on the numerical tolerances of the inner loops. For instance, the lubricant flow rate Q is adjusted to obtain a lubricant pressure p_l equal to zero at the end of the roll bite. This adjustment is located in a loop which adapts the entry speed of the strip v_{in} so that the computed front tension $\sigma_x(x_{\text{out}})$ becomes equal to the specified front tension σ_{out}. Due to the nested loop structure, very close values of v_{in} do not necessarily imply that the corresponding values of $\sigma_x(x_{\text{out}})$ are almost identical, too. In fact, a small speed increment could lead to a significantly different choice of Q in the inner bisection loop, if the tolerance of Q is relatively loose. In consequence, adjusting v_{in} to have $\sigma_x(x_{\text{out}})$ as close as required to the user-specified value σ_{out} could be impossible.

The previous explanation is *illustrated* in Fig. 5.1. The different dots represent the successive values of the front tension, which were determined by the bisection method. Due to a very loose tolerance of the flow rate tol_Q with respect to the front tension tolerance $\text{tol}_{\sigma_{\text{out}}}$, the computed front tensions $\sigma_x(x_{\text{out}})$ could be locally discontinuous and the adjustment loop of the entry speed could not converge.

In consequence, the tolerance of Q has to be determined depending on the tolerance of σ_{out}. Or, the other way round, the *tolerances of the outer loops should not be too strict with respect to the tolerances of the inner loops in order to render convergence possible*. For instance, in the previous example (Fig. 5.1), choosing a greater tolerance for σ_{out} would solve the convergence problem.

Entity	Parameter	Value	Unit
Roll bite	Type	Full-flooded lub.	-
	Heating by friction	On	-
	Heating by plastic deformation	On	-
Strip material	Name	S2	-
	E_s	210000	MPa
	ν_s	0.3	-
	Law	Ludwik	-
	Viscoplasticity	Off	-
	Thermoplasticity	Off	-
	A	776	MPa
	B	147	MPa
	n	1.52	-
	$\overline{\epsilon}_0^p$	0	-
	ρ_s	$7.850 \cdot 10^{-9}$ [7850]	t/mm^3 [kg/m^3]
	c_s	$500 \cdot 10^6$ [500]	N.mm/(t.°C) [J/(kg.°C)]
	β_s	0.9	-
Strip	t_{in}	0.75	mm
	t_{out}	0.584	mm
	σ_{in}	122.0	MPa
	σ_{out}	184.3	MPa
	$T_{s,\text{in}}$	25	°C
Lubricant	Name	L3	-
	Law	WLF (enhanced)	-
	A_1	49.64	°C
	A_2	0.000365	MPa^{-1}
	b_1	0.00578	MPa^{-1}
	b_2	−0.565	-
	C_1	16.11	-
	C_2	26.00	°C
	η_g	10^6	MPa.s
	$T_g(0)$	−85.96	°C
	T_l	60 (constant)	°C
Interface	Asperity profile	Christensen	-
	$R_{q,r}$	0.773	μm
	$R_{q,s}$	0.123	μm
	$\bar{l}$	51.28	μm
	Flattening equation	Wilson-Sheu	-
	γ	9	-
	Friction law	Coulomb-Tresca	-
	μ_C	0.08	-
	μ_T	1	-
	Flow factors ϕ_x and ϕ_s	On	-
	Shear stress factors	Off	-
Roll	Deformation method	Meindl (full)	-
	Deformation mode	Plane strain	-
	R_0	195.5	mm
	v_r	3291	mm/s
	E_r	210000	MPa
	ν_r	0.3	-
	x_{12}	?	mm
	x_{23}	?	mm
	$\Delta\theta_1$	?	°
	$\Delta\theta_2$	?	°
	$\Delta\theta_3$	?	°
	Relaxation method	Constant	-
	$w^{(0)}$	?	-
Other numerical parameters	Integration method	RK4	-
	x_{12}	?	mm
	Δx_1	?	mm
	Δx_2	?	mm
	tol_Q	?	-
	$\text{tol}_{\sigma_{\text{out}}}$	?	-
	$\text{tol}_{t_{\text{out}}}$	?	-
	tol_R	?	-
	$\Delta x_{\text{extr},1}$	?	mm
	$\Delta x_{\text{extr},2}$	?	mm
	CIEFS step	Off	-

Table 5.1: Base case for the numerical parameter calibration. This case represents Test 5B-4, which was presented in Chap. 3 and which is detailed in Sec. E.7. The interrogation marks indicate which numerical parameters have to be determined.

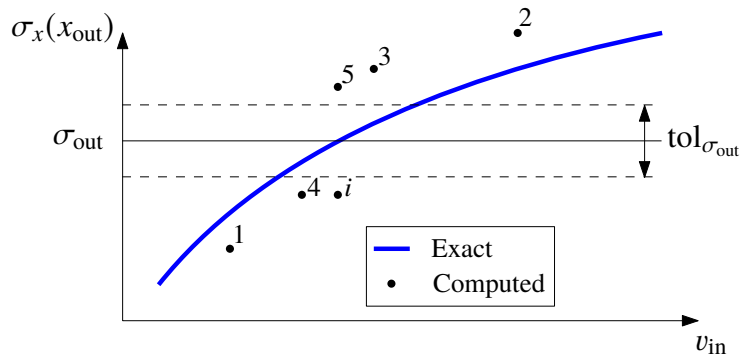

Figure 5.1: Illustration of a problem that may arise due to the interdependence of numerical parameters in METALUB: after successive adjustments of the entry speed of the strip v_{in}, the resulting front tension $\sigma_x(x_{out})$ does not fall within the interval around the specified front tension σ_{out}.

Besides this condition, the numerical parameters at each adjustment stage should allow to *predict the rolling force per width and the forward slip with a given accuracy* as explained previously. These parameters can be structured as follows from the innermost to the outermost adjustment loop in METALUB:

$$\begin{Bmatrix} x_{12} \\ \Delta x_1 \\ \Delta x_2 \end{Bmatrix} \Rightarrow \text{tol}_Q \Rightarrow \text{tol}_{\sigma_{out}} \Rightarrow \begin{Bmatrix} \text{tol}_{t_{out}} \\ x_{12} \\ x_{23} \\ \Delta\theta_1 \\ \Delta\theta_2 \\ \Delta\theta_3 \\ w^{(0)} \end{Bmatrix} \Rightarrow \begin{Bmatrix} \text{tol}_R \\ \Delta x_{\text{extr},1} \\ \Delta x_{\text{extr},2} \end{Bmatrix} \Rightarrow \begin{Bmatrix} \text{tol}_{\overline{F}_r} \\ \text{tol}_{s_f} \end{Bmatrix} \tag{5.1}$$

Hence, the parameters of the roll bite integration have to be adjusted first, then, those of the lubricant flow rate, the front tension, the final strip thickness, the roll flattening and ultimately those of the data extraction so that prediction error of the rolling force per width $\Delta\overline{F}_r$ and the forward slip Δs_f are smaller than $\text{tol}_{\overline{F}_r}$ and tol_{s_f}, respectively. These tolerances $\text{tol}_{\overline{F}_r}$ and tol_{s_f}, which should be equal to about 1% as mentioned previously, are no direct parameters in the METALUB model. The other numerical parameters are rather determined as a function of these tolerances in the following section.

It should be noted that *the previous structure of numerical parameters (Eq. 5.1) was far more complex in the past* than it is today since even more numerical parameters were required. For instance, (1) the fully adaptive Runge-Kutta integrator with its numerous tolerances (Δx_1, Δx_2, tol_{int}, tol_{abs}, tol_{crit}, Sec. 4.10.1.4) was used by default; (2) in addition to the tolerance of Q, a tolerance of the lubricant pressure at the exit was implemented since no high-speed outlet zones existed (Sec. 4.10.3.1); (3) the roll flattening had two tolerances, one with respect to the rolling

load, and the other with respect to the forward slip (Sec. 4.10.3.4); (4) and finally, too many data points were extracted since no extraction method with $\Delta x_{\text{extr},1}$ and $\Delta x_{\text{extr},2}$ did exist in the past.

Aside from the disadvantageous interdependence of the numerical tolerances, the nested loop structure has, however, the *advantage of allowing to study the influence of the numerical parameters in an inner loop when the adjusted variables of the outer loops are fixed*. For instance, the influence of the integration parameters on the rolling load and the forward slip can be studied for a given lubricant flow rate, entry strip speed, vertical position of the roll axis and profile of the roll. Thus, the full problem can be *reduced into sub-problems*.

5.2.3 Summary of the numerical parameter calibration

Since the numerical calibration is a lengthy procedure, it is only summarized in this section, while all details can be found in appendix O.

First, three different *accuracy classes* were defined, for which the values of the numerical parameters were then determined. These classes were labeled as high, medium and reasonable accuracy if the *relative error* of the predicted rolling force per width $\Delta\overline{F}_r$ and the forward slip Δs_f with respect to the most accurate prediction available are smaller than 0.01%, 0.1% and 1%, respectively.

On the basis of the scenario in Tab. 5.1, the values of the numerical parameters were then determined *layer after layer from the innermost to the outermost loop* of the METALUB model (Eq. 5.1). At a given layer, the relative errors with respect to the most accurate predictions were computed for different values of the respective free numerical parameters. For instance, the integration errors were computed for different values of the integration steps Δx_1 and Δx_2 in the innermost loop. *Depending on these errors, the values of the parameters were then assigned to one of the three previous error classes.* Simultaneously, it was checked that the chosen values of the tolerances are not in conflict due their *interdependence by the nested loop structure* (Sec. 5.2.2). In fact, non-convergence was observed when the tolerance of the front tension $\text{tol}_{\sigma_{\text{out}}}$ was too strict with respect to tolerances of more inner loops, like the integration steps Δx_1 and Δx_2, or the lubricant flow rate tolerance tol_Q.

Based on the previous strategy, ***the numerical parameters in the METALUB model were for the first time systematically calibrated***. In other words, *three different sets of numerical parameters* were determined to limit numerical errors and to reduce the occurrence of non-converging computations due to the nested loop structure of METALUB. The values of the numerical parameters of the most accurate prediction available (highest), those of each accuracy class (high, medium, reasonable) as well as the old default values are summarized in Tab. 5.2.

The results that were obtained with the values of the different parameter sets (Tab. 5.2) in the rolling scenario of Tab. 5.1 are shown in Tab. 5.3. First, it can be seen that the different *accuracy conditions are satisfied*. Moreover, the prediction with the old default parameters is (on average) less accurate than the computation with reasonable accuracy, although it takes about twice as much computation time.

Parameter	Highest	High	Medium	Reasonable	Old default	Units
Δx_1	1	1	1	1	1	mm
Δx_2	10^{-5}	10^{-5}	10^{-4}	10^{-3}	10^{-3}	mm
x_{12} (integration)	-10	-10	-10	-10	-10	mm
tol_Q	10^{-8}	10^{-8}	10^{-6}	10^{-4}	10^{-14}	-
$\text{tol}_{\sigma_{\text{out}}}$	10^{-5}	10^{-5}	10^{-4}	10^{-3}	$3 \cdot 10^{-3}$	-
$\text{tol}_{t_{\text{out}}}$	10^{-6}	10^{-6}	10^{-5}	10^{-4}	$3 \cdot 10^{-3}$	-
$\Delta x_{\text{extr},1}$	1	1	1	1	1	mm
$\Delta x_{\text{extr},2}$	10^{-2}	10^{-2}	10^{-2}	10^{-2}	10^{-2}	mm
x_{12} (roll)	-10	-10	-10	-10	-10	mm
x_{23}	5	5	5	5	5	mm
$\Delta\theta_1, \Delta\theta_3$	10^{-1}	1	1	1	1	°
$\Delta\theta_2$	10^{-3}	10^{-3}	$5 \cdot 10^{-3}$	$5 \cdot 10^{-3}$	$5 \cdot 10^{-2}$	°
$w^{(0)}$	0.5	0.5	0.5	0.5	0.5	-
tol_R	10^{-9}	10^{-8}	10^{-7}	10^{-6}	10^{-5}	-

Table 5.2: New values of the numerical parameters of the most accurate prediction available (highest), those of each accuracy class (high, medium, reasonable) as well as the old default values.

Accuracy	$\overline{F}_r$ [N/mm]	$\Delta\overline{F}_r$ [%]	s_f [%]	Δs_f [%]	Duration [h:min:s]
high	8638.2	0.000	4.816	0.005	03:00:37
medium	8637.9	0.005	4.818	0.039	00:05:47
reasonable	8638.0	0.003	4.826	0.208	00:00:13
old default	8624.6	0.158	4.823	0.145	00:00:27

Table 5.3: Results and computation time with the different parameter sets (Tab. 5.2) in the rolling scenario of Tab. 5.1. The relative error values $\Delta\overline{F}_r$ and Δs_f were computed with respect to the most accurate predictions available ("highest" in Tab. 5.2).

Finally, one should notice that the strict applicability of the previous parameter study is obviously restricted to the particular scenario in Tab. 5.1 since it is based on this rolling scenario. The *extrapolation* of the following findings to other cases is an assumption. The strictness of this assumption is, however, reduced by the similarities with other rolling cases and the introduction of relatively objective convergence criteria. This statement also implies that numerical parameters, which are chosen to restrict numerical errors to a certain threshold, do not always guarantee this limitation. On average, this should, however, be true.

5.3 Physical parameter calibration

As explained in Sec. 5.1, some *physical parameters had to be adjusted* in the past so that the numerical predictions by METALUB would be equal to the experimental results since these parameters could not be precisely measured or were not measured at all, e.g. the boundary

coefficient of friction.

In the first part of this section, a general *calibration strategy of the physical parameters* is presented on the basis of the previous rolling scenario, i.e. Test 5B of the experimental campaign at Maizières-lès-Metz (Chap. 3) for similar reasons (Sec. 5.2.1). Instead of focusing only on a single rolling speed as in the calibration study of the numerical parameter (Sec. 5.2), the *full Test 5B* will be considered. This is required to assess the predictive capabilities of the METALUB model with respect to the rolling force per width $\overline{F}_r$ and the forward slip s_f as accurately as possible. In fact, if only one operating point was considered, it would be relatively simple to adjust the physical parameters in order to predict these values perfectly. The predictions at other rolling speeds with the same parameters would, however, potentially be relatively inaccurate.

In the second part of this section, *further influence studies* are presented to understand to what extent some model components, like the roll flattening model or starvation, impact the results.

5.3.1 Calibration of significant parameters

In this section, the *most significant physical parameters will be calibrated* to predict the rolling load and forward slip as precisely as possible in the context of Test 5B (Sec. E.7).

In a similar way to the numerical parameter calibration (Sec. 5.2), the physical parameter calibration is based on the METALUB model of *Test 5B* in Tab. 5.1 with the numerical parameters of Tab. 5.2 (reasonable accuracy) and the operating conditions, i.e. the rolling speed v_r, the final thickness t_{out}, the back tension σ_{in} and the front tension σ_{out}, of Tab. E.21. In this test, the influence of the rolling speed on the rolling load and the forward slip is analyzed.

It is important to notice that the *rolling speed v_r is not the only operating parameter that changes from one rolling scenario to the next in Test 5B*, although the variations of other parameters were reduced as much as possible. Due to the significant influence of some parameters, like the final thickness on the rolling load, it is, however, required to also take their small fluctuations from one rolling speed to the next into account in order to obtain meaningful comparisons between the experimental and numerical results. One should also notice that the lubricant temperature is assumed to be constant for now since its precise value at the entry of the bite and along it is not known.

As shown in Tab. 5.1, the METALUB model depends on numerous physical parameters. On the one hand, some of them have been measured precisely, e.g. the final thickness, while others have not, e.g. the boundary coefficient of friction. On the other hand, some of them significantly impact the rolling load and forward slip, e.g. the boundary coefficient of friction, while others do not, e.g. the Poisson's ratio. Although it can be anticipated which parameters are probably the most influential ones by physical reasoning and previous results (Sec. 5.1), the influence of essentially all of them was computed to better understand the METALUB model as illustrated in Fig. 5.2 for the Coulomb coefficient of friction (at solid interfaces). In this document, we will, however, only *focus on the most uncertain and most influential physical parameters*.

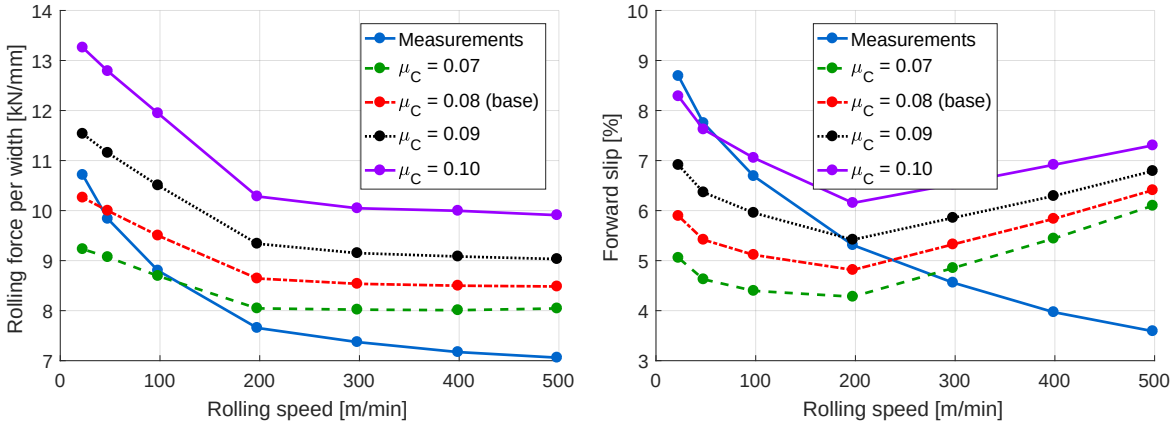

(a) Rolling force per width.

(b) Forward slip.

Figure 5.2: Influence of the boundary coefficient of friction μ_C in Test 5B (Sec. E.7) based on Tab. 5.1 with numerical parameters of Tab. 5.2 (reasonable accuracy).

5.3.1.1 Influence of the boundary Coulomb coefficient of friction

As stated earlier, the *boundary Coulomb coefficient of friction* μ_C is probably one of the most uncertain and influential physical parameters of the model as shown in Fig. 5.2. This figure shows the evolution of the rolling force per width $\overline{F}_r$ and the forward slip s_f as a function of the rolling speed. The experimental measurements as well as the numerical results for different coefficients of friction are represented to compare them.

Concerning the base case, the *prediction of the rolling force is rather good* but certainly perfectible. This quite good prediction is due to the initial choice of the boundary coefficient of friction, i.e. $\mu_C = 0.08$. The predicted rolling force decreases with the rolling speed in a similar way to the measured rolling force due to the *lubricant film build-up by viscous entrainment*, which decreases the relative contact area (Fig. 5.3) and thus the equivalent coefficient of friction (Fig. 5.4) by decreasing the contribution of solid friction.

The *prediction of the forward slip could be far better* at low and high rolling speeds, as shown in Fig. 5.2b. Like the rolling force, it decreases with the rolling speed when $v_r < 200$ m/min since friction decreases (Fig. 5.4). *Its sudden increase at higher rolling speeds can be traced back to the increase of the lubricant shear stress with the rolling speed.* In fact, to better fit the experimental measurements, friction should further decrease at high rolling speeds in the computation. This implies that the equivalent Coulomb coefficient of friction $\overline{\mu}$ seems not to decrease enough with the rolling speed, e.g. it even increases at high rolling speeds for some coefficients of friction (Fig. 5.4). The underlying reason of this hypothesis can be revealed by partitioning the local coefficient of friction μ into a *local* coefficient of friction on the asperity tops μ_a and a local

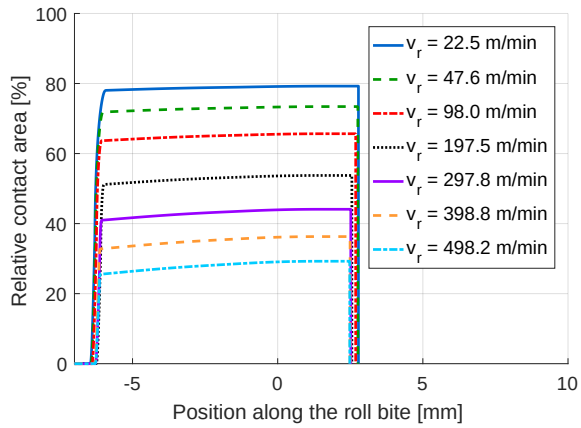

Figure 5.3: Evolution of the relative contact area A along the roll bite for the different rolling speeds v_r in Test 5B (Sec. E.7) based on Tab. 5.1 with numerical parameters of Tab. 5.2 (reasonable accuracy).

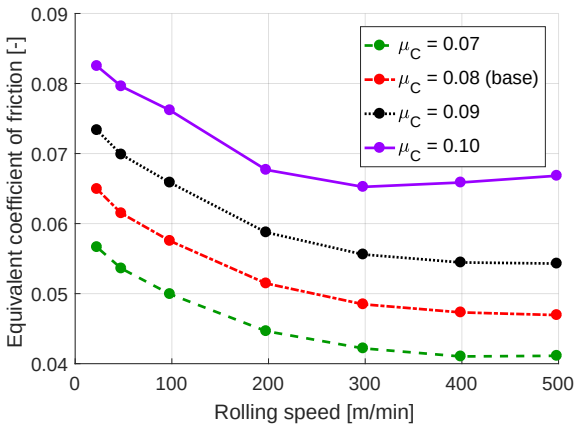

Figure 5.4: Equivalent coefficient of friction $\overline{\mu}$ as a function of rolling speed for different Coulomb coefficients of friction μ_C (at the solid interface) in Test 5B (Sec. E.7) based on Tab. 5.1 with numerical parameters of Tab. 5.2 (reasonable accuracy).

coefficient of friction due to the lubricant μ_l by the sharing law (Eq. 4.5):

$$\left|\frac{\tau_i}{p_i}\right| = \left|\frac{A\tau_a}{p_i}\right| + \left|\frac{(1-A)\tau_l}{p_i}\right| \quad \Rightarrow \quad \mu = \mu_a + \mu_l \quad \text{with} \quad \begin{cases} \mu_a = \left|\frac{A\tau_a}{p_i}\right| \\ \mu_l = \left|\frac{(1-A)\tau_l}{p_i}\right| \end{cases} \tag{5.2}$$

Based on these definitions, the *equivalent* coefficient of friction on the asperity tops $\overline{\mu}_a$ and the equivalent coefficient of friction due to the lubricant $\overline{\mu}_l$ can be computed like the equivalent coefficient of friction $\overline{\mu}$ in Eq. (4.311). The evolution of these coefficients with the rolling speed is shown in Fig. 5.5. On the one hand, friction due to contact at the asperity tops decreases with the rolling speed since the relative contact area decreases (Fig. 5.3), as mentioned previously. On the other hand, friction due to the lubricant shear stress increases with the rolling speed. Since the forward slip increases with the rolling speed in Fig. 5.2b, this could either imply, that $\overline{\mu}_a$ decreases too little or $\overline{\mu}_l$ increases too much with this speed. A direct but certainly oversimplifying solution to this problem is to neglect the influence of the lubricant shear stress τ_l on the results. Fig. 5.6 clearly shows that this hypothesis improves the prediction of the trend when comparing it to Fig. 5.2.

Before focusing on further improving the quantitative agreement, one might wonder *why neglecting the lubricant shear stress improved the results*. Several reasons can be suggested: first, the significant overprediction of the forward slip in Fig. 5.2b could stem from the *computation of the viscosity in the lubricant shear stress by the enhanced WLF law in a condition, where this law is not valid anymore*. In fact, the viscosity of the L3 lubricant was only measured up to a pressure of 500 MPa at a temperature of 75°C because it solidifies at higher pressures so that the falling ball viscometer cannot measure the lubricant viscosity anymore. While the lubricant pressure is still close to the measurement range at the entry of the roll bite, it increases significantly along the

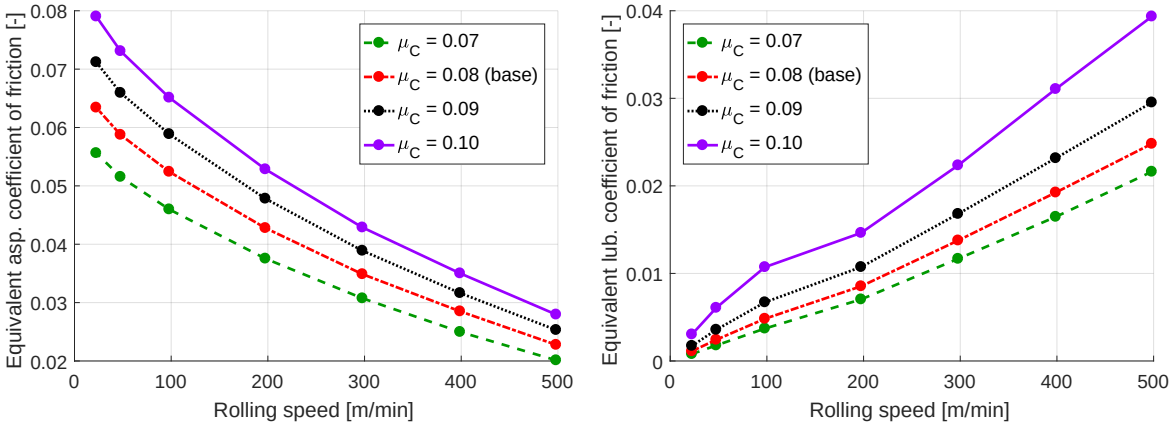

(a) Equivalent asperity coefficient of friction $\overline{\mu}_a$. **(b)** Equivalent lubricant coefficient of friction $\overline{\mu}_l$.

Figure 5.5: Influence of the boundary coefficient of friction μ_C in Test 5B (Sec. E.7) based on Tab. 5.1 with numerical parameters of Tab. 5.2 (reasonable accuracy).

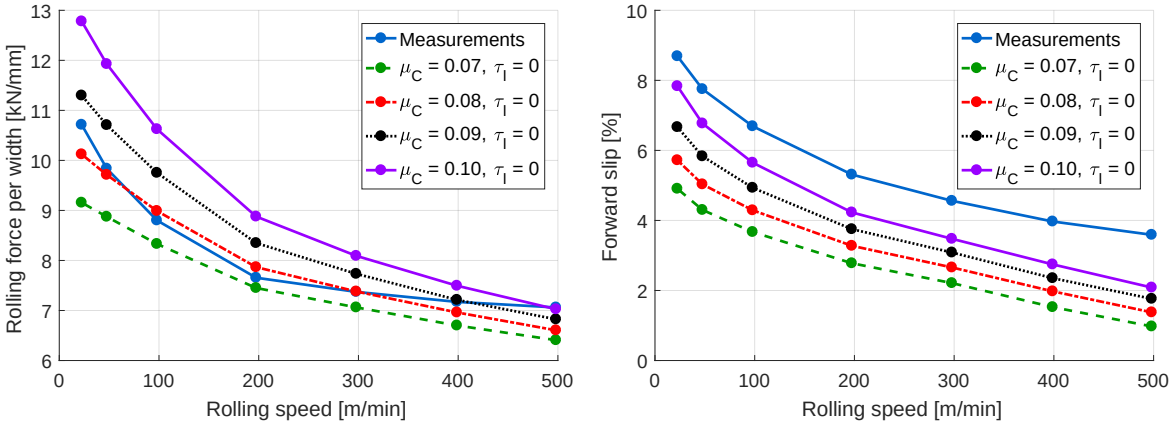

(a) Rolling force per width. **(b)** Forward slip.

Figure 5.6: Influence of the boundary coefficient of friction μ_C with zero lubricant shear stress ($\tau_l = 0$) in Test 5B (Sec. E.7) based on Tab. 5.1 with numerical parameters of Tab. 5.2 (reasonable accuracy).

roll bite as illustrated in Fig. 5.7 for the corrected case, i.e. $\tau_l = 0$. Thus, the lubricant viscosity could be overpredicted by the WLF law and the lubricant shear stress by Eq. (4.204) as well. This effect further builds on itself since viscous friction increases the rolling load, which leads to an increased interface pressure and thus an increased lubricant pressure due to their identity in most of the roll bite in the current rolling scenario (Fig. 5.7). The increased lubricant pressure then increases its viscosity and friction even more.

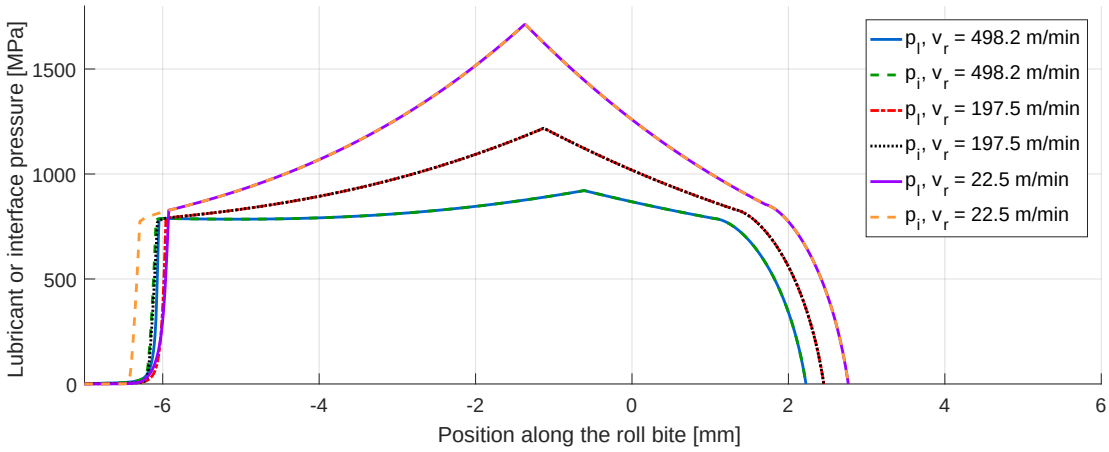

Figure 5.7: Evolution of the lubricant and interface pressures along the roll bite with zero lubricant shear stress ($\tau_l = 0$) for the different cases of Test 5B (Sec. E.7) based on Tab. 5.1 with numerical parameters of Tab. 5.2 (reasonable accuracy). Due to the high-speed hypothesis, i.e. $p_l = p_i$, curves of the lubricant and interface pressure at the same rolling speed v_r can be superimposed.

Secondly, the overprediction of the lubricant shear stress could also be explained by the assumption of the *constant lubricant temperature* in the model. In fact, it seems more realistic that this temperature *increases* along the roll bite due to the immediate proximity of the lubricant to relatively dissipative solid friction zones, due to the heat generation by plastic deformation of the strip and due to the very small lubricant quantity in the bite. One should keep in mind that the thickness of the lubricant layer has the same order of magnitude as the root-mean-square roughness, i.e. μm, in mixed lubrication. Hence, it is very thin and its heat capacity low. Since the viscosity of the lubricant is strongly reduced when its temperature increases, this viscosity and therefore the lubricant shear stress can be expected to be relatively small in the roll bite. The influence of the increasing lubricant temperature along the roll bite on the lubricant shear stresses is studied more thoroughly in Sec. 5.3.1.5.

At best, the lubricant shear stress should obviously not be neglected, especially in consideration of the small friction levels, which should be reached in cold rolling and at which the influence of viscous friction probably becomes closer and closer to solid friction. Moreover, the lubricant shear stress seems to be a fundamental component of micro-plastohydrodynamic lubrication, which occurs in lubricated cold rolling. *In the absence of a better prediction of this stress, possibly, by a full thermal model of the roll bite and the heuristic extrapolation of the laboratory measurements by the extended WLF law to compute the viscosity, it is, however, neglected since this leads to more reasonable predictions of the rolling force and the forward slip.*

One could wonder why the viscosity term in the Reynolds equation is not neglected when the lubricant shear stress is. And the answer to this question is that the viscosity in the Reynolds equation is actually neglected in the high-speed zones, since the Poiseuille term is removed from the equations. As shown in Fig. 5.7, these zones start close to the entry of the roll bite in the current rolling scenario. In consequence, it seems acceptable to set $\tau_l = 0$ in the entire roll bite while the influence of the viscosity in the Reynolds equation disappears very shortly after the entry of the roll bite[3]. Moreover, the small speed differential between the roll and strip could justify the negligence of the lubricant shear stress at low rolling speeds.

Regarding the influence of the boundary coefficient of friction μ_C in the boundary region, the rolling force and the forward slip rise with this coefficient as anticipated (Fig. 5.6). Increasing its value improves the prediction of the forward slip, while the rolling force is more and more overpredicted. It seems reasonable to further *increase μ_C as suggested in Fig. 5.6 to match the forward slip at low rolling speeds since friction is mainly determined by the boundary coefficient of friction at solid interfaces for these speeds* due to the limited load supported by the lubricant film.

5.3.1.2 Influence of the initial yield stress

After adjusting the boundary coefficient of friction to match the forward slip at low rolling speeds, it becomes clearly visible in Fig. 5.6a that the rolling force is overpredicted. This might suggest that the *yield stress* is too significant in the model since it is the parameter that impacts most strongly the rolling force as shown in Fig. 5.8a; *the more resistant the strip material, the greater the rolling load*.

Meanwhile, the *forward slip does not change significantly with the yield stress* (Fig. 5.8b). This could be explained by the insensitivity of the asperity crushing equation to the yield stress σ_Y at low rolling speeds, i.e. when the lubricant pressure is small with respect to the pressure on the asperity tops. Indeed, the pressure on the asperity tops p_a, which increases linearly with σ_Y (first-order approximation) [267, p. 25][324] is divided by $\tau_Y = \sigma_Y/\sqrt{3}$ to compute the non-dimensional effective hardness in the flattening equation (Eq. 4.90). Thus, this equation is essentially independent of σ_Y at low rolling speeds. Surprisingly, the forward slip increases for high rolling speeds with a decreasing yield stress although a decreasing equivalent coefficient of friction with a decreasing yield stress is suggested by the Wilson and Walowit formula (Eq. 2.18) due to a greater lubricant film thickness. Because of the relatively small variations, it is difficult and also not really required to trace back this observation to a physical principle. A possible explanation could be the piezoviscosity of the lubricant, which increases the viscosity and the film thickness when the pressure increases.

Before *simultaneously adjusting the boundary coefficient of friction μ_C and the initial yield stress* σ_Y^0, this approach can be *criticized* since the yield stress should be known precisely by the plane-

[3] In the model, it is obviously possibly to only set τ_l equal to zero in the high-speed zones but this small improvement was not implemented, since the transition occurs so early in the roll bite that the corresponding lubricant shear stress has only a very small influence.

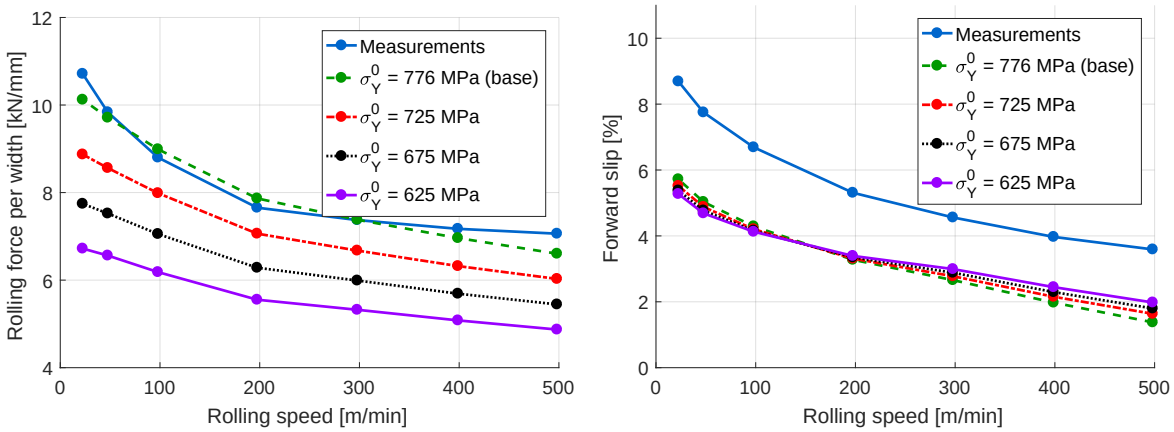

(a) Rolling force per width. **(b)** Forward slip.

Figure 5.8: Influence of the initial yield stress σ_Y^0 with zero lubricant shear stress ($\tau_l = 0$) in Test 5B (Sec. E.7) based on Tab. 5.1 with numerical parameters of Tab. 5.2 (reasonable accuracy).

strain compression test (Sec. 3.1.2). Adjusting its value therefore seems incoherent. Counter-arguments to this criticism are that the *Ludwik law* (Eq. 4.54) approximates not sufficiently well the measured hardening behavior at small effective strain (Fig. 3.3). A second counter-argument could be that the *plane-strain compression test systematically overpredicts* the theoretical yield stress, maybe due to the specific tribological conditions at the interface between the strip material and the compressive platens. Finally, *thermal softening* of the strip was not considered in the model, yet. This phenomenon could, however, physically explain the required reduction of yield stress when the boundary coefficient of friction is adjusted.

The first of the previous counter-arguments can be put to the test by defining a more general material (Sec. 4.5.2.2) in METALUB that computes the yield stress directly on the basis of the yield curve in Fig. 3.3 instead of the Ludwik law. The experimental curve in the METALUB computation was very slightly smoothed to prevent any possible convergence issues. The resulting change of the rolling force and forward slip was, however, insignificant, which is why the curves are not represented in this document.

The second counter-argument can be addressed by adjusting simultaneously the boundary Coulomb coefficient of friction μ_C and the initial yield stress σ_Y^0 to determine the best fit between the experimental measurements and the numerical results. Provided that the correction of the yield stress is then not too significant, it could be justified by a slight deviation of the yield stress in the plane-strain compression test from the theoretical yield stress. To adjust μ_C and σ_Y^0 simultaneously, μ_C was set to either 0.08, 0.10, 0.11 or 0.12, and σ_Y^0 was changed by decades until reaching the smallest mean square error for the prediction of the rolling force per width, except for the base case, which was already optimal for σ_Y^0. Boundary coefficients of friction smaller than 0.08 were not considered since they did not improve the prediction of the forward slip, while those greater than 0.12 did not improve the prediction of the rolling load. The results in Fig. 5.9 show that a significant improvement of the prediction is possible by adjusting both parameters,

i.e. the reduction of the yield stress lowers the increase of the rolling force when the boundary coefficient of friction is increased to better fit the forward slip. Since the yield stress has to be reduced relatively significantly to obtain a very good prediction of the forward slip, it seems not to be due to a slight deviation of the yield stress in the plane-strain compression test from the theoretical yield stress.

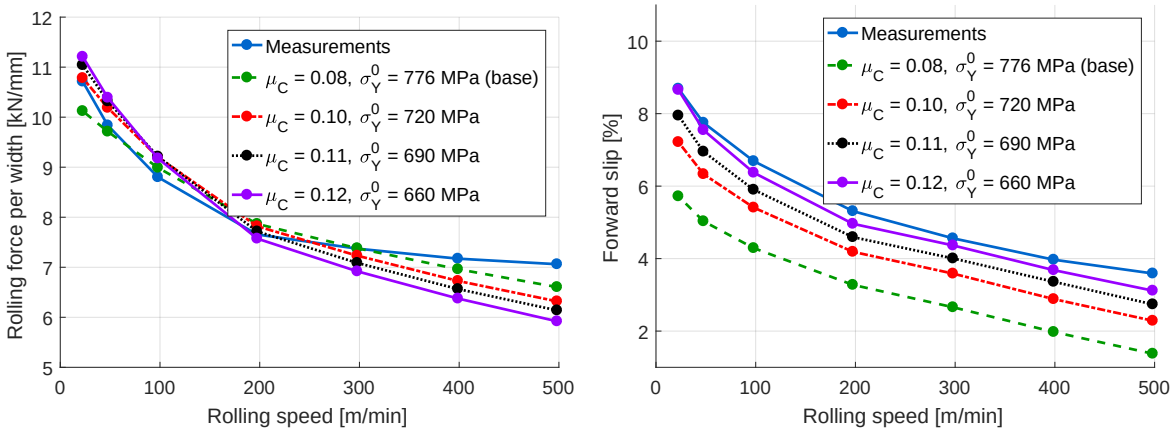

(a) Rolling force per width. **(b)** Forward slip.

Figure 5.9: Simultaneous adjustment of the boundary coefficient of friction μ_C and the initial yield stress σ_Y^0 with zero lubricant shear stress ($\tau_l = 0$) in Test 5B (Sec. E.7) based on Tab. 5.1 with numerical parameters of Tab. 5.2 (reasonable accuracy).

The remaining explanation in this context is therefore thermal softening, which will be explored in the following section.

5.3.1.3 Influence of thermal softening

The rolling load in general and the forward slip at high rolling speeds are significantly overpredicted as shown in Fig. 5.2, when only the boundary coefficient of friction is adjusted. This incongruence could be decisively reduced in the previous section by adjusting simultaneously the boundary coefficient of friction and the yield stress, as usually done in METALUB models (Sec. 5.1), in addition to neglecting the lubricant shear stress. If the measurements of the yield stress by the plane-strain compression test in Fig. 3.3 describe, however, validly the evolution of this stress with the effective deformation, another phenomenon should be able to explain the previous overprediction. This phenomenon could be *thermal softening*.

The accurate prediction of thermal softening depends on the *thermal model and the thermal dependence of the yield stress* in the current METALUB model (Chap. 4). Both of these components can certainly be improved since the thermal model does not consider heat exchanges with the roll and since the thermoplastic material behavior was not measured. Nevertheless, it should be possible to obtain a first estimation of the thermal influence.

First, Fig. 5.10 shows the *temperature evolution of the strip along the roll bite* in the base case, i.e. without thermal softening, for the different rolling scenarios in Test 5B (Tab. E.21). It

can be seen that the temperature contribution due to friction is far smaller than that due to plastic deformation and that it decreases with the rolling speed due to the reduction of friction by lubrication. Moreover, the final total temperature increase lies within the measured limits (Tab. E.21). It is, however, clear that heat transfers to the roll cannot be neglected since the computed temperature increase is almost identical for all rolling speeds, which is not true for the measurements (Tab. E.21). In fact, at low rolling speeds, the real final temperature of the strip can be expected to be smaller than the predicted one due to increased cooling of the roll per length of rolled strip.

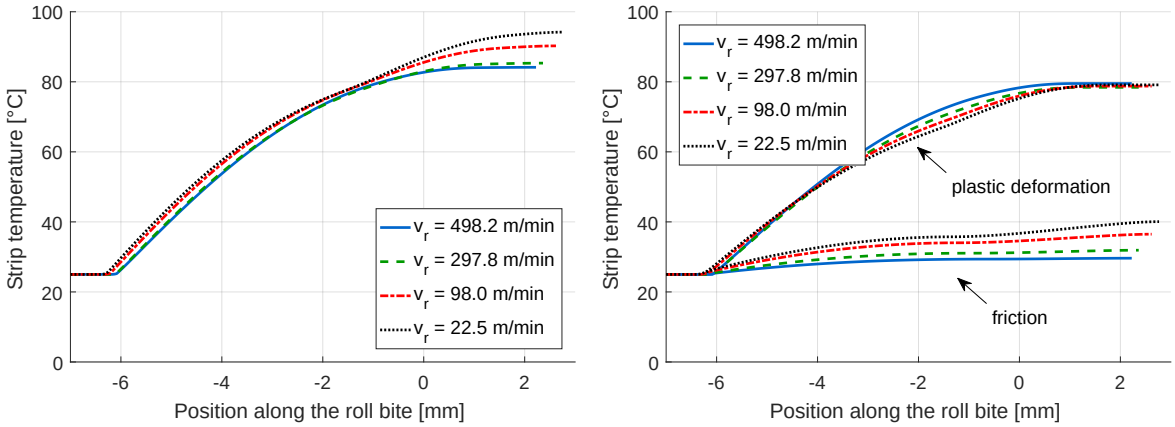

(a) Total temperature increase.

(b) Temperature increases respectively due to plastic deformation and friction.

Figure 5.10: Temperature evolution along the roll bite in Test 5B (Sec. E.7) based on Tab. 5.1 with numerical parameters of Tab. 5.2 (reasonable accuracy).

The increase of the strip temperature can be included in the computation of the yield stress via the thermoplastic component of the Johnson-Cook law (Eq. 4.62). Fig. 5.11a shows that the *influence of thermoplasticity is similar to the reduction of the yield stress*. In fact, thermplasticity reduces the rolling force like the yield stress (Fig. 5.8a), while the forward slip is almost unchanged (Fig. 5.11b) as shown previously in Fig. 5.8b.

If the *boundary coefficient of friction is adjusted simultaneously with the thermoplasticity coefficient*, a relatively good agreement with the experimental results can be obtained as illustrated in Fig. 5.12. To determine the values of the parameters in these figures, the thermoplasticity coefficient m was adjusted by increments of 0.05 for $\mu_C = 0.10$, 0.11 and 0.12 to minimize the root-mean-square error of the rolling load prediction[4]. The values of m for the best predictions, i.e. 0.55 or 0.65, are actually realistic values [161, 349]. This is the ***first time that the physical parameters are adjusted in a physically consistent way*** in the context of METALUB computations, i.e. without manually reducing the initial yield stress[5].

[4]No improvement could be obtained by thermoplasticity for $\mu_C = 0.08$.

[5]Although one could argue that one parameter was replaced by another, the new model computes the yield stress as a function of the temperature along the roll bite, so that the model seems more predictive, especially, if a full thermal model was added in the future and if the thermal softening coefficient was measured.

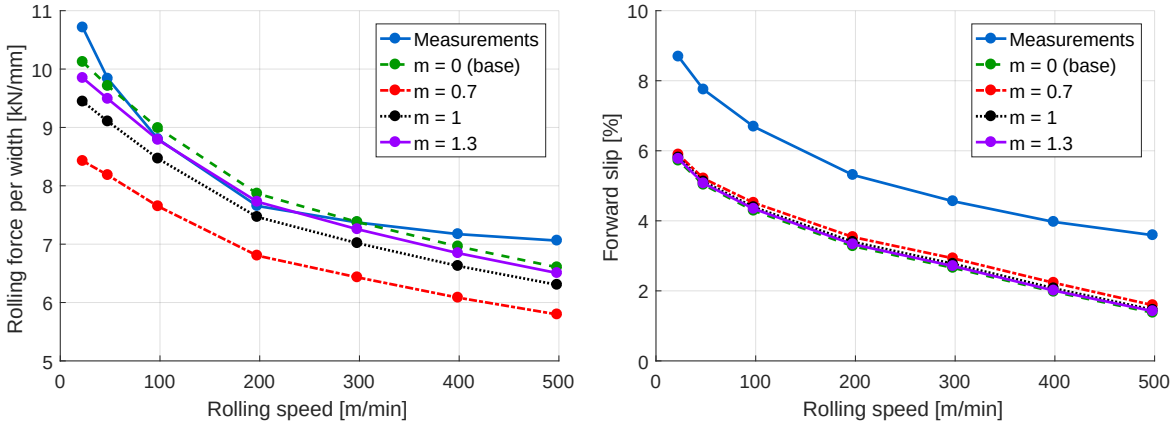

(a) Rolling force per width. **(b)** Forward slip.

Figure 5.11: Influence of the thermal softening coefficient m (Eq. 4.62) with zero lubricant shear stress ($\tau_l = 0$) in Test 5B (Sec. E.7) based on Tab. 5.1 with numerical parameters of Tab. 5.2 (reasonable accuracy).

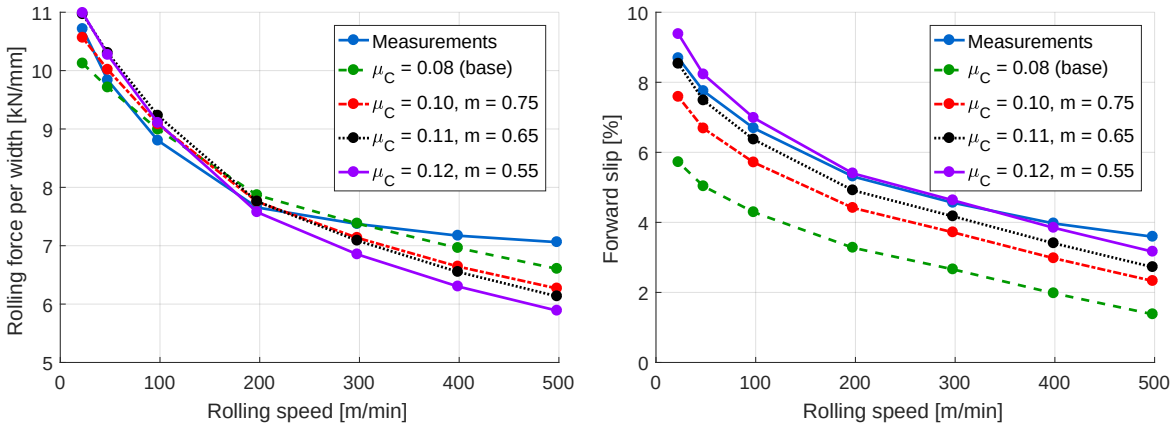

(a) Rolling force per width. **(b)** Forward slip.

Figure 5.12: Influence of the boundary coefficient of friction μ_C and the thermal softening coefficient m (Eq. 4.62) with zero lubricant shear stress ($\tau_l = 0$) in Test 5B (Sec. E.7) based on Tab. 5.1 with numerical parameters of Tab. 5.2 (reasonable accuracy).

One might now wonder whether the combined adjustment of the coefficients of friction and thermoplasticity improves the predictions by the combined adjustment of the boundary coefficient of friction and the initial yield stress. Fig. 5.13 shows that both predictions are relatively accurate, which suggests that the *manual reduction of the yield stress in the past can be explained by thermal softening*.

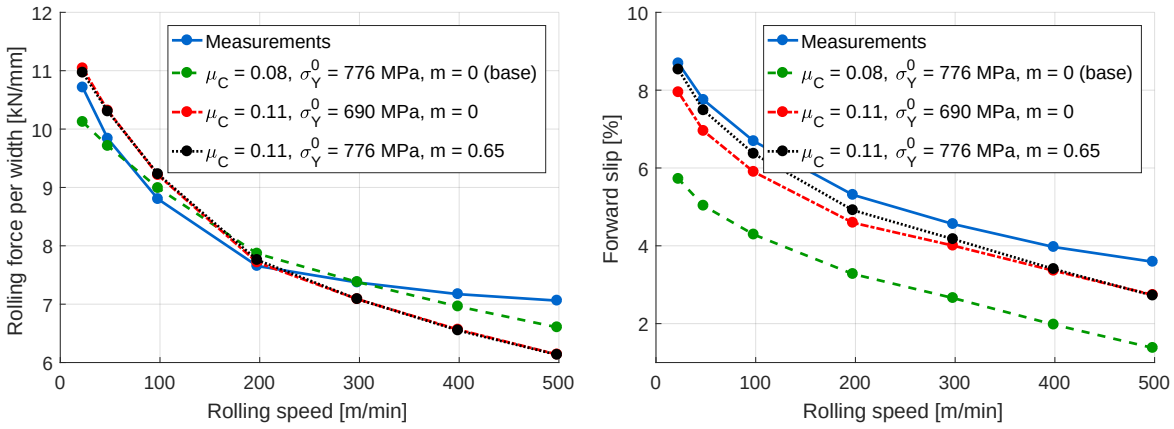

(a) Rolling force per width. **(b)** Forward slip.

Figure 5.13: Best predictions, either by adjusting the boundary coefficient of friction μ_C and the yield stress σ_Y^0, or the boundary coefficient of friction μ_C and the thermal softening coefficient m with zero lubricant shear stress ($\tau_l = 0$) in Test 5B (Sec. E.7) based on Tab. 5.1 with numerical parameters of Tab. 5.2 (reasonable accuracy).

The *underprediction of the rolling force* is present in both models and various mechanisms could explain this observation: strain rate hardening, the increasing lubricant temperature at the bite entry due to the gradual heating of the roll with rolling speed, ... These influences are studied in the following sections.

5.3.1.4 Influence of viscoplasticity

Strain rates in cold rolling are relatively significant, especially at high rolling speeds, as shown in Fig. 5.14. The equivalent rate reaches a maximum close to the entry of the roll bite due to the maximum reduction speed in this region.

Despite these important strain rates, improving the predictions by the inclusion of viscoplasticity does not seem possible. In fact, Fig. 5.15a shows that the *rolling force rises by an almost equal amount for each rolling speed* when the viscoplasticity coefficient is incremented, although one would expect it to increase more and more significantly due to viscoplasticity when the rolling speed increases. This can be explained by the decreasing influence of the yield stress on the rolling force in this scenario, when the rolling speed increases. While the material resistance increases due to viscoplasticity, when the rolling speed increases, the length of the roll bite decreases due to the significant reduction of friction by hydrodynamic lubrication. And since, the rolling force per width is approximately the product of the yield stress and the length of the

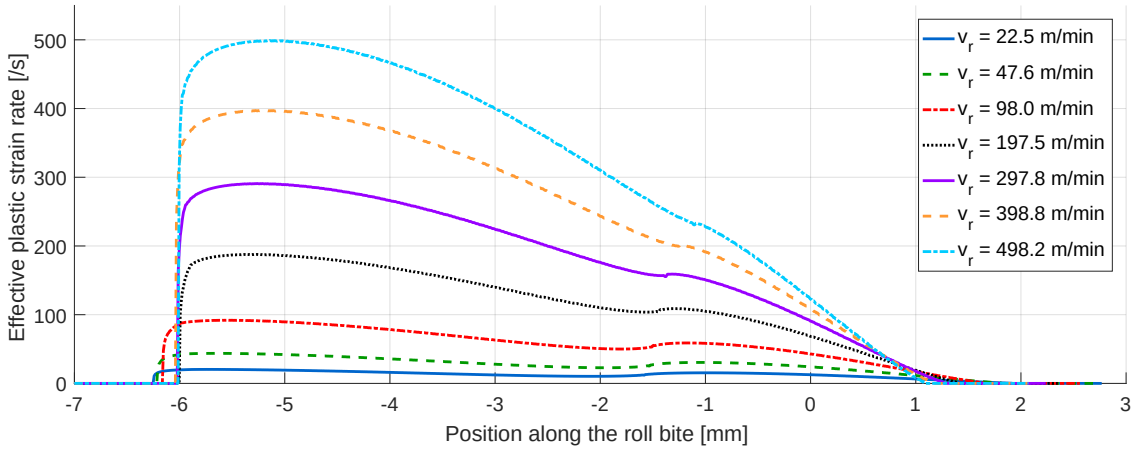

Figure 5.14: Evolution of the effective plastic strain rate along the roll bite for the different rolling speeds after the adjustment of the boundary coefficient of friction $\mu_C = 0.11$ and the thermoplasticity coefficient $m = 0.65$ with zero lubricant shear stress ($\tau_l = 0$) in Test 5B (Sec. E.7) based on Tab. 5.1 with numerical parameters of Tab. 5.2 (reasonable accuracy).

roll bite (Eqs. 3.11, 3.12 and 4.296), the influence of the yield stress decreases, when the rolling speed increases. Hence, a small yield stress increment at low speeds leads to almost the same rolling force increment as a greater yield stress increment at higher speeds in this specific rolling scenario.

Furthermore, the prediction of the forward slip does not really improve, when viscoplasticity is included in the model as shown in Fig. 5.15b. In fact, the yield stress has a small influence on the forward slip, which rather depends on friction.

Simultaneously adjusting the thermoplastic and viscoplastic parameters m and η_s in Eqs. (4.60) and (4.62) is certainly possible but it becomes more and more evident that real improvements and well-grounded conclusions are only possible if the *thermo-viscoplastic material parameters* m and η_s are *measured*, and if a *full thermal model* is included in the existing METALUB model.

5.3.1.5 Influence of the lubricant temperature

Besides the temperature of the strip, the temperature of the lubricant also has an important influence on the results as shown in Fig. 5.16. In fact, *increasing the isothermal lubricant temperature (in the model) increases the rolling force and the forward slip* since friction increases by the reduction of the lubricant film thickness with temperature due to the reduced viscosity of the lubricant. Slightly increasing the lubricant temperature in the prediction to 65°C improves it, which is why this value is selected.

Nevertheless, it is unclear whether choosing the same lubricant temperature at each rolling speed is actually a reasonable choice: in fact, the temperature of the roll increases with the rolling speed as suggested by the increasing temperature of the strip after the bite (see T_{out} in Tab. E.21). Moreover, the duration of heat exchanges decreases with the rolling speed. For instance, if the

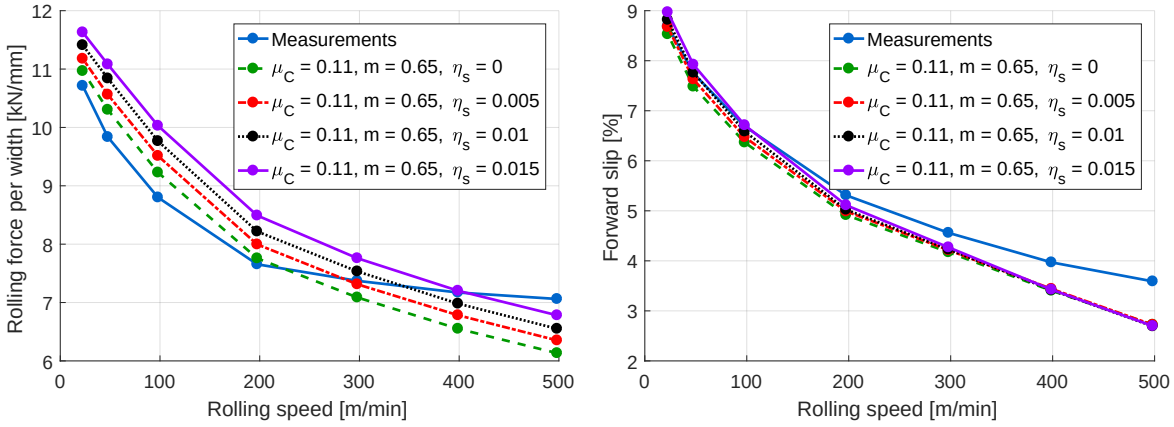

(a) Rolling force per width. **(b)** Forward slip.

Figure 5.15: Influence of viscoplasticity coefficient η_s after the adjustment of the boundary coefficient of friction $\mu_C = 0.11$ and the thermoplasticity coefficient $m = 0.65$ with zero lubricant shear stress ($\tau_l = 0$) in Test 5B (Sec. E.7) based on Tab. 5.1 with numerical parameters of Tab. 5.2 (reasonable accuracy).

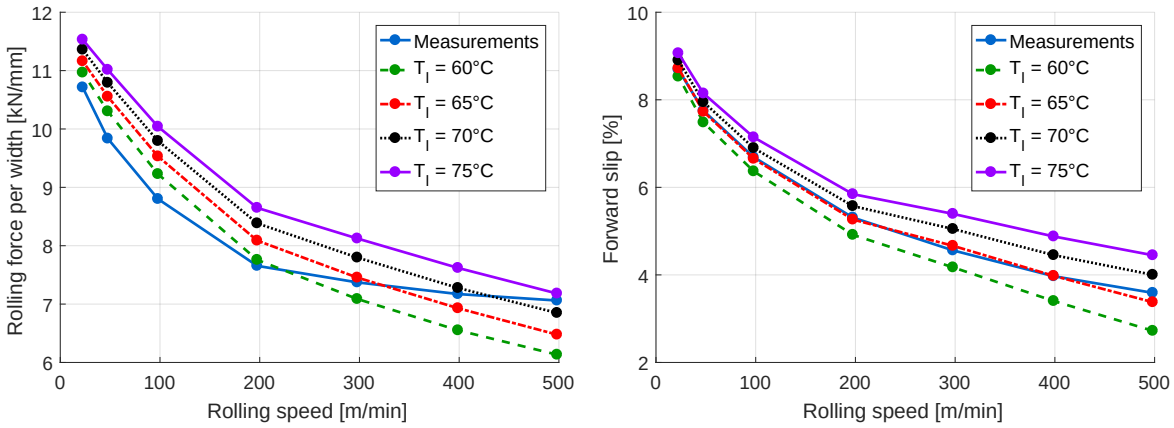

(a) Rolling force per width. **(b)** Forward slip.

Figure 5.16: Influence of the lubricant temperature T_l after the adjustment of the boundary coefficient of friction $\mu_C = 0.11$ and the thermoplasticity coefficient $m = 0.65$ with zero lubricant shear stress ($\tau_l = 0$) in Test 5B (Sec. E.7) based on Tab. 5.1 with numerical parameters of Tab. 5.2 (reasonable accuracy).

lubricant is applied directly about 1.5 m before the bite at 60°C, it can exchange heat with the 25°C cold strip at most during 4 s (22.5 m/min) and at least during 0.18 s (498.2 m/min). Depending on the lubricant quantity and the heat exchanges with the rolls and the strip, it can thus be expected that the lubricant is either colder or warmer than 60°C at the entry of the bite. The resulting influence on the rolling force and the forward slip could be tested numerically by imposing different lubricant temperatures at different rolling speeds, but the conclusion can already be anticipated on the basis of Fig. 5.16. To avoid fitting unknown parameters for each rolling case and to develop an even more predictive model, it becomes again evident that METALUB should be extended by a *full thermal model*, which allows to compute the temperature of the lubricant at the entry of the roll bite and along it.

Before concluding this section about the calibration of the most significant physical parameters, the previous *hypothesis about the negligence of the lubricant shear stress*, i.e. $\tau_l = 0$, can be analyzed more thoroughly. As mentioned above, the lubricant shear stress was neglected since it led to increasingly wrong predictions at higher rolling speeds (Sec. 5.3.1.1). Besides the application of the viscosity law in a condition, in which it is possibly not valid anymore, the isothermality of the lubricant in the METALUB model was suggested to be a reason of these wrong predictions. This hypothesis can be tested by introducing several simplified thermal scenarios for the lubricant, as explained in Sec. 4.9.3:

- *Isothermal* reference case: $T_l = 60°C$;
- The lubricant temperature is equal to its initial temperature and becomes equal to that of the strip, when the *strip* temperature becomes *greater* than that of the lubricant:

$$T_l = \begin{cases} 60°C & \text{, if } T_s < 60°C \\ T_s & \text{, otherwise.} \end{cases} \tag{5.3}$$

- The lubricant temperature increases due to local *friction*:

$$\frac{\partial T_l}{\partial x} = \frac{\beta_l}{\rho_l c_l v_s} \frac{\tau_i (v_r - v_s)}{h_t} \tag{5.4}$$

  where the density ρ_l and the specific heat capacity c_l of the lubricant are equal to 910 kg/m^3 (Sec. 3.1.3) and 1670 J/(kg.°C) [328], respectively. A percentage $\beta_l = 0.1\%$ or 0.2% of the friction energy is transformed into thermal energy of the lubricant. This percentage was determined to obtain a reasonable temperature increase at the exit of the bite according to Tab. E.21 (see Fig. 5.18a as explained later on), when the initial temperature of the lubricant is 60°C. A better prediction seems not to be possible without a full thermal model.

Since, the previous scenarios are introduced to possibly explain the negligence of the lubricant shear stress in the model, the *computation of this stress τ_l was added again to it*, instead of assuming $\tau_l = 0$.

The resulting predictions of the rolling loads and forward slips in Test 5B are represented in Fig. 5.17 for the different temperature scenarios. This figure clearly shows that *considering the*

increase of the lubricant temperature due to friction improves the predictions, especially those of the forward slip. This is not true for the second scenario, i.e. $T_l = 60°C$ or T_s, probably since only the negative lubricant shear stress is reduced significantly in amplitude, as shown hereafter (Fig. 5.18c).

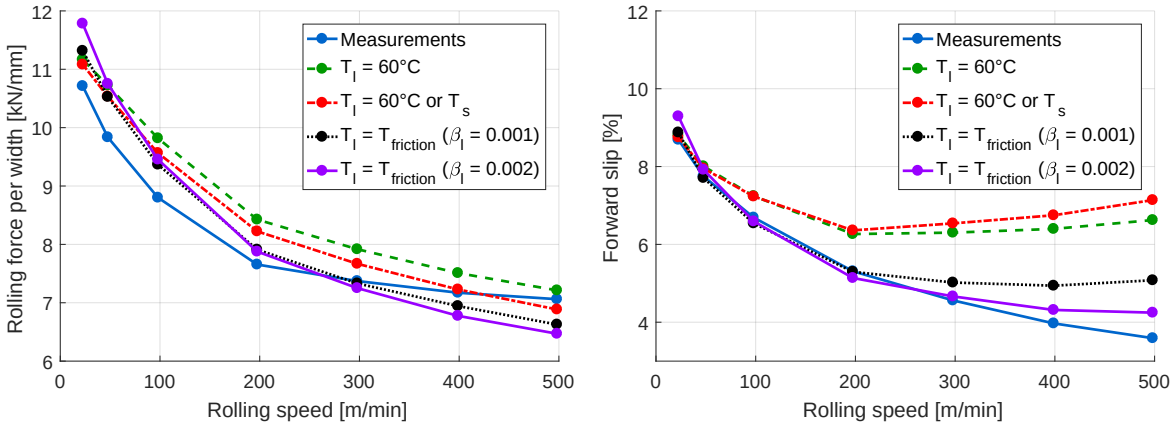

(a) Rolling force per width. **(b)** Forward slip.

Figure 5.17: Influence of the lubricant temperature scenario after the adjustment of the boundary coefficient of friction $\mu_C = 0.11$ and the thermoplasticity coefficient $m = 0.65$ with non-zero lubricant shear stress ($\tau_l \neq 0$) in Test 5B (Sec. E.7) based on Tab. 5.1 with numerical parameters of Tab. 5.2 (reasonable accuracy).

More precisely, Fig. 5.18 demonstrates that the previous improvements are due to the reduction of the lubricant shear stress by the heating of the lubricant in the bite. In fact, Fig. 5.18a shows the variation of the lubricant temperature along the roll bite. In all scenarios, it is initially equal to 60°C and it increases then sooner or later. In consequence, the viscosity of the lubricant decreases (Fig. 5.18b) and its shear stress, too (Fig. 5.18c). The viscosity in the isothermal case is significantly extrapolated with respect to the measured range since the highest viscosity in the experimental data (Fig. 3.5) is only equal to about 10 Pa.s. *Hence, neglecting the lubricant shear stress in the roll bite due to the decrease of viscosity by the temperature seems to be a reasonable hypothesis, in the absence of better temperature predictions*.

It is also important to notice that the mean film thickness is essentially independent of the temperature increase of the lubricant in the roll bite (Fig. 5.18d). This suggests that this thickness only depends on the lubricant temperature at the entry of the bite via the lubricant viscosity.

5.3.1.6 Intermediate conclusion

In the previous sections, the *most significant physical parameters* were adjusted to predict the experimental measurements as accurately as possible. These parameters are summarized in Tab. 5.4 for Test 5B-4 after combining Tab. 5.1 with the adjustments $\mu_C = 0.11$, $m = 0.65$, $T_l = 65°C$, $\tau_l = 0$ MPa and the numerical parameters of Tab. 5.2 (reasonable accuracy).

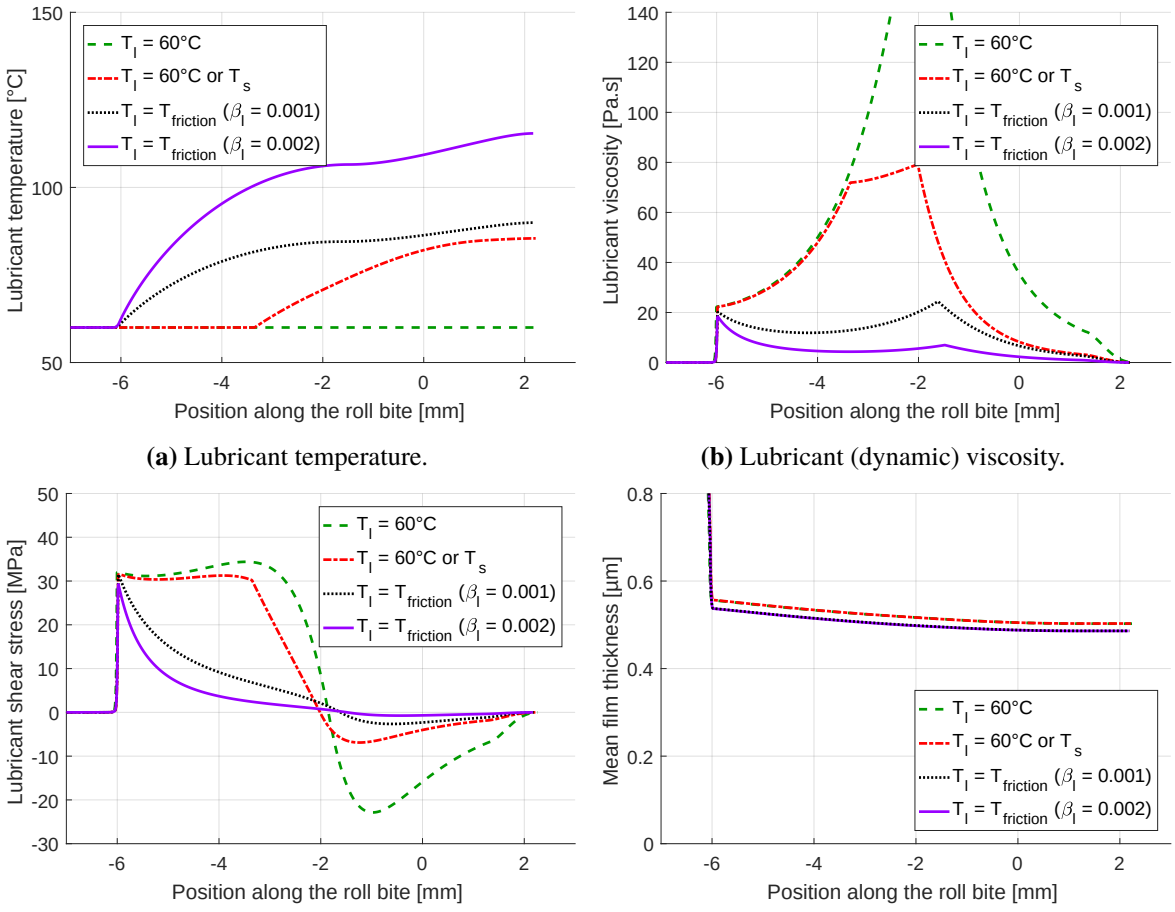

(a) Lubricant temperature.

(b) Lubricant (dynamic) viscosity.

(c) Lubricant shear stress.

(d) Mean film thickness.

Figure 5.18: Influence of the lubricant temperature scenario after the adjustment of the boundary coefficient of friction $\mu_C = 0.11$ and the thermoplasticity coefficient $m = 0.65$ with non-zero lubricant shear stress ($\tau_l \neq 0$) in Test 5B-2 (Sec. E.7, $v_r = 398.8$ m/min) based on Tab. 5.1 with numerical parameters of Tab. 5.2 (reasonable accuracy).

Entity	Parameter	Value	Unit
Roll bite	Type	Full-flooded lub.	-
	Heating by friction	On	-
	Heating by plastic deformation	On	-
Strip material	Name	S2	-
	E_s	210000	MPa
	ν_s	0.3	-
	Law	Ludwik	-
	Viscoplasticity	Off	-
	Thermoplasticity	**On**	-
	A	776	MPa
	B	147	MPa
	n	1.52	-
	m	**0.65**	-
	$\overline{\epsilon}_0^p$	0	-
	ρ_s	$7.850 \cdot 10^{-9}$ [7850]	t/mm^3 [kg/m^3]
	c_s	$500 \cdot 10^6$ [500]	N.mm/(t.°C) [J/(kg.°C)]
	β_s	0.9	-
Strip	t_{in}	0.75	mm
	t_{out}	0.584	mm
	σ_{in}	122.0	MPa
	σ_{out}	184.3	MPa
	$T_{s,\text{in}}$	25	°C
Lubricant	Name	L3	-
	Law	WLF (enhanced)	-
	A_1	49.64	°C
	A_2	0.000365	MPa^{-1}
	b_1	0.00578	MPa^{-1}
	b_2	−0.565	-
	C_1	16.11	-
	C_2	26.00	°C
	η_g	10^6	MPa.s
	$T_g(0)$	−85.96	°C
	T_l	**65** (constant)	°C
Interface	Asperity profile	Christensen	-
	$R_{q,r}$	0.773	μm
	$R_{q,s}$	0.123	μm
	$\overline{l}$	51.28	μm
	Flattening equation	Wilson-Sheu	-
	γ	9	-
	Friction law	Coulomb-Tresca	-
	μ_C	**0.11**	-
	μ_T	1	-
	Flow factors ϕ_x and ϕ_s	On	-
	Shear stress factors	Off	-
	τ_l	**0**	MPa
Roll	Deformation method	Meindl (full)	-
	Deformation mode	Plane strain	-
	R_0	195.5	mm
	v_r	3291	mm/s
	E_r	210000	MPa
	ν_r	0.3	-
	x_{12}	**−10**	mm
	x_{23}	**5**	mm
	$\Delta\theta_1$	**1**	°
	$\Delta\theta_2$	$\mathbf{5 \cdot 10^{-3}}$	°
	$\Delta\theta_3$	**1**	°
	Relaxation method	Constant	-
	$w^{(0)}$	**0.5**	-
Other numerical parameters	Integration method	RK4	-
	x_{12}	**−10**	mm
	Δx_1	**1**	mm
	Δx_2	$\mathbf{10^{-3}}$	mm
	tol_Q	$\mathbf{10^{-4}}$	-
	$\text{tol}_{\sigma_{\text{out}}}$	$\mathbf{10^{-3}}$	-
	$\text{tol}_{t_{\text{out}}}$	$\mathbf{10^{-4}}$	-
	tol_R	$\mathbf{10^{-6}}$	-
	$\Delta x_{\text{extr},1}$	**1**	mm
	$\Delta x_{\text{extr},2}$	$\mathbf{10^{-2}}$	mm
	CIEFS step	Off	-

Table 5.4: Model parameters of Test 5B-4 (Chap. 3 and Sec. E.7) after adjustment of numerical parameters and most significant physical parameters (bold).

The corresponding results in Fig. 5.19 are very *accurate*, especially the prediction of the forward slip, although differences still exist. On the one hand, the overprediction of the rolling force at low rolling speeds could be due to the estimation of the lubricant temperature at the entry of the bite. As stated previously (Sec. 5.3.1.5), it is possible that the lubricant temperature is lower than 65°C at low rolling speeds because of heat exchanges with the rolls and the strip. A lower lubricant temperature would result in a thicker lubricant film, and thus, less friction and a smaller rolling force. This would obviously also impact the forward slip, whose adjustment is probably possible by a corresponding compensation via another parameter. On the other hand, the underprediction of the rolling force at higher rolling speeds could be explained by greater lubricant temperatures than 65°C due to the heating of the rolls.

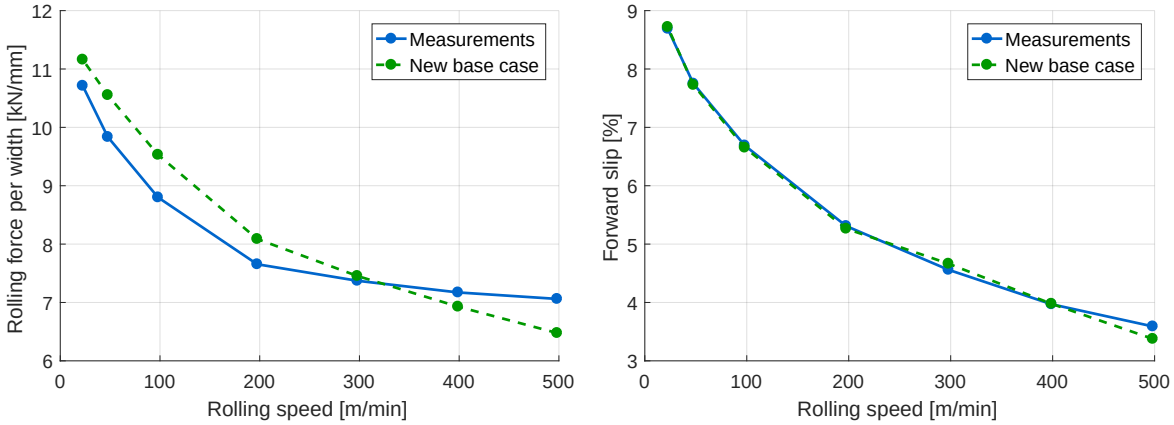

(a) Rolling force per width.

(b) Forward slip.

Figure 5.19: Best prediction (new base case) of Test 5B (Chap. 3 and Sec. E.7) based on Tab. 5.4 with v_r, t_{out}, σ_{in} and σ_{out} of Tab. E.21.

Furthermore, it is absolutely possible that some *parameter adjustments* do not correspond to their actual values. For instance, the thermoplasticity coefficient m was purely numerically adjusted without any measured values of the analyzed material, except for those in the literature of similar materials. Eliminating these shortcomings requires measuring material properties, like the thermoplasticity coefficient, the viscoplasticity coefficient, as well as developing a more advanced thermal model, which allows to compute the temperature of the lubricant at the entry of the roll bite and along it.

It is obvious that more parameters could have been adjusted in the previous sections, but the analysis becomes increasingly complex for increasingly smaller improvements of the predictions. Hence, the *influence of these remaining parameters will only be illustrated in the following sections* based on the best adjustment of the previous parameters (new base case in Tab. 5.4) to understand the importance of these parameters in the model.

5.3.2 Further influence studies

Further influence studies are presented in the following sections to even better understand the predictive capabilities and the limitations of the METALUB model.

5.3.2.1 Importance of accurate measurements

In Test 5B, only the influence of the rolling speed was tried to be studied experimentally while keeping all other operating parameters constant. Since *some operating parameters, besides the rolling speed, changed, however, slightly from one rolling scenario to another* as shown in Tab. E.21, the variations of the final thickness t_{out}, the back tension σ_{in} and front tension σ_{out} were also included in the computations to have modeling conditions that are as close as possible to the real conditions.

In the past, Carretta already reproduced some of the experimental results in Chap. 3 by his version of METALUB (not published, see Sec. 5.3.2.2) but he did *not take the previous fluctuations into account*. Hence, it is interesting to know to what extent this hypothesis impacts the predictions. Thus, if the elongation e_x is equal to 30% for all rolling speeds, and if the back and front tensions are equal to their respective averages in Tab. E.21, then t_{out} = 0.577 mm, σ_{in} = 118.1 MPa and σ_{out} = 187.0 MPa.

Figure 5.20 compares the results with real and ideal operating parameters t_{out}, σ_{in} and σ_{out}. It is clearly visible that *choosing the ideal parameters is an acceptable hypothesis, which should, however, not be applied when further measurement details are available*, e.g. at v_r = 197.5 m/min where the measured final thickness of 0.584 mm is quite different from 0.577 mm.

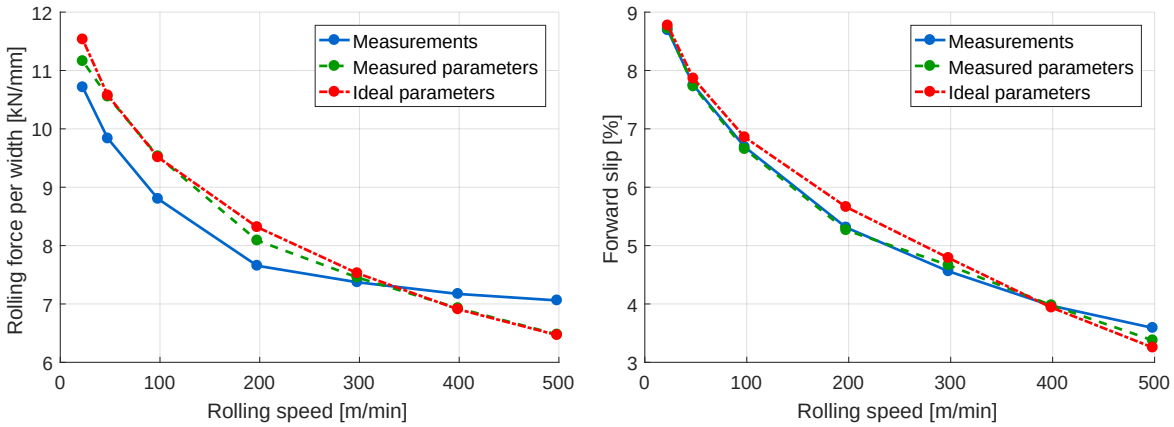

(a) Rolling force per width.

(b) Forward slip.

Figure 5.20: Influence of ideal operating parameter hypothesis in Test 5B (Chap. 3 and Sec. E.7) based on Tab. 5.4. In the case with measured parameters, t_{out}, σ_{in} and σ_{out} are provided in Tab. E.21, while they are respectively equal to 0.577 mm, 118.1 MPa and 187.0 MPa in the case with ideal parameters.

5.3.2.2 Comparison with old results by Carretta

As mentioned in the previous section, *Carretta* already analyzed Test 5B of the test campaign at Maizières-lès-Metz with his version of METALUB but he never published the results. In this section, these results will be *confronted to our results* in order to determine if the predictions were improved by the explanations, which were developed in this thesis.

Carretta used the values in Tab. 5.5 in his computations, which differ from the current values: (1) He assumed that the final thickness t_{out}, the back tension σ_{in} and the front tension σ_{out} are equal in all scenarios. It was, however, already shown in Fig. 5.20 that the results can be relatively different, if the values of the parameters do not correspond to those that were measured. (2) Carretta assumed that the asperities make an angle of about 8° with the mean line, if they are represented as triangular asperities. Hence, the half spacing $\bar{l}$ between asperities in his computations is about 5 times smaller than the spacing, which was chosen based on the measured peak count R_{pc}. (3) The lubricant shear stress was not neglected in Carretta's computations although the lubricant temperature was assumed to be constant along the roll bite. (4) Finally, he reduced artificially the yield stress of the strip material instead of considering thermal softening. (5) In consequence to these changes with respect to our model, different values of the boundary coefficient of friction μ_C were determined by Carretta.

Parameters	Carretta	Boemer (new)	Units
t_{out}	0.577	Tab. E.21	mm
σ_{in}	120	Tab. E.21	MPa
σ_{out}	185	Tab. E.21	MPa
$R_{q,r}$	/ (0)	0.773	μm
$R_{q,s}$	/ (0.78235)	0.123	μm
R_q	0.78235	0.783	μm
$\bar{l}$	9.4249	51.28	μm
Hardening law	Smatch (Eq. 4.56)	Ludwik (Eq. 4.54)	-
Hardening parameters	Tab. 3.3a with $E = -100$	Tab. 3.3b	MPa
Thermal softening	No	$m = 0.65$ (Eq. 4.62)	-
Lubricant temperature	60°C	65°C	-
μ_C	0.125	0.11	-
Roll flat. method	Jortner	Meindl	-

Table 5.5: Parameters in Carretta's and Boemer's computations of Test 5B (Chap. 3 and Sec. E.7), which are different.

Fig. 5.21 clearly shows that ***Carretta's results were significantly improved***. While the new predictions of the rolling load have a similar or slightly worse accuracy than Carretta's results, the new predictions of the forward slip are decisively more accurate than the old predictions. It would certainly be possible to adjust our parameters in such a way to better fit the rolling load than in Carretta's results but a good average prediction of the rolling load and the forward slip was preferred instead of a good prediction of just one of them. The improvement is mostly due to

the negligence of the lubricant shear stress, which was analyzed in Sec. 5.3.1.5, and the inclusion of thermal softening instead of the artificial reduction of the yield stress.

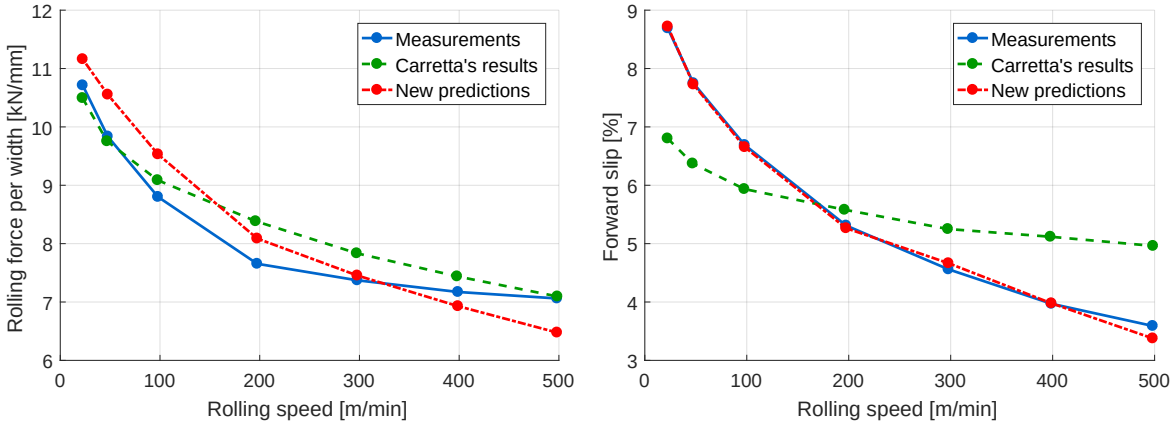

(a) Rolling force per width. **(b)** Forward slip.

Figure 5.21: Comparison of Carretta's results (with his version of METALUB) and our results (Tab. 5.4 with v_r, t_{out}, σ_{in} and σ_{out} of Tab. E.21) for the Test 5B (Chap. 3 and Sec. E.7).

5.3.2.3 Influence of the roll flattening model

Several *roll flattening models* were introduced in the METALUB model. Their influence is shown in Fig. 5.22 and the corresponding roll profiles of Test 5B-6 (Tab. E.21, v_r = 47.6 m/min) in Fig. 5.23.

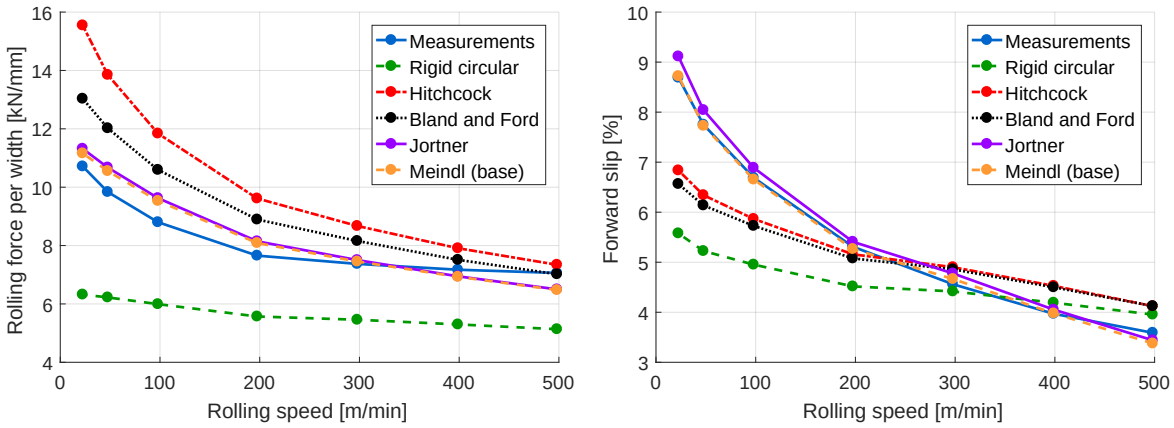

(a) Rolling force per width. **(b)** Forward slip.

Figure 5.22: Influence of the roll flattening model in Test 5B (Chap. 3 and Sec. E.7) based on Tab. 5.4 with v_r, t_{out}, σ_{in} and σ_{out} of Tab. E.21.

The comparison of the results, which were obtained by the rigid circular roll, with the other results in Fig. 5.22 clearly shows that *a roll flattening model is required* in the current rolling

scenario to predict the rolling load and forward slip relatively accurately. In fact, roll flattening *increases the rolling load by the extension of the contact arc* between the roll and the strip as illustrated in Fig. 5.23. Hence, Hitchcock's model and even more its extension, i.e. Bland and Ford's model, improve the previous prediction, that was obtained with a rigid circular roll. While the roll is circular in these models, the *effective flattening with local indentation by Jortner's and Meindl's methods further improves the prediction*. The results by these latter methods are essentially identical since the interface shear stress is relatively small with respect to the interface pressure as shown in Fig. 5.24.

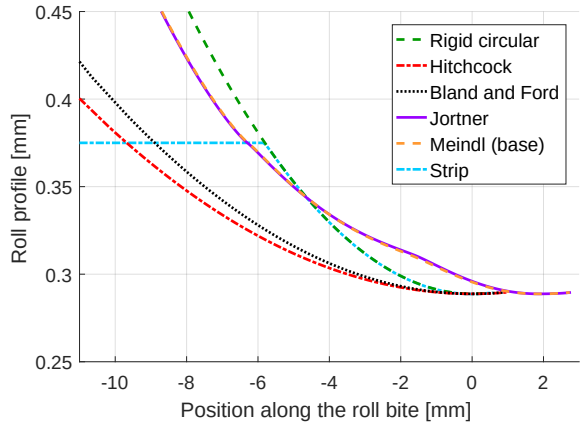

Figure 5.23: Final roll profiles of the different roll flattening models and the initial strip profile in Test 5B-6 (Chap. 3 and Sec. E.7) based on Tab. 5.4 with v_r, t_{out}, σ_{in} and σ_{out} of Tab. E.21.

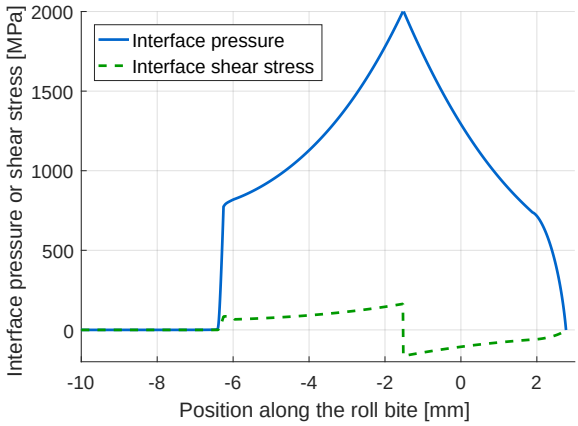

Figure 5.24: Interface pressure p_i and shear stress τ_i along the roll bite in Test 5B-6 (Chap. 3 and Sec. E.7) based on Tab. 5.4 (Meindl) with v_r, t_{out}, σ_{in} and σ_{out} of Tab. E.21.

Finally, the *influence of the roll deformation modes* (Sec. 4.6.4) was assessed with Meindl's method. According to Krimpelstätter [171, p. 120], Meindl [220, p. 135] claims that the generalized plane-strain state is the most realistic deformation mode since work rolls are bodies with axially constant strain and lateral free surfaces. Fig. 5.25 shows that in the current rolling scenario, the choice of either the generalized plane-strain state or the classical plane-strain state has no significant importance. It is, however, surprising that the plane-stress formulation of Meindl's method was used by Dbouk et al. [90, 89], although the classical deformation hypothesis in cold rolling is the plane-strain state [276, p. 246]. As illustrated in Fig. 5.25, this choice has, fortunately, no significant influence on the results, at least in the current scenario, but it is clearly visible. Choosing the plane-stress state rather than the plane-strain state increases the rolling load and forward slip due to the increased flattening of the roll, which is not kinematically constrained anymore along its axis.

5.3.2.4 Dry smooth and dry rough rolling models

Previously, asperity flattening and lubrication have mainly been included in the model via the asperity flattening equation by Wilson and Sheu, the Reynolds equation and the sharing law. One

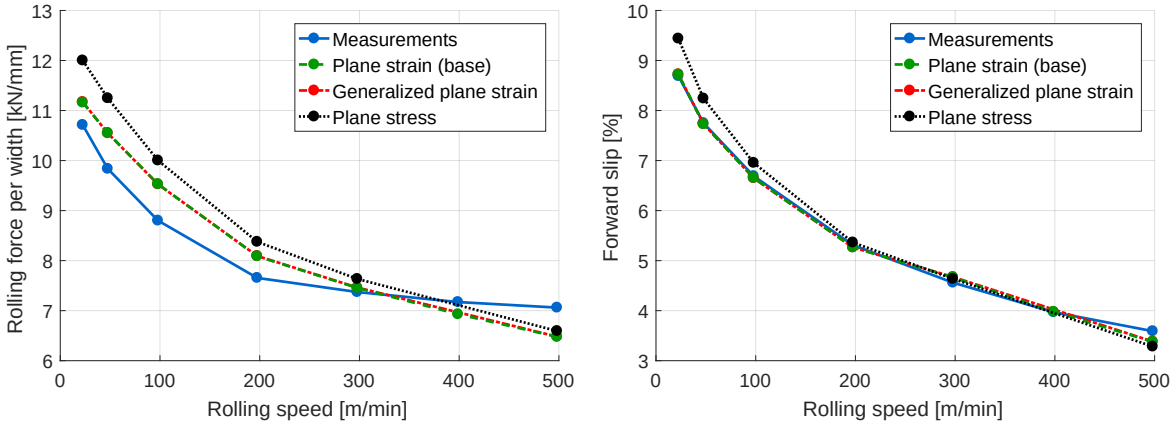

(a) Rolling force per width.

(b) Forward slip.

Figure 5.25: Influence of the roll deformation mode of Meindl's roll flattening model in Test 5B (Chap. 3 and Sec. E.7) based on Tab. 5.4 with v_r, t_{out}, σ_{in} and σ_{out} of Tab. E.21.

might wonder *how accurate a prediction can be, if asperity flattening and lubrication are not considered*.

As anticipated, Fig. 5.26 shows that the *rolling load is significantly reduced by lubrication due to the reduced friction*. To highlight this observation, the dry rolling cases were also represented with a reduced boundary coefficient of friction, i.e. $\mu_C = 0.07$. Furthermore, due to the absence of the lubricant in the dry scenarios, the reduction of the rolling load with the rolling speed by the hydrodynamic effect can obviously not be observed in these scenarios. The remaining fluctuations are due to slightly changing operating conditions from one rolling speed to another (Tab. E.21). In fact, if only the rolling speed was changed and not also the final thickness, the back tension and the front tension, the prediction of the rolling load and the forward slip would be constant in the model, since neither fluid viscosity nor viscoplasticity are included in this version of the model.

The results by the *dry smooth and dry rough formulations* are both represented in Fig. 5.26 to show that their results are essentially *identical*. This seems consistent since the friction forces depend on the boundary coefficient of friction μ_C, which is the same in both cases. The small difference is probably due to the additional roughness layer in the dry rough computation, which leads to an earlier contact between the roll and the strip at the entry of the bite.

5.3.2.5 Influence of starvation

Previously, the rolling load was significantly increased by eliminating the lubricant from the model. If the METALUB model takes *starvation* sufficiently well into account (Sec. 4.10.4), it should be possible to *gradually increase the lubricant quantity to continuously predict the variation of the rolling load from the dry configuration to the fully lubricated one*. This is illustrated in Fig. 5.27 for some scenarios of Test 5B, which can be compared to the results

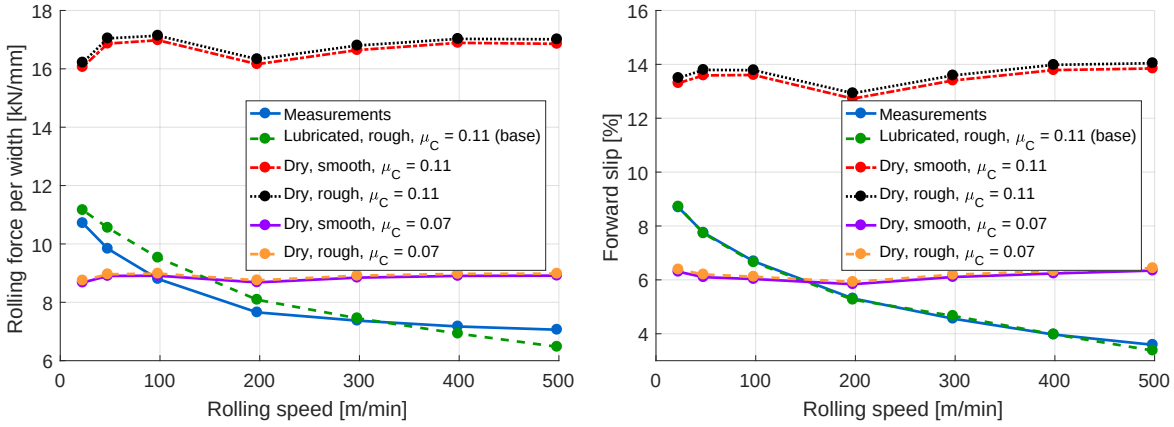

(a) Rolling force per width. **(b)** Forward slip.

Figure 5.26: Influence of lubrication in Test 5B (Chap. 3 and Sec. E.7) based on Tab. 5.4 with v_r, t_{out}, σ_{in} and σ_{out} of Tab. E.21. The dry smooth case was computed with the system of equations in Sec. N.2 while the dry variation of the system in Sec. N.1 was used for the dry rough case.

in Fig. 5.26. In fact, the rolling load and the forward slip decrease from their values in the dry configuration to their values in the fully lubricated configuration, when the lubricant film thickness at the entry increases.

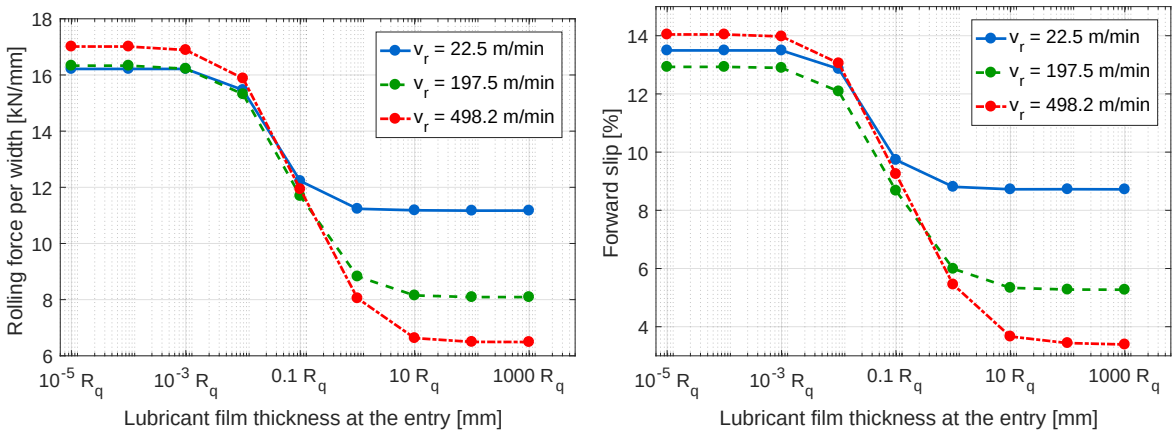

(a) Rolling force per width. **(b)** Forward slip.

Figure 5.27: Influence of the lubricant film thickness at the entry $h_{t,\text{in}}$ in Test 5B (Chap. 3 and Sec. E.7) based on Tab. 5.4 with v_r, t_{out}, σ_{in} and σ_{out} of Tab. E.21 and with activated starvation.

One should notice that this computation is *only possible since the lubricant shear stress in the bite was assumed to be negligible*. Otherwise, i.e. when the lubricant shear stress is computed classically by Eq. (4.204) and when the lubricant temperature is not increased along the roll bite by a thermal model, the *shear stress can become so important that the model does not converge anymore*. In fact, due to the relatively important elongation ($e_x = 30\%$), the smooth interface ($R_q = 0.783$ μm) and the important coefficient of friction at solid interfaces $\mu_C = 0.11$,

the relative contact area A in the dry rolling scenario is close to one, i.e. the mean distance h_t between the interfaces is very small. Moreover, some of the previous elements imply an important rolling load, thus an important interface and lubricant pressure in the METALUB model. Since the viscosity of the lubricant increases with its pressure, the small film thickness results in important viscous shear stresses (Eq. 4.204), when small lubricant film thicknesses at the entry are chosen. These shear stresses should not have a significant influence on the more macroscopic results, like the rolling load, since the lubricant shear stress is multiplied by $1 - A$, which is close to 0 in this scenario, to obtain the interface shear stress. Since the physical laws are, however, *evaluated close to their continuum and experimental limits*, the estimations seem not to be accurate anymore. The resulting high shear stress increases the rolling load until the indentation of the roll becomes so important that the adjustment of the entry speed does not converge anymore. Therefore, the following *limitation of the lubricant shear stress* was introduced:

$$\tau_l = \begin{cases} \tau_{l,\max} & \text{, if } \tau_l > \tau_{l,\max} \\ -\tau_{l,\max} & \text{, if } \tau_l < -\tau_{l,\max} \\ \tau_l & \text{, otherwise.} \end{cases} \tag{5.5}$$

where a good numerical choice of $\tau_{l,\max}$ for convergence is about 250 MPa in the current test scenario. In physical terms, $\tau_{l,\max}$ should be the maximum shear stress that can be transferred by the lubricant from the roll to the strip.

After the negligence of the lubricant shear stress in this rolling scenario (Sec. 5.3.1.5), this limitation is, however, not necessary anymore to reach convergence.

Furthermore, the *impact of starvation on the rolling load and forward slip with respect to the fully lubricated scenario increases with the rolling speed* as shown in Fig. 5.28. This is obviously due to the more severe reduction of the lubricant film thickness at higher rolling speeds. In other words, at high rolling speeds, the bite can absorb much more lubricant than at low rolling speeds due to viscous entrainment so that the film thickness increases, if no limitation by starvation exists. If this limitation, however, applies, the lubricant film thickness can be significantly reduced at high rolling speeds, while the theoretical film thickness could still be below the limitation for small rolling speeds.

5.3.2.6 Influence of the asperity height distribution

In the previous computations, the *pseudo-Gaussian asperity height distribution of Christensen* was chosen since it seems more realistic than the triangular asperity profile with never ending grooves along the rolling direction, which is also implemented in the METALUB model. Fig. 5.29 shows that the curves of the rolling load and forward slip are translated vertically towards greater values, when the asperity height distribution changes from the Christensen distribution to the distribution of triangular asperities. This shift is mostly due to the *flow factors* in the Reynolds equation, as explained in the following section.

One should also notice that the *scaling factor changes when transforming the arithmetical average roughness* R_a, which was measured, to the root-mean-square roughness R_q in the model depending

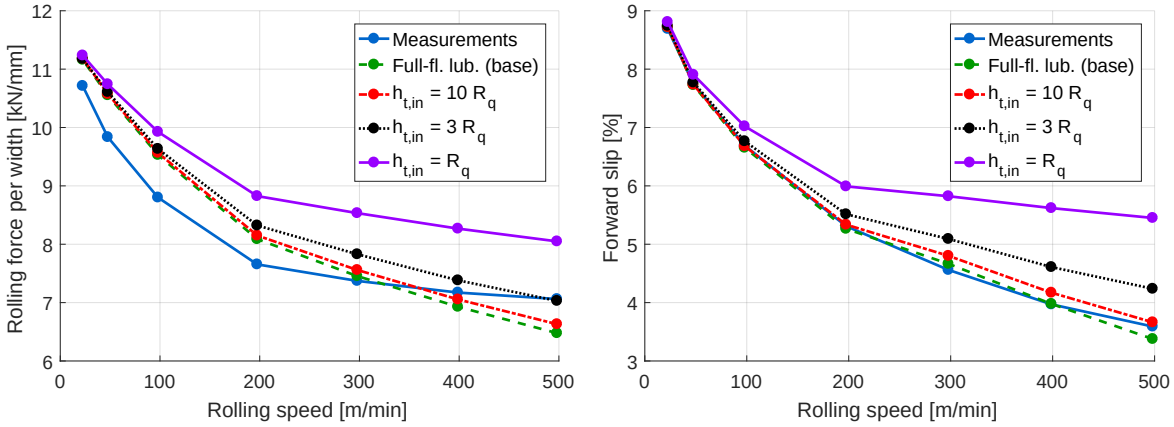

(a) Rolling force per width. **(b)** Forward slip.

Figure 5.28: Influence of the lubricant film thickness at the entry $h_{t,\text{in}}$ in Test 5B (Chap. 3 and Sec. E.7) based on Tab. 5.4 with v_r, t_{out}, σ_{in} and σ_{out} of Tab. E.21 and with activated starvation.

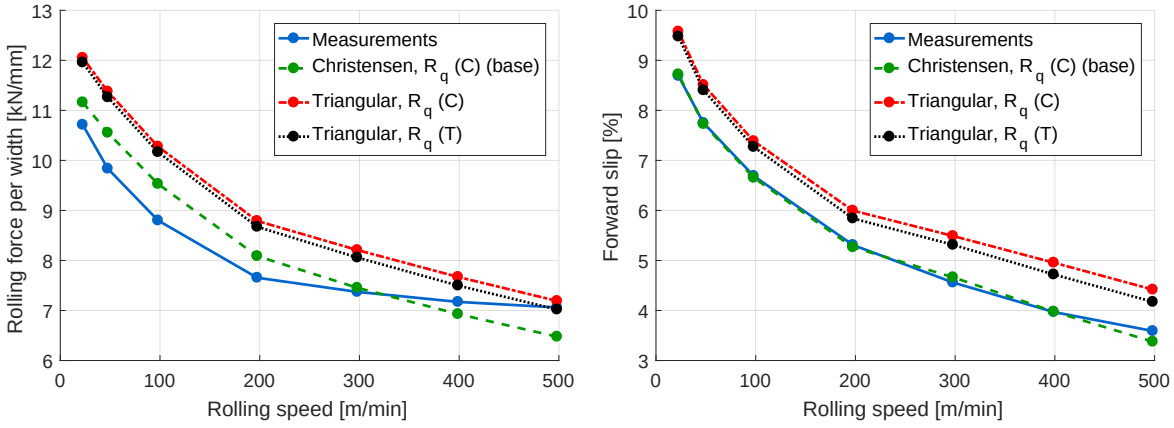

(a) Rolling force per width. **(b)** Forward slip.

Figure 5.29: Influence of the asperity height distribution in Test 5B (Chap. 3 and Sec. E.7) based on Tab. 5.4 with v_r, t_{out}, σ_{in} and σ_{out} of Tab. E.21, and R_q (C) and R_q (T) of Tab. E.20.

on the assumed asperity profile. Hence, one distinguishes R_q (C), which was obtained by assuming that the real asperity profile follows a Christensen distribution, from R_q (T) for the triangular asperity distribution (appendix F). Fig. 5.29 shows that the rolling force and forward slip slightly decrease, when only the value of R_q changes from R_q (C) to R_q (T). This decrease is due to R_q (T) being smaller than R_q (C). More precisely, if the roughness decreases, the lubricant film thickness h_t decreases, too. Therefore, the convergent effect at the entry of the bite becomes stronger and the gradient of the lubricant pressure increases (Eq. 4.191). Hence, the part of the load supported by the lubricant increases. In consequence, friction as well as the rolling force and the forward slip decrease with decreasing roughness.

5.3.2.7 Influence of flow factors

Fig. 5.30 shows that the *rolling force and forward slip increase when the Peklenik surface pattern parameter γ increases*. This is consistent since a more longitudinal asperity pattern, i.e. with grooves that are preferentially oriented along the rolling direction, entrains less lubricant into the bite than a more transversal pattern. Therefore, the lubricant film thickness decreases and friction increases. In addition, the influence of the Peklenik parameter diminishes when the rolling speed increases since the thickness of the lubricant film increases. Hence, it is less influenced by the rough boundary.

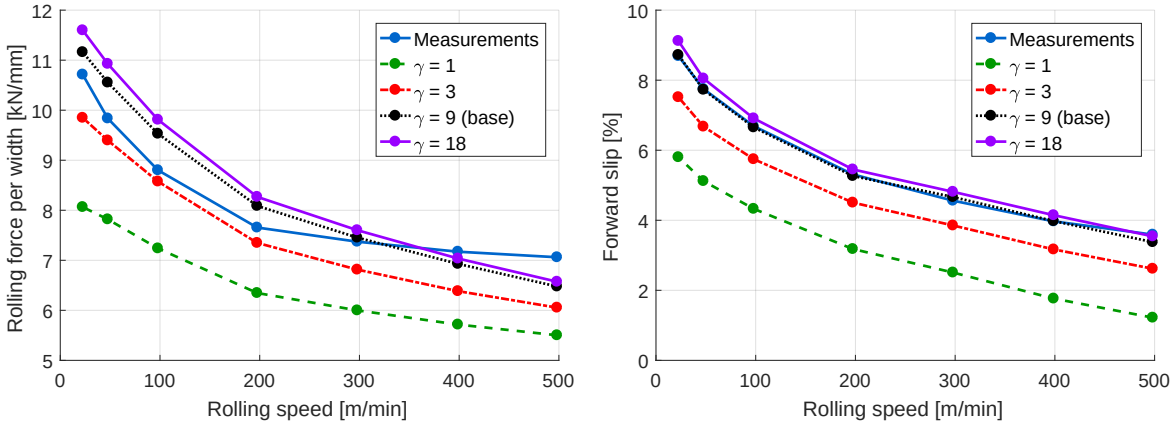

(a) Rolling force per width.

(b) Forward slip.

Figure 5.30: Influence of the Peklenik surface pattern parameter in Test 5B (Chap. 3 and Sec. E.7) based on Tab. 5.4 with v_r, t_{out}, σ_{in} and σ_{out} of Tab. E.21.

When the Peklenik parameter increases, the results with the Christensen roughness become more similar to those with the triangular asperity distribution as shown by Figs. 5.29 and 5.30. This is due to the flow factors of the Christensen height distribution converging to those of the triangular asperity distribution with grooves along the rolling direction, when the Peklenik parameter γ increases, as can be seen in Figs. 4.29 and 4.31 and Eq. (4.169). This observation is consistent, since $\gamma = +\infty$ for this latter surface pattern. Further increasing γ in Fig. 5.30 does, however, not necessarily increase the rolling load and the forward slip since the regression relations in

Eq. (4.170) of the flow factors were determined for $\gamma \in [-9, 9]$.

The *influence of the individual flow factors* was determined by selectively activating or deactivating them as shown in Fig. 5.31. This figure illustrates that the *pressure flow factor has a much more significant influence than the shear flow factor*, which could be neglected due to the small shearing velocity $v_r - v_s$ and the essentially longitudinal asperity pattern, i.e. with grooves along the rolling direction. The pressure flow factor increases friction since less lubricant is entrained into the bite by the longitudinal roughness than the smooth surface.

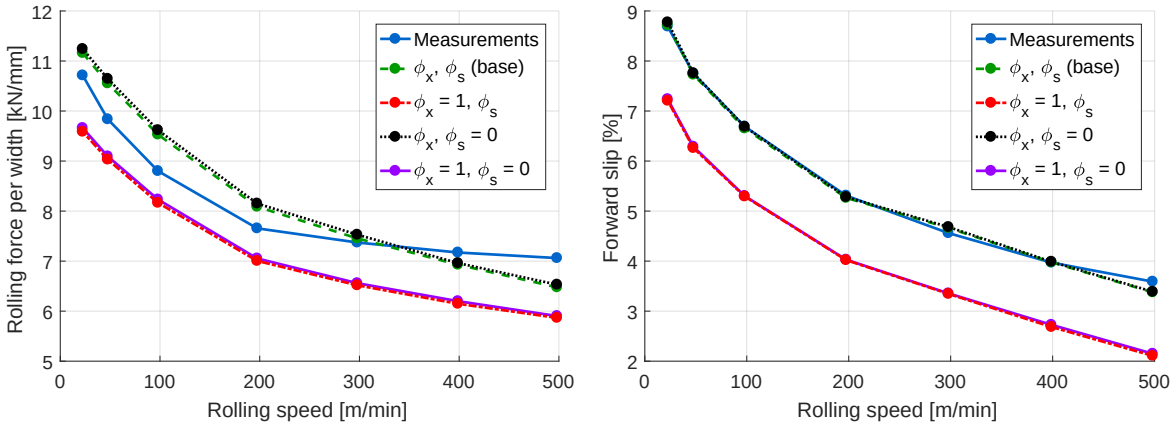

(a) Rolling force per width.

(b) Forward slip.

Figure 5.31: Influence of the flow factors with the Christensen asperity height distribution in Test 5B (Chap. 3 and Sec. E.7) based on Tab. 5.4 with v_r, t_{out}, σ_{in} and σ_{out} of Tab. E.21.

Fig. 5.32 confirms the claim of the previous section, according to which *differences between rolling forces and forward slips for different asperity height distributions (Fig. 5.29) are mainly due to the flow factors* in the current rolling scenarios. In fact, if the pressure flow factor is deactivated, i.e. $\phi_x = 1$, the rolling force and forward slip are essentially identical for both asperity height distributions.

5.3.2.8 Influence of the asperity flattening equation

It was previously shown in Fig. 5.26, that the asperity flattening equation has essentially no influence in dry rolling, for a given boundary coefficient of friction μ_C. Simply deactivating the flattening equation in the model with lubrication is, however, impossible since the model was developed for mixed lubrication. In this case, the *influence of the different asperity flattening equations*, that were implemented in METALUB, can be studied: Wilson and Sheu (Sec. 4.7.1.1), Sutcliffe and Marsault (Sec. 4.7.1.2) and the regression of Korzekwa, Dawson and Wilson's FE results by Sutcliffe (Sec. 4.7.1.3).

Fig. 5.33 shows that the equations by Sutcliffe-Marsault and Korzekwa et al.-Sutcliffe lead to almost identical results while Wilson and Sheu's equation increases slightly the rolling force and forward slip with respect to the previous equations. This can be explained by the *smaller hardness*

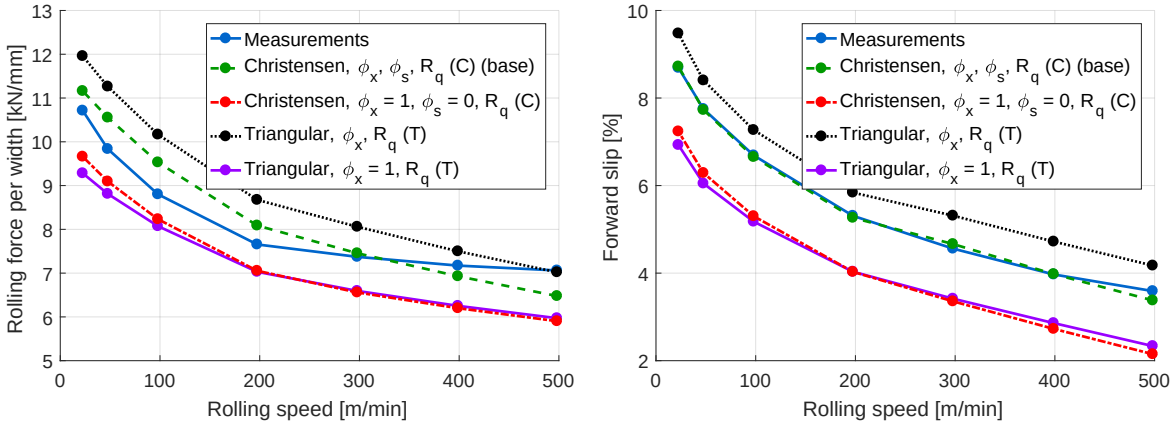

(a) Rolling force per width. **(b)** Forward slip.

Figure 5.32: Influence of the flow factors with the Christensen and triangular asperity height distributions in Test 5B (Chap. 3 and Sec. E.7) based on Tab. 5.4 with v_r, t_{out}, σ_{in} and σ_{out} of Tab. E.21. The shear flow factor ϕ_s of the triangular asperity distribution with grooves along the rolling direction is zero in any case.

of the asperities in Wilson and Sheu's equation with respect to the two others as illustrated in Figs. 4.18 and 4.19. Although the upper bound method of Wilson and Sheu overestimates the non-dimensional effective hardness, its regression relation (Eq. 4.92), which is used in METALUB, seems to underestimate the hardness with respect to the other results according to Fig. 4.19. In consequence, more significant asperity flattening with the equation by Wilson and Sheu increases friction and therefore, the rolling force and forward slip, too.

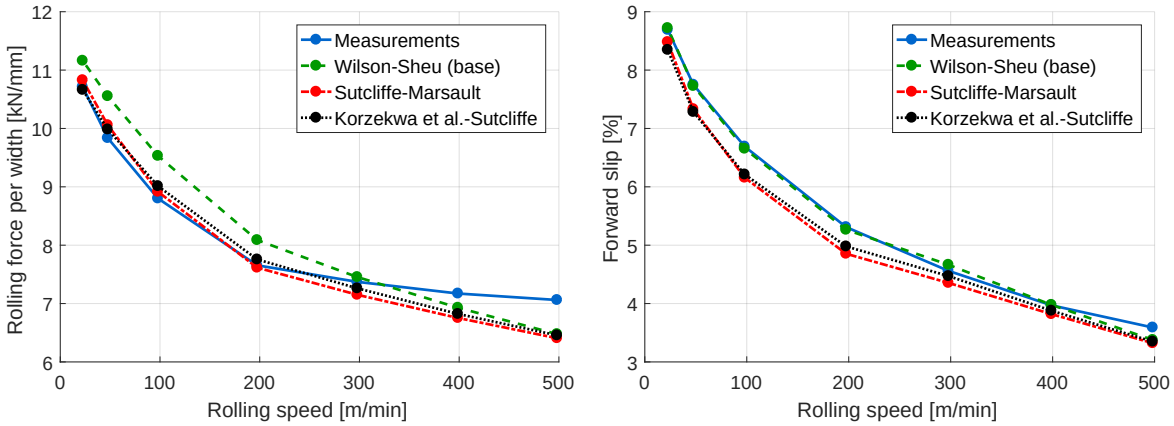

(a) Rolling force per width. **(b)** Forward slip.

Figure 5.33: Influence of the asperity flattening equation in Test 5B (Chap. 3 and Sec. E.7) based on Tab. 5.4 with v_r, t_{out}, σ_{in} and σ_{out} of Tab. E.21.

5.4 Validation cases

Previously, the *predictive capabilities* of the METALUB model were assessed based on *Test 5B* of the experimental rolling campaign (Chap. 3, Sec. E.7), which was selected because it is one of the most likely reproducible scenarios by METALUB (Sec. 5.2.1).

In this section, the parameter calibration strategy of the previous section is applied to *additional rolling scenarios* of the experimental campaign to further test the METALUB model and to determine its *limitations*. The following analysis is structured by gradually *increasing the complexity* of the rolling scenarios. First, rolling scenarios with increasing rolling speed are studied and later those with increasing reduction. Further validation cases can be found in appendix P.

5.4.1 Test 4B - Rolling speed, weak starvation

During the experimental campaign, the *influence of starvation* was tested by reducing the lubricant quantity of Test 5B (flexible lubrication by 100% L3[6], Sec. E.7) in Test 4B (flexible lubrication by 20% L3 and recirculated 2% L2, Sec. E.5) and more severely in Test 4A (recirculated 2% L2, Sec. E.4), while all other parameters remain essentially constant.

Fig. 5.34 shows that the measured rolling force and forward slip in *Test 4B* increase slightly with respect to Test 5B at higher rolling speeds due to the reduction of the oil concentration from 100% to 20% in the flexible lubrication system. This increase of the rolling force and forward slip can be included in the METALUB prediction by decreasing the lubricant film thickness $h_{t,\text{in}}$ at the entry of the bite via the *starvation model* as shown in Fig. 5.34. All other parameters are identical to those of Test 5B (except for the slight variations of the rolling speed, the final thickness and the tensions). As expected, the *film thickness $h_{t,in}$ has to decrease*, when the rolling speed increases to better reproduce on average the experimental measurements due to starvation.

5.4.2 Test 4A - Rolling speed, strong starvation

Starvation is even more significant in *Test 4A* (recirculated 2% L2), whose experimental measurements are compared to those of Test 5B (direction application 100% L3) in Fig. 5.35. To reproduce this case numerically, *only the lubricant and its temperature were first modified with respect to Test 5B* as shown in Tab. 5.6. These tables are introduced in this section instead of the appendix to clearly show the parameter values in the computations. Variations of values in these tables with respect to prior rolling scenarios are written in bold to emphasize the modifications. The measured values of the lubricant viscosity and temperature are used. Hence, *no additional calibration* was required up to now. The comparison of the experimental measurements of Test 4A and its prediction with full-flooded lubrication in Fig. 5.35 shows, however, that *starvation modeling is required* after 50 m/min. By reducing the film thickness at the entry of the bite, it is thus possible to reproduce the rolling force and forward slip relatively accurately. Nevertheless,

[6]As explained in Chap. 3, L1, L2 and L3 are the different lubricants that were used during the experimental campaign.

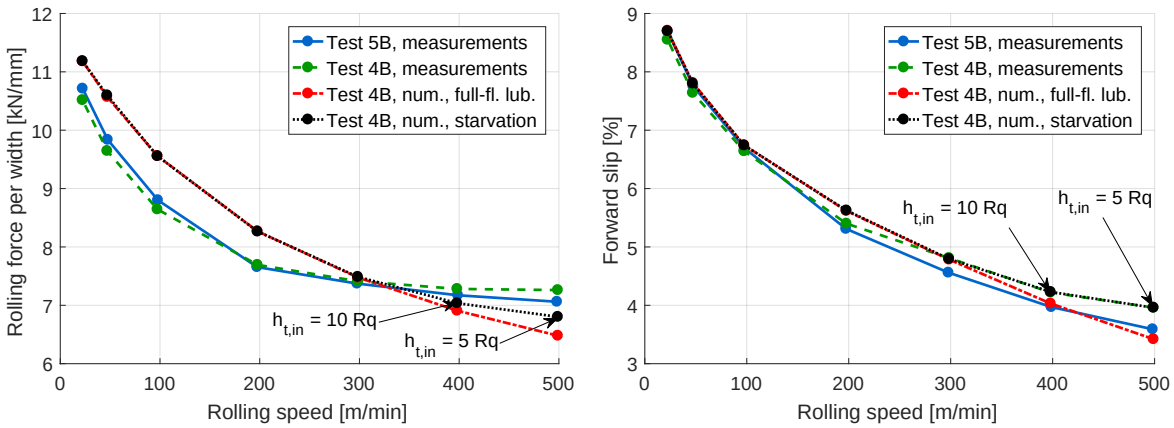

(a) Rolling force per width.

(b) Forward slip.

Figure 5.34: Experimental and numerical results of Tests 5B (Chap. 3 and Sec. E.7) and 4B (Chap. 3 and Sec. E.5) to illustrate the influence of weak starvation. Numerical results of 4B are based on Tab. 5.4 with v_r, t_{out}, σ_{in} and σ_{out} of Tab. E.15. In the case with starvation, the starvation model is only activated for v_r = 398.1 m/min and 499.0 m/min with $h_{t,\text{in}} = 10R_q$ and $5R_q$, respectively.

the reductions of the film thickness $h_{t,\text{in}}$ are manual and therefore, the model is not fully predictive. In consequence, a *film formation model*, like the one by Cassarini [63] is required to remove this limitation of METALUB.

Despite this shortcoming, the *old predictions by Carretta*, who also adjusted the film thickness $h_{t,\text{in}}$, *could again be improved* as illustrated in Fig. 5.36, possibly to a great extent by the negligence of the lubricant shear stress in the bite.

5.4.3 Test 6 - Rolling speed, different product

In Test 6 (Sec. E.8), a different product with a rougher surface[7] than in the previous scenarios is rolled (Tab. 5.7). As shown in Fig. 5.37, the material of this product is seemingly viscoplastic since the measured rolling force increases with the rolling speed, while the forward slip decreases (Sec. 3.2.1.2). For this reason, *viscoplasticity* was activated in the model and the influence of the corresponding coefficient η_s is illustrated in Fig. 5.37. Although the predicted rolling force takes the shape of the measured rolling force for the realistic value $\eta_s = 0.06$ [161], its vertical offset is unrealistic.

For this reason, the *thermoplasticity coefficient m* was adjusted according to the explanations in Sec. 5.3.1.3. In fact, thermal softening allows to reduce the rolling force as shown in Fig. 5.38 in

[7]Shortly after writing this document, the author found out that the S1 product has a more isotropic surface pattern due to pickling than the other products (S2 and S3), which were already cold rolled. Hence, the Peklenik parameter γ is presumably closer to 1 than to 9. In Carretta's results, it was also assumed to be equal to 9. Furthermore, this hypothesis could explain why the adjusted boundary coefficient of friction μ_C will be relatively small in this section. In fact, if the lubricant film thickness decreases because of an increasing γ, boundary friction has to become less severe to still reproduce the experimental results.

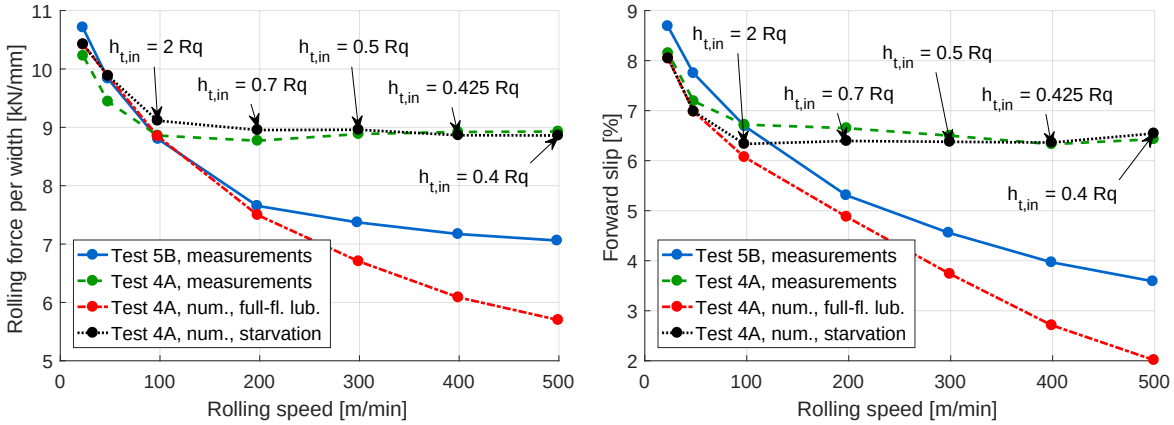

(a) Rolling force per width. **(b)** Forward slip.

Figure 5.35: Experimental and numerical results of Tests 5B (Chap. 3 and Sec. E.7) and 4A (Chap. 3 and Sec. E.4) to illustrate the influence of strong starvation. Numerical results of Test 4A are based on Tab. 5.6 with v_r, t_{out}, σ_{in} and σ_{out} of Tab. E.12. In the case with starvation, starvation is activated for v_r = 97.6 m/min, 197.8 m/min, 299.1 m/min, 399.1 m/min and 499.3 m/min with $h_{t,\text{in}} = 2R_q$, $0.7R_q$, $0.5R_q$, $0.425R_q$ and $0.4R_q$, respectively.

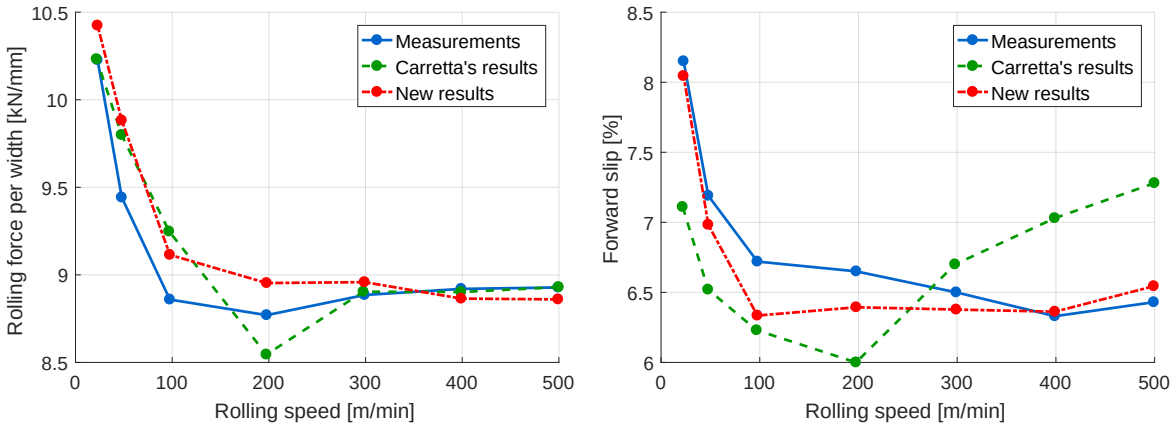

(a) Rolling force per width. **(b)** Forward slip.

Figure 5.36: Comparison of our results (Tab. 5.6 with v_r, t_{out}, σ_{in} and σ_{out} of Tab. E.12 and activated starvation for v_r = 97.6 m/min, 197.8 m/min, 299.1 m/min, 399.1 m/min and 499.3 m/min with $h_{t,\text{in}} = 2R_q$, $0.7R_q$, $0.5R_q$, $0.425R_q$ and $0.4R_q$, respectively) with those obtained by Carretta for Test 4A (Chap. 3 and Sec. E.4).

Entity	Parameter	Value	Unit
Roll bite	Type	Full-flooded lub.	-
	Heating by friction	On	-
	Heating by plastic deformation	On	-
Strip material	Name	S2	-
	E_s	210000	MPa
	ν_s	0.3	-
	Law	Ludwik	-
	Viscoplasticity	Off	-
	Thermoplasticity	On	-
	A	776	MPa
	B	147	MPa
	n	1.52	-
	m	0.65	-
	$\overline{\epsilon}_0^p$	0	-
	ρ_s	$7.850 \cdot 10^{-9}$ [7850]	t/mm^3 [kg/m^3]
	c_s	$500 \cdot 10^6$ [500]	N.mm/(t.°C) [J/(kg.°C)]
	β_s	0.9	-
Strip	t_{in}	0.75	mm
	t_{out}	0.578	mm
	σ_{in}	114.7	MPa
	σ_{out}	189.9	MPa
	$T_{s,\text{in}}$	25	°C
Lubricant	Name	**L2**	-
	Law	WLF (enhanced)	-
	A_1	**47.67**	°C
	A_2	**0.000704**	MPa^{-1}
	b_1	**0.00611**	MPa^{-1}
	b_2	**−0.517**	-
	C_1	**16.08**	-
	C_2	**25.80**	°C
	η_g	**10^6**	MPa.s
	$T_g(0)$	**−90.60**	°C
	T_l	**50** (constant)	°C
Interface	Asperity profile	Christensen	-
	$R_{q,r}$	0.773	μm
	$R_{q,s}$	0.123	μm
	$\bar{l}$	51.28	μm
	Flattening equation	Wilson-Sheu	-
	γ	9	-
	Friction law	Coulomb-Tresca	-
	μ_C	0.11	-
	μ_T	1	-
	Flow factors ϕ_x and ϕ_s	On	-
	Shear stress factors	Off	-
	τ_l	0	MPa
Roll	Deformation method	Meindl (full)	-
	Deformation mode	Plane strain	-
	R_0	195.5	mm
	v_r	3297	mm/s
	E_r	210000	MPa
	ν_r	0.3	-
	x_{12}	−10	mm
	x_{23}	5	mm
	$\Delta\theta_1$	1	°
	$\Delta\theta_2$	$5 \cdot 10^{-3}$	°
	$\Delta\theta_3$	1	°
	Relaxation method	Constant	-
	$w^{(0)}$	0.5	-
Other numerical parameters	Integration method	RK4	-
	x_{12}	−10	mm
	Δx_1	1	mm
	Δx_2	10^{-3}	mm
	tol_Q	10^{-4}	-
	$\text{tol}_{\sigma_{\text{out}}}$	10^{-3}	-
	$\text{tol}_{t_{\text{out}}}$	10^{-4}	-
	tol_R	10^{-6}	-
	$\Delta x_{\text{extr},1}$	1	mm
	$\Delta x_{\text{extr},2}$	10^{-2}	mm
	CIEFS step	Off	-

Table 5.6: Model parameters of Test 4A-4 (Chap. 3 and Sec. E.4, with deactivated starvation). Changes with respect to parameters of Test 5B-4 in Tab. 5.4 are written in bold (except for v_r, t_{out}, σ_{in} and σ_{out}).

Entity	Parameter	Value	Unit
Roll bite	Type	Full-flooded lub.	-
	Heating by friction	On	-
	Heating by plastic deformation	On	-
Strip material	Name	**S1**	-
	E_s	210000	MPa
	ν_s	0.3	-
	Law	Ludwik	-
	Viscoplasticity	Off	-
	Thermoplasticity	**Off**	-
	A	**263**	MPa
	B	**338**	MPa
	n	**0.356**	-
	$\overline{\epsilon}_0^p$	0	-
	ρ_s	$7.850 \cdot 10^{-9}$ [7850]	t/mm^3 [kg/m^3]
	c_s	$500 \cdot 10^6$ [500]	N.mm/(t.°C) [J/(kg.°C)]
	β_s	0.9	-
Strip	t_{in}	**2.8**	mm
	t_{out}	2.146	mm
	σ_{in}	36.6	MPa
	σ_{out}	120.3	MPa
	$T_{s,\text{in}}$	25	°C
Lubricant	Name	L3	-
	Law	WLF (enhanced)	-
	A_1	49.64	°C
	A_2	0.000365	MPa^{-1}
	b_1	0.00578	MPa^{-1}
	b_2	−0.565	-
	C_1	16.11	-
	C_2	26.00	°C
	η_g	10^6	MPa.s
	$T_g(0)$	−85.96	°C
	T_l	**60** (constant)	°C
Interface	Asperity profile	Christensen	-
	$R_{q,r}$	0.773	μm
	$R_{q,s}$	**1.835**	μm
	$\bar{l}$	**57.00**	μm
	Flattening equation	Wilson-Sheu	-
	γ	9	-
	Friction law	Coulomb-Tresca	-
	μ_C	0.11	-
	μ_T	1	-
	Flow factors ϕ_x and ϕ_s	On	-
	Shear stress factors	Off	-
	τ_l	0	MPa
Roll	Deformation method	Meindl (full)	-
	Deformation mode	Plane strain	-
	R_0	195.5	mm
	v_r	3297	mm/s
	E_r	210000	MPa
	ν_r	0.3	-
	x_{12}	**−15**	mm
	x_{23}	5	mm
	$\Delta\theta_1$	1	°
	$\Delta\theta_2$	$5 \cdot 10^{-3}$	°
	$\Delta\theta_3$	1	°
	Relaxation method	Constant	-
	$w^{(0)}$	0.5	-
Other numerical parameters	Integration method	RK4	-
	x_{12}	**−15**	mm
	Δx_1	1	mm
	Δx_2	10^{-3}	mm
	tol_Q	10^{-4}	-
	$\text{tol}_{\sigma_{\text{out}}}$	10^{-3}	-
	$\text{tol}_{t_{\text{out}}}$	10^{-4}	-
	tol_R	10^{-6}	-
	$\Delta x_{\text{extr},1}$	1	mm
	$\Delta x_{\text{extr},2}$	10^{-2}	mm
	CIEFS step	Off	-

Table 5.7: Model parameters of Test 6-3 (Chap. 3 and Sec. E.8). Changes with respect to parameters of Test 5B-4 in Tab. 5.4 are written in bold (except for v_r, t_{out}, σ_{in} and σ_{out}).

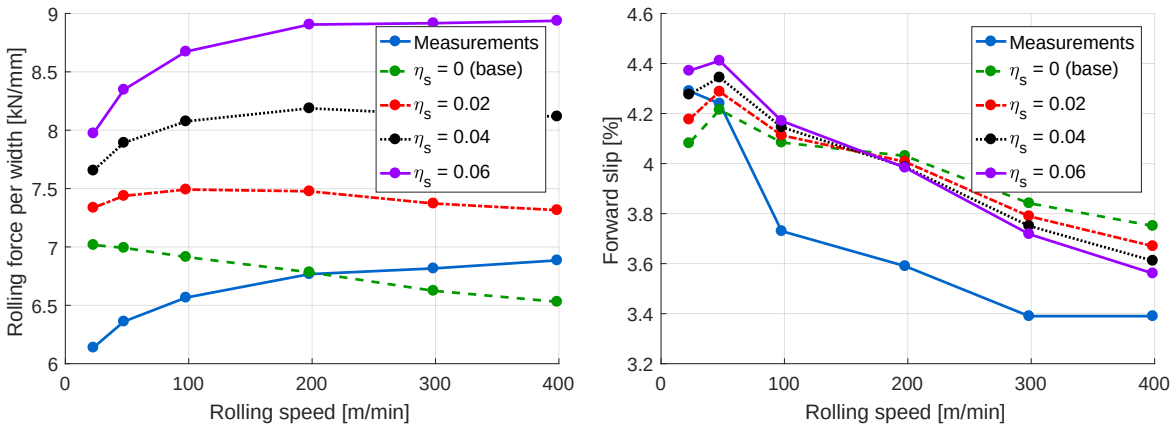

(a) Rolling force per width.

(b) Forward slip.

Figure 5.37: Influence of the viscoplasticity coefficient η_s in Test 6 (Chap. 3 and Sec. E.8) based on Tab. 5.7 with v_r, t_{out}, σ_{in} and σ_{out} of Tab. E.24.

which the thermoplasticity coefficient m was adjusted for different values of the viscoplasticity coefficients η_s to reduce the difference between the measurements and predictions of the rolling force. While a very good agreement could be obtained for $\eta_s = 0.06$ and $m = 0.4$, which are both realistic values [161], the vertical offset of the forward slip is, however, relatively significant.

In consequence, the *boundary coefficient of friction* μ_C was also adjusted due to its significant influence on the forward slip according to Sec. 5.3.1.1. More precisely, the thermoplasticity coefficient m is adjusted for different values of the boundary coefficient of friction μ_C and $\eta_s = 0.06$ in Fig. 5.39 to minimize the differences between the experimental and numerical values of the rolling force. Hence, the parameter set $\eta_s = 0.06$, $\mu_C = 0.08$ and $m = 0.48$ leads to the best prediction, when μ_C and m are adjusted by increments of 0.01.

The previous *parameter adjustment procedure* can certainly be criticized due to its fitting approach, i.e. if there are enough parameters in the model any experimental curve can be reproduced. This might possibly explain why the boundary coefficient of friction $\mu_C = 0.08$ takes a relatively small value with respect to the value $\mu_C = 0.11$ in Test 5B and those suggested in Sec. 2.1.3. Furthermore, MPH lubrication might reduce friction in the experimental case, while this mechanism is not yet included in the rolling model. In consequence, the boundary coefficient of friction is underpredicted. Since the parameters η_s, μ_C and m were not measured, certainly because of the difficulty to determine their values, they could only be adjusted via the experimental data. Besides the good agreement between the measurements and the predictions in Fig. 5.39, an additional argument in favor of this approach will be presented in the following section.

Finally, the new results can be compared to the previous *predictions by Carretta* in Fig. 5.40. Carretta assumed that the increasing rolling force with the rolling speed was due to starvation. Hence, it is no surprise that the rolling force is predicted perfectly in his results by manually adjusting the lubricant film thickness at the entry of the roll bite for each rolling speed. In consequence, his prediction of the forward slip does, however, not agree quantitatively nor

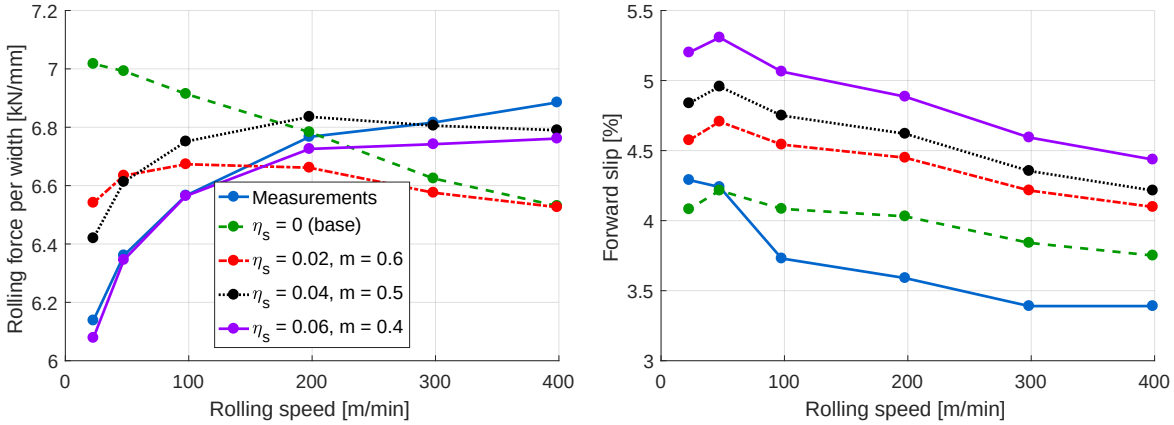

(a) Rolling force per width. **(b)** Forward slip.

Figure 5.38: Influence of the viscoplasticity coefficient η_s and the thermoplasticity coefficient m in Test 6 (Chap. 3 and Sec. E.8) based on Tab. 5.7 with v_r, t_{out}, σ_{in} and σ_{out} of Tab. E.24. For a given value of the viscoplasticity coefficient η_s, the thermoplasticity coefficient m is adjusted by increments of 0.1 to obtain the lowest mean squared error between the measurements and the predictions of the rolling force. The legend was not included in Fig. 5.38b to improve the readability but it is identical to the one in Fig. 5.38a.

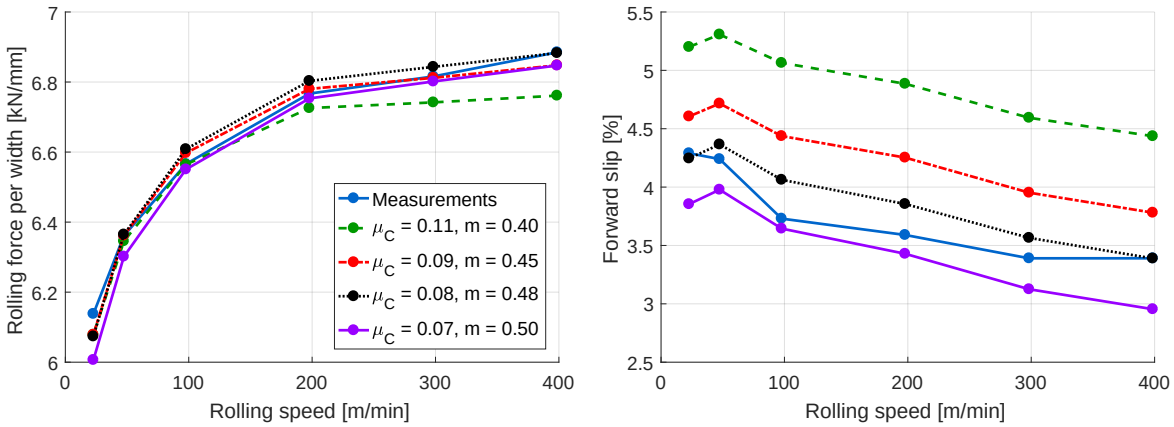

(a) Rolling force per width. **(b)** Forward slip.

Figure 5.39: Influence of the boundary coefficient of friction μ_C and the thermoplasticity coefficient m with the viscoplasticity coefficient $\eta_s = 0.06$ in Test 6 (Chap. 3 and Sec. E.8) based on Tab. 5.7 with v_r, t_{out}, σ_{in} and σ_{out} of Tab. E.24. For a given value of the boundary coefficient of friction μ_C, the thermoplasticity coefficient m is adjusted by increments of 0.01 to obtain the lowest mean squared error between the measurements and the predictions of the rolling force. The legend was not included in Fig. 5.39b to improve the readability but it is identical to the one in Fig. 5.39a.

qualitatively with the measurements. ***By introducing new material laws in METALUB, i.e. thermo-viscoplasticity, it was thus possible for the first time to reproduce the measurements in this scenario by the actual underlying physical mechanisms.***

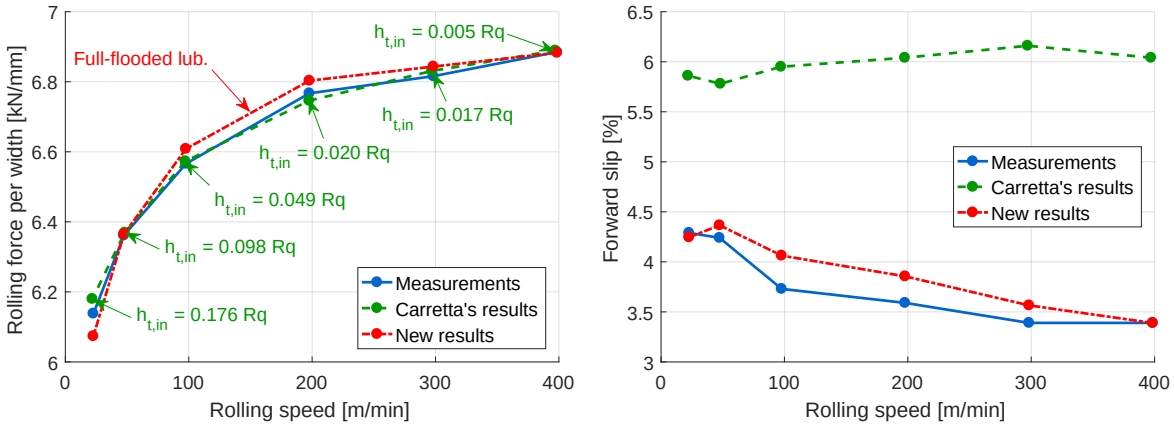

(a) Rolling force per width.

(b) Forward slip.

Figure 5.40: Comparison of our results (Tab. 5.7 with v_r, t_{out}, σ_{in} and σ_{out} of Tab. E.24 and after the adustement of $\mu_C = 0.08$, $\eta_s = 0.06$ and $m = 0.48$) with those obtained by Carretta for Test 6 (Chap. 3 and Sec. E.8). Carretta assumed that starvation occurred, which is why he adjusted the lubricant film thickness at the entry of the bite $h_{t,\text{in}}$.

5.4.4 Test 11 - Rolling speed, different product and more viscous lubricant

In addition to a different rolled product than in the base case (Test 5B), a different lubricant is introduced in this scenario. From an experimental stand point, only the lubricant changes from the less viscous L3 in Test 6 of the previous section to the more viscous L1 in Test 11 of this section. Hence, *only the values of the lubricant parameters were changed* in the final parameter set of the previous section to model Test 11 besides roughness modifications due to wear (Tab. 5.8).

Thus, without any additional parameter calibration, the predictions of the measurements in Fig. 5.41 are still relatively good and overall better than the past predictions by Carretta. This is an additional argument in favor of the parameter adjustment approach since it ***allows to obtain quite accurate predictions in rolling scenarios that are not too far from those for which the material and friction parameters were adjusted***.

Nevertheless, one might criticize that the lubricant shear stress is still neglected although a more viscous lubricant is applied. In the future, this issue should be addressed by activating again this stress and by computing a more realistic prediction of the lubricant temperature (than a constant temperature) to determine the viscosity.

Entity	Parameter	Value	Unit
Roll bite	Type	Full-flooded lub.	-
	Heating by friction	On	-
	Heating by plastic deformation	On	-
Strip material	Name	S1	-
	E_s	210000	MPa
	ν_s	0.3	-
	Law	Ludwik	-
	Viscoplasticity	**On**	-
	Thermoplasticity	**On**	-
	A	263	MPa
	B	338	MPa
	n	0.356	-
	η_s	**0.06**	-
	m	**0.48**	-
	$\overline{\epsilon}_0^p$	0	-
	ρ_s	$7.850 \cdot 10^{-9}$ [7850]	t/mm^3 [kg/m^3]
	c_s	$500 \cdot 10^6$ [500]	N.mm/(t.°C) [J/(kg.°C)]
	β_s	0.9	-
Strip	t_{in}	2.8	mm
	t_{out}	2.146	mm
	σ_{in}	37.2	MPa
	σ_{out}	118.7	MPa
	$T_{s,\text{in}}$	25	°C
Lubricant	Name	**L1**	-
	Law	WLF (enhanced)	-
	A_1	**102.77**	°C
	A_2	**0.000226**	MPa^{-1}
	b_1	**0.00573**	MPa^{-1}
	b_2	**−0.547**	-
	C_1	**15.95**	-
	C_2	**26.98**	°C
	η_g	**10^6**	MPa.s
	$T_g(0)$	**−73.16**	°C
	T_l	60 (constant)	°C
Interface	Asperity profile	Christensen	-
	$R_{q,r}$	**0.695**	μm
	$R_{q,s}$	1.835	μm
	$\overline{l}$	**67.11**	μm
	Flattening equation	Wilson-Sheu	-
	γ	9	-
	Friction law	Coulomb-Tresca	-
	μ_C	**0.08**	-
	μ_T	1	-
	Flow factors ϕ_x and ϕ_s	On	-
	Shear stress factors	Off	-
	τ_l	0	MPa
Roll	Deformation method	Meindl (full)	-
	Deformation mode	Plane strain	-
	R_0	195.5	mm
	v_r	3295	mm/s
	E_r	210000	MPa
	ν_r	0.3	-
	x_{12}	−15	mm
	x_{23}	5	mm
	$\Delta\theta_1$	1	°
	$\Delta\theta_2$	$5 \cdot 10^{-3}$	°
	$\Delta\theta_3$	1	°
	Relaxation method	Constant	-
	$w^{(0)}$	0.5	-
Other numerical parameters	Integration method	RK4	-
	x_{12}	−15	mm
	Δx_1	1	mm
	Δx_2	10^{-3}	mm
	tol_Q	10^{-4}	-
	$\text{tol}_{\sigma_{\text{out}}}$	10^{-3}	-
	$\text{tol}_{t_{\text{out}}}$	10^{-4}	-
	tol_R	10^{-6}	-
	$\Delta x_{\text{extr},1}$	1	mm
	$\Delta x_{\text{extr},2}$	10^{-2}	mm
	CIEFS step	Off	-

Table 5.8: Model parameters of Test 11-3 (Chap. 3 and Sec. E.14). Changes with respect to parameters of Test 6-3 in Tab. 5.7 are written in bold (except for v_r, t_{out}, σ_{in} and σ_{out}).

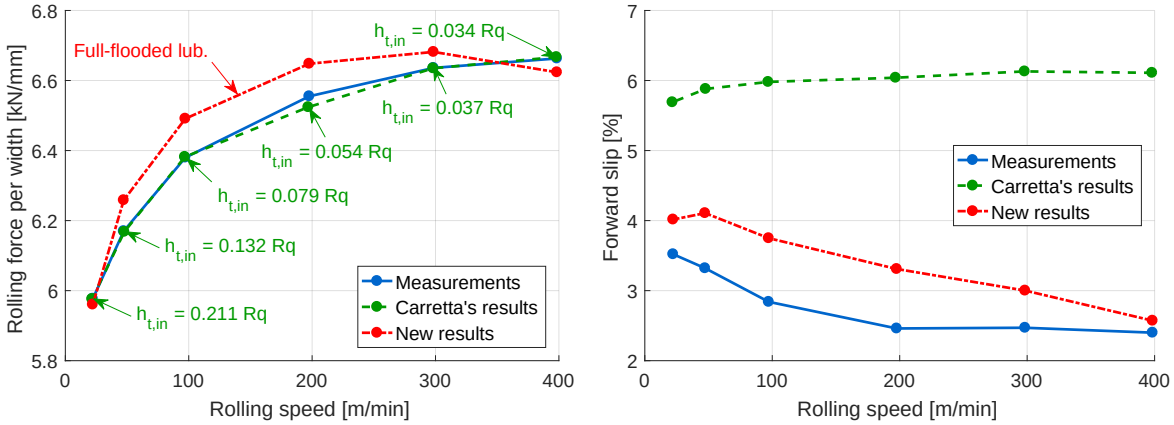

(a) Rolling force per width. **(b)** Forward slip.

Figure 5.41: Comparison of experimental results of Test 11 (Chap. 3 and Sec. E.14) with our results (Tab. 5.8 with v_r, t_{out}, σ_{in} and σ_{out} of Tab. E.42) and those of Carretta. Carretta assumed that starvation occurred, which is why he adjusted the lubricant film thickness at the entry of the bite $h_{t,\text{in}}$.

5.4.5 Tests 15/8 - Reduction

Previously, the evolution of the rolling force and the forward slip was studied as a function of the rolling speed. In this section, their evolution is studied as a function of the *reduction* or equivalently, the *elongation*.

Figs. 5.42 and 5.43 show the influence of the reduction for the same rolled product (S2) and lubricant (pure L3) as in the base case (Test 5B) at different rolling speeds, i.e. about 50 and 100 m/min in *Tests 15 and 8*, respectively. These tests were modeled based on the calibrated parameters of Sec. 5.3. Hence, *no additional calibration* was required to obtain the predictions with constant boundary coefficients of friction in the previous figures.

While these predictions are relatively good at small elongations in both cases, the difference between them and the measurements increases at greater elongations, especially in Fig. 5.42 at about 50% of elongation. The underlying reason seems to be *micro-plasto-hydrodynamic/static (MPH) lubrication* as explained in Sec. 3.2.4. In fact, if the *boundary coefficient of friction is reduced* in the model with increasing elongation, which is equivalent to the permeation of the lubricant in the solid/solid contact region, the predictions in Figs. 5.42 and 5.43 improve. This suggests that a *model of MPH lubrication is required in* METALUB. Furthermore, the greater difference between the experimental results and the predictions with a constant boundary coefficient of friction in Fig. 5.42 than in Fig. 5.43 could be explained by the greater elongation interval in the first figure and the increasing MPH effect with increasing elongation. In fact, if the elongation increases, underlying causes of MPH, like the reduction and the differential speed between the strip and the rolls, are intensified.

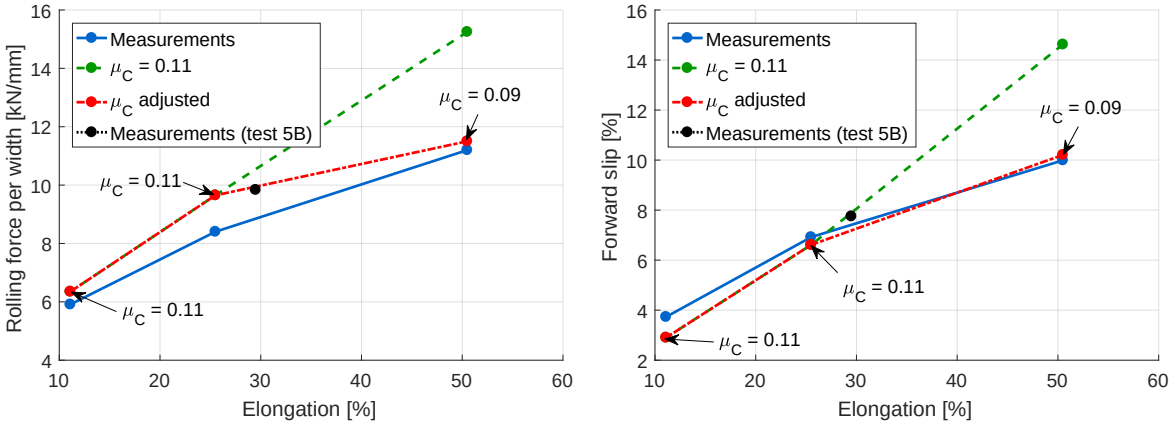

(a) Rolling force per width. **(b)** Forward slip.

Figure 5.42: Comparison of experimental and numerical results in Test 15 (Chap. 3 and Sec. E.20). The numerical results are based on Tab. 5.4 with v_r, t_{out}, σ_{in} and σ_{out} of Tab. E.60 except for $R_{q,r} = 0.657$ μm and $\bar{l} = 72.46$ μm.

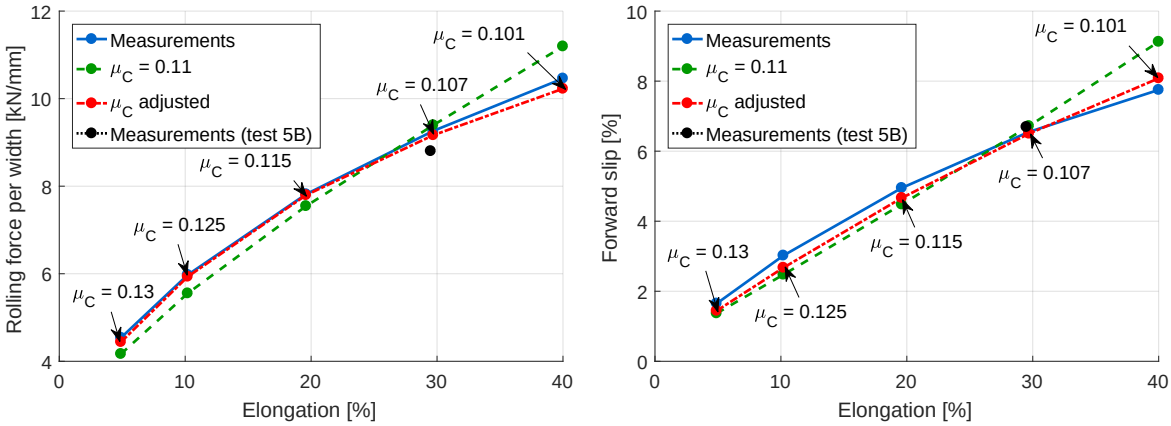

(a) Rolling force per width. **(b)** Forward slip.

Figure 5.43: Comparison of experimental and numerical results in Test 8 (Chap. 3 and Sec. E.10). The numerical results are based on Tab. 5.4 with v_r, t_{out}, σ_{in} and σ_{out} of Tab. E.21.

5.4.6 Test 7 - Reduction, different product

In this last validation case, a different rolled product with a rougher surface finish (S1) than in the base case (Test 5B) is analyzed.

The prediction with a constant boundary coefficient of friction in Fig. 5.44 was again obtained *without any additional parameter calibration* after the calibration of the coefficients of friction, thermoplasticity and viscoplasticity in Sec. 5.4.3 (Tab. 5.9). This prediction is relatively accurate for the rolling force even without further adjusting the boundary coefficient of friction, although the complex variation of the forward slip could only be reproduced qualitatively and on average quantitatively. The same is true for Carretta's predictions.

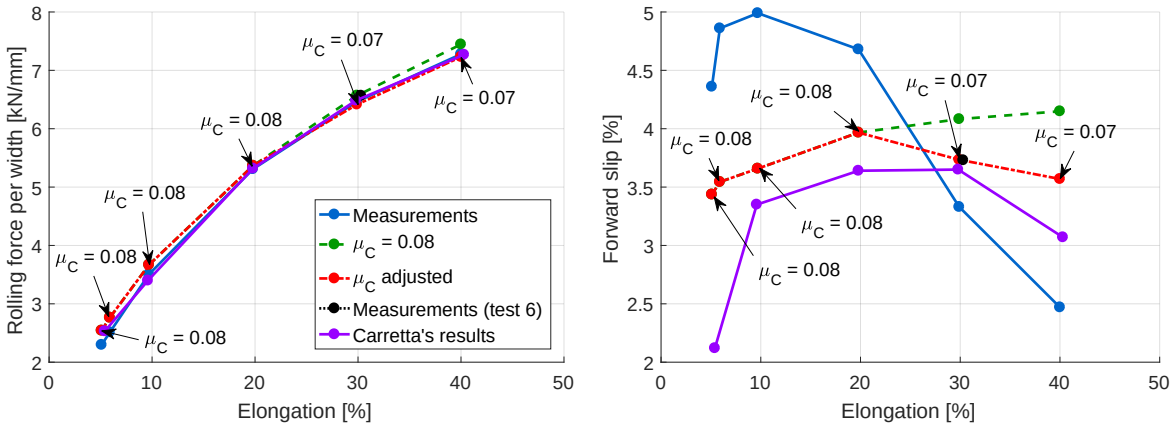

(a) Rolling force per width.

(b) Forward slip.

Figure 5.44: Comparison of experimental and numerical results in Test 7. The numerical results are based on Tab. 5.9 with v_r, t_{out}, σ_{in} and σ_{out} of Tab. E.27. Carretta also adjusted the boundary coefficient of friction. The legend was not included in Fig. 5.44b to improve the readability but it is identical to the one in Fig. 5.44a.

5.5 Conclusion

In this chapter, the *METALUB model of Chap. 4 was calibrated and validated on the basis of the most comprehensive industrial data* to the best of our knowledge (Chap. 3) in order to evaluate its *predictive capabilities* and to single out its *limitations*.

First, the *literature about the validation of METALUB was reviewed* to explain why this model had to be further validated. Despite a very comprehensive sensitivity analysis, Marsault (1998) [215] compared only very few experimental results of industrial rolling scenarios with his predictions. Later, Stephany (2008) [305] numerically reproduced numerous industrial scenarios but with sometimes limited experimental data (unknown viscosity, roughness parameters, ...) and limited capabilities of his version of the METALUB model (no thermoplasticity, viscoplasticity, temperature increase of the lubricant, ...). Finally, Carretta (2014) [54] reproduced the rolling force and forward

Entity	Parameter	Value	Unit
Roll bite	Type	Full-flooded lub.	-
	Heating by friction	On	-
	Heating by plastic deformation	On	-
Strip material	Name	S1	-
	E_s	210000	MPa
	ν_s	0.3	-
	Law	Ludwik	-
	Viscoplasticity	**On**	-
	Thermoplasticity	**On**	-
	A	263	MPa
	B	338	MPa
	n	0.356	-
	η_s	**0.06**	-
	m	**0.48**	-
	$\overline{\epsilon}_0^p$	0	-
	ρ_s	$7.850 \cdot 10^{-9}$ [7850]	t/mm^3 [kg/m^3]
	c_s	$500 \cdot 10^6$ [500]	N.mm/(t.°C) [J/(kg.°C)]
	β_s	0.9	-
Strip	t_{in}	2.8	mm
	t_{out}	2.155	mm
	σ_{in}	37.5	MPa
	σ_{out}	118.4	MPa
	$T_{s,\text{in}}$	25	°C
Lubricant	Name	L3	-
	Law	WLF (enhanced)	-
	A_1	49.64	°C
	A_2	0.000365	MPa^{-1}
	b_1	0.00578	MPa^{-1}
	b_2	−0.565	-
	C_1	16.11	-
	C_2	26.00	°C
	η_g	10^6	MPa.s
	$T_g(0)$	−85.96	°C
	T_l	60 (constant)	°C
Interface	Asperity profile	Christensen	-
	$R_{q,r}$	0.773	μm
	$R_{q,s}$	1.835	μm
	$\overline{l}$	57.00	μm
	Flattening equation	Wilson-Sheu	-
	γ	9	-
	Friction law	Coulomb-Tresca	-
	μ_C	**0.08**	-
	μ_T	1	-
	Flow factors ϕ_x and ϕ_s	On	-
	Shear stress factors	Off	-
	τ_l	0	MPa
Roll	Deformation method	Meindl (full)	-
	Deformation mode	Plane strain	-
	R_0	195.5	mm
	v_r	1625	mm/s
	E_r	210000	MPa
	ν_r	0.3	-
	x_{12}	−15	mm
	x_{23}	5	mm
	$\Delta\theta_1$	1	°
	$\Delta\theta_2$	$5 \cdot 10^{-3}$	°
	$\Delta\theta_3$	1	°
	Relaxation method	Constant	-
	$w^{(0)}$	0.5	-
Other numerical parameters	Integration method	RK4	-
	x_{12}	−15	mm
	Δx_1	1	mm
	Δx_2	10^{-3}	mm
	tol_Q	10^{-4}	-
	$\text{tol}_{\sigma_{\text{out}}}$	10^{-3}	-
	$\text{tol}_{t_{\text{out}}}$	10^{-4}	-
	tol_R	10^{-6}	-
	$\Delta x_{\text{extr},1}$	1	mm
	$\Delta x_{\text{extr},2}$	10^{-2}	mm
	CIEFS step	Off	-

Table 5.9: Model parameters of Test 7-4 (Chap. 3 and Sec. E.9). Changes with respect to parameters of Test 6-3 in Tab. 5.7 are written in bold (except for v_r, t_{out}, σ_{in} and σ_{out}).

slip for flexible lubrication conditions on the tandem mill at Tilleur but he manually adjusted the lubricant film thickness at the entry of the bite for all operating points, which renders it difficult to assess the real predictive ability of the model. Hence, further validation of the METALUB model, which now includes additional features, by the most complete industrial data was justified.

Secondly, the *numerical parameters* of the METALUB model, like the integration steps and tolerances, were *for the first time systematically calibrated* in the particular rolling scenario of Test 5B-4 (Chap. 3, Sec. E.7) to eliminate convergence issues and to reduce the computation time with a controlled accuracy of the results. More precisely, the numerical parameters were adjusted layer by layer in the numerical shooting procedure of METALUB to limit numerical, relative errors of the rolling force and forward slip by either 0.01, 0.1 or 1% and without compromising the convergence due to the interdependence of these parameters by the nested loop structure of METALUB. In this way, the computation time of the past was also divided in half for similar relative errors.

Thirdly, the influence of some *physical parameters* was studied to *calibrate* the values of those that were or could not be measured accurately in the rolling scenario of Test 5B (Chap. 3, Sec. E.7). Hence, the boundary coefficient of friction and the yield stress were adjusted as in the past [54, 305]. The yield stress was, however, reduced via thermal softening, which is more physically consistent than the manual reduction of the yield stress in the past. Furthermore, the lubricant shear stress was neglected to improve the predictions in the absence of a better estimation of this stress than by the viscosity at constant temperature. This assumption was justified by the small speed differential at low rolling speeds and the increase of the lubricant temperature in the bite at high rolling speeds. After these adjustments, further influence studies provided additional information about the predictive capabilities of the model in the context of Test 5B: (1) Previous predictions by Carretta, which have never been published before, were significantly improved by the new results. (2) The successive roll flattening models (rigid circular, Hitchcock, Bland and Ford, Jortner, Meindl) gradually improved the predictions and no significant difference could be observed between the predictions by Jortner's and Meindl's methods. (3) The starvation model allowed to continuously switch from a dry roll bite to a fully lubricated one. (4) The surface height distribution mainly influenced the rolling force and forward slip via the flow factors. (5) Wilson and Sheu's asperity flattening equation slightly increased the rolling force and forward slip with respect to the other flattening equations (Sutcliffe-Marsault, Korzekwa et al.-Sutcliffe).

Finally, additional *validation cases*, which were introduced in Chap. 3, were analyzed to study the predictive capabilities of METALUB and its limitations, when the rolled product, the lubricant, its quantity, the reduction, ... are changed. The *most important conclusions* are the following ones: (1) Carretta's past predictions were in general significantly improved, especially those of the forward slip, by the new predictions. (2) No additional parameter calibration was required when rolling scenarios, that are not too far from scenarios, for which the parameters were calibrated, were modeled. Hence, the model is predictive to some extent (see limitations hereafter). (3) Viscoplasticity allowed to predict the measurements of Tests 6 and Tests 7 for the first time in a physically consistent way. (4) Adjustments of the lubricant film thickness at the entry of the bite for each operating point improved the predictions, when starvation should be observed.

(5) Similarly, adjustments of the boundary coefficient of friction improved the predictions, when micro-plasto-hydrodynamic/static lubrication presumably occurred. Nevertheless, the METALUB model has the following *limitations*: (1) The lubricant film thickness at the entry of the bite had to be adjusted manually for each operating point, when starvation seemed to occur. To become actually predictive, a film formation model, like the one by Cassarini [63] possibly, should be added to METALUB. (2) Neglecting the lubricant shear stress is an oversimplification. This term should again be activated in the model but with a better prediction of the viscosity in its computation. More precisely, a full thermal model of the rolling scenario, like THERMROLL [58], should be included in METALUB to predict the increase of the lubricant temperature along the roll bite. Hence, the viscosity could be determined by a better temperature prediction than isothermality. Furthermore, a full thermal model could improve the prediction of thermal softening. (3) Instead of manually reducing the boundary coefficient of friction when the reduction increases, micro-plasto-hydrodynamic/static lubrication should be modeled. (4) Numerous material parameters, like thermal softening and viscoplasticity coefficients, were adjusted previously. If they were measured, modeling uncertainties could be eliminated and the model could become more predictive.

Obviously, some of the previous conclusions and recommendations are not new since coupling strategies with Cassarini's film formation model and THERMROLL were already tested in the past. Nevertheless, they were usually abandoned due to convergence issues. Therefore, it was tried in this thesis to build a *solid foundation for future developments* by rederiving the entire METALUB model with additional feature, enhanced robustness and industrial validation cases, which are the most comprehensive ones to the best of our knowledge.

Instead of focusing on problems, for which solutions were already suggested in the past, i.e. Cassarini's film formation model and THERMROLL, and whose reintegration in METALUB rather seems to be a technical than an innovative challenge, the possibility of modeling *micro-plasto-hydrodynamic/static lubrication in the context of METALUB* is investigated in the following chapter.

Chapter 6

Coupling of METALUB with METAFOR - FE Asperity Flattening

In the previous chapter, it was shown that METALUB overpredicts the rolling force and forward slip when the reduction of the strip increases (Secs. 5.4.5, 5.4.6 and P.2). A possible explanation of this observation is the decrease of friction by *micro-plasto-hydrodynamic/static (MPH) lubrication*, i.e. the permeation of the lubricant from pressurized surface pockets into the solid/solid contact region (Sec. 2.2.4.3), which is not yet included in the model.

Classically, *asperity flattening*, which determines the solid/solid contact region and thus friction, is modeled by *analytical equations* like those of Wilson and Sheu [367] (Sec. 4.7.1.1), Sutcliffe and Marsault [215, 311] (Sec. 4.7.1.2) and Korzekwa et al. and Sutcliffe [169, 313] (Sec. 4.7.1.3). These equations have several *shortcomings* in the current METALUB context:

- *Simplified geometry*: an initially flat surface, which represents the strip, is deformed by rigid flat indenters (Wilson and Sheu, Sutcliffe and Marsault) or the strip surface has a small slope angle where it is not in contact with the rigid flat roll surface (Korzekwa et al. and Sutcliffe) in the flattening models. Furthermore, composite asperity profiles in METALUB are either triangular or they have a Christensen height distribution with a profile conservation hypothesis during flattening. In addition, their composite roughness (Eq. 2.14) is computed without considering the possible correlation between the surface patterns of the roll and the strip. Hence, the geometry of the real surfaces is roughly approximated in the model.

- *Simplified material model*: the material is either assumed to be rigid-perfectly plastic in the upper bound method (Wilson and Sheu) and the slip-line field theory (Sutcliffe and Marsault) or viscoplastic (Korzekwa et al. and Sutcliffe). Work hardening is therefore not directly taken into account in the model, although it is included indirectly by changing the yield stress, which is used to compute the non-dimensional effective hardness (Eq. 4.90).

- *Approximate method*: the upper bound method is applied by Wilson and Sheu and it

overpredicts the internal power dissipation by the assumed velocity field, and thus, the non-dimensional effective hardness H_a, too. This overprediction is, however, reduced by the derivation of the corresponding asperity flattening equation (Eq. 4.92), which is used in METALUB, as illustrated previously in Fig. 4.19. In fact, the flattening equation rather underpredicts the non-dimensional effective hardness H_a, which is equivalent to overpredicting the relative contact area A, since this area generally increases when the non-dimensional effective hardness H_a increases, for a constant non-dimensional plastic strain rate E_p.

- *Micro-plasto-hydrodynamic/static lubrication is not included in the analytical flattening equations.*

Because of the previous shortcomings, Carretta [61] started to simulate dry flattening of asperities with parallel grooves to the transverse direction, i.e. normal to the rolling/longitudinal direction, by the *finite element (FE) method* in the non-linear FE software METAFOR for large deformations [258], which will be described in Sec. 6.2.2.1. The numerical results by the finite element method were compared to experimental measurements by Sutcliffe [311]. The good agreement between Carretta's numerical results and Sutcliffe's experimental results then led to FE simulations of dry asperity flattening in the longitudinal direction with boundary conditions of cold rolling computations by METALUB [56, 57, 61]. These finite element simulations were finally integrated in a coupling procedure with METALUB to fully replace the analytical flattening equation by more realistic FE asperity flattening simulations [54]. Hence, real asperity profiles and more sophisticated material laws could be included in asperity flattening computations by a more general method than the upper bound method or slip-line field theory. Thus, essentially three of the previous four shortcomings were eliminated from the model.

Up to this point, the *influence of the lubricant* was, however, not included in the FE asperity flattening model, which implies that micro-plasto-hydrodynamic/static lubrication cannot not be modeled. For this reason, Carretta proved that it is possible to model a Newtonian fluid behavior by the Norton-Hoff law alongside solid deformations in METAFOR [54]. This feature allowed him later on to model micro-plasto-hydrodynamic/static lubrication in plane strip drawing test by METAFOR simulations [54, 55] (Sec. 2.2.4.3). Finally, the same idea was tried to be integrated in the context of cold rolling to model the permeation of the lubricant into the solid/solid contact zone via a coupling procedure between METALUB and METAFOR.

Since this *coupling procedure by Carretta* has never been published in the past, it will be described in the following section before introducing a *new coupling procedure*, in which shortcomings of Carretta's procedure are attempted to be solved. The old coupling procedure will be described in more general terms, while the details are explained for the new coupling procedure. Finally, some *numerical results of the new coupling procedure* are presented.

6.1 Coupling procedure by Carretta

The objective of the coupling procedure by Carretta was to *replace the analytical asperity flattening equation*, e.g. the equation by Wilson and Sheu (Sec. 4.7.1.1), *by FE simulations of asperity flattening with the lubricant* to include micro-plasto-hydrodynamic/static lubrication in METALUB.

Due to the *multiscale* nature of the problem, it is clear that the roll bite cannot be simulated geometrically in its entirety with the asperities by the finite element method. In fact, the roll bite has a length l_{rb} of about 10 mm, while the RMS roughness R_q is equal to about 0.001 mm with a half spacing between asperities $\bar{l}$ of around 0.01 mm. Only simulating a strip width of several asperities in 3D would require an excessive number of discretization points, which would lead to impractical computation times.

For this reason, a *2D slice* of the roll bite was simulated. This slice could either be orthogonal to the rolling direction or orthogonal to the axis of the roll. Because of the common longitudinal asperity pattern in cold rolling, i.e. the grooves of the asperities are parallel to the rolling direction due to roll grinding (Sec. 2.1.2.2), the slice *orthogonal to the rolling direction* was chosen. This had the additional benefit of not having to simulate the possibly significant relative displacement between the roll and the strip along the rolling direction in the asperity flattening micro-model.

Fig. 6.1 illustrates the expected asperity flattening process with the lubricant in the normal plane along the roll bite. First, no contact exists between the roll and the strip (1). Then, the asperities of the roll break up the lubricant film and indent the surface of the strip, which is softer than the roll (2). The lubricant is compressed more and more (3) until it finally escapes from the pressurized pockets to lubricate the asperity tops (4).

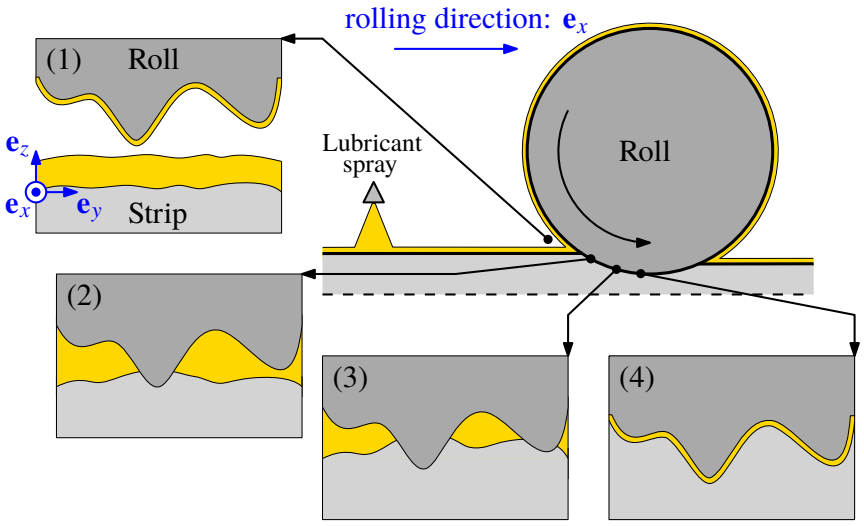

Figure 6.1: Asperity flattening with lubricant in the normal plane to the rolling direction (yellow = lubricant; white = air).

In the next sections, the three following elements are successively introduced and explained: the

old finite element micro-model of asperity flattening, the resulting *coupling procedure* of the cold rolling software METALUB with the FE solver METAFOR as well as the *shortcomings* of this coupling procedure and their successive solutions.

6.1.1 Finite element micro-model of asperity flattening

The *finite element micro-model of asperity flattening* in the FE solver METAFOR (Sec. 6.2.2.1) is schematized in Fig. 6.2. It shows the lubricant and strip portions in the orthogonal plane to the rolling direction, which are pushed against the roll (contact tool) by the local interface pressure $p_i(x)$ of the METALUB computation.

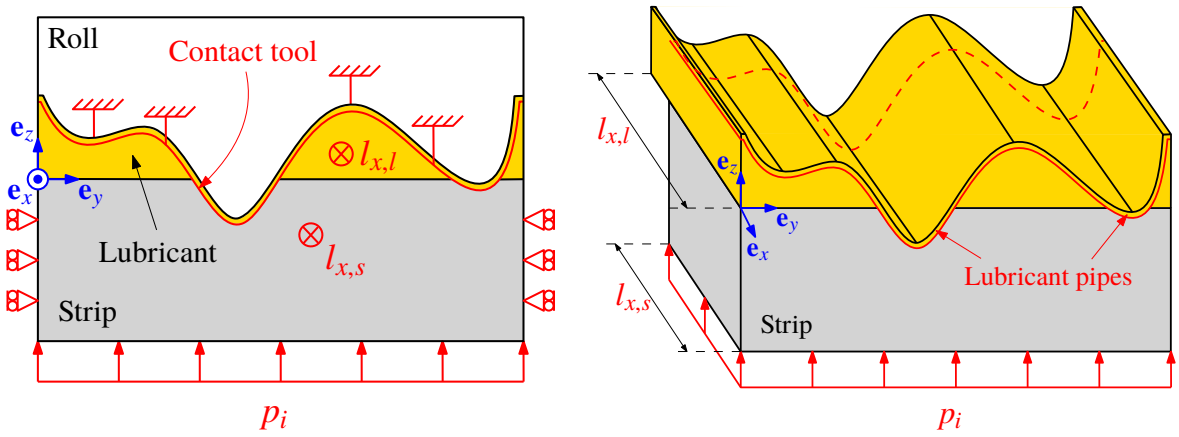

(a) 2D representation with schematized boundary conditions: discretized strip and lubricant portions with out-of-plane lengths $l_{x,l}$ and $l_{x,s}$, interface pressure p_i, contact tool, and prevention of lateral expansion.

(b) 3D representation to put emphasis on the out-of-plane lengths $l_{x,l}$ and $l_{x,s}$, and their influence on the application of the contact tool and the interface pressure p_i.

Figure 6.2: FE asperity flattening micro-model of Carretta's coupling procedure with lubricant.

Regarding the *geometry and spatial discretization*, the roll is modeled by a rigid and fixed contact tool, that interacts with the top edge of the strip by the penalty method [372]. The profiles of the roll and the strip can essentially take any shape although the profile of the strip is represented initially flat in Fig. 6.2 for simplicity. The strip and the lubricant domains are discretized by a mesh, which is not represented in Fig. 6.2. The lubricant domain takes advantage of the Arbitrary Lagrangian Eulerian (ALE) formulation in METAFOR [35, 94] to prevent mesh distortions due to large deformations of the fluid lubricant by uncoupling the material flow from the mesh displacement. Since the lubricant can only circulate where the space has been discretized by a mesh, very thin lubricant pipes were added by offsetting the contact tool with respect to the fixed rigid top edge of the lubricant. These pipes potentially allow the rise of the lubricant to the asperity tops. Fig. 6.3 shows more precisely how micro-plasto-hydrodynamic/static lubrication was imagined to be modeled. When the lubricant pressure is relatively low, the strip can be in contact at some points with the roll, i.e. the contact tool. When, the pressure, however, rises, the introduction of lubricant pipes enables the separation between the roll and the strip.

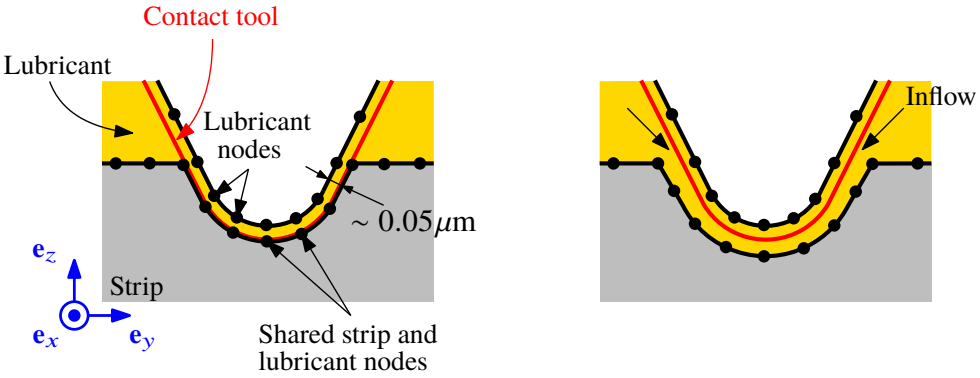

Figure 6.3: Contact loss between the roll and the strip due to the lubricant inflow in the thin lubricant pipes. The roll is represented by the contact tool. The pipes are initially created by positioning some nodes of the lubricant behind the contact tool (inside the roll) at a very small and fixed distance of this tool, i.e. about 0.05 μm. Only the nodes of the strip can be in contact with the contact tool. Hence, the figure on the left shows the initial contact between the strip and the roll, while the figure on the left shows their separation due to the inflow of the lubricant in the thin pipes.

Concerning the *material*, the strip is modeled by the same elastoplastic laws with isotropic hardening as in the METALUB model, while the lubricant has a possibly pressure-dependent compressibility and a Newtonian viscous behavior by the Norton-Hoff law [54].

With regard to the *boundary conditions*, the lateral spread of the strip and lubricant portions is prevented (Fig. 6.2a) because of the classical plane-strain hypothesis in cold rolling (Sec. 4.5.1) and symmetry. As mentioned above, the interface pressure of the METALUB computation is applied to the bottom edge of the strip, which is constrained to remain horizontal due to symmetry considerations. This constraint is applied by imposing the vertical displacements of the nodes on the bottom edge of the strip to be equal. Furthermore, the computations are performed in a generalized plane-strain state, i.e. the strip and the lubricant portions can elongate along the rolling direction by imposing their local out-of-plane lengths $l_{x,s}(x)$ and $l_{x,l}(x)$ in the bite (Fig. 6.2b), instead of a tension along the rolling direction in the past (Fig. 2.20). The elongation of the strip is a natural consequence of the rolling process, which reduces the thickness of the strip. By material conservation and the neglected elastic compressibility, the out-of-plane length of the simulated strip portion can be deduced from the local strip thickness $t_s(x)$ of the METALUB model, if this portion has a unit length when the roll gets into contact with the strip at x_{im} (Sec. 4.10.1):

$$l_{x,s}(x) = \frac{t_s(x_{\text{im}})}{t_s(x)} \tag{6.1}$$

The out-of-plane lengths of the interface pressure elements and the contact elements are the same as that of the strip portion (Fig. 6.2b).

Concerning the lubricant, the out-of-plane length $l_{x,l}(x)$ was introduced to take into account the hydrodynamic effect of the Reynolds equation, i.e. the pressure generation by the combined effects of velocity and viscosity, of the METALUB computation in the FE micro-model. Hence,

this length was computed based on the definition of the bulk modulus K_l of the lubricant, which is assumed to be constant in this explanation, to generate the lubricant pressure $p_l(x)$ of the METALUB computation in the lubricant domain:

$$K_l = -V_l \frac{\mathrm{d}p_l}{\mathrm{d}V_l} \tag{6.2}$$

where V_l is the volume occupied by the lubricant. By integrating this equation, the volume change from one position in the roll bite x_1 to the next x_2 can be derived from the pressure modification:

$$\int_{V_l(x_1)}^{V_l(x_2)} \frac{1}{V_l}\,\mathrm{d}V_l = -\int_{p_l(x_1)}^{p_l(x_2)} \frac{1}{K_l}\,\mathrm{d}p_l \quad \Rightarrow \quad V_l(x_2) = V_l(x_1)\exp\left(\frac{p_l(x_1) - p_l(x_2)}{K_l}\right) \tag{6.3}$$

If a lubricant volume initially has a unit length (like the strip portion), its length at other positions of the roll bite can be deduced from the previous equation and the mean film thickness h_t, since its lateral spread is assumed to be constant, as mentioned above:

$$l_{x,l}(x) = \frac{h_t(x_{\mathrm{im}})}{h_t(x)}\exp\left(\frac{p_l(x_{\mathrm{im}}) - p_l(x)}{K_l}\right) \tag{6.4}$$

Finally, since the FE simulation replaces the asperity crushing equation, some *results* are recorded during its execution to use them in the METALUB computation. These results are the time variations of the relative contact area $A(t)$, the mean film thickness $h_t(t)$, the mean pressure on the asperity tops $p_a(t)$ and the lubricant pressure $p_l(t)$. The computation methods of $A(t)$ and $h_t(t)$ will be explained in Sec. 6.2.2.2 for the new coupling procedure, while those of $p_a(t)$ and $p_l(t)$ are defined in appendix Q since they would only add unnecessary complexity to this section.

All parameter changes of METALUB that are applied in the finite element model, i.e. the interface pressure $p_i(x)$, the out-of-plane lengths of the strip $l_{x,s}(x)$ and the lubricant $l_{x,l}(x)$ are functions of the position x in the roll bite. The finite element method in METAFOR simulates, however, the asperity flattening as a function of time. Therefore, *space dependencies are transformed into time dependencies*, by assuming that the time t is 0, when the roll and the strip get into contact at $x = x_{\mathrm{im}}$, i.e.

$$t = \frac{x - x_{\mathrm{im}}}{v} \tag{6.5}$$

where v is the conversion speed from space to time which should be equal to the local strip speed $v_s(x)$, but which can be equal to 1, if inertial and viscous effects are neglected. The inverse change of variables is applied to transform the resulting evolutions of the METAFOR simulation to functions of space, which are used in METALUB.

6.1.2 Coupling procedure between METALUB and METAFOR

The previous FE micro-model of asperity flattening in METAFOR should replace the analytical flattening equation in METALUB. Various ways of combining both models can be envisioned.

Directly replacing each evaluation of the analytical flattening equation by a FE computation would require too much computation time since the roll bite is integrated about 1000 times in a classical METALUB computation. Therefore, the *partitioned coupling structure* in Fig. 6.4 was chosen.

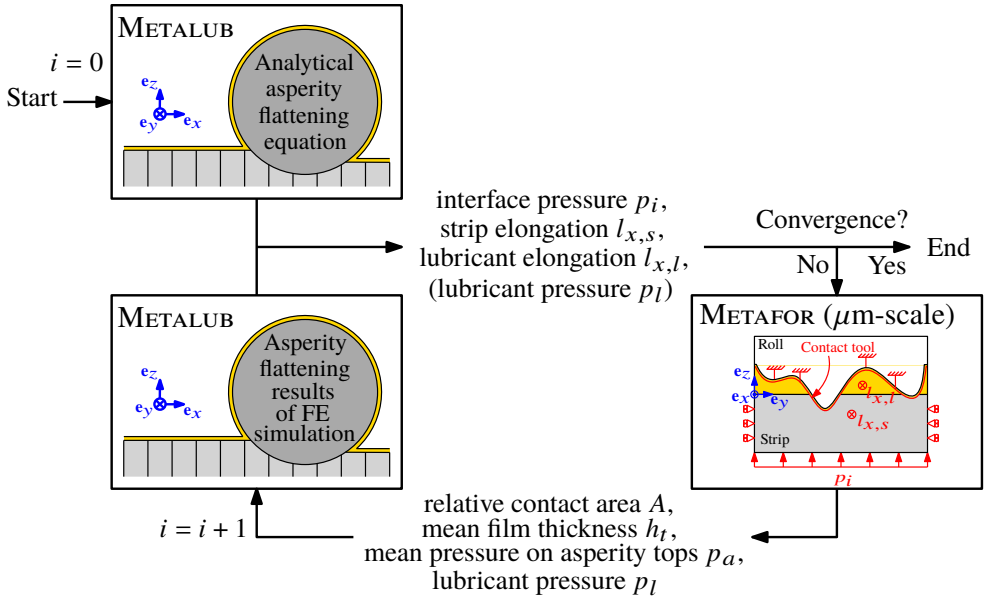

Figure 6.4: Flow chart of the coupling procedure by Carretta (i = iteration counter). An enlarged view of the asperity flattening model in METAFOR is represented in Fig. 6.2.

More precisely, the coupling procedure starts by a full *classical* METALUB *computation*, which determines the strip elongation $l_{x,s}(x)$, the lubricant elongation $l_{x,l}(x)$ and the interface pressure $p_i(x)$ along the roll bite, by using the analytical asperity flattening equation.

These influences are then applied in the *FE micro-model of asperity flattening* in METAFOR. In this way, the variations of the relative contact area $A(x)$, the mean film thickness $h_t(x)$, the average pressure on top of the asperities $p_a(x)$ and the lubricant pressure $p_l(x)$ are computed along the entire roll bite, i.e. from the initial contact between the roll and the strip at $x = x_{\text{im}}$ until the end of the roll bite at $x = x_{\text{out}}$, as explained in the previous section.

The sampled values of $A(x)$, $h_t(x)$, $p_a(x)$ and $p_l(x)$ along the roll bite from the FE computation are then interpolated along x during a subsequent METALUB *computation in its coupled version*, instead of evaluating the analytical asperity flattening equation. Since replacing the analytical equation by a FE model most likely introduces modifications of the resulting relative contact area, for instance, and since this area impacts other state variables in the bite, which again impact the relative contact area, and so on, the coupling procedure iterates between full METALUB and METAFOR computations until the state variables do not change significantly anymore from one iteration to the next.

6.1.3 Shortcomings and possible solutions

The coupling procedure in its previous form had several *shortcomings*, which were tried to be solved by the following ideas.

First, the resulting equality between the lubricant and interface pressures in the initial classical METALUB computation due to the high-speed hypothesis led to a *non-physical separation of the roll and the strip in the FE micro-model*. More precisely, if the lubricant pressure became equal to the interface pressure, the resulting force, that pushes the strip portion downwards in Fig. 6.2, became equal to the resulting force of the interface pressure, that pushes it upwards, because of the lubricant pipes. In fact, the existence of the pipes implied that the lubricant pressure was applied to the entire width of the strip portion. Thus, there was no reason for this portion to remain in contact with the roll, when the lubricant pressure became equal to the interface pressure. Hence, the separation between the roll and the strip could take an arbitrary amplitude.

Carretta tried to solve this shortcoming by adding the *relaxation loop with the finite difference resolution of the Reynolds equation* of Sec. 4.10.5 at the end of the initial METALUB computation. In the past, it was shown that the lubricant pressure was generally lower by this method than by the classical METALUB algorithm. Therefore, the lubricant pressure was less frequently equal to the interface pressure [305] and the separation between the roll and the strip could be prevented. The relaxation loop was, however, not added by default to the classical METALUB computation outside the context of the coupling procedure, because it invalidates user-specified rolling conditions, like the imposed front tension, as explained in Sec. 4.10.5. This seems, however, not to be a problem in the coupling procedure since the solution is iteratively improved and since the classical resolution of the Reynolds equation during the integration of the roll bite was replaced by the relaxation loop in the coupled version of the METALUB computation, as stated in the next paragraphs. Hence, the invalidation of user-specified rolling conditions in a classical METALUB computation could be corrected in the coupling procedure due to its iterative nature.

A second shortcoming of the old coupling procedure was the interpolation of the lubricant pressure of the micro-model during the integration of the roll bite in the coupled version of METALUB instead of the integration of the Reynolds equation as in the classical version. This interpolation was introduced to take into account the variation of the lubricant pressure due to the volume reduction and viscous effects in the FE micro-model. Therefore, *hydrodynamic lubrication along the rolling direction was not taken into account anymore*.

To solve this problem, the *relaxation loop* with the finite difference resolution of the Reynolds equation should also be added *at the end of the coupled METALUB computation*, instead of only at the end of the initial classical METALUB computation. Hence, this relaxation loop with the finite difference resolution of the Reynolds equation could not only solve the non-physical separation problem of the roll and the strip, but also include again hydrodynamic lubrication along the rolling direction in the model.

The relaxation loop was, however, never added in the past because the coupling procedure was already *very complex and non-robust*. Therefore, Carretta tried to *simplify* the coupling procedure

as much as possible to gradually improve its robustness until effectively replacing the asperity crushing equation by FE simulations.

Consequently, the lubricant pressure of the METALUB computations was directly applied to the lubricant portion in the FE model via *pressure elements*, thus rendering the variation of the out-of-plane length of the lubricant portion in Fig. 6.2b unnecessary because the lubricant pressure in the FE model became equal to the lubricant pressure of the METALUB computation. This is indicated by the lubricant pressure between parentheses in Fig. 6.4. Furthermore, the lubricant pressure was also extracted of the FE model as explained before. Thus, this pressure did not change anymore from one iteration to the next of the coupling procedure since the additional relaxation loop with the Reynolds equation was not added, yet. Hence, neither the pressure increase due to the volume reduction of the lubricant domain or viscous effects in the FE computation, nor the pressure increase by the Reynolds equation in METALUB were correctly included in the model, except for the integration of the Reynolds equation in the initial classical METALUB computation. In other words, the coupling procedure was *not representative anymore* of the process that had to be modeled. For this reason, a new coupling procedure, which was developed on the basis of the procedure by Carretta, is explained in the following section.

6.2 New coupling procedure

As mentioned previously, the *old coupling procedure by Carretta* suffered from robustness issues, which were tried to be solved by simplifying this procedure. Nevertheless, these simplifications led the procedure to *not being representative anymore of the process that had to be simulated*. On the one hand, hydrostatic compressibility effects were removed from the model by applying the lubricant pressure of the METALUB computation to the lubricant portion in the FE micro-model of asperity flattening, instead of computing the lubricant pressure by the volume reduction in METAFOR. On the other hand, the removal of the Reynolds equation from the METALUB computation in its coupled version eliminated the proper integration of hydrodynamic lubrication, which is a fundamental mechanism in cold rolling lubrication.

Hence, a *new coupling procedure was developed to take the Reynolds equation correctly into account, while applying directly the lubricant pressure to the top edge of the strip portion* in the FE micro-model of asperity flattening instead of the lubricant domain via pressure elements in the old micro-model. In other words, it was tried to gradually increase the complexity of the rolling model by re-using the functioning parts of the old coupling procedure and by correcting those that required it. In contrast to the old coupling procedure, permeation of the lubricant into the solid contact zone, i.e. MPH lubrication, seems, however, not possible anymore since the lubricant pressure is limited by the interface pressure in the METALUB model. This seems to be a necessary step of development before further improving the model to include MPH lubrication in the future.

In the following three sections, the new coupling procedure is first explained from a *general* perspective before introducing the *details about its micro- and macro-models*.

6.2.1 General description of the new coupling procedure

The key idea behind the new coupling procedure is to *exclusively*[1] *replace the analytical asperity flattening equation in* METALUB *by FE simulations*, and to keep all other equations unchanged. This idea is different from the old coupling procedure, in which also other equations than the flattening equation were modified in the coupled version of METALUB, e.g. the Reynolds equation was not integrated during the integration of all other equations as in a classical METALUB computation.

Figs. 6.5 and 6.6 show the general and detailed *flow diagrams* of the new coupling procedure. Like the old procedure, the new procedure starts by a classical (full) METALUB computation, in which the interface pressure $p_i(x)$, the elongation of the strip $l_{x,s}(x)$ and the lubricant pressure $p_l(x)$ are computed along the roll bite. These profiles are then applied after the METALUB computation in the micro-model to determine the relative contact area $A(x)$ and the mean film thickness $h_t(x)$ by the FE method.

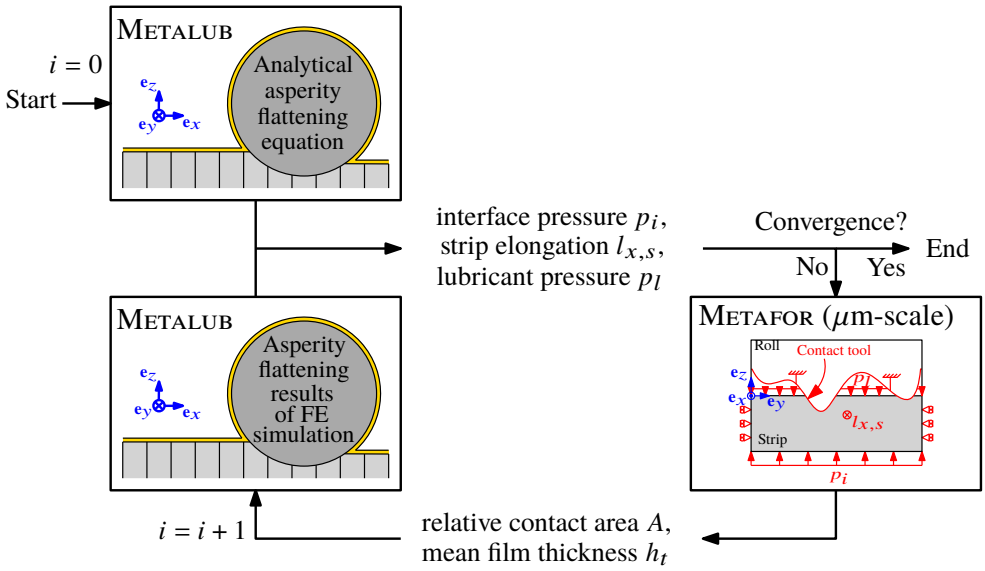

Figure 6.5: General flow chart of the new coupling procedure. An enlarged view of the asperity flattening model in METAFOR is represented in Fig. 6.10 of the following section, where it will be explained in detail.

One should notice that the new micro-model (Sec. 6.2.2) takes *equivalent variables to those of the analytical asperity flattening equation, e.g. Eq.* (4.92)*, as inputs and provides equivalent values as outputs*: concerning the inputs, the interface and lubricant pressures are equivalent to the pressure on top of the asperities (via the sharing law) and the lubricant pressure, which are combined to compute the non-dimensional effective hardness H_a, while the elongation of the strip is the counterpart of the non-dimensional plastic strain rate E_p in the flattening equation. Concerning the outputs, the relative contact area is computed by the analytical asperity flattening

[1]Strictly speaking, the analytical asperity flattening equation is replaced but also the equations that describe the profile conservation hypothesis, i.e. $A = A(h)$ and $h = h(h_t)$ (Sec. 4.4).

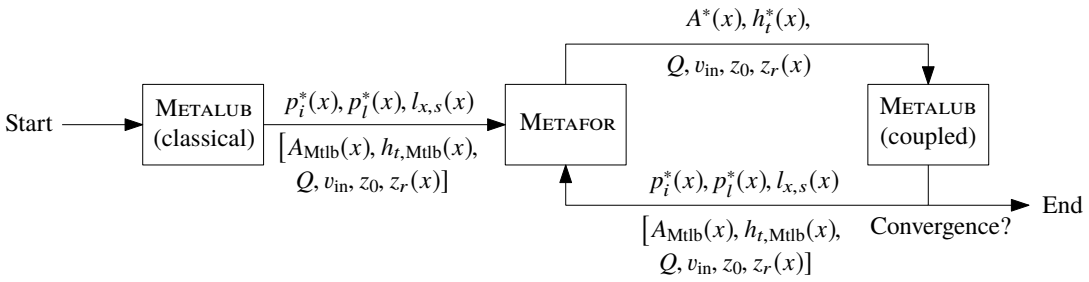

Figure 6.6: Detailed flow chart of the new coupling procedure.

equation as well as by the FE micro-model. In a classical METALUB computation, the mean film thickness h_t is then deduced from the relative contact area A by the profile conservation hypothesis, while it is explicitly computed in the micro-model (see Sec. 6.2.2.2).

Based on the profiles of the relative contact area and the mean film thickness along the roll bite by the FE micro-model, the *coupled version of METALUB then computes again the input values of the micro-model to propagate the influence of the new asperity flattening model in the solution* until this solution does not change significantly anymore from one iteration of the coupling procedure to the next. As mentioned previously, the key modification of METALUB in its coupled version is that only the equations directly related to the asperity flattening equation were replaced and no other equations (see Sec. 6.2.3) in contrast to the old coupling procedure.

Beyond that, the *detailed flow chart* in Fig. 6.6 shows that more data are exchanged between both programs than in the general flow chart (Fig. 6.5). These *additional exchanges* were introduced to improve the convergence behavior.

First, p_i^* and p_l^* are the interface and lubricant pressures, for which negative values were set to 0 since they are non-physical. In fact, both pressures can become slightly negative due to the criterion in METALUB (Eq. 4.241).

Secondly, the coupling procedure is essentially based on *fixed-point iterations*, i.e. the relative contact area profile $A(x)$ of the classical METALUB computation is used to compute a new profile of the relative contact area and so on until the results do not change anymore. To always start from an intermediate solution, which is as close as possible to the final solution in an intermediate METALUB computation, the *state variables of the previous* METALUB *computation* are used as restart points. These state variables are the lubricant flow rate Q, the strip speed at the entry of the bite v_{in}, the vertical position of the roll axis z_0 and the deformed profile of the roll $z_r(x)$.

Thirdly, it is likely that the first results of the micro-model are significantly different from the results of the initial METALUB computation depending on the modeling accuracy of the flattening process by both models. If these results are significantly different, it is also likely that the following intermediate METALUB computation does not converge. Therefore, a *relaxation strategy* was introduced to converge more smoothly to the solution, i.e. the relative contact area and the mean film thickness are gradually adapted by the following equations:

$$A^*(x) = wA_{\text{Mtfr}}(x) + (1-w)A_{\text{Mtlb}}(x) \tag{6.6}$$

$$h_t^*(x) = w h_{t,\mathrm{Mtfr}}(x) + (1-w) h_{t,\mathrm{Mtlb}}(x) \tag{6.7}$$

where w is a relaxation coefficient, which takes a value between 0 and 1, where $A_{\mathrm{Mtfr}}(x)$ and $h_{t,\mathrm{Mtfr}}(x)$ are the predictions of the relative contact area and the mean film thickness by the micro-model in METAFOR, and where $A_{\mathrm{Mtlb}}(x)$ and $h_{t,\mathrm{Mtlb}}(x)$ are their values of the previous METALUB computation.

From a programming point of view, the coupling procedure is managed by a PYTHON script, which calls METALUB and METAFOR by their PYTHON interfaces. Data exchanges are performed via files due to the limited information transit between both programs and to easily restart a computation, since these files are the data sets of each computation.

In the following sections, the *details about the FE micro-model* of asperity flattening in METAFOR and the *macro-model* of cold rolling in METALUB are explained.

6.2.2 FE micro-model of asperity flattening in METAFOR

The *FE micro-model of asperity flattening* in the new coupling procedure is very similar to the one of the old procedure (Sec. 6.1). The main modification is the *application of the lubricant pressure on the strip portion, where it is not in contact with the roll*, instead of the explicit simulation of the lubricant. This model is described more thoroughly in the following sections after a short summary about the specific implementation of the finite element method, which is used to predict asperity flattening.

6.2.2.1 Finite element method

Asperity flattening is simulated by the *non-linear FE solver* METAFOR [258]. In this section, the specific implementation of the finite element method in this solver is briefly summarized, mainly on the basis of [29, 35, 158, 249, 258, 259], in order to explain how the generalized plane-strain state and how the pressure in the non-contacting zones are defined in the following section.

Conservation law

The finite element method was developed to solve the *conservation laws of a continuum*, like, the linear momentum balance, in this case (see Sec. H.1 for the continuum formulation):

$$\rho\ddot{\mathbf{x}} = \nabla\cdot\boldsymbol{\sigma} + \rho\bar{\mathbf{b}} \quad \text{for } \mathbf{x}\in\mathbb{V}(t) \qquad \text{or} \qquad \rho\ddot{x}_i = \frac{\partial\sigma_{ij}}{\partial x_j} + \rho\bar{b}_i \quad \text{for } x_i\in\mathbb{V}(t) \tag{6.8}$$

with the *boundary condition*

$$\bar{\mathbf{t}} = \boldsymbol{\sigma}\mathbf{n} \quad \text{for } \mathbf{x}\in\mathbb{S}_\sigma(t) \qquad \text{or} \qquad \bar{t}_i = \sigma_{ij}n_j \quad \text{for } x_i\in\mathbb{S}_\sigma(t) \tag{6.9}$$

where ρ is the material density, $\ddot{\mathbf{x}}$ the acceleration vector, $\boldsymbol{\sigma}$ the Cauchy stress tensor (symmetric), $\mathbf{x}$ the position vector, $\rho\bar{\mathbf{b}}$ the applied volume force vector, $\mathbb{V}(t)$ the continuum space, $\bar{\mathbf{t}}$ the applied surface traction, $\mathbf{n}$ the unit outward-pointing normal to the surface of the continuum and $\mathbb{S}_\sigma(t)$ the surface of the continuum, on which surface tractions are applied.

Principle of virtual work

The previous strong form of the linear momentum balance and the respective boundary condition is transformed into a weak form by their multiplication with a kinematically admissible virtual displacement $\delta\mathbf{u}(\mathbf{x})$, i.e. an arbitrary weighting function $\delta\mathbf{u}(\mathbf{x})$ such that $\delta\mathbf{u}(\mathbf{x}) = \mathbf{0}$ for $\mathbf{x} \in \mathbb{S}_u(t)$, to obtain the *principle of virtual work* after their summation and the application of Gauss's theorem:

$$\delta\mathcal{M} + \delta\mathcal{W}_{\text{int}} = \delta\mathcal{W}_{\text{ext}} \tag{6.10}$$

with the virtual work done by inertia forces, internal forces and external, i.e. applied forces, respectively:

$$\delta\mathcal{M} = \int_{\mathbb{V}(t)} \delta u_i \, \rho \ddot{x}_i \, \mathrm{d}\mathbb{V} \tag{6.11}$$

$$\delta\mathcal{W}_{\text{int}} = \int_{\mathbb{V}(t)} \frac{\partial(\delta u_i)}{\partial x_j} \sigma_{ij} \, \mathrm{d}\mathbb{V} \tag{6.12}$$

$$\delta\mathcal{W}_{\text{ext}} = \int_{\mathbb{V}(t)} \delta u_i \, \rho \overline{b}_i \, \mathrm{d}\mathbb{V} + \int_{\mathbb{S}_\sigma(t)} \delta u_i \, \overline{t}_i \, \mathrm{d}\mathbb{S} \tag{6.13}$$

Discretization by finite elements

The continuum is *discretized by isoparametric finite elements*, i.e. the positions as well as all other fields are interpolated by the same shape functions. Thus, the nodal positions $\mathbf{x}^I$, for instance, can be interpolated as follows to compute the current positions inside the mesh:

$$\mathbf{x} = N^I \mathbf{x}^I \tag{6.14}$$

where N^I is the I-th shape function. The shape functions are such that $N^I(\boldsymbol{\xi}^J) = \delta_{IJ}$ with $\boldsymbol{\xi}^J$ being the position of node J in the parent space, δ being the Kronecker delta and $I, J \in [1, 2, \ldots, N]$, where N is the number of nodes in the finite element discretization.

The introduction of the discretized virtual displacement, i.e. $\delta\mathbf{u} = N^I \, \delta\mathbf{u}^I$, and that of the accelerations in Eq. (6.10) then leads to the *semi-discretized*, i.e. with respect to space, *momentum balance in its weak form* since these displacements are arbitrary except for their kinematic admissibility:

$$M^{IJ} \, \ddot{x}_i^J + F^I_{\text{int},i} - F^I_{\text{ext},i} = 0 \qquad \text{or} \qquad \mathbf{M}\ddot{\mathbf{x}} + \mathbf{F}_{\text{int}} - \mathbf{F}_{\text{ext}} = \mathbf{0} \tag{6.15}$$

where matrix notations are introduced for readability and where $\mathbf{M}$ is the consistent mass matrix, $\mathbf{F}_{\text{int}}$ the vector of nodal internal forces and $\mathbf{F}_{\text{ext}}$ the vector of nodal external forces:

$$M^{IJ} = \int_{\mathbb{V}(t)} \rho \, N^I N^J \, \mathrm{d}\mathbb{V} = \int_{\mathbb{V}_0} \rho_0 \, N^I N^J \, \mathrm{d}\mathbb{V}_0 \tag{6.16}$$

$$F^I_{\text{int},i} = \int_{\mathbb{V}(t)} \frac{\partial N^I}{\partial x_j} \sigma_{ij} \, \mathrm{d}\mathbb{V} \qquad \text{or} \qquad \mathbf{F}_{\text{int}} = \int_{\mathbb{V}(t)} \mathbf{B}^T \boldsymbol{\sigma} \, \mathrm{d}\mathbb{V} \tag{6.17}$$

$$F^I_{\text{ext},i} = \int_{\mathbb{V}(t)} N^I \, \rho \overline{b}_i \, \mathrm{d}\mathbb{V} + \int_{\mathbb{S}_\sigma(t)} N^I \, \overline{t}_i \, \mathrm{d}\mathbb{S} \tag{6.18}$$

where $\mathbf{B}$ is the strain-displacement matrix.

The mass matrix as well as the vectors of internal and external forces can be computed by *assembling* the contributions of the individual finite elements since the integral over the entire continuum space $\mathbb{V}(t)$ can be separated into integrals over each element due to the finite support of classical shape functions.

Time integration

The discretized momentum balance in Eq. (6.15) is integrated implicitly by the *generalized α-method* [78] to determine the nodal positions $\mathbf{x}_{n+1}$ of the discretized continuum for consecutive, discrete steps in time $t_{n+1} = t_n + \Delta t_n$. Hence, the time-discretized version of Eq. (6.15), which has to be satisfied, is the following one:

$$(1-\alpha_M)\mathbf{M}\ddot{\mathbf{x}}_{n+1} + \alpha_M \mathbf{M}\ddot{\mathbf{x}}_n + (1-\alpha_F)\left[\mathbf{F}_{\text{int},n+1} - \mathbf{F}_{\text{ext},n+1}\right] + \alpha_F\left[\mathbf{F}_{\text{int},n} - \mathbf{F}_{\text{ext},n}\right] = 0 \tag{6.19}$$

where $\mathbf{F}_{\text{int},n} = \mathbf{F}_{\text{int}}(\mathbf{x}_n, \dot{\mathbf{x}}_n)$ and $\mathbf{F}_{\text{ext},n} = \mathbf{F}_{\text{ext}}(\mathbf{x}_n, \dot{\mathbf{x}}_n)$, and where α_M and α_F are numerical parameters.

To compute the nodal positions based on the previous equations, the accelerations are related to the velocities and the velocities to the positions by the following equations of the *Newmark algorithm* [246]:

$$\dot{\mathbf{x}}_{n+1} = \dot{\mathbf{x}}_n + (1-\gamma)\Delta t\, \ddot{\mathbf{x}}_n + \gamma \Delta t\, \ddot{\mathbf{x}}_{n+1} \tag{6.20}$$

$$\mathbf{x}_{n+1} = \mathbf{x}_n + \Delta t\, \dot{\mathbf{x}}_n + (1/2-\beta)\,\Delta t^2\, \ddot{\mathbf{x}}_n + \beta \Delta t^2\, \ddot{\mathbf{x}}_{n+1} \tag{6.21}$$

where β and γ are again numerical parameters. The four previous numerical parameters take the values $\alpha_M = -0.97$, $\alpha_F = 0.01$, $\beta = \beta_0(1-\alpha_M+\alpha_F)^2$ and $\gamma = \gamma_0(1-2\alpha_M+2\alpha_F)$ with $\beta_0 = 1/4$ and $\gamma_0 = 1/2$ to achieve second-order accuracy with respect to the time step for the harmonic oscillator, to minimize low-frequency dissipation and to maximize high-frequency dissipation [249].

Eqs. (6.20) and (6.21) can be inserted into Eq. (6.19) so that the only remaining unknowns are the positions $\mathbf{x}_{n+1}$ at the following time step. The values of these unknowns are then determined by the *Newton-Raphson method* on the basis of the previous configuration, i.e. the final configuration at time step t_n, which is why Metafor is said to implement the *updated Lagrangian formalism*. Hence, the residual at a *mechanical* iteration i of this method, i.e.

$$\Delta\mathbf{F}^i_{n+1} = (1-\alpha_M)\mathbf{M}\ddot{\mathbf{x}}^i_{n+1} + \alpha_M \mathbf{M}\ddot{\mathbf{x}}_n + (1-\alpha_F)\left[\mathbf{F}^i_{\text{int},n+1} - \mathbf{F}^i_{\text{ext},n+1}\right] + \alpha_F\left[\mathbf{F}_{\text{int},n} - \mathbf{F}_{\text{ext},n}\right] \tag{6.22}$$

is gradually reduced by the following correction of the nodal positions,

$$\mathbf{x}^{i+1}_{n+1} = \mathbf{x}^i_{n+1} + \Delta\mathbf{x}^{i+1}_{n+1} \quad \text{with} \quad \mathbf{S}^i_{n+1}\Delta\mathbf{x}^{i+1}_{n+1} = -\Delta\mathbf{F}^i_{n+1} \tag{6.23}$$

which is the result of equating the linearized residual $\Delta\mathbf{F}^{i+1}_{n+1} = \Delta\mathbf{F}^i_{n+1} + \mathbf{S}^i_{n+1}\Delta\mathbf{x}^{i+1}_{n+1}$ to $\mathbf{0}$, where $\mathbf{S}^i_{n+1} = \partial\Delta\mathbf{F}^i_{n+1}/\partial\mathbf{x}^i_{n+1}$ is the tangent Jacobian matrix. The expression of this matrix can be

derived either analytically from the previous equations with the appropriate constitutive equations or numerically by finite differences.

Fig. 6.7 shows a *flow chart of the time integration procedure* in METAFOR without the thermo-mechanical component, which is not included in the asperity flattening computations. Thus, the time integration starts by initializing the positions and velocities. Then, their values at the following time step are predicted and corrected by the Newton-Raphson method until the residual of the out-of-balance forces becomes sufficiently small, i.e. until

$$\frac{\left\|\Delta \mathbf{F}^i_{n+1}\right\|}{\left\|\mathbf{F}^i_{\text{int},n+1}\right\| + \left\|\mathbf{F}^i_{\text{ext},n+1}\right\| + \left\|\mathbf{F}^i_{\text{inert},n+1}\right\|} < \text{tol}_{\Delta \mathbf{F}} \tag{6.24}$$

where $\text{tol}_{\Delta \mathbf{F}}$ is a user-specified tolerance, which is chosen equal to 10^{-5} and where $\mathbf{F}^i_{\text{inert},n+1}$ is the vector of inertial forces. When this condition is satisfied, the time integration continues with the following time step until the final time is reached.

Integration of constitutive equations

While the computation of the mass matrix $\mathbf{M}$ is relatively straightforward by Eq. (6.16) in the initial configuration, the *computation of internal forces* $\mathbf{F}_{\text{int}}$ by Eq. (6.17) is more complex due to the evaluation of the stresses $\boldsymbol{\sigma}$ and due to the computation of the integral in the current configuration.

The stresses are calculated by the material law and the strain increments, which are computed by the estimated nodal positions $\mathbf{x}^i_{n+1}$ and the configuration of the discretized continuum at the previous time step t_n, i.a. the positions $\mathbf{x}_n$. In fact, the *incremental deformation gradient* $\mathbf{F}^i_{n,n+1}$ from the final configuration at the time step n to the configuration i at the time step $n+1$ is computed via the following equation:

$$\mathbf{F}^i_{n,n+1} = \mathbf{J}^i_{n+1} \left(\mathbf{J}_n\right)^{-1} \tag{6.25}$$

where $\mathbf{J}^i_{n+1} = \partial \mathbf{x}^i_{n+1} / \partial \boldsymbol{\xi}$, or componentwise, $J_{ij} = \partial x_i / \partial \xi_j$ without the indices of the mechanical and time iterations, is the Jacobian matrix of the transformation from the parent space to the physical space in its configuration i at time step $n+1$, as illustrated in Fig. 6.8 for a 2D quadrilateral finite element. The *Jacobian matrix of motion* can be computed by the nodal positions $\mathbf{x}^{i,I}_{n+1}$:

$$\mathbf{J}^i_{n+1} = \mathbf{x}^{i,I}_{n+1} \otimes \frac{\partial N^I}{\partial \boldsymbol{\xi}} \tag{6.26}$$

where $\boldsymbol{\xi}$ is the position vector in the parent space. Since the incremental deformation gradient $\mathbf{F}^i_{n,n+1}$ can thus be computed by the given nodal positions $\mathbf{x}^i_{n+1}$, the *incremental natural strain* $\mathbf{E}^i_{n,n+1}$ can be deduced from the definition of this strain measure (Sec. H.1.5).

As mentioned earlier, the stresses are the results of the strain increments and the material law. On the one hand, the strain increments can be computed by the previous equations. On the other

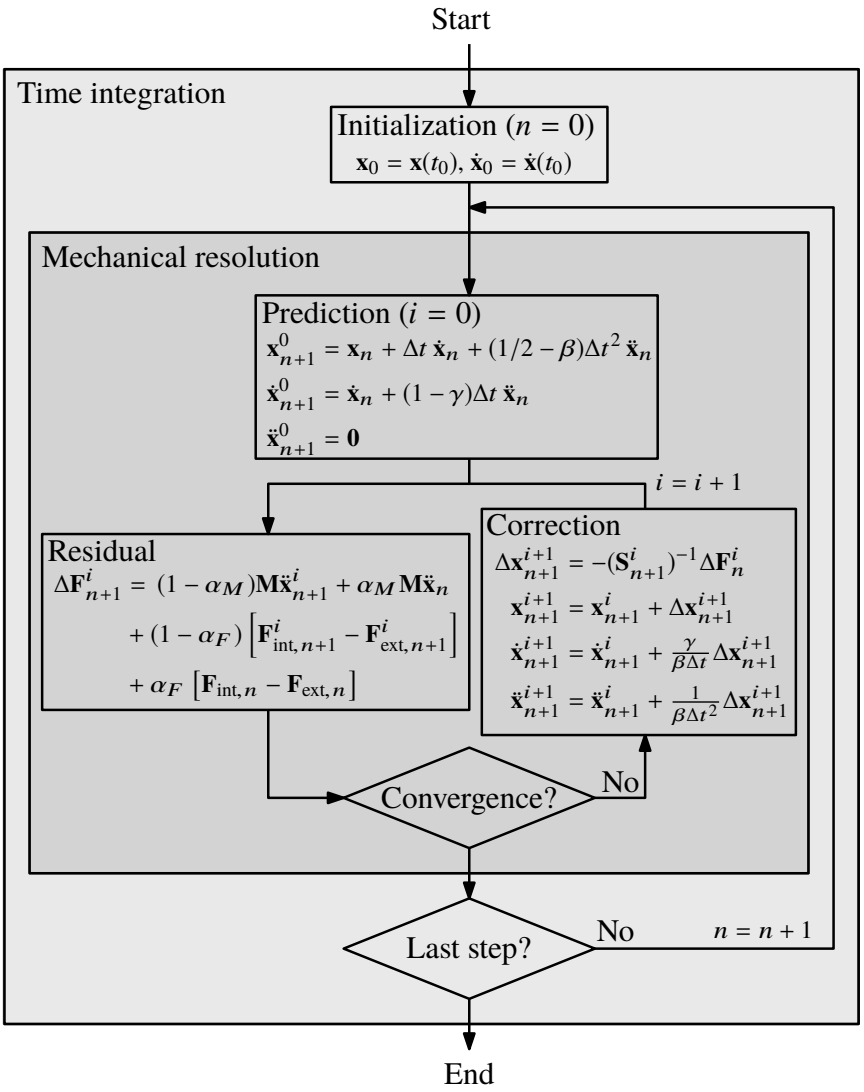

Figure 6.7: Flow chart of the time integration in METAFOR without the thermal component.

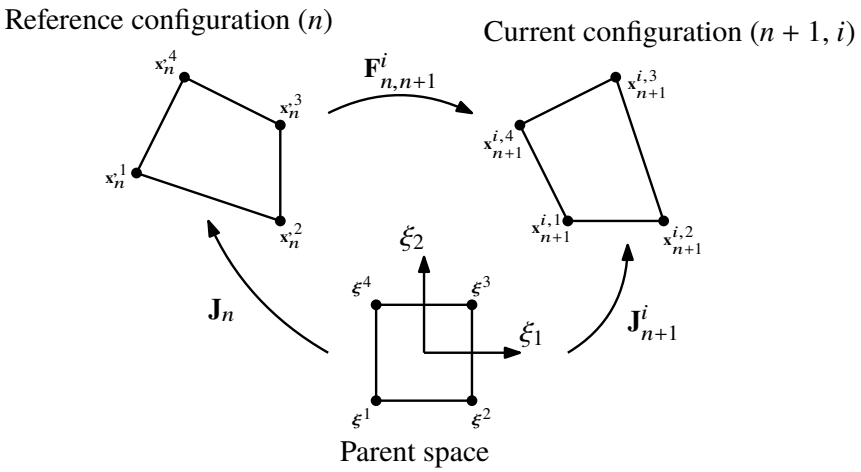

Figure 6.8: Mapping of the reference configuration to the current configuration via the parent space.

hand, the material behavior is assumed to be *elastoplastic* in asperity flattening simulations and the constitutive equations are written in their *hypoelastic* form, i.e. the stress rates are related to the strain rates (Sec. H.3.2). Moreover, only *isotropic hardening* with the *Von Mises yield criterion* (Eq. H.53) is considered here.

The resulting constitutive equations are solved by the *radial return algorithm*, i.e. the stresses are first elastically predicted by the previous strain increments and then corrected by returning the stress state onto the yield surface. More precisely, the pressure at a Gauss point of a finite element is directly computed by Eq. (H.49), since it is independent of the plastic deformation (for a given total deformation)[2],

$$p^i_{n+1} = p_n + K \operatorname{tr} \mathbf{E}^i_{n,n+1} \tag{6.27}$$

while the stress deviator is predicted elastically,

$$\mathbf{s}^{e,i}_{n+1} = \mathbf{s}_n + 2G \operatorname{dev} \mathbf{E}^i_{n,n+1} \tag{6.28}$$

by Eq. (H.50), where K and G are the bulk modulus and the shear modulus. The deviatoric stresses are then rotated to ensure objectivity by writing the following equations in a corotational frame of reference, i.e. a system of coordinates that rotates with the material:

$$\mathbf{s}^{c,i}_{n+1} = \mathbf{R}^i_{n,n+1} \mathbf{s}^{e,i}_{n+1} \mathbf{R}^{i^T}_{n,n+1} \tag{6.29}$$

where $\mathbf{R}^i_{n,n+1}$ is the incremental rotation matrix, which is derived from the incremental deformation gradient $\mathbf{F}^i_{n,n+1}$ by Eq. (H.12).

The previous elastic prediction of the incremental stresses with their rotation is based on the incremental formulation of the equation $\dot{\boldsymbol{\sigma}} = \mathbb{H} : \mathbf{D}$ in the corotational coordinate system, where

[2]To be consistent, the minus sign should rather be used, i.e. $p^i_{n+1} = p_n - K \operatorname{tr} \mathbf{E}^i_{n,n+1}$, since the convention of a positive pressure in a compressive state is chosen in this document and in METALUB. In the context of METAFOR, the opposite convention is, however, chosen, which is why the plus sign was used in Eq. (6.27).

$\mathbb{H}$ is the Hooke tensor (Eq. H.42) and $\mathbf{D}$ the strain rate tensor. Furthermore, the elastic and plastic strain rates are assumed to be additive (Eq. H.52). Hence, the plastic correction should take the following form in the corotational coordinate system by the normal plastic flow hypothesis (Eq. H.62), provided that the Von Mises stress, which is estimated by the elastic prediction, is greater than the yield stress:

$$\dot{\boldsymbol{\sigma}}_{\text{corr}} = -\mathbb{H} : \mathbf{D}^p = -\lambda \mathbb{H} : \mathbf{N} = -2G\lambda \mathbf{N} \tag{6.30}$$

When the normal $\mathbf{N}$ to the yield surface (not the shape function, similar notation) is evaluated by the elastic trial stress, the previous equation can be integrated between t_n and t_{n+1} for the deviatoric stresses:

$$\mathbf{s}_{\text{corr}} = -2G\mathbf{N} \int_{t_n}^{t_{n+1}} \lambda(t)\ \mathrm{d}t = -2G\Gamma\mathbf{N} \tag{6.31}$$

where Γ is an unknown scalar value.

Similarly, the effective plastic strain can be calculated by integrating Eq. (H.64). Thus, the stress state and the proportion of the plastic deformation with respect to the total deformation can be written as a function of Γ:

$$\mathbf{s}^i_{n+1} = \mathbf{s}^{c,i}_{n+1} - 2G\Gamma\mathbf{N} \tag{6.32}$$

$$\overline{\epsilon}^{p,i}_{n+1} = \overline{\epsilon}^p_n + \sqrt{\frac{2}{3}}\Gamma \tag{6.33}$$

The Von Mises yield criterion can therefore finally also be written as a function of the remaining unknown Γ, i.e. $f_Y\{\mathbf{s}^i_{n+1}(\Gamma), \sigma_Y[\overline{\epsilon}^{p,i}_{n+1}(\Gamma)]\} = 0$, which is computed by Newton-Raphson iterations to satisfy this criterion.

Hence, the stresses are known and the integral related to the internal forces in Eq. (6.17) can be computed by *Gaussian quadrature* in the parent space to obtain an exact integration with a minimum number of integrand evaluations, e.g. for one element with full integration (see Sec. 6.2.2.2 for reduced integration):

$$F^{e,I}_{\text{int},i} = \int_{\mathbb{V}^e(t)} \frac{\partial N^I}{\partial \xi_k}\frac{\partial \xi^k}{\partial x_j}\sigma_{ij}\ \mathrm{d}\mathbb{V} \approx \sum_{g=1}^{N_{\text{GP}}} w_g \left(\frac{\partial N^I}{\partial \xi_k}\frac{\partial \xi_k}{\partial x_j}\sigma_{ij} \det\frac{\partial \mathbf{x}}{\partial \boldsymbol{\xi}}\right)\Bigg|_{\boldsymbol{\xi}_g} \tag{6.34}$$

where the configuration (i) and time step (n) suffixes have not been written for readability. Hence, $F^{e,I}_{\text{int},i}$ are the components of the internal force vector $\mathbf{F}^{e,I,i}_{\text{int},n+1}$ of the element e at the node I and at the time step $n+1$ in the configuration i. The integrand is evaluated at the N_{GP} Gauss points of the element whose coordinates in the parent space are $\boldsymbol{\xi}_g$. It is important to notice that $\partial\xi_k/\partial x_j$ are the components of the inverse Jacobian matrix of motion, i.e. $(\mathbf{J}^i_{n+1})^{-1}$, while $\det(\partial\mathbf{x}/\partial\boldsymbol{\xi}) = \det\mathbf{J}^i_{n+1}$, since the Jacobian matrix of motion is slightly modified to impose the out-of-plane length of the strip in the generalized plane-strain state (Sec. 6.2.2.2).

Normal contact and tangential friction forces

To prevent contacting bodies from significantly penetrating each other, normal contact forces between their surfaces are computed thanks to the *penalty method*, which allows a slight overlap (Fig. 6.9a). These contact forces push nodes of the first surface (slave surface) back onto the second surface (master surface), when they penetrate the master surface. The nodal external force due to normal contact is computed linearly with respect to the normal gap between both surfaces:

$$\mathbf{F}_n = -p_c A \mathbf{n} \quad \text{with} \quad p_c = \begin{cases} k_n g_n & \text{, if } g_n < 0 \\ 0 & \text{, otherwise.} \end{cases} \tag{6.35}$$

where p_c is the contact pressure, A the equivalent nodal slave area, $\mathbf{n}$ the unit outward-pointing normal of the master surface, k_n the normal penalty coefficient and g_n the normal gap ($g_n < 0$, if in contact). The value of the normal penalty coefficient k_n should neither be too small nor too large in order to prevent important non-physical penetrations or convergence issues, respectively. As hinted at in Fig. 6.9, the equivalent nodal slave area A of a node is equal to the sum of the half-lengths of the incident segments of this node multiplied by the out-of-plane length in 2D simulations.

(a) Normal contact interaction. The normal contact force $\mathbf{F}_n$ is proportional to the small normal overlap g_n.

(b) Tangential contact interaction. The tangential contact force $\mathbf{F}_t$ is proportional to the tangential gap g_t.

Figure 6.9: Penalty method to model normal and tangential contact interaction.

In addition to the normal contact forces, *tangential friction forces* between contacting surfaces are computed by a tangential gap, which is limited by the Coulomb friction force. More precisely, the projection of the overlapping node onto the master surface is computed, when this node first enters into contact with the master surface. This projection is called the sticking point $\mathbf{x}_s$. The tangential gap g_t is then defined as the distance between this point and the projection $\mathbf{x}_p$ of the current nodal position $\mathbf{x}$ (Fig. 6.9b). Hence, the following equation quantifies the nodal tangential contact force due to friction:

$$\mathbf{F}_t = \tau_c A \frac{\mathbf{x}_s - \mathbf{x}_p}{\|\mathbf{x}_s - \mathbf{x}_p\|} \quad \text{with} \quad \tau_c = \begin{cases} \min\left(k_t g_t, \mu_C \|\mathbf{F}_n\|\right) & \text{, if } g_n < 0 \\ 0 & \text{, otherwise.} \end{cases} \tag{6.36}$$

where τ_c is the contact shear stress, k_t the tangential penalty coefficient and μ_C the coefficient of friction. When the Coulomb friction limit is reached and when the tangential motion between both surface further increases, the position of the sticking point is updated such that $k_t g_t = \mu_C \|\mathbf{F}_n\|$ to return to a state of sticking friction, when the tangential gap decreases.

6.2.2.2 Asperity flattening model

In this section, the details about the new *FE model of asperity flattening* are explained.

Geometry

The *geometry* of the new FE model in Fig. 6.10 is similar to the one of the old procedure apart from not simulating the lubricant portion and its tubes (Sec. 6.1.1). The profiles of the roll and the strip are initially rigidly translated to be in minimal contact since the METALUB data start at the position $x = x_{\text{im}}$, where the first contact occurs.

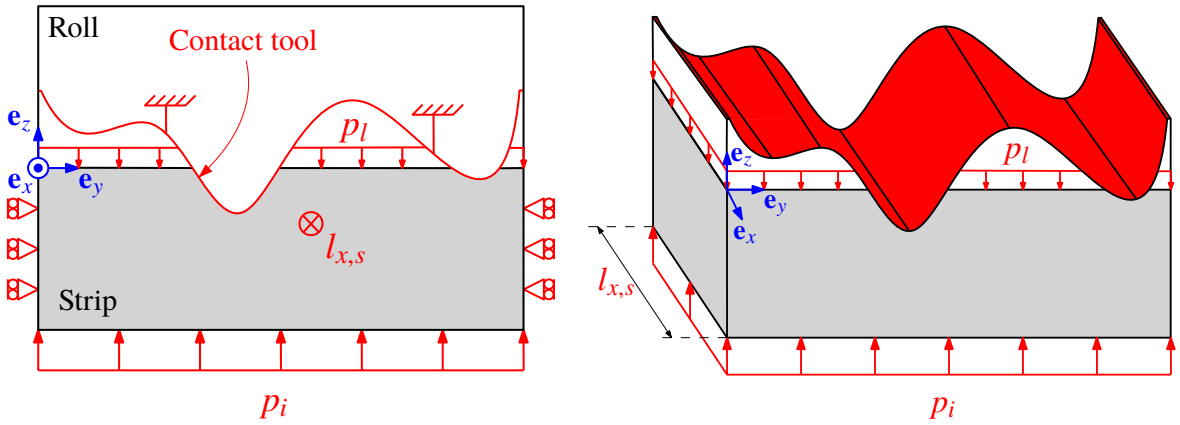

(a) 2D representation with all schematized boundary conditions: discretized strip portion with out-of-plane length $l_{x,s}$, interface pressure p_i, lubricant pressure p_l, contact tool, and prevention of lateral expansion.

(b) 3D representation to put emphasis on the out-of-plane length of the strip $l_{x,s}$ and its influence on the application of the contact tool and the interface pressure p_i.

Figure 6.10: FE asperity flattening micro-model of the new coupling procedure.

Arbitrary geometrical profiles of the roll and strip, like measured profiles, can be included in the FE model. To start with a simple configuration, the roll is assumed to have a triangular asperity profile while the strip is flat, as shown in Fig. 6.11. This configuration is similar to the one of Test 5B, which was used in Sec. 5.3 to quantify the predictive ability of the classical METALUB model, i.e. the roll is significantly rougher than the strip. Due to symmetry, only the red parts in Fig. 6.11 have to be included in the model. This geometry is completely parameterized by the RMS roughness R_q, the half spacing between asperities $\bar{l}$ and the substrate thickness H_0, which has to be sufficiently large to not impact the results (Sec. 6.3.2.1).

Material

The *material law of the strip portion* in the micro-model will be identical to the one in the corresponding METALUB model. This is obviously an assumption since the surface layer of the strip might have different properties than the underlying bulk material. Furthermore, to only gradually increase the complexity of the model, thermo- and viscoplasticity are for now not

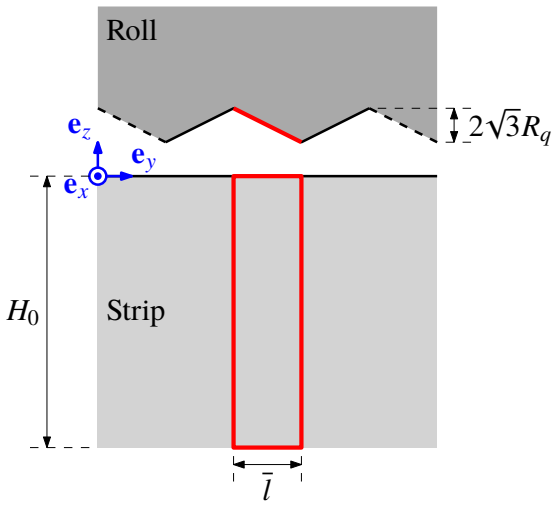

Figure 6.11: Geometry of the strip indentation by a roll with a triangular asperity profile. The red elements are the strip portion and the part of the roll profile that are modeled in the FE model due to symmetry.

included in the micro-model. This implies that these characteristics were also not included in the corresponding METALUB computations (Sec. 6.3).

The contact between the roll and the strip is modeled with friction according to Coulomb's law. The Coulomb coefficient μ_C in the FE model is the same as the boundary coefficient of friction μ_C in the METALUB model.

Mesh

Two different discretization strategies are introduced: on the one hand, the geometry is discretized by a transfinite mesh with n_y quadrilateral elements along $\mathbf{e}_y$ and n_z elements along $\mathbf{e}_z$ by adjusting the length ratio along $\mathbf{e}_z$ so that the elements of the top layer are almost square (Fig. 6.12a). On the other hand, the geometry is recursively divided into quadrangles by the GEN4 mesh generator in METAFOR to allow the specification of a different number of elements along $\mathbf{e}_y$ at the top edge ($n_{y,1}$) of the strip portion than at the bottom edge ($n_{y,2}$, see Fig. 6.12b), where the stress field is probably more uniform.

The meshes are composed of four node *2D quadrilateral (bilinear) Lagrange elements* due to volumetric locking of first-order triangular elements and complex contact treatment of higher-order elements [258].

When the internal forces are integrated as suggested in Eq. (6.34), i.e. by a full integration, with linear elements, the FE model might underestimate the deformations because of *volumetric locking* [258]. This is due to the limited ability of the linear elements to represent isochoric deformation modes, which are dominant when plastic deformations are more significant than elastic ones. In fact, the incompressibility constraint of plastic deformations introduces dependencies between the degrees of freedoms, which lead to an increased stiffness. This problem could be solved

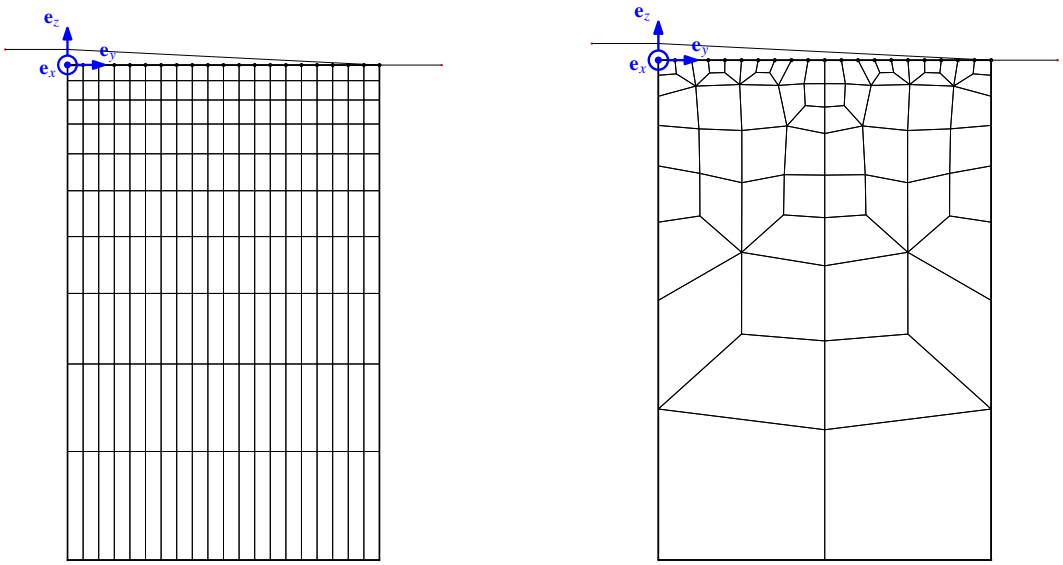

(a) Transfinite mesh with $n_y = 20$ and $n_z = 10$.

(b) GEN4 mesh with $n_{y,1} = 20$, $n_{y,2} = 2$ and $n_z = 8$.

Figure 6.12: Discretization strategies of the strip portion in the micro-model with the contact tool.

by a (fully) reduced integration, e.g. the stresses are integrated at one Gauss point instead of 4 (in 2D), but hourglass modes would be introduced in the solution. Therefore, *selective reduced integration* was applied: instead of evaluating the stresses at all 4 Gauss points of an element to compute the internal forces (e.g. Eq. 6.34), the pressure p is only integrated at the central Gauss point while the deviatoric stresses $\mathbf{s}$ are integrated again at all 4 Gauss points[3]:

$$\mathbf{F}_{\text{int}} = \underbrace{\int_{\mathbb{V}(t)} \mathbf{B}^T \mathbf{s} \, \mathrm{d}\mathbb{V}}_{\text{at 4 Gauss points}} + \underbrace{\int_{\mathbb{V}(t)} p\mathbf{B}^T \mathbf{I} \, \mathrm{d}\mathbb{V}}_{\text{at central Gauss point}} \tag{6.37}$$

where $\mathbf{I}$ is the identity matrix. This method was enhanced by extrapolating the pressure, which is still evaluated at the central Gauss point, to the 4 Gauss points to improve the approximation of the volume integral:

$$\mathbf{F}_{\text{int}} = \underbrace{\int_{\mathbb{V}(t)} \mathbf{B}^T (\mathbf{s} + \overline{p}\mathbf{I}) \, \mathrm{d}\mathbb{V}}_{\text{at 4 Gauss points}} \tag{6.38}$$

where $\overline{p}$ is the pressure evaluation at the central Gauss point of the element, which is assumed to be constant for this entire element. The previous method was adopted with the linear quadrilateral Lagrange elements in the micro-model of asperity flattening.

[3] In this equation, the METAFOR convention, i.e. a negative pressure in compression (plus sign in equation), was used, although the opposite choice was made in this document and in METALUB unless stated otherwise.

Boundary conditions

The boundary conditions are identical to those of the old micro-model (Sec. 6.1.1) except for the *application of the lubricant pressure, where the roll is not in contact with the strip* (Fig. 6.10). In the old model, the lubricant pressure was essentially applied to the entire top edge of the strip portion due to the existence of the lubricant pipes. This resulted in the separation of the roll and the strip with a non-physical amplitude, when the lubricant pressure p_l became equal to the interface pressure p_i. To try preventing this problem from occurring in the new micro-model, the lubricant pressure is directly applied and it is set to zero, where the strip is in contact with the roll, which is more physically consistent.

Practically, this boundary conditions is implemented by setting the contribution of the lubricant pressure in the nodal external force vector either totally (Fig. 6.13a) or partially (Fig. 6.13b) to zero, if the corresponding node is in contact with the roll at the previous time step. More precisely, the contact status of the previous time step is used to implement this functionality in a simple way without introducing any oscillatory behavior. In fact, oscillations could occur if the contact information of the current time step would be used without a continuous loading or unloading mechanism. In consequence, the two scenarios in Fig. 6.13 can be considered: either the contribution of the lubricant pressure on the element between nodes 2 and 3 is or is not added to the external force at node 3. Both configurations are tested in Sec. 6.3.2.1.

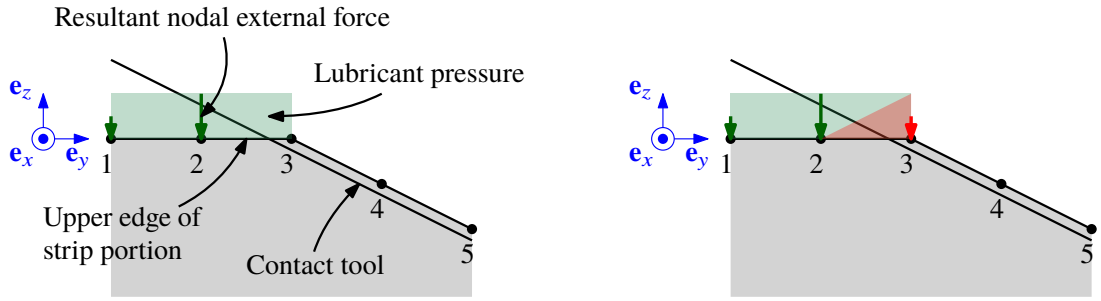

(a) Contribution at transition is zero.

(b) Contribution at transition is not zero (represented in red).

Figure 6.13: Computation of the nodal external forces due to the lubricant pressure when the nodes 3, 4 and 5 are in contact with the roll at the previous time step. The small gap between the contact tool, which represents the roll, and these nodes schematizes the overlap due to the penalty method. The green area represents the lubricant pressure distribution, which is applied to the top edge of the strip portion. The green and red arrows are the resulting nodal forces due to this pressure distribution in consideration of the contact status.

Previously, it was mentioned that the asperity flattening is simulated in a *generalized plane-strain state* to take into account the out-of-plane elongation of the strip portion due to its thickness reduction during rolling. This feature is implemented in classical plane-strain computations by setting the component J_{xx} of the Jacobian matrix of motion $\mathbf{J}^i_{n+1}$ equal to the out-of-plane length of the strip $l_{x,s}$ at the time t_{n+1}. Hence, not only is the elongation directly included in the

computation of the strains to compute the stress state via the incremental deformation gradient (Eq. 6.25) but it is also included in the integrals of internal and external forces via the determinant of the Jacobian matrix of motion (e.g. Eq. 6.34).

It is important to notice that the out-of-plane length $l_{x,s}$ of the strip portion also has to be included in the computation of the equivalent slave area of the contact force (Eqs. 6.35 and 6.36) to keep the gap constant, when the out-of-plane length increases.

Post-processing

As shown in Fig. 6.5, the results of the FE asperity flattening model are the relative contact area $A(x)$ and the mean film thickness $h_t(x)$ along the roll bite.

The *relative contact area* $A = A_r/A_a$ is computed by the method which is schematized in Fig. 6.14b: the intersections between the profiles of the roll and the strip are calculated to project the resulting contact patches onto the horizontal plane, which provide the real contact area A_r (or length in 2D). The relative contact area is then obtained by dividing A_r by the apparent contact area (or width of the reference strip portion in 2D).

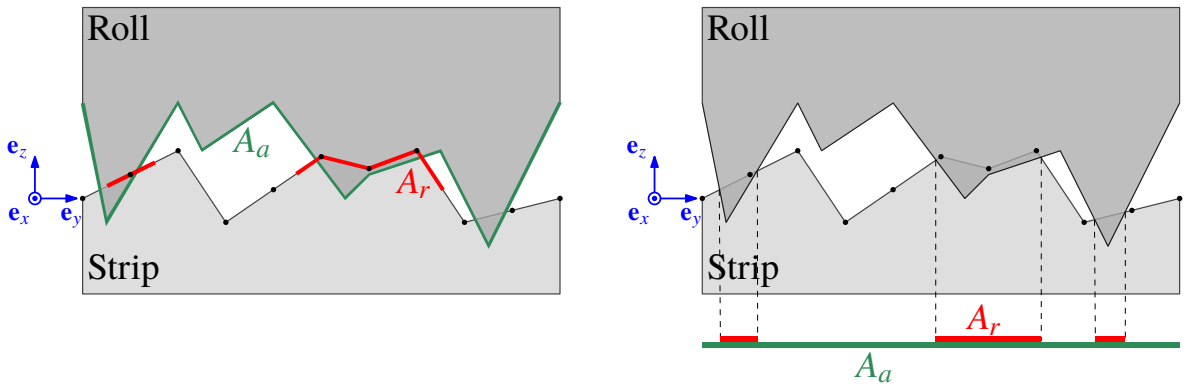

(a) Computation based on slave areas of contacting nodes (old method).

(b) Computation based on projected intersections (new method).

Figure 6.14: Computation of the relative contact area $A = A_r/A_a$ by the real contact area A_r and the apparent contact area A_a.

In the past, the relative contact area was rather computed by the sum of the slave areas (Sec. 6.2.2.1) divided by the total area of the roll profile (Fig. 6.14a). This method was easier to implement than the new method but the old method was not geometrically consistent[4] with the definition of the contact pressures and shear stresses in Eq. (4.3). Nevertheless, differences between both methods should be small due to the small slope of the asperities.

[4]For instance, if the oscillations of the roll profile increase in a region without contact, the apparent contact area in this method increases although the expected apparent contact area, which corresponds to the width of the roll along $\mathbf{e}_y$ in Fig. 6.14a, does not increase. Hence, the relative contact area would be lower than expected.

The *mean film thickness* is determined by computing the following integral:

$$h_t(x) = \int_0^{l_y} [z_r(y) - z_s(y)] \, \mathrm{d}z \tag{6.39}$$

where $z_r(y)$ and $z_s(y)$ are the profiles of the roll and the strip in the normal plane at position x of the roll bite and where l_y is the length of the reference strip portion along $\mathbf{e}_y$. For the geometry in Fig. 6.11, $l_y = \bar{l}$.

The values of the relative contact area and the mean film thickness are written to file at each time step Δt of METAFOR. The maximum value of this time step will be determined in Sec. 6.3.2.1.

6.2.3 Macro-model of cold rolling in METALUB

The *initial METALUB computation* of the coupling procedure in Fig. 6.5 is a *classical* METALUB computation (Chap. 4). To promote the convergence of the coupling procedure, it seems reasonable that the asperity profiles in this initial computation should be as close[5] as possible to those in the FE micro-model, although this is not necessarily a required condition of convergence.

The *following evaluations of METALUB* (*in its coupled version*) in the procedure are identical to those of the classical version except for essentially two modifications: a changed system of equations and the restart from a previous converged configuration.

First, the *analytical equations related to the computation of the relative contact area and the mean film thickness* by the profile conservation hypothesis, e.g. $h = h(h_t)$ and $A = A(h)$, and by the analytical asperity flattening equation, e.g. $E_p = E_p(A, H_a)$, are *replaced by interpolations of the METAFOR results*. Hence, the discrete values $A(x_i)$ and $h_t(x_i)$ of the METAFOR simulation are introduced by the following interpolating equations in the coupled version of METALUB at a position $x \in [x_i, x_{i+1}]$ of the roll bite:

$$A(x) = A(x_i) + \frac{A(x_{i+1}) - A(x_i)}{x_{i+1} - x_i}(x - x_i) \tag{6.40}$$

$$h_t(x) = h_t(x_i) + \frac{h_t(x_{i+1}) - h_t(x_i)}{x_{i+1} - x_i}(x - x_i) \tag{6.41}$$

$$\frac{\partial h_t}{\partial x}(x) = \frac{h_t(x_{i+1}) - h_t(x_{i-1})}{x_{i+1} - x_{i-1}} \tag{6.42}$$

In contrast to the old coupling procedure, no other equations were modified. The resulting system of equations can be found in appendix N.

[5] It seems reasonable that they should even be identical at best. This is, however, not always possible since the modeling hypotheses in METALUB are limited, i.e. the rolls are assumed to be flat, while the strip is rough with a triangular or Christensen asperity profile. One should notice that this flatness hypothesis of the rolls is mitigated by the introduction of the composite roughness, which contains the roughness of the rolls, in METALUB (Sec. 4.4) and the small slops of asperities. This latter condition ensure that indentation and flattening are (almost) equivalent in terms of the pressures involved [367].

Besides replacing the analytical equations by the METAFOR results, the end-of-zone criterion of the hydrodynamic entry zone in Eqs. (4.234) and (4.235) had to be changed to the following condition to detect the contact between the roll and the strip:

$$\frac{t_s}{2} - z_r + h_t > 0 \quad \text{and} \quad \frac{h_t - z_r + t_s/2}{R_q} < \text{tol}_{\text{crit}} \tag{6.43}$$

where the second condition is only required in the integration method with adaptive stepsize, and where h_t is computed by the FE results.

It is worth mentioning that the structured system of equations of previous METALUB versions was entirely rederived to obtain a *structured system of equations* in the classical and coupled versions of METALUB which are as similar as possible. More precisely, one distinguishes the structured system of equations, which is implemented in the METALUB computer program, from the underlying equations since these equations have to be structured so that they can be integrated explicitly, as explained in Sec. 4.10.2. Due to the important number of equations in the model, this non-trivial operation is documented in appendix N. As mentioned previously, great attention was paid to derive the structured system of equations in the most general and modular way possible, i.e. to combine all possible cases in one single structured system of equations, whether the analytical asperity flattening equation, the METAFOR micro-model, a dry roll bite or a lubricated roll bite are included in the model.

Secondly, METALUB in its coupled version is *restarted from the converged configuration of the previous* METALUB *computation*, as mentioned in Sec. 6.2.1, to start from a configuration, which is most likely already closer to the new converged configuration than the default initial state. More precisely, the final state variables of the previous METALUB computation are used as initial guesses of these variables in the current computation. Thus, the initial guess of the deformed roll profile $z_r^{(0)}(x)$ (Sec. 4.10.3.4) in the current computation is assumed to be the final deformed profile of the previous computation. Similarly, the initial guesses of the vertical position of the roll axis $z_0^{(0)}$ (Sec. 4.10.3.3), of the entry speed of the strip $v_{\text{in}}^{(0)}$ (Sec. 4.10.3.2) and of the lubricant flow rate $Q^{(0)}$ (Sec. 4.10.3.1) take their final values of the previous METALUB computation.

One should also notice that the vectors of space x, interface pressure p_i and lubricant pressure p_l, which are created by METALUB to use them in METAFOR, start at x_{im}, i.e. when the roll and the strip get into contact, and that they are written to file for every $\Delta x_{\text{extr},2}$. The value of this data extraction step was determined in Sec. 5.2.3.

6.3 Numerical results of the new coupling procedure

In this section, some *numerical results* of the new coupling procedure are presented to illustrate its strengths and weaknesses. First, each component of the model is tested separately before the results of the complete coupling procedure are presented.

In the same way as in Chap. 5, the numerical procedure is analyzed based on *Test 5B* of the

experimental campaign at Maizières-lès-Metz (Chap. 3 and Sec. E.7), as it will be explained in Sec. 6.3.1.1.

6.3.1 Results of the classical cold rolling model

This section focuses on the macro-model of cold rolling, i.e. METALUB in its classical and coupled versions. First, a numerical *base case* is defined by the classical METALUB model to study exclusively the influence of the flattening model on the rolling force and forward slip in the experimental scenario 5B (Chap. 3 and Sec. E.7). Secondly, a *necessary condition for convergence* of the coupling procedure is introduced and tested.

6.3.1.1 Definition of the base case

As mentioned previously, the test case 5B, in particular 5B-4, of the experimental campaign at Maizières-lès-Metz (Chap. 3 and Sec. E.7) is chosen again for the same reasons as in Sec. 5.2.1 to analyze the predictive ability of the numerical procedure. The parameters of the classical METALUB model were calibrated in Secs. 5.2 and 5.3 to predict the experimental results of this test case as well as possible. These results are summarized in Sec. 5.3.1.6.

To isolate the influence of the asperity flattening model on the results, the previous model of Test 5B is, however, slightly modified. First, *thermoplastic effects* have not yet been introduced in the FE micro-model of asperity flattening to only gradually increase its complexity, if required. Thus, the thermoplastic law in the METALUB model is replaced by an equivalent reduction of the yield stress, as in the past. In any case, the parameters of this law were not measured. Secondly, it seems reasonable to start with the simplest asperity profile in the FE model and to increase its complexity afterwards, if necessary. Either way, the precise profile is not known for the analyzed test case. To use asperity profiles in METALUB that are as close as possible[6] to those in the FE model (Fig. 6.11), the Christensen model, which was previously introduced in the classical METALUB model to study the influence of the surface pattern directionality, is replaced by the *triangular asperity profile* with parallel grooves to the rolling direction.

Fig. 6.15 shows the influence of the previous changes of the model on the results. The yield stress was adjusted by multiples of 10 MPa to reproduce the experimental results. The scenario without thermoplasticity and with a triangular asperity profile is used to test the coupling procedure (Tab. 6.1) in the following sections, as mentioned above.

6.3.1.2 Necessary condition of convergence

In this section, a necessary condition for convergence of the coupling procedure is *defined*. Then, it is explained why it is *not satisfied* before introducing a possible *improvement* of this shortcoming.

[6] Strictly speaking, this would imply that $R_{q,s}$ should be equal to 0 in Tab. 6.1. Since choosing identical parameters of the asperity profiles in METALUB and METAFOR is, however, not necessarily a required condition of convergence, the measured values are preferred here.

Entity	Parameter	Value	Unit
Roll bite	Type	Full-flooded lub.	-
	Heating by friction	On	-
	Heating by plastic deformation	On	-
Strip material	Name	S2	-
	E_s	210000	MPa
	ν_s	0.3	-
	Law	Ludwik	-
	Viscoplasticity	Off	-
	Thermoplasticity	**Off**	-
	A	**660**	MPa
	B	147	MPa
	n	1.52	-
	$\overline{\epsilon}_0^p$	0	-
	ρ_s	$7.850 \cdot 10^{-9}$ [7850]	t/mm^3 [kg/m^3]
	c_s	$500 \cdot 10^6$ [500]	N.mm/(t.°C) [J/(kg.°C)]
	β_s	0.9	-
Strip	t_{in}	0.75	mm
	t_{out}	0.584	mm
	σ_{in}	122.0	MPa
	σ_{out}	184.3	MPa
	$T_{s,\text{in}}$	25	°C
Lubricant	Name	L3	-
	Law	WLF (enhanced)	-
	A_1	49.64	°C
	A_2	0.000365	MPa^{-1}
	b_1	0.00578	MPa^{-1}
	b_2	−0.565	-
	C_1	16.11	-
	C_2	26.00	°C
	η_g	10^6	MPa.s
	$T_g(0)$	−85.96	°C
	T_l	65 (constant)	°C
Interface	Asperity profile	**Triangular**	-
	$R_{q,r}$	**0.732**	μm
	$R_{q,s}$	**0.117**	μm
	$\bar{l}$	51.28	μm
	Flattening equation	Wilson-Sheu	-
	Friction law	Coulomb-Tresca	-
	μ_C	0.11	-
	μ_T	1	-
	Flow factors ϕ_x and ϕ_s	On	-
	Shear stress factors	Off	-
	τ_l	0	MPa
Roll	Deformation method	Meindl (full)	-
	Deformation mode	Plane strain	-
	R_0	195.5	mm
	v_r	3291	mm/s
	E_r	210000	MPa
	ν_r	0.3	-
	x_{12}	−10	mm
	x_{23}	5	mm
	$\Delta\theta_1$	1	°
	$\Delta\theta_2$	$5 \cdot 10^{-3}$	°
	$\Delta\theta_3$	1	°
	Relaxation method	Constant	-
	$w^{(0)}$	0.5	-
Other numerical parameters	Integration method	RK4	-
	x_{12}	−10	mm
	Δx_1	1	mm
	Δx_2	10^{-3}	mm
	tol_Q	10^{-4}	-
	$\text{tol}_{\sigma_{\text{out}}}$	10^{-3}	-
	$\text{tol}_{t_{\text{out}}}$	10^{-4}	-
	tol_R	10^{-6}	-
	$\Delta x_{\text{extr},1}$	1	mm
	$\Delta x_{\text{extr},2}$	10^{-2}	mm
	CIEFS step	Off	-

Table 6.1: Model parameters of Test 5B (Chap. 3 and Sec. E.7) with v_r, t_{out}, σ_{in} and σ_{out} of Tab. E.21 to study the isolated impact of the asperity flattening equation in the coupling procedure. These parameters are based on Tab. 5.4 with the modifications in bold.

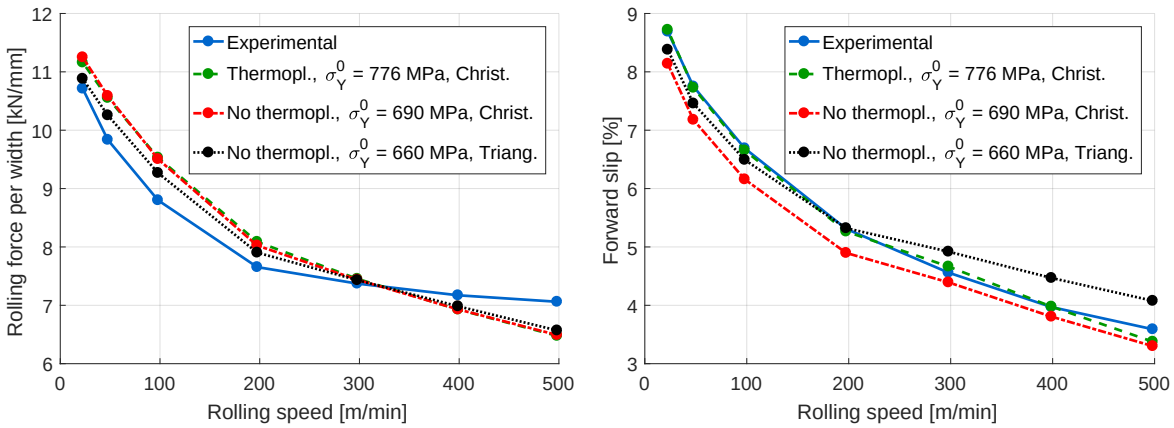

(a) Rolling force per width.

(b) Forward slip.

Figure 6.15: Influence of the required simplifications of the METALUB model to study the isolated impact of the flattening equation in the coupling procedure. The predictions of Test 5B (Chap. 3 and Sec. E.7) are based on Tab. 5.4 with v_r, t_{out}, σ_{in} and σ_{out} of Tab. E.21. The modifications with respect to Tab. 5.4 are mentioned in the legend. To eliminate any misunderstandings, the parameters of the last scenario (no thermoplasticity, $\sigma_Y^0 = 660$ MPa and triangular asperity profile) can be found in Tab. 6.1 with v_r, t_{out}, σ_{in} and σ_{out} of Tab. E.21.

Definition of the necessary condition of convergence

The METALUB-METAFOR coupling procedure is conceptually based on *fixed point iterations*, i.e. it starts from a state, which should be relatively close to the solution, to compute a new state. This state is then again used as input to compute another new state, until these states do not change anymore from one iteration to the next. For instance, the coupling procedure starts with the prediction of the relative contact area by the analytical flattening equation in the classical computation. Then, this relative contact area is progressively updated by using its previous prediction to compute a new prediction until reaching a stationary converged state. In other words, the influence of the FE asperity flattening model is propagated in the solution until, for instance, the rolling force does not change anymore from one iteration to the next.

This implies that *no (significant) change of the results should be observed, if no new component is added to the model*. Hence, the rolling force by a classical METALUB computation, i.e. with the analytical asperity flattening equation, should be equal to the rolling force by the corresponding METALUB computation in its coupled version, which takes the evolution of the relative contact area (amongst others) of the classical METALUB computation as input (Fig. 6.16). This is the *necessary condition for convergence* of the coupling procedure.

While this condition is satisfied for the test scenario in Tab. 6.1 with a dry bite, it is not satisfied when the scenario in Tab. 6.1 is simulated as such, i.e. with a lubricated bite, even by restarting the coupled METALUB computation from the previous final configuration $[Q, v_{\text{in}}, z_0, z_r(x)]$. In general terms, the reason of this non-satisfaction is the *insufficient strength/tightness of the coupling*. In other words, data exchanges between METALUB and METAFOR do not happen frequently enough.

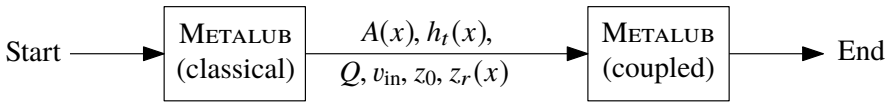

Figure 6.16: Illustration of the necessary condition for convergence of the coupling procedure. The METALUB computation in its coupled version should return the same results as the classical METALUB computation, when it takes the final values of the coupling parameters, i.e. $A(x)$ and $h_t(x)$ mainly, and Q, v_{in}, z_0 and $z_r(x)$ to further ease the convergence, from the classical METALUB computation as inputs.

More specifically, configurations, which are not acceptable in the classical version of METALUB, become acceptable in its coupled version. Hence, the values of the final state variables Q, v_{in}, z_0 and $z_r(x)$ in the coupled computation are different from those in the classical computation, although they should be identical. For this reason, the rolling forces are (significantly) different, too, and the necessary condition for convergence is not satisfied. This explanation is detailed in the following section with an example.

Explanation of the non-satisfied necessary condition of convergence

In the following paragraphs, the *insufficient strength/tightness of the coupling procedure* is proven to be at the cause of the non-satisfaction of the necessary condition for convergence in less abstract words than previously to understand how it could be tentatively solved by keeping the partitioned coupling structure, i.e. without having to replace each evaluation of the asperity flattening equation by a FE computation, which would be very costly (Sec. 6.1.2).

As mentioned previously, it is necessary that the computation of METALUB in its coupled version returns the same results as the computation of METALUB in its classical version, provided that the resulting profiles of the relative contact area and the mean film thickness of the classical METALUB computation are used as inputs of the coupled METALUB computation.

To facilitate the satisfaction of this condition, the coupled METALUB computation is started in a configuration, which is close to the final configuration of the classical METALUB computation (Sec. 6.2.3). Despite these similar configurations, i.e. for the same deformed profile of the roll $z_r(x)$, for the same position of the axis of the roll z_0 and for the same speed at the entry of the bite v_{in}, a decisively different lubricant flow rate Q is chosen in the first adjustment loop of the lubricant flow rate in the coupled METALUB computation with respect to the final lubricant flow rate of the classical computation.

This different choice is due to a different evolution of the lubricant pressure along the roll bite in the classical and coupled METALUB computations. In fact, for identical values of the lubricant flow rate (and identical other state variables), it is possible that the lubricant pressure becomes equal to the interface pressure in the coupled METALUB computation, while it becomes negative in the classical METALUB computation before the end of the roll bite. Fig. 6.17 illustrates this observation considering that the lubricant pressure of the classical computation is only *about to* become negative in this figure, since the integration and the result extraction is stopped in the adjustment loop of the lubricant flow rate, when the lubricant pressure becomes negative, in order

to readjust this rate (Sec. 4.10.3.1). Nevertheless, the results are fundamentally different, which can be explained as follows. The lubricant pressure is generally greater in the coupled METALUB computation than in the classical METALUB computation (in the same configuration), since, in the first case, the relative contact area and the mean film thickness are based on the data of the ***final*** configuration of the classical computation, while they are continuously computed by the analytical flattening equation in the ***current*** configuration in the second case. *In other words, all integrations of the roll bite in the coupled computation are carried out with the final curves $A(x)$ and $h_t(x)$ of the classical computation, so that a different flow rate Q is selected than in the classical computation, where $A(x)$ and $h_t(x)$ are computed during each integration.*

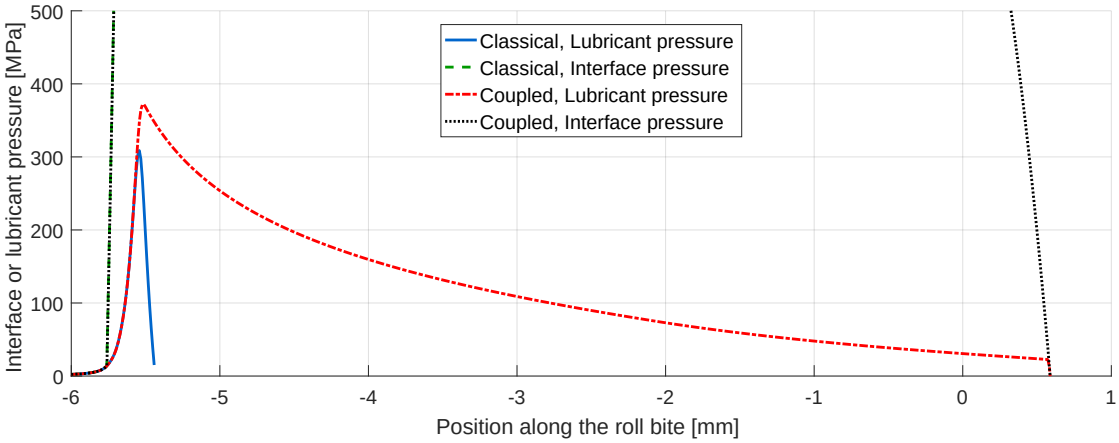

Figure 6.17: Different evolutions of the lubricant pressure along the roll bite in the classical and coupled METALUB computation in the same configuration (z_0 = 195.79134 mm, v_{in} = 2676.6803 mm/s and Q = 0.44680568 mm^2/s) for Tab. 6.1 but with a rigid circular roll. In the coupled METALUB computation, the lubricant pressure can become equal to the interface pressure, while it becomes zero in the classical computation. The variations of the interface pressure of the classical and coupled computations are initially identical. The results of the classical computation are only represented until the lubricant pressure is about to become negative since the integration is stopped at that point to readjust the lubricant flow rate (Sec. 4.10.3.1).

If Q^* is the final lubricant flow rate of the classical METALUB computation and if Q is the flow rate for which the lubricant pressure becomes equal to the interface pressure in the coupled METALUB computation, while it becomes negative before the end of the roll bite in the same configuration in the classical computation (e.g. Fig. 6.17), then $Q^* < Q$, according to the Reynolds equation (Eq. 4.191), i.e.

$$\frac{\partial p_l}{\partial x} = \frac{12\eta}{\phi_x h_t^3}\left(\frac{v_s + v_r}{2} h_t + \frac{v_s - v_r}{2} R_q \phi_s - Q\right) \tag{6.44}$$

In fact, if $Q^* < Q$, the lubricant pressure for Q^* is in general greater than for Q, i.e. $p_l(Q^*) > p_l(Q)$, in the classical METALUB computation again in the same configuration due to the previous equation. In consequence, the non-dimensional effective hardness in the flattening equation is

smaller for Q^* than for Q, i.e. $H_a(Q^*) < H_a(Q)$, because of its definition by Eq. (4.90):

$$H_a = \frac{p_a - p_l}{\tau_Y} \tag{6.45}$$

By the asperity flattening equation (Eq. 4.92), namely,

$$E_p = \frac{1}{0.515 + 0.345A - 0.860A^2}\left(\frac{2}{H_a} - \frac{1}{2.571 - A - A\ln(1-A)}\right) \tag{6.46}$$

this implies that the non-dimensional plastic strain rate is greater for Q^* than for Q, i.e. $E_p(Q^*) > E_p(Q)$. The last inequality means that the decrease of the mean film thickness along the roll bite is smaller for Q^* than for Q, i.e. $\partial h_t/\partial x(Q^*) > \partial h_t/\partial x(Q)$ because of Eq. (N.286) with all terms being positive on the right-hand side except $\partial z_r/\partial x$ (before the outlet zone):

$$\frac{\partial h_t}{\partial x} = \frac{\frac{\partial z_r}{\partial x}}{1 + \frac{t_s E_p}{2\bar{l}}\frac{\partial h}{\partial h_t}} \tag{6.47}$$

Still in the classical METALUB computation, this implies that the mean film thickness is in general greater for Q^* than for Q, i.e. $h_t(Q^*) > h_t(Q)$.

In the coupled METALUB computation, the lubricant pressure for the flow rate Q in the same configuration (v_{in}, z_0 and $z_r(x)$) as the classical computation and with the mean film thickness of this classical computation as input, i.e. $h_t(Q^*)$, is then greater than the lubricant pressure in the classical computation for the same flow rate. This is due to $h_t(Q^*) > h_t(Q)$ which finally implies that $p_l[h_t(Q), Q] < p_l[h_t(Q^*), Q]$ by the expression between parentheses in the Reynolds equation (Eq. 4.191), i.e.

$$\frac{\partial p_l}{\partial x} = \frac{12\eta}{\phi_x h_t^3}\left(\frac{v_s + v_r}{2}h_t + \frac{v_s - v_r}{2}R_q\phi_s - Q\right) \tag{6.48}$$

in the considered range of values. Hence, the lubricant pressure is generally greater in the coupled METALUB computation than in the classical METALUB computation (in the same configuration). This leads then to configurations becoming acceptable, i.e. having a non-negative lubricant pressure before the end of the roll bite, in the coupled version, which are not acceptable in the classical version, as explained before.

Tentative solution to satisfy the necessary condition of convergence

A *tentative numerical solution* to the non-satisfaction of the necessary convergence condition is to select the lubricant flow rate by a stricter criterion than the sign of the lubricant pressure to prevent inadmissible configurations from becoming acceptable in the coupled version.

More precisely, the lubricant flow rate Q is *classically adjusted depending on the sign of the lubricant pressure* p_l, i.e. Q is reduced, if $p_l < 0$ before the end of the bite (Sec. 4.10.3.1). The

resulting evolution of the lubricant and interface pressures along the bite by the classical METALUB computation is shown in Fig. 6.18a. If the same criterion is used in the coupled computation, which takes $A(x)$ and $h_t(x)$ of the classical computation as inputs, the result is significantly different from the one by the classical computation. This is observed by comparing the interface and lubricant pressure profiles for the classical criterion ($p_l < 0$) in Figs. 6.18a and 6.18b. In other words, the necessary convergence condition is not satisfied.

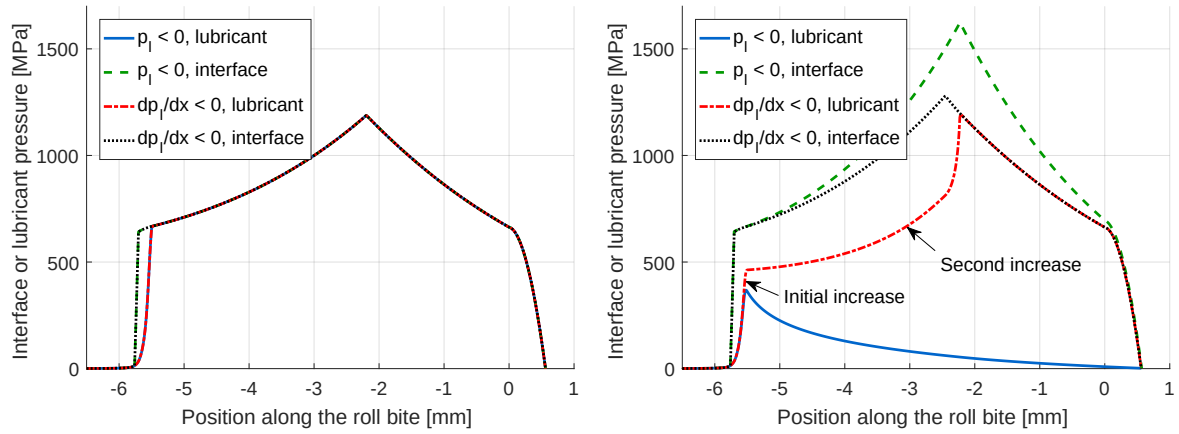

(a) Classical METALUB computation. The curves of the lubricant pressure for the different criteria are superimposed. The same is true for the curves of the interface pressure.

(b) Coupled METALUB computation.

Figure 6.18: Influence of the lubricant flow rate adjustment criterion on the lubricant and interface pressure profiles along the roll bite in the classical and coupled METALUB computations. The results are based on Test 5B-4 (Chap. 3 and Sec. E.7) with the parameters of Tab. 6.1 but with a rigid circular roll. In the coupled computations of METALUB, the flattening equation is replaced by the *final* data of the classical computation, with the same lubricant flow rate adjustment criterion, as illustrated in Fig. 6.16.

Figs. 6.18a and 6.18b show that the significant difference between the results of the classical and coupled computations with the criterion $p_l < 0$ is due to the decrease of the lubricant pressure early on in the bite of the coupled computation. As explained previously, this decrease is caused by using the mean film thickness of another configuration instead of calculating it in the current configuration via the asperity flattening equation and the profile conservation hypothesis. Since the origin of this problem is numerical, a numerical solution is suggested. Hence, the tentative solution is a practical one without necessarily strong physical grounds. It consists in reducing the difference between the results of the classical and coupled computations by replacing the criterion $p_l < 0$ by a criterion based on the *first derivative of the lubricant pressure*, i.e. $\partial p_l/\partial x < 0$ instead of $p_l < 0$. This criterion prevents the lubricant pressure from decreasing unnaturally. To push this idea even further, the second derivative of the lubricant pressure could also be used. Nevertheless, it is more susceptible to numerical errors in the complete coupling procedure than the first derivative. Moreover, the model is already a relatively strong approximation. Thus, the criterion based on the second derivative was not further investigated, although it was implemented.

The introduction of the new criterion for the adjustment of lubricant flow rate causes no changes of the results in the classical computation (Fig. 6.18a). The necessary condition for convergence is still not satisfied but the *differences between the results of the classical and the coupled computations are reduced* (Figs. 6.18a and 6.18b) for this new criterion with respect to the old one. The initial increase of p_l in Fig. 6.18b with the stricter criterion is essentially due to the rapid initial decrease of h_t as in the classical computation, while the second non-linear increase is mainly a consequence of piezoviscosity.

Other tentative solutions could be considered, e.g. only introducing the profiles of $A(x)$ and $h_t(x)$ in the high-speed zones of the coupled computation, or the second derivative in the lubricant flow criterion, as mentioned previously. All of them seem, however, to be strong hypotheses. Hence, it becomes increasingly clear that a stronger coupling or a more general method is required to solve the problem on more solid physical grounds.

In the current absence of a better solution, the criterion $\partial p_l / \partial x < 0$ is introduced in the coupling procedure after analyzing some results of the FE asperity flattening model in the following section.

6.3.2 Results of the FE asperity flattening model

In this section, the results of the FE asperity flattening model in METAFOR are analyzed based on the interface pressure $p_i(x)$, lubricant pressure $p_l(x)$ and strip elongation $l_{x,s}(x)$ of the classical METALUB computation in the test scenario 5B-4 (Chap. 3 and Sec. E.7) in Tab. 6.1. These values are written to file during the final integration in METALUB by starting at the position where the roll gets into contact with the strip and then for every $\Delta x_{\text{extr},2} = 0.01$ mm (Sec. 5.2.3).

The *influence of numerical parameters* on the relative contact area and the mean film thickness is analyzed to show that their values have been chosen thoughtfully before explaining the general results and some *physical influences*.

6.3.2.1 Influence of numerical parameters

The influence of numerical parameters, e.g. the *spatial discretization*, the *penalty coefficient*, the *substrate thickness*, and *other parameters* like the maximum time step and the tolerance of the Newton-Raphson method, is studied in this section.

The respective sensitivity analyses are based on the *reference case* is Tab. 6.2 for the Test 5B-4 (Chap. 3 and Sec. E.7) and deviations are explicitly mentioned. The different choices in this table are successively explained in the following paragraphs unless they have already been mentioned in Sec. 6.2.2.

Influence of the spatial discretization

In a very extensive sensitivity analysis, of which only the results are summarized here for brevity, the influence of the spatial discretization was studied from the $n_y = 20$ by $n_z = 20$ transfinite mesh (Fig. 6.12a) up to the $n_{y,1} = 2560$, $n_{y,2} = 16$ by $n_z = 80$ GEN4 mesh. Even after decreasing the

Entity	Parameter	Value	Unit
Geometry	Model	Fig. 6.11	-
	R_q	0.741	μm
	$\bar{l}$	51.28	μm
	H_0	$30 \cdot 2\sqrt{3}R_q$	μm
Mesh	Mesher	GEN4 (Fig. 6.12b)	-
	$n_{y,1}$	320	-
	$n_{y,2}$	4	-
	n_z	40	-
Strip material	ρ_s	7850	kg/m^3
	E_s	210000	MPa
	ν_s	0.3	-
	Hardening law	Ludwik (Eq. 4.54)	-
	A	660	MPa
	B	147	MPa
	n	1.52	-
Contact	Law	Coulomb	-
	μ_C	0.11	-
	k_n	10^9	MPa/mm
	k_t	$\mu_C k_n$	MPa/mm
Boundary conditions	Application of $l_{x,s}(x)$	On	-
	Application of $p_l(x)$	On	-
	Percentage of p_l	95	‰
	Application of $p_i(x)$	On	-
	Pressure at transition	On, i.e. Fig. 6.13b	-
	v	1	mm/s
Time integration	$\text{tol}_{\Delta\mathbf{F}}$	10^{-5}	-
	$\Delta t_{\max}$	10^{-2}	s
	Δt_0	$\Delta t_{\max}$	s

Table 6.2: METAFOR FE model parameters of Test 5B-4 (Chap. 3 and Sec. E.7).

tolerance $\text{tol}_{\Delta\mathbf{F}}$ to 10^{-9} (non-convergence for smaller values) and increasing the normal penalty coefficient k_n up to 10^{11} MPa/mm (non-convergence for greater values), a *mesh dependence* could still be observed as illustrated for slightly lower values in Fig. 6.19 for the meshes in Fig. 6.20. This observation is explained step-by-step hereafter.

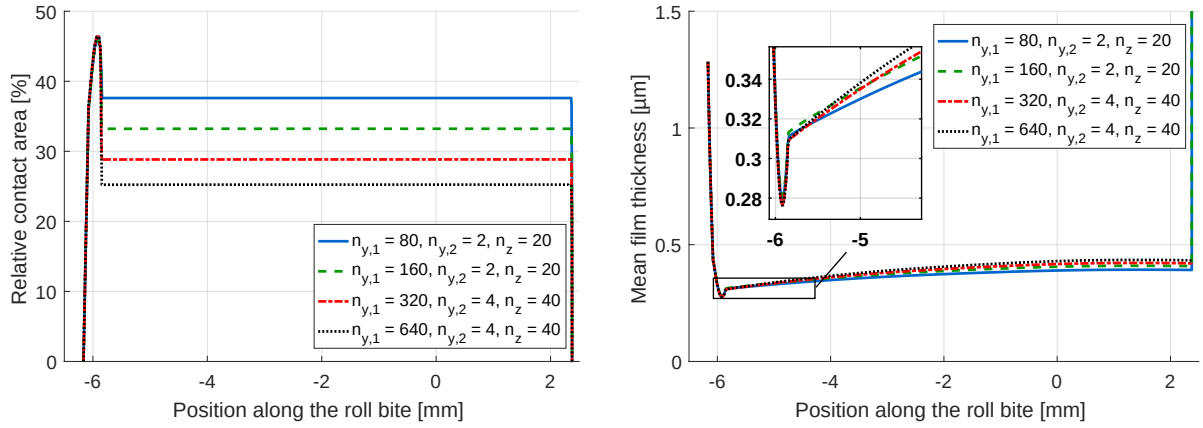

(a) Relative contact area.

(b) Mean film thickness.

Figure 6.19: Influence of the spatial discretization with the parameters of Tab. 6.2 (but 100% p_l), $k_n = 10^{10}$ MPa/mm and $\text{tol}_{\Delta\mathbf{F}} = 10^{-9}$ based on the METALUB computation with the parameters of Tab. 6.1. The results are clearly mesh dependent. The corresponding meshes are shown in Fig. 6.20.

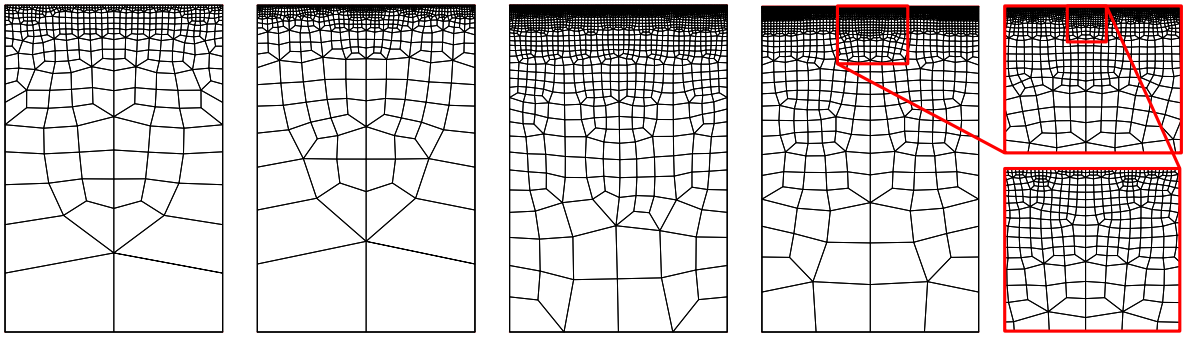

(a) $n_{y,1} = 80$, $n_{y,2} = 2$ and $n_z = 20$ (466 elements).

(b) $n_{y,1} = 160$, $n_{y,2} = 2$ and $n_z = 20$ (820 elements).

(c) $n_{y,1} = 320$, $n_{y,2} = 4$ and $n_z = 40$ (3090 elements).

(d) $n_{y,1} = 640$, $n_{y,2} = 4$ and $n_z = 40$ (5646 elements) with enlarged views.

Figure 6.20: Different meshes whose influence on the relative contact area and the mean film thickness is studied in this section.

First, transfinite meshes are in general more expensive than GEN4 meshes in this context for a given number of elements along the slave edge (n_y or $n_{y,1}$, respectively) and the lateral edges (n_z) due to the greater number of elements, which is due to the mesh structure of transfinite meshes. Nevertheless, the results are almost identical under these conditions, i.e. same n_y or $n_{y,1}$, respectively and n_z. For this reason and since the results mainly depend on the number of elements along the slave edge, *GEN4 meshes are preferred to transfinite meshes*.

Secondly, one might wonder whether the mesh dependence is related to the specific *way of applying the lubricant pressure* or not (Sec. 6.2.2.2, Fig. 6.13). Hence, Fig. 6.21a shows the influence of both methods, which were implemented to only apply the lubricant pressure where no contact exists between the roll and the strip. The relative contact area A is greater with the first method (Fig. 6.13a) than with the second (Fig. 6.13b) due to the absence of the lubricant pressure contribution on the node at the contact transition. Nevertheless, the mesh dependence still exists. It can presumably be explained as follows.

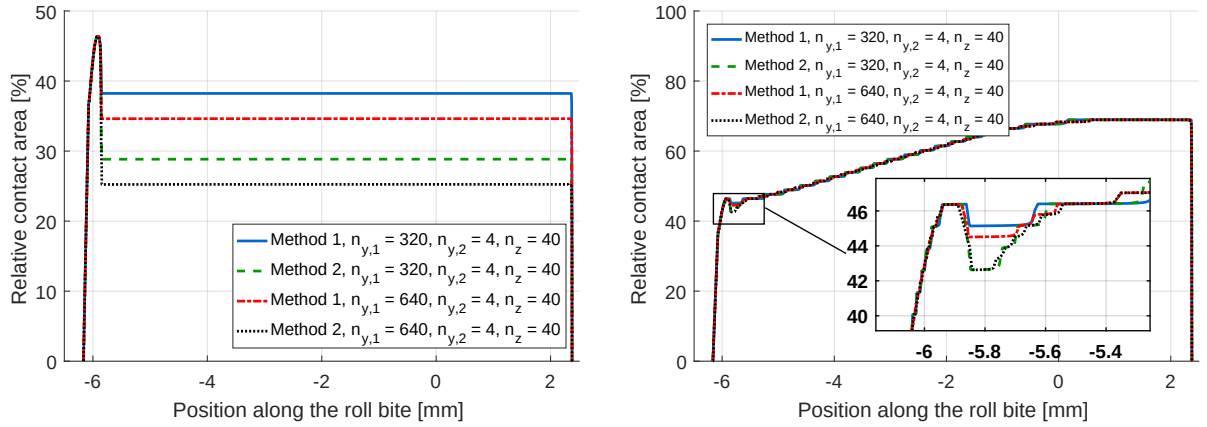

(a) 100% lubricant pressure.

(b) 95% of the lubricant pressure.

Figure 6.21: Influence of the method which only applies the lubricant pressure where the strip is not in contact with the roll. The results were obtained with the parameters of Tab. 6.2, $k_n = 10^{10}$ MPa/mm and $\text{tol}_{\Delta\mathbf{F}} = 10^{-9}$ or $\text{tol}_{\Delta\mathbf{F}} = 10^{-5}$ (in Figs. 6.21a and 6.21b, respectively) based on the METALUB computation with the parameters of Tab. 6.1. Methods 1 and 2 are those in Figs. 6.13a and 6.13b, respectively. The corresponding meshes are shown in Fig. 6.20.

Initially, the relative contact area increases and the mean film thickness decreases since the interface pressure p_i and the out-of-plane length $l_{x,s}$ increase (Figs. 6.18a and 6.19, Sec. 6.3.2.2). When the lubricant pressure p_l then becomes more and more important with respect to the interface pressure, the relative contact area decreases and the mean film thickness increases since the lubricant pressure pushes the top edge of the strip downwards. Ultimately, the *lubricant pressure becomes equal to the interface pressure*. It can be assumed that configuration 1 in Fig. 6.22a represents the configuration, in which the local asperity contact pressure p_a^* is not yet in equilibrium, when the lubricant pressure just became equal to the interface pressure. To reach the equilibrium configuration, the average asperity contact pressure p_a has to be equal to the lubricant pressure by the vertical force balance. Moreover, the local contact pressure p_a^* is assumed to have a linear distribution, which takes its lowest values where the asperity just got in contact with the roll while the highest value is reached where the strip got indented most. Since the contact pressure is on average equal to the lubricant pressure, this results in the contact pressure being smaller than the lubricant pressure where the asperity just got in contact with the roll as illustrated in Fig. 6.22a. In consequence, the lubricant pressure locally breaks the contact between the roll and the strip as shown by configuration 2 with respect to configuration 1 in Fig. 6.22.

Due to the vertical force balance, the asperity contact pressure is flatter in configuration 2 than in configuration 1. In "reality", i.e. without FE discretization, this process would continue since the lubricant pressure remains greater than the contact pressure at the transition point between the contacting and non-contacting interfaces. In the FE model, this process, however, depends on the fineness of the mesh and the normal penalty coefficient. In fact, if the fineness of the mesh decreases, so that the discretization approaches "reality", the relative contact area decreases as previously shown in Fig. 6.21a.

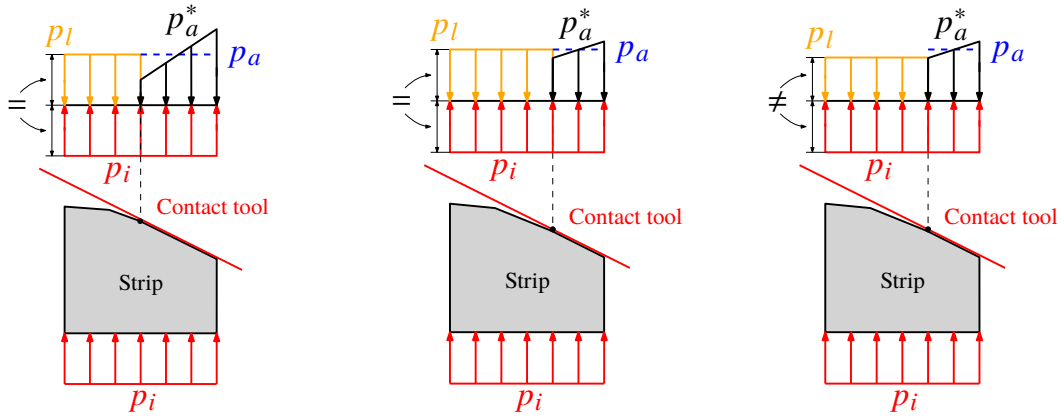

(a) Configuration 1 ($p_l = p_i$). **(b)** Configuration 2 ($p_l = p_i$). **(c)** Configuration 3 ($p_l \neq p_i$).

Figure 6.22: Progressive loss of contact from configuration 1 to configuration 2, when the lubricant pressure p_l just became equal to the interface pressure p_i. If the lubricant pressure is reduced so that it cannot become equal to the interface pressure, the contact loss stops at some point (configuration 3).

One might wonder whether an artificial reduction of the lubricant pressure could solve the problem since the asperity contact pressure could then become equal to the lubricant pressure at the transition point between the contacting and non-contacting interfaces as illustrated in Fig. 6.22c. And, in fact, the mesh dependence essentially disappears when the *lubricant pressure is reduced*, for instance, to about 95% of its initial value, as shown in Fig. 6.21b. Nevertheless, the relative contact area and the mean film thickness are highly-dependent on this percentage as shown in Fig. 6.23. This very strong dependence is probably due to the flatness of asperities, which are $2\sqrt{3}R_q/(2\bar{l}) \approx 40$ times wider than high and the reduction of resistance to indentation by the out-of-plane elongation (Sec. 6.3.2.2).

To push the boundaries of asperity flattening simulations as much as possible, this *study is continued despite the criticizable hypothesis of applying only 95% of the lubricant pressure*. No other method seems currently to exist to solve the previous problem, except for the *classical* METALUB *model*, which is, however, based on the analytical flattening equation. In fact, the mesh dependence does not exist in this model, when $p_l = p_i$, because $H_a \to 0$ (by Eqs. 4.4 and 4.90), $E_p \to +\infty$ (by Eq. 4.92) and $\partial h_t/\partial x \to 0$ (by Eq. N.286), when $p_l \to p_i$. This means that the relative contact area does not change anymore when $p_l \to p_i$ since $A = A(h_t)$.

With only 95% of the lubricant pressure, the *influence of the spatial discretization* can finally be analyzed without a significant mesh dependence based on Fig. 6.24. The influence of the

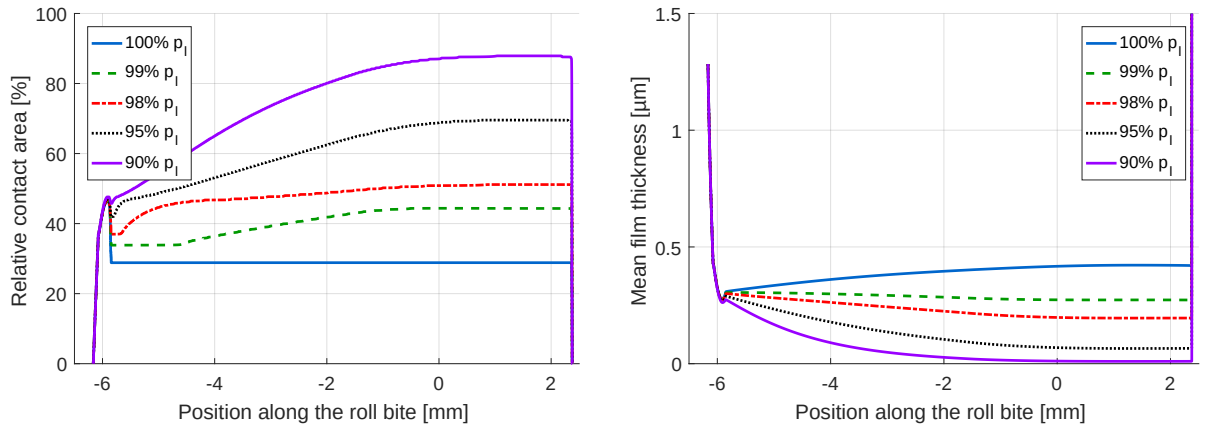

(a) 100% lubricant pressure.

(b) 95% of the lubricant pressure.

Figure 6.23: Influence of the lubricant pressure reduction. The results were obtained with the parameters of Tab. 6.2, $k_n = 10^{10}$ MPa/mm and $\text{tol}_{\Delta\mathbf{F}} = 10^{-9}$ based on the METALUB computation with the parameters of Tab. 6.1.

mesh is still visible for $n_{y,1} = 80$, where one element is equivalent to a little more than 1% of relative contact area, while it is almost not visible for $n_{y,1} = 320$. The mean film thickness is less dependent on the mesh refinement since it is an average value of the geometrical configuration.

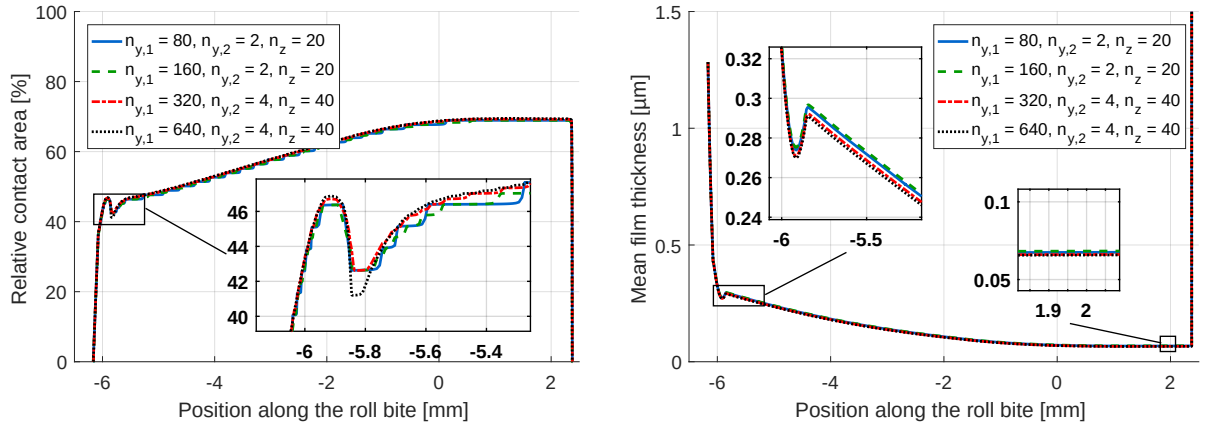

(a) Relative contact area.

(b) Mean film thickness.

Figure 6.24: Influence of the spatial discretization with the parameters of Tab. 6.2 (in particular, 95% of the lubricant pressure) and $k_n = 10^{10}$ MPa/mm based on the METALUB computation with the parameters of Tab. 6.1. The corresponding meshes are shown in Fig. 6.20.

Influence of the contact parameters

The *contact parameters* were entirely defined by setting the value of the normal penalty coefficient k_n because the coefficient of friction μ_C was assumed to be equal to the boundary coefficient of

friction μ_C of the METALUB model and since normal and tangential gaps are usually imposed to have the same amplitude by setting $k_t = \mu_C k_n$.

Fig. 6.25 shows that choosing a greater normal penalty coefficient than 10^9 MPa/mm does not substantially change the results and that the computation with $k_n = 10^{11}$ MPa/mm leads to convergence issues.

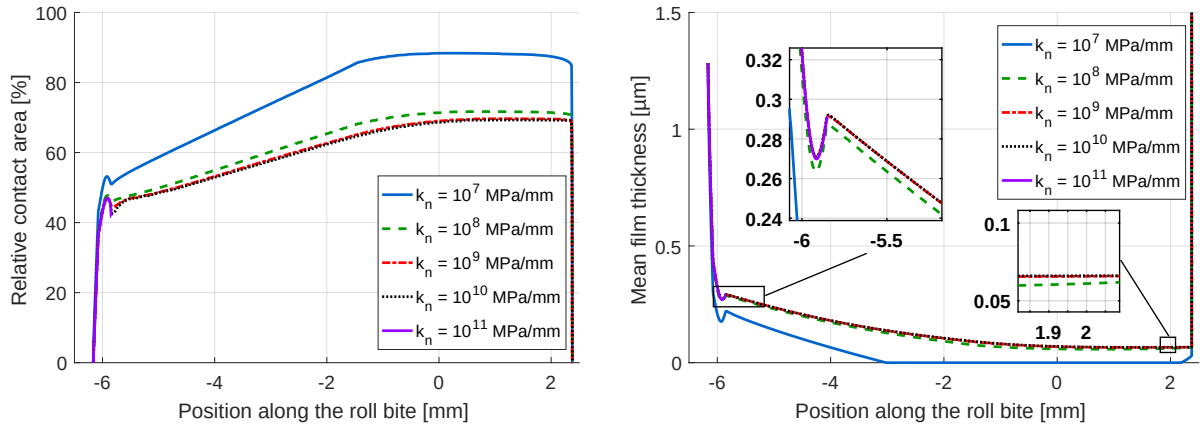

(a) Relative contact area.

(b) Mean film thickness.

Figure 6.25: Influence of the normal penalty coefficient k_n with the parameters of Tab. 6.2 based on the METALUB computation with the parameters of Tab. 6.1.

Influence of the substrate thickness

Fig. 6.26 indicates that the *substrate thickness* H_0 should be equal to about $30 \cdot 2\sqrt{3}R_q$ to obtain results which are essentially independent of this value. The influence of the mesh quality was controlled during to modifications of the geometry: it had no influence.

Influence of other numerical parameters

Additional parameters had to be specified for the simulation to run as expected. First, the tolerance of the mechanical iterations $\text{tol}_{\Delta\mathbf{F}}$ (Eq. 6.24) had essentially no influence on the results when it was increased from 10^{-7} to 10^{-3}, which is why the default value 10^{-5} was chosen. This was not true for the simulations in which the full lubricant pressure was included. In fact, the results were highly dependent on the tolerance.

Secondly, the maximum time step $\Delta t_{\max}$ was set equal to 0.01 s, which is equivalent to the extraction step $\Delta x_{\text{extr, 2}} = 0.01$ mm of the METALUB model, if the conversion factor $v = 1$ mm/s. The results do not change significantly when $\Delta t_{\max}$ takes different values between 0.0025 s and 0.04 s, which can be explained by the automatic step adaptation in METAFOR, when the mechanical iterations do not converge. This is also the reason why the initial time step Δt_0 was set equal to $\Delta t_{\max}$.

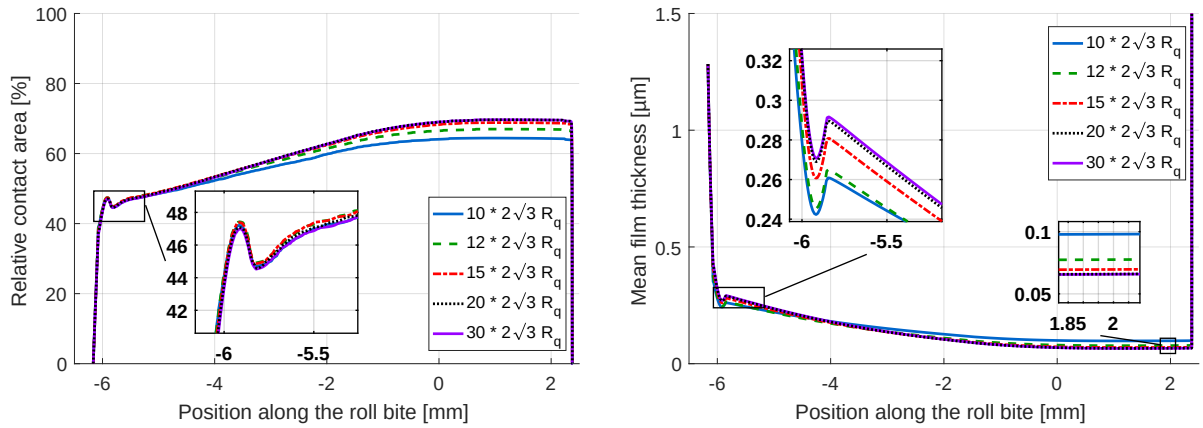

(a) Relative contact area.

(b) Mean film thickness.

Figure 6.26: Influence of the substrate thickness H_0 with the parameters of Tab. 6.2 based on the METALUB computation with the parameters of Tab. 6.1.

Finally, the independence of velocity and inertia effects was checked by varying the conversion factor v between 1 and 1000 mm/s and the density between ρ_s and $1000\rho_s$ (Tab. 6.2). No modifications of the results were observed, which is coherent with the chosen rate-independency of the material and the small spatial size of the model.

6.3.2.2 General results and influence of physical parameters

In the previous section, it was explained how the numerical parameters in Tab. 6.2 were chosen. On the basis of these parameters, some *general results* and the *influence of physical parameters* are presented in this section.

Fig. 6.27 shows the evolution of the relative contact area and the mean film thickness along the roll bite when the lubricant pressure and the out-of-plane elongation of the strip are included in the model or not. First, if *only the interface pressure is activated*, i.e. the lubricant pressure p_l and the out-of-plane elongation $l_{x,s}$ are not applied, the evolution of the relative contact area along the roll bite actually resembles that of the interface pressure (Fig. 6.18a) for obvious reasons. The mean film thickness resembles the inverse of the interface pressure, which is coherent, because it decreases when the interface pressure increases. Secondly, if 95% of the *lubricant pressure are also activated*, the relative contact area decreases as soon as the lubricant pressure becomes significant. The solid/solid contact is, however, not entirely lost since the lubricant pressure is limited to 95%. The remaining variation resembles again that of the interface pressure but at a lower amplitude than without the lubricant pressure. Thirdly, *activating the out-of-plane elongation* significantly increases the relative contact area due to the reduced resistance of the strip material to indentation (Sec. 2.2.2.2). If the lubricant pressure is not applied, i.e. if no lubricant is in the FE model, the roll and the strip are in full contact at some point of the bite. Finally, if *all boundary conditions* are activated, the full solid/solid contact is not reached and a small bump after the position $x = -6$ mm is still present due to the influence of the lubricant

pressure.

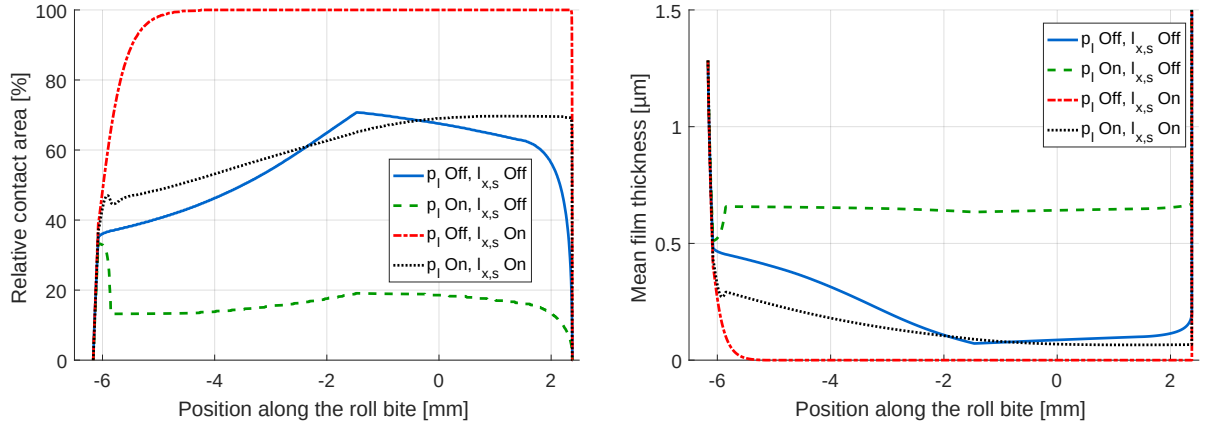

(a) Relative contact area.

(b) Mean film thickness.

Figure 6.27: General results of the FE asperity flattening model with the parameters of Tab. 6.2 based on the METALUB computation with the parameters of Tab. 6.1. The lubricant pressure p_l and the out-of-plane elongation of the strip $l_{x,s}$ are either included in the model or not.

The *explanation of this bump* is a little more subtle than one might think. In fact, Fig. 6.28a shows that the relative contact area is still increasing, when the lubricant pressure is increasing, provided that the out-of-plane elongation is activated in the FE model. The increase of the relative contact area is due to two mechanisms. First, the lubricant pressure is applied where the strip portion is not in contact with the roll, while the interface pressure is applied along the entire width of the portion. Hence, the resulting force of the lubricant pressure is smaller than this pressure multiplied by the width of the strip portion. Secondly, the resistance of the material to indentation is reduced by the out-of-plane elongation.

The results of the classical METALUB computation can be compared to the results of the FE METAFOR computation, which takes $p_i(x)$, $p_l(x)$ and $l_{x,s}(x)$ of the METALUB computation as inputs. The FE results are obviously strongly dependent on the reduction of the lubricant pressure, as mentioned previously. Qualitatively, the correspondence is best for the FE results without reduction of the lubricant pressure, while, quantitatively, it is better for a 95% reduction. Due to the mesh dependence and the non-physical reduction of the lubricant pressure, it is, however, not possible to advance further conclusions.

Finally, for the sake of completeness, Fig. 6.30 shows the Von Mises stress in the strip portion at different locations in the roll bite, which are indicated in Fig. 6.29a. The mesh is also represented in this figure to illustrate the required fineness. One notices that the Von Mises stress is essentially identical in the whole strip portion after the position $x = -6$ mm because of the relatively important out-of-plane elongation.

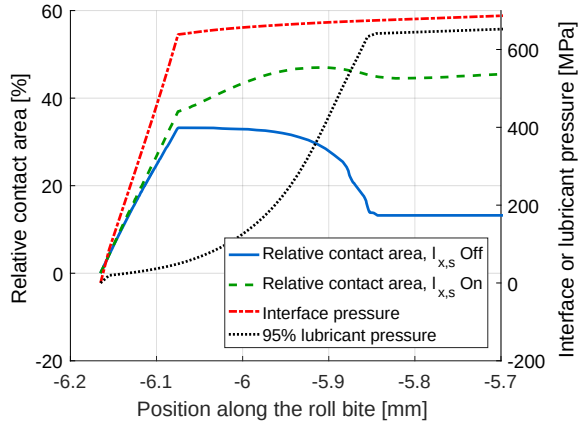

(a) Confrontation with pressures.

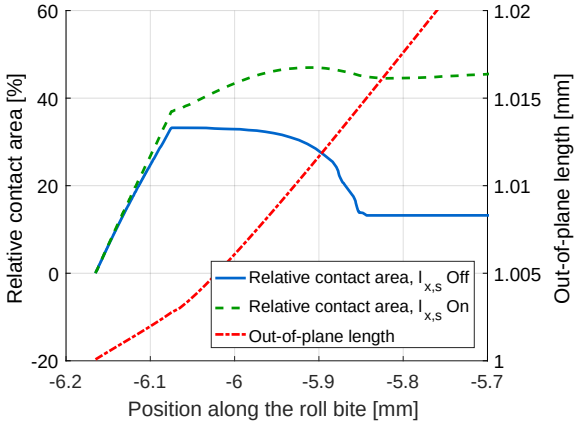

(b) Confrontation with out-of-plane length.

Figure 6.28: Explanation of the bump after the position $x = -6$ mm in Fig. 6.27a based on the boundary conditions. The relative contact area is computed by the FE asperity flattening model with the parameters of Tab. 6.2 based on the METALUB computation with the parameters of Tab. 6.1. The out-of-plane elongation $l_{x,s}$ is either included in the FE model or not.

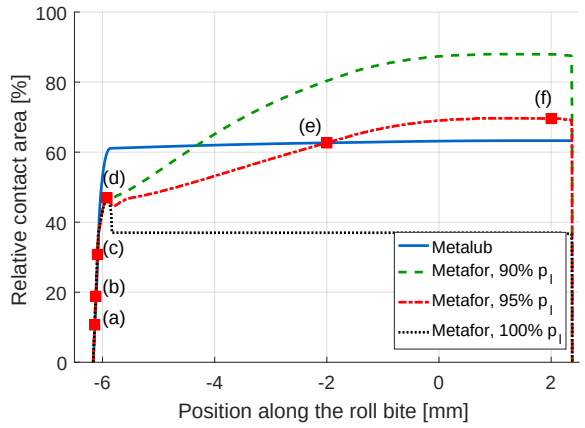

(a) Relative contact area.

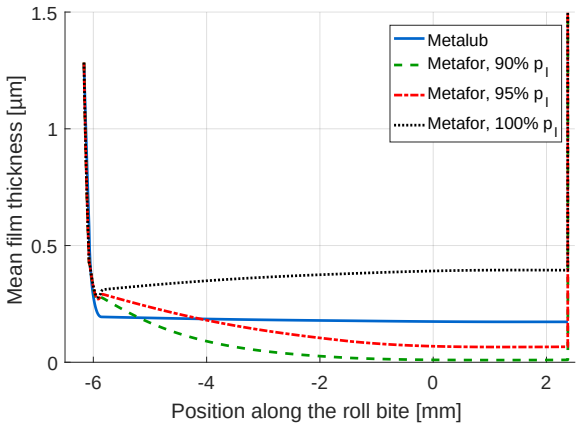

(b) Mean film thickness.

Figure 6.29: Comparison of the classical METALUB results to the FE METAFOR results with different reductions of the lubricant pressure. The square markers in Fig. 6.29a indicate the positions in the roll bite, for which the Von Mises stress is represented in Fig. 6.30. The METAFOR results were computed by the asperity flattening model with the parameters of Tab. 6.2 (except for the reduction percentage of the lubricant pressure) based on the METALUB computation with the parameters of Tab. 6.1.

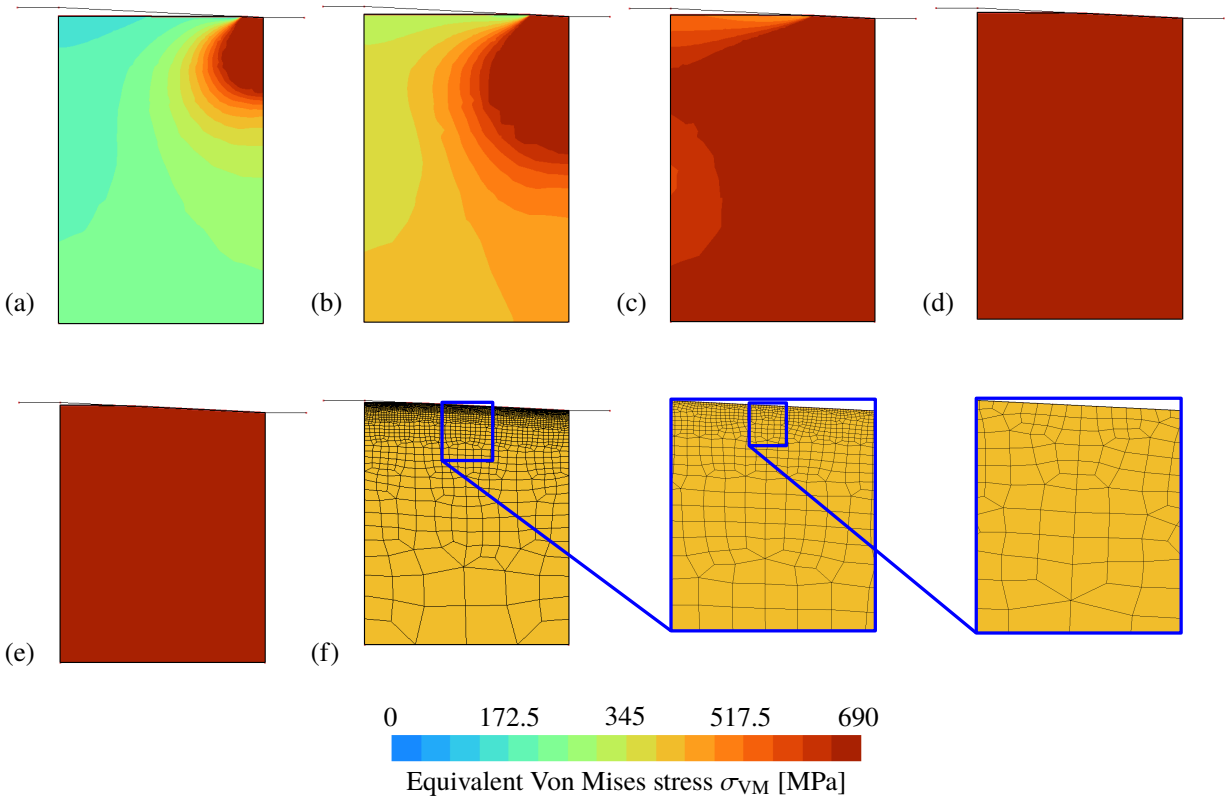

Figure 6.30: Equivalent Von Mises stress in the strip portion for different positions in the roll bite from (a) to (f), which correspond to $x = -6.14, -6.12, -6.09, -5.92, -2$ and 2 mm. These positions are highlighted in Fig. 6.29a. For the configuration (f), the GEN4 mesh is represented with two magnified views to show the required fineness of the mesh. The Von Mises stresses and displacements were computed by the asperity flattening model with the parameters of Tab. 6.2 based on the METALUB computation with the parameters of Tab. 6.1.

6.3.3 Results of the complete coupling procedure

Previously, it was shown that the individual components of the new coupling procedure have two major shortcomings. On the one hand, the *coupling is not strong enough*, which leads to the non-satisfaction of the necessary convergence condition. This weakness was numerically mitigated by changing the criterion of the loop, which adjusts the lubricant flow rate (Sec. 6.3.1.2). On the other hand, the results of the FE asperity flattening model are *mesh dependent when the lubricant pressure becomes equal to the interface pressure*. This issue was tried to be solved by slightly reducing the lubricant pressure in the FE model (Sec. 6.3.2.1).

Considering the severity of the previous hypotheses, results of the coupling procedure have to be considered *with caution*. They are, however, presented in this section to potentially simplify the development of a future, improved coupling procedure in this context.

A critical point of the coupling procedure is *computation time*. While a classical METALUB computation takes about 10 s (Tab. 5.3), a METAFOR asperity flattening simulation takes around 0.5, 1.5, 5, or 12 min for the different meshes in Fig. 6.24 ($n_{y,1}$ = 80, 160, 320, 640 elements along the top edge of the strip portion, respectively) with the remaining parameters of Tab. 6.2. Depending on the number of iterations which are required for convergence, the computation time can be relatively important. To minimize this time, it would be advantageous if the rolling force and the forward slip are not too dependent on the *mesh refinement*. Previously, this dependence was only illustrated for the relative contact area and the mean film thickness in Fig. 6.24. Fig. 6.31, however, directly quantifies this dependence for the results of the coupling procedure. Although differences between the results are visible in the specific case of Test 5B-4 (Fig. 6.31a), they are negligible in consideration of the full range of the rolling force in Test 5B (Fig. 6.31b). The same is true for the forward slip. Hence, the coarse mesh with $n_{y,1}$ = 80, $n_{y,2}$ = 2 and n_z = 20 is sufficient to obtain accurate results.

Besides the mesh refinement, the computation time also depends on the required *number of iterations* to reach convergence and, thus, on the *coefficient of relaxation* w in Eqs. (6.6) and (6.7). Their influence is illustrated in Fig. 6.32a for the coarse mesh ($n_{y,1}$ = 80, $n_{y,2}$ = 2 and n_z = 20) and the rolling force; similar conclusions can be drawn for the forward slip. First, the results oscillate more and more, if the relaxation coefficient increases. Secondly, their mean values over the last iterations are, however, almost identical. Considering, the important number of components in the model, it is difficult to pinpoint the precise reason behind the oscillations and their slightly different mean values. The value 0.1 seems to be a good choice for the relaxation coefficient w due to the small amplitude of the oscillations and the relatively smooth convergence behavior. Thirdly, a stationary state seems to be reached after about 45 iterations with this value of the relaxation coefficient. The value w = 0.1 was previously used in Fig. 6.31 to study the influence of the mesh refinement.

Before comparing the results of the coupling procedure to the experimental ones and those of the classical METALUB computation, the influence of the *lubricant pressure reduction* is shown in Fig. 6.32b. From a numerical standpoint, oscillations appear when the lubricant pressure approaches the interface pressure. These oscillations are due to the mesh dependence, or more

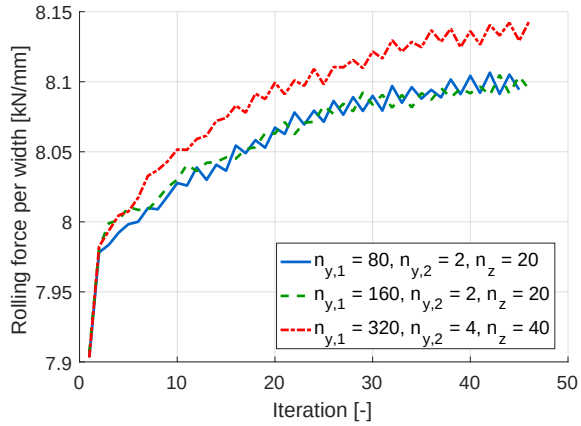

(a) Convergence history of Test 5B-4.

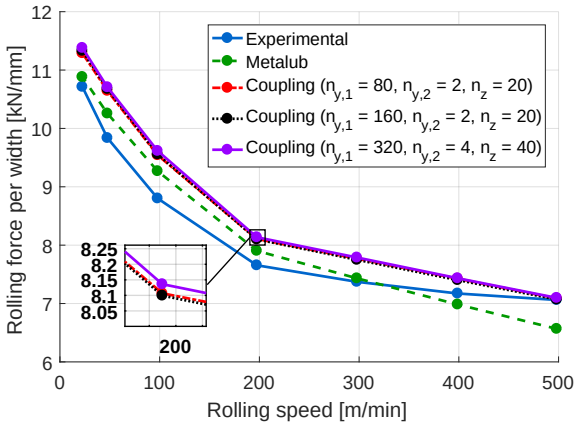

(b) Comparison with full range of Test 5B.

Figure 6.31: Influence of the mesh refinement on the results of the coupling procedure. The results were computed based on Tab. 6.1 for the METALUB component (classical and in the coupling procedure) with v_r, t_{out}, σ_{in} and σ_{out} of Tab. E.21, on Tab. 6.2 with $n_{y,1}$, $n_{y,2}$ and n_z of the legends in this figure for the METAFOR component, with the relaxation coefficient $w = 0.1$ (Eqs. 6.6 and 6.7) and after 45 iterations, in the context of Test 5B (Chap. 3 and Sec. E.7).

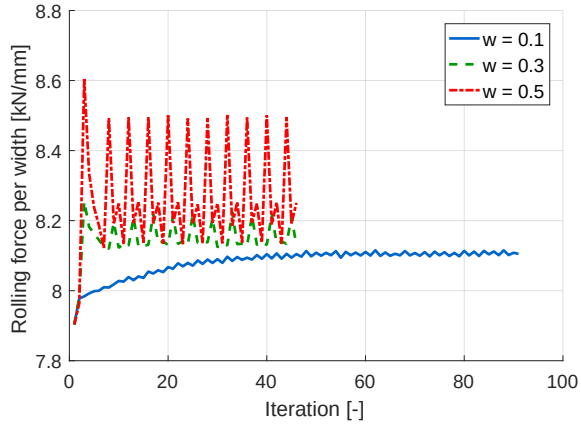

(a) Influence of the number of iterations and the coefficient of relaxation w.

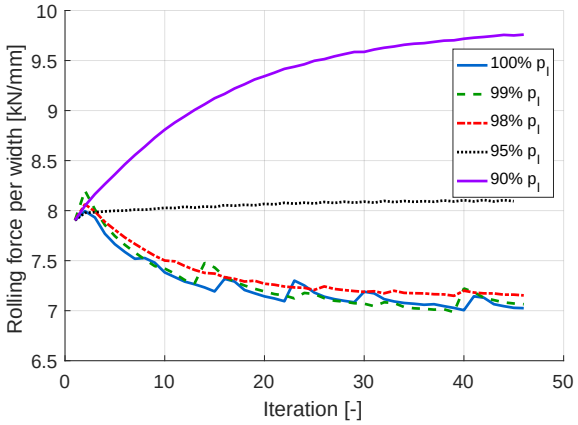

(b) Influence of the lubricant pressure reduction ($w = 0.1$).

Figure 6.32: The results were computed based on Tab. 6.1 for the METALUB component and on Tab. 6.2 for the METAFOR component with $n_{y,1} = 80$, $n_{y,2} = 2$ and $n_z = 20$.

precisely, the non-uniqueness of the solution in this case.

Finally, Fig. 6.33 highlights the *influence of the lubricant pressure reduction* in the context of the entire testing range, while allowing the *comparison with the experimental results and those of the classical METALUB computation*. Due to the oscillations when the lubricant pressure approaches the interface pressure (Fig. 6.32b), the resulting values of the few last iterations of the coupling procedure were averaged to obtain the values in Fig. 6.33. The comparison between the results of the classical METALUB computations and those of the coupling procedure shows in general a reduction of the rolling force and the forward slip. This reduction can be explained by the decrease of the relative contact area in the FE model with respect to the model by Wilson and Sheu (Fig. 6.29a), since less solid/solid contact implies less friction and thus, smaller rolling forces and forward slips. This explanation is consistent with the statement in the introduction to this chapter, according to which *the analytical asperity flattening equation by Wilson and Sheu seems to overpredict the relative contact area*. When the lubricant pressure is, however, reduced in the FE model, the relative contact area increases on average, which explains the increase of the rolling force. It is unclear why the forward slip does not increase likewise, though. Maybe, the more progressive increase of the relative contact area in the coupling procedure (Fig. 6.29a) instead of its almost constant value in the classical METALUB could be behind this observation.

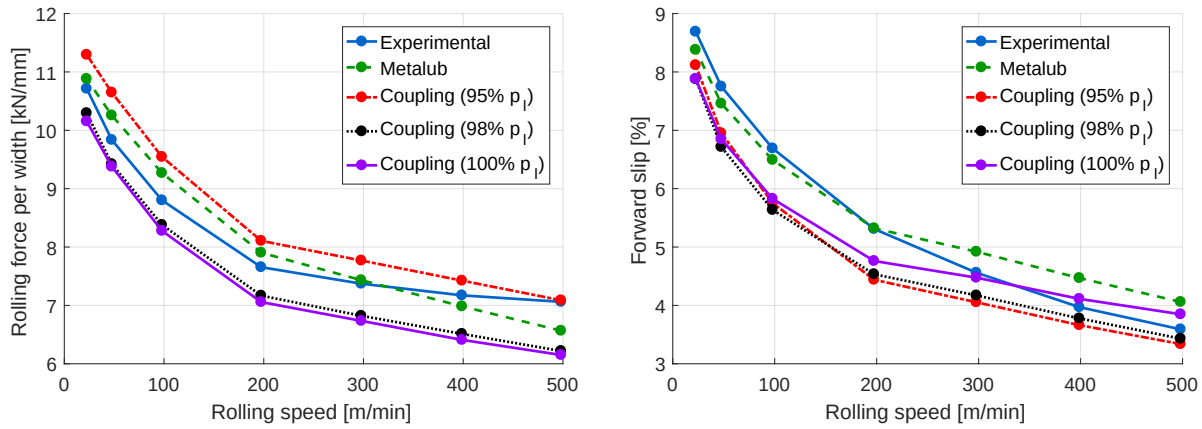

(a) Rolling force per width.

(b) Forward slip.

Figure 6.33: Comparison of the experimental results with those of the classical METALUB model and those of the METALUB/METAFOR coupling procedure for different reductions of the lubricant pressure. These results were computed based on Tab. 6.1 for the METALUB component (classical and in the coupling procedure) with v_r, t_{out}, σ_{in} and σ_{out} of Tab. E.21, on Tab. 6.2 with $n_{y,1} = 80$, $n_{y,2} = 2$ and $n_z = 20$ for the METAFOR component, with the relaxation coefficient $w = 0.1$ and after 45 iterations, in the context of Test 5B (Chap. 3 and Sec. E.7). The results of the coupling procedure with 100% p_l correspond to the average values of the rolling force per width and the forward slip from iteration 38 to 45 (8 iterations) of this procedure.

6.4 Conclusion

In this chapter, a *coupling procedure of the cold rolling model METALUB and the finite element (FE) solver METAFOR was developed in order to simulate asperity flattening with the lubricant by the FE method* instead of using analytical flattening equations.

6.4.1 Summary

In classical METALUB computations, asperity flattening is quantified by *analytical equations* like the one by Wilson and Sheu [367]. Hence, the relative contact area and the mean film thickness are predicted by *approximate methods* based on *simplified asperity profiles with simplified material laws and without micro-plasto-hydrodynamic/static lubrication*. This lubrication mechanism seems, however, to be the reason why the METALUB model overpredicts the rolling force and the forward slip when the reduction of the strip increases.

To eliminate these shortcomings, Carretta developed a *partitioned coupling procedure between METALUB and the FE solver METAFOR to simulate asperity flattening with the lubricant by FE computations*. This procedure was described in this chapter since it has never been published before and since it is the basis of the new coupling procedure. Carretta's procedure consists in computing the interface pressure, the strip elongation and the lubricant elongation by the classical METALUB model along the roll bite. These data are then applied in a FE simulation of asperity flattening in an orthogonal plane to the rolling direction. In this plane, a representative strip portion is pushed against a rigid, fixed contact tool, which represents the roll, by the interface pressure. The lubricant is simulated between the strip portion and the contact tool by the Arbitrary Lagrangian Eulerian formulation. To allow the lubricant to permeate into the solid/solid contact region, very thin lubricant pipes are included in the model. Furthermore, these FE computations are defined in an extended plane-strain state, i.e. the lateral edges of the strip portion do not deform in the transverse direction due to the classical plane-strain hypothesis in cold rolling, while the elongation of the strip and the lubricant along the rolling direction is imposed based on the METALUB results. By the time-space equivalence, the relative contact area, the mean film thickness, the pressure on top of the asperities and the lubricant pressure are computed along the roll bite in the FE model. These results are then injected in a coupled version of METALUB, which computes again the interface pressure, the lubricant elongation and the strip elongation. This procedure continues until the influence of the new FE flattening model has been fully propagated into the solution. The previous method has, however, *numerous shortcomings*, like the non-physical separation of the roll and the strip, the negligence of the Reynolds equation along the rolling direction, and later, also the negligence of hydrostatic compressibility effects in the FE model.

Since this method was ultimately not representative anymore of the process that had to be modeled, a *new coupling procedure* between METALUB and METAFOR was developed in this chapter. This method is similar to Carretta's partitioned coupling method but, instead of directly simulating the lubricant in the FE model, it is rather included indirectly by *applying the lubricant pressure of the METALUB computation to the top edge of the strip portion, where it is not in contact with the roll*.

This hypothesis unfortunately eliminated the possibility to include the pressure generation by the volume reduction with the possible permeation of the lubricant into the boundary region in the model but it rendered the replacement of the analytical equation by a FE asperity flattening model possible. In fact, before including complex MPH lubrication by a FE model, "simple" FE asperity flattening should first be possible in METALUB. Furthermore, instead of entirely modifying the system of equations in METALUB as in Carretta's method, *only the analytical asperity flattening equation and the profile conservation hypothesis were replaced by the interpolation of the FE results*. Hence, the METALUB model computes the interface pressure, the lubricant pressure and the elongation of the strip along the rolling direction. Based on these data, the FE model then determines the relative contact area and the mean film thickness along the bite. This geometrical contact information is then used again in METALUB to update the lubricant pressure, ... and so on until the results do not change anymore from one iteration to the next.

Subsequently, *numerical results* of each separate component of the coupling procedure were analyzed based on Test 5B of the experimental campaign at Maizières-lès-Metz (Chap. 3 and Sec. E.7). Concerning the METALUB component, it turned out that a necessary condition of convergence is not satisfied because the coupling procedure is not sufficiently strong/tight, i.e. that the FE model should be evaluated at each integration step of the equations along the roll bite instead of using the FE results from a different configuration. This shortcoming was, however, tentatively alleviated by introducing a new criterion of the lubricant flow rate adjustment loop. Concerning the METAFOR component, it proved to be mesh dependent when the lubricant pressure became equal to the interface pressure. This dependence was eliminated by slightly reducing the lubricant pressure. Finally, results of the full coupling procedure showed that the analytical asperity flattening equation by Wilson and Sheu overestimates the new predictions of the rolling force because the relative contact area is greater by the analytical model, which leads to increased friction. These results have, however, to be considered with caution due to the previous hypotheses.

6.4.2 Outlook

To advance in the prediction of rolling forces and forward slips, in particular, by including micro-plasto-hydrodynamic/static lubrication in the rolling model, it is necessary to solve its current shortcomings.

First, the *coupling procedure is not sufficiently strong*, i.e. data exchanges between METALUB and METAFOR should occur more frequently than after a full METALUB computation. Evaluating, however, the FE model at each integration step of the METALUB model, like the analytical asperity flattening equation, is expected to be very costly in terms of computation time. In fact, the roll bite is integrated about 1000 times in a classical METALUB computation. An additional difficulty would be the evaluation order of the flattening model. In the classical METALUB model, the flattening equation returns the local strain rate along the rolling direction (Eq. N.278), while the out-of-plane elongation is imposed in the FE micro-model.

Secondly, the results of the FE micro-model are *mesh dependent when the lubricant pressure*

becomes equal to the interface pressure. It is currently unclear how this problem could be solved since the possible equality of the lubricant and interface pressures is an integral part of the METALUB model.

Even if the previous problems could be solved, the permeation of the lubricant into the solid contact area by micro-plasto-hydrodynamic/static lubrication seems impossible in the current micro-model since the lubricant is not included in this model via its discretization as in Carretta's model (Sec. 2.2.4.3). This issue will be addressed in the following chapter by a *new discretization strategy of the lubricant and the asperities*.

Chapter 7

SPH Simulation of Lubricated Asperity Flattening in LAMMPS

Micro-plasto-hydrodynamic/static (MPH) lubrication is an intrinsic component of lubrication in cold rolling. It consists in the permeation of the lubricant from pressurized surface pockets into the solid/solid contact zone, where it decreases friction, as explained in Chap. 2. According to Chap. 3, it thus decreases the rate at which the rolling force rises, when the reduction ratio increases. Since the rolling capacity of a mill stand, i.e. its maximum rolling force, is limited, harder strips can therefore be rolled or more significant reduction ratios can be achieved thanks to this physical mechanism. Hence, it is crucial to take MPH lubrication into account when the lubrication conditions are adjusted to reach minimum friction without skidding in lubricated cold rolling.

Adjusting for instance the oil concentration in the oil-in-water emulsion, which is sprayed onto the strip by the flexible lubrication system, to reach the previous objective requires to known which concentration is optimal. Besides experimental testing, e.g. Chap. 3 and [182], *numerical models* were developed to answer this question. Nevertheless, METALUB (Chap. 4), which seems to be the most predictive model in the field of lubricated cold rolling today (Chap. 5), is currently incapable of modeling MPH lubrication.

Numerous models were proposed to simulate MPH lubrication (Sec. 2.2.4.3), and it was tried to couple Carretta's FE model [54, 55], which seems to be the most promising one, with METALUB in the previous chapter. Besides the complexity of this coupling, the FE model has several *drawbacks*: first, it requires small *artificial lubricant pipes* to simulate MPH lubrication via the Arbitrary Lagrangian Eulerian (ALE) formulation (Figs. 2.36 and 6.3). In other words, the lubricant can only rise to the asperity tops, where such pipes were added to the model. Hence, the way of introducing MPH lubrication seems predetermined and unnatural, although the pipes are relatively small. Secondly, *large solid deformations* due to indentation and ploughing via the relative movement between the roll and the strip can only be simulated to a limited extent because of resulting mesh distortions, which would require costly and sometimes non-robust remeshing

operations [35]. These limitations are essentially due to the *mesh-based nature* of the FE method.

A possible solution to this fluid-structure interaction (FSI) problem seems to be the introduction of a *Lagrangian meshless particle method*[1]. In such a method, the mesh is replaced by spatial points, which are called particles (meshless particle method) and which move with the continuum that they describe (Lagrangian method). These features eliminate mesh distortions and the need for artificial lubricant pipes. In this chapter, the most well-known Lagrangian meshless particle method, i.e. *Smoothed Particle Hydrodynamics (SPH)* [115, 207] (Sec. 7.1), is introduced to test its ability of modeling MPH lubrication.

The *SPH method* will be described more thoroughly in the first section of this chapter, by introducing specific SPH formulations, i.e. total Lagrangian SPH for solids with zero-energy mode suppression and elastoplasticity, and Eulerian SPH (ESPH) for fluids, both with kernel gradient correction. The implementation of these SPH formulations in the USER-SMD software package by Ganzenmüller [113] in the molecular dynamics simulator LAMMPS [257] is then used to simulate some validation tests in order to test the implementation and to illustrate some characteristics of the method. These validation tests are based on those that were recently reproduced by Cerquaglia [65] via the Particle Finite Element Method (PFEM) [155] in the MN2L research group. This choice should allow the comparison between both methods, i.e. SPH and PFEM, which is, however, not the main focus in this document. One should also notice that the developments in this chapter constitute the *first time* that the SPH method is extensively studied in the MN2L research group except for Cerquaglia's Master's thesis [64] and a student project [5]. Hence, this chapter focuses on the *exploration* of SPH strategies to model asperity flattening in the presence of a lubricant. With this in mind, the implementation of the USER-SMD package is essentially not modified, except for the introduction of the Wendland kernel function and additional post-processing capabilities.

To only *gradually* increase the complexity from relatively simple verification tests to full MPH lubrication with realistic surface topographies, varying compression and sliding speeds, the case of *micro-plasto-hydrostatic lubrication* is studied in the second section of this chapter in a simplified scenario. More precisely, elastoplastic asperity flattening with a non-linearly compressible fluid in the interface is simulated by the *SPH method* to reproduce equivalent FE computations by Sharvts and Yastrebov [291]. Despite the good predictive ability of their FE model, it is limited to deformations without significant mesh distortions, as explained previously, and to hydrostatic lubrication, since the lubricant is only included in the model via its compressibility. In theory, the elimination of these shortcomings seems to be possible by the SPH method, which also considers the kinematics of the fluid flow, its inertia and, most notably, its viscosity. While this final statement has to be proven in future research, the possibility of reproducing the existing FE results by SPH is assessed in this document by developing the *first SPH model of lubricated*

[1]The combination of the attributes "*meshless*" and "*particle*" might seem to be a pleonasm but the distinction can be explained by the following definitions, which are introduced to consistently classify simulation methods as stated by Cerquaglia [65]: (1) A *meshless* method is a method in which "shape functions depend only on the node positions" [154]. (2) Methods without any mesh, nor background mesh, are called *truly* meshless. (3) A *particle* method is a method where "all the physical and mathematical properties are attached to particles" [153].

asperity flattening.

7.1 Smoothed particle hydrodynamics

In this section about the smoothed particle hydrodynamics (SPH) method, a *literature review* briefly summarizes the evolution of the method since its initial development, and its application to model solid deformations and lubrication. Then, the *fundamental concepts* of the method, i.e. the kernel approximation, the particle approximation and the kernel gradient correction, are defined. These concepts allow writing the SPH formulation of the governing equations, which describe *solid deformations* and *fluid flows*. To solve these equations, the *numerical solution method* in the USER-SMD package of LAMMPS is subsequently explained. Finally, some *validation tests* are presented to study the capabilities of the specific SPH formulation and its implementation.

7.1.1 Literature review

Smoothed particle hydrodynamics (SPH) was initially developed independently by Lucy (1977) [207] and Gingold and Monaghan (1977) [115] to model astrophysical phenomena. The method is thoroughly reviewed in the articles [82, 117, 198, 224, 227, 228, 263, 342, 346] and the books [196, 345].

7.1.1.1 Principle and advantages of SPH

SPH has the objective of solving partial differential equations, like the conservation equations (Sec. H.2), by transforming them into ordinary differential equations, which can be time-integrated. The underlying principle of this transformation (details in Sec. 7.1.2) is the discretization of a continuum by spatial points that are called *particles*, where physical and mathematical properties, like the particle mass or the size of the smoothing kernel functions, are stored. These *smoothing kernel functions*, also known as kernel functions or kernels, are comparable to shape functions in the FE method [29] in the sense that they allow to compute field values inside the continuum based on particle values.

Since the particles move with the continuum, which they describe, and since no auxiliary mesh is required the method is by default *Lagrangian* and *truly*[2] *meshless*. Due to these characteristics, SPH has *in general* several *advantages* with respect to classical simulation methods, i.e. the Lagrangian FE method for solid mechanics [29] and the Eulerian Finite Volume or Finite Difference methods for fluid mechanics [140]: (1) no mesh distortions can occur due to large deformations, no overly complex treatment is required for (2) moving boundaries, (3) free surfaces, (4) interfaces with mixing of fluids and (5) fracture at least in simple cases, (6) the computation takes place only where the material is, (7) the history of field variables can be easily tracked, (8) complex

[2]The term *truly* refers to the fact that no auxiliary mesh is required as in the Particle Finite Element Method (PFEM) [65, 155] or the Material Point Method (MPM) [309].

physics can be included due to the similarity with molecular dynamics, (9) the method is highly-parallelizable by domain decomposition (Sec. 7.1.4) unlike PFEM so far[3], which, however, shares a lot of the previous advantages [65] ... These advantages suggest the possibility of simulating FSI problems, like mixed lubrication, which include large displacements/deformations, free surfaces, metal/oil/water interfaces, complex material laws with history and possible surface wear, by a unique monolithic simulation method instead of having to couple explicitly different solvers for the fluid and solid parts of the problem.

Numerous strategies were developed to model the features that are required in the simulation of mixed lubrication by SPH, as summarized hereafter.

7.1.1.2 SPH modeling of fluids

Concerning the simulation of *viscous compressible fluid flows*, weakly compressible SPH (WCSPH) was introduced by Monaghan [225] to model incompressible free-surface flows. The underlying idea is to compute the pressure via the density with a sufficiently low speed of sound (or bulk modulus) to allow the explicit time-integration in a reasonable computation time (CFL condition, Sec. 7.1.4.3) but large enough to not compromise incompressibility too much. Since this formulation is based on a compressible fluid, although it was introduced to simulate incompressible flows, various compressibility dependencies can be included in it to simulate *compressible* fluid flows. WCSPH is probably the most widespread SPH formulation due to its great modeling efficiency to simplicity ratio.

Regarding *viscous* flows, Monaghan [224, 230] first introduced an artificial viscosity in WCSPH, which is based on a bulk viscosity to remove numerical oscillations. Numerous methods were developed later on to model physical viscosity [73], like (1) the finite difference approach by Brookshaw [50], which enjoys great popularity [79, 80, 241], (2) nested summations [103, 354], which are computationally inefficient, or (3) the second derivative computation of the kernel functions, which is sensitive to particle order [326, 293]. Despite the introduction of an artificial viscosity, WCSPH suffers from spurious high-frequency pressure oscillations [83] due to the collocational nature of the method (amongst others) [346], which estimates all quantities at the same locations, i.e. at the particles. Numerous methods have been developed to solve this issue, like density filtering [83] or density diffusion, most notably δ-SPH [213, 214]. Furthermore, WCSPH can be applied to model multiphase flows, like O/W emulsions in cold rolling, provided that the density ratio of the fluids is close to one [229], while extensions of the method were developed for greater density ratios [111].

WCSPH was adopted by Kyle and Terrell [175, 176] to model hydrodynamic thick film lubrication in a sliding pad bearing geometry and by Hermange et al. [136, 137] to model aquaplaning with SPH for the water and FEM for the tire. These publications seem to be the only ones about SPH modeling of lubrication as such, i.e. with emphasis on the pressure generation due to the lubricant flow. Further articles study the oil flow in gear boxes [159] and aquaplaning [191], but without this emphasis.

[3]To the best of our knowledge, no domain decomposition technique has yet been applied to parallelize PFEM.

7.1.1.3 SPH modeling of solids

Solids were first modeled via SPH by Libersky and Petschek [192, 193]. Their elastic-perfectly plastic model was shortly afterwards extended to include damage and fracture by Benz and Asphaug [30], and more recently by Gray and Monaghan [119]. While SPH quickly became popular in the field of free-surface flows, numerical issues prevented this method from competing with classical FEM for solids. These issues are mainly the tensile instability, zero-energy modes and the lack of consistency. They also exist in SPH models of fluids, e.g. the tensile instability in [310] or spurious pressure oscillations in [83], but they were seemingly a smaller obstacle to the dissemination of the method than for solids, probably because the fluid is mainly compressed in gravity-driven free-surface flows while the kinematics appears realistic, unlike the pressure field [213].

Tensile instability

The *tensile instability* was first analyzed by Swegle et al. [318] who observed artificial particle clustering when a continuum was subjected to tension, although no clustering occurred in compression. This instability was initially explained by the shape of the kernel function [318], which suggested that it could be solved by adapting this function. Recently, it was shown that this shape is at the origin of another kind of instability, i.e. the pairing instability [263], which has similar symptoms to the tensile instability. The pairing instability can be solved by choosing kernel functions with a non-negative Fourier transform [91, 277], like the Wendland functions [357] instead of the classical cubic spline kernel [224].

Despite this improvement, the tensile instability still causes particle clustering in a tensile state as illustrated by Spreng [301, p. 49]. Therefore, numerous methods were tested in the literature, like modifications of the kernel functions [239, 240], conservative smoothing [269, 356], corrective SPH [75] or the introduction of artificial repulsive forces [120, 226], which should prevent particles from clumping. These solutions are, however, not generally applicable since they require, for instance, the calibration of the repulsive force amplitude [120, 226].

In 2000, Belytschko et al. [27] showed that the tensile instability can be eliminated by total Lagrangian[4] SPH (TLSPH), in which the initial (reference) configuration is used to compute the gradients and to integrate the stresses [38, 112, 266, 272, 344]. While TLSPH eliminates the tensile instability, the magnitude of deformations that can be simulated is, however, limited since this method is based on the (non-updated) reference configuration. Therefore, fluids are

[4]One should notice that the term "Lagrangian" does here refer to the formulation and not the discretization as at the beginning of the chapter, where it is used to mention that the particles move with the continuum, which they describe, like Lagrangian meshes [29].

preferably modeled by classical SPH, which will be called Eulerian[5] SPH (ESPH) due to the computation in the current configuration, and solids by TLSPH [266]. Nevertheless, to allow very large solid distortions, Vidal et al. [341] and Leroch et al. [189] successfully updated the reference configuration in TLSPH when zero-energy modes were suppressed. These updates were not performed at each time step but only when the relative displacements between particles become too important. Hence, this method can be called updated Lagrangian SPH (ULSPH).

Zero-energy modes

Spurious *zero-energy modes*, also known as hourglass modes in FEM [102], exist in SPH due to the rank deficiency of the discrete divergence operator [27], which resembles a central finite difference [342], as illustrated in [196, Fig. 4.9]. Their existence is a consequence of the collocational nature of the method [346].

To solve this problem, Dyka [96, 97] suggested the introduction of stress points, where stresses are computed, between classical SPH particles, similar to Gauss points in fully integrated finite elements. Despite extensions to higher dimensions of this method [270, 343], stress points in TLSPH seem not to have found widespread usage [112]. Later, Vidal et al. [341] suggested stabilizing TLSPH based on higher order derivatives, which requires, however, the costly computation of a third-order tensor. Alternatively, Ganzenmüller [112] developed a suppression algorithm for zero-energy modes based on the hourglass control of finite elements with reduced integration by Flanagan and Belytschko [102]. This method currently seems to be the best one in terms of efficiency and versatility.

Lack of consistency

In SPH, the field values of a particle, like the pressure at that particle, are computed based on values of neighboring particles. In general, particle disorder[6] and boundaries, i.e. less neighbors or different types of neighbors, therefore negatively affect the accuracy of the results [196, 239]. This accuracy is commonly characterized by reproducing conditions in SPH [28], which imply completeness (to some order, Sec. 7.1.2.3), similarly to FEM, where consistency is very difficult to establish for arbitrary meshes [29]. For these reasons, completeness and consistency are commonly used interchangeably in the general SPH literature [196].

An approximation is complete to order k, if it can reproduce any polynomial up to order k exactly. Classical SPH is, however, not even zeroth-order complete, i.e. it cannot reproduce exactly a

[5]This denomination is not unique. In fact, Ganzenmüller [113] rather labels classical SPH as updated Lagrangian SPH following the FE denomination, which states that derivatives are computed with respect to the spatial (Eulerian) coordinates and that integrals are computed over the current configuration in the updated Lagrangian formulation [29]. Nevertheless, in some total Lagrangian SPH formulations, the reference configuration is updated, as mentioned hereafter. Hence, it seems more reasonable to qualify these formulations as updated Lagrangian than the classical SPH formulation with Eulerian kernels, i.e. kernels that depend on the positions of the particles in the current configuration [27].

[6]Particles are *disordered*, when they are not located at the nodes of a Cartesian grid. Hence, disorder could, for instance, be quantified by the amplitude of the particle shifts with respect to the nodes of the Cartesian grid [74].

constant field [196]. Hence, various techniques were developed to restore completeness for function evaluations, like Shepard kernel normalization [284, 28], or for derivative evaluations [197, 266]: (1) the symmetrization of SPH equations by Monaghan [223], which yields zeroth-order completeness for the derivatives, (2) the normalization via a kernel sum by Johnson and Beissel [160], which was generalized and extended by Randles and Libersky [269] to reach first-order completeness for derivatives or (3) the kernel gradient correction by Bonet and Lok [39], which also ensures first-order completeness for derivatives.

Applications

Regarding the flattening of metallic asperities, some *applications* of the SPH method for solids, which go beyond small theoretical test cases, can be mentioned. Cleary et al. [81] simulated metal forging of industrial parts with linear hardening but without any treatment of the tensile instability, zero-energy modes or the lack of consistency. In contrast, Spreng et al. [302, 301] modeled metal cutting after extensive validation of the method with artificial repulsive forces and Shepard kernel normalization. Only negligible high-frequency oscillations were observed, which is why no method was used to suppress zero-energy modes. Islam et al. [157] transitioned from Eulerian (ESPH) to Lagrangian kernels (TLSPH) to model metal cutting, but without consistency restoration nor zero-energy mode supression, since TLSPH provided more realistic results. Finally, Leroch and Varga et al. [189, 339, 340] combined the correction methods of the tensile instability, zero-energy modes and the consistency to study scratch-induced surface damage of an elasto-viscoplastic material, i.e. a process, which strongly resembles asperity flattening. More precisely, they used TLSPH with a first-order correction of the kernel gradient, hourglass control according to Ganzenmüller [112] and updates of the reference condition, when relative displacements of interacting particles exceeded a given threshold (ULSPH).

7.1.1.4 Boundary and fluid/solid interactions

While the pressure becomes automatically equal to zero at free surfaces in classical WCSPH, numerous methods were developed to model rigid walls. As mentioned by Violeau and Rogers [346], these methods can be categorized as repulsive functions, fictitious particles and boundary integrals for complex boundary conditions. Monaghan [225] introduced the first wall boundary condition in SPH by applying a repulsive force, which was derived from a Lennard-Jones potential, between fluid particles and boundary particles of the wall. Due to its simplicity, this penalty approach enjoys great popularity. Hence, various versions of this method were used in the previous applications of the SPH method for solids (Sec. 7.1.1.3), i.e. in metal forging, cutting and scratch test simulations. While repulsive functions only prevent particles from penetrating the wall, the fictitious particle approach also allows the definition of no-slip conditions. Morris et al. [241] introduced such an approach by discretizing the boundary with several layers of dummy particles, which are included in the density and force computations of the fluid particles in their neighborhood. Instead of evolving the positions of the boundary particles by the resulting forces, their movement is prescribed by the motion of the boundary. These approaches with fictitious particles were, for instance, applied in the previous SPH applications of the SPH method for

fluids (Sec. 7.1.1.2) to model thick film lubrication and the oil flow in a gearbox, in particular, Adami et al.'s [1] popular extension of Morris et al.'s [241] method.

The previous methods for boundary interactions led to SPH fluid-structure interactions in a natural way due to the same discretization method for fluids and solids. More precisely, instead of prescribing the motion of the boundary particles, it can be computed as a result of the boundary interaction forces. For instance, if a boundary particle applies a repulsive force to a fluid particle, the reaction force can be applied to the boundary particle, which is not prescribed anymore but a part of a solid SPH structure. This idea was introduced by Antoci et al. [9] to model FSI by WCSPH with artificial repulsive forces to suppress the tensile instability. Recently, similar methods were developed but with TLSPH for solids in FSI interactions [133], including δ-SPH, hourglass control and GPU-acceleration [378].

7.1.1.5 Intermediate conclusion

Numerous strategies were developed over time to model fluids, solids and their interactions by SPH while eliminating its main drawbacks, i.e. the tensile instability, the pairing instability, zero-energy modes and the lack of consistency. Considering this important number of method extensions, which were added to traditional WCSPH, it is out of the scope of this chapter to develop a new implementation of the SPH method, which includes all of the previous best practices. For this reason, the USER-SMD SPH implementation by Ganzenmüller [113] in the molecular dynamics simulator LAMMPS [257] was selected to perform the simulations of this chapter. Besides its strong parallelization capabilities (Sec. 7.1.4.2), this implementation was chosen because it is the only open-source code to the best of our knowledge, which contains the majority of the required features, which were described above, i.e. weakly compressible viscous SPH with Eulerian kernels (ESPH) for the fluid and TLSPH with elasto-viscoplasticity, zero-energy mode suppression, kernel gradient correction and possible updates of the reference configuration (ULSPH) for the solid.

7.1.2 Fundamental concepts

In the previous section, SPH was reviewed in a very general way because of the significant amount of information, which was examined to select the formulation that seems to be best suited to simulate asperity flattening in the presence of a lubricant. In this section, this *formulation is described in more detail* to understand the underlying method. Since the formulation by Ganzenmüller was selected, as motivated at the end of the previous section, the following explanations are significantly based on [112, 189] and the source code of the USER-SMD SPH package in LAMMPS [113].

In the following sections, the fundamental concepts of SPH are summarized, i.e. how partial differential equations can be transformed into ordinary differential equations via the *kernel and particle approximations*. Emphasis is put on the *kernel gradient correction* to restore first-order completeness for the derivatives.

7.1.2.1 Kernel approximation

The kernel approximation of a scalar function $f(\cdot)$ of space, like the pressure field of a continuum, stems from the following identity:

$$f(\mathbf{x}) = \int_{\mathbb{V}} f(\mathbf{x}')\, \delta(\mathbf{x} - \mathbf{x}')\, \mathrm{d}\mathbf{x}' \tag{7.1}$$

where $\mathbf{x}$ is the position vector, $\delta(\cdot)$ the Dirac delta function and $\mathbb{V} \in \mathbb{R}^3$ the domain of $f(\cdot)$. In a similar way, the *kernel approximation* $\langle f(\cdot)\rangle^k$ of the function $f(\cdot)$ is defined by the following operation:

$$\langle f(\mathbf{x})\rangle^k = \int_{\mathbb{V}} f(\mathbf{x}')\, W(\mathbf{x} - \mathbf{x}', h)\, \mathrm{d}\mathbf{x}' \tag{7.2}$$

where the delta Dirac function $\delta(\cdot)$ was replaced by the *smoothing kernel function* $W(\mathbf{x}, h)$, also known as kernel function or kernel. The variable h denotes the *smoothing length*, which defines the compact support of the kernel function, i.e. the kernel is such that $W(\mathbf{x} - \mathbf{x}', h) = 0$, if $|\mathbf{x} - \mathbf{x}'| > \zeta h$, where ζ is a kernel dependent scale factor. This property transforms the kernel approximation from a global to a local operation. Besides the compact support, kernel functions should have additional properties to obtain good numerical approximations [196]. For instance, they should be normalized to ensure zeroth-order completeness of the kernel approximation, i.e.

$$\int_{\mathbb{V}} W(\mathbf{x} - \mathbf{x}', h)\, \mathrm{d}\mathbf{x}' = 1 \tag{7.3}$$

Numerous kernel functions were defined since the development of SPH, most notably, the spline kernels, which become, however, unstable to pairing (Sec. 7.1.1.3). For this reason and because of its relatively small computational cost, the radially symmetric Wendland C^2 kernel (twice continuously differentiable) is adopted in this chapter [91, 357]:

$$W(R, h) = \begin{cases} \dfrac{\alpha_d}{h^d}\,(1 - R)^4\,(1 + 4R) & \text{, if } 0 \leq R < 1 \\ 0 & \text{, otherwise.} \end{cases} \tag{7.4}$$

where $d = 2$ in 2D and 3 in 3D, α_d is the normalization factor (Eq. 7.3) equal to $7/\pi$ in 2D or $21/(2\pi)$ in 3D, and $R = \|\mathbf{x} - \mathbf{x}'\|/h$ is the relative distance between the points $\mathbf{x}$ and $\mathbf{x}'$, i.e. $\zeta = 1$.

In order to transform partial differential equations into ordinary differential equations with respect to time, it is necessary to define the kernel approximation of the derivative of a function. Similarly to Eq. (7.2), the gradient of $f(\cdot)$ can be approximated as follows

$$\langle \nabla f(\mathbf{x})\rangle^k = \int_{\mathbb{V}} [\nabla_{\mathbf{x}'} f(\mathbf{x}')]\; W(\mathbf{x} - \mathbf{x}', h)\, \mathrm{d}\mathbf{x}' \tag{7.5}$$

By the product rule $\nabla(ab) = a\nabla b + b\nabla a$, where a and b are scalars, and the divergence theorem, the previous equation becomes

$$\langle \nabla f(\mathbf{x})\rangle^k = \int_{\mathbb{S}} f(\mathbf{x}')\, \mathbf{n}\, W(\mathbf{x} - \mathbf{x}', h)\, \mathrm{d}\mathbb{S} - \int_{\mathbb{V}} f(\mathbf{x})\, \nabla_{\mathbf{x}'} W(\mathbf{x} - \mathbf{x}', h)\, \mathrm{d}\mathbf{x}' \tag{7.6}$$

where $\mathbf{n}$ is the unit outward-pointing normal to the surface $\mathbb{S}$ of $\mathbb{V}$. This equation can be further simplified by noticing that the first integral is equal to 0 due to the compact support property of the kernel, if its support domain is located entirely within the problem domain $\mathbb{V}$. In addition, the minus sign in the second integral can be removed by noticing that $\nabla_{\mathbf{x}'} W(\mathbf{x}-\mathbf{x}', h) = -\nabla_{\mathbf{x}} W(\mathbf{x}-\mathbf{x}', h)$ due to the symmetry property of the kernel function, i.e. because its value only depends on the distance between $\mathbf{x}$ and $\mathbf{x}'$. Hence, the *kernel approximation of the spatial derivative* of $f(\cdot)$ is given by the following equation for the gradient operator:

$$\langle \nabla f(\mathbf{x}) \rangle^k = \int_{\mathbb{V}} f(\mathbf{x}')\, \nabla_{\mathbf{x}} W(\mathbf{x}-\mathbf{x}', h)\, \mathrm{d}\mathbf{x}' \tag{7.7}$$

The previous equation is key to understanding why the kernel approximation can transform partial differential equations into ordinary differential equations. In fact, the gradient of the function $f(\cdot)$ becomes a gradient of the kernel function $W(\cdot)$ in this equation.

7.1.2.2 Particle approximation

The *particle approximation* consists in discretizing the continuum, which is modeled, by a finite number of particles as illustrated in Fig. 7.1. Each particle carries a constant mass $m_a = \rho_a^0 V_a^0$, where ρ_a^0 is its density and V_a^0 its individual volume in the initial configuration. Hence, the kernel approximation (Eq. 7.2) can be re-written as follows by the particle approximation:

$$\langle f(\mathbf{x}) \rangle^{kp} = \sum_b f(\mathbf{x}_b)\, W(\mathbf{x}-\mathbf{x}_b, h) V_b \tag{7.8}$$

where $\mathbf{x}_b$ are the positions of the particles. Due to the compact support property of the kernel, this sum can be restricted to the particles in the *kernel support domain* $\mathcal{S}_a$ of the particle located at $\mathbf{x}_a$. If the kernel is further radially symmetric, the combined kernel and particle approximation can be rewritten as follows, where the Macaulay brackets $\langle\cdot\rangle^{kp}$ are omitted for readability, to use similar notations to those of Ganzenmüller [112]:

$$f(\mathbf{x}_a) = \sum_{b\in\mathcal{S}_a} V_b\, f(\mathbf{x}_b)\, W(x_{ab}) \tag{7.9}$$

where x_{ab} is the distance between the particles a and b, i.e. $x_{ab} = \|\mathbf{x}_b - \mathbf{x}_a\|$.

The *particle approximation of the spatial derivative* of $f(\cdot)$ can be obtained in a similar way for the gradient operator on the basis of its kernel approximation in Eq. (7.7):

$$\nabla f(\mathbf{x}_a) = \sum_{b\in\mathcal{S}_a} V_b\, f(\mathbf{x}_b)\, \nabla_a W(x_{ab}) \tag{7.10}$$

where the gradient of the kernel function is computed as follows:

$$\nabla_a W(x_{ab}) = \left[\frac{\partial W(x_{ab})}{\partial x_{ab}}\right] \frac{\mathbf{x}_a - \mathbf{x}_b}{x_{ab}} \tag{7.11}$$

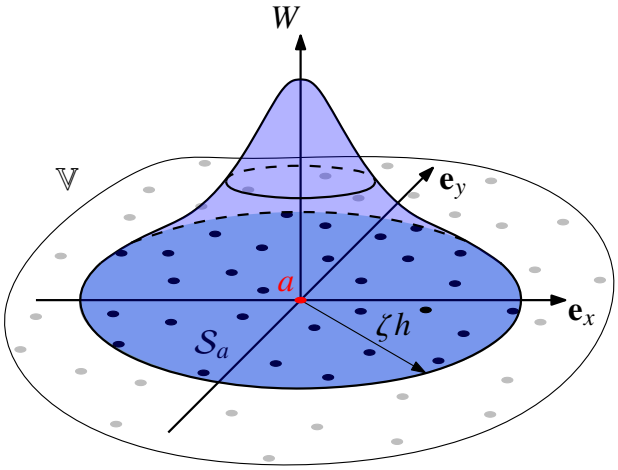

Figure 7.1: Particle approximation of a 2D continuum $\mathbb{V}$. A reference particle a (in red) is surrounded by other particles. The particles in black are contained in the support domain $\mathcal{S}_a$ of the kernel function W whose smoothing length is h. The kernel function has a circular symmetry around the axis of W according to Eq. (7.4).

7.1.2.3 Kernel gradient correction

As mentioned in Sec. 7.1.1.3, the basic particle approximation of SPH in Eq. (7.9) is not even zeroth-order complete, i.e. it cannot approximate exactly a constant field. In fact, if $f(\cdot)$ is a constant (non-zero) function, the following reproducing condition has to be satisfied according to Eq. (7.9):

$$1 = \sum_{b \in \mathcal{S}_a} V_b \, W(x_{ab}) \tag{7.12}$$

It is, however, generally not satisfied, for instance, due to particle disorder or close to the boundary of the continuum, which is deficient in particles.

The lack of completeness also exists for the particle approximation of the spatial derivative in Eq. (7.10). In other words, the gradient of a constant field is not uniformly equal to 0 using this approximation. Therefore, the symmetrization of SPH equations was introduced, as mentioned in Sec. 7.1.1.3, to restore zeroth-order completeness for the derivatives. In fact, this is possible by the following reasoning,

$$\nabla f(\mathbf{x}_a) = \nabla f(\mathbf{x}_a) - f(\mathbf{x}_a)\,\mathbf{0} = \nabla f(\mathbf{x}_a) - f(\mathbf{x}_a)\,\nabla 1 \tag{7.13}$$

Applying the SPH approximation (Eq. 7.10) to the previous equation yields

$$\nabla f(\mathbf{x}_a) = \sum_{b \in \mathcal{S}_a} V_b \, f(\mathbf{x}_b)\, \nabla_a W(x_{ab}) - f(\mathbf{x}_a) \sum_{b \in \mathcal{S}_a} V_b \, \nabla_a W(x_{ab}) \tag{7.14}$$

$$= \sum_{b \in \mathcal{S}_a} V_b \, \left[f(\mathbf{x}_b) - f(\mathbf{x}_a) \right] \, \nabla_a W(x_{ab}) \tag{7.15}$$

which is zeroth-order complete due to the difference in the last term. Zeroth-order completeness for the derivatives is, however, not sufficient to conserve angular momentum according to Bonet and Lok [39]. More precisely, they showed that enforcing first-order completeness for the derivatives of the velocity field results in the conservation of angular momentum because the internal potential energy then becomes invariant to rigid body rotations, provided that this energy function exists. For this reason, a kernel gradient correction is described in this section based on their work.

First, Eq. (7.15) can be extended[7] to a vector-valued function $\mathbf{f}(\cdot)$:

$$[\nabla \mathbf{f}(\mathbf{x}_a)]^T = \sum_{b \in \mathcal{S}_a} V_b \ [\mathbf{f}(\mathbf{x}_b) - \mathbf{f}(\mathbf{x}_a)] \otimes \nabla_a W(x_{ab}) \tag{7.16}$$

or componentwise,

$$\frac{\partial f_i(\mathbf{x}_a)}{\partial x_j} = \sum_{b \in \mathcal{S}_a} V_b \ [f_i(\mathbf{x}_b) - f_i(\mathbf{x}_a)] \ \frac{\partial W(x_{ab})}{\partial x_{a,j}} \tag{7.17}$$

If the vector-valued function is a linear field, i.e. $\mathbf{f}(\mathbf{x}) = \mathbf{A}\mathbf{x} + \mathbf{b}$ where $\mathbf{A}$ is a constant second-order tensor and $\mathbf{b}$ a constant first-order tensor, then $\nabla \mathbf{f}(\mathbf{x})$ is equal[8] to $\mathbf{A}^T$. To enforce first-order completeness via a kernel gradient correction, the following condition, which is obtained by substituting the linear field in Eq. (7.16), has to be satisfied:

$$\mathbf{I} = \sum_{b \in \mathcal{S}_a} V_b \ (\mathbf{x}_b - \mathbf{x}_a) \otimes \nabla_a W(x_{ab}) \tag{7.18}$$

This is the case, if the classical kernel gradient $\nabla_a W(x_{ab})$ is replaced by a *corrected kernel gradient*

$$\tilde{\nabla}_a W(x_{ab}) = \mathbf{K}_a^{-1} \nabla_a W(x_{ab}) \tag{7.19}$$

in the previous equation, i.e.[9]

$$\mathbf{I} = \sum_{b \in \mathcal{S}_a} V_b \ (\mathbf{x}_b - \mathbf{x}_a) \otimes \mathbf{K}_a^{-1} \nabla_a W(x_{ab}) = \left(\sum_{b \in \mathcal{S}_a} V_b \ (\mathbf{x}_b - \mathbf{x}_a) \otimes \nabla_a W(x_{ab}) \right) \mathbf{K}_a^{-T} \tag{7.20}$$

which is satisfied provided that the *shape matrix* $\mathbf{K}_a$ has the following form

$$\mathbf{K}_a = \sum_{b \in \mathcal{S}_a} V_b \ \nabla_a W(x_{ab}) \otimes (\mathbf{x}_b - \mathbf{x}_a) \tag{7.21}$$

according to Eq. (7.20). Thus, the derivative of a linear field can be correctly approximated by the following equation for the gradient operator:

$$[\nabla \mathbf{f}(\mathbf{x}_a)]^T = \sum_{b \in \mathcal{S}_a} V_b \ [\mathbf{f}(\mathbf{x}_b) - \mathbf{f}(\mathbf{x}_a)] \otimes \mathbf{K}_a^{-1} \nabla_a W(x_{ab}) \tag{7.22}$$

[7] We use the left gradient of a vector field as defined in Belytschko et al. [29], i.e. $[\nabla \mathbf{f}]_{ij} = \partial f_j / \partial x_i$.

[8] $[\nabla \mathbf{f}]_{ij} = \partial f_j / \partial x_i = \partial (A_{jk} x_k + b_j) / \partial x_i = A_{jk} \delta_{ik} = A_{ji} = A_{ij}^T = \left[\mathbf{A}^T\right]_{ij}$

[9] The second equality can be proven by the following identity $[\mathbf{A}\mathbf{x}]_i = A_{ij} x_j = x_j A_{ij} = x_j A_{ji}^T = \left[\mathbf{x}\mathbf{A}^T\right]_i$, where $\mathbf{x}$ and $\mathbf{A}$ are arbitrary first- and second-order tensors.

7.1.3 SPH formulation of the governing equations

The previous SPH approximation allows to evaluate complex field gradients $\nabla \mathbf{f}(\mathbf{x}_a)$ by gradients of the kernel functions $\nabla_a W(x_{ab})$, which can be easily evaluated by the particle values $f(\mathbf{x}_b)$ and their positions $\mathbf{x}_b$. In this section, its is shown *how this approximation can be applied to the governing equations of the continuum to compute the particle forces*. These forces are later explicitly integrated (Sec. 7.1.4.3) to ultimately determine the time evolution of the continuum. It is important to mention, that ***all the concepts of this section are combined in Sec. 7.1.4.3, which is why it might be interesting to confront the explanations of the current section with the Algorithms 1 and 2*** **in Sec. 7.1.4.3**. Due to different SPH formulations for fluids and solids, as mentioned in Sec. 7.1.1, Eulerian SPH and total Lagrangian SPH are summarized in this section. Updated Lagrangian SPH will not be treated in this document.

7.1.3.1 Eulerian SPH for fluids

In a Eulerian description of a continuum (Sec. H.1.1), the independent variables are the spatial coordinates $\mathbf{x}$ and the time t. In *Eulerian SPH*, spatial derivatives are written with respect to spatial coordinates and the internal forces are integrated in the current configuration of the continuum. In this section, the underlying Eulerian *governing equations* and the corresponding *SPH formulation* are summarized.

Governing equations

In a Eulerian description, the *conservation equations* of mass (continuity equation) and linear momentum are the following continuum equations (Sec. H.2.1):

$$\frac{\mathrm{d}\rho}{\mathrm{d}t} = -\rho \nabla \cdot \mathbf{v} \tag{7.23}$$

$$\rho \frac{\mathrm{d}\mathbf{v}}{\mathrm{d}t} = \nabla \cdot \boldsymbol{\sigma} + \rho \mathbf{b} \tag{7.24}$$

where ρ is the density, t the time, $\mathbf{v}$ the velocity vector, $\boldsymbol{\sigma}$ the Cauchy stress tensor and $\mathbf{b}$ the force per unit mass vector.

Furthermore, different *equations of state* can be defined to link the consequences of the particle displacement, e.g. the density or shear strains, to the Cauchy stress tensor $\boldsymbol{\sigma} = -p\mathbf{I} + \mathbf{s}$, where p is the pressure (positive in compression) and $\mathbf{s}$ the deviatoric Cauchy stress tensor (Sec. H.1.6):

- *Linear compressibility*[10], i.e. with a constant bulk modulus K:

$$p = K\left(\frac{\rho}{\rho_0} - 1\right) \tag{7.25}$$

  where ρ_0 is the initial density.

[10] Eq. (7.25) can be obtained by integrating the definition of the bulk modulus, i.e. $K = -V(\partial p/\partial V)$, with V being the volume, from the initial state to the current one by assuming that $p = 0$ for $\rho = \rho_0$, by the conservation of mass, i.e. $m = \rho V$, and by the hypothesis of small volume change, i.e. $\ln(V_0/V) \approx V_0/V - 1$.

- *Non-linear compressibility*[11], i.e. with a pressure-dependent bulk modulus $K = K_0 + K_1 p$:

$$p = \frac{K_0}{K_1}\left[\left(\frac{\rho}{\rho_0}\right)^{K_1} - 1\right] \tag{7.26}$$

  where K_0 and K_1 are material constants.

- *Newtonian law of viscosity* (by Eqs. H.27 and H.126):

$$\mathbf{s} = 2\eta \operatorname{dev} \mathbf{D} \tag{7.27}$$

  where η is the dynamic viscosity and $\mathbf{D}$ the strain rate tensor (Eq. H.17).

Eulerian SPH formulation

First, the right-hand side of the *continuity equation* (Eq. 7.23) can be evaluated via the SPH approximation (Eq. 7.16) of the velocity gradient $\mathbf{L} = (\nabla \mathbf{v})^T$ (Eq. H.14) at the particle a, i.e.

$$\mathbf{L}_a = \sum_{b \in \mathcal{S}_a} V_b \, (\mathbf{v}_b - \mathbf{v}_a) \otimes \mathbf{K}_a^{-1} \nabla_a W(x_{ab}) \tag{7.28}$$

since the divergence of the velocity in the continuity equation is then provided by the strain rate tensor $\mathbf{D}$ (Eq. H.17):

$$\nabla \cdot \mathbf{v} = \operatorname{tr} \mathbf{D} \quad \text{with} \quad \mathbf{D} = \frac{1}{2}\left(\mathbf{L} + \mathbf{L}^T\right) \tag{7.29}$$

Furthermore, the continuity equation (Eq. 7.23) is rather written in terms of the particle volume $V_a = m_a/\rho_a$ instead of the density. Thus, the *SPH approximation of the continuity equation* is the following one with $\mathbf{D}_a$ computed by Eqs. (7.28) and (7.29):

$$\frac{\mathrm{d}V_a}{\mathrm{d}t} = V_a \operatorname{tr} \mathbf{D}_a \tag{7.30}$$

Secondly, the SPH approximation of the internal forces $\mathbf{f}_a^{\text{int}}$ due to the stresses $\boldsymbol{\sigma}$ in the right-hand side of the *momentum equation* (Eq. 7.24 multiplied by V_a) was derived via a variational approach by Bonet and Lok [39]:

$$\mathbf{f}_a^{\text{int}} = \sum_{b \in \mathcal{S}_a} \underbrace{V_a V_b \, (\boldsymbol{\sigma}_a + \boldsymbol{\sigma}_b) \, \nabla_a W(x_{ab})}_{= \mathbf{f}_{ab}^{\text{int}}} \tag{7.31}$$

It is important to notice that the previous expression of the internal forces is based on the continuity equation (Eq. 7.23), instead of the classical summation density[12], which implies that Eq. (7.31) is variationnally consistent with Eq. (7.23) according to Bonet and Lok [39]. The derivation of

[11] Eq. (7.26) is derived in the same way as Eq. (7.25) but without the hypothesis of small volume change.

[12] The classical summation density, i.e. $\rho_a = \sum_{b \in \mathcal{S}_a} m_b W(x_{ab})$, is obtained by setting $f(\mathbf{x}) = \rho(\mathbf{x})$ in Eq. (7.9). It is an alternative way to enforce the conservation of mass in SPH.

the SPH formulation from a variational principle has the advantage that it conserves linear and angular momentum (in the absence of external forces) provided that the internal energy function is invariant with respect to rigid body motion. In fact, linear momentum is conserved since $\mathbf{f}_{ab}^{\text{int}} = -\mathbf{f}_{ba}^{\text{int}}$ due to the symmetry property of the kernel function, i.e. $\nabla_a W(x_{ab}) = -\nabla_b W(x_{ab})$. Concerning angular momentum, Bonet and Lok [39] showed that it is conserved, if Eq. (7.18) is satisfied, i.e. if the kernel gradient is corrected for the derivatives of the velocity field as explained in Sec. 7.1.2.3.

To introduce the kernel gradient correction in the previous equation without compromising the linear momentum conservation, Eq. (7.31) can be written as follows by the symmetry property of the kernel [112]:

$$\mathbf{f}_a^{\text{int}} = \sum_{b \in \mathcal{S}_a} V_a V_b \left[\boldsymbol{\sigma}_a \nabla_a W(x_{ab}) + \boldsymbol{\sigma}_b \nabla_a W(x_{ab}) \right] \tag{7.32}$$

$$= \sum_{b \in \mathcal{S}_a} V_a V_b \left[\boldsymbol{\sigma}_a \nabla_a W(x_{ab}) - \boldsymbol{\sigma}_b \nabla_b W(x_{ba}) \right] \tag{7.33}$$

If the uncorrected kernel gradient is substituted by the corrected kernel gradient (Eq. 7.19) in the previous equation, it becomes

$$\mathbf{f}_a^{\text{int}} = \sum_{b \in \mathcal{S}_a} V_a V_b \left[\boldsymbol{\sigma}_a \mathbf{K}_a^{-1} \nabla_a W(x_{ab}) - \boldsymbol{\sigma}_b \mathbf{K}_b^{-1} \nabla_b W(x_{ba}) \right] \tag{7.34}$$

The components of the sum are again symmetric, which ensures the conservation of linear momentum. This equation can be rewritten more compactly as follows, again by the symmetry of the kernel function:

$$\mathbf{f}_a^{\text{int}} = \sum_{b \in \mathcal{S}_a} V_a V_b \left[\boldsymbol{\sigma}_a \mathbf{K}_a^{-1} + \boldsymbol{\sigma}_b \mathbf{K}_b^{-1} \right] \nabla_a W(x_{ab}) \tag{7.35}$$

Thirdly, to prevent artifical noise due to zero-energy modes, which could compromise the numerical stability [213], the *artificial Monaghan-type bulk viscosity term* [227, 230] is introduced:

$$\Pi_{ab} = \frac{\alpha \overline{c}_{ab} \phi_{ab}}{\overline{\rho}_{ab}} \tag{7.36}$$

with

$$\phi_{ab} = \frac{\overline{h}_{ab} \mathbf{v}_{ab} \cdot \mathbf{x}_{ab}}{(x_{ab} + 0.1 \overline{h}_{ab})^2} \qquad \overline{c}_{ab} = \frac{c_a + c_b}{2} \qquad \overline{\rho}_{ab} = \frac{\rho_a + \rho_b}{2} \qquad \overline{h}_{ab} = \frac{h_a + h_b}{2} \tag{7.37}$$

where α is a non-dimensional numerical parameter with typical values between 0.01 and 1 [113, 213], $\mathbf{v}_{ab} = \mathbf{v}_b - \mathbf{v}_a$ and $\mathbf{x}_{ab} = \mathbf{x}_b - \mathbf{x}_a$ so that ϕ_{ab} introduces repulsive forces, when particles approach each other and attractive forces, if they are separated (see Eq. 7.38 hereafter).

The variables $\overline{c}_{ab}$, $\overline{\rho}_{ab}$ and $\overline{h}_{ab}$ are, respectively, the average speed of sound, the average density and the average smoothing length of two particles with $c_a = \sqrt{K_a/\rho_a}$ and K_a the bulk modulus.

The internal forces in Eq. (7.34), the artificial viscosity term in Eq. (7.36) and the external forces per unit mass can be combined to obtain the *SPH approximation of the linear momentum equation* (Eq. 7.24 multiplied by V_a):

$$m_a \frac{\mathrm{d}\mathbf{v}_a}{\mathrm{d}t} = \sum_{b \in \mathcal{S}_a} \left[V_a V_b \left(\boldsymbol{\sigma}_a \mathbf{K}_a^{-1} + \boldsymbol{\sigma}_b \mathbf{K}_b^{-1} \right) + m_a m_b \Pi_{ab} \right] \nabla_a W(x_{ab}) + m_a \mathbf{b}_a \tag{7.38}$$

Finally, the Cauchy stress tensor $\boldsymbol{\sigma} = -p\mathbf{I} + \mathbf{s}$ in the previous equation can be evaluated by computing the values of its components. On the one hand, the pressure p is determined by the constitutive equations (Eq. 7.25 or 7.26), the density calculation via the continuity equation (Eq. 7.30) and the constant particle mass, i.e. $\rho_a = m_a/V_a$. On the other hand, the Cauchy stress deviator $\mathbf{s}$ is the result of the Newtonian viscosity law (Eq. 7.27), in which the deviatoric strain tensor is computed by the SPH approximation of the velocity gradient (Eqs. 7.28 and 7.29).

7.1.3.2 Total Lagrangian SPH for solids

In a Lagrangian description of a continuum (Sec. H.1.1), the independent variables are the (material) coordinates $\mathbf{X}$ of the continuum in the reference configuration and the time t. In *total Lagrangian SPH* (TLSPH) spatial derivatives are written with respect to material coordinates and the internal forces are integrated in the initial (reference) configuration to eliminate the tensile instability. This method is mainly used for solids due to their smaller deformations with respect to fluids, as explained in Sec. 7.1.1.3. Hence, the *governing equations*, the *total Lagrangian SPH formulation* and *Ganzenmüller's algorithm for zero-energy mode suppression* are described in this section.

Governing equations

In a Lagrangian description, the *conservation equations* of mass and linear momentum can be written as follows (Sec. H.2.2):

$$\rho J = \rho_0 \tag{7.39}$$

$$\rho_0 \frac{\mathrm{d}\mathbf{v}}{\mathrm{d}t} = \nabla_0 \cdot \mathbf{P} + \rho_0 \mathbf{b} \tag{7.40}$$

where J is the determinant of the deformation gradient $\mathbf{F}$ (Eq. H.9), ρ_0 the density in the reference configuration and $\nabla_0 \cdot \mathbf{P}$ the divergence of the first Piola-Kirchhoff stress tensor (Eq. H.29) with respect to the reference configuration.

Concerning the *equations of state*, the material is assumed to be elastoplastic with the following hypotheses, which are summarized in Sec. H.3.2 and explained throughly in [27, 258]: hypoelasticity, additive decomposition of elastic and plastic strain rates, linear elasticity and Von Mises associated plasticity with isotropic hardening.

Total Lagrangian SPH formulation

First, the *continuity equation* (Eq. 7.39) can be used to compute the density ρ in the current configuration of the continuum by the SPH approximation of the deformation gradient $\mathbf{F} = (\nabla_{\mathbf{X}}\mathbf{u})^T + \mathbf{I}$ (Eqs. H.4 and H.9). This approximation is obtained in a similar way to the approximation of the velocity gradient (Eq. 7.28) but in the reference configuration:

$$\mathbf{F}_a = \sum_{b \in \mathcal{S}_a^0} V_b^0 \ (\mathbf{u}_b - \mathbf{u}_a) \otimes \mathbf{K}_{0,a}^{-1} \nabla_a W(X_{ab}) + \mathbf{I} \tag{7.41}$$

with

$$\mathbf{K}_{0,a} = \sum_{b \in \mathcal{S}_a^0} V_b^0 \, \nabla_a W(X_{ab}) \otimes (\mathbf{X}_b - \mathbf{X}_a) \tag{7.42}$$

$$\nabla_a W(X_{ab}) = \left(\frac{\partial W(X_{ab})}{\partial X_{ab}} \right) \frac{\mathbf{X}_a - \mathbf{X}_b}{X_{ab}} \tag{7.43}$$

where $V_b^0 = m_b / \rho_b^0$ is the particle volume in the reference configuration, $\mathbf{u}_b = \mathbf{x}_b - \mathbf{X}_b$ the particle displacement, $\mathbf{K}_{0,a}$ the shape matrix in the reference configuration, $\mathbf{X}_b$ the particle position in the reference configuration and $X_{ab} = \|\mathbf{X}_b - \mathbf{X}_a\|$. It is important to notice that only the particles, which are in the support domain in the reference configuration, i.e. $\mathcal{S}_a^0$ instead of $\mathcal{S}_a$, are considered in the summation. In fact, the kernel and its derivative are equal to zero outside this domain.

Secondly, the *conservation equation of linear momentum* is approximated in exactly the same way as in the Eulerian description (Eq. 7.38) but in the reference configuration:

$$m_a \frac{\mathrm{d}\mathbf{v}_a}{\mathrm{d}t} = \sum_{b \in \mathcal{S}_a^0} \left[V_a^0 V_b^0 \left(\mathbf{P}_a \mathbf{K}_{0,a}^{-1} + \mathbf{P}_b \mathbf{K}_{0,b}^{-1} \right) \nabla_a W(X_{ab}) + m_a m_b \Pi_{ab} \nabla_a W(x_{ab}, X_{ab}) \right] + m_a \mathbf{b}_a \tag{7.44}$$

where the artificial bulk viscosity term Π_{ab} is still computed according to Eq. (7.36)[13].

Finally, the evaluation of the first Piola-Kirchhoff tensor is less obvious than the evaluation of the Cauchy stress tensor in ESPH for fluids (Sec. 7.1.3.1) due to the non-objectivity of the stress rate, i.e. the dependence of the stress rate to the observer [29], and plasticity. More precisely, because of the hypoelastic formulation (Eq. H.51), it is necessary to compute the strain rate tensor $\mathbf{D}_a$ to integrate the stresses. This is possible by the SPH approximation of the velocity gradient $\mathbf{L}_a$ (Eq. H.17). However, instead of computing the velocity gradient in the current configuration of the continuum (Eq. 7.28), it is determined via the reference configuration in TLSPH (Eq. H.15), i.e.

$$\mathbf{L}_a = \dot{\mathbf{F}}_a \mathbf{F}_a^{-1} \tag{7.45}$$

[13] It can be noticed that the kernel gradient is computed differently in Eq. (7.44) than in Eq. (7.38). In fact, $\nabla_a W(x_{ab}, X_{ab}) = \partial W(X_{ab}) / \partial X_{ab} [(\mathbf{x}_a - \mathbf{x}_b)/x_{ab}]$ instead of $\nabla_a W(x_{ab}) = \partial W(x_{ab}) / \partial x_{ab} [(\mathbf{x}_a - \mathbf{x}_b)/x_{ab}]$. This difference was not further investigated since the artificial viscosity is not required in the following simulations of solids. The previous term was probably introduced to test the artificial viscosity in TLSPH without having to update the set $\mathcal{S}_a$, which is required in the consistent implementation of the artificial viscosity according to Eq. (7.38).

which can be evaluated by the SPH approximation of the deformation gradient in Eq. (7.41) and the SPH approximation of its time derivative:

$$\dot{\mathbf{F}}_a = \sum_{b \in \mathcal{S}_a^0} V_b^0 \ (\mathbf{v}_b - \mathbf{v}_a) \otimes \mathbf{K}_{0,a}^{-1} \nabla_a W(X_{ab}) \tag{7.46}$$

To ensure objectivity, a *corotational approach* is adopted, i.e. the components of the strain rate tensor are rotated to the corotational coordinate system, which rotates with the material. In this system, the constitutive equations are evaluated via the *radial return algorithm*, which is derived in appendix R, and the Cauchy stresses are time-integrated. The resulting stresses are then rotated back to the current configuration. Since these methods are thoroughly explained in the literature [29, 258], they are only summarized in the Algorithms 1 and 2 of Sec. 7.1.4.3. The resulting Cauchy stresses $\boldsymbol{\sigma}_a$ in the current configuration can ultimately be transformed into the first Piola-Kirchhoff stresses, which are space-integrated in Eq. (7.44), via Eq. (H.32), i.e. $\mathbf{P}_a = J_a \boldsymbol{\sigma}_a \mathbf{F}_a^{-T}$, and the SPH approximation of the deformation gradient (Eq. 7.41).

Algorithm for zero-energy mode suppression

As mentioned in Sec. 7.1.1.3, SPH is rank-deficient since various particle fields can lead to the same SPH approximation of the gradient. In consequence, non-physical *zero-energy modes* can be introduced in the solution. To suppress these modes, Ganzenmüller [112] developed a method that is similar to the *FE hourglass control algorithm by Flanagan and Belytschko* [102]. This method can be summarized as follows (see details in [112, 189]).

A linear finite element with a single integration point, also known as constant strain element, can only accurately capture a fully linear displacement field. For instance, in 1D, if the displacement is $u(X) = \alpha_0 + \alpha_1 X + \alpha_2 X^2$, the deformation gradient is $F = \partial u / \partial X + 1 = \alpha_1 + 2\alpha_2 X + 1$. If the element is integrated at $X = 0$, its deformation gradient is computed as $F^* = \alpha_1 + 1$. Hence, the non-linear component of the displacement field cannot be captured since α_2 is not included in the previous deformation gradient. In consequence, Flanagan and Belytschko identified hourglass modes as the part of the nodal displacement field, which does not correspond to the fully linear field that can be described by the element, e.g. via F^*.

Similarly, Ganzenmüller identified the error due to zero-energy modes in SPH as the difference between the particle position field and the linear position field, which is defined by the deformation gradient. More precisely, if $\mathbf{X}_{ab} = \mathbf{X}_b - \mathbf{X}_a$ is the distance vector between neighboring particles in the reference configuration, then this distance vector should be

$$\langle \mathbf{x}_{ab} \rangle^a = \mathbf{F}_a \mathbf{X}_{ab} \tag{7.47}$$

in the current configuration, where $\mathbf{F}_a$ is the SPH approximation of the deformation gradient. Because of integration errors, the distance vector in the current configuration is, however, $\mathbf{x}_{ab} = \mathbf{x}_b - \mathbf{x}_a$, so that the *error vector due to zero-energy modes* can be defined as follows:

$$\mathcal{E}_{ab}^a = \langle \mathbf{x}_{ab} \rangle^a - \mathbf{x}_{ab} \tag{7.48}$$

To ensure linear momentum conservation later on by symmetry, i.e. $\mathcal{E}_{ab} = -\mathcal{E}_{ba}$, the error vector is rather defined as follows:

$$\mathcal{E}_{ab} = \frac{1}{2}\left(\langle \mathbf{x}_{ab}\rangle^a - \mathbf{x}_{ab} + \langle \mathbf{x}_{ab}\rangle^b - \mathbf{x}_{ab}\right) = \frac{1}{2}\left(\mathbf{F}_a + \mathbf{F}_b\right)\mathbf{X}_{ab} - \mathbf{x}_{ab} \tag{7.49}$$

This error vector has to be minimized to reduce the amplitude of zero-energy modes. For this reason, a *penalty force* is defined on the basis of the error vector, which is projected on the current particle separation vector $\mathbf{x}_{ab}$ to ensure the conservation of angular momentum in addition to the conservation of linear momentum due to its symmetry:

$$\mathbf{f}_{ab}^{\mathrm{HG},e} = -\frac{1}{2}\xi E \frac{V_a^0 V_b^0 W(X_{ab})}{X_{ab}^2}\frac{\mathcal{E}_{ab}\cdot\mathbf{x}_{ab}}{x_{ab}}\frac{\mathbf{x}_{ab}}{x_{ab}} \tag{7.50}$$

where E is the Young's modulus and where ξ is a dimensionless numerical parameter, which should be chosen large enough to eliminate zero-energy modes while not adding to much artificial stiffness to the model (recommended value: 1 to 20 [113]).

Finally, one should notice that plasticity introduces locally non-linear displacements. To avoid suppressing these displacements by the previous method, the correction force is replaced by an *artificial viscous force for plastic deformations*. This force is similar to the artificial Monaghan-type bulk viscosity term (Eq. 7.36) but amplified by the non-dimensional error vector, if the repulsive or attractive force, that it possibly generates, contributes to the reduction of the error vector[14]:

$$\mathbf{f}_{ab}^{\mathrm{HG},v} = \begin{cases} m_a m_b \frac{\|\mathcal{E}_{ab}\|}{X_{ab}}\Pi_{ab}^*\nabla_a W(x_{ab}, X_{ab}) & \text{, if } (\mathbf{x}_{ab}\cdot\mathbf{v}_{ab})(\mathcal{E}_{ab}\cdot\mathbf{x}_{ab}) < 0 \\ 0 & \text{, otherwise.} \end{cases} \quad \text{with} \quad \Pi_{ab}^* = \frac{\xi c_0 \phi_{ab}}{\rho_0} \tag{7.51}$$

where ρ_0 is the reference density, $c_0 = \sqrt{K/\rho_0}$ the reference speed of sound and ϕ_{ab} of Eq. (7.37). The same value of the non-dimensional parameter ξ is used in the elastic and viscous hourglass correction methods to not over-complicate the parameter space in this first exploratory analysis.

In conclusion, the *zero-energy mode suppression force* is computed as follows:

$$\mathbf{f}_a^{\mathrm{HG}} = \sum_{b\in\mathcal{S}_a^0}\mathbf{f}_{ab}^{\mathrm{HG}} \qquad \text{with} \qquad \mathbf{f}_{ab}^{\mathrm{HG}} = \begin{cases} \mathbf{f}_{ab}^{\mathrm{HG},v} & \text{, if } \max\left(\bar{\epsilon}_a^p, \bar{\epsilon}_b^p\right) > 0 \\ \mathbf{f}_{ab}^{\mathrm{HG},e} & \text{, otherwise.} \end{cases} \tag{7.52}$$

where $\bar{\epsilon}_a^p$ is the effective plastic strain at particle a.

[14] This force has never been documented in the literature (to the best of our knowledge) but it was found in the USER-SMD SPH package of LAMMPS. Hence, its underlying working principle is not exactly known but it can be estimated. In particular, the condition in Eq. (7.51) can be illustrated by the following example. If particles are approaching, i.e. $\mathbf{x}_{ab}\cdot\mathbf{v}_{ab} < 0$, and if $\mathcal{E}_{ab}\cdot\mathbf{x}_{ab} > 0$, the error vector $\mathcal{E}_{ab}$ can be reduced by increasing the distance vector $\mathbf{x}_{ab}$ between the particles. In this case, the viscous hourglass force is repulsive according to Eq. (7.51). If $\mathcal{E}_{ab}\cdot\mathbf{x}_{ab} < 0$, however, the hourglass force is set to zero, since the resulting repulsive force would increase the error vector. Hence, the repulsive or attractive force is only applied, if it contributes to the reduction of the error vector.

7.1.3.3 Formulation of contact interactions

As mentioned in Sec. 7.1.1.4, various techniques can be used to model interactions with boundaries or between fluids and solids in SPH. In this chapter, purely repulsive penalty forces between particles of different groups are introduced to model their interactions. The particles of a group could, for instance, be those of a fluid, another fluid, a solid or a boundary wall, which thus also have to be discretized by particles. More specifically, the repulsive force acting on a particle a due to a particle b is computed by the Hertz contact theory [138, 177]:

$$\mathbf{f}_{ab}^{c} = -\frac{4}{3}E^{*}\sqrt{R^{*}}\delta^{3/2}\,\frac{\mathbf{x}_{ab}}{x_{ab}} \quad \text{if} \quad x_{ab} < R_a + R_b \tag{7.53}$$

where E^{*} is the effective contact stiffness[15] such that $1/E^{*} = (1-\nu_a^2)/E_a + (1-\nu_b^2)/E_b$, E_a the Young's modulus, ν_a the Poisson's ratio, $R^{*} = R_a R_b/(R_a + R_b)$ the effective contact radius and $\delta = R_a + R_b - x_{ab}$ the numerical overlap of contacting particles, which are assumed to be initially spherical. It is important to mention that the specific form of the penalty force has no real importance in this context provided that it increases sufficiently when particles approach each other to prevent significant overlaps. The Hertz contact force was selected because it was already implemented in the USER-SMD SPH package but a linear penalty force would certainly lead to identical results, if the contact stiffness is large enough.

7.1.4 Numerical solution method

Previously, the partial differential conservation equations were transformed into ordinary differential equations by the Eulerian and Total Lagrangian SPH approximations. In this section, it is explained, how these equations are numerically evaluated via an efficient *neighbor search algorithm* and how they are *time-integrated* to compute the evolution of the continuum over time. Before focusing on the neighbor search algorithm and the time-integration, the *computational framework*, in which these operations are executed, is briefly described in the following section.

7.1.4.1 LAMMPS USER-SMD

As explained in Sec. 7.1.1.5, the USER-SMD SPH package in LAMMPS was selected essentially because it is the only open-source software that includes most of the required features to model lubricated asperity flattening by SPH (to the best of our knowledge[16]).

LAMMPS (Large-scale Atomic/Molecular Massively Parallel Simulator) was originally developed for molecular dynamics (MD) simulations [257]. Since such simulations are usually large in the sense that millions of atoms are modeled for hundreds of thousands of time steps, LAMMPS is strongly parallelized by using the message-passing interface (MPI) standard between computing

[15] Here, the contact law was derived from a physical model. Numerically, the physical distance between centers of contacting particles has, however, no real importance provided that the overlap is sufficiently small to prevent unreasonable artificial penetration. Thus, the effective contact stiffness E^{*} is generally adjusted to limit the overlap instead of choosing physical material values.

[16] A list of SPH codes can be found in [298].

cores and a spatial decomposition of the simulation domain. The advanced extensibility of its source code and the similarity of MD to other particle methods led to the implementation of these methods within the framework of LAMMPS as packages. The *USER-SMD* (USER Smooth Mach Dynamics) SPH package by Ganzenmüller [113] is one of these packages. Practically, the code is mainly written in C++ with few dependencies (Eigen [127] and, optionally, Vtk [282]), and simulations are parameterized by input scripts with a custom syntax.

Due to the exploratory nature of this chapter, the USER-SMD package was not significantly modified: the implemented Spiky kernel [93] was replaced by the more commonly used Wendland kernel (Eq. 7.4), which prevents the pairing instability, and a method to compute the relative contact area was added (Sec. 7.2.3). Although the software changes are minor, the underlying equations of the source code were almost entirely derived and documented in this thesis to simplify future developments of the method. In fact, *no other document combines all these elements* to the best of our knowledge[17].

7.1.4.2 Neighbor search

Due to the compact support property of the kernel function, i.e. the kernel is equal to zero outside its compact support domain $\mathcal{S}_a$, the kernel approximation is transformed from a global to a local operation. This implies that only particles in the support domain have to be considered in the sum of the particle approximation. Particles b in the support domain of the kernel centered at particle a, i.e. $b \in \mathcal{S}_a$, are called *neighbors* of a. Mathematically, particles a and b are neighbors, if the condition $\|\mathbf{x}_b - \mathbf{x}_a\| < h$ is satisfied, provided that the smoothing length h is constant and $\zeta = 1$ (Sec. 7.1.2). Since these neighbors are not known initially, it is required to perform a *neighbor search*, either only once for TLSPH or at each time step in ESPH. In fact, the reference configuration does not change in TLSPH, which implies that neighbors in the reference configuration remain neighbors throughout the simulation.

Intuitively, neighbors could be searched for by computing the distance between one particle and all remaining particles. If the total number of particles is n_p, this strategy would lead to $n_p(n_p-1)$ distance tests or $n_p(n_p-1)/2$ tests due to the symmetry property of the neighborhood, i.e. if a is a neighbor of b, b is a neighbor of a (if h has the same value for all particles). Nevertheless, this implies that the number of operations is $\mathcal{O}(n_p^2)$ for each time step in ESPH[18], which could be relatively costly in terms of computation time, when the number of particles increases.

To accelerate the neighbor search, link-cell binning and neighbor lists (Verlet lists) were introduced in LAMMPS [156, 257]. In *link-cell binning*, a grid is laid over the simulation domain as in Fig. 7.2a. If the bin size is h, only particles in neighboring bins have to be locally tested via the condition $\|\mathbf{x}_b - \mathbf{x}_a\| < h$. Hence, the neighbor search becomes $\mathcal{O}(n_p)$, since binning, i.e. the

[17] Ganzenmüller focuses mainly on TLSPH and the zero-energy suppression algorithm in [112], while he provides the application programming interface (API) of the USER-SMD package in [113]. Leroch et al. focus again on TLSPH and its application to scratch test simulations in [189]. Thus, the details of ESPH are, for instance, never mentioned.

[18] The Bachmann-Landau notation $\mathcal{O}(n_p^2)$ denotes the quadratic increase of the number of neighbor search operations, when the total number of particles n_p increases.

cell identification of a particle, is done only once for each particle and since the local number of tests is $\mathcal{O}(1)$. Furthermore, instead of having to test the particles in all neighboring cells and the central cell, only the particles in the upper left cells and the central cell have to be tested due to the symmetry property of a neighborhood. In LAMMPS, this operation is slightly more complex since stencils are applied to further accelerate the neighbor search. More precisely, as illustrated in Fig. 7.2b, the bin size is $(h + s)/2$, where s is the skin distance, which will be explained hereafter. The stencil is then defined as the set of cells that could contain neighboring particles. Hence, only particles in a stencil centered on a particle a are tested.

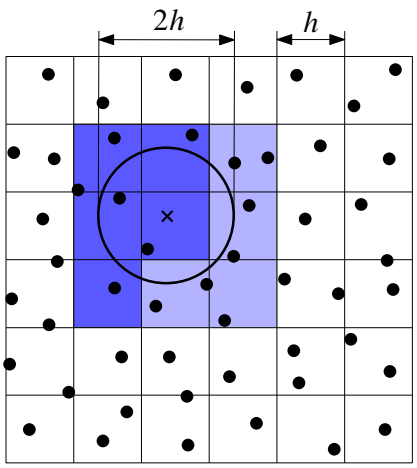

(a) All direct neighbor cells and the central cell (light and dark blue): 13 local tests (number of particles in blue cells, except central particle). Upper left neighbor cells and central cell (dark blue): 6 local tests.

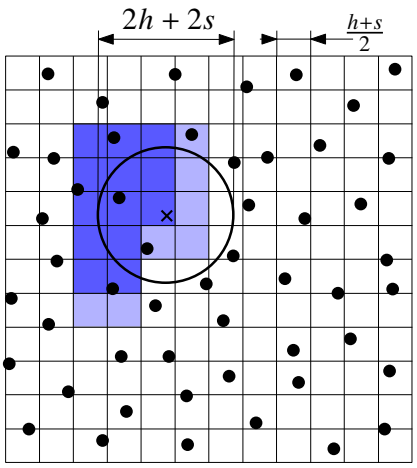

(b) Stencil with smaller bin size in dark blue: 4 local tests. The light blue zone corresponds to the dark blue zone in Fig. 7.2a to show why the number of local tests can be reduced by choosing a smaller bin size.

Figure 7.2: Illustration of link-cell binning with a different number of local tests depending on the stencil, i.e. the set of cells that could contain neighboring particles. The skin distance s was assumed to be very small in this example to allow the comparison between both figures.

Based on link-cell binning, a *neighbor list*, i.e. a list with all neighbors of a particle can be built, for each particle. Instead of determining the neighbors in the neighbor list by the condition $\|\mathbf{x}_b - \mathbf{x}_a\| < h$, they are rather selected by the condition $\|\mathbf{x}_b - \mathbf{x}_a\| < h + s$, where s is the skin distance. Adding this distance has the advantage that the same neighbor list can be reused for several time steps, which further reduces the computation time. In fact, neighbor list only have to be rebuilt, when the distance between particles is reduced by the skin distance. Hence, a conservative condition is to only rebuild neighbor lists, when a particle moved more than the distance $s/2$ since the last build of neighbor lists.

In addition to this neighbor search algorithm, LAMMPS allows to *spatially decompose the simulation domain with dynamic load balancing*. This means that this domain can be decomposed into spatial zones. The computational work load of each zone is then distributed between computing cores of one or several processors. Ideally, one core is allocated to each zone and the number of particles is the same in each zone so that each core is used optimally. Since the number

of particles could, however, change significantly from one zone to another at a given time step and over time, LAMMPS is able to spatially modify the zones in order to dynamically balance the work load of the computing cores. These ideas are illustrated in Fig. 7.3.

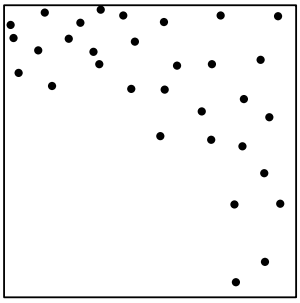

(a) Serial computation: 32 particles are simulated on one core

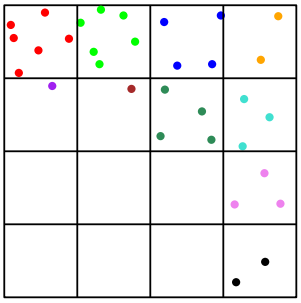

(b) Parallel computation by domain decomposition with one core per zone: some cores are empty and others have a lot of particles.

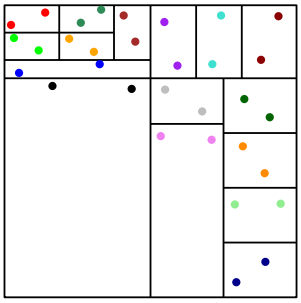

(c) Parallel computation by domain decomposition with one core per zone and with dynamic load balancing: each core has two particles.

Figure 7.3: Simplified illustration of parallel computations by domain decomposition with dynamic load balancing.

7.1.4.3 Time integration

While the SPH approximation allowed to transform the partial differential continuum equations into ordinary differential equations, the previous neighbor search algorithm makes it possible to evaluate the terms in these equations efficiently. Finally, the resulting differential equations have to be time-integrated to obtain the evolution of the studied continuum over time.

In this section, the *time-integration scheme* in LAMMPS and the respective *time step stability limit* are briefly described.

Velocity-Verlet integration scheme

The standard time integration algorithm in LAMMPS is the *explicit velocity-Verlet integration scheme* [320], which can be derived from a Taylor series expansion [108]. Hence, if the equation

$$m_a \frac{\mathrm{d}\mathbf{v}_a}{\mathrm{d}t} = \mathbf{f}_a \quad \text{with} \quad \frac{\mathrm{d}\mathbf{x}_a}{\mathrm{d}t} = \mathbf{v}_a \tag{7.54}$$

has to be time-integrated, the velocity-Verlet integration scheme is defined as follows with the time step Δt:

1. Compute $\mathbf{v}_a(t + \Delta t/2) = \mathbf{v}_a(t) + \frac{\mathbf{f}_a(t)}{m_a}\frac{\Delta t}{2}$;
2. Compute $\mathbf{x}_a(t + \Delta t) = \mathbf{x}_a(t) + \mathbf{v}_a(t + \Delta t/2)\Delta t$;
3. Evaluate $\mathbf{f}_a(t + \Delta t)$ based on $\mathbf{x}_a(t + \Delta t)$ and $\mathbf{v}_a(t + \Delta t/2)$;

4. Compute $\mathbf{v}_a(t+\Delta t) = \mathbf{v}_a(t+\Delta t/2) + \frac{\mathbf{f}_a(t+\Delta t)}{m_a}\frac{\Delta t}{2}$.

The velocity-Verlet algorithm has numerous advantages according to Frenkel and Smit [108], e.g. (1) it is locally forth-order accurate, i.e. the local error of the position is $\mathcal{O}(\Delta t^4)$, (2) it is relatively fast since it requires only one force evaluation per time step, (3) it has minimal memory requirements, (4) the positions and velocities are defined at the same time in contrast to the leapfrog algorithm, and (5) although the total energy is not conserved exactly, it shows small long-term energy drifts, which is related to its time-reversible and area-preserving (symplectic) properties.

All the previous equations of this chapter are finally combined in the Algorithms 1 and 2, which summarize the operations that are required to simulate a compressible fluid by Eulerian SPH with artificial and Newtonian viscosity, as well as a solid by total Lagrangian SPH with elastoplasticity, and both with a kernel gradient correction[19]**.**

Time step stability limit

Due to the explicit time-integration, the time step Δt has to satisfy the *Courant-Friedrichs-Lewy (CFL) condition* [88] to be stable. A derivation of the CFL condition for a specific SPH formulation by the Von Neumann stability analysis can be found in [345]. In general, the time step is therefore chosen by the following equation in *SPH*:

$$\Delta t = \beta_t \Delta t_{\text{cr}}^{\text{SPH}} \quad \text{with} \quad \Delta t_{\text{cr}}^{\text{SPH}} = \min_a \frac{h_a}{c_a} \tag{7.55}$$

where β_t is a safety factor that depends on the specific SPH scheme, e.g. $\beta_t = 0.4$ according to numerical tests in Monaghan [224], h_a is the smoothing length of particle a and c_a is its speed of sound [168]:

$$c_a = \sqrt{\frac{K_a + 4G_a/3}{\rho_a}} \tag{7.56}$$

where K_a is the effective bulk modulus, G_a the effective shear modulus and ρ_a the density of the particle a.

Furthermore, the *penalty contact formulation* (Sec. 7.1.3.3) introduces an additional stability limit. The corresponding critical time step is estimated as follows in the USER-SMD SPH package based on the stability analysis of the harmonic oscillator[20] [292]:

$$\Delta t_{\text{cr}}^c = \min_{ab}\left(\pi\sqrt{\frac{(m_a+m_b)\delta}{2f_{ab}^c}}\right) \tag{7.57}$$

[19]The sum of the contact forces is computed in Algorithm 2 as in Algorithm 1. It was not added explicitly in Algorithm 2 to keep this algorithm on a single page.

[20]It is unclear why the factor π was included in the USER-SMD SPH package (Eq. 7.57) since the critical time step of the harmonic oscillator is $\Delta t_{\text{cr}} = 2/\omega$, where ω is its frequency. This frequency is usually equal to $\sqrt{k/m}$, where m is the mass and k the stiffness of the oscillator. In any case, the factor π has no significant importance since the critical time step is multiplied by a safety factor β_t (Eq. 7.58).

Algorithm 1 Eulerian SPH with kernel gradient correction, artificial and Newtonian viscosity.

for $i = 1 : n_t$ **do** ▷ Time integration loop for n_t time steps

  for $a = 1 : n_p$ **do** ▷ First part of velocity Verlet time integration
    $\mathbf{v}_a = \mathbf{v}_a + (\Delta t\ \mathbf{f}_a)/(2m_a)$ ▷ Velocity update with half time step
    $\mathbf{x}_a = \mathbf{x}_a + \Delta t\ \mathbf{v}_a$ ▷ Position update
  end for

  for $a = 1 : n_p$ **do** ▷ Mechanical integration loop: strains and stresses
    $\mathbf{K}_a = \mathbf{L}_a = \mathbf{0}$ ▷ Initialization

    for $b \in \mathcal{S}_a$ **do** ▷ Loop over neighbors
      $\mathbf{K}_a = \mathbf{K}_a + V_b \nabla_a W(x_{ab}) \otimes (\mathbf{x}_b - \mathbf{x}_a)$ ▷ Shape matrix
      $\mathbf{L}_a = \mathbf{L}_a + V_b (\mathbf{v}_b - \mathbf{v}_a) \nabla_a W(x_{ab})$ ▷ Velocity gradient
    end for

    $\mathbf{L}_a = \mathbf{L}_a \mathbf{K}_a^{-T}$ ▷ Corrected velocity gradient
    $\mathbf{D}_a = \left(\mathbf{L}_a + \mathbf{L}_a^T\right)/2$ ▷ Strain rate tensor
    $\rho_a = m_a / V_a$ ▷ Density
    $p_a = p_a(\rho_a)$ ▷ Pressure computation by Eq. (7.25) or (7.26)
    $\mathbf{s}_a = 2\eta \operatorname{dev} \mathbf{D}_a$ ▷ Deviatoric Cauchy stresses
    $\boldsymbol{\sigma}_a = -p_a \mathbf{I} + \mathbf{s}_a$ ▷ Cauchy stress tensor
  end for

  for $a = 1 : n_p$ **do** ▷ Mechanical integration loop: particle forces
    $\mathbf{f}_a = m_a \mathbf{b}_a$ ▷ Body forces

    for $b \in \mathcal{S}_a$ **do** ▷ Loop over neighbors
      $\mathbf{f}_a = \mathbf{f}_a + V_a V_b \left(\boldsymbol{\sigma}_a \mathbf{K}_a^{-1} + \boldsymbol{\sigma}_b \mathbf{K}_b^{-1}\right) \nabla_a W(x_{ab})$ ▷ Force due to internal stresses
      $\mathbf{f}_a = \mathbf{f}_a + m_a m_b \Pi_{ab} \nabla_a W(x_{ab})$ ▷ Force due to artificial bulk viscosity
    end for

    for $b \in \mathcal{S}_a^c$ **do** ▷ Loop over particles in contact
      $\mathbf{f}_a = \mathbf{f}_a + \mathbf{f}_{ab}^c$ ▷ Contact force by Eq. (7.53)
    end for
  end for

  for $a = 1 : n_p$ **do** ▷ Second part of velocity-Verlet time integration
    $\mathbf{v}_a = \mathbf{v}_a + (\Delta t\ \mathbf{f}_a)/(2m_a)$ ▷ Velocity update at end of time step
    $V_a = V_a + \Delta t\, V_a \operatorname{tr} \mathbf{D}_a$ ▷ Particle volume
  end for

  $t = t + \Delta t$ ▷ Time incrementation
end for

Algorithm 2 Total Lagrangian SPH with kernel gradient correction and elastoplasticity.

for $i = 1 : n_t$ **do** ▷ Time integration loop for n_t time steps

  for $a = 1 : n_p$ **do** ▷ First part of velocity-Verlet time integration
    $\mathbf{v}_a = \mathbf{v}_a + (\Delta t\ \mathbf{f}_a)/(2m_a)$ ▷ Velocity update with half time step
    $\mathbf{x}_a = \mathbf{x}_a + \Delta t\ \mathbf{v}_a$ ▷ Position update
  end for

  for $a = 1 : n_p$ **do** ▷ Mechanical integration loop: strains and stresses
    $\mathbf{K}_{0,a} = \mathbf{F}_a = \dot{\mathbf{F}}_a = \mathbf{0}$ ▷ Initialization

    for $b \in \mathcal{S}_a^0$ **do** ▷ Loop over neighbors
      $\mathbf{K}_{0,a} = \mathbf{K}_{0,a} + V_b^0 \nabla_a W(X_{ab}) \otimes (\mathbf{X}_b - \mathbf{X}_a)$ ▷ Shape matrix
      $\mathbf{F}_a = \mathbf{F}_a + V_b^0 (\mathbf{u}_b - \mathbf{u}_a) \nabla_a W(X_{ab})$ ▷ Deformation gradient
      $\dot{\mathbf{F}}_a = \dot{\mathbf{F}}_a + V_b^0 (\mathbf{v}_b - \mathbf{v}_a) \nabla_a W(X_{ab})$ ▷ Rate-of-deformation gradient
    end for

    $\mathbf{F}_a = \mathbf{F}_a \mathbf{K}_{0,a}^{-T} + \mathbf{I}$ ▷ Corrected deformation gradient
    $\dot{\mathbf{F}}_a = \dot{\mathbf{F}}_a \mathbf{K}_{0,a}^{-T}$ ▷ Corrected rate-of-deformation gradient
    $\mathbf{L}_a = \dot{\mathbf{F}}_a \mathbf{F}_a^{-1}$ ▷ Velocity gradient
    $\mathbf{D}_a = \left(\mathbf{L}_a + \mathbf{L}_a^T\right)/2$ ▷ Strain rate tensor
    $\mathbf{F}_a \rightarrow \mathbf{R}_a \mathbf{U}_a$ ▷ Polar decomposition
    $\mathbf{D}'_a = \mathbf{R}_a^T \mathbf{D}_a \mathbf{R}_a$ ▷ Rotation to corotational coordinate system
    $p_a = p_a - K \Delta t \operatorname{tr} \mathbf{D}'_a$ ▷ Time integration of pressure
    $\mathbf{s}^e = \mathbf{s}'_a + 2G\Delta t \operatorname{dev} \mathbf{D}'_a$ ▷ Time integration of deviatoric stresses via elastic prediction
    $\sigma_{\mathrm{VM}}^e = \sqrt{(3/2)\mathbf{s}^e : \mathbf{s}^e}$ ▷ Von Mises stress of elastic prediction

    if $\sigma_{\mathrm{VM}}^e < \sigma_{Y,a}(\bar{\epsilon}_a^p)$ **then** ▷ Elastic prediction does not exceed yield stress
      $\mathbf{s}'_a = \mathbf{s}^e$ ▷ Deviatoric Cauchy stresses
    else
      $\mathbf{s}'_a = (\sigma_{Y,a}/\sigma_{\mathrm{VM}}^e)\ \mathbf{s}^e$ ▷ Plastic correction of deviatoric Cauchy stresses
      $\Delta\bar{\epsilon}^p = (\sigma_{\mathrm{VM}}^e - \sigma_{Y,a})/(3G)$ ▷ Effective plastic strain increment
      $\bar{\epsilon}_a^p = \bar{\epsilon}_a^p + \Delta\bar{\epsilon}^p$ ▷ Effective plastic strain
    end if

    $\boldsymbol{\sigma}'_a = -p_a \mathbf{I} + \mathbf{s}'_a$ ▷ Cauchy stresses in corotational coordinate system
    $\boldsymbol{\sigma}_a = \mathbf{R}_a \boldsymbol{\sigma}'_a \mathbf{R}_a^T$ ▷ Rotation to stationary coordinate system
    $\mathbf{P}_a = J_a \boldsymbol{\sigma}_a \mathbf{F}_a^{-T}$ ▷ First Piola-Kirchhoff stresses
  end for

  for $a = 1 : n_p$ **do** ▷ Mechanical integration loop: particle forces
    $\mathbf{f}_a = m_a \mathbf{b}_a$ ▷ Body forces

    for $b \in \mathcal{S}_a^0$ **do** ▷ Loop over neighbors
      $\mathbf{f}_a = \mathbf{f}_a + V_a^0 V_b^0 \left(\mathbf{P}_a \mathbf{K}_{0,a}^{-1} + \mathbf{P}_b \mathbf{K}_{0,b}^{-1}\right) \nabla_a W(X_{ab})$ ▷ Force due to internal stresses
      $\mathbf{f}_a = \mathbf{f}_a + m_a m_b \Pi_{ab} \nabla_a W(x_{ab}, X_{ab})$ ▷ Force due to artificial bulk viscosity
      $\mathbf{f}_a = \mathbf{f}_a + \mathbf{f}_{ab}^{\mathrm{HG}}$ ▷ Hourglass control force by Eq. (7.52)
    end for
  end for

  for $a = 1 : n_p$ **do** ▷ Second part of velocity-Verlet time integration
    $\mathbf{v}_a = \mathbf{v}_a + (\Delta t\ \mathbf{f}_a)/(2m_a)$ ▷ Velocity update at end of time step
  end for

  $t = t + \Delta t$ ▷ Time incrementation
end for

where m_a and m_b are the masses of the interacting particles, δ their overlap (Sec. 7.1.3.3) and f^c_{ab} the norm of the contact force $\mathbf{f}^c_{ab}$.

The critical time steps due to the SPH discretization and the penalty contact formulation are finally combined to compute the *time step of the SPH simulation*:

$$\Delta t = \beta_t \min\left(\Delta t^{\text{SPH}}_{\text{cr}}, \Delta t^{c}_{\text{cr}}\right) \tag{7.58}$$

where β_t is now the global reduction factor of the critical time steps to integrate the equations with a given accuracy and without instabilities.

7.1.5 Validation tests

In this section, some *validation tests*, which were simulated by the USER-SMD package of LAMMPS, are presented to test this SPH solver and to illustrate some characteristics of the method. In the literature, exclusively solid validation tests were reproduced by the USER-SMD package to evaluate the zero-energy mode suppression algorithm by Ganzenmüller [112], like (1) the patch test, (2) the bending of a beam, (3) the punch test, (4) a rubber pull test, (5) the Taylor bar impact and (6) a 3D tensile test with damage. Hence, *no validation results of the USER-SMD package have been published for fluids nor for FSI problems so far* (to the best of our knowledge). In order to ultimately simulate lubricated asperity flattening, such validation tests are presented hereafter. These tests were selected based on Cerquaglia's thesis [65], in which the capabilities of the Particle Finite Element Method (PFEM) and its coupling with the classical FE method were studied to model FSI problems.

In the subsequent sections, the following validation tests are analyzed: (1) dam break, (2) dam break on a long bed, (3) dam break against a curved, rigid obstacle, (4) sloshing of a water reservoir, (5) dam break against an elastic obstacle, (6) dam break against an elastoplastic obstacle and (7) gravity-driven viscous unsteady flow.

7.1.5.1 Dam break

The *dam break* is a classical validation test for free-surface flows. As shown in Fig. 7.4, it consists of a fluid column in a rigid container, which is initially retained by a vertical wall. At the beginning of the simulation, this wall is entirely and instantaneously removed so that the fluid flows through the container due to gravity. In the literature, different fluid column and container dimensions were studied, e.g. [83, 213] with SPH or [65, 67] with PFEM. Here, the PFEM results by Cerquaglia et al. [65, 67] are used as explained before. The characteristic length scale in Fig. 7.4 is $L = 146$ mm. The fluid is water with a density $\rho = 1000\,\text{kg/m}^3$ and a dynamic viscosity $\eta = 0.001$ Pa.s. The gravitational acceleration is applied to the water, i.e. $\mathbf{g} = -9.81\mathbf{e}_z\ \text{m/s}^2$. Air flow is not modeled in this example.

The *parameters of the SPH simulation* are summarized in Tab. 7.1. The results in this section are based on these parameters and explanations about variations of parameters were obtained with respect to these values. More specifically, the problem is simulated in 2D (plane-strain state) as

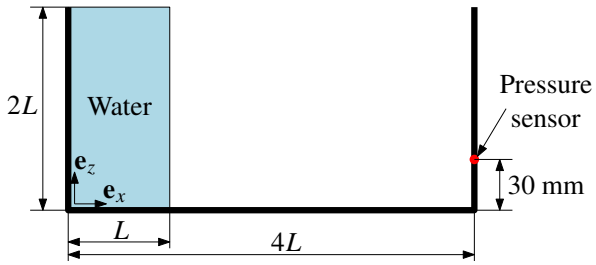

Figure 7.4: Dam break problem. Geometry of the reservoir and water column with the location of the pressure sensor.

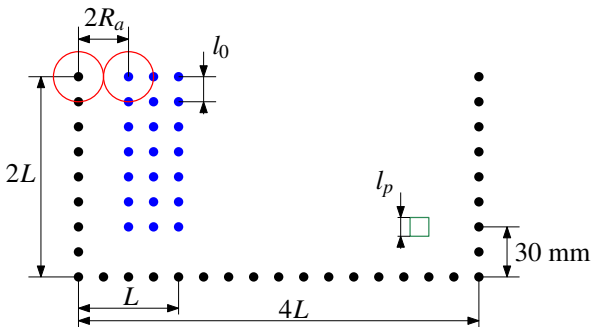

Figure 7.5: Dam break problem. Schematic SPH discretization with pressure box and contact circles.

schematized in Fig. 7.5. The container is modeled by discretizing its boundaries by a single-layer of *particles spaced* by a distance l_0 from each other (either along $\mathbf{e}_x$ or $\mathbf{e}_z$). Similarly, the water column is discretized by positioning particles at the nodes of a square lattice whose cell spacing is l_0. The first left column of water particles and the bottom row start at a distance $2R_a$ from the container walls to prevent any initial contact overlap, as illustrated by some contact circles in red in Fig. 7.5. The particle spacing was chosen to have a roughly similar fineness of the discretization than in Cerquaglia et al. [65, 67] (4500 particles, 8800 elements), while having an integer particle spacing l_0. Hence, 10440 water particles and 584 container particles were created with $l_0 = 2$ mm. The square pressure box with side length l_p and center coordinates $(4L - 2R_a - l_p/2; 30)$ (due to the repulsive boundary condition) in Fig. 7.5 will be explained later on in this section.

The *smoothing length* h varies generally in the literature between $2l_0$ and $4l_0$ (if the kernel scale factor $\zeta = 1$), e.g. [112, 189, 213, 301]. Here, $h = 2.5l_0$ was chosen since it leads to sufficiently accurate results, as shown below, while reducing the computation time and the consequences of the boundary deficiency. On the one hand, the computation time is reduced since a particle has fewer neighbors, if the smoothing length decreases. This argument is partially weakened by the CFL condition, which requires a reduction of the time step, when the smoothing length decreases. In practice, a smaller computation time was, however, observed, when the smoothing length was reduced. On the other hand, the particle deficiency near the boundary results in particle clustering (accumulation; Fig. 7.6a and more importantly, in Fig. 7.6b) in this region since the integral of the kernel approximation is not evaluated over the full support of the kernel function[21]. Since a reduction of the smoothing length decreases the influence zone of a particle, it also decreases the region, which is impaired by the boundary. The previous problem can be solved by the kernel gradient correction, which was, however, not activated in the reference case (Tab. 7.1). This is due

[21] More specifically, this observation can be explained as follows in a simplified way. If the SPH approximation (Eq. 7.9) is applied to the density field, it can be written as follows:

$$\rho_a = \sum_{b \in \mathcal{S}_a} m_b \, W(x_{ab}) \tag{7.59}$$

Parameters	Values	Units
Particle spacing l_0	2	mm
Smoothing length h	2.5 l_0	mm
Initial density ρ_0	1000	kg/m^3
Equation of state (pressure)	linear (Eq. 7.25, $K = \rho_0 c^2$)	-
Speed of sound c	10	m/s
Contact stiffness E^*	$\rho_0 c^2$	Pa
Artificial viscosity α	0.05	-
Dynamic viscosity η	0 (neglected)	Pa.s
Contact scale factor β_c	2	-
Contact radius R_a	$\beta_c\, l_0/2$	mm
Time step factor β_t	0.025	-
Gradient correction	not activated ($\mathbf{K}_a = \mathbf{I}$)	-
Side length of pressure box l_p	$3l_0$	mm
Skin distance s	h	mm
Gravitational acceleration $\mathbf{g}$	-9.81 $\mathbf{e}_z$	m/s^2

Table 7.1: Dam break problem. Parameters of the SPH model.

to the fact that it causes a different kind of local particle clustering (Fig. 7.6c), which originates at the walls of the reservoir and then travels into the bulk. Since very satisfactory results can be obtained without activating the kernel gradient correction, the precise reason for its existence was not further investigated. It is likely related to the repulsive boundary condition, since the clustering develops close to the container walls.

The *speed of sound* c was chosen to maximize the time step (due to the CFL condition), while keeping compressibility effects sufficiently small since the fluid is assumed to be incompressible. In fact, a volume reduction can be visually observed when $c = 5$ m/s, whereas no significant difference can be seen between the results for $c = 10$ m/s and $c = 20$ m/s. Further parameter choices are explained hereafter in the description of the validation results.

Fig. 7.7 shows the experimentally measured and numerically predicted positions of the *wave front as a function of time*. The best correspondence with the experimental measurements is reached by PFEM with the strong-imposition of free-slip (SFS) between the water and the container, whereas the SPH results are almost identical to those obtained by PFEM with the weak imposition of free-slip (WFS). The discrepancy between the experimental measurements and the SPH results can be explained mainly by two reasons. First, the repulsive boundary condition (Sec. 7.1.3.3) does not only act normally to the wall but also increasingly tangentially, when the contact radius

If the particle a is close to the boundary of the fluid domain and the particle distribution is uniform, this approximation provides a smaller value of ρ_a than its real value because the support domain of the kernel extends outside the fluid domain, where no particles do exist. In other words, the previous sum does not contain enough terms to correctly predict the density. In consequence, the local pressure decreases due to the low local density according to Eqs. (7.25) or (7.26). Therefore, particles in the bulk are pushed towards the fluid boundary, where clusters develop.

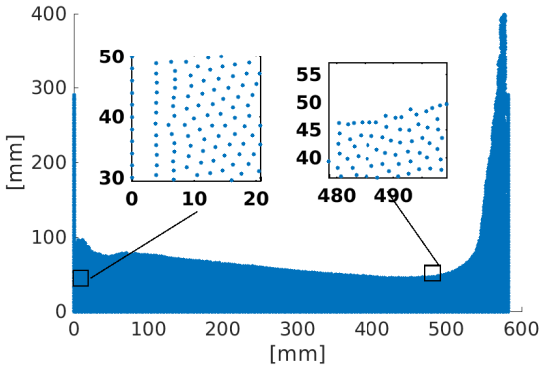

(a) $h = 2.5l_0$. Particles cluster near the free surface but the effect remains smaller than in Fig. 7.6b.

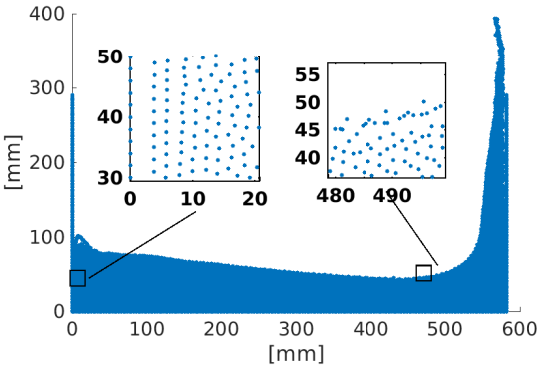

(b) $h = 4.0l_0$. Particles cluster near the free surface.

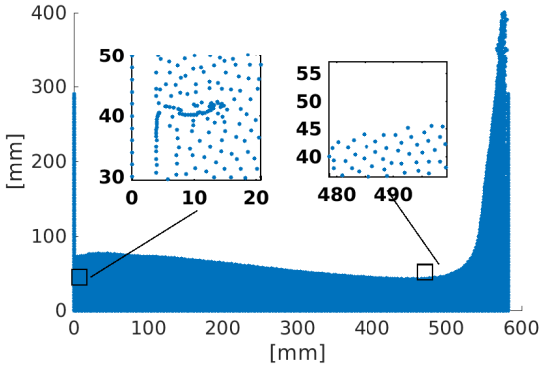

(c) $h = 2.5l_0$ and corrected kernel gradient. Particles cluster near the container wall and then move into the bulk.

Figure 7.6: Dam break problem. Different types of particle clustering in the SPH simulation at $t = 0.4$.

decreases, as illustrated in Fig. 7.8. For this reason, the *contact radius* $R_a = \beta_c l_0/2$ is increased by the contact scale factor β_c. Although the speed of the wave front slightly increases when β_c is changed from 1 to 2, no significant improvement can be observed from 2 to 3. This can possibly be explained by the required elimination of water particles to prevent any initial contact overlap with the container, when the contact radius R_a is increased, due to the discretization in Fig. 7.5. Hence, the force that pushes the wave front becomes smaller since less water particles, i.e. less mass, are included in the model. This problem can be solved by further reducing the particle spacing l_0 or by creating a smooth repulsive boundary, e.g. a repulsive line. Secondly, the *artificial viscosity* in the computation could excessively slow down the wave front. More precisely, the artificial viscosity is a requirement in the SPH computation to obtain a stable solution. When it is reduced to $\alpha = 0.0125$, strong numerical oscillations appear. A similar behavior was observed by Marrone [213] when $\alpha < 0.01$. This value can possibly also be reached in our computations, if the time

step is even further decreased. The reduction of the artificial viscosity α from 0.05 to 0.025 (at constant time step) accelerates, however, only very slightly the wave front. Hence, an additional parameter optimization with an additional computational cost and with further smoothing of the wall contact, as mentioned previously, could likely remove the small gap between the curves in Fig. 7.7.

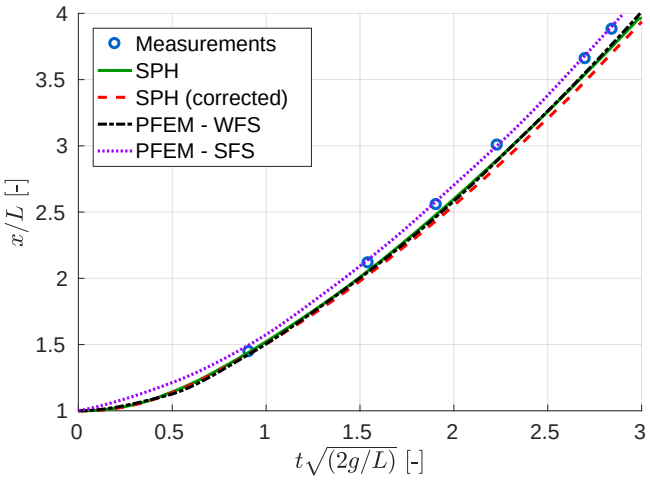

Figure 7.7: Dam break problem. Time evolution of the wave front by experimental measurements [141], by SPH, by SPH with the kernel gradient correction, by PFEM with a weak imposition of free-slip (WFS) [67] and by PFEM with a strong imposition of the free-slip (SFS) [67]. The SPH (without correction) and PFEM-WFS curves are superimposed.

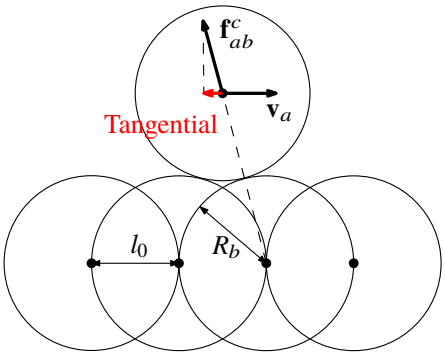

Figure 7.8: Tangential component of the contact force $\mathbf{f}^c_{ab}$ in the opposite direction to the speed $\mathbf{v}_a$. The variables l_0 and R_b denote the particle spacing and the contact radius (R_b, since R_a of particle b), respectively.

With regard to the *viscosity*, it can be added that the computation remains unstable for a small artificial viscosity, i.e. $\alpha = 0.0125$, even if the physical viscosity $\eta = 0.001$ Pa.s is added to the computation. Simulation results actually showed that the physical viscosity is so small that it does not influence the results, which is why it was neglected in the reference case (Tab. 7.1).

Besides comparing the position of the wave front, the SPH results can also be validated by *comparing the shape of the flowing water*, which is either obtained by PFEM with the strong imposition of free-slip (SFS) or by SPH in Fig. 7.9. The results are very similar until $t = 0.6$ s, except for the small water fountain near the left wall of the container in Fig. 7.9b and the slowdown near the bottom wall of the container. This slowdown can be explained by the tangential force due to the non-smooth wall contact, as explained previously, although the classical contact radius was already slightly increased ($\beta_c = 2$). The small water fountain could also be explained by the relatively rough wall contact or by a boundary deficiency effect since the kernel gradient correction mostly reduces this fountain in Fig. 7.10b. Real differences between PFEM and SPH results become visible when the wave closes at $t = 0.8$ s (Figs. 7.9g and 7.9h). These differences can also be reduced by the kernel gradient correction, as shown in Figs. 7.10c and 7.10d. At the end of the computation, i.e. at $t = 1$ s, neither SPH (Fig. 7.9j) nor corrected SPH (Fig. 7.10f) really correspond to the PFEM solution, which seems incorrect (Fig. 7.9i).

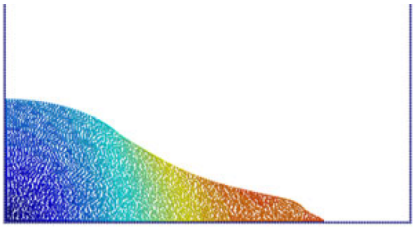

(a) $t = 0.2$ s, $t\sqrt{(2g/L)} = 2.32$, PFEM-SFS.

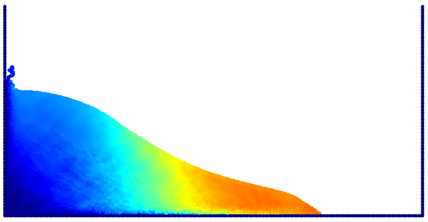

(b) $t = 0.2$ s, $t\sqrt{(2g/L)} = 2.32$, SPH.

(c) $t = 0.4$ s, $t\sqrt{(2g/L)} = 4.64$, PFEM-SFS.

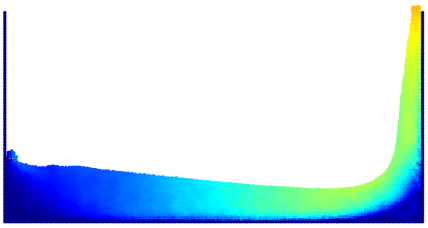

(d) $t = 0.4$ s, $t\sqrt{(2g/L)} = 4.64$, SPH.

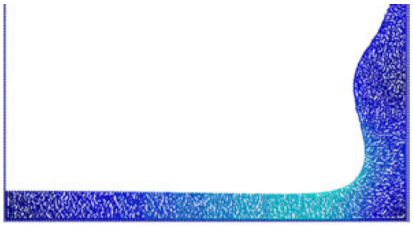

(e) $t = 0.6$ s, $t\sqrt{(2g/L)} = 6.96$, PFEM-SFS.

(f) $t = 0.6$ s, $t\sqrt{(2g/L)} = 6.96$, SPH.

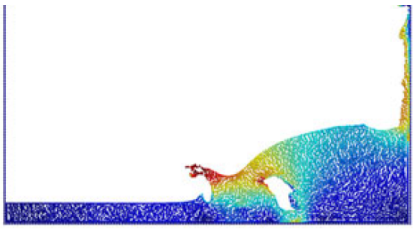

(g) $t = 0.8$ s, $t\sqrt{(2g/L)} = 9.27$, PFEM-SFS.

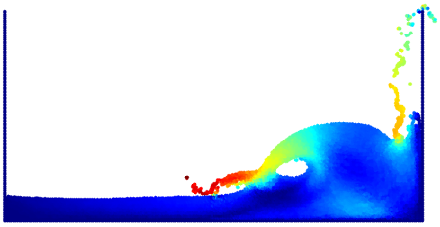

(h) $t = 0.8$ s, $t\sqrt{(2g/L)} = 9.27$, SPH.

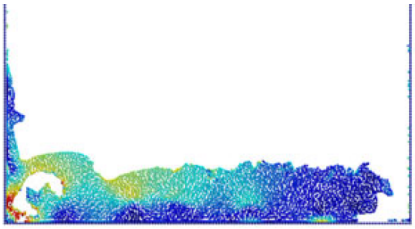

(i) $t = 1$ s, $t\sqrt{(2g/L)} = 11.6$, PFEM-SFS.

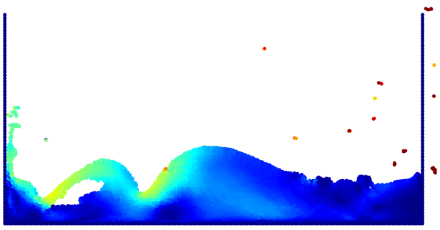

(j) $t = 1$ s, $t\sqrt{(2g/L)} = 11.6$, SPH.

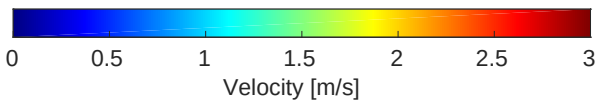

Figure 7.9: Dam break problem. Comparison of the free-surface flow over time by PFEM and SPH (**without** kernel gradient correction). The PFEM results are those by Cerquaglia et al. [65, 67], which were obtained with the strong imposition of free-slip (SFS).

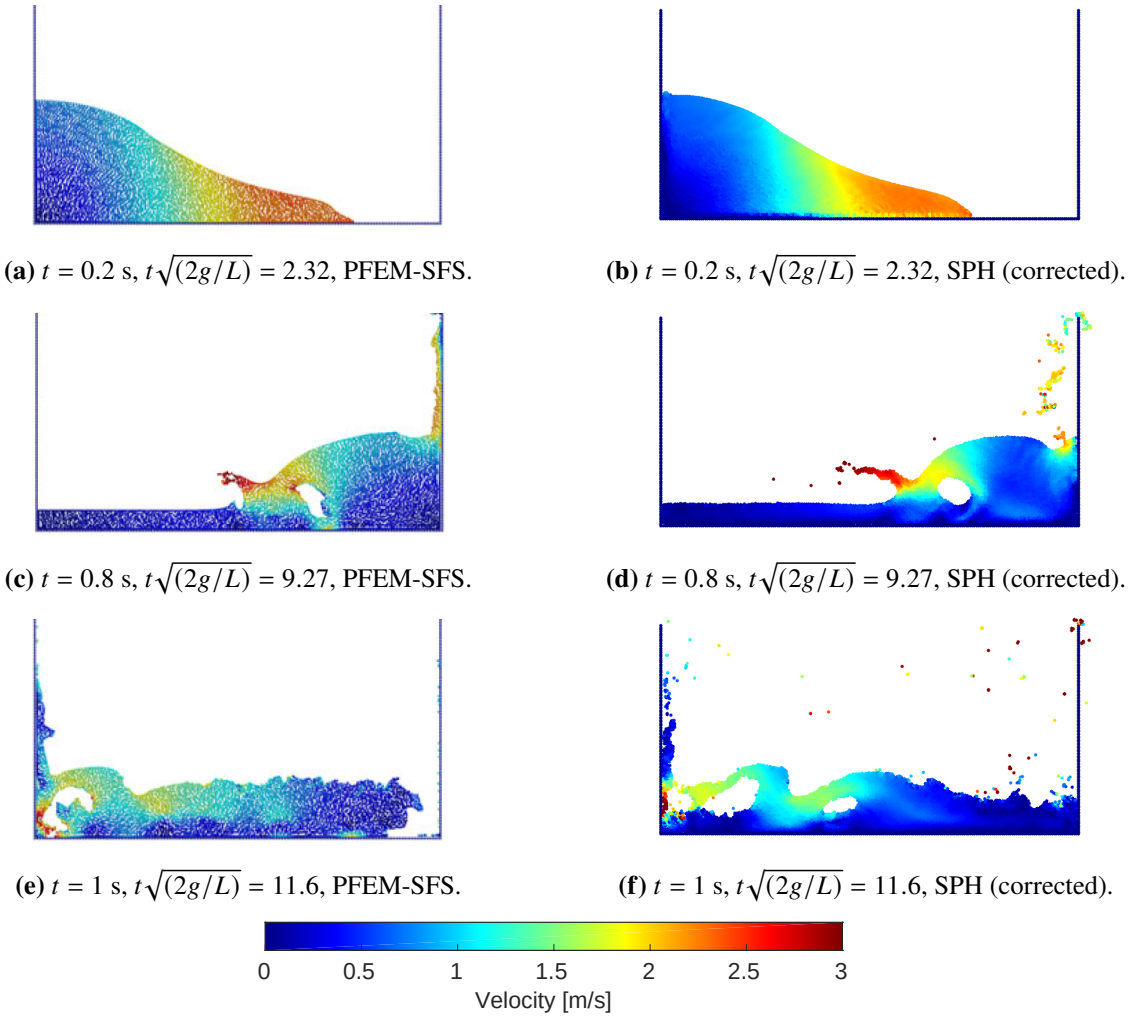

(a) $t = 0.2$ s, $t\sqrt{(2g/L)} = 2.32$, PFEM-SFS.

(b) $t = 0.2$ s, $t\sqrt{(2g/L)} = 2.32$, SPH (corrected).

(c) $t = 0.8$ s, $t\sqrt{(2g/L)} = 9.27$, PFEM-SFS.

(d) $t = 0.8$ s, $t\sqrt{(2g/L)} = 9.27$, SPH (corrected).

(e) $t = 1$ s, $t\sqrt{(2g/L)} = 11.6$, PFEM-SFS.

(f) $t = 1$ s, $t\sqrt{(2g/L)} = 11.6$, SPH (corrected).

Figure 7.10: Dam break problem. Comparison of the free-surface flow over time by PFEM and SPH (**with** kernel gradient correction). The PFEM results are those by Cerquaglia et al. [65, 67], which were obtained with the strong imposition of free-slip (SFS).

Aside from the wave front and flow field validation, the *pressure at the sensor* in Fig. 7.4 can be compared for the different methods. Due to the repulsive boundary condition in the SPH model, the pressure at this position cannot be directly computed. Therefore, a square box with the side length l_p was introduced as illustrated in Fig. 7.5. The pressure at the sensor is then approximated as the average pressure of the particles in this box at a given moment in time. The side length l_p was set equal to $3l_0$ in order to not be too strongly influenced by particles entering and leaving the box, while being sufficiently small to capture only the local pressure variation. Fig. 7.11a shows the pressure fluctuations, if the resulting pressure is plotted for each time step. Their amplitude is smaller than that computed by PFEM with the weak imposition of free-slip (WFS) but greater than that computed by PFEM with the strong imposition of free-slip (SFS) [65, 67]. To allow the comparison of the PFEM and SPH results, the SPH results were averaged over the previous 0.005 s of an average data point. Fig. 7.11b shows that the general trend is similar but the peak pressure is smaller for SPH than PFEM. The initial negative pressure of the SPH results in Fig. 7.11 is due to two upwards splashing particles, which are separating. Even the kernel gradient correction was unable to correctly capture the impact pressure, probably due to the SPH pressure computation in a box, although the second peak is better predicted. An improved pressure computation seems to require a different boundary condition, which includes the boundary particles in the particle sum (Sec. 7.1.1.4), so that the pressure can be directly measured at a fixed particle of the boundary.

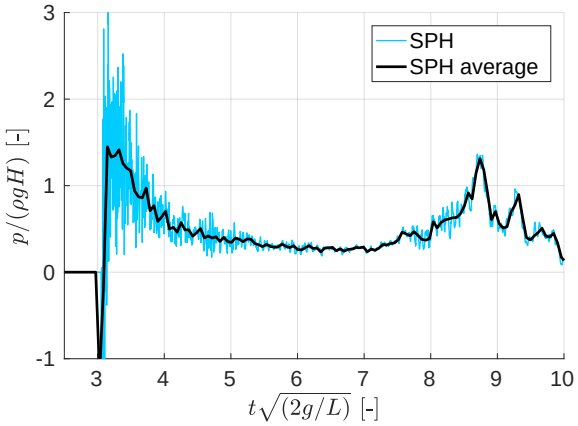

(a) Pressure over time at all time steps or averaged.

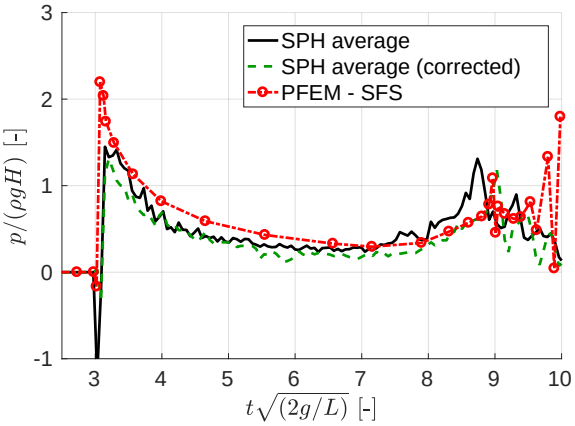

(b) Validation based on PFEM results, which are interpolated in this figure for better readability.

Figure 7.11: Dam break problem. Comparison of the non-dimensional pressure over time obtained by SPH, corrected SPH (kernel gradient correction) or PFEM. The average SPH values were computed over the previous 0.005 s. The PFEM results are those by Cerquaglia et al. [65, 67], which were obtained with the strong imposition of free-slip (SFS).

Finally, one may wonder what influence the kernel gradient correction has on the pressure field. Hence, Fig. 7.12 shows that the kernel gradient correction seems to slightly smooth the pressure field, although pressure fluctuations still exist, especially, near the boundary. This observation suggests again the necessity of a smoother boundary condition and a zero-energy

mode suppression algorithm to improve the results. The pressure fluctuations could be reduced by increasing the artificial viscosity, which would, however, be detrimental to the accuracy of the flow. Therefore, a diffusive solution like δ-SPH (Sec. 7.1.1.2) seems to be a better solution to this problem.

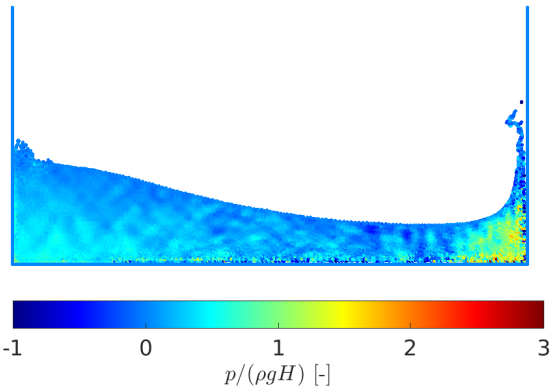

(a) SPH without kernel gradient correction. Water elevation visible near the left container wall. Stronger pressure fluctuations in the domain than by corrected SPH.

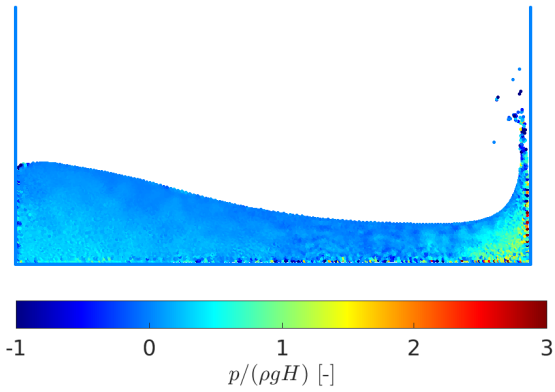

(b) SPH with kernel gradient correction. Strong pressure fluctuations only visible near the boundary.

Figure 7.12: Dam break problem. Non-dimensional pressure field obtained by the SPH computation at $t = 0.3$ s ($t\sqrt{(2g/L)} = 3.48$). The limits of the color bars were determined by the limiting values in Fig. 7.12a. The pressure fluctuations might be harder to see in the printed version of this document than in its digital version.

In conclusion, SPH is able to solve the dam break problem relatively satisfactorily in about 10 minutes of computation time without particular execution time optimization besides the domain decomposition with dynamic load balancing[22]. Differences between SPH and PFEM results seem mainly to be due to (1) the repulsive boundary condition, which should be smoother and allow a better evaluation of the pressure at the sensor, and (2) zero-energy modes, which are seemingly slightly reduced by the kernel gradient correction. This correction creates, however, particle clusters near the repulsive boundary, possibly because of this particular boundary formulation. The previous problems can probably be solved by introducing a boundary condition that includes water and boundary particles in the SPH sum, e.g. Adami et al. [1], and by Marrone et al.'s δ-SPH [213, 214]. Overall, the results are, however, relatively satisfactory considering the complexity of the problem at hand.

[22]The computations were run on 6 cores of a virtual machine on a 4-core physical machine with hyper-threading (8 virtual cores). Dynamic load balancing is performed every 1000 steps. This value was not optimized, nor the skin distance in Tab. 7.1.

7.1.5.2 Dam break on a long bed

The *dam break on a long bed* is similar to the previous dam break problem but the bed is much longer so that extremely large deformations without a returning wave have to be modeled. A fluid column is initially retained by two vertical walls, as shown in Fig. 7.13, which are entirely and instantaneously removed at the beginning of the simulation so that the water flows due to gravity. The density of water, its viscosity and the gravitational acceleration are unchanged with respect to the previous validation test, i.e. $\rho = 1000$ kg/m^3, $\eta = 0.001$ Pa.s and $\mathbf{g} = -9.81\mathbf{e}_z$ m/s^2. The SPH parameters are identical to those of the previous example in Tab. 7.1 except for the initial particle spacing l_0. In fact, the spacing is reduced to $l_0 = 1$ mm (6384 water and 1371 container particles) since the characteristic length scale L in Fig. 7.13 is decreased to 57.15 mm (with respect to the previous validation case). The computation time is equal to about 5 minutes under the same conditions as in the previous validation case.

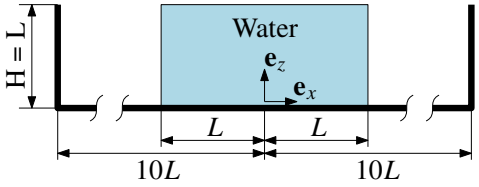

Figure 7.13: Geometry of the dam break problem on a long bed ($L = 57.15$ mm).

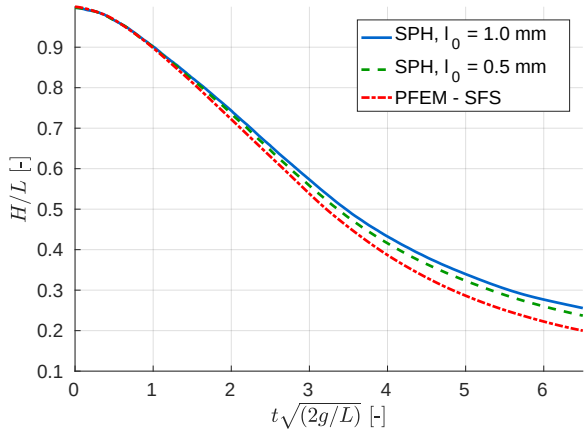

Figure 7.14: Dam break problem on a long bed. Time evolution of the water column height, by SPH and by PFEM with a strong imposition of the free-slip (SFS) [67].

Fig. 7.14 shows the time evolution of the water height obtained by SPH and PFEM. It can be seen that the height decreases more slowly in the reference SPH computation ($l_0 = 1$ mm) than in the PFEM computation. To understand this difference, a sensitivity analysis was performed by studying the influence of the division or multiplication of all parameters in Tab. 7.1 by the factor 2. The most significant change towards the PFEM solution, which is not necessarily the exact solution of the problem, is obtained by the reduction of the particle spacing, i.e. $l_0 = 0.5$ mm, as shown in Fig. 7.14. Reducing the artificial viscosity to $\alpha = 0.025$, which requires decreasing the time step ($\beta_t = 0.0125$), or activating the kernel gradient correction do not markedly decrease the evolution of the water column height.

7.1.5.3 Dam break against a curved obstacle

Cerquaglia et al. [65, 67] also analyzed the *dam break against a curved obstacle*. This scenario is essentially identical to the classical dam break problem in Sec. 7.1.5.1 except for the curved and rigid obstacle as shown in Fig. 7.15 (L = 146 mm, l = 24 mm). Hence, the SPH simulation with the same parameters as in Sec. 7.1.5.1 yields a relatively good agreement with the PFEM results in under 5 minutes of computation time as shown in Fig. 7.16. The PFEM results with the no-slip boundary condition correspond best to the SPH results, probably, because of the relatively rough boundary in SPH. In fact, we chose to pixelate the arc, i.e. to select the particles on a square lattice that are closest to the arc, which is the standard way of creating spatial discretizations in LAMMPS, instead of positioning those particles precisely on the arc.

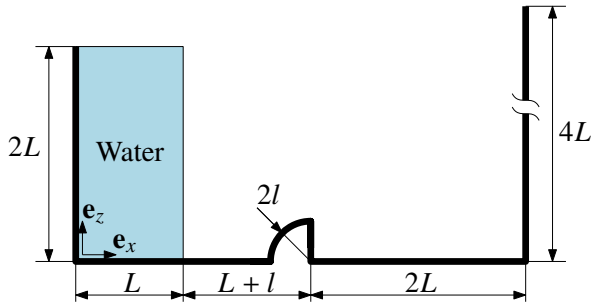

Figure 7.15: Geometry of the dam break against a curved obstacle.

7.1.5.4 Water sloshing in an oscillating reservoir

While the container was fixed in the previous validation test, *water sloshing in an oscillating reservoir* is analyzed in this section based on test 10 of SPHERIC (SPH rEsearch and engineeRing International Community) [41, 92, 296, 297]. It consists of a rectangular tank with the dimensions a = 900 mm and b = 520 mm that is filled with water up to a height h_w = 93 mm, as illustrated in Fig. 7.17. The water has a density ρ = 998 kg/m^3 and a dynamic viscosity $\eta = 8.94 \cdot 10^{-4}$ Pa.s, while the gravitational acceleration is still $\mathbf{g} = -9.81\mathbf{e}_z$ m/s^2. Water flow is created by periodic oscillations of the tank between about $\Phi = -4°$ and 4°. The measured time-evolution of the angle can be found online in the corresponding data set to the previous references, as well as videos of the water flow and the pressure measurements at the sensor location, which is indicated in Fig. 7.17.

Concerning the SPH computations, the same parameters as in Tab. 7.1 were used, except for l_0 = 4 mm (4862 water and 706 container particles) and ρ_0 = 998 kg/m^3. Figs. 7.18 and 7.19 show the respective pressure and flow field comparisons between the experimental measurements and the SPH results. The pressure at the sensor location is again approximated by the average pressure of the particles in the pressure box near the sensor. In contrast to the dam break problem (Sec. 7.1.5.1), the pressure box moves with the container and the numerical pressure prediction in Fig. 7.18 is not time-averaged.

Overall, the predictions are relatively accurate and similar conclusions than in previous examples

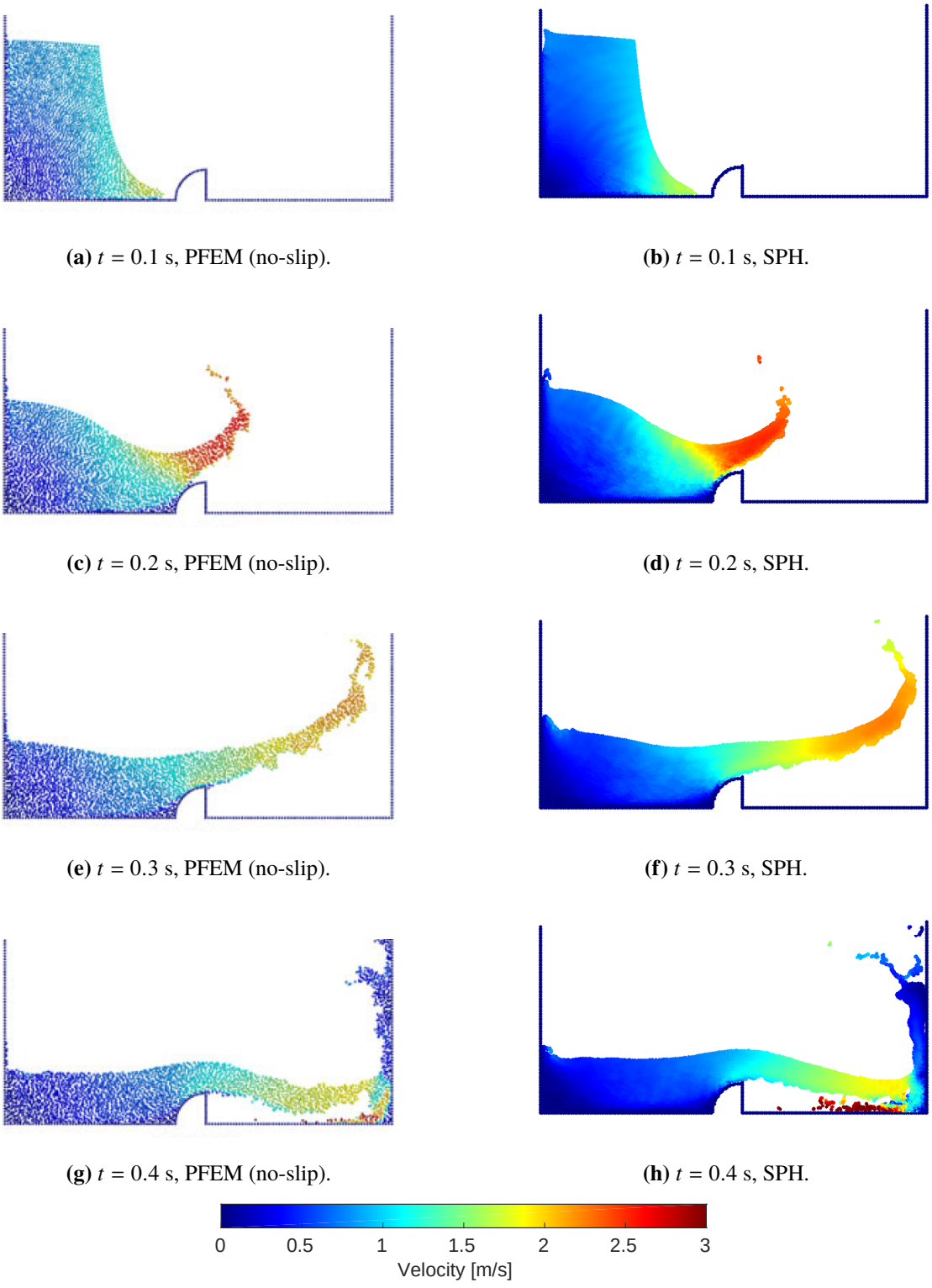

(a) $t = 0.1$ s, PFEM (no-slip).

(b) $t = 0.1$ s, SPH.

(c) $t = 0.2$ s, PFEM (no-slip).

(d) $t = 0.2$ s, SPH.

(e) $t = 0.3$ s, PFEM (no-slip).

(f) $t = 0.3$ s, SPH.

(g) $t = 0.4$ s, PFEM (no-slip).

(h) $t = 0.4$ s, SPH.

Figure 7.16: Dam break against a curved obstacle. Comparison of the free-surface flow over time by PFEM and SPH. The PFEM results are those of Cerquaglia et al. [65, 67], which were obtained with a no-slip boundary condition.

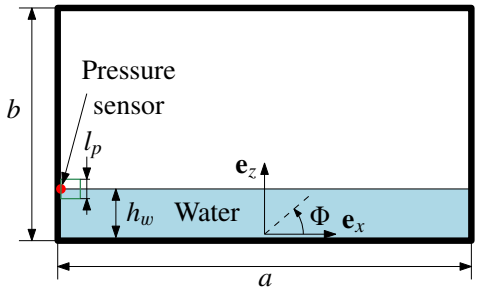

Figure 7.17: Geometry of the water sloshing problem in an oscillating reservoir. The pressure box near the pressure sensor is used to compute the local pressure by SPH. The initial center coordinates of the box are $(-a/2+2R_a+l_p/2; h_w)$ due to the repulsive boundary condition. Its center rotates with the reservoir.

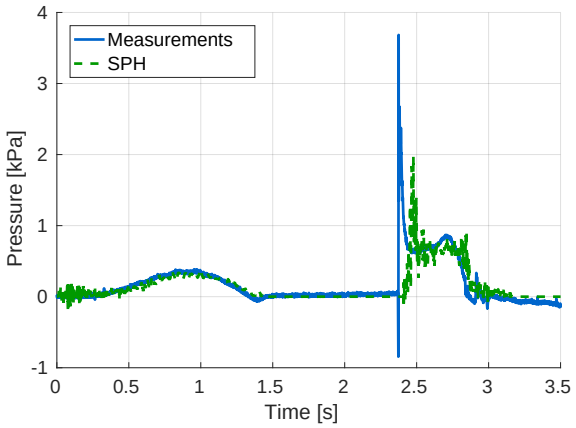

Figure 7.18: Water sloshing in an oscillating reservoir. Time evolution of the pressure at the location of the sensor, either measured by the pressure sensor or predicted by SPH.

apply. The numerical time-evolution of the pressure lags behind the experimental one and its amplitude is smaller than the latter. These shortcomings should be reconsidered after the implementation of a better adapted boundary condition to measure the pressure at the specific position of the container wall, like Adami et al. [1]. Furthermore, the pressure prediction and the flow field can be improved by increasing the spatial discretization and by slightly reducing the artificial viscosity. To illustrate this conclusion, Fig. 7.19 also shows the predicted water flow with $l_0 = 2$ mm (20070 water and 1416 container particles), $\alpha = 0.025$ and $\beta_t = 0.0125$. In general, the overlapping of the measurements and the prediction increases in Fig. 7.19 with these parameters. In particular, the wave breaks in Fig. 7.19h, which is not the case in Fig. 7.19g for the coarser discretization. One should notice that wave breaking, however, also occurs at that time with the coarser discretization, if the kernel gradient correction is activated, again with particle clumping at the container walls, though. The computation time of the coarse discretization (Tab. 7.1 and $l_0 = 4$ mm) still amounts to about 10 min, while the finer discretization takes about 2 h under the same conditions as in Sec. 7.1.5.1.

7.1.5.5 Dam break against an elastic obstacle

In this section, *fluid-structure interaction is for the first time modeled by the USER-SMD package of LAMMPS to analyze the dam break against an elastic obstacle*. This problem was first suggested by Walhorn et al. [351]. It consists of the classical dam break problem (Sec. 7.1.5.1, $L = 146$ mm, $H = 365$ mm), still in the 2D plane-strain state, with a solid linear elastic obstacle (Young's modulus $E = 1$ MPa, Poisson's ratio $\nu = 0$, density $\rho_s = 2500$ kg/m^3) of width $w = 12$ mm at the center of the container as illustrated in Fig. 7.20. Due to the gravitational acceleration

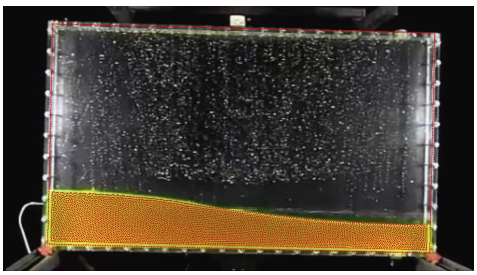

(a) $t = 1.0$ s, $l_0 = 4$ mm.

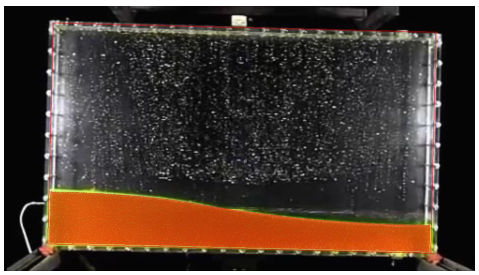

(b) $t = 1.0$ s, $l_0 = 2$ mm.

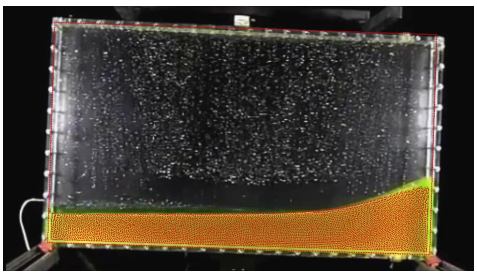

(c) $t = 1.6$ s, $l_0 = 4$ mm.

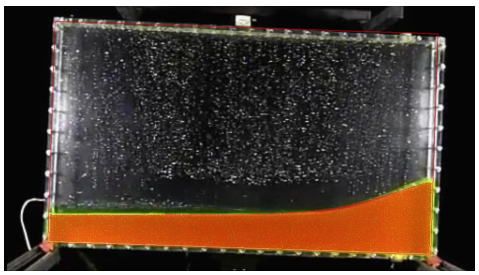

(d) $t = 1.6$ s, $l_0 = 2$ mm.

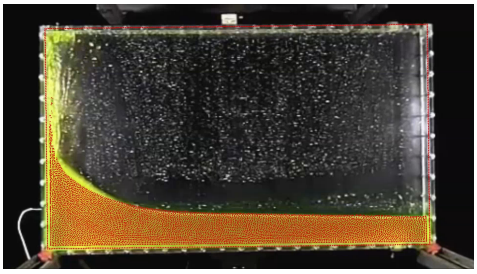

(e) $t = 2.5$ s, $l_0 = 4$ mm.

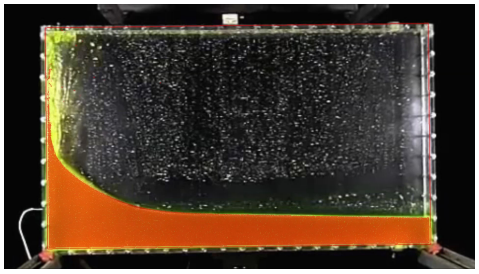

(f) $t = 2.5$ s, $l_0 = 2$ mm.

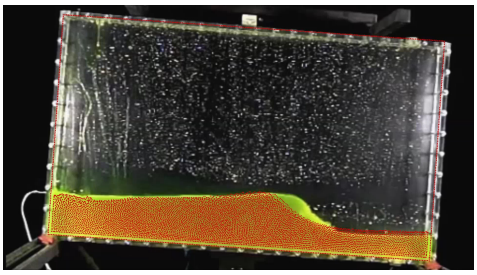

(g) $t = 3.0$ s, $l_0 = 4$ mm.

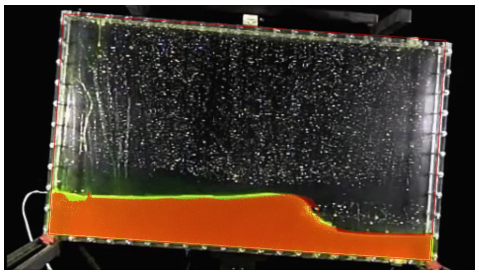

(h) $t = 3.0$ s, $l_0 = 2$ mm.

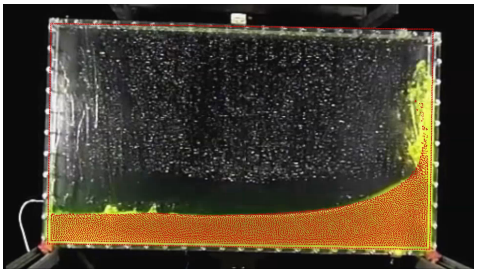

(i) $t = 3.3$ s, $l_0 = 4$ mm.

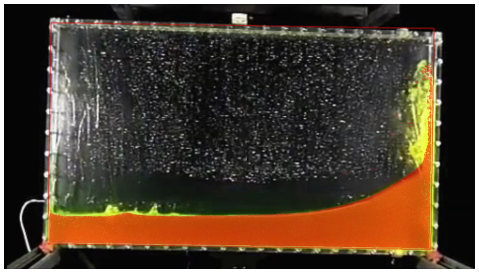

(j) $t = 3.3$ s, $l_0 = 2$ mm.

Figure 7.19: Water sloshing in an oscillating reservoir. Comparison of the recorded experimental water flow in yellow-green with the overlaid numerical solution in red for the reference discretization ($l_0 = 4$ mm, i.e. 4862 water particles, $\alpha = 0.05$) and a finer discretization with reduced artificial viscosity ($l_0 = 2$ mm, i.e. 20070 water particles, $\alpha = 0.025$). This latter parameter set required a further reduction of the time step to be stable, i.e. $\beta_t = 0.0125$.

$\mathbf{g} = -9.81\mathbf{e}_z$ m/s^2, the water (density $\rho_w = 1000$ kg/m^3, dynamic viscosity $\eta = 0.001$ Pa.s) hits the obstacle, which is deformed.

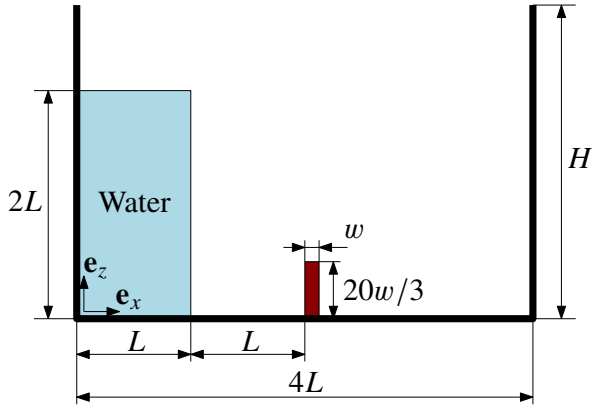

Figure 7.20: Geometry of the dam break against an elastic obstacle.

The SPH parameters are essentially identical to those of the classical dam break problem (Tab. 7.1). All parameters are summarized in Tab. 7.2. The water is simulated by ESPH (10440 particles), while the obstacle is modeled by TLSPH (7×41 particles), for which the kernel gradient correction is activated by default in the USER-SMD package. The time step is still computed via the numerical speed of sound of water since the Young's modulus of the obstacle is sufficiently small.

The results of the SPH computation, which are again obtained in about 10 minutes of computation time (same conditions as in Sec. 7.1.5.1), can be compared to results of the literature. Hence, Fig. 7.21 shows the comparison between the PFEM/FEM results by Cerquaglia et al. [65, 66] and the SPH results. They modeled the problem by coupling their PFEM solver with the Metafor FE solver (Sec. 6.2.2.1), which computes the deformation of the obstacle. From a kinematic point of view, the flows in Fig. 7.21 are very similar. The pressure field of the SPH results is, however, strongly dominated by zero-energy modes.

A more quantitative validation is possible by comparing the time evolution of the horizontal displacement of the upper-left corner of the obstacle for different numerical models, as shown in Fig. 7.22. These models are the following: (1) space-time FEM by Walhorn et al. [351], who included air in the remaining domain unlike the other models, (2) SPH with artificial repulsive forces to suppress the tensile instability (Sec. 7.1.1.3) by Rafiee and Thiagarajan [268], (3) PFEM by Marti et al. [216], which was not represented in Fig. 7.22 for readability and because it is quite different from the other curves like the SPH curve by Rafiee and Thiagarajan, (4) PFEM by Idelsohn et al. [152] and PFEM/FEM by Cerquaglia et al. [66, 65]. In comparison to the SPH solution by Rafiee and Thiagarajan, the new SPH solution seems to be far more consistent with other solutions, although differences exist between all of them.

These variations can at least partially be explained by the great sensitivity of the solution to the modeling conditions. More precisely, Fig. 7.23 shows that the SPH solutions can even be quite

Parameters	Values	Units
Water column width L	146	mm
Container height H	365	mm
Obstacle width w	12	mm
Particle spacing l_0	2	mm
Smoothing length h	2.5 l_0	mm
Initial density (water) $\rho_{w,0}$	1000	kg/m^3
Equation of state (water)	linear (Eq. 7.25, $K = \rho_{w,0}c^2$)	-
Speed of sound (water) c	10	m/s
Initial density (solid) $\rho_{s,0}$	2500	kg/m^3
Equation of state (solid)	linear elasticity	-
Young's modulus (solid) E	1	MPa
Poisson's ratio (solid) ν	0	-
Contact stiffness E^*	$\rho_{w,0}c^2$	Pa
Artificial viscosity α	0.05	-
Dynamic viscosity (water) η	0 (neglected)	Pa.s
Hourglass parameter (solid) ξ	10	-
Contact scale factor β_c	2	-
Contact radius R_a	$\beta_c\, l_0/2$	mm
Time step factor β_t	0.025	-
Gradient correction (water)	not activated ($\mathbf{K}_a = \mathbf{I}$)	-
Gradient correction (solid)	activated	-
Skin distance s	h	mm
Gravitational acceleration $\mathbf{g}$	-9.81 $\mathbf{e}_z$	m/s^2

Table 7.2: Dam break against an elastic obstacle. Parameters of the SPH model.

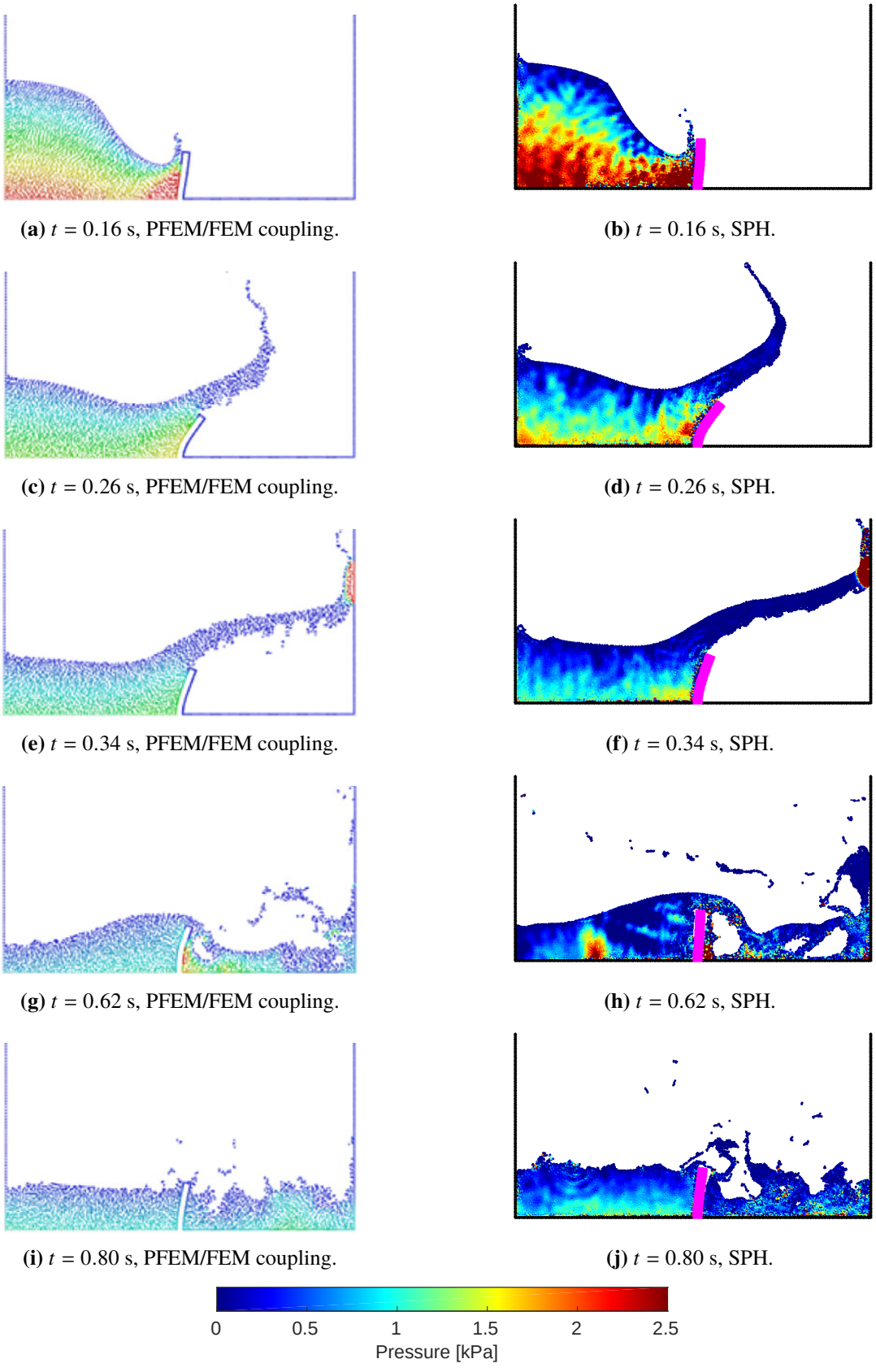

(a) $t = 0.16$ s, PFEM/FEM coupling.

(b) $t = 0.16$ s, SPH.

(c) $t = 0.26$ s, PFEM/FEM coupling.

(d) $t = 0.26$ s, SPH.

(e) $t = 0.34$ s, PFEM/FEM coupling.

(f) $t = 0.34$ s, SPH.

(g) $t = 0.62$ s, PFEM/FEM coupling.

(h) $t = 0.62$ s, SPH.

(i) $t = 0.80$ s, PFEM/FEM coupling.

(j) $t = 0.80$ s, SPH.

Figure 7.21: Dam break against an elastic obstacle. Comparison of the results by PFEM/FEM and SPH. The PFEM/FEM results are those of Cerquaglia et al. [65, 66].

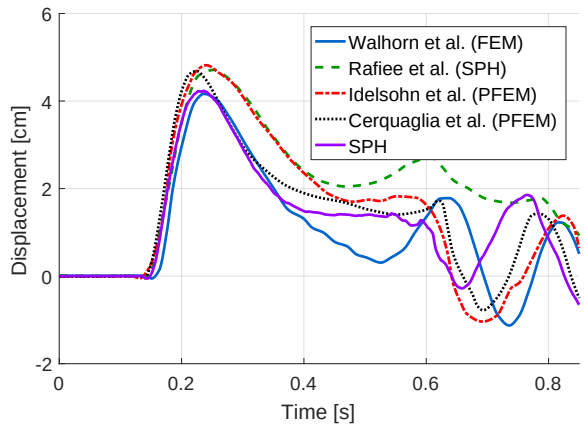

Figure 7.22: Dam break against an elastic obstacle. Time-evolution of the horizontal displacement of the upper-left corner of the obstacle according to the literature and our SPH results.

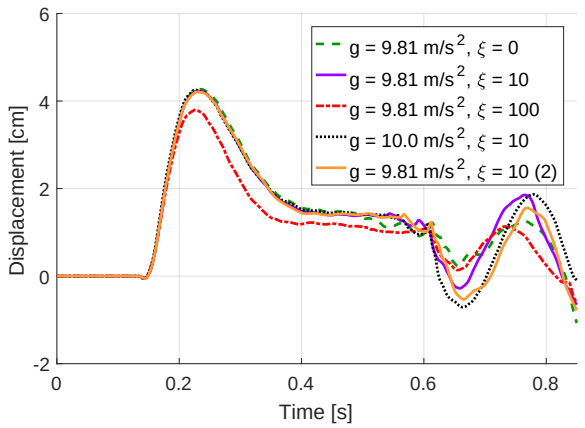

Figure 7.23: Dam break against an elastic obstacle. Influence of the hourglass parameter ξ and the gravitational acceleration g on the horizontal displacement of the upper-left corner of the obstacle.

different for identical parameters (solid line curves; the "(2)" in the legend of Fig. 7.23 indicates the second run with the values $g = 9.81$ m/s^2 and $\xi = 10$). This observation can be explained by the indeterminism of parallel computations, since the results of two serial runs with the same parameters are identical. In fact, due to the parallelization, the order of arithmetical operations, e.g. in the force summation over all neighbors, might change for successive parallel runs. As a result of finite precision computation, this order has an influence on the solution, e.g.

$$(1/10.) + (1/13.) + (1/17.) = 0.23574660633484162 \tag{7.60}$$

$$(1/17.) + (1/13.) + (1/10.) = 0.23574660633484165 \tag{7.61}$$

These differences accumulate due to the important number of time steps, so that the solution is not fully deterministic. Furthermore, it can be noticed that the gravitational acceleration is not always the same in the literature: Walhorn et al. used 10 m/s^2, while Cerquaglia et al. chose 9.81 m/s^2. The resulting difference is, however, of the same order of magnitude as variations due to parallelization as shown in Fig. 7.23. Finally, this figure illustrates that the zero-energy suppression algorithm increases the stiffness of the structure, if the corresponding parameter ξ increases. The value $\xi = 10$ seems to be adequate, since the artificial stiffness is not increased too significantly, while zero-energy modes are at least penalized to some extent. In the future, this value should be controlled more systematically by adding the computation of the work done by the forces that resist zero-energy modes to the implementation.

7.1.5.6 Dam break against an elastoplastic obstacle

The previous validation test was extended by Zhu and Scott [382] to a more complex material law by assuming that the *obstacle has an elastoplastic behavior with linear isotropic hardening*,

i.e.

$$\sigma_Y = \sigma_Y^0 + h_i \overline{\epsilon}^p \qquad \text{with} \qquad h_i = \frac{E E_p}{E - E_p} \tag{7.62}$$

where σ_Y is the yield stress, $\sigma_Y^0 = 0.05$ MPa the initial yield stress, h_i the isotropic hardening coefficient[23], $\overline{\epsilon}^p$ the effective plastic strain, $E_p = 0.02$ MPa the plastic modulus and $E = 1$ MPa the Young's modulus. All other parameters are identical to those of the previous example (Tab. 7.2).

Zhu and Scott [382] modeled the water by PFEM and the obstacle by beam elements. The width of the obstacle is, however, not geometrically included in their computation of the water flow. Cerquaglia et al. [65, 68] also predicted the water flow by PFEM but they included the width of the obstacle, whose deformation is computed by the Metafor FE solver (Sec. 6.2.2.1), in the computation of the water flow. As in the previous example, the time-evolution of the horizontal displacement of the upper-left corner of the obstacle can be compared for the different methods in Fig. 7.24. All the results show a *positive final displacement*, which is due to the non-reversible plastic deformation. Cerquaglia et al. [65, 68] explained their greater final displacement than Zhu and Scott [382] by the fact that they took into account the width of the obstacle in the computation of the water flow unlike Zhu and Scott. In our SPH computation, the final displacement is even more significant, which could be the consequence of a different water flow pattern. In fact, the almost full spring back of the obstacle in Zhu and Scott and Cerquaglia et al. seems only to be possible by the force of a strong returning wave from the right container wall.

Besides this explanation, other influences were studied to understand the differences between the results. A dependency on the discretization fineness of the obstacle was observed as illustrated in Fig. 7.25: the displacement increases when the particle spacing of the obstacle $l_{0,o}$ decreases, i.e. for 7×41, 13×81 and finally 25×161 particles. The results by Cerquaglia et al. [65, 68] are, however, almost identical when the mesh of the obstacle is refined from 4×31 to 10×64 elements. Furthermore, the hourglass control parameter ξ allows to reduce the amplitude of the displacement by increasing its stiffness as shown in Fig. 7.25. This operation distorts, however, the predictive ability of the model, if the value of this parameter becomes too significant. As in the previous section, the computation of the work done by the forces that resist zero-energy modes is required to assess the predictive ability of the model more thoroughly. Finally, one should notice that the artificial viscosity between particles of the obstacle has no influence, if $\alpha \in [0, 0.2]$; the influence of greater values was not studied since 0.05 is already sufficient to stabilize the water flow.

In conclusion, a quantitatively consistent prediction of the obstacle displacement is possible in 50 minutes (5 s of physical time in the simulation, under the same conditions as in Sec. 7.1.5.1). It is, however, unclear why a dependency on the fineness of the discretization was observed with SPH and not with PFEM/FEM by Cerquaglia et al. [65, 68].

[23] The previous expression of h_i can be obtained by combining the following equations: incremental form of Hooke's law ($d\sigma = E d\epsilon^e$), incremental definition of the plastic modulus ($d\sigma = E_p d\epsilon$), the additive decomposition of the strain increments ($d\epsilon = d\epsilon^e + d\epsilon^p$) and the monotonic tensile test hypothesis ($d\sigma_Y = d\sigma$ and $d\overline{\epsilon}^p = d\epsilon^p$) [258].

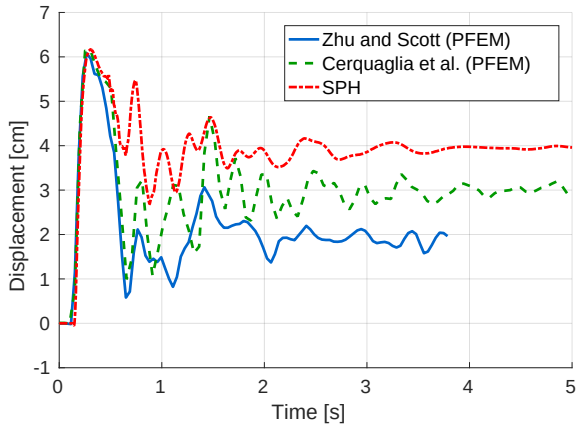

Figure 7.24: Dam break against an elastoplastic obstacle. Time-evolution of the horizontal displacement of the upper-left corner of the obstacle according to the literature and our SPH results.

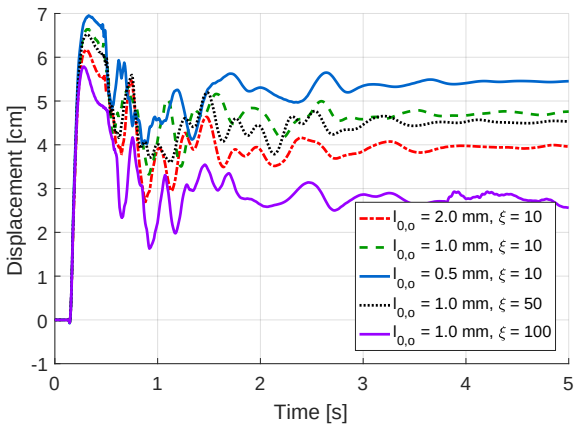

Figure 7.25: Dam break against an elastoplastic obstacle. Influence of the particle spacing of the obstacle $l_{0,o}$ and the hourglass parameter ξ on the horizontal displacement of the upper-left corner of the obstacle. All other parameters, except for the smoothing length $h_o = 2.5l_{0,o}$ and the particle mass $m_{a,o} = \rho_{s,0} l_{0,o}^2$ of the obstacle particles, are unchanged.

7.1.5.7 Gravity-driven viscous unsteady flow

In the previous examples, various components that are required in lubricated asperity flattening, like an elastoplastic material behavior and the FSI interaction, were illustrated. An additional key component in lubrication is the viscosity of the lubricant and its viscous interaction with the boundary. To briefly illustrate how this component can be integrated in future models via a no-slip boundary condition, a strategy to predict the *gravity-driven viscous unsteady flow* is described in this section. This problem consists of the 2D (plane-strain) laminar flow of an incompressible Newtonian fluid (density $\rho = 1000$ kg/m^3, dynamic viscosity $\eta = 10$ Pa.s) in an infinite channel between vertical walls due to gravity $\mathbf{g} = -9.81\mathbf{e}_z$ m/s^2 as shown in Fig. 7.26 [65]. The domain has an infinite height along $\mathbf{e}_z$ but in the computation only a sample of height $4L$ is considered, as in Cerquaglia [65], thanks to a periodic boundary condition, i.e. that particles leaving the domain from the bottom are reinjected at its top.

Instead of studying the flow in the steady state, which would take quite some time to be reached with a Lagrangian methodology like SPH, the unsteady state is rather analyzed. Therefore, Cerquaglia [65] computed a harmonic expansion approximation of the vertical velocity profile along $\mathbf{e}_x$ as a function of time t:

$$v_z(x,t) = \sum_{k=1}^{+\infty} b_k e^{-\left(\frac{k\pi}{L}\right)^2 \frac{\eta t}{\rho}} \sin\left(\frac{k\pi}{L}x\right) + \frac{\rho g}{2\eta}x(x-L) \tag{7.63}$$

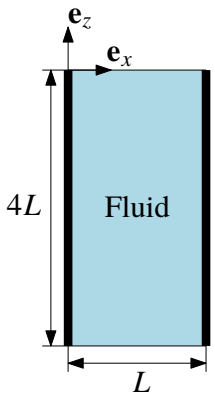

Figure 7.26: Gravity-driven viscous unsteady flow. Geometry with $L = 0.5$ m.

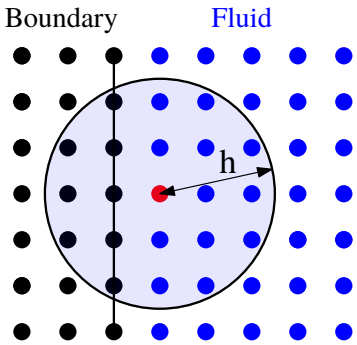

Figure 7.27: Layers of fixed boundary particles are included in the particle sum of moving particles to create a non-deficient no-slip boundary condition.

with

$$b_k = -2\left(\frac{\rho g L^2}{\eta k^3 \pi^3}\right)\left[(-1)^k - 1\right] \tag{7.64}$$

which can be time-integrated to obtain the vertical displacement:

$$u_z(x,t) = \sum_{k=1}^{+\infty} b_k \left(\frac{L}{k\pi}\right)^2 \frac{\rho}{\eta}\left(1 - e^{-\left(\frac{k\pi}{L}\right)^2 \frac{\eta t}{\rho}}\right) \sin\left(\frac{k\pi}{L}x\right) + \frac{\rho g}{2\eta} x(x-L)t \tag{7.65}$$

The SPH parameters are essentially identical to those in Tab. 7.1 for the dam break problem (Sec. 7.1.5.1) except for the initial particle spacing, which is $l_0 = 10$ mm here (11457 particles, about 4 minutes of computation time under the same conditions as in Sec. 7.1.5.1), and the dynamic viscosity η. Its value is not negligible anymore but equal to 10 Pa.s. To model the no-slip condition at the boundary for the viscous fluid, Fig. 7.27 shows that fixed boundary particles were created as in Morris et al. [241]. These particles are classical fluid particles, which are included in the particle sums and whose velocity is equal to that of the boundary, i.e. they are fixed in the current case. If a moving fluid particle approaches the boundary, the local density increases so that the local pressure increases as well. Thus, moving fluid particles are prevented from penetrating the boundary. This is, however, only possible, if no boundary deficiency artificially reduces the local pressure as explained in Sec. 7.1.5.1. Therefore, three layers of boundary particles were added to the computation as illustrated in Fig. 7.27.

Figs. 7.28a and 7.28b compare the harmonic expansion approximation and the SPH prediction of the vertical displacement and velocity for different moments in time. The agreement is relatively good but the difference between the solutions increases close to the boundary. This difference can be reduced either by increasing the fineness of the discretization or by giving the boundary particles a fictitious velocity, while still keeping their positions fixed. The precise approach is explained by Morris et al. [241] and its extension by Adami et al. [1]. It can also be mentioned that the computation becomes unstable when the velocity increases as time advances. This

observation was traced back to the inability of WCSPH to suppress transverse oscillations of particles to the flow direction [22, 294].

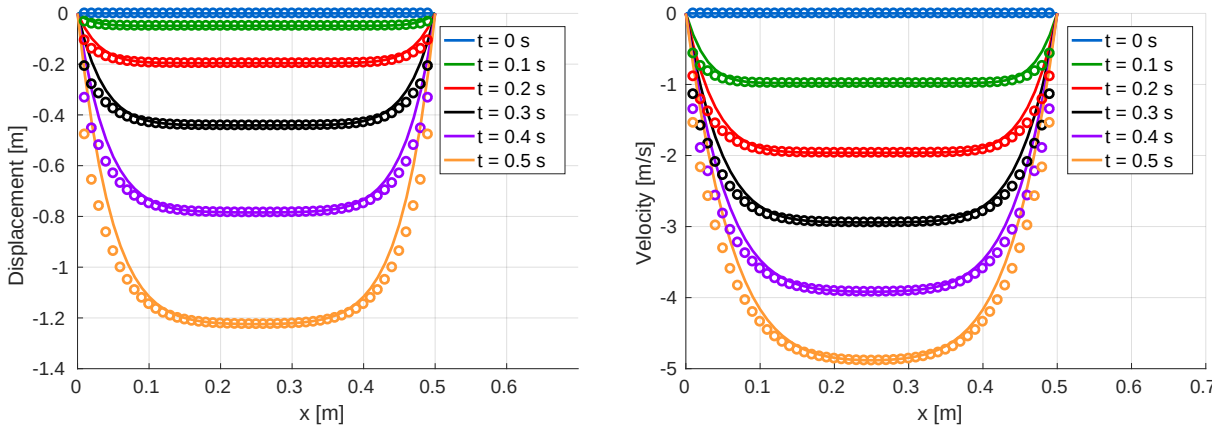

(a) Vertical displacement.

(b) Vertical velocity.

Figure 7.28: Gravity-driven viscous unsteady flow. Time evolution of the vertical displacement and vertical velocity profiles along $\mathbf{e}_x$. Analytical solution (solid lines) and SPH prediction (circles corresponding to particles).

7.2 Micro-plasto-hydrostatic lubrication

Previously, it was shown that relatively complex FSI problems, which contain the different components of micro-plasto-hydrostatic/dynamic lubrication, can be modeled by SPH. In this section, this *methodology is applied to a simplified problem of micro-plasto-hydrostatic lubrication* in order to gradually converge to a complete SPH model of MPH lubrication in cold rolling. This problem consists of a trapped fluid in a contact interface that was studied via the FE method of Shvarts and Yastrebov [291].

In the following sections, the *problem* of a trapped fluid in a contact interface is first defined with a summary of existing solutions based on the previous reference. Then, the SPH model of lubricated asperity flattening is incrementally constructed. First, the *uniaxial compression of an elastoplastic solid* is modeled by SPH. Secondly, SPH results of *dry asperity flattening* are compared to results by the FE solver Metafor. Before introducing the lubricant in the computation, its *compressive behavior* is verified. And finally, the full SPH model of *lubricated asperity flattening* is described.

7.2.1 Problem statement and existing solutions

Shvarts and Yastrebov [291] analyzed the compression of a semi-infinite deformable half-space with a periodic wavy surface against a rigid horizontal plane by an external pressure at infinity. The half-space is assumed to be either elastic or elastic J_2-perfectly plastic (Sec. H.3.2.2) and the

problem is defined in the plane-strain state. Furthermore, the free volume between the bodies is partially filled with a compressible or incompressible fluid as illustrated in Fig. 7.29. The initial gap between both bodies is provided by the following equation depending on the wavelength λ and the amplitude Δ:

$$g_0(x) = \Delta\left(1 - \cos\frac{2\pi x}{\lambda}\right) \tag{7.66}$$

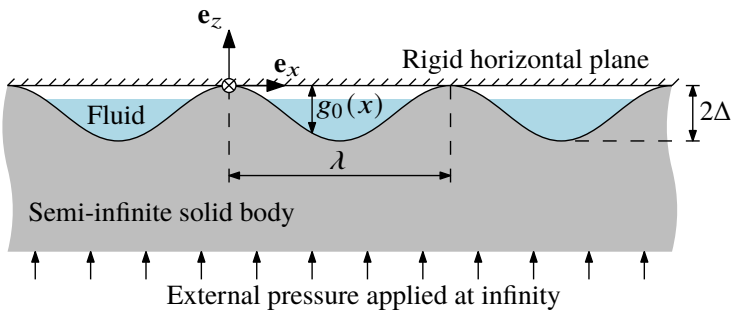

Figure 7.29: Geometry of the trapped fluid in a contact interface.

The relative contact area A between both bodies can then be computed as a function of the external pressure at infinity, i.e. the interface pressure $p_i \geq 0$, by various methods, which are briefly summarized hereafter.

7.2.1.1 Westergaard's analytical solution

Westergaard [162, 359] solved analytically the previous problem, if the deformable half-space is *elastic*, if *no fluid* is located in the free volumes and if the characteristic *slope* Δ/λ *is very small*:

$$A(p_i) = \frac{2}{\pi}\arcsin\sqrt{\frac{p_i}{p^*}} \quad \text{with} \quad p^* = \frac{\pi E\Delta}{\lambda(1-\nu^2)} \tag{7.67}$$

with the Young's modulus E and the Poisson's ratio ν. The pressure p^* is such that $A = 1$, i.e. full contact, if $p_i > p^*$.

7.2.1.2 Shvarts and Yastrebov's analytical solution

Kuznetsov [174] generalized the previous solution by including a *compressible fluid* in the valleys of the wavy surface. This solution was then extended by Shvarts and Yastrebov [291] to *partially* fluid-filled free volumes in the contact interface. While the relative contact area A could previously be written as a function of the interface pressure p_i (Eq. 7.67), i.e. $A = A(p_i)$, an analytical form of the inverse relation seems not to exist in this case. Thus, to compute the interface pressure as a function of the relative contact area, the volume V_g (per out-of-plane thickness along $\mathbf{e}_y$) of a single deformed pocket has first to be computed:

$$V_g = V_{g,0}\left\{1 - \sin^2\frac{\pi A}{2}\left[1 - \ln\left(\sin^2\frac{\pi A}{2}\right)\right]\right\} \tag{7.68}$$

with the initial pocket volume (per out-of-plane thickness) $V_{g,0} = \lambda\Delta$. If $V_{f,0}$ is the initial fluid volume (per out-of-plane thickness) in the pocket, its filling ratio is defined as $\theta = V_{f,0}/V_{g,0}$. Hence, if the fluid is not yet compressed, i.e. $V_g \geq \theta V_{g,0}$, Eq. (7.67) is still valid to compute the interface pressure. Otherwise, the interface pressure is computed as follows depending on the compressibility law of the fluid:

- Linear compressibility (Eq. 7.25):

$$p_i(A) = p^* \sin^2 \frac{\pi A}{2} + \frac{K}{\theta} \left\{ \theta - 1 + \sin^2 \frac{\pi A}{2} \left[1 - \ln \left(\sin^2 \frac{\pi A}{2} \right) \right] \right\} \tag{7.69}$$

- Non-linear compressibility (Eq. 7.26):

$$p_i(A) = p^* \sin^2 \frac{\pi A}{2} + \frac{K_0}{K_1} \left(\theta^{K_1} \left\{ 1 - \sin^2 \frac{\pi A}{2} \left[1 - \ln \left(\sin^2 \frac{\pi A}{2} \right) \right] \right\}^{-K_1} - 1 \right) \tag{7.70}$$

7.2.1.3 Shvarts and Yastrebov's FE solution

Shvarts and Yastrebov [291] finally extended the previous solutions by the FE method to take into account the *geometrical modification of the pocket* during its *elastic-perfectly plastic deformation*. In contrast to the previous methods, FEM allowed to model the escape of the fluid from the pockets, which then permeates into the solid/solid contact zone and thereby reduces the relative contact area. It is important to notice that the permeation occurs at unrealistically high pressure in their model, e.g. $p_i \approx 23000$ MPa for the combination of an elastoplastic steel with a non-linearly compressible oil [291, Fig. 13a]. Furthermore, the *mechanism of permeation* is not precisely identified in this reference. Thus, it can only be assumed to occur when the bulk modulus of the solid becomes smaller than that of the fluid. This mechanism seems not to be the one that occurs in cold rolling (Sec. 2.2.4.3), where the interface pressure is much smaller. The problem of Shvarts and Yastrebov [291], however, still remains of interest due to its simplicity and the asperity flattening with elastoplastic deformations and the compressible fluid, before considering problems that are more closely related to lubricated cold rolling, like lubricated plane strip drawing.

The FE model by Shvarts and Yastrebov is based either on the penalty method or on Lagrange multipliers to compute the forces that are applied to the nodes of the solid in the pocket by the fluid. These forces are, however, only the result of the fluid volume variation inside the pocket. Hence, the kinematics of the fluid flow, its inertia and, especially, its viscosity are not included in the model, so that it cannot describe *hydrodynamic effects*. Furthermore, *mesh distortions* limit the applicability of this method, when significant indentation and ploughing have to be modeled. In theory, it seems possible that these shortcomings can be solved by SPH. To assess this statement, SPH is used in the following sections to gradually reproduce the current problem of micro-plasto-hydrostatic lubrication. Future research is then required to test whether SPH is also capable of eliminating the previous shortcomings in practice.

7.2.2 Compression of an elastoplastic solid with contact

A first step towards the SPH simulation of lubricated asperity flattening is to determine how the *compression of an elastoplastic solid* can be modeled *with contact* (Fig. 7.30) by this method and if the model accurately solves this problem. In other words, asperity flattening is studied in this section without a specific asperity height profile and without the lubricant, which will be added in the following sections.

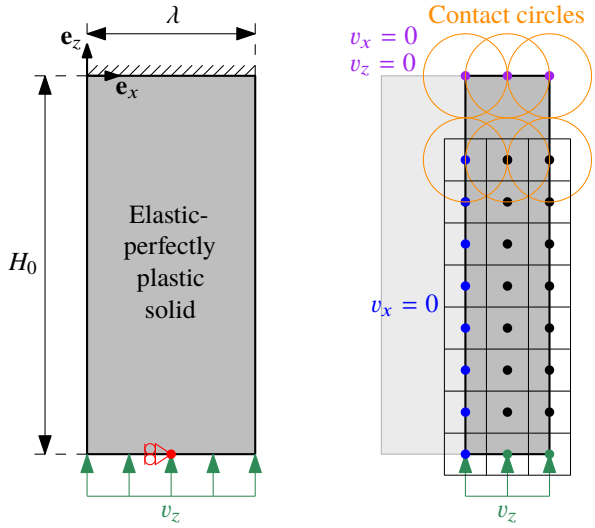

Figure 7.30: Compression of an elastoplastic solid with contact. Geometry (left) and schematic SPH discretization with symmetry condition (right). The cell around each solid particle schematizes its initial volume.

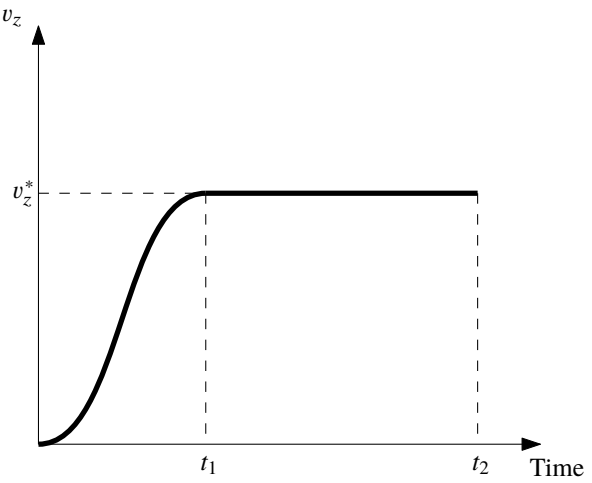

Figure 7.31: Time-evolution of the applied velocity v_z to the bottom edge of the solid.

The plane-strain compression problem is *defined* on the basis of the same *geometry* as in the FE model of Shvarts and Yastrebov [291] but without the asperity profile. As shown in Fig. 7.30, the solid thus[24] has an initial height $H_0 = 200$ μm and a width $\lambda = 100$ μm. The *material law* is also assumed to be the same as in Shvarts and Yastrebov [291], i.e. elastic-perfectly plastic with classical values of steel: Young's modulus $E = 200$ GPa, Poisson's ratio $\nu = 0.28$ and the constant yield stress $\sigma_Y = 250$ MPa. The density is not mentioned in their study, which is why it is assumed to be equal to $\rho_{s,0} = 7850$ kg/m^3 as in Sec. 5.2.1. Concerning the *boundary conditions*, the bottom edge of the solid is pushed upwards, while its horizontal displacement is not prevented (except for one point). The upward speed v_z increases gradually from 0 to v_z^* over

[24] Shvarts and Yastrebov [291] did not mention any absolute length scales in their article due to nondimensionalization, but only the relations $\Delta/H_0 = 0.005$ and $\Delta/\lambda = 0.01$. Hence, the absolute dimensions were chosen by setting the asperity amplitude Δ equal to 1 μm (Eq. 7.66 and Fig. 7.29), which is a realistic value (e.g. Sec. 2.1.2.2), and by conserving the previous relations.

time t, as illustrated in Fig. 7.31:

$$v_z = \begin{cases} \dfrac{v_z^*}{2}\left[1 - \cos\left(\dfrac{\pi t}{t_1}\right)\right] & \text{, if } 0 \leq t \leq t_1 \\ v_z^* & \text{, if } t_1 < t \leq t_2 \end{cases} \tag{7.71}$$

where the characteristic time $t_1 = 0.1\, t_2$. The gradual increase was included in the model in order to have a slow start without excessive inertial forces. This statement obviously also depends on the choice of v_z^*, which will be selected afterwards. The time t_2 is chosen such that[25] the vertical strain $\epsilon_z = \ln H/H_0$, with H being the varying height of the solid, is equal to -0.004 at $t = t_2$. This strain ensures yielding of the solid, which is pushed against the frictionless and rigid horizontal plane.

These boundary conditions were selected since they are similar to those of Shvarts and Yastrebov [291] and since an *analytical solution* to this problem exists in the literature to verify the SPH results. According to Chakrabarty [69, pp. 127-130], the relation between the vertical strain ϵ_z and the vertical stress σ_z can be written as follows:

- Elastic deformation before yielding:

$$\sigma_z = \frac{E}{1-\nu^2}\epsilon_z \tag{7.72}$$

- Elastic-perfectly plastic deformation:

$$\sigma_z = -\frac{2\sigma_Y}{\sqrt{3}}\cos\theta \tag{7.73}$$

$$\epsilon_z = -\frac{\sigma_Y}{E}\left\{\frac{2}{\sqrt{3}}(1-2\nu)\sin\left(\frac{\pi}{6}-\theta\right) + \frac{\sqrt{3}}{2}\ln\left[\cot\left(\frac{\theta}{2}\right)\tan\left(\frac{\theta_0}{2}\right)\right] + \sqrt{1-\nu+\nu^2}\right\} \tag{7.74}$$

  where θ is the deviatoric angle (or Lode angle). Its value equals $\theta_0 = \arctan\left[(1-2\nu)/\sqrt{3}\right]$ at the initial yielding and then decreases to 0.

Concerning the *SPH model*, the previous Fig. 7.30 schematizes the initial particle positions in addition to the geometry. Furthermore, Tab. 7.3 summarizes the values of the simulation parameters. Due to symmetry, only one half of the solid is included in the simulation. This half is discretized by positioning particles at the nodes of a square lattice with a particle spacing $l_0 = 2.5\ \mu$m along the principal axes. The same particle spacing is used for the rigid horizontal plane that is in contact with the solid via the penalty formulation of Sec. 7.1.3.3. It was ensured that the distance between particles of the rigid horizontal plane and the solid is sufficient to have

[25] More precisely, if $t_1 = \gamma t_2$ ($\gamma = 0.1$, here), the vertical displacement of the bottom edge at $t = t_1$ is $u_{z,1} = v_z^* t_1/2$ by integrating Eq. (7.71), and the final displacement is $u_{z,2} = u_{z,1} + v_z^*(t_2 - t_1)$ due to the constant upward speed between t_1 and t_2. Hence, $t_2 = 2u_{z,2}/[v_z^*(2-\gamma)]$ where the final displacement $u_{z,2}$ is known by the imposed final vertical strain.

no initial overlap depending on the contact radius $R_a = \beta_c l_0/2$, where β_c is again the scale factor to slightly smooth the contact profile. Alternatively, the particles of the horizontal plane could be translated upwards and particles could be added to the solid so that the contact interface is located precisely at the frontier of the solid, instead of inside the solid as shown in Fig. 7.30. Since the importance of this geometrical approximation decreases with the particle spacing, its impact on the results decreases with the fineness of the discretization, which will have to be relatively fine in the following sections. The solid is modeled by TLSPH with the kernel gradient correction and zero-energy mode control. Moreover, the boundary conditions are applied as shown in Fig. 7.30 by imposing some velocities to take into account the symmetry condition, the imposed displacement of the bottom edge and the fixation of the rigid horizontal plane. To allow the comparison of the SPH results with the analytical solution, the vertical stress σ_z is computed by taking the sum F_b of the vertical forces applied to the particles of the bottom edge in Fig. 7.30 and dividing it by the width of the solid in the SPH simulation, i.e. $\lambda/2$. A computation with the parameters of Tab. 7.3 contains 1659 particles and it takes about 3 minutes of computation time under the same conditions as in Sec. 7.1.5.1.

Parameters	Values	Units
Solid height H_0	200	μm
Solid width λ	100	μm
Particle spacing l_0	2.5	μm
Smoothing length h	2.5 l_0	μm
Initial solid density $\rho_{s,0}$	7850	kg/m^3
Equation of state	elastic-perfectly plastic	-
Young's modulus E	200	GPa
Poisson's ratio ν	0.28	-
Yield stress σ_Y	250	MPa
Contact stiffness E^*	$10^3 E$	GPa
Artificial viscosity α	0	-
Hourglass parameter ξ	10	-
Contact scale factor β_c	2	-
Contact radius R_a	$\beta_c\, l_0/2$	μm
Loading speed v^*	100	mm/s
Time step factor β_t	0.1	-
Gradient correction	activated	-
Skin distance s	h	μm

Table 7.3: Compression of an elastoplastic solid with contact. Parameters of the SPH model.

Fig. 7.32 finally shows the comparison between the previous analytical *results* of the stress-strain curve and the SPH results for different particle spacings l_0. More precisely, the SPH results converge to the analytical solution, when the particle spacing l_0 decreases. This observation can be explained by the improved approximation of the solid geometry by the SPH particles, when the particle spacing decreases. In fact, the initial particle volume (per out-of-plane thickness)

is l_0^2 (see the cell around each particle in Fig. 7.30) due to the square lattice discretization, so that the width of the solid in the simulation, i.e. $\lambda/2$, is overvalued by l_0. In consequence, its effective stiffness decreases, when the particle spacing l_0 decreases. It can, however, also be seen in Fig. 7.32 that the stress falls off at some point (in absolute value), when the particle spacing decreases to $l_0 = 1.25\ \mu$m. This trend is due to the lateral plastic flow in the contact region so that the centers of the contact circles of the rigid horizontal plane in Fig. 7.30 are not vertically aligned anymore with those of the elastoplastic solid but more and more shifted sideways. In consequence, these centers can further approach each other without additional deformation so that the stress drops (in absolute value) by vertical elastic unloading. The occurrence of this circumstance is encouraged by the greater curvature of the contact circles when the particle spacing decreases.

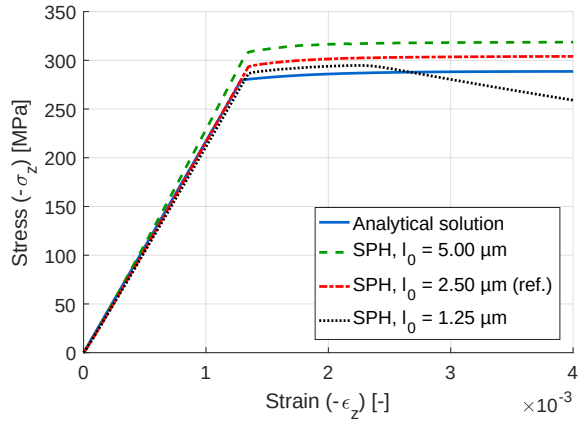

Figure 7.32: Compression of an elastoplastic solid with contact. Comparison between analytical and SPH results for different particle spacings l_0.

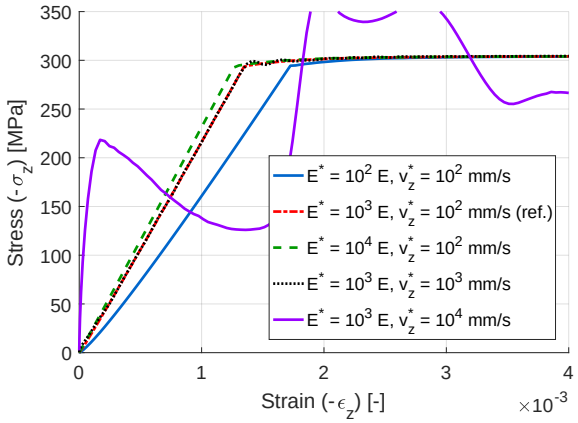

Figure 7.33: Compression of an elastoplastic solid with contact. Influence of the contact stiffness E^* and the loading speed v_z^* with respect to the reference case (ref) in Tab. 7.3.

Concerning the *influences of other parameters* with respect to the configuration in Tab. 7.3, the following observations were made: (1) The yield stress is reached a bit earlier, if the contact radius $R_a = \beta_c l_0/2$ increases due to the geometrical approximation and the relatively stiff penalty contact. (2) As illustrated in Fig. 7.33, the contact stiffness E^* increases the stress for a given strain and this increase converges around the value, which was selected in the reference case (Tab. 7.3), i.e. $E^* = 10^3 E$. (3) The artificial viscosity α is set to 0, since the computation converges without it. If its value is set to 1, the stress increases very slightly. (4) No difference can be observed when the hourglass parameter ξ is increased from 1 to 10 but the solution becomes unstable if $\xi = 100$, probably because the CFL condition is not satisfied anymore. (5) The loading speed v^* introduces almost unnoticeable oscillations due to inertia when its values in the reference case is multiplied by 10. When it is multiplied by 100, inertia effects dominate the solution, as shown in Fig. 7.33. (6) If the time step is increased by increasing β_t from 0.1 to 0.4, the solution becomes unstable, while no modification is observed, if it is further reduced. (7) Decreasing or increasing the smoothing length h to $2l_0$ or $4l_0$ has no visible influence on the stress-strain curve.

In conclusion, SPH approximates relatively accurately the compression of an elastoplastic solid with contact but discrepancies exists between the analytical and numerical solutions, mainly, for two reasons: first, the *rippled contact boundary condition* introduces a numerical artifact in the solution due to the repulsive particles. This phenomenon can be eliminated by introducing a smooth repulsive boundary like a repulsive line. Secondly, in contrast to FEM, *SPH does not exactly approximate the geometrical boundary of a solid*. In consequence, SPH slightly overestimates its effective stiffness for the current discretization choice. The error due to this approximation can be reduced by decreasing the particle spacing.

7.2.3 Verification of dry asperity flattening by FE simulation in Metafor

The next step towards the SPH simulation of lubricated asperity flattening consists in checking *whether SPH is able to model dry asperity flattening*, i.e. whether SPH is able to predict the relative contact area A as a function of the interface pressure p_i without the lubricant. The corresponding verification case is again defined on the basis of Shvarts and Yastrebov [291]. Since they, however, provide no results for elastoplastic asperity flattening without the lubricant, the SPH results will be verified by the FE model of asperity flattening in Metafor of Sec. 6.2.2.

As explained in Sec. 7.2.1, Shvarts and Yastrebov modeled the *asperity flattening problem* in the previous Fig. 7.29. Fig. 7.34 shows a simplification of this problem due to its symmetry and the suppression of the lubricant. In contrast to the model of elastic-perfectly plastic compression with contact in the previous section, the surface of the solid is not flat anymore, the horizontal displacement of the lateral walls is prevented and the geometry is not divided one more time due to symmetry, although this is possible[26]. All remaining problem parameters take the same values as in the previous section, if not specified otherwise.

To solve the previous problem of dry asperity flattening, the *SPH model* can be defined in a similar way than in the previous section apart from some modifications: (1) The *amplitude parameter* Δ of the asperity profile has to be increased. In fact, if $\Delta = 1$ μm, as explained in the previous section, and if the pocket is discretized by around 20 particles along the vertical direction at its deepest point, the initial particle spacing l_0 should be $2\Delta/20 = 0.1$ μm. With the condition that the particle spacing is homogeneous throughout the whole domain, about $H_0\lambda/l_0^2 = 2$ million particles would then be required. This large number of particles can be simulated because of the strong parallelization of LAMMPS, but it is impractical in this feasibility analysis due to the resulting computation time and the size of the output data. Therefore, it is assumed that $\Delta = 10$ μm. In the future, the local refinement of the spatial discretization should be studied to include small geometrical features in large simulation domains without excessively increasing the number of particles. An illustration of such a refinement is provided at the end of this section. (2) The *initial particle spacing* is reduced to $l_0 = 0.5$ μm, which is even smaller than the previous suggestion ($2\Delta/20$) to further increase the accuracy of the predicted relative contact area. (3) In order to reduce the computation time even more, it was possible to *reduce the solid height* H_0 to

[26]When the lubricant is included in the model, it is not possible to simply divide the pocket so that the width of the solid in the computation would be $\lambda/2$. Therefore, the solid is modeled with its full width λ here, too.

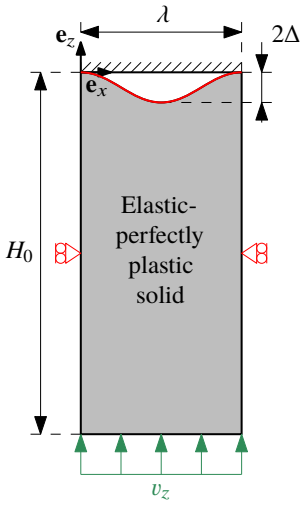

Figure 7.34: Geometry of the dry asperity flattening problem with boundary conditions and modifications with respect to the previous problem of Sec. 7.2.2 (Fig. 7.30) in red (asperity profile and no horizontal displacement of lateral edges).

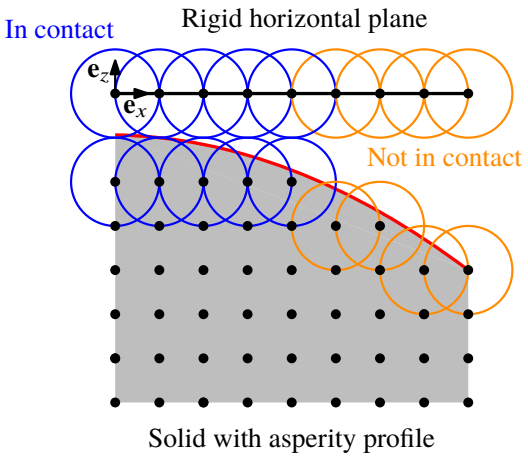

Figure 7.35: Schematic magnification of the top left zone of the initial geometry in Fig. 7.34. Discretization of the solid by SPH particles below the asperity profile, which was shifted downwards by the contact radius R_a to prevent any initial overlap of repulsive contact circles. The contact status of the particles (blue, if in contact), which belong to the rigid horizontal plane, allows to compute the relative contact area A.

100 μm. In fact, a sensitivity analysis showed that the results become only strongly dependent on H_0, when its value is close to 50 μm. Based on these parameter choices, the geometry can be discretized by SPH parameters as illustrated in Fig. 7.35 (see above). It is important to notice that the asperity profile was slightly shifted downwards by the contact radius R_a to prevent any initial contact overlap between the solid and the rigid horizontal plane. (4) *Self-contact* is introduced in the model to prevent any artificial solid penetration, when the surface pocket closes itself. This feature is implemented in a similar way to the penalty forces between the rigid horizontal plane and the solid. More precisely, if particles are such that $\|\mathbf{x}_{0,b} - \mathbf{x}_{0,a}\| > h$, i.e. they are no neighbors in the reference configuration, and if their distance in the current configuration is such that $\|\mathbf{x}_b - \mathbf{x}_a\| < R_a + R_b$, a repulsive penalty force is included in between them. (5) The introduction of self-contact requires the *reduction of the contact radius* R_a to $l_0/2$, i.e. the contact scale factor β_c equals 1 instead of 2, which was previously suggested to smooth the contact interface. In fact, if $\beta_c = 2$, particles in the solid bulk start to noticeably interact by repulsive contact forces because significant plastic deformations bring bulk particles, that are initially sufficiently distant from each other, closer together. This problem could be solved by a more sophisticated identification of the solid boundary in future research. (6) The loading speed v^* (Eq. 7.71) was increased by a factor 10, i.e. to 10^3 mm/s, in order to further reduce the computation time. (7) While the interface pressure $p_i = -\sigma_z$ can be computed via the horizontal stress σ_z as in the previous section, the *relative contact area* A is computed by the contact status of the particles of the rigid horizontal plane (see Fig. 7.35 above). Hence, if n_x is the total number of particles of the rigid plane and if n_c is the number of these particles that are in contact with the

deformable solid, the relative contact area $A = n_c/n_x$. In conclusion, the SPH baseline model, whose parameters are summarized in Tab. 7.4a, contains 36200 solid particles and 201 particles for the rigid horizontal plane. It is solved in about 4.5 hours on one node of the cluster FABULOUS (2 CPUs with 6 cores each, i.e. 12 cores in total) with dynamic load balancing.

Parameters	Values	Units
Solid height H_0	**100**	μm
Solid width λ	100	μm
Asperity amplitude Δ	**10**	μm
Particle spacing l_0	**0.5**	μm
Smoothing length h	2.5 l_0	μm
Initial solid density $\rho_{s,0}$	7850	kg/m^3
Equation of state	elastic-perfectly plastic	-
Young's modulus E	200	GPa
Poisson's ratio ν	0.28	-
Yield stress σ_Y	250	MPa
Contact stiffness E^*	$10^3 E$	GPa
Artificial viscosity α	0	-
Hourglass parameter ξ	10	-
Contact scale factor β_c	**1**	-
Contact radius R_a	$\beta_c\, l_0/2$	μm
Self-contact	**activated**	-
Loading speed v^*	**10^3**	mm/s
Time step factor β_t	0.1	-
Gradient correction	activated	-
Skin distance s	h	μm

(a) SPH parameters. Modifications of parameter values with respect to those in the previous problem (Tab. 7.3) are written in bold.

Parameters	Values	Units
Solid height H_0	100	μm
Solid width λ	100	μm
Asperity amplitude Δ	10	μm
Mesher	GEN4	-
No. of elements $n_{y,1}$	320	-
No. of elements $n_{y,2}$	**16**	-
No. of elements n_z	40	-
Density ρ_s	7850	kg/m^3
Equation of state	elastic-perfectly plastic	-
Young's modulus E	200	GPa
Poisson's ratio ν	0.28	-
Yield stress σ_Y	250	MPa
Contact law	**sticking contact**	-
Normal penalty k_n	10^9	MPa/mm
Tangential penalty k_t	$0.11 \cdot 10^9$	MPa/mm
Self-contact	**activated**	-
Imposed displacement	**activated**	-
Loading speed v^*	**decreased**	mm/s
Tolerance $\text{tol}_{\Delta\mathbf{F}}$	10^{-5}	-
Max. time step $\Delta t_{\max}$	10^{-2}	s
Initial time step Δt_0	$\Delta t_{\max}$	s

(b) FEM parameters. Non-obvious modifications of parameter values with respect to those in Chap. 6 (Tab. 6.2) are written in bold.

Table 7.4: Dry asperity flattening. Parameters of the SPH and FEM models.

The plane-strain *FE model*, which is used to verify the SPH results, is essentially identical to the one in Chap. 6 apart from (1) changing the *geometry* to that in Fig. 7.34, (2) using the *material* parameters of the SPH model and (3) imposing an *upward displacement* to the bottom edge of the solid instead of the METALUB boundary conditions. Besides these obvious adaptations, the following modifications were introduced, as summarized in Tab. 7.4b: (4) The *solid height* H_0 was reduced to 100 μm as in the SPH model. Fig. 7.36 shows that the relation between the interface pressure and the relative contact area changes if H_0 is reduced to 50 μm. The results for greater values of H_0 than 100 μm were not represented in Fig. 7.36 since they are identical to those for $H_0 = 100$ μm. (5) The *number of elements* of the bottom edge was increased from 4 to 16 (in total, 3814 elements, Fig. 7.37) since this slightly delays the breakdown of the resolution

due to element distortions. This breakdown, however, also occurs in the reference case when the interface pressure is equal to about 1000 MPa as shown in Figs. 7.36 and 7.37. (6) Friction is modeled by the *sticking contact* model (negligible tangential displacement at the interface) to be consistent with the relatively rough interface in the SPH model, which is due to the required reduction of the contact scale factor β_c to 1. Fig. 7.36 illustrates the influence of friction by FE results that were obtained with a frictionless interface. (7) And finally, the *loading speed* v^* is decreased in the FE computation by applying the interpolated upward displacement of the bottom edge $u_z = 0$ to 14 μm from $t = 0$ s to 1 s. Otherwise, i.e. if the time-displacement relation of the SPH computation is applied in the FEM computation, high-frequency oscillations start to appear in the FE computation as illustrated in Fig. 7.36. These oscillations are due to the particular choice of the loading speed in the SPH computations, which is just at the limit of inertia effects to minimize the computation time. The FEM computation with the reference parameters in Fig. 7.4b takes about 20 minutes.

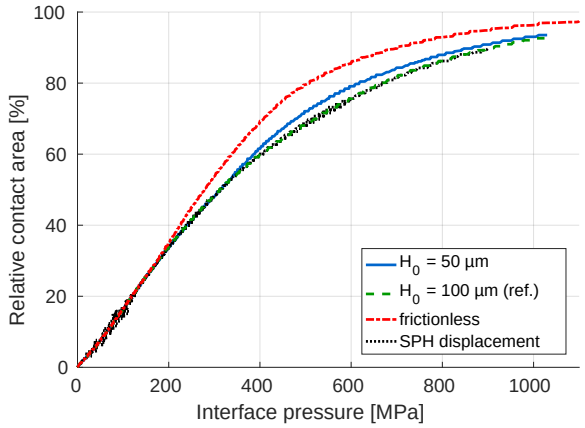

Figure 7.36: Dry asperity flattening. FEM results based on the reference case with sticking contact (ref.) in Tab. 7.4b.

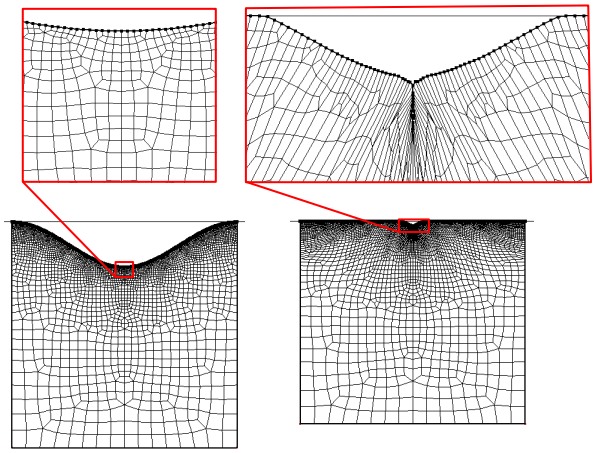

Figure 7.37: Dry asperity flattening. Initial FE mesh (left) and final mesh (right), when the computation stops due to element distortions.

The *comparison of the FEM and SPH results* in Fig. 7.38 finally shows that SPH is able to model dry asperity flattening *seemingly better than FEM*, which is limited by mesh distortions. More precisely, these figures show the relative contact area A as a function of the displacement of the bottom solid edge u_z and the interface pressure p_i. In particular, the first one of these figures illustrates the convergence to full contact with SPH, which is not possible with the FE model. Although the SPH model seems superior to the FE model from this point of view it has several drawbacks: (1) The *boundary of the solid pocket is discretized in a pixelated way* as schematized in Fig. 7.35. In consequence, the relative contact area increases strongly at the beginning of the simulation. In the current model, this discrepancy can only be solved by reducing the particle spacing l_0, which extends the computation time by increasing the number of particles and by the CFL condition. In the future, methods to spatially discretize boundaries more accurately and local refinement strategies should be investigated to solve this problem. (2) These methods would also allow to reduce the *computation time*, which is currently about 13.5 time longer with SPH

than with FEM due to the significantly larger number of elements/particles and time steps. It should be noted that the computation time of the SPH model can certainly still be significantly reduced by using more computing cores due to its domain decomposition approach, which does not exist in the FE solver. (3) Simulating truly large deformations is currently limited by the TLSPH formulation since the *reference configuration is not updated*. Although this was no problem so far, updating the reference configuration (ULSPH) should be studied, if even more complex deformation modes have to be simulated in the future.

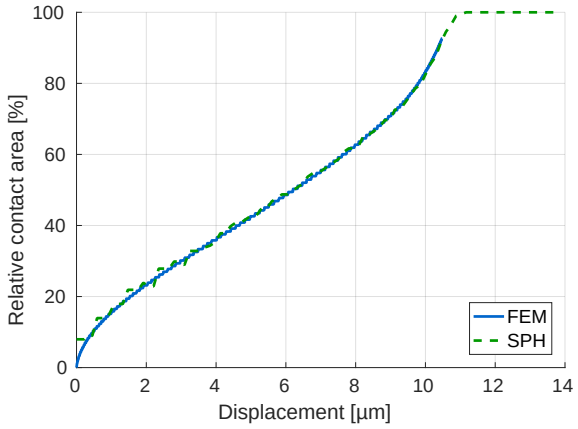

(a) Relative contact area A as a function of the vertical displacement of the bottom solid edge u_z.

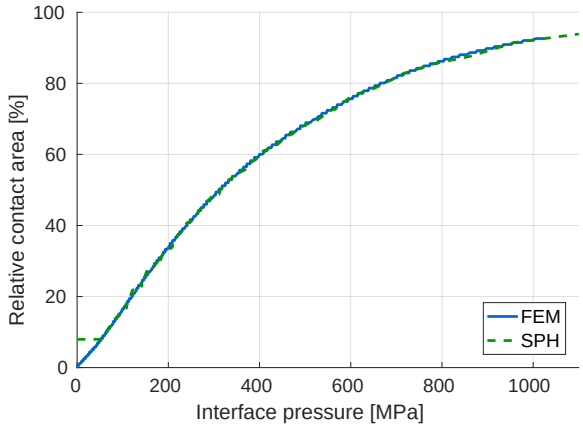

(b) Relative contact area A as a function of the interface pressure p_i.

Figure 7.38: Dry asperity flattening. Comparison of FEM and SPH results.

The *influences of all parameters* in the SPH model were meticulously studied and the conclusions are very similar to those in the previous section, which is why they are not mentioned here. The SPH results can be marginally improved, if the number of particles is increased and if the loading speed is reduced as shown in Fig. 7.39. Since these operations substantially increase the computation time ($l_0 = 0.25$ μm: 35 h; $v^* = 10^2$ mm/s: 44 h), locally refining/coarsening the discretization seems advantageous, as mentioned earlier. A preliminary investigation of this suggestion is possible by creating two zones with different particles spacings as illustrated in Fig. 7.40. Besides reducing the number of particles in the lower region of the solid, this approach requires increasing their initial volume (per out-of-plane thickness) to $4l_0^2$ and increasing their smoothing length h to $2 \cdot 2.5l_0$. The respective results with the refined discretization around the pocket such that the transition occurs at $d = 4\Delta$ (Fig. 7.40) are shown in Fig. 7.39. While these results are essentially identical to those of the base case, they are calculated in less than half the computation time (2 h) since the number of particles (17839 particles) is reduced to less than half of the number of particles in the base case (36401 particles). In addition to optimizing the spatial approximation in future research, using greater time steps for larger particles instead of the same time step for all particles could possibly reduce the computation time even more.

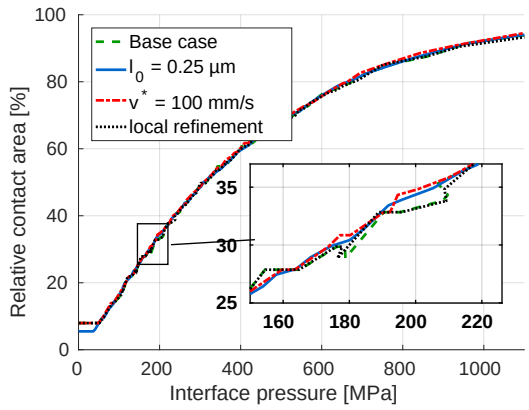

Figure 7.39: Dry asperity flattening. Influences of a reduced particle spacing l_0, a reduced loading speed v^* and a refinement of the spatial discretization around the pocket (see Fig. 7.40) with respect to the base case in Tab. 7.4a.

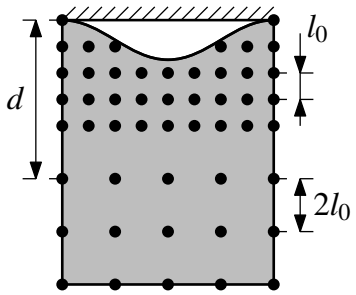

Figure 7.40: Dry asperity flattening. Schematic representation of a method to locally refine the discretization.

7.2.4 Compression of a fluid

The next step towards the SPH model of lubricated asperity flattening consists in simulating the plane-strain *compression of a fluid* without the deformable solid. More precisely, the fluid compression problem in this section is based on the rigid piston-cylinder apparatus, which is schematized in Fig. 7.41. Its dimensions are similar to those of the asperity profile in the previous section, i.e. $\Delta = 10\,\mu$m and $\lambda = 100\,\mu$m. The piston moves upwards at a sufficiently slow speed v_z to neglect inertial forces, while viscous forces are still neglected. In consequence, the pressure of the lubricant, which is initially assumed to be zero, increases. In this section, it is tested whether SPH is able to accurately predict this increase in pressure, if the bulk modulus is either constant, i.e. $K = K_0$, or linearly increasing with the lubricant pressure p_l, i.e. $K = K_0 + K_1 p_l$. The lubricant is assumed to be an ordinary oil with the density $\rho_0 = 910$ kg/m^3 (Sec. 3.1.3) and the compressibility parameters $K_0 = 2000$ MPa and $K_1 = 9.25$ according to Shvarts and Yastrebov [291].

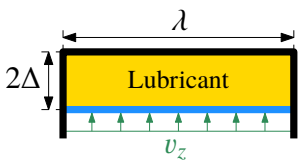

Figure 7.41: Compression of a fluid. Geometry of a rigid piston-cylinder apparatus to compress the lubricant, when the piston (in blue) moves upwards with the speed v_z.

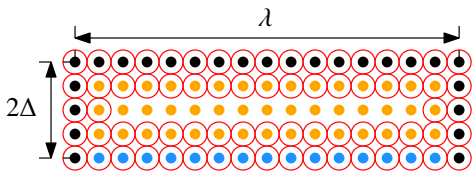

Figure 7.42: Compression of a fluid. Schematic representation of the SPH discretization. Cylinder particles in black, piston particles in blue, lubricant particles in orange and contact circles in red.

The *analytical solutions* to this problem can be derived by Eqs. (7.25) and (7.26) via the conser-

vation of mass ($\rho V = \rho_0 V_0$) depending on the constitutive equation:

- Linear compressibility[27] (Eq. 7.25):

$$p_l = K_0 \left(\frac{V_0}{V} - 1 \right) \tag{7.75}$$

- Non-linear compressibility (Eq. 7.26):

$$p_l = \frac{K_0}{K_1} \left[\left(\frac{V_0}{V} \right)^{K_1} - 1 \right] \tag{7.76}$$

where $V_0 = 2\Delta\lambda$ is the initial volume and V the current volume.

The *SPH model*, whose discretization is schematized in Fig 7.42 (see above), is built like the previous SPH models with a fluid, e.g. the dam break problem in Sec. 7.1.5.1. Some parameter values of the previous section (Sec. 7.2.3) are, however, reused due to similarities to the previous problem, like the length scale (same particle spacing l_0), the expected force amplitude (same contact stiffness E^*), and the prevention of inertial forces (same upward speed v_z by Eq. 7.71). The most significant difference with respect to the dam break problem in Sec. 7.1.5.1 is certainly the compressibility of the fluid. Instead of increasing its speed of sound or bulk modulus in order to converge to the behavior of an incompressible fluid, the pressure is computed by Eq. (7.25) or (7.26) with *physical material values to introduce linear or non-linear compressibility* in the model. The values of all parameters are summarized in Tab. 7.5. To ultimately compare the analytical and numerical results, the displacement of the piston and the average pressure of the lubricant (average over all lubricant particles) are recorded during the SPH computation. This model contains 8241 particles and it is solved in about 45 minutes on one node of the cluster Fabulous (2 CPUs with 6 cores each, i.e. 12 cores in total) with dynamic load balancing.

Fig. 7.43 shows the *comparison between the analytical solutions and the SPH results* for the lubricants with linear and non-linear compressibility. The pressure increases obviously significantly more with the displacement of the piston in the second case than in the first one. Although, the SPH results reproduce quite satisfactorily the analytical solutions, some differences between them still exist. For this reason, the influences of the particle spacing l_0 and the contact scale factor β_c as well as magnifications close to the origin are also represented in Fig. 7.43. It can be seen that the analytical prediction of the pressure increases immediately, when the displacement increases, while the pressure by the SPH model increases more gradually. This slower increase is due to a *reorganization of the particle structure to optimally fill the available space*. More precisely, the particles are initially positioned at the nodes of a square lattice as shown in Fig. 7.42 (see above). Because of the repulsive boundary condition, particles can first slide in the free space between the contact circles of the boundary, as previously illustrated in Fig. 7.8, before the pressure increases more significantly. If this free space is reduced, either by decreasing the

[27] In Shvarts and Yastrebov [291, Eq. 7], the equation $p_l = K_0(1 - V/V_0)$ is wrongly mentioned.

Parameters	Values	Units
Fluid width λ	100	μm
Initial fluid height 2Δ	20	μm
Particle spacing l_0	0.5	μm
Smoothing length h	2.5 l_0	mm
Initial density ρ_0	910	kg/m^3
Equation of state (pressure)	linear (Eq. 7.25) or non-linear (Eq. 7.26)	-
Bulk modulus K	K_0 or $K_0 + K_1 p_l$	MPa
Compressibility parameter K_0	2000	MPa
Compressibility parameter K_1	9.25	-
Young's modulus E	200	GPa
Contact stiffness E^*	$10^3 E$	GPa
Artificial viscosity α	0.05	-
Dynamic viscosity η	0 (neglected)	Pa.s
Contact scale factor β_c	1	-
Contact radius R_a	$\beta_c\, l_0/2$	mm
Loading speed v^*	10^3	mm/s
Time step factor β_t	0.025	-
Gradient correction	not activated ($\mathbf{K}_a = \mathbf{I}$)	-
Skin distance s	h	mm

Table 7.5: Compression of a fluid. Parameters of the SPH model.

particle spacing l_0 or by increasing the contact scale factor β_c, Fig. 7.43 shows that the pressure in the SPH computation increases earlier, so that the SPH results converge to the analytical solution. This effect is amplified by the reduction of the effective initial volume V_0, when β_c is increased. Finally, it should be noticed that *particle pairing* occurs at the boundary, when the compression becomes significant, although the Wendland C^2 kernel was used to prevent this type of instability (Sec. 7.1.1.3). Further research is required to determine the precise origin of this instability. It could possibly be related to the deficiency of the kernel support near the boundary, which is why considering a different boundary implementation, e.g. Adami et al. [1], could solve the problem. Nevertheless, the pairing instability is rather benign, as mentioned by Price [263], since it has a small influence on the density estimation, but it wastes computation time due to a reduced spatial resolution.

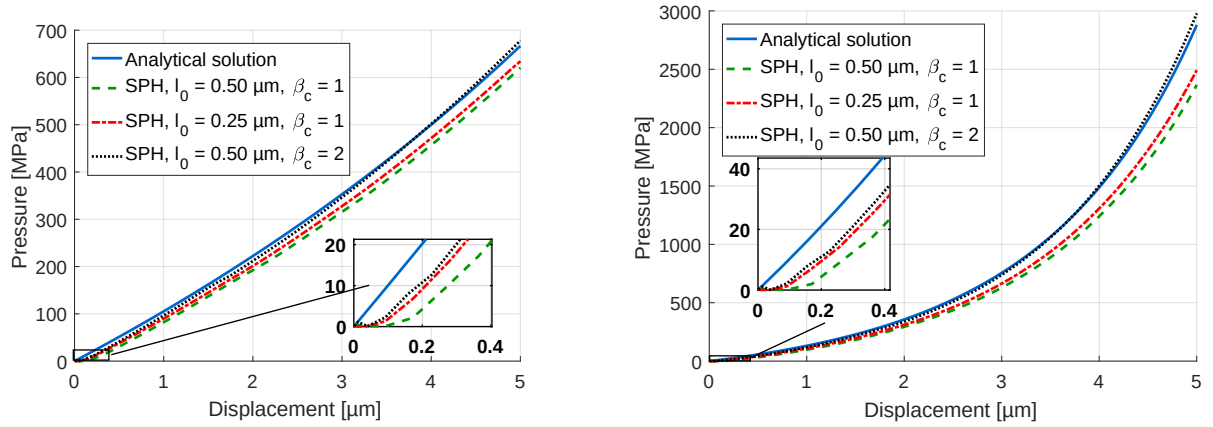

(a) Linear compressibility (Eq. 7.25). **(b)** Non-linear compressibility (Eq. 7.26).

Figure 7.43: Compression of a fluid. Comparison of the analytical solution and SPH results with influences of the particle spacing l_0 and the contact scale factor β_c.

7.2.5 Lubricated asperity flattening

In this last section, the models of the previous sections are finally combined to simulate *lubricated asperity flattening by SPH* in the plane-strain state based on the problem of Shvarts and Yastrebov [291] (Sec. 7.2.1). Due to its geometrical symmetry, this problem can be simplified as illustrated in Fig. 7.44. It consists of an elastic-perfectly plastic solid, which is compressed against a rigid horizontal plane, in the presence of a surface pocket, that is partially filled by a lubricant[28]. In comparison to Shvarts and Yastrebov [291], the amplitude Δ of the wavy surface pattern is increased and the substrate height H_0 is reduced to facilitate the simulation of the problem by SPH, as explained in Sec. 7.2.3. More precisely, $\Delta = 10\ \mu$m (instead of 1 μm), $\lambda = 100\ \mu$m and $H_0 = 100\ \mu$m (instead of 200 μm). Half of the volume of the surface pocket $V_{g,0} = \lambda\Delta$ is initially assumed to be filled by the lubricant whose volume $V_{f,0}$ can be computed by the following

[28] Air in the remaining volume of the surface pocket is not considered since its bulk modulus is about 10^4 smaller than that of the lubricant.

equation as a function of the position of its free surface Δ_l (Fig. 7.44):

$$V_{f,0} = \int_{x_l}^{\lambda - x_l} \left[\Delta \left(1 - \cos \frac{2\pi x}{\lambda} \right) - \Delta_l \right] \mathrm{d}x \quad \text{with} \quad x_l = \frac{\lambda}{2\pi} \arccos \left(1 - \frac{\Delta_l}{\Delta} \right) \tag{7.77}$$

where x_l is the coordinate of the first intersection between the asperity profile and the free surface of the lubricant. The numerical resolution of the equation $V_{f,0} = 0.5V_{g,0}$, then provides the position of the free surface $\Delta_l = 6.713$ μm. As in the previous sections and as in Shvarts and Yastrebov [291], the solid is assumed to be elastic-perfectly plastic steel (Young's modulus $E = 200$ GPa, Poisson's ratio $\nu = 0.28$, constant yield stress $\sigma_Y = 250$ MPa, density $\rho_s = 7850$ kg/m^3) while the lubricant is a typical mineral oil whose bulk modulus $K_l = K_0 + K_1 p_l$ increases with its pressure p_l ($K_0 = 2000$ MPa, $K_1 = 9.25$, density $\rho_l = 910$ kg/m^3 by Sec. 3.1.3). Viscous effects are still neglected as in [291]. Furthermore, the loading speed v_z is again gradually increased according to Eq. (7.71).

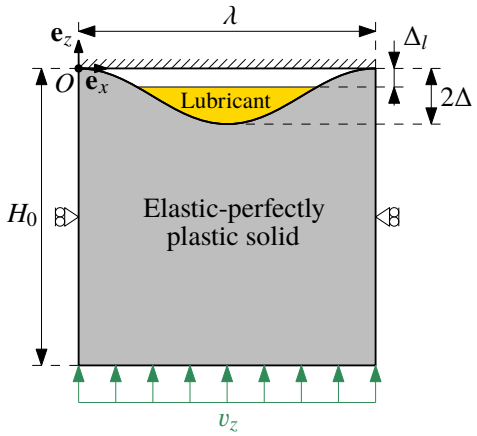

Figure 7.44: Lubricated asperity flattening. Geometry of a partially filled pocket at the surface of a deformable solid, which is pushed against a rigid horizontal plane by applying a speed v_z to its bottom edge. The horizontal displacement of the lateral edges of the solid is prevented.

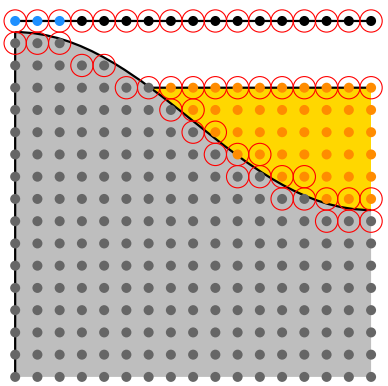

Figure 7.45: Lubricated asperity flattening. Schematic representation of the top left corner of the SPH discretization. Particles of the rigid horizontal plane in black or in blue, if in contact with the solid, solid particles in gray, lubricant particles in orange, and some contact circles in red.

The *SPH model* is essentially the combination of the previous models (Secs. 7.2.3 and 7.2.4) except for the following modifications: (1) the *initial positions of the lubricant particles* are such that they take the form of the surface pocket as illustrated in Fig. 7.45. More precisely, the initial positions of the particles are provided by the nodes of a square lattice (centered in O, Fig. 7.44). The particles of the lubricant are then those that satisfy the inequalities $z < -\Delta_l$ and $z > -R_a + 2R_a - \Delta[1 - \cos(2\pi x/\lambda)]$ (or $z > -R_a - \Delta[1 - \cos(2\pi x/\lambda)]$, if $\beta_c = 1$ as in Fig. 7.45), while those of the solid satisfy the inequality $z \leq -R_a - \Delta[1 - \cos(2\pi x/\lambda)]$, where x and z are the coordinates of a particle and where R_a is the contact radius. The shift by $-R_a$ in the previous inequalities was introduced to ensure no initial overlap between particles of the solid and the rigid horizontal plane, whereas the factor $2R_a$ was introduced to have no such overlap between the

solid and the lubricant. The influence of these geometrical hypotheses vanishes when the particle spacing l_0 decreases, since $R_a = \beta_c l_0/2$. (2) The *interaction between the lubricant and the solid, or the lubricant and the rigid horizontal plane* is modeled by the same method as the interaction between the solid and the plane, i.e. by a repulsive penalty formulation (Sec. 7.1.3.3). The contact scale factor β_c in this method was increased from 1 to 2 with respect to the previous models for reasons that will be explained in the following paragraphs. The numerical parameters of the SPH model, which are based on those of the previous sections, are summarized in Tab. 7.6. Hence, the model contains 36097 solid particles, 1870 lubricant particles and 201 particles, which discretize the rigid horizontal plane. It is solved in about 20 hours on one node of the cluster FABULOUS (2 CPUs with 6 cores each, i.e. 12 cores) with dynamic load balancing. This increase of the computation time is consistent with that of dry asperity flattening (Sec. 7.2.3), since the time step factor β_t was reduced from 0.1 to 0.025 like in the fluid compression problem (Sec. 7.2.4).

The *results of the SPH model* with the lubricant are compared to those of the FE method without the lubricant in Fig. 7.46 for different parameters values. More specifically, the figure shows the relative contact area A as a function of the vertical displacement of the bottom solid edge u_z and the interface pressure p_i. If the same parameters as in dry asperity flattening (Sec. 7.2.3) are used in the SPH simulation, i.e. $\beta_c = 1$ with activated self-contact for the deformable solid, the SPH results are essentially identical to the FEM result, as long as the lubricant is not compressed. In fact, Fig. 7.47a shows that the lubricant is initially free to move, while it enters into contact with the rigid horizontal plane in Fig. 7.47b, when $u_z = 4.56\ \mu$m and $p_i = 243$ MPa. Subsequently, the pressure in the lubricant rises so that the interface pressure is partially supported by the lubricant. In consequence, the increase of the relative contact area (either with the displacement u_z or the interface pressure p_i) slows down with respect to the FEM results without the lubricant.

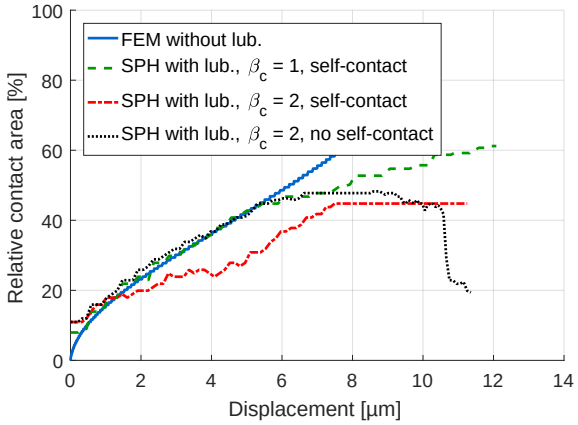

(a) Relative contact area A as a function of the vertical displacement of the bottom solid edge u_z.

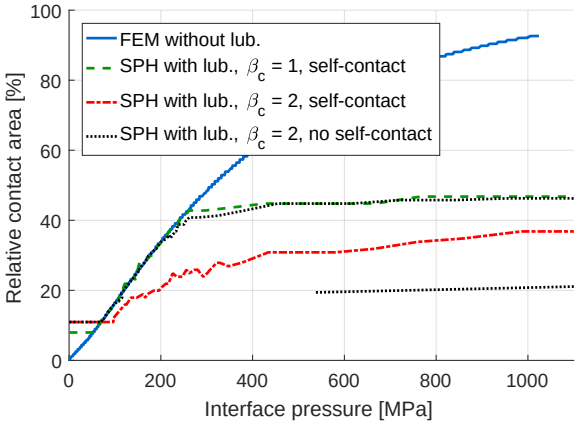

(b) Relative contact area A as a function of the interface pressure p_i.

Figure 7.46: Lubricated asperity flattening. Comparison of FEM results (without lubricant) and SPH results (with lubricant) including the influences of the contact scale factor β_c and self-contact of the deformable solid.

So far, the SPH model seems *quite promising since it solves at least partially a very complex*

Parameters	Values	Units
Solid height H_0	100	μm
Solid width λ	100	μm
Asperity amplitude Δ	10	μm
Lubricant free surface Δ_r	6.713	μm
Particle spacing l_0	0.5	μm
Smoothing length h	2.5 l_0	mm
Initial density (solid) $\rho_{s,0}$	7850	kg/m^3
Equation of state (solid)	elastic-perfectly plastic	-
Young's modulus (solid) E	200	GPa
Poisson's ratio (solid) ν	0.28	-
Yield stress (solid) σ_Y	250	MPa
Initial density (lubricant) $\rho_{l,0}$	910	kg/m^3
Equation of state (lubricant)	non-linear (Eq. 7.26)	-
Bulk modulus (lubricant) K	$K_0 + K_1 p_l$	MPa
Compressibility parameter K_0	2000	MPa
Compressibility parameter K_1	9.25	-
Contact stiffness E^*	$10^3 E$	GPa
Artificial viscosity (solid) α_s	0	-
Hourglass parameter (solid) ξ	10	-
Artificial viscosity (lubricant) α_l	0.05	-
Dynamic viscosity (lubricant) η	0 (neglected)	Pa.s
Contact scale factor β_c	2	-
Contact radius R_a	$\beta_c\, l_0/2$	mm
Self-contact (solid)	not activated	-
Loading speed v^*	10^3	mm/s
Time step factor β_t	0.025	-
Gradient correction (solid)	activated	-
Gradient correction (lubricant)	not activated ($\mathbf{K}_a = \mathbf{I}$)	-
Skin distance s	h	mm

Table 7.6: Lubricated asperity flattening. Parameters of the SPH model.

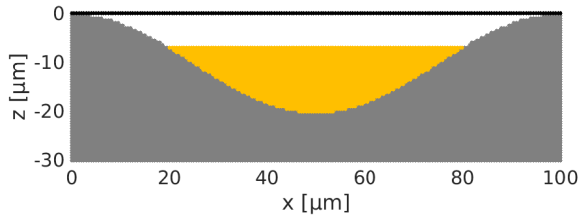

(a) Initial state ($u_z = 0$ μm, $p_i = 0$ MPa).

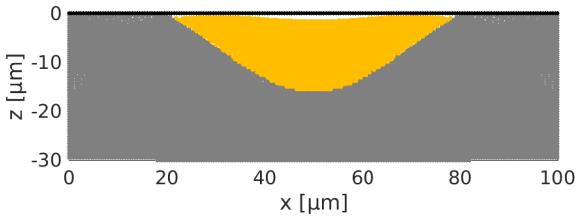

(b) First contact between the lubricant and the rigid horizontal plane ($u_z = 4.56$ μm, $p_i = 243$ MPa).

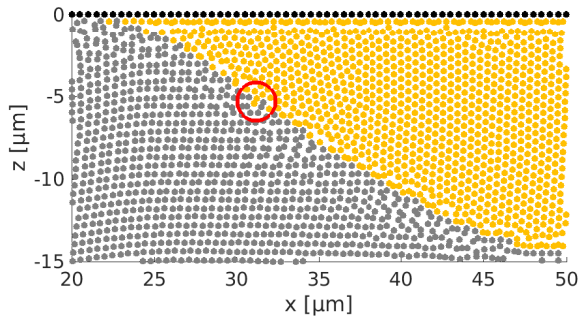

(c) Onset of lubricant infiltration into the solid ($u_z = 6.19$ μm, $p_i = 860$ MPa). The red circle indicates the onset of lubricant infiltration in the solid.

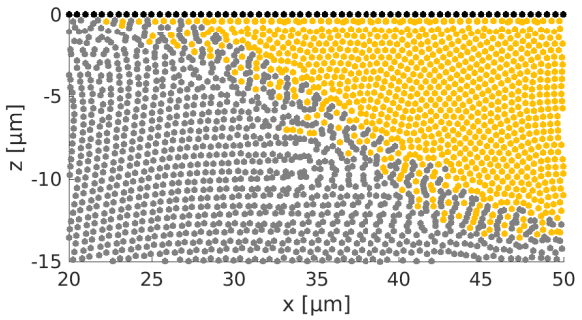

(d) Infiltration of the lubricant into the solid ($u_z = 8.06$ μm, $p_i = 2001$ MPa).

Figure 7.47: Lubricated asperity flattening. SPH particles at characteristic moments of the flattening process. Results obtained with the *contact scale factor* $\beta_c = 1$ and *activated self-contact* for the solid. Rigid horizontal plane in black, solid in gray and lubricant in yellow.

problem but its improvement is required for various reasons. First, the *lubricant particles infiltrate the solid* at rather high interface pressure as shown in Fig. 7.47d. This infiltration seems to start when $u_z = 6.19$ μm or $p_i = 860$ MPa according to Fig. 7.47c, in which the interface between the lubricant and the solid is still relatively clear. Under these circumstances, the pressure in the lubricant is seemingly strong enough that its particles can separate solid particles by their contact forces. Hence, it stands to reason that increasing the contact radius $R_a = \beta_c l_0/2$ via the contact scale factor β_c could at least delay this problem since it decreases the tangential force that could separate solid particles as illustrated in Fig. 7.48. Their separation is further prevented because it has to be even larger to let lubricant particles pass in between these solid particles, when the contact radius is increased.

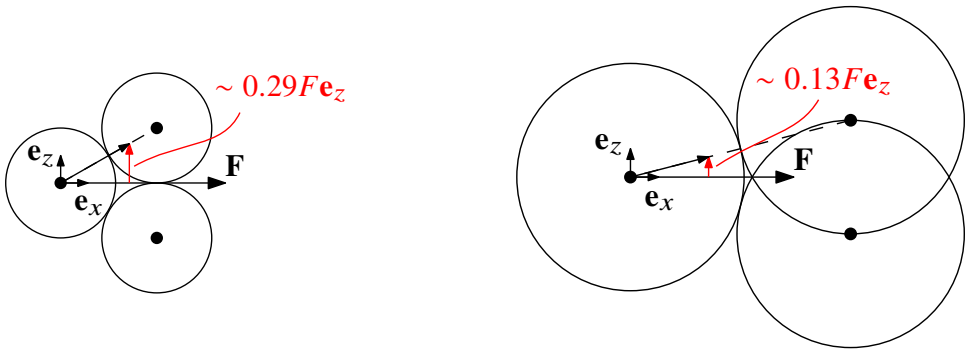

(a) $\beta_t = 1$. **(b)** $\beta_t = 2$.

Figure 7.48: Lubricated asperity flattening. Particles with their contact circles to illustrate the reduction of the separating force (in red) by an increase of the contact scale factor β_c for a given projected force $\mathbf{F}$ along $\mathbf{e}_x$.

Simply increasing the contact scale factor β_c from 1 to 2 in order to increase the contact radius while keeping self-contact activated does, however, not solve the problem according to Fig. 7.46. In fact, the SPH solution does not reproduce its FEM counterpart anymore before the compression of the lubricant under these circumstances. This erroneous behavior is caused by the self-contact algorithm as stated in Sec. 7.2.3. Since the occurrence of self-contact is less likely in lubricated asperity flattening than in dry flattening, not activating this feature seems a reasonable option before improving its implementation in future research. Indeed, increasing the contact scale factor β_c to 2 and not activating self-contact solves the previous problems. On the one hand, the FEM solution of dry asperity flattening can be replicated quite well before the compression of the lubricant as illustrated in Fig. 7.46. It could even be improved by further reducing the particle spacing l_0, which reduces the contact radius $R_a = \beta_c l_0/2$ and thus, the geometrical approximation. On the other hand, the interface pressure, at which the lubricant starts to infiltrate the solid, is increased above the interface pressure that commonly applies in lubricated cold rolling [86]. For instance, Fig. 7.49a ($\beta_c = 2$) shows no real lubricant infiltration at about $p_i = 2000$ MPa while it is significant for the same level of pressure in the previous Fig. 7.47d ($\beta_c = 1$). If the interface pressure comes close to 4500 MPa, the infiltration also starts with greater contact radii as illustrated in Fig. 7.49b. One should notice that the surface of the solid is roughened

in this model as in *free surface roughening* (Sec. 2.2.2.4). In contrast to physical free surface roughening, which is due to the emergence of grains at the surface of a polycrystalline solid, its origin is purely numerical in the SPH model.

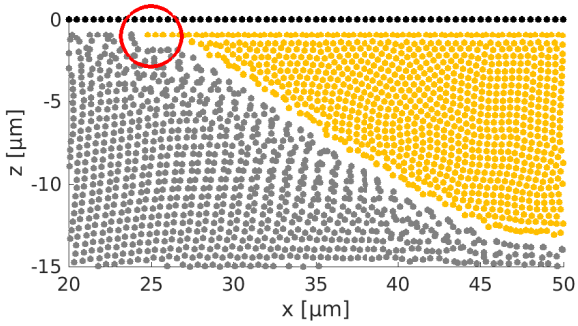

(a) No infiltration for similar interface pressure than in Fig. 7.47c (u_z = 7.18 μm, p_i = 2137 MPa). The red circle indicates that lubricant particles get stuck in the contact zone.

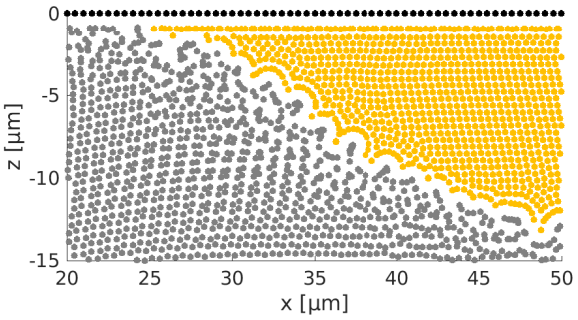

(b) Numerical roughening of the solid with infiltration of lubricant into the solid (u_z = 9.02 μm, p_i = 4499 MPa).

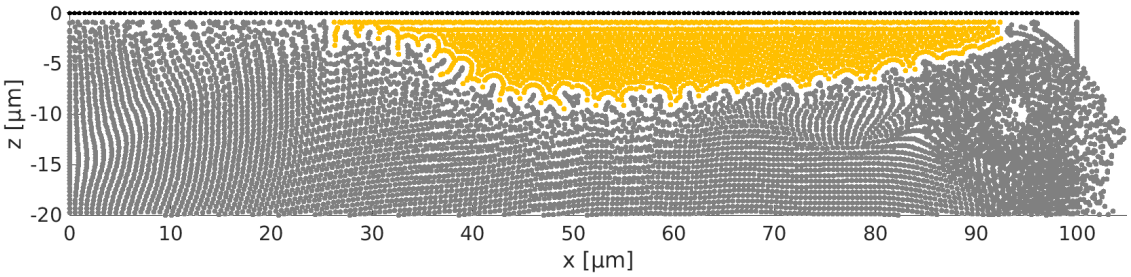

(c) Illustration of the non-physical permeation of the lubricant into the solid contact zone due to particle deletion because of excessive deformation (u_z = 10.85 μm, p_i = 1531 MPa).

Figure 7.49: Lubricated asperity flattening. SPH particles at characteristic moments of the flattening process. Results obtained with the *contact scale factor* $\beta_c = 2$ and *no self-contact* for the solid. Rigid horizontal plane in black, solid in gray and lubricant in yellow.

Secondly, the model can be criticized because of its *failure, when solid deformations become too large*. SPH was introduced in this chapter to allow the simulation of greater deformations than FEM, which is limited by mesh distortions. This statement was verified in Sec. 7.2.3, where FEM breaks down unlike SPH. Nevertheless, the TLSPH method in this study also has its limitations since it is based on the initial reference configuration, which is not updated. Thus, to guarantee the stability of the method, particles, whose Jacobian $\det \mathbf{F}_a$ is such that $\det \mathbf{F}_a < 0.2$ or $\det \mathbf{F}_a > 2$, are removed from the computation when one of these conditions is satisfied. This mechanism is at the origin of the sudden reduction of the relative contact area in Fig. 7.46a and the relative contact area at about 20% in Fig. 7.46b, when $\beta_c = 2$ without self-contact. A particle at the surface of the deformable solid is actually deleted close to the end of the computation. Consequently, the solid penetrates itself at this position since the particle, which counteracted this behavior, was

removed. Due to the violent unloading of the solid contact pressure, the lubricant permeates into the solid contact area and the relative contact area is reduced. The resulting state of the SPH particles is shown in Fig. 7.49c. As mentioned previously, this problem could possibly be solved by updating the reference configuration, i.e. by ULSPH (Sec. 7.1.1.3), in future research. Either way, this failure of the method occurs at very high pressure, which is usually not reached in lubricated cold rolling. Although, the permeation of the lubricant in the solid contact area is due to this failure, its *resemblance to micro-plasto-hydrostatic lubrication by a reduction of the solid contact pressure at the front of the lubricant pocket in strip drawing* (Sec. 2.2.4.3) should be noticed.

Thirdly, *lubricant particles get stuck at the lateral tops of the pocket* during the compression since the surfaces of the rigid horizontal plane and the solid are not perfectly smooth because of their contact circles. This behavior is visible in Fig. 7.49a. For this reason, it can be expected that the SPH model would predict a lower relative contact area than the FEM model of Shvarts and Yastrebov [291] at a given interface pressure. This shortcoming could probably be solved by treating the interaction between the solid, the horizontal plane and the lubricant by another method than the repulsive penalty formulation. Such methods were suggested in Sec. 7.1.1.4.

Fourthly, the *SPH results could not be compared to the results of Shvarts and Yastrebov* [291] due to the required increase of the asperity amplitude in the SPH model. If $\Delta/H_0 = 0.005$ and $\Delta/\lambda = 0.01$ as in their article and if the number of SPH particles along the vertical direction at the deepest point of the pocket was the same as in the current model, the new SPH model would contain 200 times more particles than the current model, which corresponds to about 8 million[29]. Furthermore, the required number of time steps would be multiplied by 10 due to the CFL condition. Since the computation time is proportional to the number of particles and the number of time steps, the current computation time of 20 h would hypothetically be multiplied by 2000. This factor can, however, be reduced (1) by locally refining the discretization, which has the most significant impact on the computation time, (2) by increasing the number of computing cores and (3) by further optimizing the parameters of the model, like the time step factor β_t, the loading speed v^* and the artificial viscosity α.

7.3 Conclusion

In this chapter, *lubricated asperity flattening was for the first time simulated by the Lagrangian meshless particle method Smoothed Particle Hydrodynamics (SPH)* to eliminate shortcomings of the existing finite element (FE) model [54, 55], namely, mesh distortions and the need for artificial lubricant pipes, which allow the permeation of the lubricant into the solid contact zone.

More precisely, in the first section of this chapter, *smoothed particle hydrodynamics* was introduced from a general point of view. Initially, the *literature about this method was reviewed* and

[29] In more detail, the current model contains about $2\Delta/l_0 = 40$ particles (where $\Delta = 10\ \mu$m) along the vertical direction at the deepest point of the pocket. Hence, the particle spacing l_0 in the new model is $2\Delta/40 = 0.05\ \mu$m (where $\Delta = 1\ \mu$m). Thus, the total number of particles in the new model is approximately $H_0\lambda/l_0^2 = 200 \cdot 100/0.05^2 = 8 \cdot 10^6$.

its *fundamental concepts* were defined. The method is based on the discretization of a continuum by spatial points, which are called particles, instead of a mesh. These particles move with the continuum (Lagrangian discretization) and they interact via kernel functions. Hence, mesh distortions, as in classical FEM, and the creation of a mesh at each time step, as in PFEM, do not exist in this method. In consequence, SPH seems to have numerous advantages with respect to these methods, like the possibility to simulate complex fluid-structure interactions (FSI) with a great parallel scalability by domain decomposition.

Various *SPH formulations* exist in the literature to implement different features, e.g. Newtonian viscosity, within the framework of this method and to eliminate its inherent deficiencies. In this chapter, the formulation of the USER-SMD SPH implementation by Ganzenmüller [113] in the molecular dynamics simulator LAMMPS [257] was chosen because its open-source and strongly parallelized code contains most of the features that are required to model lubricated asperity flattening. More specifically, this implementation allows the simulation of linearly or non-linearly compressible, viscous fluids by weakly-compressible SPH with physical and artificial viscosity to reduce the influence of zero-energy modes, with the Wendland kernel to eliminate the pairing instability (clustering of particles) and with a kernel gradient correction to improve the consistency of the approximation. Unlike fluids, elastoplastic solids are modeled by total Lagrangian SPH (TLSPH), in which the underlying equations are integrated in a reference configuration, to eliminate the tensile instability, i.e. an instability that arises when a solid is subjected to tension[30]. Furthermore, zero-energy modes in solids can be suppressed by a similar method to Flanagan and Belytschko's [102] hourglass control algorithm for finite elements. The interaction between fluids and solids is modeled by a normal penalty approach, so that contacting particles do not penetrate each other. The SPH approximations are *numerically computed* by efficient neighbor search algorithms with domain decomposition and dynamic load balancing inherited from LAMMPS before being explicitly time-integrated by the velocity-Verlet algorithm. Besides our implementation of the Wendland kernel and some new post-processing features in the USER-SMD SPH package, the applied SPH formulation was fully derived in this chapter to facilitate its extension in the future. *No other single document combines all this information (to the best of our knowledge).*

Before simulating lubricated asperity flattening, classical *validation tests* of the literature were reproduced in this chapter to test the USER-SMD SPH package of LAMMPS and to illustrate some characteristics of the method. These examples were chosen from Cerquaglia's thesis [65], in which the capabilities of the Particle Finite Element Method (PFEM) and its coupling with the classical FE method were studied to model FSI problems: (1) dam break, (2) dam break on a long bed, (3) dam break against a curved, rigid obstacle, (4) sloshing of a water reservoir, (5) dam break against an elastic obstacle, (6) dam break against an elastoplastic obstacle and (7) gravity-driven viscous unsteady flow. In general, *SPH allowed to solve these quite complicated problems relatively satisfactorily within a few minutes of computation time on a laptop. It is also worth*

[30] Although asperity flattening generally leads to a compressive state, TLSPH was also chosen in anticipation of future SPH models of asperity flattening, in which local tension could be created by the friction between surfaces due to their relative displacement.

mentioning that these problems have never before been modeled with the USER-SMD SPH solver (to the best of our knowledge). Improvements of the results seem mainly to be possible by the implementation of a different contact formulation, like the one by Adami et al. [1], and a zero-energy mode suppression method for fluids, like δ-SPH by Marrone et al. [213, 214]: in fact, (1) the normal penalty contact formulation between particles leads to non-smooth boundaries, (2) it might be at the origin of particle clustering, if the kernel gradient correction is activated for fluids, (3) it only allows normal interactions between particles, i.e. without viscous shear stresses, (4) it renders the measurement of pressure fluctuations at positions of the boundary more difficult than a formulation, which includes the boundary particles in the SPH approximation, and (5) the pressure field contains high-frequency numerical oscillations. Moreover, the computation of the work done by the forces that suppress zero-energy modes of solids should be added to the software in the future to monitor their influence more carefully.

In the second section of this chapter, SPH is applied to model a problem of *micro-plasto-hydrostatic lubrication* (MPHSL) in the plane-strain state to incrementally develop a method, which is able to simulate MPH lubrication in cold rolling without mesh distortions and artificial lubricant pipes of previous models [54, 55]. This problem consists of the compression of an elastoplastic solid with a wavy surface pattern, whose free volumes are partially filled with a compressible lubricant, against a rigid horizontal plane. Shvarts and Yastrebov [291] solved this problem by the FE method but it cannot take the kinematics of the fluid flow and hydrodynamic effects, which are required to completely model MPH lubrication, into account, unlike SPH. Thus, an SPH model of lubricated asperity flattening was constructed step-by-step in this chapter.

First, the *compression of a flat elastoplastic solid against a rigid horizontal plane* was simulated by TLSPH. Small differences between the analytical and numerical solutions exist because of the rippled contact condition (due to the penalty approach) and the inexact geometrical approximation of the solid by particles, which can be improved by increasing the fineness of the discretization.

Secondly, *dry asperity flattening* was simulated by SPH after adding a wavy surface pattern to the solid of the previous compression problem. This model was verified by the FE model of asperity flattening in Metafor of Sec. 6.2.2. While the FEM and SPH results are almost identical during most of the compression phase, the FE model broke down due to mesh distortions before reaching the full contact between the solid and the horizontal plane. The SPH model, however, also has some shortcomings: the fineness of the discretization has to be excessively increased to approximate the asperity profile with sufficient accuracy and the computation time increases accordingly from a few minutes to a few hours.

Thirdly, a *compressible lubricant was squeezed* in a rigid piston-cylinder apparatus by Eulerian SPH (ESPH) to check whether the pressure increases in the simulation as the analytical law would predict it. Small differences, which could be reduced by refining the discretization, were observed due to the reorganization of the particle structure, again because of the penalty contact formulation.

Finally, the previous models were combined to model lubricated asperity flattening by SPH for the first time via the compression of an elastoplastic solid with partially filled surface pockets by a non-

linearly compressible lubricant against a rigid horizontal plane. The method is promising since it allows to solve at least partially a very complex problem but it has still several shortcomings: (1) SPH results could not be compared to FE results by Shvarts and Yastrebov [291] since the amplitude of the asperity profile had to be increased to simulate the problem in a reasonable computation time. This shortcoming could possibly be solved by reducing the number of particles via a local refinement strategy of the spatial discretization [301, 303] around the pocket to not use the same particle density in the whole simulation domain, before considering a massively parallel computation. (2) The contact formulation by the normal penalty force allows the infiltration of the lubricant into the solid at very high pressure (> 2000 MPa) and it causes lubricant particles to get stuck in the interface between the solid and the horizontal plane, which falsifies the prediction of the relative contact area (with respect to the FE results). Thus, alternative contact formulations should be considered in the future, e.g. the formulation by Adami et al. [1, 133, 378].

Chapter 8

Conclusion

This thesis is concluded by *summarizing its chapters including the main contributions*. Then, some guidelines about how to improve the existing models in *future research* are described.

8.1 Summary and main contributions

Chapter 2: Contextualization and Literature Review

The increasing demand for harder and thinner steel strips challenge European *cold rolling* mills that were designed several decades ago to roll softer steel grades. If friction between the rolls and the strip is too low, undesired skidding occurs. If friction is, however, too high, it unnecessarily increases the energy consumption, the wear of the rolls, the forward slip and the rolling force. To improve the performance of rolling by controlling friction, the concept of flexible lubrication, was developed. It consists in continuously adapting the lubrication conditions, like the oil concentration in the oil-in-water emulsion, depending on the operating conditions, such as the decreasing roughness of the rolls due to wear. Flexible lubrication requires the prediction of the optimal lubrication conditions in order to apply them in the industrial process. These conditions can either be determined experimentally for a number of rolling scenarios, or in combination with numerical models, which allow to extrapolate the experimental data to numerous other scenarios as far as they are validated.

Therefore, the *physics of friction* was summarized in the context of lubricated cold rolling. Metallic surface are rough at the micro-scale so that they only enter into contact at their peaks, also known as asperities, which are flattened along the way through the roll bite. Dry friction, i.e. without a lubricant, can be explained by adhesion at contacting asperities and by their mechanical interaction in the presence of contaminating films. In lubricated cold rolling, a lubricant film is created by the plate-out and dynamic concentration mechanisms between the surfaces of the rolls and the strip. Hence, the interface pressure is partially supported by the solid/solid contact and partially by the lubricant, so that cold rolling occurs in the mixed lubrication regime. Besides macro-plasto-hydrodynamic, boundary and hydrostatic lubrication,

an additional lubrication mechanism in this regime is micro-plasto-hydrodynamic/static (MPH) lubrication, which consists in the permeation of the lubricant from pressurized surface pockets into the solid/solid contact zone where friction is thereby reduced.

Numerous *models of lubricated cold rolling* were developed in earlier research but none of them is able to forecast the optimal lubrication conditions depending on the rolling condition, yet. The METALUB model, which was jointly developed by research groups at ArcelorMittal, Mines ParisTech (CEMEF) and ULiège (LTAS-MN2L), seems to be the most predictive model so far. As explained more thoroughly in the following chapters, its predictive capabilities are, however, limited: it requires a few manual parameter adjustments to replicate the experimental results since some parameters were not measured and since some physical mechanisms, specifically, those of the lubricant film formation and MPH lubrication, are not included in the model.

Chapter 3: Experimental data

To overcome the previous shortcomings and to build a strong foundation on prior research before extending it, the *most comprehensive experimental data of lubricated cold rolling* available were introduced and analyzed. These data are essentially measurements of the rolling force and the forward slip, which were recorded by ArcelorMittal on a semi-industrial pilot mill for different steel grades, lubrication conditions, rolling speeds and reduction ratios. Besides the previous number of different operating conditions, these data stand out due to the availability of the following measurements: the hardening laws of the strips by plane-strain compression tests, their roughness and that of the rolls, as well as the thermo-piezoviscous material laws of the lubricants at high pressure. Furthermore, the experimental results were carefully post-processed in appendix E in order to validate numerical models in this thesis and those in future research.

On the basis of these data, different *physical mechanisms were detailed to explain the influences* of the rolling speed, the strip material, the lubricant quantity, the lubricant type, the lubricant temperature, and the elongation of the strip on the rolling force and the forward slip, and to ultimately ensure that these interacting mechanisms are included in the rolling model: (1) the hydrodynamic effect due to the creation of a lubricant film between the rolls and the strip by viscous entrainment of the lubricant into the roll bite, (2) starvation, which occurs when less lubricant is available at the entry of the bite than it can absorb, (3) viscous friction, (4) viscoplasticity, i.e. strain rate hardening, (5) work hardening, (6) the geometry of the roll bite, that depends on the reduction ratio and roll flattening, amongst others, (7) asperity flattening and (8) micro-plasto-hydrodynamic/static lubrication.

Chapter 4: METALUB - A Mixed Lubrication Cold Rolling Model

In addition to the previous shortcomings of the METALUB model, several versions of it existed in the past without a centralized and detailed documentation, thus hindering its extension. Therefore, *METALUB was completely rederived, documented and improved*. In particular, the underlying systems of equations were thoroughly derived in a standardized form for different modeling hypotheses in appendix N.

Thus, METALUB is presently a 2D cold rolling model with applied front and back tensions in the mixed lubrication regime. In the model, the *geometric contact of asperities* is described

by their composite mean-square-roughness, the half-spacing between asperities, the roughness orientation and a surface height distribution, which is either that of triangular asperities or the quasi-Gaussian Christensen distribution [77]. The *mechanics of the strip* is quantified by the slab method and a thermo-elastoviscoplastic material model. In particular, the dependencies on the temperature and the strain rate were added in this thesis since earlier research and the previous rolling data suggested their necessity to accurately model lubricated cold rolling. Besides circular rolls and non-circular roll profiles, *roll flattening* can be computed via the methods of Hitchcock [142], Bland and Ford [33], Jortner et al. [163], or Meindl [171, 220], which is the most accurate of them all and which was added in this thesis. *Solid contact* is modeled by the asperity flattening equations of Wilson and Sheu [367], Sutcliffe and Marsault [215, 311], or Korzekwa et al. and Sutcliffe (added in this thesis) [169, 313], as well as by the boundary friction models of Coulomb [85], Tresca [252, 373] or Coulomb-Tresca with possible linear regularization for significant roll flattening. The *lubricant flow* is included in the model through the average Reynolds equation with flow factors due to the roughness, which were partially corrected, and the thermo-piezoviscous material description by Barus [21], Roelands [278] or the extended WLF law [20]. Lubricant shear stresses can be computed either by the average film thickness in the surface valleys or by the new shear stress factor approach of Patir and Cheng [254], which, was, however, not extended to large fractional contact areas. *Starvation* is modeled by switching from the equations of a dry roll bite to those of a lubricated one, when the average distance between surfaces becomes smaller than the lubricant film thickness at the entry of the bite. The *temperature computation* of the strip by an adiabatic model and some thermal laws for the lubricant are additional new features of the rederived METALUB model. All the previous components were combined in one *full model*, in which parameters, like the roll position, are adjusted after explicitly integrating the underlying system of equations along the roll bite until some conditions, such as the strip thickness at the end of the roll bite being equal to the imposed final thickness, are satisfied. The *robustness* and the speed of the model were significantly improved by reducing the number of numerical parameters and by smarter initial conditions of iterative solvers.

From a computational standpoint, METALUB is implemented in object-oriented C++ with a PYTHON wrapper, version control, regression tests and a PYQT graphical user interface (GUI). To ensure that the notations, equations and methods of the rederived model match with those in the computer code, and to improve the coding style as well as the robustness of the implementation, the existing source code of the METALUB model was entirely refactored.

Chapter 5: METALUB - Numerical results

Earlier validations of the METALUB model suffered from limited experimental data. Hence, the new version of the METALUB model was tested on the basis of the previous experimental data (Chap. 3) to *evaluate its predictive capabilities and to determine its shortcomings*.

Therefore, the *numerical parameters of the model were for the first time systematically calibrated*. Adjusting these parameters layer by layer of the nested loop structure in METALUB allowed to eliminate convergence issues and to reduce the computation time with a controlled accuracy of the results.

Afterwards, the experimental rolling results of Chap. 3 were reproduced by METALUB, first by

detailing the method based on a single test scenario and then, by applying it to numerous other scenarios. Concerning the *predictive capabilities* of METALUB, *predictions in earlier research were improved* by the following assumptions: (1) Instead of manually reducing the yield stress, thermal softening was introduced in the model. (2) The lubricant shear stress was neglected in the roll bite due to the decreasing viscosity of the lubricant by the rising temperature along the roll bite. (3) Viscoplasticity allowed to reproduce rolling scenarios with increasing rolling forces and decreasing forward slips when the rolling speed increased. (4) Adjustments of the lubricant film thickness at the entry of the roll bite enabled accurate predictions of experimental results in scenarios with starvation. (5) In a similar way, rolling scenarios, in which MPH lubrication presumably occurs, were reproduced by manually reducing the boundary coefficient of friction. (6) Finally, it was shown that material parameters had not to be re-calibrated to still reproduce the experimental results in rolling scenarios, that are not too far from scenarios, for which these parameters were calibrated. Thus, the model is actually quantitatively predictive to some extent.

Nevertheless, the following *limitations* were identified: (1) Accurate predictions still depend on the calibration of material parameters. If they were measured, some modeling uncertainties could be eliminated. (2) Neglecting the lubricant shear stress seems to be an oversimplification. To improve the prediction of the viscosity in this stress by a better temperature estimation than isothermality, and of thermal softening, a full thermal model, like THERMROLL [42], should be added to METALUB. (3) The lubricant film thickness at the entry of the roll bite is manually adjusted. Hence, a film formation model, like the one by Cassarini [63], is required in METALUB to have a fully predictive model. (4) Likewise, an MPH lubrication model is required to avoid manually adjusting the boundary coefficient of friction, when this lubrication mechanism becomes significant.

Chapter 6: Coupling of METALUB with METAFOR - FE Asperity Flattening

Besides their inability to model MPH lubrication, analytical asperity flattening equations in METALUB are based on approximate methods and simplified asperity profiles with simplified material laws. For these reasons, the *first coupling procedure between METALUB and the finite element (FE) solver METAFOR [258] was developed to replace the flattening equations by FE simulations of lubricated asperity flattening*.

First, *Carretta's coupling procedure, which is based on his MPH lubrication model in METAFOR* [54, 55], was described. In his FE micro-model of asperity flattening, a rough strip portion is pushed against a rigid, fixed contact tool, which represents the roll, in the orthogonal plane to the rolling direction. Hence, the solid/solid contact area and the lubricant pressure, which are used in the METALUB model, are calculated by the FE method as a function of the interface pressure and the elongations of the strip and the lubricant from the METALUB computation. Between the contact tool and the strip portion, the lubricant is modeled by the Arbitrary Lagrangian Eulerian formulation with artificial lubricant pipes to allow the permeation of the lubricant into the solid/solid contact zone. Nevertheless, the procedure suffers from a non-physical separation of the roll and the strip, and the negligence of the Reynolds equation.

To eliminate the previous shortcomings, a *new coupling procedure* was developed by simplifying Carretta's FE model of lubricated asperity flattening. Instead of directly simulating the lubricant in the FE model, the lubricant pressure of the METALUB computation is rather applied to the top edge of the strip portion, where this edge is not in contact with the roll.

Finally, the *new procedure was tested* by rolling scenarios of Chap. 3, which were modeled by METALUB in Chap. 5. It turned out that the METALUB component of the coupling procedure did not satisfy a necessary condition of convergence, while the METAFOR component was mesh-dependent. These deficiencies were alleviated by strong hypotheses, which, however, cast doubt on the potential improvement of the predictions by this method.

Chapter 7: SPH Simulation of Lubricated Asperity Flattening in LAMMPS

As mentioned previously, Carretta's FE model of MPH lubrication [54, 55] requires artificial lubricant pipes. Moreover, mesh distortions are expected to limit this model, when large deformations due to indentation and ploughing at the micro-scale are simulated. For these reasons, the *first model of lubricated asperity flattening by the Lagrangian meshless particle method "smoothed particle hydrodynamics" (SPH) was developed*.

After a *literature review* of this method and the definition of its *fundamental concepts*, the *SPH formulation* of the USER-SMD SPH package [113] in the molecular dynamics solver LAMMPS [257] was described since its open-source and strongly parallelized implementation contains most of the features required for the simulation of lubricated asperity flattening: linearly and non-linearly compressible SPH with physical Newtonian viscosity and artificial Monaghan viscosity to simulate fluids, total Lagrangian SPH with elastoplastic material laws, the kernel gradient correction and a method of zero-energy mode suppression for solids, and a penalty method for interactions between fluids and solids. Several validation tests of relatively complex fluid and FSI problems were then for the first time (to the best of our knowledge) reproduced by the previous SPH implementation, and the computation time on a laptop was only a few minutes long.

Ultimately, lubricated asperity flattening was modeled by SPH after gradually building this model by simulating the compression of a flat elastoplastic solid, dry asperity flattening partially validated by FEM, which was limited by mesh distortions unlike SPH, and the compression of a fluid. The main shortcomings of this SPH model are the computational overhead resulting from the required number of particles, if the geometrical discretization is not locally refined, and the contact formulation between the solid and the fluid.

8.2 Future research perspectives

To build on the developments in this thesis, our estimation of the *most promising steps towards the numerical prediction of the optimal lubrication conditions in cold rolling* are summarized hereafter. These steps are sorted by decreasing feasibility and impact on reaching the previous objective.

Incorporation of a full thermal model into METALUB

In Sec. 5.3.1.1, the predictions by METALUB were significantly improved by neglecting the lubricant shear stress. This hypothesis was justified by the decreasing viscosity of the lubricant along the roll bite due to its temperature increase. In Sec. 5.3.1.5, this hypothesis was even successfully tested by estimating the temperature increase via a simplified thermal model. However, in consideration of the temperature variations at the exit of the roll bite in Tab. E.21 for instance, the question arises whether simply neglecting the lubricant shear stress is not an oversimplification. In fact, the temperature in the roll bite strongly depends on the rolling speed, so that different lubricant shear stresses can be expected at different rolling speeds. In addition, Figs. 5.17 and 5.18 illustrate the important influence of the lubricant temperature on the rolling force via the lubricant shear stress, provided that the thermo-piezviscous material law of the lubricant is still valid. Aside from the influence of the temperature on the lubricant shear stress, thermal softening of the strip (instead of the manual reduction of the yield stress) improved the predictive ability of METALUB in Sec. 5.3.1.3. Although the thermal softening coefficient of the strip was not measured unlike the thermo-piezviscous material law of the lubricant, the previous reasons justify the *necessity of more accurate temperature predictions in the model*.

In the past, the finite volume model THERMROLL was coupled with Stephany's version of METALUB as explained in Sec. 4.9.1. It seems, however, suboptimal to couple THERMROLL as such again with METALUB for three reasons. First, THERMROLL has *convergence issues*, which have, however, never been documented. Secondly, such a coupling procedure would bear the risk of loosing again the thermal model component due to *laborious software management*. THERMROLL is actually implemented in FORTRAN, unlike METALUB, so that an additional compiler as well as a developer, who is still able to handle the growing number of technologies, would be required. Thirdly, a program, which manages data exchanges between THERMROLL and METALUB, is needed to coupled them, so that their *usage would be further complicated*.

In a long-term perspective, it therefore seems preferable to *incorporate a thermal solver*, which is specifically dedicated to lubricated cold rolling as explained by Tseng [334, 335, 336, 337, 338], *directly within the METALUB software project*. From a modeling point of view, this solver would still be coupled to METALUB like THERMROLL in the past [54, 58], i.e. by a fifth loop outside of METALUB's nested loop structure (Fig. 4.35). In this way, the resulting model could fully take advantage of the development environment of METALUB, like the creation of PYTHON data sets and regression tests, which is required for models that are as sophisticated as METALUB.

Incorporation of a MPH lubrication model into METALUB

Despite significant efforts to include MPH lubrication (MPHL) into METALUB in Chap. 6, *the model can still not predict this lubrication mechanism*, which is most likely at the origin of differences between experimental and numerical results in Secs. 5.4.5, 5.4.6 and P.2, though.

To solve the existing challenges of MPHL modeling in METALUB, some research perspectives were described in Sec. 6.4.2. However, the question arises *whether the cost and the complexity of the suggested solutions do not outweigh their potential benefits*. In fact, evaluating the FE

model of asperity flattening *at each integration step of the roll bite* in METALUB, as previously suggested, seems very costly, specifically, in consideration of the important number of tests in sensitivity analyses that are still required to calibrate the model (see Chap. 5). For instance, the roll bite is integrated about 1000 times in a classical METALUB computation in a few seconds altogether and a simple FE simulation of asperity flattening takes about 2 minutes. Hence, a coupled computation would take about $1000 \cdot 2/60 \approx 33$ hours, without considering the time for data exchanges between the solvers.

While Carretta's MPHL model [54, 55] and the SPH model are still valuable to better quantitatively characterize MPHL, *it seems more promising to integrate simpler models of this lubrication mechanism in METALUB* for the previous reasons. Such a model could possibly be the one by Lo and Wilson [201], which was introduced in the rolling models of Sutcliffe et al. [316] and Le and Sutcliffe [186] (see Sec. 2.2.4.3).

In particular, the following idea could be a first avenue of research: in METALUB, the relative contact area becomes almost constant, when the lubricant pressure converges to the interface pressure, i.e. when MPHL can be expected. Indeed, if $p_l \to p_i$, $H_a \to 0$ (by Eqs. 4.4 and 4.90), $E_p \to +\infty$ (by Eq. 4.92), $\partial h_t/\partial x \to 0$ (by Eq. N.286) and $\partial A/\partial x \to 0$ (by Eqs. N.263 and N.265). And in high-speed zones of the roll bite in the model, i.e. when $p_l = p_i$, any variation of the relative contact area A is essentially due to a variation of the strip speed v_s according to the volume conservation in Eq. (4.239) and $A = A(h_t)$ (by Eqs. N.373 and N.374). ***Instead of computing the relative contact area A as a function of the mean film thickness h_t in the high-speed zones, it could be decreased, when values that favor MPHL increase, in order to model this mechanism***. An example of such a value is the following ratio by Ahmed and Sutcliffe [6], which quantifies the oil volume drawn out of a surface pocket with respect to the initial pocket volume:

$$\Lambda_m = \frac{6\,\eta_0\,\gamma_l\,(v_r - v_{\text{in}})\,x_{rs}^*}{\delta^2\left[\exp\left(-\gamma_l\sigma_Y^0/2\right) - \exp\left(-3\gamma_l\sigma_Y^0/2\right)\right]} \tag{8.1}$$

where η_0 is the dynamic viscosity in the reference state, γ_l the pressure coefficient in the Barus equation (Eq. 4.192), v_r the rolling speed, v_{in} the speed of the strip at the entry of the bite, δ the depth of the surface pocket and σ_Y^0 the initial yield stress of the strip. The sliding distance x_{rs}^* between the roll and the strip at the end of the bite is the distance between two material points, one on the roll and one on the strip, which were located at the same x-position at the entry of the bite, at the end of the bite.

Instead of computing the relative contact area by Eq. (N.374), but on the basis of the previous relation, MPHL could possibly be modeled in METALUB by integrating the following equation along the roll bite, *starting at the transition from the low-speed to the high-speed equations*:

$$\frac{\partial A}{\partial x} = -\frac{\beta_m\,\eta_0\,\gamma_l\,(v_r - v_s)^2}{R_q^2\,v_r\left[\exp\left(-\gamma_l\sigma_Y^0/2\right) - \exp\left(-3\gamma_l\sigma_Y^0/2\right)\right]} \quad \text{with} \quad \gamma_l = \frac{1}{\eta_0}\left.\frac{\partial\eta}{\partial p_l}\right|_{p_l=0} \tag{8.2}$$

where β_m is the non-dimensional MPHL factor that has to be adjusted by experimental data and R_q the composite root-mean-square roughness of the rolls and the strip. The previous differential

equation was derived from Eq. (8.1) by imposing that the outflow of the lubricant from a surface pocket results in a reduction of the relative contact area, i.e.

$$\frac{\partial A}{\partial x} = -\frac{\partial \Lambda_m}{\partial x}, \tag{8.3}$$

and by taking only the derivative of x_{rs} in Λ_m, since the sliding distance between the roll and the strip increases (in general) along the roll bite, while the other variables in Λ_m are assumed to be constant. This derivative can be computed by considering the coordinates of two material points at time t, one on the roll and the other on the strip, which are located at the same x-position, when the lubricant pressure becomes equal to the pressure on top of the asperities ($t = 0$), i.e. at the high-speed transition, since MPH lubrication then seems to become possible:

$$x_{rs}(t) = x_r(t) - x_s(t) = \int_0^t \left[v_r - v_s(t_r)\right] \, \mathrm{d}t_r \tag{8.4}$$

where v_r is assumed to be constant along the roll bite due to its small length with respect to the radius of the roll. The previous integral can be written as a function of $x = v_r\, t + x_0$, so that the derivative of the sliding distance is the following one:

$$x_{rs}(x) = \int_{x_0}^{x} \left[\frac{v_r - v_s(x_r)}{v_r}\right] \mathrm{d}x_r \qquad \Rightarrow \qquad \frac{\partial x_{rs}}{\partial x} = \frac{v_r - v_s(x)}{v_r} \tag{8.5}$$

Moreover, the strip speed at the entry v_{in} in Eq. (8.1) was replaced by the local strip speed v_s in Eq. (8.2) since it seems more consistent that the outflow of the lubricant pocket depends on the local sliding speed than on the sliding speed at the entry of the bite. The derivative of v_s was, however, not computed to not excessively complicate the model.

This model is expected to be *promising* since it reduces the relative contact area and thus, friction, when the lubricant pressure becomes equal to the contact pressure at the asperity tops, when the thickness reduction increases (via the sliding speed), when the rolling speed increases (also via the sliding speed) and when the viscosity of the lubricant increases. All these influences were observed in the experimental data in Sec. 3.2.4.

Incorporation of a lubricant film formation model into Metalub

After the previous integration of thermal and MPHL models in Metalub, it is still necessary to compute the lubricant quantity that enters into the roll bite depending on the lubrication and operating conditions to ultimately minimize friction while preventing skidding. To date, e.g. in Sec. 5.4.2, the *lubricant film thickness at the entry of the roll bite is manually adjusted* in Metalub, when starvation occurs, so that the model is indeed not fully predictive.

Hence, a film formation model, which includes the plate-out and dynamic concentration mechanisms, should be incorporated into Metalub. In the past, a coupling procedure between Stephany's version of Metalub [305] and Cassarini's film formation model [63] was not successful [237]. The improvements of Metalub in terms of robustness in this thesis could potentially

render a coupling between a film formation model and METALUB possible via a sixth adjustment loop on top of METALUB's nested loop structure including the previous thermal model. It is, however, clear that this additional layer of complexity does not simplify the model, which is already highly sophisticated.

Extension of experimental data

In this thesis, *strain rate hardening* was for the first time introduced in the METALUB model (Sec. 5.4.3) because it was the most consistent explanation of some experimental observations. Since this material property was, however, not measured beforehand, its corresponding material parameter in the model had to be adjusted based on the rolling data, like the boundary coefficient of friction, the coefficient of thermal softening and the lubricant film thickness at the entry of the bite, in some cases.

When the number of unknown parameters becomes too important with respect to experimental results, their values can be wrongly adjusted, similar to unknowns in an underdetermined system of linear equations. In consequence, the model could return accurate predictions for the rolling scenarios, which were used to adjust the parameters, while the predictions could be wrong for other scenarios. To eliminate this risk, every parameter that can be measured by a simpler method than cold rolling, which combines numerous physical mechanisms, should be measured by this method.

Furthermore, the following extensions of the experimental data could be envisioned:

- Instead of characterizing the roughness only by the root-mean-square roughness, the half-spacing between asperities and the assumption that the Peklenik parameter is equal to 9, *3D surface topographies* could be measured. Hence, more realistic relations between the relative contact area and the mean film thickness could be computed by sampled height distribution functions. In addition, more accurate flow factors could be calculated by CFD based on these data.
- The lubricant viscosity was determined up to 800 MPa in the experimental data of this thesis as shown in Fig. 3.5, since the falling ball, which is used to measure the viscosity, gets stuck when the lubricant solidifies. *Higher pressures* are, however, expected to occur in the roll bite, e.g. in Fig. 5.7. Thus, the *viscosity should be measured at those pressures*, provided that this is possible and meaningful.
- Concerning the *lubrication and cooling systems*, flow rates, oil concentrations, oil droplet sizes, nozzle positions and any other factor that influences the oil supply to the roll bite and cooling should also be recorded to become input parameters of future thermal and lubricant film formation models.

Improvements of lubricated asperity flattening by SPH

As mentioned previously, although the significant computational overhead of FEM or SPH models impedes their usefulness in full models of lubricated cold rolling, as long as computing

technology is not decisively improved, they are still valuable to better understand, quantify and build simplified models of complex problems like lubricated asperity flattening. Specifically with regard to the SPH model of this problem in Chap. 7, the *most significant shortcomings are the boundary condition by the penalty method and the discretization with a uniform particle density*, which unnecessarily increases the number of particles and thus, the computation time.

First, a different formulation of the boundary condition could be introduced to possibly prevent lubricant particles from getting stuck at the solid/solid contact interface and from penetrating into the solid. In particular, the *boundary condition by Adami et al.* [1] seems to be a promising choice due to its successful application in recent FSI simulations by SPH [133, 378] and due to its versatility since it can be used between solid boundaries and fluids as well as between different fluids.

Secondly, before taking advantage of the strong parallel computation capabilities of LAMMPS, the calculation time can be reduced by decreasing the number of particles in a simulation. This is possible by *locally refining the SPH discretization at the beginning of the computation or even by adaptively refining it during the computation*. Adaptivity is actually one of the grand challenges of the international SPH community SPHERIC [299] and it was implemented in the context of solid deformations by Spreng et al. [301, 303], which suggests its application in lubricated asperity flattening simulations.

Bibliography

[1] S. Adami, X. Y. Hu, and N. A. Adams. A generalized wall boundary condition for smoothed particle hydrodynamics. *Journal of Computational Physics*, 231(21):7057–7075, 2012.

[2] R. A. Adams and C. Essex. *Calculus. A complete course*. Pearson, seventh edition, 2009.

[3] A. Adine. Contrainte d'écoulement: cas des aciers au titane et rephosphorés. Technical Report LAMEF.N.944, Irsid (Groupe Usinor, ArcelorMittal), 14/02/1991.

[4] A. Adine and R. Schwarz. Calcul de la contrainte d'écoulement en laminage à froid. Technical Report LAMEF 93 n 77, Irsid (Groupe Usinor, ArcelorMittal), 29/03/1993.

[5] X. Adriaens, A. Attipoe, S. Brialmont, G. Digregorio, J. Dular, and R. Hanus. Smoothed-particle hydrodynamic. MATH0471 - Multiphysics Integrated Computational Project, 2017.

[6] R. Ahmed and M. P. F. Sutcliffe. An experimental investigation of surface pit evolution during cold-rolling or drawing of stainless steel strip. *Journal of Tribology*, 123(1):1–7, 2001.

[7] J. M. Alexander. On the theory of rolling. *Proceedings of the Royal Society, Series A*, 326(1567):535–563, 1972.

[8] G. Amontons. De la resistance causée dans les machines. *Mémoires de l'Académie royale des sciences in Histoire de l'Académie royale des sciences*, pages 206–222, 1699.

[9] C. Antoci, M. Gallati, and S. Sibilla. Numerical simulation of fluid-structure interaction by SPH. *Computers & Structures*, 85(11–14):879–890, 2007.

[10] ArcelorMittal. A guide to the language of steel. https://corporate.arcelormittal.com/news-and-media/factfile/steel-terminology, 2019.

[11] J. F. Archard. Elastic deformation and the laws of friction. *Proceedings of the Royal Society, Series A*, 243(1233):190–205, 1957.

[12] A. Azushima. FEM analysis of hydrostatic pressure generated within lubricant entrapped into pocket on workpiece surface in upsetting process. *Journal of Tribology*, 122(4):822–827, 2000.

[13] A. Azushima. Chapter 5 - Direct observation of interface for tribology in metal forming. In J. G. Lenard, editor, *Metal Forming Science and Practice*. Elsevier Trade Monographs, 2002.

[14] A. Azushima. *Tribology in sheet rolling technology*. Springer, 2016.

[15] A. Azushima and H. Kudo. Direct observation of contact behaviour to interpret the pressure dependence of the coefficient of friction in sheet metal forming. *CIRP Annals*, 44(1):209–212, 1995.

[16] A. Azushima, M. Tsubouchi, H. Kudo, N. Furuta, and K. Minemura. Experimental confirmation of the micro-plasto-hydrodynamic lubrication mechanism at the interface between workpiece and forming die. *Journal of the Japan Society for Technology of Plasticity*, 30(347):1631–1638, 1989. In Japanese.

[17] A. Azushima, A. Yanagida, and S. Tani. Permeation of lubricant trapped within pocket into real contact area on the end surface of cylinder. *Journal of Tribology*, 133(1):011501–1–011501–6, 2011.

[18] S. Bair. A routine high-pressure viscometer for accurate measurements to 1 GPa. *Tribology Transactions*, 47(3):356–360, 2004.

[19] S. Bair. *High pressure rheology for quantitative elastohydrodynamics*. Elsevier Science, 2007.

[20] S. Bair, C. Mary, N. Bouscharain, and P. Vergne. An improved Yasutomi correlation for viscosity at high pressure. *Proceedings of the Institution of Mechanical Engineers, Part J: Journal of Engineering Tribology*, 227(9):1056–1060, 2013.

[21] C. Barus. Isothermals, isopiestics and isometrics relative to viscosity. *American Journal of Science*, 45(266):87–96, 1893.

[22] M. Basa, N. J. Quinlan, and M. Lastiwka. Robustness and accuracy of SPH formulations for viscous flow. *International Journal for Numerical Methods in Fluids*, 60(10):1127–1148, 2009.

[23] N. Bay, J. I. Bech, J. L. Andreasen, and I. Shimizu. Chapter 7 - Studies on micro plasto hydrodynamic lubrication in metal forming. In J. G. Lenard, editor, *Metal Forming Science and Practice*. Elsevier Trade Monographs, 2002.

[24] J. Bech, N. Bay, and M. Eriksen. Entrapement and escape of liquid lubricant in metal forming. *Wear*, 232(2):134–139, 1999.

[25] J. I. Bech. Lubrication mechanisms in metal forming. Master's thesis, Technical University of Denmark, 1997. In Danish.

[26] B. Becker and N. Legrand. Analyse expérimentale et numérique de la validité de l'essai rhéologique de bipoinçonnement à froid. Technical Report LAMEF n, LAF 267, Irsid (Groupe Usinor, ArcelorMittal), 25/08/2001.

[27] T. Belytschko, Y. Guo, W. K. Liu, and S. P. Xiao. A unified stability analysis of meshless particle methods. *International Journal for Numerical Methods in Engineering*, 48(9):1359–1400, 2000.

[28] T. Belytschko, Y. Krongauz, J. Dolbow, and C. Gerlach. On the completeness of meshfree particle methods. *International Journal for Numerical Methods in Engineering*, 43(5):785–819, 1998.

[29] T. Belytschko, W. K. Liu, B. Moran, and K. I. Elkhodary. *Nonlinear finite elements for continua and structures*. John Wiley & Sons, first edition, 2000.

[30] W. Benz and E. Asphaug. Simulations of brittle solids using smooth particle hydrodynamics. *Computer Physics Communications*, 87(1–2):253–265, 1995.

[31] B. Bhushan. *Introduction to tribology*. John Wiley & Sons, second edition, 2013.

[32] D. R. Bland and H. Ford. The calculation of roll force and torque in cold strip rolling with tensions. *Proceedings of the Institution of Mechanical Engineers*, 159(1):144–163, 1948.

[33] D. R. Bland and H. Ford. Cold rolling with strip tension, Part 3 - An approximate treatment of the elastic compression of the strip in cold rolling. *Journal of Iron and Steel Institute*, 171:245–249, 1952.

[34] N. Bockiau. Modélisation et étude des conditions de lubrification d'une cage de laminoir à froid. Technical report, Université de Liège, 2012.

[35] R. Boman. *Development of a tridimensional Arbitrary Lagrangian Eulerian formalism for dynamic implicit problems. Application to forming processes*. PhD thesis, Université de Liège, 2010. In French.

[36] R. Boman and J.-P. Ponthot. Numerical simulation of lubricated contact in rolling processes. *Journal of Material Processing Technology*, 125-126:405–411, 2002.

[37] R. Boman and J.-P. Ponthot. Finite element simulation of lubricated contact in rolling using the arbitrary Lagrangian-Eulerian formulation. *Computer Methods in Applied Mechanics and Engineering*, 193(39-41):4323–4353, 2004.

[38] J. Bonet and S. Kulasegaram. Remarks on tension instability of Eulerian and Lagrangian corrected smooth particle hydrodynamics (CSPH) methods. *International Journal for Numerical Methods in Engineering*, 52(11):1203–1220, 2001.

[39] J. Bonet and T.-S. L. Lok. Variational and momentum preservation aspects of Smooth Particle Hydrodynamic formulations. *Computer Methods in Applied Mechanics and Engineering*, 180(1–2):97–115, 1999.

[40] J. Bonet and R. D. Wood. *Nonlinear continuum mechanics for finite element analysis*. Cambridge university press, 1997.

[41] E. Botia-Vera, A. Souto-Iglesias, G. Bulian, and L. Lebovský. Three SPH novel benchmark test cases for free surface flows. In *5th ERCOFTAC SPHERIC workshop on SPH applications*, 2010.

[42] T. Bouache, N. Legrand, and P. Montmitonnet. A numerical heat transfer analysis in mixed film lubrication for cold strip rolling. In M. Steeper, editor, *5th European Rolling Conference*, London, 2009.

[43] N. Bouscharain and P. Vergne. Étude d'huiles de laminage sous hautes pressions. Technical report, Laboratoire de Mécanique des Contacts et des Structures, Institut Européen de Tribologie, INSA-Lyon, 2010.

[44] N. Bouscharain and P. Vergne. Comportement rhéologique d'huiles de laminage sous hautes pressions. Technical report, Laboratoire de Mécanique des Contacts et des Structures, Institut Européen de Tribologie, INSA-Lyon, 2013.

[45] F. P. Bowden and D. Tabor. The area of contact between stationary and moving surfaces. *Proceedings of the Royal Society, Series A*, 169(938):391–413, 1939.

[46] F. P. Bowden and D. Tabor. Mechanism of metallic friction. *Nature*, 150(3798):197–199, 1942.

[47] F. P. Bowden and D. Tabor. *The friction and lubrication of solids*. Oxford University Press, 1950.

[48] P. W. Bridgeman. The effect of hydrostatic pressure on the fracture of brittle substances. *Journal of Applied Physics*, 18(2):246–258, 1947.

[49] P. W. Bridgeman. *Studies in large plastic flow and fracture with special emphasis on the effects of hydrostatic pressure*. McGraw-Hill, 1952.

[50] L. Brookshaw. A method of calculating radiative heat diffusion in particle simulations. *Astronomical Society of Australia, Proceedings*, 6(2):207–210, 1985.

[51] BS EN 10111:2008. Continuously hot rolled low carbon steel sheet and strip for cold forming. Technical delivery conditions, 2008.

[52] BS EN 10130:2006. Cold rolled low carbon steel flat products for cold forming. Technical delivery conditions, 2006.

[53] R. L. Burden and J. D. Faires. *Numerical analysis*. Brooks/Cole, ninth edition, 2011.

[54] Y. Carretta. *Modélisation des conditions d'apparition du micro-hydrodynamisme via la méthode des éléments finis dans la perspective d'intégrer ce phénomène dans un modèle numérique de laminage à froid*. PhD thesis, Université de Liège, 2014. In French.

[55] Y. Carretta, J. Bech, N. Legrand, M. Laugier, J.-P. Ponthot, and R. Boman. Numerical modelling of micro-plasto-hydrodynamic lubrication in plane strip drawing. *Tribology International*, 110:378–391, 2017.

[56] Y. Carretta, R. Boman, N. Legrand, M. Laugier, and J.-P. Ponthot. Three-dimensional modelling of asperity crushing. In *Journées Annuelles de la SF2M 2012*, 2012.

[57] Y. Carretta, R. Boman, N. Legrand, M. Laugier, and J.-P. Ponthot. Numerical simulation of asperity crushing using boundary conditions encountered in cold-rolling. *Key Engineering Materials*, 554-557:850–857, 2013.

[58] Y. Carretta, R. Boman, A. Stephany, T. Bouache, R. Canivenc, P. Montmitonnet, N. Legrand, M. Laugier, and J.-P. Ponthot. Thermomechanical simulation of roll forming process based on the coupling of two independent solvers. In B. Schrefler, E. Oñate, and M. Papadrakakis, editors, *IV International Conference on Computational Methods for Coupled Problems in Science and Engineering*, Venice, Italy, 2011.

[59] Y. Carretta, R. Boman, A. Stephany, N. Legrand, M. Laugier, and J.-P. Ponthot. Metalub - A slab method software for the numerical simulation of mixed lubrication regime in cold strip rolling. *Proceedings of the Institution of Mechanical Engineers, Part J: Journal of Engineering Tribology*, 225(9):894–904, 2011.

[60] Y. Carretta, A. Hunter, R. Boman, J.-P. Ponthot, N. Legrand, M. Laugier, and R. Dwyer-Joyce. Ultrasonic roll bite measurements in cold rolling: Contact length and strip thickness. *Proceedings of the Institution of Mechanical Engineers, Part J: Journal of Engineering Tribology*, 232(2):179–192, 2018.

[61] Y. Carretta, N. Legrand, M. Laugier, and J.-P. Ponthot. Numerical simulation of asperity crushing - application to cold rolling. In G. Menary, editor, *Proceedings of ESAFORM*, Belfast, UK, 2011.

[62] Y. Carretta, A. Stephany, N. Legrand, M. Laugier, and J.-P. Ponthot. Metalub - A slab method software for the numerical simulation of mixed lubrication regime. Application to cold rolling. In E. Felder and P. Montmitonnet, editors, *Proceedings of the 4th International Conference on Tribology in Manufacturing Processes*, Nice, France, 2010.

[63] S. Cassarini. *Modélisation du film lubrifiant dans la zone d'entrée pour la lubrification par émulsion en laminage à froid*. PhD thesis, École Nationale Supérieure des Mines de Paris, 2007. In French.

[64] M. L. Cerquaglia. Contribution in bird impact numerical simulation on composite aircraft using SPH method. Master's thesis, Politecnico di Milano, 2013.

[65] M. L. Cerquaglia. *Development of a fully-partitioned PFEM-FEM approach for fluid-structure interaction problems characterized by free surfaces, large solid deformations, and strong added-mass effects*. PhD thesis, Université de Liège, 2019.

[66] M. L. Cerquaglia, G. Deliège, R. Boman, and J. P. Ponthot. The particle finite element method for the numerical simulation of bird strike. *International Journal of Impact Engineering*, 109:1–13, 2017.

[67] M. L. Cerquaglia, G. Deliège, R. Boman, V. Terrapon, and J.-P. Ponthot. Free-slip boundary conditions for simulating free-surface incompressible flows through the particle finite element method. *International Journal for Numerical Methods in Engineering*, 110(10):921–946, 2016.

[68] M. L. Cerquaglia, D. Thomas, R. Boman, V. Terrapon, and J.-P. Ponthot. A fully partitioned Lagrangian framework for FSI problems characterized by free surfaces, large solid deformations and displacements, and strong added-mass effects. *Computer Methods in Applied Mechanics and Engineering*, 348:409–442, 2019.

[69] J. Chakrabarty. *Theory of plasticity*. Butterworth-Heinemann, third edition, 2006.

[70] J. M. Challen and P. L. B. Oxley. An explanation of the different regimes of friction and wear using asperity deformation models. *Wear*, 53(2):229–243, 1979.

[71] J. M. Challen and P. L. B. Oxley. Slip-line fields for explaining the mechanis of polishing and related processes. *International Journal of Mechanical Sciences*, 26(6-8):403–418, 1984.

[72] D.-F. Chang, N. Marsault, and W. R. D. Wilson. Lubrication of strip rolling in the low-speed mixed regime. *Tribology Transactions*, 39(2):407–415, 1996.

[73] A. K. Chaniotis, D. Poulikakos, and P. Koumoutsakos. Remeshed smoothed particle hydrodynamics for the simulation of viscous and heat conducting flows. *Journal of Computational Physics*, 182(1):67–90, 2002.

[74] G. Chaussonnet, S. Braun, L. Wieth, R. Koch, and H.-J. Bauer. Influence of particle disorder and smoothing length on SPH operator accuracy. In *10th International SPHERIC Workshop*, Parma, Italy, 2015.

[75] K. J. Chen, E. J. Beraun, and J. C. Jih. An improvement for tensile instability in smoothed particle hydrodynamics. *Computational Mechanics*, 23(4):279–287, 1999.

[76] H. S. Cheng. Plastohydrodynamic lubrication. In F. Ling, et al., editor, *Friction and lubrication in metal processing*. ASME, New York, 1966.

[77] H. Christensen. Stochastic models for hydrodynamic lubrication of rough surfaces. *Proceedings of the Institution of Mechanical Engineers*, 184:1013–1022, 1970.

[78] J. Chung and G. M. Hulbert. A time integration algorithm for structural dynamics with improved numerical dissipation: the generalized-α method. *Journal of Applied Mechanics*, 60(2):371–375, 1993.

[79] P. W. Cleary. Modelling confined multi-material heat and mass flows using SPH. *Applied Mathematical Modelling*, 22(12):981–993, 1998.

[80] P. W. Cleary and J. J. Monaghan. Conduction modelling using smoothed particle hydrodynamics. *Computational Physics*, 148(1):227–264, 1999.

[81] P. W. Cleary, M. Prakash, R. Das, and J. Ha. Modelling of metal forging using SPH. *Applied Mathematical Modelling*, 36(8):3836–3855, 2012.

[82] P. W. Cleary, M. Prakash, J. Ha, N. Stokes, and C. Scott. Smoothed particle hydrodynamics: status and future potential. *Progress in Computational Fluid Dynamics*, 7(2-4):70–90, 2007.

[83] A. Colagrossi and M. Landrini. Numerical simulation of interfacial flows by smoothed particle hydrodynamics. *Computational Physics*, 191(2):448–475, 2003.

[84] P. Cosse and M. Economopoulos. Mathematical study of cold rolling. *C.N.R.M.*, 17:15–32, 1968.

[85] C. A. Coulomb. Théorie des machines simples, en ayant regard au frottement de leurs parties, et à la roideur des cordages. *Mem. Math. Phys. X*, pages 161–342, 1785.

[86] C. Counhaye. *Modélisation et contrôle industriel de la géométrie des aciers laminés à froid*. PhD thesis, Université de Liège, 2000.

[87] C. Counhaye. Contribution du frottement à la consommation d'énergie en laminage à froid. In French, 2012.

[88] R. Courant, K. Friedrichs, and H. Lewy. Über die partiellen Differenzengleichungen der mathematischen Physik. *Mathematische Annalen*, 100(1):32–74, 1928.

[89] T. Dbouk, P. Montmitonnet, and N. Legrand. Two-dimensional roll bite model with lubrication for cold strip rolling. *Advanced Materials Research*, 966-967:48–62, 2014.

[90] T. Dbouk, P. Montmitonnet, H. Matsumoto, N. Suzuki, Y. Takahama, N. Legrand, and T. Ngo. Advanced roll bite models for cold and temper rolling processes. In *9th International & 6th European Rolling Conference*, Venice, Italy, 2013.

[91] W. Dehnen and H. Aly. Improving convergence in smoothed particle hydrodynamics simulations without pairing instability. *Monthly Notices of the Royal Astronomical Society*, 425(2):1–15, 2012.

[92] L. Delorme, A. Colagrossi, A. Souto-Iglesias, R. Zamora-Rodriguez, and E. Botia-Vera. A set of canonical problems in sloshing, Part I: Pressure field in forced roll - comparison between experimental results and SPH. *Ocean Engineering*, 36(2):168–178, 2009.

[93] M. Desbrun and M. P. Gascuel. Smoothed particles: a new paradigm for animating highly deformable bodies. In *Proceedings of Eurographics Workshop on Computer Animation and Simulation*, 1996.

[94] J. Donéa, A. Huerta, J.-P. Ponthot, and A. Rodriguez-Ferran. *Encyclopedia of Computational Mechanics, Part 1. Fundamentals*, chapter 14: Arbitrary Lagrangian-Eulerian Methods, pages 413–437. E. Stein, R. de Borst and T. J. R. Hughes, 2004.

[95] L. Dubar, C. Hubert, P. Christiansen, N. Bay, and A. Dubois. Analysis of fluid lubrication mechanisms in metal forming at mescopic scale. *CIRP Annals*, 61(1):271–274, 2012.

[96] C. T. Dyka and R. P. Ingel. An approach for tension instability in smoothed particle hydrodynamics (SPH). *Computers & Structures*, 57(4):573–580, 1995.

[97] C. T. Dyka, P. W. Randles, and R. P. Ingel. Stress points for tension instability in SPH. *International Journal for Numerical Methods in Engineering*, 40(13):2325–2341, 1997.

[98] C. M. Edwards and J. Halling. An analysis of the plastic interaction of surface asperities and its relevance to the value of the coefficient of friction. *Journal of Mechanical Engineering Science*, 10(2):101–110, 1968.

[99] H. Ernst and M. E. Merchant. Surface friction of clean metals: a basic factor in the metal cutting process. In *Proc. of the Special Summer Conf., Friction and Surface Finish, MIT Press*, pages 76–101, 1940. See also a synopsis of this article in Merchant M.E., The mechanism of static friction. J. Appl. Phys. 11, 230. (doi:10.1063/1.1712761).

[100] European Union. Regulation (EC) No 443/2009 of the European Parliament and of the Council of 23 April 2009 setting emission performance standards for new passenger cars as part of the Community's integrated approach to reduce CO 2 emissions from light-duty vehicles. http://data.europa.eu/eli/reg/2009/443/2018-05-17.

[101] W. S. Farren and G. I. Taylor. The heat developed during plastic extension of metals. *Proceedings of the Royal Society, Series A*, 107(743):422–451, 1925.

[102] D. P. Flanagan and T. Belytschko. A uniform strain hexahedron and quadrilateral with orthogonal hourglass control. *International Journal for Numerical Methods in Engineering*, 17(5):679–706, 1981.

[103] O. Flebbe, S. Muenzel, H. Herold, H. Riffert, and H. Ruder. Smoothed particle hydrodynamics: hysical viscosity and the simulation of accretion disks. *Astrophysical Journal*, 431(2):754–760, 1994.

[104] N. A. Fleck and K. L. Johnson. Towards a new theory of cold rolling thin foil. *International Journal of Mechanical Sciences*, 29(7):507–524, 1987.

[105] N. A. Fleck, K. L. Johnson, M. E. Mear, and L. C. Zhang. Cold rolling of foil. *Proceedings of the Institution of Mechanical Engineers, Part B: Journal of Engineering Manufacture*, 206(2):119–131, 1992.

[106] B. Fogg. Preliminary study of the influence of stress and deformation in the substrate on junction growth and friction. *Proceedings of the Institution of Mechanical Engineers*, 182(Pt/3K):152–161, 1967.

[107] H. Ford, F. Ellis, and D. R. Bland. Cold rolling with strip tension, Part I. A new approximate method of calculation and a comparison with other methods. *Journal of the Iron and Steel Institute*, 168:57–72, 1951.

[108] D. Frenkel and B. Smit. *Understanding molecular simulation*. Academic Press, second edition, 2002.

[109] N. Fujita and Y. Kimura. Plate-out efficiency related to oil-in-water emulsions supply conditions on cold rolling strip. *Proceedings of the Institution of Mechanical Engineers, Part J: Journal of Engineering Tribology*, 227(5):413–422, 2012.

[110] N. Fujita, Y. Kimura, K. Kobayashi, K. Itoh, Y. Amanuma, and Y. Sodani. Dynamic control of lubrication characteristics in high speed tandem cold rolling. *Journal of Materials Processing Technology*, 229:407–416, 2016.

[111] J. P. Fürstenau, B. Avci, and P. Wriggers. A numerical review of multi-fluid SPH algorithms for high density ratios. In Y. Bazilevs and K. Takizawa, editors, *Advances in computational fluid-structure interaction and flow simulation. Modeling and simulation in science, engineering and technology*, pages 139–150, Birkhäuser, Cham, 2015. Springer.

[112] G. C. Ganzenmüller. An hourglass control algorithm for Lagrangian smooth particle hydrodynamics. *Computer Methods in Applied Mechanics and Engineering*, 286:87–106, 2015.

[113] G. C. Ganzenmüller. Smooth Mach Dynamics package for LAMMPS, Fraunhofer Ernst-Mach Institute for high-speed dynamics. https://lammps.sandia.gov/doc/PDF/SMD_LAMMPS_userguide.pdf, 2015. Version 0.12.

[114] C. W. Gear. *Numerical initial value problems in ordinary differential equations*. Prentice-Hall, 1971.

[115] R. A. Gingold and J. J. Monaghan. Smoothed particle hydrodynamics - Theory and applications to non-spherical stars. *Monthly Notices of the Royal Astronomical Society*, 181:375–389, 1977.

[116] J. W. Golten. *Analysis of cold rolling with particular reference to roll deformations*. PhD thesis, Swansea University, 1969.

[117] M. Gomez-Gesteira, B. D. Rogers, R. A. Dalrymple, and A. J. C. Crespo. State-of-the-art of classical SPH for free-surface flows. *Hydraulic Research*, 48(1):6–27, 2010.

[118] P. Gratacos, P. Montmitonnet, C. Fromholz, and J. L. Chenot. A plane-strain elastoplastic finite-element model for cold rolling of thin strip. *International Journal of Mechanical Sciences*, 34(3):195–210, 1992.

[119] J. P. Gray and J. J. Monaghan. Numerical modelling of stress fields and fracture around magma chambers. *Volcanology and Geothermal Research*, 135(3):259–283, 2004.

[120] J. P. Gray, J. J. Monaghan, and R. P. Swift. SPH elastic dynamics. *Computer Methods in Applied Mechanics and Engineering*, 190(49-50):6641–6662, 2001.

[121] A. P. Green. The plastic yielding of metal junctions due to combined shear and pressure. *Journal of the Mechanics and Physics of Solids*, 2(3):197–211, 1954.

[122] A. P. Green. Friction between unlubricated metals: a theoretical analysis of the junction model. *Proceedings of the Royal Society, Series A*, 228(1173):191–204, 1955.

[123] J. A. Greenwood. A note on Nayak's third paper. *Wear*, 262(1-2):225–227, 2007.

[124] J. A. Greenwood and G. W. Rowe. Deformation of surface asperities during bulk plastic flow. *Journal of Applied Physics*, 36:667–668, 1965.

[125] J. A. Greenwood and J. B. P. Williamson. Contact of nominally flat surfaces. *Proceedings of the Royal Society of London, Series A*, 295(1442):300–319, 1966.

[126] M. J. Grimble, M. A. Fuller, and G. F. Bryant. A non-circular arc roll force model for cold rolling. *International Journal for Numerical Methods in Engineering*, 12(4):643–663, 1978.

[127] G. Guennebaud, B. Jacob, et al. Eigen v3. http://eigen.tuxfamily.org, 2010.

[128] R. Guillaument. *Modélisation globale de l'alimentation d'une emprise lubrifiée par émulsion: simulation numérique directe et analyse physique des phénomènes*. PhD thesis, Université Bordeaux I, 2010. In French.

[129] R. Guillaument, S. Vincent, and J. P. Caltagirone. Plate-out modelling for cold-rolling systems lubricated with oil-in-water emulsions. *Proceedings of the Institution of Mechanical Engineers, Part J: Journal of Engineering Tribology*, 225(9):905–914, 2011.

[130] A. Hacquin. *Modélisation thermomécanique 3D du laminage: couplage bande - cylindre (3D thermomecanical modelling of rolling processes: strip/roll coupling)*. PhD thesis, École des Mines de Paris, 1996.

[131] A. Hacquin, P. Montmitonnet, and J.-P. Guillerault. A steady state thermo-elastoviscoplastic finite element model of rolling with coupled thermo-elastic roll deformation. *Journal of Materials Processing Technology*, 60(1-4):109–116, 1996.

[132] B. J. Hamrock, S. R. Schmid, and B. O. Jacobson. *Fundamentals of fluid film lubrication*. Marcel Dekker, Inc., 2004.

[133] L. Han and X. Hu. SPH modeling of fluid-structure interaction. *Journal of Hydrodynamics*, 30(1):62–69, 2018.

[134] W. B. Hardy and I. Doubleday. Boundary lubrication. The paraffin series. *Proceedings of the Royal Society, Series A*, 100(707):550–574, 1922.

[135] P. Hartley, I. Pillinger, and C. E. N. Sturgess. *Numerical modelling of material deformation*. Springer Verlag, 1992.

[136] C. Hermange. *Numerical simulation of the fluid-structure interactions inside the aquaplaning problem*. PhD thesis, Ecole Centrale de Nantes, 2017.

[137] C. Hermange, G. Oger, Y. Le Chenadec, and D. Le Touzé. A 3D SPH-FE coupling for FSI problems and its application to tire hydroplaning simulations on rough ground. *Computer Methods in Applied Mechanics and Engineering*, 355:558–590, 2019.

[138] H. Hertz. Über die Berührung fester elastischer Körper. *Journal für die reine und angewandte Mathematik*, 92:156–171, 1881.

[139] R. Hill. *The mathematical theory of plasticity*. Oxford University Press, Oxford, 1950.

[140] C. Hirsch. *Numerical computation of internal and external flows: The fundamentals of computational fluid dynamics*. Butterworth-Heineman, 2007.

[141] C. W. Hirt and B. D. Nichols. Volume of fluid (VOF) method for the dynamics of free boundaries. *Journal of Computational Physics*, 39(1):201–225, 1981.

[142] J. H. Hitchcock. Elastic deformation of rolls during cold-rolling. *Roll Neck Bearings. Report of A.S.M.E. Special Research Committee on Heavy-Duty Anti-friction Bearings*, pages 33–41, 1935.

[143] K. Hokkirigawa and K. Kato. An experimental and theoretical investigation of ploughing, cutting and wedge formation during abrasive wear. *Tribology International*, 21(1):51–57, 1988.

[144] J. Hol. *Multi-scale friction modeling for sheet metal forming*. PhD thesis, University of Twente, 2013.

[145] J. Hol, M. V. C. Alfaro, M. B. de Rooij, and T. Meinders. Advanced friction modeling for sheet metal forming. *Wear*, 286-287:66–78, 2012.

[146] J. Hol, V. T. Meinders, M. B. de Rooij, and A. H. van den Boogaard. Multi-scale friction modeling for sheet metal forming: The boundary lubrication regime. *Tribology International*, 81:112–128, 2015.

[147] J. Hol, V. T. Meinders, H. J. M. Geijselaers, and A. H. van den Boogaard. Multi-scale friction modeling for sheet metal forming: The mixed lubrication regime. *Tribology International*, 85:10–25, 2015.

[148] R. Holm. Über die auf die wirkliche Berührungsfläche bezogene Reibungskraft. Technical report, Forschungslaboratorium I der Siemens-Werke zu Siemensstadt, 1938. pp. 38-42. In German.

[149] C. Hubert, A. Dubois, L. Dubar, M. Laugier, N. Legrand, R. Boman, J.-P. Ponthot, and Y. Carretta. Complementary approaches for the numerical simulation of the micro-plasto-hydrodynamic lubrication regime. *Key Engineering Materials*, 651–653:492–497, 2015.

[150] A. K. Hunter. *Ultrasonic measurements of the strip thickness, lubricant film thickness, roll deflection and roll stress in the roll bite in the cold rolling of steel*. PhD thesis, The University of Sheffield, 2018.

[151] S. Hyun, L. Pei, J.-F. Molinari, and M. O. Robbins. Finite-element analysis of contact between elastic self-affine surfaces. *Physical Review E*, 70(2):026117, 2004.

[152] S. R. Idelsohn, J. Marti, A. Limache, and E. Oñate. Unified Lagrangian formulation for elastic solids and incompressible fluids: Application to fluid-structure interaction problem

via the PFEM. *Computer Methods in Applied Mechanics and Engineering*, 197(19-20):1762–1776, 2008.

[153] S. R. Idelsohn and E. Oñate. To mesh or not to mesh. That is the question... *Computer Methods in Applied Mechanics and Engineering*, 195(37–40):4681–4696, 2006.

[154] S. R. Idelsohn, E. Oñate, and F. D. Pin. A Lagrangian meshless finite element method applied to fluid-structure interaction problems. *Computers & Structures*, 81(8-11):655–671, 2003.

[155] S. R. Idelsohn, E. Oñate, and F. D. Pin. The particle finite element method: a powerful tool to solve incompressible flows with free-surfaces and breaking waves. *International Journal for Numerical Method in Engineering*, 61(7):964–989, 2004.

[156] P. J. in 't Veld, S. Plimpton, and G. S. Grest. Accurate and efficient methods for modeling colloidal mixtures in an explicit solvent using molecular dynamics. *Computer Physics Communications*, 179(5):320–329, 2008.

[157] M. R. I. Islam, A. Bansal, and C. Peng. Numerical simulation of metal machining process with Eulerian and total Lagrangian SPH. *Preprint*, 2019.

[158] P.-P. Jeunechamps. *Simulation numérique, à l'aide d'algorithmes thermomécaniques implicites, de matériaux endommageables pouvant subir de grandes vitesses de déformation*. PhD thesis, Université de Liège, 2008. In French.

[159] Z. Ji, M. Stanic, E. A. Hartono, and V. Chernoray. Numerical simulation of oil flow inside a gearbox by smoothed particle hydrodynamics (SPH) method. *Tribology International*, 127:47–58, 2018.

[160] G. R. Johnson and S. R. Beissel. Normalized smoothing functions for SPH impact computation. *International Journal for Numerical Methods in Engineering*, 39(16):2725–2741, 1996.

[161] G. R. Johnson and W. H. Cook. A constitutive model and data for metals subjected to large strains, high-strain rates and high-temperatures. *Proceedings of the 7th International Symposium on Ballistics*, pages 541–547, 1983.

[162] K. L. Johnson, J. A. Greenwood, and J. G. Higginson. The contact of elastic regular wavy surfaces. *International Journal of Mechanical Sciences*, 27(6):383–396, 1985.

[163] S. Jortner, J. F. Osterle, and C. F. Zorowski. An analysis of cold strip rolling. *International Journal of Mechanical Sciences*, 2:179–194, 1960.

[164] H. Keife and T. Jonsäter. Influence of rolling speed upon friction in cold rolling of foils. *Journal of Tribology*, 119(2):349–357, 1997.

[165] H. Keife and C. Sjögren. A friction model applied in the cold rolling of aluminum strips. *Wear*, 179(1-2):137–142, 1994.

[166] A. S. Khan and S. Huang. *Continuum theory of plasticity*. John Wiley & Sons, 1995.

[167] Y. Kimura, N. Fujita, Y. Matsubara, K. Kobayashi, Y. Amanuma, O. Yoshioka, and Y. Sodani. High-speed rolling by hybrid-lubrication system in tandem cold rolling mills. *Journal of Material Processing Technology*, 216:357–368, 2015.

[168] L. E. Kinsler, A. R. Frey, A. B. Coppens, and J. V. Sanders. *Fundamentals of acoustics*. John Wiley & Sons, 2000.

[169] D. A. Korzekwa, P. R. Dawson, and W. R. D. Wilson. Surface asperity deformation during sheet forming. *International Journal of Mechanical Sciences*, 34(7):521–539, 1992.

[170] P. B. Kosasih, A. K. Tieu, W. H. Li, and C. Lu. The effects of oil concentration and droplet diameter in oil-in-water emulsion on strip rolling. In *8th International Conference on Technology of Plasticity*, Verona, Italy, Oct. 2005. Paper 47.

[171] K. Krimpelstätter. *Non-circular arc temper rolling model considering radial and circumferential work roll displacements*. PhD thesis, Johannes Kepler Universität Linz, 2005.

[172] H. Kudo. A note on the role of microscopically trapped lubricant at the tool-work interface. *International Journal of Mechanical Sciences*, 7(5):383–388, 1965.

[173] P. K. Kundu and I. M. Cohen. *Fluid mechanics*. Elsevier, 2008.

[174] Y. A. Kuznetsov. Effect of fluid lubricant on the contact characteristics of rough elastic bodies in compression. *Wear*, 103(3):177–194, 1985.

[175] J. P. Kyle. *The rheology of nanoparticle additives: an investigation utilizing mesh free methods*. PhD thesis, Columbia University, 2014.

[176] J. P. Kyle and E. J. Terrell. Application of smoothed particle hydrodynamics to full-film lubrication. *Journal of Tribology*, 135(4):041705, 2013.

[177] L. D. Landau and E. M. Lifshitz. *Theory of elasticity*. Pergamon Press, second edition, 1970.

[178] M. Laugier. Flexible lubrication concept. The future of cold rolling lubrication. In *4th International Conference on Tribology in Manufacturing Processes (ICTMP)*, Nice, France, June 2010.

[179] M. Laugier. Numerical model of cold rolling lubricated with FL. 3rd generation of cold rolling model / tribology-lubrication. Meeting on February 13th, 2019.

[180] M. Laugier, R. Boman, N. Legrand, J.-P. Ponthot, M. Tornicelli, J. I. Bech, and Y. Carretta. Micro-plasto-hydrodynamic lubrication. A fundamental mechanism in cold rolling. *Advanced Materials Research*, 966-967:228–241, 2014.

[181] M. Laugier and G. Hauret. Cold rolling lubrication; state of the art and probable future. In *Proceedings of the 9th International and 4th European Steel Rolling Conference*, Paris, France, 2006.

[182] M. Laugier, M. Tornicelli, J. Cebey, L. Schiavone, D. Lopez Peris, A. Devolder, R. Guillard, and F. Kop. Flexible lubrication for controlling friction in cold rolling, crucial to be successful for AHSS challenge. In *Proceedings of the METEC and 2nd ESTAD*, Düsseldorf, Germany, 2015.

[183] M. Laugier, M. Tornicelli, C. S. Leligois, D. Bouquegneau, D. Launet, and J. A. Alvarez. Flexible lubrication concept. The future of cold rolling lubrication. *Proceedings of the Institution of Mechanical Engineers, Part J: Journal of Engineering Tribology*, 225(9):949–958, 2011.

[184] H. R. Le and M. P. F. Sutcliffe. A two-wavelength model of surface flattening in cold metal rolling with mixed lubrication. *Tribology Transactions*, 43(4):595–602, 2000.

[185] H. R. Le and M. P. F. Sutcliffe. A semi-empirical friction model for cold metal rolling. *Tribology Transactions*, 44(2):284–290, 2001.

[186] H. R. Le and M. P. F. Sutcliffe. Evolution of surface pits on stainless steel strip in cold rolling and strip drawing. *Journal of Tribology*, 125(2):384–390, 2003.

[187] H. R. Le and M. P. F. Sutcliffe. A multi-scale model for friction in cold rolling of aluminium alloy. *Tribology Letters*, 22(1):95–104, 2006.

[188] N. Legrand, D. Patrault, N. Labbe, D. Gade, D. Piesak, N. G. Jonsson, A. Nilsson, J. Horsky, T. Luks, P. Montmitonnet, R. Canivenc, R. D. Joyce, A. Hunter, C. Pinna, and L. Maurin. Advanced roll gap sensors for enhanced hot and cold rolling processes (rollgap sensors). Technical report, Research Fund for Coal and Steel, European Commission, 2015.

[189] S. Leroch, M. Varga, S. J. Eder, A. Vernes, M. R. Ripoll, and G. Ganzenmüller. Smooth particle hydrodynamics simulation of damage induced by a spherical indenter scratching a viscoplastic material. *International Journal of Solids and Structures*, 81:188–202, 2016.

[190] N. Letalleur. Génération de pression en régime hydrodynamique piézovisqueux dans une géométrie de type plateau-vallée. Private communication. In French, 1997.

[191] Z. Li, J. Leduc, J. Nunez-Ramirez, A. Combescure, and J.-C. Marongiu. A non-intrusive partitioned approach to couple smoothed particle hydrodynamics and finite element methods for transient fluid-structure interaction problems with large interface motion. *Computational Mechanics*, 55(4):697–718, 2015.

[192] L. D. Libersky and A. G. Petschek. Smooth particle hydrodynamics with strength of materials. In H. E.Trease, M. F. Fritts, and W. P. Crowley, editors, *Advances in the free-Lagrange method including contributions on adaptive gridding and the smooth particle hydrodynamics method: Proceedings of the next free-Lagrange conference held at Jackson Lake Lodge, Moran, WY, USA 3–7 June 1990*, pages 248–257, Berlin, Heidelberg, 1991. Springer Berlin Heidelberg.

[193] L. D. Libersky, A. G. Petschek, T. C. Carney, J. R. Hipp, and F. A. Allahdadi. High strain Lagrangian hydrodynamics: a three-dimensional SPH code for dynamic material response. *Journal of Computational Physics*, 109(1):67–75, 1993.

[194] H.-S. Lin, N. Marsault, and W. R. D. Wilson. A mixed lubrication model for cold strip rolling - Part I: Theoretical. *Tribology Transactions*, 41(3):317–326, 1998.

[195] D. Liu, A. Azushima, and T. Shima. Behavior of hydrostatic pressure of lubricant trapped in surface pocket on workpiece at upsetting process. *Journal of the Japan Society for Technology of Plasticity*, 34(394):1240–1245, 1993. In Japanese.

[196] G. R. Liu and M. B. Liu. *Smoothed Particle Hydrodynamics: a meshfree particle method*. World Scientific Publishing Co. Pte. Ltd., 2003.

[197] M. B. Liu and G. R. Liu. Restoring particle consistency in smoothed particle hydrodynamics. *Applied Numerical Mathematics*, 56(1):19–36, 2006.

[198] M. B. Liu and G. R. Liu. Smoothed particle hydrodynamics (SPH): an overview and recent developments. *Archives of Computational Methods in Engineering*, 17(1):25–76, 2010.

[199] Y. J. Liu, A. K. Tieu, D. D. Wang, and W. Y. D. Yuen. Friction measurement in cold rolling. *Journal of Material Processing Technology*, 111(1):142–145, 2001.

[200] S.-W. Lo. A study on flow phenomena in mixed lubrication regime by porous medium model. *Journal of Tribology*, 116(3):640–647, 1994.

[201] S.-W. Lo and W. R. D. Wilson. A theoretical model of micro-pool lubrication in metal forming. *Journal of Tribology*, 121(4):731–738, 1999.

[202] S.-W. Lo, T.-C. Yang, Y.-A. Cian, and K.-C. Huang. A model for lubrication by oil-in-water emulsions. *Journal of Tribology*, 132(1):011801–1–9, 2010.

[203] S.-W. Lo, T.-C. Yang, and H.-S. Lin. The lubricity of oil-in-water emulsion in cold strip rolling process under mixed lubrication. *Tribology International*, 66(1):125–133, 2013.

[204] S.-W. Lo, T.-C. Yang, Z.-M. Shih, and S.-C. Lin. Effects of surface roughening on asperity flattening. *Tribology Letters*, 35(1):67–75, 2009.

[205] LTAS-MN2L, University of Liège. Metafor, An object-oriented Finite Element code for the simulation of solids submitted to large deformations, commit messages. http://metafor.ltas.ulg.ac.be/dokuwiki/commit/start, 2019.

[206] C. Lu and A. K. Tieu. Measurement of the forward slip in cold strip rolling using a high speed digital camera. *Journal of Mechanical Science and Technology*, 21:1528–1533, 2007.

[207] L. B. Lucy. A numerical approach to testing of the fission hypothesis. *Astronomical Journal*, 82:1013–1024, 1977.

[208] P. Ludwik. *Elemente der Technologischen Mechanik*. Springer, Berlin, Heidelberg, 1909.

[209] B. Ma, A. K. Tieu, C. Lu, and Z. Jiang. A finite-element simulation of asperity flattening in metal forming. *Journal of Material Processing Technology*, 130-131:450–455, 2002.

[210] B. Ma, A. K. Tieu, C. Lu, and Z. Y. Jiang. Comparison of asperity flattening under different wavelength models for sheet metal forming. *Journal of Material Processing Technology*, 140(1-3):635–640, 2003.

[211] X. Ma, M. de Rooij, and D. Schipper. A load dependent friction model for fully plastic contact conditions. *Wear*, 269(11-12):790–796, 2010.

[212] A. Makinouchi, H. Ike, M. Murakawa, and N. Koga. A finite element analysis of flattening of surface asperities by perfectly lubricated rigid dies in metal working processes. *Wear*, 128(2):109–122, 1988.

[213] S. Marrone. *Enhanced SPH modeling of free-surface flows with large deformations*. PhD thesis, Università di Roma, 2011.

[214] S. Marrone, M. Antuono, A. Colagrossi, G. Colicchio, D. L. Touzé, and G. Graziani. δ-SPH model for simulating violent impact flows. *Computer Methods in Applied Mechanics and Engineering*, 200(13-16):1526–1542, 2011.

[215] N. Marsault. *Modélisation du régime de lubrification mixte en laminage à froid*. PhD thesis, École Nationale Supérieure des Mines de Paris, 1998. In French.

[216] J. Marti, S. Idelsohn, A. Limache, N. Calvo, and J. D'Elía. A fully coupled particle method for quasi incompressible fluid-hypoelastic structure interactions. *Mecánica Computacional*, 25:809–827, 2006.

[217] H. Matsumoto. Elastic-plastic theory of cold and temper rolling. In *8th International Conference on Technology of Plasticity*, Verona, Italy, 2005. Paper 359.

[218] H. Matsumoto and T. Shiraishi. Elastic-plastic theory of temper rolling with noncircular roll flattening. *Journal of the Japan Society for Technology of Plasticity*, 49(565):153–157, 2008. In Japanese.

[219] J. S. McFarlane and D. Tabor. Relation between friction and adhesion. *Proceedings of the Royal Society, Series A*, 202(1069):244–253, 1950.

[220] W. Meindl. *Walzenabplattung unter Berücksichtigung der Kontaktschubspannungen*. PhD thesis, Johannes Kepler Universität Linz, 2001. In German.

[221] P. L. Menezes, S. P. Ingole, M. Nosonovsky, S. V. Kailas, and M. R. Lovell. *Tribology for scientists and engineers*. Springer, 2013.

[222] T. Mizuno and M. Okamoto. Effects of lubricant viscosity at pressure and sliding velocity on lubrication conditions in the compression-friction test on sheet metals. *Journal of Lubrication Technology*, 104(1):53–59, 1982.

[223] J. J. Monaghan. An introduction to SPH. *Computer Physics Communications*, 48(1):89–96, 1988.

[224] J. J. Monaghan. Smoothed particle hydrodynamics. *Annual review of astronomy and astrophysics*, 30:543–574, 1992.

[225] J. J. Monaghan. Simulating free surface flows with SPH. *Journal of Computational Physics*, 110(2):399–406, 1994.

[226] J. J. Monaghan. SPH without a tensile instability. *Computational Physics*, 159(2):290–311, 2000.

[227] J. J. Monaghan. Smoothed particle hydrodynamics. *Reports on Progress in Physics*, 68:1703–1759, 2005.

[228] J. J. Monaghan. Smoothed particle hydrodynamics and its diverse applications. *Annual Review of Fluid Mechanics*, 44:323–346, 2012.

[229] J. J. Monaghan, R. A. Cas, A. M. Kos, and M. Hallworth. Gravity currents descending a ramp in a stratified tank. *Fluid Mechanics*, 379:39–69, 1999.

[230] J. J. Monaghan and R. A. Gingold. Shock simulation by the particle method SPH. *Journal of Computational Physics*, 52(2):374–389, 1983.

[231] P. Montmitonnet. Modélisation du contact lubrifié - exemple de la mise en forme des métaux. *Mécanique & Industries*, 1(6):621–637, 2000. In French.

[232] P. Montmitonnet. Plasto-hydrodynamic lubrication (PHD) - application of lubrication theory to metal forming processes. *Comptes Rendus de l'Académie des Sciences*, 2(5):729–737, 2001.

[233] P. Montmitonnet. Laminage: objectifs et modélisation. *Techniques de l'ingénieur*, M3065 v1, 2002. In French.

[234] P. Montmitonnet. Hot and cold strip rolling processes. *Computer Methods in Applied Mechanics and Engineering*, 195(48–49):6604–6625, 2006.

[235] P. Montmitonnet. Scientific approaches of metal forming processes: Chapter 10. Rolling processes. Lecture notes, 2009.

[236] P. Montmitonnet, L. Fourment, U. Ripert, Q. T. Ngo, and A. Ehrlacher. State of the art in rolling process modelling. *BHM, Berg- und Hüttenmännische Monatshefte*, 161(9):396–404, 2016.

[237] P. Montmitonnet, A. Stephany, S. Cassarini, J.-P. Ponthot, M. Laugier, and N. Legrand. Modelling of metal forming lubrication by O/W emulsions. In A. Azushima, editor, *Proceedings of the 3rd International Conference on Tribology in Manufacturing Processes*, Yokohama, Japan, 2007.

[238] P. Montmitonnet, E. Wey, F. Delamare, J.-L. Chenot, C. Fromholz, and M. de Vathaire. A mechanical model of cold rolling. Influence of the friction law on roll flattening calculated by a Finite Element Method. In *4th International Steel Rolling Conference*, Deauville, France, 1987.

[239] J. P. Morris. *Analysis of smoothed particle hydrodynamics with applications*. PhD thesis, Monash University, 1996.

[240] J. P. Morris. A study of the stability properties of smooth particle hydrodynamics. *Astronomical Society of Australia*, 13(1):97–102, 1996.

[241] J. P. Morris, P. J. Fox, and Y. Zhu. Modeling low Reynolds number incompressible flows using SPH. *Computational Physics*, 136(1):214–226, 1997.

[242] H. Muramoto, M. Matsumoto, T. Teshiba, F. Yanagishima, and Y. Yamada. Curtailment of the unit consumption of the rolling oil with hybrid system. *Tetsu-to-Hagane*, 68(5):S370, 1982. In Japanese.

[243] A. Nadai. The forces required for rolling steel strip under tension. *Journal of Applied Mechanics*, 6:A54–A62, 1939.

[244] P. R. Nayak. Random process model of rough surfaces in plastic contact. *Wear*, 26(3):305–333, 1973.

[245] T. Nellemann, N. Bay, and T. Wanheim. Real area of contact and friction stress - The role of trapped lubricant. *Wear*, 43(1):45–53, 1977.

[246] N. M. Newmark. A method of computation for structural dynamics. *Journal of the Engineering Mechanics Division*, 85(3):67–94, 1959.

[247] C. V. Nielsen and N. Bay. Overview of friction modelling in metal forming processes. *Procedia Engineering*, 207:2257–2262, 2017.

[248] C. V. Nielsen, P. A. F. Martins, and N. Bay. Modelling of real area of contact between tool and workpiece in metal forming processes including the influence of substance deformation. *CIRP Annals - Manufacturing Technology*, 65(1):261–264, 2016.

[249] L. Noels. *Contributions aux algorithmes d'intégration temporelle conservant l'énergie en dynamique*. PhD thesis, Université de Liège, 2004. In French.

[250] OECD. *Glossary of terms and definitions in the field of friction, wear and lubrication. Tribology*. Organisation for Economic Co-operation and Development. Research Group on Wear of Engineering Materials, 1969.

[251] OICA. 2017 production statistics by the International Organization of Motor Vehicle Manufacturers. http://www.oica.net/category/production-statistics/, 2019.

[252] E. Orowan. The calculation of roll pressure in hot and cold flat rolling. *Proceedings of the Institution of Mechanical Engineers*, 150(1):140–167, 1943.

[253] N. Patir and H. S. Cheng. An average flow model for determining effects of three-dimensional roughness on partial hydrodynamic lubrication. *Journal of Lubrication Technology*, 100(1):12–17, 1978.

[254] N. Patir and H. S. Cheng. Application of average flow model to lubrication between rough sliding surfaces. *Journal of Lubrication Technology*, 101(2):220–229, 1979.

[255] L. Pei, S. Hyun, J. F. Molinari, and M. O. Robbins. Finite element modeling of elasto-plastic contact between rough surfaces. *Journal of the Mechanics and Physics of Solids*, 53(11):2385–2409, 2005.

[256] J. Peklenik. New developments in surface characterization and measurements by means of random process analysis. *Proceedings of the Institution of Mechanical Engineers*, 182:108–126, 1967.

[257] S. Plimpton. Fast parallel algorithms for short-range molecular dynamics. *Journal of Computational Physics*, 117(1):1–19, 1995.

[258] J.-P. Ponthot. *Traitement unifié de la mécanique des milieux continus solides en grandes transformations par la méthode des éléments finis*. PhD thesis, Université de Liège, 1995. In French.

[259] J.-P. Ponthot. Unified stress update algorithms for the numerical simulation of large deformation elasto-plastic and elasto-viscoplastic processes. *International Journal of Plasticity*, 18(1):91–126, 2002.

[260] W. Prager and P. G. Hodge. *Theory of perfectly plastic solids*. John Wiley & Sons, 1951.

[261] J. Prescott. *Applied elasticity*. Dover Publications, 1946.

[262] W. H. Press, S. A. Teukolsky, W. T. Vetterling, and B. P. Flannery. *Numerical recipes. The art of scientific computing*. Cambridge University Press, third edition, 2007.

[263] D. J. Price. Smoothed particle hydrodynamics and magnetohydrodynamics. *Journal of Computational Physics*, 231(3):759–794, 2012.

[264] J. Pullen and J. B. P. Williamson. On the plastic contact of rough surfaces. *Proceedings of the Royal Society of London, Series A*, 327:159–173, 1972.

[265] Z. L. Qiu, W. Y. D. Yuen, and A. K. Tieu. Mixed-film lubrication theory and tension effects on metal rolling processes. *Journal of Tribology*, 121(4):908–915, 1999.

[266] T. Rabczuk, T. Belytschko, and S. P. Xiao. Stable particle methods based on Lagrangian kernels. *Computer Methods in Applied Mechanics and Engineering*, 193(12–14):1035–1063, 2004.

[267] E. Rabinowicz. *Friction and wear of materials*. John Wiley & Sons, Canada, second edition, 1995.

[268] A. Rafiee and K. P. Thiagarajan. An SPH projection method for simulating fluid-hypoelastic structure interaction. *Computer Method in Applied Mechanics and Engineering*, 198(33-36):2785–2795, 2009.

[269] P. W. Randles and L. D. Libersky. Smoothed particle hydrodynamics: some recent improvements and applications. *Computer Methods in Applied Mechanics and Engineering*, 139(1–4):375–408, 1996.

[270] P. W. Randles and L. D. Libersky. Normalized SPH with stress points. *International Journal for Numerical Methods in Engineering*, 48(10):1445–1462, 2000.

[271] R. Reich, N. Panseri, and J. Bohaychick. The effect of lubricant starvation in the cold rolling of aluminum metal when using an oil-in-water emulsion. *Lubrication Engineering*, 57(4):15–18, 2001.

[272] J. R. Reveles. *Development of a total Lagrangian SPH code for the simulation of solids under dynamic loading*. PhD thesis, Cranfield University, 2007.

[273] O. Reynolds. On the theory of lubrication and its applications to Mr. Beauchamp Tower's experiments, including an experimental determination of the viscosity of olive oil. *Philosophical Transactions of the Royal Society of London*, 177(1):157–234, 1886.

[274] D. Rittel, L. H. Zhang, and S. Osovski. The dependence of the Taylor-Quinney coefficient on the dynamic loading mode. *Journal of the Mechanics and Physics of Solids*, 107:96–114, 2017.

[275] W. L. Roberts. *Friction and lubrication in metal processing*. American Society of Mechanical Engineers, 1966.

[276] W. L. Roberts. *Cold rolling of steel*. Marcel Dekker, New York, 1978.

[277] M. Robinson. *Turbulence and viscous mixing using smoothed particle hydrodynamics*. PhD thesis, Monash University, 2009.

[278] C. J. A. Roelands. *Correlational aspects of the viscosity-temperature-pressure relationship of lubricating oils*. PhD thesis, Technische Hogeschool Delft, 1966.

[279] P. K. Saha and W. R. D. Wilson. Influence of plastic strain on friction in sheet metal forming. *Wear*, 172(2):167–173, 1994.

[280] T. Saito, K. Hamagami, T. Kaneko, K. Kawashima, K. Takezawa, and T. Chonan. Technologies of the highest speed rolling in the world at a cold tandem mill. *Revue de métallurgie*, 97(7-8):931–940, 2000.

[281] J. A. Schey. *Tribology in metalworking: friction, lubrication, and wear*. American Society for Metals, 1984.

[282] W. Schroeder, K. Martin, and B. Lorensen. *The visualization toolkit*. Kitware, fourth edition, 2006.

[283] M. C. Shaw, A. Ber, and P. A. Mamin. Friction characteristics of sliding surfaces undergoing subsurface plastic flow. *Journal of Basic Engineering*, 82(2):342–345, 1960.

[284] D. Shepard. A two-dimensional interpolation function for irregularly-spaced data. *Proceedings of the 1968 23rd ACM national conference*, pages 517–524, 1968.

[285] S. Sheu and W. R. D. Wilson. Mixed lubrication of strip rolling. *Tribology Transactions*, 37(3):483–493, 1994.

[286] Y. Shigaki, R. Nakhoul, and P. Montmitonnet. Numerical treatments of slipping/no-slip zones in cold rolling of thin sheets with heavy roll deformation. *Lubricants*, 3:113–131, 2015.

[287] I. Shimizu, J. L. Andreasen, J. I. Bech, and N. Bay. Influence of workpiece surface topography on the mechanisms of liquid lubrication in strip drawing. *Journal of Tribology*, 123(2):290–294, 2001.

[288] I. Shimizu, P. A. F. Martins, N. Bay, J. L. Andreasen, and J. I. Bech. Influences of lubricant pocket geometry and working conditions upon micro-lubrication mechanisms in upsetting and strip drawing. *International Journal of Surface Science and Engineering*, 4(1):42–54, 2010.

[289] T. Shiraishi, H. Yamamoto, J. Hashimoto, and T. Niitome. Characteristics of cold rolling in consideration of negative forward slip ratio. *Journal of the Japan Society for Technology of Plasticity*, 36(412):457–462, 1995.

[290] A. G. Shvarts and V. A. Yastrebov. Fluid flow across a wavy channel brought in contact. *Tribology International*, 126(1):116–126, 2018.

[291] A. G. Shvarts and V. A. Yastrebov. Trapped fluid in contact interface. *Journal of the Mechanics and Physics of Solids*, 119(1):140–162, 2018.

[292] R. D. Skeel, G. Zhang, and T. Schlick. A family of symplectic integrators: stability, accuracy, and molecular dynamics applications. *SIAM Journal on Scientific Computing*, 18(1):203–222, 1997.

[293] B. Solenthaler, J. Schläfli, and R. Pajarola. A unified particle model for fluid-solid interactions. *Computer Animation and Virtual Worlds*, 18(1):69–82, 2007.

[294] B. Song, A. Pazouki, and T. Pöschel. Instability of smoothed particle hydrodynamics applied to Poiseuille flows. *Computers & Mathematics with Applications*, 76(6):1447–1457, 2018.

[295] C. G. Sørensen, J. I. Bech, J. L. Andreasen, N. Bay, U. Engel, and T. Neudecker. A basic study of the influence of surface topography on mechanisms of liquid lubrication in metal forming. *CIRP Annals*, 48(1):203–208, 1999.

[296] A. Souto-Iglesias, E. Botia-Vera, and G. Bulian. Repeatability and two-dimensionality of model scale sloshing impacts. In *International Offshore and Polar Engineering Conference. The International Society of Offshore and Polar Engineers (ISOPE)*, June 2011.

[297] A. Souto-Iglesias, E. Botia-Vera, A. Martin, and F. Pérez-Arribas. A set of canonical problems in sloshing. Part 0: Experimental setup and data processing. *Ocean Engineering*, 38(16):1823–1830, 2011.

[298] SPHERIC. SPH codes. https://spheric-sph.org/sph-projects-and-codes, 2019.

[299] SPHERIC. SPH grand challenges. https://spheric-sph.org/grand-challenges, 2019.

[300] T. Spittel and M. Spittel. *Ferrous alloys*. Springer-Verlag Berlin Heidelberg, first edition, 2009.

[301] F. Spreng. *Smoothed particles hydrodynamics for ductile solids*. PhD thesis, Universität Stuttgart. Institut für Technische und Numerische Mechanik, 2017.

[302] F. Spreng and P. Eberhard. Machining process simulations with smoothed particle hydrodynamics. *Procedia CIRP*, 31:94–99, 2015.

[303] F. Spreng, D. Schnabel, A. Mueller, and P. Eberhard. A local adaptive discretization algorithm for smoothed particle hydrodynamics. *Computational Particle Mechanics*, 1:131–145, 2014.

[304] A. Stephany. Modèle semi-empirique de la lubrification en régime mixte pour le laminage à froid. Mémoire présenté pour le Diplôme d'études Approfondies (DEA) de troisième cycle en sciences appliquées. Technical report, Université de Liège, 2004. In French.

[305] A. Stephany. *Contribution à l'étude numérique de la lubrification en régime mixte en laminage à froid*. PhD thesis, Université de Liège, 2008. In French.

[306] A. Stephany, H. R. Le, and M. P. F. Sutcliffe. An efficient finite element model of surface pit reduction on stainless steel in metal forming processes. *Journal of Material Processing Technology*, 170(1-2):310–316, 2005.

[307] A. Stephany, J.-P. Ponthot, C. Collette, and J. Schelings. Efficient algorithmic approach for mixed-lubrication in cold rolling. *Journal of Materials Processing Technology*, 153–154:307–313, 2004.

[308] J. Stoer and R. Bulirsch. *Introduction to numerical analysis*. Springer, third edition, 2002.

[309] D. Sulsky, Z. Chen, and H. L. Schreyer. A particle method for history-dependent materials. *Computer Methods in Applied Mechanics and Engineering*, 118(1-2):179–196, 1994.

[310] P. N. Sun, A. Colagrossi, S. Marrone, M. Antuono, and A. M. Zhang. Multi-resolution Delta-plus-SPH with tensile instability control: Towards high Reynolds number flows. *Computer Physics Communications*, 224:63–80, 2018.

[311] M. P. F. Sutcliffe. Surface asperity deformation in metal forming processes. *International Journal of Mechanical Sciences*, 30(11):847–868, 1988.

[312] M. P. F. Sutcliffe. Experimental measurements of lubricant film thickness in cold strip rolling. *Proceedings of the Institution of Mechanical Engineers, Part B: Journal of Engineering Manufacture*, 204(4):263–273, 1990.

[313] M. P. F. Sutcliffe. Flattening of random rough surfaces in metal-forming processes. *Journal of Tribology*, 121(3):433–440, 1999.

[314] M. P. F. Sutcliffe. Chapter 4 - Surface finish and friction in cold metal rolling. In J. G. Lenard, editor, *Metal Forming Science and Practice*. Elsevier Trade Monographs, 2002.

[315] M. P. F. Sutcliffe and K. L. Johnson. Lubrication in cold strip rolling in the 'mixed' regime. *Proceedings of the Institution of Mechanical Engineers, Part B: Journal of Engineering Manufacture*, 204(4):249–261, 1990.

[316] M. P. F. Sutcliffe, H. R. Le, and R. Ahmed. Modeling of micro-pit evolution in rolling or strip-drawing. *Journal of Tribology*, 123(4):791–798, 2001.

[317] M. P. F. Sutcliffe and P. Montmitonnet. Numerical modelling of lubricated foil rolling. *Revue de Métallurgie*, 98(5):435–442, 2001.

[318] J. W. Swegle, D. L. Hicks, and S. W. Attaway. Smoothed particle hydrodynamics stability analysis. *Computational Physics*, 116(1):123–134, 1995.

[319] H. W. Swift. Length changes in metals under torsional overstrain. *Engineering*, 163:253–257, 1947.

[320] W. C. Swope, H. C. Andersen, P. H. Berens, and K. R. Wilson. A computer simulation method for the calculation of equilibrium constants for the formation of physical clusters of molecules: application to small water clusters. *The Journal of Chemical Physics*, 76(1):637–649, 1982.

[321] A. Z. Szeri. On the flow of emulsions in tribological contacts. *Wear*, 200(1-2):353–364, 1996.

[322] A. Z. Szeri. *Fluid film lubrication*. Cambridge University Press, 2011.

[323] P. E. Tabary, M. P. F. Sutcliffe, F. Porral, and P. Deneuville. Measurements of friction in cold metal rolling. *Journal of Tribology*, 118(3):629–636, 1996.

[324] D. Tabor. *The hardness of metals*. Oxford University Press, 1951.

[325] D. Tabor. Junction growth in metallic friction: The role of combined stresses and surface contamination. *Proceedings of the Royal Society of London, Series A*, 251:378–393, 1959.

[326] H. Takeda, S. M. Miyama, and M. Sekiya. Numerical simulation of viscous flow by smoothed particle hydrodynamics. *Progress of Theoretical Physics*, 92(5):939–960, 1994.

[327] G. I. Taylor and H. Quinney. The latent energy remaining in a metal after cold working. *Proceedings of the Royal Society, Series A*, 143(849):307–326, 1934.

[328] The Engineering ToolBox. Specific heat of liquids and fluids. https://www.engineeringtoolbox.com/specific-heat-fluids-d_151.html, 2019.

[329] A. K. Tieu, P. B. Kosasih, and A. Godbole. A thermal analysis of strip-rolling in mixed-film lubrication with O/W emulsions. *Tribology International*, 39(12):1591–1600, 2006.

[330] J. Tlusty, G. Chandra, S. Critchley, and D. Paton. Chatter in cold rolling. *CIRP Annals*, 31(1):195–199, 1982.

[331] J. H. Tripp. Surface roughness effects in hydrodynamic lubrication: The flow factor method. *Journal of Lubrication Technology*, 105(3):458–463, 1983.

[332] A. Troost and P. Köller. Extension of the elementary theory of elasto- and plastostatics in plane deformation. *Archiv für das Eisenhüttenwesen*, 42:325–334, 1972.

[333] Y. H. Tsao and L. B. Sargent Jr. A mixed lubrication model for cold rolling of metals. *ASLE Transactions*, 20(1):55–63, 1977.

[334] A. A. Tseng. Finite-difference solutions for heat transfer in a roll rotating at high speed. *Numerical Heat Transfer*, 7(1):113–125, 1984.

[335] A. A. Tseng. A generalized finite difference scheme for convection-dominated metal-forming. *International Journal for Numerical Methods in Engineering*, 20(10):1885–1900, 1984.

[336] A. A. Tseng. A numerical heat transfer analysis of strip rolling. *Journal of Heat Transfer*, 106(3):512–517, 1984.

[337] A. A. Tseng. Thermal modeling of roll and strip interface in rolling processes: Part 1 - review. *Numerical Heat Transfer*, 35(2):115–133, 1999.

[338] A. A. Tseng. Thermal modeling of roll and strip interface in rolling processes: Part 2 - simulation. *Numerical Heat Transfer*, 35(2):135–154, 1999.

[339] M. Varga, S. Leroch, S. J. Eder, and M. Rodriguez Ripoll. Meshless microscale simulation of wear mechanisms in scratch testing. *Wear*, 376-377(Part B):1122–1129, 2017.

[340] M. Varga, S. Leroch, H. Rojacz, and M. Rodriguez Ripoll. Study of wear mechanisms at high temperature scratch testing. *Wear*, 388–389:112–118, 2017.

[341] Y. Vidal, J. Bonet, and A. Huerta. Stabilized updated Lagrangian corrected SPH for explicit dynamic problems. *International Journal for Numerical Methods in Engineering*, 69(13):2687–2710, 2007.

[342] R. Vignjevic and J. Campbell. Review of development of the smooth particle hydrodynamics (SPH) method. In S. Hiermaier, editor, *Predictive Modeling of Dynamic Processes*, pages 367–396. Springer US, 2009.

[343] R. Vignjevic, J. Campbell, and L. Libersky. A treatment of zero-energy modes in the smoothed particle hydrodynamics method. *Computer Methods in Applied Mechanics and Engineering*, 184(1):67–85, 2000.

[344] R. Vignjevic, J. R. Reveles, and J. Campbell. SPH in a total Lagrangian formalism. *Computer Modeling in Engineering & Science*, 14(3):181–198, 2006.

[345] D. Violeau. *Fluid mechanics and the SPH method*. Oxford University Press, Oxford, 2012.

[346] D. Violeau and B. D. Rogers. Smoothed particle hydrodynamics (SPH) for free-surface flows: past, present and future. *Journal of Hydraulic Research*, 54(1):1–26, 2016.

[347] E. Voce. The relationship between stress and strain for homogeneous deformations. *Journal of the Institute of Metals*, 74:537–562, 1948.

[348] T. von Karman. Beitrag zur Theorie des Walzvorgangs. *Zeitschrift für Angewandte Mathematik und Mechanik*, 5(2):139–141, 1925.

[349] M. Vural, G. Ravichandran, and D. Rittel. Large strain mechanical behavior of 1018 cold-rolled steel over a wide range of strain rates. *Metallurgical and Materials Transactions A*, 34(12):2873–2885, 2003.

[350] P. Vyas. Effects of stochastic (random) surface roughness on hydrodynamic lubrication of deterministic asperity. Master's thesis, University of Kentucky, 2005.

[351] E. Walhorn, A. Kölke, B. Hübner, and D. Dinkler. Fluid-structure coupling within a monolithic model involving free surface flows. *Computers & Structures*, 83(25-26):2100–2111, 2005.

[352] T. Wanheim and N. Bay. A model for friction in metal forming processes. *CIRP Annals*, 27:189–194, 1978.

[353] T. Wanheim, N. Bay, and A. S. Peterson. A theoretically determined model for friction in metal working processes. *Wear*, 28(2):251–258, 1974.

[354] S. J. Watkins, A. S. Bhattal, N. Francis, J. A. Turner, and A. P. Whitworth. A new prescription for viscosity in smoothed particle hydrodynamics. *Astronomy & Astrophysics Supplement Series*, 119(1):177–187, 1996.

[355] A. B. Watts and H. Ford. An experimental investigation of the yield of strip between smooth dies. *Proceedings of the Institution of Mechanical Engineers, Part B: Journal of Engineering Manufacture*, 1(1-10):448–453, 1953.

[356] Y. Wen, D. L. Hicks, and J. W. Swegle. Stabilizing SPH with conservative smoothing. Technical Report SAND94-1932, Sandia, 1994.

[357] H. Wendland. Piecewise polynomial, positive definite and compactly supported radial functions of minimal degree. *Advances in Computational Mathematics*, 4(1):389–396, 1995.

[358] A. Westeneng. *Modelling of contact and friction in deep drawing processes*. PhD thesis, University of Twente, 2001.

[359] H. M. W. Westergaard. Bearing pressures and cracks. *Journal of Applied Mechanics*, 6:A49–A53, 1939.

[360] M. L. Williams, R. F. Landel, and J. D. Ferry. The temperature dependence of relaxation mechanisms in amorphous polymers and other glass-forming liquids. *Journal of the American Chemical Society*, 77(14):3701–3707, 1955.

[361] W. R. D. Wilson. Friction and lubrication in bulk metal-forming processes. *Journal of Applied Metalworking*, 1(1):7–19, 1978.

[362] W. R. D. Wilson. Friction models for metal forming in the boundary lubrication regime. *Journal of Engineering Materials and Technology*, 113(1):60–68, 1991.

[363] W. R. D. Wilson and D. Chang. Low speed mixed lubrication of bulk metal forming processes. *Journal of Tribology*, 118(1):83–89, 1996.

[364] W. R. D. Wilson and N. Marsault. Partial hydrodynamic lubrication with large fractional contact areas. *Journal of Tribology*, 120(1):16–20, 1998.

[365] W. R. D. Wilson, Y. Sakaguchi, and S. R. Schmid. A dynamic concentration model for lubrication with oil-in-water emulsions. *Wear*, 161(1-2):207–212, 1993.

[366] W. R. D. Wilson, Y. Sakaguchi, and S. R. Schmid. A mixed flow model for lubrication with emulsions. *Tribology Transactions*, 37(3):543–551, 1994.

[367] W. R. D. Wilson and S. Sheu. Real area of contact and boundary friction in metal forming. *International Journal of Mechanical Sciences*, 30(7):475–489, 1988.

[368] W. R. D. Wilson and J. A. Walowit. An isothermal hydrodynamic lubrication theory for strip rolling with front and back tension. *Proceedings of Tribology Convention, Douglas, Isle of Man, UK*, pages 164–172, 1971.

[369] F. S. Woods. *Advanced calculus: a course arranged with special reference to the needs of students of applied mathematics. 60. Differentiation of a definite integral*. Ginn and Company, new edition, 1934. pages 141–144.

[370] World Steel Association. Fact sheet. Advanced steel applications. Technical report, World Steel Association (https://www.worldsteel.org/en/dam/jcr:4864507f-7f52-446b-98d6-f0ac19da8c6d/fact_Advanced+steel+applications_2016.pdf), 2018.

[371] World Steel Association. Steel statistical yearbook 2018. Technical report, World Steel Association (https://www.worldsteel.org/en/dam/jcr:e5a8eda5-4b46-4892-856b-00908b5ab492/SSY_2018.pdf), 2018.

[372] P. Wriggers. *Computational contact mechanics*. Springer Verlag, second edition, 2006.

[373] P. Wriggers and P. Panagiotopoulos. *New developments in contact problems*. Springer Verlag Wien GmbH, 1999.

[374] C. Wu, L. Zhang, P. Qu, S. Li, and Z. Jiang. A multi-field analysis of hydrodynamic lubrication in high speed rolling of metals. *International Journal of Mechanical Sciences*, 142-143:468–479, 2018.

[375] S. Yasutomi, S. Bair, and W. O. Winer. An application of a free volume model to lubricant rheology I - Dependence of viscosity on temperature and pressure. *Journal of Tribology*, 106(2):291–302, 1984.

[376] I. S. Yun, W. R. D. Wilson, and K. F. Ehmann. Review of chatter studies in cold rolling. *International Journal of Machine Tools and Manufacture*, 38(12):1499–1530, 1998.

[377] H. Zahrouni. Projet ANR - PLATFORM: Maîtrise de la PLAnéité des Tôles métalliques FORmées par laMinage. Technical report, Agence nationale de la recherche, 2011.

[378] L. Zhan, C. Peng, B. Zhang, and W. Wu. A stabilized TL-WC SPH appoach with GPU acceleration for three-dimensional fluid-structure interaction. *Journal of Fluids and Structures*, 86:329–353, 2019.

[379] S. Zhang and J. G. Lenard. The effects of the reduction, speed and lubricant viscosity on friction in cold rolling. *Journal of Material Processing Technology*, 30(2):197–209, 1992.

[380] D. Zhu, G. Biresaw, S. J. Clark, and T. J. Kasun. Elastohydrodynamic lubrication with O/W emulsions. *Journal of Tribology*, 116(2):310–319, 1994.

[381] D. Zhu and Q. J. Wang. Elastohydrodynamic lubrication: A gateway to interfacial mechanics - Review and prospect. *Journal of Tribology*, 133(4), 2011.

[382] M. Zhu and M. H. Scott. Improved fractional step method for simulating fluid-structure interaction using the PFEM. *International Journal for Numerical Methods in Engineering*, 99(12):925–944, 2014.

University of Liège - School of Engineering
Department of Aerospace and Mechanical Engineering
Non-Linear Computational Mechanics - MN2L Research Group

Numerical Modeling of Friction in Lubricated Cold Rolling
-
Appendices

Dominik Boemer
M. Sc. Eng., Mechanical Engineer
FNRS Research Fellow

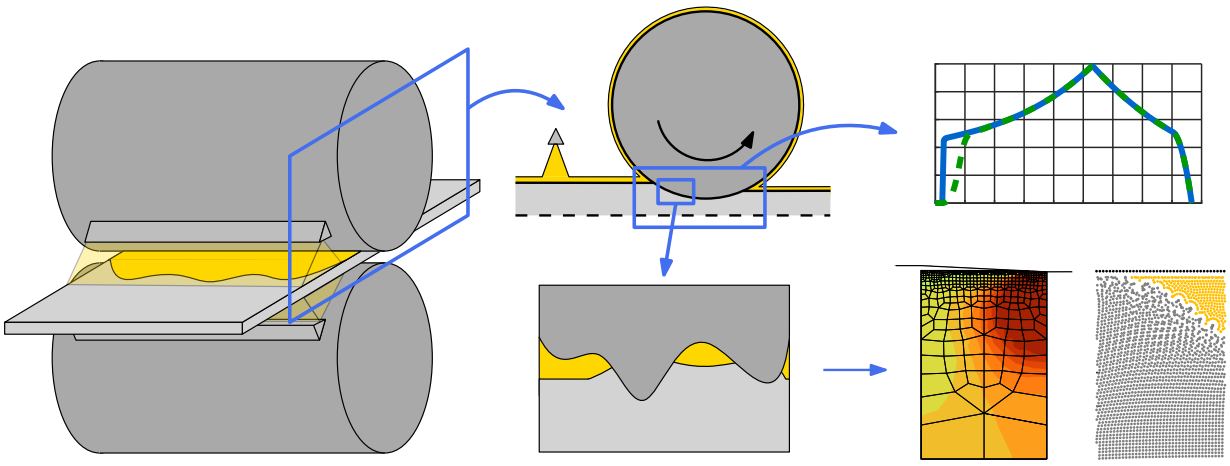

Thesis submitted in partial fulfillment of the requirements
for the Ph.D. Degree in Engineering Sciences and Technology
("Docteur en Sciences de l'Ingénieur et Technologie")

February 2020

First printing, February 2020

Appendix A

Proof of the triangular asperity height distribution function

In this section, the height distribution function $f_Z(z)$ of the triangular asperity profile in Fig. A.1 is derived.

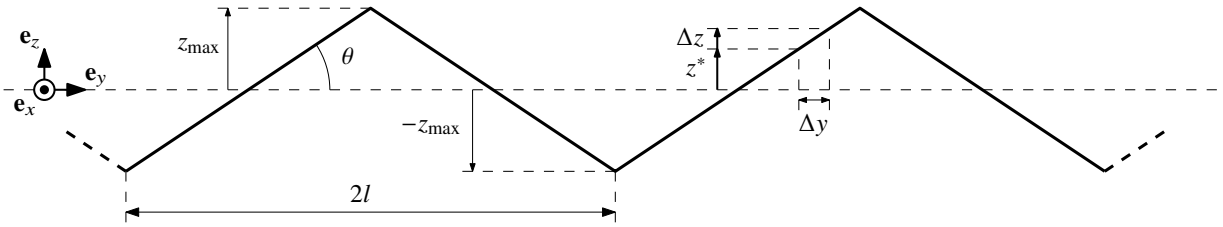

Figure A.1: Triangular asperity profile with an amplitude $2z_{\max}$ and a wavelength $2l$.

By the definition of the height distribution function, for an arbitrary value $z^* \in [-z_{\max}; z_{\max}]$,

$$\int_{z^*}^{z^*+\Delta z} f_Z(z)\, \mathrm{d}z = \Pr\left[z^* \leq Z < z^* + \Delta z\right] \tag{A.1}$$

For $\Delta z \to 0$, the integral can be approximated and the probability can be computed as follows (by taking into account only one tooth due to symmetry):

$$f_Z(z^*)\, \Delta z = \frac{2\Delta y}{2l} \tag{A.2}$$

Moreover, $z = y \tan\theta$ and $\tan\theta = 2z_{\max}/l$. Therefore, $\Delta z/\Delta y$ can be replaced by $2z_{\max}/l$ in the previous equation,

$$f(z^*) = \frac{1}{2z_{\max}} \tag{A.3}$$

This value can be written as a function of the root-mean-square roughness R_q. By definition (Eq. 2.9), if the reference line coincides with the mean line,

$$R_q^2 = \int_{-z_{\max}}^{z_{\max}} z^2 \, f_Z(z) \, \mathrm{d}z \tag{A.4}$$

$$= \frac{1}{2z_{\max}} \left[\frac{z^3}{3} \right]_{-z_{\max}}^{z_{\max}} \tag{A.5}$$

$$= \frac{z_{\max}^2}{3} \tag{A.6}$$

Accordingly, $z_{\max}$ can be replaced by $\sqrt{3}R_q$, which results in

$$f_Z(z) = \begin{cases} \dfrac{1}{2\sqrt{3}R_q} & \text{, if } z \in [-\sqrt{3}R_q; \sqrt{3}R_q] \\ 0 & \text{, otherwise.} \end{cases} \tag{A.7}$$

Appendix B

Proof of the composite RMS roughness formula

If Z is a random variable, which represents the composite roughness of the roll Z_r and the strip Z_s, the composite root-mean-square (RMS) roughness R_q can be written as a function of the RMS roughness of the roll $R_{q,r}$ and the strip $R_{q,s}$ based on the joined probability density function $f_{Z_r,Z_s}(z_r, z_s)$ of the composite roughness, which satisfies the following identities

$$\int_{-\infty}^{+\infty}\int_{-\infty}^{+\infty} f_{Z_r,Z_s}(z_r, z_s)\,\mathrm{d}z_r\,\mathrm{d}z_s = 1 \tag{B.1}$$

$$\int_{-\infty}^{+\infty} f_{Z_r,Z_s}(z_r, z_s)\,\mathrm{d}z_r = f_{Z_s}(z_s) \tag{B.2}$$

$$\int_{-\infty}^{+\infty} f_{Z_r,Z_s}(z_r, z_s)\,\mathrm{d}z_s = f_{Z_r}(z_r) \tag{B.3}$$

Hence, by definition of the RMS roughness (Eq. 2.9),

$$R_q^2 = \int_{-\infty}^{+\infty}\int_{-\infty}^{+\infty} (z_r + z_s)^2 f_{Z_r,Z_s}(z_r, z_s)\,\mathrm{d}z_r\,\mathrm{d}z_s \tag{B.4}$$

$$= \int_{-\infty}^{+\infty} z_r^2 f_{Z_r}(z_r)\,\mathrm{d}z_r + \int_{-\infty}^{+\infty} z_s^2 f_{Z_s}(z_s)\,\mathrm{d}z_s + 2\int_{-\infty}^{+\infty}\int_{-\infty}^{+\infty} z_r z_s f_{Z_r,Z_s}(z_r, z_s)\,\mathrm{d}z_r\,\mathrm{d}z_s \tag{B.5}$$

$$= R_{q,r}^2 + R_{q,s}^2 + 2\mathrm{cov}(Z_r, Z_s) \tag{B.6}$$

The last term in the previous equation is the covariance, which is zero, when both height profiles are uncorrelated.

Appendix C

Dry friction models

In this appendix, more advanced *dry friction models* than Coulomb's law with a constant coefficient of friction are shortly reviewed.

After the analysis of isolated asperity contacts by Green [121, 122] via the slip-line field theory and by Edwards and Halling [98] via the upper bound method, *slip-line fields* were developed for interacting asperities contacts by Wanheim et al. [353, 352]. Since their model quantified asperity flattening due to normal loading and shear stresses (Sec. 2.2.2.3), and since the resulting real contact area is assumed to be proportional to the friction force due to adhesion, it allowed to predict the friction force from low to high normal pressures (Fig. C.1). Their model did, however, not consider different *deformation modes* depending on the asperity angle, i.e. relatively flat asperities with weak adhesion simply rub against each other, while material is worn away by adhesion when this force is strong. When pointed asperities move, however, tangentially through a softer material, this material is cut away by abrasion. Scanning electron micrographs of these deformation modes were obtained by Hokkirigawa and Kato [143]. A model with different slip-line fields for each of these modes was developed by Challen and Oxley [70, 71] to compute the coefficient of friction (Fig. C.2).

Up to this point, the geometry of asperities was strongly simplified in friction models, although joining asperities form contact patches of various shapes in reality [123, 244]. Ma et al. [211] recently developed a method to approximate the asperity angle in the model by Challen and Oxley [70] via elliptical paraboloids for contact patches, that were determined by surface height matrices, i.e. matrices, which define the height at a position of a surface (Fig. C.3). Hence, it became possible to predict the friction force for arbitrarily shaped surfaces: asperity flattening models are used to compute the real contact areas, over which the friction forces, that were computed by the local coefficients of friction via the formula by Challen and Oxley [70], are integrated.

Finally, the most general model of dry friction to our knowledge was developed by Hol, who combined his asperity flattening model for arbitrary surfaces, which includes the three asperity flattening mechanisms and strain hardening (Sec. 2.2.2), initially, with a model by Westeneng

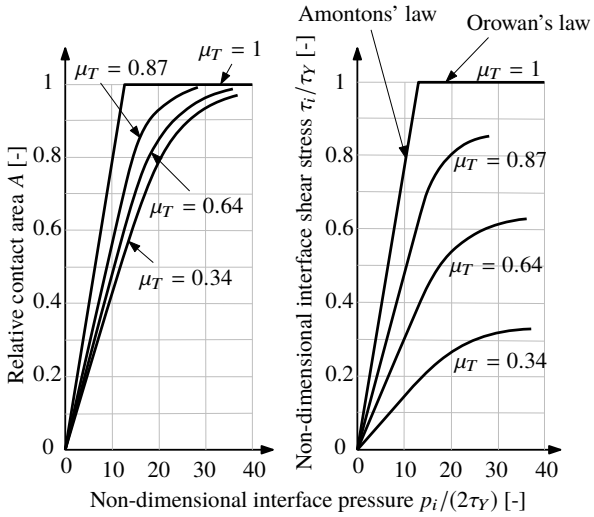

Figure C.1: Results of the slip-line field model by Wanheim et al. [353]. The relative contact area A increases with the normal interface pressure p_i and the friction factor $\mu_T = \tau_{Y,a}/\tau_Y$, where $\tau_{Y,a}$ and τ_Y are the shear strength of the solid interface due to adhesion, i.e. in the solid-solid contact zone, and the bulk shear yield stress, respectively. Since the relative contact area increases with the normal interface pressure p_i, the interface shear stress τ_i increases due to adhesion, too.

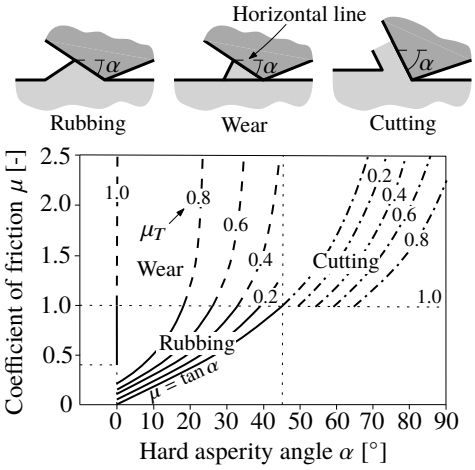

Figure C.2: Results of the slip-line field theory with different interaction scenarios by Challen and Oxley [70]. Based on the asperity angle α and the friction factor $\mu_T = \tau_{Y,a}/\tau_Y$, which characterizes the shear strength of the solid interface due to adhesion at the top of the asperities, i.e. at the contact, with respect the the bulk shear yield stress, an interaction scenario of asperities can be determined. The slip-line field of this interaction scenario then allows to compute the coefficient of friction depending on the angle and the friction factor.

[358] to compute the angle in the model by Challen and Oxley [70], and later, with the model by Ma et al. [211] as explained in Hol et al. [144, 145, 146].

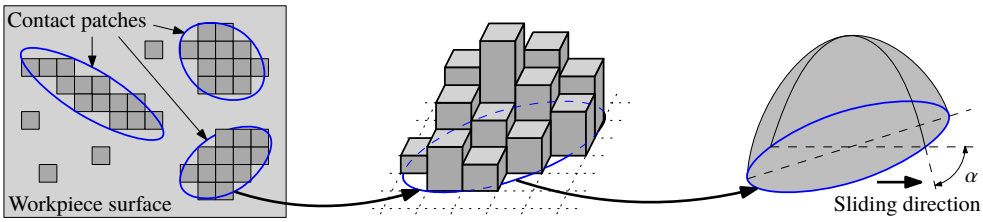

Figure C.3: Illustration of the connection between surface height matrices and the asperity angle α by Ma et al. [211], which is required in the friction model by Challen and Oxley [70], based on Fig. 2.7 in Hol [144]. Contact patches are identified via the surface height matrix of the workpiece surface. An equivalent paraboloid is then constructed by the shape of the contact patch and its volume. The angle in the friction model by Challen and Oxley [70] corresponds to the angle between the surface of the paraboloid and the horizontal plane in the sliding direction.

Appendix D

Proof of the formula by Wilson and Walowit

In this appendix, the formula of the lubricant film thickness by Wilson and Walowit [368] is proven based on explanations in the thesis by Marsault [215, p. 59] after deriving approximations of the length and the contact angle of the roll bite.

D.1 Length and contact angle of the roll bite

Fig. D.1 defines the rolling process of a strip with the initial and final thicknesses t_{in} and t_{out} by a rigid roll with the radius R_0. The length and the contact angle of the roll bite are denoted by the variables l_{rb} and α, respectively, while β_1 and β_2 are intermediate variables to define some angles as shown in this figure. Hence, the roll bite has the following length:

$$l_{\mathrm{rb}} = R_0 \sin\beta_1 + R_0 \sin\beta_2 \tag{D.1}$$

This formula can be simplified ($\beta_2 = 0$) since the elastic return after the position, where the rolls are closest to each other, is assumed to be negligible:

$$l_{\mathrm{rb}} \approx R_0\sqrt{1-\cos^2\beta_1} \approx R_0\sqrt{1-\left[\frac{R_0-(t_{\mathrm{in}}/2-t_{\mathrm{out}}/2)}{R_0}\right]^2} \approx \sqrt{R_0(t_{\mathrm{in}}-t_{\mathrm{out}})-\frac{(t_{\mathrm{in}}-t_{\mathrm{out}})^2}{4}} \tag{D.2}$$

This last equation can finally be simplified since the thickness of the strip is significantly smaller than the radius of the roll in cold rolling. Hence, the *length of the roll bite* l_{rb} can be approximated as follows:

$$l_{\mathrm{rb}} \approx \sqrt{R_0(t_{\mathrm{in}}-t_{\mathrm{out}})} \tag{D.3}$$

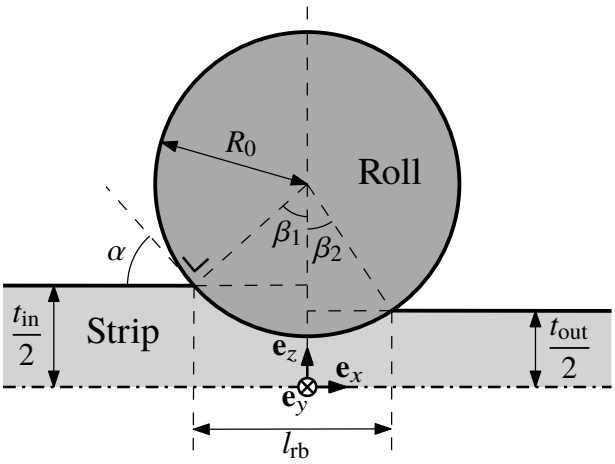

Figure D.1: Geometry of the roll bite to approximate the length l_{rb} and the contact angle α of the roll bite.

The angle at the entry of the roll bite can also be written as a function of R_0, t_{in} and t_{out}:

$$\tan\alpha = \tan\beta_1 = \frac{\sqrt{1-\cos^2\beta_1}}{\cos\beta_1} = \frac{\sqrt{1-\left[\frac{R_0-(t_{\text{in}}/2-t_{\text{out}}/2)}{R_0}\right]^2}}{\frac{R_0-(t_{\text{in}}/2-t_{\text{out}}/2)}{R_0}} = \frac{\sqrt{\frac{t_{\text{in}}-t_{\text{out}}}{R_0}-\left(\frac{t_{\text{in}}-t_{\text{out}}}{2R_0}\right)^2}}{\frac{R_0-(t_{\text{in}}/2-t_{\text{out}}/2)}{R_0}} \tag{D.4}$$

The previous equation can finally be simplified to obtain an approximation of the *contact angle of the roll bite* α since the thickness of the strip is negligible with respect to the radius of the roll:

$$\tan\alpha \approx \sqrt{\frac{t_{\text{in}}-t_{\text{out}}}{R_0}} \tag{D.5}$$

D.2 Lubricant film thickness

The lubricant film thickness $h_{l,\text{iw}}$ at the transition from the inlet to the work zone, i.e. where the strip starts to yield (Sec. 4.10.1), can be derived by integrating the Reynolds equation (Eq. 4.146), i.e.

$$\frac{\partial}{\partial x}\left(\frac{\rho h_l^3}{12\eta}\frac{\partial p_l}{\partial x}\right)+\frac{\partial}{\partial y}\left(\frac{\rho h_l^3}{12\eta}\frac{\partial p_l}{\partial y}\right)=\frac{\partial}{\partial x}\left(\rho h_l\frac{v_s+v_r}{2}\right)+\frac{\partial(\rho h_l)}{\partial t} \tag{D.6}$$

The Reynolds equations is first simplified by assuming that no pressure gradient exists along the transverse direction $\mathbf{e}_y$ due to symmetry, that the rolling process has reached the steady state and that the lubricant is incompressible:

$$\frac{\partial}{\partial x}\left(\frac{h_l^3}{12\eta}\frac{\partial p_l}{\partial x}-\frac{v_s+v_r}{2}h_l\right)=0 \tag{D.7}$$

This equation is then integrated along $\mathbf{e}_x$ and the constant of integration is determined by assuming that $p_l = \sigma_Y^0$ and $\partial p_l/\partial x = 0$ at the position $x = x_{\text{iw}}$ ($x_{\text{iw}} = x_{\text{wmls}}$ in Sec. 4.10.1), where the strip starts to yield and where $h_l = h_{l,\text{iw}}$:

$$\frac{h_l^3}{12\eta}\frac{\partial p_l}{\partial x} - \frac{v_s + v_r}{2}h_l = -\frac{v_{\text{in}} + v_r}{2}h_{l,\text{iw}} \tag{D.8}$$

Since the speed of the strip is assumed to not change significantly from the entry of the bite until it starts to yield because elastic deformations are small, the previous equation can be re-written:

$$\frac{\partial p_l}{\partial x} = 6\eta(v_{\text{in}} + v_r)\frac{h_l - h_{l,\text{iw}}}{h_l^3} \tag{D.9}$$

Furthermore, the lubricant film thickness at the entry of the bite can be linearly approximated and written as follows by Eqs. (D.3) and (D.5):

$$h_l = h_{l,\text{iw}} - \tan\alpha\,(x + l_{\text{rb}}) = h_{l,\text{iw}} - \frac{l_{\text{rb}}}{R_0}\,(x + l_{\text{rb}}) \tag{D.10}$$

By the chain rule and the previous equation, i.e. $\partial p_l/\partial x = (\partial p_l/\partial h_l)(\partial h_l/\partial x) = (\partial p_l/\partial h_l)(-l_{\text{rb}}/R_0)$, it is possible to re-write Eq. (D.9):

$$\frac{\partial p_l}{\partial h_l} = -6\eta(v_{\text{in}} + v_r)\frac{R_0}{l_{\text{rb}}}\frac{h_l - h_{l,\text{iw}}}{h_l^3} \tag{D.11}$$

This equation can be integrated with the following boundary conditions, where the first condition is based on the *full-flooded lubrication assumption*,

$$\begin{cases} p_l = 0 & \text{when } h_l = +\infty \\ p_l = \sigma_Y^0 & \text{when } h_l = h_{l,\text{iw}} \end{cases} \tag{D.12}$$

and by replacing η either by η_0, if the lubricant is assumed to be isoviscous, or by $\eta_0 e^{\gamma_l p_l}$, if its piezoviscous behavior is modeled by the Barus equation (Eq. 4.192):

$$\int_0^{\sigma_Y^0}\frac{1}{\eta}\,\mathrm{d}p_l = \int_{+\infty}^{h_{l,\text{iw}}} -6(v_{\text{in}} + v_r)\frac{R_0}{l_{\text{rb}}}\left(\frac{1}{h_l^2} - \frac{h_{l,\text{iw}}}{h_l^3}\right)\mathrm{d}h_l \tag{D.13}$$

Hence, the previous integral provides an approximation of the *lubricant film thickness* in the bite, and more precisely, at the position *where the strip starts to yield*, respectively for an isoviscous lubricant and a piezoviscous lubricant described by the Barus equation:

$$h_{l,\text{iw}} = \frac{3\eta_0(v_{\text{in}} + v_r)R_0}{\sigma_Y^0\, l_{\text{rb}}} \qquad \text{or} \qquad h_{l,\text{iw}} = \frac{3\eta_0(v_{\text{in}} + v_r)\gamma_l R_0}{\left[1 - \exp\left(-\gamma_l\,\sigma_Y^0\right)\right] l_{\text{rb}}} \tag{D.14}$$

Appendix E

Experimental data

In this appendix, the detailed experimental data, which were measured in the context of the *roll gap sensors* project [188], are provided as explained in Chap. 3. Each of the following sections in this chapter corresponds to a test scenario, in which the influences of the *strip product*, the *lubrication* and the *mill operating conditions* are studied. Hence, the following section titles are based on the summarized data in Tab. 3.6. Some values were rounded in this table for brevity. Therefore, the values in the titles and those in the corresponding section may differ. The values in the following sections are the most precise ones. Each test scenario can be structured into 4 *components*: the coil, the roughness parameters, the lubrication and other measurements.

The *coil* is characterized by its number during the test campaign (as mentioned earlier), its full number in the ArcelorMittal database, its material (Sec. 3.1.2), its thickness and its width.

Only the *roughness* values of some coils have been measured (Tab. 3.4). Likewise, the roughness of the rolls is not measured after each pass (Tabs. 3.2a and 3.2b). For these reasons, the roughness parameters of a coil are assumed to be equal to those of a coil, which is made of the same material, which comes from the same production plant and for which the roughness parameters have been measured. Similarly, the roughness parameters of the rolls for a given test are assumed to be equal to those that were measured closest in time to this current test. To know which measurement was selected in a given test, the respective coil and the coil after which the roll roughness was measured are mentioned in the caption of the following tables about the roughness parameters. Furthermore, the measured roughness values cannot be directly introduced in the METALUB model (Chap. 4) and some conversions are required. First, the mean of the average roughness of the top $R_{a,r,t}$ and the bottom roll $R_{a,r,b}$ is computed to obtain the average roughness of the rolls $R_{a,r}$:

$$R_{a,r} = \frac{R_{a,r,t} + R_{a,r,b}}{2} \tag{E.1}$$

Then, the average roughness of the roll and the strip are transformed to the root-mean-square roughness by assuming that their asperity profiles are triangular or that they follow a Christensen

distribution, respectively:

$$R_{q,r/s} = \frac{2}{\sqrt{3}} R_{a,r/s} \text{ (triangular)} \qquad R_{q,r/s} = \frac{128}{105} R_{a,r/s} \text{ (Christensen)} \tag{E.2}$$

The conversion factor is determined in appendix F. Its is equal to $2/\sqrt{3} \approx 1.154$ for the triangular height distribution, while $128/105 \approx 1.219$ for the Christensen distribution, which is not significantly different from the first value. The composite root-mean-square roughness R_q of the roll and the strip is computed according to Eq. (2.14).

Besides the root-mean-square roughness, the Metalub model also requires the half spacing between the asperities. An estimation of this value can be derived from the peak counts of the rolls and the strip. First, the average peak count of the rolls is computed as follows:

$$R_{pc,r} = \frac{R_{pc,r,t} + R_{pc,r,b}}{2} \tag{E.3}$$

Then, the composite peak count of the roll and the strip is assumed to be equal to the following value:

$$R_{pc} = \frac{1}{R_{pc,r} + R_{pc,s}} \left(R_{pc,r}^2 + R_{pc,s}^2 \right) \tag{E.4}$$

This previous formula was chosen since, $R_{pc} = R_{pc,r}$, if $R_{pc,s} = 0$, and $R_{pc} = (R_{pc,r} + R_{pc,s})/2$, if $R_{pc,r} = R_{pc,s}$. The half spacing between asperities is then equal to:

$$\bar{l} = \frac{1}{2R_{pc}} \tag{E.5}$$

Other measurements, like the rolling speed, the elongation or the back tension, were extracted at characteristic points in time from data files, which were recorded during the test campaign. Checking whether the system is in a steady state was done based on the figures of the rolling speed, outlet thickness, back tension, front tension, rolling force per width and forward slip as a function of time. This evaluation is subjective and debatable in a lot of cases. Nevertheless, it was tried to be as objective as possible.

As mentioned in Sec. 3.1.4, some measurements are converted to more easily comparable and useful values in the context of the Metalub model:

- The rolling speed is assumed to be equal to the average peripheral speed of the top and bottom rolls:

$$v_r = \frac{v_{r,t} + v_{r,b}}{2} \tag{E.6}$$

- The final strip thickness t_{out} can be deduced from the definition of the elongation e_x, the conservation of volume ($t_{\text{in}} l_{\text{in}} = t_{\text{out}} l_{\text{out}}$), and the initial thickness t_{in}:

$$e_x = \frac{l_{\text{out}} - l_{\text{in}}}{l_{\text{in}}} = \frac{t_{\text{in}} - t_{\text{out}}}{t_{\text{out}}} \quad \Rightarrow \quad t_{\text{out}} = \frac{t_{\text{in}}}{1 + e_x} \tag{E.7}$$

- The reduction ratio is defined as follows:

$$r = \frac{t_{\text{in}} - t_{\text{out}}}{t_{\text{in}}} \tag{E.8}$$

- The back and front tension stresses are deduced from the back and front tension loads:

$$\sigma_{\text{in}} = \frac{L_{\text{in}}}{t_{\text{in}} w_{\text{in}}} \qquad \sigma_{\text{out}} = \frac{L_{\text{out}}}{t_{\text{out}} w_{\text{out}}} \tag{E.9}$$

- The mean temperature in the roll bite $\overline{T}$ is assumed to be equal to the average of the entry and exit temperatures, which is obviously an assumption:

$$\overline{T} = \frac{T_{\text{in}} + T_{\text{out}}}{2} \tag{E.10}$$

- The rolling force per width $\overline{F}_r$ is obtained by dividing the rolling load L_r by the width of the strip w and converting the mass per unit length to a force per unit length:

$$\overline{F}_r = \frac{g\, L_r}{w} \tag{E.11}$$

  where $g = 9.81$ m/s^2 is the norm of the gravitational acceleration.

- The rolling torque per width (of the strip) $\overline{M}_r$ was computed by averaging the torque of both rolls (with sign correction due to different torque orientations) and dividing this average torque by the width of the strip.

E.1 Test 1 - S1/RE L2 2%/Rolling speed

- Coil: Tab. E.1
- Roughness: Tab. E.2
- Lubrication: recirculated emulsion with 1.95% L2 (50°C)
- Other measurements: Tab. E.3

Number	Material	t_{in} [mm]	w [mm]
1	S1	2.8	100

Table E.1: Test 1 - coil.

$R_{a,r,t}$	$R_{a,r,b}$	$R_{a,s}$	$R_{q,r}$ (T)	$R_{q,s}$ (T)	R_q (T)	$R_{q,r}$ (C)	$R_{q,s}$ (C)	R_q (C)	$R_{pc,r,t}$	$R_{pc,r,b}$	$R_{pc,s}$	R_{pc}	$\bar{l}$
μm	μm	μm	μm	μm	μm	μm	μm	μm	peaks/cm	peaks/cm	peaks/cm	peaks/cm	μm
0.618	0.614	1.505	0.711	1.738	1.878	0.751	1.835	1.982	89.0	103.0	75.0	86.8	57.61

Table E.2: Test 1 - roughness of rolls after coil 2 and of coil 2.

Steady	v_r	v_r	e_x	r	t_{out}	σ_{in}	σ_{out}	T_{in}	T_{out}	$\overline{T}$	$\overline{F}_r$	L_r	s_f	$\overline{M}_r$	Data file
-	mm/s	m/min	%	%	mm	MPa	MPa	°C	°C	°C	N/mm	t	%	kN	-
No (t_{out})	6647	398.8	28.6	22.2	2.177	37.8	120.0	25	81	53	6939	70.7	4.61	22.2	2014-03-04_11.35.28
Almost (σ_{in})	4970	298.2	29.9	23.0	2.155	38.1	118.3	25	87	56	6972	71.1	4.66	23.5	
No (t_{out})	3297	197.8	27.2	21.4	2.201	39.5	116.5	25	76	50	6461	65.9	4.70	20.0	2014-03-04_11.46.21
Almost (σ_{out})	1633	98.0	31.1	23.7	2.135	37.5	117.7	25	81	53	6497	66.2	4.78	21.2	
Yes	794	47.6	29.8	23.0	2.157	37.4	117.1	25	71	48	6076	61.9	4.96	17.9	
Yes	375	22.5	29.9	23.0	2.155	44.6	118.8	25	50	38	5823	59.4	4.90	17.8	
Yes	377	22.6	29.5	22.8	2.162	44.7	117.1	25	54	39	5842	59.6	4.88	18.6	2014-03-04_13.35.44

Table E.3: Test 1 - other measurements.

E.2 Test 2 - S1/RE L2 2% + FL L3 20%/Rolling speed

- Coil: Tab. E.4
- Roughness: Tab. E.5
- Lubrication: recirculated emulsion with 1.95% L2 (50°C) and flexible lubrication by emulsion with 20% L3 (60°C)
- Other measurements: Tab. E.6

Number	Material	t_{in} [mm]	w [mm]
2	S1	2.8	100

Table E.4: Test 2 - coil.

$R_{a,r,t}$	$R_{a,r,b}$	$R_{a,s}$	$R_{q,r}$ (T)	$R_{q,s}$ (T)	R_q (T)	$R_{q,r}$ (C)	$R_{q,s}$ (C)	R_q (C)	$R_{pc,r,t}$	$R_{pc,r,b}$	$R_{pc,s}$	R_{pc}	$\bar{l}$
μm	μm	μm	μm	μm	μm	μm	μm	μm	peaks/cm	peaks/cm	peaks/cm	peaks/cm	μm
0.618	0.614	1.505	0.711	1.738	1.878	0.751	1.835	1.982	89.0	103.0	75.0	86.8	57.61

Table E.5: Test 2 - roughness of rolls after coil 2 and of coil 2.

Steady	v_r	v_r	e_x	r	t_{out}	σ_{in}	σ_{out}	T_{in}	T_{out}	$\overline{T}$	$\overline{F}_r$	L_r	s_f	$\overline{M}_r$	Data file
-	mm/s	m/min	%	%	mm	MPa	MPa	°C	°C	°C	N/mm	t	%	kN	-
No (t_{out})	6632	397.9	29.0	22.5	2.170	36.5	119.0	25	77	51	6769	69.0	3.26	21.3	2014-03-04_14.36.42
Yes	4964	297.8	30.4	23.3	2.148	36.9	119.6	25	79	52	6760	68.9	3.18	22.0	
Yes	3304	198.2	30.6	23.4	2.144	36.9	119.9	25	74	50	6662	67.9	3.38	21.5	
Yes	1623	97.4	30.3	23.3	2.148	37.4	117.9	25	69	47	6455	65.8	3.78	20.3	
Yes	794	47.6	29.8	23.0	2.156	37.1	117.7	25	58	42	6309	64.3	4.27	19.0	
Yes	373	22.4	29.7	22.9	2.159	44.4	116.5	25	42	34	6037	61.5	4.33	19.5	

Table E.6: Test 2 - other measurements.

E.3 Test 3 - S1/RE L2 0 - 2% + FL L3 0 - 20%/Lubrication

- Coil: Tab. E.7
- Roughness: Tab. E.8
- Lubrication:
  - recirculated emulsion with 1.95% L2 (50°C) and flexible lubrication by emulsion with 20% L3 (60°C)
  - recirculated emulsion with 1.95% L2 (50°C)
  - no lubrication
- Other measurements: Tab. E.9

Number	Material	t_{in} [mm]	w [mm]
3	S1	2.8	100

Table E.7: Test 3 - coil.

$R_{a,r,t}$	$R_{a,r,b}$	$R_{a,s}$	$R_{q,r}$ (T)	$R_{q,s}$ (T)	R_q (T)	$R_{q,r}$ (C)	$R_{q,s}$ (C)	R_q (C)	$R_{pc,r,t}$	$R_{pc,r,b}$	$R_{pc,s}$	R_{pc}	$\bar{l}$
μm	μm	μm	μm	μm	μm	μm	μm	μm	peaks/cm	peaks/cm	peaks/cm	peaks/cm	μm
0.618	0.614	1.505	0.711	1.738	1.878	0.751	1.835	1.982	89.0	103.0	75.0	86.8	57.61

Table E.8: Test 3 - roughness of rolls after coil 2 and of coil 2.

Steady	v_r	v_r	e_x	r	t_{out}	σ_{in}	σ_{out}	T_{in}	T_{out}	$\overline{T}$	$\overline{F}_r$	L_r	s_f	$\overline{M}_r$	Data file
-	mm/s	m/min	%	%	mm	MPa	MPa	°C	°C	°C	N/mm	t	%	kN	-
Yes	4972	298.3	29.7	22.9	2.159	38.7	117.8	25	85	55	6704	68.3	3.28	22.3	
Yes	4974	298.4	29.9	23.0	2.155	37.1	118.2	25	82	53	6963	71.0	4.00	23.1	2014-03-04_17.35.57
Yes	4974	298.4	30.2	23.2	2.151	37.2	118.0	25	79	52	7137	72.8	3.97	24.3	

Table E.9: Test 3 - other measurements.

E.4 Test 4A - S2/RE L2 2%/Rolling speed

- Coil: Tab. E.10
- Roughness: Tab. E.11
- Lubrication: recirculated emulsion with 2.25% L2 (50°C)
- Other measurements: Tab. E.12

Number	Material	t_{in} [mm]	w [mm]
4	S2	0.75	75

Table E.10: Test 4A - coil.

$R_{a,r,t}$	$R_{a,r,b}$	$R_{a,s}$	$R_{q,r}$ (T)	$R_{q,s}$ (T)	R_q (T)	$R_{q,r}$ (C)	$R_{q,s}$ (C)	R_q (C)	$R_{pc,r,t}$	$R_{pc,r,b}$	$R_{pc,s}$	R_{pc}	$\bar{l}$
μm	μm	μm	μm	μm	μm	μm	μm	μm	peaks/cm	peaks/cm	peaks/cm	peaks/cm	μm
0.651	0.617	0.101	0.732	0.117	0.741	0.773	0.123	0.783	103.0	92.0	0.0	97.5	51.28

Table E.11: Test 4A - roughness of rolls after coil 5 and of coil 4.

Steady	v_r	v_r	e_x	r	t_{out}	σ_{in}	σ_{out}	T_{in}	T_{out}	$\overline{T}$	$\overline{F}_r$	L_r	s_f	$\overline{M}_r$	Data file
-	mm/s	m/min	%	%	mm	MPa	MPa	°C	°C	°C	N/mm	t	%	kN	-
Yes	8321	499.3	29.9	23.0	0.577	111.7	198.3	25	110	67	8928	68.3	6.43	19.0	
Yes	6651	399.1	29.8	23.0	0.578	116.8	192.7	25	108	66	8920	68.2	6.33	19.6	
Yes	4985	299.1	30.1	23.2	0.576	116.7	189.5	25	103	64	8885	67.9	6.50	19.5	
Yes	3297	197.8	29.8	23.0	0.578	114.7	189.9	25	90	58	8770	67.0	6.65	19.0	
Yes	1627	97.6	29.4	22.7	0.580	115.3	182.0	25	68	47	8859	67.7	6.72	18.9	2014-03-05_10.53.18
Yes	798	47.9	28.8	22.3	0.582	118.0	180.9	25	40	33	9442	72.2	7.19	19.4	
Yes	381	22.9	29.0	22.5	0.581	123.0	203.9	25	26	26	10227	78.2	8.15	20.3	
Yes	783	47.0	29.6	22.8	0.579	116.0	188.3	25	34	30	9555	73.0	7.50	19.9	
Yes	377	22.6	29.5	22.8	0.579	123.4	203.4	25	25	25	10259	78.4	8.38	20.5	

Table E.12: Test 4A - other measurements.

E.5 Test 4B - S2/RE L2 2% + FL L3 20%/Rolling speed

- Coil: Tab. E.13
- Roughness: Tab. E.14
- Lubrication: recirculated emulsion with 1.95% L2 (50°C) and flexible lubrication by emulsion with 20% L3 (60°C)
- Other measurements: Tab. E.15

Number	Material	t_{in} [mm]	w [mm]
4	S2	0.75	75

Table E.13: Test 4B - coil.

$R_{a,r,t}$	$R_{a,r,b}$	$R_{a,s}$	$R_{q,r}$ (T)	$R_{q,s}$ (T)	R_q (T)	$R_{q,r}$ (C)	$R_{q,s}$ (C)	R_q (C)	$R_{pc,r,t}$	$R_{pc,r,b}$	$R_{pc,s}$	R_{pc}	$\bar{l}$
μm	μm	μm	μm	μm	μm	μm	μm	μm	peaks/cm	peaks/cm	peaks/cm	peaks/cm	μm
0.651	0.617	0.101	0.732	0.117	0.741	0.773	0.123	0.783	103.0	92.0	0.0	97.5	51.28

Table E.14: Test 4B - roughness of rolls after coil 5 and of coil 4.

Steady	v_r	v_r	e_x	r	t_{out}	σ_{in}	σ_{out}	T_{in}	T_{out}	$\overline{T}$	$\overline{F}_r$	L_r	s_f	$\overline{M}_r$	Data file
-	mm/s	m/min	%	%	mm	MPa	MPa	°C	°C	°C	N/mm	t	%	kN	-
Yes	8317	499.0	30.3	23.2	0.576	114.6	191.0	25	109	67	7261	55.5	3.96	16.9	
Yes	6635	398.1	30.0	23.1	0.577	116.8	189.6	25	104	64	7281	55.7	4.22	16.7	
Yes	4974	298.4	29.5	22.8	0.579	114.1	188.0	25	99	62	7413	56.7	4.81	16.5	
Yes	3297	197.8	29.7	22.9	0.578	118.7	188.3	25	88	57	7693	58.8	5.40	17.3	2014-03-05_11.48.05
Yes	1625	97.5	29.7	22.9	0.578	119.0	181.7	25	75	50	8644	66.1	6.64	18.8	
Yes	785	47.1	29.7	22.9	0.578	118.0	184.9	25	43	34	9645	73.7	7.64	20.4	
Yes	373	22.4	29.8	23.0	0.578	121.6	199.0	25	30	28	10516	80.4	8.55	21.3	

Table E.15: Test 4B - other measurements.

E.6 Test 5A - S2/RE L2 2% + FL L3 0 - 20%/Lubrication

- Coil: Tab. E.16
- Roughness: Tab. E.17
- Lubrication:
  - recirculated emulsion with 2% L2 (50°C) and flexible lubrication by emulsion with 20% L3 (60°C)
  - recirculated emulsion with 2% L2 (50°C) and flexible lubrication by emulsion with 5% L3 (60°C)
  - recirculated emulsion with 2% L2 (50°C)
  - recirculated emulsion with 2% L2 (50°C) and flexible lubrication by emulsion with 20% L3 (60°C)
- Other measurements: Tab. E.18

Number	Material	t_{in} [mm]	w [mm]
5	S2	0.75	75

Table E.16: Test 5A - coil.

$R_{a,r,t}$	$R_{a,r,b}$	$R_{a,s}$	$R_{q,r}$ (T)	$R_{q,s}$ (T)	R_q (T)	$R_{q,r}$ (C)	$R_{q,s}$ (C)	R_q (C)	$R_{pc,r,t}$	$R_{pc,r,b}$	$R_{pc,s}$	R_{pc}	$\bar{l}$
μm	μm	μm	μm	μm	μm	μm	μm	μm	peaks/cm	peaks/cm	peaks/cm	peaks/cm	μm
0.651	0.617	0.101	0.732	0.117	0.741	0.773	0.123	0.783	103.0	92.0	0.0	97.5	51.28

Table E.17: Test 5A - roughness of rolls after coil 5 and of coil 4.

Steady	v_r	v_r	e_x	r	t_{out}	σ_{in}	σ_{out}	T_{in}	T_{out}	$\overline{T}$	$\overline{F}_r$	L_r	s_f	$\overline{M}_r$	Data file
-	mm/s	m/min	%	%	mm	MPa	MPa	°C	°C	°C	N/mm	t	%	kN	-
Yes	6641	398.4	29.9	23.0	0.577	114.3	185.9	25	108	67	7511	57.4	4.59	17.1	
Yes	6641	398.4	29.8	23.0	0.578	117.2	184.2	25	108	67	7845	60.0	5.01	17.6	2014-03-05_15.23.53
Yes	6643	398.6	29.8	23.0	0.578	115.8	184.7	25	111	68	8806	67.3	6.02	19.3	
Yes	377	22.6	29.6	22.8	0.579	120.9	206.4	25	28	27	10672	81.6	8.67	21.2	2014-03-05_15.34.12

Table E.18: Test 5A - other measurements.

E.7 Test 5B - S2/FL L3 100%/Rolling speed

- Coil: Tab. E.19
- Roughness: Tab. E.20
- Lubrication: flexible lubrication by pure L3 (60°C)
- Other measurements: Tab. E.21

Number	Material	t_{in} [mm]	w [mm]
5	S2	0.75	75

Table E.19: Test 5B - coil.

$R_{a,r,t}$	$R_{a,r,b}$	$R_{a,s}$	$R_{q,r}$ (T)	$R_{q,s}$ (T)	R_q (T)	$R_{q,r}$ (C)	$R_{q,s}$ (C)	R_q (C)	$R_{pc,r,t}$	$R_{pc,r,b}$	$R_{pc,s}$	R_{pc}	$\bar{l}$
μm	μm	μm	μm	μm	μm	μm	μm	μm	peaks/cm	peaks/cm	peaks/cm	peaks/cm	μm
0.651	0.617	0.101	0.732	0.117	0.741	0.773	0.123	0.783	103.0	92.0	0.0	97.5	51.28

Table E.20: Test 5B - roughness of rolls after coil 5 and of coil 4.

Steady	v_r	v_r	e_x	r	t_{out}	σ_{in}	σ_{out}	T_{in}	T_{out}	$\overline{T}$	$\overline{F}_r$	L_r	s_f	$\overline{M}_r$	Data file
-	mm/s	m/min	%	%	mm	MPa	MPa	°C	°C	°C	N/mm	t	%	kN	-
Yes	8303	498.2	30.0	23.1	0.577	113.2	189.0	25	111	68	7061	54.0	3.59	16.4	
Yes	6647	398.8	29.9	23.0	0.577	117.3	187.3	25	108	67	7172	54.8	3.97	16.6	
Yes	4964	297.8	29.3	22.7	0.580	116.7	185.3	25	104	65	7372	56.4	4.56	16.9	
Yes	3291	197.5	28.4	22.1	0.584	122.0	184.3	25	94	60	7655	58.5	5.31	17.0	2014-03-05_16.26.43
Yes	1633	98.0	29.5	22.8	0.579	119.6	180.0	25	82	54	8801	67.3	6.69	19.3	
Yes	794	47.6	29.5	22.8	0.579	117.4	183.0	25	63	44	9836	75.2	7.75	20.8	
Yes	375	22.5	29.7	22.9	0.578	120.5	199.9	26	40	33	10713	81.9	8.69	21.6	
Yes	371	22.2	30.1	23.2	0.576	120.2	198.0	25	53	39	10753	82.2	8.79	21.6	2014-03-05_17.44.35

Table E.21: Test 5B - other measurements.

E.8 Test 6 - S1/FL L3 100%/Rolling speed

- Coil: Tab. E.22
- Roughness: Tab. E.23
- Lubrication: flexible lubrication by pure L3 (60°C)
- Other measurements: Tab. E.24

Number	Material	t_{in} [mm]	w [mm]
6	S1	2.8	100

Table E.22: Test 6 - coil.

$R_{a,r,t}$	$R_{a,r,b}$	$R_{a,s}$	$R_{q,r}$ (T)	$R_{q,s}$ (T)	R_q (T)	$R_{q,r}$ (C)	$R_{q,s}$ (C)	R_q (C)	$R_{pc,r,t}$	$R_{pc,r,b}$	$R_{pc,s}$	R_{pc}	$\bar{l}$
μm	μm	μm	μm	μm	μm	μm	μm	μm	peaks/cm	peaks/cm	peaks/cm	peaks/cm	μm
0.651	0.617	1.505	0.732	1.738	1.886	0.773	1.835	1.991	103.0	92.0	75.0	87.7	57.00

Table E.23: Test 6 - roughness of rolls after coil 5 and of coil 2.

Steady	v_r	v_r	e_x	r	t_{out}	σ_{in}	σ_{out}	T_{in}	T_{out}	$\overline{T}$	$\overline{F}_r$	L_r	s_f	$\overline{M}_r$	Data file
-	mm/s	m/min	%	%	mm	MPa	MPa	°C	°C	°C	N/mm	t	%	kN	-
Yes	6643	398.6	29.7	22.9	2.158	37.4	119.9	25	86	56	6885	70.2	3.39	22.3	2014-03-06_11.01.26
Yes	4972	298.3	30.0	23.1	2.154	37.6	119.8	25	83	54	6816	69.5	3.39	22.1	
Yes	3297	197.8	30.5	23.4	2.146	36.6	120.3	25	80	53	6767	69.0	3.59	21.5	
Yes	1629	97.7	30.3	23.3	2.148	37.9	117.9	25	75	50	6566	66.9	3.73	20.8	
Yes	791	47.5	29.9	23.0	2.155	37.3	117.5	25	70	47	6361	64.8	4.24	19.0	
Yes	379	22.7	29.7	22.9	2.158	43.7	115.8	25	66	46	6138	62.6	4.29	19.6	
Yes	377	22.6	29.7	22.9	2.159	44.5	115.5	25	63	44	6115	62.3	4.32	19.7	2014-03-06_11.11.28

Table E.24: Test 6 - other measurements.

E.9 Test 7 - S1/FL L3 100%/Elongation

- Coil: Tab. E.25
- Roughness: Tab. E.26
- Lubrication: flexible lubrication by pure L3 (60°C)
- Other measurements: Tab. E.27

Number	Material	t_{in} [mm]	w [mm]
7	S1	2.8	100

Table E.25: Test 7 - coil.

$R_{a,r,t}$	$R_{a,r,b}$	$R_{a,s}$	$R_{q,r}$ (T)	$R_{q,s}$ (T)	R_q (T)	$R_{q,r}$ (C)	$R_{q,s}$ (C)	R_q (C)	$R_{pc,r,t}$	$R_{pc,r,b}$	$R_{pc,s}$	R_{pc}	$\bar{l}$
μm	μm	μm	μm	μm	μm	μm	μm	μm	peaks/cm	peaks/cm	peaks/cm	peaks/cm	μm
0.651	0.617	1.505	0.732	1.738	1.886	0.773	1.835	1.991	103.0	92.0	75.0	87.7	57.00

Table E.26: Test 7 - roughness of rolls after coil 5 and of coil 2.

Steady	v_r	v_r	e_x	r	t_{out}	σ_{in}	σ_{out}	T_{in}	T_{out}	$\overline{T}$	$\overline{F}_r$	L_r	s_f	$\overline{M}_r$	Data file
-	mm/s	m/min	%	%	mm	MPa	MPa	°C	°C	°C	N/mm	t	%	kN	-
Yes	1623	97.4	5.9	5.6	2.643	38.4	118.9	25	38	32	2513	25.6	4.86	-12.7	
Yes	1621	97.2	9.7	8.9	2.551	38.3	118.6	25	48	36	3506	35.7	4.99	-6.7	
Yes	1623	97.4	19.8	16.5	2.337	37.7	119.1	25	68	47	5308	54.1	4.68	7.7	2014-03-06_14.57.47
Yes	1625	97.5	29.9	23.0	2.155	37.5	118.4	25	85	55	6466	65.9	3.33	20.3	
Yes	1625	97.5	40.0	28.6	2.000	38.1	118.5	25	95	60	7277	74.2	2.47	30.5	
Yes	1621	97.2	5.1	4.9	2.663	38.7	119.3	25	32	29	2297	23.4	4.36	-13.9	

Table E.27: Test 7 - other measurements.

E.10 Test 8 - S2/FL L3 100%/Elongation

- Coil: Tab. E.28
- Roughness: Tab. E.29
- Lubrication: flexible lubrication by pure L3 (60°C)
- Other measurements: Tab. E.30

Number	Material	t_{in} [mm]	w [mm]
8	S2	0.75	75

Table E.28: Test 8 - coil.

$R_{a,r,t}$	$R_{a,r,b}$	$R_{a,s}$	$R_{q,r}$ (T)	$R_{q,s}$ (T)	R_q (T)	$R_{q,r}$ (C)	$R_{q,s}$ (C)	R_q (C)	$R_{pc,r,t}$	$R_{pc,r,b}$	$R_{pc,s}$	R_{pc}	$\bar{l}$
μm	μm	μm	μm	μm	μm	μm	μm	μm	peaks/cm	peaks/cm	peaks/cm	peaks/cm	μm
0.651	0.617	0.101	0.732	0.117	0.741	0.773	0.123	0.783	103.0	92.0	0.0	97.5	51.28

Table E.29: Test 8 - roughness of rolls after coil 5 and of coil 4.

Steady	v_r	v_r	e_x	r	t_{out}	σ_{in}	σ_{out}	T_{in}	T_{out}	$\overline{T}$	$\overline{F}_r$	L_r	s_f	$\overline{M}_r$	Data file
-	mm/s	m/min	%	%	mm	MPa	MPa	°C	°C	°C	N/mm	t	%	kN	-
Yes	1623	97.4	4.9	4.6	0.715	123.5	192.2	25	66	46	4539	32.4	1.65	1.0	
Yes	1625	97.5	10.2	9.3	0.681	124.0	192.8	25	82	54	5974	42.6	3.02	5.5	
Yes	1621	97.2	19.6	16.4	0.627	123.5	190.0	25	105	65	7817	55.8	4.95	13.1	2014-03-06_16.35.24
Yes	1623	97.4	29.7	22.9	0.578	124.2	188.6	25	125	75	9263	66.1	6.55	20.3	
Yes	1627	97.6	40.0	28.6	0.536	125.7	188.0	25	136	81	10460	74.6	7.75	26.7	

Table E.30: Test 8 - other measurements.

E.11 Test 9 - S3/FL L3 100%/Rolling speed

- Coil: Tab. E.31
- Roughness: Tab. E.32
- Lubrication: flexible lubrication by pure L3 (40°C)
- Other measurements: Tab. E.33

Number	Material	t_{in} [mm]	w [mm]
9	S3	0.634	100

Table E.31: Test 9 - coil.

$R_{a,r,t}$	$R_{a,r,b}$	$R_{a,s}$	$R_{q,r}$ (T)	$R_{q,s}$ (T)	R_q (T)	$R_{q,r}$ (C)	$R_{q,s}$ (C)	R_q (C)	$R_{pc,r,t}$	$R_{pc,r,b}$	$R_{pc,s}$	R_{pc}	$\bar{l}$
μm	μm	μm	μm	μm	μm	μm	μm	μm	peaks/cm	peaks/cm	peaks/cm	peaks/cm	μm
0.651	0.617	0.189	0.732	0.218	0.764	0.773	0.230	0.806	103.0	92.0	3.5	94.2	53.05

Table E.32: Test 9 - roughness of rolls after coil 5 and of coil 12.

Steady	v_r	v_r	e_x	r	t_{out}	σ_{in}	σ_{out}	T_{in}	T_{out}	$\overline{T}$	$\overline{F}_r$	L_r	s_f	$\overline{M}_r$	Data file
-	mm/s	m/min	%	%	mm	MPa	MPa	°C	°C	°C	N/mm	t	%	kN	-
Yes	19923	1195.4	29.9	23.0	0.488	137.3	227.5	25	102	63	5436	55.4	2.24	14.0	
No ($\overline{F}_r$)	16598	995.9	30.7	23.5	0.485	135.4	232.3	25	107	66	5028	51.3	3.50	11.3	2014-03-07_11.05.39
Almost (s_f)	11611	696.7	29.6	22.8	0.489	139.1	230.0	25	100	63	4938	50.3	3.96	10.5	

Table E.33: Test 9 - other measurements.

E.12 Test 10A - S2/FL L1 100%/Rolling speed

- Coil: Tab. E.34
- Roughness: Tab. E.35
- Lubrication: flexible lubrication by pure L1 (40°C)
- Other measurements: Tab. E.36

Number	Material	t_{in} [mm]	w [mm]
10	S2	0.75	75

Table E.34: Test 10A - coil.

$R_{a,r,t}$	$R_{a,r,b}$	$R_{a,s}$	$R_{q,r}$ (T)	$R_{q,s}$ (T)	R_q (T)	$R_{q,r}$ (C)	$R_{q,s}$ (C)	R_q (C)	$R_{pc,r,t}$	$R_{pc,r,b}$	$R_{pc,s}$	R_{pc}	$\bar{l}$
μm	μm	μm	μm	μm	μm	μm	μm	μm	peaks/cm	peaks/cm	peaks/cm	peaks/cm	μm
0.577	0.563	0.101	0.658	0.117	0.668	0.695	0.123	0.706	73.0	75.0	0.0	74.0	67.57

Table E.35: Test 10A - roughness of rolls after coil 11 and of coil 4.

Steady	v_r	v_r	e_x	r	t_{out}	σ_{in}	σ_{out}	T_{in}	T_{out}	$\overline{T}$	$\overline{F}_r$	L_r	s_f	$\overline{M}_r$	Data file
-	mm/s	m/min	%	%	mm	MPa	MPa	°C	°C	°C	N/mm	t	%	kN	-
Yes	8317	499.0	30.0	23.1	0.577	113.1	190.2	25	100	63	6870	52.5	3.01	15.8	2014-03-07_14.53.02
No (t_{out})	3295	197.7	29.8	23.0	0.578	118.7	184.0	25	81	53	6596	50.4	3.25	15.6	
Yes	796	47.8	29.7	22.9	0.578	116.3	183.3	25	33	29	7935	60.7	6.63	17.2	
Yes	375	22.5	29.8	23.0	0.578	123.1	202.7	25	35	30	8605	65.8	7.84	17.9	

Table E.36: Test 10A - other measurements.

E.13 Test 10B - S2/FL L1 100%/Rolling speed

- Coil: Tab. E.37
- Roughness: Tab. E.38
- Lubrication: flexible lubrication by pure L1 (60°C)
- Other measurements: Tab. E.39

Number	Material	t_{in} [mm]	w [mm]
10	S2	0.75	75

Table E.37: Test 10A - coil.

$R_{a,r,t}$	$R_{a,r,b}$	$R_{a,s}$	$R_{q,r}$ (T)	$R_{q,s}$ (T)	R_q (T)	$R_{q,r}$ (C)	$R_{q,s}$ (C)	R_q (C)	$R_{pc,r,t}$	$R_{pc,r,b}$	$R_{pc,s}$	R_{pc}	$\bar{l}$
μm	μm	μm	μm	μm	μm	μm	μm	μm	peaks/cm	peaks/cm	peaks/cm	peaks/cm	μm
0.577	0.563	0.101	0.658	0.117	0.668	0.695	0.123	0.706	73.0	75.0	0.0	74.0	67.57

Table E.38: Test 10B - roughness of rolls after coil 11 and of coil 4.

Steady	v_r	v_r	e_x	r	t_{out}	σ_{in}	σ_{out}	T_{in}	T_{out}	$\overline{T}$	$\overline{F}_r$	L_r	s_f	$\overline{M}_r$	Data file
-	mm/s	m/min	%	%	mm	MPa	MPa	°C	°C	°C	N/mm	t	%	kN	-
Yes	8311	498.7	30.1	23.1	0.576	113.2	188.1	25	103	64	6756	51.7	2.69	15.6	
Yes	6632	397.9	30.0	23.1	0.577	116.4	187.2	25	100	62	6679	51.1	2.65	15.5	
Yes	4964	297.8	29.4	22.7	0.580	121.0	186.8	25	93	59	6555	50.1	2.62	15.4	
Yes	3297	197.8	29.5	22.8	0.579	120.0	184.8	25	82	53	6587	50.4	3.18	15.2	2014-03-07_15.20.05
Yes	1623	97.4	28.3	22.0	0.585	116.4	178.6	25	55	40	7034	53.8	4.93	15.5	
Yes	792	47.5	30.0	23.1	0.577	118.5	186.6	25	38	32	7885	60.3	6.59	17.2	
Yes	373	22.4	30.1	23.1	0.576	122.1	200.1	25	31	28	8768	67.0	7.84	18.3	

Table E.39: Test 10B - other measurements.

E.14 Test 11 - S1/FL L1 100%/Rolling speed

- Coil: Tab. E.40
- Roughness: Tab. E.41
- Lubrication: flexible lubrication by pure L1 (60°C)
- Other measurements: Tab. E.42

Number	Material	t_{in} [mm]	w [mm]
11	S1	2.8	100

Table E.40: Test 11 - coil.

$R_{a,r,t}$	$R_{a,r,b}$	$R_{a,s}$	$R_{q,r}$ (T)	$R_{q,s}$ (T)	R_q (T)	$R_{q,r}$ (C)	$R_{q,s}$ (C)	R_q (C)	$R_{pc,r,t}$	$R_{pc,r,b}$	$R_{pc,s}$	R_{pc}	$\bar{l}$
μm	μm	μm	μm	μm	μm	μm	μm	μm	peaks/cm	peaks/cm	peaks/cm	peaks/cm	μm
0.577	0.563	1.505	0.658	1.738	1.858	0.695	1.835	1.962	73.0	75.0	75.0	74.5	67.11

Table E.41: Test 11 - roughness of rolls after coil 11 and of coil 2.

Steady	v_r	v_r	e_x	r	t_{out}	σ_{in}	σ_{out}	T_{in}	T_{out}	$\overline{T}$	$\overline{F}_r$	L_r	s_f	$\overline{M}_r$	Data file
-	mm/s	m/min	%	%	mm	MPa	MPa	°C	°C	°C	N/mm	t	%	kN	-
No (σ_{in})	6641	398.4	29.4	22.7	2.164	39.4	118.5	25	95	60	6663	67.9	2.40	22.1	
Yes	4974	298.4	30.1	23.1	2.153	36.5	119.0	25	94	60	6636	67.6	2.47	21.3	
Yes	3295	197.7	30.5	23.4	2.146	37.2	118.7	25	90	58	6555	66.8	2.46	21.0	2014-03-10_14.51.03
Yes	1621	97.2	30.4	23.3	2.148	37.2	117.9	25	84	55	6380	65.0	2.84	19.9	
Yes	789	47.4	29.9	23.0	2.156	37.3	117.5	25	75	50	6170	62.9	3.32	18.3	
Yes	371	22.2	29.5	22.8	2.163	43.9	115.4	26	56	41	5977	60.9	3.52	19.0	

Table E.42: Test 11 - other measurements.

E.15 Test 12A - S3/FL L1 100%/Rolling speed

- Coil: Tab. E.43
- Roughness: Tab. E.44
- Lubrication: flexible lubrication by pure L1 (40°C)
- Other measurements: Tab. E.45

Number	Material	t_{in} [mm]	w [mm]
12	S3	0.634	100

Table E.43: Test 12A - coil.

$R_{a,r,t}$	$R_{a,r,b}$	$R_{a,s}$	$R_{q,r}$ (T)	$R_{q,s}$ (T)	R_q (T)	$R_{q,r}$ (C)	$R_{q,s}$ (C)	R_q (C)	$R_{pc,r,t}$	$R_{pc,r,b}$	$R_{pc,s}$	R_{pc}	$\bar{l}$
μm	μm	μm	μm	μm	μm	μm	μm	μm	peaks/cm	peaks/cm	peaks/cm	peaks/cm	μm
0.563	0.569	0.189	0.654	0.218	0.689	0.690	0.230	0.727	83.0	72.0	3.5	74.3	67.29

Table E.44: Test 12A - roughness of rolls after coil 12 and of coil 12.

Steady	v_r	v_r	e_x	r	t_{out}	σ_{in}	σ_{out}	T_{in}	T_{out}	$\overline{T}$	$\overline{F}_r$	L_r	s_f	$\overline{M}_r$	Data file
-	mm/s	m/min	%	%	mm	MPa	MPa	°C	°C	°C	N/mm	t	%	kN	-
Almost (σ_{in})	19954	1197.2	29.8	23.0	0.488	137.0	221.9	25	105	65	5314	54.2	3.92	11.8	2014-03-11_10.28.56
Yes	11593	695.6	30.1	23.1	0.487	136.4	226.4	25	95	60	5217	53.2	4.15	11.5	
No (σ_{out})	6641	398.4	30.2	23.2	0.487	133.5	221.1	25	89	57	5092	51.9	3.99	11.3	2014-03-11_11.18.18
Yes	3304	198.2	30.0	23.1	0.488	141.4	223.9	25	69	47	4825	49.2	3.69	11.0	
Yes	1621	97.2	31.2	23.8	0.483	137.6	220.3	25	42	33	5018	51.1	5.90	10.6	
Yes	373	22.4	30.7	23.5	0.485	147.3	235.6	25	26	26	5827	59.4	8.28	11.8	

Table E.45: Test 12A - other measurements.

E.16 Test 12B - S3/RE L1 2%/Rolling speed

- Coil: Tab. E.46
- Roughness: Tab. E.47
- Lubrication: recirculated emulsion with 2% L1 (50°C)
- Other measurements: Tab. E.48

Number	Material	t_{in} [mm]	w [mm]
12	S3	0.634	100

Table E.46: Test 12B - coil.

$R_{a,r,t}$	$R_{a,r,b}$	$R_{a,s}$	$R_{q,r}$ (T)	$R_{q,s}$ (T)	R_q (T)	$R_{q,r}$ (C)	$R_{q,s}$ (C)	R_q (C)	$R_{pc,r,t}$	$R_{pc,r,b}$	$R_{pc,s}$	R_{pc}	$\bar{l}$
μm	μm	μm	μm	μm	μm	μm	μm	μm	peaks/cm	peaks/cm	peaks/cm	peaks/cm	μm
0.563	0.569	0.189	0.654	0.218	0.689	0.690	0.230	0.727	83.0	72.0	3.5	74.3	67.29

Table E.47: Test 12B - roughness of rolls after coil 12 and of coil 12.

Steady	v_r	v_r	e_x	r	t_{out}	σ_{in}	σ_{out}	T_{in}	T_{out}	$\overline{T}$	$\overline{F}_r$	L_r	s_f	$\overline{M}_r$	Data file
-	mm/s	m/min	%	%	mm	MPa	MPa	°C	°C	°C	N/mm	t	%	kN	-
Yes	379	22.7	30.3	23.3	0.486	149.3	230.1	25	25	25	6283	64.0	8.55	12.1	2014-03-12_11.11.21

Table E.48: Test 12B - other measurements.

E.17 Test 13 - S1/RE L1 2%/Rolling speed

- Coil: Tab. E.49
- Roughness: Tab. E.50
- Lubrication: recirculated emulsion with 2% L1 (50°C)
- Other measurements: Tab. E.51

Number	Material	t_{in} [mm]	w [mm]
13	S1	2.8	100

Table E.49: Test 13 - coil.

$R_{a,r,t}$	$R_{a,r,b}$	$R_{a,s}$	$R_{q,r}$ (T)	$R_{q,s}$ (T)	R_q (T)	$R_{q,r}$ (C)	$R_{q,s}$ (C)	R_q (C)	$R_{pc,r,t}$	$R_{pc,r,b}$	$R_{pc,s}$	R_{pc}	$\bar{l}$
μm	μm	μm	μm	μm	μm	μm	μm	μm	peaks/cm	peaks/cm	peaks/cm	peaks/cm	μm
0.563	0.569	1.505	0.654	1.738	1.857	0.690	1.835	1.960	83.0	72.0	75.0	76.3	65.56

Table E.50: Test 13 - roughness of rolls after coil 12 and of coil 2.

Steady	v_r	v_r	e_x	r	t_{out}	σ_{in}	σ_{out}	T_{in}	T_{out}	$\overline{T}$	$\overline{F}_r$	L_r	s_f	$\overline{M}_r$	Data file
-	mm/s	m/min	%	%	mm	MPa	MPa	°C	°C	°C	N/mm	t	%	kN	-
Almost ($\overline{F}_r$)	6639	398.3	29.0	22.5	2.170	36.7	118.6	25	82	54	7037	71.7	3.84	22.8	
Yes	4976	298.6	30.1	23.1	2.152	36.6	119.4	25	79	52	6985	71.2	3.78	23.0	
Yes	3297	197.8	30.3	23.3	2.149	36.7	119.0	25	89	57	6864	70.0	3.83	22.3	2014-03-12_14.31.51
Yes	1627	97.6	30.0	23.1	2.153	37.0	117.1	25	80	52	6589	67.2	3.76	20.6	
Yes	794	47.6	29.9	23.0	2.156	37.1	117.2	25	67	46	6351	64.7	3.99	18.9	
Yes	375	22.5	30.0	23.1	2.154	35.4	52.2	25	40	33	6599	67.3	1.69	32.2	

Table E.51: Test 13 - other measurements.

E.18 Test 14A - S2/FL L1 100%/Elongation

- Coil: Tab. E.52
- Roughness: Tab. E.53
- Lubrication: flexible lubrication by pure L1 (60°C)
- Other measurements: Tab. E.54

Number	Material	t_{in} [mm]	w [mm]
14	S2	0.75	75

Table E.52: Test 14A - coil.

$R_{a,r,t}$	$R_{a,r,b}$	$R_{a,s}$	$R_{q,r}$ (T)	$R_{q,s}$ (T)	R_q (T)	$R_{q,r}$ (C)	$R_{q,s}$ (C)	R_q (C)	$R_{pc,r,t}$	$R_{pc,r,b}$	$R_{pc,s}$	R_{pc}	$\bar{l}$
μm	μm	μm	μm	μm	μm	μm	μm	μm	peaks/cm	peaks/cm	peaks/cm	peaks/cm	μm
0.543	0.535	0.079	0.622	0.091	0.629	0.657	0.096	0.664	67.0	71.0	0.0	69.0	72.46

Table E.53: Test 14A - roughness of rolls after coil 14 and of coil 14.

Steady	v_r	v_r	e_x	r	t_{out}	σ_{in}	σ_{out}	T_{in}	T_{out}	$\overline{T}$	$\overline{F}_r$	L_r	s_f	$\overline{M}_r$	Data file
-	mm/s	m/min	%	%	mm	MPa	MPa	°C	°C	°C	N/mm	t	%	kN	-
Almost (σ_{out})	1625	97.5	9.8	9.0	0.683	114.5	200.8	25	43	34	4206	32.2	3.71	2.0	
Yes	1623	97.4	19.9	16.6	0.626	115.3	183.4	25	49	37	5496	42.0	4.42	9.2	
Yes	1621	97.2	29.4	22.7	0.580	116.3	176.1	25	52	39	6321	48.3	4.22	14.8	2014-03-12_16.36.37
Yes	1621	97.2	39.5	28.3	0.538	117.2	176.9	26	49	38	6922	52.9	3.87	19.1	
Yes	1627	97.6	4.9	4.7	0.715	116.9	182.8	25	44	34	3371	25.8	1.95	0.2	
No ($\overline{F}_r$)	1629	97.7	40.8	29.0	0.533	117.8	174.3	25	36	31	6834	52.3	3.51	19.4	
Yes	1629	97.7	39.8	28.5	0.536	116.0	183.0	25	46	36	6754	51.6	3.89	18.7	2014-03-13_11.32.13
Yes	1631	97.8	49.5	33.1	0.502	118.2	196.6	25	49	37	7192	55.0	3.98	21.6	
Yes	1631	97.8	49.5	33.1	0.502	118.4	185.5	25	41	33	7267	55.6	3.63	22.2	

Table E.54: Test 14A - other measurements.

E.19 Test 14B - S2/FL L1 100%/Elongation

- Coil: Tab. E.55
- Roughness: Tab. E.56
- Lubrication: flexible lubrication by pure L1 (60°C)
- Other measurements: Tab. E.57

Number	Material	t_{in} [mm]	w [mm]
14	S2	0.75	75

Table E.55: Test 14B - coil.

$R_{a,r,t}$	$R_{a,r,b}$	$R_{a,s}$	$R_{q,r}$ (T)	$R_{q,s}$ (T)	R_q (T)	$R_{q,r}$ (C)	$R_{q,s}$ (C)	R_q (C)	$R_{pc,r,t}$	$R_{pc,r,b}$	$R_{pc,s}$	R_{pc}	$\bar{l}$
μm	μm	μm	μm	μm	μm	μm	μm	μm	peaks/cm	peaks/cm	peaks/cm	peaks/cm	μm
0.543	0.535	0.079	0.622	0.091	0.629	0.657	0.096	0.664	67.0	71.0	0.0	69.0	72.46

Table E.56: Test 14B - roughness of rolls after coil 14 and of coil 14.

Steady	v_r	v_r	e_x	r	t_{out}	σ_{in}	σ_{out}	T_{in}	T_{out}	$\overline{T}$	$\overline{F}_r$	L_r	s_f	$\overline{M}_r$	Data file
-	mm/s	m/min	%	%	mm	MPa	MPa	°C	°C	°C	N/mm	t	%	kN	-
Yes	8319	499.2	9.6	8.7	0.685	114.0	194.3	25	44	35	4592	35.1	2.66	3.2	2014-03-13_11.13.23
Almost (σ_{in})	8317	499.0	19.3	16.1	0.629	115.9	192.8	25	59	42	5645	43.2	3.28	9.1	
Almost (σ_{out})	8319	499.2	30.7	23.5	0.574	119.0	191.0	25	79	52	6203	47.4	1.99	15.0	
No (σ_{in})	8317	499.0	39.2	28.2	0.539	116.4	194.0	25	77	51	6438	49.2	1.09	18.4	

Table E.57: Test 14B - other measurements.

E.20 Test 15 - S2/FL L3 100%/Elongation

- Coil: Tab. E.58
- Roughness: Tab. E.59
- Lubrication: flexible lubrication by pure L3 (60°C)
- Other measurements: Tab. E.60

Number	Material	t_{in} [mm]	w [mm]
8	S2	0.75	75

Table E.58: Test 15 - coil.

$R_{a,r,t}$	$R_{a,r,b}$	$R_{a,s}$	$R_{q,r}$ (T)	$R_{q,s}$ (T)	R_q (T)	$R_{q,r}$ (C)	$R_{q,s}$ (C)	R_q (C)	$R_{pc,r,t}$	$R_{pc,r,b}$	$R_{pc,s}$	R_{pc}	$\bar{l}$
μm	μm	μm	μm	μm	μm	μm	μm	μm	peaks/cm	peaks/cm	peaks/cm	peaks/cm	μm
0.543	0.535	0.101	0.622	0.117	0.633	0.657	0.123	0.669	67.0	71.0	0.0	69.0	72.46

Table E.59: Test 15 - roughness of rolls after coil 14 and of coil 4.

Steady	v_r	v_r	e_x	r	t_{out}	σ_{in}	σ_{out}	T_{in}	T_{out}	$\overline{T}$	$\overline{F}_r$	L_r	s_f	$\overline{M}_r$	Data file
-	mm/s	m/min	%	%	mm	MPa	MPa	°C	°C	°C	N/mm	t	%	kN	-
Yes	798	47.9	50.5	33.5	0.498	117.4	189.5	25	25	25	11199	85.6	9.99	30.7	
Yes	796	47.8	25.7	20.5	0.597	117.1	185.1	25	25	25	8402	64.2	6.92	16.5	2014-03-14_10.20.00
Yes	794	47.6	11.1	10.0	0.675	118.1	185.9	25	25	25	5910	45.2	3.73	5.6	

Table E.60: Test 15 - other measurements.

Appendix F

Roughness conversion

In this appendix, the *conversion from the arithmetical average roughness R_a to the root-mean-square roughness R_q* is explained for a given roughness profile. According to Eq. (2.13), the average roughness of a surface along a direction can be computed based on the height distribution function $f_Z(z)$, if the mean line corresponds with the reference line, i.e. $z_m = 0$:

$$R_a = \int_{-\infty}^{+\infty} |z| f_Z(z)\, \mathrm{d}z \tag{F.1}$$

If the surface asperity profile follows a *triangular asperity height distribution* (Eq. 2.11), by symmetry,

$$R_a = 2 \int_0^{\sqrt{3}R_q} z\, \frac{1}{2\sqrt{3}R_q}\, \mathrm{d}z = \frac{\sqrt{3}}{2} R_q \tag{F.2}$$

On the other hand, if the surface asperity profile follows a *Christensen height distribution* (Eq. 2.12), again by symmetry,

$$R_a = 2 \int_0^{3R_q} z\, \frac{35}{96R_q} \left[1 - \left(\frac{z}{3R_q}\right)^2\right]^3 \mathrm{d}z = \frac{105}{128} R_q \tag{F.3}$$

Appendix G

Graphical user interface of METALUB

In this appendix, the graphical user interface (GUI) of METALUB, which is coded in PYQT, is illustrated by focusing on its main tabs. It was initially created by Yves Carretta and then completely refactored and extended by the author of this document. Fig. G.1 shows the main window of the GUI with the configurator of a test case on the left and the information about the computation on the right. The Test 5B-4, i.e. Test 5B at 197.5 m/min in Sec. E.7, was run with the parameters of Tab. 5.4 as illustration. Figs. G.2-G.6 show the configuration tabs of the strip, the lubricant, the interface, the roll and the numerical parameters, respectively. The right side of the main window (Fig. G.7) and an additional window (Fig. G.8) display information about the computation during a METALUB run and the final results. Especially, the information during a run was crucial to debug and extend the computational core of METALUB, which is programmed in C++.

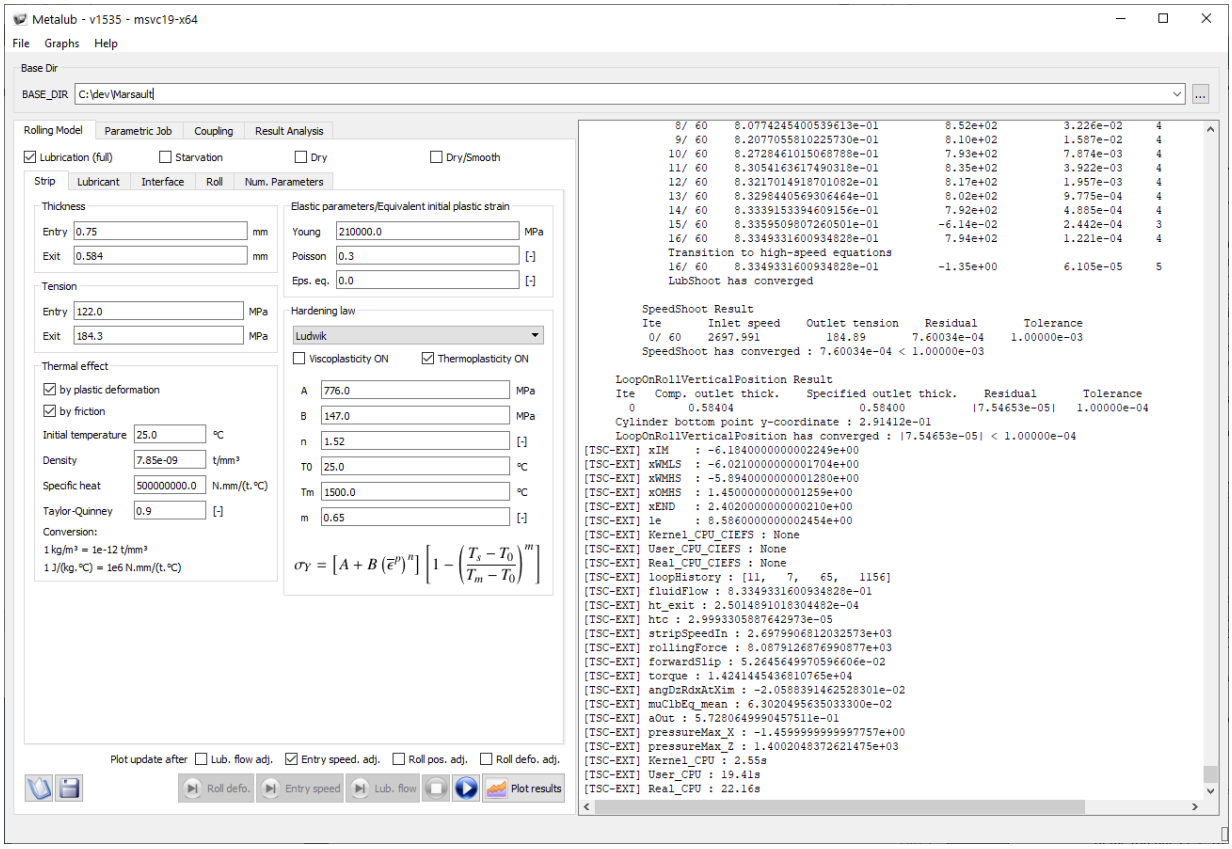

Figure G.1: Main window of the METALUB GUI.

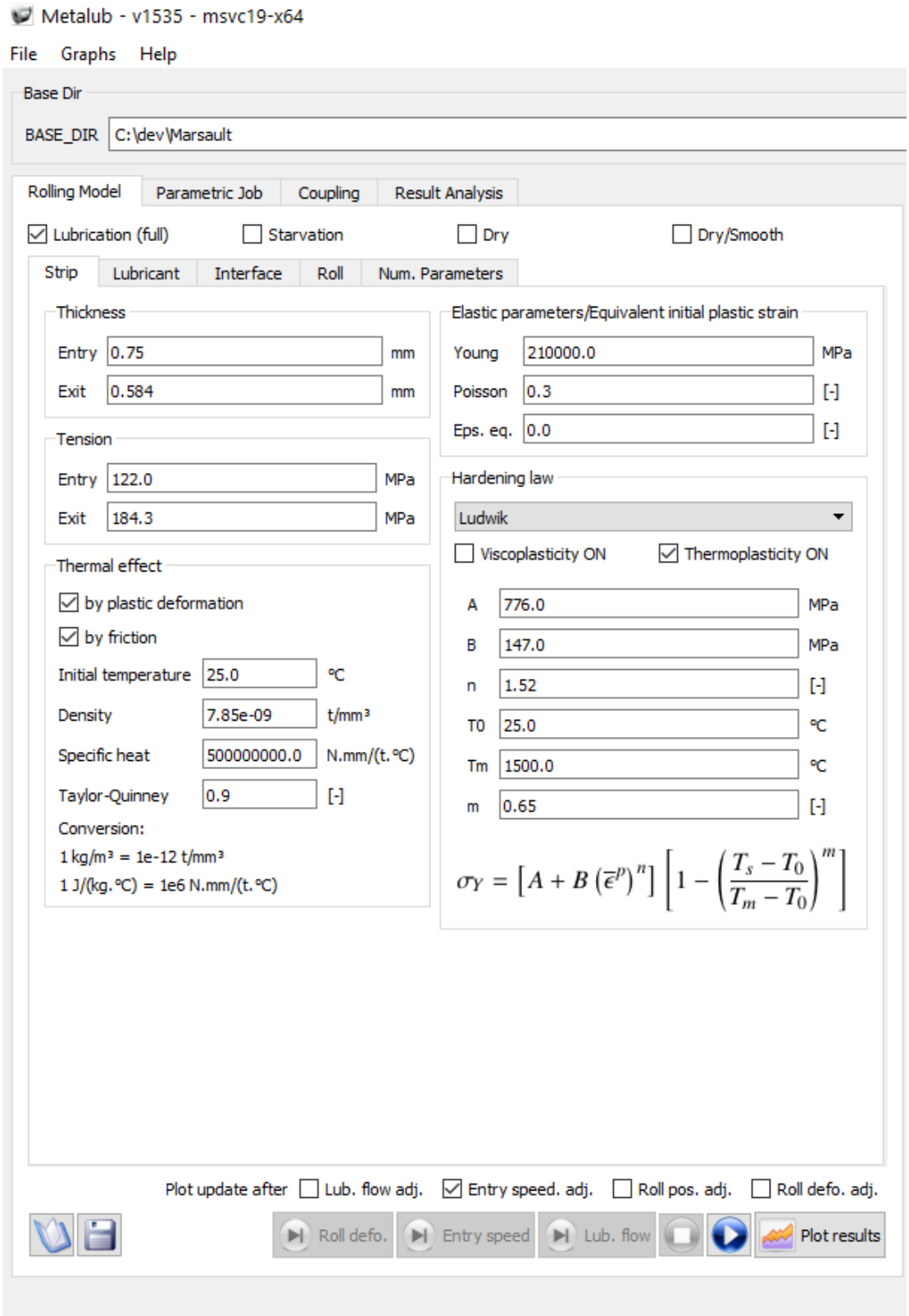

Figure G.2: Strip tab of the METALUB GUI.

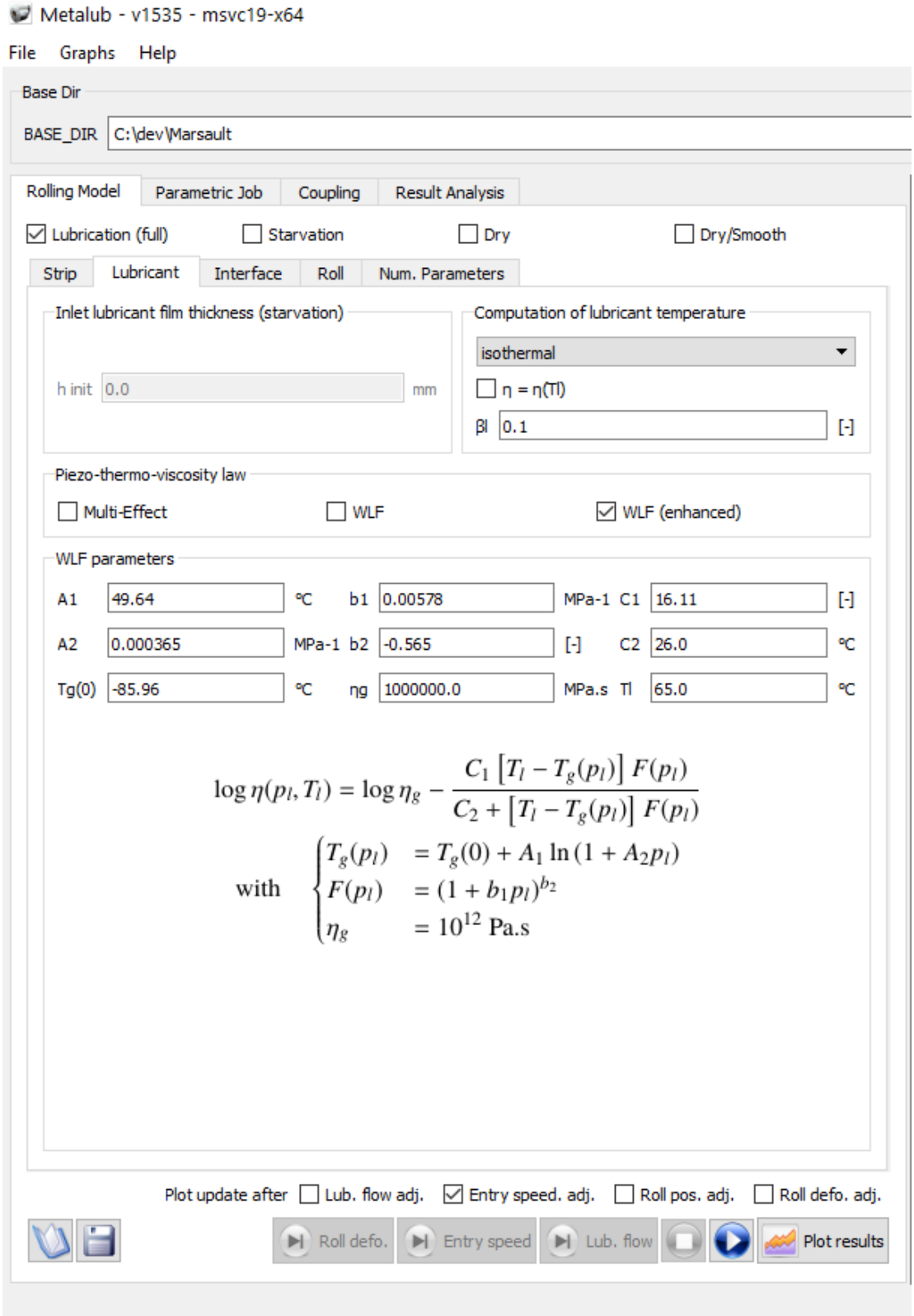

Figure G.3: Lubricant tab of the METALUB GUI.

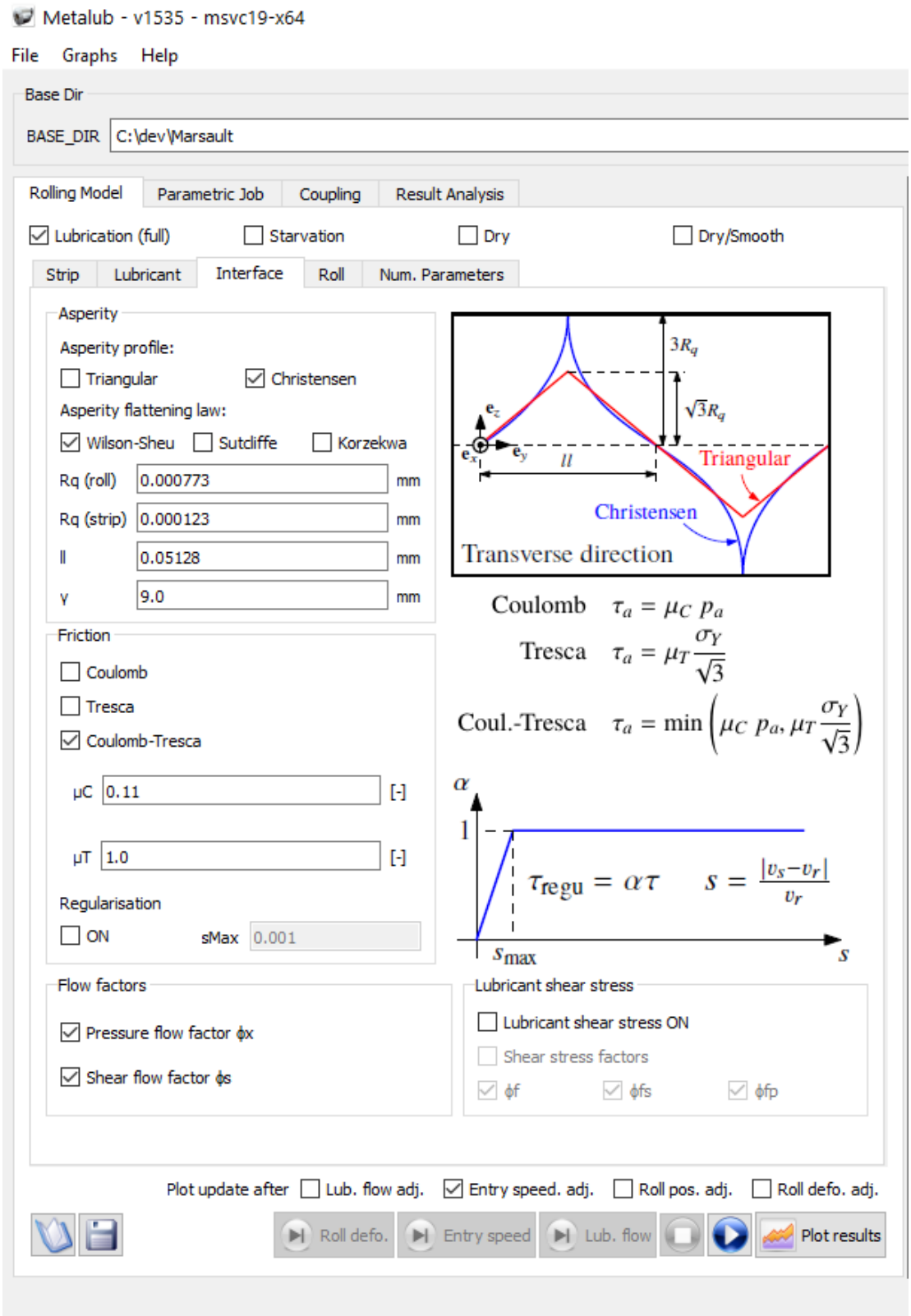

Figure G.4: Interface tab of the METALUB GUI.

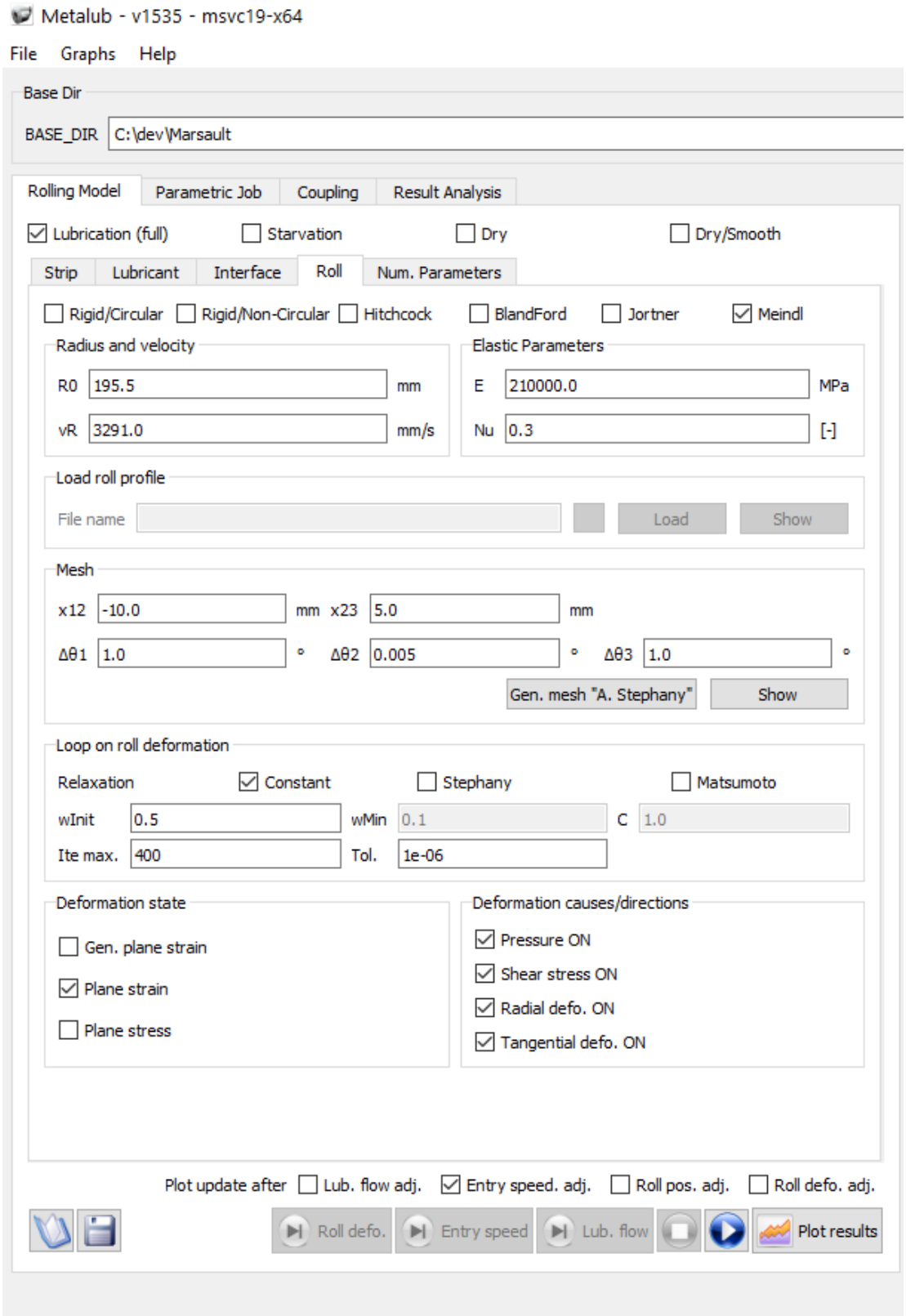

Figure G.5: Roll tab of the METALUB GUI.

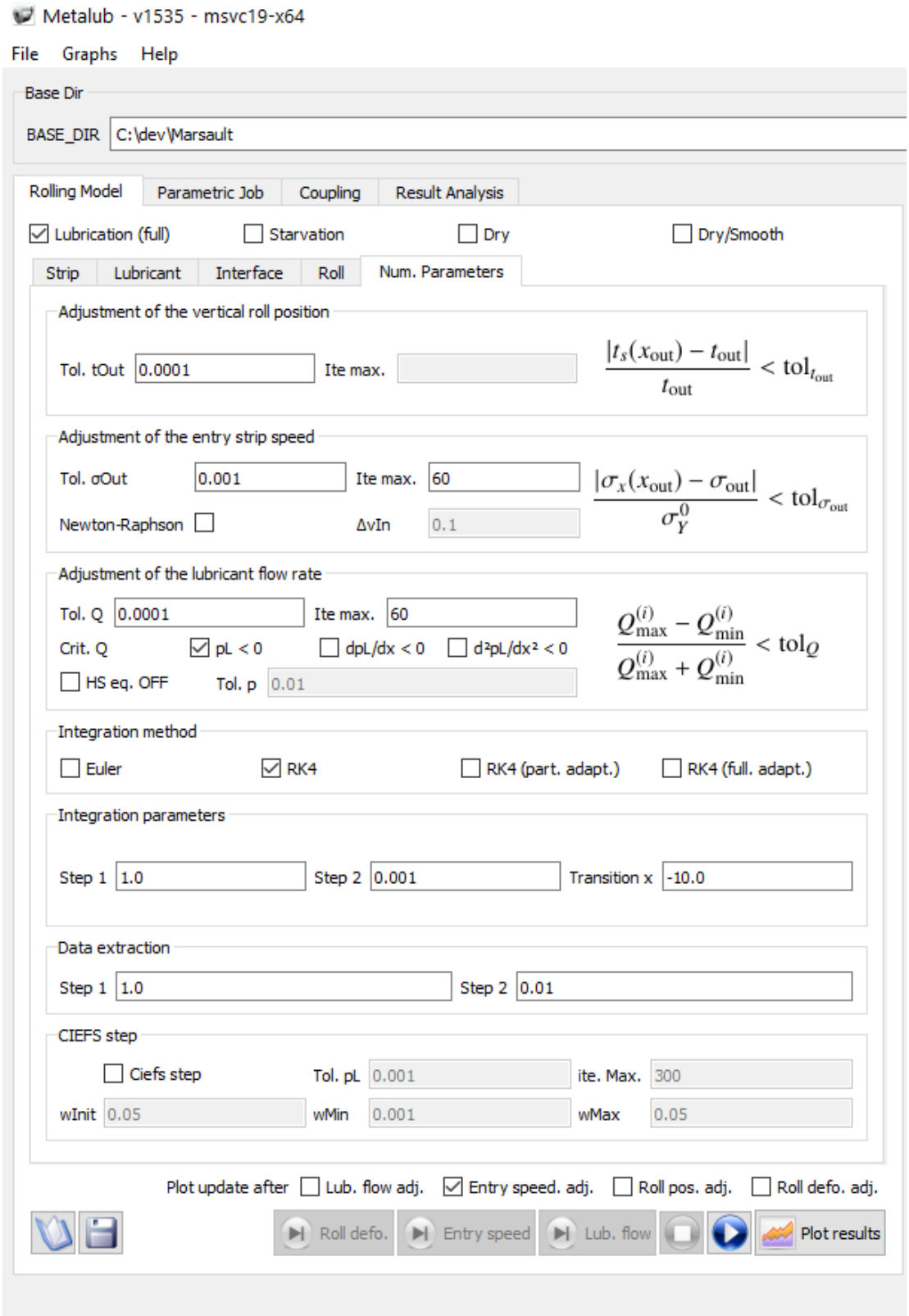

Figure G.6: Numerical parameter tab of the METALUB GUI.

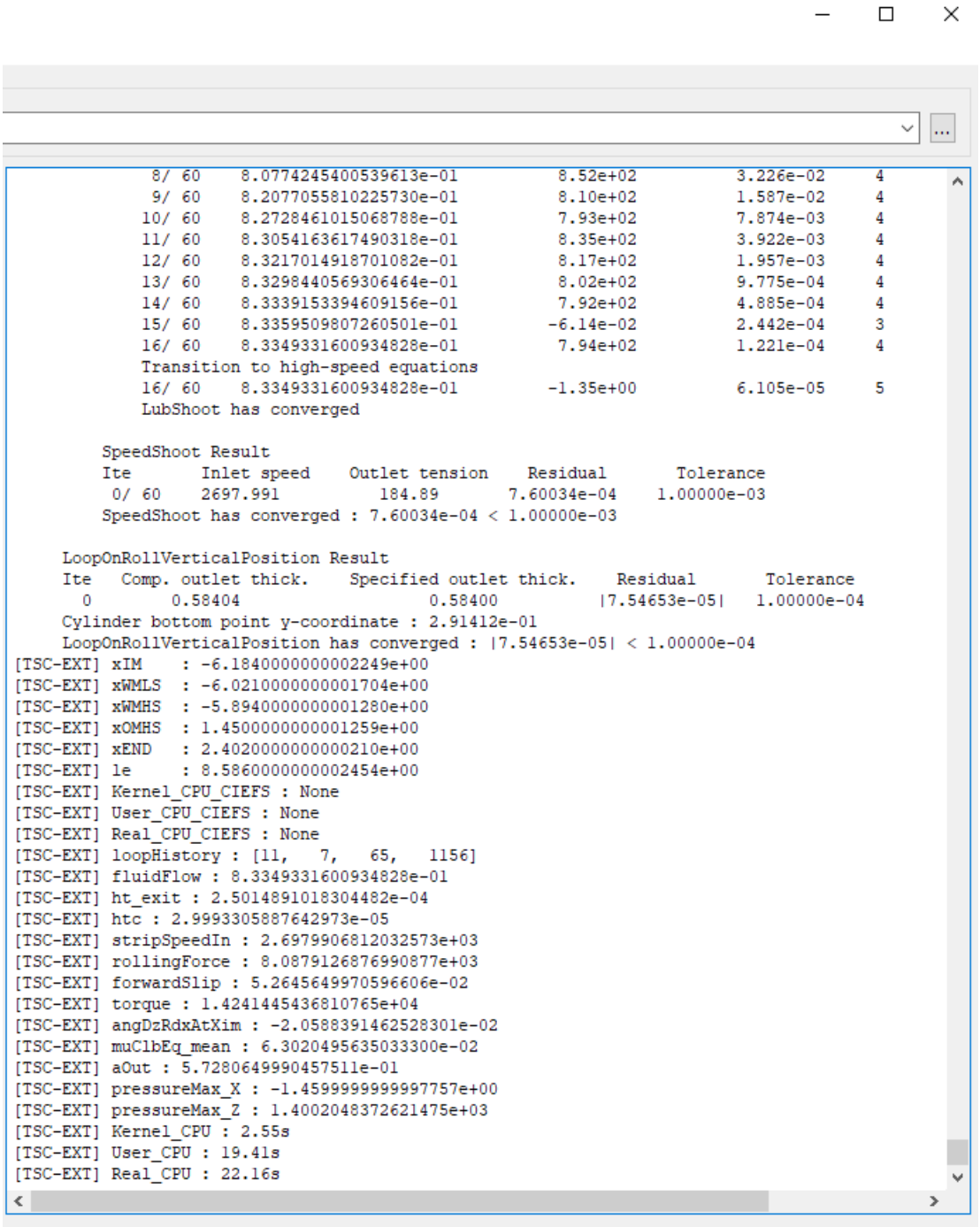

Figure G.7: Information about the computation during a METALUB run and the final results in the METALUB GUI.

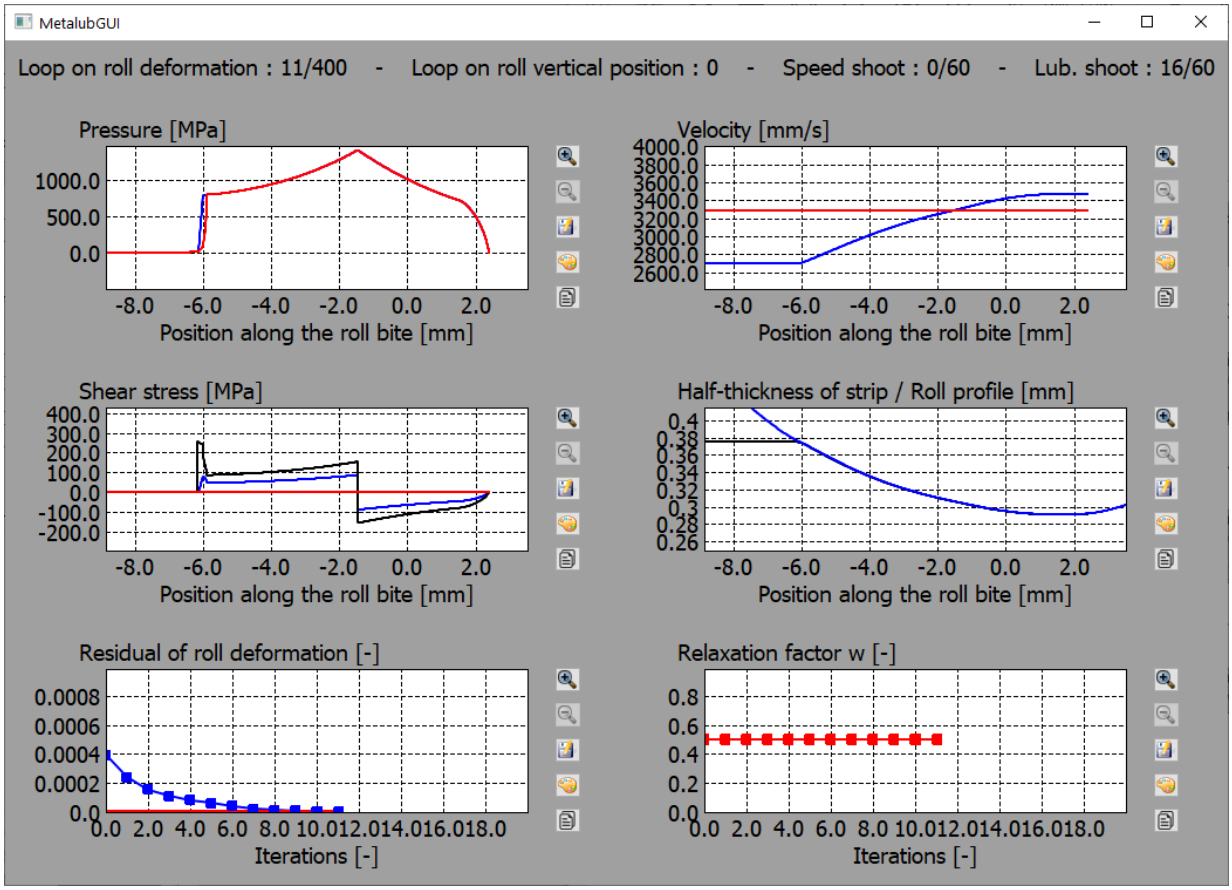

Figure G.8: Additional window of the METALUB GUI with information about the computation during a METALUB run and the final results.

Appendix H

Fundamentals of mechanics

H.1 Continuum mechanics

For reasons of completeness, some fundamentals of continuum mechanics are summarized in this appendix based on Khan and Huang [166], Bonet and Wood [40] Belytschko et al. [29], and especially Ponthot [258].

H.1.1 Configurations of a continuum

Let $\mathbb{V}_0 \subset \mathbb{R}^3$ be a set of points, which defines the *reference configuration* of a continuum (Fig. H.1). Usually, $\mathbb{V}_0$ is the *initial configuration* of the continuum at time $t = 0$ but it could be any other configuration. As time passes, the continuum changes its configuration from $\mathbb{V}_0$ to $\mathbb{V}$. Therefore, $\mathbb{V}(t)$ denotes the *current configuration* at time t. The variables relating to the reference configuration have the suffix 0.

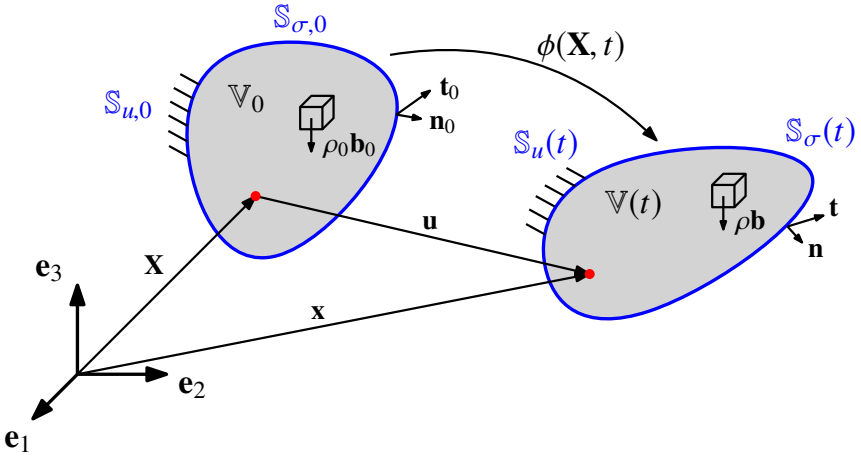

Figure H.1: Mapping of a reference configuration $\mathbb{V}_0$ to the current configuration $\mathbb{V}$ of a continuum.

The *position of a material point*, i.e. an infinitesimal element of the continuum, in the reference position is defined by the vector $\mathbf{X} = X_A \mathbf{E}_A$, where X_A ($A = 1, 2$ or 3) are the coordinates of $\mathbf{X}$ in the reference configuration and where $\mathbf{E}_A$ are the unit base vectors of a Cartesian coordinate system. Hence, the vector $\mathbf{X}$ contains the material or Lagrangian coordinates of a material point. Similarly, the position of a material point in the current configuration, also known as its spatial or Eulerian coordinates, is defined by the vector $\mathbf{x} = x_i \mathbf{e}_i$, where $\mathbf{e}_i$ ($i = 1, 2$ or 3) are the unit base vectors of a different Cartesian coordinate system. The vectors $\mathbf{E}_A$ are usually chosen identical to the vectors $\mathbf{e}_i$. Unlike the coordinates x_i, material coordinates X_A are independent of time, since a material point is by definition initially labeled with a material coordinate.

The surface points of the current configuration define the subset $\mathbb{S}(t) \subset \mathbb{V}(t)$ such that $\mathbb{S}(t) = \mathbb{S}_u(t) \cup \mathbb{S}_\sigma(t)$ and $\emptyset = \mathbb{S}_u(t) \cap \mathbb{S}_\sigma(t)$, where $\mathbb{S}_u(t)$ and $\mathbb{S}_\sigma(t)$ are the sets of surface points whose displacements are imposed and on which surface forces are applied, respectively, and where $\emptyset$ is the empty set symbol. The unit normal vector to the surface is denoted by $\mathbf{n}$.

While the surface forces are described by the surface traction $\mathbf{t}$ in the current configuration, the continuum is also subjected to external volume forces $\rho\mathbf{b}$, where ρ is the material density and where $\mathbf{b}$ are the body forces per unit mass.

H.1.2 Motion

The *motion* of a continuum is described by an assumed continuous mapping function $\boldsymbol{\phi}(\mathbf{X}, t)$,

$$\mathbf{x} = \boldsymbol{\phi}(\mathbf{X}, t) \qquad \text{or} \qquad x_i = \phi_i(\mathbf{X}, t) \tag{H.1}$$

If the initial configuration and the reference configuration are identical,

$$\mathbf{X} = \mathbf{x}(\mathbf{X}, 0) \equiv \boldsymbol{\phi}(\mathbf{X}, 0) \qquad \text{or} \qquad X_i = x_i(\mathbf{X}, 0) \equiv \phi_i(\mathbf{X}, 0) \tag{H.2}$$

Based on the previous explanations, a continuum can either be described as a function of two different sets of independent variables: the material coordinates $\mathbf{X}$ and time t or the spatial coordinates $\mathbf{x}$ and time t. The first description is called the *material or Lagrangian description*, while the second description is called the *spatial or Eulerian description*.

H.1.3 Displacement, velocity and acceleration

The *displacement* of a material point with respect to the reference configuration, which is assumed to be the initial configuration, is defined as

$$\mathbf{u}(\mathbf{X}, t) = \boldsymbol{\phi}(\mathbf{X}, t) - \boldsymbol{\phi}(\mathbf{X}, 0) \qquad \text{or} \qquad u_i(\mathbf{X}, t) = \phi_i(\mathbf{X}, t) - \phi_i(\mathbf{X}, 0) \tag{H.3}$$

which can also be written as follows provided that these vectors are defined in the same system of coordinates:

$$\mathbf{u} = \mathbf{x} - \mathbf{X} \qquad \text{or} \qquad u_i = x_i - X_i \tag{H.4}$$

The *velocity* of a material point is the time derivative of its position:

$$\mathbf{v}(\mathbf{X},t) = \frac{\partial \boldsymbol{\phi}(\mathbf{X},t)}{\partial t} \qquad \text{or} \qquad v_i(\mathbf{X},t) = \frac{\partial \phi_i(\mathbf{X},t)}{\partial t} \tag{H.5}$$

The *acceleration* of a material point is the time derivative of its velocity:

$$\mathbf{a}(\mathbf{X},t) = \frac{\partial \mathbf{v}(\mathbf{X},t)}{\partial t} \qquad \text{or} \qquad a_i(\mathbf{X},t) = \frac{\partial v_i(\mathbf{X},t)}{\partial t} \tag{H.6}$$

Previously, the velocity and acceleration were written for a particular material point, which is located at $\mathbf{X}$ in the reference configuration. These functions could, however, also be written as functions of $\mathbf{x}$. In other words, a function f can either be a *Lagrangian function* $f(\mathbf{X},t)$, i.e. a function of the material coordinates $\mathbf{X}$ and time t or a *Eulerian function* $f(\mathbf{x},t)$, i.e. a function of the spatial coordinates $\mathbf{x}$ and time t [166, p. 31]. For a Lagrangian function, the *total time derivative*, or *material derivative*, is computed as follows, by the chain rule,

$$\frac{\mathrm{d}f(\mathbf{X},t)}{\mathrm{d}t} = \frac{\partial f(\mathbf{X},t)}{\partial t} + \frac{\partial f(\mathbf{X},t)}{\partial X_i}\frac{\partial X_i}{\partial t} = \frac{\partial f(\mathbf{X},t)}{\partial t} \tag{H.7}$$

since $\mathbf{X}$ does not change with time, while for a Eulerian function, the position $\mathbf{x}$ is also a function of time. Hence,

$$\frac{\mathrm{d}f(\mathbf{x},t)}{\mathrm{d}t} = \frac{\partial f(\mathbf{x},t)}{\partial t} + \frac{\partial f(\mathbf{x},t)}{\partial x_i}\frac{\partial x_i}{\partial t} = \frac{\partial f(\mathbf{x},t)}{\partial t} + \frac{\partial f(\mathbf{x},t)}{\partial x_i}v_i \tag{H.8}$$

The first term and the second term on the right hand side are respectively called the *spatial time derivative* and the *convective* or *transport term*.

H.1.4 Deformation gradient

The *deformation gradient* is defined by

$$\mathbf{F} = \frac{\partial \boldsymbol{\phi}}{\partial \mathbf{X}} \equiv \frac{\partial \mathbf{x}}{\partial \mathbf{X}} \qquad \text{or} \qquad F_{iA} = \frac{\partial \phi_i}{\partial X_A} \equiv \frac{\partial x_i}{\partial X_A} \tag{H.9}$$

Mathematically, it is the Jacobian matrix of the vector function $\boldsymbol{\phi}(\mathbf{X},t)$. The determinant of the deformation gradient is the *Jacobian determinant* or simply the *Jacobian*

$$J = \det \mathbf{F} \tag{H.10}$$

The Jacobian can be used to relate an integral of a function f in the reference configuration $\mathbb{V}_0$ to an integral in the current configuration $\mathbb{V}$:

$$\int_{\mathbb{V}} f \,\mathrm{d}\mathbb{V} = \int_{\mathbb{V}_0} fJ \,\mathrm{d}\mathbb{V}_0 \tag{H.11}$$

If the deformation gradient $\mathbf{F}$ is non-singular, it can be decomposed into the product of an orthogonal matrix $\mathbf{R}$, the *rotation tensor*, and a symmetric positive definite matrix $\mathbf{U}$, the *right stretch tensor*:

$$\mathbf{F} = \mathbf{R}\mathbf{U} \tag{H.12}$$

H.1.5 Strain measures

Strain measures describe the deformation of a body. Thus, it should vanish for any rigid body motion but increase when the deformation increases. Numerous strain measures can be defined, e.g. the Biot, Green-Lagrange or natural/logarithmic strain tensors.

H.1.5.1 Strain tensors

The *natural or logarithmic strain tensor* is defined as follows:

$$\mathbf{E}^N = \ln \mathbf{U} \tag{H.13}$$

H.1.5.2 Rate of deformation tensors

Besides quantifying the deformation, the rate of deformation can also be measured by introducing the *velocity gradient* $\mathbf{L}$, which is defined by the following equation:

$$\mathbf{L} = (\nabla \mathbf{v})^T \qquad \text{or} \qquad L_{ij} = \frac{\partial v_i}{\partial x_j} \tag{H.14}$$

It can be related to the deformation gradient $\mathbf{F}$ as follows:

$$\mathbf{L} = \frac{\partial \dot{\mathbf{x}}}{\partial \mathbf{x}} = \frac{\partial \dot{\mathbf{x}}}{\partial \mathbf{X}} \frac{\partial \mathbf{X}}{\partial \mathbf{x}} = \dot{\mathbf{F}} \mathbf{F}^{-1} \qquad \text{or} \qquad L_{ij} = \frac{\partial \dot{x}_i}{\partial x_j} = \frac{\partial \dot{x}_i}{\partial X_A} \frac{\partial X_A}{\partial x_j} = \dot{F}_{iA} F^{-1}_{Aj} \tag{H.15}$$

The velocity gradient can be decomposed into its symmetric and skew symmetric parts by

$$\mathbf{L} = \frac{1}{2}\left(\mathbf{L} + \mathbf{L}^T\right) + \frac{1}{2}\left(\mathbf{L} - \mathbf{L}^T\right) \qquad \text{or} \qquad L_{ij} = \frac{1}{2}\left(L_{ij} + L_{ji}\right) + \frac{1}{2}\left(L_{ij} - L_{ji}\right) \tag{H.16}$$

The *strain rate tensor* $\mathbf{D}$ can then defined as the symmetric part of $\mathbf{L}$, while the skew symmetric part is the *spin tensor* $\mathbf{W}$:

$$\mathbf{D} = \frac{1}{2}\left(\mathbf{L} + \mathbf{L}^T\right) \qquad \text{or} \qquad D_{ij} = \frac{1}{2}\left(\frac{\partial v_i}{\partial x_j} + \frac{\partial v_j}{\partial x_i}\right) \tag{H.17}$$

$$\mathbf{W} = \frac{1}{2}\left(\mathbf{L} - \mathbf{L}^T\right) \qquad \text{or} \qquad W_{ij} = \frac{1}{2}\left(\frac{\partial v_i}{\partial x_j} - \frac{\partial v_j}{\partial x_i}\right) \tag{H.18}$$

H.1.5.3 Incompressibility

The volume of an *incompressible* material does not change by definition. According to Eq. (H.11), this implies that the Jacobian is equal to 1. Alternatively, since the density is constant for an incompressible material, the continuity equation (Eq. H.33 with $\mathrm{d}\rho/\mathrm{d}t = 0$) implies that the divergence of the velocity is zero, which means that the trace of the strain rate tensor is zero (Eq. H.17), too:

$$J = \det \mathbf{F} = 1 \qquad \text{or} \qquad \nabla \cdot \mathbf{v} = \operatorname{tr} \mathbf{D} = 0 \tag{H.19}$$

In particular, if the natural strain matrix $\mathbf{E}^N$ is diagonal, the stretch matrix $\mathbf{U}$ is also diagonal:

$$\mathbf{E}^N = \begin{pmatrix} \epsilon_x & 0 & 0 \\ 0 & \epsilon_y & 0 \\ 0 & 0 & \epsilon_z \end{pmatrix} \quad \Rightarrow \quad \mathbf{U} = \begin{pmatrix} e^{\epsilon_x} & 0 & 0 \\ 0 & e^{\epsilon_y} & 0 \\ 0 & 0 & e^{\epsilon_z} \end{pmatrix} \tag{H.20}$$

If the material is incompressible, the following identity is satisfied due to Eq. H.12, the identity $\det(\mathbf{AB}) = \det\mathbf{A}\det\mathbf{B}$, Eq. H.20, and $\det\mathbf{R} = 1$ (property of rotation matrices):

$$\det\mathbf{F} = \det(\mathbf{RU}) = \det\mathbf{U} = e^{\epsilon_x+\epsilon_y+\epsilon_z} = 1 \quad \Rightarrow \quad \epsilon_x + \epsilon_y + \epsilon_z = 0 \tag{H.21}$$

H.1.5.4 Deviatoric strain rate tensor

The *deviatoric strain rate tensor* is defined as follows:

$$\mathbf{D}^d = \mathbf{D} - \frac{\operatorname{tr}\mathbf{D}}{3}\mathbf{I} \quad \text{or} \quad D^d_{ij} = D_{ij} - \frac{D_{kk}}{3}\delta_{ij} \tag{H.22}$$

H.1.6 Stress measures

The reference configuration $\mathbb{V}_0$ and the current configuration $\mathbb{V}$ of a continuum are represented in Fig. H.2 to define two different stress measures, i.e. the Cauchy stress tensor $\boldsymbol{\sigma}$ in the current configuration and the first Piola-Kirchhoff stress tensor $\mathbf{P}$ in the reference configuration.

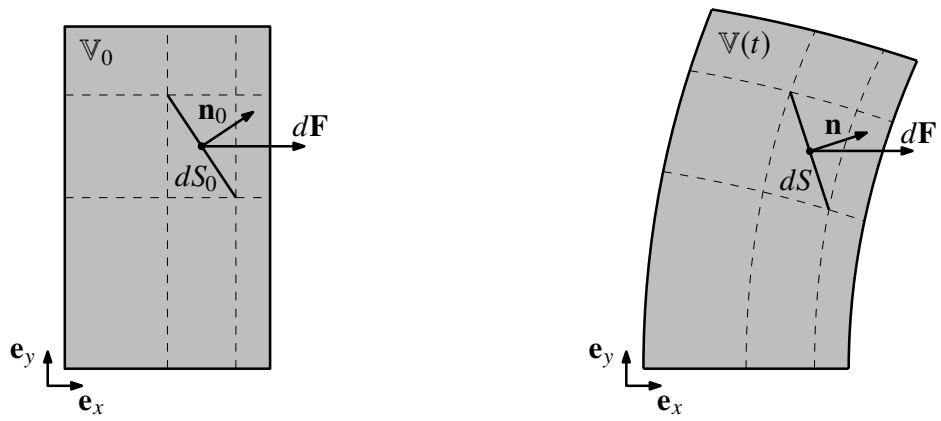

(a) Reference configuration. **(b)** Current configuration.

Figure H.2: Definition of stress measures based on an infinitesimal force $d\mathbf{F}$ which is acting on a material point. Due to the deformation of the continuum from its reference configuration $\mathbb{V}_0$ to its current configuration $\mathbb{V}$, an infinitesimal surface facet changes its orientation from $\mathbf{n}_0$ to $\mathbf{n}$ and its area from dS_0 to dS.

H.1.6.1 Cauchy stress tensor

In the current configuration $\mathbb{V}(t)$, the stress vector $\mathbf{t}$ is defined as the force per unit area that acts on the continuum at a given point of this continuum and for a given internal surface orientation, i.e.

$$d\mathbf{F} = \mathbf{t}\, dS \tag{H.23}$$

where $d\mathbf{F}$ is an infinitesimal force and dS an infinitesimal surface area, according to Fig. H.2b.

The *Cauchy stress tensor* or true stress $\boldsymbol{\sigma}$ can be defined based on the stress vector $\mathbf{t}$ and the local surface orientation $\mathbf{n}$ in the current configuration:

$$\mathbf{t} = \boldsymbol{\sigma}\mathbf{n} \qquad \text{or} \qquad t_i = \sigma_{ij} n_j \tag{H.24}$$

where σ_{ij} denotes the i-th component of the stress vector acting on the positive side of the plane x_j = constant. Notice that this definition was chosen by Ponthot [258], which is used in this document, while Belytschko et al. [29] define the Cauchy stress tensor differently, i.e. $\mathbf{t} = \mathbf{n}\boldsymbol{\sigma}$.

The *hydrostatic stress* is defined as the average of the three diagonal stress components of the stress tensor:

$$\sigma_{\text{hyd}} = \frac{\operatorname{tr}\boldsymbol{\sigma}}{3} = \frac{\sigma_{ii}}{3} \tag{H.25}$$

The *mechanical pressure* or simply *pressure* is the opposite of the hydrostatic stress:

$$p = -\sigma_{\text{hyd}} = -\frac{\operatorname{tr}\boldsymbol{\sigma}}{3} = -\frac{\sigma_{ii}}{3} \tag{H.26}$$

This definition of the mechanical pressure is the one which is commonly used in fluid mechanics, e.g. [322], while the opposite sign is preferred in solid mechanics, e.g. [258]. In this document, we will, however, use the first definition, since positive pressure is associated with a compressive state in cold rolling.

The *Cauchy stress deviator*, *stress deviator tensor*, *deviatoric stress* or *deviatoric stress tensor* is defined as follows:

$$\mathbf{s} = \boldsymbol{\sigma} - \sigma_{\text{hyd}}\mathbf{I} \qquad \text{or} \qquad \mathbf{s} = \boldsymbol{\sigma} + p\mathbf{I} \qquad \text{or} \qquad s_{ij} = \sigma_{ij} - \frac{\sigma_{kk}}{3}\delta_{ij} \tag{H.27}$$

H.1.6.2 First Piola-Kirchhoff stress tensor

In contrast to the Cauchy stress tensor, the first Piola-Kirchhoff stress tensor defines the stress state of a given force in the reference configuration instead of the current configuration. In a similar way to the derivation of the Cauchy stress tensor, the stress vector $\mathbf{t}_0$ in the reference configuration is thus defined by

$$d\mathbf{F} = \mathbf{t}_0\, dS_0 \tag{H.28}$$

Considering the orientation of the surface in the reference configuration $\mathbf{n}_0$, the first *Piola-Kirchhoff stress tensor* is defined as follows:

$$\mathbf{t}_0 = \mathbf{P}\,\mathbf{n}_0 \qquad \text{or} \qquad t_{0,i} = P_{iA} n_{0,A} \tag{H.29}$$

The first Piola-Kirchhoff stress tensor can be written as a function of the Cauchy stress tensor. In fact, since the infinitesimal force is the same whether it is written in the reference configuration or the current configuration, Eqs. (H.23), (H.24), (H.28) and (H.29) can be combined:

$$\mathbf{P}\,\mathbf{n}_0\; dS_0 = \boldsymbol{\sigma}\mathbf{n}\; dS \qquad \text{or} \qquad P_{iA}\, n_{0,A}\; dS_0 = \sigma_{ij}\, n_j\; dS \tag{H.30}$$

Nanson's relation allows to quantify the area change from the reference configuration to the current configuration [29, 258]:

$$\mathbf{n}\; dS = J\mathbf{F}^{-T}\mathbf{n}_0\; dS_0 \qquad \text{or} \qquad n_i\; dS = JF^{-T}_{iA} n_{0,A}\; dS_0 \tag{H.31}$$

By combining the previous equations, the first Piola-Kirchhoff stress tensor can be written as a function of the Cauchy stress tensor:

$$\mathbf{P} = J\boldsymbol{\sigma}\mathbf{F}^{-T} \qquad \text{or} \qquad P_{iA} = J\sigma_{ij}F^{-T}_{jA} \tag{H.32}$$

H.2 Conservation equations

The derivation of the conservation equations in the Eulerian and Lagrangian descriptions of the following sections can be found in Ponthot [258] or Belytschko et al. [29].

H.2.1 Eulerian description

- Conservation of mass:

$$\frac{\mathrm{d}\rho}{\mathrm{d}t} + \rho\nabla\cdot\mathbf{v} = 0 \qquad \text{or} \qquad \frac{\mathrm{d}\rho}{\mathrm{d}t} + \rho\frac{\partial v_i}{\partial x_i} = 0 \tag{H.33}$$

- Conservation of linear momentum:

$$\rho\frac{\mathrm{d}\mathbf{v}}{\mathrm{d}t} = \nabla\cdot\boldsymbol{\sigma} + \rho\mathbf{b} \qquad \text{or} \qquad \rho\frac{\mathrm{d}v_i}{\mathrm{d}t} = \frac{\partial\sigma_{ij}}{\partial x_j} + \rho b_i \tag{H.34}$$

- Conservation of energy:

$$\rho\frac{\mathrm{d}e}{\mathrm{d}t} = \mathbf{D}:\boldsymbol{\sigma} - \nabla\cdot\mathbf{q} + \rho s \qquad \text{or} \qquad \rho\frac{\mathrm{d}e}{\mathrm{d}t} = D_{ij}\sigma_{ij} - \frac{\partial q_i}{\partial x_i} + \rho s \tag{H.35}$$

H.2.2 Lagrangian description

- Conservation of mass:

$$\rho J = \rho_0 \tag{H.36}$$

- Conservation of linear momentum:

$$\rho_0 \frac{\mathrm{d}\mathbf{v}}{\mathrm{d}t} = \nabla_0 \cdot \mathbf{P} + \rho_0 \mathbf{b} \qquad \text{or} \qquad \rho_0 \frac{\mathrm{d}v_i}{\mathrm{d}t} = \frac{\partial P_{iA}}{\partial X_A} + \rho_0 b_i \tag{H.37}$$

- Conservation of energy:

$$\rho_0 \frac{\mathrm{d}e}{\mathrm{d}t} = \dot{\mathbf{F}} : \mathbf{P} - \nabla_0 \cdot \mathbf{Q} + \rho_0 s \qquad \text{or} \qquad \rho_0 \frac{\mathrm{d}e}{\mathrm{d}t} = \dot{F}_{iA} P_{iA} - \frac{\partial Q_A}{\partial X_A} + \rho_0 s \tag{H.38}$$

  with $\mathbf{Q} = J\mathbf{F}^{-1}\mathbf{q}$.

H.3 Solid mechanics

In this section, the equations governing *small strain elasticity* and *elastoplasticity* are derived, in particular the *Prandtl-Reuss equations*.

H.3.1 Small strain elasticity

In small strain elasticity, the *strain tensor* reduces to

$$\boldsymbol{\epsilon} = \frac{1}{2}\left(\nabla \mathbf{u} + (\nabla \mathbf{u})^T\right) \qquad \text{or} \qquad \epsilon_{ij} = \frac{1}{2}\left(\frac{\partial u_j}{\partial x_i} + \frac{\partial u_i}{\partial x_j}\right) \tag{H.39}$$

The linear isotropic homogeneous material behavior can be described by *Hooke's law*:

$$\boldsymbol{\sigma} = \mathbb{H} : \boldsymbol{\epsilon} \qquad \text{or} \qquad \sigma_{ij} = \mathbb{H}_{ijkl}\epsilon_{kl} \tag{H.40}$$

with the 4th order Hooke tensor

$$\mathbb{H}_{ijkl} = G(\delta_{ik}\delta_{jl} + \delta_{il}\delta_{kj}) + \lambda\delta_{ij}\delta_{kl} \tag{H.41}$$

$$= K\delta_{ij}\delta_{kl} + G\left(\delta_{ik}\delta_{jl} + \delta_{il}\delta_{kj} - \frac{2}{3}\delta_{ij}\delta_{kl}\right) \tag{H.42}$$

Lamé's first parameter λ, Lamé's second parameters G, also known as the shear modulus, and the bulk modulus K in the previous equations are respectively related to the Young's modulus E and the Poisson's ratio ν by the following equations:

$$G = \frac{E}{2(1+\nu)} \qquad \lambda = \frac{\nu E}{(1+\nu)(1-2\nu)} \qquad K = \frac{E}{3(1-2\nu)} \tag{H.43}$$

Replacing the Hooke tensor in Eq. (H.40) by its form in Eq. (H.42), one gets

$$\sigma_{ij} = \mathbb{H}_{ijkl}\epsilon_{kl} \tag{H.44}$$

$$= K\epsilon_{kk}\delta_{ij} + G\left(\epsilon_{ij} + \epsilon_{ji} - \frac{2}{3}\delta_{ij}\epsilon_{kk}\right) \tag{H.45}$$

$$= K\epsilon_{kk}\delta_{ij} + 2G\left(\epsilon_{ij} - \frac{1}{3}\epsilon_{kk}\delta_{ij}\right) \tag{H.46}$$

$$\tag{H.47}$$

In tensor form, the previous equation becomes

$$\boldsymbol{\sigma} = K\,\mathrm{tr}\,\boldsymbol{\epsilon} + 2G\,\mathrm{dev}\,\boldsymbol{\epsilon} \tag{H.48}$$

Since the stress tensor can be decomposed into pressure and deviator parts (Eq. H.27), one obtains, by identification,

$$p = -K\,\mathrm{tr}\,\boldsymbol{\epsilon} \tag{H.49}$$

$$\mathbf{s} = 2G\,\mathrm{dev}\,\boldsymbol{\epsilon} \tag{H.50}$$

H.3.2 Elastoplasticity

Due to the path-dependent strain history, it is necessary in plasticity to write the constitutive equation in a rate form. This equation can take the following hypoelastic form by introducing the material tensor $\mathbb{M}$:

$$\dot{\boldsymbol{\sigma}} = \mathbb{M} : \mathbf{D} \tag{H.51}$$

To ensure objectivity, i.e. the invariance of the constitutive equations to the change of observer, objective rates, like the Jaumann rate, are commonly introduced. To simplify the explanations, these rates are not introduced hereafter but details can be found in [29, 258].

H.3.2.1 Additive decomposition of strain rate

A common hypothesis in plasticity is to assume that the strain rate can be decomposed into a strain rate due to elastic deformations and a strain rate due to plastic deformations:

$$\mathbf{D} = \mathbf{D}^e + \mathbf{D}^p \tag{H.52}$$

H.3.2.2 Existence of a yield criterion

A second hypothesis is to assume the existence of a yield criterion, i.e. a function $f_Y(\boldsymbol{\sigma}, \mathbf{p})$ which is negative, when the deformations are elastic, and which becomes zero, when the deformations are plastic. This function depends only on the stress state $\boldsymbol{\sigma}$ and history dependent internal parameters $\mathbf{p}$.

A classical yield criterion for steel is the *Von Mises yield criterion*:

$$f_Y = J_2 - \frac{1}{3}\sigma_Y^2 \tag{H.53}$$

where

$$J_2 = \frac{1}{2}s_{ij}s_{ij} \tag{H.54}$$

is the second invariant of the deviatoric stress tensor and where σ_Y is the yield stress. A plasticity model based on the Von Mises yield criterion is called *J_2-plasticity*. The *equivalent Von Mises stress* is a scalar value computed from the Cauchy stress tensor, which is equal to σ_Y when the material deforms plastically. By the symmetry of the Cauchy stress tensor and Eqs. (H.27), (H.53) and (H.54):

$$\sigma_{\text{VM}} = \sqrt{\frac{1}{2}\left[\left(\sigma_x - \sigma_y\right)^2 + \left(\sigma_y - \sigma_z\right)^2 + \left(\sigma_z - \sigma_x\right)^2 + 6\left(\sigma_{xy}^2 + \sigma_{yz}^2 + \sigma_{zx}^2\right)\right]} \tag{H.55}$$

The *shear yield stress* τ_Y can be defined as the shear stress, which induces plastic yielding by itself. Based on the previous equation and $\sigma_{\text{VM}} = \sigma_Y$, when the material yields,

$$\tau_Y = \frac{\sigma_Y}{\sqrt{3}} \tag{H.56}$$

H.3.2.3 Evolution of the yield function

During plastic deformations, the yield function changes due microscopic changes of the material, which can be described by the evolution of internal parameters, like the dislocation density. A parameter, which is commonly used in metal plasticity models to quantify these changes is the effective plastic strain $\overline{\epsilon}^p$:

$$\overline{D}^p = \frac{\mathrm{d}\overline{\epsilon}^p}{\mathrm{d}t} \tag{H.57}$$

where $\overline{D}^p$ is the effective plastic strain rate

$$\overline{D}^p = \sqrt{\frac{2}{3}\mathbf{D}^p : \mathbf{D}^p} \tag{H.58}$$

It is generally assumed that the plastic strain rate is normal to the plastic flow potential g:

$$D_{ij}^p = \Upsilon\frac{\partial g}{\partial \sigma_{ij}} \tag{H.59}$$

where Υ is the plastic multiplier. The previous equation is the flow rule. It can be rewritten by introducing the unit normal to the flow potential:

$$N_{ij} = \frac{\frac{\partial g}{\partial \sigma_{ij}}}{\left(\frac{\partial g}{\partial \boldsymbol{\sigma}} : \frac{\partial g}{\partial \boldsymbol{\sigma}}\right)^{1/2}} \tag{H.60}$$

Hence,

$$D_{ij}^{p} = \Upsilon \left(\frac{\partial g}{\partial \boldsymbol{\sigma}} : \frac{\partial g}{\partial \boldsymbol{\sigma}} \right)^{1/2} N_{ij} \tag{H.61}$$

$$= \lambda N_{ij} \tag{H.62}$$

where λ is the flow intensity.

The time derivative of the internal parameters can take a similar form:

$$\dot{\mathbf{p}}^{(k)} = \lambda r^{(k)}(\boldsymbol{\sigma}, \mathbf{p}) \tag{H.63}$$

The superscript (k) was introduced since a yield function might depend on k internal parameters, which could be scalars, vectors (first-order tensors) or tensors (second-order tensors). Hence, the nomenclature convention for scalars, vectors (bold) and tensors (bold) was not respected here.

Furthermore, the flow intensity can be related to the effective plastic strain rate:

$$\overline{D}^{p} = \sqrt{\frac{2}{3}\mathbf{D}^{p} : \mathbf{D}^{p}} = \sqrt{\frac{2}{3} D_{ij}^{p} D_{ij}^{p}} = \sqrt{\frac{2}{3}\lambda\lambda \underbrace{N_{ij}N_{ij}}_{=1}} = \sqrt{\frac{2}{3}}\lambda \tag{H.64}$$

Moreover, the yield function has to change in such a way that it remains zero, while the deformations are plastic. This condition is called the consistency conditions, which can be stated mathematically as follows:

$$\dot{f}_Y = \frac{\partial f_Y}{\partial \sigma_{ij}} \dot{\sigma}_{ij} + \frac{\partial f_Y}{\partial \mathbf{p}^{(v)}} * \dot{\mathbf{p}}^{(v)} = 0 \tag{H.65}$$

The sign $*$ is used to represent a general product, i.e. a product between scalars, if $\mathbf{p}^{(v)}$ is a scalar, a dot product, if $\mathbf{p}^{(v)}$ is a vector (first-order tensor) or a double-dot product, if $\mathbf{p}^{(v)}$ is a tensor (second-order tensor).

The flow intensity λ can be determined based on the consistency condition (Eq. H.65), which becomes the following equation by taking the time derivative of Hooke's law (Eq. H.40) and by introducing the expression for the rate of internal parameters (Eq. H.63):

$$\frac{\partial f_Y}{\partial \sigma_{ij}} \mathbb{H}_{ijkl} (D_{kl} - \underbrace{D_{kl}^{p}}_{=\lambda N_{kl}}) + \frac{\partial f_Y}{\partial \mathbf{p}^{(v)}} * \lambda r^{(v)}(\boldsymbol{\sigma}, \mathbf{p}) = 0 \tag{H.66}$$

$$\Leftrightarrow \quad \lambda \left(\frac{\partial f_Y}{\partial \sigma_{ij}} \mathbb{H}_{ijkl} N_{kl} - \frac{\partial f_Y}{\partial \mathbf{p}^{(v)}} * r^{(v)} \right) = \frac{\partial f_Y}{\partial \sigma_{ij}} \mathbb{H}_{ijkl} D_{kl} \tag{H.67}$$

$$\Leftrightarrow \quad \lambda = \frac{\dfrac{\partial f_Y}{\partial \sigma_{ij}} \mathbb{H}_{ijkl} D_{kl}}{\dfrac{\partial f_Y}{\partial \sigma_{pq}} \mathbb{H}_{pqtu} N_{tu} - \dfrac{\partial f_Y}{\partial \mathbf{p}^{(v)}} * r^{(v)}} \tag{H.68}$$

H.3.2.4 Elastoplastic material tensor

The elastoplastic material tensor $\mathbb{M}$ in Eq. (H.75) can be computed by starting from the time derivative of Hooke's law (Eq. H.40):

$$\dot{\sigma}_{ij} = \mathbb{H}_{ijkl} D^e_{kl} \tag{H.69}$$

$$= \mathbb{H}_{ijkl}(D_{kl} - D^p_{kl}) \tag{H.70}$$

$$= \mathbb{H}_{ijkl}(D_{kl} - \lambda N_{kl}) \tag{H.71}$$

$$= \mathbb{H}_{ijkl}\left(D_{kl} - \frac{\dfrac{\partial f_Y}{\partial \sigma_{rs}} \mathbb{H}_{rsnm} D_{nm} N_{kl}}{\dfrac{\partial f_Y}{\partial \sigma_{pq}} \mathbb{H}_{pqtu} N_{tu} - \dfrac{\partial f_Y}{\partial \mathbf{p}^{(v)}} * r^{(v)}} \right) \tag{H.72}$$

$$= \mathbb{H}_{ijkl} D_{kl} - \frac{\mathbb{H}_{ijkl} \dfrac{\partial f_Y}{\partial \sigma_{rs}} \mathbb{H}_{rsnm} D_{nm} N_{kl}}{\dfrac{\partial f_Y}{\partial \sigma_{pq}} \mathbb{H}_{pqtu} N_{tu} - \dfrac{\partial f_Y}{\partial \mathbf{p}^{(v)}} * r^{(v)}} \tag{H.73}$$

$$= \mathbb{H}_{ijkl} D_{kl} - \frac{\mathbb{H}_{ijnm} \dfrac{\partial f_Y}{\partial \sigma_{rs}} \mathbb{H}_{rskl} D_{kl} N_{nm}}{\dfrac{\partial f_Y}{\partial \sigma_{pq}} \mathbb{H}_{pqtu} N_{tu} - \dfrac{\partial f_Y}{\partial \mathbf{p}^{(v)}} * r^{(v)}} \tag{H.74}$$

$$= \underbrace{\left(\mathbb{H}_{ijkl} - \frac{\mathbb{H}_{ijnm} \dfrac{\partial f_Y}{\partial \sigma_{rs}} \mathbb{H}_{rskl} N_{nm}}{\dfrac{\partial f_Y}{\partial \sigma_{pq}} \mathbb{H}_{pqtu} N_{tu} - \dfrac{\partial f_Y}{\partial \mathbf{p}^{(v)}} * r^{(v)}} \right)}_{=\mathbb{M}_{ijkl}} D_{kl} \tag{H.75}$$

H.3.2.5 Associated flow rule

A common hypothesis in plasticity theory is to assume that the flow potential g is the yield function $f_Y(\boldsymbol{\sigma}, \mathbf{q})$. Since the flow rule is associated with the yield function, this plasticity model is called *associated plasticity*.

H.3.3 Prandtl-Reuss equations

The Prandtl-Reuss equations can be derived from the previous equations by assuming isotropic elasticity, isotropic hardening and J_2-based plasticity (Von Mises).

In the following sections, the expressions of the normal to the flow potential $\mathbf{N}$, the material tensor $\mathbb{M}$ and the flow intensity λ are particularized based on the previous hypotheses.

H.3.3.1 Normal to the flow potential N

First, the following equation will be proven:

$$\frac{\partial f_Y}{\partial \sigma_{ij}} = \frac{\partial f_Y}{\partial s_{ij}} \tag{H.76}$$

In fact, f_Y is a function of the stress deviator $\mathbf{s}$ according to its definition (Eq. H.53). Therefore,

$$\begin{aligned}
\frac{\partial f_Y}{\partial \sigma_{ij}} &= \frac{\partial f_Y}{\partial s_{kl}} \frac{\partial s_{kl}}{\partial \sigma_{ij}} && \text{(H.77)}\\
&= \frac{\partial f_Y}{\partial s_{kl}} \frac{\partial}{\partial \sigma_{ij}} \left(\sigma_{kl} - \frac{\sigma_{mm}}{3} \delta_{kl} \right) && \text{(H.78)}\\
&= \frac{\partial f_Y}{\partial s_{kl}} \frac{\partial}{\partial \sigma_{ij}} \left((\delta_{ik}\delta_{jl} - \frac{1}{3}\delta_{ij}\delta_{kl})\sigma_{ij} \right) && \text{(H.79)}\\
&= \frac{\partial f_Y}{\partial s_{kl}} (\delta_{ik}\delta_{jl} - \frac{1}{3}\delta_{ij}\delta_{kl}) && \text{(H.80)}\\
&= \frac{\partial f_Y}{\partial s_{ij}} - \frac{1}{3}\delta_{ij} \frac{\partial f_Y}{\partial s_{kk}} && \text{(H.81)}\\
&= \frac{\partial f_Y}{\partial s_{ij}} && \text{(H.82)}
\end{aligned}$$

since $s_{ii} = 0$, which leads to

$$\frac{\partial f_Y}{\partial s_{33}} = \frac{\partial f_Y}{\partial s_{11}} \underbrace{\frac{\partial s_{11}}{\partial s_{33}}}_{=-1} + \frac{\partial f_Y}{\partial s_{22}} \underbrace{\frac{\partial s_{22}}{\partial s_{33}}}_{=-1} \quad \rightarrow \quad \frac{\partial f_Y}{\partial s_{kk}} = 0 \tag{H.83}$$

By the definition of the Von Mises yield criterion (Eq. H.53), it is possible to compute

$$\frac{\partial f_Y}{\partial s_{ij}} = \frac{\partial}{\partial s_{ij}} \left(\frac{1}{2} s_{ij} s_{ij} - \frac{1}{3} \sigma_Y^2 \right) = s_{ij} \tag{H.84}$$

Finally, the normal to the associated flow potential $\mathbf{N}$ (Eq. H.60) becomes

$$N_{ij} = \frac{s_{ij}}{\sqrt{s_{kl} s_{kl}}} \tag{H.85}$$

H.3.3.2 Material tensor $\mathbb{M}$

The material tensor determined in Eq. (H.75) can be rewritten by simplifying its different components:

$$\mathbb{M}_{ijkl} = \mathbb{H}_{ijkl} - \frac{\mathbb{H}_{ijnm} \dfrac{\partial f_Y}{\partial \sigma_{rs}} \mathbb{H}_{rskl} N_{nm}}{\dfrac{\partial f_Y}{\partial \sigma_{pq}} \mathbb{H}_{pqtu} N_{tu} - \dfrac{\partial f_Y}{\partial \mathbf{p}^{(v)}} * r^{(v)}} \tag{H.86}$$

Based on the definition of the Hooke tensor (Eq. H.42),

$$\mathbb{H}_{ijnm}N_{nm} = \left[K\delta_{ij}\delta_{nm} + G\left(\delta_{in}\delta_{jm} + \delta_{im}\delta_{nj} - \frac{2}{3}\delta_{ij}\delta_{mn}\right)\right]N_{nm} \tag{H.87}$$

$$= K\delta_{ij}\underbrace{N_{nn}}_{=0\text{ , since }s_{nn}=0} + G\left(N_{ij} + \underbrace{N_{ji}}_{=N_{ij}\text{ , since }s_{ij}=s_{ji}} - \frac{2}{3}\delta_{ij}\underbrace{N_{nn}}_{=0}\right) \tag{H.88}$$

$$= 2GN_{ij} \tag{H.89}$$

$$\frac{\partial f_Y}{\partial \sigma_{rs}}\mathbb{H}_{rskl} = s_{rs}\left[K\delta_{rs}\delta_{kl} + G\left(\delta_{rk}\delta_{sl} + \delta_{rl}\delta_{ks} - \frac{2}{3}\delta_{rs}\delta_{kl}\right)\right] \tag{H.90}$$

$$= K\delta_{kl}\underbrace{s_{ss}}_{=0} + G\left(s_{kl} + s_{lk} - \frac{2}{3}\delta_{kl}\underbrace{s_{ss}}_{=0}\right) \tag{H.91}$$

$$= 2Gs_{kl} \tag{H.92}$$

$$= 2G\sqrt{\frac{2}{3}}\sigma_Y N_{kl} \tag{H.93}$$

$$\frac{\partial f_Y}{\partial \sigma_{pq}}\mathbb{H}_{pqtu}N_{tu} = 2G\sqrt{\frac{2}{3}}\sigma_Y N_{tu}N_{tu} \quad \text{(see Eq. H.93)} \tag{H.94}$$

$$= 2G\sqrt{\frac{2}{3}}\sigma_Y \tag{H.95}$$

For isotropic hardening, we suppose that the yield stress σ_Y changes only with the effective plastic strain $\overline{\epsilon}^p$. Hence,

$$\dot{\sigma}_Y = \frac{\mathrm{d}\sigma_Y}{\mathrm{d}\overline{\epsilon}^p}\overline{D}^p = h_i(\overline{\epsilon}^p)\overline{D}^p = \underbrace{\sqrt{\frac{2}{3}}h_i(\overline{\epsilon}^p)}_{r^{(v)}}\lambda \tag{H.96}$$

where h_i is the isotropic hardening coefficient, which might depend on $\overline{\epsilon}^p$. Hence, the remaining term of the material tensor can finally be simplified:

$$\frac{\partial f_Y}{\partial \mathbf{p}^{(v)}} * r^{(v)} = \frac{\partial f_Y}{\partial \sigma_Y}\sqrt{\frac{2}{3}}h_i \tag{H.97}$$

$$= -\frac{2}{3}\sigma_Y\sqrt{\frac{2}{3}}h_i \tag{H.98}$$

Introducing all simplifications in Eq. (H.86),

$$\mathbb{M}_{ijkl} = \mathbb{H}_{ijkl} - \frac{2G}{1 + \dfrac{h_i}{3G}} N_{ij} N_{kl} \tag{H.99}$$

This equation can also be written

$$\mathbb{M}_{ijkl} = \mathbb{H}_{ijkl} - \beta 2G N_{ij} N_{kl} \qquad \text{with} \qquad \beta = \frac{1}{1 + \dfrac{h_i}{3G}} \tag{H.100}$$

H.3.3.3 Flow intensity λ

The flow intensity

$$\lambda = \frac{\dfrac{\partial f_Y}{\partial \sigma_{ij}} \mathbb{H}_{ijkl} D_{kl}}{\dfrac{\partial f_Y}{\partial \sigma_{pq}} \mathbb{H}_{pqtu} N_{tu} - \dfrac{\partial f_Y}{\partial \mathbf{p}^{(v)}} * r^{(v)}} \tag{H.101}$$

can be simplified in the same way as the material tensor:

$$\frac{\partial f_Y}{\partial \sigma_{ij}} \mathbb{H}_{ijkl} = 2G \sqrt{\frac{2}{3}} \sigma_Y N_{kl} \tag{H.102}$$

$$\frac{\partial f_Y}{\partial \sigma_{pq}} \mathbb{H}_{pqtu} N_{tu} = 2G \sqrt{\frac{2}{3}} \sigma_Y \tag{H.103}$$

$$\frac{\partial f_Y}{\partial \mathbf{p}^{(v)}} * r^{(v)} = -\frac{2}{3} \sigma_Y \sqrt{\frac{2}{3}} h_i \tag{H.104}$$

Hence,

$$\lambda = \frac{N_{kl} D_{kl}}{1 + \dfrac{h_i}{3G}} \tag{H.105}$$

H.3.3.4 Split between hydrostatic and deviatoric parts

Hydrostatic part

$$\dot{p} = -\frac{\dot{\sigma}_{ii}}{3} \tag{H.106}$$

$$= -\frac{\mathbb{M}_{iikl} D_{kl}}{3} \tag{H.107}$$

$$= -\frac{1}{3} \mathbb{H}_{iikl} D_{kl} - \frac{2G\beta}{3} \underbrace{N_{ii}}_{=0} N_{kl} D_{kl} \tag{H.108}$$

$$= -\frac{1}{3}\left[K \underbrace{\delta_{ii}}_{=3} \delta_{kl} + G\left(\delta_{ik}\delta_{il} + \delta_{il}\delta_{ki} - \frac{2}{3}\delta_{ii}\delta_{kl}\right)\right] D_{kl} \tag{H.109}$$

$$= -\frac{1}{3}\left[3KD_{kk} + G\left(D_{kl}\delta_{kl} + D_{kl}\delta_{kl} - 2\delta_{kl}D_{kl}\right)\right] \tag{H.110}$$

$$= -KD_{kk} \tag{H.111}$$

which can also be written

$$\dot{p} = -K \operatorname{tr} \mathbf{D} \tag{H.112}$$

Deviatoric part

$$\dot{s}_{ij} = \dot{\sigma}_{ij} - \dot{p}\delta_{ij} \tag{H.113}$$

$$= \mathbb{M}_{ijkl} D_{kl} - KD_{kk}\delta_{ij} \tag{H.114}$$

$$= \left(\mathbb{M}_{ijkl} - K\delta_{kl}\delta_{ij}\right) D_{kl} \tag{H.115}$$

$$= \left(\mathbb{H}_{ijkl} - K\delta_{kl}\delta_{ij} - 2G\beta N_{ij}N_{kl}\right) D_{kl} \tag{H.116}$$

$$= \left[G\left(\delta_{ik}\delta_{jl} + \delta_{il}\delta_{kj} - \frac{2}{3}\delta_{ij}\delta_{kl}\right) - 2G\beta N_{ij}N_{kl}\right] D_{kl} \tag{H.117}$$

$$\text{with} \quad \delta_{il}\delta_{kj} = \delta_{ik}\delta_{lj} \text{ since } D_{kl} = D_{lk}$$

$$= 2G\left(\delta_{ik}\delta_{jl} - \frac{1}{3}\delta_{ij}\delta_{kl} - \beta N_{ij}N_{kl}\right) D_{kl} \tag{H.118}$$

$$= 2G\left(D^d_{ij} - \beta N_{ij}N_{kl}D_{kl}\right) \tag{H.119}$$

The normal $\mathbf{N}$ to the associated flow potential can be replaced by the following relation, which was derived from Eq. (H.53) and Eq. (H.85):

$$N_{ij}N_{kl} = \frac{s_{ij}s_{kl}}{\frac{2}{3}\sigma_Y^2} \tag{H.120}$$

Thus,

$$\dot{s}_{ij} = 2G\left(D^d_{ij} - \beta_1 s_{ij}s_{kl}D_{kl}\right) \quad \text{with} \quad \beta_1 = \frac{1}{\frac{2}{3}\sigma_Y^2\left(1 + \frac{h_i}{3G}\right)} \tag{H.121}$$

Finally, to write the evolution of $\dot{\mathbf{s}}$ only as a function of the material parameters, the strain rate gradient $\mathbf{D}$ and the deviatoric stress tensor $\mathbf{s}$, the deviatoric strain rate tensor can be replaced by Eq. (H.22):

$$\dot{s}_{ij} = 2G\left(D_{ij} - \frac{D_{kk}}{3}\delta_{ij} - \beta_1 s_{ij}s_{kl}D_{kl}\right) \tag{H.122}$$

H.3.3.5 Relation between Cauchy stresses for a rigid plastic material in the plane-strain state

For a rigid plastic material with associated plasticity in the plane-strain state, a relation between the Cauchy stresses can be derived by noticing that the total strain rate is equal to the plastic strain rate, and by Eqs. (H.62) and (H.85):

$$D_{ij} = D_{ij}^{p} = \lambda N_{ij} = \lambda \frac{s_{ij}}{\sqrt{s_{kl} s_{kl}}} \tag{H.123}$$

In fact, if the plane-strain hypothesis applies in the normal plane to $\mathbf{e}_y$, i.e. $D_{yy} = 0$, the stress deviator s_{yy} is equal to zero according to the previous equation. By the definition of the stress deviator (Eq. H.27), this implies that:

$$\sigma_{yy} = \frac{\sigma_{xx} + \sigma_{zz}}{2} \tag{H.124}$$

Furthermore, the Von Mises yield criterion can be simplified by the previous relation in the principal axes, i.e. the non-diagonal terms of the Cauchy stress tensor are zero, via Eq. (H.55):

$$|\sigma_x - \sigma_z| = \frac{2}{\sqrt{3}} \sigma_Y \tag{H.125}$$

H.4 Fluid mechanics

H.4.1 Constitutive equation of a Newtonian fluid

The constitutive equation of a Newtonian fluid is derived in Kundu and Cohen [173] or Szeri [322]:

$$\boldsymbol{\sigma} = -p_{\text{th}} \mathbf{I} + 2\eta \mathbf{D} + \zeta (\nabla \cdot \mathbf{v}) \mathbf{I} \qquad \text{or} \qquad \sigma_{ij} = -p_{\text{th}} \delta_{ij} + 2\eta D_{ij} + \zeta D_{kk} \delta_{ij} \tag{H.126}$$

where p_{th}, η and ζ are the thermodynamic pressure, the dynamic viscosity and the second viscosity parameter, respectively.

By the definition of the mechanical pressure p (Eq. H.26) and the previous constitutive equation of a Newtonian fluid, we can write

$$p = p_{\text{th}} - \left(\frac{2}{3} \eta + \zeta \right) \nabla \cdot \mathbf{v} \tag{H.127}$$

The factor $2\eta/3 + \zeta$ is the coefficient of bulk viscosity. In practice, this coefficient is commonly assumed to be equal to 0 [173, 322]. This hypothesis is called the *Stokes assumption*. In this case, $p = p_{\text{th}}$. If p is the (mechanical) pressure in the lubricant, the notation p_l is used.

H.4.2 Navier-Stokes equation

The Navier-Stokes equation can be derived from the Eulerian description of the conservation of momentum, which is also known as the Cauchy momentum equation:

$$\rho \frac{\mathrm{d}\mathbf{v}}{\mathrm{d}t} = \nabla \cdot \boldsymbol{\sigma} + \rho \mathbf{b} \qquad \text{or} \qquad \rho \frac{\mathrm{d}v_i}{\mathrm{d}t} = \frac{\partial \sigma_{ij}}{\partial x_j} + \rho b_i \tag{H.128}$$

If the fluid is isotropic and Newtonian, the flow is described by the constitutive equation of the previous section, i.e. Eq. (H.126). Hence, one obtains the Navier-Stokes equation:

$$\rho \frac{\mathrm{d}\mathbf{v}}{\mathrm{d}t} = \nabla \left[-p_{\mathrm{th}} + \zeta (\nabla \cdot \mathbf{v}) \right] + \nabla \cdot (2\eta \mathbf{D}) + \rho \mathbf{b} \tag{H.129}$$

In a Cartesian coordinate system, this equation can successively be expanded:

$$\rho \frac{\mathrm{d}v_i}{\mathrm{d}t} = \frac{\partial}{\partial x_i} \left[-p_{\mathrm{th}} + \zeta \left(\frac{\partial v_k}{\partial x_k} \right) \right] + \frac{\partial}{\partial x_j} (2\eta D_{ij}) + \rho b_i \tag{H.130}$$

Then,

$$\rho \left(\frac{\partial v_i}{\partial t} + v_j \frac{\partial v_i}{\partial x_j} \right) = \frac{\partial}{\partial x_i} \left[-p_{\mathrm{th}} + \zeta \left(\frac{\partial v_k}{\partial x_k} \right) \right] + \frac{\partial}{\partial x_j} (2\eta D_{ij}) + \rho b_i \tag{H.131}$$

And finally, in its full form,

$$\begin{aligned} &\rho \left(\frac{\partial v_x}{\partial t} + v_x \frac{\partial v_x}{\partial x} + v_y \frac{\partial v_x}{\partial y} + v_z \frac{\partial v_x}{\partial z} \right) \\ &\quad = \frac{\partial}{\partial x} \left[-p_{\mathrm{th}} + \zeta \left(\frac{\partial v_x}{\partial x} + \frac{\partial v_y}{\partial y} + \frac{\partial v_z}{\partial z} \right) + 2\eta \frac{\partial v_x}{\partial x} \right] + \frac{\partial}{\partial y} \left[\eta \left(\frac{\partial v_x}{\partial y} + \frac{\partial v_y}{\partial x} \right) \right] \\ &\qquad + \frac{\partial}{\partial z} \left[\eta \left(\frac{\partial v_x}{\partial z} + \frac{\partial v_z}{\partial x} \right) \right] + \rho b_x \end{aligned} \tag{H.132a}$$

$$\begin{aligned} &\rho \left(\frac{\partial v_y}{\partial t} + v_x \frac{\partial v_y}{\partial x} + v_y \frac{\partial v_y}{\partial y} + v_z \frac{\partial v_y}{\partial z} \right) \\ &\quad = \frac{\partial}{\partial x} \left[-p_{\mathrm{th}} + \zeta \left(\frac{\partial v_x}{\partial x} + \frac{\partial v_y}{\partial y} + \frac{\partial v_z}{\partial z} \right) + 2\eta \frac{\partial v_y}{\partial y} \right] + \frac{\partial}{\partial x} \left[\eta \left(\frac{\partial v_x}{\partial y} + \frac{\partial v_y}{\partial x} \right) \right] \\ &\qquad + \frac{\partial}{\partial z} \left[\eta \left(\frac{\partial v_y}{\partial z} + \frac{\partial v_z}{\partial y} \right) \right] + \rho b_y \end{aligned} \tag{H.132b}$$

$$\begin{aligned} &\rho \left(\frac{\partial v_z}{\partial t} + v_x \frac{\partial v_z}{\partial x} + v_y \frac{\partial v_z}{\partial y} + v_z \frac{\partial v_z}{\partial z} \right) \\ &\quad = \frac{\partial}{\partial z} \left[-p_{\mathrm{th}} + \zeta \left(\frac{\partial v_x}{\partial x} + \frac{\partial v_y}{\partial y} + \frac{\partial v_z}{\partial z} \right) + 2\eta \frac{\partial v_z}{\partial z} \right] + \frac{\partial}{\partial x} \left[\eta \left(\frac{\partial v_x}{\partial z} + \frac{\partial v_z}{\partial x} \right) \right] \end{aligned}$$

$$+\frac{\partial}{\partial y}\left[\eta\left(\frac{\partial v_y}{\partial z}+\frac{\partial v_z}{\partial y}\right)\right]+\rho b_z \tag{H.132c}$$

H.4.3 Reynolds equation from continuity equation

The *continuity equation* (Eq. H.33) can be successively written as follows

$$\frac{\mathrm{d}\rho}{\mathrm{d}t}+\rho\frac{\partial v_i}{\partial x_i}=0 \quad\Rightarrow\quad \frac{\partial\rho}{\partial t}+v_i\frac{\partial\rho}{\partial x_i}+\rho\frac{\partial v_i}{\partial x_i}=0 \quad\Rightarrow\quad \frac{\partial\rho}{\partial t}+\frac{\partial(\rho v_i)}{\partial x_i}=0 \tag{H.133}$$

In its full form, the previous equation becomes

$$\frac{\partial\rho}{\partial t}+\frac{\partial(\rho v_x)}{\partial x}+\frac{\partial(\rho v_y)}{\partial y}+\frac{\partial(\rho v_z)}{\partial z}=0 \tag{H.134}$$

This equation can be integrated along z from $z=0$ to $z=h_l(x,t)$, which does not depend on y by assumption:

$$[\rho v_z]_0^{h_l(x,t)}=-\int_0^{h_l(x,t)}\frac{\partial(\rho v_x)}{\partial x}\mathrm{d}z-\int_0^{h_l(x,t)}\frac{\partial(\rho v_y)}{\partial y}\mathrm{d}z-\int_0^{h_l(x,t)}\frac{\partial\rho}{\partial t}\mathrm{d}z \tag{H.135}$$

By interchanging integration and differentiation in the previous equation,

$$[\rho v_z]_0^{h_l(x,t)}=-\frac{\partial}{\partial x}\int_0^{h_l(x,t)}\rho v_x\,\mathrm{d}z+(\rho v_x)\,|_{h_l(x,t)}\frac{\partial h_l}{\partial x}-\frac{\partial}{\partial y}\int_0^{h_l(x,t)}\rho v_y\,\mathrm{d}z-\int_0^{h_l(x,t)}\frac{\partial\rho}{\partial t}\,\mathrm{d}z \tag{H.136}$$

is obtained by applying Leibnitz's rule for differentiation under the integral sign [369]:

$$\frac{\mathrm{d}}{\mathrm{d}x}\int_{a(x)}^{b(x)}f(x,t)\,\mathrm{d}t=\int_{a(x)}^{b(x)}\frac{\partial f(x,t)}{\partial x}\,\mathrm{d}t+f\,[x,b(x)]\,\frac{\mathrm{d}b(x)}{\mathrm{d}x}-f\,[x,a(x)]\,\frac{\mathrm{d}a(x)}{\mathrm{d}x} \tag{H.137}$$

The unknown quantities v_x and v_y in Eq. (H.136) can be substituted by their expressions from Eq. (4.139):

$$\begin{aligned}[\rho v_z]_0^{h_l(x,t)}=&-\frac{1}{2}\frac{\partial}{\partial x}\left[\frac{\partial p_l}{\partial x}\int_0^{h_l}\frac{\rho}{\eta}(z^2-zh_l)\,\mathrm{d}z\right]-\frac{1}{2}\frac{\partial}{\partial y}\left[\frac{\partial p_l}{\partial y}\int_0^{h_l}\frac{\rho}{\eta}(z^2-zh_l)\,\mathrm{d}z\right]\\&-\frac{\partial}{\partial x}\int_0^{h_l}\rho\left[\left(1-\frac{z}{h_l}\right)v_s+\frac{z}{h_l}v_r\right]\mathrm{d}z+\rho v_r\frac{\partial h_l}{\partial x}-\int_0^{h_l}\frac{\partial\rho}{\partial t}\,\mathrm{d}z\end{aligned} \tag{H.138}$$

The dynamic viscosity η and the density ρ are assumed to not change along $\mathbf{e}_z$ due to the thin film hypothesis. Thus, the previous integrals can be computed:

$$[\rho v_z]_0^{h_l(x,t)}=\frac{\partial}{\partial x}\left(\frac{\rho h_l^3}{12\eta}\frac{\partial p_l}{\partial x}\right)+\frac{\partial}{\partial y}\left(\frac{\rho h_l^3}{12\eta}\frac{\partial p_l}{\partial y}\right)-\frac{\partial}{\partial x}\left(\rho h_l\frac{v_s+v_r}{2}\right)+\rho v_r\frac{\partial h_l}{\partial x}-h_l\frac{\partial\rho}{\partial t} \tag{H.139}$$

Moreover, by the boundary conditions (Eq. 4.138),

$$[\rho v_z]_0^{h_l(x,t)} = \rho(W_r - W_s) = \rho \frac{\mathrm{d}h_l}{\mathrm{d}t} \tag{H.140}$$

The *Reynolds equation* can finally be written by combining Eqs. (H.139) and (H.140):

$$\frac{\partial}{\partial x}\left(\frac{\rho h_l^3}{12\eta}\frac{\partial p_l}{\partial x}\right) + \frac{\partial}{\partial y}\left(\frac{\rho h_l^3}{12\eta}\frac{\partial p_l}{\partial y}\right) = \frac{\partial}{\partial x}\left(\rho h_l \frac{v_s + v_r}{2}\right) + \rho\frac{\mathrm{d}h_l}{\mathrm{d}t} - \rho v_r \frac{\partial h_l}{\partial x} + h_l \frac{\partial \rho}{\partial t} \tag{H.141}$$

This equation can be simplified in the context of rolling since the vertical distance $h_l = h_l(x,t)$ between a point of the roll and the strip surface changes either locally or convectively due to the rotation of the roll, which is why the rolling speed appears in the following equation:

$$\frac{\mathrm{d}h_l}{\mathrm{d}t} = \frac{\partial h_l}{\partial t} + v_r \frac{\partial h_l}{\partial x} \tag{H.142}$$

Hence, the general Reynolds equation can be written as follows:

$$\frac{\partial}{\partial x}\left(\frac{\rho h_l^3}{12\eta}\frac{\partial p_l}{\partial x}\right) + \frac{\partial}{\partial y}\left(\frac{\rho h_l^3}{12\eta}\frac{\partial p_l}{\partial y}\right) = \frac{\partial}{\partial x}\left(\rho h_l \frac{v_s + v_r}{2}\right) + \frac{\partial(\rho h_l)}{\partial t} \tag{H.143}$$

Appendix I

Proof of an incoherence in Jortner's roll deformation formula

In this appendix, it will be shown that Eq. (8) in Jortner et al. [163], i.e.

$$\overline{u}(a,\theta,\alpha) = u(a,\theta,\alpha) - \frac{pa}{\pi}(1-\nu-2\nu^2) \tag{I.1}$$

should be replaced by

$$\overline{u}(a,\theta,\alpha) = u(a,\theta,\alpha) - \frac{pa}{E}(1-\nu-2\nu^2) \tag{I.2}$$

This correction was necessary to compute coherent roll deformations by Jortner's method as explained in Sec. 4.6.3. In the following proof, as well as in the previous equations, the same notations as in Jortner et al. [163] are used.

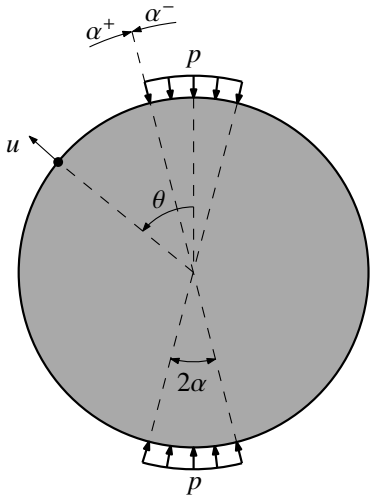

Figure I.1: Definition of the approach directions α^- and α^+.

According to Eq. (7) in Jortner et al. [163], the deformation at a position θ due to the applied pressures in the 2α sector, for $|\theta| > \alpha$ (Fig. I.1) is given by the following equation:

$$u(a,\theta,\alpha) = \frac{pa}{\pi E}\left\{(1-\nu-2\nu^2)\left[\cos(\theta+\alpha)\left(\tan^{-1}\frac{1+\cos(\theta+\alpha)}{\sin(\theta+\alpha)}+\tan^{-1}\frac{1-\cos(\theta+\alpha)}{\sin(\theta+\alpha)}\right)\right.\right.$$
$$\left.-\cos(\theta-\alpha)\left(\tan^{-1}\frac{1+\cos(\theta-\alpha)}{\sin(\theta-\alpha)}+\tan^{-1}\frac{1-\cos(\theta-\alpha)}{\sin(\theta-\alpha)}\right)\right]$$
$$\left.+(1-\nu^2)\left[\sin(\theta+\alpha)\ln\frac{1-\cos(\theta+\alpha)}{1+\cos(\theta+\alpha)}-\sin(\theta-\alpha)\ln\frac{1-\cos(\theta-\alpha)}{1+\cos(\theta-\alpha)}\right]\right\} \quad \text{(I.3)}$$

On the one hand, the limit from below yields the following result:

$$\lim_{\theta\to\alpha^-} u(a,\theta,\alpha) = \frac{pa}{\pi E}\left\{(1-\nu-2\nu^2)\left[\cos 2\alpha\left(\tan^{-1}\frac{1+\cos 2\alpha}{\sin 2\alpha}+\tan^{-1}\frac{1-\cos 2\alpha}{\sin 2\alpha}\right)+\frac{\pi}{2}\right]\right.$$
$$\left.+(1-\nu^2)\sin 2\alpha\ln\frac{1-\cos 2\alpha}{1+\cos 2\alpha}\right\} \quad \text{(I.4)}$$

On the other hand, the limit from above is computed as follows:

$$\lim_{\theta\to\alpha^+} u(a,\theta,\alpha) = \frac{pa}{\pi E}\left\{(1-\nu-2\nu^2)\left[\cos 2\alpha\left(\tan^{-1}\frac{1+\cos 2\alpha}{\sin 2\alpha}+\tan^{-1}\frac{1-\cos 2\alpha}{\sin 2\alpha}\right)-\frac{\pi}{2}\right]\right.$$
$$\left.+(1-\nu^2)\sin 2\alpha\ln\frac{1-\cos 2\alpha}{1+\cos 2\alpha}\right\} \quad \text{(I.5)}$$

Since the expression of $u(a,\theta,\alpha)$ in Eq. (I.3) is the correct value for $|\theta| > \alpha$, $\lim_{\theta\to\alpha^+} u(a,\theta,\alpha)$ should be the value at $\theta = \alpha$. The offset between $\lim_{\theta\to\alpha^+} u(a,\theta,\alpha)$ and $\lim_{\theta\to\alpha^-} u(a,\theta,\alpha)$ was introduced by the integration of a singularity at $\theta = \alpha$, as explaine in [163]. Subtracting this offset of $u(a,\theta,\alpha)$ in Eq. (I.3) then yields an expression of $u(a,\theta,\alpha)$ for $|\theta| < \alpha$. Equation (8) in [163] can therefore be corrected as follows:

$$\overline{u}(a,\theta,\alpha) = u(a,\theta,\alpha) + \lim_{\theta\to\alpha^+} u(a,\theta,\alpha) - \lim_{\theta\to\alpha^-} u(a,\theta,\alpha) \quad \text{(I.6)}$$
$$= u(a,\theta,\alpha) - \frac{pa}{E}\left(1-\nu-2\nu^2\right) \quad \text{(I.7)}$$

Appendix J

Jortner influence functions

In this appendix, the *Jortner influence functions*, which are required to compute radial roll flattening due to pressure stresses (Sec. 4.6.4), are written down based on [163]:

- $-\frac{\pi}{2} < \theta < \alpha$ or $\alpha < \theta < \frac{\pi}{2}$:

$$\begin{aligned}
&\mathrm{JIF}_{r,p}\left(\theta, \alpha, \nu_r\right) = \left(1 - \nu_r - 2\nu_r^2\right) \\
&\left(\cos\left(\theta + \alpha\right)\left\{\tan^{-1}\left[\frac{1 + \cos\left(\theta + \alpha\right)}{\sin\left(\theta + \alpha\right)}\right] + \tan^{-1}\left[\frac{1 - \cos\left(\theta + \alpha\right)}{\sin\left(\theta + \alpha\right)}\right]\right\} - \cos\left(\theta - \alpha\right)\left\{\tan^{-1}\left[\frac{1 + \cos\left(\theta - \alpha\right)}{\cos\left(\theta - \alpha\right)}\right] + \tan^{-1}\left[\frac{1 - \cos\left(\theta - \alpha\right)}{\sin\left(\theta - \alpha\right)}\right]\right\}\right) \\
&+ \left(1 - \nu_r^2\right)\left\{\sin\left(\theta + \alpha\right)\ln\left[\frac{1 - \cos\left(\theta + \alpha\right)}{1 + \cos\left(\theta + \alpha\right)}\right] - \sin\left(\theta - \alpha\right)\ln\left[\frac{1 - \cos\left(\theta - \alpha\right)}{1 + \cos\left(\theta - \alpha\right)}\right]\right\}
\end{aligned} \tag{J.1}$$

- $\theta = -\alpha$:

$$\begin{aligned}
&\mathrm{JIF}_{r,p}\left(\theta, \alpha, \nu_r\right) = \left(1 - \nu_r - 2\nu_r^2\right) \\
&\left(\cos\left(\theta + \alpha\right)\left\{-\frac{\pi}{2} + 0\right\} - \cos\left(\theta - \alpha\right)\left\{\tan^{-1}\left[\frac{1 + \cos\left(\theta - \alpha\right)}{\cos\left(\theta - \alpha\right)}\right] + \tan^{-1}\left[\frac{1 - \cos\left(\theta - \alpha\right)}{\sin\left(\theta - \alpha\right)}\right]\right\}\right) \\
&+ \left(1 - \nu_r^2\right)\left\{0 - \sin\left(\theta - \alpha\right)\ln\left[\frac{1 - \cos\left(\theta - \alpha\right)}{1 + \cos\left(\theta - \alpha\right)}\right]\right\}
\end{aligned} \tag{J.2}$$

- $-\alpha < \theta < \alpha$:

$$\begin{aligned}
&\mathrm{JIF}_{r,p}\left(\theta, \alpha, \nu_r\right) = \left(1 - \nu_r - 2\nu_r^2\right) \\
&\left(\cos\left(\theta + \alpha\right)\left\{\tan^{-1}\left[\frac{1 + \cos\left(\theta + \alpha\right)}{\sin\left(\theta + \alpha\right)}\right] + \tan^{-1}\left[\frac{1 - \cos\left(\theta + \alpha\right)}{\sin\left(\theta + \alpha\right)}\right]\right\} - \cos\left(\theta - \alpha\right)\left\{\tan^{-1}\left[\frac{1 + \cos\left(\theta - \alpha\right)}{\cos\left(\theta - \alpha\right)}\right] + \tan^{-1}\left[\frac{1 - \cos\left(\theta - \alpha\right)}{\sin\left(\theta - \alpha\right)}\right]\right\}\right) \\
&+ \left(1 - \nu_r^2\right)\left\{\sin\left(\theta + \alpha\right)\ln\left[\frac{1 - \cos\left(\theta + \alpha\right)}{1 + \cos\left(\theta + \alpha\right)}\right] - \sin\left(\theta - \alpha\right)\ln\left[\frac{1 - \cos\left(\theta - \alpha\right)}{1 + \cos\left(\theta - \alpha\right)}\right]\right\} - \pi\left(1 - \nu_r - 2\nu_r^2\right)
\end{aligned} \tag{J.3}$$

- $\theta = \alpha$:

$$\begin{aligned}
&\mathrm{JIF}_{r,p}\left(\theta, \alpha, \nu_r\right) = \left(1 - \nu_r - 2\nu_r^2\right) \\
&\left(\cos\left(\theta + \alpha\right)\left\{\tan^{-1}\left[\frac{1 + \cos\left(\theta + \alpha\right)}{\sin\left(\theta + \alpha\right)}\right] + \tan^{-1}\left[\frac{1 - \cos\left(\theta + \alpha\right)}{\sin\left(\theta + \alpha\right)}\right]\right\} - \cos\left(\theta - \alpha\right)\left\{\frac{\pi}{2} + 0\right\}\right) \\
&+ \left(1 - \nu_r^2\right)\left\{\sin\left(\theta + \alpha\right)\ln\left[\frac{1 - \cos\left(\theta + \alpha\right)}{1 + \cos\left(\theta + \alpha\right)}\right] - 0\right\}
\end{aligned} \tag{J.4}$$

Appendix K

Meindl influence functions

In this appendix, the *Meindl influence functions*, which are required to compute radial and tangential roll flattening due to radial and tangential stresses (Sec. 4.6.4), are written down based on Meindl [220] and Krimpelstätter [171]. These functions are structured in the following order: radial displacement due to pressure, tangential displacement due to pressure, radial displacement due to shear stress and tangential displacement due to shear stress. For each case, the formulas of the generalized plane-strain state, the plane-strain state and the plane-stress state are listed. The formulas start on the following page to have a separate page for each case.

K.1 Radial displacement due to pressure

K.1.1 Generalized plane-strain state

- $-\frac{\pi}{2} < \theta < \alpha$:

$$\begin{aligned}\mathrm{MIF}_{r,p}(\theta,\alpha,\nu_r) = &\left(1-\nu_r^2\right)\left\{\frac{\pi}{2}\left(\frac{\nu_r}{1-\nu_r}-1\right)\cos(\theta+\alpha)+\sin(\theta+\alpha)\ln\left[\tan^2\left(\frac{\theta+\alpha}{2}\right)\right]\right\}\\ &-\left(1-\nu_r^2\right)\left\{\frac{\pi}{2}\left(\frac{\nu_r}{1-\nu_r}-1\right)\cos(\theta-\alpha)+\sin(\theta-\alpha)\ln\left[\tan^2\left(\frac{\theta-\alpha}{2}\right)\right]\right\}-4\alpha\nu_r^2\end{aligned} \quad \text{(K.1)}$$

- $\theta = -\alpha$:

$$\begin{aligned}\mathrm{MIF}_{r,p}(\theta,\alpha,\nu_r) = &\left(1-\nu_r^2\right)\left\{\frac{\pi}{2}\left(\frac{\nu_r}{1-\nu_r}-1\right)\cos(\theta+\alpha)+0\right\}\\ &-\left(1-\nu_r^2\right)\left\{\frac{\pi}{2}\left(\frac{\nu_r}{1-\nu_r}-1\right)\cos(\theta-\alpha)+\sin(\theta-\alpha)\ln\left[\tan^2\left(\frac{\theta-\alpha}{2}\right)\right]\right\}-4\alpha\nu_r^2\end{aligned} \quad \text{(K.2)}$$

- $-\alpha < \theta < \alpha$:

$$\begin{aligned}\mathrm{MIF}_{r,p}(\theta,\alpha,\nu_r) = &\frac{\pi}{2}\left(1-\nu_r^2\right)\left(\frac{\nu_r}{1-\nu_r}-1\right)\left[2-\cos(\theta-\alpha)-\cos(\theta+\alpha)\right]\\ &+\left(1-\nu_r^2\right)\left\{\sin(\theta+\alpha)\ln\left[\tan^2\left(\frac{\theta+\alpha}{2}\right)\right]-\sin(\theta-\alpha)\ln\left[\tan^2\left(\frac{\theta-\alpha}{2}\right)\right]\right\}-4\alpha\nu_r^2\end{aligned} \quad \text{(K.3)}$$

- $\theta = \alpha$:

$$\begin{aligned}\mathrm{MIF}_{r,p}(\theta,\alpha,\nu_r) = &\left(1-\nu_r^2\right)\left\{-\frac{\pi}{2}\left(\frac{\nu_r}{1-\nu_r}-1\right)\cos(\theta+\alpha)+\sin(\theta+\alpha)\ln\left[\tan^2\left(\frac{\theta+\alpha}{2}\right)\right]\right\}\\ &-\left(1-\nu_r^2\right)\left\{-\frac{\pi}{2}\left(\frac{\nu_r}{1-\nu_r}-1\right)\cos(\theta-\alpha)+0\right\}-4\alpha\nu_r^2\end{aligned} \quad \text{(K.4)}$$

- $\alpha < \theta < \frac{\pi}{2}$:

$$\begin{aligned}\mathrm{MIF}_{r,p}(\theta,\alpha,\nu_r) = &\left(1-\nu_r^2\right)\left\{-\frac{\pi}{2}\left(\frac{\nu_r}{1-\nu_r}-1\right)\cos(\theta+\alpha)+\sin(\theta+\alpha)\ln\left[\tan^2\left(\frac{\theta+\alpha}{2}\right)\right]\right\}\\ &-\left(1-\nu_r^2\right)\left\{-\frac{\pi}{2}\left(\frac{\nu_r}{1-\nu_r}-1\right)\cos(\theta-\alpha)+\sin(\theta-\alpha)\ln\left[\tan^2\left(\frac{\theta-\alpha}{2}\right)\right]\right\}-4\alpha\nu_r^2\end{aligned} \quad \text{(K.5)}$$

K.1.2 Plane-strain state

- $-\frac{\pi}{2} < \theta < \alpha$:

$$\begin{aligned}\mathrm{MIF}_{r,p}(\theta,\alpha,\nu_r) = &\left(1-\nu_r^2\right)\left\{\frac{\pi}{2}\left(\frac{\nu_r}{1-\nu_r}-1\right)\cos(\theta+\alpha)+\sin(\theta+\alpha)\ln\left[\tan^2\left(\frac{\theta+\alpha}{2}\right)\right]\right\}\\ &-\left(1-\nu_r^2\right)\left\{\frac{\pi}{2}\left(\frac{\nu_r}{1-\nu_r}-1\right)\cos(\theta-\alpha)+\sin(\theta-\alpha)\ln\left[\tan^2\left(\frac{\theta-\alpha}{2}\right)\right]\right\}\end{aligned} \tag{K.6}$$

- $\theta = -\alpha$:

$$\begin{aligned}\mathrm{MIF}_{r,p}(\theta,\alpha,\nu_r) = &\left(1-\nu_r^2\right)\left\{\frac{\pi}{2}\left(\frac{\nu_r}{1-\nu_r}-1\right)\cos(\theta+\alpha)+0\right\}\\ &-\left(1-\nu_r^2\right)\left\{\frac{\pi}{2}\left(\frac{\nu_r}{1-\nu_r}-1\right)\cos(\theta-\alpha)+\sin(\theta-\alpha)\ln\left[\tan^2\left(\frac{\theta-\alpha}{2}\right)\right]\right\}\end{aligned} \tag{K.7}$$

- $-\alpha < \theta < \alpha$:

$$\begin{aligned}\mathrm{MIF}_{r,p}(\theta,\alpha,\nu_r) = &\frac{\pi}{2}\left(1-\nu_r^2\right)\left(\frac{\nu_r}{1-\nu_r}-1\right)\left[2-\cos(\theta-\alpha)-\cos(\theta+\alpha)\right]\\ &+\left(1-\nu_r^2\right)\left\{\sin(\theta+\alpha)\ln\left[\tan^2\left(\frac{\theta+\alpha}{2}\right)\right]-\sin(\theta-\alpha)\ln\left[\tan^2\left(\frac{\theta-\alpha}{2}\right)\right]\right\}\end{aligned} \tag{K.8}$$

- $\theta = \alpha$:

$$\begin{aligned}\mathrm{MIF}_{r,p}(\theta,\alpha,\nu_r) = &\left(1-\nu_r^2\right)\left\{-\frac{\pi}{2}\left(\frac{\nu_r}{1-\nu_r}-1\right)\cos(\theta+\alpha)+\sin(\theta+\alpha)\ln\left[\tan^2\left(\frac{\theta+\alpha}{2}\right)\right]\right\}\\ &-\left(1-\nu_r^2\right)\left\{-\frac{\pi}{2}\left(\frac{\nu_r}{1-\nu_r}-1\right)\cos(\theta-\alpha)+0\right\}\end{aligned} \tag{K.9}$$

- $\alpha < \theta < \frac{\pi}{2}$:

$$\begin{aligned}\mathrm{MIF}_{r,p}(\theta,\alpha,\nu_r) = &\left(1-\nu_r^2\right)\left\{-\frac{\pi}{2}\left(\frac{\nu_r}{1-\nu_r}-1\right)\cos(\theta+\alpha)+\sin(\theta+\alpha)\ln\left[\tan^2\left(\frac{\theta+\alpha}{2}\right)\right]\right\}\\ &-\left(1-\nu_r^2\right)\left\{-\frac{\pi}{2}\left(\frac{\nu_r}{1-\nu_r}-1\right)\cos(\theta-\alpha)+\sin(\theta-\alpha)\ln\left[\tan^2\left(\frac{\theta-\alpha}{2}\right)\right]\right\}\end{aligned} \tag{K.10}$$

K.1.3 Plane-stress state

- $-\frac{\pi}{2} < \theta < \alpha$:

$$\begin{aligned}\mathrm{MIF}_{r,p}(\theta,\alpha,\nu_r) = {} & \frac{\pi}{2}(\nu_r - 1)\cos(\theta+\alpha) + \sin(\theta+\alpha)\ln\left[\tan^2\left(\frac{\theta+\alpha}{2}\right)\right] \\ & - \left\{\frac{\pi}{2}(\nu_r - 1)\cos(\theta-\alpha) + \sin(\theta-\alpha)\ln\left[\tan^2\left(\frac{\theta-\alpha}{2}\right)\right]\right\}\end{aligned} \tag{K.11}$$

- $\theta = -\alpha$:

$$\begin{aligned}\mathrm{MIF}_{r,p}(\theta,\alpha,\nu_r) = {} & \frac{\pi}{2}(\nu_r - 1)\cos(\theta+\alpha) + 0 \\ & - \left\{\frac{\pi}{2}(\nu_r - 1)\cos(\theta-\alpha) + \sin(\theta-\alpha)\ln\left[\tan^2\left(\frac{\theta-\alpha}{2}\right)\right]\right\}\end{aligned} \tag{K.12}$$

- $-\alpha < \theta < \alpha$:

$$\begin{aligned}\mathrm{MIF}_{r,p}(\theta,\alpha,\nu_r) = {} & \frac{\pi}{2}(\nu_r - 1)\left[2 - \cos(\theta-\alpha) - \cos(\theta+\alpha)\right] \\ & + \sin(\theta+\alpha)\ln\left[\tan^2\left(\frac{\theta+\alpha}{2}\right)\right] - \sin(\theta-\alpha)\ln\left[\tan^2\left(\frac{\theta-\alpha}{2}\right)\right]\end{aligned} \tag{K.13}$$

- $\theta = \alpha$:

$$\begin{aligned}\mathrm{MIF}_{r,p}(\theta,\alpha,\nu_r) = {} & -\frac{\pi}{2}(\nu_r - 1)\cos(\theta+\alpha) + \sin(\theta+\alpha)\ln\left[\tan^2\left(\frac{\theta+\alpha}{2}\right)\right] \\ & - \left[-\frac{\pi}{2}(\nu_r - 1)\cos(\theta-\alpha) + 0\right]\end{aligned} \tag{K.14}$$

- $\alpha < \theta < \frac{\pi}{2}$:

$$\begin{aligned}\mathrm{MIF}_{r,p}(\theta,\alpha,\nu_r) = {} & -\frac{\pi}{2}(\nu_r - 1)\cos(\theta+\alpha) + \sin(\theta+\alpha)\ln\left[\tan^2\left(\frac{\theta+\alpha}{2}\right)\right] \\ & - \left\{-\frac{\pi}{2}(\nu_r - 1)\cos(\theta-\alpha) + \sin(\theta-\alpha)\ln\left[\tan^2\left(\frac{\theta-\alpha}{2}\right)\right]\right\}\end{aligned} \tag{K.15}$$

K.2 Tangential displacement due to pressure

K.2.1 Generalized plane-strain state and plane-strain state

- $-\frac{\pi}{2} < \theta < \alpha$:

$$\begin{aligned}\mathrm{MIF}_{\theta,p}(\theta,\alpha,\nu_r) = {} & \left(1-\nu_r^2\right)\left\{-\frac{\pi}{2}\left(\frac{\nu_r}{1-\nu_r}-1\right)\sin(\theta+\alpha) - 2\sin^2\left(\frac{\theta+\alpha}{2}\right)\ln\left[\tan^2\left(\frac{\theta+\alpha}{2}\right)\right] - 2\ln\left[\cos^2\left(\frac{\theta+\alpha}{2}\right)\right]\right\} \\ & - \left(1-\nu_r^2\right)\left\{-\frac{\pi}{2}\left(\frac{\nu_r}{1-\nu_r}-1\right)\sin(\theta-\alpha) - 2\sin^2\left(\frac{\theta-\alpha}{2}\right)\ln\left[\tan^2\left(\frac{\theta-\alpha}{2}\right)\right] - 2\ln\left[\cos^2\left(\frac{\theta-\alpha}{2}\right)\right]\right\}\end{aligned} \tag{K.16}$$

- $\theta = -\alpha$:

$$\begin{aligned}\mathrm{MIF}_{\theta,p}(\theta,\alpha,\nu_r) = {} & \left(1-\nu_r^2\right)\left\{-\frac{\pi}{2}\left(\frac{\nu_r}{1-\nu_r}-1\right)\sin(\theta+\alpha) - 0 - 2\ln\left[\cos^2\left(\frac{\theta+\alpha}{2}\right)\right]\right\} \\ & - \left(1-\nu_r^2\right)\left\{-\frac{\pi}{2}\left(\frac{\nu_r}{1-\nu_r}-1\right)\sin(\theta-\alpha) - 2\sin^2\left(\frac{\theta-\alpha}{2}\right)\ln\left[\tan^2\left(\frac{\theta-\alpha}{2}\right)\right] - 2\ln\left[\cos^2\left(\frac{\theta-\alpha}{2}\right)\right]\right\}\end{aligned} \tag{K.17}$$

- $-\alpha < \theta < \alpha$:

$$\begin{aligned}\mathrm{MIF}_{\theta,p}(\theta,\alpha,\nu_r) = {} & \frac{\pi}{2}\left(1-\nu_r^2\right)\left(\frac{\nu_r}{1-\nu_r}-1\right)\left[\sin(\theta+\alpha)+\sin(\theta-\alpha)\right] \\ & - 2\left(1-\nu_r^2\right)\left\{\sin^2\left(\frac{\theta+\alpha}{2}\right)\ln\left[\tan^2\left(\frac{\theta+\alpha}{2}\right)\right] + \ln\left[\cos^2\left(\frac{\theta+\alpha}{2}\right)\right]\right\} \\ & + 2\left(1-\nu_r^2\right)\left\{\sin^2\left(\frac{\theta-\alpha}{2}\right)\ln\left[\tan^2\left(\frac{\theta-\alpha}{2}\right)\right] + \ln\left[\cos^2\left(\frac{\theta-\alpha}{2}\right)\right]\right\}\end{aligned} \tag{K.18}$$

- $\theta = \alpha$:

$$\begin{aligned}\mathrm{MIF}_{\theta,p}(\theta,\alpha,\nu_r) = {} & \left(1-\nu_r^2\right)\left\{\frac{\pi}{2}\left(\frac{\nu_r}{1-\nu_r}-1\right)\sin(\theta+\alpha) - 2\sin^2\left(\frac{\theta+\alpha}{2}\right)\ln\left[\tan^2\left(\frac{\theta+\alpha}{2}\right)\right] - 2\ln\left[\cos^2\left(\frac{\theta+\alpha}{2}\right)\right]\right\} \\ & - \left(1-\nu_r^2\right)\left\{\frac{\pi}{2}\left(\frac{\nu_r}{1-\nu_r}-1\right)\sin(\theta-\alpha) - 0 - 2\ln\left[\cos^2\left(\frac{\theta-\alpha}{2}\right)\right]\right\}\end{aligned} \tag{K.19}$$

- $\alpha < \theta < \frac{\pi}{2}$:

$$\begin{aligned}\mathrm{MIF}_{\theta,p}(\theta,\alpha,\nu_r) = {} & \left(1-\nu_r^2\right)\left\{\frac{\pi}{2}\left(\frac{\nu_r}{1-\nu_r}-1\right)\sin(\theta+\alpha) - 2\sin^2\left(\frac{\theta+\alpha}{2}\right)\ln\left[\tan^2\left(\frac{\theta+\alpha}{2}\right)\right] - 2\ln\left[\cos^2\left(\frac{\theta+\alpha}{2}\right)\right]\right\} \\ & - \left(1-\nu_r^2\right)\left\{\frac{\pi}{2}\left(\frac{\nu_r}{1-\nu_r}-1\right)\sin(\theta-\alpha) - 2\sin^2\left(\frac{\theta-\alpha}{2}\right)\ln\left[\tan^2\left(\frac{\theta-\alpha}{2}\right)\right] - 2\ln\left[\cos^2\left(\frac{\theta-\alpha}{2}\right)\right]\right\}\end{aligned} \tag{K.20}$$

K.2.2 Plane-stress state

- $-\frac{\pi}{2} < \theta < \alpha$:

$$\begin{aligned}\mathrm{MIF}_{\theta,p}(\theta,\alpha,\nu_r) = &-\frac{\pi}{2}(\nu_r-1)\sin(\theta+\alpha) - 2\sin^2\left(\frac{\theta+\alpha}{2}\right)\ln\left[\tan^2\left(\frac{\theta+\alpha}{2}\right)\right] - 2\ln\left[\cos^2\left(\frac{\theta+\alpha}{2}\right)\right]\\ &-\left\{-\frac{\pi}{2}(\nu_r-1)\sin(\theta-\alpha) - 2\sin^2\left(\frac{\theta-\alpha}{2}\right)\ln\left[\tan^2\left(\frac{\theta-\alpha}{2}\right)\right] - 2\ln\left[\cos^2\left(\frac{\theta-\alpha}{2}\right)\right]\right\}\end{aligned} \tag{K.21}$$

- $\theta = -\alpha$:

$$\begin{aligned}\mathrm{MIF}_{\theta,p}(\theta,\alpha,\nu_r) = &-\frac{\pi}{2}(\nu_r-1)\sin(\theta+\alpha) - 0 - 2\ln\left[\cos^2\left(\frac{\theta+\alpha}{2}\right)\right]\\ &-\left\{-\frac{\pi}{2}(\nu_r-1)\sin(\theta-\alpha) - 2\sin^2\left(\frac{\theta-\alpha}{2}\right)\ln\left[\tan^2\left(\frac{\theta-\alpha}{2}\right)\right] - 2\ln\left[\cos^2\left(\frac{\theta-\alpha}{2}\right)\right]\right\}\end{aligned} \tag{K.22}$$

- $-\alpha < \theta < \alpha$:

$$\begin{aligned}\mathrm{MIF}_{\theta,p}(\theta,\alpha,\nu_r) = &\frac{\pi}{2}(\nu_r-1)\left[\sin(\theta+\alpha)+\sin(\theta-\alpha)\right]\\ &-2\left\{\sin^2\left(\frac{\theta+\alpha}{2}\right)\ln\left[\tan^2\left(\frac{\theta+\alpha}{2}\right)\right] + \ln\left[\cos^2\left(\frac{\theta+\alpha}{2}\right)\right]\right\}\\ &+2\left\{\sin^2\left(\frac{\theta-\alpha}{2}\right)\ln\left[\tan^2\left(\frac{\theta-\alpha}{2}\right)\right] + \ln\left[\cos^2\left(\frac{\theta-\alpha}{2}\right)\right]\right\}\end{aligned} \tag{K.23}$$

- $\theta = \alpha$:

$$\begin{aligned}\mathrm{MIF}_{\theta,p}(\theta,\alpha,\nu_r) = &\frac{\pi}{2}(\nu_r-1)\sin(\theta+\alpha) - 2\sin^2\left(\frac{\theta+\alpha}{2}\right)\ln\left[\tan^2\left(\frac{\theta+\alpha}{2}\right)\right] - 2\ln\left[\cos^2\left(\frac{\theta+\alpha}{2}\right)\right]\\ &-\left\{\frac{\pi}{2}(\nu_r-1)\sin(\theta-\alpha) - 0 - 2\ln\left[\cos^2\left(\frac{\theta-\alpha}{2}\right)\right]\right\}\end{aligned} \tag{K.24}$$

- $\alpha < \theta < \frac{\pi}{2}$:

$$\begin{aligned}\mathrm{MIF}_{\theta,p}(\theta,\alpha,\nu_r) = &\frac{\pi}{2}(\nu_r-1)\sin(\theta+\alpha) - 2\sin^2\left(\frac{\theta+\alpha}{2}\right)\ln\left[\tan^2\left(\frac{\theta+\alpha}{2}\right)\right] - 2\ln\left[\cos^2\left(\frac{\theta+\alpha}{2}\right)\right]\\ &-\left\{\frac{\pi}{2}(\nu_r-1)\sin(\theta-\alpha) - 2\sin^2\left(\frac{\theta-\alpha}{2}\right)\ln\left[\tan^2\left(\frac{\theta-\alpha}{2}\right)\right] - 2\ln\left[\cos^2\left(\frac{\theta-\alpha}{2}\right)\right]\right\}\end{aligned} \tag{K.25}$$

K.3 Radial displacement due to shear stress

K.3.1 Generalized plane-strain state and plane-strain state

- $-\frac{\pi}{4} < \theta < \alpha$:

$$\begin{aligned}\mathrm{MIF}_{r,\tau}(\theta,\alpha,\nu_r) = {} & \left(1-\nu_r^2\right)\left\{-2\sin^2\left(\frac{\theta+\alpha}{2}\right)\ln\left[\tan^2\left(\frac{\theta+\alpha}{2}\right)\right]-2\ln\left[\cos^2\left(\frac{\theta+\alpha}{2}\right)\right]-2\ln\left[\frac{2}{1+\sin(\theta+\alpha)}\right]\right. \\ & \left.+\left[1-\sin(\theta+\alpha)\right]\ln\left[\frac{1-\sin(\theta+\alpha)}{1+\sin(\theta+\alpha)}\right]+\frac{\pi}{2}\left(1-\frac{\nu_r}{1-\nu_r}\right)\left[\sin(\theta+\alpha)+\cos(\theta+\alpha)\right]\right\} \\ & -\left(1-\nu_r^2\right)\left\{-2\sin^2\left(\frac{\theta-\alpha}{2}\right)\ln\left[\tan^2\left(\frac{\theta-\alpha}{2}\right)\right]-2\ln\left[\cos^2\left(\frac{\theta-\alpha}{2}\right)\right]-2\ln\left[\frac{2}{1+\sin(\theta-\alpha)}\right]\right. \\ & \left.+\left[1-\sin(\theta-\alpha)\right]\ln\left[\frac{1-\sin(\theta-\alpha)}{1+\sin(\theta-\alpha)}\right]+\frac{\pi}{2}\left(1-\frac{\nu_r}{1-\nu_r}\right)\left[\sin(\theta-\alpha)+\cos(\theta-\alpha)\right]\right\}\end{aligned} \tag{K.26}$$

- $\theta = -\alpha$:

$$\begin{aligned}\mathrm{MIF}_{r,\tau}(\theta,\alpha,\nu_r) = {} & \left(1-\nu_r^2\right)\left\{0-2\ln\left[\cos^2\left(\frac{\theta+\alpha}{2}\right)\right]-2\ln\left[\frac{2}{1+\sin(\theta+\alpha)}\right]\right. \\ & \left.+\left[1-\sin(\theta+\alpha)\right]\ln\left[\frac{1-\sin(\theta+\alpha)}{1+\sin(\theta+\alpha)}\right]+\frac{\pi}{2}\left(1-\frac{\nu_r}{1-\nu_r}\right)\left[\sin(\theta+\alpha)+\cos(\theta+\alpha)\right]\right\} \\ & -\left(1-\nu_r^2\right)\left\{-2\sin^2\left(\frac{\theta-\alpha}{2}\right)\ln\left[\tan^2\left(\frac{\theta-\alpha}{2}\right)\right]-2\ln\left[\cos^2\left(\frac{\theta-\alpha}{2}\right)\right]-2\ln\left[\frac{2}{1+\sin(\theta-\alpha)}\right]\right. \\ & \left.+\left[1-\sin(\theta-\alpha)\right]\ln\left[\frac{1-\sin(\theta-\alpha)}{1+\sin(\theta-\alpha)}\right]+\frac{\pi}{2}\left(1-\frac{\nu_r}{1-\nu_r}\right)\left[\sin(\theta-\alpha)+\cos(\theta-\alpha)\right]\right\}\end{aligned} \tag{K.27}$$

- $-\alpha < \theta < \alpha$:

$$\begin{aligned}\mathrm{MIF}_{r,\tau}(\theta,\alpha,\nu_r) = {} & \frac{\pi}{2}\left(1-\nu_r^2\right)\left(1-\frac{\nu_r}{1-\nu_r}\right)\left[-\sin(\theta-\alpha)-\sin(\theta+\alpha)+\cos(\theta+\alpha)-\cos(\theta-\alpha)\right] \\ & +\left(1-\nu_r^2\right)\left\{-2\sin^2\left(\frac{\theta+\alpha}{2}\right)\ln\left[\tan^2\left(\frac{\theta+\alpha}{2}\right)\right]-2\ln\left[\cos^2\left(\frac{\theta+\alpha}{2}\right)\right]\right. \\ & \left.-2\ln\left[\frac{2}{1+\sin(\theta+\alpha)}\right]+\left[1-\sin(\theta+\alpha)\right]\ln\left[\frac{1-\sin(\theta+\alpha)}{1+\sin(\theta+\alpha)}\right]\right\} \\ & -\left(1-\nu_r^2\right)\left\{-2\sin^2\left(\frac{\theta-\alpha}{2}\right)\ln\left[\tan^2\left(\frac{\theta-\alpha}{2}\right)\right]-2\ln\left[\cos^2\left(\frac{\theta-\alpha}{2}\right)\right]\right. \\ & \left.-2\ln\left[\frac{2}{1+\sin(\theta-\alpha)}\right]+\left[1-\sin(\theta-\alpha)\right]\ln\left[\frac{1-\sin(\theta-\alpha)}{1+\sin(\theta-\alpha)}\right]\right\}\end{aligned} \tag{K.28}$$

- $\theta = \alpha$:

$$\begin{aligned}\mathrm{MIF}_{r,\tau}(\theta,\alpha,\nu_r) = {} & \left(1-\nu_r^2\right)\left\{-2\sin^2\left(\frac{\theta+\alpha}{2}\right)\ln\left[\tan^2\left(\frac{\theta+\alpha}{2}\right)\right]-2\ln\left[\cos^2\left(\frac{\theta+\alpha}{2}\right)\right]-2\ln\left[\frac{2}{1+\sin(\theta+\alpha)}\right]\right. \\ & \left.+\left[1-\sin(\theta+\alpha)\right]\ln\left[\frac{1-\sin(\theta+\alpha)}{1+\sin(\theta+\alpha)}\right]-\frac{\pi}{2}\left(1-\frac{\nu_r}{1-\nu_r}\right)\left[\sin(\theta+\alpha)-\cos(\theta+\alpha)\right]\right\} \\ & -\left(1-\nu_r^2\right)\left\{0-2\ln\left[\cos^2\left(\frac{\theta-\alpha}{2}\right)\right]-2\ln\left[\frac{2}{1+\sin(\theta-\alpha)}\right]\right. \\ & \left.+\left[1-\sin(\theta-\alpha)\right]\ln\left[\frac{1-\sin(\theta-\alpha)}{1+\sin(\theta-\alpha)}\right]-\frac{\pi}{2}\left(1-\frac{\nu_r}{1-\nu_r}\right)\left[\sin(\theta-\alpha)-\cos(\theta-\alpha)\right]\right\}\end{aligned} \tag{K.29}$$

- $\alpha < \theta < \frac{\pi}{4}$:

$$\mathrm{MIF}_{r,\tau}(\theta,\alpha,\nu_r) = \left(1-\nu_r^2\right)\left\{-2\sin^2\left(\frac{\theta+\alpha}{2}\right)\ln\left[\tan^2\left(\frac{\theta+\alpha}{2}\right)\right]-2\ln\left[\cos^2\left(\frac{\theta+\alpha}{2}\right)\right]-2\ln\left[\frac{2}{1+\sin(\theta+\alpha)}\right]\right.$$

$$
\begin{aligned}
&+ [1 - \sin(\theta + \alpha)] \ln\left[\frac{1 - \sin(\theta + \alpha)}{1 + \sin(\theta + \alpha)}\right] - \frac{\pi}{2}\left(1 - \frac{\nu_r}{1 - \nu_r}\right)[\sin(\theta + \alpha) - \cos(\theta + \alpha)]\Bigg\} \\
&- \left(1 - \nu_r^2\right)\Bigg\{-2\sin^2\left(\frac{\theta - \alpha}{2}\right)\ln\left[\tan^2\left(\frac{\theta - \alpha}{2}\right)\right] - 2\ln\left[\cos^2\left(\frac{\theta - \alpha}{2}\right)\right] - 2\ln\left[\frac{2}{1 + \sin(\theta - \alpha)}\right] \\
&+ [1 - \sin(\theta - \alpha)] \ln\left[\frac{1 - \sin(\theta - \alpha)}{1 + \sin(\theta - \alpha)}\right] - \frac{\pi}{2}\left(1 - \frac{\nu_r}{1 - \nu_r}\right)[\sin(\theta - \alpha) - \cos(\theta - \alpha)]\Bigg\}
\end{aligned}
\tag{K.30}
$$

K.3.2 Plane-stress state

- $-\frac{\pi}{4} < \theta < \alpha$:

$$\begin{aligned}\mathrm{MIF}_{r,\tau}(\theta,\alpha,\nu_r) = {} & -2\sin^2\left(\frac{\theta+\alpha}{2}\right)\ln\left[\tan^2\left(\frac{\theta+\alpha}{2}\right)\right] - 2\ln\left[\cos^2\left(\frac{\theta+\alpha}{2}\right)\right] - 2\ln\left[\frac{2}{1+\sin(\theta+\alpha)}\right] \\ & + [1-\sin(\theta+\alpha)]\ln\left[\frac{1-\sin(\theta+\alpha)}{1+\sin(\theta+\alpha)}\right] + \frac{\pi}{2}(1-\nu_r)[\sin(\theta+\alpha)+\cos(\theta+\alpha)] \\ & - \left\{-2\sin^2\left(\frac{\theta-\alpha}{2}\right)\ln\left[\tan^2\left(\frac{\theta-\alpha}{2}\right)\right] - 2\ln\left[\cos^2\left(\frac{\theta-\alpha}{2}\right)\right] - 2\ln\left[\frac{2}{1+\sin(\theta-\alpha)}\right]\right. \\ & \left. + [1-\sin(\theta-\alpha)]\ln\left[\frac{1-\sin(\theta-\alpha)}{1+\sin(\theta-\alpha)}\right] + \frac{\pi}{2}(1-\nu_r)[\sin(\theta-\alpha)+\cos(\theta-\alpha)]\right\}\end{aligned} \tag{K.31}$$

- $\theta = -\alpha$:

$$\begin{aligned}\mathrm{MIF}_{r,\tau}(\theta,\alpha,\nu_r) = {} & 0 - 2\ln\left[\cos^2\left(\frac{\theta+\alpha}{2}\right)\right] - 2\ln\left[\frac{2}{1+\sin(\theta+\alpha)}\right] \\ & + [1-\sin(\theta+\alpha)]\ln\left[\frac{1-\sin(\theta+\alpha)}{1+\sin(\theta+\alpha)}\right] + \frac{\pi}{2}(1-\nu_r)[\sin(\theta+\alpha)+\cos(\theta+\alpha)] \\ & - \left\{-2\sin^2\left(\frac{\theta-\alpha}{2}\right)\ln\left[\tan^2\left(\frac{\theta-\alpha}{2}\right)\right] - 2\ln\left[\cos^2\left(\frac{\theta-\alpha}{2}\right)\right] - 2\ln\left[\frac{2}{1+\sin(\theta-\alpha)}\right]\right. \\ & \left. + [1-\sin(\theta-\alpha)]\ln\left[\frac{1-\sin(\theta-\alpha)}{1+\sin(\theta-\alpha)}\right] + \frac{\pi}{2}(1-\nu_r)[\sin(\theta-\alpha)+\cos(\theta-\alpha)]\right\}\end{aligned} \tag{K.32}$$

- $-\alpha < \theta < \alpha$:

$$\begin{aligned}\mathrm{MIF}_{r,\tau}(\theta,\alpha,\nu_r) = {} & \frac{\pi}{2}(1-\nu_r)[-\sin(\theta-\alpha)-\sin(\theta+\alpha)+\cos(\theta+\alpha)-\cos(\theta-\alpha)] \\ & - 2\sin^2\left(\frac{\theta+\alpha}{2}\right)\ln\left[\tan^2\left(\frac{\theta+\alpha}{2}\right)\right] - 2\ln\left[\cos^2\left(\frac{\theta+\alpha}{2}\right)\right] - 2\ln\left[\frac{2}{1+\sin(\theta+\alpha)}\right] + [1-\sin(\theta+\alpha)]\ln\left[\frac{1-\sin(\theta+\alpha)}{1+\sin(\theta+\alpha)}\right] \\ & - \left\{-2\sin^2\left(\frac{\theta-\alpha}{2}\right)\ln\left[\tan^2\left(\frac{\theta-\alpha}{2}\right)\right] - 2\ln\left[\cos^2\left(\frac{\theta-\alpha}{2}\right)\right] - 2\ln\left[\frac{2}{1+\sin(\theta-\alpha)}\right] + [1-\sin(\theta-\alpha)]\ln\left[\frac{1-\sin(\theta-\alpha)}{1+\sin(\theta-\alpha)}\right]\right\}\end{aligned} \tag{K.33}$$

- $\theta = \alpha$:

$$\begin{aligned}\mathrm{MIF}_{r,\tau}(\theta,\alpha,\nu_r) = {} & -2\sin^2\left(\frac{\theta+\alpha}{2}\right)\ln\left[\tan^2\left(\frac{\theta+\alpha}{2}\right)\right] - 2\ln\left[\cos^2\left(\frac{\theta+\alpha}{2}\right)\right] - 2\ln\left[\frac{2}{1+\sin(\theta+\alpha)}\right] \\ & + [1-\sin(\theta+\alpha)]\ln\left[\frac{1-\sin(\theta+\alpha)}{1+\sin(\theta+\alpha)}\right] - \frac{\pi}{2}(1-\nu_r)[\sin(\theta+\alpha)-\cos(\theta+\alpha)] \\ & - \left\{0 - 2\ln\left[\cos^2\left(\frac{\theta-\alpha}{2}\right)\right] - 2\ln\left[\frac{2}{1+\sin(\theta-\alpha)}\right]\right. \\ & \left. + [1-\sin(\theta+\alpha)]\ln\left[\frac{1-\sin(\theta-\alpha)}{1+\sin(\theta-\alpha)}\right] - \frac{\pi}{2}(1-\nu_r)[\sin(\theta-\alpha)-\cos(\theta-\alpha)]\right\}\end{aligned} \tag{K.34}$$

- $\alpha < \theta < \frac{\pi}{4}$:

$$\begin{aligned}\mathrm{MIF}_{r,\tau}(\theta,\alpha,\nu_r) = {} & -2\sin^2\left(\frac{\theta+\alpha}{2}\right)\ln\left[\tan^2\left(\frac{\theta+\alpha}{2}\right)\right] - 2\ln\left[\cos^2\left(\frac{\theta+\alpha}{2}\right)\right] - 2\ln\left[\frac{2}{1+\sin(\theta+\alpha)}\right] \\ & + [1-\sin(\theta+\alpha)]\ln\left[\frac{1-\sin(\theta+\alpha)}{1+\sin(\theta+\alpha)}\right] - \frac{\pi}{2}(1-\nu_r)[\sin(\theta+\alpha)-\cos(\theta+\alpha)] \\ & - \left\{-2\sin^2\left(\frac{\theta-\alpha}{2}\right)\ln\left[\tan^2\left(\frac{\theta-\alpha}{2}\right)\right] - 2\ln\left[\cos^2\left(\frac{\theta-\alpha}{2}\right)\right] - 2\ln\left[\frac{2}{1+\sin(\theta-\alpha)}\right]\right. \\ & \left. + [1-\sin(\theta+\alpha)]\ln\left[\frac{1-\sin(\theta-\alpha)}{1+\sin(\theta-\alpha)}\right] - \frac{\pi}{2}(1-\nu_r)[\sin(\theta-\alpha)-\cos(\theta-\alpha)]\right\}\end{aligned} \tag{K.35}$$

K.4 Tangential displacement due to shear stress

K.4.1 Generalized plane-strain state and plane-strain state

- $-\frac{\pi}{4} < \theta < \alpha$:

$$\begin{aligned}
&\mathrm{MIF}_{\theta,\tau}(\theta,\alpha,\nu_r) = \\
&\left(1-\nu_r^2\right)\left\{-\sin(\theta+\alpha)\ln\left[\tan^2\left(\frac{\theta+\alpha}{2}\right)\right]-\cos(\theta+\alpha)\ln\left[\frac{1-\sin(\theta+\alpha)}{1+\sin(\theta+\alpha)}\right]+\frac{\pi}{2}\left(1-\frac{\nu_r}{1-\nu_r}\right)[\cos(\theta+\alpha)-\sin(\theta+\alpha)]\right\} \\
&-\left(1-\nu_r^2\right)\left\{-\sin(\theta-\alpha)\ln\left[\tan^2\left(\frac{\theta-\alpha}{2}\right)\right]-\cos(\theta-\alpha)\ln\left[\frac{1-\sin(\theta-\alpha)}{1+\sin(\theta-\alpha)}\right]+\frac{\pi}{2}\left(1-\frac{\nu_r}{1-\nu_r}\right)[\cos(\theta-\alpha)-\sin(\theta-\alpha)]\right\}
\end{aligned} \tag{K.36}$$

- $\theta = -\alpha$:

$$\begin{aligned}
&\mathrm{MIF}_{\theta,\tau}(\theta,\alpha,\nu_r) = \\
&\left(1-\nu_r^2\right)\left\{0-\cos(\theta+\alpha)\ln\left[\frac{1-\sin(\theta+\alpha)}{1+\sin(\theta+\alpha)}\right]+\frac{\pi}{2}\left(1-\frac{\nu_r}{1-\nu_r}\right)[\cos(\theta+\alpha)-\sin(\theta+\alpha)]\right\} \\
&-\left(1-\nu_r^2\right)\left\{-\sin(\theta-\alpha)\ln\left[\tan^2\left(\frac{\theta-\alpha}{2}\right)\right]-\cos(\theta-\alpha)\ln\left[\frac{1-\sin(\theta-\alpha)}{1+\sin(\theta-\alpha)}\right]+\frac{\pi}{2}\left(1-\frac{\nu_r}{1-\nu_r}\right)[\cos(\theta-\alpha)-\sin(\theta-\alpha)]\right\}
\end{aligned} \tag{K.37}$$

- $-\alpha < \theta < \alpha$:

$$\begin{aligned}
\mathrm{MIF}_{\theta,\tau}(\theta,\alpha,\nu_r) = &-\frac{\pi}{2}\left(1-\nu_r^2\right)\left(1-\frac{\nu_r}{1-\nu_r}\right)[-2+\cos(\theta-\alpha)+\cos(\theta+\alpha)+\sin(\theta+\alpha)-\sin(\theta-\alpha)] \\
&+\left(1-\nu_r^2\right)\left[-\sin(\theta+\alpha)\ln\left[\tan^2\left(\frac{\theta+\alpha}{2}\right)\right]-\cos(\theta+\alpha)\ln\left[\frac{1-\sin(\theta+\alpha)}{1+\sin(\theta+\alpha)}\right]\right] \\
&-\left(1-\nu_r^2\right)\left[-\sin(\theta-\alpha)\ln\left[\tan^2\left(\frac{\theta-\alpha}{2}\right)\right]-\cos(\theta-\alpha)\ln\left[\frac{1-\sin(\theta-\alpha)}{1+\sin(\theta-\alpha)}\right]\right]
\end{aligned} \tag{K.38}$$

- $\theta = \alpha$:

$$\begin{aligned}
&\mathrm{MIF}_{\theta,\tau}(\theta,\alpha,\nu_r) = \\
&\left(1-\nu_r^2\right)\left\{-\sin(\theta+\alpha)\ln\left[\tan^2\left(\frac{\theta+\alpha}{2}\right)\right]-\cos(\theta+\alpha)\ln\left[\frac{1-\sin(\theta+\alpha)}{1+\sin(\theta+\alpha)}\right]-\frac{\pi}{2}\left(1-\frac{\nu_r}{1-\nu_r}\right)[\cos(\theta+\alpha)+\sin(\theta+\alpha)]\right\} \\
&-\left(1-\nu_r^2\right)\left\{0-\cos(\theta-\alpha)\ln\left[\frac{1-\sin(\theta-\alpha)}{1-\sin(\theta-\alpha)}\right]-\frac{\pi}{2}\left(1-\frac{\nu_r}{1-\nu_r}\right)[\cos(\theta-\alpha)+\sin(\theta-\alpha)]\right\}
\end{aligned} \tag{K.39}$$

- $\alpha < \theta < \frac{\pi}{4}$:

$$\begin{aligned}
&\mathrm{MIF}_{\theta,\tau}(\theta,\alpha,\nu_r) = \\
&\left(1-\nu_r^2\right)\left\{-\sin(\theta+\alpha)\ln\left[\tan^2\left(\frac{\theta+\alpha}{2}\right)\right]-\cos(\theta+\alpha)\ln\left[\frac{1-\sin(\theta+\alpha)}{1+\sin(\theta+\alpha)}\right]-\frac{\pi}{2}\left(1-\frac{\nu_r}{1-\nu_r}\right)[\cos(\theta+\alpha)+\sin(\theta+\alpha)]\right\} \\
&-\left(1-\nu_r^2\right)\left\{-\sin(\theta-\alpha)\ln\left[\tan^2\left(\frac{\theta-\alpha}{2}\right)\right]-\cos(\theta-\alpha)\ln\left[\frac{1-\sin(\theta-\alpha)}{1-\sin(\theta-\alpha)}\right]-\frac{\pi}{2}\left(1-\frac{\nu_r}{1-\nu_r}\right)[\cos(\theta-\alpha)+\sin(\theta-\alpha)]\right\}
\end{aligned} \tag{K.40}$$

K.4.2 Plane-stress state

- $-\frac{\pi}{4} < \theta < \alpha$:

$$\begin{aligned}
&\mathrm{MIF}_{\theta,\tau}(\theta, \alpha, \nu_r) = \\
&\quad -\sin(\theta+\alpha)\ln\left[\tan^2\left(\frac{\theta+\alpha}{2}\right)\right] - \cos(\theta+\alpha)\ln\left[\frac{1-\sin(\theta+\alpha)}{1+\sin(\theta+\alpha)}\right] + \frac{\pi}{2}(1-\nu_r)\left[\cos(\theta+\alpha)-\sin(\theta+\alpha)\right] \\
&\quad -\left\{-\sin(\theta-\alpha)\ln\left[\tan^2\left(\frac{\theta-\alpha}{2}\right)\right] - \cos(\theta-\alpha)\ln\left[\frac{1-\sin(\theta-\alpha)}{1+\sin(\theta-\alpha)}\right] + \frac{\pi}{2}(1-\nu_r)\left[\cos(\theta-\alpha)-\sin(\theta-\alpha)\right]\right\}
\end{aligned} \tag{K.41}$$

- $\theta = -\alpha$:

$$\begin{aligned}
&\mathrm{MIF}_{\theta,\tau}(\theta, \alpha, \nu_r) = \\
&\quad 0 - \cos(\theta+\alpha)\ln\left[\frac{1-\sin(\theta+\alpha)}{1+\sin(\theta+\alpha)}\right] + \frac{\pi}{2}(1-\nu_r)\left[\cos(\theta+\alpha)-\sin(\theta+\alpha)\right] \\
&\quad -\left\{-\sin(\theta-\alpha)\ln\left[\tan^2\left(\frac{\theta-\alpha}{2}\right)\right] - \cos(\theta-\alpha)\ln\left[\frac{1-\sin(\theta-\alpha)}{1+\sin(\theta-\alpha)}\right] + \frac{\pi}{2}(1-\nu_r)\left[\cos(\theta-\alpha)-\sin(\theta-\alpha)\right]\right\}
\end{aligned} \tag{K.42}$$

- $-\alpha < \theta < \alpha$:

$$\begin{aligned}
\mathrm{MIF}_{\theta,\tau}(\theta, \alpha, \nu_r) = &-\frac{\pi}{2}(1-\nu_r)\left[-2+\cos(\theta-\alpha)+\cos(\theta+\alpha)+\sin(\theta+\alpha)-\sin(\theta-\alpha)\right] \\
&-\sin(\theta+\alpha)\ln\left[\tan^2\left(\frac{\theta+\alpha}{2}\right)\right] - \cos(\theta+\alpha)\ln\left[\frac{1-\sin(\theta+\alpha)}{1+\sin(\theta+\alpha)}\right] \\
&-\left\{-\sin(\theta-\alpha)\ln\left[\tan^2\left(\frac{\theta-\alpha}{2}\right)\right] - \cos(\theta-\alpha)\ln\left[\frac{1-\sin(\theta-\alpha)}{1+\sin(\theta-\alpha)}\right]\right\}
\end{aligned} \tag{K.43}$$

- $\theta = \alpha$:

$$\begin{aligned}
&\mathrm{MIF}_{\theta,\tau}(\theta, \alpha, \nu_r) = \\
&\quad -\sin(\theta+\alpha)\ln\left[\tan^2\left(\frac{\theta+\alpha}{2}\right)\right] - \cos(\theta+\alpha)\ln\left[\frac{1-\sin(\theta+\alpha)}{1+\sin(\theta+\alpha)}\right] - \frac{\pi}{2}(1-\nu_r)\left[\cos(\theta+\alpha)+\sin(\theta+\alpha)\right] \\
&\quad -\left\{0 - \cos(\theta-\alpha)\ln\left[\frac{1-\sin(\theta-\alpha)}{1+\sin(\theta-\alpha)}\right] - \frac{\pi}{2}(1-\nu_r)\left[\cos(\theta-\alpha)+\sin(\theta-\alpha)\right]\right\}
\end{aligned} \tag{K.44}$$

- $\alpha < \theta < \frac{\pi}{4}$:

$$\begin{aligned}
&\mathrm{MIF}_{\theta,\tau}(\theta, \alpha, \nu_r) = \\
&\quad -\sin(\theta+\alpha)\ln\left[\tan^2\frac{(\theta+\alpha)}{2}\right] - \cos(\theta+\alpha)\ln\left[\frac{1-\sin(\theta+\alpha)}{1+\sin(\theta+\alpha)}\right] - \frac{\pi}{2}(1-\nu_r)\left[\cos(\theta+\alpha)+\sin(\theta+\alpha)\right] \\
&\quad -\left\{-\sin(\theta-\alpha)\ln\left[\tan^2\left(\frac{\theta-\alpha}{2}\right)\right] - \cos(\theta-\alpha)\ln\left[\frac{1-\sin(\theta-\alpha)}{1+\sin(\theta-\alpha)}\right] - \frac{\pi}{2}(1-\nu_r)\left[\cos(\theta-\alpha)+\sin(\theta-\alpha)\right]\right\}
\end{aligned} \tag{K.45}$$

Appendix L

Roelands viscosity equation

In this appendix, the form of the *Roelands viscosity equation* in the METALUB model is derived based on Roelands' thesis [278]. In particular, this derivation shows that Eqs. (A2.11), (A2.56), (A2.104), (A2.155), (A2.192) and (A2.219) in Marsault's thesis [215] with both components of the Roelands equation, i.e. pressure and temperature, are incorrect.

According to Eq. (V-9b) in [278, p. 123], the dynamic viscosity η (in cP) can be computed as a function of the lubricant pressure p_l (in kgf/cm^2) and its temperature T_l (in °C):

$$\frac{\log_{10}\eta + 1.2}{\log_{10}\eta_0 + 1.2} = \left(1 + \frac{p_l}{p_r}\right)^{z_{p_l}} \left(\frac{T_0 + 135}{T_l + 135}\right)^{S_0} \tag{L.1}$$

where η_0 is the reference (atmospheric) viscosity [278, p. 115], $p_r = 2000\,\text{kgf/cm}^2 = 196.2\,\text{MPa}$, z_{p_l} the viscosity pressure index, T_0 the reference temperature and S_0 the atmospheric slope index.

The previous equation can be rewritten since $\log_{10}(\cdot) = \ln(\cdot)/\ln 10$,

$$\ln\eta = (\ln\eta_0 + 2.763)\left(1 + \frac{p_l}{p_r}\right)^{z_{p_l}} \left(\frac{T_0 + 135}{T_l + 135}\right)^{S_0} - 2.763 \tag{L.2}$$

Furthermore, if the units of the dynamic viscosity are Pa.s ($= 10^3$ cP) instead of cP,

$$\ln\eta = (\ln\eta_0 + 9.67)\left(1 + \frac{p_l}{p_r}\right)^{z_{p_l}} \left(\frac{T_0 + 135}{T_l + 135}\right)^{S_0} - 9.67 \tag{L.3}$$

This equation can then be factorized:

$$\eta = \exp\left[(\ln\eta_0 + 9.67)\left(1 + \frac{p_l}{p_r}\right)^{z_{p_l}} \left(\frac{T_0 + 135}{T_l + 135}\right)^{S_0} + \ln\eta_0 - \ln\eta_0 - 9.67\right] \tag{L.4}$$

$$= \exp\left\{(\ln\eta_0 + 9.67)\left[\left(1 + \frac{p_l}{p_r}\right)^{z_{p_l}} \left(\frac{T_0 + 135}{T_l + 135}\right)^{S_0} - 1\right] + \ln\eta_0\right\} \tag{L.5}$$

Finally, the Reynolds equation in METALUB can be written as follows:

$$\eta = \eta_0 \exp\left\{\left[\ln\left(10^6\,\eta_0\right) + 9.67\right]\left[\left(1 + \frac{p_l}{p_r}\right)^{z_{p_l}}\left(\frac{T_0 + 135}{T_l + 135}\right)^{S_0} - 1\right]\right\} \tag{L.6}$$

where the factor 10^6 was introduced so that the units of the dynamic viscosity are MPa.s since the unit system in this model was chosen to be N, mm, s.

If the Eqs. (A2.11), (A2.56), (A2.104), (A2.155), (A2.192) and (A2.219) in Marsault's thesis [215] (with the unit adaptation) were used with both components of the Roelands equation, i.e. pressure and temperature, the dynamic viscosity would be computed as follows, which is ***wrong*** according to the previous equation:

$$\eta = \eta_0 \exp\left\{\left[\ln\left(10^6\,\eta_0\right) + 9.67\right]\left[\left(1 + \frac{p_l}{p_r}\right)^{z_{p_l}} + \left(\frac{T_0 + 135}{T_l + 135}\right)^{S_0} - 2\right]\right\} \tag{L.7}$$

Appendix M

Viscous shear stress computation based on shear stress factors

The computation of the lubricant shear stress by Eq. (4.204), i.e.

$$\tau_l = \frac{\eta(v_r - v_s)}{h_v} \quad \text{with} \quad h_v = \frac{h_t}{1 - A} \tag{M.1}$$

has essentially two shortcomings. First, the local film thickness h_l in the velocity differential term in Eq. (4.200) was replaced by the mean film thickness in the valleys h_v. Hence, a mean film thickness is computed instead of a *mean shear stress*, although a mean shear stress is deduced of this mean film thickness. In other words, the average of h_l is not necessarily equal to the inverse of the average of $1/h_l$. Secondly, the *lubricant pressure gradient* term in Eq. (4.200) is neglected. A solution to these shortcomings was introduced by Patir and Cheng [254], who computed the lubricant shear stress as follows, if $h > 0$:

$$\tau_l = \frac{\eta(v_r - v_s)}{h}(\phi_f - \phi_{fs}) - \phi_{fp}\frac{h}{2}\frac{\partial p_l}{\partial x} \tag{M.2}$$

The variables ϕ_f, ϕ_{fs} and ϕ_{fp} are the *shear stress factors* that depend on the Peklenik surface pattern parameter γ and the lubricant film thickness h with respect to the composite root-mean-square roughness R_q. The shear stress factors were derived for close rough surfaces with no or moderate contact, i.e. $h > 0$, by Patir and Cheng [254].

No mathematical expression similar to the flow factors for significant real contact areas, i.e. $h \leq 0$, in Wilson and Marsault [364] seems yet to exist in the literature for the shear stress factors. Hence, instead of assuming that the lubricant shear stress is zero, if $h \leq 0$, the current best models are used to extend it. These models are Eq. (4.204) for the Couette shear stress and the explanation about the mean film thickness in valleys in Sec. 4.8.3, which is more reasonably applied to h_l in the pressure gradient term of Eq. (4.200) than $1/h_l$ in the Couette shear stress

term:

$$\tau_l = \begin{cases} \dfrac{\eta(v_r - v_s)}{h}(\phi_f - \phi_{fs}) - \phi_{fp}\dfrac{h}{2}\dfrac{\partial p_l}{\partial x} & \text{, if } h > 0 \\ \dfrac{\eta(v_r - v_s)}{h_v} - \dfrac{h_v}{2}\dfrac{\partial p_l}{\partial x} & \text{, otherwise.} \end{cases} \tag{M.3}$$

In the following sections, the three different shear stress factors in the previous equation are defined.

M.1 First shear stress factor

The *first shear stress factor* ϕ_f is computed by averaging the velocity differential term of the shear stress for the different asperity heights, by assuming that the velocities and the viscosity are independent of the asperity height:

$$\mathbf{E}\left(\frac{\eta(v_r - v_s)}{h_l}\right) = \phi_f \frac{\eta(v_r - v_s)}{h} \quad \Rightarrow \quad \phi_f = h\mathbf{E}\left(\frac{1}{h_l}\right) \tag{M.4}$$

where $\mathbf{E}(\cdot)$ is the expected value operator. This expression can be evaluated by integration for a given surface height distribution. Since the continuum hypothesis, which is required in the constitutive law, is certainly invalidated below a small film thickness $\epsilon > 0$, the hydrodynamic shear stress is assumed to be zero below ϵ. Otherwise, the integral becomes unbounded because of the singularity at the contact points where $h_l = 0$. Thus[1],

$$\phi_f = \begin{cases} h\displaystyle\int_{z_{\min}}^{z_{\max}} \frac{f_Z(z)}{h - z}\,\mathrm{d}z & \text{, if } z_{\max} < h \quad \text{(M.6)} \\ h\displaystyle\int_{z_{\min}}^{h-\epsilon} \frac{f_Z(z)}{h - z}\,\mathrm{d}z & \text{, if } h \leq z_{\max} \quad \text{(M.7)} \end{cases}$$

This integral can be computed for the triangular asperity (grooves aligned with rolling direction) height distribution (Eq. 2.11) and the Christensen height distributions (Eq. 2.12). For the first distribution,

$$\phi_f = \begin{cases} \dfrac{h}{2\sqrt{3}R_q}\ln\left(\dfrac{h + \sqrt{3}R_q}{h - \sqrt{3}R_q}\right) & \text{, if } \sqrt{3}R_q < h \\ \dfrac{h}{2\sqrt{3}R_q}\ln\left(\dfrac{h + \sqrt{3}R_q}{\epsilon}\right) & \text{, if } h \leq \sqrt{3}R_q \end{cases} \tag{M.8}$$

[1] In Patir and Cheng [254], the following equation is mentioned:

$$\phi_f = h\int_{-h+\epsilon}^{+\infty} \frac{f_Z(z)}{h + z}\,\mathrm{d}z \tag{M.5}$$

It is equivalent to Eq. (M.7), if $f_Z(z)$ is an even function. If this is not true and if $f_Z(z)$ is defined such that asperities at higher z-positions enter into contact before asperities at lower z-positions, Eq. (M.7) should be used exclusively since the height distribution function is not evaluated at the correct position otherwise.

For the Christensen distribution, according to Patir and Cheng [254], if $3R_q < h$,

$$\phi_f = \frac{35}{32} H \left[(1 - H^2)^3 \ln \frac{H+1}{H-1} + \frac{H}{15} \left(66 + H^2 (30H^2 - 80) \right) \right] \tag{M.9}$$

In order to obtain a numerically stable value, the previous expression of ϕ_f is set to 1 for $h \geq 10 \cdot 3R_q$. Otherwise, if $h \leq 3R_q$,

$$\phi_f = \frac{35}{32} H \left[(1 - H^2)^3 \ln \frac{H+1}{\epsilon^*} + \frac{1}{60} \left(-55 + 132H + 345H^2 \right. \right.$$
$$\left. \left. -160H^3 - 405H^4 + 60H^5 + 147H^6 \right) \right] \tag{M.10}$$

where $H = h/(3R_q)$, $\epsilon^* = \epsilon/(3R_q)$ and $\epsilon = R_q/100$.

Figure M.1 shows the evolution of the first shear stress factor ϕ_f with the nominal film thickness h for the triangular asperity and Christensen height distributions. The dependence in ϵ is relatively important. Since no precise value of where the continuum hypothesis breaks down is, however, known, $\epsilon = R_q/100$ is chosen as suggested by Patir and Cheng [254]. It is also important to notice that $\phi_f \to 1$, if h increases, which is coherent with Eq. (4.200).

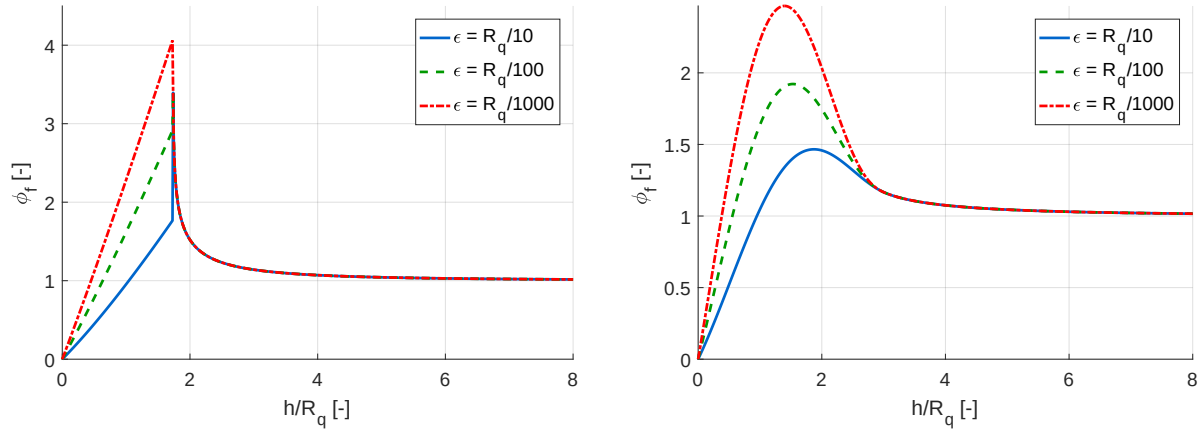

(a) Triangular asperity height distribution.

(b) Christensen height distribution.

Figure M.1: Evolution of the first shear stress factor ϕ_f with the nominal film thickness h.

M.2 Second shear stress factor

The *second shear stress factor* ϕ_{fs} was obtained through simulation by Patir and Cheng [254] for the Gaussian height distribution, which is almost similar to the Christensen height distribution as explained in Sec. 2.2.1.2. If the roll is assumed to be locally flat (Sec. 4.4), the expression in the reference simplifies to

$$\phi_{fs} = A_3 \mathcal{H}^{\alpha_4} e^{-\alpha_5 \mathcal{H} + \alpha_6 \mathcal{H}^2} \tag{M.11}$$

where $\mathcal{H} = h/R_q$ and the coefficients are listed in Tab. M.1. The previous equation is valid for $0.5 < \mathcal{H} < 7$. For larger values of $\mathcal{H}$ than 7, it has to converge to 0, since the influence of the roughness vanishes.

γ	A_3	α_4	α_5	α_6
1/9	14.1	2.45	2.30	0.10
1/6	13.4	2.42	2.30	0.10
1/3	12.3	2.32	2.30	0.10
1	11.1	2.31	2.38	0.11
3	9.8	2.25	2.80	0.18
6	10.1	2.25	2.90	0.18
9	8.7	2.15	2.97	0.18

Table M.1: Parameter values in the expression of the second shear stress factor ϕ_{fs} (Eq. M.11).

Figure M.2 shows the evolution of the second shear stress factor ϕ_{fs} with the nominal film thickness for the Gaussian height distribution. If one surface is smooth and the other one is rough, ϕ_{fs} decreases the mean shear stress on the rough surface while it increases the shear stress on the smooth surface. In simple words, the roughness seems to be protecting the surface parts in the valleys from viscous forces, thus decreasing the average shear stress.

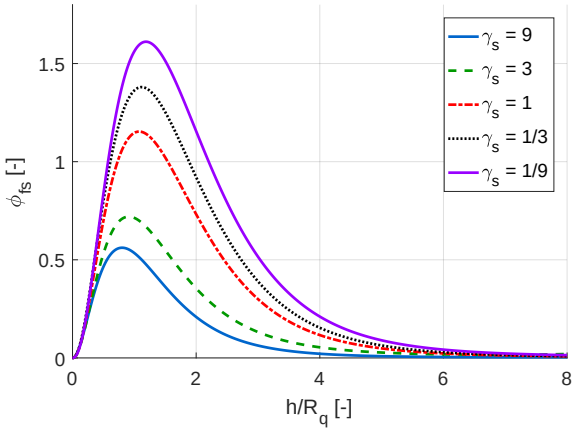

Figure M.2: Evolution of the second shear stress factor ϕ_{fs} as a function of the nominal film thickness h for the Gaussian height distribution.

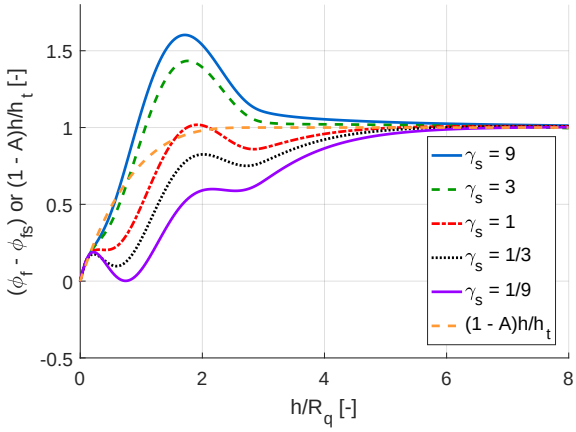

Figure M.3: Evolution of the combined shear stress factor related to the sliding velocity $\phi_f - \phi_{fs}$ as a function of the nominal film thickness h for the Gaussian height distribution ($\epsilon = R_q/100$).

This second shear stress factor is combined with the first shear factor as shown in Eq. (M.3), i.e. $\phi_f - \phi_{fs}$, for the stress applied to the strip. This combination is plotted in Fig. M.3 for $\epsilon = R_q/100$. It is unclear why the evolution of $\phi_f - \phi_{fs}$ as a function of h is relatively alternating.

In order to compare the Couette shear stress computation by the mean film thickness in the valleys (Sec. 4.8.3, Eq. 4.204) with the shear stress factor approach (Eq. M.3), the evolution of

$(1-A)h/h_t$ is also represented in Fig. M.3 since

$$\left.\begin{array}{ll} \frac{\eta(v_r-v_s)}{h_t}(1-A) & \text{by Eq. (4.204)} \\ \frac{\eta(v_r-v_s)}{h}(\phi_f-\phi_{fs}) & \text{by Eq. (M.3)} \end{array}\right\} \quad \Rightarrow \quad \phi_f-\phi_{fs} \overset{?}{\sim} \frac{(1-A)h}{h_t} \tag{M.12}$$

On average, $(1-A)h/h_t$ matches relatively well the combined shear stress factor, although this extension is theoretically questionable but extendable to larger contact areas, as explained before.

The values in Tab. M.1 can be fitted by the least squares method to obtain the following relations:

$$A_3 = 11.0850 - 0.8822\ln\gamma + 0.1030\ln\gamma^2 - 0.0600\ln\gamma^3 \tag{M.13}$$

$$\alpha_4 = 2.3001 - 0.0159\ln\gamma + 0.0026\ln\gamma^2 - 0.0107\ln\gamma^3 \tag{M.14}$$

$$\alpha_5 = 2.4555 + 0.2369\ln\gamma + 0.0412\ln\gamma^2 - 0.0183\ln\gamma^3 \tag{M.15}$$

$$\alpha_6 = 0.1259 + 0.0391\ln\gamma + 0.0037\ln\gamma^2 - 0.0045\ln\gamma^3 \tag{M.16}$$

For a longitudinal lay of triangular asperities, the second shear stress factor ϕ_{fs} is zero since the lubricant can neither be considered to be carried along in the valleys with a uniform velocity nor be considered stagnant, like it would be the case for some lubricant in surface pockets. This conclusion is coherent with Eq. (M.11), where $\phi_{fs} \to 0$, when $\gamma \to +\infty$ as suggested in Fig. M.3.

M.3 Third shear stress factor

In the same way as the previous factor, the *shear stress factor related to the pressure gradient* was also obtained through simulation for the Gaussian height distribution [254]:

$$\phi_{fp} = 1 - De^{-s\mathcal{H}} \tag{M.17}$$

where $\mathcal{H} = h/R_q$ and the coefficients are listed in Tab. M.2. Depending on the value of γ, the previous relation is only valid for $\mathcal{H} > 1$, > 0.75 or > 0.5.

Figure M.4 shows the evolution of the third shear stress factor with the nominal film thickness for the Gaussian height distribution. In order to determine the values of D and s in Eq. (M.17) based on Tab. M.2, the following fitting curves were obtained by the least-squares method:

$$D = 1.3364 - 0.1741\ln\gamma - 0.0425\ln^2\gamma \tag{M.18}$$

$$s = 0.6713 + 0.0947\ln\gamma + 0.0114\ln^2\gamma \tag{M.19}$$

$$\tag{M.20}$$

For the triangular asperity height distribution, whose grooves are aligned with the rolling direction, the third shear stress factor ϕ_{fp} is equal to 1 or h_v/h, if $h > \sqrt{3}R_q$ or $h \leq \sqrt{3}R_q$, respectively. These results can be derived as follows. First, for $h > \sqrt{3}R_q$ and Fig. 4.25,

$$\phi_{fp} = \frac{\frac{1}{\Delta y}\int_0^{\Delta y} h_l \,\mathrm{d}y}{h} = \frac{\frac{1}{\Delta y}\int_0^{\Delta y}\left(h - \sqrt{3}R_q + \frac{2\sqrt{3}R_q}{\Delta y}y\right)\mathrm{d}y}{h} = \frac{h}{h} = 1 \tag{M.21}$$

γ	D	s
1/9	1.51	0.52
1/6	1.51	0.54
1/3	1.47	0.58
1	1.40	0.66
3	0.98	0.79
6	0.97	0.91
9	0.73	0.91

Table M.2: Parameter values in the expression of the shear stress factor related to the pressure gradient ϕ_{fp} (Eq. M.17).

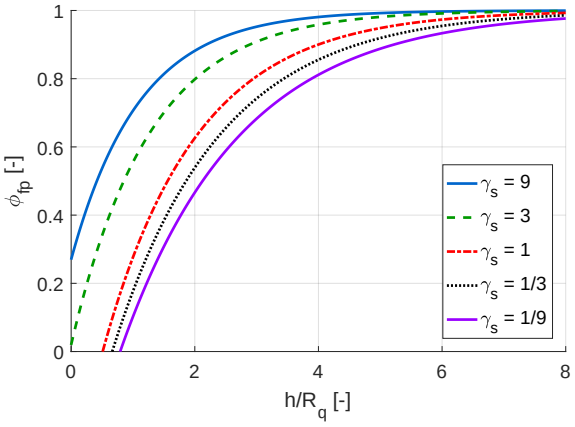

Figure M.4: Evolution of the third shear stress factor ϕ_{fp} with the nominal film thickness h for the Gaussian height distribution.

Secondly, for $h \leq \sqrt{3}R_q$ and Fig. 4.27,

$$\phi_{fp} = \frac{\frac{1}{\Delta y\left(\frac{1}{2}+\frac{h}{2\sqrt{3}R_q}\right)}\int_{\Delta y\left(\frac{1}{2}-\frac{h}{2\sqrt{3}R_q}\right)}^{\Delta y}\left(h-\sqrt{3}R_q+\frac{2\sqrt{3}R_q}{\Delta y}y\right)\,\mathrm{d}y}{h} \tag{M.22}$$

$$= \frac{\sqrt{3}R_q}{h}\left(\frac{1}{2}+\frac{h}{2\sqrt{3}R_q}\right) = \frac{h_v}{h} \tag{M.23}$$

by Eqs. (4.13), (4.15) and (4.203). An important subtlety in the previous calculation is that the average is not computed over the whole length Δy, like for the flow factors, e.g. Eq. (4.168), but only over the domain with the lubricant. This is due to the fact, that τ_l is defined with respect to $A_a - A_r$ in Eq. (4.5) and not A_a, while the flow factors are introduced to average the flow over the whole domain.

Appendix N

Derivation of METALUB equations

Explicitly solving a system of differential equations requires that these equations can be structured in a way allowing for their integration. Determining this structure is not straightforward in the METALUB model due to the important number of underlying equations. Therefore, the *particular form of equations, which is integrated, is derived in this chapter*.

As explained in Chap. 4, dry rough, lubricated rough, rough with starvation and smooth rolling models are implemented in METALUB, with and without finite element (FE) coupling. Since the rolling scenario with starvation is a combination of the dry rough and lubricated rough scenarios, essentially three different systems of equations exist in METALUB: dry rough, lubricated rough and smooth. Since the equations of the *dry rough and lubricated rough* rolling scenarios are similar, the corresponding equations are presented in the first section, while those of a *smooth* roll bite are presented in the second section.

Each of these two sections is divided into subsections depending on the *zones* in the roll bite, i.e. if the deformation mode is elastic and/or plastic, if the roll is in contact with the asperities or not, or if the transition to the high-speed equations occurred or not. For each zone, the *underlying equations* are first mentioned, then the *derivation* of their structured form for integration is explained, and finally, this *structured form* is specified. *This form is implemented verbatim in the METALUB software*. All systems are derived by considering the rough lubricated rolling scenario to be the base case. To simplify the presentation and the implementation, the corresponding names of the zones in this base case are used in other scenarios although they are not necessarily coherent when no lubricant is in the roll bite, e.g. the inlet zone of a dry roll bite is not hydrodynamic, or when the roll bite is assumed to be smooth.

In order to distinguish the equations of the dry and lubricated roll bites with or without FE coupling in the first section, different abbreviations were introduced. Thus, when equations are different in the dry and lubricated scenarios, the alternative dry value is written at the end of the same equation, but separated by the word "or", e.g.:

$$\frac{\partial p_l}{\partial x} = \frac{12\eta}{\phi_x h_t^3}\left(\frac{v_s + v_r}{2} h_t + \frac{v_s - v_r}{2} R_q \phi_s - Q\right) \text{ or } 0 \tag{N.1}$$

which is equivalent to

$$\frac{\partial p_l}{\partial x} = \frac{12\eta}{\phi_x h_t^3}\left(\frac{v_s + v_r}{2} h_t + \frac{v_s - v_r}{2} R_q \phi_s - Q\right), \text{ if lubricated.} \tag{N.2}$$

$$\frac{\partial p_l}{\partial x} = 0, \text{ if dry.} \tag{N.3}$$

Concerning the equations with and without the FE coupling in the first section, the following notations are used in the "Underlying system of equations" and "Structured system of equations" sections:

- $=$: equation used with and without FE coupling;
- $\overset{\text{cpl}}{=}$: equation used only with FE coupling;
- $\overset{\cancel{\text{cpl}}}{=}$: equation used only without FE coupling.

Finally, the different arrows, i.e. $\rightarrow$ and $\Rightarrow$, are used in the "Derivation" and "Structured system of equations" sections. In the "Derivation" sections, $\rightarrow$ and $\Rightarrow$ denote the following stages of a algebraic transformations. In particular, $\Rightarrow$ represents that this final transformation is used in the structured form of equations, which is implemented in METALUB. In the "Structured system of equations" sections, $\Rightarrow$ means that the corresponding differential equation has to be explicitly integrated, while $\rightarrow$ is not used in these sections.

N.1 Rough roll bite

N.1.1 Hydrodynamic inlet zone

N.1.1.1 Underlying system of equations

$z_r = z_r(x)$	by Secs. 4.6.1, 4.6.2, 4.6.3 or 4.6.4	(N.4)
$h_t = z_r - \frac{t_s}{2}$	Eq. (4.23)	(N.5)
$h = h(h_t)$	by Eqs. (4.15) or (4.20)	(N.6)
$A = A(h)$	by Eqs. (4.13) or (4.18)	(N.7)
$\overline{\epsilon}^p = \overline{\epsilon}^p_0$	No plastic deformation	(N.8)
$\sigma_Y = \sigma_Y(\overline{\epsilon}^p, \overline{D}^p, T_s)$	by Eqs. (4.50), (4.52), (4.54), (4.56), (4.60) or (4.62)	(N.9)
$\tau_Y = \frac{\sigma_Y}{\sqrt{3}}$	Eq. (H.56)	(N.10)
$p_a = p_l + 5.142\tau_Y$ or $5.142\tau_Y$	Eqs. (4.90) and (4.91); or $p_a = 0$	(N.11)
$p_i = Ap_a + (1-A)p_l$ or Ap_a	Eq. (4.4)	(N.12)
$\tau_a = 0$	No aspertity contact	(N.13)
$T_l = T_l(T_l^*, T_s, T_l)$ or /	by Eqs. (4.212), (4.213), (4.214) or (4.215)	(N.14)
$\eta = \eta(p_l, T_l)$ or /	by Eqs. (4.192), (**??**) or (4.195)	(N.15)
$\tau_l = \tau_l\left(h, h_t, A, \eta, v_s, v_r, \frac{\partial p_l}{\partial x}\right)$ or 0	by Eqs. (4.204) or (4.205)	(N.16)
$\tau_i = A\tau_a + (1-A)\tau_l$ or $A\tau_a$	Eq. (4.5)	(N.17)
$\phi_x = \phi_x(h_t)$ or /	by Eqs. (4.157) or (4.160)	(N.18)
$\phi_s = \phi_s(h_t)$ or /	by Eqs. (4.159) or (4.163) and (4.174) with (4.182)	(N.19)
$\frac{\partial p_l}{\partial x} = \frac{12\eta}{\phi_x h_t^3}\left(\frac{v_s + v_r}{2}h_t + \frac{v_s - v_r}{2}R_q\phi_s - Q\right)$ or 0	Eq. (4.191)	(N.20)
$\frac{\partial(\sigma_x t_s)}{\partial x} = -p_i\frac{\partial t_s}{\partial x} - 2\tau_i$	Eq. (4.65)	(N.21)
$\sigma_z = -p_i$	Eq. (4.68)	(N.22)
$\epsilon_x^e = \frac{1}{E_s}\left[\sigma_x - \nu_s(\sigma_y + \sigma_z)\right]$	Eq. (4.34a)	(N.23)
$\sigma_y = \nu_s(\sigma_x + \sigma_z)$	Eq. (4.34b)	(N.24)
$\epsilon_z^e = \frac{1}{E_s}\left[\sigma_z - \nu_s(\sigma_x + \sigma_y)\right]$	Eq. (4.34c)	(N.25)

$$\frac{\partial v_s}{\partial x} = v_s \frac{\partial \epsilon_x^e}{\partial x} \qquad \text{Eq. (4.30) and } \epsilon_x = \epsilon_x^e \tag{N.26}$$

$$\frac{\partial \epsilon_z^e}{\partial x} = \frac{1}{t_s}\frac{\partial t_s}{\partial x} \qquad \text{Eq. (4.31) and } \epsilon_z = \epsilon_z^e \tag{N.27}$$

$$p = -\frac{\sigma_x + \sigma_y + \sigma_z}{3} \qquad \text{Eq. (H.26)} \tag{N.28}$$

$$s_x = \sigma_x + p \qquad \text{Eq. (H.27)} \tag{N.29}$$

$$s_z = \sigma_z + p \qquad \text{Eq. (H.27)} \tag{N.30}$$

$$\frac{\partial T_s}{\partial x} = \frac{1}{\rho_s c_s v_s}\frac{\tau_i (v_r - v_s)}{t_s} \qquad \text{Eq. (4.211) and no plastic deformation} \tag{N.31}$$

$$\frac{\partial T_l}{\partial x} = \frac{\beta_l}{\rho_l c_l v_s}\frac{\tau_i (v_r - v_s)}{h_t} \text{ or } 0 \qquad \text{Eq. (4.215)} \tag{N.32}$$

N.1.1.2 Derivation

- Eq. (N.24) in Eq. (N.25):

$$\epsilon_z^e = \frac{1}{E_s}\left[\sigma_z - \nu_s \sigma_x - \nu_s^2(\sigma_x + \sigma_z)\right] \tag{N.33}$$

$$\rightarrow \epsilon_z^e = \frac{1}{E_s}\left[-\nu_s(1+\nu_s)\sigma_x + (1-\nu_s^2)\sigma_z\right] \tag{N.34}$$

$$\rightarrow \epsilon_z^e = \frac{1+\nu_s}{E_s}\left[-\nu_s \sigma_x + (1-\nu_s)\sigma_z\right] \tag{N.35}$$

- Eq. (N.22) in Eq. (N.35):

$$\epsilon_z^e = \frac{-(1+\nu_s)}{E_s}\left[\nu_s \sigma_x + (1-\nu_s)p_i\right] \tag{N.36}$$

$$\rightarrow \frac{\partial \epsilon_z^e}{\partial x} = \frac{-(1+\nu_s)}{E_s}\left[\nu_s \frac{\partial \sigma_x}{\partial x} + (1-\nu_s)\frac{\partial p_i}{\partial x}\right] \tag{N.37}$$

- Eq. (N.27) in Eq. (N.37):

$$\frac{1}{t_s}\frac{\partial t_s}{\partial x} = \frac{-(1+\nu_s)}{E_s}\left[\nu_s \frac{\partial \sigma_x}{\partial x} + (1-\nu_s)\frac{\partial p_i}{\partial x}\right] \tag{N.38}$$

- Eq. (N.21) and $p_i = p_l$, since $A = 0$ by definition in the hydrodynamic inlet zone:

$$\frac{\partial \sigma_x}{\partial x} t_s + \sigma_x \frac{\partial t_s}{\partial x} = -p_l \frac{\partial t_s}{\partial x} - 2\tau_i \tag{N.39}$$

$$\Rightarrow \frac{\partial \sigma_x}{\partial x} = -\frac{1}{t_s}\left[(\sigma_x + p_l)\frac{\partial t_s}{\partial x} + 2\tau_i\right] \tag{N.40}$$

- Eq. (N.40) in Eq. (N.38), and again $p_i = p_l$:

$$\frac{1}{t_s}\frac{\partial t_s}{\partial x} = \frac{-(1+\nu_s)}{E_s}\left[\frac{-\nu_s}{t_s}(\sigma_x + p_l)\frac{\partial t_s}{\partial x} - \frac{2\nu_s}{t_s}\tau_i + (1-\nu_s)\frac{\partial p_l}{\partial x}\right] \tag{N.41}$$

$$\rightarrow E_s\frac{\partial t_s}{\partial x} = \nu_s(1+\nu_s)(\sigma_x + p_l)\frac{\partial t_s}{\partial x} + 2\nu_s(1+\nu_s)\tau_i - (1-\nu_s^2)\frac{\partial p_l}{\partial x}t_s \tag{N.42}$$

$$\rightarrow \frac{\partial t_s}{\partial x}\left[E_s - \nu_s(1+\nu_s)(\sigma_x + p_l)\right] = (1+\nu_s)\left[2\nu_s\tau_i - (1-\nu_s)\frac{\partial p_l}{\partial x}t_s\right] \tag{N.43}$$

$$\Rightarrow \frac{\partial t_s}{\partial x} = \frac{(1+\nu_s)\left[(1-\nu_s)\frac{\partial p_l}{\partial x}t_s - 2\nu_s\tau_i\right]}{\nu_s(1+\nu_s)(\sigma_x + p_l) - E_s} \tag{N.44}$$

- Eq. (N.24) in Eq. (N.23):

$$\epsilon_x^e = \frac{1}{E_s}\left[\sigma_x - \nu_s^2(\sigma_x + \sigma_z) - \nu_s\sigma_z\right] \tag{N.45}$$

$$\rightarrow \epsilon_x^e = \frac{1}{E_s}\left[(1-\nu_s^2)\sigma_x - \nu_s(1+\nu_s)\sigma_z\right] \tag{N.46}$$

$$\rightarrow \epsilon_x^e = \frac{1+\nu_s}{E_s}\left[(1-\nu_s)\sigma_x - \nu_s\sigma_z\right] \tag{N.47}$$

- Eq. (N.22) in Eq. (N.47) and again $p_i = p_l$:

$$\epsilon_x^e = \frac{1+\nu_s}{E_s}\left[(1-\nu_s)\sigma_x + \nu_s p_l\right] \tag{N.48}$$

$$\rightarrow \frac{\partial \epsilon_x^e}{\partial x} = \frac{1+\nu_s}{E_s}\left[(1-\nu_s)\frac{\partial \sigma_x}{\partial x} + \nu_s\frac{\partial p_l}{\partial x}\right] \tag{N.49}$$

- Eq. (N.49) in Eq. (N.26):

$$\Rightarrow \frac{\partial v_s}{\partial x} = \frac{v_s(1+\nu_s)}{E_s}\left[(1-\nu_s)\frac{\partial \sigma_x}{\partial x} + \nu_s\frac{\partial p_l}{\partial x}\right] \tag{N.50}$$

N.1.1.3 Structured system of equations

Values required in differential equations

$$z_r = z_r(x) \qquad \text{by Secs. 4.6.1, 4.6.2, 4.6.3 or 4.6.4} \tag{N.51}$$

$$h_t = z_r - \frac{t_s}{2} \tag{N.52}$$

$$h = h_t \tag{N.53}$$

$$A = 0 \tag{N.54}$$

$$T_l = T_l(T_l^*, T_s, T_l) \text{ or } / \qquad \text{by Eqs. (4.212), (4.213), (4.214) or (4.215)} \tag{N.55}$$

$$\eta = \eta(p_l, T_l) \text{ or } / \qquad \text{by Eqs. (4.192), (??) or (4.195)} \tag{N.56}$$

$$\phi_x = \phi_x(h_t) \text{ or } / \qquad \text{by Eqs. (4.157) or (4.160)} \tag{N.57}$$

$$\phi_s = \phi_s(h_t) \text{ or } / \qquad \text{by Eqs. (4.159) or (4.163) and (4.174) with (4.182)} \tag{N.58}$$

Differential equations (mainly)

$$\Rightarrow \frac{\partial p_l}{\partial x} = \frac{12\eta}{\phi_x h_t^3}\left(\frac{v_s + v_r}{2} h_t + \frac{v_s - v_r}{2} R_q \phi_s - Q\right) \text{ or } 0 \tag{N.59}$$

$$\tau_l = \tau_l\left(h, h_t, A, \eta, v_s, v_r, \frac{\partial p_l}{\partial x}\right) \text{ or } 0 \qquad \text{by Eqs. (4.204) or (4.205)} \tag{N.60}$$

$$\tau_i = \tau_l \text{ or } 0 \qquad \text{Eq. (N.17) and } A = 0 \tag{N.61}$$

$$\Rightarrow \frac{\partial t_s}{\partial x} = \frac{(1+\nu_s)\left[(1-\nu_s)\frac{\partial p_l}{\partial x} t_s - 2\nu_s \tau_i\right]}{\nu_s(1+\nu_s)(\sigma_x + p_l) - E_s} \text{ or } 0 \tag{N.62}$$

$$\Rightarrow \frac{\partial \sigma_x}{\partial x} = -\frac{1}{t_s}\left[(\sigma_x + p_l)\frac{\partial t_s}{\partial x} + 2\tau_i\right] \text{ or } 0 \tag{N.63}$$

$$\Rightarrow \frac{\partial v_s}{\partial x} = \frac{v_s(1+\nu_s)}{E_s}\left[(1-\nu_s)\frac{\partial \sigma_x}{\partial x} + \nu_s \frac{\partial p_l}{\partial x}\right] \text{ or } 0 \tag{N.64}$$

$$\Rightarrow \frac{\partial T_s}{\partial x} = \frac{1}{\rho_s c_s v_s}\frac{\tau_i(v_r - v_s)}{t_s} \tag{N.65}$$

$$\Rightarrow \frac{\partial T_l}{\partial x} = \frac{\beta_l}{\rho_l c_l v_s}\frac{\tau_i(v_r - v_s)}{h_t} \text{ or } 0 \tag{N.66}$$

Values not directly required in differential equations

$$\overline{\epsilon}^p = \overline{\epsilon}_0^p \tag{N.67}$$

$$\sigma_Y = \sigma_Y(\overline{\epsilon}^p, \overline{D}^p, T_s) \qquad \text{by Eqs. (4.50), (4.52), (4.54), (4.56), (4.60) or (4.62)} \tag{N.68}$$

$$\tau_Y = \frac{\sigma_Y}{\sqrt{3}} \tag{N.69}$$

$$p_a = p_l + 5.142\tau_Y \text{ or } 5.142\tau_Y \tag{N.70}$$

$$p_i = p_l \text{ or } 0 \tag{N.71}$$

$$\tau_a = 0 \tag{N.72}$$

$$\sigma_z = -p_i \text{ or } 0 \tag{N.73}$$

$$\sigma_y = \nu_s(\sigma_x + \sigma_z) \text{ or } \nu_s\sigma_x \tag{N.74}$$

$$p = -\frac{\sigma_x + \sigma_y + \sigma_z}{3} \tag{N.75}$$

$$s_x = \sigma_x + p \tag{N.76}$$

$$s_z = \sigma_z + p \tag{N.77}$$

N.1.2 Mixed inlet zone

N.1.2.1 Underlying system of equations

$z_r = z_r(x)$	by Secs. 4.6.1, 4.6.2, 4.6.3 or 4.6.4	(N.78)
$h_t = z_r - \frac{t_s}{2}$	Eq. (4.23)	(N.79)
$h_t \overset{\text{cpl}}{=} h_t(x)$	by Eq. (6.41)	(N.80)
$h = h(h_t)$	by Eqs. (4.15) or (4.20)	(N.81)
$A \overset{\text{epl}}{=} A(h)$	by Eqs. (4.13) or (4.18)	(N.82)
$A \overset{\text{cpl}}{=} A(x)$	by Eq. (6.40)	(N.83)
$\overline{\epsilon}^p = \overline{\epsilon}^p(x_{\text{ihm}})$	No plastic deformation	(N.84)
$\sigma_Y = \sigma_Y(\overline{\epsilon}^p, \overline{D}^p, T_s)$	by Eqs. (4.50), (4.52), (4.54), (4.56), (4.60) or (4.62)	(N.85)
$\tau_Y = \frac{\sigma_Y}{\sqrt{3}}$	Eq. (H.56)	(N.86)
$E_p \overset{\text{epl}}{=} 0$	Eq. (4.89) and no plastic deformation	(N.87)
$H_a \overset{\text{epl}}{=} H_a(A, E_p)$	by Eq. (4.92)	(N.88)
$p_a \overset{\text{epl}}{=} p_l + H_a\tau_Y$ or $H_a\tau_Y$	Eq. (4.90)	(N.89)
$p_i = Ap_a + (1-A)p_l$ or Ap_a	Eq. (4.4)	(N.90)
$\tau_a = \tau_a(v_s, v_r, p_a, \tau_Y)$	by Eqs. (4.123), (4.124) or (4.125)	(N.91)
$T_l = T_l(T_l^*, T_s, T_l)$ or /	by Eqs. (4.212), (4.213), (4.214) or (4.215)	(N.92)
$\eta = \eta(p_l, T_l)$ or /	by Eqs. (4.192), (**??**) or (4.195)	(N.93)
$\tau_l = \tau_l\left(h, h_t, A, \eta, v_s, v_r, \frac{\partial p_l}{\partial x}\right)$ or 0	by Eqs. (4.204) or (4.205)	(N.94)
$\tau_i = A\tau_a + (1-A)\tau_l$ or $A\tau_a$	Eq. (4.5)	(N.95)
$\phi_x = \phi_x(h_t)$ or /	by Eqs. (4.168) or (4.170)	(N.96)
$\phi_s = \phi_s(h_t)$ or /	by Eqs. (4.169) or (4.174) with (4.182)	(N.97)
$\frac{\partial p_l}{\partial x} = \frac{12\eta}{\phi_x h_t^3}\left(\frac{v_s+v_r}{2}h_t + \frac{v_s-v_r}{2}R_q\phi_s - Q\right)$ or 0	Eq. (4.191)	(N.98)
$\frac{\partial(\sigma_x t_s)}{\partial x} = -p_i\frac{\partial t_s}{\partial x} - 2\tau_i$	Eq. (4.65)	(N.99)
$\sigma_z = -p_i$	Eq. (4.68)	(N.100)

$$\epsilon_x^e = \frac{1}{E_s}\left[\sigma_x - \nu_s(\sigma_y + \sigma_z)\right] \quad \text{Eq. (4.34a)} \tag{N.101}$$

$$\sigma_y = \nu_s(\sigma_x + \sigma_z) \quad \text{Eq. (4.34b)} \tag{N.102}$$

$$\epsilon_z^e = \frac{1}{E_s}\left[\sigma_z - \nu_s(\sigma_x + \sigma_y)\right] \quad \text{Eq. (4.34c)} \tag{N.103}$$

$$\frac{\partial v_s}{\partial x} = v_s \frac{\partial \epsilon_x^e}{\partial x} \quad \text{Eq. (4.30) and } \epsilon_x = \epsilon_x^e \tag{N.104}$$

$$\frac{\partial \epsilon_z^e}{\partial x} = \frac{1}{t_s}\frac{\partial t_s}{\partial x} \quad \text{Eq. (4.31) and } \epsilon_z = \epsilon_z^e \tag{N.105}$$

$$p = -\frac{\sigma_x + \sigma_y + \sigma_z}{3} \quad \text{Eq. (H.26)} \tag{N.106}$$

$$s_x = \sigma_x + p \quad \text{Eq. (H.27)} \tag{N.107}$$

$$s_z = \sigma_z + p \quad \text{Eq. (H.27)} \tag{N.108}$$

$$\frac{\partial T_s}{\partial x} = \frac{1}{\rho_s c_s v_s}\frac{\tau_i(v_r - v_s)}{t_s} \quad \text{Eq. (4.211) and no plastic deformation} \tag{N.109}$$

$$\frac{\partial T_l}{\partial x} = \frac{\beta_l}{\rho_l c_l v_s}\frac{\tau_i(v_r - v_s)}{h_t} \text{ or } 0 \quad \text{Eq. (4.215)} \tag{N.110}$$

N.1.2.2 Derivation

- Eq. (N.79):

$$t_s = 2(z_r - h_t) \tag{N.111}$$

$$\Rightarrow \frac{\partial t_s}{\partial x} = 2\left(\frac{\partial z_r}{\partial x} - \frac{\partial h_t}{\partial x}\right) \tag{N.112}$$

- Eq. (N.99):

$$\frac{\partial \sigma_x}{\partial x} t_s + \sigma_x \frac{\partial t_s}{\partial x} = -p_i \frac{\partial t_s}{\partial x} - 2\tau_i \tag{N.113}$$

$$t_s \frac{\partial \sigma_x}{\partial x} = -(\sigma_x + p_i)\frac{\partial t_s}{\partial x} - 2\tau_i \tag{N.114}$$

$$\Rightarrow \frac{\partial \sigma_x}{\partial x} = -\frac{1}{t_s}\left[(\sigma_x + p_i)\frac{\partial t_s}{\partial x} + 2\tau_i\right] \tag{N.115}$$

- Eq. (N.102) in Eq. (N.103):

$$\epsilon_z^e = \frac{1}{E_s}\left[\sigma_z - \nu_s\sigma_x - \nu_s^2(\sigma_x + \sigma_z)\right] \tag{N.116}$$

$$\rightarrow \epsilon_z^e = \frac{1}{E_s}\left[-\nu_s(1 + \nu_s)\sigma_x + (1 - \nu_s^2)\sigma_z\right] \tag{N.117}$$

$$\rightarrow \frac{\partial \epsilon_z^e}{\partial x} = \frac{-\nu_s(1 + \nu_s)}{E_s}\frac{\partial \sigma_x}{\partial x} + \frac{1 - \nu_s^2}{E_s}\frac{\partial \sigma_z}{\partial x} \tag{N.118}$$

- Eq. (N.105) in Eq. (N.118):

$$\frac{1}{t_s}\frac{\partial t_s}{\partial x} = \frac{-\nu_s(1+\nu_s)}{E_s}\frac{\partial \sigma_x}{\partial x} + \frac{1-\nu_s^2}{E_s}\frac{\partial \sigma_z}{\partial x} \tag{N.119}$$

$$\rightarrow \frac{1-\nu_s^2}{E_s}\frac{\partial \sigma_z}{\partial x} = \frac{1}{t_s}\frac{\partial t_s}{\partial x} + \frac{\nu_s(1+\nu_s)}{E_s}\frac{\partial \sigma_x}{\partial x} \tag{N.120}$$

$$\Rightarrow \frac{\partial \sigma_z}{\partial x} = \frac{E_s}{t_s(1-\nu_s^2)}\frac{\partial t_s}{\partial x} + \frac{\nu_s}{1-\nu_s}\frac{\partial \sigma_x}{\partial x} \tag{N.121}$$

- Eq. (N.89) in Eq. (N.90):

$$p_i = A p_l + A H_a \tau_Y + p_l - A p_l \tag{N.122}$$

$$\rightarrow p_i = p_l + A H_a \tau_Y \tag{N.123}$$

- Eq. (N.123) in Eq. (N.100):

$$\sigma_z = -p_l - A H_a \tau_Y \tag{N.124}$$

$$\rightarrow \frac{\partial \sigma_z}{\partial x} = -\frac{\partial p_l}{\partial x} - \frac{\partial A}{\partial x} H_a \tau_Y - A\frac{\partial H_a}{\partial x}\tau_Y \tag{N.125}$$

$$\rightarrow \frac{\partial \sigma_z}{\partial x} = -\frac{\partial p_l}{\partial x} - \left(\frac{\partial A}{\partial h}\frac{\partial h}{\partial h_t}\frac{\partial h_t}{\partial x} H_a + A\frac{\partial H_a}{\partial A}\frac{\partial A}{\partial h}\frac{\partial h}{\partial h_t}\frac{\partial h_t}{\partial x}\right)\tau_Y \tag{N.126}$$

$$\rightarrow \frac{\partial \sigma_z}{\partial x} = -\frac{\partial p_l}{\partial x} - \frac{\partial A}{\partial h}\frac{\partial h}{\partial h_t}\left(H_a + A\frac{\partial H_a}{\partial A}\right)\tau_Y\frac{\partial h_t}{\partial x} \tag{N.127}$$

$$\rightarrow \frac{\partial \sigma_z}{\partial x} = -\frac{\partial p_l}{\partial x} - \beta\frac{\partial h_t}{\partial x} \quad \text{with} \quad \beta = \frac{\partial A}{\partial h}\frac{\partial h}{\partial h_t}\left(H_a + A\frac{\partial H_a}{\partial A}\right)\tau_Y \tag{N.128}$$

- Eq. (N.112) in Eq. (N.115):

$$\frac{\partial \sigma_x}{\partial x} = -\frac{1}{t_s}\left[2(\sigma_x + p_i)\left(\frac{\partial z_r}{\partial x} - \frac{\partial h_t}{\partial x}\right) + 2\tau_i\right] \tag{N.129}$$

- Eq. (N.112) and Eq. (N.129) in Eq. (N.121):

$$\frac{\partial \sigma_z}{\partial z} = \frac{2E_s}{t_s(1-\nu_s^2)}\left(\frac{\partial z_r}{\partial x} - \frac{\partial h_t}{\partial x}\right) - \frac{\nu_s}{t_s(1-\nu_s)}\left[2(\sigma_x + p_i)\left(\frac{\partial z_r}{\partial x} - \frac{\partial h_t}{\partial x}\right) + 2\tau_i\right] \tag{N.130}$$

- Eq. (N.130) in Eq. (N.128):

$$\frac{2E_s}{t_s(1-\nu_s^2)}\left(\frac{\partial z_r}{\partial x} - \frac{\partial h_t}{\partial x}\right) - \frac{\nu_s}{t_s(1-\nu_s)}\left[2(\sigma_x + p_i)\left(\frac{\partial e_r}{\partial x} - \frac{\partial h_t}{\partial x}\right) + 2\tau_i\right] = -\frac{\partial p_l}{\partial x} - \beta\frac{\partial h_t}{\partial x} \tag{N.131}$$

$$\rightarrow 2E_s\left(\frac{\partial z_r}{\partial x}-\frac{\partial h_t}{\partial x}\right)-\nu_s(1+\nu_s)\left[2(\sigma_x+p_i)\left(\frac{\partial z_r}{\partial x}-\frac{\partial h_t}{\partial x}\right)+2\tau_i\right]$$
$$=-t_s(1-\nu_s^2)\left(\frac{\partial p_l}{\partial x}+\beta\frac{\partial h_t}{\partial x}\right) \tag{N.132}$$

$$\rightarrow 2E_s\frac{\partial z_r}{\partial x}-2E_s\frac{\partial h_t}{\partial x}-2\nu_s(1+\nu_s)(\sigma_x+p_i)\frac{\partial z_r}{\partial x}+2\nu_s(1+\nu_s)(\sigma_x+p_i)\frac{\partial h_t}{\partial x}$$
$$-2\nu_s(1+\nu_s)\tau_i=-t_s(1-\nu_s^2)\frac{\partial p_l}{\partial x}-t_s\beta(1-\nu_s^2)\frac{\partial h_t}{\partial x} \tag{N.133}$$

$$\rightarrow\frac{\partial h_t}{\partial x}\left[2\nu_s(1+\nu_s)(\sigma_x+p_i)+t_s\beta(1-\nu_s^2)-2E_s\right] \tag{N.134}$$

$$=\left[2\nu_s(1+\nu_s)(\sigma_x+p_i)-2E_s\right]\frac{\partial z_r}{\partial x}-t_s(1-\nu_s^2)\frac{\partial p_l}{\partial x}+2\nu_s(1+\nu_s)\tau_i \tag{N.135}$$

$$\rightarrow\frac{\partial h_t}{\partial x}\left\{(1+\nu_s)\left[2\nu_s(\sigma_x+p_i)+t_s\beta(1-\nu_s)\right]-2E_s\right\} \tag{N.136}$$

$$=\left[2\nu_s(1+\nu_s)(\sigma_x+p_i)-2E_s\right]\frac{\partial z_r}{\partial x}+(1+\nu_s)\left[2\nu_s\tau_i-t_s(1-\nu_s)\frac{\partial p_l}{\partial x}\right] \tag{N.137}$$

$$\Rightarrow\frac{\partial h_t}{\partial x}=\frac{\left[2\nu_s(1+\nu_s)(\sigma_x+p_i)-2E_s\right]\frac{\partial z_r}{\partial x}+(1+\nu_s)\left[2\nu_s\tau_i-t_s(1-\nu_s)\frac{\partial p_l}{\partial x}\right]}{(1+\nu_s)\left[2\nu_s(\sigma_x+p_i)+t_s\beta(1-\nu_s)\right]-2E_s} \tag{N.138}$$

- Eq. (N.102) in Eq. (N.101):

$$\epsilon_x^e=\frac{1}{E_s}\left[\sigma_x-\nu_s^2(\sigma_x+\sigma_z)-\nu_s\sigma_z\right] \tag{N.139}$$

$$\rightarrow\epsilon_x^e=\frac{1}{E_s}\left[(1-\nu_s^2)\sigma_x-\nu_s(1+\nu_s)\sigma_z\right] \tag{N.140}$$

$$\rightarrow\frac{\partial\epsilon_x^e}{\partial x}=\frac{1+\nu_s}{E_s}\left[(1-\nu_s)\frac{\partial\sigma_x}{\partial x}-\nu_s\frac{\partial\sigma_z}{\partial x}\right] \tag{N.141}$$

- Eq. (N.141) in Eq. (N.104):

$$\Rightarrow\frac{\partial v_s}{\partial x}=\frac{v_s(1+\nu_s)}{E_s}\left[(1-\nu_s)\frac{\partial\sigma_x}{\partial x}-\nu_s\frac{\partial\sigma_z}{\partial x}\right] \tag{N.142}$$

N.1.2.3 Structured system of equations

Values required in differential equations

$$z_r = z_r(x) \quad \text{by Secs. 4.6.1, 4.6.2, 4.6.3 or 4.6.4} \tag{N.143}$$

$$\frac{\partial z_r}{\partial x} = \frac{\partial z_r}{\partial x}(x) \quad \text{by Secs. 4.6.1, 4.6.2, 4.6.3 or 4.6.4} \tag{N.144}$$

$$h_t \overset{\text{cpl}}{=} h_t(x) \quad \text{by Eq. (6.41)} \tag{N.145}$$

$$t_s = 2(z_r - h_t) \tag{N.146}$$

$$h = h(h_t) \quad \text{by Eqs. (4.15) or (4.20)} \tag{N.147}$$

$$\frac{\partial h}{\partial h_t} \overset{\text{epl}}{=} \frac{\partial h}{\partial h_t}(h_t) \quad \text{by Eqs. (4.17) or (4.22)} \tag{N.148}$$

$$A \overset{\text{epl}}{=} A(h) \quad \text{by Eqs. (4.13) or (4.18)} \tag{N.149}$$

$$A \overset{\text{cpl}}{=} A(x) \quad \text{by Eq. (6.40)} \tag{N.150}$$

$$\frac{\partial A}{\partial h} \overset{\text{epl}}{=} \frac{\partial A}{\partial h}(h) \quad \text{by Eqs. (4.14) or (4.19)} \tag{N.151}$$

$$H_a \overset{\text{epl}}{=} H_a(A) \quad \text{by Eq. (4.94)} \tag{N.152}$$

$$\frac{\partial H_a}{\partial A} \overset{\text{epl}}{=} \frac{\partial H_a}{\partial A}(A) \quad \text{by Eq. (4.95)} \tag{N.153}$$

$$\overline{\epsilon}^p = \overline{\epsilon}^p(x_{\text{ihm}}) \tag{N.154}$$

$$\sigma_Y = \sigma_Y(\overline{\epsilon}^p, \overline{D}^p, T_s) \quad \text{by Eqs. (4.50), (4.52), (4.54), (4.56), (4.60) or (4.62)} \tag{N.155}$$

$$\tau_Y = \frac{\sigma_Y}{\sqrt{3}} \tag{N.156}$$

$$\beta \overset{\text{epl}}{=} \frac{\partial A}{\partial h}\frac{\partial h}{\partial h_t}\left(H_a + A\frac{\partial H_a}{\partial A}\right)\tau_Y \tag{N.157}$$

$$p_i = -\sigma_z \tag{N.158}$$

$$p_a = \frac{p_i - (1-A)p_l}{A} \text{ or } \frac{p_i}{A} \tag{N.159}$$

$$\tau_a = \tau_a(v_s, v_r, p_a, \tau_Y) \quad \text{by Eqs. (4.123), (4.124) or (4.125)} \tag{N.160}$$

$$T_l = T_l(T_l^*, T_s, T_l) \text{ or } / \quad \text{by Eqs. (4.212), (4.213), (4.214) or (4.215)} \tag{N.161}$$

$$\eta = \eta(p_l, T_l) \text{ or } / \quad \text{by Eqs. (4.192), (??) or (4.195)} \tag{N.162}$$

$$\phi_x = \phi_x(h_t) \text{ or } / \quad \text{by Eqs. (4.168) or (4.170)} \tag{N.163}$$

$$\phi_s = \phi_s(h_t) \text{ or } / \quad \text{by Eqs. (4.169) or (4.174) with (4.182)} \tag{N.164}$$

Differential equations (mainly)

$$\Rightarrow \frac{\partial p_l}{\partial x} = \frac{12\eta}{\phi_x h_t^3}\left(\frac{v_s + v_r}{2}h_t + \frac{v_s - v_r}{2}R_q\phi_s - Q\right) \text{ or } 0 \tag{N.165}$$

$$\tau_l = \tau_l\left(h, h_t, A, \eta, v_s, v_r, \frac{\partial p_l}{\partial x}\right) \text{ or } 0 \qquad \text{by Eqs. (4.204) or (4.205)} \tag{N.166}$$

$$\tau_i = A\tau_a + (1 - A)\tau_l \text{ or } A\tau_a \tag{N.167}$$

$$\Rightarrow \frac{\partial h_t}{\partial x} \overset{\text{cpl}}{=} \frac{[2\nu_s(1+\nu_s)(\sigma_x + p_i) - 2E_s]\frac{\partial z_r}{\partial x} + (1+\nu_s)\left[2\nu_s\tau_i - t_s(1-\nu_s)\frac{\partial p_l}{\partial x}\right]}{(1+\nu_s)\left[2\nu_s(\sigma_x + p_i) + t_s\beta(1-\nu_s)\right] - 2E_s} \tag{N.168}$$

$$\frac{\partial h_t}{\partial x} \overset{\text{cpl}}{=} \frac{\partial h_t}{\partial x}(x) \qquad \text{by Eq. (6.42)} \tag{N.169}$$

$$\frac{\partial t_s}{\partial x} = 2\left(\frac{\partial z_r}{\partial x} - \frac{\partial h_t}{\partial x}\right) \tag{N.170}$$

$$\Rightarrow \frac{\partial \sigma_x}{\partial x} = -\frac{1}{t_s}\left[(\sigma_x + p_i)\frac{\partial t_s}{\partial x} + 2\tau_i\right] \tag{N.171}$$

$$\Rightarrow \frac{\partial \sigma_z}{\partial x} = \frac{E_s}{t_s(1-\nu_s^2)}\frac{\partial t_s}{\partial x} + \frac{\nu_s}{1-\nu_s}\frac{\partial \sigma_x}{\partial x} \tag{N.172}$$

$$\Rightarrow \frac{\partial v_s}{\partial x} = \frac{v_s(1+\nu_s)}{E_s}\left[(1-\nu_s)\frac{\partial \sigma_x}{\partial x} - \nu_s\frac{\partial \sigma_z}{\partial x}\right] \tag{N.173}$$

$$\Rightarrow \frac{\partial T_s}{\partial x} = \frac{1}{\rho_s c_s v_s}\frac{\tau_i(v_r - v_s)}{t_s} \tag{N.174}$$

$$\Rightarrow \frac{\partial T_l}{\partial x} = \frac{\beta_l}{\rho_l c_l v_s}\frac{\tau_i(v_r - v_s)}{h_t} \text{ or } 0 \tag{N.175}$$

Values not directly required in differential equations

$$\sigma_y = \nu_s(\sigma_x + \sigma_z) \tag{N.176}$$

$$p = -\frac{\sigma_x + \sigma_y + \sigma_z}{3} \tag{N.177}$$

$$s_x = \sigma_x + p \tag{N.178}$$

$$s_z = \sigma_z + p \tag{N.179}$$

N.1.3 Low-speed work zone

N.1.3.1 Underlying system of equations

$$z_r = z_r(x) \quad \text{by Secs. 4.6.1, 4.6.2, 4.6.3 or 4.6.4} \quad \text{(N.180)}$$

$$h_t = z_r - \frac{t_s}{2} \quad \text{Eq. (4.23)} \quad \text{(N.181)}$$

$$h_t \overset{\text{cpl}}{=} h_t(x) \quad \text{by Eq. (6.41)} \quad \text{(N.182)}$$

$$h = h(h_t) \quad \text{by Eqs. (4.15) or (4.20)} \quad \text{(N.183)}$$

$$A \overset{\cancel{\text{epl}}}{=} A(h) \quad \text{by Eqs. (4.13) or (4.18)} \quad \text{(N.184)}$$

$$A \overset{\text{cpl}}{=} A(x) \quad \text{by Eq. (6.40)} \quad \text{(N.185)}$$

$$\sigma_Y = \sigma_Y(\overline{\epsilon}^p, \overline{D}^p, T_s) \quad \text{by Eqs. (4.50), (4.52), (4.54), (4.56), (4.60) or (4.62)} \quad \text{(N.186)}$$

$$\tau_Y = \frac{\sigma_Y}{\sqrt{3}} \quad \text{Eq. (H.56)} \quad \text{(N.187)}$$

$$H_a \overset{\cancel{\text{epl}}}{=} \frac{p_a - p_l}{\tau_Y} \text{ or } \frac{p_a}{\tau_Y} \quad \text{Eq. (4.90)} \quad \text{(N.188)}$$

$$E_p \overset{\cancel{\text{epl}}}{=} E_p(A, H_a) \quad \text{by Eqs. (4.92), (4.96) or (4.97)} \quad \text{(N.189)}$$

$$p_i = Ap_a + (1-A)p_l \text{ or } Ap_a \quad \text{Eq. (4.4)} \quad \text{(N.190)}$$

$$\tau_a = \tau_a(v_s, v_r, p_a, \tau_Y) \quad \text{by Eqs. (4.123), (4.124) or (4.125)} \quad \text{(N.191)}$$

$$T_l = T_l(T_l^*, T_s, T_l) \text{ or } / \quad \text{by Eqs. (4.212), (4.213), (4.214) or (4.215)} \quad \text{(N.192)}$$

$$\eta = \eta(p_l, T_l) \text{ or } / \quad \text{by Eqs. (4.192), (??) or (4.195)} \quad \text{(N.193)}$$

$$\tau_l = \tau_l\left(h, h_t, A, \eta, v_s, v_r, \frac{\partial p_l}{\partial x}\right) \text{ or } 0 \quad \text{by Eqs. (4.204) or (4.205)} \quad \text{(N.194)}$$

$$\tau_i = A\tau_a + (1-A)\tau_l \text{ or } A\tau_a \quad \text{Eq. (4.5)} \quad \text{(N.195)}$$

$$\phi_x = \phi_x(h_t) \text{ or } / \quad \text{by Eqs. (4.168) or (4.170)} \quad \text{(N.196)}$$

$$\phi_s = \phi_s(h_t) \text{ or } / \quad \text{by Eqs. (4.169) or (4.174) with (4.182)} \quad \text{(N.197)}$$

$$\frac{\partial p_l}{\partial x} = \frac{12\eta}{\phi_x h_t^3}\left(\frac{v_s + v_r}{2} h_t + \frac{v_s - v_r}{2} R_q \phi_s - Q\right) \text{ or } 0 \quad \text{Eq. (4.191)} \quad \text{(N.198)}$$

$$\frac{\partial(\sigma_x t_s)}{\partial x} = -p_i \frac{\partial t_s}{\partial x} - 2\tau_i \quad \text{Eq. (4.65)} \quad \text{(N.199)}$$

$$\sigma_z = -p_i \quad \text{Eq. (4.68)} \quad \text{(N.200)}$$

$$\epsilon_x^e = \frac{1}{E_s}\left[\sigma_x - \nu_s(\sigma_y + \sigma_z)\right] \quad \text{Eq. (4.34a)} \quad \text{(N.201)}$$

$$\sigma_y = \nu_s(\sigma_x + \sigma_z) \quad \text{Eq. (4.34b), elastic deformations} \quad \text{(N.202)}$$

$$\epsilon_z^e = \frac{1}{E_s}\left[\sigma_z - \nu_s(\sigma_x + \sigma_y)\right] \quad \text{Eq. (4.34c)} \quad \text{(N.203)}$$

$$h_{i,s} = h_{i,s}(\overline{\epsilon}^p, \overline{D}^p, T_s) \quad \text{by Eqs. (4.51), (4.53), (4.55), (4.57), (4.61) or (4.63)} \quad \text{(N.204)}$$

$$\beta_1 = \frac{1}{\frac{2}{3}\sigma_Y^2\left(1 + \frac{h_{i,s}}{3G_s}\right)} \quad \text{Eq. (4.37)} \quad \text{(N.205)}$$

$$\dot{s}_x = \frac{2G_s}{3}\left[\left(2 - 3\beta_1 s_x^2\right) D_x - (1 + 3\beta_1 s_x s_z)\, D_z\right] \quad \text{Eq. (4.39)} \quad \text{(N.206)}$$

$$\dot{s}_z = \frac{2G_s}{3}\left[-(1 + 3\beta_1 s_x s_z)\, D_x + \left(2 - 3\beta_1 s_z^2\right) D_z\right] \quad \text{Eq. (4.40)} \quad \text{(N.207)}$$

$$\dot{s}_x = v_s \frac{\partial s_x}{\partial x} \quad \text{Eq. (4.45)} \quad \text{(N.208)}$$

$$\dot{s}_z = v_s \frac{\partial s_z}{\partial x} \quad \text{Eq. (4.45)} \quad \text{(N.209)}$$

$$0 = s_x + s_y + s_z \quad \text{Eq. (H.27)} \quad \text{(N.210)}$$

$$D_x = \frac{\partial v_s}{\partial x} \quad \text{Eq. (4.41)} \quad \text{(N.211)}$$

$$D_z = \frac{v_s}{t_s}\frac{\partial t_s}{\partial x} \quad \text{Eq. (4.44)} \quad \text{(N.212)}$$

$$\dot{p} = -K_s(D_x + D_z) \quad \text{Eq. (4.38)} \quad \text{(N.213)}$$

$$\dot{p} = v_s \frac{\partial p}{\partial x} \quad \text{Eq. (4.45)} \quad \text{(N.214)}$$

$$D_x^e = v_s \frac{\partial \epsilon_x^e}{\partial x} \quad \text{Eq. (4.48)} \quad \text{(N.215)}$$

$$D_z^e = v_s \frac{\partial \epsilon_z^e}{\partial x} \quad \text{Eq. (4.49)} \quad \text{(N.216)}$$

$$0 = D_x^p + D_y^p + D_z^p \quad \text{Plastic incompressibility, Eq. (H.19)} \quad \text{(N.217)}$$

$$D_y^p = 0 \quad \text{Plane-strain state} \quad \text{(N.218)}$$

$$D_z = D_z^e + D_z^p \quad \text{Eq. (H.52)} \quad \text{(N.219)}$$

$$\frac{\partial h}{\partial x} = \frac{-D_x^p \bar{l}}{v_s E_p} \quad \text{Eq. (4.122)} \quad \text{(N.220)}$$

$$\overline{D}^p = v_s \frac{\partial \overline{\epsilon}^p}{\partial x} \quad \text{Eq. (4.46)} \quad \text{(N.221)}$$

$$\overline{D}^p = \sqrt{\frac{2}{3}\left[(D_x - D_x^e)^2 + (D_z - D_z^e)^2\right]} \quad \text{Eq. (4.47)} \quad \text{(N.222)}$$

$$s_x = \sigma_x + p \qquad \text{Eq. (H.27)} \tag{N.223}$$

$$s_z = \sigma_z + p \qquad \text{Eq. (H.27)} \tag{N.224}$$

$$s_y = \sigma_y + p \qquad \text{Eq. (H.27)} \tag{N.225}$$

$$\frac{\partial T_s}{\partial x} = \frac{1}{\rho_s c_s v_s}\left[\beta_s\left(D_x^p \sigma_x + D_z^p \sigma_z\right) + \frac{\tau_i(v_r - v_s)}{t_s}\right] \qquad \text{Eq. (4.211)} \tag{N.226}$$

$$\frac{\partial T_l}{\partial x} = \frac{\beta_l}{\rho_l c_l v_s}\frac{\tau_i(v_r - v_s)}{h_t} \text{ or } 0 \qquad \text{Eq. (4.215)} \tag{N.227}$$

N.1.3.2 Derivation

- Eq. (N.181):

$$t_s = 2(z_r - h_t) \tag{N.228}$$

$$\Rightarrow \frac{\partial t_s}{\partial x} = 2\left(\frac{\partial z_r}{\partial x} - \frac{\partial h_t}{\partial x}\right) \tag{N.229}$$

- Eq. (N.190):

$$\Rightarrow p_a = \frac{p_i - (1 - A)p_l}{A} \tag{N.230}$$

- D_z^e is assumed to be negligible in the work zone. Hence, Eq. (N.219):

$$D_z = D_z^p \tag{N.231}$$

- Eqs. (N.218) (plane strain) and (N.231) in Eq. (N.217):

$$D_x^p = -D_z \tag{N.232}$$

- Eq. (N.232) in Eq. (N.220):

$$\frac{\partial h}{\partial x} = \frac{D_z \bar{l}}{v_s E_p} \tag{N.233}$$

- Eq. (N.212) in Eq. (N.233):

$$\frac{\partial h}{\partial x} = \frac{\partial t_s}{\partial x}\frac{\bar{l}}{t_s E_p} \tag{N.234}$$

- Eq. (N.229) in Eq. (N.234):

$$\frac{\partial h}{\partial h_t}\frac{\partial h_t}{\partial x} = 2\left(\frac{\partial z_r}{\partial x} - \frac{\partial h_t}{\partial x}\right)\frac{\bar{l}}{t_s E_p} \tag{N.235}$$

$$\rightarrow \frac{\partial h_t}{\partial x}\left(\frac{\partial h}{\partial h_t}+\frac{2\bar{l}}{t_s E_p}\right)=\frac{2\bar{l}}{t_s E_p}\frac{\partial z_r}{\partial x} \tag{N.236}$$

$$\Rightarrow \frac{\partial h_t}{\partial x}=\frac{\frac{\partial z_r}{\partial x}}{1+\frac{t_s E_p}{2\bar{l}}\frac{\partial h}{\partial h_t}} \tag{N.237}$$

- Eq. (N.199):

$$\frac{\partial \sigma_x}{\partial x}t_s+\sigma_x\frac{\partial t_s}{\partial x}=-p_i\frac{\partial t_s}{\partial x}-2\tau_i \tag{N.238}$$

$$\rightarrow t_s\frac{\partial \sigma_x}{\partial x}=-(\sigma_x+p_i)\frac{\partial t_s}{\partial x}-2\tau_i \tag{N.239}$$

$$\Rightarrow \frac{\partial \sigma_x}{\partial x}=-\frac{1}{t_s}\left[(\sigma_x+p_i)\frac{\partial t_s}{\partial x}+2\tau_i\right] \tag{N.240}$$

- Eq. (N.214) in Eq. (N.213):

$$v_s\frac{\partial p}{\partial x}=-K_s(D_x+D_z) \tag{N.241}$$

$$\Rightarrow \frac{\partial p}{\partial x}=-\frac{K_s}{v_s}(D_x+D_z) \tag{N.242}$$

- Eq. (N.223):

$$p=s_x-\sigma_x \tag{N.243}$$

$$\rightarrow \frac{\partial p}{\partial x}=\frac{\partial s_x}{\partial x}-\frac{\partial \sigma_x}{\partial x} \tag{N.244}$$

- Eq. (N.206) in Eq. (N.208):

$$\frac{\partial s_x}{\partial x}=\frac{2G_s}{3v_s}\left[\left(2-3\beta_1 s_x^2\right)D_x-(1+3\beta_1 s_x s_z)\,D_z\right] \tag{N.245}$$

- Eq. (N.244) in Eq. (N.242):

$$\frac{\partial s_x}{\partial x}-\frac{\partial \sigma_x}{\partial x}=-\frac{K_s}{v_s}(D_x+D_z) \tag{N.246}$$

- Eq. (N.245) in Eq. (N.246):

$$\frac{2G_s}{3v_s}\left[\left(2-3\beta_1 s_x^2\right)D_x-(1+3\beta_1 s_x s_z)\,D_z\right]-\frac{\partial \sigma_x}{\partial x}=-\frac{K_s}{v_s}(D_x+D_z) \tag{N.247}$$

$$\rightarrow 2G_s\left(2-3\beta_1 s_x^2\right)D_x-2G_s\,(1+3\beta_1 s_x s_z)\,D_z-3v_s\frac{\partial \sigma_x}{\partial x}=-3K_s(D_x+D_z) \tag{N.248}$$

$$\rightarrow D_x \left[2G_s \left(2 - 3\beta_1 s_x^2\right) + 3K_s\right] = \left[2G_s \left(1 + 3\beta_1 s_x s_z\right) - 3K_s\right] D_z + 3v_s \frac{\partial \sigma_x}{\partial x} \tag{N.249}$$

$$\Rightarrow D_x = \frac{\left[2G_s \left(1 + 3\beta_1 s_x s_z\right) - 3K_s\right] D_z + 3v_s \frac{\partial \sigma_x}{\partial x}}{2G_s \left(2 - 3\beta_1 s_x^2\right) + 3K_s} \tag{N.250}$$

- Eq. (N.202) in Eq. (N.201):

$$\epsilon_x^e = \frac{1}{E_s}\left[\sigma_x - \nu_s^2(\sigma_x + \sigma_z) - \nu_s \sigma_z\right] \tag{N.251}$$

$$\rightarrow \epsilon_x^e = \frac{1}{E_s}\left[(1 - \nu_s^2)\sigma_x - \nu_s(1 + \nu_s)\sigma_z\right] \tag{N.252}$$

$$\rightarrow \epsilon_x^e = \frac{1 + \nu_s}{E_s}\left[(1 - \nu_s)\sigma_x - \nu_s \sigma_z\right] \tag{N.253}$$

$$\Rightarrow \frac{\partial \epsilon_x^e}{\partial x} = \frac{1 + \nu_s}{E_s}\left[(1 - \nu_s)\frac{\partial \sigma_x}{\partial x} - \nu_s \frac{\partial \sigma_z}{\partial x}\right] \tag{N.254}$$

- Eq. (N.254) in Eq. (N.215):

$$\Rightarrow D_x^e = \frac{v_s(1 + \nu_s)}{E_s}\left[(1 - \nu_s)\frac{\partial \sigma_x}{\partial x} - \nu_s \frac{\partial \sigma_z}{\partial x}\right] \tag{N.255}$$

- Eq. (N.202) in Eq. (N.203):

$$\epsilon_z^e = \frac{1}{E_s}\left[\sigma_z - \nu_s \sigma_x - \nu_s^2\left(\sigma_x + \sigma_z\right)\right] \tag{N.256}$$

$$\rightarrow \epsilon_z^e = \frac{1}{E_s}\left[-\nu_s\left(1 + \nu_s\right)\sigma_x + \left(1 - \nu_s^2\right)\sigma_z\right] \tag{N.257}$$

$$\rightarrow \epsilon_z^e = \frac{1 + \nu_s}{E_s}\left[-\nu_s \sigma_x + (1 - \nu_s)\sigma_z\right] \tag{N.258}$$

$$\Rightarrow \frac{\partial \epsilon_z^e}{\partial x} = \frac{1 + \nu_s}{E_s}\left[-\nu_s \frac{\sigma_x}{\partial x} + (1 - \nu_s)\frac{\sigma_z}{\partial x}\right] \tag{N.259}$$

- Eq. (N.259) in Eq. (N.216):

$$\Rightarrow D_z^e = \frac{v_s(1 + \nu_s)}{E_s}\left[-\nu_s \frac{\sigma_x}{\partial x} + (1 - \nu_s)\frac{\sigma_z}{\partial x}\right] \tag{N.260}$$

- Eq. (N.225) in Eq. (N.210):

$$\Rightarrow \sigma_y = -(s_x + s_z) - p \tag{N.261}$$

N.1.3.3 Structured system of equations

Values required in differential equations

$$h_t \overset{\text{cpl}}{=} h_t(x) \quad \text{by Eq. (6.41)} \tag{N.262}$$

$$h = h(h_t) \quad \text{by Eqs. (4.15) or (4.20)} \tag{N.263}$$

$$\frac{\partial h}{\partial h_t} \overset{\text{cpl}}{=} \frac{\partial h}{\partial h_t}(h_t) \quad \text{by Eqs. (4.17) or (4.22)} \tag{N.264}$$

$$A \overset{\text{cpl}}{=} A(h) \quad \text{by Eqs. (4.13) or (4.18)} \tag{N.265}$$

$$A \overset{\text{cpl}}{=} A(x) \quad \text{by Eq. (6.40)} \tag{N.266}$$

$$\sigma_x = s_x - p \tag{N.267}$$

$$\sigma_z = s_z - p \tag{N.268}$$

$$p_i = -\sigma_z \tag{N.269}$$

$$p_a = \frac{p_i - (1-A)p_l}{A} \text{ or } \frac{p_i}{A} \tag{N.270}$$

$$\sigma_Y = \sigma_Y(\overline{\epsilon}^p, \overline{D}^p, T_s) \quad \text{by Eqs. (4.50), (4.52), (4.54), (4.56), (4.60) or (4.62)} \tag{N.271}$$

$$\tau_Y = \frac{\sigma_Y}{\sqrt{3}} \tag{N.272}$$

$$\tau_a = \tau_a(v_s, v_r, p_a, \tau_Y) \quad \text{by Eqs. (4.123), (4.124) or (4.125)} \tag{N.273}$$

$$z_r = z_r(x) \quad \text{by Secs. 4.6.1, 4.6.2, 4.6.3 or 4.6.4} \tag{N.274}$$

$$\frac{\partial z_r}{\partial x} = \frac{\partial z_r}{\partial x}(x) \quad \text{by Secs. 4.6.1, 4.6.2, 4.6.3 or 4.6.4} \tag{N.275}$$

$$t_s = 2(z_r - h_t) \tag{N.276}$$

$$H_a \overset{\text{cpl}}{=} \frac{p_a - p_l}{\tau_Y} \text{ or } \frac{p_a}{\tau_Y} \tag{N.277}$$

$$E_p \overset{\text{cpl}}{=} E_p(A, H_a) \quad \text{by Eqs. (4.92), (4.96) or (4.97)} \tag{N.278}$$

$$T_l = T_l(T_l^*, T_s, T_l) \text{ or } / \quad \text{by Eqs. (4.212), (4.213), (4.214) or (4.215)} \tag{N.279}$$

$$\eta = \eta(p_l, T_l) \text{ or } / \quad \text{by Eqs. (4.192), (??) or (4.195)} \tag{N.280}$$

$$\phi_x = \phi_x(h_t) \text{ or } / \quad \text{by Eqs. (4.168) or (4.170)} \tag{N.281}$$

$$\phi_s = \phi_s(h_t) \text{ or } / \quad \text{by Eqs. (4.169) or (4.174) with (4.182)} \tag{N.282}$$

Differential equations (mainly)

$$\Rightarrow \frac{\partial p_l}{\partial x} = \frac{12\eta}{\phi_x h_t^3}\left(\frac{v_s + v_r}{2}h_t + \frac{v_s - v_r}{2}R_q\phi_s - Q\right) \text{ or } 0 \tag{N.283}$$

$$\tau_l = \tau_l\left(h, h_t, A, \eta, v_s, v_r, \frac{\partial p_l}{\partial x}\right) \text{ or } 0 \quad \text{by Eqs. (4.204) or (4.205)} \tag{N.284}$$

$$\tau_i = A\tau_a + (1-A)\tau_l \text{ or } A\tau_a \tag{N.285}$$

$$\Rightarrow \frac{\partial h_t}{\partial x} \overset{\cancel{\text{epl}}}{=} \frac{\frac{\partial z_r}{\partial x}}{1 + \frac{t_s E_p}{2\bar{l}} \frac{\partial h}{\partial h_t}} \tag{N.286}$$

$$\frac{\partial h_t}{\partial x} \overset{\text{cpl}}{=} \frac{\partial h_t}{\partial x}(x) \qquad \text{by Eq. (6.42)} \tag{N.287}$$

$$\frac{\partial t_s}{\partial x} = 2\left(\frac{\partial z_r}{\partial x} - \frac{\partial h_t}{\partial x}\right) \tag{N.288}$$

$$\frac{\partial \sigma_x}{\partial x} = -\frac{1}{t_s}\left[(\sigma_x + p_i)\frac{\partial t_s}{\partial x} + 2\tau_i\right] \tag{N.289}$$

$$h_{i,s} = h_{i,s}(\overline{\epsilon}^p, \overline{D}^p, T_s) \qquad \text{by Eqs. (4.51), (4.53), (4.55), (4.57), (4.61) or (4.63)} \tag{N.290}$$

$$\beta_1 = \frac{1}{\frac{2}{3}\sigma_Y^2\left(1 + \frac{h_{i,s}}{3G_s}\right)} \tag{N.291}$$

$$D_z = \frac{v_s}{t_s}\frac{\partial t_s}{\partial x} \tag{N.292}$$

$$D_x = \frac{\left[2G_s(1 + 3\beta_1 s_x s_z) - 3K_s\right] D_z + 3v_s \frac{\partial \sigma_x}{\partial x}}{2G_s(2 - 3\beta_1 s_x^2) + 3K_s} \tag{N.293}$$

$$\Rightarrow \frac{\partial v_s}{\partial x} = D_x \tag{N.294}$$

$$\Rightarrow \frac{\partial s_x}{\partial x} = \frac{2G_s}{3v_s}\left[(2 - 3\beta_1 s_x^2)D_x - (1 + 3\beta_1 s_x s_z)D_z\right] \tag{N.295}$$

$$\Rightarrow \frac{\partial s_z}{\partial x} = \frac{2G_s}{3v_s}\left[-(1 + 3\beta_1 s_x s_z)D_x + (2 - 3\beta_1 s_z^2)D_z\right] \tag{N.296}$$

$$\Rightarrow \frac{\partial p}{\partial x} = -\frac{K_s}{v_s}(D_x + D_z) \tag{N.297}$$

$$\frac{\partial \sigma_z}{\partial x} = \frac{\partial s_z}{\partial x} - \frac{\partial p}{\partial x} \tag{N.298}$$

$$D_x^e = \frac{v_s(1+\nu_s)}{E_s}\left[(1-\nu_s)\frac{\partial \sigma_x}{\partial x} - \nu_s \frac{\partial \sigma_z}{\partial x}\right] \tag{N.299}$$

$$D_z^e = \frac{v_s(1+\nu_s)}{E_s}\left[-\nu_s \frac{\partial \sigma_x}{\partial x} + (1-\nu_s)\frac{\partial \sigma_z}{\partial x}\right] \tag{N.300}$$

$$\Rightarrow \frac{\partial \overline{\epsilon}^p}{\partial x} = \frac{1}{v_s}\sqrt{\frac{2}{3}\left[(D_x - D_x^e)^2 + (D_z - D_z^e)^2\right]} \tag{N.301}$$

$$\Rightarrow \frac{\partial T_s}{\partial x} = \frac{1}{\rho_s c_s v_s}\left[\beta_s\left(D_x^p \sigma_x + D_z^p \sigma_z\right) + \frac{\tau_i(v_r - v_s)}{t_s}\right] \tag{N.302}$$

$$\Rightarrow \frac{\partial T_l}{\partial x} = \frac{\beta_l}{\rho_l c_l v_s}\frac{\tau_i(v_r - v_s)}{h_t} \text{ or } 0 \tag{N.303}$$

Values not directly required in differential equations

$$\sigma_y = -(s_x + s_z) - p \tag{N.304}$$

$$\overline{D}^p = v_s \frac{\partial \overline{\epsilon}^p}{\partial x} \tag{N.305}$$

N.1.4 High-speed work zone

N.1.4.1 Underlying system of equations

$$z_r = z_r(x) \quad \text{by Secs. 4.6.1, 4.6.2, 4.6.3 or 4.6.4} \quad \text{(N.306)}$$

$$h_t = z_r - \frac{t_s}{2} \quad \text{Eq. (4.23)} \quad \text{(N.307)}$$

$$h_t \overset{\text{cpl}}{=} h_t(x) \quad \text{by Eq. (6.41)} \quad \text{(N.308)}$$

$$h = h(h_t) \quad \text{by Eqs. (4.15) or (4.20)} \quad \text{(N.309)}$$

$$A \overset{\cancel{\text{epl}}}{=} A(h) \quad \text{by Eqs. (4.13) or (4.18)} \quad \text{(N.310)}$$

$$A \overset{\text{cpl}}{=} A(x) \quad \text{by Eq. (6.40)} \quad \text{(N.311)}$$

$$\sigma_Y = \sigma_Y(\overline{\epsilon}^p, \overline{D}^p, T_s) \quad \text{by Eqs. (4.50), (4.52), (4.54), (4.56), (4.60) or (4.62)} \quad \text{(N.312)}$$

$$\tau_Y = \frac{\sigma_Y}{\sqrt{3}} \quad \text{Eq. (H.56)} \quad \text{(N.313)}$$

$$p_i = A p_a + (1 - A) p_l \quad \text{Eq. (4.4)} \quad \text{(N.314)}$$

$$p_l = p_i \quad \text{Hypothesis} \quad \text{(N.315)}$$

$$\tau_a = \tau_a(v_s, v_r, p_a, \tau_Y) \quad \text{by Eqs. (4.123), (4.124) or (4.125)} \quad \text{(N.316)}$$

$$T_l = T_l(T_l^*, T_s, T_l) \text{ or } / \quad \text{by Eqs. (4.212), (4.213), (4.214) or (4.215)} \quad \text{(N.317)}$$

$$\eta = \eta(p_l, T_l) \quad \text{by Eqs. (4.192), (??) or (4.195)} \quad \text{(N.318)}$$

$$\tau_l = \tau_l\left(h, h_t, A, \eta, v_s, v_r, \frac{\partial p_l}{\partial x}\right) \quad \text{by Eqs. (4.204) or (4.205)} \quad \text{(N.319)}$$

$$\tau_i = A\tau_a + (1 - A)\tau_l \quad \text{Eq. (4.5)} \quad \text{(N.320)}$$

$$\phi_s = \phi_s(h_t) \quad \text{by Eqs. (4.169) or (4.174) with (4.182)} \quad \text{(N.321)}$$

$$Q = \frac{v_s + v_r}{2} h_t + \frac{v_s - v_r}{2} R_q \phi_s \quad \text{Eq. (4.239)} \quad \text{(N.322)}$$

$$\frac{\partial(\sigma_x t_s)}{\partial x} = -p_i \frac{\partial t_s}{\partial x} - 2\tau_i \quad \text{Eq. (4.65)} \quad \text{(N.323)}$$

$$\sigma_z = -p_i \quad \text{Eq. (4.68)} \quad \text{(N.324)}$$

$$\epsilon_x^e = \frac{1}{E_s}\left[\sigma_x - \nu_s(\sigma_y + \sigma_z)\right] \quad \text{Eq. (4.34a)} \quad \text{(N.325)}$$

$$\sigma_y = \nu_s(\sigma_x + \sigma_z) \quad \text{Eq. (4.34b), elastic deformations} \quad \text{(N.326)}$$

$$\epsilon_z^e = \frac{1}{E_s}\left[\sigma_z - \nu_s(\sigma_x + \sigma_y)\right] \quad \text{Eq. (4.34c)} \quad \text{(N.327)}$$

$$h_{i,s} = h_{i,s}(\overline{\epsilon}^p, \overline{D}^p, T_s) \quad \text{by Eqs. (4.51), (4.53), (4.55), (4.57), (4.61) or (4.63)} \quad \text{(N.328)}$$

$$\beta_1 = \frac{1}{\frac{2}{3}\sigma_Y^2\left(1+\frac{h_{i,s}}{3G_s}\right)} \qquad \text{Eq. (4.37)} \qquad \text{(N.329)}$$

$$\dot{s}_x = \frac{2G_s}{3}\left[\left(2-3\beta_1 s_x^2\right)D_x - \left(1+3\beta_1 s_x s_z\right)D_z\right] \qquad \text{Eq. (4.39)} \qquad \text{(N.330)}$$

$$\dot{s}_z = \frac{2G_s}{3}\left[-\left(1+3\beta_1 s_x s_z\right)D_x + \left(2-3\beta_1 s_z^2\right)D_z\right] \qquad \text{Eq. (4.40)} \qquad \text{(N.331)}$$

$$\dot{s}_x = v_s\frac{\partial s_x}{\partial x} \qquad \text{Eq. (4.45)} \qquad \text{(N.332)}$$

$$\dot{s}_z = v_s\frac{\partial s_z}{\partial x} \qquad \text{Eq. (4.45)} \qquad \text{(N.333)}$$

$$0 = s_x + s_y + s_z \qquad \text{Eq. (H.27)} \qquad \text{(N.334)}$$

$$D_x = \frac{\partial v_s}{\partial x} \qquad \text{Eq. (4.41)} \qquad \text{(N.335)}$$

$$D_z = \frac{v_s}{t_s}\frac{\partial t_s}{\partial x} \qquad \text{Eq. (4.44)} \qquad \text{(N.336)}$$

$$\dot{p} = -K_s(D_x + D_z) \qquad \text{Eq. (4.38)} \qquad \text{(N.337)}$$

$$\dot{p} = v_s\frac{\partial p}{\partial x} \qquad \text{Eq. (4.45)} \qquad \text{(N.338)}$$

$$D_x^e = v_s\frac{\partial \epsilon_x^e}{\partial x} \qquad \text{Eq. (4.48)} \qquad \text{(N.339)}$$

$$D_z^e = v_s\frac{\partial \epsilon_z^e}{\partial x} \qquad \text{Eq. (4.49)} \qquad \text{(N.340)}$$

$$\overline{D}^p = v_s\frac{\partial \overline{\epsilon}^p}{\partial x} \qquad \text{Eq. (4.46)} \qquad \text{(N.341)}$$

$$\overline{D}^p = \sqrt{\frac{2}{3}\left[(D_x - D_x^e)^2 + (D_z - D_z^e)^2\right]} \qquad \text{Eq. (4.47)} \qquad \text{(N.342)}$$

$$s_x = \sigma_x + p \qquad \text{Eq. (H.27)} \qquad \text{(N.343)}$$

$$s_z = \sigma_z + p \qquad \text{Eq. (H.27)} \qquad \text{(N.344)}$$

$$s_y = \sigma_y + p \qquad \text{Eq. (H.27)} \qquad \text{(N.345)}$$

$$\frac{\partial T_s}{\partial x} = \frac{1}{\rho_s c_s v_s}\left[\beta_s\left(D_x^p\sigma_x + D_z^p\sigma_z\right) + \frac{\tau_i(v_r - v_s)}{t_s}\right] \qquad \text{Eq. (4.211)} \qquad \text{(N.346)}$$

$$\frac{\partial T_l}{\partial x} = \frac{\beta_l}{\rho_l c_l v_s}\frac{\tau_i(v_r - v_s)}{h_t} \text{ or } 0 \qquad \text{Eq. (4.215)} \qquad \text{(N.347)}$$

N.1.4.2 Derivation

- Eq. (N.307):

$$t_s = 2(z_r - h_t) \tag{N.348}$$

$$\Rightarrow \frac{\partial t_s}{\partial x} = 2\left(\frac{\partial z_r}{\partial x} - \frac{\partial h_t}{\partial x}\right) \tag{N.349}$$

- Eq. (N.315) in Eq. (N.314):

$$p_a = p_i \tag{N.350}$$

- Eq. (N.322):

$$\frac{1}{2}\frac{\partial v_s}{\partial x}h_t + \frac{v_s + v_r}{2}\frac{\partial h_t}{\partial x} + \frac{1}{2}\frac{\partial v_s}{\partial x}R_q\phi_s + \frac{v_s - v_r}{2}R_q\frac{\partial \phi_s}{\partial h_t}\frac{\partial h_t}{\partial x} = 0 \tag{N.351}$$

$$\rightarrow \frac{\partial h_t}{\partial x}\left(v_s + v_r + (v_s - v_r)R_q\frac{\partial \phi_s}{\partial h_t}\right) = -\frac{\partial v_s}{\partial x}(h_t + R_q\phi_s) \tag{N.352}$$

$$\rightarrow \frac{\partial h_t}{\partial x} = -\frac{1}{v_s\frac{v_s + v_r + (v_s - v_r)R_q\frac{\partial \phi_s}{\partial h_t}}{v_s(h_t + R_q\phi_s)}}\frac{\partial v_s}{\partial x} \tag{N.353}$$

$$\rightarrow \frac{\partial h_t}{\partial x} = -\frac{1}{v_s\beta_3}\frac{\partial v_s}{\partial x} \quad \text{with} \quad \Rightarrow \beta_3 = \frac{v_s + v_r + (v_s - v_r)R_q\frac{\partial \phi_s}{\partial h_t}}{\left(h_t + R_q\phi_s\right)v_s} \tag{N.354}$$

- Eq. (N.323):

$$\frac{\partial \sigma_x}{\partial x}t_s + \sigma_x\frac{\partial t_s}{\partial x} = -p_i\frac{\partial t_s}{\partial x} - 2\tau_i \tag{N.355}$$

$$\rightarrow t_s\frac{\partial \sigma_x}{\partial x} = -(\sigma_x + p_i)\frac{\partial t_s}{\partial x} - 2\tau_i \tag{N.356}$$

$$\Rightarrow \frac{\partial \sigma_x}{\partial x} = -\frac{1}{t_s}\left[(\sigma_x + p_i)\frac{\partial t_s}{\partial x} + 2\tau_i\right] \tag{N.357}$$

- Eq. (N.330) in Eq. (N.332):

$$\frac{\partial s_x}{\partial x} = \frac{2G_s}{3v_s}\left[\left(2 - 3\beta_1 s_x^2\right)D_x - (1 + 3\beta_1 s_x s_z)\,D_z\right] \tag{N.358}$$

- Eq. (N.338) in Eq. (N.337):

$$v_s\frac{\partial p}{\partial x} = -K_s(D_x + D_z) \tag{N.359}$$

$$\Rightarrow \frac{\partial p}{\partial x} = -\frac{K_s}{v_s}(D_x + D_z) \tag{N.360}$$

- Based on Eqs. (N.343), (N.358) and (N.360), the following expression can be derived in the same way as in the low-speed work zone (Eq. N.250):

$$\Rightarrow D_x = \frac{\left[2G_s\left(1+3\beta_1 s_x s_z\right)-3K_s\right]D_z + 3v_s\frac{\partial \sigma_x}{\partial x}}{2G_s\left(2-3\beta_1 s_x^2\right)+3K_s} \tag{N.361}$$

- Eq. (N.335), Eq. (N.336) and Eq. (N.357) in Eq. (N.361):

$$\frac{\partial v_s}{\partial x} = \frac{\left[2G_s\left(1+3\beta_1 s_x s_z\right)-3K_s\right]\frac{v_s}{t_s}\frac{\partial t_s}{\partial x} - \frac{3v_s}{t_s}\left[\left(\sigma_x+p_i\right)\frac{\partial t_s}{\partial x}+2\tau_i\right]}{2G_s\left(2-3\beta_1 s_x^2\right)+3K_s} \tag{N.362}$$

$$\rightarrow \frac{\partial v_s}{\partial x} = \frac{\left[2G_s\left(1+3\beta_1 s_x s_z\right)-3K_s-3(\sigma_x+p_i)\right]\frac{v_s}{t_s}\frac{\partial t_s}{\partial x} - \frac{6v_s}{t_s}\tau_i}{2G_s\left(2-3\beta_1 s_x^2\right)+3K_s} \tag{N.363}$$

$$\rightarrow \frac{\partial v_s}{\partial x} = \frac{v_s\left(\beta_4\frac{\partial t_s}{\partial x}-6\tau_i\right)}{t_s\left[2G_s\left(2-3\beta_1 s_x^2\right)+3K_s\right]} \quad \text{with} \quad \beta_4 = 2G_s\left(1+3\beta_1 s_x s_z\right)-3(\sigma_x+p_i+K_s) \tag{N.364}$$

- Eq. (N.364) in Eq. (N.354):

$$\frac{\partial h_t}{\partial x} = \frac{-\beta_4\frac{\partial t_s}{\partial x}+6\tau_i}{t_s\beta_3\left[2G_s\left(2-3\beta_1 s_x^2\right)+3K_s\right]} \tag{N.365}$$

- Eq. (N.349) in Eq. (N.365):

$$\frac{\partial h_t}{\partial x} = \frac{2\beta_4\left(\frac{\partial h_t}{\partial x}-\frac{\partial z_r}{\partial x}\right)+6\tau_i}{t_s\beta_3\left[2G_s\left(2-3\beta_1 s_x^2\right)+3K_s\right]} \tag{N.366}$$

$$\rightarrow t_s\beta_3\left[2G_s\left(2-3\beta_1 s_x^2\right)+3K_s\right]\frac{\partial h_t}{\partial x} = 2\beta_4\frac{\partial h_t}{\partial x} - 2\beta_4\frac{\partial z_r}{\partial x}+6\tau_i \tag{N.367}$$

$$\rightarrow \frac{\partial h_t}{\partial x}\left\{\left[2G_s\left(2-3\beta_1 s_x^2\right)+3K_s\right]\beta_3 t_s - 2\beta_4\right\} = 2\left(3\tau_i-\beta_4\frac{\partial z_r}{\partial x}\right) \tag{N.368}$$

$$\rightarrow \frac{\partial h_t}{\partial x} = \frac{3\tau_i-\beta_4\frac{\partial z_r}{\partial x}}{\left[G_s\left(2-3\beta_1 s_x^2\right)+\frac{3}{2}K_s\right]\beta_3 t_s-\beta_4} \tag{N.369}$$

$$\Rightarrow \frac{\partial h_t}{\partial x} = \frac{3\tau_i-\left[2G_s(1+3\beta_1 s_x s_z)-3(\sigma_x+p_i+K_s)\right]\frac{\partial z_r}{\partial x}}{\left[G_s\left(2-3\beta_1 s_x^2\right)+\frac{3}{2}K_s\right]\beta_3 t_s-\left[2G_s(1+3\beta_1 s_x s_z)-3(\sigma_x+p_i+K_s)\right]} \tag{N.370}$$

- Eq. (N.345) in Eq. (N.334):

$$\Rightarrow \sigma_y = -(s_x+s_z)-p \tag{N.371}$$

N.1.4.3 Structured system of equations

Values required in differential equations

$$h_t \overset{\text{cpl}}{=} h_t(x) \quad \text{by Eq. (6.41)} \tag{N.372}$$

$$h = h(h_t) \quad \text{by Eqs. (4.15) or (4.20)} \tag{N.373}$$

$$A \overset{\cancel{\text{epl}}}{=} A(h) \quad \text{by Eqs. (4.13) or (4.18)} \tag{N.374}$$

$$A \overset{\text{cpl}}{=} A(x) \quad \text{by Eq. (6.40)} \tag{N.375}$$

$$\sigma_x = s_x - p \tag{N.376}$$

$$\sigma_z = s_z - p \tag{N.377}$$

$$p_i = -\sigma_z \tag{N.378}$$

$$p_l = p_i \tag{N.379}$$

$$p_a = p_i \tag{N.380}$$

$$\sigma_Y = \sigma_Y(\overline{\epsilon}^p, \overline{D}^p, T_s) \quad \text{by Eqs. (4.50), (4.52), (4.54), (4.56), (4.60) or (4.62)} \tag{N.381}$$

$$\tau_Y = \frac{\sigma_Y}{\sqrt{3}} \tag{N.382}$$

$$\tau_a = \tau_a(v_s, v_r, p_a, \tau_Y) \quad \text{by Eqs. (4.123), (4.124) or (4.125)} \tag{N.383}$$

$$T_l = T_l(T_l^*, T_s, T_l) \text{ or } / \quad \text{by Eqs. (4.212), (4.213), (4.214) or (4.215)} \tag{N.384}$$

$$\eta = \eta(p_l, T_l) \quad \text{by Eqs. (4.192), (??) or (4.195)} \tag{N.385}$$

$$\tau_l = \tau_l\left(h, h_t, A, \eta, v_s, v_r, \frac{\partial p_l}{\partial x} = 0\right) \quad \text{by Eqs. (4.204) or (4.205), Hyp.} \tag{N.386}$$

$$\tau_i = A\tau_a + (1 - A)\tau_l \tag{N.387}$$

$$z_r = z_r(x) \quad \text{by Secs. 4.6.1, 4.6.2, 4.6.3 or 4.6.4} \tag{N.388}$$

$$\frac{\partial z_r}{\partial x} = \frac{\partial z_r}{\partial x}(x) \quad \text{by Secs. 4.6.1, 4.6.2, 4.6.3 or 4.6.4} \tag{N.389}$$

$$t_s = 2(z_r - h_t) \tag{N.390}$$

$$\phi_s \overset{\cancel{\text{epl}}}{=} \phi_s(h_t) \quad \text{by Eqs. (4.169) or (4.174) with (4.182)} \tag{N.391}$$

$$\frac{\partial \phi_s}{\partial h_t} \overset{\cancel{\text{epl}}}{=} \frac{\partial \phi_s}{\partial h_t}(h_t) \quad \text{by Eq. (4.188)} \tag{N.392}$$

$$h_{i,s} = h_{i,s}(\overline{\epsilon}^p, \overline{D}^p, T_s) \quad \text{by Eqs. (4.51), (4.53), (4.55), (4.57), (4.61) or (4.63)} \tag{N.393}$$

$$\beta_1 = \frac{1}{\frac{2}{3}\sigma_Y^2\left(1 + \frac{h_{i,s}}{3G_s}\right)} \tag{N.394}$$

$$\beta_3 \overset{\cancel{\text{epl}}}{=} \frac{v_s + v_r + (v_s - v_r) R_q \frac{\partial \phi_s}{\partial h_t}}{(h_t + R_q \phi_s) v_s} \tag{N.395}$$

Differential equations (mainly)

$$\Rightarrow \frac{\partial h_t}{\partial x} \overset{\cancel{\text{epl}}}{=} \frac{3\tau_i - \left[2G_s(1 + 3\beta_1 s_x s_z) - 3(\sigma_x + p_i + K_s)\right] \frac{\partial z_r}{\partial x}}{\left[G_s\left(2 - 3\beta_1 s_x^2\right) + \frac{3}{2}K_s\right]\beta_3 t_s - \left[2G_s(1 + 3\beta_1 s_x s_z) - 3(\sigma_x + p_i + K_s)\right]} \tag{N.396}$$

$$\frac{\partial h_t}{\partial x} \overset{\text{cpl}}{=} \frac{\partial h_t}{\partial x}(x) \qquad \text{by Eq. (6.42)} \tag{N.397}$$

$$\frac{\partial t_s}{\partial x} = 2\left(\frac{\partial z_r}{\partial x} - \frac{\partial h_t}{\partial x}\right) \tag{N.398}$$

$$\frac{\partial \sigma_x}{\partial x} = -\frac{1}{t_s}\left[(\sigma_x + p_i)\frac{\partial t_s}{\partial x} + 2\tau_i\right] \tag{N.399}$$

$$D_z = \frac{v_s}{t_s}\frac{\partial t_s}{\partial x} \tag{N.400}$$

$$D_x = \frac{\left[2G_s(1 + 3\beta_1 s_x s_z) - 3K_s\right] D_z + 3v_s \frac{\partial \sigma_x}{\partial x}}{2G_s(2 - 3\beta_1 s_x^2) + 3K_s} \tag{N.401}$$

$$\Rightarrow \frac{\partial v_s}{\partial x} = D_x \tag{N.402}$$

$$\Rightarrow \frac{\partial s_x}{\partial x} = \frac{2G_s}{3v_s}\left[(2 - 3\beta_1 s_x^2)D_x - (1 + 3\beta_1 s_x s_z)D_z\right] \tag{N.403}$$

$$\Rightarrow \frac{\partial s_z}{\partial x} = \frac{2G_s}{3v_s}\left[-(1 + 3\beta_1 s_x s_z)D_x + (2 - 3\beta_1 s_z^2)D_z\right] \tag{N.404}$$

$$\Rightarrow \frac{\partial p}{\partial x} = -\frac{K_s}{v_s}(D_x + D_z) \tag{N.405}$$

$$\frac{\partial \sigma_z}{\partial x} = \frac{\partial s_z}{\partial x} - \frac{\partial p}{\partial x} \tag{N.406}$$

$$D_x^e = v_s \frac{1 + \nu_s}{E_s}\left[(1 - \nu_s)\frac{\partial \sigma_x}{\partial x} - \nu_s \frac{\partial \sigma_z}{\partial x}\right] \tag{N.407}$$

$$D_z^e = v_s \frac{1 + \nu_s}{E_s}\left[-\nu_s \frac{\partial \sigma_x}{\partial x} + (1 - \nu_s)\frac{\partial \sigma_z}{\partial x}\right] \tag{N.408}$$

$$\Rightarrow \frac{\partial \bar{\epsilon}^p}{\partial x} = \frac{1}{v_s}\sqrt{\frac{2}{3}\left[(D_x - D_x^e)^2 + (D_z - D_z^e)^2\right]} \tag{N.409}$$

$$\Rightarrow \frac{\partial T_s}{\partial x} = \frac{1}{\rho_s c_s v_s}\left[\beta_s\left(D_x^p \sigma_x + D_z^p \sigma_z\right) + \frac{\tau_i(v_r - v_s)}{t_s}\right] \tag{N.410}$$

$$\Rightarrow \frac{\partial T_l}{\partial x} = \frac{\beta_l}{\rho_l c_l v_s}\frac{\tau_i(v_r - v_s)}{h_t} \text{ or } 0 \tag{N.411}$$

Values not directly required in differential equations

$$\sigma_y = -(s_x + s_z) - p \tag{N.412}$$

$$\overline{D}^p = v_s \frac{\partial \overline{\epsilon}^p}{\partial x} \tag{N.413}$$

N.1.5 High-speed work zone 2

N.1.5.1 Underlying system of equations

$$z_r = z_r(x) \quad \text{by Secs. 4.6.1, 4.6.2, 4.6.3 or 4.6.4} \quad \text{(N.414)}$$

$$h_t = z_r - \frac{t_s}{2} \quad \text{Eq. (4.23)} \quad \text{(N.415)}$$

$$h = h(h_t) \quad \text{by Eqs. (4.15) or (4.20)} \quad \text{(N.416)}$$

$$A = A(h) \quad \text{by Eqs. (4.13) or (4.18)} \quad \text{(N.417)}$$

$$\sigma_Y = \sigma_Y(\overline{\epsilon}^p, \overline{D}^p, T_s) \quad \text{by Eqs. (4.50), (4.52), (4.54), (4.56), (4.60) or (4.62)} \quad \text{(N.418)}$$

$$\tau_Y = \frac{\sigma_Y}{\sqrt{3}} \quad \text{Eq. (H.56)} \quad \text{(N.419)}$$

$$p_i = A p_a + (1 - A) p_l \quad \text{Eq. (4.4)} \quad \text{(N.420)}$$

$$H_a = \frac{p_a - p_l}{\tau_Y} \quad \text{Eq. (4.90)} \quad \text{(N.421)}$$

$$H_a = H_a(A, E_p) \quad \text{by Eqs. (4.92), (4.96) or (4.97)} \quad \text{(N.422)}$$

$$\tau_a = \tau_a(v_s, v_r, p_a, \tau_Y) \quad \text{by Eqs. (4.123), (4.124) or (4.125)} \quad \text{(N.423)}$$

$$T_l = T_l(T_l^*, T_s, T_l) \text{ or } / \quad \text{by Eqs. (4.212), (4.213), (4.214) or (4.215)} \quad \text{(N.424)}$$

$$\eta = \eta(p_l, T_l) \quad \text{by Eqs. (4.192), (??) or (4.195)} \quad \text{(N.425)}$$

$$\tau_l = \tau_l\left(h, h_t, A, \eta, v_s, v_r, \frac{\partial p_l}{\partial x}\right) \quad \text{by Eqs. (4.204) or (4.205)} \quad \text{(N.426)}$$

$$\tau_i = A\tau_a + (1 - A)\tau_l \quad \text{Eq. (4.5)} \quad \text{(N.427)}$$

$$\phi_s = \phi_s(h_t) \quad \text{by Eqs. (4.169) or (4.174) with (4.182)} \quad \text{(N.428)}$$

$$Q = \frac{v_s + v_r}{2} h_t + \frac{v_s - v_r}{2} R_q \phi_s \quad \text{Eq. (4.239)} \quad \text{(N.429)}$$

$$\frac{\partial(\sigma_x t_s)}{\partial x} = -p_i \frac{\partial t_s}{\partial x} - 2\tau_i \quad \text{Eq. (4.65)} \quad \text{(N.430)}$$

$$\sigma_z = -p_i \quad \text{Eq. (4.68)} \quad \text{(N.431)}$$

$$\epsilon_x^e = \frac{1}{E_s}\left[\sigma_x - \nu_s(\sigma_y + \sigma_z)\right] \quad \text{Eq. (4.34a)} \quad \text{(N.432)}$$

$$\sigma_y = \nu_s(\sigma_x + \sigma_z) \quad \text{Eq. (4.34b), elastic deformations} \quad \text{(N.433)}$$

$$\epsilon_z^e = \frac{1}{E_s}\left[\sigma_z - \nu_s(\sigma_x + \sigma_y)\right] \quad \text{Eq. (4.34c)} \quad \text{(N.434)}$$

$$h_{i,s} = h_{i,s}(\overline{\epsilon}^p, \overline{D}^p, T_s) \quad \text{by Eqs. (4.51), (4.53), (4.55), (4.57), (4.61) or (4.63)} \quad \text{(N.435)}$$

$$\beta_1 = \frac{1}{\frac{2}{3}\sigma_Y^2\left(1+\frac{h_{i,s}}{3G_s}\right)} \quad \text{Eq. (4.37)} \quad \text{(N.436)}$$

$$\dot{s}_x = \frac{2G_s}{3}\left[\left(2-3\beta_1 s_x^2\right)D_x - \left(1+3\beta_1 s_x s_z\right)D_z\right] \quad \text{Eq. (4.39)} \quad \text{(N.437)}$$

$$\dot{s}_z = \frac{2G_s}{3}\left[-\left(1+3\beta_1 s_x s_z\right)D_x + \left(2-3\beta_1 s_z^2\right)D_z\right] \quad \text{Eq. (4.40)} \quad \text{(N.438)}$$

$$\dot{s}_x = v_s\frac{\partial s_x}{\partial x} \quad \text{Eq. (4.45)} \quad \text{(N.439)}$$

$$\dot{s}_z = v_s\frac{\partial s_z}{\partial x} \quad \text{Eq. (4.45)} \quad \text{(N.440)}$$

$$0 = s_x + s_y + s_z \quad \text{Eq. (H.27)} \quad \text{(N.441)}$$

$$D_x = \frac{\partial v_s}{\partial x} \quad \text{Eq. (4.41)} \quad \text{(N.442)}$$

$$D_z = \frac{v_s}{t_s}\frac{\partial t_s}{\partial x} \quad \text{Eq. (4.44)} \quad \text{(N.443)}$$

$$\dot{p} = -K_s(D_x + D_z) \quad \text{Eq. (4.38)} \quad \text{(N.444)}$$

$$\dot{p} = v_s\frac{\partial p}{\partial x} \quad \text{Eq. (4.45)} \quad \text{(N.445)}$$

$$D_x^e = v_s\frac{\partial \epsilon_x^e}{\partial x} \quad \text{Eq. (4.48)} \quad \text{(N.446)}$$

$$D_z^e = v_s\frac{\partial \epsilon_z^e}{\partial x} \quad \text{Eq. (4.49)} \quad \text{(N.447)}$$

$$0 = D_x^p + D_y^p + D_z^p \quad \text{Plastic incompressibility, Eq. (H.19)} \quad \text{(N.448)}$$

$$D_y^p = 0 \quad \text{Plane-strain state} \quad \text{(N.449)}$$

$$D_z = D_z^e + D_z^p \quad \text{Eq. (H.52)} \quad \text{(N.450)}$$

$$\frac{\partial h}{\partial x} = \frac{-D_x^p \bar{l}}{v_s E_p} \quad \text{Eq. (4.122)} \quad \text{(N.451)}$$

$$\overline{D}^p = v_s\frac{\partial \overline{\epsilon}^p}{\partial x} \quad \text{Eq. (4.46)} \quad \text{(N.452)}$$

$$\overline{D}^p = \sqrt{\frac{2}{3}\left[(D_x - D_x^e)^2 + (D_z - D_z^e)^2\right]} \quad \text{Eq. (4.47)} \quad \text{(N.453)}$$

$$s_x = \sigma_x + p \quad \text{Eq. (H.27)} \quad \text{(N.454)}$$

$$s_z = \sigma_z + p \quad \text{Eq. (H.27)} \quad \text{(N.455)}$$

$$s_y = \sigma_y + p \quad \text{Eq. (H.27)} \quad \text{(N.456)}$$

$$\frac{\partial T_s}{\partial x} = \frac{1}{\rho_s c_s v_s}\left[\beta_s\left(D_x^p\sigma_x + D_z^p\sigma_z\right)\right.$$

$$+\frac{\tau_i(v_r - v_s)}{t_s}\Bigg] \qquad \text{Eq. (4.211)} \tag{N.457}$$

$$\frac{\partial T_l}{\partial x} = \frac{\beta_l}{\rho_l c_l v_s}\frac{\tau_i(v_r - v_s)}{h_t} \text{ or } 0 \qquad \text{Eq. (4.215)} \tag{N.458}$$

N.1.5.2 Derivation

In contrast to the other sections about the derivation of the structured system of equations, this section illustrates why an explicitly solvable system cannot be derived for the equations in the previous section.

In fact, if the lubricant pressure is computed by the asperity flattening equation as explained in Sec. 4.10.2.4, this evaluation can be written as follows by combining Eqs. (N.420) and (N.421):

$$p_l = p_i - H_a A \tau_Y \tag{N.459}$$

According to Eq. (N.422), the non-dimensional plastic strain rate E_p is required to compute H_a in the previous equation. This strain rate can be written as a function of the mean film thickness rate $\partial h_t/\partial x$. First, by Eqs. (N.448), (N.449), (N.450) and (N.451), and by assuming that D_z^e is negligible with respect to D_z^p in this zone,

$$\frac{\partial h}{\partial x} = \frac{D_z \bar{l}}{v_s E_p} \tag{N.460}$$

$$\rightarrow E_p = \frac{D_z \bar{l}}{v_s \frac{\partial h}{\partial h_t}\frac{\partial h_t}{\partial x}} \tag{N.461}$$

Moreover, D_z in the previous equation is a function of $\partial h_t/\partial x$ according to Eq. (N.443) and the following transformation of Eq. (N.415):

$$t_s = 2(z_r - h_t) \tag{N.462}$$

$$\rightarrow \frac{\partial t_s}{\partial x} = 2\left(\frac{\partial z_r}{\partial x} - \frac{\partial h_t}{\partial x}\right) \tag{N.463}$$

Thus, the value of E_p depends on $\partial h_t/\partial x$, which can be written as follows by combining Eqs. (N.429), (N.430), (N.437), (N.439), (N.442), (N.443), (N.444), (N.445), (N.454) and (N.463) as in Sec. N.1.4.2:

$$\frac{\partial h_t}{\partial x} = \frac{3\tau_i - \left[2G_s(1 + 3\beta_1 s_x s_z) - 3(\sigma_x + p_i + K_s)\right]\frac{\partial z_r}{\partial x}}{\left[G_s\left(2 - 3\beta_1 s_x^2\right) + \frac{3}{2}K_s\right]\beta_3 t_s - \left[2G_s(1 + 3\beta_1 s_x s_z) - 3(\sigma_x + p_i + K_s)\right]} \tag{N.464}$$

The interface shear stress τ_i in the previous equation depends on p_l according to Eqs. (N.420), (N.423) and (N.427):

$$p_a = \frac{p_i - (1 - A)p_l}{A} \tag{N.465}$$

$$\tau_a = \tau_a(v_s, v_r, p_a, \tau_Y) \tag{N.466}$$

$$\tau_i = A\tau_a + (1 - A)\tau_l \tag{N.467}$$

In conclusion, the evaluation of $\partial h_t/\partial x$ depends on the value of p_l and the evaluation of p_l depends on the value of $\partial h_t/\partial x$. Therefore, it is required to combine the previous equations and to extract a value for $\partial h_t/\partial x$, which is independent of p_l, to solve the system explicitly. This is, however, not possible since Eq. (N.466) cannot be inverted, i.e. it is not possible to write $p_a = p_a(v_s, v_r, \tau_a, \tau_Y)$ due to the possible Coulomb-Tresca friction model.

N.1.6 Low-speed outlet zone

N.1.6.1 Underlying system of equations

$z_r = z_r(x)$	by Secs. 4.6.1, 4.6.2, 4.6.3 or 4.6.4	(N.468)
$h_t = z_r - \frac{t_s}{2}$	Eq. (4.23)	(N.469)
$h \overset{\cancel{\text{epl}}}{=} h(x_{\text{wo}})$	Hypothesis	(N.470)
$h \overset{\text{cpl}}{=} h(h_t)$	by Eqs. (4.15) or (4.20)	(N.471)
$h_t \overset{\cancel{\text{epl}}}{=} h_t(x_{\text{wo}})$	Hypothesis	(N.472)
$h_t \overset{\text{cpl}}{=} h_t(x)$	by Eq. (6.41)	(N.473)
$A \overset{\cancel{\text{epl}}}{=} A(x_{\text{wo}})$	Hypothesis	(N.474)
$A \overset{\text{cpl}}{=} A(x)$	by Eq. (6.40)	(N.475)
$p_i = Ap_a + (1-A)p_l$ or Ap_a	Eq. (4.4)	(N.476)
$\overline{\epsilon}^p = \overline{\epsilon}^p(x_{\text{wo}})$	No plastic deformation	(N.477)
$\sigma_Y = \sigma_Y(\overline{\epsilon}^p, \overline{D}^p, T_s)$	by Eqs. (4.50), (4.52), (4.54), (4.56), (4.60) or (4.62)	(N.478)
$\tau_Y = \frac{\sigma_Y}{\sqrt{3}}$	Eq. (H.56)	(N.479)
$\tau_a = \tau_a(v_s, v_r, p_a, \tau_Y)$	by Eqs. (4.123), (4.124) or (4.125)	(N.480)
$T_l = T_l(T_l^*, T_s, T_l)$ or /	by Eqs. (4.212), (4.213), (4.214) or (4.215)	(N.481)
$\eta = \eta(p_l, T_l)$ or /	by Eqs. (4.192), (**??**) or (4.195)	(N.482)
$\tau_l = \tau_l\left(h, h_t, A, \eta, v_s, v_r, \frac{\partial p_l}{\partial x}\right)$ or 0	by Eqs. (4.204) or (4.205)	(N.483)
$\tau_i = A\tau_a + (1-A)\tau_l$ or $A\tau_a$	Eq. (4.5)	(N.484)
$\phi_x = \phi_x(h_t)$ or /	by Eqs. (4.168) or (4.170)	(N.485)
$\phi_s = \phi_s(h_t)$ or /	by Eqs. (4.169) or (4.174) with (4.182)	(N.486)
$\frac{\partial p_l}{\partial x} = \frac{12\eta}{\phi_x h_t^3}\left(\frac{v_s+v_r}{2}h_t + \frac{v_s-v_r}{2}R_q\phi_s - Q\right)$ or 0	Eq. (4.191)	(N.487)
$\frac{\partial(\sigma_x t_s)}{\partial x} = -p_i\frac{\partial t_s}{\partial x} - 2\tau_i$	Eq. (4.65)	(N.488)
$\sigma_z = -p_i$	Eq. (4.68)	(N.489)

$$\epsilon_x^e = \frac{1}{E_s}\left[\sigma_x - \nu_s(\sigma_y + \sigma_z)\right] \quad \text{Eq. (4.34a)} \tag{N.490}$$

$$\sigma_y = \nu_s(\sigma_x + \sigma_z) \quad \text{Eq. (4.34b)} \tag{N.491}$$

$$\epsilon_z^e = \frac{1}{E_s}\left[\sigma_z - \nu_s(\sigma_x + \sigma_y)\right] \quad \text{Eq. (4.34c)} \tag{N.492}$$

$$\frac{\partial v_s}{\partial x} = v_s \frac{\partial \epsilon_x^e}{\partial x} \quad \text{Eq. (4.30) and } \epsilon_x = \epsilon_x^e \tag{N.493}$$

$$\frac{\partial \epsilon_z^e}{\partial x} = \frac{1}{t_s}\frac{\partial t_s}{\partial x} \quad \text{Eq. (4.31) and } \epsilon_z = \epsilon_z^e \tag{N.494}$$

$$p = -\frac{\sigma_x + \sigma_y + \sigma_z}{3} \quad \text{Eq. (H.26)} \tag{N.495}$$

$$s_x = \sigma_x + p \quad \text{Eq. (H.27)} \tag{N.496}$$

$$s_z = \sigma_z + p \quad \text{Eq. (H.27)} \tag{N.497}$$

$$\frac{\partial T_s}{\partial x} = \frac{1}{\rho_s c_s v_s}\frac{\tau_i(v_r - v_s)}{t_s} \quad \text{Eq. (4.211) and no plastic deformation} \tag{N.498}$$

$$\frac{\partial T_l}{\partial x} = \frac{\beta_l}{\rho_l c_l v_s}\frac{\tau_i(v_r - v_s)}{h_t} \text{ or } 0 \quad \text{Eq. (4.215)} \tag{N.499}$$

N.1.6.2 Derivation

- Eq. (N.469) and Eq. (N.472):

$$\frac{\partial t_s}{\partial x} = 2\frac{\partial z_r}{\partial x} \tag{N.500}$$

- Eq. (N.488):

$$\frac{\partial \sigma_x}{\partial x} t_s + \sigma_x \frac{\partial t_s}{\partial x} = -p_i \frac{\partial t_s}{\partial x} - 2\tau_i \tag{N.501}$$

$$\rightarrow t_s \frac{\partial \sigma_x}{\partial x} = -(\sigma_x + p_i)\frac{\partial t_s}{\partial x} - 2\tau_i \tag{N.502}$$

$$\Rightarrow \frac{\partial \sigma_x}{\partial x} = -\frac{1}{t_s}\left[(\sigma_x + p_i)\frac{\partial t_s}{\partial x} + 2\tau_i\right] \tag{N.503}$$

- Eq. (N.491) in Eq. (N.492):

$$\epsilon_z^e = \frac{1}{E_s}\left[\sigma_z - \nu_s\sigma_x - \nu_s^2(\sigma_x + \sigma_z)\right] \tag{N.504}$$

$$\rightarrow \epsilon_z^e = \frac{1}{E_s}\left[-\nu_s(1 + \nu_s)\sigma_x + (1 - \nu_s^2)\sigma_z\right] \tag{N.505}$$

$$\rightarrow \frac{\partial \epsilon_z^e}{\partial x} = \frac{-\nu_s(1 + \nu_s)}{E_s}\frac{\partial \sigma_x}{\partial x} + \frac{1 - \nu_s^2}{E_s}\frac{\partial \sigma_z}{\partial x} \tag{N.506}$$

- Eq. (N.494) in Eq. (N.506):

$$\frac{1}{t_s}\frac{\partial t_s}{\partial x} = \frac{-\nu_s(1+\nu_s)}{E_s}\frac{\partial \sigma_x}{\partial x} + \frac{1-\nu_s^2}{E_s}\frac{\partial \sigma_z}{\partial x} \tag{N.507}$$

$$\rightarrow \frac{1-\nu_s^2}{E_s}\frac{\partial \sigma_z}{\partial x} = \frac{1}{t_s}\frac{\partial t_s}{\partial x} + \frac{\nu_s(1+\nu_s)}{E_s}\frac{\partial \sigma_x}{\partial x} \tag{N.508}$$

$$\Rightarrow \frac{\partial \sigma_z}{\partial x} = \frac{E_s}{t_s(1-\nu_s^2)}\frac{\partial t_s}{\partial x} + \frac{\nu_s}{1-\nu_s}\frac{\partial \sigma_x}{\partial x} \tag{N.509}$$

- Eq. (N.491) in Eq. (N.490):

$$\epsilon_x^e = \frac{1}{E_s}\left[\sigma_x - \nu_s^2(\sigma_x+\sigma_z) - \nu_s\sigma_z\right] \tag{N.510}$$

$$\rightarrow \epsilon_x^e = \frac{1}{E_s}\left[(1-\nu_s^2)\sigma_x - \nu_s(1+\nu_s)\sigma_z\right] \tag{N.511}$$

$$\rightarrow \frac{\partial \epsilon_x^e}{\partial x} = \frac{1+\nu_s}{E_s}\left[(1-\nu_s)\frac{\partial \sigma_x}{\partial x} - \nu_s\frac{\partial \sigma_z}{\partial x}\right] \tag{N.512}$$

- Eq. (N.512) in Eq. (N.493):

$$\Rightarrow \frac{\partial v_s}{\partial x} = \frac{v_s(1+\nu_s)}{E_s}\left[(1-\nu_s)\frac{\partial \sigma_x}{\partial x} - \nu_s\frac{\partial \sigma_z}{\partial x}\right] \tag{N.513}$$

N.1.6.3 Structured system of equations

Values required in differential equations

$$h_t \overset{\text{epl}}{=} h_t(x_{\text{wo}}) \tag{N.514}$$

$$h_t \overset{\text{cpl}}{=} h_t(x) \quad \text{by Eq. (6.41)} \tag{N.515}$$

$$z_r = z_r(x) \quad \text{by Secs. 4.6.1, 4.6.2, 4.6.3 or 4.6.4} \tag{N.516}$$

$$\frac{\partial z_r}{\partial x} = \frac{\partial z_r}{\partial x}(x) \quad \text{by Secs. 4.6.1, 4.6.2, 4.6.3 or 4.6.4} \tag{N.517}$$

$$t_s = 2(z_r - h_t) \tag{N.518}$$

$$h \overset{\text{epl}}{=} h(x_{\text{wo}}) \tag{N.519}$$

$$h \overset{\text{cpl}}{=} h(h_t) \quad \text{by Eqs. (4.15) or (4.20)} \tag{N.520}$$

$$A \overset{\text{epl}}{=} A(x_{\text{wo}}) \tag{N.521}$$

$$A \overset{\text{cpl}}{=} A(x) \quad \text{by Eq. (6.40)} \tag{N.522}$$

$$\overline{\epsilon}^p = \overline{\epsilon}^p(x_{\text{wo}}) \tag{N.523}$$

$$\sigma_Y = \sigma_Y(\overline{\epsilon}^p, \overline{D}^p, T_s) \quad \text{by Eqs. (4.50), (4.52), (4.54), (4.56), (4.60) or (4.62)} \tag{N.524}$$

$$\tau_Y = \frac{\sigma_Y}{\sqrt{3}} \tag{N.525}$$

$$p_i = -\sigma_z \tag{N.526}$$

$$p_a = \frac{p_i - (1-A)p_l}{A} \text{ or } \frac{p_i}{A} \tag{N.527}$$

$$\tau_a = \tau_a(v_s, v_r, p_a, \tau_Y) \quad \text{by Eqs. (4.123), (4.124) or (4.125)} \tag{N.528}$$

$$\frac{\partial t_s}{\partial x} \overset{\text{epl}}{=} 2\frac{\partial z_r}{\partial x} \tag{N.529}$$

$$\frac{\partial h_t}{\partial x} \overset{\text{cpl}}{=} \frac{\partial h_t}{\partial x}(x) \quad \text{by Eq. (6.42)} \tag{N.530}$$

$$\frac{\partial t_s}{\partial x} \overset{\text{cpl}}{=} 2\left(\frac{\partial z_r}{\partial x} - \frac{\partial h_t}{\partial x}\right) \tag{N.531}$$

$$T_l = T_l(T_l^*, T_s, T_l) \text{ or } / \quad \text{by Eqs. (4.212), (4.213), (4.214) or (4.215)} \tag{N.532}$$

$$\eta = \eta(p_l, T_l) \text{ or } / \quad \text{by Eqs. (4.192), (??) or (4.195)} \tag{N.533}$$

$$\phi_x = \phi_x(h_t) \text{ or } / \quad \text{by Eqs. (4.168) or (4.170)} \tag{N.534}$$

$$\phi_s = \phi_s(h_t) \text{ or } / \quad \text{by Eqs. (4.169) or (4.174) with (4.182)} \tag{N.535}$$

Differential equations (mainly)

$$\Rightarrow \frac{\partial p_l}{\partial x} = \frac{12\eta}{\phi_x h_t^3}\left(\frac{v_s + v_r}{2} h_t + \frac{v_s - v_r}{2} R_q \phi_s - Q\right) \text{ or } 0 \tag{N.536}$$

$$\tau_l = \tau_l\left(h, h_t, A, \eta, v_s, v_r, \frac{\partial p_l}{\partial x}\right) \text{ or } 0 \qquad \text{by Eqs. (4.204) or (4.205)} \tag{N.537}$$

$$\tau_i = A\tau_a + (1 - A)\tau_l \text{ or } A\tau_a \tag{N.538}$$

$$\Rightarrow \frac{\partial \sigma_x}{\partial x} = -\frac{1}{t_s}\left[(\sigma_x + p_i)\frac{\partial t_s}{\partial x} + 2\tau_i\right] \tag{N.539}$$

$$\Rightarrow \frac{\partial \sigma_z}{\partial x} = \frac{E_s}{(1 - \nu_s^2)t_s}\frac{\partial t_s}{\partial x} + \frac{\nu_s}{1 - \nu_s}\frac{\partial \sigma_x}{\partial x} \tag{N.540}$$

$$\Rightarrow \frac{\partial v_s}{\partial x} = \frac{v_s(1 + \nu_s)}{E_s}\left[(1 - \nu_s)\frac{\partial \sigma_x}{\partial x} - \nu_s \frac{\partial \sigma_z}{\partial x}\right] \tag{N.541}$$

$$\Rightarrow \frac{\partial T_s}{\partial x} = \frac{1}{\rho_s c_s v_s}\frac{\tau_i(v_r - v_s)}{t_s} \tag{N.542}$$

$$\Rightarrow \frac{\partial T_l}{\partial x} = \frac{\beta_l}{\rho_l c_l v_s}\frac{\tau_i(v_r - v_s)}{h_t} \text{ or } 0 \tag{N.543}$$

Values not directly required in differential equations

$$\sigma_y = \nu_s(\sigma_x + \sigma_z) \tag{N.544}$$

$$p = -\frac{\sigma_x + \sigma_y + \sigma_z}{3} \tag{N.545}$$

$$s_x = \sigma_x + p \tag{N.546}$$

$$s_z = \sigma_z + p \tag{N.547}$$

N.1.7 High-speed outlet zone

N.1.7.1 Underlying system of equations

$z_r = z_r(x)$	by Secs. 4.6.1, 4.6.2, 4.6.3 or 4.6.4	(N.548)
$h_t = z_r - \frac{t_s}{2}$	Eq. (4.23)	(N.549)
$h = h(x_{\mathrm{wo}})$	Hypothesis	(N.550)
$h_t \overset{\text{epl}}{=} h_t(x_{\mathrm{wo}})$	Hypothesis	(N.551)
$h_t \overset{\text{cpl}}{=} h_t(x)$	by Eq. (6.41)	(N.552)
$A = A(x_{\mathrm{wo}})$	Hypothesis	(N.553)
$A \overset{\text{epl}}{=} A(x)$	by Eq. (6.40)	(N.554)
$p_i = Ap_a + (1-A)p_l$	Eq. (4.4)	(N.555)
$\overline{\epsilon}^p = \overline{\epsilon}^p(x_{\mathrm{wo}})$	No plastic deformation	(N.556)
$\sigma_Y = \sigma_Y(\overline{\epsilon}^p, \overline{D}^p, T_s)$	by Eqs. (4.50), (4.52), (4.54), (4.56), (4.60) or (4.62)	(N.557)
$\tau_Y = \frac{\sigma_Y}{\sqrt{3}}$	Eq. (H.56)	(N.558)
$\tau_a = \tau_a(v_s, v_r, p_a, \tau_Y)$	by Eqs. (4.123), (4.124) or (4.125)	(N.559)
$p_l = p_i$	Hypothesis	(N.560)
$T_l = T_l(T_l^*, T_s, T_l)$ or /	by Eqs. (4.212), (4.213), (4.214) or (4.215)	(N.561)
$\eta = \eta(p_l, T_l)$	by Eqs. (4.192), (**??**) or (4.195)	(N.562)
$\tau_l = \tau_l\left(h, h_t, A, \eta, v_s, v_r, \frac{\partial p_l}{\partial x}\right)$	by Eqs. (4.204) or (4.205)	(N.563)
$\tau_i = A\tau_a + (1-A)\tau_l$	Eq. (4.5)	(N.564)
$\frac{\partial(\sigma_x t_s)}{\partial x} = -p_i\frac{\partial t_s}{\partial x} - 2\tau_i$	Eq. (4.65)	(N.565)
$\sigma_z = -p_i$	Eq. (4.68)	(N.566)
$\epsilon_x^e = \frac{1}{E_s}\left[\sigma_x - \nu_s(\sigma_y + \sigma_z)\right]$	Eq. (4.34a)	(N.567)
$\sigma_y = \nu_s(\sigma_x + \sigma_z)$	Eq. (4.34b)	(N.568)
$\epsilon_z^e = \frac{1}{E_s}\left[\sigma_z - \nu_s(\sigma_x + \sigma_y)\right]$	Eq. (4.34c)	(N.569)
$\frac{\partial v_s}{\partial x} = v_s\frac{\partial \epsilon_x^e}{\partial x}$	Eq. (4.30) and $\epsilon_x = \epsilon_x^e$	(N.570)
$\frac{\partial \epsilon_z^e}{\partial x} = \frac{1}{t_s}\frac{\partial t_s}{\partial x}$	Eq. (4.31) and $\epsilon_z = \epsilon_z^e$	(N.571)

$$p = -\frac{\sigma_x + \sigma_y + \sigma_z}{3} \quad \text{Eq. (H.26)} \quad \text{(N.572)}$$

$$s_x = \sigma_x + p \quad \text{Eq. (H.27)} \quad \text{(N.573)}$$

$$s_z = \sigma_z + p \quad \text{Eq. (H.27)} \quad \text{(N.574)}$$

$$\frac{\partial T_s}{\partial x} = \frac{1}{\rho_s c_s v_s} \frac{\tau_i (v_r - v_s)}{t_s} \quad \text{Eq. (4.211) and no plastic deformation} \quad \text{(N.575)}$$

$$\frac{\partial T_l}{\partial x} = \frac{\beta_l}{\rho_l c_l v_s} \frac{\tau_i (v_r - v_s)}{h_t} \text{ or } 0 \quad \text{Eq. (4.215)} \quad \text{(N.576)}$$

N.1.7.2 Derivation

The derivation of the structured system of equations in the high-speed outlet zone is identical to the derivation in the low-speed outlet zone (Sec. N.1.6.2).

N.1.7.3 Structured system of equations

Values required in differential equations

$$h_t \overset{\text{epl}}{=} h_t(x_{\text{wo}}) \tag{N.577}$$

$$h_t \overset{\text{cpl}}{=} h_t(x) \quad \text{by Eq. (6.41)} \tag{N.578}$$

$$z_r = z_r(x) \quad \text{by Secs. 4.6.1, 4.6.2, 4.6.3 or 4.6.4} \tag{N.579}$$

$$\frac{\partial z_r}{\partial x} = \frac{\partial z_r}{\partial x}(x) \quad \text{by Secs. 4.6.1, 4.6.2, 4.6.3 or 4.6.4} \tag{N.580}$$

$$t_s = 2(z_r - h_t) \tag{N.581}$$

$$h \overset{\text{epl}}{=} h(x_{\text{wo}}) \tag{N.582}$$

$$h \overset{\text{cpl}}{=} h(h_t) \quad \text{by Eqs. (4.15) or (4.20)} \tag{N.583}$$

$$A \overset{\text{epl}}{=} A(x_{\text{wo}}) \tag{N.584}$$

$$A \overset{\text{cpl}}{=} A(x) \quad \text{by Eq. (6.40)} \tag{N.585}$$

$$\overline{\epsilon}^p = \overline{\epsilon}^p(x_{\text{wo}}) \tag{N.586}$$

$$\sigma_Y = \sigma_Y(\overline{\epsilon}^p, \overline{D}^p, T_s) \quad \text{by Eqs. (4.50), (4.52), (4.54), (4.56), (4.60) or (4.62)} \tag{N.587}$$

$$\tau_Y = \frac{\sigma_Y}{\sqrt{3}} \tag{N.588}$$

$$p_i = -\sigma_z \tag{N.589}$$

$$p_l = p_i \tag{N.590}$$

$$p_a = p_i \tag{N.591}$$

$$\tau_a = \tau_a(v_s, v_r, p_a, \tau_Y) \quad \text{by Eqs. (4.123), (4.124) or (4.125)} \tag{N.592}$$

$$T_l = T_l(T_l^*, T_s, T_l) \text{ or } / \quad \text{by Eqs. (4.212), (4.213), (4.214) or (4.215)} \tag{N.593}$$

$$\eta = \eta(p_l, T_l) \quad \text{by Eqs. (4.192), (??) or (4.195)} \tag{N.594}$$

$$\tau_l = \tau_l\left(h, h_t, A, \eta, v_s, v_r, \frac{\partial p_l}{\partial x}\right) \quad \text{by Eqs. (4.204) or (4.205)} \tag{N.595}$$

$$\tau_i = A\tau_a + (1 - A)\tau_l \tag{N.596}$$

$$\frac{\partial t_s}{\partial x} \overset{\text{epl}}{=} 2\frac{\partial z_r}{\partial x} \tag{N.597}$$

$$\frac{\partial h_t}{\partial x} \overset{\text{cpl}}{=} \frac{\partial h_t}{\partial x}(x) \quad \text{by Eq. (6.42)} \tag{N.598}$$

$$\frac{\partial t_s}{\partial x} \overset{\text{cpl}}{=} 2\left(\frac{\partial z_r}{\partial x} - \frac{\partial h_t}{\partial x}\right) \tag{N.599}$$

Differential equations (mainly)

$$\Rightarrow \frac{\partial \sigma_x}{\partial x} = -\frac{1}{t_s}\left[(\sigma_x + p_i)\frac{\partial t_s}{\partial x} + 2\tau_i\right] \tag{N.600}$$

$$\Rightarrow \frac{\partial \sigma_z}{\partial x} = \frac{E_s}{(1-\nu_s^2)t_s}\frac{\partial t_s}{\partial x} + \frac{\nu_s}{1-\nu_s}\frac{\partial \sigma_x}{\partial x} \tag{N.601}$$

$$\Rightarrow \frac{\partial v_s}{\partial x} = v_s\frac{1+\nu_s}{E_s}\left[(1-\nu_s)\frac{\partial \sigma_x}{\partial x} - \nu_s\frac{\partial \sigma_z}{\partial x}\right] \tag{N.602}$$

$$\Rightarrow \frac{\partial T_s}{\partial x} = \frac{1}{\rho_s c_s v_s}\frac{\tau_i(v_r - v_s)}{t_s} \tag{N.603}$$

$$\Rightarrow \frac{\partial T_l}{\partial x} = \frac{\beta_l}{\rho_l c_l v_s}\frac{\tau_i(v_r - v_s)}{h_t} \text{ or } 0 \tag{N.604}$$

Values not directly required in differential equations

$$h = h(x_{\text{wo}}) \tag{N.605}$$

$$\sigma_y = \nu_s(\sigma_x + \sigma_z) \tag{N.606}$$

$$p = -\frac{\sigma_x + \sigma_y + \sigma_z}{3} \tag{N.607}$$

$$s_x = \sigma_x + p \tag{N.608}$$

$$s_z = \sigma_z + p \tag{N.609}$$

N.2 Smooth roll bite

In this section, the equations of a smooth roll bite are provided. Parameter of surface asperities, like h, h_t, A, the lubricant pressure, the Reynolds equation and the asperity flattening equation are not included. This is why this model is called smooth. Nevertheless, asperity effects and lubrication are included in the model via macroscopic friction laws. Hence, it is not strictly smooth.

In this model, the number of the dependent variables in a rough lubricated roll bite (Sec. 4.10.1) is reduced to the following ones:

$$v_s, t_s, p_i, \tau_i, \sigma_x, \sigma_y, \sigma_z, s_x, s_z, p, \overline{\epsilon}^p \tag{N.610}$$

The underlying equations and the structured systems of equations in the following sections are deduced of those in Sec. N, in the same order. Since this derivation is relatively straightforward and since it can usually by found in Sec. N, no specific section about their derivation was added here.

Although no hydrodynamic or mixed inlet zones exist as such in this case, since the lubricant is not explicitly included in the computation via the Reynolds equation, the roll bite is divided into the same zones as in the rough lubricated roll bite (Sec. N,) in order to simplify the presentation and the implementation. No high-speed zones do obviously exist in this case.

Moreover, only the end-of-zone criterion of the hydrodynamic inlet zone is provided in the following sections because it differs from those in Sec. 4.10.2, which are still valid for the other zones.

N.2.1 Hydrodynamic inlet zone zone

N.2.1.1 Underlying system of equations

$$z_r = z_r(x) \quad \text{by Secs. 4.6.1, 4.6.2, 4.6.3 or 4.6.4} \tag{N.611}$$

$$\overline{\epsilon}^p = \overline{\epsilon}_0^p \quad \text{No plastic deformation} \tag{N.612}$$

$$p_i = 0 \quad \text{No contact} \tag{N.613}$$

$$\tau_i = 0 \quad \text{No contact} \tag{N.614}$$

$$\frac{\partial(\sigma_x t_s)}{\partial x} = -p_i \frac{\partial t_s}{\partial x} - 2\tau_i \quad \text{Eq. (4.65)} \tag{N.615}$$

$$\sigma_z = -p_i \quad \text{Eq. (4.68)} \tag{N.616}$$

$$\epsilon_x^e = \frac{1}{E_s}\left[\sigma_x - \nu_s(\sigma_y + \sigma_z)\right] \quad \text{Eq. (4.34a)} \tag{N.617}$$

$$\sigma_y = \nu_s(\sigma_x + \sigma_z) \quad \text{Eq. (4.34b)} \tag{N.618}$$

$$\epsilon_z^e = \frac{1}{E_s}\left[\sigma_z - \nu_s(\sigma_x + \sigma_y)\right] \quad \text{Eq. (4.34c)} \tag{N.619}$$

$$\frac{\partial v_s}{\partial x} = v_s \frac{\partial \epsilon_x^e}{\partial x} \quad \text{Eq. (4.30) and } \epsilon_x = \epsilon_x^e \tag{N.620}$$

$$\frac{\partial \epsilon_z^e}{\partial x} = \frac{1}{t_s}\frac{\partial t_s}{\partial x} \quad \text{Eq. (4.31) and } \epsilon_z = \epsilon_z^e \tag{N.621}$$

$$p = -\frac{\sigma_x + \sigma_y + \sigma_z}{3} \quad \text{Eq. (H.26)} \tag{N.622}$$

$$s_x = \sigma_x + p \quad \text{Eq. (H.27)} \tag{N.623}$$

$$s_z = \sigma_z + p \quad \text{Eq. (H.27)} \tag{N.624}$$

$$\frac{\partial T_s}{\partial x} = 0 \quad \text{No friction and no plastic deformation} \tag{N.625}$$

N.2.1.2 Structured system of equations

$$z_r = z_r(x) \qquad \text{by Secs. 4.6.1, 4.6.2, 4.6.3 or 4.6.4} \tag{N.626}$$
$$\tau_i = 0 \tag{N.627}$$
$$t_s = t_{\text{in}} \tag{N.628}$$
$$\sigma_x = \sigma_{\text{in}} \tag{N.629}$$
$$v_s = v_{\text{in}} \tag{N.630}$$
$$\overline{\epsilon}^p = \overline{\epsilon}^p_0 \tag{N.631}$$
$$p_i = 0 \tag{N.632}$$
$$\sigma_z = -p_i \tag{N.633}$$
$$\sigma_y = \nu_s(\sigma_x + \sigma_z) \tag{N.634}$$
$$p = -\frac{\sigma_x + \sigma_y + \sigma_z}{3} \tag{N.635}$$
$$s_x = \sigma_x + p \tag{N.636}$$
$$s_z = \sigma_z + p \tag{N.637}$$
$$T_s = T_{s_{\text{in}}} \tag{N.638}$$

N.2.1.3 End-of-zone criterion

$$z_r < \frac{t_s}{2} \quad \text{and} \quad \frac{z_r - \frac{t_s}{2}}{t_{\text{in}}} > -\text{tol}_{\text{crit}} \tag{N.639}$$

N.2.2 Mixed inlet zone zone

N.2.2.1 Underlying system of equations

$$z_r = z_r(x) \quad \text{by Secs. 4.6.1, 4.6.2, 4.6.3 or 4.6.4} \tag{N.640}$$

$$0 = z_r - \frac{t_s}{2} \quad \text{Eq. (4.23) and } h_t = 0 \tag{N.641}$$

$$\overline{\epsilon}^p = \overline{\epsilon}^p(x_{\text{ihm}}) \quad \text{No plastic deformation} \tag{N.642}$$

$$\sigma_Y = \sigma_Y(\overline{\epsilon}^p, \overline{D}^p, T_s) \quad \text{by Eqs. (4.50), (4.52), (4.54), (4.56), (4.60) or (4.62)} \tag{N.643}$$

$$\tau_Y = \frac{\sigma_Y}{\sqrt{3}} \quad \text{Eq. (H.56)} \tag{N.644}$$

$$p_i = p_a \quad \text{Eq. (4.4) and } A = 1 \tag{N.645}$$

$$\tau_a = \tau_a(v_s, v_r, p_a, \tau_Y) \quad \text{by Eqs. (4.123), (4.124) or (4.125)} \tag{N.646}$$

$$\tau_i = \tau_a \quad \text{Eq. (4.5) and } A = 1 \tag{N.647}$$

$$\frac{\partial(\sigma_x t_s)}{\partial x} = -p_i \frac{\partial t_s}{\partial x} - 2\tau_i \quad \text{Eq. (4.65)} \tag{N.648}$$

$$\sigma_z = -p_i \quad \text{Eq. (4.68)} \tag{N.649}$$

$$\epsilon_x^e = \frac{1}{E_s}\left[\sigma_x - \nu_s(\sigma_y + \sigma_z)\right] \quad \text{Eq. (4.34a)} \tag{N.650}$$

$$\sigma_y = \nu_s(\sigma_x + \sigma_z) \quad \text{Eq. (4.34b)} \tag{N.651}$$

$$\epsilon_z^e = \frac{1}{E_s}\left[\sigma_z - \nu_s(\sigma_x + \sigma_y)\right] \quad \text{Eq. (4.34c)} \tag{N.652}$$

$$\frac{\partial v_s}{\partial x} = v_s \frac{\partial \epsilon_x^e}{\partial x} \quad \text{Eq. (4.30) and } \epsilon_x = \epsilon_x^e \tag{N.653}$$

$$\frac{\partial \epsilon_z^e}{\partial x} = \frac{1}{t_s}\frac{\partial t_s}{\partial x} \quad \text{Eq. (4.31) and } \epsilon_z = \epsilon_z^e \tag{N.654}$$

$$p = -\frac{\sigma_x + \sigma_y + \sigma_z}{3} \quad \text{Eq. (H.26)} \tag{N.655}$$

$$s_x = \sigma_x + p \quad \text{Eq. (H.27)} \tag{N.656}$$

$$s_z = \sigma_z + p \quad \text{Eq. (H.27)} \tag{N.657}$$

$$\frac{\partial T_s}{\partial x} = \frac{1}{\rho_s c_s v_s}\frac{\tau_i(v_r - v_s)}{t_s} \quad \text{Eq. (4.211) and no plastic deformation} \tag{N.658}$$

N.2.2.2 Structured system of equations

Values required in differential equations

$$z_r = z_r(x) \quad \text{by Secs. 4.6.1, 4.6.2, 4.6.3 or 4.6.4} \tag{N.659}$$

$$\frac{\partial z_r}{\partial x} = \frac{\partial z_r}{\partial x}(x) \quad \text{by Secs. 4.6.1, 4.6.2, 4.6.3 or 4.6.4} \tag{N.660}$$

$$t_s = 2z_r \tag{N.661}$$

$$\overline{\epsilon}^p = \overline{\epsilon}^p(x_{\text{ihm}}) \tag{N.662}$$

$$\sigma_Y = \sigma_Y(\overline{\epsilon}^p, \overline{D}^p, T_s) \quad \text{by Eqs. (4.50), (4.52), (4.54), (4.56), (4.60) or (4.62)} \tag{N.663}$$

$$\tau_Y = \frac{\sigma_Y}{\sqrt{3}} \tag{N.664}$$

$$p_i = -\sigma_z \tag{N.665}$$

$$\tau_i = \tau_a(v_s, v_r, p_i, \tau_Y) \quad \text{by Eqs. (4.123), (4.124) or (4.125)} \tag{N.666}$$

$$\frac{\partial t_s}{\partial x} = 2\frac{\partial z_r}{\partial x} \tag{N.667}$$

Differential equations (mainly)

$$\Rightarrow \frac{\partial \sigma_x}{\partial x} = -\frac{1}{t_s}\left[(\sigma_x + p_i)\frac{\partial t_s}{\partial x} + 2\tau_i\right] \tag{N.668}$$

$$\Rightarrow \frac{\partial \sigma_z}{\partial x} = \frac{E_s}{t_s(1-\nu_s^2)}\frac{\partial t_s}{\partial x} + \frac{\nu_s}{1-\nu_s}\frac{\partial \sigma_x}{\partial x} \tag{N.669}$$

$$\Rightarrow \frac{\partial v_s}{\partial x} = \frac{v_s(1+\nu_s)}{E_s}\left[(1-\nu_s)\frac{\partial \sigma_x}{\partial x} - \nu_s\frac{\partial \sigma_z}{\partial x}\right] \tag{N.670}$$

$$\Rightarrow \frac{\partial T_s}{\partial x} = \frac{1}{\rho_s c_s v_s}\frac{\tau_i(v_r - v_s)}{t_s} \tag{N.671}$$

Values not directly required in differential equations

$$\sigma_y = \nu_s(\sigma_x + \sigma_z) \tag{N.672}$$

$$p = -\frac{\sigma_x + \sigma_y + \sigma_z}{3} \tag{N.673}$$

$$s_x = \sigma_x + p \tag{N.674}$$

$$s_z = \sigma_z + p \tag{N.675}$$

N.2.3 Work zone

N.2.3.1 Underlying system of equations

$$z_r = z_r(x) \quad \text{by Secs. 4.6.1, 4.6.2, 4.6.3 or 4.6.4} \quad \text{(N.676)}$$

$$0 = z_r - \frac{t_s}{2} \quad \text{Eq. (4.23) and } h_t = 0 \quad \text{(N.677)}$$

$$\sigma_Y = \sigma_Y(\overline{\epsilon}^p, \overline{D}^p, T_s) \quad \text{by Eqs. (4.50), (4.52), (4.54), (4.56), (4.60) or (4.62)} \quad \text{(N.678)}$$

$$\tau_Y = \frac{\sigma_Y}{\sqrt{3}} \quad \text{Eq. (H.56)} \quad \text{(N.679)}$$

$$p_i = p_a \quad \text{Eq. (4.4) and } A = 1 \quad \text{(N.680)}$$

$$\tau_a = \tau_a(v_s, v_r, p_a, \tau_Y) \quad \text{by Eqs. (4.123), (4.124) or (4.125)} \quad \text{(N.681)}$$

$$\tau_i = \tau_a \quad \text{Eq. (4.5) and } A = 1 \quad \text{(N.682)}$$

$$\frac{\partial(\sigma_x t_s)}{\partial x} = -p_i \frac{\partial t_s}{\partial x} - 2\tau_i \quad \text{Eq. (4.65)} \quad \text{(N.683)}$$

$$\sigma_z = -p_i \quad \text{Eq. (4.68)} \quad \text{(N.684)}$$

$$\epsilon_x^e = \frac{1}{E_s}\left[\sigma_x - \nu_s(\sigma_y + \sigma_z)\right] \quad \text{Eq. (4.34a)} \quad \text{(N.685)}$$

$$\sigma_y = \nu_s(\sigma_x + \sigma_z) \quad \text{Eq. (4.34b), elastic deformations} \quad \text{(N.686)}$$

$$\epsilon_z^e = \frac{1}{E_s}\left[\sigma_z - \nu_s(\sigma_x + \sigma_y)\right] \quad \text{Eq. (4.34c)} \quad \text{(N.687)}$$

$$h_{i,s} = h_{i,s}(\overline{\epsilon}^p, \overline{D}^p, T_s) \quad \text{by Eqs. (4.51), (4.53), (4.55), (4.57), (4.61) or (4.63)} \quad \text{(N.688)}$$

$$\beta_1 = \frac{1}{\frac{2}{3}\sigma_Y^2\left(1 + \frac{h_{i,s}}{3G_s}\right)} \quad \text{Eq. (4.37)} \quad \text{(N.689)}$$

$$\dot{s}_x = \frac{2G_s}{3}\left[\left(2 - 3\beta_1 s_x^2\right) D_x - \left(1 + 3\beta_1 s_x s_z\right) D_z\right] \quad \text{Eq. (4.39)} \quad \text{(N.690)}$$

$$\dot{s}_z = \frac{2G_s}{3}\left[-\left(1 + 3\beta_1 s_x s_z\right) D_x + \left(2 - 3\beta_1 s_z^2\right) D_z\right] \quad \text{Eq. (4.40)} \quad \text{(N.691)}$$

$$\dot{s}_x = v_s \frac{\partial s_x}{\partial x} \quad \text{Eq. (4.45)} \quad \text{(N.692)}$$

$$\dot{s}_z = v_s \frac{\partial s_z}{\partial x} \quad \text{Eq. (4.45)} \quad \text{(N.693)}$$

$$0 = s_x + s_y + s_z \quad \text{Eq. (H.27)} \quad \text{(N.694)}$$

$$D_x = \frac{\partial v_s}{\partial x} \quad \text{Eq. (4.41)} \quad \text{(N.695)}$$

$$D_z = \frac{v_s}{t_s}\frac{\partial t_s}{\partial x} \qquad \text{Eq. (4.44)} \qquad \text{(N.696)}$$

$$\dot{p} = -K_s(D_x + D_z) \qquad \text{Eq. (4.38)} \qquad \text{(N.697)}$$

$$\dot{p} = v_s\frac{\partial p}{\partial x} \qquad \text{Eq. (4.45)} \qquad \text{(N.698)}$$

$$D_x^e = v_s\frac{\partial \epsilon_x^e}{\partial x} \qquad \text{Eq. (4.48)} \qquad \text{(N.699)}$$

$$D_z^e = v_s\frac{\partial \epsilon_z^e}{\partial x} \qquad \text{Eq. (4.49)} \qquad \text{(N.700)}$$

$$0 = D_x^p + D_y^p + D_z^p \qquad \text{Plastic incompressibility, Eq. (H.19)} \qquad \text{(N.701)}$$

$$D_y^p = 0 \qquad \text{Plane-strain state} \qquad \text{(N.702)}$$

$$D_z = D_z^e + D_z^p \qquad \text{Eq. (H.52)} \qquad \text{(N.703)}$$

$$\frac{\partial h}{\partial x} = \frac{-D_x^p \bar{l}}{v_s E_p} \qquad \text{Eq. (4.122)} \qquad \text{(N.704)}$$

$$\overline{D}^p = v_s\frac{\partial \overline{\epsilon}^p}{\partial x} \qquad \text{Eq. (4.46)} \qquad \text{(N.705)}$$

$$\overline{D}^p = \sqrt{\frac{2}{3}\left[(D_x - D_x^e)^2 + (D_z - D_z^e)^2\right]} \qquad \text{Eq. (4.47)} \qquad \text{(N.706)}$$

$$s_x = \sigma_x + p \qquad \text{Eq. (H.27)} \qquad \text{(N.707)}$$

$$s_z = \sigma_z + p \qquad \text{Eq. (H.27)} \qquad \text{(N.708)}$$

$$s_y = \sigma_y + p \qquad \text{Eq. (H.27)} \qquad \text{(N.709)}$$

$$\frac{\partial T_s}{\partial x} = \frac{1}{\rho_s c_s v_s}\left[\beta_s\left(D_x^p\sigma_x + D_z^p\sigma_z\right) + \frac{\tau_i(v_r - v_s)}{t_s}\right] \qquad \text{Eq. (4.211)} \qquad \text{(N.710)}$$

N.2.3.2 Structured system of equations

Values required in differential equations

$$\sigma_x = s_x - p \tag{N.711}$$

$$\sigma_z = s_z - p \tag{N.712}$$

$$p_i = -\sigma_z \tag{N.713}$$

$$\sigma_Y = \sigma_Y(\overline{\epsilon}^p, \overline{D}^p, T_s) \quad \text{by Eqs. (4.50), (4.52), (4.54), (4.56), (4.60) or (4.62)} \tag{N.714}$$

$$\tau_Y = \frac{\sigma_Y}{\sqrt{3}} \tag{N.715}$$

$$z_r = z_r(x) \quad \text{by Secs. 4.6.1, 4.6.2, 4.6.3 or 4.6.4} \tag{N.716}$$

$$\frac{\partial z_r}{\partial x} = \frac{\partial z_r}{\partial x}(x) \quad \text{by Secs. 4.6.1, 4.6.2, 4.6.3 or 4.6.4} \tag{N.717}$$

$$t_s = 2z_r \tag{N.718}$$

$$\tau_i = \tau_a(v_s, v_r, p_i, \tau_Y) \quad \text{by Eqs. (4.123), (4.124) or (4.125)} \tag{N.719}$$

$$\frac{\partial t_s}{\partial x} = 2\frac{\partial z_r}{\partial x} \tag{N.720}$$

$$\frac{\partial \sigma_x}{\partial x} = -\frac{1}{t_s}\left[(\sigma_x + p_i)\frac{\partial t_s}{\partial x} + 2\tau_i\right] \tag{N.721}$$

$$h_{i,s} = h_{i,s}(\overline{\epsilon}^p, \overline{D}^p, T_s) \quad \text{by Eqs. (4.51), (4.53), (4.55), (4.57), (4.61) or (4.63)} \tag{N.722}$$

$$\beta_1 = \frac{1}{\frac{2}{3}\sigma_Y^2\left(1 + \frac{h_{i,s}}{3G_s}\right)} \tag{N.723}$$

$$D_z = \frac{v_s}{t_s}\frac{\partial t_s}{\partial x} \tag{N.724}$$

$$D_x = \frac{\left[2G_s(1 + 3\beta_1 s_x s_z) - 3K_s\right] D_z + 3v_s\frac{\partial \sigma_x}{\partial x}}{2G_s(2 - 3\beta_1 s_x^2) + 3K_s} \tag{N.725}$$

Differential equations (mainly)

$$\Rightarrow \frac{\partial v_s}{\partial x} = D_x \tag{N.726}$$

$$\Rightarrow \frac{\partial s_x}{\partial x} = \frac{2G_s}{3v_s}\left[(2 - 3\beta_1 s_x^2)D_x - (1 + 3\beta_1 s_x s_z)D_z\right] \tag{N.727}$$

$$\Rightarrow \frac{\partial s_z}{\partial x} = \frac{2G_s}{3v_s}\left[-(1 + 3\beta_1 s_x s_z)D_x + (2 - 3\beta_1 s_z^2)D_z\right] \tag{N.728}$$

$$\Rightarrow \frac{\partial p}{\partial x} = -\frac{K_s}{v_s}(D_x + D_z) \tag{N.729}$$

$$\frac{\partial \sigma_z}{\partial x} = \frac{\partial s_z}{\partial x} - \frac{\partial p}{\partial x} \tag{N.730}$$

$$D_x^e = \frac{v_s(1+\nu_s)}{E_s}\left[(1-\nu_s)\frac{\partial \sigma_x}{\partial x} - \nu_s \frac{\partial \sigma_z}{\partial x}\right] \tag{N.731}$$

$$D_z^e = \frac{v_s(1+\nu_s)}{E_s}\left[-\nu_s\frac{\partial \sigma_x}{\partial x} + (1-\nu_s)\frac{\partial \sigma_z}{\partial x}\right] \tag{N.732}$$

$$\Rightarrow \frac{\partial \overline{\epsilon}^p}{\partial x} = \frac{1}{v_s}\sqrt{\frac{2}{3}\left[(D_x - D_x^e)^2 + (D_z - D_z^e)^2\right]} \tag{N.733}$$

$$\Rightarrow \frac{\partial T_s}{\partial x} = \frac{1}{\rho_s c_s v_s}\left[\beta_s\left(D_x^p \sigma_x + D_z^p \sigma_z\right) + \frac{\tau_i(v_r - v_s)}{t_s}\right] \tag{N.734}$$

Values not directly required in differential equations

$$\sigma_y = -(s_x + s_z) - p \tag{N.735}$$

$$\overline{D}^p = v_s \frac{\partial \overline{\epsilon}^p}{\partial x} \tag{N.736}$$

N.2.4 Outlet zone

The underlying and structured systems of equations are identical to those of the mixed inlet zone (Sec. N.2.2).

Appendix O

Calibration of numerical parameters

In this chapter, the *calibration procedure of numerical parameters* in the METALUB model of test 5B-4 (Chap. 3, appendix E.7) is explained in detail while a summarized version can be found in Sec. 5.2.3.

Before studying the influence of the numerical parameters layer by layer based on the full structure in Eq. (5.1), i.e.

$$\begin{Bmatrix} x_{12} \\ \Delta x_1 \\ \Delta x_2 \end{Bmatrix} \Rightarrow \text{tol}_Q \Rightarrow \text{tol}_{\sigma_{\text{out}}} \Rightarrow \begin{Bmatrix} \text{tol}_{t_{\text{out}}} \\ x_{12} \\ x_{23} \\ \Delta\theta_1 \\ \Delta\theta_2 \\ \Delta\theta_3 \\ w^{(0)} \end{Bmatrix} \Rightarrow \begin{Bmatrix} \text{tol}_R \\ \Delta x_{\text{extr},1} \\ \Delta x_{\text{extr},2} \end{Bmatrix} \Rightarrow \begin{Bmatrix} \text{tol}_{\overline{F}_r} \\ \text{tol}_{s_f} \end{Bmatrix} \tag{O.1}$$

this structure can be *further simplified* by assuming that the roll is rigid and circular. In fact, the remaining numerical tolerances should be valid whether the roll is deformable or not[1]:

$$\begin{Bmatrix} x_{12} \\ \Delta x_1 \\ \Delta x_2 \end{Bmatrix} \Rightarrow \text{tol}_Q \Rightarrow \text{tol}_{\sigma_{\text{out}}} \Rightarrow \text{tol}_{t_{\text{out}}} \Rightarrow \begin{Bmatrix} \Delta x_{\text{extr},1} \\ \Delta x_{\text{extr},2} \end{Bmatrix} \Rightarrow \begin{Bmatrix} \text{tol}_{\overline{F}_r} \\ \text{tol}_{s_f} \end{Bmatrix} \tag{O.2}$$

In order *to determine first the numerical parameters* in Eq. (O.2) and then the remaining ones in Eq. (O.1), it is necessary to *run a full METALUB computation of the simplified case*, i.e. with rigid

[1]This statement is not entirely true, since x_{12} depends on the length of the roll bite, which increases with roll flattening. Hence, its value is chosen sufficiently small and its influence is tested again, when roll flattening is taken into account.

circular rolls, to have a prediction of the lubricant flow rate Q, the entry rolling speed v_{in} and the vertical position of the roll axis z_0. These values are not necessarily satisfactory solutions of the full problem after adjusting the numerical parameters but they are realistic values. These three values are required to run a single integration of the roll bite. Then, when the integration parameters have been determined, the tolerance of the lubricant flow rate Q can be studied for the values of v_{in} and z_0, *and so on*. The simplified scenario of the base case in Tab. 5.1 can be found in Tab. O.1. Some *choices* were made to be as systematic as possible:

- The coordinate x_{12} at which the integration step switches from Δx_1 to Δx_2 was chosen equal to -10 mm based on preliminary computations. In the past, it was rare that the roll bite started before $x = -10$ mm for a rigid roll.
- The values of the integration steps Δx_1 and Δx_2 in Tab. O.1 were chosen on purpose. In fact, if the lubricant pressure becomes zero in the roll bite, i.e. before its end, the computation stops and no results in terms of rolling load and forward slip are returned. Hence, it is necessary for all combinations of Δx_1 and Δx_2, which are tested hereafter, that the lubricant pressure does not become negative in the roll bite for the lubricant flow rate Q, which was computed in the simplified base case. Thus, it was necessary to choose a relatively small value for Δx_1 and a relatively big value for Δx_2.
- The tolerances of Q, σ_{out} and t_{out} are equal to those of previous versions of Metalub but they were rounded to the closest decade because determining more precise tolerances in a justified way would be very time-consuming and it would not necessarily improve the results significantly.
- The extraction steps $\Delta x_{extr,1}$ and $\Delta x_{extr,1}$ are equal to 10^{-15}, which is equivalent to extracting the data at all integration steps (and not every 10^{-15} mm). Their values will be determined later on to reduce the data, which are saved to file.

In the following subsections, the influence of the numerical parameters on the results are studied *incrementally*, i.e. first, only by studying the integration of the roll bite, then the adjustment of the lubricant flow rate, and so on. Moreover, *three different sets of numerical parameters* are determined depending on the relative error with respect to the most accurate prediction that can be obtained in an acceptable computation time and with satisfactory accuracy. These errors are $< 0.01\%$ (high accuracy), $< 0.1\%$ (medium accuracy) and $< 1\%$ (reasonable accuracy) for the parameter sets, with high, medium and reasonable accuracy, respectively. In order to present this study as clearly as possible, a color code was introduced for each set and the computed relative errors. These colors are green, yellow, red and dark red for $< 0.01\%$, $< 0.1\%$, $< 1\%$ and $> 1\%$, respectively.

O.1 Integration of the roll bite

To integrate the roll bite, the values of Q, v_{in} and z_0 were determined in the simplified base case of Tab. O.1. For these values and $x_{12} = -10$ mm, the influence of the *integration steps* Δx_1 and

Entity	Parameter	Value	Unit
Roll bite	Type	Full-flooded lub.	-
	Heating by friction	On	-
	Heating by plastic deformation	On	-
Strip material	Name	S2	-
	E_s	210000	MPa
	ν_s	0.3	-
	Law	Johnson-Cook	-
	Viscoplasticity	Off	-
	Thermoplasticity	Off	-
	A	776	MPa
	B	147	MPa
	n	1.52	-
	$\overline{\epsilon}_0^p$	0	-
	ρ_s	$7.850 \cdot 10^{-9}$ [7850]	t/mm^3 [kg/m^3]
	c_s	$500 \cdot 10^6$ [500]	N.mm/(t.°C) [J/(kg.°C)]
	β_s	0.9	-
Strip	t_{in}	0.75	mm
	t_{out}	0.584	mm
	σ_{in}	122.0	MPa
	σ_{out}	184.3	MPa
	$T_{s,\text{in}}$	25	°C
Lubricant	Name	L3	-
	Law	WLF (enhanced)	-
	A_1	49.64	°C
	A_2	0.000365	MPa^{-1}
	b_1	0.00578	MPa^{-1}
	b_2	−0.565	-
	C_1	16.11	-
	C_2	26.00	°C
	η_g	10^6	MPa.s
	$T_g(0)$	−85.96	°C
	T_l	60 (constant)	°C
Interface	Asperity profile	Christensen	-
	R_{q_r}	0.773	μm
	R_{q_s}	0.123	μm
	$\bar{l}$	51.28	μm
	Flattening equation	Wilson-Sheu	-
	γ	9	-
	Friction law	Coulomb-Tresca	-
	μ_C	0.08	-
	μ_T	1	-
	Flow factors ϕ_x and ϕ_s	On	-
	Shear stress factors	Off	-
Roll	Deformation method	Rigid	-
	Deformation mode	Circular	-
	R_0	195.5	mm
	v_r	3291	mm/s
	E_r	210000	MPa
Other numerical parameters	Integration method	RK4	-
	x_{12}	−10	mm
	Δx_1	10^{-3}	mm
	Δx_2	10^{-2}	mm
	tol_Q	10^{-14}	-
	$\text{tol}_{\sigma_{\text{out}}}$	10^{-3}	-
	$\text{tol}_{t_{\text{out}}}$	10^{-3}	-
	$\Delta x_{\text{extr},1}$	10^{-15}	mm
	$\Delta x_{\text{extr},2}$	10^{-15}	mm
	CIEFS step	Off	-

Table O.1: Simplified base case for the numerical parameter calibration. This case represents test 5B-4, which was presented in Chap. 3 and which is detailed in appendix E.7.

Δx_2 on the results is shown[2] in Tab. O.2. Thus, Δx_1 has seemingly no influence on the results. For $\Delta x_1 = 10$ mm (not in Tab. O.2), the integration was, however, not possible. This is due to the fact that the integration step changes not precisely at x_{12} from Δx_1 to Δx_2 but rather when this value is exceeded. Therefore, Δx_1 can take any value provided that the integration step is reduced before reaching significant variations of values in the roll bite. In this case, $\Delta x_1 = 1$ mm is chosen since it provides an idea about rolling values before the bite, while having a negligible computation cost.

Δx_1 [mm]	Δx_2 [mm]	$\overline{F}_r$ [N/mm]	$\Delta\overline{F}_r$ [%]	s_f [%]	Δs_f [%]	σ_{out} [MPa]	$\Delta\sigma_{\text{out}}$ [-]	t_{out} [mm]	Δt_{out} [-]
1E-03	1E-05	5723.6	0.000	4.132	0.000	191.59	0.0E+00	0.584284	0.0E+00
1E-02	1E-05	5723.6	0.000	4.132	0.000	191.59	1.0E-07	0.584284	1.0E-11
1E-01	1E-05	5723.6	0.000	4.132	0.000	191.59	1.0E-07	0.584284	9.4E-12
1E+00	1E-05	5723.6	0.000	4.132	0.000	191.59	8.7E-08	0.584284	2.1E-10
1E-03	1E-04	5723.8	0.004	4.132	0.002	191.57	2.8E-05	0.584284	1.3E-06
1E-02	1E-04	5723.8	0.004	4.132	0.002	191.57	2.9E-05	0.584284	1.3E-06
1E-01	1E-04	5723.8	0.004	4.132	0.002	191.57	2.9E-05	0.584284	1.3E-06
1E+00	1E-04	5723.8	0.004	4.132	0.002	191.57	2.9E-05	0.584284	1.3E-06
1E-03	1E-03	5727.6	0.071	4.131	0.024	191.24	4.6E-04	0.584291	1.3E-05
1E-02	1E-03	5727.6	0.070	4.131	0.024	191.23	4.7E-04	0.584291	1.3E-05
1E-01	1E-03	5727.6	0.070	4.131	0.024	191.23	4.7E-04	0.584291	1.3E-05
1E+00	1E-03	5727.6	0.071	4.131	0.024	191.24	4.6E-04	0.584291	1.3E-05
1E-03	1E-02	5826.4	1.797	4.113	0.449	191.24	4.6E-04	0.584291	1.3E-05
1E-02	1E-02	5826.5	1.798	4.113	0.447	191.23	4.7E-04	0.584291	1.3E-05
1E-01	1E-02	5826.5	1.798	4.113	0.447	191.23	4.7E-04	0.584291	1.3E-05
1E+00	1E-02	5826.3	1.796	4.113	0.447	191.24	4.6E-04	0.584291	1.3E-05

Table O.2: Influence of the integration steps Δx_1 and Δx_2 in a single integration ($x_{12} = -10$ mm, $Q = 0.69806895466161301$ mm^2/s, $v_{\text{in}} = 2670.1204270356079$ mm/s and $z_0 = 195.79141834370725$ mm). The values $\Delta\overline{F}_r$ and Δs_f, and the criterion value Δt_{out} are relative errors with respect to the most accurate result, i.e. $\Delta x_1 = 10^{-3}$ mm and $\Delta x_2 = 10^{-5}$ mm. The criterion value $\Delta\sigma_{\text{out}}$ is computed as follows: $\Delta\sigma_{\text{out}} = |\sigma_x(x_{\text{out}}) - \sigma_{\text{out}}|/\sigma_Y^0$, where $\sigma_Y^0 = 776$ MPa based on Tab. O.1.

Considering the impact of Δx_2, three different values classes can be defined, as already mentioned:

- *high* accuracy, relative error (on average) at most equal to 0.01%: $\Delta x_1 = 1$ mm and $\Delta x_2 = 10^{-5}$ mm;
- *medium* accuracy, relative error (on average) at most equal to 0.1%: $\Delta x_1 = 1$ mm and $\Delta x_2 = 10^{-4}$ mm;
- *reasonable* accuracy, relative error (on average) at most equal to 1%: $\Delta x_1 = 1$ mm and $\Delta x_2 = 10^{-3}$ mm.

Referring to our previous explanations (Sec. 5.2.2), the *variation of the criterion value* (with respect to the exact value) due to inaccuracies in an inner loop of the method, i.e. here, inaccuracies due to the spatial step, should be smaller than the corresponding tolerance. Based on the results

[2]The error percentages $\Delta\overline{F}_r$ or Δs_f and the criterion values $\Delta\sigma_{\text{out}}$ and Δt_{out} were computed based on the full float numbers of $\overline{F}_r$, s_f, σ_{out} and t_{out} while the values of these results in the different tables are limited to a certain number of decimal places.

in Tab. O.2 (blue fields), the tolerances corresponding to the criteria of σ_{out} (Eq. 4.262) and t_{out} (Eq. 4.265) should at minimum be equal to approximately 10^{-7} and 10^{-9}, 10^{-4} and 10^{-5}, and 10^{-3} and 10^{-4}, respectively for the parameter sets with high, medium and reasonable accuracy, if they are rounded to the closest decade.

Concerning the *transition* at x_{12}, it was observed that x_{12} has no significant influence on the results, if it is sufficiently far away from the roll bite and if Δx_1 is sufficiently small, as stated above. For instance, if $\Delta x_1 = 1$ mm, x_{12} has no influence on the result until reaching -6 mm (starting from -10 by integer increments), when the integration is not possible anymore. The influence of x_{12} will be illustrated in Sec. O.6.2 with roll flattening.

O.2 Adjustment of the lubricant flow rate

In a single adjustment loop of the *lubricant flow rate*, v_{in} and z_0 are given by the values which were determined in the simplified base case (Tab. O.1) and Q is adjusted until the criterion in Eq. (4.253) is satisfied. Hence, the results depend on tol_Q in addition to Δx_1, Δx_2 and x_{12}.

Based on the previous parameters sets, the influence of tol_Q is studied for the parameters set with high, medium and reasonable accuracy as shown in Tab. O.3. The values $\text{tol}_Q = 10^{-8}$, $\text{tol}_Q = 10^{-6}$ and $\text{tol}_Q = 10^{-4}$ are selected for the respective sets, with reasonable caution to not fall into a lower accuracy class. It is also important to notice that the relative values in Tab. O.3 were computed with respect to the configuration $\text{tol}_Q = 10^{-14}$ in Tab. O.3a instead of the configuration $\Delta x_1 = 10^{-3}$ mm and $\Delta x_2 = 10^{-5}$ mm in Tab. O.2, to isolate the effect of tol_Q. In fact, the prediction of Q in both cases is different since the value Q of the previous entry speed adjustement loop is used in the full computation (Sec. 4.10.3.1), which is not available in the single adjustment loop of the lubricant flow rate.

Concerning the *condition of the minimum tolerances*, good estimations of $\text{tol}_{\sigma_{\text{out}}}$ and $\text{tol}_{t_{\text{out}}}$ are 10^{-4} and 10^{-6}, 10^{-4} and 10^{-6}, and 10^{-3} and 10^{-5}, respectively for the parameter sets with high, medium and reasonable accuracy.

O.3 Adjustment of the entry strip speed

In a single adjustment loop of the *entry strip speed*, the vertical position of the roll axis z_0 is the only state parameter that is set equal to the value from the resolution of the simplified base case, i.e. v_{in} and Q have to be adjusted. The values of Δx_1, Δx_2, x_{12} and tol_Q were determined in the previous sections. In this section, the influence of the tolerance related to the outlet tension $\text{tol}_{\sigma_{\text{out}}}$ is studied. As mentioned previously, convergence could not be possible if $\text{tol}_{\sigma_{\text{out}}} \leq 10^{-4}$, 10^{-4} or 10^{-3} for the parameter sets with high, medium or reasonable accuracy, in the worst case scenario, by selecting the most limiting conditions from Secs. O.1 and O.2. *This convergence problem due to the interdependence of tolerance actually occurred* for $\text{tol}_{\sigma_{\text{out}}} = 10^{-6}$ in Tab. O.4b, and also for $\text{tol}_{\sigma_{\text{out}}} = 10^{-5}$ in Tab. O.4c. Hence, the real limiting values seem to be much smaller than those which were predicted by gross but save approximations.

tol_Q [-]	$\overline{F}_r$ [N/mm]	$\Delta\overline{F}_r$ [%]	s_f [%]	Δs_f [%]	σ_{out} [MPa]	$\Delta\sigma_{\text{out}}$ [-]	t_{out} [mm]	Δt_{out} [-]
1E-14	5810.8	0.000	4.118	0.000	185.12	0.0E+00	0.584349	0.0E+00
1E-08	5811.1	0.006	4.118	0.001	185.08	5.9E-05	0.584349	2.1E-07
1E-07	5811.1	0.006	4.118	0.001	185.08	6.3E-05	0.584349	1.3E-07
1E-06	5810.8	0.000	4.118	0.001	185.09	3.9E-05	0.584348	3.7E-07
1E-05	5809.5	0.022	4.118	0.006	185.18	6.6E-05	0.584347	2.1E-06
1E-04	5805.8	0.086	4.118	0.021	185.43	4.0E-04	0.584345	7.0E-06
1E-03	5805.8	0.086	4.118	0.021	185.43	4.0E-04	0.584345	7.0E-06
1E-02	5777.1	0.580	4.123	0.135	187.54	3.1E-03	0.584323	4.3E-05

(a) High accuracy ($\Delta x_1 = 1$ mm and $\Delta x_2 = 10^{-5}$ mm).

tol_Q [-]	$\overline{F}_r$ [N/mm]	$\Delta\overline{F}_r$ [%]	s_f [%]	Δs_f [%]	σ_{out} [MPa]	$\Delta\sigma_{\text{out}}$ [-]	t_{out} [mm]	Δt_{out} [-]
1E-14	5810.9	0.002	4.118	0.000	185.11	1.7E-05	0.584349	2.2E-08
1E-08	5811.2	0.006	4.118	0.002	185.08	6.2E-05	0.584349	1.1E-06
1E-07	5811.1	0.006	4.118	0.002	185.07	6.6E-05	0.584349	9.8E-07
1E-06	5811.0	0.003	4.118	0.001	185.08	6.0E-05	0.584349	8.2E-07
1E-05	5809.7	0.019	4.118	0.005	185.16	5.0E-05	0.584348	1.5E-06
1E-04	5807.1	0.063	4.118	0.015	185.34	2.8E-04	0.584346	5.0E-06
1E-03	5807.1	0.063	4.118	0.015	185.34	2.8E-04	0.584346	5.0E-06
1E-02	5777.3	0.576	4.123	0.133	187.52	3.1E-03	0.584324	4.3E-05

(b) Medium accuracy ($\Delta x_1 = 1$ mm and $\Delta x_2 = 10^{-4}$ mm).

tol_Q [-]	$\overline{F}_r$ [N/mm]	$\Delta\overline{F}_r$ [%]	s_f [%]	Δs_f [%]	σ_{out} [MPa]	$\Delta\sigma_{\text{out}}$ [-]	t_{out} [mm]	Δt_{out} [-]
1E-14	5812.0	0.021	4.117	0.011	185.02	1.4E-04	0.584353	7.2E-06
1E-08	5812.3	0.026	4.117	0.011	184.98	1.9E-04	0.584353	7.2E-06
1E-07	5812.3	0.026	4.117	0.011	184.98	1.9E-04	0.584353	7.2E-06
1E-06	5812.1	0.022	4.117	0.010	184.98	1.8E-04	0.584353	6.9E-06
1E-05	5812.1	0.022	4.117	0.010	184.98	1.8E-04	0.584353	6.9E-06
1E-04	5808.6	0.038	4.118	0.003	185.22	1.3E-04	0.584351	3.6E-06
1E-03	5800.2	0.183	4.119	0.032	185.82	9.0E-04	0.584346	3.9E-06
1E-02	5785.4	0.437	4.122	0.096	186.94	2.3E-03	0.584333	2.7E-05

(c) Reasonable accuracy ($\Delta x_1 = 1$ mm and $\Delta x_2 = 10^{-3}$ mm).

Table O.3: Influence of the lubricant flow rate tolerance tol_Q in a single adjustment loop of the lubricant flow rate ($x_{12} = -10$ mm, $v_{\text{in}} = 2670.1204270356079$ mm/s and $z_0 = 195.79141834370725$ mm). The values $\Delta\overline{F}_r$ and Δs_f, and the criterion value Δt_{out} are relative errors with respect to the most accurate result, i.e. $\text{tol}_Q = 10^{-14}$ in Tab. O.3a. The criterion value $\Delta\sigma_{\text{out}}$ is computed as follows: $\Delta\sigma_{\text{out}} = |\sigma_x(x_{\text{out}}) - \sigma_{\text{out}}|/\sigma_Y^0$, where $\sigma_Y^0 = 776$ MPa based on Tab. O.1.

$\text{tol}_{\sigma_{\text{out}}}$ [-]	$\overline{F}_r$ [N/mm]	$\Delta\overline{F}_r$ [%]	s_f [%]	Δs_f [%]	t_{out} [mm]	Δt_{out} [-]	Duration [h:min:s]
1E-06	5814.2	0.000	4.107	0.000	0.584351	0.0E+00	00:09:21
1E-05	5814.2	0.000	4.107	0.001	0.584351	7.9E-09	00:08:23
1E-04	5814.3	0.002	4.107	0.011	0.584351	2.2E-07	00:07:37
1E-03	5813.9	0.006	4.108	0.028	0.584351	4.4E-07	00:06:32
1E-02	5802.7	0.197	4.147	0.975	0.584343	1.4E-05	00:04:36
1E-01	5687.7	2.175	4.561	11.046	0.584265	1.5E-04	00:03:40

(a) High accuracy ($\Delta x_1 = 1$ mm, $\Delta x_2 = 10^{-5}$ mm and $\text{tol}_Q = 10^{-8}$).

$\text{tol}_{\sigma_{\text{out}}}$ [-]	$\overline{F}_r$ [N/mm]	$\Delta\overline{F}_r$ [%]	s_f [%]	Δs_f [%]	t_{out} [mm]	Δt_{out} [-]	Duration [h:min:s]
1E-06	/	/	/	/	/	/	/
1E-05	5814.0	0.003	4.107	0.001	0.584351	2.5E-07	00:00:55
1E-04	5814.2	0.001	4.107	0.003	0.584351	5.0E-07	00:00:44
1E-03	5813.6	0.010	4.109	0.037	0.584350	7.8E-07	00:00:38
1E-02	5802.6	0.199	4.147	0.984	0.584343	1.4E-05	00:00:24
1E-01	5687.4	2.181	4.561	11.056	0.584265	1.5E-04	00:00:20

(b) Medium accuracy ($\Delta x_1 = 1$ mm, $\Delta x_2 = 10^{-4}$ mm and $\text{tol}_Q = 10^{-6}$).

$\text{tol}_{\sigma_{\text{out}}}$ [-]	$\overline{F}_r$ [N/mm]	$\Delta\overline{F}_r$ [%]	s_f [%]	Δs_f [%]	t_{out} [mm]	Δt_{out} [-]	Duration [h:min:s]
1E-06	/	/	/	/	/	/	/
1E-05	/	/	/	/	/	/	/
1E-04	5810.3	0.067	4.104	0.070	0.584350	2.2E-06	00:00:03
1E-03	5812.9	0.022	4.096	0.266	0.584350	1.8E-06	00:00:02
1E-02	5796.6	0.303	4.148	0.995	0.584343	1.4E-05	00:00:02
1E-01	5684.8	2.226	4.561	11.060	0.584263	1.5E-04	00:00:02

(c) Reasonable accuracy ($\Delta x_1 = 1$ mm, $\Delta x_2 = 10^{-3}$ mm and $\text{tol}_Q = 10^{-4}$).

Table O.4: Influence of the front tension tolerance $\text{tol}_{\sigma_{\text{out}}}$ in a single adjustment loop of the strip entry speed ($x_{12} = -10$ mm and $z_0 = 195.79141834370725$ mm). The values $\Delta\overline{F}_r$ and Δs_f, and the criterion value Δt_{out} are relative errors with respect to the most accurate result, i.e. $\text{tol}_{\sigma_{\text{out}}} = 10^{-6}$ in Tab. O.4a.

The relative errors in Tab. O.4 were computed with respect to the most accurate computation in this table instead of the values in Tab. O.2 ($\Delta x_1 = 10^{-3}$ mm and $\Delta x_2 = 10^{-5}$ mm) because the final values of Q and v_{in} are different in both cases. This difference is due to different initial values of Q and v_{in} in the adjustment loops. In the full computation, their values are those of the previous adjustment loop of vertical roll position, which is not available in the isolated single adjustment loop of the strip speed. Based on the relative errors in Tab. O.4, 10^{-5}, 10^{-4} and 10^{-3} seem to be adequate values of $\text{tol}_{\sigma_{\text{out}}}$ in the numerical parameters sets with high, medium and reasonable accuracy, respectively.

Concerning the *tolerance interdependence criterion*, Tab. O.4 suggests that $\text{tol}_{t_{\text{out}}}$ should be greater than 10^{-8}, 10^{-6} and 10^{-5}, if computations are executed with high, medium and reasonable accuracy.

O.4 Adjustment of the vertical roll position

When the *vertical roll position* is adjusted, the computation is equivalent to a full METALUB computation without roll flattening. Tab. O.5 shows that $\text{tol}_{t_{\text{out}}}$ has to be equal to 10^{-6}, 10^{-5} and 10^{-4} to keep the computation errors below 0.01%, 0.1% and 1% on average, respectively. These values are also not in conflict with their limits that were previously chosen (Secs. O.1, O.2 and O.3) to prevent potential non-convergence due to the nested loop structure.

Interestingly, the computation time (duration) in Tab. O.5b for $\text{tol}_{t_{\text{out}}} = 10^{-7}$ and, more significantly, in Tab. O.5 for $\text{tol}_{t_{\text{out}}} = 10^{-7}$ show a significant increase with respect to the computations for greater values of $\text{tol}_{t_{\text{out}}}$. This clearly illustrates the *influence of the tolerances on the convergence behavior*. Strict tolerances of an outer loop are only effective in terms of computation time and accuracy when the tolerances of inner loops are also relatively strict.

It is also interesting to notice as an intermediate conclusion that a METALUB computation without roll flattening and with a numerical error smaller than about 1% (for $\overline{F}_r$ and s_f) is *on average 4 seconds long*.

O.5 Determination of the data extraction steps

The *extraction steps* $\Delta x_{\text{extr},1}$ and $\Delta x_{\text{extr},2}$ determine how often data are extracted during the final roll bite integration in order to save the evolution of results, like the lubricant pressure, to file, and to compute synthetic rolling parameters, like the rolling force (Sec. 4.10.6). Previously, $\Delta x_{\text{extr},1}$ and $\Delta x_{\text{extr},2}$ were both equal to 10^{-15} mm in order to extract the data at all integration steps. This required, however, large amounts of storage space and it increased the computation time of other post-processing operations. Hence, it it necessary to determine what values $\Delta x_{\text{extr},1}$ and $\Delta x_{\text{extr},2}$ should take to reduce the stored data while satisfying the previous accuracy criteria, i.e. the relative error of the rolling force per width $\overline{F}_r$ and the forward slip s_f should be smaller than 0.01%, 0.1% and 1%, respectively for each numerical parameter set.

$\text{tol}_{t_{\text{out}}}$ [-]	$\overline{F}_r$ [N/mm]	$\Delta\overline{F}_r$ [%]	s_f [%]	Δs_f [%]	Duration [h:min:s]
1E-07	5822.7	0.000	4.117	0.000	00:33:51
1E-06	5822.7	0.000	4.117	0.001	00:31:13
1E-05	5822.6	0.002	4.117	0.004	00:29:39
1E-04	5821.6	0.020	4.116	0.033	00:24:18
1E-03	5813.5	0.158	4.106	0.257	00:17:23
1E-02	5785.8	0.634	4.074	1.031	00:09:29

(a) High accuracy ($\Delta x_1 = 1$ mm, $\Delta x_2 = 10^{-5}$ mm, $\text{tol}_Q = 10^{-8}$ and $\text{tol}_{\sigma_{\text{out}}} = 10^{-5}$).

$\text{tol}_{t_{\text{out}}}$ [-]	$\overline{F}_r$ [N/mm]	$\Delta\overline{F}_r$ [%]	s_f [%]	Δs_f [%]	Duration [h:min:s]
1E-07	5822.6	0.003	4.117	0.002	00:02:26
1E-06	5822.4	0.006	4.117	0.002	00:02:02
1E-05	5822.0	0.012	4.117	0.008	00:01:49
1E-04	5821.7	0.018	4.115	0.045	00:01:38
1E-03	5813.4	0.161	4.106	0.259	00:01:15
1E-02	5785.5	0.640	4.075	1.011	00:00:41

(b) Medium accuracy ($\Delta x_1 = 1$ mm, $\Delta x_2 = 10^{-4}$ mm, $\text{tol}_Q = 10^{-6}$ and $\text{tol}_{\sigma_{\text{out}}} = 10^{-4}$).

$\text{tol}_{t_{\text{out}}}$ [-]	$\overline{F}_r$ [N/mm]	$\Delta\overline{F}_r$ [%]	s_f [%]	Δs_f [%]	Duration [h:min:s]
1E-07	5819.1	0.063	4.120	0.070	00:00:40
1E-06	5819.4	0.058	4.120	0.069	00:00:06
1E-05	5817.4	0.092	4.119	0.048	00:00:05
1E-04	5822.5	0.003	4.111	0.149	00:00:04
1E-03	5810.5	0.210	4.108	0.225	00:00:03
1E-02	5784.7	0.653	4.069	1.157	00:00:02

(c) Reasonable accuracy ($\Delta x_1 = 1$ mm, $\Delta x_2 = 10^{-3}$ mm, $\text{tol}_Q = 10^{-4}$ and $\text{tol}_{\sigma_{\text{out}}} = 10^{-3}$).

Table O.5: Influence of the final thickness tolerance $\text{tol}_{t_{\text{out}}}$ in a single adjustment loop of the vertical roll position ($x_{12} = -10$ mm). The values $\Delta\overline{F}_r$ and Δs_f are relative errors with respect to the most accurate result, i.e. $\text{tol}_{t_{\text{out}}} = 10^{-7}$ in Tab. O.5a.

Since the number of integration points before the roll bite is relatively low by the choice of Δx_1, it was decided that the data at all these points can be extracted, i.e. $\Delta x_{\text{extr},1} = \Delta x_1 = 1$ mm. In regard to this choice, Tab. O.6 shows that $\Delta x_{\text{extr},2}$ should be equal to 0.01 mm to satisfy the accuracy criteria. Relative errors were computed with respect to the corresponding configurations in Tab. O.5 to isolate the influence of $\Delta x_{\text{extr},2}$ (strictly). The *relative error of the forward slip* was not added to this table since it is zero. In fact, its value depends on the speed of the strip at the last integration point, which is extracted by default to compute the forward slip.

$\Delta x_{\text{extr},2}$ [mm]	$\overline{F}_r$ [N/mm]	$\Delta\overline{F}_r$ [%]
1E-05	5822.8	0.000
1E-04	5822.8	0.000
1E-03	5822.8	0.000
1E-02	5822.8	0.002
1E-01	5832.0	0.159

(a) High accuracy ($\Delta x_1 = 1$ mm, $\Delta x_2 = 10^{-5}$ mm, $\text{tol}_Q = 10^{-8}$, $\text{tol}_{\sigma_{\text{out}}} = 10^{-5}$ and $\text{tol}_{t_{\text{out}}} = 10^{-6}$). The values $\Delta\overline{F}_r$ and Δs_f are relative errors with respect to the configuration for $\text{tol}_{t_{\text{out}}} = 10^{-6}$ in Tab. O.5a.

$\Delta x_{\text{extr},2}$ [mm]	$\overline{F}_r$ [N/mm]	$\Delta\overline{F}_r$ [%]
1E-04	5822.0	0.006
1E-03	5822.0	0.006
1E-02	5822.1	0.005
1E-01	5831.3	0.152

(b) Medium accuracy ($\Delta x_1 = 1$ mm, $\Delta x_2 = 10^{-4}$ mm, $\text{tol}_Q = 10^{-6}$, $\text{tol}_{\sigma_{\text{out}}} = 10^{-4}$ and $\text{tol}_{t_{\text{out}}} = 10^{-5}$). The values $\Delta\overline{F}_r$ and Δs_f are relative errors with respect to the configuration for $\text{tol}_{t_{\text{out}}} = 10^{-5}$ in Tab. O.5b.

$\Delta x_{\text{extr},2}$ [mm]	$\overline{F}_r$ [N/mm]	$\Delta\overline{F}_r$ [%]
1E-03	5822.6	0.000
1E-02	5822.6	0.002
1E-01	5831.9	0.160

(c) Reasonable accuracy ($\Delta x_1 = 1$ mm, $\Delta x_2 = 10^{-3}$ mm, $\text{tol}_Q = 10^{-4}$, $\text{tol}_{\sigma_{\text{out}}} = 10^{-3}$ and $\text{tol}_{t_{\text{out}}} = 10^{-4}$). The values $\Delta\overline{F}_r$ and Δs_f are relative errors with respect to the configuration for $\text{tol}_{t_{\text{out}}} = 10^{-6}$ in Tab. O.5c.

Table O.6: Influence of the extraction step $\Delta x_{\text{extr},2}$ ($x_{12} = -10$ mm, $\Delta x_{\text{extr},1} = 1$ mm).

O.6 Adjustment of the roll profile

In the previous subsections, the numerical parameters were determined in such a way that the relative errors of the rolling force per width $\overline{F}_r$ and the forward slip s_f with respect to the most accurate computation without roll flattening are on average smaller than 0.01%, 0.1% and 1% depending on the parameter set. In this section, the values of the *numerical parameters related to the roll flattening* are chosen to maintain these conditions.

Roll flattening is predicted by Meindl's method (Sec. 4.6.4), which is the most accurate method that is currently implemented in METALUB. This method is based on 7 parameters, i.e. tol_R, x_{12}, x_{23}, $\Delta\theta_1$, $\Delta\theta_2$, $\Delta\theta_3$ and $w^{(0)}$.

The first parameter is the tolerance of the roll flattening loop tol_R (in Eq. 4.273), which is calibrated in the first of the two following subsections. This calibration is only possible by choosing a very fine roll discretization to isolate the effect of the tolerance. The discretization is

parameterized by the 5 following parameters of the previous ones, i.e. x_{12}, x_{23}, $\Delta\theta_1$, $\Delta\theta_2$ and $\Delta\theta_3$. Their calibration is described in the second subsection. Finally, the last parameter is the constant relaxation coefficient (Sec. 4.10.3.4). This coefficient is assumed to be equal to 0.5, which is the immediate choice after it turned out that the convergence with $w^{(0)} = 1$, i.e. without relaxations, is either not possible or very slow.

O.6.1 Calibration of the roll flattening tolerance

In order to calibrate the *roll flattening tolerance* tol_R exclusively, it is important to limit the influence of the roll discretization. Thus, relatively strict values were chosen for the roll discretization as mentioned in Tab. O.7. The reason behind these choices are explained in the following section. Based on Tab. O.7, the roll flattening tolerances should be equal to 10^{-8}, 10^{-7} and 10^{-6} to obtain predictions with high, moderate and reasonable accuracy.

It is interesting to notice that the satisfaction of the criterion with the previous tolerances became only possible after restarting the adjustment loop of the strip speed with the speed prediction of the previous vertical position iteration, thus starting from a configuration which is already closer to the solution than the initial speed prediction (Sec. 4.10.3.2). In other words, these tolerances could not be satisfied with old versions of the METALUB model.

O.6.2 Calibration of the roll discretization

The parameters of the roll discretization are x_{12}, x_{23}, $\Delta\theta_1$, $\Delta\theta_2$ and $\Delta\theta_3$, as stated before. The parameters x_{12} and x_{23} determine the coordinates of the transition from zone 1 to zone 2 and from zone 2 to zone 3, respectively. In these different zones, the roll is discretized by the angular increments $\Delta\theta_1$, $\Delta\theta_2$ and $\Delta\theta_3$, respectively. It can be expected that $\Delta\theta_2$ should be much smaller than the other angular increments since the roll bite is supposed to be located between x_{12} and x_{23}.

Although x_{12} of the roll discretization can be different from x_{12} of the spatial discretization, which is used with the Runge-Kutta 4 integrator (Sec. 4.10.1.2 and Eq. 4.218), they are assumed to be equal since they define the same location, i.e. the position where the evolutions of the key unknowns become significant at the entry of the roll bite. This is also the reason why the same nomenclature was used. As indicated previously, $x_{12} = -10$ mm and its influence on the results is studied later on in this section. While x_{12} defines the entry position of the roll bite, x_{23} defines the exit position with some margin. A save estimate of x_{23} is 5 mm as will be shown hereafter.

Concerning the *angular discretization*, it seems coherent to say that $\Delta\theta_1$ and $\Delta\theta_3$ have a negligible influence on the results provided that x_{12} and x_{23} were chosen correctly, since the interface pressure and the interface shear stress are negligible outside these bounds. Previously, in the study of the roll flattening tolerance, $\Delta\theta_1$ and $\Delta\theta_3$ were therefore equal to the relatively coarse value of 0.1°. Tab. O.8 shows, however, that even coarser values are acceptable, since only $\Delta\theta_2$ has a significant influence on the results. The value of 1° is chosen for $\Delta\theta_1$ and $\Delta\theta_2$ due to its limited additional

tol_R [-]	$\overline{F}_r$ [N/mm]	$\Delta\overline{F}_r$ [%]	s_f [%]	Δs_f [%]	Duration [h:min:s]
1E-09	8638.3	0.000	4.816	0.000	03:03:45
1E-08	8638.2	0.001	4.816	0.003	02:52:51
1E-07	8637.9	0.005	4.817	0.020	02:49:58
1E-06	8646.3	0.093	4.838	0.450	02:36:58
1E-05	8669.6	0.363	4.876	1.239	02:27:20
1E-04	8690.3	0.602	5.067	5.198	01:52:54

(a) High accuracy ($\Delta x_1 = 1$ mm, $\Delta x_2 = 10^{-5}$ mm, $\text{tol}_Q = 10^{-8}$, $\text{tol}_{\sigma_{\text{out}}} = 10^{-5}$ and $\text{tol}_{t_{\text{out}}} = 10^{-6}$).

tol_R [-]	$\overline{F}_r$ [N/mm]	$\Delta\overline{F}_r$ [%]	s_f [%]	Δs_f [%]	Duration [h:min:s]
1E-09	/	/	/	/	/
1E-08	8636.2	0.024	4.817	0.007	00:09:29
1E-07	8637.0	0.015	4.817	0.006	00:07:58
1E-06	8644.3	0.070	4.838	0.447	00:06:45
1E-05	8668.1	0.345	4.876	1.236	00:06:10
1E-04	8690.2	0.601	5.065	5.169	00:04:32

(b) Medium accuracy ($\Delta x_1 = 1$ mm, $\Delta x_2 = 10^{-4}$ mm, $\text{tol}_Q = 10^{-6}$, $\text{tol}_{\sigma_{\text{out}}} = 10^{-4}$ and $\text{tol}_{t_{\text{out}}} = 10^{-5}$).

tol_R [-]	$\overline{F}_r$ [N/mm]	$\Delta\overline{F}_r$ [%]	s_f [%]	Δs_f [%]	Duration [h:min:s]
1E-09	/	/	/	/	/
1E-08	/	/	/	/	/
1E-07	8632.7	0.065	4.810	0.139	00:01:02
1E-06	8638.9	0.007	4.837	0.421	00:00:51
1E-05	8661.9	0.273	4.861	0.923	00:00:44
1E-04	8678.3	0.464	5.061	5.088	00:00:28

(c) Reasonable accuracy ($\Delta x_1 = 1$ mm, $\Delta x_2 = 10^{-3}$ mm, $\text{tol}_Q = 10^{-4}$, $\text{tol}_{\sigma_{\text{out}}} = 10^{-3}$ and $\text{tol}_{t_{\text{out}}} = 10^{-4}$).

Table O.7: Influence of the roll flattening tolerance tol_R ($x_{12} = -10$ mm, $\Delta x_{\text{extr},1} = 1$ mm, $\Delta x_{\text{extr},2} = 10^{-2}$ mm, $x_{23} = 5$ mm, $\Delta\theta_1 = \Delta\theta_3 = 10^{-1}$ °, $\theta_2 = 10^{-3}$ ° and $w^{(0)} = 0.5$). The values $\Delta\overline{F}_r$ and Δs_f are relative errors with respect to the most accurate result, i.e. $\text{tol}_R = 10^{-9}$ in Tab. O.7a.

computation cost for a relatively accurate representation of the roll outside the roll bite, which is, however, not necessarily required.

To study the *influence of* $\Delta\theta_2$, half decades were introduced since the possible range of this parameter is relatively small. On the one hand, choosing values smaller than $\Delta\theta_2 = 0.001°$ are inefficient due to the important memory requirement of the influence function computation[3]. On the other hand, 0.1° corresponds to an equivalent arc length of about 0.34 mm, which is very coarse when the roll bite has a length of about 10 mm. Based on Tab. O.8, appropriate values of $\Delta\theta_2$ are 0.001°, 0.005° and 0.005°, respectively, for the parameter sets to obtain highly, moderately and reasonably accurate predictions. According to the previous definitions of these sets and the values in Tab. O.8, $\Delta\theta_2$ could even take the value 0.05°, which is relatively coarse. This coarseness can easily cause the non-convergence of the computation considering that the roll flattening tolerance is relatively small, even in the case with reasonable accuracy. To improve the convergence behavior, 0.005° was chosen instead of 0.01° or even 0.05°. One should notice that the resulting computation overhead is negligible (Tab. O.8). Finally, it is necessary to mention that the *relaxation coefficient* had to be reduced from 0.5 to 0.4 in some scenarios in Tab. O.8b. Indeed, it might happen that an adjustment loop of the strip speed does not converge. Whether this is due to a strong deformation of the roll as explained in Sec. 4.10.3.4 or another cause is unclear. Nevertheless, *this non-convergence can usually be solved by reducing the relaxation coefficient*, which suggests the first explanation to be true.

Concerning the parameters x_{12} (discretization of the roll bite and of the roll) and x_{23}, Tabs. O.9 and O.10 show that they have only a negligible influence on the results provided that they delimit the roll bite appropriately. Interestingly, these tables also show that the error limits of 0.001%, 0.01% and 0.1% are satisfied, respectively for the parameters sets with highly, moderately and reasonably accurate results. Moreover, the computation time can be significantly reduced, when the fine discretization zone is reduced. While this influence can be seen for x_{12} in Tab. O.9, it is not shown in Tab. O.10 for x_{23} because the integration generally ends before x_{23}, thus not requiring additional computation time when x_{23} increases. Hereafter, x_{12} and x_{23} are respectively equal to −10 mm and 5 mm in order to anticipate more important roll flattening than in the current rolling scenario (Tab. 5.1).

Finally, the *computation time* with the reasonable parameter set is only 13 seconds long. Hence, a relaxation scheme with a constant relaxation coefficient $w^{(0)} = 0.5$ seems to be sufficient at the current stage of development.

[3]These functions are precomputed at the beginning of a METALUB computation in order to not have to compute them at each update of the roll profile. Since the required memory space is $\mathcal{O}(n^2)$, where n is the number of discretization points of the roll, the RAM memory limit can be easily exceeded when $\Delta\theta_2$ takes values smaller than 0.001°.

$\Delta\theta_1, \Delta\theta_3$ [°]	$\Delta\theta_2$ [°]	$\overline{F}_r$ [N/mm]	$\Delta\overline{F}_r$ [%]	s_f [%]	Δs_f [%]	Duration [h:min:s]
0.001	0.1	8638.2	0.001	4.816	0.003	03:06:16
0.005	0.1	8638.6	0.003	4.818	0.034	03:05:41
0.01	0.1	8639.1	0.009	4.823	0.147	03:26:15
0.05	0.1	8629.6	0.100	4.833	0.347	03:30:42
0.001	1	8638.2	0.000	4.816	0.005	03:00:37
0.005	1	8638.6	0.004	4.818	0.034	03:18:34
0.01	1	8639.1	0.010	4.823	0.149	03:10:34
0.05	1	8629.7	0.099	4.833	0.346	03:08:14
0.001	10	8638.2	0.000	4.816	0.005	02:39:44
0.005	10	8638.6	0.004	4.818	0.034	02:49:16
0.01	10	8639.1	0.010	4.823	0.149	02:41:21
0.05	10	8629.7	0.099	4.833	0.346	02:59:06

(a) High accuracy ($\Delta x_1 = 1$ mm, $\Delta x_2 = 10^{-5}$ mm, $\text{tol}_Q = 10^{-8}$, $\text{tol}_{\sigma_{\text{out}}} = 10^{-5}$, $\text{tol}_{t_{\text{out}}} = 10^{-6}$ and $\text{tol}_R = 10^{-7}$).

$\Delta\theta_1, \Delta\theta_3$ [°]	$\Delta\theta_2$ [°]	$\overline{F}_r$ [N/mm]	$\Delta\overline{F}_r$ [%]	s_f [%]	Δs_f [%]	Duration [h:min:s]
0.001	0.1	8637.0	0.015	4.817	0.006	00:06:39
0.005	0.1	8636.0	0.027	4.818	0.037	00:06:23
0.01	0.1	8637.4	0.010	4.824	0.164	00:06:00*
0.05	0.1	8629.0	0.108	4.834	0.377	00:06:58
0.001	1	8637.0	0.014	4.818	0.028	00:06:48*
0.005	1	8637.9	0.005	4.818	0.039	00:05:47
0.01	1	8639.0	0.008	4.824	0.167	00:05:26
0.05	1	8627.7	0.123	4.834	0.369	00:05:35*
0.001	10	8637.0	0.014	4.818	0.028	00:05:39*
0.005	10	8637.9	0.005	4.818	0.039	00:05:47
0.01	10	8639.0	0.008	4.824	0.167	00:05:28
0.05	10	8627.7	0.123	4.834	0.369	00:05:10*

(b) Medium accuracy ($\Delta x_1 = 1$ mm, $\Delta x_2 = 10^{-4}$ mm, $\text{tol}_Q = 10^{-6}$, $\text{tol}_{\sigma_{\text{out}}} = 10^{-4}$, $\text{tol}_{t_{\text{out}}} = 10^{-5}$ and $\text{tol}_R = 10^{-7}$). The asterisk ($*$) in some duration fields indicates that the roll relaxation coefficient $w^{(0)}$ had to be reduced from 0.5 to 0.4 to converge.

$\Delta\theta_1, \Delta\theta_3$ [°]	$\Delta\theta_2$ [°]	$\overline{F}_r$ [N/mm]	$\Delta\overline{F}_r$ [%]	s_f [%]	Δs_f [%]	Duration [h:min:s]
0.001	0.1	8638.9	0.007	4.837	0.421	00:00:50
0.005	0.1	8632.7	0.064	4.821	0.105	00:00:19
0.01	0.1	8636.7	0.019	4.834	0.376	00:00:17
0.05	0.1	8633.1	0.059	4.837	0.434	00:00:16
0.001	1	8632.8	0.064	4.820	0.077	00:00:33
0.005	1	8638.0	0.003	4.826	0.208	00:00:13
0.01	1	8637.2	0.013	4.833	0.347	00:00:14
0.05	1	8627.7	0.122	4.843	0.547	00:00:14
0.001	10	8632.8	0.064	4.820	0.077	00:00:33
0.005	10	8638.0	0.003	4.826	0.208	00:00:13
0.01	10	8637.2	0.013	4.833	0.347	00:00:14
0.05	10	8627.7	0.122	4.843	0.547	00:00:14

(c) Reasonable accuracy ($\Delta x_1 = 1$ mm, $\Delta x_2 = 10^{-3}$ mm, $\text{tol}_Q = 10^{-4}$, $\text{tol}_{\sigma_{\text{out}}} = 10^{-3}$, $\text{tol}_{t_{\text{out}}} = 10^{-4}$ and $\text{tol}_R = 10^{-6}$).

Table O.8: Influence of the angular discretization parameters $\Delta\theta_1 = \Delta\theta_3$ and $\Delta\theta_2$ ($x_{12} = -10$ mm, $\Delta x_{\text{extr},1} = 1$ mm, $\Delta x_{\text{extr},2} = 10^{-2}$ mm, $x_{23} = 5$ mm, and $w^{(0)} = 0.5$). The values $\Delta\overline{F}_r$ and Δs_f are relative errors with respect to the most accurate result, i.e. $\text{tol}_R = 10^{-9}$ in Tab. O.7a.

x_{12} [mm]	$\overline{F}_r$ [N/mm]	$\Delta\overline{F}_r$ [%]	s_f [%]	Δs_f [%]	Duration [h:min:s]
-15	8638.0	0.003	4.817	0.008	06:28:25
-14	8638.0	0.004	4.817	0.010	05:36:49
-13	8638.1	0.002	4.817	0.006	05:15:46
-12	8637.8	0.006	4.817	0.013	04:31:13
-11	8638.0	0.003	4.817	0.009	04:00:05
-10	8638.2	0.000	4.816	0.005	02:44:52
-9	8638.2	0.001	4.817	0.011	02:14:03
-8	8638.4	0.002	4.817	0.019	01:42:13
-7	8632.0	0.073	4.810	0.126	01:00:09
-6	/	/	/	/	/

(a) High accuracy ($\Delta x_1 = 1$ mm, $\Delta x_2 = 10^{-5}$ mm, $\text{tol}_Q = 10^{-8}$, $\text{tol}_{\sigma_{\text{out}}} = 10^{-5}$, $\text{tol}_{t_{\text{out}}} = 10^{-6}$, $\text{tol}_R = 10^{-8}$, $\Delta\theta_1 = \Delta\theta_3 = 1°$ and $\Delta\theta_2 = 0.001°$).

x_{12} [mm]	$\overline{F}_r$ [N/mm]	$\Delta\overline{F}_r$ [%]	s_f [%]	Δs_f [%]	Duration [h:min:s]
-15	8636.0	0.026	4.819	0.048	00:11:49
-14	8637.1	0.014	4.818	0.026	00:11:15
-13	8638.5	0.002	4.817	0.017	00:09:48
-12	8638.3	0.000	4.817	0.022	00:09:16
-11	8637.5	0.009	4.818	0.033	00:07:46
-10	8637.9	0.005	4.818	0.039	00:06:19
-9	8639.0	0.008	4.818	0.033	00:05:08
-8	8637.4	0.010	4.819	0.062	00:03:49
-7	8631.9	0.074	4.811	0.100	00:02:35
-6	/	/	/	/	/

(b) Medium accuracy ($\Delta x_1 = 1$ mm, $\Delta x_2 = 10^{-4}$ mm, $\text{tol}_Q = 10^{-6}$, $\text{tol}_{\sigma_{\text{out}}} = 10^{-4}$, $\text{tol}_{t_{\text{out}}} = 10^{-5}$, $\text{tol}_R = 10^{-7}$, $\Delta\theta_1 = \Delta\theta_3 = 1°$ and $\Delta\theta_2 = 0.005°$).

x_{12} [mm]	$\overline{F}_r$ [N/mm]	$\Delta\overline{F}_r$ [%]	s_f [%]	Δs_f [%]	Duration [h:min:s]
-15	8635.4	0.033	4.827	0.227	00:00:25
-14	8638.0	0.003	4.820	0.085	00:00:23
-13	8647.5	0.107	4.813	0.066	00:00:22
-12	8627.6	0.123	4.828	0.247	00:00:19
-11	8629.9	0.097	4.819	0.057	00:00:17
-10	8638.0	0.003	4.826	0.208	00:00:14
-9	8623.0	0.177	4.812	0.096	00:00:13
-8	8638.3	0.001	4.826	0.212	00:00:09
-7	8626.6	0.135	4.815	0.030	00:00:06
-6	/	/	/	/	/

(c) Reasonable accuracy ($\Delta x_1 = 1$ mm, $\Delta x_2 = 10^{-3}$ mm, $\text{tol}_Q = 10^{-4}$, $\text{tol}_{\sigma_{\text{out}}} = 10^{-3}$, $\text{tol}_{t_{\text{out}}} = 10^{-4}$, $\text{tol}_R = 10^{-6}$, $\Delta\theta_1 = \Delta\theta_3 = 1°$ and $\Delta\theta_2 = 0.005°$).

Table O.9: Influence of position x_{12} at which the fine discretization of the roll bite and the roll starts ($\Delta x_{\text{extr},1} = 1$ mm, $\Delta x_{\text{extr},2} = 10^{-2}$ mm, $x_{23} = 5$ mm, and $w^{(0)} = 0.5$). The values $\Delta\overline{F}_r$ and Δs_f are relative errors with respect to the most accurate result, i.e. $\text{tol}_R = 10^{-9}$ in Tab. O.7a.

x_{23} [mm]	$\overline{F}_r$ [N/mm]	$\Delta\overline{F}_r$ [%]	s_f [%]	Δs_f [%]	Duration [h:min:s]
5	8638.2	0.000	4.816	0.005	03:08:52
4	8638.2	0.000	4.816	0.005	03:07:54
3	8638.2	0.000	4.816	0.005	03:08:20
2	/	/	/	/	/
1	7092.6	17.894	5.542	15.065	02:32:14
0	6038.6	30.095	6.521	35.395	03:09:11

(a) High accuracy ($\Delta x_1 = 1$ mm, $\Delta x_2 = 10^{-5}$ mm, $\text{tol}_Q = 10^{-8}$, $\text{tol}_{\sigma_{\text{out}}} = 10^{-5}$, $\text{tol}_{t_{\text{out}}} = 10^{-6}$, $\text{tol}_R = 10^{-8}$, $\Delta\theta_1 = \Delta\theta_3 = 1°$ and $\Delta\theta_2 = 0.001°$).

x_{23} [mm]	$\overline{F}_r$ [N/mm]	$\Delta\overline{F}_r$ [%]	s_f [%]	Δs_f [%]	Duration [h:min:s]
5	8637.9	0.005	4.818	0.039	00:06:09
4	8637.9	0.005	4.818	0.039	00:06:08
3	8637.9	0.005	4.818	0.039	00:06:06
2	/	/	/	/	/
1	7109.7	17.696	5.539	15.004	00:05:28
0	6028.4	30.213	6.553	36.054	00:06:46

(b) Medium accuracy ($\Delta x_1 = 1$ mm, $\Delta x_2 = 10^{-4}$ mm, $\text{tol}_Q = 10^{-6}$, $\text{tol}_{\sigma_{\text{out}}} = 10^{-4}$, $\text{tol}_{t_{\text{out}}} = 10^{-5}$, $\text{tol}_R = 10^{-7}$, $\Delta\theta_1 = \Delta\theta_3 = 1°$ and $\Delta\theta_2 = 0.005°$).

x_{12} [mm]	$\overline{F}_r$ [N/mm]	$\Delta\overline{F}_r$ [%]	s_f [%]	Δs_f [%]	Duration [h:min:s]
5	8638.0	0.003	4.826	0.208	00:00:13
4	8638.0	0.003	4.826	0.208	00:00:13
3	8638.0	0.003	4.826	0.208	00:00:13
2	7885.6	8.713	5.255	9.102	00:00:45
1	7104.5	17.756	5.542	15.059	00:00:13
0	6019.1	30.321	6.554	36.079	00:00:10

(c) Reasonable accuracy ($\Delta x_1 = 1$ mm, $\Delta x_2 = 10^{-3}$ mm, $\text{tol}_Q = 10^{-4}$, $\text{tol}_{\sigma_{\text{out}}} = 10^{-3}$, $\text{tol}_{t_{\text{out}}} = 10^{-4}$, $\text{tol}_R = 10^{-6}$, $\Delta\theta_1 = \Delta\theta_3 = 1°$ and $\Delta\theta_2 = 0.005°$).

Table O.10: Influence of position x_{23} at which the fine discretization of the roll bite and the roll ends ($x_{12} = -10$ mm, $\Delta x_{\text{extr},1} = 1$ mm, $\Delta x_{\text{extr},2} = 10^{-2}$ mm, and $w^{(0)} = 0.5$). The values $\Delta\overline{F}_r$ and Δs_f are relative errors with respect to the most accurate result, i.e. $\text{tol}_R = 10^{-9}$ in Tab. O.7a.

Appendix P

Additional METALUB validation cases

The following validation cases, i.e. Tests 10B, 14A and 14B are added to this appendix since they were analyzed by a physical mechanism, i.e. starvation, which probably is not the real underlying mechanism. In fact, a pure oil was applied in these tests so that starvation is unlikely to occur, provided that enough oil was sprayed onto the strip. Moreover, the lubricant shear stress was neglected, although it seems reasonable that this stress becomes more predominant, when the viscosity is relatively important, like in these tests (lubricant L1).

Despite these inconsistencies, these tests further highlight the *necessity of a thermal model, which includes the rolls*, to predict the lubricant temperature, and a *model of micro-plastohydrodynamic/static lubrication* to compute the decrease of friction with the reduction.

P.1 Test 10B - Rolling speed, more viscous lubricant

In Test 10B (Sec. E.13), the less viscous L3 lubricant of Test 5B was replaced by the *more viscous L1 lubricant*. In consequence, the measured rolling forces and forward slips decrease as shown in Fig. P.1.

Similarly, only the lubricant was first replaced in the METALUB model of Test 5B as well as the roughness parameters of the roll due to wear in order to simulate Test 10B (Tab. P.1). Hence, no additional calibration was performed. In the resulting computation with *full-flooded lubrication, the predictions of the rolling force and forward slip are too low at high rolling speeds* (Fig. P.1), which also explains why the computations at about 400 and 500 m/min did not converge.

The previous observation suggests that friction should be greater in the model at higher rolling speeds. This can be explained by three mechanisms. First, *starvation* allows to reproduce relatively precisely the rolling force and forward slip at higher rolling speeds, when the lubricant film thickness at the entry of the bite is reduced with the rolling speed as shown in Fig. P.1. This explanation can, however, be criticized since the lubrication system in this scenario is the flexible lubrication system with pure L1 and no emulsion with only a few percent of oil. Hence,

Entity	Parameter	Value	Unit
Roll bite	Type	Full-flooded lub.	-
	Heating by friction	On	-
	Heating by plastic deformation	On	-
Strip material	Name	S2	-
	E_s	210000	MPa
	ν_s	0.3	-
	Law	Ludwik	-
	Viscoplasticity	Off	-
	Thermoplasticity	On	-
	A	776	MPa
	B	147	MPa
	n	1.52	-
	m	0.65	-
	$\overline{\epsilon}_0^p$	0	-
	ρ_s	$7.850 \cdot 10^{-9}$ [7850]	t/mm^3 [kg/m^3]
	c_s	$500 \cdot 10^6$ [500]	N.mm/(t.°C) [J/(kg.°C)]
	β_s	0.9	-
Strip	t_{in}	0.75	mm
	t_{out}	0.579	mm
	σ_{in}	120.0	MPa
	σ_{out}	184.8	MPa
	$T_{s,\text{in}}$	25	°C
Lubricant	Name	**L1**	-
	Law	WLF (enhanced)	-
	A_1	**102.77**	°C
	A_2	**0.000226**	MPa^{-1}
	b_1	**0.00573**	MPa^{-1}
	b_2	**−0.547**	-
	C_1	**15.95**	-
	C_2	**26.98**	°C
	η_g	**10^6**	MPa.s
	$T_g(0)$	**−73.16**	°C
	T_l	65 (constant)	°C
Interface	Asperity profile	Christensen	-
	$R_{q,r}$	**0.695**	μm
	$R_{q,s}$	0.123	μm
	$\bar{l}$	**67.57**	μm
	Flattening equation	Wilson-Sheu	-
	γ	9	-
	Friction law	Coulomb-Tresca	-
	μ_C	0.11	-
	μ_T	1	-
	Flow factors ϕ_x and ϕ_s	On	-
	Shear stress factors	Off	-
	τ_l	0	MPa
Roll	Deformation method	Meindl (full)	-
	Deformation mode	Plane strain	-
	R_0	195.5	mm
	v_r	3297	mm/s
	E_r	210000	MPa
	ν_r	0.3	-
	x_{12}	−10	mm
	x_{23}	5	mm
	$\Delta\theta_1$	1	°
	$\Delta\theta_2$	$5 \cdot 10^{-3}$	°
	$\Delta\theta_3$	1	°
	Relaxation method	Constant	-
	$w^{(0)}$	0.5	-
Other numerical parameters	Integration method	RK4	-
	x_{12}	−10	mm
	Δx_1	1	mm
	Δx_2	10^{-3}	mm
	tol_Q	10^{-4}	-
	$\text{tol}_{\sigma_{\text{out}}}$	10^{-3}	-
	$\text{tol}_{t_{\text{out}}}$	10^{-4}	-
	tol_R	10^{-6}	-
	$\Delta x_{\text{extr},1}$	1	mm
	$\Delta x_{\text{extr},2}$	10^{-2}	mm
	CIEFS step	Off	-

Table P.1: Model parameters of Test 10B-4 (Chap. 3 and Sec. E.13, with deactivated starvation). Changes with respect to parameters of Test 5B-4 in Tab. 5.4 are written in bold (except for v_r, t_{out}, σ_{in} and σ_{out}).

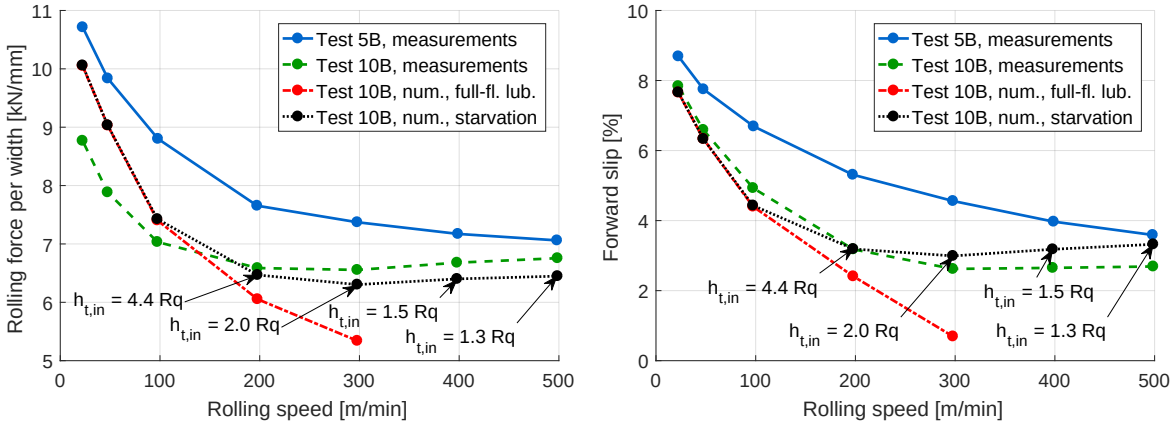

(a) Rolling force per width.

(b) Forward slip.

Figure P.1: Experimental and numerical results of Tests 5B (Chap. 3 and Sec. E.7) and 10B (Chap. 3 and Sec. E.13) to illustrate the influence of a more viscous lubricant than L3. Numerical results of Test 10B are based on Tab. P.1 with v_r, t_{out}, σ_{in} and σ_{out} of Tab. E.39. In the cases with starvation, it is activated for v_r = 197.8 m/min, 297.8 m/min, 397.9 m/min and 498.7 m/min with $h_{t_{\text{in}}} = 4.4R_q$, $2.0R_q$, $1.5R_q$ and $1.3R_q$.

starvation should be unlikely provided that the lubrication system delivers a sufficient quantity of oil to the strip. A second explanation could be the *heating of the lubricant at the entry of the bite by the roll whose temperature rises with the rolling speed* (see T_{out} in Tab. E.39). In fact, Fig. P.2 shows that the experimental measurements can be reproduced as well by starvation as by an increase of the lubricant temperature, which also reduces the film thickness. Thirdly, it is important to mention that the lubricant shear stress was neglected so far since this assumption improved the predictions in Sec. 5.3.1.1 while being reasonable. If the viscosity increases, it becomes, however, more likely that this stress is not negligible anymore, so that *viscous friction* becomes significant at higher rolling speeds. This scenario should be studied in the future with the lubricant temperature computation by a *full thermal model, which includes the rolls*.

Finally, the *new results can be compared to Carretta's results* in Fig. P.2, which were obtained with $\tau_l \neq 0$ by adjusting the lubricant temperature to reproduce the rolling force and by decreasing the yield stress of the strip in Test 5B by 40 MPa in Test 10B. Although Carretta's predictions of the rolling forces are better than the new predictions, especially at low rolling speeds, the *new predictions are better overall considering the forward slip*.

P.2 Tests 14A/14B - Reduction, more viscous lubricant

The influence of elongation was studied by *Tests 14A and 14B*, in which a *more viscous lubricant* (L1) was used than in Tests 8 and 15. Thus, the increase of the rolling force is slower with the elongation than in these latter tests and the forward slip can even decrease as shown in Figs. P.3 and P.4.

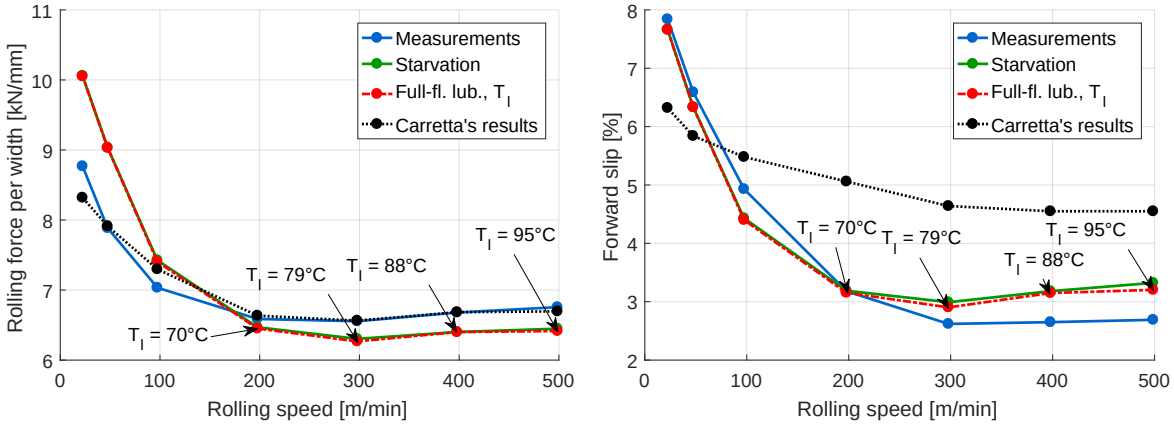

(a) Rolling force per width. **(b)** Forward slip.

Figure P.2: Comparison of our results (Tab. P.1 with v_r, t_{out}, σ_{in} and σ_{out} of Tab. E.39, either with activated starvation or modified lubricant temperature for v_r = 197.8 m/min, 297.8 m/min, 397.9 m/min and 498.7 m/min with $h_{t_{\text{in}}} = 4.4R_q$, $2.0R_q$, $1.5R_q$ and $1.3R_q$ or T_l = 70, 79, 88 and 95°C, respectively) with those obtained by Carretta for Test 10B (Chap. 3 and Sec. E.13). Carretta also adjusted the temperature in his computations.

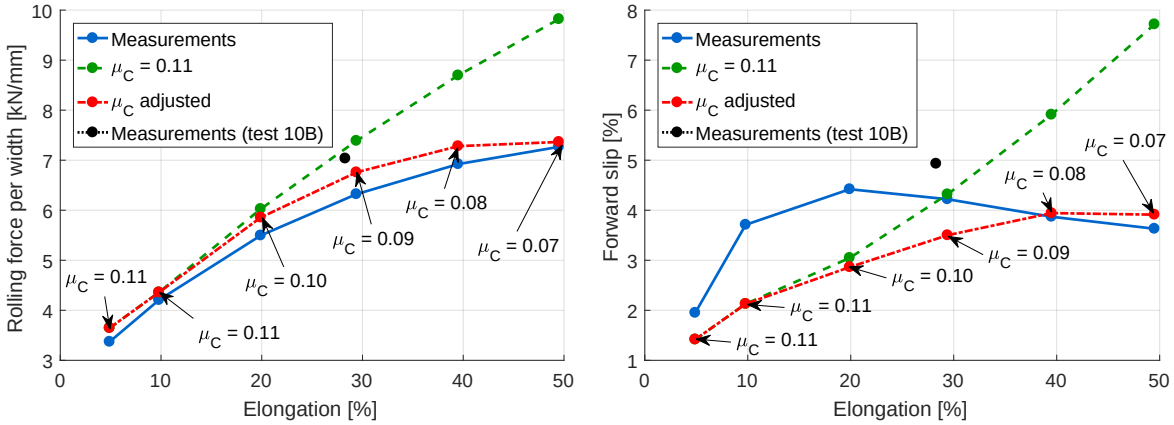

(a) Rolling force per width. **(b)** Forward slip.

Figure P.3: Comparison of experimental and numerical results in Test 14A (Chap. 3 and Sec. E.18). The numerical results are based on Tab. P.1 with v_r, t_{out}, σ_{in} and σ_{out} of Tab. E.54, except for $R_{q,r}$ = 0.657 μm, $R_{q,s}$ = 0.096 μm and $\bar{l}$ = 72.46 μm.

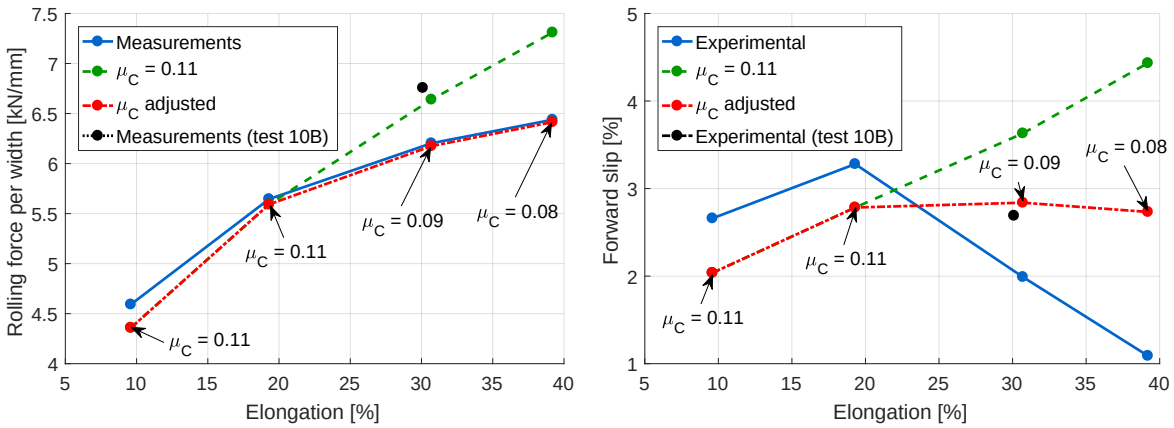

(a) Rolling force per width. **(b)** Forward slip.

Figure P.4: Comparison of experimental and numerical results in Test 14B (Chap. 3 and Sec. E.19). The numerical results are based on Tab. P.1 with v_r, t_{out}, σ_{in} and σ_{out} of Tab. E.57, except for $R_{q,r} = 0.657$ μm, $R_{q,s} = 0.096$ μm, $\bar{l} = 72.46$ μm and activated starvation with $h_{t,\text{in}} = 1.1R_q$.

The predictions with a constant boundary coefficient of friction were obtained essentially *without any additional calibration* on the basis of the results in Sec. P.1 (Test 10B). This is particularly interesting in Test 14B since the starvation regime was kept activated, with $h_{t,\text{in}} = 1.3R_q$ instead of $h_{t,\text{in}} = 1.1R_q$ though, due to a slightly better fitting. The METALUB model overpredicts the rolling force and forward slip, when the boundary coefficient of friction is constant. Therefore, a reduction of this coefficient with increasing elongation allows to obtain better predictions, which suggests that a model of micro-plasto-hydrodynamic/static lubrication has to be included in METALUB. The required reduction of the boundary coefficient of friction is more significant in Tests 14A and 14B with the more viscous lubricant than in Tests 8 and 15. This suggests that the *viscosity promotes the permeation* of the lubricant in the solid contact region via micro-plasto-hydro*dynamic* lubrication.

Appendix Q

Details of the coupling procedure by Carretta

In this appendix, the *computation of the lubricant pressure* $p_l(t)$ and the *pressure on the asperity tops* $p_a(t)$ in the coupling procedure of METALUB and METAFOR by Carretta is explained. This computation is required in the finite element micro-model of asperity flattening as mentioned in Sec. 6.1.1. The following explanation is based on [205, commit 3071].

The *lubricant pressure* $p_l(t)$, which is applied to the strip portion, is determined by calculating the average lubricant pressure along the top edge of the lubricant portion outside the lubricant pipes and by rescaling this pressure due to the different out-of-plane lengths of the strip portion $l_{x,s}$ and the lubricant portion $l_{x,l}$ (Fig. Q.1). More precisely, the top edge of the lubricant portion is meshed in such a way that its nodes have corresponding nodes on the top edge of the strip portion along the direction $\mathbf{e}_z$ as illustrated in Fig. Q.1. Hence, the length of the top edge of the lubricant l_{nc} outside the lubricant pipes, i.e. whose corresponding nodes on the strip are not in contact (nc) with the roll, is computed as follows (in the non-discretized form):

$$l_{nc} = \int_0^{l_{y,s}} c(y^*) \sqrt{1 + \left(\left. \frac{\partial z_l}{\partial y} \right|_{y=y^*} \right)^2} \, \mathrm{d}y^* \tag{Q.1}$$

where $l_{y,s}$ is the width of the strip portion along $\mathbf{e}_y$, $c(y)$ the contact status, which is equal to 0 in a lubricant pipe, i.e. if the corresponding node of the strip is in contact with the roll (contact tool), and $z_l(y)$ is the profile of the top lubricant edge. The arc length is computed according to Adams and Essex [2, p. 404] in the previous equation.

The average lubricant pressure $\overline{p}_l(t)$ outside the lubricant pipes and positive in compression is then given by the following equation (in the non-discretized form):

$$\overline{p}_l(t) = \frac{1}{l_{nc}} \int_0^{l_{y,s}} -p(y^*) \, c(y^*) \sqrt{1 + \left(\left. \frac{\partial z_l}{\partial y} \right|_{y=y^*} \right)^2} \, \mathrm{d}y^* \tag{Q.2}$$

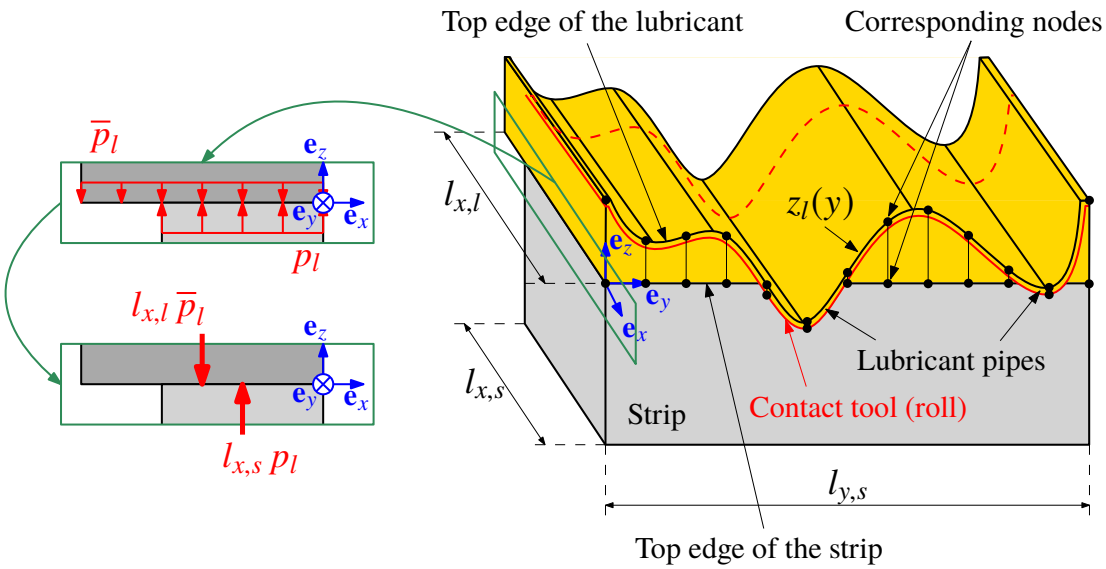

Figure Q.1: 3D representation of the generalized plane-strain FE asperity flattening micro-model of Carretta's coupling procedure with lubricant (on the right). The sections on the left show the vertical force equilibrium between the lubricant and the strip portions.

where $p(y)$ is the pressure (negative in compression in METAFOR) along the top edge of the lubricant portion. The pressure in the lubricant pipes is not considered since they are numerical artifices, where solid/solid contact would prevail in reality.

Due to the different elongations of the strip and lubricant portions (via the Jacobian matrix, see Sec. 6.2.2.2) and the volume integration in the FE method (Eq. 6.17), it is necessary to convert the previous average lubricant pressure $\overline{p}_l(t)$ to compute the lubricant pressure $p_l(t)$ that is actually applied to the strip portion on average. As illustrated in Fig. Q.1, the following equilibrium equation provides this pressure:

$$l_{x,l}(t)\,\overline{p}_l(t) = l_{x,s}(t)\,p_l(t) \qquad \Rightarrow \qquad p_l(t) = \frac{l_{x,l}(t)\,\overline{p}_l(t)}{l_{x,s}(t)} \tag{Q.3}$$

Besides possible extrapolation errors from the Gauss points to the nodes, it is unclear why the stress $-\sigma_{zz}$ was not simply averaged at the interface between the lubricant and strip portions along $\mathbf{e}_y$, where no contact between the roll and the strip exists, to compute the lubricant pressure instead of applying the previous method. This alternative method was, however, not further investigated due to more severe shortcomings of Carretta's coupling procedure (see Sec. 6.1.3).

Finally, the *pressure on the asperity tops* $p_a(t)$ is calculated by the load sharing equation (Eq. 4.4), i.e.

$$p_a(t) = \frac{p_i(t) - [1 - A(t)]p_l(t)}{A(t)} \tag{Q.4}$$

where the interface pressure $p_i(t)$ is the result of the preceding METALUB computation, while the relative contact area $A(t)$ and the lubricant pressure $p_l(t)$ are computed by the current asperity

flattening simulation in METAFOR.

Appendix R

Radial return algorithm in explicit integration scheme

In this appendix, the *radial return algorithm in the explicit integration scheme* of the USER-SMD SPH package of LAMMPS is derived. This algorithm is required to integrate the Cauchy stresses in the corotational system of coordinates in Sec. 7.1.3.2. The following explanations resemble those in Sec. 6.2.2.1 but they are slightly different since the integration is explicit in this section instead of being implicit in Sec. 6.2.2.1. Thus, the strain increment in the elastic prediction is computed by explicitly integrating the strain rate rather than by predicting the strain increment by enforcing the yield criterion and the equilibrium of forces via the Newton-Raphson algorithm.

In the corotational coordinate system and from the time step t_n to the time step $t_{n+1} = t_n + \Delta t$, the stress state $\boldsymbol{\sigma}_{n+1} = -p_{n+1}\mathbf{I} + \mathbf{s}_{n+1}$ can be elastically predicted via the rate version of Hooke's law (Eq. H.40)[1], i.e. $\dot{\boldsymbol{\sigma}} = \mathbb{H} : \mathbf{D}$:

$$p^e = p_n - K\Delta t \operatorname{tr}\mathbf{D} \tag{R.1}$$

$$\mathbf{s}^e = \mathbf{s}_n + 2G\Delta t \operatorname{dev}\mathbf{D} \tag{R.2}$$

The previous prediction of the pressure is valid, whether the material flows plastically or not due to the pressure-independence of Von Mises plasticity, i.e. $p_{n+1} = p^e$. The elastic prediction of the Cauchy stress deviator $\mathbf{s}^e$ has, however, to be corrected if the resulting Von Mises stress (Eq. H.53)

$$\sigma^e_{\mathrm{VM}} = \sqrt{\frac{3}{2}\mathbf{s}^e : \mathbf{s}^e} \tag{R.3}$$

is greater than the current yield stress $\sigma_{Y,n}$ due to the plastic flow. Otherwise, $\mathbf{s}_{n+1} = \mathbf{s}^e$.

The correction of the Cauchy stress deviator results from the previous rate version of Hooke's law and the additive decomposition of the strain rate (Eq. H.52), which can be simplified by the

[1]The variables $\boldsymbol{\sigma}$, $\mathbf{s}$ and $\mathbf{D}$ are assumed to denote the expressions of the Cauchy stress tensor, the deviatoric Cauchy stress tensor and the strain rate tensor *in the corotational coordinate system*, respectively.

hypotheses of normal plastic flow (Eq. H.62) and the Von Mises associated plasticity (Eq. H.85):

$$\dot{\boldsymbol{\sigma}}_{\text{corr}} = -\mathbb{H} : \mathbf{D}^p = -\lambda \mathbb{H} : \mathbf{N} = -2G\lambda \mathbf{N} \tag{R.4}$$

If the normal $\mathbf{N}$ is assumed to be constant over the time step, the previous equation can be integrated as follows:

$$\mathbf{s}_{\text{corr}} = -2G\mathbf{N} \int_{t_n}^{t_{n+1}} \lambda(t)\, \mathrm{d}t = -2G\Gamma\mathbf{N} \tag{R.5}$$

where Γ is an unknown scalar value. Furthermore, the effective plastic strain increment can be computed by integrating Eq. (H.64), and the yield stress by integrating the following equation for isotropic hardening, again by assuming that $\mathbf{N}$ is constant from t_n to t_{n+1}:

$$\dot{\sigma}_Y = \frac{\mathrm{d}\sigma_Y}{\mathrm{d}\overline{\epsilon}^p} \overline{D}^p = h_i \sqrt{\frac{2}{3}} \lambda \tag{R.6}$$

where h_i is the isotropic hardening coefficient. Hence, to correct the Cauchy stress deviator, the value of Γ has to be determined in the following equations

$$\mathbf{s}_{n+1} = \mathbf{s}^e - 2G\Gamma\mathbf{N} \tag{R.7}$$

$$\overline{\epsilon}^p_{n+1} = \overline{\epsilon}^p_n + \sqrt{\frac{2}{3}}\Gamma \tag{R.8}$$

$$\sigma_{Y,n+1} = \sigma_{Y,n} + \sqrt{\frac{2}{3}}\Gamma h_i \tag{R.9}$$

such that the yield criterion is satisfied, i.e.

$$\sqrt{\frac{3}{2}\mathbf{s}_{n+1} : \mathbf{s}_{n+1}} = \sigma_{Y,n+1} \tag{R.10}$$

where the normal to the yield surface is evaluated by the elastic trial stress (radial return), i.e. $\mathbf{N} = \mathbf{s}^e / \sqrt{\mathbf{s}^e : \mathbf{s}^e}$ (Eq. H.85).

To simplify the notations, Γ is replaced by the effective plastic strain increment:

$$\Delta\overline{\epsilon}^p = \overline{\epsilon}^p_{n+1} - \overline{\epsilon}^p_n = \sqrt{\frac{2}{3}}\Gamma \tag{R.11}$$

Substituting Γ by the previous equation, and $\mathbf{N} = \sqrt{3/2}\ \mathbf{s}^e / \sigma^e_{\text{VM}}$ (via Eq. R.3) in Eq. (R.7), we obtain:

$$\mathbf{s}_{n+1} = \left(1 - \frac{3G\Delta\overline{\epsilon}^p}{\sigma^e_{\text{VM}}}\right)\mathbf{s}^e \tag{R.12}$$

This value as well as the yield stress $\sigma_{Y,n+1} = \sigma_{Y,n} + h_i\Delta\overline{\epsilon}^p$ (Eqs. R.9 and R.11) can be substituted in the yield criterion (Eq. R.10), which is solved for the effective plastic strain increment:

$$\Delta\overline{\epsilon}^p = \frac{\sigma^e_{\text{VM}} - \sigma_{Y,n}}{3G + h_i} \tag{R.13}$$

This expression can be inserted in the previous equation of the corrected Cauchy stress deviator (Eq. R.12):

$$\mathbf{s}_{n+1} = \frac{3G\sigma_{Y,n} + h_i\sigma^e_{\text{VM}}}{\sigma^e_{\text{VM}}(3G + h_i)}\mathbf{s}^e \tag{R.14}$$

Finally, since the isotropic hardening coefficient h_i is generally much smaller than the shear modulus G, the following simplified versions of Eqs. (R.13) and (R.14) are used to correct the Cauchy stress deviator in order to integrate the stresses with plasticity:

$$\Delta\bar{\epsilon}^p = \frac{\sigma^e_{\text{VM}} - \sigma_{Y,n}}{3G} \tag{R.15}$$

$$\mathbf{s}_{n+1} = \frac{\sigma_{Y,n}}{\sigma^e_{\text{VM}}}\mathbf{s}^e \tag{R.16}$$